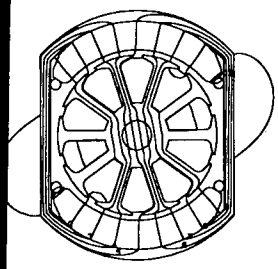

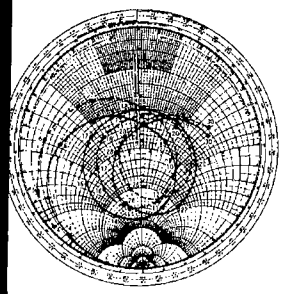

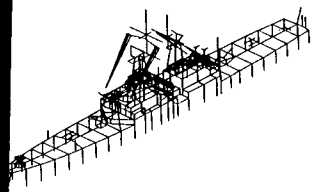

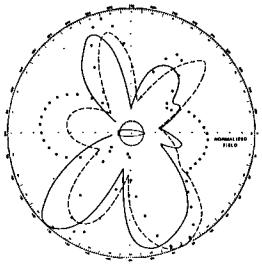

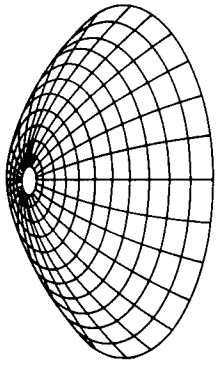

13th Annual Review of Progress in

APPLIED
COMPUTATIONAL
ELECTROMAGNETICS

at the

Naval Postgraduate School

Monterey, CA

March 17-21, 1997

CONFERENCE PROCEEDINGS

CONFERENCE PROCEEDINGS

VOLUME II

13th Annual Review of Progress in APPLIED COMPUTATIONAL ELECTROMAGNETICS

at the

Naval Postgraduate School

Monterey, CA

March 17-21, 1997

TECHNICAL PROGRAM CHAIRMAN

Eric C. Michielssen

Sponsored by

The Applied Computational Electromagnetics Society

Naval Postgraduate School, DOE/LLNL, University of Illinois, University of Kentucky,

USAF, DOD AND DOE IN COOPERATION WITH IEEE, URSI, ASEE, SIAM AND AMTA

THE NAVAL POSTGRADUATE SCHOOL

Contents

SESSION 2: continued

SESSION 7: continued

SESSION 8: FDTD AND FVTD I
Chair: Melinda Picket-May

SESSION 9A: FDTD AND FVTD II

SESSION 9B: INTEGRATED CIRCUITS AND PHOTONICS

SESSION 11: continued

VOLUME II

SESSION 24: continued

SESSION 25: PLANAR AND CONFORMAL ANTENNAS AND CIRCUITS
Chair: Giuseppe Vecchi

SESSION 13:

COMPOSITE MATERIALS

Chairs: K. Whites and R.E. Diaz

APPLICATION OF THE ANALYTIC THEORY OF MATERIALS TO THE MODELING OF COMPOSITES IN ELECTROMAGNETIC ENGINEERING

Rodolfo E. Díaz
Northrop Grumman Corporation
Military Aircraft Systems Division
2500 W. Frye Rd., Chandler, AZ 85224
(602) 786-8800, FAX(602)786-9796

Abstract -All materials are, by nature, frequency dependent. Although this variation of the permittivity (or permeability) as a function of frequency is generally viewed as a nuisance, it clearly provides the engineer with an additional degree of freedom in the design of electromagnetic devices. Just as man-made composite materials allow the design of aerospace structures with tailored mechanical properties, electromagnetic composite materials should enable the design of structures with a tailored, optimized, electromagnetic response. To do this, the designer must have access to an accurate, compact, and ultrabroadband model of the constitutive properties of existing materials, even in the presence of measurement error. In addition, a framework of guidelines for the evaluation of the physical realizability of new materials is needed to guide in their synthesis. The analytic theory of materials fulfills these requirements.

Just like the Kramers-Krönig relations, this theory is based on the well known analyticity of the permittivity function that results from the requirements of causality. However, since the Kramers-Krönig relations require the user to know at least half of the answer to begin with, their utility is limited. The analytic theory, based on an expansion of the constitutive properties into a natural set of complex functions, does not suffer from this limitation. By virtue of the analytic continuation properties of these functions, data measured on the same material over separate bands of frequencies, can be combined into a unified, self-consistent, ultrabroadband representation of the material.

In this work, the application of the theory is demonstrated through a set of examples. The examples illustrate the realities of electromagnetic measurements, whereby tests results from different devices on different configurations of the same material do not necessarily yield data that is self-consistent. In that case, the analytic model actually serves to eliminate test error because it forces data measured over different frequency bands to fit the same set of analytic functions. The examples also illustrate the pit-falls and limitations of extrapolations, the danger of taking published "typical" data on materials at face value, and the best approach to take when analyzing a very limited or corrupt set of data. Finally, the application of the theory to the synthesis problem is illustrated by calculating the expected properties of an iron-loaded composite, compatible with published commercial data.

I - Introduction

The natural frequency dependence of the constitutive properties of materials is known to be an analytic necessity of causality, independent of any particular physical models used to describe the material. Thus it would be expected that the rich field of analytic function theory would lend a tremendous boost to the theory and development of electromagnetic materials. Yet, in practice, very little use is made of this analytic foundation. One of the reasons, is that the Kramers-Krönig relations, the principal result of the analytic work, are really only useful in elucidating the properties of materials when half of the answer is already known: Either the real part leads to knowledge of the imaginary part or vice-versa. Therefore, when new materials need to be modeled, for which neither part is fully known, practitioners rely almost exclusively on variations or combinations of the two fully understood classic physical models: the Debye Relaxation and the Lorentz Resonance. When the data deviates from these models, they are declared incomplete and other unknown phenomena are postulated. This state of affairs weakens our understanding of the fundamental processes of materials. Furthermore, given the analyticity of the permittivity function, it is fundamentally unjustified. It has been shown [1] that a set of analytic functions exists that is free of these limitations, is able to model other physical phenomena beyond the two classical models, and is useful for both synthesis and analysis of arbitrary materials. The completeness associated with the analyticity of this set implies that when data cannot be fit with these functions, we must acknowledge the presence of error in the data.

That error exists in the experimental data of materials is of course no surprise to experimentalists. However, what the degree of error is and which portions of the data are to be believed is, historically, an unaddressed question. It is proposed here that the best approach we can take to resolving this question, and obtaining valid models of materials, is to

exploit the compactness and ease of derivation of this set of analytic functions. By using the broadest band of data possible on the materials, and properly weighting those ranges of frequencies, or constitutive parameters, that the experimentalist knows are probably the most correct, an analytic function fit results that is the best, physically realizable representation of that material. Any significant deviation from this fit, particularly one that violates the Hilbert Transform complementarity between the real and imaginary parts of the data, must be recognized to be impossible. Such a deviation would violate causality, and, experimental data notwithstanding, time can only march forwards.

In this paper we will apply this approach to the analysis of a variety of measured data on materials. The resulting models have an ultra broad bandwidth of validity, are compact and are physically realizable. They are ideally suited for the modeling of microwave structures incorporating realistic dispersive materials such as man-made absorbing composites.

II - Derivation of the analytic functions

Assume that the experimentally observed phenomenon of dielectric polarization is a macroscopic manifestation of a microscopic dynamics. In other words, assume that there is some physical mechanism but do not specify its form. Then, the following three physical requirements follow: First, because by polarization we mean the separation of charges in response to an applied field, it follows that exchange and transport of energy between the field and the material is occurring. Any such exchange can at most occur at the speed of light and therefore it must be causal. Second, because the phenomenon involves the reaction of microscopic "systems" to an applied force, it must be expressible in the form of an equation of motion. Third, because the dielectric is ultimately not a continuum but a granular ensemble of individual "particles", any model derived under the assumption of a continuum must break down at high enough frequencies. (Fortunately, for most materials, this latter limit of validity occurs beyond the ultraviolet.)

Given these requirements plus the assumption of invariance under translation in time and the assumption of linearity (to allow the use of superposition), the connection between the dielectric displacement vector (as an output) and the applied electric field (as the causing input) leads to a formulation of the permittivity as an analytic function in the complex frequency plane [2]. (To remain consistent with the notation of these references we assume an implicit time dependence for harmonic waves of the form $e^{-i\omega t}$.) This formulation shows that *in the upper half-plane* the permittivity is: An analytic, one-valued, regular, zero-less function. Its imaginary part only vanishes on the imaginary frequency axis. And its only singularity is a simple pole at the origin. This knowledge leads to the Kramers-Krönig relations. But as noted above, these relations are only useful if you know half of the answer. To find a compact more generally useful representation we follow a suggestion by Landau and Lifshitz and analytically continue the permittivity function into the lower half-plane. There it can be shown that the permittivity only has simple poles and zeros, thus being a rational function. In particular it can be expressed as the partial fraction expansion:

$$\varepsilon(\omega) - 1 = \sum_{n=1}^{N} \frac{An}{\{(\omega-\pi_n)(\omega-\pi_n^*)\}} \qquad (1)$$

When one of the poles π_n is close to the real axis (say $\pi_n = \omega_o+\delta$, $\delta<<1$), the imaginary part of this function attains a very high peak value in the neighborhood of ω_o, given by $1/(2\delta\omega_0)$. This behavior is reminiscent of the behavior of the classic Lorentzian function $\Delta\nu/((\nu-\nu_0)^2+(\Delta\nu)^2)$ at $\nu=\nu_0$. Therefore we will call each of the terms $A_n/\{(\omega-\pi_n)(\omega+\pi_n^*)\}$ a Complex Lorentzian. And so equation 1 tells us that the complex permittivity of any physically realizable material must be expressible as a sum of Complex Lorentzians.

The significance of these functions is grasped immediately upon further examination of one term. Let the pole be given by $\pi_1 = a + ib$, and let $a= (1/LC - R^2/4L^2)^{1/2}$ and $b=-R/2L$. Then each term in (1) reduces to the form:

$$C_1 = A'_1/\{1-i\omega RC-\omega^2 LC\} \qquad (2)$$

which is the effective complex capacitance (defined as $C=Y/(-i\omega)$) of a series LRC circuit; with the poles located at

$$\pi_1 = -iR/2L \pm (1/LC-R^2/4L^2)^{1/2} \qquad (3)$$

This representation is very convenient for lossy, conducting and semiconducting materials. In particular, for most composites made of inert matrices filled with lossy particles, whose characteristic size is much smaller than the wavelength, the "inductive" term L in these functions can be ignored. The resulting function is then just a sum of parallel RC branches, which is the same as a sum of multiple Debye Relaxation terms. Despite the simplicity of such a representation, it remains fully analytic and as such it is the physically realizable model applicable to those materials.

The simplest way to describe the collective behavior of multiple Debye Relaxations is in the Cole-Cole plot (introduced by R. H. Cole and K. S. Cole in the Journal Of Chemistry and Physics in 1941) and its extension by Grant [3]. In these plots the real part of the permittivity (conductivity) is plotted against the imaginary part. The resulting curve is a smooth blending of semicircular arcs, each representing one relaxation. In the Cole-Cole plot, an arc's diameter is a measure of the capacitance of that relaxation, whereas the diameter of the same arc in the Grant plane is a measure of its conductance. Therefore by working back and forth between the two planes, we can successively extract the circuit parameters of a set of measured data.

The first step in this approach is to recognize that in the Cole-Cole plot, the zero frequency point occurs at the rightmost extreme of the data and that frequency increases as we walk counter-clockwise along the curve. In the Grant plane the zero frequency point is at the leftmost end of the curve and frequency increases by moving along the curve clockwise. The high frequency limit of the data appears at the leftmost point in the Cole-Cole plot and at the rightmost point in the Grant plane. (See Figures 1a and 1b). These two limits, zero frequency and high frequency, are specially important because the parallel sum of RC circuits simplifies at both of them. At zero frequency, the only conductance is the DC conductivity term. Therefore the intersection of the curve in the Grant plane with the real conductivity axis, near the origin, reveals the presence of DC conductivity in the material. Once this term is isolated, it can be subtracted out from the data, thus removing the DC pole in the permittivity. The removal of this term removes the infinite tail in Figure 1a and clarifies the trend towards the real axis of the curve in the Cole Cole plot, at zero frequency . This intersection is a measure of the sum total capacitance of all RC circuits. Similarly, in the high frequency limit, the only capacitance that can be seen is the background material's capacitance (free space or a resin matrix). Once this term is identified and subtracted from the data, the infinite tail in Figure 1b disappears and the high frequency intersection of the curve in the Grant plane with the real axis can be obtained. This intersection is the sum of all the conductances. Thus, an initial analysis of the four end points of the two curves in Figure 1 allows us to determine the sum total of all capacitors, the sum total of all conductors, the DC conductivity and the high frequency limit permittivity of the material. After this is done, the curves in each plane look like blended arcs, with no tails, and their component semicircles can be obtained by a variety of suitable optimization procedures. Let us illustrate the application of this procedure with measured data.

III - Application to analysis of measured data.

The most broadband test set-up for dielectrometry, besides a coax transmission line, is the free space admittance tunnel with a vector network analyzer. With material samples greater than two wavelengths across, it is the preferred measurement method because it does not require careful machining of the sample or full contact to a metallic fixture. Since the sampled material is large it is also more representative of the real application of these materials, where the inhomogeneities in the whole are averaged during the measurement. Many small samples of the same material would need to be measured in a coax to guarantee a statistical validity comparable to that of the free space measured data. Furthermore, in the presence of anisotropy with well defined principal axes, the coax method becomes invalid. The free space method, though, is not free of problems. At low frequencies (below 500 MHz) the size of the sample starts to become unwieldy. Any deviations of the wave from a true plane wave at its incidence on the sample invalidates the assumptions used to derive the constitutive parameters from the measured transmission Amplitude and Phase data. Finally, the data at the band edges is usually corrupted by the set-up in two ways: The use of an iris to minimize cross talk causes choking at low frequency and collimated diffraction at the high end, while the use of time domain gating causes distortions near the window edges. Whatever the test method used, the practitioner must be aware of its limitations and of the typical error that can be expected. Fortunately, since different test methods incur different errors, the measurement of the same material over many bands and in different set-ups can actually be used to reduce the errors, because all the measurements must fit the same analytic function. The low frequency data and the high frequency data measured on the same material are not independent of each other, they are analytic continuations of each other.

Whenever we are dealing with man made composite materials we know the constitutive properties of the matrix inside which the lossy fillers are dispersed. If this matrix is lossless, it is recommended that this value be divided out of the measured data. The resulting data set is therefore always located near the origin in the Cole Cole plot and normalized to free space. Figure 2 shows one such measured Cole Cole plot for a lossy composite. The free space data was measured in two different set-ups, one over the range from 1.5 GHz to 20 GHz, the other, over the range from 400 MHz to 2.5 GHz. The fact that the set-ups overlap between 1.5 GHz and 2.5 GHz serves to illustrate the typical discrepancy that can be expected in such measurements. The two set-ups agree on the value of the imaginary part (y-axis value) over this range, but there is a clear difference in the value of the real part. Another typical discrepancy is shown when the same material is measured at two different thicknesses. The 2 inch thick material provides a greater phase shift to the wave at low frequen-

cies and so yields a better measurement of the real part of the permittivity in that range than the 1 inch sample. Given all this data, the best guess of experimental reality for this material is the curve of Figure 3.

By examining the low and high frequency extremes of this data, we can identify the sum total low frequency conductivity and the high frequency limit permittivity. Subtracting these, changes the Cole Cole plot and the Grant plane as shown in Figures 4a and 4b. The resulting blended arcs can be fit with two Debye Relaxation terms, and as Figure 5 shows, the full range of data from 400 MHz to 20 GHz is accurately modeled. Figure 5 also illustrates the next dilemma we encounter. If we need to know the value of this material's permittivity below 400 MHz, can we extrapolate from the measured data? The answer is, no. Two equally valid analytic fits to the data are shown in Figure 5, differing by a reasonable + or - 6.5% error at the lowest measured frequency. Depending on which fit is true, the real permittivity at 100 MHz may be 5.5 or it may be 10.8, the imaginary part may be 11.7 or it may be 7.4. An error of nearly 100% can easily result from a naive attempt at extrapolating. Clearly, lower frequency data is needed. However, because of the analytic continuation properties of the functions involved we do not need to measure near 100 MHz (where the sample size is prohibitive for free space methods and where capacitor methods have to deal with radiation corrections). Just measuring below 100 MHz suffices. In fact, we choose to measure well below 100 MHz, from 10 KHz to 1 MHz, using a simple parallel plate capacitor with an impedance meter. That measurement shows that the real part at low frequencies tends to 25.5 and also gives an upper bound to the value of the true DC conductivity. These two facts narrow down the options of Figure 5 to the results shown in Figure 6.

The data in this model in the unmeasured range from 1 MHz to 400 MHz is a rigorous analytic continuation of the data in the measured range (above 400 MHz and below 1 MHz). Because the analytic functions are "clamped" at both the low and high ends, any significant deviation of the data between 1 MHz and 400 MHz from the results of this fit would cause the data in the measured bands to be in error by more than 10%. If we know that the error in the measured data cannot be greater than 10% then any deviation from this model would constitute a violation of causality and therefore would be physically unrealizable.

Now let us consider data measured without the benefit of modern equipment. For instance, Emerson and Cumings sells a variety of lossy materials with data that, in some cases, is over two decades old. Can we estimate the validity of this data before using the materials? Whenever a lossy material is being fit, and there is a discrepancy in the agreement with the model between the real and the imaginary parts, we prefer to give the benefit of the doubt to the imaginary part because loss of energy is a real physical phenomenon, more detectable and usually less subject to falsification by artifacts than the phase shifts or wavelengths used to determine the real part. Following this philosophy, Figure 7 shows that in some cases the data is quite good. In the Figure we show the reported permittivity of a very lossy material, MF-124, from 100 Hz to 18 GHz. A fit with 8 Debye terms accurately matches the imaginary part of the data and deviates from the real part significantly only below 10 KHz. However, Figure 8 shows that the same is not true of the data for LS 20. If as in Figure 9 we match the imaginary part well, we obtain a severe disagreement in the real part starting just below 1 GHz. Knowing that LS20 is a foam material, its conductivity at high frequency is to be trusted more than at low frequency, because any artifacts due to imperfect contact with the test set-up are minimized at the high end. Conversely, the low frequency permittivity, if derived by capacitor methods, should not be in error by a factor of two. Therefore, based on these considerations, and knowing nothing else about the test set-ups and the data, Figure 10 is the best guess of the true behavior of LS20 over the entire band. The inability to generate a satisfactory physically realizable model of this material means that this "old" data needs to be verified experimentally at a few points before any device dependent on its constitutive properties is designed.

The above examples demonstrate the typical problems that are encountered in the measurement of the constitutive properties of lossy composite materials. Fitting the data to the analytic functions advocated here is the simplest method of assessing the validity of the data. It also enables us to estimate the reasonable range of variation that can be expected about the modeled values, given the known fidelity of the test set-ups. The presence of Lorentz-like resonances in the data does not present a particular problem to this approach. As discussed in [1], even Lorentz terms, which we think of as narrow band, have sufficient analytic effects outside their band to be detectable in a good set of broad band measurements. The above examples thus constitute a demonstration of the usefulness in analysis of this analytic model of materials. We conclude by giving an example of the application of the model to a synthesis problem.

IV- A synthesis problem.

Given the constitutive properties of the filler particles and the matrix in which they are to be suspended, can we estimate the properties of the composite that will result? The answer is, yes, provided we have one more piece of information. We need to know how the particles disperse and agglomerate during the manufacturing process. The modeling of such

phenomena belongs to the realm of Percolation Theory. Percolation Theory recognizes the stochastic nature of the mixing mechanism and describes the resulting material in terms of a distribution of clusters. Since the size and mutual proximity of these clusters determines the capacitance they contribute to the analytic function, and since their morphology determines their conductance, the distribution of clusters corresponds to a distribution of Debye Relaxations.

It has been shown [4] that the permeability of materials can be represented by the same analytic functions used for the permittivity, with a corresponding set of analytic circuits. Therefore, we should be able to model a composite of magnetic metal particles dispersed in a nonmagnetic matrix, as a collection of Debye Relaxation capacitors filled with the complex permeability of the filler particles. First, a model for the complex permeability of the particles must be obtained. For Iron, we refer to the original work of Kittel, where he postulated that the complex permeability of magnetic metals should be controlled by skin-depth-limited forces on the domain boundaries. Figure 11 shows the data points from Kittel's theory and the best analytic fit to it. It should be noted that Kittel's model calls for the real part of the permeability to rise Lorentz-like before the peak of the imaginary part occurs. However, after the peak, the real part does not drop sharply as would be required by a Lorentz behavior. In fact, the drop in real part and the gentle tails of the peak in imaginary part are best fit by a single Debye term, which cannot show a rise in real part at all. Kittel's model cannot be fit exactly with the present set of analytic functions. This is not alarming since none of the measurements Kittel used to derive his theory showed the rise in real part either, and he acknowledged that his formulation was only approximate.

This model of the particles represents the highest frequency position for the loss peak that can be obtained from Iron, since Kittel assumed single domain films. Thicker films or particles will exhibit the skin-depth shielding at lower frequencies and so a distribution of particle sizes would result in a distribution of Debye Relaxation behaviors in the filler itself. However, the distribution of Relaxations that results from the random clustering of the particles in the mixture is probably the dominant behavior in the composite. So, we assume a single Debye term representation for the filler and three Debye Relaxation terms in the composite's equivalent cluster capacitors to represent a typical 80% volume concentration of Iron particles in the composite. The result is shown by the curves of Figure 12. Overlaid on the same plot are data points from Emerson and Cuming's datasheet for MF-124. The agreement is of the same order as the typical agreement obtained for dielectric data.

V- Conclusion

The modeling of materials using a set of analytic functions that intrinsically satisfies the requirements of causality, linearity, and completeness, results in a compact, ultrabroadband, physically realizable model of real materials. This analytic theory of materials has been applied to the analysis and synthesis of man made lossy composites. In the case of analysis, the theory helps identify experimental error in measured data and, with the use of measurements at low and high frequency bands, generates a valid model for the material in question. This model actually reduces the errors in the measurements by enforcing the analytic continuation character of the measured data. In the case of synthesis, it has been shown that the model can correctly represent the properties of disperse mixtures of magnetic particles. The success is based on recognizing that the composite's properties are a combination of the filler's intrinsic dispersion and the dispersion induced by the random clustering induced by the manufacturing process.

References

[1] R. E. Diaz, The Analytic Continuation Method for the Analysis and Design of Dispersive Materials, UCLA Ph.D. Dissertation, 1992.

[2] J. S. Toll, "Causality and the Dispersion Relation: Logical Foundations", *Physical Review*, vol. 104, 1956, pp. 1760-1770. , L. D. Landau and E. M. Lifshitz, Electrodynamics of Continuous Media, Pergamon Press, New York, 1960, pp. 249-268. L. D. Landau and E. M. Lifshitz, Statistical Physics, Pergamon Press, New York, 1977, section 125, pp. 387-389.

[3] Grant, F.A., "Use of Complex Conductivity in the Representation of Dielectric Phenomena", *J. Appl. Phys.*, vol. 29, 1958, pp.76-80.

[4] W. M. Merrill, Percolation Theory in the Design and Analysis of Artificial Dielectrics, UCLA M.S.Thesis, 1996.

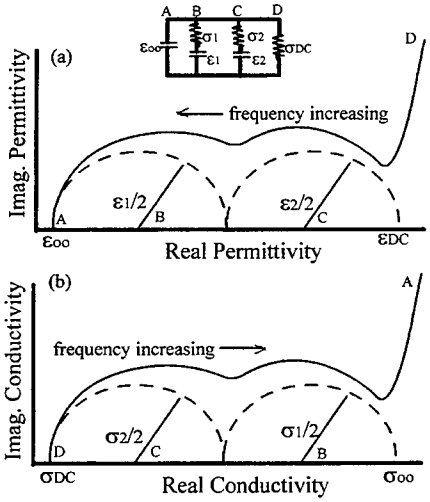

Figure 1. Sketch of the Cole Cole plot (a) and the Grant Plane (b) of a typical lossy material defined by four analytic circuit branches. Each circuit branch describes a semicircle centered on the real axis or an infinite tail.

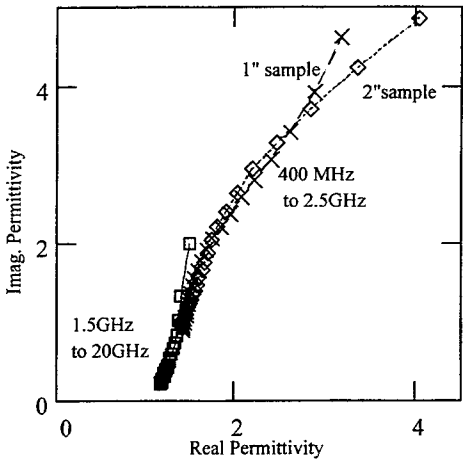

Figure 2. Cole Cole plot of the normalized data of a lossy composite material. The data has been measured over two different bands with different free space test set-ups and on two thicknesses of the material. The disagreement between the curves is typical.

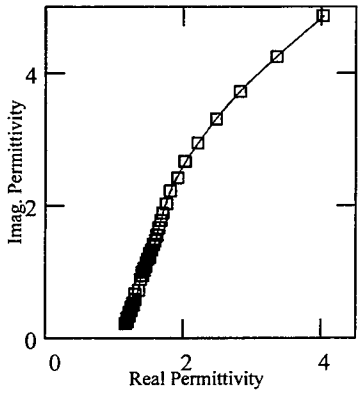

Figure 3. Best guess of reality for the material of Figure 2. The low frequency data has been taken from the 2-inch thick sample. The high frequency data has been taken from the high frequency set-up. The data between 1.5 GHz and 2.5 GHz has been taken as the average of the two set-ups.

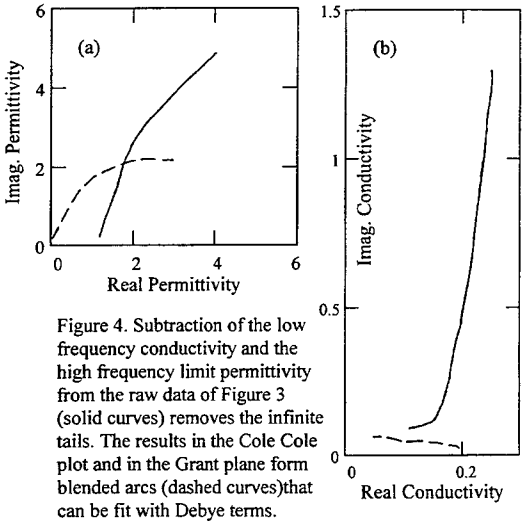

Figure 4. Subtraction of the low frequency conductivity and the high frequency limit permittivity from the raw data of Figure 3 (solid curves) removes the infinite tails. The results in the Cole Cole plot and in the Grant plane form blended arcs (dashed curves)that can be fit with Debye terms.

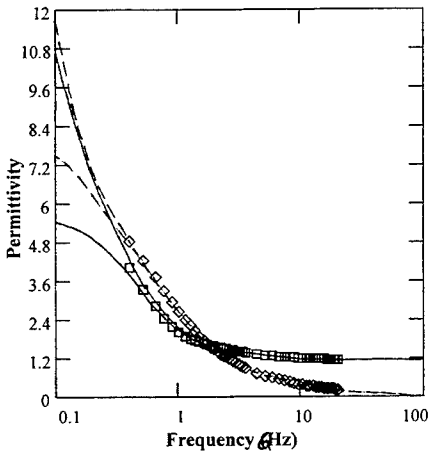

Figure 5. Plot of the real (solid) and imaginary (dashed) parts of the permittivity versus frequency for the material of Figures 1 through 4. The points represent the measured data. The curves represent two analytic models that fit the data within + or - 6.5% of error. Note that it is impossible to reliably extrapolate this data to lower frequencies.

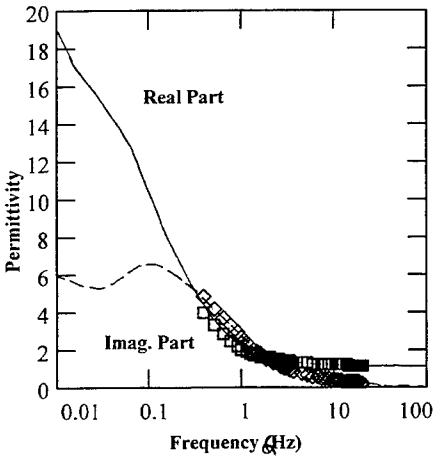

Figure 6. The use of low frequency data below 100 MHz reduces the range of possible analytic fits to the measured data and yields a representation of the material valid over a 2,000,000:1 bandwidth. The solid line is the real part, the dashed is the imaginary.

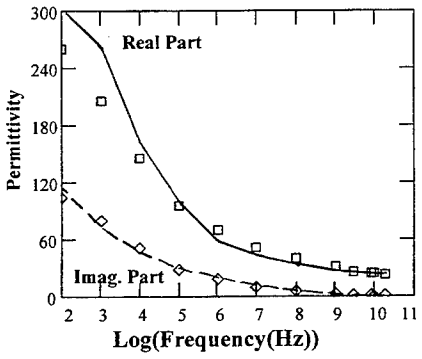

Figure 7. Analytic fit (curves) to Emerson and Cuming's data for the permittivity of MF-124(points). Eight Debye terms accurately match the imaginary part over the entire band and only deviate from the real part's data below 10 KHz.

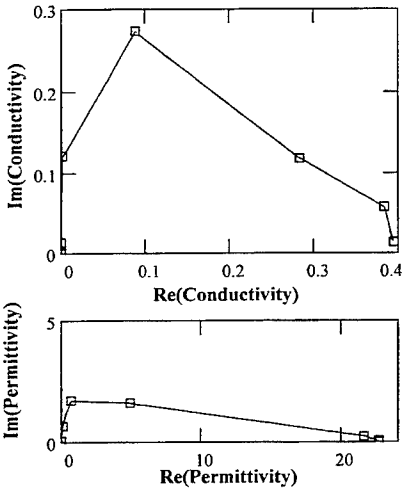

Figure 8. Grant Plane (top) and Cole Cole plot (bottom) of LS20 data after removal of endpoint contributions. Neither curve can be composed of semicircular arcs, showing that the data is not error free.

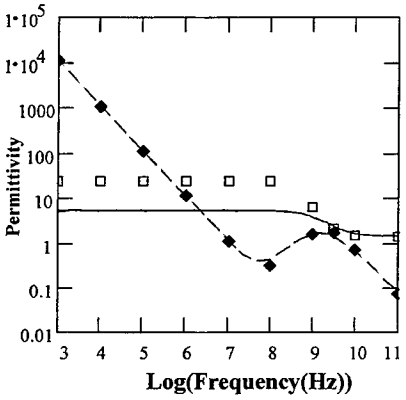

Figure 9. Fitting the imaginary permittivity data (dashed line and diamonds) of LS20, leaves a significant deviation in the real part (solid line versus boxes), showing that the data for this material is not causal.

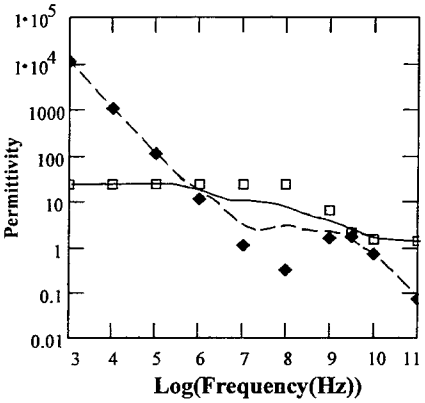

Figure 10. In the absence of guidelines for which range of data or constitutive parameter to believe, the best that can be done to estimate the true properties of LS20 is a compromise across the middle of the band.

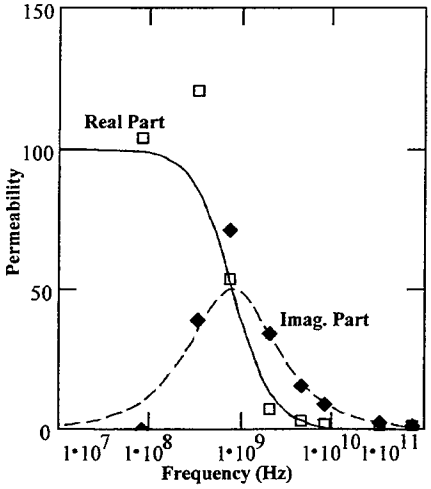

Figure 11. Analytic fit to Kittel's model for the high frequency dispersive permeability of Iron. The model's sharp rise in the real part before a gentle drop is not consistent with causal analytic functions, nor with the empirical data. So we adopt a single Debye term representation.

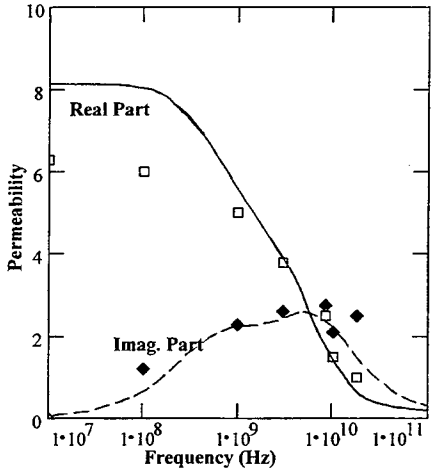

Figure 12. Model of the permeability of a composite with 82% volume content of Iron powder in a nonmagnetic matrix (curves), compared to the data for Emerson and Cuming's MF-124 (points).

Scattering from inhomogeneous chiral cylindrical composites using axial Beltrami fields and the fast multipole method

Balasubramaniam Shanker, Eric Michielssen, and Weng C. Chew
Center for Computational Electromagnetics,
Department of Electrical and Computer Engineering
University of Illinois at Urbana-Champaign,
1406 W. Green St., Urbana, IL 61801
Email: shanker@socrates.ece.uiuc.edu

Abstract

A fast multipole accelerated integral equation based technique for analyzing oblique scattering from two-dimensional inhomogeneous chiral objects immersed in a chiral host is presented. The analysis is performed in terms of Beltrami fields, as these provide a natural representation of fields in a chiral medium. Volume integral equations in terms of solely axial components of Beltrami fields are derived, and are discretized using pyramidal basis functions. Our numerical results are validated against exact solutions for scattering from circular cylinders and shells. Scattering from large shells and corrugated curved gratings are presented and the reduced computational complexity of our algorithm is demonstrated.

Introduction

Optical activity or chirality was first discovered in the early 1800's, and early research was more or less restricted to the realm of chemists and physicists. It was only after Lindman [1] discovered that a dispersion of macroscopic metallic helices in an achiral host displayed the characteristics of an optically active medium that microwave engineering applications emerged. Since then, studies have focused on every aspect of wave propagation in, and wave interaction with chiral materials; see [2] for a sample of the literature in this field. One of the many probable applications of chiral materials is to control an object's scattering properties. As opposed to a dielectric material, a chiral material is described by three constitutive parameters, namely the permittivity, permeability, and the chirality pseudo-scalar. Thus, there is an additional design parameter that one can manipulate.

In this paper, oblique scattering from large two-dimensional inhomogeneous chiral bodies is analyzed using a purely Volumetric Integral Equation (VIE) approach. The scatterer is assumed to be z invariant but can be of arbitrary cross-section (Fig. 1). The ambient host medium is also assumed to be chiral. Analytical methods for analyzing scattering from such objects are restricted to simple shapes. If the scatterer is inhomogeneous and/or of arbitrary shape [3], one resorts to numerical techniques, e.g., by formulating the problem in terms of integral equations and subsequently solving them using the Method of Moments (MoM). Kluskens and Newman [3] were the first to analyze scattering from an inhomogeneous chiral cylinder using a VIE in terms of all six volumetric field components. In a more recent paper, Rojas [4] studied scattering from homogeneous chiral cylinders using a surface integral equation in terms of four surface unknowns, and scattering from inhomogeneous chiral bodies using a combined surface-volume integral equation in terms of two surface and two volume unknowns.

This paper introduces an algorithm for analyzing scattering from chiral cylinders with extended capabilities and improved numerical efficiency when compared to previously published techniques. More specifically, the main contributions of this paper are threefold:

- In contrast to previous works which focussed on chiral-in-dielectric inhomogeneities illuminated by normally incident plane waves, our algorithm analyzes oblique scattering from chiral-in-chiral inhomogeneous bodies.
- The analysis is performed in terms of Beltrami fields. Using the fact that in a quasi two-dimensional system transverse fields can be represented in terms of the axial field components [2, 4], integral equations can be constructed in terms of *only* two volume unknowns, thereby realizing an absolute minimum number of unknowns.
- To further expand the applicability of this algorithm to the analysis of scattering from electrically large structures, the Fast Multipole Method (FMM) is implemented to accelerate the MoM–based solution to these equations.

Analysis: Integral equations using axial Beltrami fields

Let all space be divided into two mutually exclusive regions, V_{ext} and V_{int}, such that a host medium obeying the Drude-Born-Federov constitutive relations

$$\mathbf{D}(\mathbf{r}) = \epsilon_a \mathbf{E}(\mathbf{r}) + \epsilon_a \beta_a \nabla \times \mathbf{E}(\mathbf{r}); \quad \mathbf{B}(\mathbf{r}) = \mu_a \mathbf{H}(\mathbf{r}) + \mu_a \beta_a \nabla \times \mathbf{H}(\mathbf{r}) \tag{1}$$

occupies V_{ext}. Here ϵ_a and μ_a are the permittivity and permeability, and β_a is the chirality parameter of the medium. An $\exp[-i\omega t]$ time harmonic dependence has been implicitly assumed. The region V_{int} is occupied by a z invariant inhomogeneous cylindrical scatterer which obeys the constitutive relations

$$\mathbf{D}(\mathbf{r}) = \epsilon_b(\mathbf{r})\mathbf{E}(\mathbf{r}) + \epsilon_b(\mathbf{r})\beta_b(\mathbf{r})\nabla \times \mathbf{E}(\mathbf{r}); \quad \mathbf{B}(\mathbf{r}) = \mu_b(\mathbf{r})\mathbf{H}(\mathbf{r}) + \mu_b(\mathbf{r})\beta_b(\mathbf{r})\nabla \times \mathbf{H}(\mathbf{r}) \tag{2}$$

where $\epsilon_b(\mathbf{r})$, $\mu_b(\mathbf{r})$ and $\beta_b(\mathbf{r})$ are the inhomogeneous permittivity, permeability and the chirality parameter of the scatterer. In a manner similar to Ref. [5], the scatterer is replaced by equivalent sources which radiate everywhere as if all space were occupied by the host medium. It is assumed that the scatterer is illuminated by an obliquely incident wave which imposes an $\partial/\partial z = i\alpha$ on all fields such that any field or current can be written as $\mathbf{X}(\mathbf{r}) = \mathbf{X}(\boldsymbol{\rho})\exp[i\alpha z]$. By expressing the fields and the equivalent current densities in terms their equivalent Beltrami analogues [2], and using $\nabla = \nabla_t + \mathbf{u}_z \partial/\partial z$ with $\mathbf{X} = \mathbf{X}_t + \mathbf{u}_z X_z$, it can be shown that the field equations take the form [6]

$$\frac{\gamma_1}{\kappa_1^2}\left(\nabla_t^2 + \kappa_1^2\right) Q_{1z}(\boldsymbol{\rho}) = -W_{1z}(\boldsymbol{\rho}) + \frac{\gamma_1 \nabla_t \cdot \mathbf{u}_z \times \mathbf{W}_{1t}(\boldsymbol{\rho}) - i\alpha \nabla_t \cdot \mathbf{W}_{1t}(\boldsymbol{\rho})}{\kappa_1^2} \tag{3a}$$

$$\frac{\gamma_2}{\kappa_2^2}\left(\nabla_t^2 + \kappa_2^2\right) Q_{2z}(\boldsymbol{\rho}) = W_{2z}(\boldsymbol{\rho}) + \frac{\gamma_2 \nabla_t \cdot \mathbf{u}_z \times \mathbf{W}_{2t}(\boldsymbol{\rho}) + i\alpha \nabla_t \cdot \mathbf{W}_{2t}(\boldsymbol{\rho})}{\kappa_2^2} \tag{3b}$$

with the source densities being

$$\begin{aligned} W_{1z}(\boldsymbol{\rho}) &= a_{11}(\boldsymbol{\rho})Q_{1z}(\boldsymbol{\rho}) + a_{12}(\boldsymbol{\rho})Q_{2z}(\boldsymbol{\rho}) \\ W_{2z}(\boldsymbol{\rho}) &= a_{21}(\boldsymbol{\rho})Q_{1z}(\boldsymbol{\rho}) + a_{22}(\boldsymbol{\rho})Q_{2z}(\boldsymbol{\rho}) \end{aligned} \tag{4a}$$

$$\begin{aligned} \mathbf{W}_{1t}(\boldsymbol{\rho}) = &\frac{a_{11}(\boldsymbol{\rho})}{\Delta(\boldsymbol{\rho})}\left[c_{11}(\boldsymbol{\rho})\nabla_t Q_{1z} + c_{12}(\boldsymbol{\rho})\nabla_t Q_{2z} + c_{13}(\boldsymbol{\rho})\mathbf{u}_z \times \nabla_t Q_{1z} + c_{14}(\boldsymbol{\rho})\mathbf{u}_z \times \nabla_t Q_{2z}\right] \\ &+\frac{a_{12}(\boldsymbol{\rho})}{\Delta(\boldsymbol{\rho})}\left[c_{21}(\boldsymbol{\rho})\nabla_t Q_{1z} + c_{22}(\boldsymbol{\rho})\nabla_t Q_{2z} + c_{23}(\boldsymbol{\rho})\mathbf{u}_z \times \nabla_t Q_{1z} + c_{24}(\boldsymbol{\rho})\mathbf{u}_z \times \nabla Q_{2z}\right] \end{aligned} \tag{4b}$$

$$\begin{aligned} \mathbf{W}_{2t}(\boldsymbol{\rho}) = &\frac{a_{21}(\boldsymbol{\rho})}{\Delta(\boldsymbol{\rho})}\left[c_{11}(\boldsymbol{\rho})\nabla_t Q_{1z} + c_{12}(\boldsymbol{\rho})\nabla_t Q_{2z} + c_{13}(\boldsymbol{\rho})\mathbf{u}_z \times \nabla_t Q_{1z} + c_{14}(\boldsymbol{\rho})\mathbf{u}_z \times \nabla_t Q_{2z}\right] \\ &+\frac{a_{22}(\boldsymbol{\rho})}{\Delta(\boldsymbol{\rho})}\left[c_{21}(\boldsymbol{\rho})\nabla_t Q_{1z} + c_{22}(\boldsymbol{\rho})\nabla_t Q_{2z} + c_{23}(\boldsymbol{\rho})\mathbf{u}_z \times \nabla_t Q_{1z} + c_{24}(\boldsymbol{\rho})\mathbf{u}_z \times \nabla_t Q_{2z}\right] \end{aligned} \tag{4c}$$

Using Eqns. (4a-c) together with Eqns. (3a,b), it is seen that $Q_{1z}(\boldsymbol{\rho})$ and $Q_{2z}(\boldsymbol{\rho})$ satisfy the integral equations [7]

$$\begin{aligned} Q_{lz}(\boldsymbol{\rho}) = &\; Q_{lz,inc}(\boldsymbol{\rho}) + (-1)^{(l-1)}\frac{\kappa_l^2}{\gamma_l}\left[a_{l1}(\boldsymbol{\rho})Q_{1z}(\boldsymbol{\rho}) + a_{l2}(\boldsymbol{\rho})Q_{1z}(\boldsymbol{\rho})\right] * g_0(\kappa_l|\boldsymbol{\rho}|) \\ &- \frac{1}{\gamma_l}\nabla_t \cdot \left[b_{l1}(\boldsymbol{\rho})\nabla_t Q_{1z}(\boldsymbol{\rho}) + b_{l2}(\boldsymbol{\rho})\nabla_t Q_{2z}(\boldsymbol{\rho})\right] * g_0(\kappa_l|\boldsymbol{\rho}|) \\ &- \frac{1}{\gamma_l}\nabla_t \cdot \left[b_{l3}(\boldsymbol{\rho})\mathbf{u}_z \times \nabla_t Q_{1z}(\boldsymbol{\rho}) + b_{l4}(\boldsymbol{\rho})\mathbf{u}_z \times \nabla_t Q_{2z}(\boldsymbol{\rho})\right] * g_0(\kappa_l|\boldsymbol{\rho}|); \quad \forall \; l = 1,2 \end{aligned} \tag{5}$$

Here $Q_{1z,inc}(\boldsymbol{\rho})$ and $Q_{2z,inc}(\boldsymbol{\rho})$ are the left and right circularly polarized waves incident on the scatterer, $g_0(\kappa_l|\boldsymbol{\rho}|) = \frac{i}{4}H_0^1(\kappa_l|\boldsymbol{\rho}|)$ for $l = 1,2$ is the scalar Green's function, and the asterisk denotes convolution over two-dimensional space. These equations simplify considerably for a homogeneous scatterer as $\nabla_t \cdot (\mathbf{u}_z \times \nabla_t Q_{lz}(\boldsymbol{\rho})) = 0$

and $\mathbf{u}_z \times \mathbf{u}_z \times \nabla_t Q_{lz}(\boldsymbol{\rho}) = -\nabla_t Q_{lz}(\boldsymbol{\rho})$ for $l = 1, 2$. Also, setting $\beta_a = \beta_b(\boldsymbol{\rho}) = 0$, and reverting back to the E_z and H_z system, reduces these expressions to those obtained by Michielssen *et al* [7].

Method of Moments and the Fast Multipole Method

To develop an MoM algorithm, the cylinder is discretized into triangular cells, and the unknowns $Q_{1z}(\boldsymbol{\rho})$ and $Q_{2z}(\boldsymbol{\rho})$ are linearly interpolated in between the N nodes comprising the mesh by expanding them in terms of a set of pyramidal basis functions $B_n(\boldsymbol{\rho})$, $n = 1, \cdots, N$ as [7]

$$Q_{lz}(\boldsymbol{\rho}) \approx \sum_{n=1}^{N} q_{ln} B_n(\boldsymbol{\rho}); \quad \forall \quad l = 1, 2 \tag{6}$$

Inserting Eqns. (6) into Eqns. (5), and enforcing the resulting equations at the N mesh nodes, results in a system of $2N$ linear equations in the $2N$ expansion coefficients q_{1n} and q_{2n} which are given by

$$\begin{bmatrix} \mathbf{Q}_{1inc} \\ \mathbf{Q}_{2inc} \end{bmatrix} = \begin{bmatrix} \bar{\mathbf{A}}_{11} & \bar{\mathbf{A}}_{12} \\ \bar{\mathbf{A}}_{21} & \bar{\mathbf{A}}_{22} \end{bmatrix} \begin{bmatrix} \mathbf{q}_1 \\ \mathbf{q}_2 \end{bmatrix} \tag{7}$$

where $Q_{1inc,m} = Q_{1z,inc}(\boldsymbol{\rho}_m)$. Henceforth, only one of the coefficients in Eqn. (7) will be use for illustration, namely

$$A_{11,mn} = \delta_{mn} + \frac{1}{\gamma_1}\left[-\kappa_1^2 a_{11}(\boldsymbol{\rho}) + \nabla_t b_{11}(\boldsymbol{\rho})\nabla_t + \nabla_t b_{13}(\boldsymbol{\rho})\mathbf{u}_z \times \nabla_t\right] B_n(\boldsymbol{\rho}) * g_0(\kappa_1|\boldsymbol{\rho}|)\Big|_{\boldsymbol{\rho}=\boldsymbol{\rho}_m} \tag{8}$$

where δ_{mn} represents the Kronecker's delta. The convolution integrals in this equation are evaluated using numerical quadrature after extraction of the singular terms.

Storage of all matrix elements in Eqn. (7) requires $O(N^2)$ memory. Direct solution of the matrix equation (Eqn. (7)), e.g., using LU decomposition, requires $O(N^3)$ operations which is impractical for analyzing scattering from electrically large objects. The application of classical iterative solvers to the solution of Eqn. (7) requires $O(N^2)$ operations per iteration. However, the FMM permits a reduction [8] in the computational complexity of matrix-vector multiplications as well as the memory requirements of an iterative solver. To apply the FMM, the scatterer is subdivided into a large set of N_g sub-scatterers, each of which is contained in a square box whose centers are denoted by $\boldsymbol{\rho}_j, j = 1, \cdots, N_g$. Matrix elements corresponding to the interaction between the nodes in the same or adjacent boxes (near field) are computed as usual. The "far-field" terms are computed using [8]

$$A_{11,mn} = \frac{1}{2\pi}\int_0^{2\pi} d\theta \mathcal{B}_{1,mj}(\theta)\mathcal{T}_{1,jj'}(\theta)\mathcal{C}_{11,j'n}(\theta) \tag{9}$$

where it is assumed that nodes m and n belong to boxes j and j', respectively, with

$$\mathcal{B}_{1,mj}(\theta) = e^{i\boldsymbol{\kappa}_1 \cdot \boldsymbol{\rho}_{mj}} \tag{10a}$$

$$\mathcal{T}_{1,jj'}(\theta) = \sum_{p=-P}^{P} H_p^{(1)}(\kappa_1 |\boldsymbol{\rho}_{jj'}|) e^{-ip(\phi_{jj'} - \theta - \pi/2)} \tag{10b}$$

$$\mathcal{C}_{11,j'n}(\theta) = \frac{1}{\gamma_1}\left[-\kappa_1^2 a_{11}(\boldsymbol{\rho}) + \nabla_t b_{11}(\boldsymbol{\rho})\nabla_t + \nabla_t b_{13}(\boldsymbol{\rho})\mathbf{u}_z \times \nabla_t\right] B_n(\boldsymbol{\rho}) * e^{-i\boldsymbol{\kappa}_1 \cdot \boldsymbol{\rho}}\Big|_{\boldsymbol{\rho}=\boldsymbol{\rho}_{j'}} \tag{10c}$$

In these equations $\boldsymbol{\kappa}_l = \kappa_l(\hat{\mathbf{x}}\cos\theta + \hat{\mathbf{y}}\sin\theta)$ for $l = 1, 2$, $\boldsymbol{\rho}_{sr} = \boldsymbol{\rho}_s - \boldsymbol{\rho}_r$, and $\phi_{jj'}$ is the angle that $\boldsymbol{\rho}_{jj'}$ makes with the positive x–axis. In a computationally efficient algorithm, the operators $\mathcal{C}_{lk,j'n}(\theta)$, $\mathcal{B}_{l,mj}(\theta)$, and $\mathcal{T}_{l,jj'}(\theta)$ are first pre-computed for a set of directions $\theta_p = 2\pi p/P; p = 1, \cdots, P$, and the integrals in Eqns (9a-d) are evaluated numerically in the following manner. Tabulation of $\mathcal{C}_{lk,j'n}(\theta)$ permits the computation of the left and right circularly polarized far–field patterns associated with $Q_{1z}(\boldsymbol{\rho})$ and $Q_{2z}(\boldsymbol{\rho})$ sources in a given box. Given these far–field patterns, the plane wave spectrum of the fields incident upon a receiving box is obtained through the use of the translation operators $\mathcal{T}_{l,jj'}(\theta)$ for all pairs of boxes residing in each other's far field. Finally, and only after the spectrum of the total field incident upon a box due to all far–field interacting boxes has been obtained, the $\mathcal{B}_{l,mj}(\theta)$ are used to obtain the fields at the observers.

The total computational cost associated with a matrix vector multiplication using this procedure is considerably less that N^2. The cost associated with multiplying all near-field elements by a trial solution vector is given by

$$C_{near} = C_1 N_g M^2 \tag{11a}$$

The corresponding far-field multiplication requires the computation of the plane wave spectra for each group, and the translation of field for all interacting far-field box pairs. The costs associated with these operations are given by

$$C_{far} = C_2 N_g M P + C_3 N_g^2 P \tag{11b}$$

In Eqns. (11a,b) C_1, C_2, and C_3 are some arbitrary constants. For a volumetric scatterer it follows form Nyquist's sampling theorem that $P \propto \sqrt{M}$. Hence, assuming that $C_2 N_g M P$ is negligible compared to C_{near}, it is seen that $M \propto N^{0.4}$. Therefore, one expects the CPU time per iteration to scale as $O(N^{1.4})$, as is seen in Fig. 1(b).

Numerical Results

Before discussing the validity of this approach, it should be noted that, as the external medium is chiral, the incident plane wave is chosen to be either right or left circularly polarized. Since z-variation of the fields is of the form $e^{i\alpha z}$, it follows that

$$\alpha = -\gamma_1 \cos(\psi_1) = -\gamma_2 \cos(\psi_2) \tag{12}$$

where ψ_1 and ψ_2 denote the angles at which either the LCP or RCP waves are incident on the cylindrical scatterer.

Next, to validate and test the limits of the integral equation formulation, a battery of tests is conducted. In all the examples presented, the magnitude of the incident field is assumed to be unity, and the closed-form solutions used for comparison are derived in Ref. [6]. Figure 2(a) shows a comparison of the exact and the MoM solutions for the magnetic field on the surface of a 0.1λ cylinder excited by a normally incident RCP wave. The constitutive parameters of the host and the scatterer are $\epsilon_a = 3\epsilon_0, \mu_a = 2\mu_0, \beta_a = 0.001$ and $\epsilon_b = 3\epsilon_0, \mu_b = 2\mu_0, \beta_b = 0.002$ respectively. To test an extremum case, scattering from a body with unrealistically high chirality parameter is computed. The constitutive parameters of the scatterer and the host are assumed to be $\epsilon_b = 8\epsilon_0, \mu_b = 4\mu_0, \beta_b = 0.1$, and $\epsilon_a = 2\epsilon_0, \mu_a = \mu_0, \beta_a = 0.001$, respectively. The computed fields on the surface and the corresponding closed form solutions are in excellent agreement(Fig. 2(b)).

Finally, in Figs. 3(a,b), the RCS for scattering from two large objects are presented. Scattering from a shell of mean radius 16.5λ (19,200 unknowns) and thickness 0.1λ being illuminated by an LCP wave incident at $\psi_1 = 90°$ is shown in Fig. 3(a). The RCS of a curved corrugated grating of mean radius 150λ, thickness of 0.1λ, and 23 equally spaced teeth of height 0.05λ is shown in Fig. 3(b). In this example, the total number of unknowns is 16,230, and the scatterer is illuminated by an LCP wave incident at $\psi_1 = 80°$ and making an angle of 150° with the positive x axis.

In other tests, we studied scattering from both larger circular cylinders and shells, where the contrast was high. In all cases, the numerical results converged to the exact solution as the cylinder models were refined. Indeed, the refinement required is problem specific and depends on the shape of the scatterer, the contrast between the two materials, and the chirality parameter of the cylinder. A higher contrast requires a finer mesh as does a larger chirality parameter. In keeping with the usual requirements, it is recommended that a minimum of 10 nodes per linear wavelength be used in any computation. One should also remember that a chiral material is birefringent and the number of nodes chosen should reflect the size of the smaller of the two wavelengths.

Summary

This paper presented a very general approach for analyzing oblique scattering from inhomogeneous chiral cylinders of arbitrary cross-section immersed in a chiral host. Using the method of equivalent current densities, two coupled integral equations were obtained in terms of volume unknowns representing axial Beltrami fields. These equations were then solved using an iterative FMM accelerated MoM technique. The numerical results obtained using this approach agree very well with closed form solutions for scattering from circular cylinders and shells. It has also been demonstrated that the computational complexity scales as $O(N^{1.4})$; hence our technique can be applied to the analysis of very large scatterers. By using a multilevel FMM, the complexity of the algorithm can be further reduced to $O(N)$ or $O(N \log(N))$ for volume-and surface-like scatterers, respectively. In addition, the proposed

algorithm can be applied to the study of homogenization models of random chiral composites. This is the focus of our current research.

Acknowledgments: This work was supported in part by a grant from AFOSR via the MURI Program under contract no F49620-96-1-0025.

References

[1] K. Lindman, "Über die durch ein isotropes system von spiralförmigen r esonatoren erzeugte rotationspolarization der electromagnetischen wellen," *Ann. Phys. Leipzig*, vol. 63, p. 621, 1920.

[2] A. Lakhtakia, *Beltrami Fields in Chiral Media*. Singapore: World Scientific, 1995.

[3] M. S. Kluskens and E. H. Newman, "Scattering by a chiral cylinder of arbitrary cross section," *IEEE Trans. Antennas Propagat.*, vol. 38, pp. 1448–1455, 1990.

[4] R. G. Rojas, "Integral equations for EM scattering by homogeneous/inhomogeneous two-dimensional chiral bodies," *IEE Proc. Microw. Antennas Propagat.*, vol. 141, pp. 385–392, 1994.

[5] B. Shanker and A. Lakhtakia, "Extended Maxwell Garnett model for homogenizing chiral-in chiral composites," *J. Phys. D: Appl. Phys.*, vol. 26, pp. 1746–1758, 1993.

[6] B. Shanker, E. Michielssen, and W. C. Chew, "Oblique scattering from an inhomogeneous chiral cylindrical object using axial Beltrami fields and the fast multipole method," Tech. Rep., University of Illinois at Urbana-Champaign, 1997.

[7] E. Michielssen, A. F. Peterson, and R. Mittra;, "Oblique scattering from inhomogeneous cylinders using a coupled integral formulation with triangular cells," *IEEE Trans. Antennas Propagat.*, vol. 39, pp. 485–490, 1991.

[8] V. Rokhlin, "Rapid solutions of integral equations of scattering thoery in two dimensions," *J. Comput. Phys.*, vol. 86, pp. 414–439, 1990.

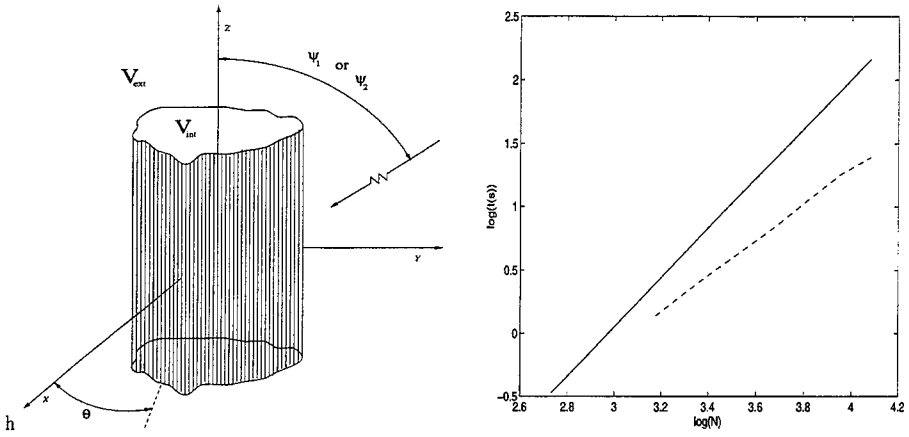

(a) (b)

Figure 1: (a) Geometry of the problem; (b) Computational complexity; (−) direct solution; (−−) iterative solution

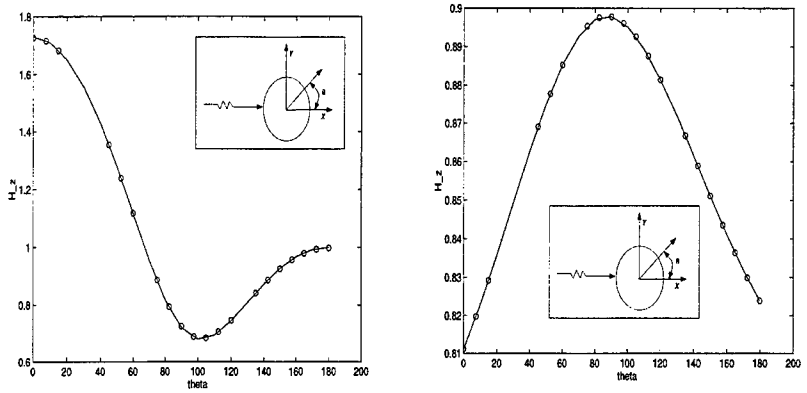

(a) (b)

Figure 2: A comparison of the magnetic field on the surface of the scatterer computed using MoM and Mie-type solutions; (-) exact solution; (o) MOM calculations

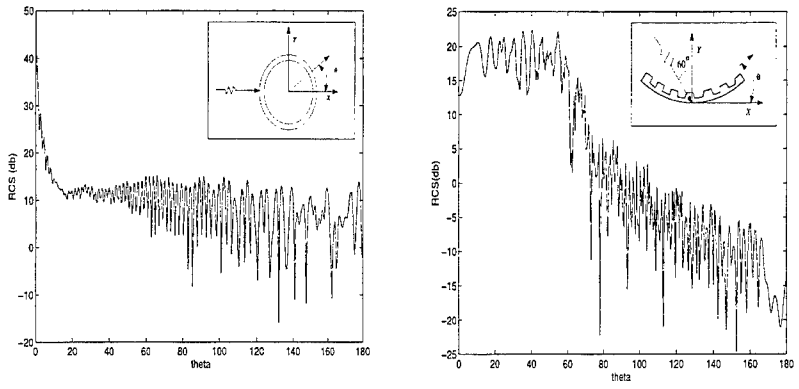

(a) (b)

Figure 3: The RCS due to an incident LCP wave for (a) 16.5λ shell of 0.1λ thickness; (b) for a corrugated surface of radius 150λ of thickness 0.1λ sub-tending an angle of 30°. There are 23 rectangular "teeth" on the surface. The constitutive parameters are $\epsilon_b = (3 + 0.1i)\epsilon_0, \mu_b = (2 + 0.1i)\mu_0, \beta_b = 0.002$, and $\epsilon_a = \epsilon_0, \mu_a = \mu_0, \beta_a = 0.001$.

DIAZ-FITZGERALD TIME DOMAIN METHOD APPLIED TO ELECTRIC AND MAGNETIC DEBYE MATERIALS

Franco De Flaviis, Massimo Noro†,
Rodolfo E.Diaz‡, and Nicolaos G. Alexopoulos

Department of Electrical Engineering, †Department of Chemistry and Biochemistry
University of California at Los Angeles, Los Angeles, CA 90095
‡Northrop Grumman, Military Aircraft System Division E.Washington Blvd., Pico Rivera, CA 90660

Abstract : Electromagnetic phenomena can be simulated by the dynamics of a mechanical system as long as the Hamiltonian of the electromagnetic and the mechanical systems coincide. It was shown by Diaz [1, 2] that George Francis FitzGerald's 1885 [3] model of electromagnetic propagation leads to a finite difference numerical formulation that is different from the conventional Finite Difference Time Domain method (FDTD). De Flaviis, Noro et al. [4, 5] showed that the mechanical finite difference scheme coincides with the discretized Maxwell's Equations in the vector potential formulation, and extended the model in order to treat lossy media.

In this work we present another extension for the modeling of electromagnetic wave interaction with complex media, namely frequency dependent electric and magnetic materials. We show a direct analogy between the mechanical model and the electric vector potential formulation.

Several engineering applications are described with examples of classical scattering problems and the simulations are validated with comparison to canonical solutions.

1. INTRODUCTION

Mechanical analog models can provide an excellent time domain visualization tool for propagation, scattering and radiation of electromagnetic waves in dispersive media. It has been known since the late 19th century that electromagnetic phenomena can be simulated by the dynamics of a mechanical system, as long as the Hamiltonians of the mechanical and the electromagnetic systems coincide. It was shown by Diaz [1, 2] that George Francis FitzGerald's 1885 [3] model of electromagnetic propagation leads to a finite difference numerical formulation that is different from the conventional Finite Difference Time Domain method (FDTD). This is because, as shown by De Flaviis and Noro [4, 5], FDTD is based upon the discretization of the Maxwell's equation in the

classical formulation, while Diaz time domain discretization of FitzGerald's mechanical model coincides with the discretization of Maxwell's equations in the vector potential formulation .

The original FitzGerald model consists of a distributed discrete system of pulleys of moment of inertial I connected to each other by means of rubber bands of elasticity constant k, as shown in Figure 1.

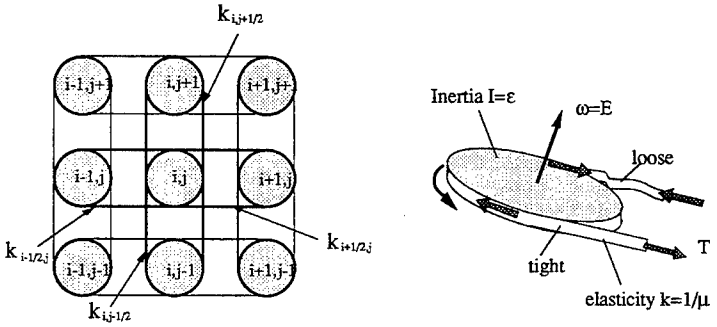

Fig.1 Array of rigid pulleys connected by rubber bands and corresponding equivalent electric quantities.

If a pulley is spun, its rotation strains the four rubber bands connecting it to its four neighbors. The total force of tension and compression applied at the peripheries of the pulleys, imparts to each one an angular acceleration α through Newton's second law: their angular velocity ω increases by αdt after a time step dt. Thus, an angular velocity pulse applied to the central pulley propagates outwards by action and reaction to all pulleys of the system. The differential equations describing the motion of the system is given by:

$$\begin{cases} \dfrac{\partial \omega}{\partial t} = \dfrac{a^2}{I}\dfrac{\partial}{\partial x}\left(ka^2\dfrac{\partial \theta}{\partial x}\right) \\ \dfrac{\partial \theta}{\partial t} = \omega \end{cases} \quad ; \qquad (1)$$

the electrical analog of the same one dimensional Maxwell's curl equations leads to[6]:

$$\begin{cases} \dfrac{\partial E_z}{\partial t} = \dfrac{1}{\varepsilon}\left[\dfrac{\partial}{\partial x}\left(\dfrac{1}{\mu}\dfrac{\partial A_z}{\partial x}\right)\right] \\ \dfrac{\partial A_z}{\partial t} = -E_z \end{cases} \quad . \qquad (2)$$

The extension to the two dimensional case is straightforward and is here omitted.

A summary of the correspondences between the mechanical, see eq.1, and the electrical quantities, see eq.2, is presented in Table I.

Electrical		*Mechanical*	
Ez	z-comp. electric field	ω	angular velocity
dEz/dt	Ez rate of change	α	angular acceleration
Az	z-comp. vector potential	$-\theta$	angle
ε	permittivity	I/a^2	inertia of the pulley
μ	permeability	$1/(ka^2)$	rubber band elasticity
Δx	mesh grid size	2a	pulley radius

Table I Equivalence between electrical and mechanical quantities in our model.

In the mechanical model the presence of a dielectric medium ($\varepsilon \neq \varepsilon_0$) is taken into account by increasing the moment of inertia of the pulley; while the presence of a magnetically permeable medium ($\mu \neq \mu_0$) is modeled by modifying the elasticity of the rubber (the elastic constant of the spring).

2. DEBYE DIELECTRIC MATERIALS FORMULATION

For a material characterized by a single Debye relaxation we can write [7, 8]

$$\mathbf{D} = \varepsilon_\infty \mathbf{E} + \mathbf{P} \tag{3}$$

where

$$\frac{\partial \mathbf{P}}{\partial t} = \frac{\varepsilon_s - \varepsilon_\infty}{\tau}\mathbf{E} - \frac{1}{\tau}\mathbf{P} \tag{4}$$

where ε_s and ε_∞ are the dielectric constants of zero (static) and "infinite" frequency, and τ is the relaxation time constant. The modification takes the form of an additional weighted ring (of moment of inertia $I^{(1)}$ resting on the pulley and connected to it through a coefficient of friction ($Q^{(1)}$) as shown in Figure 2.

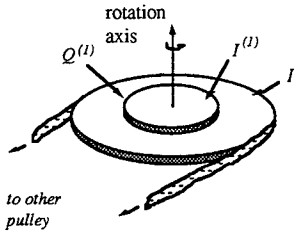

Fig.2 Mechanical model for single electrical Debye materials.

The time constant of the Debye pole τ corresponds to the ratio $I^{(1)}/Q^{(1)}$. Action and reaction of the top pulley then simulate the storage and dissipation of polarization. The new set of equations for this system can be derived starting form the original equations in the one dimensional case, by adding an inertial reaction due to the top pulley which is coupled to the bottom one through a friction coefficient.

$$\begin{cases} \dfrac{\partial \omega_i}{\partial t} = \dfrac{a^2}{I_i}\dfrac{\partial}{\partial x}\left(ka^2\dfrac{\partial \theta}{\partial x}\right) - \dfrac{a^2 Q_i^{(1)}}{I_i}\left(\omega_i - \omega_i^{(1)}\right) \\ \dfrac{\partial \theta_i}{\partial t} = \omega_i \end{cases} \tag{5}$$

Here $\omega_i^{(1)}$ represents the angular velocity of the weighted ring, $I_i^{(1)}$ its moment of inertia and $Q_i^{(1)}$, the coefficient of friction. This extension of the FitzGerald model finds as exact analogy in the vector potential formulation of the Maxwell's Equations. In this case the Polarization vector needs to be introduced, and here we just report the final equations in the one dimensional case:

$$\begin{cases} \dfrac{\partial E_z}{\partial t} = \dfrac{1}{\varepsilon_\infty}\dfrac{\partial}{\partial x}\left(\dfrac{1}{\mu}\dfrac{\partial A_z}{\partial x}\right) + \dfrac{\varepsilon_s - \varepsilon_\infty}{\tau\varepsilon_\infty}\left(\dfrac{P_z}{\varepsilon_s - \varepsilon_\infty} - E_z\right) \\ \dfrac{\partial A_z}{\partial t} = -E_z \end{cases} \tag{6}$$

By comparing eq.(5) to eq.(6) it is clear that they describe the same phenomenon.

5. FREQUENCY DEPENDENT MAGNETIC MATERIALS FORMULATION

A single Debye magnetic medium is characterized by the following equation:

$$\mathbf{B} = \mu_\infty \mathbf{H} + \mathbf{M} \tag{7}$$

where

$$\frac{\partial \mathbf{M}}{\partial t} = \frac{\mu_s - \mu_\infty}{\tau}\mathbf{H} - \frac{1}{\tau}\mathbf{M} \tag{8}$$

where μ_s and μ_∞ are the permeability of zero (static) and "infinite" frequency, τ is the relaxation time constants. In this case the mechanical model can be extended once more to describe such materials by modifying the rubber bands elasticity to attribute their elastic constants a Debye character.

The modification takes the form of an additional spring connected in series with the original one. The new spring is connected with a device immersed in a viscous fluid, so that the oscillation of the second spring will be damped according to the viscous coefficient of the fluid γ. See Figure 3. We

have already discussed how the elastic coefficient can be viewed as the reciprocal of the magnetic permeability. Now we introduce the time constant of the magnetic Debye material τ as corresponding to the ratio γ/k_1.

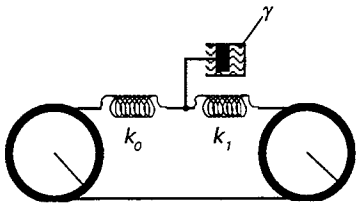

Fig.3 Magnetic Debye material model: the two springs are connected in series

The new equation of motion for the system [9] is

$$\begin{cases} \dfrac{\partial F}{\partial t} = -a^2 k_0 \dfrac{\partial}{\partial t}\left(\dfrac{\partial \theta}{\partial x}\right) - \dfrac{a^2 k_0 k_1}{\gamma}\dfrac{\partial \theta}{\partial x} - \dfrac{k_0 + k_1}{\gamma} F \\ \dfrac{\partial \omega_i}{\partial t} = -\dfrac{a^2}{I_i}\dfrac{\partial F}{\partial x} \\ \dfrac{\partial \theta_i}{\partial t} = \omega_i \end{cases} \qquad (9)$$

where F represents the restoring force, k_0 and k_1 the elastic constant of the springs and γ the damping coefficient. This extension of the Fitzgerald model finds an exact analogy in the vector potential formulation of the Maxwell's equations, giving:

$$\begin{cases} \dfrac{\partial H_y}{\partial t} = -\dfrac{1}{\mu_\infty}\dfrac{\partial}{\partial t}\left(\dfrac{\partial A_z}{\partial x}\right) - \dfrac{1}{\mu_\infty \tau}\dfrac{\partial A_z}{\partial x} - \dfrac{\mu_s}{\mu_\infty \tau} H_y \\ \dfrac{\partial E_z}{\partial t} = \dfrac{1}{\varepsilon}\dfrac{\partial H_y}{\partial x} \\ \dfrac{\partial A_z}{\partial t} = -E_z \end{cases} \qquad (10)$$

Also in this case the two equations (9) and (10) are equivalent, the only difference being in the label of the variables.

4. ECHO EXPERIMENTS

Consider a plane wave incident upon the flat infinite air-medium interface; because of the simple geometry the problem can be reduced to one dimension [10] The one dimensional space consists of 1000 cells: 700 are used to model the free space (air) and the remaining 300 are used for the complex material. Each cell corresponds to a length of 0.1 mm and the time step is 0.25 psec. The incident

wave is a Gaussian pulse with maximum frequency of 200 GHz and width of 20 time steps. The pulse is launched at the cell position 300 and the DFT of the incident pulse is performed at position i=310 for 300 time steps. This represents the spectrum of the incident wave. The simulation is time stepped for a long enough time until the pulse reaches the interface and is partially reflected.

A second DFT analysis is performed on the reflected pulse, accurately windowed, at position i=600 for the same number of time steps. This represents the spectrum of the reflected wave. The reflection coefficient as a function of the frequency is therefore calculated as the ratio of the two spectra. The calculated reflection coefficient is compared to the correspondent analytical quantity obtained in the frequency domain from the following relation:

$$|R(\omega)| = \left|\frac{\eta_1 - \eta_0}{\eta_1 + \eta_0}\right| \tag{11}$$

where η_0 and η_1 are the characteristic impedance of free space and the complex medium respectively, and are given by

$$\eta_0 = \sqrt{\frac{\mu_0}{\varepsilon_0}} \tag{12a}$$

$$\eta_1 = \sqrt{\frac{\mu_1(\omega)}{\varepsilon_1(\omega)}} \tag{12b}$$

In the first experiment we consider the water-air interface; the complex permittivity of water can be approximated by a single order Debye relaxation. We have used ε_S=81.0, ε_∞=1.8, and τ_0=9.4•10^{-12} sec [11] The results for the reflection coefficients are plotted and compared to the analytical solution in Fig. 4.

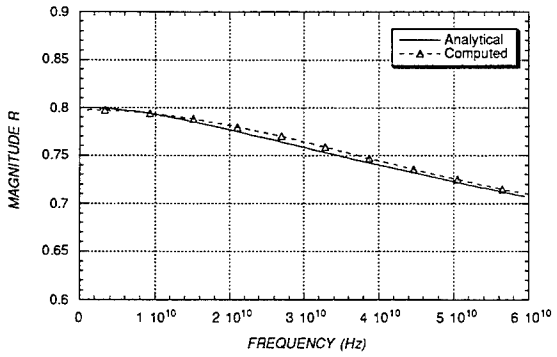

Fig.4 Reflection coefficient for air-water interface

In the next experiment we consider a single magnetic Debye material characterized by μ_S=81.0, μ_∞=1.8, and τ_0=9.4•10^{-12} sec. Results are shown in Figures 5, which compares the reflection coefficient calculated from the simulations to the analytical results.

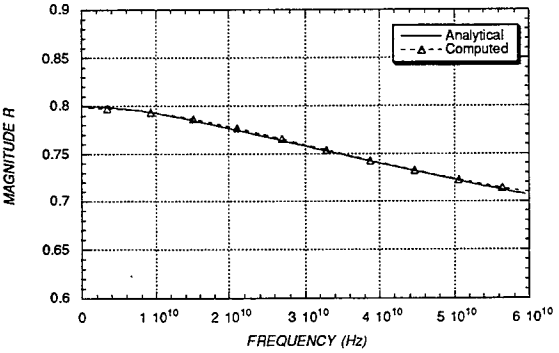

Fig.5 Reflection coefficient for single magnetic Debye materials

In the last experiment we consider complex medium characterized by an electric and magnetic Debye relaxation. The constitutive parameters of the medium are matched in order to obtain a perfect absorbing material at all frequencies. In particular we have used ε_S=81.0, ε_∞=1.8, and τ_e=9.4•10^{-12} sec, μ_S=81.0, μ_∞=1.8, and τ_m=9.4•10^{-12} sec; such that the ratio $\sqrt{\frac{\mu(\omega)}{\varepsilon(\omega)}}$ is frequency independent and equal to η_0. The results reported in Figure 6 confirm the prediction of no reflection as all frequencies, even though the calculation is affected by an error below 38 dB due to the finite cell size. In fact higher precision is achieved by decreasing the cell size up to the stability limit.

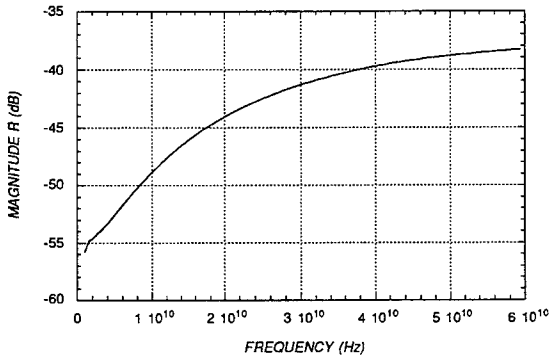

Fig.6 Reflection coefficient for wide band absorbing material.

5. CONCLUSIONS

We have extended the mechanical model first proposed by FitzGerald and then modified by De Flaviis and Noro to account for different realistic materials. The good agreement between the experimental and the predicted results confirms the validity of the new extensions introduced.

6. REFERENCES

[1] R. E. Diaz, *The Analitic Continuation Method for the Analysis and Design of Dispersive Materials*. PhD Dissertation, University of California at Los Angeles, 1992.

[2] R. E. Diaz, "A Discrete FitzGerald Time Domain Method for Computational Electromagnetics," in *International Conference on Electromagnetics in Aerospace Advanced Applications (ICEAA)*. Politecnico di Torino, ITALY 1993, pp. 391-394.

[3] G. F. FitzGerald, *Letter to Oliver Lodge, 3 Mar. 1894*, in *The Maxwellians*. Ithaca: Cornell University Press, 1991.

[4] F. De Flaviis, M. Noro, and N.G. Alexopoulos, "Diaz-FitzGerald Time Domain Method Applied to Dielectric Lossy Materials," in *Iternational Conference on Electromagnetics in Advanced Applications (ICEAA)*. Politecnico di Torino, ITALY 1995, pp. 309-311.

[5] F. De Flaviis, M. Noro, R.E.Diaz, and N.G. Alexopoulos, "Diaz-FitzGerald Time Domain (D-FTD) Technique Applied to Electromagnetic Problems," in *IEEE MTT-S International Microwave Symposium*. S. Francisco, pp.1047-1050, 1996.

[6] L. Lapidus and G. F. Pinder, *Numerical Solutions of Partial Differential Equations in Science and Engineering*. New York: John Wiley and Sons, 1982.

[7] T. Kashiwa, N. Yoshida, and I. Fukay, "A Treatment by the Finite Difference Time Domain Method of the Dispersive Characteristics Associated with Orientation Polarization," *IEICE Transactions*, vol. Vol. E-73, pp. 1326-1328, 1990.

[8] J. L. Yang, "Propagation in Linear Dispersive Media: Finite Difference Time Domain Methodologies," *IEEE Transaction Antennas Propagation*, vol. AEP-43, pp. 422-426, 1995.

[9] F. De Flaviis, M. Noro, N. G. Alexopoulos, R. E. Diaz, and G. Franceschetti, "Extensions to Complex Materials of the Fitzgerald Model for the Solution of Electromagnetic Problems," *Journal of Applied Physiscs*, vol. , To be pubblished.

[10] C. A. Balaniis, *Advanced Engineering Electromagnetics*. New York: John Wiley and Sons Inc., 1989.

[11] K. Luebbers, *The Finite Difference Time Domain Method for Electromagnetics*. Boca Raton, Florida: CRC Press, 1993.

Numerical multipole modelling of bianisotropic and complex composite materials

Luk R Arnaut

National Physical Laboratory
Centre for Electromagnetic and Time Metrology
Teddington TW11 0LW, UK

Abstract

A hybrid numerical-analytical method is presented for the electromagnetic modelling of composite media containing complex-shaped particles at arbitrary frequencies. The microscopic polyadic constitutive parameters of the individual particles are determined using a recursive multi-polarisability algorithm. This algorithm is based on a multi-polarisability expansion of the induced multipole moments. Macroscopic constitutive parameters are subsequently obtained for the homogenised effective medium using the corresponding macroscopic constitutive polyadics.

1 Introduction

Theoretical modelling of chiral, bianisotropic and more general complex composite media is important in the stages of design and validation of measurements of practical materials. Analytical modelling techniques are often difficult and approximative or have a limited range of applicability. Numerical full-wave simulations of composite media yield effective medium parameters directly, but at a large computational cost. A microscopic full-wave analysis of individual particles reduces this overhead significantly. However it requires further analytical processing of the numerical data in order to obtain macroscopic medium parameters. The latter approach is pursued in our analysis.

2 Multipole expansions

Consider the microscopic current density distribution $\underline{J}(\underline{r})$ induced in a particle of complex shape by an incident wave. If one is only concerned with the macroscopic effects caused by $\underline{J}(\underline{r})$ rather than with the detailed microscopic effects, then the actual distribution may be replaced by a set of multipole moments for the averaged (macroscopic) current density $\langle \underline{J}(\underline{r}) \rangle$. This set of equivalent sources, called a multipole expansion of $\underline{J}(\underline{r})$, is in essence a Taylor series expansion of the average density with reference to an arbitrary point in the proximity of the particle.

If the size of the particle is small in comparison with the spatial variations of the macroscopic field and provided that the magnitude of the wavenumber $\underline{k}$ is sufficiently small relative to the particle size a, i.e. $||\underline{k}||\, a \ll 1$, then the series may be limited to the first few terms. For simple non-magnetic isotropic or uniaxial anisotropic media, the multipole series may be limited to the first two terms, i.e. monopole and electric dipole moments, because these are sufficient to explain and quantify phenomena such as (normal) linear birefringence in uniaxial media. In more complex media, such as magnetic

or isotropic chiral media, the electric dipole-magnetic dipole approximation is required to explain and quantify phenomena such as circular birefringence. Unlike isotropic chiral media, quadrupole moments may be significant in anisotropic chiral media. Consequently the dipole-quadrupole approximation should then be used. The electric octopole-magnetic quadrupole approximation is needed to explain effects such as Jones linear birefringence in the absence of normal linear birefringence [1]. Rather than concentrating on particular polarisation phenomena for quasi-static excitation, the multipole modelling of general composite media aims at predicting their effective medium parameters over a wider frequency range. To this end, the contribution of each multipole moment to the macroscopic polarisation of the medium must be assessed individually and compared to the contribution of the other moments. Given the required accuracy, this enables one to decide on the truncation point in the series in any practical case of particle modelling. Whereas this truncation point can be determined *a priori* in the long-wavelength regime, it depends in general on the specific medium and microstructure as well as on the frequency of operation.

3 Microscopic modelling

The multipole moments for $\exp(j\omega t)$ time-harmonic excitations are defined in the usual manner and written here using polyadic notation. For a particle with volume V in which a current density $\underline{J}(\underline{r})$ is induced, the electric and magnetic[1] dipole, quadrupole, octopole, ... moments are:-

$$\underline{p}_e \triangleq (j\omega)^{-1}\int\int\int_V \underline{J}\,\mathrm{d}V, \quad \underline{p}_m \triangleq \frac{\mu_o}{2}\int\int\int_V (\underline{r}\times\underline{J})\,\mathrm{d}V \tag{1}$$

$$\underline{\underline{q}}_e \triangleq (j2\omega)^{-1}\int\int\int_V (\underline{J}\,\underline{r}+\underline{r}\,\underline{J})\,\mathrm{d}V, \quad \underline{\underline{q}}_m \triangleq \frac{\mu_o}{3}\int\int\int_V [(\underline{r}\times\underline{J})\,\underline{r}+\underline{r}\,(\underline{r}\times\underline{J})]\,\mathrm{d}V \tag{2}$$

$$\underline{\underline{\underline{o}}}_e \triangleq (j3\omega)^{-1}\int\int\int_V (\underline{J}\,\underline{r}\,\underline{r}+\underline{r}\,\underline{J}\,\underline{r}+\underline{r}\,\underline{r}\,\underline{J})\,\mathrm{d}V, \quad \underline{\underline{\underline{o}}}_m \triangleq \frac{\mu_o}{4}\int\int\int_V [(\underline{r}\times\underline{J})\,\underline{r}\,\underline{r}+\underline{r}\,(\underline{r}\times\underline{J})\,\underline{r}+\underline{r}\,\underline{r}\,(\underline{r}\times\underline{J})]\,\mathrm{d}V \tag{3}$$

and so on. For conducting objects the surface current density $\underline{J}_S$ gives rise to additional terms in these definitions, for example $\underline{p}_e \triangleq (j\omega)^{-1}[\int\int\int_V \underline{J}\mathrm{d}V + \int\int_{S=\partial V}\underline{J}_S\mathrm{d}S]$. The multipole moments can alternatively be expressed using the multi-polarisability polyadics that characterise the particle, as defined by the microscopic constitutive equations:-

$$\begin{aligned}\underline{p}_e &= \epsilon_o \underline{\underline{p}}_{ee}\cdot\underline{E}+\sqrt{\mu_o\epsilon_o}\,\underline{\underline{p}}_{em}\cdot\underline{H}+\frac{1}{2}\left[\epsilon_o\underline{\underline{q}}'_{ee}\cdot(\nabla\,\underline{E})+\sqrt{\mu_o\epsilon_o}\,\underline{\underline{q}}'_{em}\cdot(\nabla\,\underline{H})\right]\\ &\quad+\frac{1}{6}\left[\epsilon_o\underline{\underline{\underline{o}}}''_{ee}\cdot(\nabla\,\nabla\,\underline{E})+\sqrt{\mu_o\epsilon_o}\,\underline{\underline{\underline{o}}}''_{em}\cdot(\nabla\,\nabla\,\underline{H})\right]+\ldots \qquad (4)\\ \underline{p}_m &= \sqrt{\mu_o\epsilon_o}\,\underline{\underline{p}}_{me}\cdot\underline{E}+\mu_o\underline{\underline{p}}_{mm}\cdot\underline{H}+\frac{1}{2}\left[\sqrt{\mu_o\epsilon_o}\,\underline{\underline{q}}'_{me}\cdot(\nabla\,\underline{E})+\mu_o\underline{\underline{q}}'_{mm}\cdot(\nabla\,\underline{H})\right]\\ &\quad+\frac{1}{6}\left[\sqrt{\mu_o\epsilon_o}\,\underline{\underline{\underline{o}}}''_{me}\cdot(\nabla\,\nabla\,\underline{E})+\mu_o\underline{\underline{\underline{o}}}''_{mm}\cdot(\nabla\,\nabla\,\underline{H})\right]+\ldots \qquad (5)\end{aligned}$$

$$\underline{\underline{q}}_e = \epsilon_o\underline{\underline{q}}_{ee}\cdot\underline{E}+\sqrt{\mu_o\epsilon_o}\,\underline{\underline{q}}_{em}\cdot\underline{H}+\frac{1}{2}\left[\sqrt{\mu_o\epsilon_o}\,\underline{\underline{\underline{o}}}'_{me}\cdot(\nabla\,\underline{E})+\mu_o\underline{\underline{\underline{o}}}'_{mm}\cdot(\nabla\,\underline{H})\right]+\ldots \tag{6}$$

$$\underline{\underline{q}}_m = \sqrt{\mu_o\epsilon_o}\,\underline{\underline{q}}_{me}\cdot\underline{E}+\mu_o\underline{\underline{q}}_{mm}\cdot\underline{H}+\frac{1}{2}\left[\sqrt{\mu_o\epsilon_o}\,\underline{\underline{\underline{o}}}'_{me}\cdot(\nabla\,\underline{E})+\mu_o\underline{\underline{\underline{o}}}'_{mm}\cdot(\nabla\,\underline{H})\right]+\ldots \tag{7}$$

[1]The appearance of the factor μ_o in the definitions of the magnetic moments is due to the choice of $\underline{H}$ and its spatial derivatives as the magnetic source fields, rather than $\underline{B}$ and its derivatives.

$$\underline{\underline{o}}_{e} = \epsilon_o \underline{\underline{o}}_{ee} \cdot \underline{E} + \sqrt{\mu_o \epsilon_o}\, \underline{\underline{o}}_{em} \cdot \underline{H} + \ldots \quad (8)$$

$$\underline{\underline{o}}_{m} = \sqrt{\mu_o \epsilon_o}\, \underline{\underline{o}}_{me} \cdot \underline{E} + \mu_o \underline{\underline{o}}_{mm} \cdot \underline{H} + \ldots \quad (9)$$

where $\underline{\nabla}\,\underline{\nabla}\,\underline{A}$ represents an n-adic product, i.e.

$$\underline{\nabla}\,\underline{\nabla}\ldots\underline{\nabla}\,\underline{A} = \sum_{i_1=x,y,z} \sum_{i_2=x,y,z} \cdots \sum_{i_n=x,y,z} \nabla_{i_1} \ldots \nabla_{i_{n-1}} A_{i_n} \underline{1}_{i_1} \cdots \underline{1}_{i_n} \quad (10)$$

with $\underline{A} \equiv \underline{E}, \underline{H}$. The $\underline{\underline{p}}_{kl}, \underline{\underline{q}}_{kl}, \underline{\underline{o}}_{kl}, \ldots$ are the dipolarisability, quadrupolarisability, octopolarisability, ... polyadics of rank 2, 3, 4, ... of the particle expressed in units m^3, m^4, m^5, ..., respectively $(k, l = e, m)$. The ϵ_o and μ_o represent the permittivity and permeability of the isotropic host medium, respectively. The extension to higher-order multi-polarisabilities is straightforward. The primed quantities can be derived from the corresponding unprimed ones from perturbation theory by exploiting the hermiticity of the associated quantum mechanical multipole moment operators [2]. In determining the multi-polarisability polyadics, those of highest rank are computed first. The polyadics of lower rank are subsequently computed, in a recursive manner, until the dipolarisability dyadics are finally obtained. For example, the sequence in which Eqns (4–9) are solved, with omission of higher-order contributions, is:-

$$\underline{\underline{o}}_{kl} \rightarrow \underline{\underline{o}}'_{kl} \rightarrow \underline{\underline{o}}''_{kl} \rightarrow \underline{\underline{q}}_{kl} \rightarrow \underline{\underline{q}}'_{kl} \rightarrow \underline{\underline{p}}_{kl} \quad (11)$$

The multi-polarisabilities can be computed, for example, using the method of counterpropagating waves with averaged direction of propagation (Fig 1) by solving a system of linear equations. This method has previously been used for the characterisation of isotropic chiral [3, 4] and anisotropic chiral [5, 6, 7] particles.

4 Macroscopic medium parameters

Once the multipole moments have been determined per particle, the macroscopic (effective) medium properties can be derived. Denoting the electric and magnetic multipole moments per unit volume by $\underline{P}_e, \underline{\underline{Q}}_e, \underline{\underline{\underline{O}}}_e, \ldots$ and $\underline{P}_m, \underline{\underline{Q}}_m, \underline{\underline{\underline{O}}}_m, \ldots$ with associated multi-polarisabilities $\underline{\underline{P}}_{kl}, \underline{\underline{Q}}_{kl}, \underline{\underline{\underline{O}}}_{kl}, \ldots$, then the multipole expansion of the macroscopic constitutive equations reads:-

$$\begin{aligned} \underline{D} &= \epsilon_o \underline{E} + \underline{P}_e - \frac{1}{2}\underline{\nabla} \cdot \underline{\underline{Q}}_e + \frac{1}{6}\underline{\nabla} \cdot \underline{\nabla} \cdot \underline{\underline{\underline{O}}}_e - \ldots \\ &\quad + (j\omega\mu_o)^{-1} \left[\underline{\nabla} \times \underline{P}_m - \frac{1}{2}\underline{\nabla} \times \left(\underline{\nabla} \cdot \underline{\underline{Q}}_m \right) + \frac{1}{6}\underline{\nabla} \times \left(\underline{\nabla} \cdot \underline{\nabla} \cdot \underline{\underline{\underline{O}}}_m \right) - \ldots \right] \end{aligned} \quad (12)$$

$$\begin{aligned} \underline{B} &= \mu_o \underline{H} + \underline{P}_m - \frac{1}{2}\underline{\nabla} \cdot \underline{\underline{Q}}_m + \frac{1}{6}\underline{\nabla} \cdot \underline{\nabla} \cdot \underline{\underline{\underline{O}}}_m - \ldots \\ &\quad + (j\omega\epsilon_o)^{-1} \left[\underline{\nabla} \times \underline{P}_e - \frac{1}{2}\underline{\nabla} \times \left(\underline{\nabla} \cdot \underline{\underline{Q}}_e \right) + \frac{1}{6}\underline{\nabla} \times \left(\underline{\nabla} \cdot \underline{\nabla} \cdot \underline{\underline{\underline{O}}}_e \right) - \ldots \right] \end{aligned} \quad (13)$$

In general,

$$\underline{D} = \epsilon_o \underline{E} + \sum_{n=1}^{\infty} \frac{(-1)^{n-1}}{n!} \underline{\nabla}^{n-1} \cdot \underline{P}_e^{(2^n)} + (j\omega\mu_o)^{-1} \underline{\nabla} \times \sum_{n=1}^{\infty} \frac{(-1)^{n-1}}{n!} \underline{\nabla}^{n-1} \cdot \underline{P}_m^{(2^n)} \quad (14)$$

$$\underline{B} = \mu_o \underline{H} + \sum_{n=1}^{\infty} \frac{(-1)^{n-1}}{n!} \underline{\nabla}^{n-1} \cdot \underline{P}_m^{(2^n)} + (j\omega\epsilon_o)^{-1} \underline{\nabla} \times \sum_{n=1}^{\infty} \frac{(-1)^{n-1}}{n!} \underline{\nabla}^{n-1} \cdot \underline{P}_e^{(2^n)} \quad (15)$$

where we have denoted $\underline{P}^{(2)}_{e,m} \equiv \underline{P}_{e,m}$, $\underline{P}^{(4)}_{e,m} \equiv \underline{\underline{Q}}_{e,m}$, $\underline{P}^{(8)}_{e,m} \equiv \underline{\underline{\underline{O}}}_{e,m}$, ... For spatially non-dispersive media ($\underline{\nabla} \cdot \underline{P}_{kl} = \underline{\nabla} \cdot \underline{\nabla} \cdot \underline{\underline{Q}}_{kl} = \underline{\nabla} \cdot \underline{\nabla} \cdot \underline{\nabla} \cdot \underline{\underline{\underline{O}}}_{kl} = \ldots = \underline{0}$), we can use:-

$$\underline{\nabla} \cdot \left(\underline{\underline{Q}}_{kl} \cdot \underline{A} \right) = \underline{\underline{Q}}_{kl} \cdot \underline{\nabla}\, \underline{A}, \quad \underline{\nabla} \cdot \underline{\nabla} \cdot \left(\underline{\underline{\underline{O}}}_{kl} \cdot \underline{A} \right) = \underline{\underline{\underline{O}}}_{kl} \cdot \underline{\nabla}\, \underline{\nabla}\, \underline{A}, \quad \ldots \tag{16}$$

to express $\underline{D}$ and $\underline{B}$ in terms of the source fields and its spatial derivatives. For example, in a dipole-quadrupole model of the medium:-

$$\begin{aligned}
\underline{D} \;=\; & \epsilon_o \left(\underline{\underline{I}} + \underline{\underline{P}}_{ee} \right) \cdot \underline{E} + \frac{1}{2} \epsilon_o \left(\underline{\underline{Q}}'_{ee} - \underline{\underline{Q}}_{ee} \right) \cdot \underline{\nabla}\, \underline{E} + \ldots \\
& + (j\omega)^{-1} \sqrt{\frac{\epsilon_o}{\mu_o}} \left(\underline{\nabla} \times \underline{\underline{P}}_{me} \right) \cdot \underline{E} + \frac{1}{2} (j\omega)^{-1} \sqrt{\frac{\epsilon_o}{\mu_o}} \left[\underline{\nabla} \times \left(\underline{\underline{Q}}'_{me} - \underline{\underline{Q}}_{me} \right) \right] \cdot \underline{\nabla}\, \underline{E} + \ldots \\
& + \sqrt{\mu_o \epsilon_o}\, \underline{\underline{P}}_{em} \cdot \underline{H} + \frac{1}{2} \sqrt{\mu_o \epsilon_o} \left(\underline{\underline{Q}}'_{em} - \underline{\underline{Q}}_{em} \right) \cdot \underline{\nabla}\, \underline{H} + \ldots \\
& + (j\omega)^{-1} \left(\underline{\nabla} \times \underline{\underline{P}}_{mm} \right) \cdot \underline{H} + \frac{1}{2} (j\omega)^{-1} \left[\underline{\nabla} \times \left(\underline{\underline{Q}}'_{mm} - \underline{\underline{Q}}_{mm} \right) \right] \cdot \underline{\nabla}\, \underline{H} + \ldots
\end{aligned} \tag{17}$$

$$\begin{aligned}
\underline{B} \;=\; & \mu_o \left(\underline{\underline{I}} + \underline{\underline{P}}_{mm} \right) \cdot \underline{H} + \frac{1}{2} \mu_o \left(\underline{\underline{Q}}'_{mm} - \underline{\underline{Q}}_{mm} \right) \cdot \underline{\nabla}\, \underline{H} + \ldots \\
& + (j\omega)^{-1} \sqrt{\frac{\mu_o}{\epsilon_o}} \left(\underline{\nabla} \times \underline{\underline{P}}_{em} \right) \cdot \underline{H} + \frac{1}{2} (j\omega)^{-1} \sqrt{\frac{\mu_o}{\epsilon_o}} \left[\underline{\nabla} \times \left(\underline{\underline{Q}}'_{em} - \underline{\underline{Q}}_{em} \right) \right] \cdot \underline{\nabla}\, \underline{H} + \ldots \\
& + \sqrt{\mu_o \epsilon_o}\, \underline{\underline{P}}_{me} \cdot \underline{E} + \frac{1}{2} \sqrt{\mu_o \epsilon_o} \left(\underline{\underline{Q}}'_{me} - \underline{\underline{Q}}_{me} \right) \cdot \underline{\nabla}\, \underline{E} + \ldots \\
& + (j\omega)^{-1} \left(\underline{\nabla} \times \underline{\underline{P}}_{ee} \right) \cdot \underline{E} + \frac{1}{2} (j\omega)^{-1} \left[\underline{\nabla} \times \left(\underline{\underline{Q}}'_{ee} - \underline{\underline{Q}}_{ee} \right) \right] \cdot \underline{\nabla}\, \underline{E} + \ldots
\end{aligned} \tag{18}$$

This yields, implicitly, the expansion of the macroscopic constitutive parameters of the effective medium as a multi-polarisability series. For bianisotropic media:-

$$\underline{D} = \underline{\underline{\epsilon}} \cdot \underline{E} + \underline{\underline{\xi}} \cdot \underline{H}, \quad \underline{B} = \underline{\underline{\zeta}} \cdot \underline{E} + \underline{\underline{\mu}} \cdot \underline{H} \tag{19}$$

As the frequency increases this requires further higher-order multipole contributions.
A more general method for the multipole expansion in complex space uses a series representation with spherical harmonics as basis functions [8].

5 Numerical example

The recursive multi-polarisability algorithm (RMA) has been applied to the characterisation of a single copper helix in the dipole-quadrupole approximation. Helices can be used for the manufacturing of synthetic chiral or bianisotropic media. The helix has three turns with diameter 1mm, pitch 0.5mm, wire gauge 0.15mm and is embedded in an isotropic low-loss dielectric host medium ($[\epsilon_r]_{host} = 3.4 - j0.008$, $[\mu_r]_{host} = 1$). The helix axis defines the oz-axis. The induced currents were computed with a moment method technique in the thin-wire approximation using the Numerical Electromagnetics Code (NEC–4). The helix is modelled as a polygonal structure consisting of 60 uniform cylindrical segments inscribing the actual helix. A study on the effect of helix segmentation on the numerical accuracy has shown that near the first helix resonance frequency, a length-to-radius ratio per segment between 1.05 and 1.40 yields the smallest variation of the computed current as

a function of the segmentation [5]. The slightly coarser segmentation with somewhat longer segments was chosen here to reduce the computation time and to increase numerical accuracy at low frequencies. The dipolarisability dyadics (not shown here) were found to be similar to those shown in [6, 7] except for a shift in the resonance frequency due to the value of ϵ_{host}. The 27 components of the tryadic $\underline{\underline{\underline{q}}}_{ee}$ are shown in Figs 2–4, expressed in m^4. The first index refers to the direction of polarisation for $\underline{E}$. Of all four $\underline{\underline{\underline{q}}}_{kl}$ only $\underline{\underline{\underline{q}}}_{ee}$ was found to exhibit nonzero static components.

6 Conclusions

The RMA enables a complete and rigorous characterisation to be made of general complex-shaped particles in composite media at arbitrary frequencies. In comparison with the complex multipole expansion which is based on spherical harmonics, the method used here is iterative and computationally more intensive if the order to which the multipole moments are included in the model is high. It is, however, conceptually simpler and leads to an easier physical interpretation of the obtained expansion coefficients.

References

[1] Graham, E B and Raab, R E; Light propagation in cubic and other anisotropic crystals; *Proc Roy Soc Lond, A,* vol 430 (1990), pp 593–614.

[2] Barron, L D; *Molecular light scattering and optical activity;* Cambridge University Press, Cambridge (1982), Ch 2.

[3] Brewitt-Taylor, C R; Modelling of helix-loaded chiral radar-absorbing layers; in: Priou, A; *Progress in Electromagnetics Research (PIER 9);* Monograph series, vol 9, EMW Publishing, Cambridge, MA (1994), pp 289–310.

[4] Mariotte, F, Tretyakov, S A and Sauviac, B; Isotropic chiral composite modeling: comparison between analytical, numerical and experimental results; *Microw Opt Tech Lett,* vol 7 no 18 (1994), pp 861–864.

[5] Arnaut, L R; *Design of synthetic chirals;* UMIST report to British Aerospace, contract no 040894 (1994), part IV/1.

[6] Arnaut, L R; Computation of dipolarisability tensors of helix-based bianisotropic media; *Proc 2nd 'Journées Maxwell'* (6–9 June 1995, Bordeaux, France), pp 319–327.

[7] Arnaut, L R; Mutual coupling between bianisotropic particles: a theoretical study; in: Kong, J A; *Progress in Electromagnetics Research (PIER 16);* Monograph series, vol 16, EMW Publishing, Cambridge, MA (1997), pp 35–66.

[8] Jackson, J D; *Classical Electrodynamics;* 2nd edition (1975), Ch 16.

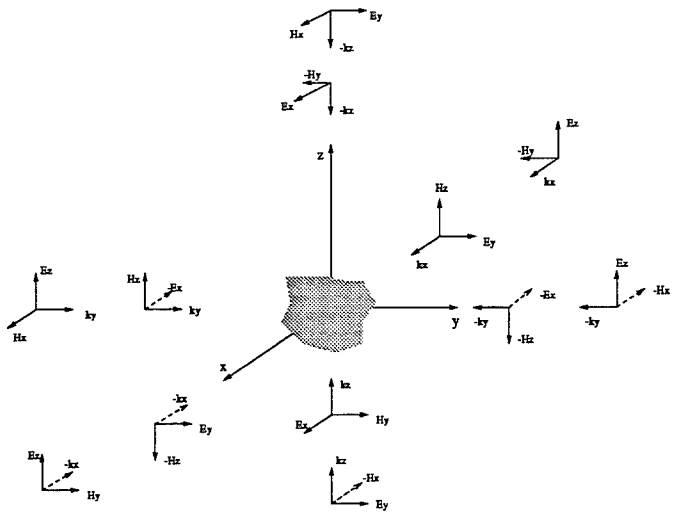

Figure 1: Excitation scheme for method of counterpropagating waves for a complex-shaped particle.

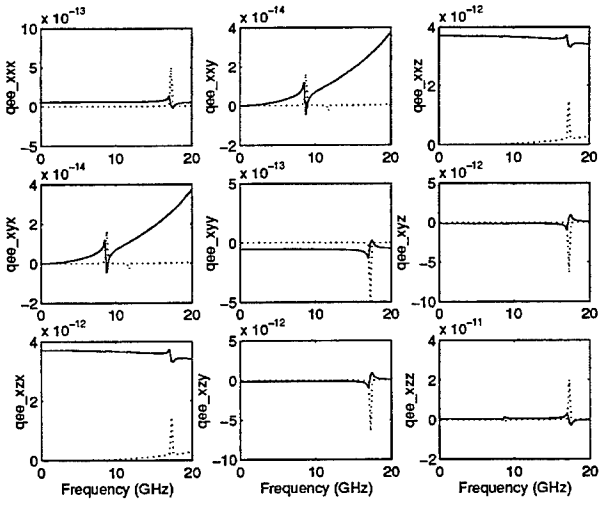

Figure 2: Components $x * *$ of $\underline{\underline{q}}_{ee}$ as a function of frequency. — = real part, $\cdots$ = imaginary part.

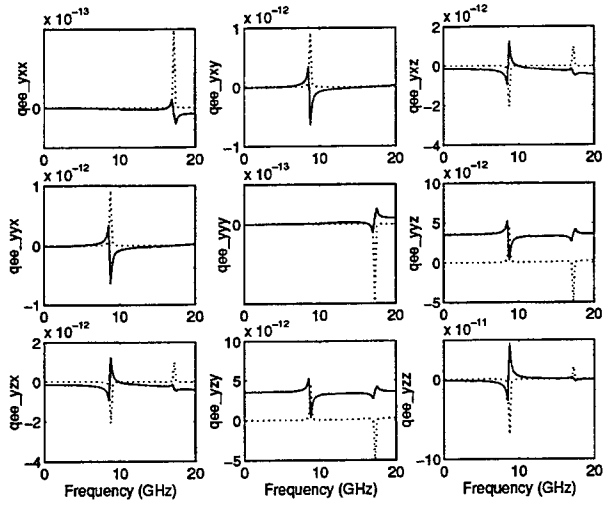

Figure 3: Components $y**$ of $\underline{\underline{q}}_{ee}$ as a function of frequency. — = real part, $\cdots$ = imaginary part.

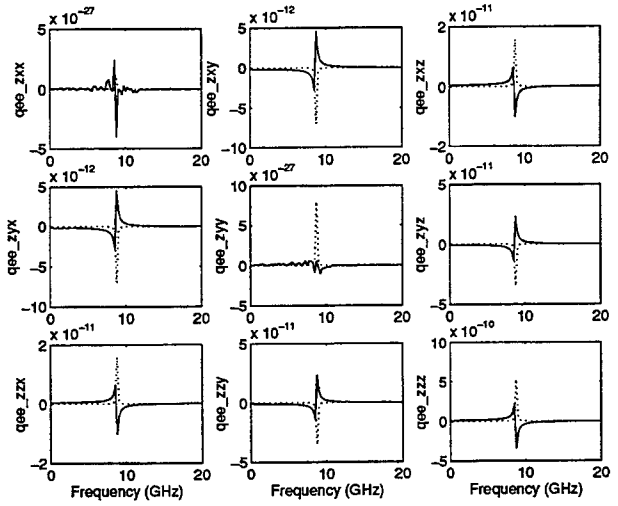

Figure 4: Components $z**$ of $\underline{\underline{q}}_{ee}$ as a function of frequency. — = real part, $\cdots$ = imaginary part.

Experimental Confirmation of a Numerical Constitutive Parameters Extraction Methodology for Uniaxial Bianisotropic Chiral Materials

Keith W. Whites
Department of Electrical Engineering
University of Kentucky
453 Anderson Hall
Lexington, KY 40506-0046

Chee Y. Chung
Intel Technology Sdn. Bhd.
Penang Package Tech. Dev.
Bayan Lepas Free Industrial Zone
11900 Penang, Malaysia

I. INTRODUCTION

A uniaxial bianisotropic chiral (UBC) material can be constructed, among other ways, by aligning "uniaxial helices" (or other uniaxial chiral particles) in a regular lattice such that their axes are parallel to each other. This type of material has possible electromagnetics applications as polarization transformers, filter devices and absorbers, among others [1-3]. (For additional references on UBC material research, the reader is referred to [4, 5].) We have previously modeled this UBC material numerically and presented a technique for extracting its effective constitutive parameters in [6]. A number of theoretical tests were undertaken there to validate this methodology and the results were promising. Since then, two UBC slabs were fabricated by embedding uniaxial helices in an epoxy host. In this paper, some of the comparisons of the measured and predicted scattering by these samples is presented.

In the characterization technique for UBC materials in [6], the effective material parameters of the composite are extracted using purely computational methods. Given the periodic arrangement, it was found that only *uniaxial helices* can be used to model a UBC material. Thus, there are restrictions on the dimensions of the helices as well as the frequency of the illuminating field such that their non-uniaxial behaviors are negligible. Provided these restrictions are satisfied, the constitutive equations for such a UBC material are [1-3]

$$\begin{aligned} \overline{D} &= \overline{\overline{\varepsilon}} \cdot \overline{E} + \overline{\overline{\xi}} \cdot \overline{H} \\ \overline{B} &= \overline{\overline{\zeta}} \cdot \overline{E} + \overline{\overline{\mu}} \cdot \overline{H} \end{aligned} \tag{1}$$

where

$$\overline{\overline{\varepsilon}} = \varepsilon_0 \begin{bmatrix} \varepsilon_{rx} & 0 & 0 \\ 0 & \varepsilon_r & 0 \\ 0 & 0 & \varepsilon_r \end{bmatrix}, \quad \overline{\overline{\mu}} = \mu_0 \begin{bmatrix} \mu_{rx} & 0 & 0 \\ 0 & \mu_r & 0 \\ 0 & 0 & \mu_r \end{bmatrix}, \quad \overline{\overline{\xi}} = \begin{bmatrix} -j\kappa\sqrt{\mu_0\varepsilon_0} & 0 & 0 \\ 0 & 0 & 0 \\ 0 & 0 & 0 \end{bmatrix} = -\overline{\overline{\zeta}} \tag{2}$$

in a Cartesian frame assuming, without loss of generality, that the optic axis of the lattice of helices is in the x-direction. In addition to the anisotropy of these materials, there is also magnetoelectric coupling on a microscopic level which is accounted for by the chirality parameter κ.

The composite UBC material slabs used in this investigation were manufactured by embedding electromagnetically small metallic helices in an epoxy host. It is believed that these are the first ever manufactured artificial UBC samples using helices as chiral inclusions and the computed effective

medium parameters are the first ever presented for physically realized UBC materials [7]. Chiral samples composed of aligned helices were previously fabricated in [8] and the scattering response was measured but these samples were neither characterized nor shown to be effective UBC materials. Another form of composite uniaxial chiral material was successfully constructed in [9, 10] by sequentially rotating "chiral hooks" through 90^{o} within a unit cell.

II. Sample Fabrication and Scattering Measurement System

Our composite UBC slabs were manufactured by embedding electromagnetically small beryllium copper helices in Stycast 1365-90 from Emerson & Cuming, Inc. Stycast 1365-90 is a two-part epoxy resin which cures to a nearly transparent, semi-flexible solid. Two UBC samples were manufactured: one composed of three and the other with four layers of particles. The wire helices used were right handed with five-turns where the radius of helix = 0.433, the pitch = 0.26 and the wire radius = 0.057 mm. With these dimensions, it was determined from studying the scattering of a single helix and its induced dipole moments, using the criterion in [6], that they closely resemble *uniaxial scatterers* within the frequency band of the measurement system (8.2-12.5 GHz). The three-layer sample had average unit-cell dimensions $D_x = 2.00$, $D_y = 1.77$ and $D_z = 2.86$ mm, as illustrated in Fig. 1, while the four-layer sample had $D_x = 3.03$, $D_y = 3.02$ and $D_z = 2.74$ mm. Scanned images of portions of both samples are shown in Fig. 2.

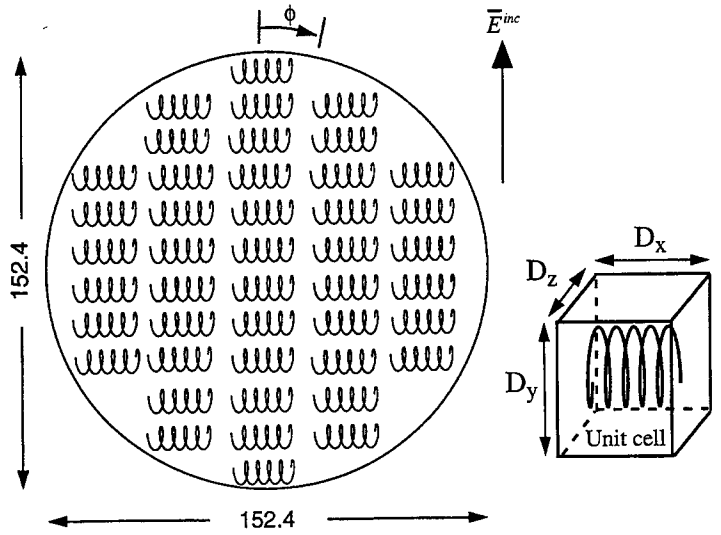

Figure 1 Geometry of the UBC samples (units of mm). The z direction is perpendicular to the sample face.

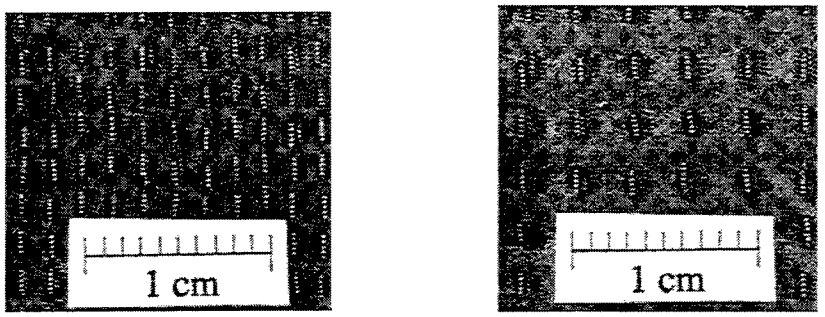

(a) (b)

Figure 2 Images of the (a) three layer and (b) four layer UBC samples.

A free-space measurement system was used to measure the scattering parameters of the UBC samples. This system has been previously used to measure the scattering of isotropic chiral materials [11, 12]. The main components of the system are two circular lensed horn antennas and a Hewlett-Packard 8510B vector network analyzer (VNA). The antennas were located on a two-piece optical plate and connected to the VNA through flexible, low-loss coaxial cables. The samples were mounted on a sample holder positioned near the common focal plane of the two antennas. This experimental set-up operates in the X-band from 8.2 to 12.5 GHz. The distance between the two antennas was measured to be 61.29 cm while the spot sizes of the two antennas in the focal plane are approximately 3.2 cm (E-plane) by 4.3 cm (H-plane) as given by the manufacturer.

The experimental set-up was calibrated using the Thru-Reflect-Line (TRL) method [13]. A firmware time gate of width 1.35 ns was used to help minimize the non-TEM multiple scattering effects between the sample and the horn antennas. No averaging of the signals was employed. The accuracy of the measured scattering parameters were previously reported to be within approximately 0.15 dB for magnitude and $\pm 5^{\circ}$ for phase [11]. The co-polarized reflected and transmitted scattering from the samples was measured by having the two antennas oriented in the same way while the cross-polarized transmission was measured by orienting the two antennas orthogonal to one other. Reflection cross-polarization cannot be measured with this configuration of the free-space measurement facility.

III. SCATTERING PARAMETER COMPARISONS

The effective constitutive parameters for these two samples were computed as a function of frequency using the methodology of [6] and can be found in [7]. It was then possible, using these material parameters, to compute the predicted plane-wave scattering by these UBC slabs with arbitrary thickness. These solutions are termed the *predicted* results in the comparisons with the measured data shown in Figs. 3 and 4. In these figures the predicted and measured scattering for the reflection co-polarized and transmission co- and cross-polarized coefficients are shown.

To quantify the repeatability and variability of the reflection and transmission coefficient measurements, the *S*-parameters for each sample orientation and frequency were measured four times for a single TRL calibration of the measurement facility. The set-up was recalibrated and the *S*-parameters

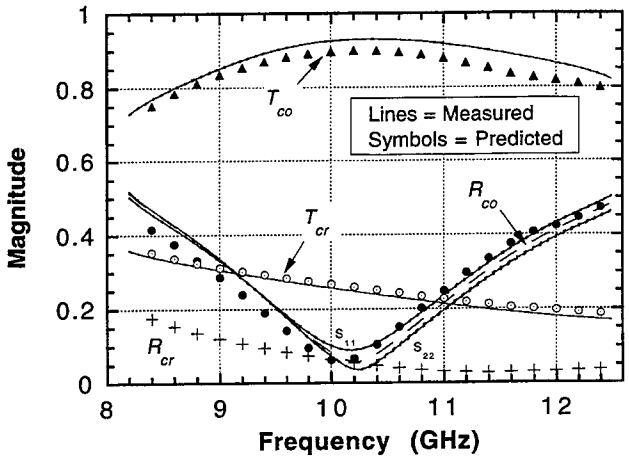

3(a)

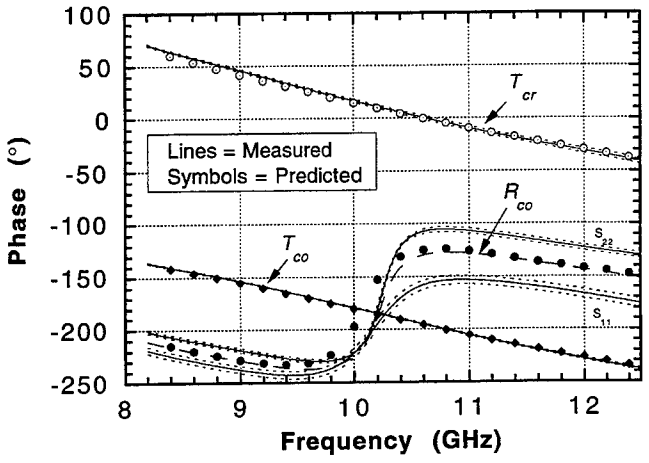

3(b)

Figure 3 Comparisons of the measured and predicted scattering by the three-layer UBC sample for $\phi = 0°$. (a) Magnitude and (b) phase. In (a), the predicted cross polarized reflection is indicated as R_{cr}.

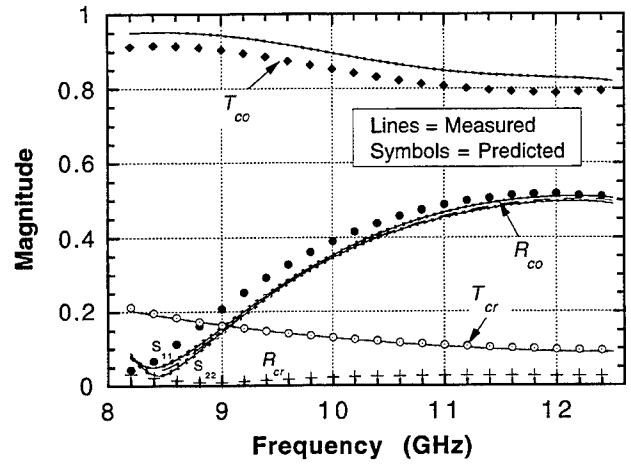

4(a)

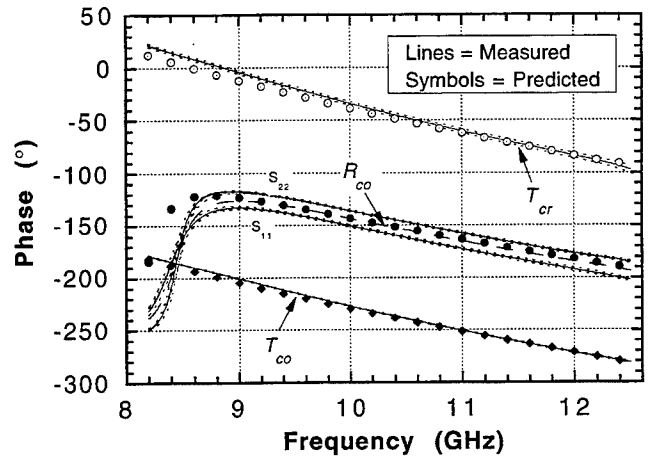

4(b)

Figure 4 Comparisons of the measured and predicted scattering by the four-layer UBC sample for $\phi = 180°$. (a) Magnitude and (b) phase. In (a), the predicted cross polarized reflection is indicated as R_{cr}.

remeasured another four times. This entire procedure was repeated four times for a total of 16 measurements. Because of the anisotropic nature of this composite material and the definition of the sample rotation angle ϕ, as shown in Fig. 1, S_{22} and S_{12} are measured at angle ϕ, while S_{11} and S_{21} are measured at 180°-ϕ. This latter angle for S_{11} and S_{21} is partially a consequence of the ideal two-fold rotational symmetry of the samples about a normal to the sample face if the sample was constructed perfectly. For the actual laboratory samples, only an approximate two-fold rotational symmetry was observed.

The average and standard deviation of these parameters S_{ij}, referenced to the planes of the slab facing each of the ports (i,j =1,2), were computed using the 16 measurements. Shown in the solid lines of Figs. 3 and 4 are the average S_{11} and S_{22} parameters while plus and minus one standard deviation is given by the dotted lines. Further averaging was then performed assuming that the sample is symmetric when viewed from ports 1 and 2. In particular, average co-polarized reflection and transmission coefficients were computed as

$$R_{co} \equiv \frac{1}{2N}\sum_{n=1}^{N}\left[S_{22}(\phi)+S_{11}(180°-\phi)\right] \quad , \quad T_{co} \equiv \frac{1}{2N}\sum_{n=1}^{N}\left[S_{12}(\phi)+S_{21}(180°-\phi)\right] \tag{3}$$

with N = 16 measurements. The average of R_{co} is given by the dashed lines in Figs. 3 and 4. Due to the high correlation between the S_{12} and S_{21} measurements, the standard deviation of T_{co} was computed from the total 32 data points, unlike that for R_{co}, and the average of the individual S_{12} and S_{21} parameters is not shown. The cross-polarized transmission coefficients, T_{cr}, are reported from only port 2 measurements (S_{12}) and orthogonal orientations of the horn antennas. The average (solid lines) and standard deviation (dotted lines) involve N = 16 measurements for S_{12} at ϕ, with the average defined as

$$T_{cr} \equiv \frac{1}{N}\sum_{n=1}^{N} S_{12}(\phi) \tag{4}$$

It is quite evident in these results that the sample is not entirely symmetric since the reflection coefficients are not the same when the excited port is switched ($S_{11} \leftrightarrow S_{22}$) as would be expected from a symmetric slab. The sources for this error are difficult to identify but one appreciable contribution to this error is probably non-uniform layer thicknesses. Consequently, the measured coefficients for both ports were averaged here with the intention of reducing this error. The transmission coefficients have a much smaller slab asymmetry error principally because of reciprocity and the fact that the orientation of the helices in the axial direction of Fig. 1 was well maintained during construction of these samples.

IV. CONCLUSION

Observing these comparisons given in Figs. 3 and 4, it can be seen that the measured and predicted results are in good agreement. These comparisons serve as a convincing verification of the accuracy and correctness of the algorithm presented in [6] as well as the accuracy of the UBC material description for these ordered arrangements of electromagnetically small, handed inclusions. Additional comparisons of the scattering by these samples with the theoretically predicted results will be shown.

REFERENCES

1. I. V. Lindell and A. J. Viitanen, "Plane wave propagation in uniaxial bianisotropic medium," *Electron. Lett.*, vol. 29, no. 2, pp. 150-152, 1993.

2. A. J. Viitanen and I. V. Lindell, "Uniaxial chiral quarter-wave polarisation transformer," *Electron. Lett.*, vol. 29, no. 12, pp. 1074-1075, 1993.

3. I. V. Lindell and A. H. Sihvola, "Plane-wave reflection from uniaxial chiral interface and its application to polarization transformation," *IEEE Trans. Antennas Propagat.*, vol. 43, no. 12, pp. 1397-1404, 1995.

4. C. Y. Chung, "Electromagnetic analysis of a composite uniaxial bianisotropic chiral material," M. S. thesis, University of Kentucky, 1995.

5. U. B. Unrau, "A bibliography on research in the field of bi-anisotropic, bi-isotropic and chiral media and their applications," *Proceedings of Chiral'94*, Perigueux, France, pp. A1-A48, 1994.

6. C. Y. Chung and K. W. Whites, "Effective constitutive parameters for an artificial uniaxial bianisotropic chiral medium," *J. Electromagn. Waves Appl.*, vol. 10, no. 10, pp. 1363-1388, 1996.

7. K. W. Whites and C. Y. Chung, "Composite uniaxial bianisotropic chiral materials characterization: comparison of predicted and measured results," *J. Electromagn. Waves Appl.*, vol. 11, pp. 271-394, to appear, 1997.

8. F. Guérin, "Contribution a l'étude théorique et expérimentale des matériaux composites chiraux et bianisotropes dans le domaine microonde (A contribution to the theoretical and experimental study of chiral and bianisotropic materials at microwave frequencies)," D. Sc. dissertation, University of Limoges, France, 1995.

9. I. P. Theron and J. H. Cloete, "The optical activity of an artificial non-magnetic uniaxial chiral crystal at microwave frequencies," *J. Electromagn. Waves Appl.*, vol. 10, no. 4, pp. 539-561, 1996.

10. I. P. Theron and J. H. Cloete, "The electric quadrupole contribution to the circular birefringence of nonmagnetic anisotropic chiral media: a circular waveguide experiment," *IEEE Trans. Microwave Theory Tech.*, vol. 44, no. 8, pp. 1451-1459, 1996.

11. K. W. Whites, "Measured and computed EM scattering comparison for chiral-material slabs," *Digest of the 1995 URSI Radio Science International Symposium*, Newport Beach, CA, p. 48, June, 1995.

12. K. W. Whites, "Comparison of computed and measured scattering by artificial chiral material," *Proceedings of Chiral'95*, State College, PA, pp. 17-20, Oct., 1995.

13. D. K. Ghodgaonkar, V. V. Varadan and V. K. Varadan, "A free-space method for measurement of dielectric constant and loss tangents at microwave frequencies," *IEEE Trans. Instrum. Meas.*, vol. 37, no. 3, pp. 789-793, 1989.

A frequency domain dispersion and absorption model for numerically extracting the constitutive parameters of an isotropic chiral slab from measured reflection and transmission coefficients

M. Bingle, I.P. Theron and J.H. Cloete
Department of Electrical and Electronic Engineering
University of Stellenbosch, Stellenbosch
7600 South Africa

email: mbingle@firga.sun.ac.za

Abstract

The constitutive parameters of a material can be determined (at each frequency) by direct inversion of measured scattering coefficients. This technique to determine the constitutive parameters of an isotropic chiral slab is accurate except for weakly absorbing samples at frequencies where the sample thickness is multiples of half a wavelength. These inaccuracies have been mostly eliminated by an inversion algorithm due to Baker-Jarvis *et al.* [1]. They use a nonlinear least-squares solution with causality constraints to determine the permittivity and permeability from scattering equations. This paper is concerned with the extension of the Baker-Jarvis technique to determine the constitutive parameters of an isotropic chiral slab with unknown permittivity, permeability and chirality from the measured scattering parameters. Material parameter models for the permittivity and permeability and chirality are chosen in accordance with the classical models of polarization and a multipole description of isotropic chiral materials. Results are presented for the material parameters of artificial isotropic chiral material slabs calculated from the measured scattering parameters. The model-based constitutive parameter extraction shows an improved and physically more credible solution than the direct inversion technique, especially for weakly absorbing samples at frequencies where the sample thickness is multiples of half a wavelength.

1 Introduction

The free-space measurement procedure for material parameters involves the measurement of the transmission and reflection coefficients at normal incidence of a material sample and the computation of the constitutive parameters from the measured scattering coefficients. The direct inversion technique [2, 3] to determine the constitutive parameters of an isotropic chiral slab involves the reduction of scattering data on a frequency-by-frequency basis. This technique is accurate except for weakly absorbing samples at frequencies where the sample thickness is multiples of half a wavelength [2].

Baker-Jarvis *et al.* [1] presented a nonlinear least-squares solution to determine the permittivity and permeability from scattering equations. Frequency dependent models for the material parameters, with constant coefficients, are chosen consistent with linearity and causality constraints. The constitutive parameters are obtained by estimating the coefficients of the models. The resulting scattering parameters are fitted to the measured scattering parameters by minimising the sum of the squares of the differences between the predicted and measured scattering parameters. An advantage of the model-based parameter extraction is that correlations are allowed between neighbouring frequency measurements.

This paper is concerned with the extension of the Baker-Jarvis technique to determine the constitutive parameters of an isotropic chiral slab from the measured scattering parameters.

2 Constitutive and scattering parameter relations

Isotropic chiral materials are sufficiently described with an additional (to ϵ and μ) constitutive parameter ξ. Raab and Cloete [4] use a multipole description to characterise chiral materials and show that for an isotropic chiral material the contribution of the electric quadrupole moment averages out. From the subsequent work of Theron and Cloete [5] it can be concluded that the frequency domain constitutive relations in the Post-Jaggard form [6],

$$\mathbf{D} = \epsilon\mathbf{E} + j\xi\mathbf{B} \quad (1)$$

$$\mathbf{H} = \mu^{-1}\mathbf{B} + j\xi\mathbf{E} \quad (2)$$

adequately represent isotropic chiral matter. Here ξ is the chiral admittance, ϵ the permittivity and μ the permeability of the isotropic chiral medium. A time-harmonic excitation in the $e^{j\omega t}$ convention is implicit. (Note that ξ is a pseudo-scalar and ours differs from Jaggard's by a factor of -1.) With the appropriate terms retained, these are consistent with the constitutive relations of Barron [7] and the chirality parameter ξ is related to the quantum mechanical expressions for the molecular property tensors derived in [7].

The scattering parameters of a chiral slab for normal incidence of a linearly polarized plane wave were derived by Bassiri *et al.* [6].

3 Model for permittivity, permeability and chirality determination

It is important (especially for wide-band data and extrapolation outside the measurement band) that the frequency dependent models for the material parameters are good and physically sound. The models for the permittivity and permeability were chosen according to the classical oscillator model of polarization. Each includes a Debye and a Lorentz term [8],

$$\epsilon_r = a_1 + \frac{a_2}{1/\tau + j\omega} + \frac{a_3}{\omega_o^2 - \omega^2 + j\Gamma\omega}. \quad (3)$$

All constants are real and positive. A complete expansion for a physical medium would need a number of resonator terms, some with resonating frequencies well into the optical frequency range. The constant a_1 may be larger than one to include the effect of resonance terms far above the measurement band.

The quantum mechanical expressions for the molecular property tensors [7] provided the frequency dependent model for ξ. The model accounts for absorption of radiation near resonance; two resonator terms are included. All constants are real and $\omega_{01,02}$ and $\Gamma_{1,2}$ are positive,

$$\xi = \frac{\omega C_1}{\omega_{01}^2 - \omega^2 + j\omega\Gamma_1} + \frac{\omega C_2}{\omega_{02}^2 - \omega^2 + j\omega\Gamma_2}. \quad (4)$$

4 Numerical algorithm

The technique of Baker-Jarvis *et al.* [1] was implemented with a different numerical algorithm. Solving for the constants defining the parameters involves a multidimensional minimisation of the error function. This function has numerous local minima and the problem is to optimise to the correct minimum. It was decided to use a non-derivative based technique. Powell's quadratically convergent method was implemented with the simplest bracketing and a Golden section search [9] for the minimum along each direction.

The existence of alternate sub-optima in the mathematical model requires a reasonable initial guess in order to converge to the correct solution. Baker-Jarvis *et al.* [1] required that the starting values be within

10% to 20% of the correct values. This is quite a tight specification. The starting values for the model constants are obtained from the direct solution for ϵ, μ and ξ [2, 3]. The models of the medium parameters are fitted in the same least squares manner (as the S-parameters) to the material parameters from the direct inversion technique. In order to avoid errors due to half-wave effects, frequencies where S_{11} is less than the average are not included in this fitting. The advantage of fitting to the material parameters of the direct inversion to initialise the constants rather than fitting to the measured S-parameters is twofold. ϵ and μ only appear as a product in the S-parameter equations and iterating ϵ with the wrong μ (and *vice versa*) may result in bad initial values for the constants. The effects of ϵ and μ are separated with the direct inversion. Secondly, the computation of ϵ and μ is much faster than that of the S-parameters.

Since the system is over determined it is possible to optimise for other variables, e.g. the sample thickness and sample position, which has to remain fixed in the direct inversion techniques [1]. The starting value of the sample thickness is, however crucial and it is important to measure the thickness reasonably accurately and only allow iterations when the other parameters have converged to a reasonable degree.

5 Measurements and results for material parameters

Artificial isotropic chiral material slabs (where chiral activity is observed at microwave frequencies) are manufactured by randomly embedding metal helices in a dielectric host medium. A macroscopic constitutive parameter ξ can still be used to describe the chiral medium. The scattering parameters are measured with an HP8510 network analyser in an 11-17 GHz Gaussian beam free space measurement set-up. An uncertainty analysis of the inversion equations for the constitutive parameters of an isotropic, non-magnetic chiral slab [2] showed that the inversion equations are highly sensitive to errors in the measured scattering parameters in the frequency region where the sample is half a wavelength thick or multiples thereof. This is especially true for low loss media where the reflection coefficient goes through deep minima where $d = n\lambda/2$.

Two examples of material measurements with parameter extraction will be presented. The first sample is an example of a lossy host material containing chiral inclusions. The sample consists of a dielectric absorber made from castable material with $70/\text{cm}^3$ right-handed chiral inclusions (40μm Cu wire wound around a 0.8mm nylon mandrel with a 1mm pitch and cut to 2 turns). The effective permittivity of the host with nylon inclusions is approximately $2.7 - j0.65$. The geometry of the chiral inclusions was chosen to show the Cotton effect in the measurement band. The sample thickness was measured to be 10mm and the sample was positioned at 0mm. The measured and predicted S-parameters are compared in Figure 1 (with the sample thickness optimised to d=10.65mm and shifted 0.14mm towards the send antenna). The medium parameters are compared in Figure 2 and there is good agreement between the direct solution and the model-based parameter extraction. Observe that the Cotton resonance is indicated in the chirality parameter ξ.

The second example is of a low loss isotropic chiral sample, with a half-wave effect present at the lower end of the measurement band. The sample was made by randomly embedding nickel-chrome coated stainless steel helices in a silcone rubber ($\epsilon_r = 2.74 - j0.06$) host medium. The three turn helices had a diameter of 1.2mm, a pitch of 0.33mm and wire diameter of 132μm. The helices were encapsulated in polyurethane ($\epsilon_r \approx 2.86 - j0.23$) to prevent them from touching and therefore cause percolation. The sample is 6.7mm thick and there are 220 helices per cubic centimeter. The predicted S-parameters are compared to the measured S-parameters in Figure 3. The material parameters for the direct inversion solution and the model-based parameter extraction are compared in Figure 4. The model-based constitutive parameter extraction shows an improved and physically more credible solution.

6 Conclusion

The inversion technique of Baker-Jarvis *et al.* [1] can be described as a model-based parameter extraction technique to numerically extract the permittivity and permeability of a material. The technique was generalised to include isotropic materials with chiral properties. A frequency dependent model for ξ was chosen to be consistent with a multipole description of an isotropic chiral material and the quantum mechanical expressions for the molecular property tensors. It was found that the initial values for the model constants should be specified quite accurately, therefore the technique is used in conjunction with the direct inversion technique [2] for permittivity, permeability and chirality characterisations in a free-space measurement setup. The material parameters from the direct solution are used to initialise the constants determining ϵ, μ and ξ. The model-based parameter extraction technique was successfully used for a number of other samples where the direct inversion technique had been found inadequate.

Acknowledgement

We wish to thank Dr. Scott Kuehl and Mundus Grové for the careful manufacture of the samples.

References

[1] J. Baker-Jarvis, R.G. Geyer and P.D. Domich, "A nonlinear least-squares solution with causality constraints applied to transmission line permittivity and permeability determination," *IEEE Trans. Instrumentation and Measurement*, vol. 41, pp. 646–652, October 1992.

[2] A.G. Smith, *An Experimental Study of Artificial Isotropic Chiral Media at Microwave Frequencies*, Ph.D. Thesis, Stellenbosch University, Stellenbosch, 1994.

[3] J.H. Cloete and A.G. Smith, "The constitutive parameters of a lossy chiral slab by inversion of plane wave scattering coefficients," *Microwave and Optical Technology Letters*, vol. 5, no. 7, pp. 303–306, 20 June 1992. "Correction", ibid, vol. 7, no. 1, p. 42, January 1994.

[4] R.E. Raab and J.H. Cloete, "An eigenvalue theory of circular birefringence and dichroism in a nonmagnetic chiral medium," *J Electromagnetic Waves and Applications*, vol. 8, no. 8, pp. 1073–1089, 1994.

[5] I.P. Theron and J.H. Cloete, "The electric quadrupole contribution to the circular birefringence of nonmagnetic anisotropic chiral media: a circular waveguide experiment," *IEEE Trans. Microwave Theory and Techniques*, vol. 44, pp. 1451–1459, August 1996.

[6] S. Bassiri, C.H. Papas and N. Engheta "Electromagnetic Wave Propagation Through a Dielectric-Chiral Interface and Through a Chiral Slab," *J Optical Society of America A*, vol. 5, pp. 1450–1459, 1988.

[7] L.D. Barron, *Molecular Light Scattering and Optical Activity*, Cambridge: Cambridge University Press, 1982.

[8] A.R. Von Hippel, *Dielectric Materials and Applications*, Cambridge, Massacusetts: MIT Press, 1954.

[9] W.H. Press, B.P. Flannery, S.A. Teukolsky and W.T. Vetterling, *Numerical Recipes in Pascal — The Art of Scientific Computing*, Cambridge: Cambridge University Press, 1989.

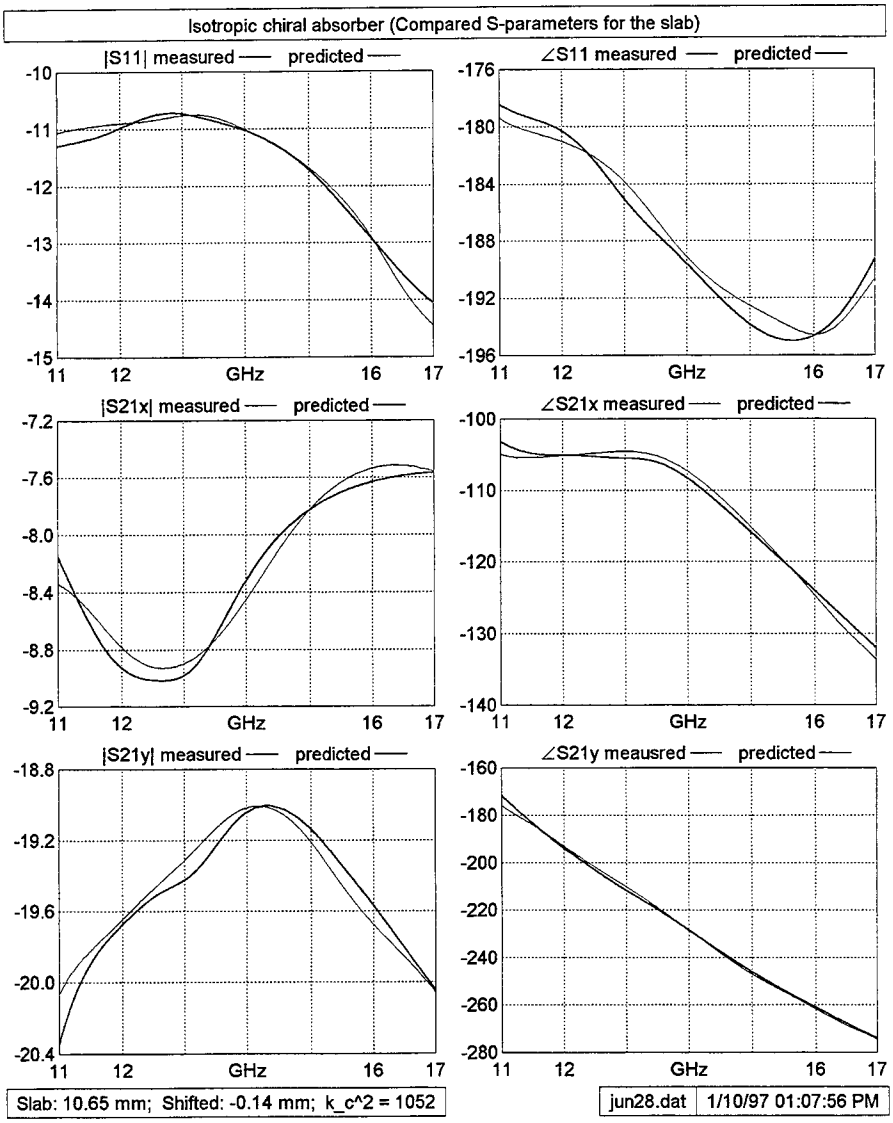

Figure 1: Comparison between the measured and predicted S-parameters of an isotropic chiral sample. (Copper helices embedded in a lossy host medium ($\epsilon_r \approx 2.7 - j0.65$). 2 turn helices of 40μm Cu wire wound around 0.8mm nylon mandrels with 1mm pitch.)

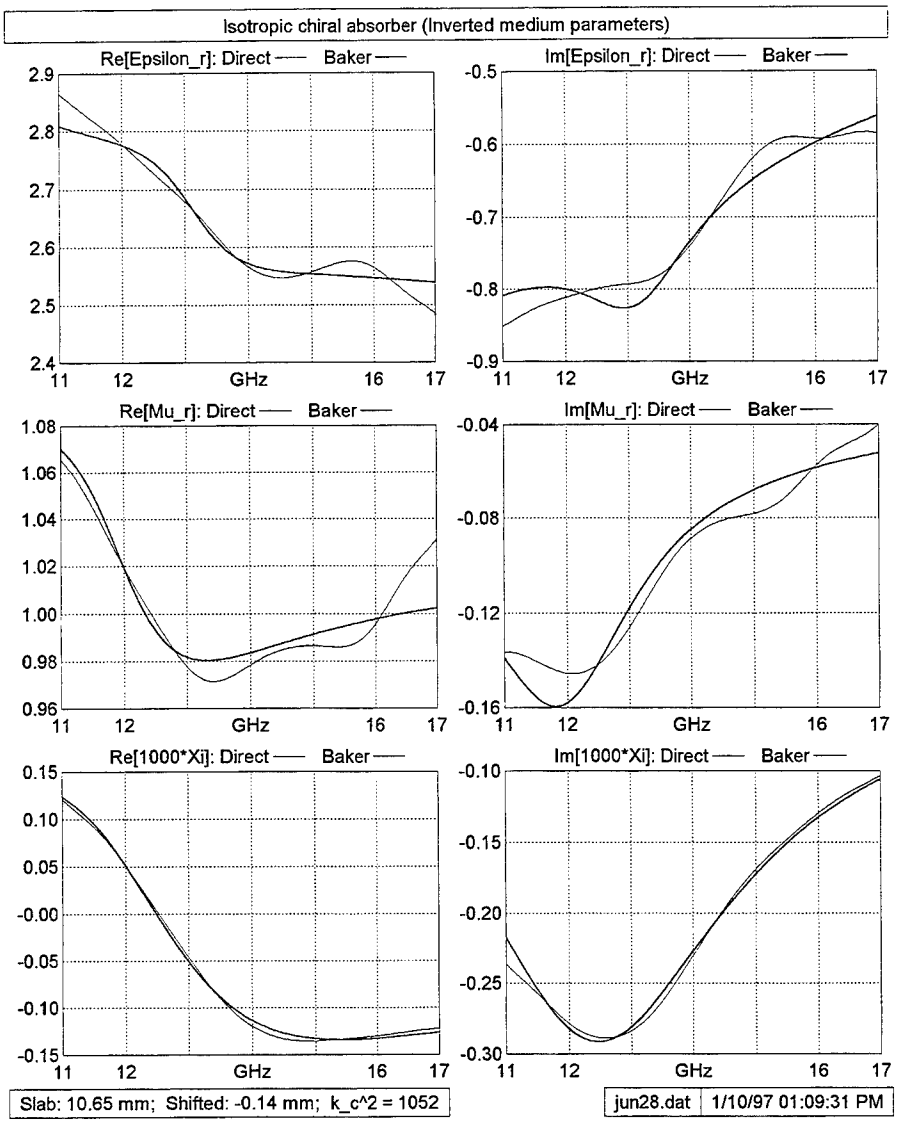

Figure 2: Comparison between the medium parameters of the direct inversion technique and the Baker-Jarvis inversion algorithm for an isotropic chiral sample. (Copper helices embedded in a lossy host medium ($\epsilon_r \approx 2.7 - j0.65$). 2 turn helices of 40$\mu$m Cu wire wound around 0.8mm nylon mandrels with 1mm pitch.)

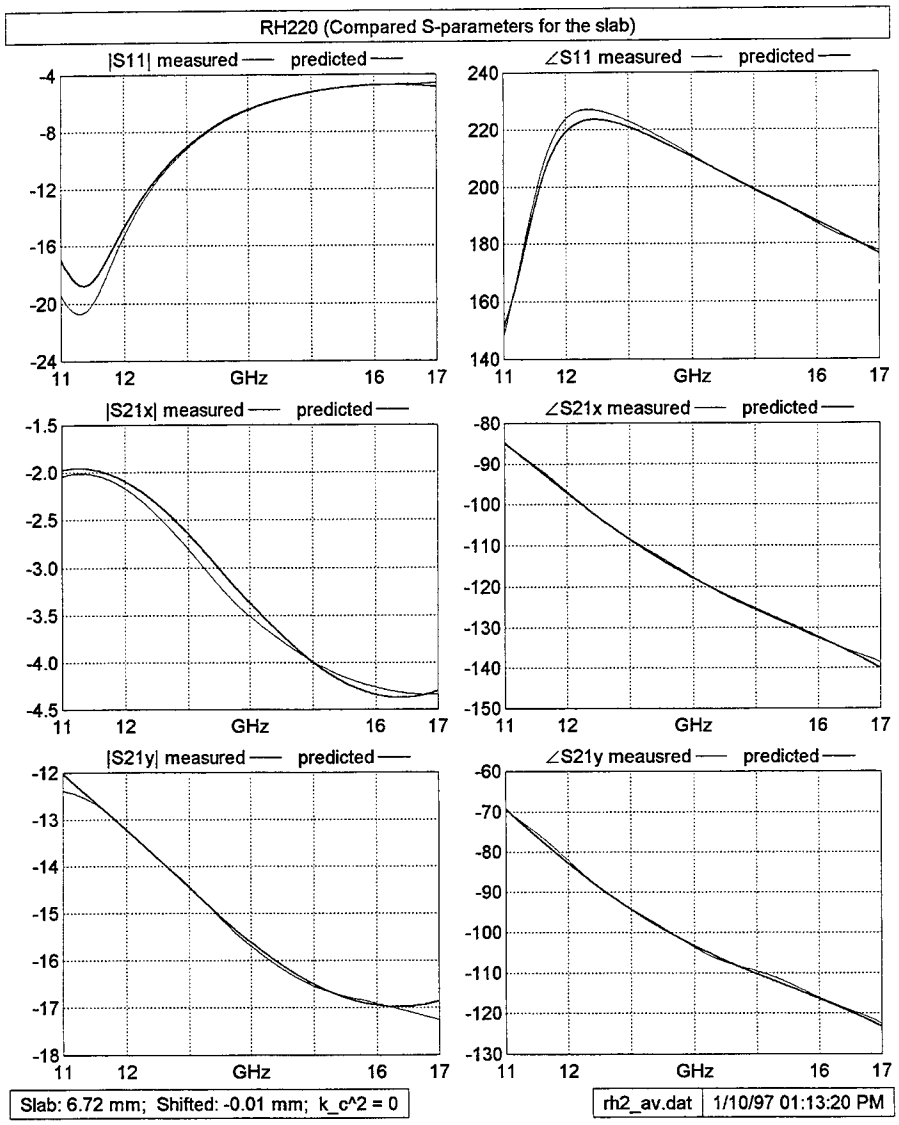

Figure 3: Compared S-parameters of an isotropic (non-magnetic) chiral sample. (Nickel-chrome coated stainless steel helices embedded in a silcone rubber ($\epsilon_r = 2.74 - j0.06$) host medium. 3 turn helices with a diameter of 1.2mm, pitch of 0.33mm and wire diameter of 132μm).)

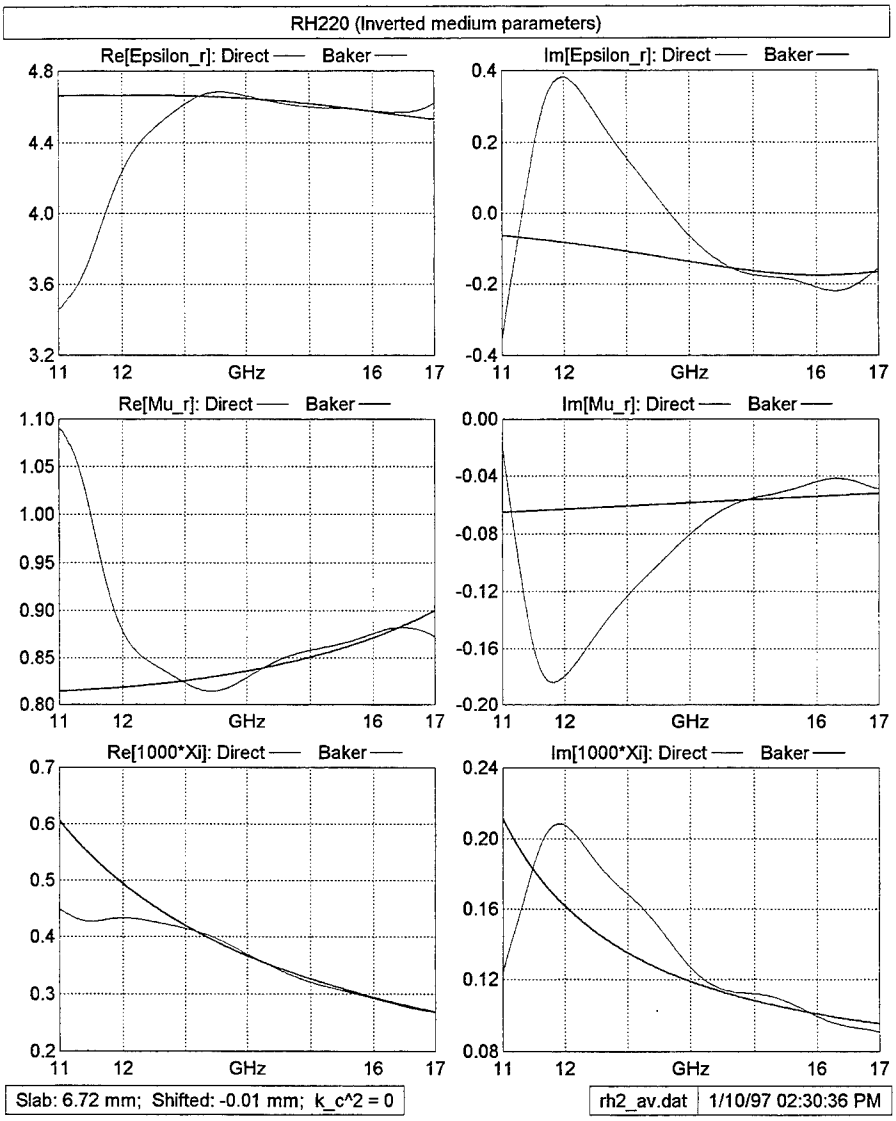

Figure 4: Compared medium parameters of an isotropic non-magnetic chiral sample. (Nickel-chrome coated stainless steel helices embedded in a silcone rubber ($\epsilon_r = 2.74 - j0.06$) host medium. 3 turn helices with a diameter of 1.2mm, pitch of 0.33mm and wire diameter of 132μm).)

SESSION 14:

NEC AND COMPUTER CODES FOR COMPUTATIONAL ELECTROMAGNETICS

Chairs: P. Foster and Richard Adler

IONEC:
Mesh generation and Data Entry for NEC

S P Walker

Imperial College, London

(s.p.walker@ic.ac.uk)

1. Introduction

The scattering code NEC[1] is powerful and widely used. Arguably the ease with which data, and particularly mesh geometrical information, can be provided to NEC does not quite match its processing power. As a consequence there has been a number of additional items of software written to accommodate this, of which a sample are referenced.[2-4].

In general these provide some mechanism to construct geometries on a screen, typically by defining them by lines, with the large surface patches so formed being subdivided by wires to define quadrilaterals or triangles. Display of the results on the same model is generally provided.

The need for analysis and modelling exists over a broad range of industrial applications, spanning far beyond electromagnetics. In general all applications share the need to enter the geometry (generally referred to as a solid model) followed by the development of a discretised form of this; the meshing process. This discretised representation is entered into some analysis software to solve the relevant differential equations. Subsequent display of their solutions on the same model is usual.

There are areas outside electromagnetics where this whole activity is much more widespread, has been under way for longer, and as a consequence is generally conducted in a more sophisticated way; perhaps the most developed area is stress analysis and mechanical modelling generally. One consequence of this longstanding activity is that there exists now a large body of sophisticated commercial software covering the activities of solid modelling (geometry entry), meshing and display. The definition is not precise, but for brevity we will refer to this as CAD (computer aided design) software.

Such software is large (possibly hundreds of Mb), a reflection of the broad functionality provided, and the complexity of providing it. It is also generally expensive, although this is obviously a subjective matter, but it is software which most industrial electromagnetic modelling organisations will tend to have anyway to support the mechanical aspects of their activities.

The intent of the IONEC code is not to provide a mechanism for geometry input and meshing for NEC, reproducing the role of the well developed commercial software. Rather it is to permit this body of general purpose software to be made available to the NEC user.

2. Objectives

The user interface of NEC, whilst not overly user-friendly, is both widely known and rich, allowing good control of what can be complex analyses. An objective in specifying IONEC was to retain the advantages of this, whilst allowing so far as possible the more difficult geometrical input to be automated by exploiting the CAD software. IONEC is thus written as a stand-alone pre-processor; it is an aid in preparing NEC input files, rather than a seamless GUI to NEC.

The other objective is to make available to the NEC analyst as many as possible of the sophisticated tools taken for granted by analysts in other disciplines. These include the complexities of solid model generation and geometry definition, tools for automatic mesh generation, localised mesh refinement, mesh testing and analysis, and so on. All this is performed in the comprehensive GUI environment of the CAD package. Various of the data for a NEC mesh are not automatically provided by the CAD software, which has been

primarily developed for other disciplines, and this is extracted by IONEC. In addition, some criteria for a NEC mesh differ from, or do not arise in the other disciplines, so IONEC performs additional tests of mesh quality and consistency.

IONEC is thus *not* a geometry entry or meshing package. It is an intermediary, run after a modelling session on the CAD system is complete, which extracts from the CAD system's output data relevant to NEC, augments it as required, performs some NEC-specific quality tests, and writes it out formatted so that it can form part of a standard NEC input file. In essence IONEC automates the provision of parts of the NEC input file; 'Lines GW' and 'Lines SP'. At present IONEC does not take NEC output and return it for postprocessing and display in the CAD package; this is an attractive and natural development, and is discussed further later.

3. Use of IONEC

- There is a large range of commercial CAD software which is highly suitable to the modelling of NEC targets; Patran, Pro-Engineer, Ideas, ... IONEC can in principle be modified to accommodate any such package; it has thus far been written to work with Patran and Ideas[5].
- With one of these the user generates a solid model of the object(s) of interest. This uses the normal modelling facilities of the CAD package. Solid modelling is a large and complicated topic in its own right; modern software will allow generation of complex, asymmetric, generally curved bodies, and this capability is then available to the NEC user.
- A surface mesh is created on this model by the meshing part of the CAD package. To suit the limitations of NEC, this must comprise (a mixture of) three noded flat triangles, or four noded flat quadrilaterals. Whilst in practice most non-electromagnetic use of such CAD software now employs curvilinear element descriptions, all package do include these simpler linear forms. Note that the underlying solid model on which this mesh is created can, and generally will, be curvilinear. There is no requirement (or temptation) to 'flatten' the geometry on a length scale greater than that to which it is eventually discretised (in contrast to the perfectly understandable approach adopted, for example, in the cases shown for WIREGRID[4]).
- This mesh creation process makes use of the full facilities of the CAD package; free and mapped meshing, mesh seeding, mesh grading, image rotation, inspection, hidden line removal, and so on, all controlled form the GUI of the CAD software. These are capabilities which are complicated and expensive to provide, *ab initio*, but which already exist in the widely available CAD software.
- The mesh file is saved.
- IONEC is run. It interrogates the CAD meshfile, and extracts or constructs the data required to provide triangular and quadrilateral wire meshes and triangular and quadrilateral patch data to NEC; Lines GW and Lines SP. IONEC output is an ASCII text file, comprising a series of datasets of logically associated, formally specified data. Some of these are 'housekeeping'; run identification and so on, others provide a full specification of the mesh (wire and node numbers, node locations, element and nodes, nodes connected to nodes, and so on) and some contain the results from the various tests. Others, of the most immediate relevance to the user, contain sets of lines written in the form of parts of a NEC input file, principally 'Lines GW' and 'Lines SP'. These contain wire and surface patch information respectively. This data is copied directly by the user into a NEC input file. The user adds to this the other data required by NEC, and runs the NEC analysis as normal.
- These stages are shown diagrammatically in figure 1.

4. Functionality of IONEC

As noted, IONEC interrogates the mesh file, and from the data there generates the basic wire and segment or patch data required by NEC. Wire data differs markedly from the element and node data provided by CAD

software, with its finite element origins. There is some searching and much housekeeping required to identify, for example, a pair of adjacent nodes as a single wire.

Once wires are identified, IONEC selects wire diameters for NEC, via the equal (or some other user specified number different from unity) area rule. Since the CAD meshers will allow easy local mesh refinement the use of a single uniform wire diameter may well not be appropriate. IONEC satisfies the equal area condition both globally and locally. The numbers of segments into which each wire is to be divided is obtained from the wire length, and a user-provided wavelength and 'segments per wavelength'. Wire radii are determined on a wire by wire basis, such that the wires associated with any portion of the mesh have an area equal to the area of that portion, which simultaneously ensures that the total wire area is equal to the total surface area. An additional advantage is that finely meshed regions automatically employ fine wires, minimising the problem of segment centres lying inside segments of other wires.

A common requirement for NEC analyses, not generally shared in other disciplines, is to include individual long thin members; an antenna protruding from a vehicle, or a cable connecting two bodies, for example. Such individual wires are entered straightforwardly in the CAD system as bar elements or the like, and the corresponding 'Lines GW' for the NEC input file are generated by IONEC.

Some mesh testing is done in NEC anyway. It is our experience that *a priori* mesh testing is very valuable, and can avoid considerable waste of time; too much testing is almost an impossibility. Much testing can be performed by the CAD package; the exact tests naturally depend on the particular package employed. The various tests performed in IONEC are:

-'Holes' in the mesh; a (say) triangular patch must have at least three neighbouring patches. The mesh is tested to determine if such criteria are met.

-Too narrow an angle between wires; The angle subtended between wires meeting at a point is calculated, and warnings written when (user specified) bounds are exceeded.

-Too big tangent mismatch: At any node, as many normals can be identified as elements meet at the node. Even if the node is intended to lie on a smooth portion of the surface, these normals will generally not be colinear. Tests are performed to locate non-colinear normals, and their locations reported. The IONEC user specifies the angle between normals which causes the warning to be written. (Note of course that on non-smooth portions of the surface, normals which are not nearly colinear are intended; the user naturally then ignores the warning.)

-Too 'squashed' a set of wires: A big a difference between the lengths of the sides of wires bordering a triangle or quadrilateral may be deliberate, but is most likely the result of poor meshing. The aspect ratio of patches is evaluated, and warnings written.

5. Examples of use

Here we show examples of the use of the CAD package for generating meshes for NEC use. Figure 2 shows a shaded mesh of a thick-walled, open ended cavity. (Screen display, using colour, of varying intensity determined by user specified illumination direction and so on, where the body can be rotated and zoomed freely to examine different parts, is naturally a much more helpful representation than this monochrome figure). The rectilinear quadrilateral surface mesh was formed on this body by the meshing part of the CAD package. It is the coordinates of the ends of the lines defining the edges of these quadrilaterals which are provided to NEC as wire endpoints, along with the number of segments into which each wire should be split.

A more complex example is shown in figures 3 (the solid model) and 4 (the mesh). The marked mesh grading the CAD packages make possible is seen in the portion of the model where the supports join the dish. IONEC-calculated wire diameters in this region are, as would be desired, much smaller than their value over the majority of the surface.

6. Future developments

The most obvious extension is to complete the process by arranging for the display by the CAD system of NEC-calculated surface currents on the same model. This is the norm for say solid mechanics applications, and indeed is routinely done for the curvilinear integral equation electromagnetic analysis we describe elsewhere in the session.

7. Observations and Conclusions

IONEC has proven to be effective in making the power and convenience of modern CAD software available to the user of NEC. More complex and more accurate models can be constructed, and more sophisticated, graded meshes produced, with much reduced effort. There is obviously a price to be paid. The cost and availability of CAD software was mentioned above. Additionally, just as for say mechanical design engineers, competent familiarity with the CAD software is a pre-requisite for its proper use and the obtaining of maximum benefit. Whilst this is greatly eased by their generally very user friendly interfaces, and comprehensive on line, context sensitive help systems, such competence is still a requirement!

8. IONEC Availability

IONEC is presently available, with full documentation, for the Ideas and Patran CAD packages; if required it could be modified to work with other packages. It can be provided to run on any Unix workstation (or indeed on a PC). For further information please contact the author.

References

1. G.J. Burke. *Numerical Electromagnetics Code - NEC-4*, UCRL-MA-109338, Lawrence Livermore National Laboratory,1992.

2. J. Peng, J. Choi and C.A. Balanis, Automation of the geometry data for the NEC and the ESP using the Super 3-D, *6th Annual Review of Progress in Applied Computational Electromagnetics* 33-38 (1990).

3. P.S. Excell and A.F. Armanious, A portable interactive graphics preprocessor for use with wire grid modelling software, *7th Annual Review of Progress in Applied Computational Electromagnetics* 1-9 (1991).

4. C.F. du Toit and D.B. Davidson, WIREGRID: A NEC2 pre-processor, *Applied Computational Electromagnetics Society Journal* **10**, 31-39 (1995).

5. *I-DEAS Master Series User Guide*, Structural Dynamics Researh Corporation, Milford, Ohio,1995.

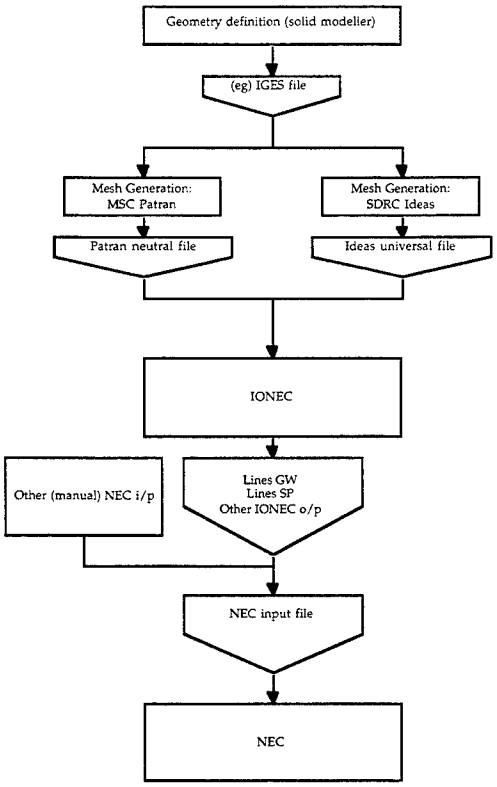

Figure 1 The overall structure and interactions of the CAD software, IONEC and NEC.

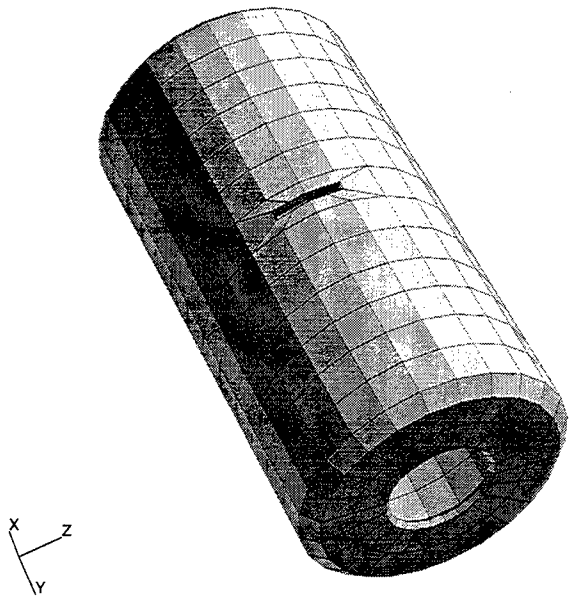

Figure 2 Shaded mesh representation of an open ended cylindrical cavity

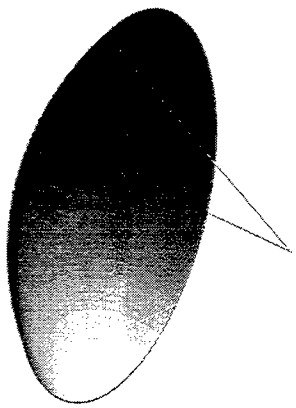

Figure 3 CAD software solid model of example dish with supports

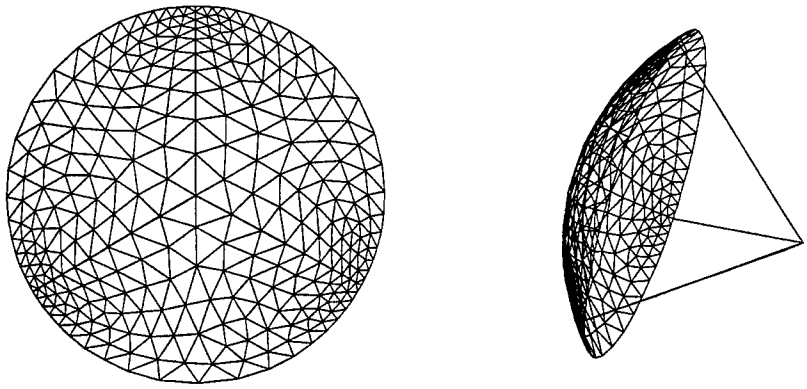

Figure 4 Mesh of example dish with supports

Experiments with NEC3 and NEC4 - Simulation of Helicopter HF Antennas

Stanley J. Kubina, Christopher W. Trueman and David Gaudine
EMC Laboratory
Electrical and Computer Engineering Department
Concordia University
Montreal, Que. Canada

Introduction

The Bell Textron BT412 Utility Helicopter in use by the Canadian Forces uses a short transmission line type of HF antenna. It consists of a tubular element fed by a feed-through insulator on the aft port side of the cabin, runs along the tail cone spaced 10" from the fuselage and terminates in an open circuit just aft of the horizontal stabilizer. It is some 20 feet in length, supported at intervals by insulators to assure sufficient rigidity of the 1" tubular element. The antenna is tuned by an HF antenna coupler over the four octave frequency range, 2-30MHz to match the 50 ohm impedance of the HF Transceiver. A wire grid representation of the helicopter and the antenna is shown in Fig. 1. This type of antenna is often used with the aft end short-circuited to the fuselage. The BT412 fuselage is similar to that of the CH-135/Twin Huey Helicopter, previously discussed at ACES[1], except that it has four 46 ft. rotor blades and a slightly different upper cowling superstructure. The rotor configuration of the BT412 was added to the CH-135 model for this study, but not the cowling detail.

Methodology

It has become standard practice at the EMC Laboratory to perform a high-resolution spectral analysis of these antennas by doing a frequency sweep with NEC at 0.1 MHz increments over the entire HF 2-30 MHz frequency band. The EMC Lab's NEC Integrated Software System[2] is used for model creation (DIDEC and AutoCad) and verification (CHECK,MESHES,FNDRAD)[3], to execute the spectral sweep and to generate a standard output file to examine impedance, radiation patterns in various formats, current distributions and HF communication system *performance parameters*[4] over the frequency range. These latter values are obtained from specific integrations of volumetric radiation patterns for both polarizations at the relevant conical sectors for ionospheric, ground wave or high vertical incidence communication(NAP-OF-EARTH). Such high-resolution spectral analysis has been performed on the wire-grid model first with NEC3 and more recently with NEC4 using the EMC Labs DEC workstations. This paper provides the first opportunity to examine the results for such complex models with an intriguing set of comparisons of the detailed data sets.

The EMC Laboratory considers *validation* an essential part of computational simulations. In this case however, the only validation that has been possible to-date and that has some limited applicability, is that previously reported for the CH-135 helicopter in comparisons with scale-model measurements[1]. The wire-grid model contains some 360 segments. The topology is

verified by our software system and the segment lengths are selected to be lambda/10 at 15 MHZ, mid-way in the frequency range, conforming to prior practice of maintaining model bandwidth. There are few precedents to anticipate the results for the two antenna types - open and short-circuited version. In this study the model was executed with the rotors in-line with the fuselage and at 45 degrees. In this paper, the 45 degree results are shown.

Results - Shorted Loop

For the shorted transmission line antenna, the impedance values vs. frequency for NEC3 and NEC4 track each other well with frequency, showing particularly the perturbations which are associated with coupling to resonant fuselage paths. The resistance vs. frequency is presented in Fig. 2. Note the features at 7.7 and 10.2 MHz, which we have labelled the 'aha!' bumps indicative of fuselage coupling.

In studies of this type, the overwhelming volume of radiation pattern information for both polarizations is best sampled at specific frequencies. However, the operationally useful details of the radiation patterns are best presented in the plots of performance parameters vs. frequency, such as radiation pattern efficiency and %E-theta and %E-theta*[4]. Note that radiation pattern efficiency is defined as the ratio of power radiated in the conical sector , 30 degrees above and below the horizon to the total power radiated, and %E-theta* is the ratio of power in E-theta for this same sector, and %E-theta is the ratio of the power in this polarization component to the total power radiated. Plots of these versus frequency are shown in Fig. 3. We also usually plot the amount of power 30 degrees around the zenith for NAP-of-EARTH application analysis. Note that the performance parameters for NEC3 and NEC4 also track each other exceptionally well over the entire frequency range, showing also the specific variations which had been identified in prior papers as associated with specific airframe resonant paths involving the rotor blades and fuselage. The current distributions on the model (to be shown in the oral presentation) are revealingly consistent with these results and provide an appreciation of the physical reality being modelled.

Is this also the case for the open-circuited version of the antenna?

Results - Open-Circuited Antenna

For the open-circuited transmission line HF antenna, the impedance values vs. frequency track well over a portion of the frequency range but show some differences in the middle of the frequency band. The resistance values are shown plotted vs. frequency in Fig. 4. Once more they show the radiation resistance peaks associated with coupling to resonant fuselage paths, but the resistance values computed with NEC4 are lower in the 8-20 MHz range. There is also a small shift in the indicated antenna resonant length peaks, which can be understood to be related to the different segment end treatment in NEC3 and NEC4.

The plots of the performance parameters show an interesting behaviour. These are shown in Fig. 5. Over a considerable portion of the frequency range, say 10 MHz to 20 MHz, the radiation pattern efficiency curves are almost identical, with peaks occurring at frequencies only slightly shifted as in the impedance curve set. However the curves show substantial differences in

the lower frequency range, 2-10MHz and above 20MHz. An examination of the E-theta curves shows little difference at the high frequencies and thus suggests that the high frequency difference is due primarily to differences in the E-phi radiation patterns.

An examination of the current distributions shows that both the NEC3 and NEC4 results have the loop current "artifacts" which had been noted in prior work[1]. In the past these have been shown to have a minimal effect on far-field radiation patterns for cases such as these.

Commentary

These results raise a number of new technical modelling issues for us. Of primary importance to us is the need for reliable scale-model measurements which can be used to *validate* the results of this study and to help to resolve the serious questions that are raised. Thus far, we have not been successful in arranging for these to be carried out.

Clearly the agreement in the case of the shorted antenna plus general correlation with CH-135 results gives us considerable confidence in the NEC3 and NEC4 values, but should not totally eliminate the need for some measurement corroboration. This comment also applies to the 10-20 MHz region of the open-circuited antenna results.

The discrepancies at both the low and high frequency portion of the range, raise the important questions:

which results are closest to real-world electromagnetic equivalence?,

what weakness in the existing guidelines for NEC3 and NEC4 for use with complex bodies, is responsible?

In the absence of scale-model measurement results, a series of model perturbation studies are in place in an attempt to understand fully the reasons for the differences and to indicate which result might be the more reliable one. Thus far, no clear elucidation has been obtained.

Acknowledgements

This project has been supported by a Canadian National Science and Engineering Research Operating Grant OGP0009340 and EMC Laboratory sustaining research funds. The model manipulation, execution and data organization was effectively carried out by research assistants Thien Huong Ha, Huong Thi Nguyen and William D'Orazio. Helpful discussions with Gerry Burke are gratefully acknowledged.

REFERENCES

[1] Kubina, S. J., "Helicopters, HF Antennas: Models, Measurements and All That", 3rd Annual Review of Progress in Applied Computational Electromagnetics, Monterey CA, March 24-26, 1987.

[2] Kubina, S. J., Trueman, C. W. Gaudine, D., and Ramos, A., "Creation, Visualization and Analysis - The Dynamics of Complex Models," 9th Annual Review of Progress in Applied Computational Electromagnetics, Monterey CA, March 22-26, 1993.

[3] Trueman, C.W., and Kubina, S. J., "Verifying Wire-Grid Model Integrity with Program - "CHECK", Applied Computational Electromagnetics Society Journal, Vol. 5, No.2, Winter 1990, pp. 17-42.

[4] Kubina, Stanley J., "Measurement and Computer Simulation of Antennas on Ships and Aircraft for Results of Operational Reliability", AGARD Lecture Series No. 165 on Modern Antenna Design Using Computers and Measurement: Application to Antenna Problems of Military Interest, October 19-27, 1989, pp. 5-1 to 5-28.

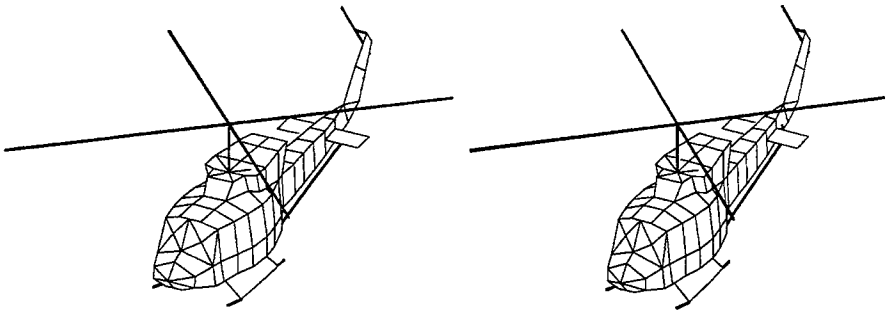

Fig. 1 - Helicopter HF Antenna Models - Open, Shorted, BT412

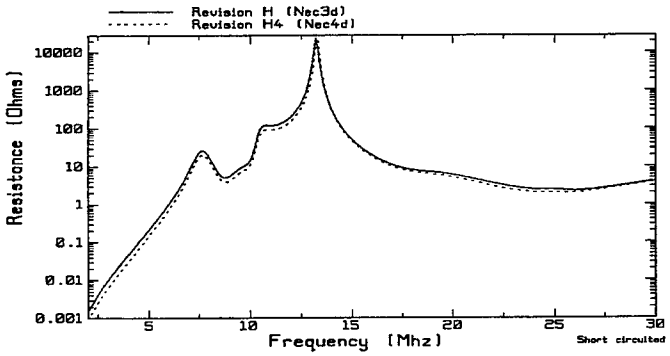

Fig. 2 Resistance vs. Frequency - Shorted Antenna(NEC3 & NEC4)

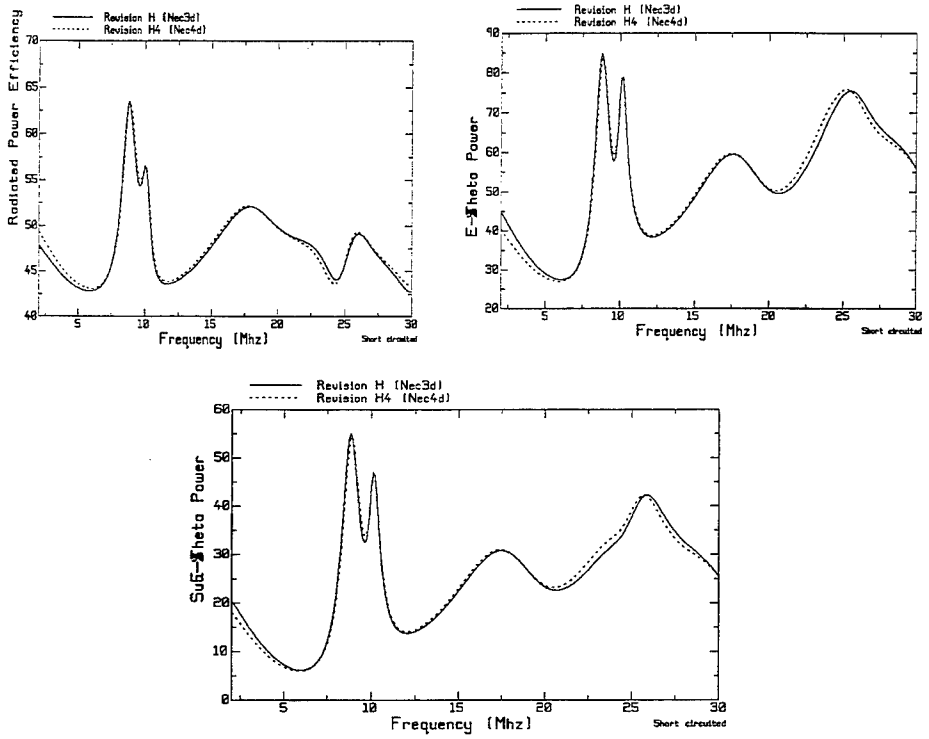

Fig. 3 Performance Parameters vs. Frequency - Shorted HF Antenna(NEC3 & NEC4)

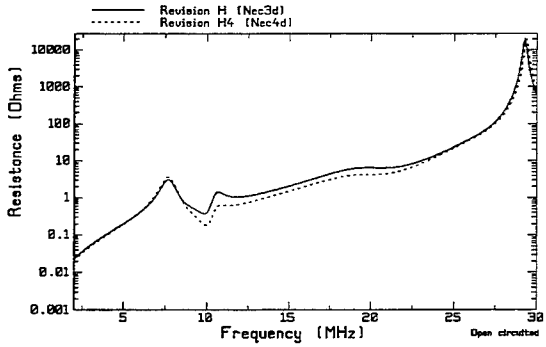

Fig. 4 Resistance vs. Frequency - Open-Circuited Antenna(NEC3 & NEC4)

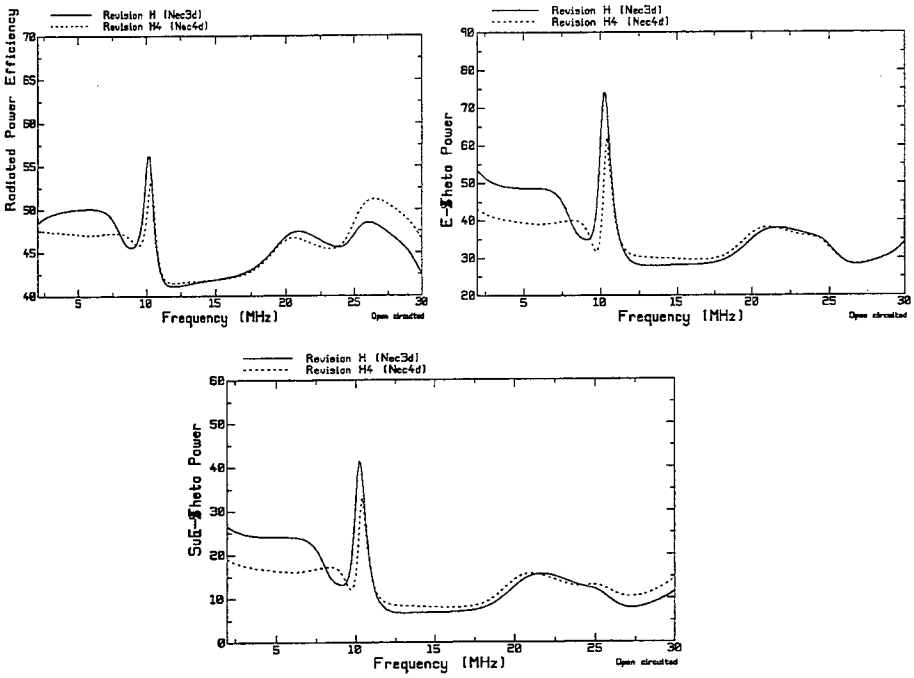

Fig. 5. Performance Parameters vs. Frequency - Open-Circuited Antenna(NEC3 & NEC4)

BUILDING MODELS FOR NEC2 AND NEC-BSC

U Lidvall
Communicator CEC AB
PO Box 1310, S-17125 Solna
Sweden

1 Abstract

A unified way to build geometry models for antenna calculations with CEM-tools like the NEC2 and the NEC-BSC codes with MATLAB-scripts and MATLAB function libraries is presented. The generated models are then displayed and checked with workbench-programs like the EAM-NEC and the BSC-Workbench.

Models for the analysis of antennas and antennas on vehicles will be demonstrated and described.

2 Introduction

Model building is often a time consuming part when performing electromagnetic calculations on different antenna problems. A flexible and effective way of creating, checking and modifying models is of great value. To have a unified way of working with models for different CEM tools enables the analyst to efficiently make corresponding models for alternative tools and to perform parallel analysis based on different formulations for better understanding of the problem and more reliable results.

In this paper we address the building of simple and medium advanced models. Advanced models, with very accurate description of surfaces and a lot of detail, normally have to be built with specialized meshing tools based on CAD data.

The geometry part of an input data file for the NEC2 [1] or the NEC-BSC [2] codes can be generated by a MATLAB-script [3] calling a set of functions that write different geometry elements to the input data file. The MATLAB functions can be arranged in libraries, one for each code, and each library can be arranged in several layers with the functions writing the basic geometry elements in the bottom layer. In the higher layers functions for more and more complicated structures can be placed all the time calling functions in lower layers to get building blocks for the structure. The libraries can easily be extended in any layer to new geometry elements. A parallel library for one more CEM tool can also be set up when ever needed.

The geometry structures built as described above can be displayed and checked in the case of NEC2 with the EAM-NEC [4] and in the case of NEC-BSC with the BSC-Workbench [5]. Modifications of models can be done directly within the workbench or by modifying the model-generating MATLAB-script and renewed treatment with a workbench.

In the following sections model building for NEC2 and NEC-BSC will be described and a couple of models will be demonstrated.

3 Building models for NEC2

3.1 MATLAB scripts and function library for NEC2 models

A library of MATLAB functions have been prepared and the functions are intended to be used when building NEC2 geometry models and antenna elements. When one of the functions is called by a MATLAB script one or more geometry elements are written to a NEC2 input data file. The library have several layers and in the bottom layer we have functions that write basic geometry elements like a straight or a curved wire. At the time being

Table 3.1 *Multilayer MATLAB function library for NEC2 modeling*

Layer 6	*Vehicle (truck, helicopter, aircraft, ...)*
Layer 5	*Antenna models*
Layer 4	*Structure (box, fuselage, wing, ...)*
Layer 3	*Polyplate surface, poly cylinder/cone/ellipsoid body*
Layer 2	*Bilinear plate, cylinder/cone/ellipsoid shell*
Layer 1	*Polywire*
Layer 0	*Wire (plate)*

only the wire modeling capability of NEC2 is used. In the next layer of the library we have functions that write wire grid modeled bilinear surfaces and wire grid modeled sections of cylinders, cones, and ellipsoids. In the next higher layer of the library there are functions for generation of multiple bilinear surfaces, multiple sections of cylindrical, conical, or ellipsoidal surfaces, and combinations of those. In one layer of the library we have functions for the generation of antenna models. At a top level of the library we can have functions for the generation of complete vehicles of different kinds. The library can easily be extended with new geometry elements or structures on any level.

In a MATLAB function for the generation of a geometry structure a fair amount of calculations pertinent to the structure can be done based on relatively few controlling input parameters. This can make the function very efficient to use in a certain modeling situation. Different regularity checks on the geometry data, related to the requirements of the CEM tool used, can easily be done within the function library.

When a geometry model for NEC2 is going to be generated a main MATLAB script is prepared. The main script sets or loads in the necessary geometry defining parameters and then calls one or more of the library functions to write the geometry part of a NEC2 input data file.

A MATLAB graphical interface to the function library have not yet been developed.

3.2 Log-periodic antenna model for NEC2

A MATLAB function for the generation of a wire model for a Log periodic antenna has been developed. It uses wire geometry element functions in lower layers of the NEC2 library. A resulting standard log-periodic antenna model as displayed by EAM-NEC is shown in fig 3.1. Other log-periodic structures can be modeled by analogous library functions.

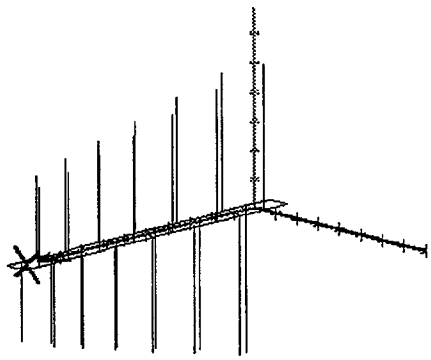

Fig. 3.1 *NEC2 model for traditional log-periodic antenna displayed with EAM-NEC*

3.3 NEC2 model for truck with communication antennas

A truck model for NEC2 analysis of some communication antennas have been generated with a main script and a package of MATLAB functions. One function used can give attached or nonattached bilinear surfaces represented by wire grid modeling. Part of the model is shown in fig 3.2 before the wire grid modeled plates are joined together. The complete model is shown in fig 3.3.

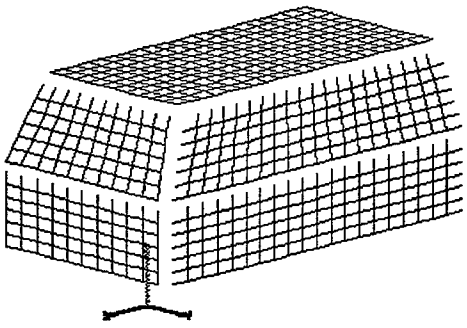

Fig. 3.2 *Part of NEC2 truck model showing pre join wire grid modeled plates*

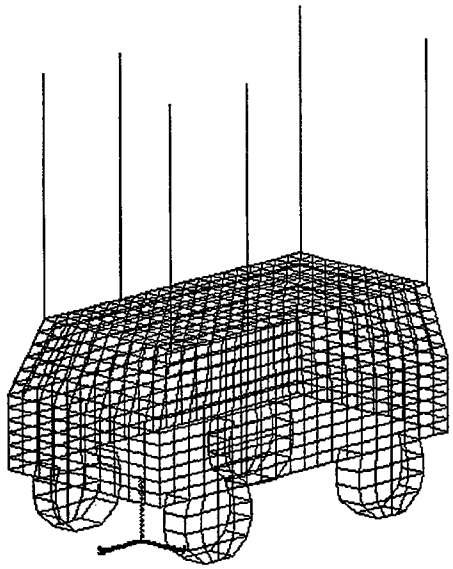

Fig. 3.3 *NEC2 model for truck with communication antennas*

4 Building models for NEC-BSC

4.1 MATLAB scripts and function libraries for NEC-BSC models

To build a model for NEC-BSC a main MATLAB-script is prepared. The main script sets the geometry defining parameters and then calls appropriate functions in a MATLAB library developed to write all the necessary geometry elements on a desired structure to a NEC-BSC input data file.

The MATLAB function library used to build NEC-BSC models is, in analogy to the NEC2 library, constructed in several layers. The 'ground' layer have functions that give the basic geometry elements of NEC-BSC, namely a plate, a cylinder, a cone, or an ellipsoid. In the next higher layers there are functions for multiple plat surfaces, multiple cylinder/cone/ellipsoids, and combinations of those. In one part of the library antenna modeling functions are collected. In the highest level of the library there are functions for generation of complete structures like e g vehicles.

Table 4.1 *Multilayer MATLAB function library for NEC-BSC modeling*

Layer 4	*Vehicle (helicopter, aircraft, ...)*
Layer 3	*Antenna models*
Layer 2	*Structure (fuselage, wing, ...)*
Layer 1	*Polyplate surface, poly cylinder/cone/ellipsoid body*
Layer 0	*Plate, cylinder, cone, ellipsoid*

The MATLAB model building library for NEC-BSC is thus a direct parallel to the library for NEC2. The libraries have corresponding functions in the model element space spanned by the respective codes.

The library group can of cause be extended to have analogous libraries for other CEM tools.

4.2 Aircraft fuselage model for NEC-BSC

To model the fuselage of an aircraft a group of MATLAB functions have been prepared to generate the general shape of the fuselage by composing appropriate NEC-BSC geometry elements and adjusting them to each other. Figure 4.1 shows a fuselage model as displayed with the BSC-Workbench. It consists of adjusted groups of ellipsoids and is based on the shielding capability of the NEC-BSC code.

Fig. 4.1a *Aircraft fuselage model for NEC-BSC, side view*

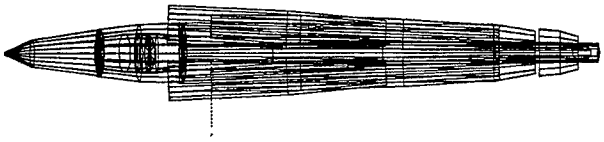

Fig. 4.1b *Aircraft fuselage model for NEC-BSC, top view*

4.3 Aircraft model for NEC-BSC

A model of the complete aircraft is shown in figure 4.2. It is generated by the use of the fuselage library functions mentioned above together with some wing generating functions joined to an aircraft modeling package for this specific aircraft.

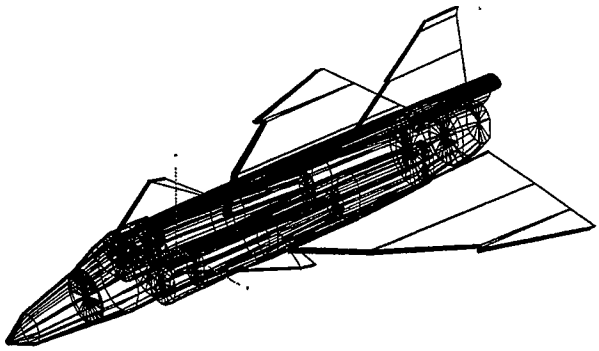

Fig. 4.2 Aircraft model for NEC-BSC

The aircraft model is intended for the analysis of antennas not placed on the aircraft fuselage.

5 Conclusions

MATLAB scripts and function libraries have been developed and used in an effort to achieve a unified, flexible, and efficient way to build models of medium complexity for CEM tools like NEC2 and NEC-BSC.

The MATLAB libraries for different tools are made 'parallel' to each other so corresponding models for alternative tools can be generated with analogous main MATLAB scripts only by using different function libraries.

The MATLAB libraries can be used to build a wide range of different types of models and they are easily extended to new model elements or new model structures and also to new CEM tools. Also relatively large and complicated models can readily be built with these libraries.

6 References

[1] G J Burke and A J Poggio, 'Numerical Electromagnetics Code (NEC) - Method of Moments', Lawrence Livermore National Laboratory Report UCID-18834, January 1981

[2] R J Marhefka and J W Silvestro, 'Near Zone - Basic Scattering Code, User's Manual with Space Station Applications', Technical Report, The Ohio State University ElectroScience Laboratory, December 1989

[3] MATLAB Reference Guide, The MathWorks Inc., Natick, MA, August 1992

[4] M J Packer, R A Powers, and A P Tsitsopoulos, 'Graphicel Shell for the Numerical Electromagnetics Code', ACES93, Conference Proceedings, Monterey, CA, March 22-26, 1993, pp 243-250

[5] L W Henderson and R J Marhefka, 'A Graphical User Interface for the NEC-BSC', ACES95, Conference Proceedings, Monterey, CA, March 20-25, 1995, pp 245-251

RECENT ENHANCEMENTS TO ALDAS V3.00

P R Foster, Microwave and Antenna Systems, UK

INTRODUCTION

ALDAS is a versatile program for computing the effects of a conducting structure on the RF performance of an antenna mounted on or off the structure. The program, which uses diffraction theory, has been described previously [1] and several papers have been published on validating this program [2], [3]. The current version, V3.0, has a number of useful new features which include

1) the ability to model an array of antennas, specified as to boresight direction and position, as one input file to ALDAS
2) the ability to plot the field over any specified plane for nearfield geometries
3) enhancements to the coupling calculations
4) the ability to plot the contributing rays for any particular direction
5) the ability to specify which higher order interactions should be included in the calculations, for example, a plane reflection followed by an edge diffraction
6) the ability to provide a rendered graphics plot of any geometry
7) a new interface which translates between a CATIA file and ALDAS input. CATIA is a standard European drafting package used extensively in the Aerospace industry

ARRAY OF FOUR DIPOLES

A validation has been carried out by using NEC to model an array of four dipoles over a flat plate and to compare these results with radiation patterns computed using ALDAS (Figure 1 and Figure 2).

ARRAYS INSTALLED ON VEHICLES

ALDAS has been used to model the installed performance of an array of 8 wire elements on a tracked vehicle at 1 GHz. The antenna patterns of the array with its integral ground planes was first modelled using NEC [4] and these radiation patterns used as a source for the complex geometry of a tracked vehicle. This procedure made it possible

1) to optimise the backlobe of the element
2) to optimise the element spacing and aperture distribution of the array
3) to examine the performance in various configurations of the vehicle to check on overall performance and to select those geometries which should be measured.

Subsequent measurements and system trials of performance were in excellent agreement with prediction [5]. Figure 3 and Figure 4 show the Sum and Control pattern of the array at an Elevation of 10.0 degrees. Measurement errors from the site are responsible for errors at the -25 dB level. Plots of the predicted Control pattern are shown in Figure 5 (Line contour) and Figure 6

(Isometric). The boresight angle is at 0.0 degrees in Azimuth and the central part of each figure shows the back radiation which is at a very low level for such a low gain antenna (about 16 dBi).

A four element array mounted on a tripod-mounted missile system was also treated this way. In both cases, the ability to predict the installed performance allowed an optimisation of the performance, when installed, which would otherwise have been very time-consuming.

Comparisons of measured and computed data for arrays on aircraft have also been carried out and found to be in good agreement.

Incorporation of Measured Radiation Patterns into ALDAS

The incorporation of measured radiation patterns of Circularly Polarised antennas directly into ALDAS for use in computing the effect of a spacecraft on a TT&C antenna has been carried out. The spacecraft geometry (produced through the ALDAS secondary program, VISALD, which provides a rendered visualisation of the ALDAS structure geometry) is shown in Figure 7 with the antenna position marked with a star and the antenna boresight direction marked with an arrow. The input data as processed for ALDAS is shown in Figure 8 and the final installed patterns in Figure 9. The fine detail of the pattern due to interference from the local structure of the spacecraft is clearly visible.

Nearfield Effects

The effects on TV coverage in North Central London caused by the proposed Millennium Ferris Wheel are a source of concern. The Millennium Ferris Wheel is on the banks of the Thames and some of the TV transmitters are on the south side of the river. The nearfield signal strength has been computed over the region of disturbance at a distance of 15 km from the transmitter (Figure 10). The predicted degradation in signal on the North side of the river can sometime reach -10 dB but the angular range of the disturbance is very small and amounts to an area about 0.5 km across.

CATIA Interface

Many ALDAS users are in the European space industry where the CAD package CATIA [6] is extensively used and there is a demand for an interface directly between ALDAS and the CATIA package. Such an interface has been completed by TDC [7] and tested. It allows a user to take a complete aircraft file in CATIA and interactively fit an ALDAS model in a single session. To generate a complex model will take less than one day. ALDAS rules are applied and warnings given, for example, when structure elements are too small. Examples of screens will be shown.

Conclusions

A number of useful utilities have been produced for ALDAS which makes interfacing data, either geometry or radiation patterns, much easier. The addition of an array feed for ALDAS and of enhanced input feed data, particularly for circular polarised antennas, has already proved useful.

References

1 Foster P R. 'Analysis of Low Directivity Antennas on Structures',, p362-369. 6th Annual Conference on Applied Computational Electromagnetics, 1989

2 B Cordery, M Gurd and P R Foster, 'Antennas on Structures: A Case Study of an Aircraft', PIERS-94, Noordwijk, Holland.

3 P R Foster, 'Validation of a Diffraction program', 10th ACES Symposium, 1994, Monterey, Vol. 1, p366 - 373.

4 J G Burke and A J Poggio,'Numerical Electromagnetic Code (NEC) - Method of Moments Parts I, II and III' Technical Document No 116, Lawrence Livermore National Laboratory,USA 1981

5 P R Foster, M W S Grigson and C Wheatley, 'D-band IFF for Short Range Army Air Defence Systems', Submitted to RADAR-97

6 CATIA Home Page at http://www.catia.ibm.com/html/catmain.html (IBM and Dassault Systemes)

7 TDC, Nene House, Drayton Way, Daventry, Northants, NN1 5EA

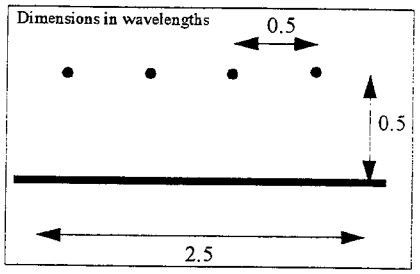

Figure 1 Geometry of 4 dipole array. The plane is in the X-Y plane and the dipoles are parallel to the X-axis.

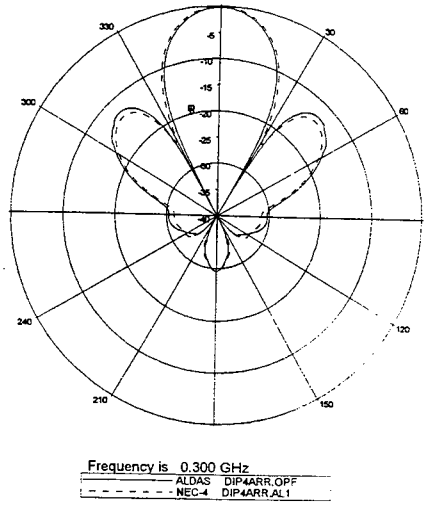

Figure 2 Radiation Patterns of 4 dipole array over a flat plate. Pattern cut in the Y-Z plane

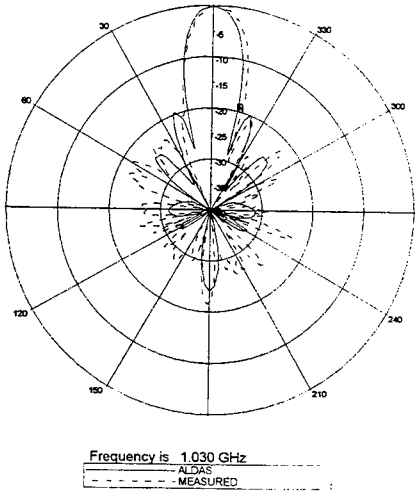

Figure 3 Radiation Pattern from 8 element installed array - Sum pattern

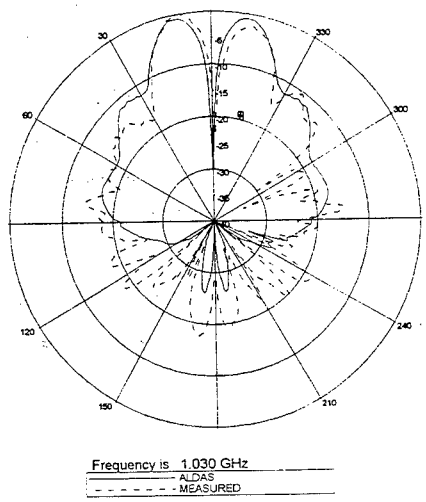

Figure 4 Radiation Pattern from 8 element installed array - Control pattern

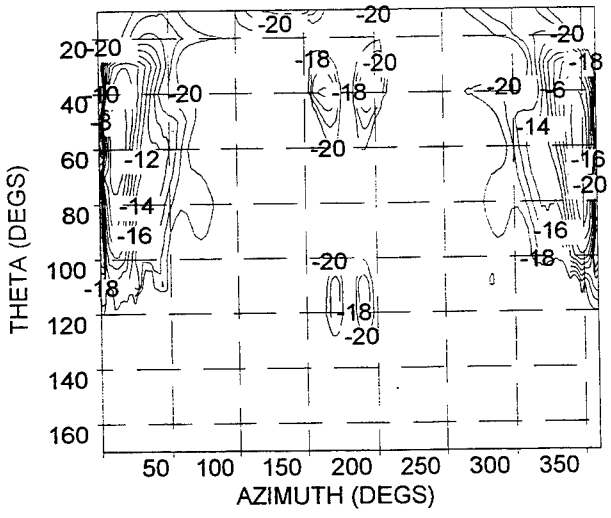

Figure 5 Contour plot of radiation from an 8-element array installed on a tracked vehicle (Control pattern)

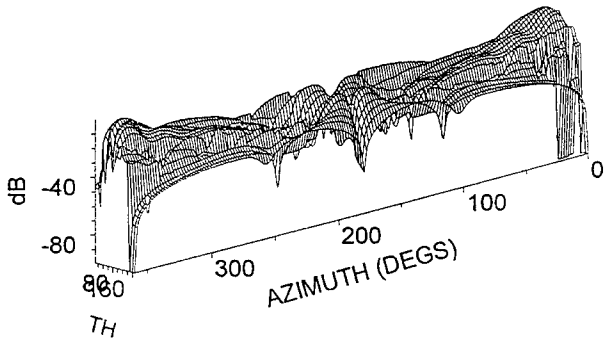

Figure 6 Isometric plot of radiation from an 8-element array installed on a tracked vehicle (Control pattern)

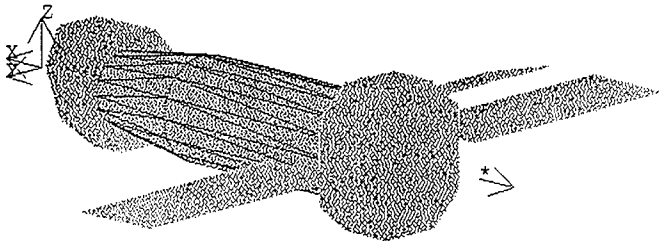

Figure 7 Geometry of Spacecraft showing Antenna Position and Boresight Direction

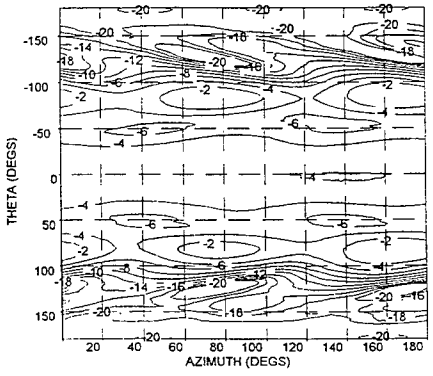

Figure 8 Contour Plot of Input Measured Radiation Patterns

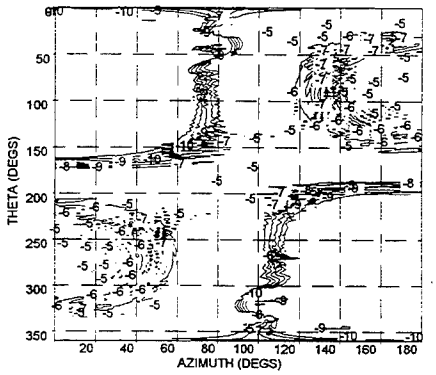

Figure 9 Final Radiation Patterns

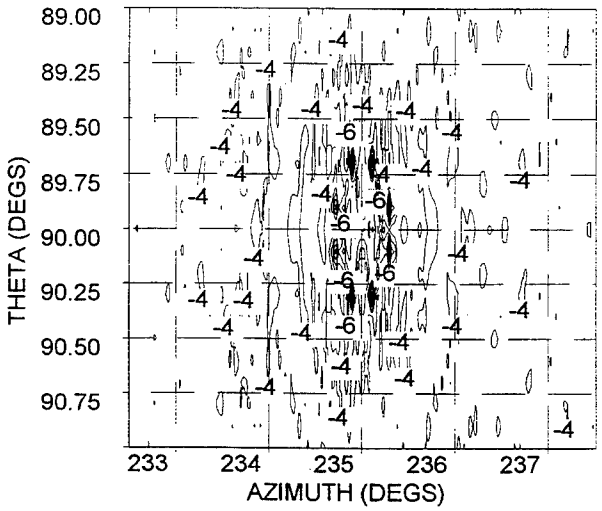

Figure 10 Nearfield Radiation from Millennium Ferris Wheel

Simulation of Portable UHF Antennas in the Presence of Certain Dielectric Structures Using the Numerical Electromagnetics Code

Robert J. DeGroot, Andrew A. Efanov, Eric Krenz and James P. Phillips

Motorola, Inc.
Cellular Subscriber Sector Research Labs
600 North U.S. Highway 45
Libertyville, IL 60048

ABSTRACT - this paper presents the results of simulations of some small dielectric structures for portable UHF applications using the Numerical Electromagnetics Code NEC-2. Two basic configurations have been considered: a coil with a dielectric core and a human's head placed near a radiating antenna. Numerical results obtained by the NEC-2 code are compared with the calculated data obtained by the FDTD and FEM codes, and with some experimental data.

1. INTRODUCTION

The NEC-2 code is a powerful tool for the simulation of various conducting structures of a complex geometry. However, the code is not able to incorporate arbitrary dielectric bodies with the conducting structure. Commercially available FDTD and FEM codes allow the analysis of complex 3-D dielectric bodies, but they are limited to describing and efficiently solving a simple conducting geometry. Usually, these algorithms are computationally intensive and very time-consuming.

This paper presents the results of the authors' simulations of some small dielectric structures for portable UHF applications using the NEC-2 code. Two basic configurations have been considered: a coil with a dielectric core and a human's head placed near a radiating antenna.

2. COIL WITH A DIELECTRIC SUPPORT

Various helical conductors (helicoils) are widely used in antenna practice. Often a helicoil is wound on a dielectric support. Such a structure is not directly suitable for the NEC-2 simulations because of the presence of the dielectric. We propose a simple method to imitate the dielectric core. Any two parallel nearby allocated turns of the coil could be considered (in some way) as a two-conductor transmission line. Such a line can be described by a well-known series LC circuit model ([1]). The presence of the dielectric can be emulated by an implementation of the additional capacitive shunt lumped loads along the line. The loads are placed on the shunt wire segments connected between the turns.

Determination of the values of the loads is quite a difficult task. The best results could be obtained by using a different accurate solver (like a FEM code) which could calculate electrical characteristics of the structure. Even static solvers can be used assuming a two-wire transmission line model of adjacent turns. Any available experimental data can be used for this purpose as well. Then, the results of the

NEC-2 simulations could be compared with the accurate solution, and the values of the lumped loads can be selected and optimized.

As an example of this approach, the following configuration (Fig. 1a) is considered here: a helicoil-type radiator with a dielectric support is connected in series to a whip. The length of the whip is 70 mm, the coil has 10 turns, 2 mm pitch, 4.5 mm diameter and it is wound on a dielectric support with $\varepsilon_r = 3.1$. This structure is excited by a short collinear dipole. First, the electrical characteristics have been analyzed by a FEM code. Then the shunt lumped capacitive loads have been implemented into the NEC-2 wire model (Fig. 1b), and their values have been adjusted. For this specific case it has been found that each load should be -j1700 Ohms. Calculated frequency characteristics of the structure (whip and coil) are shown in Figure 2. The resonant frequencies coincide very well for both models. The difference in absolute values of the radiated power is caused by the different excitation models used in FEM and NEC-2 simulations.

3. SIMULATIONS OF A HEAD

Portable UHF antennas used for personal communication systems usually work in a very close vicinity to the operator's body, especially his/her head. From the electromagnetic point of view, a human head is a lossy dielectric/conductive medium with the following average parameters: relative permittivity ε_r = 44.0 and conductivity σ = 0.9 S/m ([2]). Several papers ([3-6]) were devoted to a problem of the absorption of EM energy in a human head using FDTD methods. The reported results show that the energy mainly dissipates in a relatively thin (about 1-2 cm) surface layer of the head tissues, which corresponds well with the estimated thickness of a skin-depth for a lossy conductor with the above-mentioned conductivity at 900 MHz. This circumstance leads to an idea to use a resistively loaded wire-grid surface model of the head.

To verify this approach, a comparison between the modeling methods was conducted. The following configuration has been considered: a solid rectangular box (210 x 180 x 150 mm, $\varepsilon_r = 44.0$, $\sigma = 0.9$) is excited by a resonant half-wave dipole at 900 MHz. The distance between the box and the dipole is 20 mm. First, this problem has been analyzed by a FDTD code. Second, a corresponding NEC-2 surface wire-grid model of the box has been elaborated (Fig. 3). The sizes of the square grid facets are 30 x 30 mm, what is approximately equal to 1/10 of the operating wavelength in free space at 900 MHz. Then, the structure has been loaded (each wire segment contains a resistive lumped load), and the resistance of all the loads has been optimized using the NEC-2 code. It had been found that 90 Ohm resistive loads yield the best correspondence between the NEC-2 surface wire-grid model and the FDTD solid dielectric model (Fig. 4) at 900 MHz.

Then the surface of a head has been approximated by a wire mesh with the same size facets and the same resistive loads. The model (Fig. 5) has 512 wire segments and 512 lumped loads, correspondingly. As an example of the possible use of this model, we present calculated and measured far-field radiation patterns (Fig. 6) of a simple sleeve dipole antenna mounted on a metal box and working close to the head (Fig. 5). A dummy phantom of the upper part of the human's body (the head and an upper part of a trunk, filled by a liquid with $\varepsilon_r = 44.0$, $\sigma = 0.9$ S/m) has been used for the measurements. There is

quite good correspondence between the measured and calculated results. The measured and calculated overall antenna efficiencies are 83 and 77 percent, respectively.

4. CONCLUSIONS

The relatively simple approach suitable for NEC-2 simulations of two types of structures (a model of a wire coil wound on a dielectric support and a human head model) has been presented here. This allows the EM analysis of a highly intricate configuration in close proximity to significant dielectrics.

This approach has two main advantages. First of all, the NEC-2 code is much faster than any available FEM solver. Once the values of the lumped loads have been found, the NEC-2 model can be used for any further optimization and design of the whole antenna structure using commercially available NEC-based optimizers. Moreover, the NEC modeling makes it possible to analyze very complex wire structures, which are beyond the powers of FEM and FDTD solvers. The proposed approach requires further validation and verification. Comments and new results regarding this method would be appreciated.

ACKNOWLEDGEMENT

The authors wish to acknowledge the contribution of Dr. Hugh K. Smith who made FDTD simulations.

REFERENCES

[1] C. T. A. Johnk, *Engineering Electromagnetic Fields and Waves*, New York: John Wiley & Sons, 1975.

[2] I. G. Zubal *at al*, "Computerized three-dimensional segmented human anatomy," *Med. Phys. Biol.*, vol. 21, pp. 299-302, 1994.

[3] M. Okoniewski and M. A. Stuchly, "A study of the handset antenna and human body interaction," *IEEE Trans. Microwave Theory Tech.*, vol. 44, pp. 1855-1864, No 10, October 1996.

[4] V. Hombach, K. Meier, M. Burkhardt, E. Kuhn and N. Kuster, "The dependence of EM energy absorption upon human head modeling at 900 MHz," *IEEE Trans. Microwave Theory Tech.*, vol. 44, pp. 1865-1873, No 10, October 1996.

[5] S. Watanabe, M. Taki, T.Nojima and O. Fujiwara, "Characteristics of the SAR distribution in a head exposed to electromagnetic fields radiated by a hand-held portable radio," *IEEE Trans. Microwave Theory Tech.*, vol. 44, pp. 1874-1883, No 10, October 1996.

[6] O. P. Gandhi, G. Lazzi and C. M. Furse, "Electromagnetic absorption in the human head and neck for mobile telephones at 835 and 1900 MHz," *IEEE Trans. Microwave Theory Tech.*, vol. 44, pp. 1884-1897, No 10, October 1996.

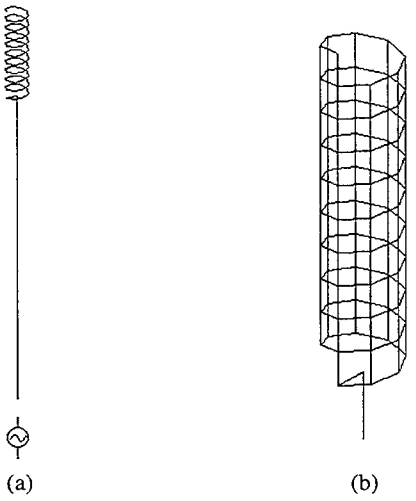

Figure 1. The whip and coil antenna: (a) overall configuration, the antenna is excited by a short collinear dipole; (b) wire-grid model of the coil with the shunt capacitive loads.

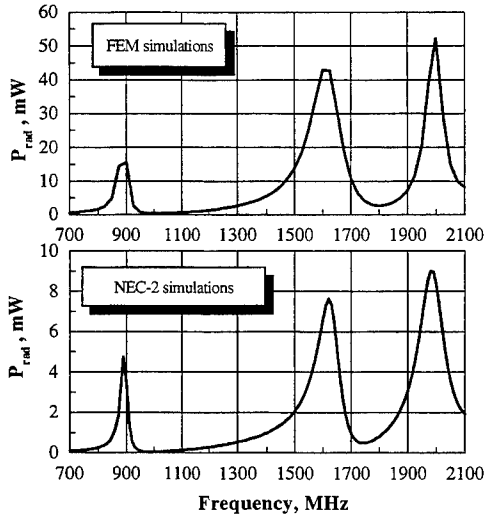

Figure 2. Calculated frequency response characteristics of the whip and coil antenna (excited by a short collinear dipole).

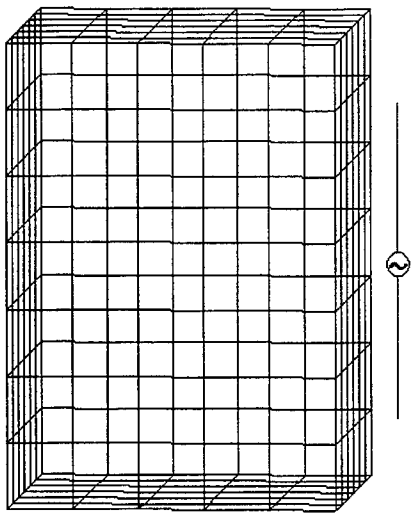

Figure 3. Surface wire-grid model of the rectangular box excited by a resonant dipole at 900 MHz.

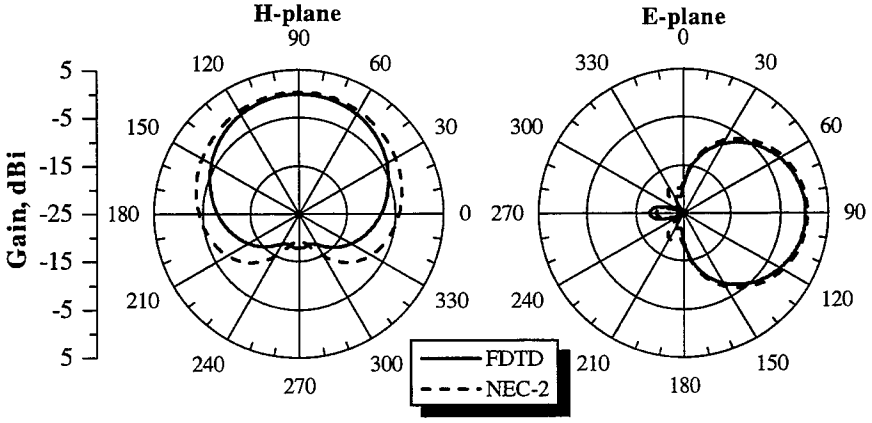

Figure 4. Calculated radiation patterns at 900 MHz of the resonant dipole placed in close vicinity to the lossy dielectric rectangular box.

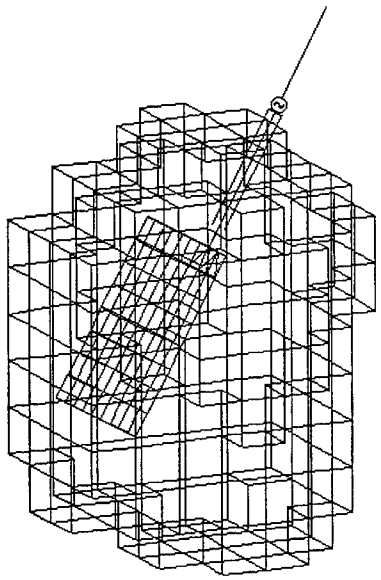

Figure 5. Wire-grid model of the resonant sleeve dipole antenna mounted on the hand-held radio placed near to the operator's head.

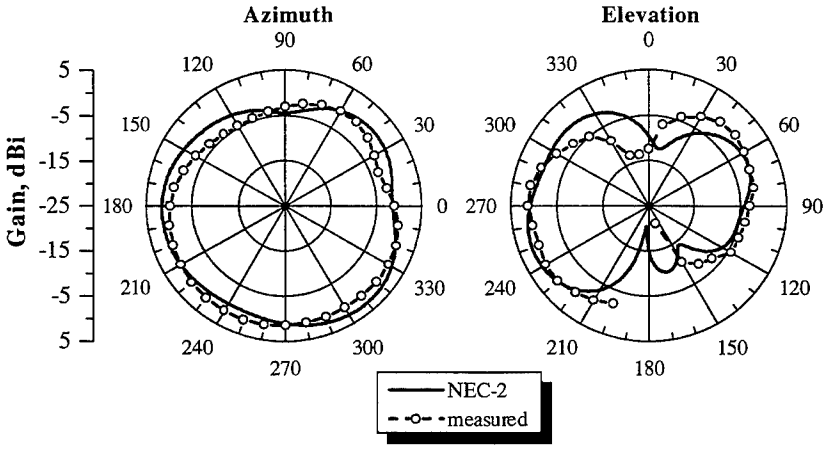

Figure 6. Calculated and measured radiation patterns at 920 MHz of the resonant sleeve dipole antenna mounted on the hand-held radio placed near to the operator's head.

"SCATTMAT: A Mode Matching and Generalized Scattering Matrix Code for Personal Computers in a Windows Environment"

Antonio Liberal, Carlos del Río, Ramón Gonzalo and Mario Sorolla
Dept. of Electrical and Electronic Engineering
Microwave and Millimeter Group
Public University of Navarra
Campus Arrosadia s/n, 31006 Pamplona, Spain
Phone: +34 48 169326 Fax: +34 48 169169 e_mail: carlos@upna.es

ABSTRACT

In this paper, a computer aided design tool is presented to simulate symmetrical radially deformed circular waveguide microwave components. This tool works with the well-known "Mode Matching and Scattering Matrix" techniques, and it has been developed in C++ language in a Windows environment, to obtain the most friendly interface between the user and the code.

The most important feature of the presented code is that it includes the possibility to display the internal mode power evolution along the component.

The code has been successfully validated with numerical and experimental results from different authors.

INTRODUCTION

Nowadays, there are a lot of microwave and millimeter waves applications like satellite communications, radar, remote sensing, plasma heating, etc., where circular waveguide components using radial deformations to achieve convenient features. Due to high fabrication cost it is very important to simulate these components before construction; in this way, then it is desirable to predict their experimental behaviors.

Mode converters, filters, tapers, horn antennas (smooth and corrugated), Bragg reflectors, resonators and many others can be analyzed readily.

The main features of the code are the following:

- It runs in a personal computers (486 or higher) under Windows environment.
- The program controls the memory resources to avoid the machine overflow. Besides it displays a message if the total machine resources are insufficient to calculate the component.
- Logically, TE and TM modes can be considered.
- A two-dimensional graphic design program to specify the component geometry is also given.
- Internal mode power evolution can be tracked down the component showing magnitude and phase at certain points given as input to the code.
- Any mode mixture is allowed at the input of the component, if needed.

The computation time, other than the processor speed, depends on the number of modes taken into account which fixes the size of the matrix. Also the number of internal component points to be

visualized determine the number of considered and stored matrices. These two parameters, number of modes and points to visualize determine the memory resources for the calculation.

NUMERICAL METHOD

The used numerical method is the well-known "Mode Matching and Scattering Matrix" method [1]. In order to visualize the internal power evolution along the whole component, it is compulsive to store all the partial scattering matrices. To get the power distribution in one particular point, it is also compulsive to know the whole scattering matrix from this point toward the input, and the whole scattering matrix from the same point toward the output or end of the component.

The calculation procedure has two differents steps:

- *Calculation of the whole scattering matrix*, in this stage, all the submatrices are stored in a binary tree form. This means, two matrices of one level are combined to get a new matrix of a higher level. Working in this way, at the end of the process, on the top of the tree, we will obtain the global scattering matrix of the whole component. This is illustrated in Fig. 1 for the case of 4 elements or sampling points. Where **z** is the longitudinal position and $\mathbf{a_s(z)}$ is the component radius function.

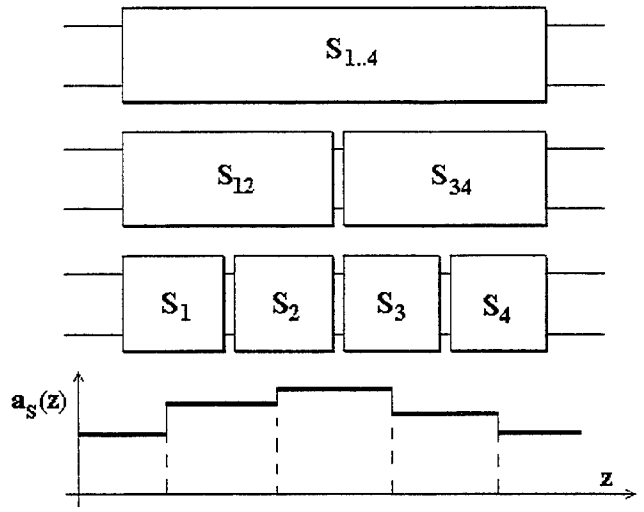

Figure 1.- Generated binary tree of scattering matrices of a simplified profile function $a_S(z)$ for the case of 4 sampling points.

- *Calculation of the internal power evolution*, from the input power data, and the calculated ones at the output, by using the previously calculated global scattering matrix, and if we go down the submatrice tree then we obtain the internal power distributions between the matrices of each level. For instance, just at the level under the top, we will have two matrices representing each one the half of the component.

In this point, we have absolutely defined the scattering matrices from the middle point of the component toward the input and the output, we are able to determinate the power distribution at the middle point of the component. At this point, we can consider the tree splitted in two, and we can apply the same process again for these two trees independently. We can work in this way since arrive to the bottom of the tree where the single scattering matrices are placed.

EXAMPLE

As a validation of the code, and to show how to proceed in order to analyze one particular component, we will develop in detail the whole calculation process from the geometrical description of the component, until the final presentation of results.

In particular, the component used to test the code will be the mode converter proposed by Vernon [2] from the TE_{02} circular smooth waveguide mode to the TE_{01} mode. The profile is defined by the formula:

$$a(z) = a_0 \left\{ 1 + 0.42\left[1 - 0.31\cos(20.9z)\right]\left[1 - \cos\left(34.9z + B_1 \sin(34.9z) + 0.2\sin(69.8z)\right)\right] \right.$$
$$\left. -0.043\left[1 + 0.6\cos(44.72z)\right]\left[1 - \cos(34.9z)\right] + E_2\left[1 - \cos(87.3z)\right] \right\} m \qquad (1)$$

where $0 \le z \le 0.18m$,

$$B_1 = \begin{cases} 0.85 & if \ z \le 0.09m \\ 1.07 & if \ z > 0.09m \end{cases} \quad \text{and} \quad E_2 = \begin{cases} -0.014 & if \ z \le 0.09m \\ 0 & if \ z > 0.09m \end{cases} \qquad (2)$$

and a_0 is the input radius value.

Such formidable expression can be introduced directly in a text file form to the SCATTMAT code to be sampled by te code or it can be introduced as sampled list of data containing the format of radius and positions. The graphical representation of mode converter profile is presented in Fig. 2.

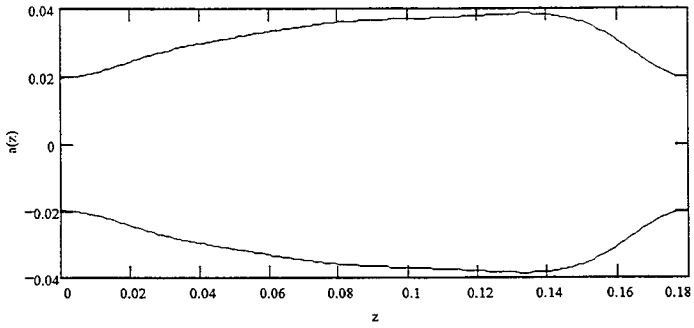

Figure 2.- Vernon's TE_{02}-TE_{01} mode converter profile. All the dimensions are given in meters.

The main idea is to sted-wise approximate the component by several waveguide slices of constant radius and to apply the mode matching techniques in order to obtain the scattering matrix at each interface between two slices. Then, combining properly all the scattering matrices of all the interfaces, we obtain the global and some partial scattering matrices definining the response of the whole or a section of the component.

Because of the symmetrically radius deformations, if we introduce at the input the TE_{02} circular smooth waveguide mode, only TE_{0m} modes can couple some power along the component [3]. Then, the mode azimuthal index value must be defined previously to start de calculations, because it will be constant.

Also the number of modes to take in account in the calculation must be defined. It is important to consider some evanescent modes, modes in cut-off, because they are also necessary to represent the fields in every interface between slices.

Obviously, the frequency has to be also defined and also some additional parameters as the metallic conductivity of the conductor employed to produce the component, the input radius, the inner media characteristics, etc. (See Fig. 3).

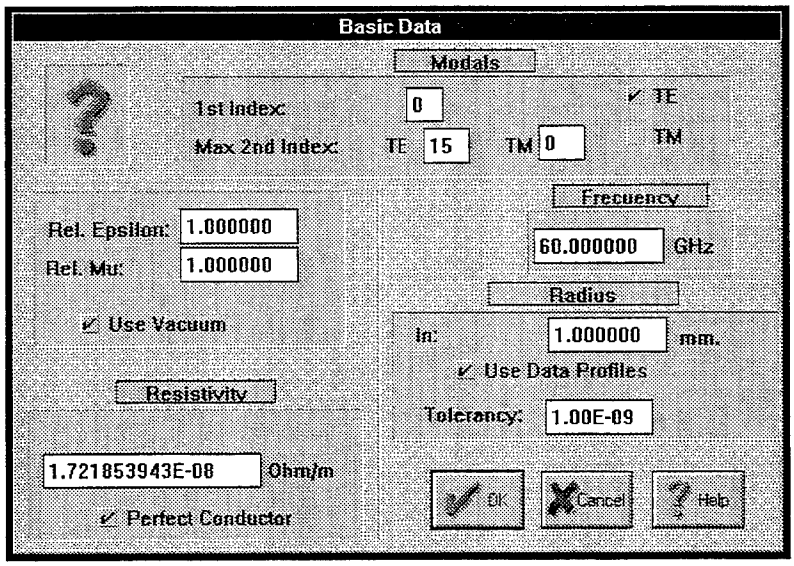

Figure 3.- Input data window of SCATTMAT

In order to define the number of points to be presented inside the component, we define a reduction factor. This factor corresponds with the number of single matrices composing one matrix of the lower level of the binary tree. This procedure allow us to save machine resources. It is important to remember that all the matrices of the binary tree have to be stored in logical or physical memory, consuming finally machine resources. Working with this factor, we can reduce the number of matrices to be stored in the calculation process, increasing probably the speed of the code (See Fig. 4).

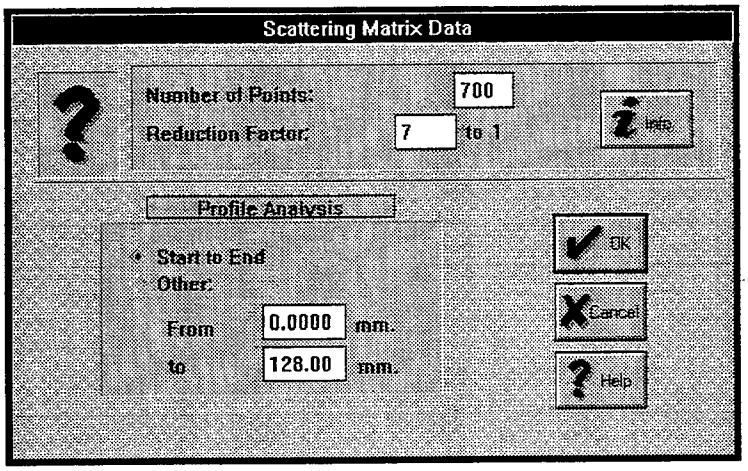

Figure 4.- Scattering Matrix data window input.

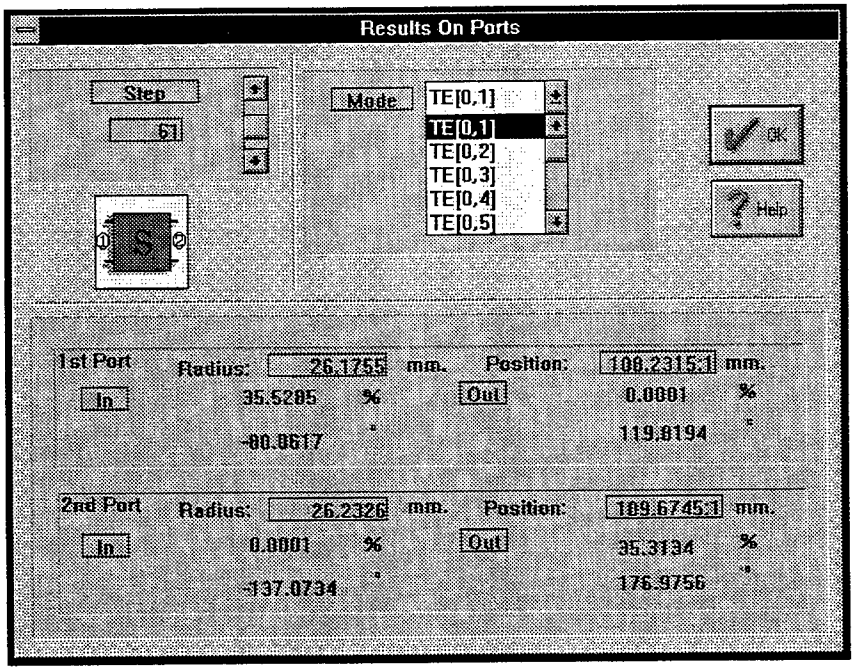

Figure 5.- Numerical data presentation of each mode power between slices.

RESULTS

The program allows different ways to present the results:

- *numerical data presentation* for each slice of the binary tree (Fig. 5). For any considered mode, it is possible to determine his amplitude at the input and output of every interface between slices.
- *graphical representation* of the mode power evolution along the component. Each mode is represented using differents colors. From the whole list of the considered modes, we have to choose six of them to be represented. We can represent the forward mode power (in the mode list, an additional "i" after the label of the mode has been added, i.e. TEi[0,1]), and the backward mode power (TEr[0,1]).

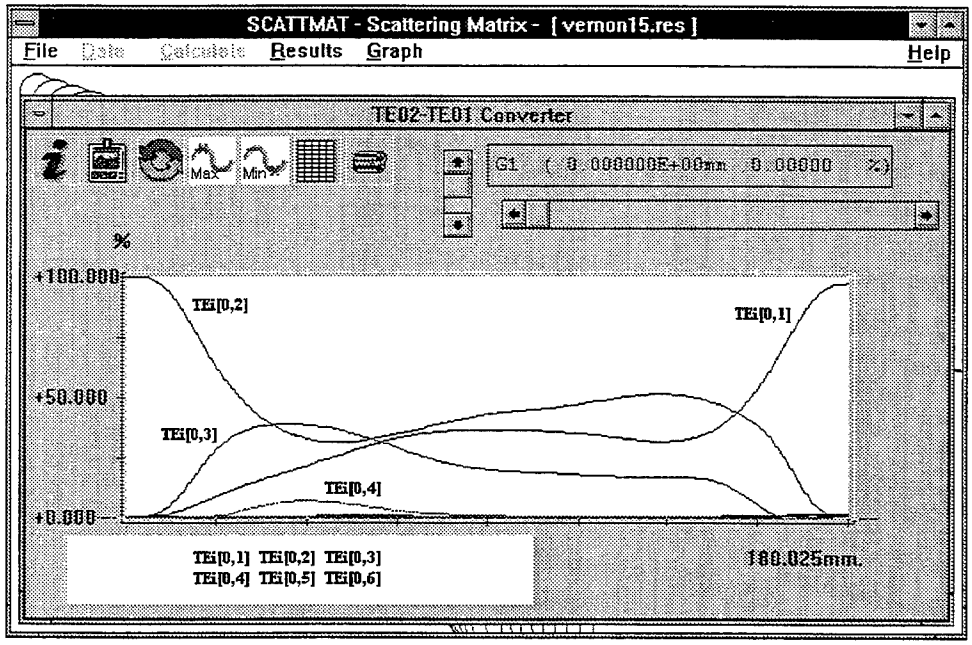

Figure 6.- Graphical representation of the internal evolution of mode power along the component.

One can see in figure 6 how the all the power at the begining of the component (converter) is in the TE_{02} mode, and the output is practically in the TE_{01} mode. A cursor is provided in order to know the instantaneously power value of every represented mode.

The obtained conversion coeficient is 97%, the same one that Vernon gave in his reference [2]. More other cases and components have been used in order to test the code, and in all cases the results have been in very good agreement with the provided by the authors.

The calculation time process depends on the number of matrices to take in account and the size ot these matrices (number of modes).

CONCLUSIONS

A new and very friendly mode matching and scattering matrix code for PC under windows environment is presented.

The code allows to analyze circular symmetric waveguide components having the capability to represent the internal mode power along the component.

The code has been proved very useful for several well known problems giving excellent processing times.

A far field radiation pattern evaluation rutine is under development to employ the code for horn antenna design. A graphical design tool, real ohmic losses calculation and tolerance effects predictions will be implemented in the near future.

REFERENCES

[1] Collin, R.E. "Field theory of guided waves". Mc Graw Hill, 1960.

[2] Buckley. M.J., Stein, D.A. and Vernon, R.J. "A single-period TE_{02}-TE_{01} mode converter in a highly overmoded circular waveguide". IEEE Transactions on Microwave Theory and Techniques, Vol. 39, N° 8, pp. 1301-1306, August 1991.

[3] Doane, J.L. "Propagation and mode coupling in corrugated and smooth-wall circular waveguides". Infrared and Millimeter Waves. Vol. 13, Millimeter Components and Techniques, Part 4, Chapter 5, pp. 123-171. K. Button Editor. Academic Press.

EVALUATION OF NEAR FIELD ELECTROMAGNETIC SCATTERING CODES FOR AIRBORNE APPLICATION

James M. Taylor, Jr., Andrew J. Terzuoli, Jr.

Air Force Institute of Technology, Wright-Patterson AFB, OH 45433

ABSTRACT

This paper details the results of simulations of experiments conducted at an indoor near field measurement range. The cone-cylinder-sphere target was used experimentally for various trajectories and antenna orientations. Each trajectory presented was simulated using two near field electromagnetic scattering codes: the Uniform Theory of Diffraction (UTD)-based Numerical Electromagnetic Code-Basic Scattering Code (NEC-BSC) and the Shooting and Bouncing Ray (SBR)-based NPATCH code. The analysis of the results showed good correlation between measured data and the response predicted by the two codes. Run time comparison between the two codes showed NEC-BSC operating much faster than NPATCH; however, NPATCH has a more precise modeling capability that can lead to more accurate results for intricate objects.

INTRODUCTION

One of the keys to validating a numerical electromagnetic code is comparing predicted results to measurements made in the laboratory. For far field prediction codes, there are dozens of large and small measurement ranges that can analyze a wide variety of targets from simple cylinders and spheres to full size aircraft. Unfortunately, near field ranges are so specialized that the Missile Engagement Simulation Arena (MESA) [1] facility at China Lake, California, is the only facility in the country overtly configured to handle the requirements of a moving transmitter/receiver in the near field.

The following discussion describes the results of simulations of near field scattering experiments using two near field electromagnetic scattering codes: the Uniform Theory of Diffraction (UTD) [2]-based Numerical Electromagnetic Code-Basic Scattering Code (NEC-BSC) [3] and the Shooting and Bouncing Ray (SBR) [4]-based NPATCH code [5].

EXPERIMENTAL CONFIGURATION

At the MESA test range, formerly known as the Encounter Simulation Laboratory (ESL), a unique capability exists to evaluate the performance of a missile fuze in a laboratory environment. This low-cost alternative to live fire testing allows objects up to 11,340 kg to be suspended from the ceiling of high bay that is 27.4 m high, 123.4 m long, and 45.7 m wide. On the floor, a 79.2 m long track is used to move the test fuze or radar system past the target, while a computer system controls data collection and the relative engagement geometry.

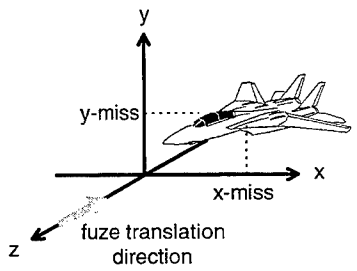

Figure 1. Target relative coordinate system used for encounters at MESA.

Target Relative Coordinate System

Figure 1 shows a typical engagement scenario using a target relative coordinate system, where the x-miss and y-miss distances are the key parameters. This location indicates the position of the centroid of the target relative to the origin of the global coordinate system. Some members of the missile simulation community prefer this system because it places the point of closest approach (PCA) between the missile and the centroid of the target in the xy-plane. At the MESA facility, the global z axis contains the track used to propel the fuze past the target, while the positive y axis is directed upward from the floor [6]. After the target is located in the desired x-miss, y-miss configuration, it can be rotated to the desired roll, pitch, and yaw angles. Furthermore, the fuze positioning device can independently rotate the fuze in roll, pitch, and yaw as well. With all of these options, nearly any real-world missile encounter geometry can be simulated at this facility.

MESA Fore Antenna

The data gathered at the MESA facility is often times classified, since it deals with actual missile hardware and full-size or scale models of operational aircraft. Fortunately, there have been some experiments conducted with unclassified targets and antennas. One such antenna was used in a series of MESA tests identified as Test Number 9303. This antenna, herein referred to as the MESA Fore Antenna, was used to gather near field data on several targets including a 0.3556 m (14 in) diameter calibration sphere. From data that included linear trajectories past the sphere, it was possible to reconstruct the majority of the far field gain pattern.

MESA Target Encounter Geometry

Another unclassified target, the cone-cylinder-sphere or MESA Target for this research, provided a perfect electric conducting object to study electromagnetic interactions encountered in the near field. Its distinctive shape, as shown in Figure 2, provides many sources of interesting electromagnetic phenomena, such as the dominant specular reflections and the less influential effects of diffraction from changes in radius of curvature, traveling waves, surface waves, and tip diffraction. Another benefit for validation purposes is that the model has no possible sources for multiple reflections which can cause ambiguities in determining the location of strong scattering centers. In the case of the MESA Target experiments, the fuze radar was operated at 12.65 GHz (λ=2.37 cm), with an 18 cm radius calibration.

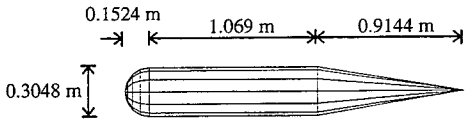

Figure 2. Diagram of MESA Target: a cone-cylinder-sphere.

For this research, several experiments were compared to simulations of the same encounter geometry using the NPATCH and NEC-BSC codes. Table 1 contains the target orientation for the tests evaluated during this portion of the research, while Figure 3 defines the yaw angle.

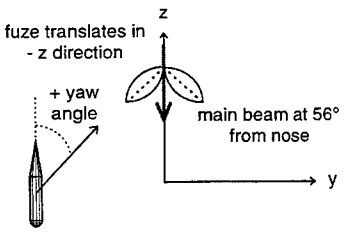

Figure 3. Target yaw angle used in simulation coordinate system.

Table 1. MESA Target orientations for measured data.

Test ID	Target Yaw
M1-1	+30°
M1-2	-60°
M1-3	-90°
M1-4	-120°

SCATTERING CODE OPERATION

NEC-BSC

NEC-BSC utilizes the principles of geometrical optics in conjunction with the Uniform Theory of Diffraction to arrive at high frequency scattering approximations in the near field. In UTD analysis, only the major structural features of a model need inclusion, since the code uses a ray optical approach to calculate the incident field at locations within the geometry. The scattering object is modeled with several solid geometries: n-sided flat plates, composite ellipsoids, cone frustums, and elliptic cylinders. For accurate UTD results, the plate edges should be larger than a wavelength of the incident field. When smaller structures are important in the model, a moment method solution can be integrated into an overall hybrid solution.

Once the incident field is known at each significant point in the geometry, edge diffraction and subsequent interactions with other structures are determined using UTD. The total field at each point in the trajectory is the coherent sum of the incident field, singly and doubly-reflected fields, diffracted fields, reflected-diffracted fields, and diffracted-reflected fields. Software options allow each of these components to be included or excluded in the final solution.

NPATCH

For NPATCH, a Shooting and Bouncing Ray (SBR) approach to the Physical Theory of Diffraction (PTD) is used for calculating the scattering solution from a test object. All of the object's surfaces, even curved ones, are described by a collection of flat triangular facets that cover the surface of the object. Segments of the model with significant edge diffraction are indicated by the user in a separate file. To satisfy the PTD accuracy requirements, the size of the integration surface is reduced during the code's execution so that no integration surface is more than a wavelength long in size. These so-called "baby facets" are then evaluated to determine the contribution from each to the overall scattered field. The total scattered field at each point along the trajectory is the coherent sum of the scattered fields from the individual baby facets.

NEAR FIELD SCATTERING FIGURE OF MERIT

Once the experiments and simulations are performed, it would be desirable to have a metric to compare the *radar observability* of an object in the near field. Unfortunately, radar cross section, a range and antenna-independent scattering descriptor loses its usefulness in the near field. To give a radar engineer an idea of the scattering strength of an object in a particular scenario, a two-step measurement technique has been developed at the MESA test facility. The first measurement sequence takes place with the target in position and the antennas rotated to their desired position for that test. A second measurement sequence is then initiated with a calibration sphere replacing the target, while the antennas are rotated such that the main beam is always directed toward the center of the sphere.

$$\text{Relative Power Return Ratio} = \frac{P_r(\text{target}) / P_t}{P_r(\text{sphere}) / P_t}$$

The result is that data from the MESA Target experiments is given in "dB Relative" units. In other words, the scattering strength of the target in a particular orientation is defined in terms of the ratio of the power returned from the target to that returned from the calibration sphere. This same procedure is used in the simulations to achieve a similar "dB Relative" output. If the relative power return ratio is scaled by a constant of proportionality equal to the far field RCS of the sphere, a new quantity can be defined representing a *near field RCS*. However, it is more straightforward and actually simple to use a relative power return ratio.

COMPARISON OF EXPERIMENTAL AND SIMULATED RESULTS

Run Time Comparisons

When NEC-BSC and NPATCH were used to simulate the MESA encounters the disparity between the two programs became obvious. The approximations made in the UTD solutions obtained by NEC-BSC allowed it to operate much faster than the more methodical process of shooting and bouncing rays in NPATCH. When executed on a Pentium®-powered personal computer, the NEC-BSC simulations took an average of 10 seconds to complete. At the other extreme, the average NPATCH trajectory lasted for approximately 1700 seconds even though it was operated on a Silicon Graphics workstation. The main reason for the long execution time is that NPATCH must divide the geometry of the model into

baby facets and perform a PTD analysis on each, as well as perform blockage checking for reflected rays. If this geometry had been more complicated and permitted multiple bounces on the object, the run time would have increased significantly.

Trajectory M1-1

The first experiment, denoted M1-1, showed the effect of the main beam of the MESA Fore Antenna oriented so that it pointed directly *down the nose* of the right circular cone on the MESA Target. This represents a target orientation where the incident energy from the radar is near grazing to the cylindrical portion of the target and thus has a low return ratio. Figure 4 shows the measured and predicted values from this trajectory. Note that the NEC-BSC and NPATCH calculations are truncated for return ratios below -30 dB, since the synthesized antenna pattern approximation makes anything below this level invalid. As seen in Figure 4, the antenna approximations seem valid for the region where the main beam illuminated the target. Despite the lack of perfect agreement, the data does capture the lobing pattern caused by constructive and destructive interference from the cylindrical and conic scattering surfaces is captured.

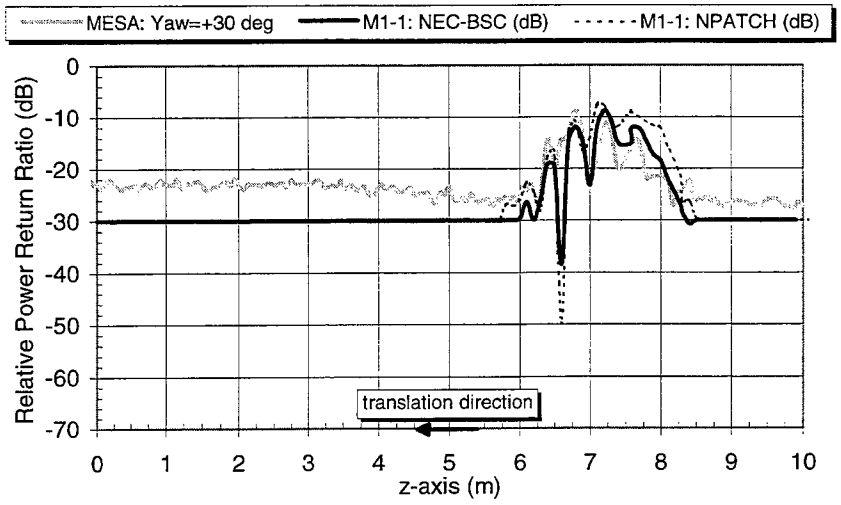

Figure 4. Test M1-1: MESA Target at f=12.65 GHz, x=0, y=-10.67 m, Yaw=+30°.

Trajectory M1-2

When the target is yawed to -60°, it presents a broadside view to the main beam of the antenna. Both NPATCH and NEC-BSC do a good job of modeling the effect seen when the main beam tracks along the long axis of the target, coplanar with the surface normal of the cylinder. From Figure 5, the few discrepancies between measured and predicted results could be the result of antenna modeling errors or the inability of the programs to model traveling waves and other scattering effects.

Trajectory M1-3

As the target yaw is varied further, the dominant specular return of the cylinder is replaced by the broad return from the spherical end cap. In the orientation described in Figure 6, the cylinder surface normal receives energy at only grazing incidence. The peak return is slightly less than 0 dB and occurs when the main beam peak is illuminating the spherical cap. This result is reasonable since the target appearance from this orientation consists of a majority of the spherical cap with portions of the cylinder only visible at grazing incidence. When compared to the 0.3556 m diameter calibration sphere, the

0.3048 m diameter MESA Target has a smaller cross section, contributing to the slightly less than 0 dB relative power return ratio at the peak.

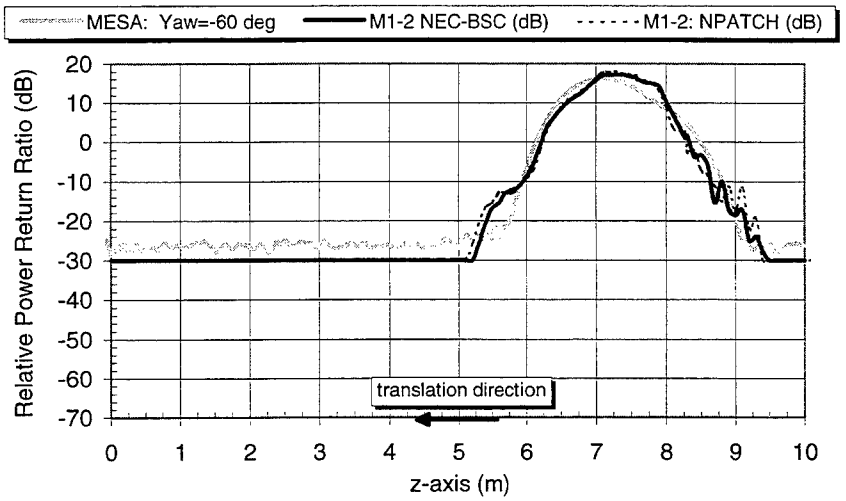

Figure 5. Test M1-2: MESA Target at f=12.65 GHz, x=0, y=-10.67 m, Yaw=-60°.

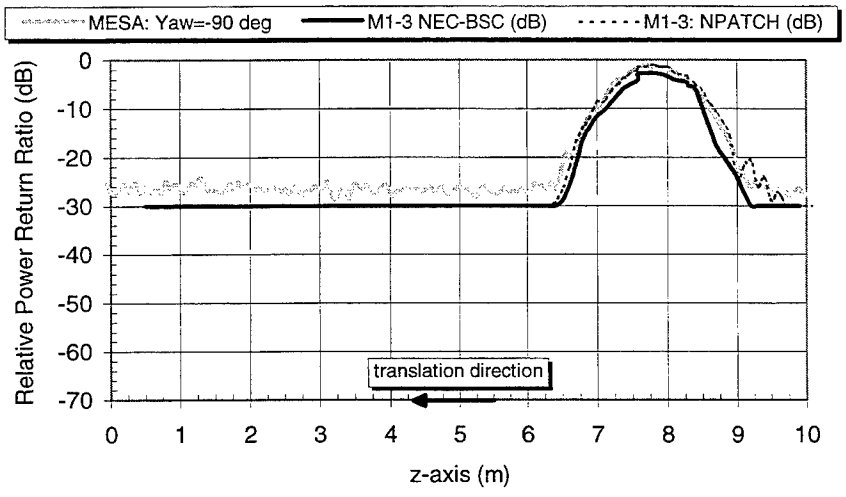

Figure 6. Test M1-3: MESA Target at f=12.65 GHz, x=0, y=-10.67 m, Yaw=-90°.

Trajectory M1-4

The final experiment had the MESA Target oriented such that the main beam was incident on the spherical cap nearly exclusively. In this orientation, as indicated in Figure 7, the broad peak is observed as in Trajectory M1-3 of Figure 6. For Trajectory M1-4, the peak return is lower than Trajectory M1-3, since less of the cylinder is visible to the main beam.

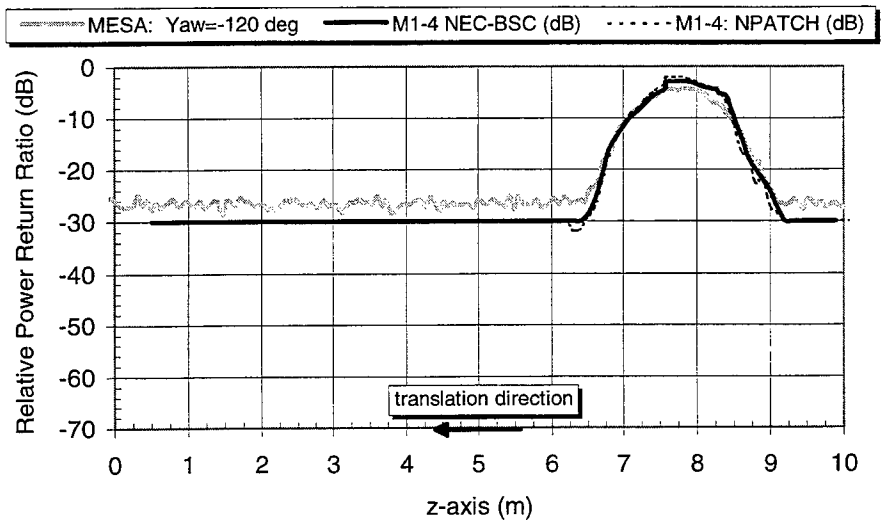

Figure 7. Test M1-4: MESA Target at f=12.65 GHz, x=0, y=-10.67 m, Yaw=-120°.

CONCLUSIONS

Overall, the results from both NPATCH and NEC-BSC simulations showed good agreement with the measured data. Given this apparent success in predictions and measured data, these codes seem well suited to make the extension from simple objects to more detailed ones, like aircraft. However, as the model details begin to deviate from shapes that NEC-BSC can model exactly, the errors introduced into the simulation increase. More detailed models in NPATCH mean longer run times and more complicated model building techniques.

ACKNOWLEDGMENTS

This work was sponsored by the United States Strategic Command (USSTRATCOM), Offutt AFB, Nebraska. The authors are indebted to the following individuals for their assistance: Ron Marhefka, Andy Lee, Cullen Lee, Dennis Andersh, Sam McKenzie, Annie Webb, Helen Wang, Grant LeBarre, James McGuire, Bill Brown and Gerry Gerace.

REFERENCES

[1] MESA, "Missile Engagement Simulation Arena," Electronic Message, 24 January 1996.

[2] R.G. Kouyoumjian and P.H. Pathak, "A uniform geometrical theory of diffraction for an edge in a perfectly-conducting surface," *Proc. IEEE*, vol. 62, pp. 1448-1461, Nov. 1974.

[3] R.J. Marhefka, J.W. Silvestro, *Near Zone - Basic Scattering Code User's Manual with Space Station Applications*, T.R. 716199-13, The Ohio State University, ElectroScience Laboratory, Columbus, OH, March 1989.

[4] H. Ling, R.C. Chou, S.W. Lee, "Shooting and bouncing rays: calculating the RCS of an arbitrarily shaped cavity," *IEEE Trans. Antennas and Propagat.*, vol 37, no. 2, pp. 194-204, Feb 1989.

[5] S.W. Lee, S.K. Jeng, *NcPTD 1.2 A High Frequency Near-Field RCS Computation Code Based on Physical Theory of Diffraction*, DEMACO, Inc., Champaign, IL, June 1991.

[6] Reg Memo C2916/000, Naval Weapons Center, China Lake, CA, 12 June 1993.

FASANT: Fast Computer Code for the Analysis of Antennas on Board Complex Structures

M. Felipe Cátedra, Jesús Pérez, Francisco Saez de Adana

Grupo de Sistemas y Radio. Departamento de Ingeniería de Comunicaciones
Universidad de Cantabria
39005 Santander, Spain
FAX: 34 42 201873, e-mail: felipe@gsr.unican.es

ABSTRACT

A computer code is presented for the analysis of antennas on board satellites, aircrafts and other complex bodies. The code is based on the Uniform Theory of Diffraction. The bodies can be modelled by plane facets and curved surfaces. The geometrical input files can be generated by the most used Computer Aided Geometrical Design (CAGD) tools. Special algorithms have been developed to speed-up the ray-tracing computation for both flat and curved surfaces. The code can also be applied to the analysis of arbitrarily shaped reflectors.

INTRODUCTION

The code combines quite advanced ray-tracing techniques and parametric surfaces in the format of Bezier's patches with GTD-UTD. All surfaces are assumed to be perfectly conducting.

The structure under analysis must be suitable to be modelled by plane polygonal facets and a set of a few curved surfaces modelled by polylines or by NURBS (Non Uniform Rational B-Splines), as is usually the case of satellites, aircraft, cars, etc. The code uses special angular Z-buffer algorithm which has made the code very efficient. Far and Near-Fields values are obtained considering direct, reflected, edge-diffracted, slope diffracted, corner diffracted, double-reflected, reflected-diffracted, diffracted-reflected and double-diffracted rays. An equivalent double-diffraction is incorporated to treat coupling by creeping waves.

The ray-tracing algorithm for curved surfaces is in part similar to that described in [1]-[2]. The angular Z-buffer algorithm is outlined in the appendix.

FUNCTIONALITIES: Near and Far Field patterns. Mutual coupling between antennas. Each ray mechanism can be evaluated separately.

SYSTEM REQUIREMENTS: PC or Workstation

LANGUAGE: FORTRAN

STATUS: Operative and validated

INSTITUTION WHICH SPONSORED THE SOFTWARE TOOL: INTA (Spanish National Agency For Aerospace)

INPUT FILES

There are four input files:

* GEOMETRY FILE:

The geometry of the body is described in terms of polygonal plane facets and arbitrary curved surfaces. They are defined with the DXF format. The file can be generated by many CAGD tools. If it is created with the AUTOCAD package the following two basic rules are used:

- The plane facets are created with the command '3DFACET'
- The arbitrary surfaces are created using the command '3DMESH'

* MAIN DATA FILE:

This file contains the following information:

- The name of the geometry file;
- The option for the field calculation: 'LEJ' if far field is required, 'CER' if one wants to calculate near field and 'ACO' when one wants to compute the coupling between a pair of antennas.
- The rays considered in the field computations: Direct field, Reflected field , Diffracted field,.., etc.
- The location and direction cosines of the reference coordinate system associated with the transmitter antenna with regard to the absolute coordinate system. The antenna coordinate systems is the coordinate system where the antennas are described. The absolute coordinate system is the coordinate system where the geometry, the observation points, the observation directions and the results are referred to.
-The type of antenna considered. There are two possibilities: DIP' when the antenna is defined as a set of infinitesimal dipoles; and 'ANT' for a generic antenna defined by its radiation pattern . If the option 'DIP' is chosen it must be given: the number of electric dipoles and the number of magnetic dipoles; the product between the length and the current of each dipole; and the location and the direction cosines of the coordinate system associated to each dipole with respect to the antennas coordinate system. If option 'ANT' has been selected it must be given: the name of a file which contains the radiation pattern of the transmitter antenna. The code works with three formats of antenna patterns: 'REV' when the radiation pattern has symmetry of revolution, 'RV2' if the radiation pattern is defined by the E-plane and H-plane patterns, and '3DE' for three dimensional radiation pattern description.
- The frequency sweep information: initial frequency, final frequency, number of frequencies analysed.

- If far field ('LEJ') has been selected the parameters which define the angular sweeps must be given.
- When coupling between antennas ('ACO') is selected, the following information describing the 'passive antenna' is provided: name of the 'passive antenna' file; type of description of the radiation pattern ('REV', 'RV2' or '3DE'); location and direction cosines of the coordinate system associated with the 'passive antenna' with regard to the antennas coordinate system
- The normalised value for the resulting fields.

* POINTS FILE:

If the user selects near field computation (option 'CER' in line two), a file called 'PUNTOS.DAT' which contains the points where the near field is calculated must be provided.

* RADIATION PATTERN FILES:

The program works with three formats of antenna patterns as is described above. The fields must be given in magnitude (in dB's) and phase (in degrees).

OUTPUT FILES

If far field or near field options have been selected (option 'LEJ' or 'CER') several output files corresponding to each one of the coupling mechanisms selected computations and the total field are generated. The format of the output files depends on the type of field computed: far-field or near-field. In the first case, for each selected frequency and for each direction of observation, the files show the amplitude and phase of the angular components (theta and phi) of the electric field. In the case of near-field computation, the output files show, for each frequency and point of observation, the Cartesian components of the electric field (magnitude and phase).

When the program calculates coupling between a pair of antennas (option 'ACO' in line two of the main data file) the coupling value is shown on the screen, so there are not output files.

EXAMPLES

Figure 1 presents far-field results relative to the simplified model of a satellite (all dimensions are in meters). The antenna is a vertical electric dipole located in (14.0,2.0,2.3). Component theta of the electric field has been computed for a phi=90° cut at frequency=1.0 GHz. Only direct, reflected and diffracted rays have been taken into account in order to compare the code with the available version of the NEC-BSC code [4].

To illustrate the performance of the program for double effects, especially double diffraction, the radiation pattern of a vertical electric dipole over the structure of figure 2 has been compared with the Moment Method prediction. The body is formed by two parallel square facets perpendicular to the Z axis. The facets dimensions in meters are 2x2 and 3x3. The dipole is located on the Z axis over the first facet.The distance between the facets are 0.9m. The distance between the dipole and the first facet is 1m. Figure 2 shows the results obtained for the E-theta component relative to the phi=90° cut at a frequency=0.3 GHz.

The coupling computation functionality has been validated with measurements of the structure shown in figure 3. Two pyramidal horn antennas and a TTC antenna were analyzed at two frequencies (8 and 12 GHz). The results correspond to five configurations relative to different locations of pairs of antennas on the structure. Table 1 shows the comparison between the code coupling values and the measurements. The measured values were obtained with four different systems and chambers. In Table 1 first and second columns present the configurations and the frequency, respectively. The third column presents the values of FASSAT and the remaining four columns show the measured values M(*) and the error with respect the code E(*). All the values are in dB.

CPU-TIME AND MEMORY REQUIREMENTS

In order to illustrate the performance of the code, the following table shows the CPU times obtained for a 70 facet model. The antenna is a vertical electric dipole and far field was analyzed. The values correspond to a cut of 181 values. The computer was a PC-Pentium at 120 MHz with 16 Mb of RAM. All the time values are in seconds.

- Geometric pre-processing: 2"
- Simple effects: 3"
- Double reflections: 1"
- Reflection-diffractions: 2"
- Diffraction-reflections: 2"
- Double diffractions: 59"

- Total time: 69"

FIGURES AND TABLES

Figure 1: Results of the simplified model of satellite.

Figure 2: Results of the two-facet structure.

Figure 3: Body for the antennas coupling calculations.

Table 1: Comparison between calculated and measured values of antennas coupling.

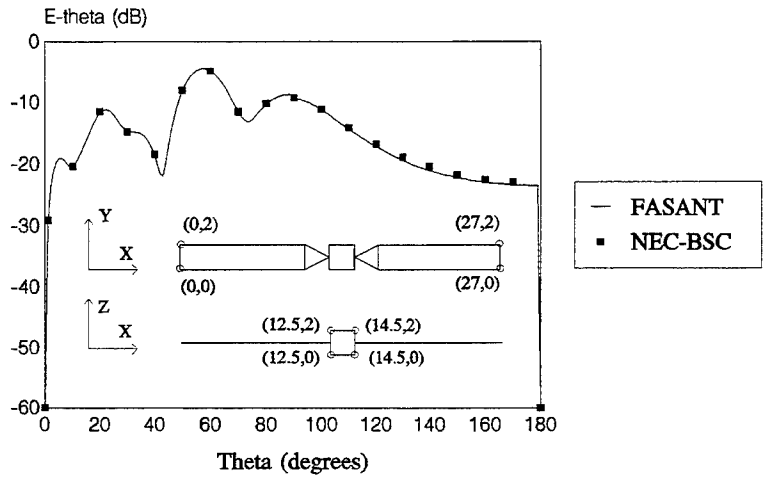

FIGURE 1.

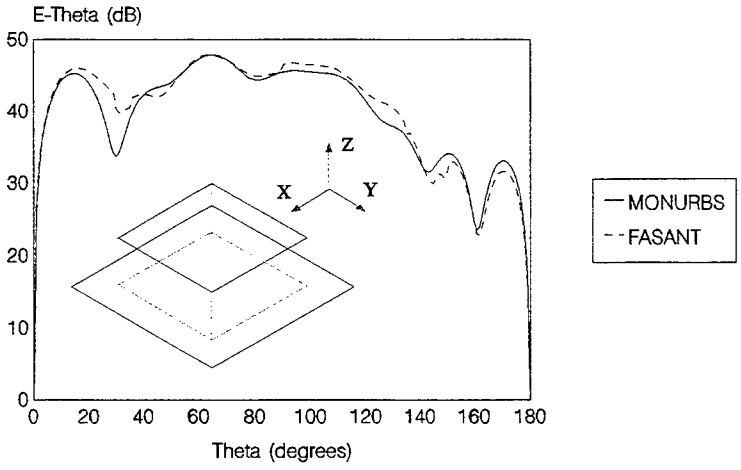

FIGURE 2.

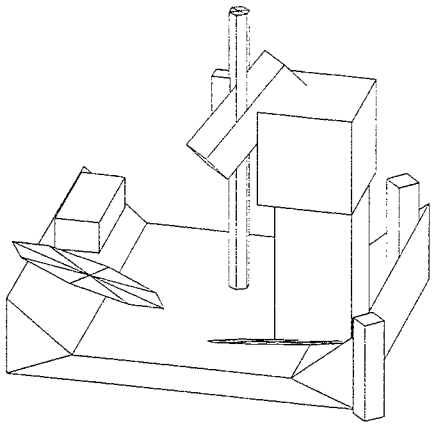

FIGURE 3.

Con.	f	C.	M(1), E(1)	M(2), E(2)	M(3), E(3)	M(4), E(4)
1	8	-69.2	-85.7, 16.5	-85.0, 15.8	-79.3, 10.1	-76.5, 7.3
1	12	-79.2	-78.9, 0.3	-80.0, 0.8	-84.3, 5.1	-80.1, 0.9
2	8	-79.4	-77.5, 1.9	-77.1, 2.3	-69.8, 9.6	-68.5, 10.9
3	8	-85.9	-80.3, 5.6	-80.4, 5.5	-78.6, 7.3	-75.1, 10.4
3	12	-88.2	-	-	-87.7, 0.5	-82.1, 6.1
4	8	-70.9	-71.4, 0.5	-71.8, 0.9	-71.6, 0.7	-70.1, 0.8
5	8	-89.4	-90.5, 1.1	-91.2, 1.8	-87.1, 2.3	-80.6, 8.8

TABLE 1.

APPENDIX: THE ANGULAR Z-BUFFER (AZB) ALGORITHM

The AZB algorithm can be considered as a modification of the Z-Buffer and the "Bounding Volumes" algorithms to speed-up the UTD analysis in Picocells. The direct-ray shadowing problem can be considered to introduce the AZB algorithm. In this problem we want to know if there is any object between the observation and the source point which can interrupt the Line of Observation (LOS) of the direct ray. In order to avoid the brute force procedure of checking if each one of the facets of the scene interrupts, the LOS the AZB algorithm proceeds as follows:

The objects of the scene are allocated in a mesh defined in the θ-φ space seen from the source. Figure A1 defines an angular region seen from the source, Figure A2 shows where the facets are allocated when the entire space seen from the source is considered. Each cell of the mesh of Fig A2 is defined by an angular margin of size $\Delta\theta\Delta\varphi$. Only the facets closer to the source are allocated in the cells.
A column of a matrix is assigned to each one of the cells of the mesh. It is the AZB matrix. The identification number of the facets allocated in each cell is arranged in the corresponding vector of the AZB matrix. The identification numbers of the facets are sorted in the vector considering the distance to the source, starting from the closest one. When a LOS is checked for a possible shadowing the $\theta_o\varphi_o$ angular coordinates of this line and the AZB cell corresponding to these coordinates are found. Only the facets of the column corresponding to the cell are checked for possible shadowing of the LOS. This procedure is the AZB algorithm which reduces by a factor of 1/N the number of facets to be checked, N being the number of cells in the mesh. This reduction is even greater in practice because the facets that have a larger possibility to shadow the LOS are those closer to the source which are arranged in the first places in the AZB matrix and therefore are checked first.

The AZB algorithm is applied to the ray reflected by a facet in a similar way. The antenna image in this facet is the source to be considered in the definition of the LOS. Now the angular margin on which the mesh is developed is much smaller than for the case of the original source (the transmitter), as is pictured in Figs. A-3 and A4. This fact means that the AZB for the reflection is smaller than for the direct ray and therefore the time applying the algorithm for reflection is also less. An AZB matrix for the reflection must be found for each facet seen from the transmitter antenna in a post-proccessing step. This implies an initial expense of time that, however, is largely recovered when the coverage in a great amount of points is required. The AZB algorithm is a quite efficient method in CPU-time but it requires some amount of memory resources (16 to 32 Mbytes can be enough).

For a double (or higher order) reflection the AZB is applied considering the second image (or higher order image) as source in the definition of the LOS

The AZB is applied for the rays diffracted by an edge considering a mesh defined by the β ϕ angles, where β is the angle of the Keller's cone and ϕ is the angle that forms the diffracted outgoing ray with the illuminated facet of the wedge. In the pre-proccessing, an AZB shall be computed for each illuminated edge.

FIGURES

Figure A1. Example of an angular region seen from the source

Figure A2. The complete angular space seen from the source is obtained varying θ from 0 to π and φ from 0 to 2π. The complete angular space is split in a set of N cells using the rectangular mesh of the figure.

Figure A3. Picture of the angular region seen from the image of a facet. This region is limited by the sides of the facet.

Figure A4. The complete angular θ-φ space seen from the image of a facet is limited by a rectangle that encloses the four-sides figure that bound the facet in the θ-φ space (in this space the sides of this figure are in general curve. This fact has not been considered in the figure).

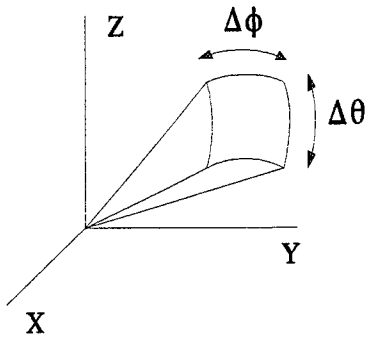

FIGURE A1.

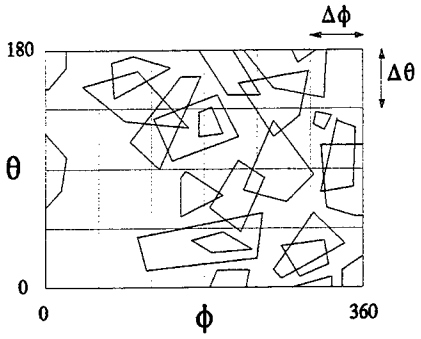

FIGURE A2.

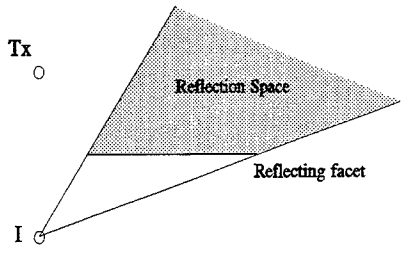

FIGURE A3.

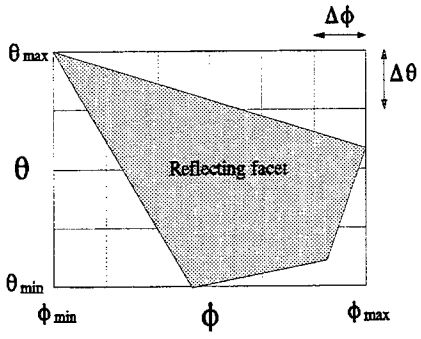

FIGURE A4.

REFERENCES

[1] J. Pérez, J. A. Saiz, O. M. Conde, R. P. Torres, M.F. Cátedra: *"Analysis of Antennas on Board Arbitrary Structures Modelled by NURBS Surfaces"*, IEEE Transactions on Antennas and Propagation. *To appear.*

[2] J. Pérez, J. Sáiz, M. F. Cátedra *"Analysis of Radiation and Scattering of bodies modelled with parametric surfaces"*. IEEE International Symposium of IEEE Antennas and Propagation Society, Baltimore, Maryland, July 21-26, 1996.. (pp. 1820-1823).

[3] A. S. Glassner, Editor: "An introduction to ray tracing", Academic Press, San Diego CA, 1989.

[4] R. J. Marhefka, W. D. Burnside: *"Numerical Electromagnetic Code-Basis Scattering Code"*, Technical Report 712242-14. The Ohio State University, December 1982.

FASPRO: Fast Computer Tool for the Analysis of Propagation in Personal Communication Network

M. Felipe Cátedra, Jesus Pérez

Grupo de Sistemas y Radio. Departamento de Ingeniería de Comunicaciones
Universidad de Cantabria
39005 Santander, Spain
FAX: 34 42 201873, e-mail: felipe@gsr.unican.es

ABSTRACT

A computer tool, FASPRO, for the analysis of propagation in urban picocells is presented. FASPRO performs fully 3-Dimensional Analyses using UTD (Uniform Theory of Diffraction). The urban geometry is represented by plane facets using the DXF format. A ray-tracing technique based on the Image Theory and on the Angular Z-Buffer (AZB) algorithm is used to speed up the computations. The code makes an extensive use of dialogue windows, graphic interfaces and can be integrated with the most employed tools for the Computed Aided Geometrical Design (CAGD) and with the tools for the analysis and planning of mobile communication systems.

CODE DESCRIPTION AND METHODOLOGY

FASPRO is an accurate and efficient tool to perform deterministic analyses of propagation in urban picocells and microcells. A fully 3D propagation model is considered. The topographical input data are based on a 3D plane-facets model of the urban environment which is given in terms of DXF files. FASPRO is able to read DXF files from AUTOCAD, Microsystem, CADDS and other CAGD and topographical tools systems. In addition, FASPRO has its own facility which allows it to create new urban scenes. FASPRO visualises the geometry on the screen as a 2D map of the urban scene. The user can make a zoom of the scene and modify it in a graphical and iterative way. The scene is arranged as a set of entities, each one of them corresponding to a building. Each building is represented by its foundation, its height and the electrical constants ε and σ of its walls.

The electromagnetic analysis is performed using UTD techniques. First order coupling mechanisms (direct, reflected and edge-diffracted rays), second order coupling mechanisms (double reflected, diffracted-reflected, diffracted-reflected, double diffracted, etc.) and third order mechanisms (e.g. reflected-diffracted-reflected, etc.) are included. The total field in the observation point is obtained as the coherent adding of the fields of all the coupling mechanisms.

The transmitter antenna can be defined by a set of electric and magnetic dipoles or by its radiation pattern.

All the reflections are computed applying Image Theory taking advantage of the fact that all the facets are flat. The antenna image is given and orientated assuming that all the facets are perfect conductors. The

material constant is considered by multiplying the reflected field by the Fresnell coefficients, taking into account the incident angle and the surface roughness . The reflection of the ground surface can be treated either by one (or several) plane facets or by considering the image of the entire urban scene.

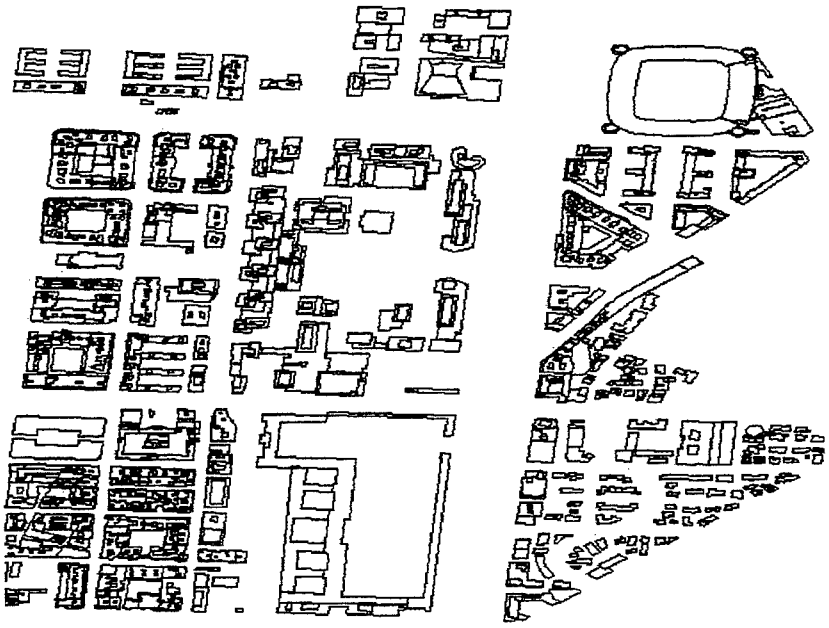

Figure 1. Example of an urban scene visualised using FASPRO. The geometrical data has been taken from a DXF file.

The diffraction coefficient is computed using UTD. This coefficient has two terms: one that takes into account the boundary between the lit and the shadow regions for the direct ray, and the other term that makes the transition boundary of the reflection to be continuous. Both terms are computed considering the facets perfect conducting. The term associated with the reflection boundary is multiplied by the Fresnell reflection coefficient of the wedge walls taking into account the incident angle in the lit wall of the wedge. It must be noted that, thanks to the incorporation of diffraction in all the edges of the 3D model, the coverage in areas in the deep shadow of the transmitter antenna can be predicted well. The coverage by diffraction in the horizontal top edges of the highest buildings is quite important because this mechanism can cover a very large area of the cell.

The diffraction-reflection is evaluated applying Image Theory, considering the appropriate rotation of the image-edge. Double-Diffraction is computed using an analytical expression to find the pair of diffraction points.

A new ray-tracing algorithm is used to speed-up the computations. This ray-tracing algorithm is based on a modification of the Z-Buffer and the "Bounding Volumes" schemes, [1], in which the elements are arranged in an angular map (AZB, Angular Z-Buffer). This algorithm is summarised in [2]-[3].

LANGUAGE

The kernel of FASPRO is written in FORTRAN. The graphics and the user´s interface has been developed using the FORTRAN Powerstation of Microsoft.

COMPUTER ON WHICH CODE RUNS

Any platform with Windows 95 or Windows NT. A minimum of 16 MB of RAM is required (32 MB or more recommended)

INPUT DATA

FASPRO reads three input files: one file defining the urban scene, another one defining the transmitting antenna and the third one specifying the remaining parameters.

The geometrical model of the scene is defined by a DXF file. This file contains information to characterise each building completely: the vertices of a polygon defining the building foundation and its height. The geometrical data should be completed with the material data of each facet. The user has two ways to define the electrical constants (ε and σ and roughness parameter): a) by introducing explicitly their numerical values; b) by a code number that associates the facet material to one of a table.

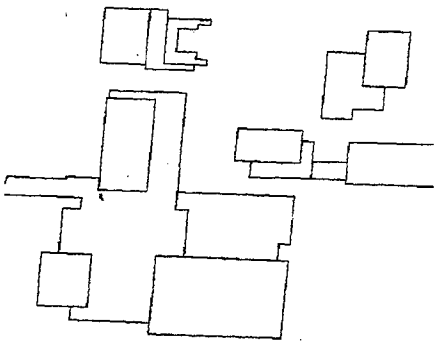

Figure 2. A part of the map of Fig. 1 is shown using the zoom capability of FASPRO.

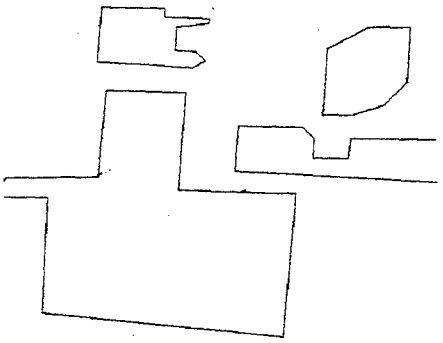

Figure 3. Many times the DXF file as it is given by a topographical data provider gives maps with to many details, as shown in Fig 1 and 2. These maps need to be cleared in order to run an electromagnetic simulator properly. FASPRO allows the user to "clear" the map. Figure 2 shows an example of an original scene and Fig 3 the corresponding cleared scene. The clearing facility of FASPRO also allows the user to investigate the impact of each building because the user can delete any one of the scene.

The second kind of input data of FASPRO contains information about the transmitter antenna. This can be defined: a) by a set of electric and magnetic dipoles (option DIP of FASPRO) or by means of its radiation pattern (option ANT of FASPRO). If option DIP is chosen then the antenna momentum and the position and orientation of each dipole relative to the antenna system shall be provided. If option ANT is chosen the antenna is described by a numerical file with its radiation pattern . In the last case we have three options: a) defined the antenna by a cut when the antenna has symmetry of revolution; b) that can be defined by the E and H-plane cuts c) the arbitrary case for which a three-dimensional numerical pattern is required.

The third set of input data required is an electrical data file that can be easily generated using the graphic user interface of FASPRO. Figure 4 shows the main screen of FASPRO to help with the input of these electrical parameters like: the ray-mechanisms to be considered (direct-ray, reflected-ray, diffracted-ray, etc.), transmitter antenna option (ANT or DIP), and the height, the ERP (Effective Radiation Power), the antenna gain, the name of the file where the radiation pattern is stored. Other parameters of the screen are: the number of points around the receiver to be considered in a statistical analysis option is chosen, the number of points along the receiver path line where the field should be evaluated in the case that the user decides to make a line path analysis, the height of the receiver antenna, the field level for the Average Duration of Fades (ADF) calculation, the mobile speed and the frequency.

The rest of the input parameters are introduced with the help of other FASPRO screens. Most of these data can be introduced either by using the keyboard or the mouse. These parameters are:

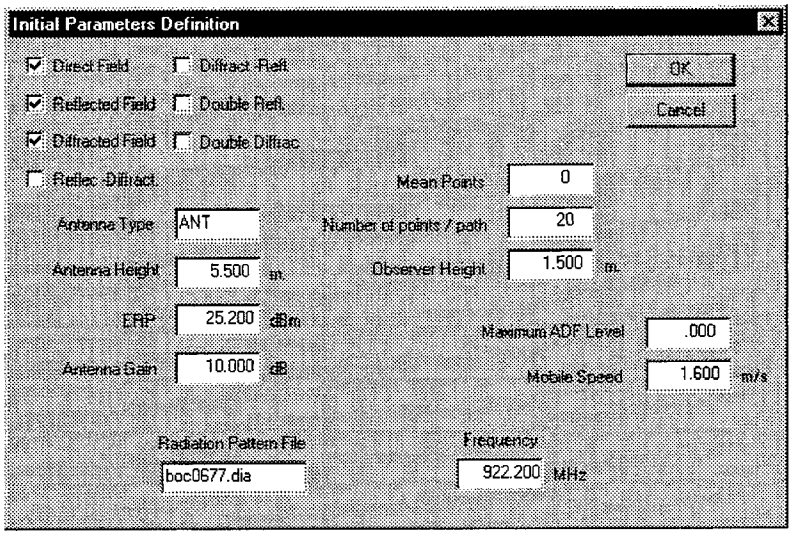

Figure 4. Main screen of FASPRO to input data.

- The location of the transmitter antenna and its axis. Figure 5 shows an example of antenna allocation and orientation.

- The option for the distribution of the observation points. These can be distributed along a line or in the nodes of a mesh. Both options can be defined graphically with the help of the zoom facility.

- The field components (E_x, E_y E_z or E_{total}) to be pictured or saved in the output files.

- The option to compute some statistical parameter such as: the PDF (Probability Distribution Function) , CPD (Cumulative Probability Distribution), ADF, LCR (level Crossing Rate) etc.

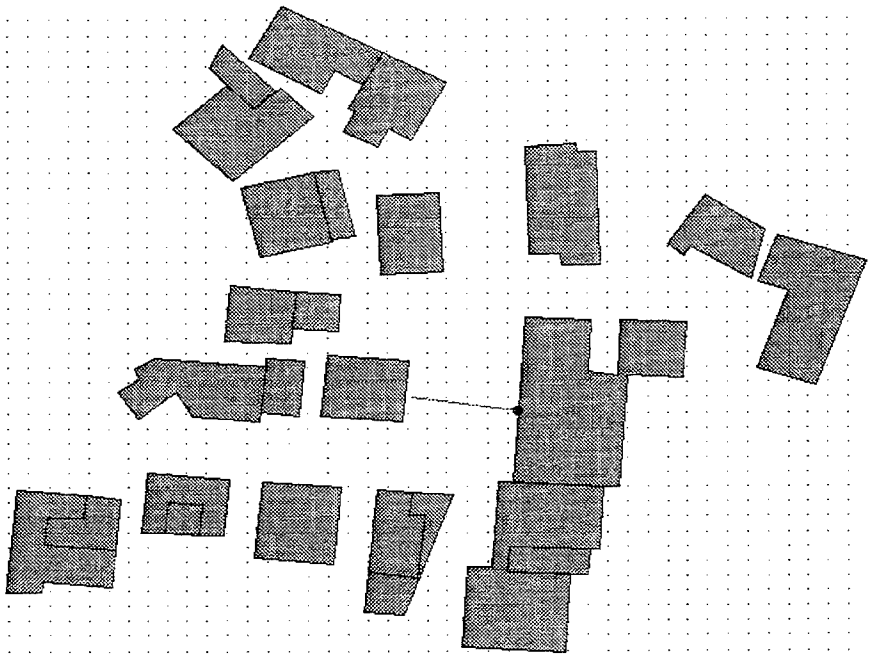

Figure 5. Example of an antenna allocation using FASPRO. The solid point indicates the transmitter antenna location and the outgoing line the antenna axis. A mesh of observation points is also indicated.

OUTPUT DATA

The main output of FASPRO is a file with the fields levels in each one of the points of the "mesh" or of the "line" previously selected. This file contains the fields due to each ray mechanism selected and the total field. The user can also visualise, by means of a colour code, the field level in the urban scene if he has selected the option "mesh" or the curve of the field intensity if he has selected the option "line". He has also the option to save both pictures as bitmap images.

FASPRO also has the possibility of presenting the PDF, CPD, ADF and LCR for each point if the user has selected the statistic study.

FASPRO can export the "cleared" DXF file which has been obtained using the geometrical processing facility of the code. This file also includes the antenna position and the material composition of the buildings.

VALIDATION / STATUS

FASPRO has been successfully validated by comparing predictions and measurements provided by TELCEL (MOTOROLA). The measurements have been

carried out in the centre of Madrid considering examples of representative picocells in a very highly urbanised area. FASPRO is operative and commercially available.

REPRESENTATIVE RESULTS

Figs 6. shows the total fields due to the direct, reflected and diffracted coupling mechanisms for the picocell indicated in Fig 5. The antenna allocation and the mesh(50x50 points) indicated in Fig 5 have been considered. The frequency is 922 MHz. The CPU time to obtain these results was about five minutes using a Pentium (133 MHz, 64 MB of RAM)

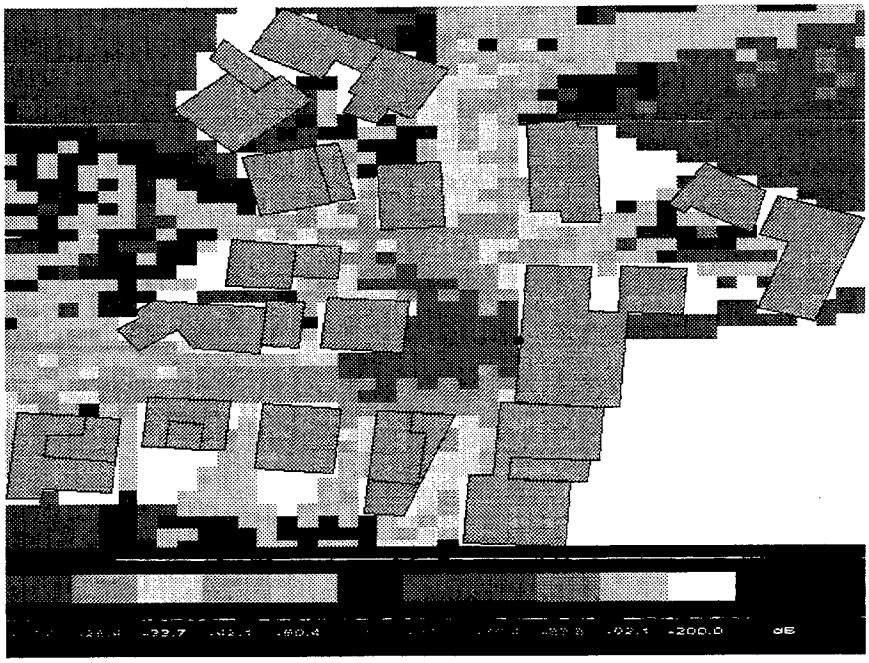

Fig 6. Field coverage for a typical microcell.

Figure 7 presents a quite demanding analysis case. Now we have the coverage of the field for the microcell of fig 1 which has an area of is about 2Kmx2Km. The observations points are defined using a mesh of 250x250 points. The antenna is located in the solid point indicated, it is 7m in height and its axis is oriented to the upper part of the figure forming 30° with the normal of the building where its placed. Simple and double effects coupling mechanisms, except double-diffraction have been considered. It can be noted that simple and double effects with diffraction provide great field coverage thanks to the downwardly directed diffraction that appears in the upper edges of the higher buildings of the scene. This can indicate that in an urban environment

with high skyscrapers the field coverage by diffraction can be greater than high order reflection, therefore a 3D analysis becomes necessary for analyses and design purposes. The CPU-time has been about 1 hour for simple effects and about 14 hours for the double effects considered using the PC outlined above.

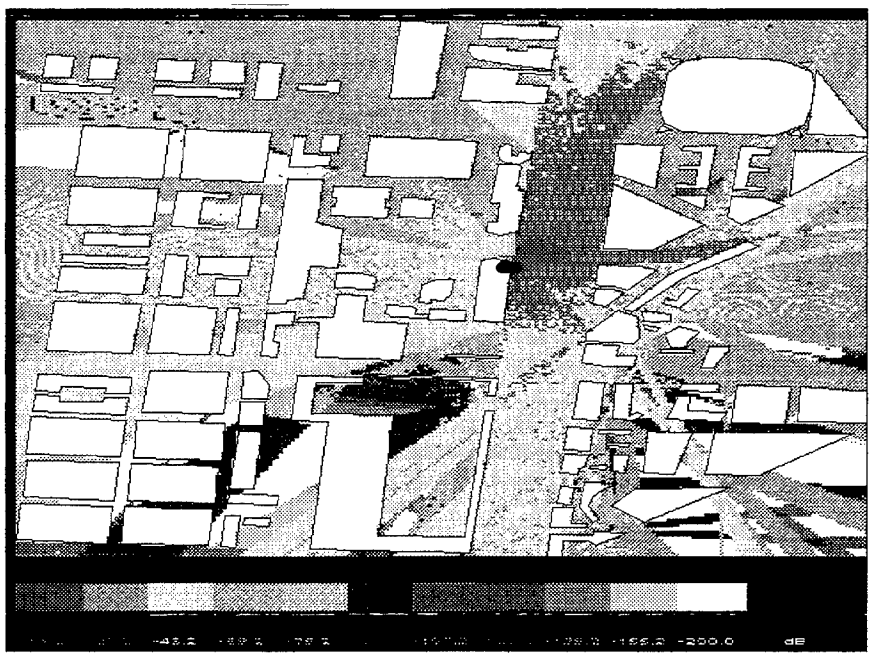

Figure 7. Field coverage for a large microcell.

ACKNOWLEDGEMENTS

The authors whish to thank Telefónica Moviles and TELCEL for all their help in the development of the code.

REFERENCES

[1] A. S. Glassner, Editor: "An introduction to ray tracing", Academic Press, San Diego CA, 1989.

[2] M. F. Cátedra, J. Pérez, F. Saiz de Adana: "FASANT: Fast Computer Code for the Analysis of Antennas on Board Complex Structures". 1997 ACES Symposium.

[3] J. Pérez, F. Saiz de Adana, M.F. Cátedra: "Efficient 3-D Ray Tracing Algorithms for Planning of Microcellular Systems in Urban and Indoor Environments". To be submitted to IEEE Antennas and Propagation Magazine.

SESSION 15:

PML: THEORETICAL AND NUMERICAL IMPLEMENTATION ISSUES

Chairs: A. Cangellaris and P. Petropoulos

ON THE CONSTRUCTION AND ANALYSIS OF ABSORBING LAYERS IN CEM *

S. ABARBANEL
DEPT. OF APPLIED MATHEMATICS
TEL AVIV UNIVERSITY
TEL AVIV, ISRAEL

D. GOTTLIEB†
DIV. OF APPLIED MATHEMATICS
BROWN UNIVERSITY
PROVIDENCE, RI

Abstract. A recently introduced system of of partial differential equations, based on physical consideration, which describes the behavior of electro-magnetic waves in artifical absorbing layer, is analysed. Analytic solutions are found, for the cases of semi-infinite layer and finite depth layers, both for primitive and characteristic boundary conditions.

A different set of equations that seem to offer some advantages is proposed in this paper. The properties of its solutions for the same geometries and boundary condition are also discussed.

1. Introduction. In this paper we examine the issue of finding infinite space solutions on a finite numerical domain to Maxwell's equations. One way of preventing outgoing waves from relecting off the artificial numerical boundaries is to introduce an absorbing layer, to which one attributes "material" properties that modify the vacuum-equations so that the field strength decays. These "material" properties may be based on a mathematical construct, such as splitting the transverse magnetic field (see Berenger [1]) – or they may be derived from physical principles, as was done by Ziolkowski who used a Lorentz-material model [2], Zhao and Cangellaris [3] and Petropoulos et al. [4], who employed similar considerations.

In a previous paper [5], we analysed the PML method proposed by Berenger [1]. It was shown there that his split equations are only a *weakly* well posed 4×4 hyperbolic system. As a consequence, under many types of perturbations the solution will have an exponentially explosive mode. Also, for any finite difference scheme, the pure initial value problem will possess an amplification matrix whose powers are not bounded, leading to instabilites (see [5]).

In section 2 we study the set of equations derived from the Lorentz-material-model for the absorbing layer. First we show that the set of 4 p.d.e.'s can be reduced to a set of 3 inhomogenous Maxwell equations augmented by a temporal O.D.E. This means that the original set of equations in the layer is strongly well posed. We then provide a closed form solution for a plane-wave traveling in the absorbing layer, under the assumption of periodcity in y, for 2 cases – the semi-infinite layer and the finite layer. In the case of the finite layer, the solution is provided for two different approaches to the imposition of boundary conditions – characteristic and non-characteristic. The results of the finding are summarized in the last section.

In section 3 we present an alternate set of strongly well posed equations (the inhomogeneous Maxwell equations, augmented by two o.d.e.'s) derived from mathematical considerations. Closed form solutions are found also for this et under the same boundary treatments of section 3. We feel this alternate set of equations possesses better decay and continuity properties.

2. Analysis of the Lorentz-Material-Model Equations. Consider the sub-set of Maxwell's equations dscribing the transverse-electric mode (TE) in two dimensional free space:

$$
\begin{aligned}
\frac{\partial \tilde{E}_x}{\partial \tilde{t}} &= \frac{1}{\varepsilon_0}\frac{\partial \tilde{H}_z}{\partial \tilde{y}} - \frac{\tilde{\sigma}}{\varepsilon_0}\tilde{E}_x \ , \\
\frac{\partial \tilde{E}_y}{\partial \tilde{t}} &= -\frac{1}{\varepsilon_0}\frac{\partial \tilde{H}_z}{\partial \tilde{x}} - \frac{\tilde{\sigma}}{\varepsilon_0}\tilde{E}_y \ , \\
\frac{\partial \tilde{H}_z}{\partial \tilde{t}} &= -\frac{1}{\mu_0}\frac{\partial \tilde{E}_y}{\partial \tilde{x}} + \frac{1}{\mu_0}\frac{\partial \tilde{E}_x}{\partial \tilde{y}} - \frac{\tilde{\sigma}^*}{\mu_0}\tilde{H}_z \ ,
\end{aligned}
\tag{1}
$$

where E_x, E_y, H_z are, respectively, the electric field components in the x, y direction and the magnetic field component normal to the domain of calculation. Here ε_0 and μ_0 are the free space permittivity and permeability, and σ and σ^* denote, respectively, possibly electric and magnetic losses assigned to free space. The speed of light in free space is given by $c = (\varepsilon_0\mu_0)^{-\frac{1}{2}}$. As usual we shall assume $\tilde{\sigma}^*\varepsilon_0 = \tilde{\sigma}\mu_0$.

* Research supported by DARPA/AFOSR grant no. F49620-96-1-0426
† Corresponding Author: *dig@cfm.brown.edu*

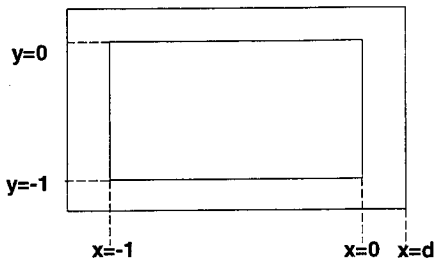

FIG. 1. *Illustration of the geometry considered.*

We non-dimensionalize the above set as follows

$$x = \tilde{x}/L \ , \ y = \tilde{y}/L \ , \ t = c\tilde{t}/L \ ,$$
$$H = \sqrt{\frac{\varepsilon_0}{\mu_0}}\tilde{H}_z \ , \ E_x = \tilde{E}_x \ , \ E_y = \tilde{E}_y$$

where we dropped the subscript z designation on the magnetic field. L is a reference length associated with a given problem. We further take $\tilde{\sigma} = 0$, in free space.

Thus the dimensionless form of (1) in free space (with $\tilde{\sigma} = 0$) becomes

$$\begin{aligned} \frac{\partial E_x}{\partial t} &= \frac{\partial H}{\partial y} \ , \\ \frac{\partial E_y}{\partial t} &= -\frac{\partial H}{\partial x} \ , \\ \frac{\partial H}{\partial t} &= \frac{\partial E_x}{\partial y} - \frac{\partial E_y}{\partial x} \ . \end{aligned} \tag{2}$$

Suppose our finite computational domain of interest, over which (2) are to be solved, is the square $-L \le \tilde{x}, \tilde{y} \le 0$, i.e., $-1 \le x, y \le 0$. This places the interface between the computational domain and the absorbing layer on the right, at $x = 0$. Our analysis will focus on this right hand side layer – similar analyses can be carried out in the other three surrounding absorbing layer (see Fig. 1).

It is in the layer $0 < x < d$ (as well as in the other three) that one posits the modified equations – either the split form of (2), as was done by in [1], or the physically derived equations [2, 3, 4]. The dimensionless form of the equations based on the Lorentz-material model, as reported in [2], is:

$$\begin{aligned} \frac{\partial E_x}{\partial t} &= \frac{\partial H}{\partial y} - J \ , \\ \frac{\partial E_y}{\partial t} &= -\frac{\partial H}{\partial x} - \sigma E_y \ , \\ \frac{\partial H}{\partial t} &= \frac{\partial E_x}{\partial y} - \frac{\partial E_y}{\partial x} - \sigma H \ , \\ \frac{\partial J}{\partial t} &= -\sigma \frac{\partial H}{\partial y} \ , \end{aligned} \tag{3}$$

where J is a polarization current [2], and σ (not to be confused with the free space parameter $\tilde{\sigma}$) is a lossy material property, which may be a function of the spatial coordinates.

First we notice that the system (3) of 4 p.d.e.'s can be reduced to a Maxwell-like system of 3 p.d.e.'s supplemented by an ordinary differential equation in time for a new parameter, $P = J + \sigma E_x$. The new set of equations for E_x, E_y, H and P becomes

(4)
$$\frac{\partial E_x}{\partial t} = \frac{\partial H}{\partial y} + \sigma E_x - P \ ,$$
$$\frac{\partial E_y}{\partial t} = -\frac{\partial H}{\partial x} - \sigma E_y \ ,$$
$$\frac{\partial H}{\partial t} = \frac{\partial E_x}{\partial y} - \frac{\partial E_y}{\partial x} - \sigma H \ ,$$

with the Debye-like equation for the polarization current being

(5)
$$\frac{\partial P}{\partial t} = -\sigma P + \sigma^2 E_x \ .$$

Notice that (5) contains no spatial derivatives and hence it is indeed as o.d.e. for P. This should lead to a considerable reduction in computational cost, since most of the numerical effort goes to evaluating the spacial derivatives.

Recall that the potential difficulties with the set of split equations [5] was due to the fact that the system was only *weakly* well posed for the initial value problem. In contrast Eqs. (4)-(5), after dropping the undifferentiated terms, become the original 3×3 Maxwell system which is symmetric hyperbolic and therefore *strongly* well posed.

We next investigate the behavior of a plane-wave impinging on the interface at $x = 0$, and entering the absorbing layer as described by (4)-(5). We note that a general "pulse" hitting the interface can be decomposed into a linear combination of plane waves. We shall actually explicitly solve (4)-(5), in the absorbing layer, for this entering plane wave under the assumption that the solution is periodic in y. The impinging plane is of the form:

$$\begin{pmatrix} E_x \\ E_y \\ H \end{pmatrix} = \begin{pmatrix} -\beta \\ \alpha \\ 1 \end{pmatrix} e^{i\omega(t-\alpha x-\beta y)} \ , \qquad x \le 0 \ ,$$

where the dimensionless frequency ω is given by $\omega = \tilde{\omega}L/c$, $\tilde{\omega}$ being the physical frequency, and $\alpha^2 + \beta^2 = 1$. We seek a solution in the layer to (4)-(5) of the form

(6)
$$\vec{U} = \begin{pmatrix} E_x \\ E_y \\ H \\ P \end{pmatrix} = e^{i\omega(t-\beta y)} \begin{pmatrix} e(x) \\ g(x) \\ h(x) \\ p(x) \end{pmatrix} = e^{i\omega(t-\beta y)}\vec{u} \ .$$

Substituting (6) into (4)-(5) we get, with $(\cdot)' = d(\cdot)/dx$,

(7)
$$i\omega e = -i\omega\beta h + \sigma e - p \ ,$$
(8)
$$i\omega g = -h' - \sigma g \ ,$$
(9)
$$i\omega h = -i\omega\beta e - g' - \sigma h \ ,$$
(10)
$$i\omega p = -\sigma p + \sigma^2 e \ .$$

From (7) and (10) we get p and e in terms of h:

(11)
$$p = -\frac{i\sigma^2\beta h}{\omega} \ , \quad e = -\beta(1 + \frac{\sigma}{i\omega})h \ .$$

Using (11) in (8)-(9) we get two coupled differential equations for h and g:

(12)
$$h' = -(i\omega + \sigma)g = -\psi(x)g \ ,$$
$$g' = -(i\omega + \sigma)\alpha^2 h = -\psi(x)\alpha^2 h \ .$$

These may be combined to yield a second order o.d.e. for h, say, with variable coefficients, viz:

$$\left(\frac{h'}{\psi}\right)' = \alpha^2 \psi h \ . \tag{13}$$

In general 2^{nd} order o.d.e.'s with variables coefficient do not possess closed form solutions. However, a closed form exists for (13) [6]. In particular

$$h = Ae^{\alpha \int_0^x \psi(\eta)d\eta} + Be^{-\alpha \int_0^x \psi(\eta)d\eta} \ , \tag{14}$$

where again $\psi(x) = i\omega + \sigma(x)$. From (12) we get g:

$$g = -\frac{h'}{\psi} = -\alpha \left[Ae^{\alpha \int_0^x (\eta)d\eta} - Be^{-\alpha \int_0^x \psi(\eta)d\eta} \right] \ . \tag{15}$$

We thus have a complete solution of the form (6) with A and B to be determined by the boundary conditions of each particular problem. At this point we examine the application of the above solution to two separate cases:

1. The absorbing layer is semi-infinite, $0 \leq x$.
2. The absorbing layer is finite, $0 \leq x \leq d$:
   (2a) Boundary conditions imposed on the primitive variables.
   (2b) Boundary conditions imposed on the characteristic variables.

2.1. The semi-infinite case. For this case we require H and E_y to be continuous across $x = 0$, i.e. $h(0) = 1$, $g(0) = x$. Using these initial values in (14)-(15), we obtain immediately, $A = 0$, $B = 1$. Thus the solution vector is:

$$\begin{pmatrix} E_x \\ E_y \\ H \\ P \end{pmatrix} = \begin{pmatrix} -\beta(1 + \frac{\sigma}{i\omega}) \\ \alpha \\ 1 \\ \frac{i\beta\sigma^2}{\omega} \end{pmatrix} e^{i\omega(t - \alpha x - \beta y)} e^{-\alpha \int_0^x \sigma(\eta)d\eta} \ . \tag{16}$$

If we want also E_x to be continuous across the interface $x = 0$, then according to (16) we must choose $\sigma(x)$ such that $\sigma(0) = 0$. (This will cause P, which vanishes in the free space interior, also to be continuous).

It is clear that

$$\alpha \frac{\partial}{\partial x}|H| \leq 0 \quad \forall \ \alpha, 0 \leq x \ ,$$

and also

$$\alpha \frac{\partial}{\partial x}|E_y| \leq 0 \quad \forall \ \alpha, 0 \leq x \ ,$$

so, that both $|E_y|$ and $|H|$ will decay in all directions of propagation. We next examine the behavior of E_x. Since $|E_x|^2$ is independent y, the directional derivative may be written as

$$\begin{aligned} \alpha \frac{\partial}{\partial x}(|E_x|^2) &= \alpha \frac{\partial}{\partial x} \left\{ \beta^2 (1 + \frac{\sigma^2}{\omega^2}) e^{-2\alpha \int_0^x \sigma(\eta)d\eta} \right\} \\ &= \frac{2\sigma\beta^2}{\omega^2} \left[\alpha\sigma' - \alpha^2(\sigma^2 + \omega^2) \right] e^{-2\alpha \int_0^x \sigma(\eta)d\eta} \ . \end{aligned}$$

We would like the directional derivation to negative, i.e.

(17) $$\alpha\sigma' - \alpha^2(\sigma^2+\omega^2) < 0 \ .$$

If $\alpha < 0$, then (17) is satisfied automatically. For $\alpha > 0$ we have

$$\sigma' < \alpha(\sigma^2+\omega^2) \ ,$$

or, since we took $\sigma(0) = 0$ for continuity

(18) $$\frac{1}{\omega}\tan^{-1}(\frac{\sigma}{\omega}) \le \alpha x \quad , \quad 0 \le x \ .$$

We see that for any given ω, x and $\sigma(x)$, there is a range of α for which the inequalilty cannot be satisfied for all α's. If ω is very large the problem occurs only for grazing angles, $\alpha << 1$. However, if in a pulse there is a significant component of moderate frequencies there might be a problem.

If one takes $\sigma = \sigma_0 =$ constant, then the directional derivative is always negative but there is a jump across $x = 0$ in $|E_x|$ of size $\frac{\beta\sigma_0}{\omega}$. This jump may, in a numerical code, cause spacious reflection from the interface.

2.1.1. The Finite Layer Case-Non characteristic boundary conditions. In practice, numerical codes use a finite absorbing layer of thickness $d = \tilde{d}/L$. The commonly used boundary conditions are to demand condinuity in H at $x = 0$, and perfect conductivity at $x = d$, i.e. $E_y(d) = 0$. This leads to the following boundary condition for the o.d.e's (12):

(19) $$h(0) = 1 \ , \ g(d) = 0 \ .$$

Using this in (14)-(15) one gets

(20) $$A = \frac{e^{-2\alpha\int_0^d \psi(\eta)d\eta}}{1+e^{-2\alpha\int_0^d \psi(\eta)d\eta}} \ , \ B = \frac{1}{1+e^{-2\alpha\int_0^d \psi(\eta)d\eta}} \ .$$

Note that if $\int_0^d \sigma(\eta)d\eta$ is large than A is exponentially small, $B \to 1$ and the solution tends to the semi-infinite case.

For the sake of completion we now write down the expressions for the field:

(21)
$$E_x = -\frac{\beta(1+\frac{\sigma}{i\omega})}{1+e^{-2I\alpha}}\left[1+e^{2i\omega\alpha(x-d)}e^{-2\alpha\int_x^d\sigma(\eta)d\eta}\right]e^{i\omega(t-\alpha x-\beta y)}e^{-\alpha\int_0^x\sigma(\eta)d\eta} \ ,$$
$$E_y = \alpha\frac{1}{1+e^{-2I\alpha}}\left[1-e^{2i\omega\alpha(x-d)}e^{-2\alpha\int_x^d\sigma(\eta)d\eta}\right]e^{i\omega(t-\alpha x-\beta y)}e^{-\alpha\int_0^x\sigma(\eta)d\eta} \ ,$$
$$H = \frac{1}{1+e^{-2I\alpha}}\left[1+e^{2i\omega\alpha(x-d)}e^{-2\alpha\int_x^d\sigma(\eta)d\eta}\right]e^{i\omega(t-\alpha x-\beta y)}e^{-\alpha\int_0^x\sigma(\eta)d\eta} \ ,$$
$$P = -\frac{i\sigma^2\beta h}{\omega(1+e^{2I\alpha})}\left[1+e^{2i\omega\alpha(x-d)}e^{-2\alpha\int_x^d\sigma(\eta)d\eta}\right]e^{i\omega(t-\alpha x-\beta y)}e^{-\alpha\int_0^x\sigma(\eta)d\eta} \ ,$$

where $I = \int_0^d \psi(\eta)d\eta$. In (21) the solution is written in such a form that the first term in each equation (corresponding to 1 in the square brackets) represents the outgoing wave (basically the decaying interface - impinging wave), while the second term is due to the wave reflected from the outer boundary at $x = d$.

2.1.2. The finite layer case with characteristic boundary condition. Hyperbolic systems of partial differential equations lend themselves more naturally to the imposition of boundary conditions on the characteristic variables. In the present case, the incoming and outgoing x-directed characteristic variables are, respectively $\Phi_1 = H + E_y$ and $\Phi_2 = H - E_y$; they correspond to the eigenvalues ± 1 of (4) under the assumption of a solution periodic in y. The relevant boundary conditions are continuity of Φ_1 at the interface $x = 0$, and $\Phi_2 = 0$ at $x = d$ (i.e. Φ_2 is not reflected at the outer boundary, $x = d$). Thus, instead of (19) we have

$$h(0) + g(0) = 1 + \alpha \quad , \quad h(d) - g(d) = 0 \ .$$

This pair yields ($\alpha \neq 0$)

$$A = -\frac{(\frac{1-\alpha}{1+\alpha})e^{-2\alpha I}}{1-(\frac{1-\alpha}{1+\alpha})^2 e^{-2\alpha I}} \ , \ B = \frac{1}{1-(\frac{1-\alpha}{1+\alpha})^2 e^{-2\alpha I}} \qquad (\alpha \neq 0) \ .$$

Note that for $\alpha = 1$ (incoming plane wave normal to the interface), we have $A = 0$ and $B = 1$; i.e. there is no reflected wave - unlike the case of solution with primitive boundary conditions (see (20)). Also note that for $\alpha = -1$, $A = B = 0$; i.e. the field strength is zero in the absorbing layer. Finally note, that even though as $\alpha \to 0$, A and B become singular, the solution itself remains finite and the boundary condition are satisfied.

3. A Mathematically Derived Set of Unsplit PML Equations. The starting point is the assumption that the behavior in the absorbing layer can be described by a set of inhomogeneous Maxwell's equations (possibly augmented by a few temporal o.d.e.'s). We thus start (in the TE case, as an illustration) with

(22)
$$\begin{aligned} \frac{\partial E_x}{\partial t} &= \frac{\partial H}{\partial y} + R_1 \ , \\ \frac{\partial E_y}{\partial t} &= -\frac{\partial H}{\partial x} + R_2 \ , \\ \frac{\partial H}{\partial t} &= \frac{\partial E_x}{\partial y} - \frac{\partial E_y}{\partial x} + R_3 \ . \end{aligned}$$

We look for solutions of the form

(23)
$$\begin{aligned} H &= e^{i\omega(t-\alpha x-\beta y)} e^{-\alpha \int_0^x \sigma(\eta)d\eta} \ , \\ E_y &= \Omega_1(x;x,\omega)H \ , \\ E_x &= \Omega_2(x;\alpha,\omega)H \ . \end{aligned}$$

Note that in Ω_1, Ω_2 dependence on β is taken care of via the restriction $\alpha^2 + \beta^2 = 1$. The five functions $R_j (j = 1,2,3), \Omega_1$ and Ω_2 are determined from the following constraints:

(i) That the R_j's be independent of α, β and ω. This way the equations will be valid for any superposition of waves.
(ii) that the solution vector be continuous across, $x = 0$, the interface between the interior free space region and the absorbing layer.
(iii) That in the absorbing layer the magnitude of the solution vector be bounded by a monotonically decaying function in all directions of propagation, *uniformly* in $\sigma(x)$ and ω.

Notice that equations (4) of the previous section (augmented by the temporal o.d.e (5) may be cast in the form (22) by choosing: $R_1 = \sigma E_x - P$, $R_2 = -\sigma E_y$, $R_3 = -\sigma H$.

As we saw, in the solution of (22) we get $\Omega_1 = \alpha$; $\Omega_2 = -\beta(1 + \frac{\sigma}{i\omega})$. As was pointed out in section 2, this set of R_j's and Ω_1, Ω_2 causes the solution to satisfy only of the constraints (ii) and (iii).

We now propose a set of equations for the absorbing layer that does satisfy all the constraints:

(24)
$$\begin{aligned} \frac{\partial E_x}{\partial t} &= \frac{\partial H}{\partial y} \ , \\ \frac{\partial E_y}{\partial t} &= -\frac{\partial H}{\partial x} - 2\sigma E_y - \sigma P \ , \\ \frac{\partial H}{\partial t} &= \frac{\partial E_x}{\partial y} - \frac{\partial E_y}{\partial x} + \sigma' Q \ , \\ \frac{\partial P}{\partial t} &= \sigma E_y \ , \ \frac{\partial Q}{\partial t} = -\sigma Q - E_y \ . \end{aligned}$$

The details of the derivation are omitted here and will be presented elsewhere. The solution for the semi-infinite case is given directly by (23) with

$$\Omega_1 = \frac{i\omega}{\sigma + i\omega}\alpha H \ , \ \Omega_2 = -\beta \ .$$

The solution for the finite absorbing layer with primitive boundary conditions, (19), is obtained from (24) exactly in the same manner as it was done in Lorentz-material-model case, section 2. The complete solution is given by:

$$E_x = -\frac{\beta}{1+e^{-2I}}\left[1+e^{2i\omega\alpha(x-d)}e^{-2\alpha\int_x^d\sigma(\eta)d\eta}\right]e^{i\omega(t-\alpha x-\beta y)}e^{-\alpha\int_0^x\sigma(\eta)d\eta}\ ,$$

$$E_y = \frac{\alpha}{1+e^{-2I}}\cdot\frac{i\omega}{\sigma+i\omega}\left[1-e^{2i\omega\alpha(x-d)}e^{-2\alpha\int_x^d\sigma(\eta)d\eta}\right]e^{i\omega(t-\alpha x-\beta y)}e^{-\alpha\int_0^x\sigma(\eta)d\eta}\ ,$$

$$H = \frac{1}{1+e^{-2I}}\left[1+e^{2i\omega\alpha(x-d)}e^{-2\alpha\int_x^d\sigma(\eta)d\eta}\right]e^{i\omega(t-\alpha x-\beta y)}e^{-\alpha\int_0^x\sigma(\eta)d\eta}\ ,$$

$$P = \frac{\sigma}{i\omega}E_y\ ,\ Q = -\frac{1}{(\sigma+i\omega)}E_y\ .$$

If we choose any $\sigma(x) > 0$, such that $\sigma(0) = 0$, then clearly

$$H(0) = \frac{1}{1+e^{-2I}}\left[1+e^{-2I}\right]e^{i\omega(t-\beta y)} = e^{i\omega(t-\beta y)}$$

which is the free space plane wave solution at $x = 0$. Similarly, $E_x(0) = -\beta H(0)$, and $E_y(0) = \alpha\frac{1-e^{-2\alpha I}}{1+e^{-2\alpha I}}H(0)$. Note that there is a jump across $x = 0$ for E_y but it is exponentially small. This is also true for E_y obtained via the Lorentz-material-model equations, section 2.

Also note that since $\left|\frac{i\omega}{\sigma+i\omega}\right| < 1$, then $|E_y|$ (as well as all the magnitude of other field components) is bounded by $|H|$ which satisfies $\alpha\frac{\partial}{\partial x}|H| < 0\forall\alpha \neq 0$. Thus all three constraints (i)-(iii) are satisfied.

If one imposes the characteristic boundary conditions, i.e. continuity of $\Phi_1 = H + E_y$ at $x = 0$, and $\Phi_2 = H - E_y = 0$ at $x = d$, then one gets

$$E_x = -\beta C\left[1+De^{2i\omega\alpha(x-d)}e^{-2\alpha\int_x^d\sigma(\eta)d\eta}\right]e^{i\omega(t-\alpha x-\beta y)}e^{-\alpha\int_0^x\sigma(\eta)d\eta}\ ,$$

$$E_y = \alpha C\frac{i\omega}{\sigma+i\omega}\left[1-De^{2i\omega\alpha(x-d)}e^{-2\alpha\int_x^d\sigma(\eta)d\eta}\right]e^{i\omega(t-\alpha x-\beta y)}e^{-\alpha\int_0^x\sigma(\eta)d\eta}\ ,$$

$$H = C\left[1+De^{2i\omega\alpha(x-d)}e^{-2\alpha\int_x^d\sigma(\eta)d\eta}\right]e^{i\omega(t-\alpha x-\beta y)}e^{-\alpha\int_0^x\sigma(\eta)d\eta}\ ,$$

$$P = \frac{\sigma}{i\omega}\ E_y\ ,\ Q = -\frac{1}{\sigma+i\omega}\ E_y\ ,$$

where

$$C = \frac{1}{1-\frac{1-\alpha}{1+\alpha}\cdot\frac{1-\alpha\gamma}{1+\alpha\gamma}e^{-2\alpha I}}\ ,\ D = -\frac{1-\alpha\gamma}{1+\alpha\gamma}\ e^{-2\alpha I}\ ,\ \gamma = \frac{i\omega}{\sigma(d)+i\omega}\ .$$

4. Summary. In this paper we considered two Maxwell like sets of p.d.e designed to surpress the electromagnetic field in artificial absorbing layers surrounding a free-space computational domain. One set of equations, introduced in [2, 3, 4] is based on a Lorentz-material model. The other set, that we present in this paper, is based on a mathematical construct. Both sets of equations are shown to strongly-well posed, unlike the set of split equations introduced in [1], and analyzed in [5].

The main results for the Lorentz-material model are as follows:

1. In the semi-infinite layer case, if $\sigma(x)$ is a variable such that $\sigma(0) = 0$, as most practitioners do, then the field variables are continuous across $x = 0$. However, in this case, there is a range of x (depending on $\sigma(x), \alpha$ and ω) in which the field strength increases, rather than decreases, in the direction of propagation. If $\sigma(x) = \sigma_0 =$ constant, then the field strength does decay in all direction. However there is a discontinuity in the absolute value of E_x at $x = 0$, proportional to $\sigma/|\omega|$.

2. In the finite layer case solution the main conclusion are the same as for the semi-infinite layer case, with the exception that now, regardless of the structure of $\sigma(x)$, E_y has a jump at $x = 0$. The jump is proportional to $e^{-2\alpha \int_0^d \sigma(\eta) d\eta}$. This provides us with guideline to choose $\sigma(x)$ and d, so that the jump is indeed exponentially small. The imposition of characteristic boundary conditions offers some advantages.
3. **The results for the alternate set of equations are as follows:**
Basically the properties of the solutios in all cases (infinite and finite layers; primitive and characteristic boundary conditions) are the same as in the Lorentz material case, with one (at least theoretically) important different – now the magnitude of the solution vector is uniformly bounded by the size of the magnetic field which decays in all directions.

REFERENCES

[1] J. P. BERENGER, *A Perfectly Matched Layer for the Absorption of Electromagnetic Waves*, J. Comp. Phys. **114**(1994), pp. 185-200.

[2] R. W. ZIOLKOWSKI, *Time-Derivative Lorentz-Material Model Based Absorbing Boundary Conditions* - preprint, 1996.

[3] L. ZHAO AND A. C. CANGELLARIS, *A General Approach for the Development of Unsplit-Field Time-Domain Implementations of Perfectly Matched Layers for FD-TD Grid Truncation*, IEEE Microwave Guided Wave Lett. **6**(1996), pp. 209-211.

[4] P. PETROPOULOS, L. ZHAO AND A. C. CANGELLARIS, *A Reflectionless Sponge Layer Absorbing Boundary Condition for the Solution of Maxwell's Equations with High-Order Staggered Finite Difference Schemes*, J. Comp. Phys. - submitted, 1996.

[5] S. ABARBANEL AND D. GOTTLIEB, *A Mathematical Analysis of the PML Method*, J. Comp. Phys. - submitted, 1996.

[6] S. BREUER AND D. GOTTLIEB, *The Reduction of Linear Ordinary Differential Equations with Constant Coefficients*, J. of Math. Anal. Appl. **32**(1970), pp. 62-76.

The Application of PML ABCs in High-Order FD-TD Schemes *

Peter G. Petropoulos
Department of Mathematics, SMU
Dallas, TX 75275

1. Introduction

Analysis of real-world electromagnetic problems requires the numerical solution of the linear Maxwell equations $\frac{\partial \vec{B}}{\partial t} = -\vec{\nabla} \times \vec{E}$ and $\frac{\partial \vec{D}}{\partial t} = \vec{\nabla} \times \vec{H} - \vec{J}$, where $\vec{J}$ is an impressed (or induced) current. In the absence of impressed charges the fields are divergence-free, i.e., $\vec{\nabla} \cdot \vec{D} = 0$, $\vec{\nabla} \cdot \vec{B} = 0$. In general, the system is closed with hereditary constitutive laws $\vec{D} = F[\vec{E}, \vec{H}]$, $\vec{B} = G[\vec{E}, \vec{H}]$. For example, in modeling transient propagation through water (or biological tissue) one would describe the propagation medium with $\vec{B} = \mu_0 \vec{H}$, where μ_0 is the permeability of free-space, and $\vec{D}(\vec{x}, t) = \epsilon(\vec{x})\vec{E}(\vec{x}, t) + \int_0^t \chi(\vec{x}, t - t')E(\vec{x}, t')dt'$, where $\min_{\vec{x} \in R^3} \epsilon(\vec{x}) = \epsilon_0$, ϵ_0 is the permittivity of free-space, and $\chi(\vec{x}, t)$ (the "memory") is the time-domain Debye susceptibility kernel. An analytical study of interesting wave phenomena in such dielectrics, and of the energies associated with them, was presented in [1]. The Finite-Difference Time-Domain method [2] has been very successful in applications-oriented settings. The FD-TD method is a second-order accurate finite difference scheme in which the field unknowns are staggered in space-time. In fact [3], it is the best second-order accurate non-dissipative finite difference scheme for the time-dependent Maxwell equations and preserves the divergence-free property of $\vec{D}$ and $\vec{B}$.

Applications typically involve structures whose size is very large in terms of some characteristic wavelength present in the problem. Electrically-large electromagnetic problems, coupled with the need to increase the predictive dynamic range of CEM modeling codes while retaining the capability to do the computation with existing computational resources, call for numerical schemes with order of accuracy greater than two. In [4] we quantified the superiority of the (2,4) staggered scheme [5] over the FD-TD scheme for a fixed amount of phase error allowed to accumulate over a given computation time interval. Also, high-order accuracy is called for when use of realistic models of materials (via hereditary constitutive laws) is made. We [6] have explored this issue for FD-TD, and have determined that the (2,4) staggered schemes are more accurate and natural for such problems.

Unfortunately, higher-order schemes, although appealing from the phase error and accuracy points of view, have not been widely accepted by the engineering CEM community. One reason is that the wider spatial stencil of such methods does not allow for a straightforward implementation of the absorbing boundary conditions needed to simulate the fact that the problem to be solved is embedded in free-space. Herein, we will address this objection by reporting results obtained by coupling a PML-type (sometimes referred to as a sponge layer) ABC [7] with (2,4) staggered schemes. We also report on theoretical analysis of well-posedness of the layer equations, and of the resulting algorithm's numerical stability [8].

*Supported in part by AFOSR Grant F49620-95-1-0014 and NSF SCREMS Grant DMS-9508273.

2. The Time-Domain Sponge Layer.

Consider, first, the case of an absorbing layer perpendicular to the $\hat{z}$ axis. The continuous equations are [7]

$$\begin{aligned}
&\frac{\partial H_x}{\partial t} + w_z'' H_x = -\frac{1}{\mu}\left(\nabla \times \mathbf{E}\right)_x \\
&\frac{\partial H_z}{\partial t} = -\frac{1}{\mu}\left(\nabla \times \mathbf{E}\right)_z - \frac{1}{\mu} w_z'' \int_0^t \left(\nabla \times \mathbf{E}\right)_z dt' \\
&\frac{\partial E_y}{\partial t} + w_z'' E_y = \frac{1}{\epsilon}\left(\nabla \times \mathbf{H}\right)_y .
\end{aligned} \tag{2.1}$$

The first and third equations above have the standard form for wave propagation in a lossy medium with electric conductivity $\sigma = \epsilon w_z''$ and magnetic conductivity $\sigma^* = \mu w_z''$, and their time discretization using central differencing (or exponential differencing) is easy. The second equation in (2.1) is different in the sense that a time integral of the $\hat{z}$ component of the curl of the electric field appears on the right-hand side. This term is interpreted as a field-dependent source term.

Consider next the corner region where an absorbing layer perpendicular to the $\hat{z}$ axis overlaps an absorbing layer perpendicular to the $\hat{x}$ axis. The relevant equations now are [7]

$$\begin{aligned}
&\frac{\partial H_x}{\partial t} + w_z'' H_x = -\frac{1}{\mu}\left(\nabla \times \mathbf{E}\right)_x - \frac{w_x''}{\mu} \int_0^t \left(\nabla \times \mathbf{E}\right)_x dt' \\
&\frac{\partial H_z}{\partial t} + w_x'' H_z = -\frac{1}{\mu}\left(\nabla \times \mathbf{E}\right)_z - \frac{w_z''}{\mu} \int_0^t \left(\nabla \times \mathbf{E}\right)_z dt' \\
&\frac{\partial E_y}{\partial t} + (w_x'' + w_z'') E_y + w_x'' w_z'' \int_0^t E_y dt' = \frac{1}{\epsilon}\left(\nabla \times \mathbf{H}\right)_y .
\end{aligned} \tag{2.2}$$

Now, along with electric and magnetic losses, there are three field-dependent source terms present. The ones in the first and second equations in (2.2) are similar to those present in (2.1) in the sense that they involve time integrals of the specific component of the curl of the electric field. The source term in the third equation in (2.2) is different. It involves the time integral of the electric field component.

3. Well-Posedness.

We now show that the extra terms appearing in the sponge-layer equations, (2.1) and (2.2), are lower-order (undifferentiated) perturbations of Maxwell's equations in a homogeneous non-dispersive dielectric (a symmetric, strongly well-posed hyperbolic system). It will follow, using Thm. (4.32) of [10], that the sponge layer equations are also well-posed.

Fourier transform (2.1) and rearrange to obtain

$$\begin{aligned}
i\omega B_x &= \frac{\partial E_y}{\partial z} \\
-i\omega B_z &= \frac{\partial E_y}{\partial x} \\
i\omega D_y &= \frac{\partial H_x}{\partial z} - \frac{\partial H_z}{\partial x},
\end{aligned} \tag{3.1}$$

closed with constitutive relations

$$\begin{aligned} B_x &= \mu(1+\frac{w_z''}{i\omega})H_x \\ B_z &= \mu\frac{i\omega}{w_z''+i\omega}H_z \\ D_y &= \epsilon(1+\frac{w_z''}{i\omega})E_y. \end{aligned} \tag{3.2}$$

Next, inverse Fourier transform (3.1)-(3.2) to obtain

$$\begin{aligned} \frac{\partial B_x}{\partial t} &= \frac{\partial E_y}{\partial z} \\ -\frac{\partial B_z}{\partial t} &= \frac{\partial E_y}{\partial x} \\ \frac{\partial D_y}{\partial t} &= \frac{\partial H_x}{\partial z} - \frac{\partial H_z}{\partial x}, \end{aligned} \tag{3.3}$$

where

$$\begin{aligned} B_x &= \mu H_x + \mu w_z'' \int_0^t H_x dt' \\ B_z &= \mu \int_0^t e^{-w_z''(t-t')}\frac{\partial H_z}{\partial t'}dt' \\ D_y &= \epsilon E_y + \epsilon w_z'' \int_0^t E_y dt'. \end{aligned} \tag{3.4}$$

Note, the first and third equations in (3.4) just indicate that there are magnetic and electric losses in the indicated direction, while the second equation indicates memory of the time rate of change of the normal to the layer magnetic field.

Take the time derivative of every equation in (3.4), and apply integration by parts (using zero initial conditions for the fields in the layer) to the second one to obtain

$$\begin{aligned} \frac{\partial B_x}{\partial t} &= \mu\frac{\partial H_x}{\partial t} + \mu w_z'' H_x \\ \frac{\partial B_z}{\partial t} &= \mu\frac{\partial H_z}{\partial t} - \mu w_z'' H_z + \mu w_z''^2 \int_0^t e^{-w_z''(t-t')}H_z dt' \\ \frac{\partial D_y}{\partial t} &= \epsilon\frac{\partial E_y}{\partial t} + \epsilon w_z'' E_y. \end{aligned} \tag{3.5}$$

Substitute (3.5) in the left hand side of (3.3) to recover the standard Maxwell equations modified by lower-order (undifferentiated) terms. Due to the equivalence of (3.3) (with (3.5)) and (2.1) we see that the extra term in (2.1) is really a lower-order term.

Next consider the corner region equations (2.2). These can be cast (using the Fourier transform) in the same form as (3.1) but now with constitutive relations

$$\begin{aligned} B_x &= \mu\frac{w_z}{w_x}H_x \\ B_z &= \mu\frac{w_x}{w_z}H_z \\ D_y &= \epsilon w_z w_x E_y, \end{aligned} \tag{3.6}$$

where $w_{z(x)} = 1 + \frac{w''_{z(x)}}{i\omega}$. Noting that

$$\frac{w_{z(x)}}{w_{x(z)}} = 1 + \frac{\frac{w''_{z(x)}}{w''_{x(z)}} - 1}{1 + \frac{i\omega}{w''_{x(z)}}}, \tag{3.7}$$

subsequent application of the inverse Fourier transform, using

$$w_x w_z = 1 + \frac{w''_x + w''_z}{i\omega} + \frac{w''_x w''_z}{(i\omega)^2}, \tag{3.8}$$

results again in (3.3) but now closed with the time-dependent constitutive laws

$$\begin{aligned} & B_{x(z)} = \mu H_{x(z)} + \\ & \mu(w''_{z(x)} - w''_{x(z)}) \int_0^t e^{-w''_{x(z)}(t-t')} H_{x(z)} dt' \\ & \frac{\partial D_y}{\partial t} = \epsilon \frac{\partial E_y}{\partial t} + \epsilon(w''_x + w''_z) E_y + \epsilon w''_x w''_z \int_0^t E_y dt'. \end{aligned} \tag{3.9}$$

Note that if $w''_x = w''_z$ then the magnetic part of (3.9) is lossless.

Time-differentiation of the first equation in (3.9), and substitution in (3.3) yields again the standard Maxwell equations modified by lower-order (undifferentiated) terms.

4. Numerical Stability.

We have already shown that the sponge layer equations are just Maxwell's equations for a homogeneous non-dispersive dielectric modified by lower-order (undifferentiated) terms. Such terms were seen to be proportional to the fields or to their weighted time-integrals, i.e., H_x, $\int_0^t H_x dt'$, or $\int_0^t e^{-w''_z(t-t')} H_x dt'$. We have shown [7]-[8] that an appropriately centered discretization of these extra terms is possible while preserving the second-order time accuracy of the FD-TD time-integration (regardless of the method used to discretize space; we have used both 2nd and 4th order accurate schemes).

If we were to calculate the amplification matrix of the discrete sponge layer equations we would find it to be that of the standard Maxwell equations but perturbed by terms that are $O(\Delta t)$ uniformly in wavenumber. For example, terms like those below will modify the amplification matrix of the staggered grid discretization of Maxwell's equations for a homogeneous non-dispersive dielectric as indicated in the order symbol:

$$\begin{aligned} & \Delta t \{H_x\}_{discrete} \sim O(\Delta t) \\ & \Delta t \{\int_0^t H_x dt'\}_{discrete} \sim O(\Delta t^2) \\ & \Delta t \{\int_0^t e^{-w''_z(t-t')} H_x dt'\}_{discrete} \sim O(\Delta t^2). \end{aligned} \tag{4.1}$$

Thus, in a von Neumann stability analysis, the original amplification matrix will be modified by terms that will be $O(\Delta t)$ and $O(\Delta t^2)$ uniformly in wavenumber. This will result in the necessary and sufficient standard CFL stability restriction for the discretized standard Maxwell equations

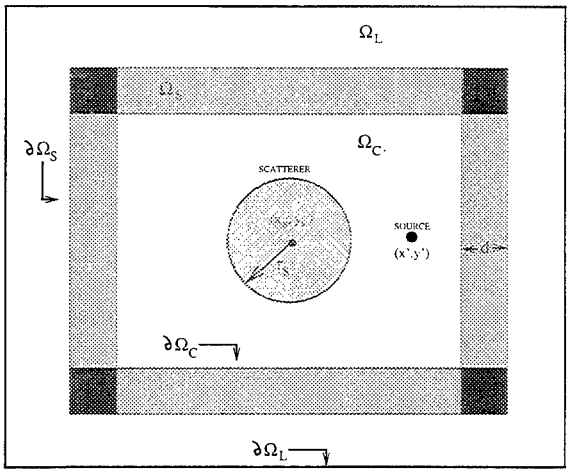

Figure 1: Geometry used in the numerical experiments.

to also be a necessary *and* sufficient stability condition for the sponge layer equations herein via Thm. 6.2.6 of [11].

We note that in the original sponge-layer equations, (2.1) and (2.2), the additional terms are proportional to $\int_0^t (\nabla \times \mathbf{E})_z \, dt'$. Upon discretization

$$\Delta t \{ \int_0^t (\nabla \times \mathbf{E})_z \, dt' \}_{discrete} \sim O(\nu \Delta t) \tag{4.2}$$

uniformly in wavenumber, with constant the CFL number ν. Thus, the standard necessary and sufficient stability restriction will hold *unmodified* for the modified Maxwell's equations in a sponge layer, or corner.

5. Numerical Experiments.

Figure 1 depicts a circular scatterer centered at (x_s, y_s) of relative permittivity ϵ_r and radius r_s illuminated by a cylindrically spreading wave generated with the pulsed electric-current point-source $J^{source}(x', y', t) = \frac{\delta_{i-i',j-j'}}{\Delta^2} g(t)$, where Δ is the spatial cell size, $\frac{\delta_{i-i',j-j'}}{\Delta^2}$ is the Kronecker delta function approximation to $\delta(x-x', y-y')$, (i', j') is the location of the source point (x', y') on the grid, $g(t) = E_0(10 - 15\cos\omega_1 t + 6\cos\omega_2 t - \cos\omega_3 t)$ is a compact smooth function supported in $t \in [0, t_s]$, and E_0 is the source amplitude. The scatterer is centered on the grid, and the point source is placed so that $|x_s - x'| = 2r_s$ and $y_s = y'$. We take $t_s = 10^{-9}$ sec, $\omega_m = 2\pi m/t_s$, $m = 1, 2, 3$, $\epsilon_r = 4$, $r_s = 2c_\infty t_s/3$, and $E_0 = Z_r/320$ with $Z_r = \sqrt{\mu_0/\epsilon_0\epsilon_r}$ being the wave impedance in the medium of relative permittivity ϵ_r where the source is placed. Our scattering problem is embedded in a two-dimensional, infinite, homogeneous, lossless, dielectric with $\epsilon_r = 1$. We solve it numerically, in a test domain Ω_C, with boundary $\partial\Omega_C$, itself embedded inside a much larger reference domain Ω_L with boundary $\partial\Omega_L$. Domain Ω_C is truncated by either placing on $\partial\Omega_C$ one of

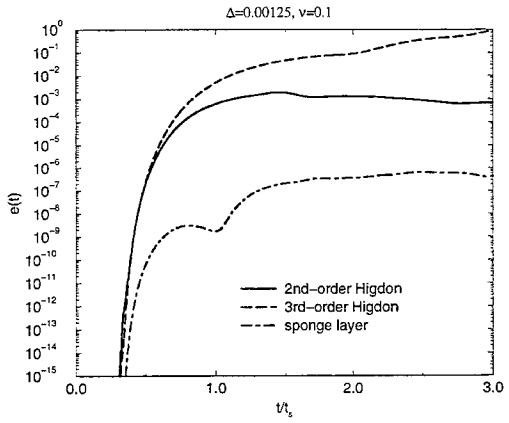

Figure 2: Time evolution of $e(n\Delta t)$.

the local Higdon RBCs (which are used for comparison with the sponge layer), or by surrounding Ω_C with a uniform width ($d = 4ct_s/15$) PML-type layer Ω_S bounded by $\partial\Omega_C$ on the inside and $\partial\Omega_S$ on the outside. On $\partial\Omega_S$ and $\partial\Omega_L$ we implement a PEC boundary condition using images [8], thus preserving the interior scheme spatial order of accuracy there. The reference domain boundary is placed sufficiently far from $\partial\Omega_C$ to provide causal isolation between all points in the test domain and reflections generated at $\partial\Omega_L$ over a given computation time interval $[0, T = 3t_s]$. The physical size of Ω_C is L^2 where $L = 5c_\infty t_s/3$. The (2,4) staggered scheme is employed with the same source, scatterer, and discretization parameters inside both domains.

To test and compare the boundary treatments considered herein we compute the error $e(n\Delta t) = ||E^{\Omega_C}(\cdot,\cdot,n\Delta t) - E^{\Omega_L}(\cdot,\cdot,n\Delta t)||_2$ introduced at each time step n by the artificial truncation of Ω_C for $n \in [0, T/\Delta t]$, where Δt is the time step, E^{Ω_C,Ω_L} is the discrete electric field in the appropriate domain indicated by the superscript, and the L_2 norm is taken over the interior of Ω_C. Note, $e(n\Delta t) = 0$ for $n \in [0, T_{int}/\Delta t]$, where T_{int} is the least time required for the wave field to start interacting with $\partial\Omega_C$. This definition of error is a measure of how well the artificial truncation approximates the true "physics" at the boundary which dictate that there should be no boundary felt by the outgoing waves. We also compute $||e(\cdot)||_2$, over $n \in [0, T/\Delta t]$, on a sequence of grids generated by successively halving Δ while keeping the CFL number constant. We assume $||e(\cdot)||_2 \sim O(\Delta^r)$ and compute the exponent r from the numerical results. On the coarsest grid $\Delta = 0.02$, while $\Delta = 0.00125$ on the finest grid. Results are presented with a CFL number $\nu = 0.1$ for the (2,4) staggered scheme. The sponge-layer/free-space interface is reflectionless for analytic waves, however, discrete waves may partially reflect from it. For this reason, the conductivities are implemented as the functions $\sigma_{max}(\frac{x}{d})^p$, where x is distance from the sponge-layer/free-space interface along the normal into the layer, and p is the order of variation. We choose the parameters so that the value of σ_{max} gives 10^{-q} for the reflection due to the PEC backing after one round-trip for plane waves entering the layer at normal incidence. For the simulations we used $q = 5$ and $p = 2$. The value for d used herein corresponds to a layer 8 grid cells wide at $\Delta = 0.01$, and gives $\sigma_{max} = 28.125/(Z_0 ct_s)$. An important parameter in the sponge layer is the relaxation time $\tau = \epsilon_0/\sigma_{max}$. The time-resolution parameter in the sponge

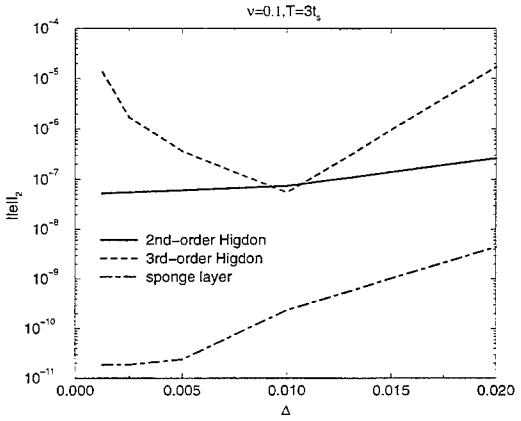

Figure 3: Convergence of the reflection properties in the L_2-norm.

layer is $h = \Delta t/\tau = 93.75\nu\Delta$ for the values given above. Then, we have $0.0117 \leq h \leq 0.1875$ for the (2,4) staggered scheme; the time-discretization is accurately approximating the effect of the relaxation time scale in the sponge layer [9]. The parameters in the 2nd- and 3rd-order Higdon operators were set as $\theta_k^{abs} = 0^o$, $k = 1, .., 3$, and $a = b = 0.5$. They provide perfect annihilation only for plane waves impinging normally on $\partial\Omega_C$. Each discrete Higdon operator is implemented with the 2nd-order accurate box scheme. The width of the sponge layer, and all other physical dimensions and parameters were kept invariant during the mesh refinement studies.

Figure 2 compares the "physical" errors introduced by the boundary truncations. We see the sponge layer to be superior to the other methods by more than 3 orders of magnitude. It is interesting to note that the 3-rd order Higdon operator performs poorly for late times and fine discretization. This is expected as it is badly behaved at zero-frequency, where it possesses a generalized eigenvalue that produces instability. The zero-frequency in our problem is introduced by the fact that in two dimensions a passing wavefront leaves behind it an algebraically decaying residue that persists for long times. Hence, after the main pulse passes through $\partial\Omega_C$, the remaining slowly-decaying residue acts as a zero-frequency forcing of the boundary operator. Figure 3 depicts the results of a convergence study using the (2,4) staggered scheme. Again, the superiority of the sponge layer is evident. The slope of the dash-dot line on the graph is roughly 3. The deterioration of the 3rd-order Higdon operator with grid refinement confirms our explanation of its poor performance as it gets worse as the continuum limit is approached. The "floor" of the error introduced by the sponge layer can be further reduced by increasing σ_{max}, and/or decreasing Δt.

References

[1] T. M. Roberts and P. G. Petropoulos, *J. Opt. Soc. Am. A*, vol. 13, no. 6, pp. 1204-1217, 1996.

[2] A. Taflove, *Computational Electrodynamics: The Finite-Difference Time-Domain Method,* Artech House, Boston (1995).

[3] Y. Liu, *J. Computational Physics,* vol. 124, pp. 396-416, 1996.

[4] P. G. Petropoulos, *IEEE Trans. on Antennas and Propagation,* vol. 42, no. 6, pp. 859-862, 1994.

[5] J. Fang, *Ph.D. Dissertation,* Dept. of Elec. Eng., University of California, Berkeley, CA, 1989.

[6] P. G. Petropoulos, *IEEE Trans. on Antennas and Propagation,* vol. 42, no. 1, pp. 62-69, 1994; *Wave Motion*, vol. 21, pp. 253-262, 1995; *ACES Journal,* vol. 11, no. 1, pp. 8-16, 1996.

[7] L. Zhao and A.C. Cangellaris, *IEEE Trans. Microwave Theory Tech.*, vol. 44, no. 12, pp. 2555-2563, 1996.

[8] P.G. Petropoulos, L. Zhao and A.C. Cangellaris, *J. Computational Physics,* submitted, Ms.# G0357, 1996. Available from first author via e-mail (peterp@golem.math.smu.edu).

[9] P. G. Petropoulos, "Analysis of Exponential Time-Differencing for FD-TD in Lossy Dielectrics," *IEEE Trans. on Antennas and Propagation,* accepted. Available from author via e-mail (peterp@golem.math.smu.edu).

[10] B. Gustafsson, H.-O. Kreiss and J. Oliger, *Time Dependent Problems and Finite Difference Methods,* Wiley Interscience, New York (1995).

[11] J. W. Thomas, *Numerical Partial Differential Equations: Finite Difference Methods,* Springer-Verlag, New York (1995).

Efficient Implementation of the Uniaxial PML Absorbing Media for the Finite-Difference Time-Domain Method

Stephen D. Gedney
University of Kentucky
Department of Electrical Engineering
Lexington, KY 40506-0046

1. Introduction

Explicit time-domain methods such as the finite-difference time-domain (FDTD) method and the planar generalized Yee (PGY) algorithm have been highly effective for the analysis of practical microwave circuit devices and antennas. One of the most challenging aspects of these methods is implementing absorbing boundary conditions that can accurately truncate the mesh over broad frequency bands. The perfectly matched layer (PML) absorbing media introduced by J.-P. Berenger [1] has been demonstrated to be a highly effective method for the termination of FDTD lattices [2, 3]. and can result in reflection errors as minute as -80 dB to -100 dB. Recently, it has been shown that the PML method can be reposed in a Maxwellian form as a uniaxial anisotropic medium [4-6]. It has been demonstrated that the uniaxial medium can be perfectly matched to lossy, inhomogeneous, dispersive, isotropic and anisotropic medium. Most significant is that the extension to such complex media in a FDTD implementation is quite trivial. Furthermore, since the uniaxial PML formulation is Maxwellian and not restricted to an orthogonal field splitting and it can be easily extended to more generalized methods such as the non-orthogonal FDTD method [7]. The focus of this paper will be on the efficient implementation of the uniaxial PML method and the expected accuracy. It will be shown that the uniaxial PML is more computationally efficient in terms of memory and computational speed as compared to Berenger's PML. Furthermore, the simple extension to more complex media will also be discussed in the context that its implementation within an existing FDTD code is quite trivial. It will also be shown that the theoretical reflection coefficient of the uniaxial PML medium in the discrete FDTD space is identical to that derived for Berenger's PML based on the split field equations [8], and extremely high levels of absorption are readily obtained.

2. The Uniaxial PML

It was shown in [4-6] that an arbitrary polarized wave incident on a planar half space (defined by the $z = 0$ plane) will be perfectly transmitted provided that the half space is a uniaxial medium with constitutive parameters

$$\bar{\bar{\varepsilon}} = \varepsilon_o \varepsilon_r \begin{bmatrix} a & 0 & 0 \\ 0 & a & 0 \\ 0 & 0 & a^{-1} \end{bmatrix}, \quad \bar{\bar{\mu}} = \mu_o \mu_r \begin{bmatrix} a & 0 & 0 \\ 0 & a & 0 \\ 0 & 0 & a^{-1} \end{bmatrix} \tag{1}$$

where ε_r and μ_r are defined by the medium of the upper half space. It can be demonstrated that this perfectly transmitting property is still valid if the upper half space is inhomogeneous, lossy, dispersive, and even anisotropic.

The intention of the PML medium is to rapidly attenuate waves entrant into the medium. Thus a suitable choice for a is:

$$a = \kappa_z + \frac{\sigma_z}{j\omega\varepsilon_o}. \tag{2}$$

Given the propagation constant of the incident wave to be $\gamma_z^i = \alpha_z^i + j\beta_z^i$, then it can be shown that the propagation constant of the transmitted wave in the uniaxial PML region is [5]

$$\gamma_z^a = \left(\kappa_z\alpha_z^i + \beta_z^i\frac{\sigma_z}{\omega\varepsilon_o}\right) + j\left(\kappa_z\beta_z^i - \alpha_z^i\frac{\sigma_z}{\omega\varepsilon_o}\right). \tag{3}$$

The real part of γ_z^a leads to the attenuation of the wave. Thus, the loss term σ_z will lead to the attenuation of all propagating modes, and the real term κ_z will lead to the amplification of the attenuation of all evanescent modes incident on the planar interface. As a result, this parameterization is analogous to the generalized PML introduced by Fang *et al.* [9], which is an extension of the original Berenger formulation.

The uniaxial PML can be used to terminate a three-dimensional FDTD space accurately and efficiently. To this end, the FDTD lattice is terminated on all 6 sides via planar PML media, which are backed by a PEC wall. Under such circumstances, it is recognized that the planar interfaces will overlap in what is referred to as the corner regions. In order to derive the constitutive relations in these corner regions, it is reasonable to match the PML to the adjacent uniaxial medium. For example, let the upper half space have permittivity and permeability tensors:

$$\overline{\overline{\varepsilon}}_1 = \varepsilon_o\varepsilon_r\begin{bmatrix} s_x^{-1} & 0 & 0 \\ 0 & s_x & 0 \\ 0 & 0 & s_x \end{bmatrix},\ \overline{\overline{\mu}}_1 = \mu_o\mu_r\begin{bmatrix} s_x^{-1} & 0 & 0 \\ 0 & s_x & 0 \\ 0 & 0 & s_x \end{bmatrix}. \tag{4}$$

Then, assuming an arbitrary polarized plane wave will be perfectly transmitted into the lower half space separated by a z = constant plane if the permittivity and permeability tensors are defined as:

$$\overline{\overline{\varepsilon}}_2 = \varepsilon_o\varepsilon_r\begin{bmatrix} s_x^{-1} & 0 & 0 \\ 0 & s_x & 0 \\ 0 & 0 & s_x \end{bmatrix}\begin{bmatrix} s_z & 0 & 0 \\ 0 & s_z & 0 \\ 0 & 0 & s_z^{-1} \end{bmatrix},\ \overline{\overline{\mu}}_2 = \mu_o\mu_r\begin{bmatrix} s_x^{-1} & 0 & 0 \\ 0 & s_x & 0 \\ 0 & 0 & s_x \end{bmatrix}\begin{bmatrix} s_z & 0 & 0 \\ 0 & s_z & 0 \\ 0 & 0 & s_z^{-1} \end{bmatrix}. \tag{5}$$

This can be further generalized to a y interface, leading to the general uniaxial tensors

$$\overline{\overline{\varepsilon}} = \varepsilon_o\varepsilon_r\overline{\overline{s}},\quad \overline{\overline{\mu}} = \mu_o\mu_r\overline{\overline{s}},\quad \text{and } \overline{\overline{s}} = \begin{bmatrix} \frac{s_y s_z}{s_x} & 0 & 0 \\ 0 & \frac{s_x s_z}{s_y} & 0 \\ 0 & 0 & \frac{s_x s_y}{s_z} \end{bmatrix} \tag{6}$$

where,

$$s_x = \left(\kappa_x + \frac{\sigma_x}{j\omega\varepsilon_o}\right),\ s_y = \left(\kappa_y + \frac{\sigma_y}{j\omega\varepsilon_o}\right),\ s_z = \left(\kappa_z + \frac{\sigma_z}{j\omega\varepsilon_o}\right). \tag{7}$$

Within this uniaxial region, Maxwell's curl equations are expressed as:

$$\nabla\times\vec{H} = j\omega\varepsilon_o\varepsilon_r(\omega)\overline{\overline{s}}\vec{E},\quad \nabla\times\vec{E} = -j\omega\mu_o\overline{\overline{s}}\vec{H} \tag{8}$$

It is from these equations that the explicit field updates will be derived. As an example, consider the update expression for E_z. Introducing the constitutive relation

$$D_z = \varepsilon_o\varepsilon_r\frac{s_x}{s_z}E_z. \tag{9}$$

where ε_r is assumed to be a function of x and y, it follows from (6) - (8):

$$\frac{\partial}{\partial x}H_y - \frac{\partial}{\partial y}H_x = j\omega D_z + \frac{\sigma_y}{\varepsilon_o}D_z. \tag{10}$$

Subsequently, this leads to the discrete field update for D_z:

$$D_{z_{i,j,k+\frac{1}{2}}}^{n+\frac{1}{2}} = \frac{\frac{\kappa_y}{\Delta t} - \frac{\sigma_y}{2\varepsilon_o}}{\frac{\kappa_y}{\Delta t} + \frac{\sigma_y}{2\varepsilon_o}} D_{z_{i,j,k+\frac{1}{2}}}^{n-\frac{1}{2}} + \frac{1}{\frac{\kappa_y}{\Delta t} + \frac{\sigma_y}{2\varepsilon_o}} \left(\left(H_{y_{i+\frac{1}{2},j,k+\frac{1}{2}}}^{n} - H_{y_{i-\frac{1}{2},j,k+\frac{1}{2}}}^{n} \right) / \Delta x - \left(H_{x_{i,j+\frac{1}{2},k+\frac{1}{2}}}^{n} - H_{x_{i,j-\frac{1}{2},k+\frac{1}{2}}}^{n} \right) / \Delta y \right) \tag{11}$$

Given D_z, an auxiliary relationship can be derived for E_z as

$$\begin{aligned} &s_z D_z = \varepsilon_o \varepsilon_r s_x E_z \text{ , or} \\ &j\omega\kappa_z D_z + \frac{\sigma_z}{\varepsilon_o} D_z = \varepsilon_o \varepsilon_r (j\omega\kappa_x E_z + \frac{\sigma_x}{\varepsilon_o} E_z). \end{aligned} \tag{12}$$

Then, transforming (12) into the time-domain, approximating the time derivatives using a central difference approximation, and averaging $\frac{\sigma_z}{\varepsilon_o}D_z$ and $\frac{\sigma_x}{\varepsilon_o}E_z$ in time, this results in a second-order accurate explicit update equation:

$$E_{z_{i,j,k+\frac{1}{2}}}^{n+\frac{1}{2}} = E_{z_{i,j,k+\frac{1}{2}}}^{n-\frac{1}{2}} \frac{(\kappa_x - \frac{\sigma_x \Delta t}{2\varepsilon_o})}{(\kappa_x + \frac{\sigma_x \Delta t}{2\varepsilon_o})} + \frac{1}{(\kappa_x + \frac{\sigma_x \Delta t}{2\varepsilon_o})\varepsilon_o \varepsilon_r} \left(D_{z_{i,j,k+\frac{1}{2}}}^{n+\frac{1}{2}} (\kappa_z + \frac{\sigma_z \Delta t}{2\varepsilon_o}) - D_{z_{i,j,k+\frac{1}{2}}}^{n-\frac{1}{2}} (\kappa_z - \frac{\sigma_z \Delta t}{2\varepsilon_o}) \right). \tag{13}$$

Similar update equations can be derived for the remaining field components.

The uniaxial PML method is easily extended to more general media such as lossy media, dispersive media, or non-linear media. This can easily be done through the addition of an additional auxiliary equation(s) [5], which is a simple extension of the above algorithm.

3. Estimating the Discretization Error of the Uniaxial PML

In a continuous space, the uniaxial PML provides a reflectionless interface that is highly attenuative. In theory, the conductivity can be made extremely large such that the wave attenuates immediately. However, due to discretization error, spurious reflections will be realized in the discrete FDTD space. Specifically, a large step discontinuity in the material medium will lead to large discretization errors. To date, this has been circumvented by scaling the PML parameters along the normal axis to eliminate large step discontinuities at the PML interface. The scaling function has been chosen to be a polynomial of some order m, where typically m is in the range $2 \leq m \leq 4$. In the discrete space, the inhomogeneous media is represented by a piecewise linear approximation. Subsequently, larger jumps in the material profile are realized deeper in the PML medium, where the reflected waves will be sufficiently attenuated before being transmitted back into the FDTD space. As a result, there is an optimal choice for the scaling order m and PML parameters that provide minimal reflection error. Unfortunately, determining the scaling order and the optimal parameters is not obvious. Through numerical experiments, a "rule-of-thumb" was derived in [6] which has provided a good estimate of the optimal parameters for PML media 5 to 10 cells thick for a wide variety of applications[5-7]. Recently, an analytical formulation was presented by Fang and Wu which provides an exact representation of the reflection error in Berenger's split field formulation [8]. The advantage of this simple model is that for a given FDTD lattice, material medium, and PML thickness, the optimal parameters can be easily extracted *a priori*. A second advantage is that the performance of the PML medium in the discrete space can be studied and optimized [10]. Using a similar procedure, the reflection error of the uniaxial PML in the discrete space is determined in the following.

Initially, it is assumed that a plane wave is propagating through a FDTD lattice with PML parameters given by (6). Inserting the plane wave expression into the discrete field equations characterized by (11) and(13), a discrete dispersion relationship is derived:

$$\left(\frac{\sin\left(\frac{\omega\Delta t}{2}\right)}{c_o\Delta t}\right)^2=\left(\frac{\sin\left(\tilde{k}_x\Delta x/2\right)}{\Delta x\left(\kappa_x-j\frac{\sigma_x}{\varepsilon_o}\frac{\Delta t}{\tan(\omega\Delta t/2)}\right)}\right)^2+\left(\frac{\sin\left(\tilde{k}_y\Delta y/2\right)}{\Delta y\left(\kappa_y-j\frac{\sigma_y}{\varepsilon_o}\frac{\Delta t}{\tan(\omega\Delta t/2)}\right)}\right)^2+\left(\frac{\sin\left(\tilde{k}_z\Delta z/2\right)}{\Delta z\left(\kappa_z-j\frac{\sigma_z}{\varepsilon_o}\frac{\Delta t}{\tan(\omega\Delta t/2)}\right)}\right)^2 \tag{14}$$

As expected, in the limit $\Delta x,\Delta y,\Delta z,\Delta t\to 0$, this reduces to the dispersion relationship in the continuous space. Next, assume that the wave is TE_y polarized and $k_y = 0$. The wave is assumed to be propagating in a PML medium with profile κ_{z1}, σ_{z1} and is incident on a planar interface backed by a PML medium with profile κ_{z2}, σ_{z2} (see Fig. 1). Furthermore, assume that $\kappa_x = \kappa_y = 1$ and $\sigma_x = \sigma_y = 0$ in both medium. The governing curl equations are then expressed as:

$$\frac{\partial}{\partial t}\varepsilon_o\kappa_z E_x+\sigma_z E_x=-\frac{\partial}{\partial z}H_y, \tag{15.a}$$

$$\frac{\partial}{\partial t}D_z=\frac{\partial}{\partial x}H_y,\quad \frac{\partial}{\partial t}\varepsilon_o E_z=\frac{\partial}{\partial t}\kappa_z D_z+\frac{\sigma_z}{\varepsilon_o}D_z \tag{15.b}$$

$$\frac{\partial}{\partial t}\mu_o\kappa_z H_y+\frac{\sigma_z\mu_o}{\varepsilon_o}H_y=-\frac{\partial}{\partial z}E_x+\frac{\partial}{\partial x}E_z. \tag{15.c}$$

which are discretized in the same manner as (11) and (13). In the discrete space, the incident wave propagating in medium 1 has the wave impedance

$$Z=\frac{E_x}{H_y}=\frac{\sin\left(\frac{\tilde{k}_{z1}\Delta z}{2}\right)\Big/\Delta z}{\left(\frac{\kappa_{z1}\varepsilon_o}{\Delta t}\sin(\omega\Delta t/2)-j\frac{\sigma_{z1}}{2}\cos(\omega\Delta t/2)\right)}=\sqrt{\eta^2-\left(\frac{\sin\left(\frac{\tilde{k}_x\Delta x}{2}\right)}{\Delta x}\right)^2} \tag{16}$$

where the right-hand-side is easily deduced from the dispersion relationship in (14). It can be shown that the wave impedance in medium 2 is identical to that in medium 1 since k_x is identical in each medium.

Assuming the TE_y wave to be incident from medium 1 to medium 2, the total fields can be written as:

$$E_{x_1}=E_o e^{j\omega t}(e^{-j\tilde{k}_x x-j\tilde{k}_{z_1}z}+R_e e^{-j\tilde{k}_x x+j\tilde{k}_{z_1}z}),\qquad E_{x_2}=E_o e^{j\omega t}(1+R_e)e^{-j\tilde{k}_x x-j\tilde{k}_{z_2}z}$$

$$H_{y_1}=E_o e^{j\omega t}(e^{-j\tilde{k}_x x-j\tilde{k}_{z_1}z}-R_e e^{-j\tilde{k}_x x+j\tilde{k}_{z_1}z})/Z,\quad H_{y_2}=E_o e^{j\omega t}(1+R_e)e^{-j\tilde{k}_x x-j\tilde{k}_{z_2}z}/Z \tag{17}$$

Inserting (17) into (15.a) in its discrete form evaluated at the $z = 0$ interface (see Fig. 2) leads to

$$R_e=-\frac{j2\varepsilon_o\left(\kappa_z-\frac{\kappa_{z1}+\kappa_{z2}}{2}\right)\sin\left(\frac{\omega\Delta t}{2}\right)\Big/\Delta t+\left(\sigma_z-\frac{\sigma_{z1}+\sigma_{z2}}{2}\right)\cos\left(\frac{\omega\Delta t}{2}\right)\Big/2+\frac{1}{Z\Delta z}\left(\cos\left(\frac{\tilde{k}_{z2}\Delta z}{2}\right)-\cos\left(\frac{\tilde{k}_{z1}\Delta z}{2}\right)\right)}{j2\varepsilon_o\left(\kappa_z-\frac{\kappa_{z1}+\kappa_{z2}}{2}\right)\sin\left(\frac{\omega\Delta t}{2}\right)\Big/\Delta t+\left(\sigma_z-\frac{\sigma_{z1}+\sigma_{z2}}{2}\right)\cos\left(\frac{\omega\Delta t}{2}\right)\Big/2+\frac{1}{Z\Delta z}\left(\cos\left(\frac{\tilde{k}_{z2}\Delta z}{2}\right)+\cos\left(\frac{\tilde{k}_{z1}\Delta z}{2}\right)\right)} \tag{18}$$

This procedure is then repeated by assuming a plane wave incident from medium 2 to medium 1, for which the reflection coefficient R_e^r is assumed. It is determined that

$$R_e^r=-\frac{j2\varepsilon_o\left(\kappa_z-\frac{\kappa_{z1}+\kappa_{z2}}{2}\right)\sin\left(\frac{\omega\Delta t}{2}\right)\Big/\Delta t+\left(\sigma_z-\frac{\sigma_{z1}+\sigma_{z2}}{2}\right)\cos\left(\frac{\omega\Delta t}{2}\right)\Big/2-\frac{1}{Z\Delta z}\left(\cos\left(\frac{\tilde{k}_{z2}\Delta z}{2}\right)-\cos\left(\frac{\tilde{k}_{z1}\Delta z}{2}\right)\right)}{j2\varepsilon_o\left(\kappa_z-\frac{\kappa_{z1}+\kappa_{z2}}{2}\right)\sin\left(\frac{\omega\Delta t}{2}\right)\Big/\Delta t+\left(\sigma_z-\frac{\sigma_{z1}+\sigma_{z2}}{2}\right)\cos\left(\frac{\omega\Delta t}{2}\right)\Big/2+\frac{1}{Z\Delta z}\left(\cos\left(\frac{\tilde{k}_{z2}\Delta z}{2}\right)+\cos\left(\frac{\tilde{k}_{z1}\Delta z}{2}\right)\right)} \tag{19}$$

It is interesting to observe that in general $R_e \neq -R_e^r$, unless $\sigma_z = \frac{\sigma_{z1}+\sigma_{z2}}{2}$ and $\kappa_z = \frac{\kappa_{z1}+\kappa_{z2}}{2}$.

To complete the analysis, the reflection coefficient must next be computed at an H_y boundary, which is offset by $\Delta z/2$ from the E_x boundary (Fig. 2). Initially, from (15.b) it is found that

$$\frac{E_z}{H_y} = -\frac{\kappa_z \sin(\omega\Delta t/2)/\Delta t - j\frac{\sigma_z}{\varepsilon_o}\cos(\omega\Delta t/2)/2}{\varepsilon_o \sin^2(\omega\Delta t/2)/\Delta t^2}\frac{\sin(\tilde{k}_x x)}{\Delta x} \tag{20}$$

Then, (15.c) is evaluated in its discrete form by assuming the fields in (17) (with reflection coefficient R_h). It can be shown that

$$R_h = -R_e. \tag{21}$$

Repeating this procedure by assuming the wave is incident from medium 2 onto medium 1, it can further be shown that

$$R_h^r = -R_e^r. \tag{22}$$

Given the reflection coefficients R_e, R_e^r, R_h, and R_h^r due to a PML/PML interface a simple transmission analogy can be used to compute the reflection coefficient due to an N-cell PML medium interfaced to an FDTD lattice, as presented by Fang and Wu in [8]. Such an analogy can be used to more fully understand the behavior of the uniaxial PML medium in the discrete space.

It is interesting to note that if $\kappa_z = \kappa_{z1} = \kappa_{z2} = 1$, then (18), (19), (21) and (22) are identical to the reflection coefficients derived for Berenger's split field formulation in [8]. While this result was not initially obvious, it is not surprising due to the relationship between Berenger's PML formulation and the uniaxial PML formulation [6]. The advantage of this, is that the optimization methods introduced by Wu and Fang in [10] can also be applied to the uniaxial PML method, enhancing the efficiency of the uniaxial PML method.

4. Efficient Implementation of the Uniaxial PML

The time-dependent electric and magnetic fields within the uniaxial PML are computed using an explicit time-marching solution scheme, as derived in (11) and (13) for E_z. The uniaxial PML can be easily and efficiently implemented within the framework of an existing FDTD code. For example, combining both (11) and (13), the discrete field updates can be expressed as a triple-nested loop (illustrated here in FORTRAN):

```
do 10 k = 1, nz - 1
  do 10 j = 2, ny - 1
    do 10 i = 2, nx - 1
      ds = dz(i, j, k)
      dz(i, j, k) = ay(j) * dz(i, j, k) + by(j) * (hy(i, j, k) - hy(i - 1, j, k) - hx(i, j, k) + hx(i, j - 1, k))
      ez(i, j, k) = ax(i) * ez(i, j, k) + bx(i) * (az(k) * dz(i, j, k) - bz(k) * ds) * er_z(i, j, k)
10 continue
```

(23)

where

$$ay(j) = \frac{2\varepsilon_o\kappa_{y_j} - \sigma_{y_j}\Delta t}{2\varepsilon_o\kappa_{y_j} + \sigma_{y_j}\Delta t},\quad by(j) = \frac{2\varepsilon_o\Delta t}{2\varepsilon_o\kappa_{y_j} + \sigma_{y_j}\Delta t}\cdot\frac{1}{\Delta x\Delta y},\quad ax(i) = \frac{2\varepsilon_o\kappa_{x_i} - \sigma_{x_i}\Delta t}{2\varepsilon_o\kappa_{x_i} + \sigma_{x_i}\Delta t},$$

$$bx(i) = \frac{2\varepsilon_o\Delta t}{2\varepsilon_o\kappa_{x_i} + \sigma_{x_i}\Delta t},\quad az(k) = \frac{\kappa_{z_k}}{\Delta t} + \frac{\sigma_{z_k}}{2\varepsilon_o},\quad bz(k) = \frac{\kappa_{z_k}}{\Delta t} - \frac{\sigma_{z_k}}{2\varepsilon_o},\quad er_z(i,j,k) = \frac{1}{\varepsilon_o\varepsilon_r(i,j,k)} \tag{24}$$

and the fields have been scaled by their edge length (e.g., $E_x = \Delta x E_x$). It is noted that the PML parameters σ_i and κ_i (i = x,y,z) are one-dimensional variables. Specifically, in the interior working volume, it is assumed that $\sigma_i = 0$, and $\kappa_i = 1$, and in the PML regions, they are assumed to have an m-th order polynomial spatial variation in the PML region along their respective axes. As a result, the update coefficients in (24) are simply one-dimensional coefficients.

Updating the fields over all space has the limitation that the additional storage arrays required to store the flux densities (e.g., D_z) must be stored over all space. However, it does offer the advantage of simplicity in the modification of existing codes. An alternative is to write a triple nested loop for the interior fields, and then write separate loops for the different PML regions (segregating corner regions). In this case, only the auxiliary variables need to be stored in the PML regions, leading to memory savings. Furthermore, in this circumstance, the uniaxial PML will require considerably less storage than Berenger's PML, since only the normal fields require dual storage as opposed to the two tangential fields as required by Berenger's PML formulation. Based on this scheme, the FDTD with a uniaxial PML truncation on all 6 boundaries will require

$$6N_xN_yN_z + 8N_{pml}(N_xN_y + N_yN_z + N_zN_x) - 16N_{pml}(N_x + N_y + N_z) + 24N_{pml}^2 \qquad (25)$$

real numbers as compared to $6N_xN_yN_z$ real numbers required by a FDTD method with a local ABC. A comparison of the storage requirements is presented in Fig. 3, which illustrates the percentage of additional memory required to implement a 4 cell and 10 cell PML boundary in a cubic grid ($N_x = N_y = N_z$) as compared to that required by an FDTD method with a local ABC of the same lattice dimension. It is illustrated that the larger the problem size, the greater the savings. Furthermore, local ABC's must be placed much further out requiring even larger lattices. Subsequently, the uniaxial PML can lead to significant memory savings.

The effectiveness of the uniaxial PML was presented in [5, 6]. Here, some additional results are provided demonstrating the efficiency of the PML method. Consider the coupled patch antenna illustrated in Fig. 4 printed on a 1.5 mm substrate with $\varepsilon_r = 2.86$. The FDTD model consisted of a 173 X 91 X 21 lattice with $\Delta x = \Delta y = 0.5$ mm, $\Delta z = 0.25$ mm. This lattice includes 10 cell thick PML boundaries on 5 sides of the lattice (the sixth side is a PEC ground) placed 5 cells from the edge of the antenna and above the antenna surface. The simulation was executed on a 4 processor SGI power challenge and required 8,000 time iterations. Table 1 illustrates the times required by the uniaxial PML (UPML) method, Berenger's PML method (BPML) and FDTD with a second-order Higdon absorbing boundary condition (ABC). For these computations, the PML is assumed to be over all space, and updates synonymous to (23) were used for both the UPML and BPML. Interestingly, the UPML was roughly 50 % faster than the BPML scheme. Similarly, the UPML was only 25 % slower than the FDTD with a local ABC *for the same grid size*. However, for the same level of accuracy, the local ABC must be pushed further out. In fact, if the ABC were pushed only 5 cells further out in each direction, the FDTD simulation would require 45 % more floating point operations to perform the 8,000 time steps!

References

[1] J. P. Berenger, "A perfectly matched layer for the absorption of electromagnetic waves," *Journal of Computational Physics*, vol. 114, pp. 185-200, October 1994.

[2] W. C. Chew and W. H. Weedon, "A 3D perfectly matched medium from modified Maxwell's equations with stretched coordinates," *IEEE Microwave and Guided Wave Letters*, vol. vol. 7, pp. 599-604, September 1994.

[3] D. S. Katz, E. T. Thiele and A. Taflove, "Validation and extension to three-dimensions of the Berenger PML absorbing boundary condition for FD-TD meshes," *IEEE Microwave and Guided Wave Letters*, vol. 4, pp. 268-270, August 1994.

[4] Z. S. Sacks, D. M. Kingsland, R. Lee and J. F. Lee, "A perfectly matched anisotropic absorber for use as an absorbing boundary condition," *IEEE Transactions on Antennas and Propagation*, vol. vol. 43, pp. 1460-1463, December 1995.

[5] S. D. Gedney, "An anisotropic PML absorbing media for FDTD simulation of fields in lossy dispersive media," *Electromagnetics*, vol. 16, pp. 399-415, July/August 1996.

[6] S. D. Gedney, "An anisotropic perfectly matched layer absorbing media for the truncation of FDTD Lattices," *IEEE Transactions on Antennas and Propagation*, vol. 44, pp. 1630-1639, December 1996.

[7] J. A. Roden and S. D. Gedney, "Efficient Implementation of the Uniaxial Based PML Media in Three-Dimensional Non-orthogonal Coordinates Using the FDTD Technique," *Microwave and Optical Technology Letters*, vol. Vol. 10, pp. February 1997.

[8] J. Fang and Z. Wu, "Closed-form expression of numerical reflection coefficient at PML interfaces and optimization of PML performance," *IEEE Microwave and Guided Wave Letters*, vol. vol. 6, pp. 332-334, September 1996.

[9] J. Fang and Z. Wu, "Generalized perfectly matched layer - an extension of Berenger's Perfectly Matched Layer Boundary Condition," *IEEE Microwave and Guided Wave Letters*, vol. vol. 5, pp. 451-453, December 1995.

[10] Z. Wu and J. Fang, "High-Performance PML Algorithms," *IEEE Microwave and Guided Wave Letters*, vol. vol. 6, pp. 335-337, September 1996.

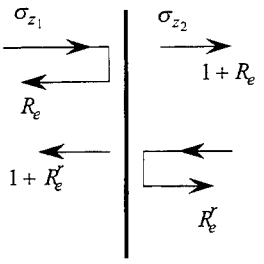

Fig. 1. Reflection at a PML/PML boundary

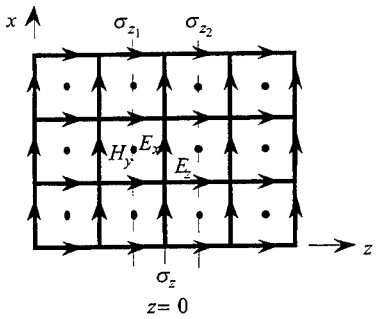

Fig. 2. Discrete Lattice at the PML/PML boundary.

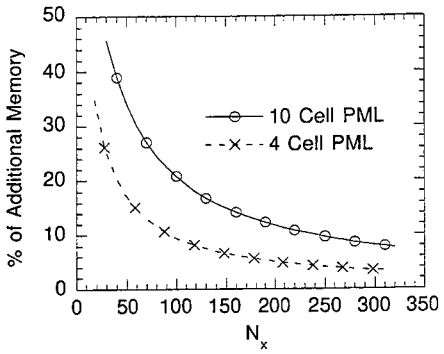

Fig. 3 Percentage of additional memory required by the uniaxial PML algorithm for 10 cell and 4 cell thick PML boundaries given $N_x = N_y = N_z$.

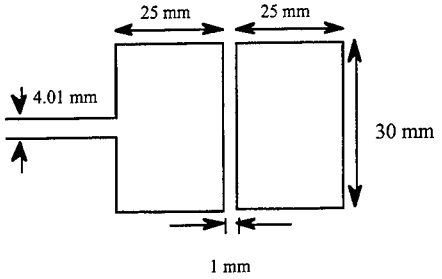

Fig. 4 Coupled patch antenna printed on a 1.5 mm substrate ($\varepsilon_r = 2.86$)

	1 Proc	4 Proc
UPML	2,684 s	601.1 s
BPML	4,113 s	1,249 s
ABC	2,064 s	512.8 s

Table 1 CPU times recorded on an SGI power challenge for a 183 x 101 x 21 Lattice

Generalization of PML to Cylindrical Geometries

Jim Maloney, Morris Kesler and Glenn Smith
Signature Technology Lab
Georgia Tech Research Institute
Atlanta, GA 30332

Introduction

There has been much work recently in the area of numerical absorbing boundary conditions, particularly the concept of a perfectly matched layer (PML). Several PML formulations have been proposed, such as the Berenger split-field [1], anisotropic material [2-3] and stretched coordinates [4], and demonstrated to provide an excellent means for truncating rectilinear, numerical grids. There are situations where it is desirable to use something other than a rectilinear grid, such as a grid in cylindrical coordinates for a problem with rotational symmetry. However, the straightforward application of these methods to non-rectilinear grids does not provide a satisfactory level of grid termination. Clearly the need exists for a PML applicable to general, orthogonal curvilinear coordinate systems.

Recently, we presented a graphical technique for obtaining a PML in cylindrical coordinates [5]. The approach was based on a piece-wise linear approximation of the boundary region, using a limiting procedure to deduce effective material properties. The result was an anisotropic material whose properties were a function of the radius of curvature at the boundary and the distance into the layer. FDTD numerical results were presented which showed the effectiveness of the cylindrical PML. However, because of the approximations inherent in discretizing the problem, the reflection coefficient will not be exactly zero, and thus it is not possible to show numerically that the new, cylindrical PML was a true PML.

In this paper we will review the graphical derivation and show that the result derived graphically is a true cylindrical PML. A modal analysis is used to obtain closed-form expressions for the reflection coefficient at an air-cylindrical PML interface (which equals zero) and the attenuation of the transmitted field. Of course, when used to truncate a grid in a numerical implementation, only a finite thickness layer is desired. Results of the reflection from a PML layer backed by a PEC boundary are included to show the level of effectiveness versus thickness and mode number.

Geometrical Construction of Cylindrical PML

Consider first an interface at the outside of a cylindrical coordinate grid, as would be the case in an FDTD numerical simulation. We want to develop an anisotropic material conforming to this geometry which has the properties of a PML material, i.e., a lossy material with no reflection at an interface with free space. If we make a piece-wise linear approximation to this problem, the geometry is as indicated in Figure 1(a).

As shown in the figure, there are two types of regions that need to be considered. The first type of region, indicated by **I**, has a planar interface with the interior region (taken to be free space for this dis-

cussion). The material parameters that make this interface with free space reflectionless are the usual rectangular PML parameters, i.e.,

$$\frac{\bar{\bar{\varepsilon}}}{\varepsilon_0} = \frac{\bar{\bar{\mu}}}{\mu_0} = \begin{bmatrix} 1/a & & \\ & a & \\ & & a \end{bmatrix} \tag{1}$$

in the coordinate system in which the x-axis is perpendicular to the interface, and where a is a complex number. We wish to find the material parameters for the triangular region **II** that make the interfaces

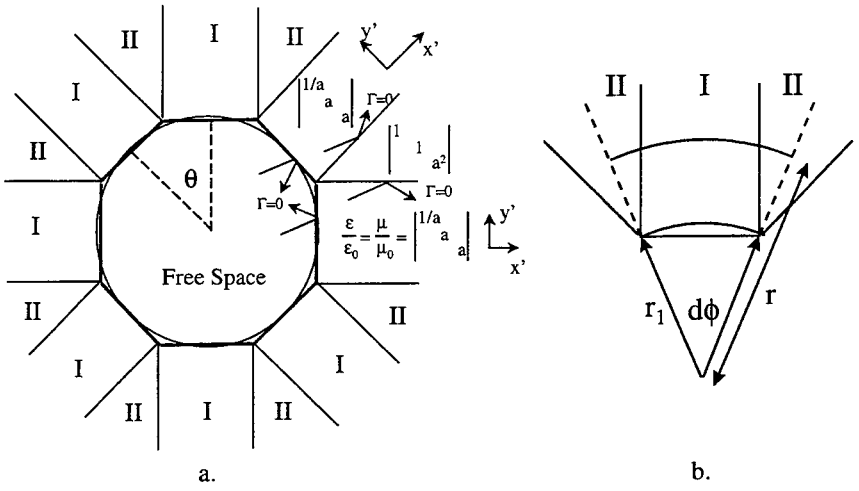

Figure 1 (a) Geometry used for cylindrical PML construction, (b) Geometry used for the averaging process.

with the two region **I**'s on either side of it reflectionless. In general, the material parameters which accomplish this for region **II** will be dependent on the angle θ, since we must rotate the material matrix into a common coordinate system when solving the interface problems. However, the solution will be independent of θ if the properties for region **II** are of the form,

$$\frac{\bar{\bar{\varepsilon}}}{\varepsilon_0} = \frac{\bar{\bar{\mu}}}{\mu_0} = \begin{bmatrix} b & & \\ & b & \\ & & c \end{bmatrix}, \tag{2}$$

since this matrix remains the same for rotations about the z-axis. If we can find a solution in the form of equation (2) that works for one of the interfaces, it will also work for the other.

It can be shown the material properties of region **II** that make the boundary reflectionless are

$$\frac{\bar{\bar{\varepsilon}}}{\varepsilon_0}=\frac{\bar{\bar{\mu}}}{\mu_0}=\begin{bmatrix}1 & & \\ & 1 & \\ & & a^2\end{bmatrix}. \tag{3}$$

To extend these results to a circular boundary, consider the limit as the angle θ gets small and each of the individual regions gets smaller. The overall material properties will be an average of the types given by equations (1) and (3). To determine how the averaging should work, consider an individual angular segment of width $d\phi$ as shown in Figure 1(b). This segment consists of regions **I** and **II** with the material properties given by equations (1) and (3). The fractional amount of each type of region depends on the distance into the layer, $r-r_1$, where r_1 denotes the radial distance to the interface. Thus, the averaged material properties will be a function of the radius of curvature of the interface.

In the limit of small $d\phi$, the fractional amount of region **I** and **II** is denoted by ζ_1 and ζ_2, respectively, where

$$\zeta_1=\frac{r_1}{r},\quad \zeta_2=\frac{r-r_1}{r}. \tag{4}$$

The r- and z-components of the material properties are both tangential to the interface boundaries, so they average the same way, while the ϕ component is normal to the interface boundaries and averages differently. The result of this averaging is

$$\begin{aligned} r &\to \zeta_1\frac{1}{a}+\zeta_2=\frac{1}{a}(\zeta_1+a\zeta_2)\\ \phi &\to \frac{1}{\zeta_1\frac{1}{a}+\zeta_2}=a\frac{1}{(\zeta_1+a\zeta_2)}\\ z &\to \zeta_1 a+\zeta_2 a^2=a(\zeta_1+a\zeta_2)\end{aligned}. \tag{5}$$

The material properties of the cylindrical PML are thus

$$\frac{\bar{\bar{\varepsilon}}}{\varepsilon_0}=\frac{\bar{\bar{\mu}}}{\mu_0}=\begin{bmatrix}\frac{1}{a}\gamma(r) & & \\ & \frac{a}{\gamma(r)} & \\ & & a\gamma(r)\end{bmatrix},\quad \gamma(r)=\frac{r_1+a(r-r_1)}{r}. \tag{6}$$

The form of the cylindrical PML is similar to that of rectangular PML, with the addition of the r-dependent factor $\gamma(r)$.

The use of PML in numerical codes, e.g. FDTD, requires the loss parameter (imaginary part of a) to be tapered smoothly from near zero to very high values. This is required because numerical implementations of PML exhibit interface reflections that are proportional to the discontinuities in the discrete taper. The cylindrical PML given in equations (6) is for a constant loss factor and can not be used for a tapered loss. The construction of a tapered, cylindrical PML will be discussed below.

Again, consider a piece-wise linear approximation to this problem as indicated in Figure 2. The regions indicated by **I** that have a planar interface with the interior region now have a planar interface with the regions indicated by **I′**. Because this interface is planar, regions **I′** are also the usual rectangular PML. The regions indicated by **II** have a planar interface with the regions marked **III**; however, because the material properties of **II** are not rectangular PML then the properties of **III** can not be rectangular PML. Furthermore, the properties of the regions indicated by **IV** must be determined. Requiring the reflection coefficient at each interface to be zero yields the material tensors given in Figure 2. This process of radial subdivision is repeated. Lastly to determine the tapered, cylindrical PML tensor, the average material properties are determined in the limit as the angle θ gets small and each individual region get smaller. The material properties of the tapered, cylindrical PML are thus

$$\frac{\overline{\overline{\varepsilon}}}{\varepsilon_0}=\frac{\overline{\overline{\mu}}}{\mu_0}=\begin{bmatrix}\frac{1}{a(r)}\gamma(r) & & \\ & \frac{a(r)}{\gamma(r)} & \\ & & a(r)\gamma(r)\end{bmatrix}, \quad \gamma(r)=\frac{r_1+\int_{r_1}^{r}a(r)dr}{r}. \tag{7}$$

Notice that the non-tapered result given above in Equation (6) is recovered from the tapered result when $a(r)$ is a constant value.

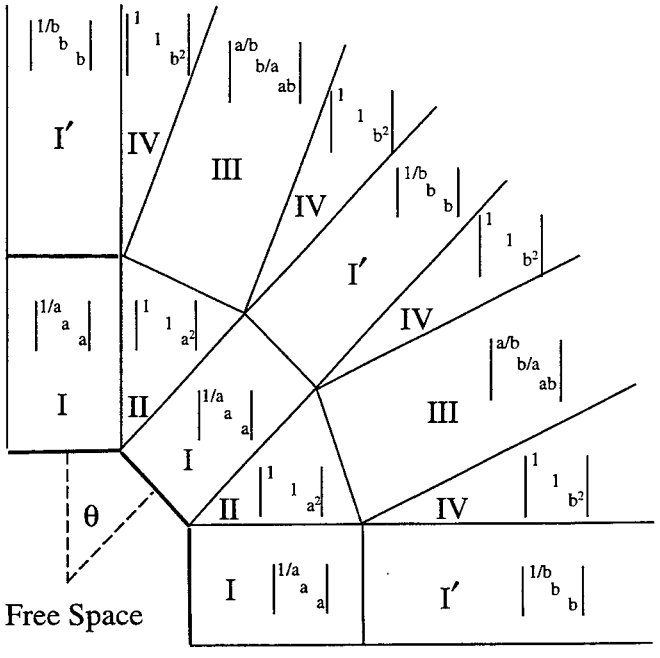

Figure 2 Geometry used for the tapered, cylindrical PML formulation.

Theoretical Evaluation of Cylindrical PML

To show that these material parameters are a true PML, we must examine the wave equation in such a material. Consider the TE case (H_r, H_ϕ, E_z) where the relevant Maxwell's equations are

$$j\omega\varepsilon_z E_z = \frac{1}{r}\left(\frac{\partial(rH_\phi)}{\partial r} - \frac{\partial H_r}{\partial \phi}\right), \quad H_\phi = \frac{1}{j\omega\mu_\phi}\frac{\partial E_z}{\partial r}, \quad H_r = -\frac{1}{j\omega\mu_r}\frac{1}{r}\frac{\partial E_z}{\partial \phi} \tag{8}$$

with

$$\frac{\mu_r}{\mu_0} = \frac{1}{a(r)}\gamma(r), \quad \frac{\mu_\phi}{\mu_0} = \frac{a(r)}{\gamma(r)}, \quad \frac{\varepsilon_z}{\varepsilon_0} = a(r)\gamma(r), \tag{9}$$

and $\gamma(r)$ given by (7). Combining equations (8) and (9) leads to the wave equation in this medium,

$$\frac{1}{r\gamma(r)}\frac{\partial}{\partial r}\left(r\gamma(r)\frac{\partial E_z}{\partial r}\right) + k_0^2 a^2 E_z + \left(\frac{a}{r\gamma(r)}\right)^2 \frac{\partial^2 E_z}{\partial \phi^2} = 0. \tag{10}$$

Defining $r' = r\gamma(r) = r_1 + \int_{r_1}^{r} a(r)dr$, then $\partial r' = a\partial r$ and (10) becomes

$$\frac{1}{r'}\frac{\partial}{\partial r'}\left(r'\frac{\partial E_z}{\partial r'}\right) + k_0^2 E_z + \left(\frac{1}{r'}\right)^2 \frac{\partial^2 E_z}{\partial \phi^2} = 0, \tag{11}$$

which is the same as the wave equation for free space. Thus, the electric field in the anisotropic material will be given by

$$\overline{E} \sim \hat{z} E_0 H_n^{(2)}(k_0(r_1 + \int_{r_1}^{r} a(r)dr))\exp(jn\phi), \tag{12}$$

where $H_n^{(2)}$ is a Hankel function of order n. The component of the magnetic field tangential to the boundary (ϕ component) is

$$\overline{H}_\phi \sim \frac{k_0\gamma(r)}{j\omega\mu_0} E_0 H_n'^{(2)}(k_0(r_1 + \int_{r_1}^{r} a(r)dr))\exp(jn\phi), \tag{13}$$

where the prime indicates a derivative with respect to the argument of the Hankel function. The reflection coefficient of the interface will be zero if the wave impedance inside the PML media and the wave impedance in the interior free space region are identical at the interface. The wave impedance in the interior free space region is

$$Z_{FS}(r) = \frac{E_z}{H_\phi} = j\eta_0 \frac{H_n^{(2)}(k_0 r)}{H_n'^{(2)}(k_0 r)}. \tag{14}$$

The wave impedance in the PML region is also a function of the radial position r; however, at the interface

$$Z_{PML}(r_1) = \frac{E_z}{H_\phi} = \frac{j\eta_0}{\gamma(r_1)} \frac{H_n^{(2)}(k_0 r)}{H_n'^{(2)}(k_0 r)} = Z_{FS}(r_1), \tag{15}$$

because $\gamma(r_1) = 1$, and thus there will be no reflection. Note also that the wave will be attenuated for proper choice of a as it propagates for $r > r_1$. This leads to the conclusion that the anisotropic material described by equations (6) or (7) is indeed a true cylindrical PML.

We can evaluate the reflection coefficient from a layer of the cylindrical PML material in a straightforward manner since there are no reflections at the air-PML interface. Consider the geometry in Figure 3, which shows a PML layer (inner radius r_1) surrounded by a metal shell of radius r_2. An outward propagating cylindrical wave is incident on the boundary, propagates through the PML region, reflects off the metal surface and propagates back through the PML layer into the free space interior region. The reflection coefficient is defined as the ratio of the E_R to E_I, and the magnitude of the reflection coefficient is determined solely by the two-way loss in the PML layer.

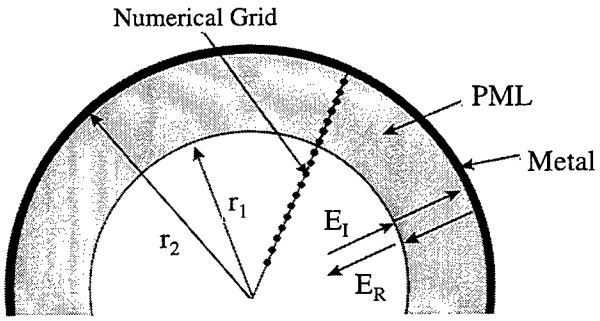

Figure 3 Geometry for evaluating the cylindrical PML.

The incident field is written as

$$E_I = E_0 H_n^{(2)}(k_0 r)\exp(jn\phi), \tag{16}$$

while the outward propagating field in the PML is

$$E_{PML}^{+} = E_0 H_n^{(2)}(k_0(r_1 + \int_{r_1}^{r} a(r)dr))\exp(jn\phi). \tag{17}$$

At the metal boundary, this field is reflected with a reflection coefficient of -1. Matching the boundary conditions at this point makes the inward propagating field

$$E_{PML}^{-} = -E_0 \frac{H_n^{(2)}(k_0(r_1 + \int_{r_1}^{r_2} a(r)dr))}{H_n^{(1)}(k_0(r_1 + \int_{r_1}^{r_2} a(r)dr))} H_n^{(1)}(k_0(r_1 + \int_{r_1}^{r} a(r)dr))\exp(jn\phi). \tag{18}$$

The field amplitude at the inner boundary determines the reflection coefficient, which is given by

$$R_{PML}^{L} = -\frac{H_n^{(2)}\left(k_0\left(r_1 + \int_{r_1}^{r_2} a(r)dr\right)\right)}{H_n^{(1)}\left(k_0\left(r_1 + \int_{r_1}^{r_2} a(r)dr\right)\right)} \frac{H_n^{(1)}(k_0 r_1)}{H_n^{(2)}(k_0 r_1)}. \tag{19}$$

We will compare the reflection of the cylindrical PML to that of rectangular PML to show the performance. Thus, we need the reflection of an individual cylindrical mode when the layer is an arbitrary, anisotropic material. In general, there is a reflection at the material interface at $r = r_1$ as well as from the metal outer boundary leading to a more complex expression for the total reflection coefficient. The result can be expressed as

$$R_{TE} = -\frac{H_n^{(2)}(k_0 r_1) - Z_{n'} H_n'^{(2)}(k_0 r_1)}{H_n^{(1)}(k_0 r_1) - Z_{n'} H_n'^{(1)}(k_0 r_1)} \frac{H_n^{(1)}(k_0 r_1)}{H_n^{(2)}(k_0 r_1)} \tag{20}$$

with

$$Z_{n'} = \sqrt{\frac{\mu_\phi \varepsilon_0}{\mu_0 \varepsilon_z}} \frac{H_{n'}^{(2)}(k_{\phi z} r_1) H_{n'}^{(1)}(k_{\phi z} r_2) - H_{n'}^{(2)}(k_{\phi z} r_2) H_{n'}^{(1)}(k_{\phi z} r_1)}{H_{n'}'^{(2)}(k_{\phi z} r_1) H_{n'}^{(1)}(k_{\phi z} r_2) - H_{n'}^{(2)}(k_{\phi z} r_2) H_{n'}'^{(1)}(k_{\phi z} r_1)} \tag{21}$$

$k_{\phi z} = \omega\sqrt{\mu_\phi \varepsilon_z}$, and $n' = n\sqrt{\mu_\phi / \mu_r}$. For the case of rectangular PML with material parameter a, the wavevector is $k_{\phi z} = a k_0$, $n' = an$ and $\sqrt{\frac{\mu_\phi \varepsilon_0}{\mu_0 \varepsilon_z}} = 1$.

We used equations (19) and (20) to calculate the cylindrical mode reflection for both rectangular and cylindrical PML. Figure 4 shows the reflection from a metal cylindrical shell coated with a rectangular PML material compared to the same shell coated with the cylindrical PML material. The geometry for the calculation is shown in Figure 3, with the coating thickness kept constant at $k_o(r_2 - r_1) = 0.633$. The material parameter for the coating was $a = 1 - j5$. The E-pol reflection as a function of radius of curvature for the n=0 cylindrical mode is shown in Figure 4(a) while the reflection as a function of mode number n for a fixed radius of curvature is shown in Figure 4(b). The cylindrical PML is dramatically better for smaller cylinders where the rectangular PML results are dominated by the interface reflection, with the results converging for very large cylinders as expected. As the mode number increases, the reflection from the layer increases, analogous to the reflection from a planar PML layer as the angle of incidence increases.

Numerical Evaluation of Cylindrical PML

The previous section demonstrated that the new cylindrical PML given by equation (7) is a true PML. To demonstrate the usefulness of the new cylindrical PML in a numerical FDTD code, consider the configuration shown in Figure 3. The inset in Figure 3 shows a schematic representation of the 1-D FDTD grid. The numerical grid begins at a fixed radius from the origin with the source excitation injected at the beginning of the grid. The reflection coefficient is determined by comparing two simulations: one with the grid truncated by the cylindrical PML and the other with an effectively infinite grid.

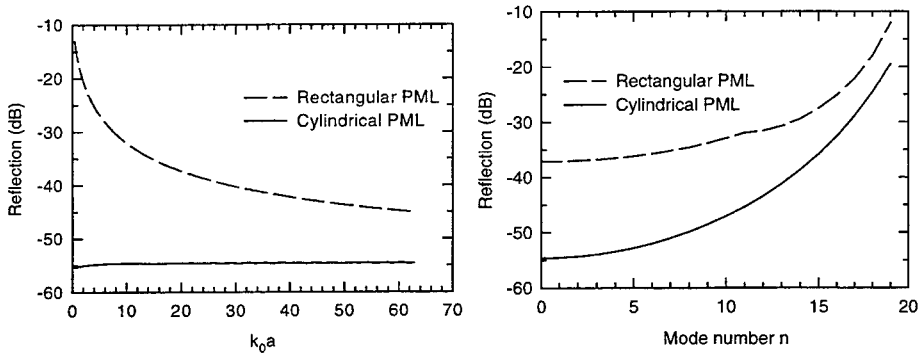

Figure 4 Reflection from a thin layer ($k_o(r_2 - r_1) = 0.633$). (a) Reflection as a function of the radius for the n=0 mode. (b) Reflection as a function of mode n for the radius $k_o r_2 = 20$.

Figure 5 shows a comparison of the reflection coefficient for the non-tapered case. The thickness of the PML layer is sufficiently large that only the front surface reflection is significant. The plot on the left shows the behavior as a function of radius for a fixed frequency with the loss and cell density indicated in the figure. As expected, the reflection coefficient for the rectangular PML is large and approaches the planar limit (indicated in figure) when the radius approaches infinity. The reflection coefficient for the cylindrical case is clearly better by approximately 30 dB. The plot on the right shows the behavior as a function of cylindrical mode number for fixed frequency and radius. Again, the cylindrical PML result is at least 30 dB better than the rectangular PML. Also shown is the reflection coefficient for a homogeneous, isotropic, matched layer.

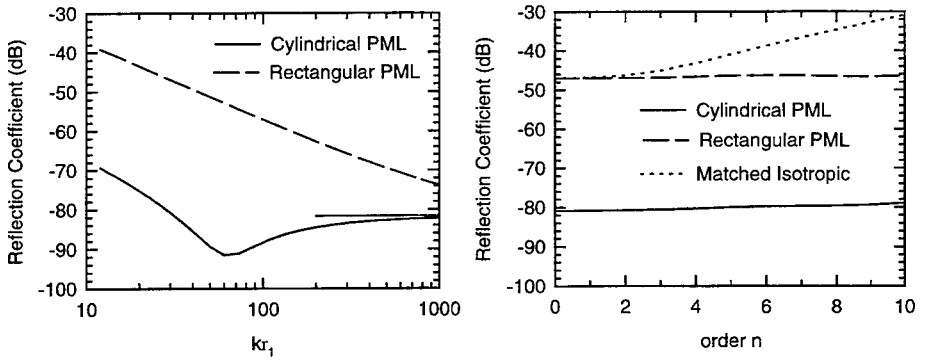

Figure 5 Reflection Coefficient of a thick, non-tapered PML region (a=1-j5)

A tapered PML is more useful for truncating FDTD grids. Figure 6 shows the results for a 10 cell PML with quadratic loss profile. Again, cylindrical PML is superior to rectangular PML. In this case, the planar limit is higher because of the trade-off between the front surface reflection and the two-way loss through the layer.

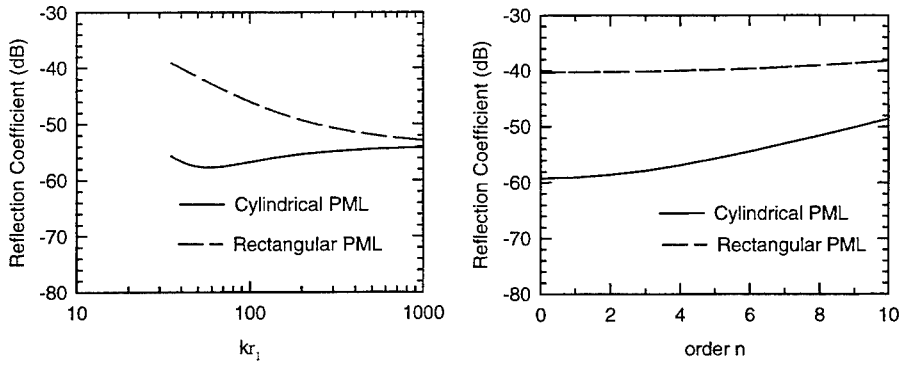

Figure 6 Reflection coefficient of a 10 cell, tapered Cylindrical PML.

References

[1] J. P. Berenger, "A Perfectly Matched Layer for the Absorption of Electromagnetic Waves," *Journal of Computational Physics*, Oct. 1994.

[2] Z. S. Sacks, D. M. Kingsland, R. Lee, and J. F. Lee, "A Perfectly Matched Anisotropic Absorber for Use as an Absorbing Boundary Condition," *IEEE Trans. Antennas Propagation*, vol. 43, pp. 1460-1463, Dec. 1995.

[3] S. D. Gedney, "An Anisotropic Perfectly Matched Layer Absorbing Medium for the Truncation of FDTD Lattices,", *IEEE Trans. Antennas Propagation*, vol. 43, pp. 1630-1639, Dec. 1996.

[4] W. C. Chew and W. H. Weedon, "A 3-D Perfectly Matched Medium From Modified Maxwell's Equations with Stretched Coordinates," *Microwave Opt. Tech. Lett.*, vol. 7, pp. 599-604, Sept. 1994.

[5] J. G. Maloney and M. P. Kesler, Proceedings of USNC/URSI Meeting, p. 365, Baltimore, MD., July 1996.

Complex Coordinate System as a Generalized Absorbing Boundary Condition †

W.C. Chew, J.M. Jin, and E. Michielssen

Center for Computational Electromagnetics
Electromagnetics Laboratory
Department of Electrical and Computer Engineering
University of Illinois
Urbana, IL 61801

Abstract

By a change of variables, we show that Maxwell's equations for PML media reduce to ordinary Maxwell's equations but with complex coordinate systems. Many closed form solutions for Maxwell's equations map to corresponding closed form solutions in complex coordinate systems. Numerical simulations with the closed form solutions show that metallic boxes lined with PML media are highly absorptive lending a better insight into the absorptive properties of PML media. More importantly, the complex coordinate system method can be easily generalized to non-Cartesian coordinate systems, providing absorbing boundary conditions in these coordinate systems.

1. Introduction

The perfectly matched layer (PML) as a material absorbing boundary condition was first proposed by Berenger [1]. Later, Katz et al [2] extended it to three dimensions, while Chew and Weedon [3] proposed a coordinate stretching viewpoint. An anisotropic media interpretation has also been proposed by Zack et al [4]. Due to its efficacy as a material absorbing boundary condition, it has been fervently studied by many workers for numerical simulations of PDE's [5-13].

In this paper, we expand on the coordinate stretching viewpoint, and introduce a change of variables to transform Maxwell's equations in PML media into ordinary-looking Maxwell's equations in a complex coordinate system. As a result, many closed form solutions that have already existed can be easily mapped into closed form solutions in these complex coordinate systems. Moreover, the method can be easily generalize to non-Cartesian coordinate systems.

---

† This work was supported by AFOSR under MURI grant F49620-96-1-0025, ONR under grant N00014-95-1-0872, and NSF under grant NSF ECS93-02145. File: aces.tex, Date: December 29, 1996.

2. Complex Coordinate System

Maxwell's equations in a stretched coordinate system are given by [3]

$$\nabla_\sigma \times \mathbf{E} = i\omega\mu\mathbf{H}, \tag{1}$$

$$\nabla_\sigma \times \mathbf{H} = -i\omega\epsilon\mathbf{E}, \tag{2}$$

$$\nabla_\sigma \cdot \epsilon\mathbf{E} = 0, \tag{3}$$

$$\nabla_\sigma \cdot \mu\mathbf{H} = 0, \tag{4}$$

where

$$\nabla_\sigma = \hat{x}\frac{1}{s_x}\frac{\partial}{\partial x} + \hat{y}\frac{1}{s_y}\frac{\partial}{\partial y} + \hat{z}\frac{1}{s_z}\frac{\partial}{\partial z}. \tag{5}$$

In the above, $s_i, i = x, y, z$ are coordinate stretching variables. When s_i's, where $i = x, y, z$, are functions of i only, then (3) and (4) are derivable from (1) and (2).

With the following change of variables,

$$\tilde{x} = \int_0^x s_x(x')\,dx', \tag{6a}$$

$$\tilde{y} = \int_0^y s_y(y')\,dy', \tag{6b}$$

$$\tilde{z} = \int_0^z s_z(z')\,dz', \tag{6c}$$

the ∇_σ operator becomes

$$\tilde{\nabla} = \hat{x}\frac{\partial}{\partial\tilde{x}} + \hat{y}\frac{\partial}{\partial\tilde{y}} + \hat{z}\frac{\partial}{\partial\tilde{z}}, \tag{7}$$

because

$$\frac{\partial}{\partial\tilde{x}} = \frac{1}{s_x}\frac{\partial}{\partial x}, \quad \frac{\partial}{\partial\tilde{y}} = \frac{1}{s_y}\frac{\partial}{\partial y}, \quad \frac{\partial}{\partial\tilde{z}} = \frac{1}{s_z}\frac{\partial}{\partial z}. \tag{8}$$

In this case, Equations (1) to (4) just become ordinary looking Maxwell's equations, except that $\tilde{x}$, $\tilde{y}$, and $\tilde{z}$ can be complex valued as well. As a result, many closed form solutions can be obtained for PML media using the mapping provided by (6a) to (6c).

When $\tilde{x}$, $\tilde{y}$, and $\tilde{z}$ are complex, the wave that travels through the complex coordinates is attenuated, but not reflected. More importantly, the complex coordinate system for Maxwell's equations can be written in any coordinate system with complex variables as the coordinate variables. We will illustrate the solutions in the complex Cartesian, cylindrical, and spherical coordinates.

3. Cartesian Coordinates

We will solve for the closed form solution of a line source inside a metallic box of width a, and truncated in the vertical direction at $y = b$. The box is filled with two half spaces with different wave numbers k_1 and k_2, and the source is located at (x', y'), with a dielectric interface at $y = h$. The box is assumed to be infinitely extended in the negative y direction. The solution is given by [for detail of the solution technique, see 14]

$$\psi(x, y) = -\sum_{n=0}^{\infty} X_n(x)X_n(x')Y_n(y, y') \tag{9a}$$

for $-\frac{a}{2} < x < \frac{a}{2}$, $y < b$, where

$$X_n(x) = \sqrt{\frac{2}{a}}\sin\left[k_{nx}\left(x + \frac{a}{2}\right)\right], \quad -\frac{a}{2} < x < \frac{a}{2}, \tag{9b}$$

$$Y_n(y, y') = \begin{cases} \frac{1}{2i\gamma_1}\left[e^{i\gamma_1|y-y'|} + \tilde{R}_{12}e^{-i\gamma_1(y-h)+i\gamma_1|h-y'|}\right], & y < h, \\ \frac{1}{2i\gamma_1}\tilde{T}_{12}\left[e^{i\gamma_2(y-h)} - e^{-i\gamma_2(y-2b+h)}\right], & b > y > h, \end{cases} \tag{9c}$$

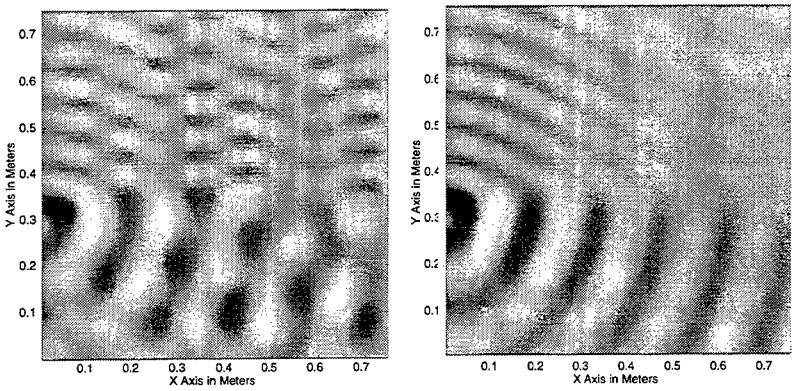

(a) (b)

Figure 1. The solution of a line source in a two-dimensional box with $a = b = 1.5$ m. The frequency is 2.2 GHz, $\epsilon_1 = 1$, $\epsilon_2 = 4$, $\Delta = 0.15$ m, $h = 0.25b$, and $(x', y') = (0, 0.2b)$. (a) $\alpha = 0$ and one can see many reflections from the walls of the box. (b) $\alpha = 2$, and little reflection is observed.

$$k_{nx} = \frac{n\pi}{a}, \quad \gamma_1 = \sqrt{k_1^2 - k_{nx}^2}, \quad \gamma_2 = \sqrt{k_2^2 - k_{nx}^2}. \tag{9d}$$

$\tilde{R}_{12}$ and $\tilde{T}_{12}$ are generalized reflection and transmission coefficients, respectively, at the upper and lower interfaces [14]. To derive the solution in the complex coordinate system, we make use of Equations (6), and define

$$s_x(x) = \begin{cases} 1, & 0 < x < x_m, \\ 1 + i\alpha \left(\frac{x - x_m}{0.5a - x_m} \right)^2, & x_m < x < \frac{a}{2}, \end{cases} \tag{10}$$

where $x_m = 0.5a - \Delta$ and Δ is a small real positive number. In this manner, in accordance to (34), we obtain the mapping

$$\tilde{x} = \begin{cases} x, & 0 < x < x_m, \\ x + i\alpha \frac{(x - x_m)^3}{3(0.5a - x_m)^2}, & x_m < x < \frac{a}{2}. \end{cases} \tag{11}$$

In other words, $\tilde{x}$ assumes complex values in this complex coordinate stretching or map. The mapping is linear for most part except when $x \approx a/2$. (This map is chosen as an illustration, because it resembles the parabolic profile often chosen in PML simulations. Other maps are also possible.) A similar map occurs for $x < 0$. Hence, in the complex coordinate system, the boundary of the box is defined by $\tilde{a}$ which is complex valued. Similar mapping can be defined for the y-axis such that $y \mapsto \tilde{y}$, $b \mapsto \tilde{b}$, where $\tilde{y}$ and $\tilde{b}$ are complex valued.

Figure 1 shows the above solution (a) with, (b) without complex coordinate mapping. In (a) ($\alpha = 0$, one clearly sees the reflection from the walls. (Only the domain $0 < x < 0.5a$ and $0 < y < 0.5b$ is plotted.) In case (b) ($\alpha = 2$), the reflection from the wall is greatly diminished. In this case, as shown by Equation (11), the boundary of the box is located in a complex space. This result explains why PML remains highly absorptive (a) when a dielectric interface extends into the PML media, and (b) at the corner region of a simulation box laced with PML.

4. Cylindrical Coordinates

The solution of a line source in a cylinder with a perfectly conducting wall is [14]

$$\psi(\rho,\phi) = \frac{i}{4}H_0^{(1)}(k|\boldsymbol{\rho}-\boldsymbol{\rho}'|) - \frac{i}{4}\sum_{n=-\infty}^{\infty} J_n(k\rho)\frac{J_n(k\rho')H_n^{(1)}(ka)}{J_n(ka)}e^{in(\phi-\phi')}. \tag{12}$$

We can define a map

$$\tilde{\rho} = \begin{cases} \rho, & 0<\rho<\rho_m, \\ \rho + i\alpha\frac{(\rho-\rho_m)^3}{3(a-\rho_m)^2}, & \rho_m<\rho<a, \end{cases} \tag{13}$$

where $\rho_m = a - \Delta$. Figure 2 shows the calculation of the above series summation formula for different values of α. When $\alpha > 0$ (case (b)), complex coordinate mapping occurs near the wall according to Equation (13) and reflection is diminished.

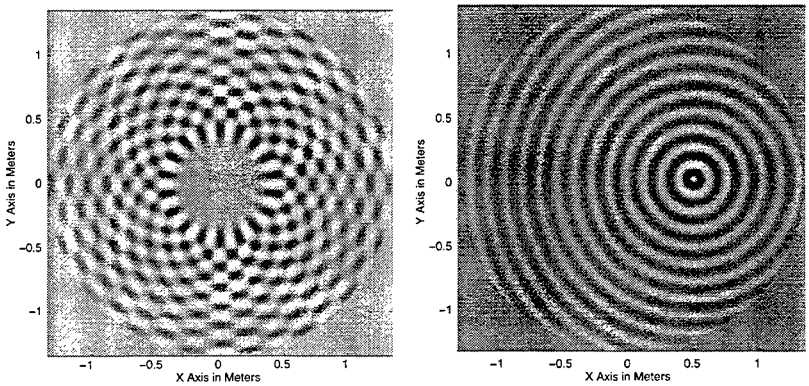

Figure 2. The solution of a line source in a circular cylinder of radius 1.5 m where $(x', y') = (0.5, 0.0)$ m. The frequency is 2.2 GHz, and $\Delta = 0.15$ m. (a) $\alpha = 0$, and one can see many reflections from the wall of the cylinder. (b) $\alpha = 2$, and one sees little reflections.

5. Spherical Coordinates

The solution of a point source in a sphere with a homogeneous Direchlet boundary condition is [14]

$$\psi(\mathbf{r}) = \frac{e^{ik|\mathbf{r}-\mathbf{r}'|}}{4\pi|\mathbf{r}-\mathbf{r}'|} - ik\sum_{n=0}^{\infty}\sum_{m=-n}^{n} j_n(kr)\,Y_{nm}(\theta,\phi)\,Y_{nm}^*(\theta',\phi')\,\frac{j_n(kr')h_n^{(1)}(ka)}{j_n(ka)}, \tag{14}$$

where

$$Y_{nm}(\theta,\phi) = \sqrt{\frac{(n-m)!}{(n+m)!}\frac{2n+1}{4\pi}}\,P_n^m(\cos\theta)e^{im\phi}. \tag{15}$$

The corresponding complex map is

$$\tilde{r} = \begin{cases} r, & 0 < r < r_m, \\ r + i\alpha \frac{(r-r_m)^3}{3(a-r_m)^2}, & r_m < r < a, \end{cases} \tag{16}$$

where $r_m = a - \Delta$. Figure 3 shows the calculation of the above series summation formula. When $\alpha > 0$ (case (b)), complex coordinate stretching occurs near the wall according to Equation (16) and little reflection is observed.

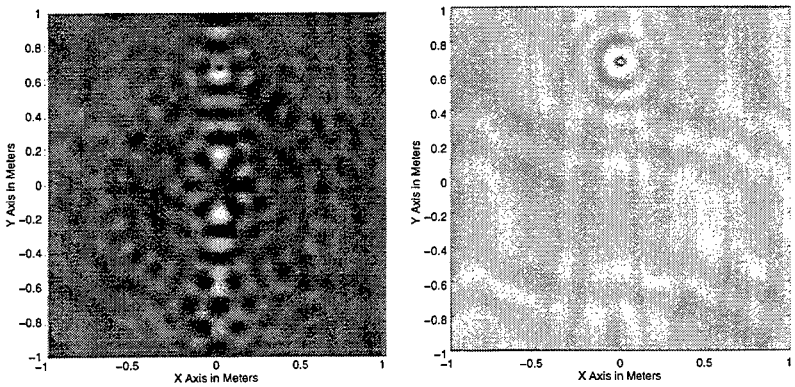

(a) (b)

Figure 3. The solution of a point source in a sphere of radius 1.0 *m with* $(x', y') = (0.0, 0.75)$ *m. The frequency is* 2.2 *GHz, and* $\Delta = 0.15$ *m. (a)* $\alpha = 0$*, and one can see much reflections from the wall of the sphere. (b)* $\alpha = 2$*, and little reflection is observed.*

6. Conclusions

We have demonstrated that PML in Cartesian coordinates is equivalent to solving the wave equation or Maxwell's equations in a complex coordinate system. Therefore, closed form solutions that exist in the real coordinate system map to solutions in the complex coordinate system. In the complex coordinate system, the boundaries exist in a complex space, providing absorbing boundary conditions. Hence, this transformation provides a new view of PML in the Cartesian coordinates, clearly showing that a mapping to a complex coordinate system does not induce reflections, explaining why PML works near the corner of a simulation region, and when a dielectric interface, or a metallic surface, extends to the edge of a simulation region.

The idea of a complex coordinate system can be further generalized to other curvilinear coordinate system. We have demonstrated the solutions and their absorbing boundary conditions in cylindrical as well as spherical coordinates.

References

[1] J. P. Berenger, "A perfectly matched layer for the absorption of electromagnetic waves," *J. Comp. Phys.*, no. 114, pp. 185-200, 1994.

[2] D. S. Katz, E. T. Thiele, and A. Taflove, "Validation and extension to three dimensions of the Berenger PML absorbing boundary condition for FD-TD meshes," *IEEE Microwave Guided Wave Lett.*, no. 4, pp. 268-270, 1994.

[3] W. C. Chew and W. H. Weedon, "A 3D perfectly matched medium from modified Maxwell's equations with stretched coordinates," *Microwave Opt. Tech. Lett.*, no. 7, pp. 599-604, 1994.

[4] Z. S. Sacks, D. M. Kingsland, R. Lee, and J.-F. Lee, "A perfectly matched anisotropic absorber for use as an absorbing boundary condition," *IEEE Trans. Antennas Propag.*, vol. 43, no. 12, pp. 1460-1463, 1995.

[5] E. A. Navarro, C. Wu, P. Y. Chung, and J. Litva, "Application of PML superabsorbing boundary condition to non-orthogonal FDTD method," *Electronics Lett.*, **30**, 20, pp. 1654-1656, 1994.

[6] R. Mittra and Ü. Pekel, "A new look at the perfectly matched layer (PML) concept for the reflectionless absorption of electromagnetic waves," *IEEE Micro. Guided Wave Lett.*, **5**, 3, pp. 84-86, 1995.

[7] W. C. Chew, W. H. Weedon, and A. Sezginer, "A 3-D perfectly matched medium by coordinate stretching and its absorption of static fields," *ACES Digest*, Monterey, CA, March, 1995.

[8] M. Gribbons, S. K. Lee, and A. C. Cangellaris, "Modification of Berenger's perfectly matched layer for the absorption of electromagnetic waves in layered media," *Proc. 11th Ann. Rev. of Progress in ACES,* Monterey, CA, March 20-25, pp. 498-503, 1995.

[9] Z.M. Liu, A.S. Mohan, T. Aubrey, and W.R. Belcher, "Techniques for implementation of FDTD method on a CM-5 parallel computer," *IEEE Antennas Propagat. Mag.*, vol. 37, no. 5, pp. 64-71, October 1995.

[10] Z. Wu and J. Fang, "High performance PML algorithms," *IEEE Microwave Guided Wave Lett.*, vol. 6, no. 9, pp. 335-337, September 1996.

[11] W.V. Andrew, C.A. Balanis, and P.A. Tirkas, "A comparison of the Berenger perfectly matched layer and the Lindman higher-order ABC's for the FDTD method," *IEEE Microwave Guided Wave Lett.*, vol. 5, pp. 192-194, June 1995.

[12] J.R. Wait, "On the PML concept: a view from outside," *IEEE Antennas Propagat. Mag.*, vol. 38, no. 2, pp. 48-51, April 1996.

[13] W. C. Chew and J. M. Jin, *Special Issue: Absorbing Boundary Condition (ABC), Electromagnetics,* vol. 16, no. 4, July-August, 1996.

[14] W. C. Chew, *Waves and Fields in Inhomogeneous Media.* Van Nostrand, New York, 1990 (reprinted by IEEE Press, 1995).

Using PML in 3D FEM Formulations for Electromagnetic Field Problems

Jin-Fa Lee
ECE Dept., WPI
100 Institute Road
Worcester, MA 01609
jinlee@ece.wpi.edu
(508)831-5778

R. Dyczij-Edlinger and Guanghua Peng
Motorola Corp., System Technologies
Motorola CCRL, IL02-EA901
1301 East Algonquin Road
Schaumburg, IL 60796

Currently, the research in using PML as an effective mesh truncation scheme has been very active, particularly in the FDTD community. The use of PML in frequency domain FEM computations, although not as popular, is also attracting interest among the CEM community as well. The results to date indicate that PMLs, specifically the coordinate stretching PML (Chew and Weedon) and the anisotropic PML (Sack etc.), work well in terms of accuracy. However, something bad does happen when using PML as a mesh truncation scheme in 3D FEM computations. That is the extremely slow convergence in the iterative solvers, such as the Preconditioned Conjugate Gradient (PCCG) method. This leads to a legitimate question: Is PML a good choice for mesh truncation in FEM computations?

The aim of this paper is not to answer this question. To answer it will require overall comparisons among various alternatives on accuracy, easy to use, versatility, and automation, etc. Therefore, our presentation shall concentrate on the performances of : (a) various FEM formulations in conjunction with PMLs (FEM+PML); and, (b) different preconditioners in PCCG algorithms for FEM+PML matrices. It will be shown that a simple switching to AV formulation, four-potential formulation, the convergence of FEM+PML will be restored to the FEM+ABC in the conventional E field formulation. Then, the presentation will continue to investigate the development of specific PML preconditioners to further improve the matrix solution process.

The Design of Maxwellian Absorbing Materials for Numerical Absorbing Boundary Conditions

Richard W. Ziolkowski
Electromagnetics Laboratory, Department of Electrical and Computer Engineering
The University of Arizona, Tucson, AZ 85721-0104

A time-derivative Lorentz material model is introduced for the polarization and magnetization fields in an uniaxial medium to generate a Maxwellian absorbing boundary condition for the finite-difference time-domain method. This Maxwellian ABC is shown to have performance characteristics that are comparable to the non-Maxwellian Berenger PML ABC.

1. INTRODUCTION

Electromagnetic absorbers have many practical usages. They have attracted much attention recently in the computational electromagnetics community with the desire to truncate the simulation domain in any finite difference or finite element approach. Many absorbing boundary conditions (ABCs) have been developed to achieve this truncation. Like with any real-life absorber, the perfect ABC would absorb perfectly any frequency of electromagnetic radiation incident upon it from any angle of incidence. The Berenger perfectly matched layer (PML) [1] ABC comes quite close to this goal. However, a major issue with the Berenger PML ABC is that it requires a non-Maxwellian implementation through the field equation splitting. This is not a serious drawback numerically, but it does mean that a PML region can not be realized physically.

A Maxwellian material interpretation of the Berenger perfectly matched layer (PML) has been developed [2] using polarization and magnetization fields. The PML material is found to be a passive lossy electric and magnetic medium with particular conductivity and Debye dispersion characteristics. A potentially realizable, Maxwellian material that has those perfect absorption properties has also been constructed with these concepts [3] and is discussed in Section 2. The numerical implementation of this time-derivative Lorentz material (TD-LM) absorber has been extended for use as a numerical ABC as described in Section 3. For broad bandwidth pulsed fields this ABC, like the non-Maxwellian PML, has absorption characteristics in the 90 dB range for large angles of incidence.

2. PERFECT ABSORBER

Following the development of Sachs, et al. [4], a broad bandwidth absorbing material that is Maxwellian is developed as follows. Consider a semi-infinite uniaxial medium whose normal is assumed (with no lack of generality) to be in the z-direction. The permittivity and permeability tensors of this medium in the frequency domain are assumed have the form

$$\frac{\overline{\overline{\epsilon}}(\omega)}{\epsilon_0} = \frac{\overline{\overline{\mu}}(\omega)}{\mu_0} = \begin{pmatrix} a_\omega & 0 & 0 \\ 0 & a_\omega & 0 \\ 0 & 0 & c_\omega \end{pmatrix} . \tag{1}$$

The permittivity and permeability components a_ω and c_ω are constructed from the corresponding frequency domain electric and magnetic susceptibilities χ_ω so that, respectively, $a_\omega = 1 + \chi_\omega$ and $c_\omega =$

$a_\omega^{-1} = (1+\chi_\omega)^{-1} = 1 - \chi_\omega\,(1+\chi_\omega)^{-1}$. An electromagnetic plane wave [$\exp(-i\omega t)$ convention assumed throughout] polarized, for example, in the xz-plane and incident on this half-space will experience no reflection from this medium for any non-grazing angle of incidence. The transmitted plane wave will lose energy to this medium if additionally $\mathrm{Im}(\chi_\omega) > 0$.

To construct an absorber that deals effectively with ultrafast pulses, one needs to introduce a model for the susceptibility $\chi_\omega$that has a large bandwidth. One can introduce a generalization of the Lorentz model for the polarization and magnetization fields that includes the time derivative of the driving fields as a driving term[3-5]. For instance, the x-directed polarization field, in such a material would be assumed to satisfy a linear time-derivative Lorentz material (TD-LM) model of the form

$$\frac{\partial^2}{\partial t^2}\,P_x + \Gamma\,\frac{\partial}{\partial t}\,P_x + \omega_0^2\,P_x = \epsilon_0\,\omega_0^2\left[\chi_\alpha\,E_x + \frac{\chi_\beta}{\omega_0}\,\frac{\partial}{\partial t}\,E_x\right], \tag{2}$$

where ω_0 is the resonance frequency and Γ is the width of that resonance. This TD-LM model leads to the following frequency-domain electric susceptibility

$$\chi_\omega^{TD} \equiv \frac{P_{\omega,x}\,(\vec{r})}{\epsilon_0\;E_{\omega,x}\,(\vec{r})} = \frac{\omega_0^2\,[\,\chi_\alpha - i\,(\omega/\omega_0)\,\chi_\beta\,]}{\omega_0^2 - \omega^2 - i\,\Gamma\,\omega}\,. \tag{3}$$

Choosing $\chi_\omega = \chi_\omega^{TD}$, one can make the uniaxial medium defined by (1) a passive absorber if $\Gamma\,\chi_\alpha > \omega_0\,\chi_\beta\,[1-(\omega/\omega_0)^2]$. Thus, a broad bandwidth absorber is realized[20] if the uniaxial TD-LM is designed so that $\chi_\alpha, \chi_\beta > 0$ and $\omega \gg \omega_0 \gg \Gamma$. This results in the susceptibility $\chi_\omega \cong -(\omega_0/\omega)^2\;\chi_\alpha + i\,\omega_0\,\chi_\beta/\omega$. A unit amplitude plane wave propagating in this material, for instance, along the z-axis will have the form: $\exp(i\,k_z\,z) = \exp[i\,(1+\chi_\omega)\,(\omega/c)\,z] = \exp\{i\,[1-(\omega_0/\omega)^2\,\chi_\alpha]\,(\omega/c)\,z\}\,\exp[-(\omega_0\,\chi_\beta)z/c]$. Clearly, the medium will be very lossy if $\omega_0\,\chi_\beta \gg \omega$ in the frequency regime of interest. It will also be effectively dispersionless if in addition $\chi_\alpha \ll 1$.

3. Constructing the Maxwellian ABC

When a TD-LM-slab having its normal in the $\hat{z}$ direction is used as a numerical absorber, it has been shown that the limits $\chi_\alpha \ll 1$, $\Gamma \ll \omega_0 \ll \omega$, and $\omega_0\,\chi_\beta \approx 10\,\omega$, are quite effective. In this limit the material quantities

$$a_\omega - 1 = \chi_\omega \cong \frac{\zeta}{-i\,\omega} \tag{5a}$$

$$c_\omega - 1 = -\frac{\chi_\omega}{1+\chi_\omega} = -\frac{\omega_0^2\,\chi_\alpha - i\,\omega\,\omega_0\,\chi_\beta}{-\omega^2 - i\,\omega\,[\Gamma + \omega_0\,\chi_\beta] + \omega_0^2\,(1+\chi_\alpha)} \cong \frac{i\,\omega\,\zeta}{-\omega^2 - i\,\omega\,\zeta}\,. \tag{5b}$$

where we have set $\omega_0\,\chi_\beta = \zeta$. In the time domain these expressions lead immediately to the desired polarization and magnetization field equations

$$\partial_t\,P_x = \zeta\,\epsilon_0\,E_x \tag{6a}$$

$$\partial_t\,M_y = \zeta\,H_y \tag{6b}$$

$$\partial_t^2\,P_z + \zeta\,\partial_t\,P_z = -\zeta\,\epsilon_0\,\partial_t\,E_z\,. \tag{6c}$$

The transverse polarization and magnetization terms insert nicely into Maxwell's equations since they have conductivity current forms. These currents arise directly from the coupling of their corresponding

field components to the material. On the other hand, to handle the longitudinal term we introduce the polarization current term $\partial_t P_z = J_z$ and make use of the fact that the time derivative of the displacement field component $D_z = \epsilon_0 E_z + P_z$ is related to the magnetic field through the Maxwell equations to convert (6c) into the form $\partial_t J_z = -\zeta \partial_x H_y$. This means that time variations in the longitudinal component of the polarization current results from the circulation of the magnetic field, i.e., the longitudinal electric polarization current is driven by the magnetic field rather than the electric field and ζ is the coupling coefficient. The corresponding electric and magnetic field equations, which govern the behavior in the uniaxial TD-LM absorber specified by Eqs. (1)-(3), are then

$$\partial_t E_x + \zeta E_x = -\frac{1}{\epsilon_0} \partial_z H_y \tag{7a}$$

$$\partial_t J_z = -\zeta \partial_x H_y \tag{7b}$$

$$\partial_t E_z = \frac{1}{\epsilon_0} \partial_x H_y - \frac{1}{\epsilon_0} J_z \tag{7c}$$

$$\partial_t H_y + \zeta H_y = -\frac{1}{\mu_0} (\partial_z E_x - \partial_x E_z) \tag{7d}$$

Clearly one observes from (7a) and (7d) that there is exponential decay imposed on the transverse field components when $\zeta > 0$. The longitudinal field component experiences this exponential decay because it is driven by terms which depend on the transverse magnetic field component H_y.

Similar equations occur with a slab having an $\hat{x}$ directed normal. If we set $\omega \chi_\beta = \xi$ along that normal, we are immediately led to the field and current equations:

$$\partial_t E_z + \xi E_z = \frac{1}{\epsilon_0} \partial_x H_y \tag{8a}$$

$$\partial_t J_x = \xi \partial_z H_y \tag{8b}$$

$$\partial_t E_x = -\frac{1}{\epsilon_0} \partial_z H_y - \frac{1}{\epsilon_0} J_x \tag{8c}$$

$$\partial_t H_y + \xi H_y = -\frac{1}{\mu_0} (\partial_z E_x - \partial_x E_z) \tag{8d}$$

The remaining issue is what to do with a corner region where there is no well-defined normal. It is straightforward to show with a plane wave analysis that in order to maintain free-space impedances at all interfaces and to maintain straight-line propagation in each medium through the interfaces, the material constants in a corner region must satisfy $\overline{\overline{\Lambda}}_{ZX} = \overline{\overline{\Lambda}}_Z \times \overline{\overline{\Lambda}}_X$. In the time domain this means we are multiplying together the operators corresponding to the separate regions. This product rule means that in the frequency domain

$$a_\omega^{ZX} = \frac{a_\omega^Z}{a_\omega^X} \tag{9a}$$

$$b_\omega^{ZX} = a_\omega^Z \times a_\omega^X \tag{9b}$$

$$c_\omega^{ZX} = \frac{a_\omega^X}{a_\omega^Z} , \tag{9c}$$

where we write $a_\omega^Z = 1+\chi_{\omega,z}$ and $a_\omega^X = 1+\chi_{\omega,x}$ to distinguish the parameters and normals in the respective regions. The magnetization equation is readily obtained since (9b) means $\chi_{yy} = \chi_{\omega,x} + \chi_{\omega,z} + \chi_{\omega,x} \times \chi_{\omega,z}$. Equations (9) lead to the following possible choice for the time domain relations in the corner

$$\partial_t J_x = +\xi\, \partial_z\, H_y \tag{10a}$$

$$\partial_t\, E_x + \zeta\, E_x = -\frac{1}{\epsilon_0}\, \partial_z\, H_y - \frac{1}{\epsilon_0}\, J_x \tag{10b}$$

$$\partial_t J_z = -\zeta\, \partial_x\, H_y \tag{10c}$$

$$\partial_t\, E_z + \xi\, E_z = \frac{1}{\epsilon_0}\, \partial_x\, H_y - \frac{1}{\epsilon_0}\, J_z \tag{10d}$$

$$\partial_t\, K_y = [\xi\, \zeta]\, H_y \tag{10e}$$

$$\partial_t\, H_y + [\xi + \zeta]\, H_y = -\frac{1}{\mu_0}\, (\, \partial_z\, E_x - \partial_x\, E_z\,) - K_y \tag{10f}$$

The resulting TD-LM ABC has been tested and absorption levels compete nicely with those obtained with the now standard PML ABC.

This work was supported in part by the Office of Naval Research under grant number N0014-95-1-0636 and by the Air Force Office of Scientific Research, Air Force Materiel Command, USAF, under grant number F49620-96-1-0039. The U.S. Government is authorized to reproduce and distribute reprints for Governmental purposes notwithstanding any copyright notation thereon.

REFERENCES

1. J.-P. Berenger, "A perfectly matched layer for the absorption of electromagnetic waves," *J. Comp. Phys.*, vol. 114, pp. 185-200, October 1994.

2. R. W. Ziolkowski, "The design of Maxwellian absorbers for numerical boundary conditions and for practical applications using engineered artificial materials," Proceedings of the Joint IEEE/AP-S and URSI Symposia, Baltimore, Maryland, July 1996.

3. Z. S. Sacks, D. M. Kingsland, R. Lee, and J.-F. Lee, "A perfectly matched anisotropic absorber for use as an absorbing boundary condition," *IEEE Transactions on Antennas and Propagation*, vol. 43(12), pp. 1460-1463, December 1995.

4. R. W. Ziolkowski, "The design of Maxwellian absorbers for numerical boundary conditions and for practical applications using engineered artificial materials," to appear in *IEEE Trans. Antennas and Propagation*, April 1997.

5. R. W. Ziolkowski, "Time-Derivative Lorentz-Materials and their utilization as electromagnetic absorbers," to appear in *Phys. Rev. A*, 1997.

A New Artificial Medium Based on Unsplit Anisotropic PML for Mesh Truncation in FDTD Analysis

[1] Yinchao Chen, [1] Ming-sze Tong, [2] Mustafa Kuzuoglu and [3] Raj Mittra

[1] Department of Electronic Engineering
Hong Kong Polytechnic University, Hong Kong

[2] Department of Electrical Engineering
Middle East Technical University, Ankara, Turkey

[3] Applied Research and Electromagnetic Communication Laboratories
Pennsylvania State University, State College, PA, USA

Abstract - In this paper we discuss the adaptation of an unsplit anisotropic perfectly matched layer (PML), previously utilized in the context of the finite element analysis, to applications in the finite difference time domain (FDTD) algorithm. The unsplit anisotropic PML is easy to implement in the existing FDTD codes, and is well-suited for truncating inhomogeneous and layered media without special treatment required in the conventional PML approach. A further advantage of the present method is that it improves the performance over the conventional PML at lower frequencies. The application of the unsplit anisotropic PML/FDTD method is illustrated by considering the problems of TEM wave propagation and transmission in an open microstrip line.

I. INTRODUCTION

The perfectly matched layer (PML), first introduced by Berenger [1], has been found to be very effective for truncating the mesh in the finite difference time domain (FDTD) analysis. In the original PML approach, each of the Maxwell's curl equations for the electric and magnetic fields are split into two, leading to twelve equations altogether. Sacks et al.[2] have introduced a different formulation in the frequency domain and have demonstrated that a medium with certain uniaxial anisotropic properties can also act as a perfectly matched layer. Furthermore, the use of such a layer requires no alteration of the conventional Maxwell's equations and, specifically, it does not call for a splitting of these equations. Recently, Kuzuogolu and Mittra [3] have investigated the causal properties of the PML-type anisotropic media and have proposed a medium with certain constitutive parameters that exhibits improved low frequency performance in the finite element analysis.

In this paper we extend the unsplit anisotropic PML approach and show that the same concept can be successfully incorporated into the finite difference time domain (FDTD) analysis for mesh truncation. The unsplit anisotropic PML is straightforward to implement in the existing FDTD codes, and is well-suited for truncating inhomogeneous as well as layered media without the special treatments required in the conventional PML approach. A further advantage of the present approach is its improved performance at lower frequencies. The application of the anisotropic PML/FDTD method is illustrated by considering the problem of a one-dimensional TEM wave propagation and transmission in an open microstrip line.

II. CONSTRUCTION OF ARTIFICIAL UNSPLIT ANISOTROPIC PML

IIa. Time-Domain Constitutive Relations in the Unsplit Anisotropic PML

It has been shown in [2, 3], that the relative permittivity and permeability of the anisotropic PML medium share the same constitutive relation, which is a diagonal tensor in the frequency domain with a general form

$$[\Lambda(\omega)]=\begin{bmatrix}\Lambda_{xx}(\omega) & 0 & 0\\ 0 & \Lambda_{yy}(\omega) & 0\\ 0 & 0 & \Lambda_{zz}(\omega)\end{bmatrix}, \tag{1}$$

where the elements, $\Lambda_{ii}(\omega)$'s ($ii = xx, yy, \text{or } zz$) of (1) are complex parameters. They must be chosen such that the PML medium is completely non-reflective irrespective of the incident angle or frequency, and the transmitted wave is rapidly attenuated along the direction normal to the PML interface. Following [2, 3], we choose $\Lambda_{ii}(\omega)$ to equal either $a(\omega)$ or $1/a(\omega)$, and, for a wideband performance, we assign $a(\omega)$ to have the form

$$a(\omega) = 1+\frac{\tau}{1+j\omega\alpha} \tag{2}$$

where α and τ are the controlling parameters that determine the rate of decay of the wave along the normal direction in the PML region. Note that the choice of $a(\omega)$ in (3) is different from the one given in [2], though it is similar to one proposed in [3] instead. The above choice has been dictated by our desire to achieve improved low frequency performance, and the results presented later in Section III will serve to validate this.

By using the phasor relations, we can transform the frequency-domain constitutive relations into those in the corresponding time domain. This leads to the relations:

$$\begin{bmatrix}B_i-\mu_0 H_i\\ D_i-\varepsilon_0 E_i\end{bmatrix}+\alpha\frac{\partial}{\partial t}\begin{bmatrix}B_i-\mu_0 H_i\\ D_i-\varepsilon_0 E_i\end{bmatrix}=\begin{bmatrix}\mu_0\tau H_i\\ \varepsilon_0\tau E_i\end{bmatrix} \tag{3}$$

for the terms associated with $\Lambda_{ii}(\omega)=a(\omega)$, and

$$(1+\tau)\begin{bmatrix}B_i-\mu_0 H_i\\ D_i-\varepsilon_0 E_i\end{bmatrix}+\alpha\frac{\partial}{\partial t}\begin{bmatrix}B_i-\mu_0 H_i\\ D_i-\varepsilon_0 E_i\end{bmatrix}=\begin{bmatrix}-\mu_0\tau H_i\\ -\varepsilon_0\tau E_i\end{bmatrix} \tag{4}$$

for the corresponding ones with $\Lambda_{ii}(\omega)=1/a(\omega)$. The index i in the above equations can be x, y or z.

IIb. Numerical Implementation

We have successfully implemented three different discretization techniques for (3) and (4) to analyze the problem of reflection coefficient from a PML wall. These are: (i) fundamental approach;

(ii) mixed fields approach; and, (iii) exponential time-stepping approach. We have found that, in principle, these three methods are equivalent except for some subtle differences, and we only discuss the fundamental approach here because of space limitations. By discretizing (3) and (4), and using the central finite difference scheme for the time derivative, we obtain

$$\begin{bmatrix} H_i^{n+1/2} \\ E_i^{n+1} \end{bmatrix} = \frac{1-\frac{\Delta t(1+\tau)}{2\alpha}}{1+\frac{\Delta t(1+\tau)}{2\alpha}} \begin{bmatrix} H_i^{n-1/2} \\ E_i^{n} \end{bmatrix} - \frac{\left(1-\frac{\Delta t}{2\alpha}\right)}{\left(1+\frac{\Delta t(1+\tau)}{2\alpha}\right)} \begin{bmatrix} B_i^{n-1/2}/\mu_0 \\ D_i^{n}/\varepsilon_0 \end{bmatrix} + \frac{\left(1+\frac{\Delta t}{2\alpha}\right)}{\left(1+\frac{\Delta t(1+\tau)}{2\alpha}\right)} \begin{bmatrix} B_i^{n+1/2}/\mu_0 \\ D_i^{n+1}/\varepsilon_0 \end{bmatrix} \quad (5)$$

$$\begin{bmatrix} H_i^{n+1/2} \\ E_i^{n+1} \end{bmatrix} = \frac{1-\frac{\Delta t}{2\alpha}}{1+\frac{\Delta t}{2\alpha}} \begin{bmatrix} H_i^{n-1/2} \\ E_i^{n} \end{bmatrix} - \frac{1-\frac{\Delta t(1+\tau)}{2\alpha}}{\left(1+\frac{\Delta t}{2\alpha}\right)} \begin{bmatrix} B_i^{n-1/2}/\mu_0 \\ D_i^{n}/\varepsilon_0 \end{bmatrix} + \frac{1+\frac{\Delta t(1+\tau)}{2\alpha}}{\left(1+\frac{\Delta t}{2\alpha}\right)} \begin{bmatrix} B_i^{n+1/2}/\mu_0 \\ D_i^{n+1}/\varepsilon_0 \end{bmatrix} \quad (6)$$

where the superscript represents the time sample. Note that the spatial index has been suppressed in the above equations because $\vec{D}$ and $\vec{E}$ fields share the same location, as do the $\vec{B}$ and $\vec{H}$ fields. By combining (5) and (6) with the conventional FDTD update algorithm derived from the Maxwell's curl equations (using $\left(\vec{E},\vec{B}\right)$ and $\left(\vec{H},\vec{D}\right)$ pairs) respectively, we can derive a complete FDTD iteration cycle for each time step. We should mention that updating the fields in the PML regions now requires a four-step operation, as opposed to the two-step updating procedure in the conventional FDTD algorithm.

It is useful to point out that the PML-based mesh truncation approach described above is well-suited for inhomogeneous materials of complex nature, for instance those found in MMIC transmission lines and discontinuities. This is because unlike the Berenger-type PML, the method does not require special treatments for such media, and the procedure for truncating the inhomogeneous medium is no different than that employed for free-space.

III. NUMERICAL VALIDATION

To validate the proposed unsplit PML algorithm, we first analyze a one-dimensional TEM wave propagation problem as shown in Fig. 1, where the computation domain is truncated by unsplit anisotropic PML walls at two ends. To examine the frequency response of the PML walls, we choose an excitation function with a wide spectrum spanning a frequency band of as much as 30 *GHz*. After accounting for the speed of wave propagation and the associated time delay, we can separate the incident and reflected waves, and derive the reflection coefficient presented by the PML absorbing boundary condition. As is evident from Fig. 2, the reflection coefficients for the right PML wall, obtained by using 4 or 8 layers of PML, are considerably superior to that of the first order Mur ABC.

Next, we further validate the proposed PML algorithm by analyzing an open microstrip line structure, which can be reduced to an equivalent two-dimensional problem. The geometrical dimensions of the structure are depicted in Fig. 3. The effective dielectric constant $\varepsilon_{eff}(f)$ as well as the characteristic impedance $Z_0(f)$ of the microstrip line are derived by using the FDTD approach with anisotropic PML medium described herein, and the results are plotted in Fig. 4. We note that the anisotropic PML works very well over the entire frequency band of interest, *viz.*, 2 to 200 GHz. Specially, we see noticeable improvement at the lower frequencies, even with only a 4-cell anisotropic PML, over the results derived by using the conventional 3-D PML approach followed in [4].

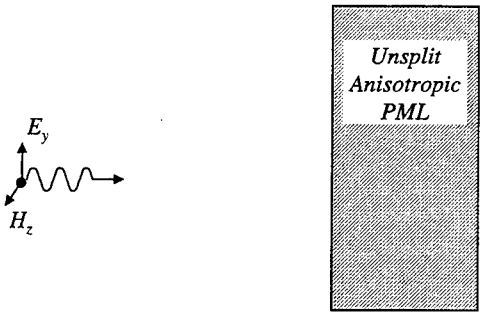

Fig. 1 A wideband *TEM* wave incident upon an unsplit anisotropic PML wall.

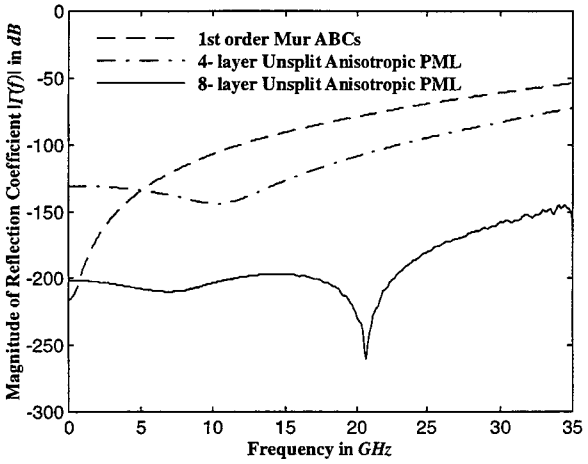

Fig. 2 Frequency dependence of the magnitude of the reflection coefficient $|\Gamma(f)|$ for unsplit anisotropic PMLs.

IV. CONCLUSIONS

In this work an unsplit-field anisotropic PML algorithm has been successfully implemented in the time domain, and has been applied to the problems of TEM wave propagation and simulation of an open microstrip line to illustrate its usefulness for FDTD mesh truncation. The proposed PML algorithm can be conveniently incorporated in the existing FDTD codes, because it does not require special treatments when truncating inhomogeneous and/or layered media. Another desirable feature of this method is that it exhibits improved performance at lower frequencies where the conventional Berenger-type PML begins to deteriorate.

REFERENCES

[1] J. P. Berenger, "A perfectly matched layer for the absorption of electromagnetic waves," *J. Comp. Phys.*, vol. 114, pp. 185-200, May 1994.

[2] Z. S. Sacks, D. M. Kingsland, R. Lee, J.-F. Lee, "A perfectly matched anisotropic absorber for use as an absorbing boundary condition," *IEEE Trans Antennas and Propgat.*, vol. 43, no 12, pp. 1460-1463, Dec. 1995.

[3] M. Kuzuoglu, and R. Mittra, "Frequency dependence of the constitutive parameters of causal perfectly matched anisotropic absorbers," to appear *IEEE Microwave Guided Wave Lett.*.

[4] J.C. Veihl, *Effective Mesh Truncation Techniques for the Solution of Maxwell's Equations using the Finite Difference Time Domain Method*, Ph.D. Dissertation, Department of Electrical Engineering, University of Illinois at Urbana-Champaign, 1996

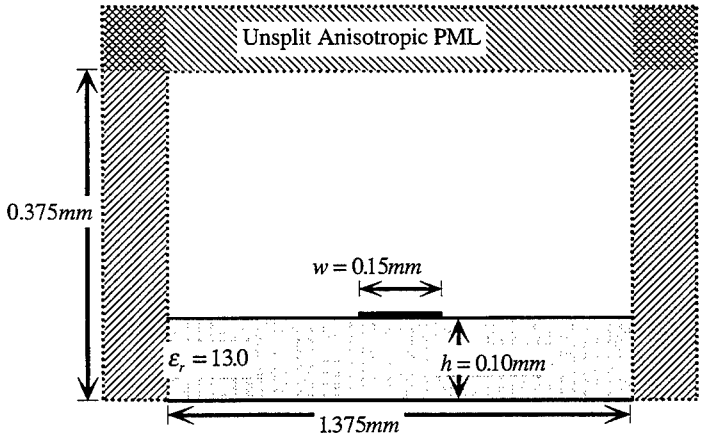

Fig. 3 Cross section of an open single microstrip line surrounded by PMLs.

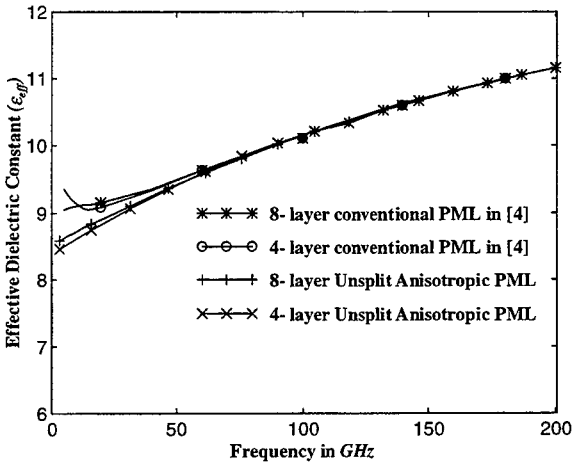

(a)

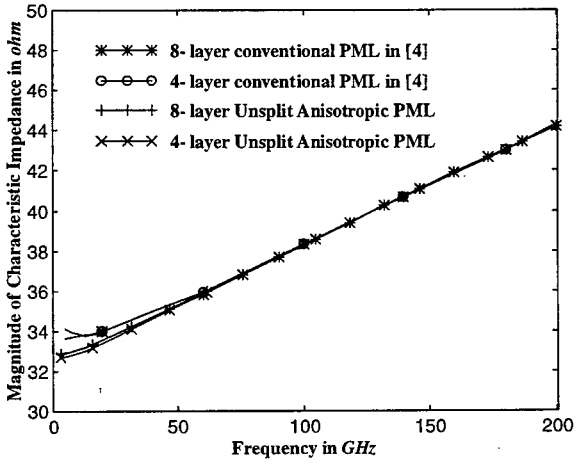

(b)

Fig. 4 Frequency dependence for an open microstrip line. (a) The effective dielectric constant (ε_{eff}); and (b) magnitude of the characteristic impedance (Z_0) in *ohms*.

ON THE USE OF PML ABC'S IN SPECTRAL TIME-DOMAIN SIMULATIONS OF ELECTROMAGNETIC SCATTERING*

B. YANG, D. GOTTLIEB AND J.S. HESTHAVEN†
DIVISION OF APPLIED MATHEMATICS,
BROWN UNIVERSITY, PROVIDENCE, RI 02912

Abstract. We discuss a time-domain spectral multi-domain method for the solution of Maxwell equations. The emphasis is on computation of TM-scattering from two-dimensional cylinders of arbitrary cross-section with the computational domains being constructed using curvilinear body-conforming quadrilaterals.

Besides from providing geometric flexibility, the multi-domain approach also supplies a very natural framework in which to deal with complicated absorbing boundary conditions such as the perfectly matched layer (PML) methods.

We present a detailed comparison between several different implementations, among them several new formulations, of PML methods in spectral methods and include comparisons with results obtained using FD-TD methods and MoM methods. These studies clearly illustrate the algorithmic as well as computational advantages of employing high-order methods coupled with properly constructed PML methods for accurately predicting the scattering by perfectly conducting objects.

1. Introduction. The Finite-Difference-Time-Domain (FD-TD) method [1], so extensively used for computing electromagnetic scattering by general objects, suffers from the requirement of having 10-20 grid points per wavelength to obtain sufficiently accurate solutions of the scattered fields. Indeed, in cases of transient excitation of the scatterer one must often use a significantly denser grid. These requirements inhibit the use of FD-TD methods for accurately computing electromagnetic scattering by electrically large objects and transient phenomena.

On the other hand, it is well known [2] that the Chebyshev spectral method requires approximately π points per wavelength to accurately resolve a wave. Hence, using spectral methods for the solution of scattering problems promises a very significant decrease in the required number of grid points compared to FD-TD methods while maintaining the accuracy in time and space. This again suggests that high-order methods, and in particular spectral methods, are well suited for the simulation of electrically large or transient problems in electromagnetics.

However, traditional spectral methods suffer from having a fixed distribution of grid points, thereby making it difficult to apply such methods for solving problems in complex geometries. Using a multi-domain approach, i.e. splitting the computational domain into several geometrically simple body conforming domains, has proven to be a powerful way of overcoming such restrictions on the applicability of spectral methods (see e.g. [3]). Moreover, this approach promises to allow for an efficient implementation on contemporary parallel computers [4] and relieves much of the computational burden of spectral methods even on serial computers, as one can increase the number of subdomains rather than the number of grid points in each subdomain.

One of the most important, and as yet unsolved, problems in computational electromagnetics is the issue of obtaining solutions of infinite domain problems from finite domain numerical computations. The truncation of the computational domain introduces an artificial boundary and the crucial issue is how to design absorbing boundary conditions (ABC) such that outgoing waves are absorbed without reflections which may otherwise re-enter the domain and falsify the computational results.

A characteristic type ABC, requiring the incoming characteristic variable to vanish at the boundary, has often been used with high order methods. However, as shown in [5], applying a characteristic type boundary condition causes significant reflections at the outer boundary, unless the outer boundary is put very far away from the scatter, i.e. at a distance of 12-20 wavelengths from the scatter, rendering such methods ill-suited for large scale problems. Similar conclusions was found when using a 2nd order one-way wave equation as the boundary conditions [5].

As a very attractive alternative to these simple ABC's, Berenger [6] proposed a perfectly matched layer (PML) method for reflectionless truncation of FD-TD wave simulations, with the property that the non-physical absorbing layer is reflectionless regardless of the angle of incidence and the frequency of the wave. However, it was recently shown [7] that the split-field equations utilized in the PML methods are only weakly well-posed and may be explosively unstable under small perturbations.

The requirement for complex absorbing boundary conditions highlights yet another advantage of the multi-domain approach as we may simply dedicate the outer subdomains to deal with such boundary conditions while

* The first two authors were supported by DARPA/AFOSR grant F49620-96-1-0426. The last author was also supported through DOE grant DE-FG02-95ER25239 and NSF grant ASC-9504002.

† Corresponding Author: *jansh@cfm.brown.edu*

solving Maxwells equations in the remaining, and main, part of the computational domain. In the FD-TD implementation of the rectangular PML method [6], a small amount of numerical reflection at the vacuum-layer interface was observed. However, in a multi-domain approach, derivatives are never computed across the vacuum-layer interface, thereby reducing the numerical reflections significantly.

The remaining part of this paper is organized as follows. In Sec. 2 we introduce the TM-form of Maxwells equations and the symmetric form of the equations utilized in the actual computations. Section 3 contains a brief discussion of the spectral multi-domain methods and the associated terminology while Sec. 4 is devoted to a presentation of several different PML methods considered in Sec. 5, where we review the computational results. Section 6 contains a few concluding remarks.

2. Maxwell's Equations on Symmetric Form. We consider the two-dimensional transverse magnetic (TM) free space Maxwells equations, given in general curvilinear coordinates, on the form

$$\frac{\partial \hat{q}}{\partial t} = \mathrm{A}_\xi \frac{\partial \hat{q}}{\partial \xi} + \mathrm{A}_\eta \frac{\partial \hat{q}}{\partial \eta} \ , \tag{1}$$

where $\hat{q} = Jq = J(H_x, H_y, E_z)^T$ represents the non-dimensional state vector containing the two transverse components of the magnetic field and the normal component of the electric field, respectively. Rather than using the dimensional magnetic and electric fields, $\tilde{q} = (\tilde{H}_x, \tilde{H}_y, \tilde{E}_z)^T$, we have introduced a normalization as

$$x = \tilde{x}/L \ , \ y = \tilde{y}/L \ , \ t = \tilde{c}\tilde{t}/L \ ,$$

where L represents a scale length and the fields are normalized as

$$H_x = \tilde{H}_x \ , \ H_y = \tilde{H}_y \ , \ E_z = \sqrt{\frac{\varepsilon_0}{\mu_0}}\tilde{E}_z = Z_0^{-1}\tilde{E}_z \ ,$$

where Z_0 represents the free space impedance, ε_0 and μ_0 the free space permitivity and permeability, respectively, while $\tilde{c} = (\sqrt{\varepsilon_0\mu_0})^{-1}$ refers to the free space speed of light.

With this normalization, the two matrices in Eq.(1) becomes

$$\mathrm{A}_\xi = \begin{bmatrix} 0 & 0 & -\xi_y \\ 0 & 0 & \xi_x \\ -\xi_y & \xi_x & 0 \end{bmatrix} \ , \ \mathrm{A}_\eta = \begin{bmatrix} 0 & 0 & -\eta_y \\ 0 & 0 & \eta_x \\ -\eta_y & \eta_x & 0 \end{bmatrix} \ . \tag{2}$$

Here, and in Eq.(1), we have introduced the general curvilinear coordinates, (ξ, η), as well as the Cartesian coordinates, (x, y), related through the transformation Jacobian, $J = x_\xi y_\eta - x_\eta y_\xi$.

The formulation of Maxwell's equations as given through Eqs.(1)-(2), are well suited for computation as well as analysis. In particular, we observe that the matrices in Eq.(2) are both symmetric and, since the actual values of ε_0 and μ_0 are hidden in the normalization, we need not concern ourselves with these constants during the computation.

The two matrices, A_ξ and A_η, are both symmetrizable under the similarity transformations,

$$\Lambda_\xi = \mathrm{S}_\xi^T \mathrm{A}_\xi \mathrm{S}_\xi = \begin{bmatrix} 0 & 0 & 0 \\ 0 & -|\nabla\xi|^2 & 0 \\ 0 & 0 & |\nabla\xi|^2 \end{bmatrix} \ , \ \Lambda_\eta = \mathrm{S}_\eta^T \mathrm{A}_\eta \mathrm{S}_\eta = \begin{bmatrix} 0 & 0 & 0 \\ 0 & -|\nabla\eta|^2 & 0 \\ 0 & 0 & |\nabla\eta|^2 \end{bmatrix} \ ,$$

where

$$\mathrm{S}_\xi = \frac{1}{\sqrt{2}} \begin{bmatrix} \sqrt{2}\xi_x & \xi_y & -\xi_y \\ \sqrt{2}\xi_y & -\xi_x & \xi_x \\ 0 & 1 & 1 \end{bmatrix} \ , \ \mathrm{S}_\eta = \frac{1}{\sqrt{2}} \begin{bmatrix} \sqrt{2}\eta_x & \eta_y & -\eta_y \\ \sqrt{2}\eta_y & -\eta_x & \eta_x \\ 0 & 1 & 1 \end{bmatrix} \ , \tag{3}$$

showing that Eq.(1) is symmetric hyperbolic and therefore strongly well-posed. Equation (3) also leads to the definition of the characteristic variables, $\boldsymbol{Q}_\xi = \mathrm{S}_\xi^T \boldsymbol{q}$ and $\boldsymbol{Q}_\eta = \mathrm{S}_\eta^T \boldsymbol{q}$, which are convected with the speeds given by the diagonal matrices, Λ_ξ and Λ_η, respectively, and shall be used for the development of the patching scheme.

3. The Spectral Multi-Domain Scheme. We shall seek solutions to Eq.(1) in the general domain $\Omega \subset \mathsf{R}^2$, enclosed by the boundary, $\delta\Omega$. To obtain such solutions we employ polynomial expansions to approximate the unknown functions and their spatial derivatives. As is well known, the most natural and computationally efficient way of applying polynomial expansions in several dimensions is through the use of tensor products. This procedure, however, requires that the computational domain is diffeomorphic to the unit square. To surround this limitation, we construct Ω using K non-overlapping general quadrilaterals, $\mathsf{D}^k \subset \mathsf{R}^2$, such that $\Omega = \bigcup_{k=1}^{K} \mathsf{D}^k$.

To apply the tensor product formulation we require that there exists a diffeomorphism, $\Psi : \mathsf{D} \rightarrow \mathsf{I}$, where $\mathsf{I} \subset \mathsf{R}^2$ is the unit square, i.e., $\mathsf{I} \in [-1,1]^2$. At this point we have the Cartesian coordinates, $(x,y) \in \mathsf{D}$, and the general curvilinear coordinates, $(\xi,\eta) \in \mathsf{I}$, related through the map, $(x,y) = \Psi(\xi,\eta)$. The map, $\Psi : \mathsf{D} \rightarrow \mathsf{I}$, plays an important role in the application of polynomial methods to problems in general geometries. To establish a one to one correspondence between the unit square and the general quadrilateral we construct the global map using transfinite blending functions. We refer to [3] for a thorough account of this procedure within the present context.

Once the global map, Ψ, has been constructed, we may compute the metric of the mapping, the corresponding transformation Jacobian and outward pointing normal vectors at all points of the enclosing edges of the quadrilateral.

Approximation in I is done by a standard pseudospectral method using tensor products of interpolating Lagrange polynomials based on the Chebyshev Gauss-Lobatto quadrature points. Hence, we seek solutions to Eq.(1) of the form

$$\mathcal{I}_N \boldsymbol{q}(x,y) = \sum_{i=0}^{N} \sum_{j=0}^{N} \boldsymbol{q}(x(\xi_i,\eta_j), y(\xi_i,\eta_j)) L_i(\xi(x,y)) L_j(\eta(x,y)) \ ,$$

where $L_i(\xi)$ and $L_j(\eta)$ correspond to the interpolating Lagrange polynomials based on the Chebyshev Gauss-Lobatto quadrature points in ξ and η, respectively. We refer to [3] for a thorough discussion of multi-domain solution of wave dominated problems using spectral methods.

Within this setting we need to solve K independent problems, Eq.(1), in the individual subdomains. However, to obtain the global solution we have to pass information between the subdomains in a way consistent with the dynamics of Maxwell equations. Since these equations constitute a hyperbolic system it is natural to transfer information between the various subdomains using the characteristic variables introduced in the previous section.

Let us consider two neighboring subdomains and also introduce the corresponding characteristic variables, $\boldsymbol{Q}_{\xi,1} = (Q^0_{\xi,1}, Q^-_{\xi,1}, Q^+_{\xi,1})^T$ and $\boldsymbol{Q}_{\xi,2} = (Q^0_{\xi,2}, Q^-_{\xi,2}, Q^+_{\xi,2})^T$, referring to the three characteristic variables in domain 1 and 2. Here Q^0_ξ represents the non-propagating characteristic, while Q^-_ξ and Q^+_ξ refers to the incoming and outgoing characteristic variable along $\nabla\xi$, respectively, as decided using the convective speeds of propagation of the characteristic variables, i.e. the elements of Λ_ξ.

We enforce the incoming characteristic variable along the normal in each subdomain to equal the outgoing characteristics variable from the neighboring subdomain, i.e. the proper boundary conditions are obtained as

$$Q^-_{\xi,1} = Q^+_{\xi,2} \ , \ \ Q^-_{\xi,2} = Q^+_{\xi,1} \ ,$$

where the right-hand-side of the equations signifies computed values and the left-hand-side refers to the sought after boundary conditions. The non-propagating characteristic variables, $Q^0_{\xi,1}$ and $Q^0_{\xi,2}$ are enforced to be continuous across the interface, while the outgoing characteristic variables, $Q^+_{\xi,1}$ and $Q^+_{\xi,2}$, are preserved in each subdomain.

This procedure of interchanging information between neighboring subdomains is applied at each time step to ensure that a global solution is obtained. The actual field values at the interfaces are then obtained by multiplying the computed characteristic functions with S_ξ. A similar procedure is applied along the remaining 3 edges of the quadrilateral. We note that this procedure is local in nature as each point along the boundary only requires information from one point at the boundary of the neighboring subdomain. Hence, in a parallel setting, the communication grows only as the surface of the quadrilateral rather than the area making the algorithm well suited for parallelization.

On the surface of the scatter we impose the exact boundary condition for E_z and use the characteristic variables to obtain the remaining field values.

4. Using PML Methods in Spectral Methods. A long standing problem in computational electromagnetics is the issue of finding infinite space solutions on a finite computational domain. The issue is to prevent outgoing waves from being reflected from the artificial numerical boundaries. Ideally, an absorbing layer should

be reflectionless with no dependence of the frequency and the direction of propagation of the waves. Such layers, termed Perfectly Matched Layers (PML) were proposed in [6] and have in recent years attracted considerable attention within the community of computational electromagnetics.

The PML methods are all characterized by the need to solve a set of equations different from Maxwells equations in the absorbing layer, e.g. Maxwells equations are split to obtain a number of additional equations. Recently it has been shown that the procedure originally proposed in [6] modifies the equations in a rather unfortunate way as the system of equations to be solved in the layer looses the property of being strongly well-posed [7]. A remedy for this, leading to a new formulation of the perfectly matched layer methods, has recently been derived and is presented elsewhere [8].

The need for solving Maxwells equations in one part of the computational domain while solving a different set of equations, the PML equations in the absorbing layer, highlights yet another advantage of the multi-domain approach developed here as we may simply dedicate the outer domains to deal with the PML equations while Maxwells equations are solved close to the scatter. Patching between the two types of domains does not pose a problem as Maxwells equations are recovered from the PML equations at the vacuum-layer interface and patching through the characteristic variables may be performed in the usual manner. Since derivatives never are computed across subdomain boundaries the amount of reflections from the vacuum-layer interface is reduced significantly compared to the original approach [6].

In the following we shall briefly discuss different formulations and implementations of the PML methods that shall provide the basis for the comparative studies in the subsequent section.

4.1. The Original Rectangular PML Method (PML). The original PML method, proposed in [6], is given in Cartesian coordinates, i.e. a rectangular vacuum-layer interface is implicitly assumed although not necessarily required as discussed in [5].

Consider the non-dimensional PML equations with spatially varying absorbing terms.

$$
\begin{aligned}
\frac{\partial H_x}{\partial t} &= -\frac{\partial (E_{zx}+E_{zy})}{\partial y} - \mu H_x \ , \\
\frac{\partial H_y}{\partial t} &= \frac{\partial (E_{zx}+E_{zy})}{\partial x} - \varepsilon H_y \ , \\
\frac{\partial E_{zx}}{\partial t} &= \frac{\partial H_y}{\partial x} - \varepsilon E_{zx} \ , \\
\frac{\partial E_{zy}}{\partial t} &= -\frac{\partial H_x}{\partial y} - \mu E_{zy} \ ,
\end{aligned}
\tag{4}
$$

where $\varepsilon = \varepsilon(x)$ and $\mu = \mu(y)$. As shown in [6] and further discussed in [5], Eq.(4) allows for plane wave solutions that decay inside the layer irrespective of the frequency and angle of propagation of the wave while remaining continuous across the vacuum-layer interface provided ε and μ are sufficiently smooth.

We assume that the PML region is outside a square bounded by $|x| = a$ and $|y| = a$ and choose $\varepsilon(x)$ as

$$
\varepsilon(x) = \begin{cases} 0 & |x| < a \\ C|x-a|^n & |x| \geq a \end{cases}
\tag{5}
$$

where $n > 2$ and $C > 0$ are constants used to control the strength of the absorbing layer. The definition of $\mu(y)$ is similar.

4.2. A Well-Posed Rectangular PML Method (WPML). As shown in [7], the original PML method discussed in the previous section suffers from being only weakly well-posed as a consequence of the splitting of Maxwells equations. Although, in a multi-domain setting, these equations are solved in a small part of the computational domain only, this property is certainly undesirable.

Recently, an unsplit well-posed PML (WPML) method was proposed to circumvent this problem [8], which, for TM-scattering, is given as

$$
\frac{\partial H_x}{\partial t} = -\frac{\partial E_z}{\partial y} - 2\mu H_x - \mu P_y \ ,
\tag{6}
$$

$$
\begin{aligned}
\frac{\partial H_y}{\partial t} &= \frac{\partial E_z}{\partial x} - 2\varepsilon H_y - \varepsilon P_x \ , \\
\frac{\partial E_z}{\partial t} &= \frac{\partial H_y}{\partial x} - \frac{\partial H_x}{\partial y} - \varepsilon' Q_x + \mu' Q_y \ , \\
\frac{\partial P_x}{\partial t} &= \varepsilon H_y \ , \quad \frac{\partial Q_x}{\partial t} = -\varepsilon Q_x - H_y \ , \\
\frac{\partial P_y}{\partial t} &= \mu H_x \ , \quad \frac{\partial Q_y}{\partial t} = -\mu Q_y - H_x \ ,
\end{aligned}
$$

where $\varepsilon = \varepsilon(x)$ and $\mu = \mu(y)$ signifies the non-dimensional lossy material parameters. We immediately note that since Maxwells equations are altered by low-order terms only, the system of partial differential equations are well-posed by construction with the introduction of 4 additional Debye-like equations describing the development of the artificial polarization currents, P_x and Q_x, along x and, likewise, P_y and Q_y, along y.

Indeed, for $\varepsilon = \mu = 0$ we recover the free space Maxwell equations ensuring that the fields are continuous at the vacuum-layer interface, at least up to the approximation error. In [8] it is shown that Eq.(6) supports plane wave solutions that decay uniformly inside the layer irrespective of the frequency and the angle of propagation of the plane wave. For a detailed analysis we refer to [8]. Following the approach developed in that paper one may also show that Eq.(6) has matched plane wave solutions in the corner regions as well.

We assume that the PML region is outside a square bounded by $|x| = a$ and $|y| = a$, with ε and μ being specified in Eq.(5).

The well-posed PML method, Eq.(6), is very similar to those advocated in e.g. [9, 10, 11], although the latter methods are derived from a physical point of view while Eq.(6) is a result of a mathematical analysis only. One significant difference is that the matched plane wave solutions to Eq.(6) are continuous across the vacuum-layer interface while the normal field components are allowed to be discontinuous across the interface in previously proposed methods in accordance with the dynamics of the physical problem. However, regarding the issue of numerical accuracy it is certainly preferable to require continuity, at the expense of rendering the absorbing material unphysical, to reduce numerical reflections from the vacuum-layer interface.

4.3. A Polar PML Method (PPML). The two PML methods considered so far share the property that they have a rectangular vacuum-layer interface, making it cumbersome, although possible as discussed in [5], to apply such methods when a non-Cartesian grid is used. However, a general vacuum-layer interface may be more natural when solving scattering problems, in particular when applying the general curvilinear formulation.

A natural vacuum-layer interface for scattering problems appears to be a cylindrical interface as the outward propagating waves, at least far away from the scatter, approach a cylindrical wave. These observations have motivated the development of a PML method (PPML) formulated in polar coordinates, (r, θ), as

(7)
$$
\begin{aligned}
\frac{\partial H_r}{\partial t} &= -\frac{1}{r}\frac{\partial (E_{zr} + E_{z\theta})}{\partial \theta} - \varepsilon \frac{H_r}{r} \ , \\
\frac{\partial H_\theta}{\partial t} &= \frac{\partial (E_{zr} + E_{z\theta})}{\partial r} - \varepsilon' H_\theta \ , \\
\frac{\partial E_{zr}}{\partial t} &= -\frac{1}{r}\frac{\partial H_r}{\partial \theta} + \frac{H_\theta}{r} - \varepsilon \frac{E_{zr}}{r} \ , \\
\frac{\partial E_{z\theta}}{\partial t} &= \frac{\partial H_\theta}{\partial r} - \varepsilon' E_{z\theta} \ ,
\end{aligned}
$$

with $\varepsilon = \varepsilon(r)$. Under certain assumptions on the smoothness of ε [5], Eq.(7) admits matched plane wave solutions that decay uniformly inside the layer regardless of the frequency and angle of propagation of the wave. In the present work we use

(8)
$$
\varepsilon(r) = \begin{cases} 0 & r < r_0 \\ C(r - r_0)^n & r \geq r_0 \end{cases}
$$

where $n > 2$ and $C > 0$ are constants used to control the strength of the absorbing layer. Here r_0 signifies the radius of the circular vacuum-layer interface.

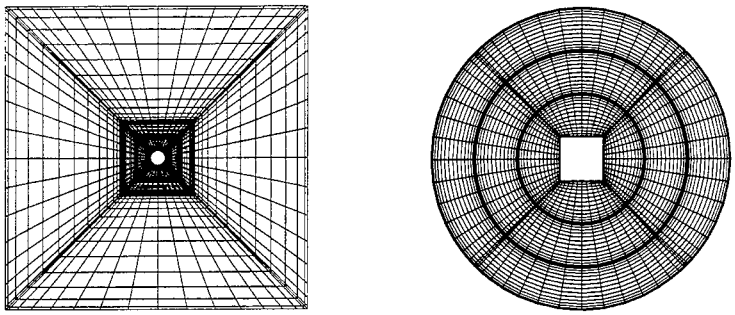

FIG. 1. *Examples of multi-domain grids used for the computation of 2D-TM scattering by cylinders with cylindrical and square cross-sections.*

The difference between the PML method proposed here and previously proposed polar PML methods, see e.g. [12, 13], lies in the way the equations are split, i.e. in the present version the low-order term is applied in the third equation while previous methods include this term in the fourth equation of Eq.(7). Although this latter choice may appear more natural it has recently been shown to lead to significantly larger errors [5].

4.4. A Well-Posed Polar PML Method (WPPML). Following the same line of reasoning leading to the well-posed PML in Cartesian coordinates, Eq.(6), we have derived a well-posed polar PML method, with a circular vacuum-layer interface, that has matched plane wave solutions that decay uniformly inside the layer independent of angle of propagation and frequency. The analysis leading to the actual scheme will be presented elsewhere.

The well-posed polar PML (WPPML) method is given as

$$
\begin{aligned}
\frac{\partial H_r}{\partial t} &= -\frac{1}{r}\frac{\partial E_z}{\partial \theta} \ , \\
\frac{\partial H_\theta}{\partial t} &= \frac{\partial E_z}{\partial r} - (2r\varepsilon' - \varepsilon)\frac{H_\theta}{r} + (2r\varepsilon' - \varepsilon)^2 \frac{P}{r^2} \ , \\
\frac{\partial E_z}{\partial t} &= -\frac{1}{r}\frac{\partial H_r}{\partial \theta} + \frac{1}{r}\frac{\partial r H_\theta}{\partial r} + \varepsilon'' Q \ , \\
\frac{\partial P}{\partial t} &= H_\theta - \varepsilon\frac{P}{r} \ , \quad \frac{\partial Q}{\partial t} = H_\theta - \varepsilon' Q \ ,
\end{aligned}
\tag{9}
$$

where $\varepsilon = \varepsilon(r)$ is given in Eq.(8).

5. Numerical Examples. We consider the case of 2D-TM scattering from perfectly conducting cylinders of circular and square cross-section, respectively. As Maxwells equations are linear we only compute the purely scattered field while the excitation is introduced through the boundary conditions as

$$E_{\rm sc} = -E_{\rm inc} \ ,$$

i.e. the total electrical field vanishes at the scatterer.

In Fig. 1 we show examples of the multi-domain grids used in the following computations. We observe that the multi-domain approach allows for dealing with rectangular and circular vacuum-layer interfaces with equal ease and that scattering by more general objects can be computed by the exact same approach as discussed here for generic shapes. We also find it advantageous to apply a cubic mapping [5] in the outer domains when considering a rectangular vacuum-layer interface while this is not the case for the circular interface.

Computation of the bistatic radar cross section (RCS) is adopted as the criterion for assessing the accuracy of the multi-domain approach as well as the effect of using the various PML methods discussed in the previous section. A near-to-far-field transformation [1] is computed along different enclosing contours and the associated

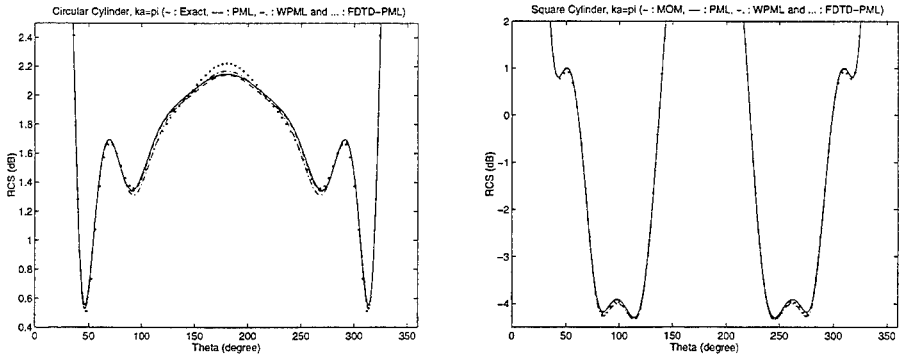

FIG. 2. *Radar-Cross-Sections (RCS) computed using the spectral multi-domain method with various choices of absorbing boundary conditions. On the left we show the RCS for scattering for a $ka = \pi$ circular cylinder computed using also the FD-TD method and compared with the exact solution. The right displays the RCS for scattering from a $ka = \pi$ square cylinder compared with the result obtained using a FD-TD scheme with the MoM result taken to be the reference solution.*

RCS's are compared to ensure that a steady state has been achieved. The equations are advanced in time using a 4th order Runge-Kutta method.

For comparison we have also computed the RCS using a 2nd order FD-TD method [1] with Eq.(4) as the absorbing boundary conditions.

5.1. Scattering by a Circular Cylinder. We first consider the problem of scattering by a $ka = \pi$ circular cylinder where a represents the radius of the cylinder and we use the exact series solution as the reference.

On the left of Fig. 2 we show the computed RCS using different methods and absorbing boundary conditions with a rectangular vacuum-layer interface, i.e. Eqs.(4)-(6). It is clear that the spectral solutions are superior to the FD-TD solution, in particular in the backscatter region.

TABLE 1

Comparison of accuracy and CPU-time from scattering by a circular cylinder, $ka = \pi$. The computational grid is constructed using K domains, each with a resolution of N, and the L_2-error and the required CPU-time are shown for the test cases considered here. The series solution is used as the exact solution against which to compare.

Method - ABC	N	K	L_2-error (dB)	CPU-time (sec)
Spectral - PML	16	12	1.43E-02	387
Spectral - WPML	16	12	2.42E-02	376
Spectral - PPML	16	12	8.60E-04	320
Spectral - WPPML	16	12	9.47E-03	330
FD-TD - PML	320	1	4.50E-02	1402

A more quantitative comparison is shown in Table 1 where we give the L_2 error of the computed RCS and the CPU-time required to obtain the result for the various versions of PML methods introduced previously. Indeed, at first we observe that the spectral scheme is significantly faster as well as more accurate than the FD-TD method. We also observe that the polar PML methods are consistently more accurate than the PML methods with a rectangular vacuum-layer interface while the well-posed formulations of the PML methods appears to be less accurate that the PML methods based on the split set of equations.

We attribute these observations to several effects. The matched plane wave solutions for the well-posed PML methods are more complicated than the solutions associated with the split field PML methods, which may explain the observed difference. The rectangular PML methods, on the other hand, suffers from the requirement that plane waves at grazing incidence must propagate all the way to the corner before experiencing the effect of the layer while no such thing is required in the polar formulation of the PML method.

5.2. Scattering by a Square Cylinder. Let us also consider the case of TM scattering from a square $ka = \pi$ cylinder with a being half a side length. No exact solution is known for this problem and we use a

10 point/wavelength MoM solution as the reference solution. We note that the MoM solution suffers from ill-conditioning for large number of points/wavelength making it impossible to obtain very accurate solutions of the RCS, i.e. it is not possible to arrive at quantitative measures of the same quality as in the previous section.

TABLE 2

Comparison of accuracy and CPU-time from scattering by a rectangular cylinder, $ka = \pi$. The computational grid is constructed using K domains, each with a resolution of N, and the L_2-error and the required CPU-time are shown for the test cases considered here. The MoM-solution with 10 points/wavelength is assumed to represent the exact solution against which to compare.

Method - ABC	N	K	L_2-error (dB)	CPU-time (sec)
Spectral - PML	16	12	2.78E-02	387
Spectral - WPML	16	12	4.16E-02	376
Spectral - PPML	16	12	1.64E-02	326
Spectral - WPPML	16	12	1.61E-02	335
FD-TD - PML	320	1	3.71E-02	1383

On the right of Fig. 2 we show the computed RCS using different methods and absorbing boundary conditions with a rectangular vacuum-layer interface, i.e. Eqs.(4)-(6). In this case we find little difference between the FD-TD solution and those obtained with the spectral scheme, although, as shown in Table 2, the spectral solutions are obtained significantly faster. Again we observe that the polar PML methods outperforms the rectangular PML methods for the reasons discussed in the previous section.

6. Concluding Remarks. The purpose of the present work has been two-fold. The development and implementation of the spectral multi-domain scheme for the solution of Maxwells equations establishes a high-order algorithm, flexible enough to handle arbitrary geometric complexity, while being computational highly efficient and suitable for parallel as well as three-dimensional extensions.

We have also addressed the issue of properly formulating and implementing perfectly absorbing boundary conditions in the context of the multi-domain approach. The results clearly illustrate the superior accuracy, obtained at lower computational cost than when using FD-TD methods, attainable when combining PML methods with the accurate spectral methods. In particular we have shown that the polar PML methods seems to offer higher accuracy than the rectangular PML methods. On the other hand, the recently proposed well-posed PML methods appear to be slightly less accurate that the PML methods based on the split equations [6] due to more complicated matched plane wave solutions. However, we do believe that using the well-posed PML methods is the proper choice, in particular when considering problems with transient excitation.

Acknowledgments. The authors would like to express their gratitude to Dr. Peter G. Petropoulos, Southern Methodist University, for many helpful discussions and some useful codes.

REFERENCES

[1] A. TAFLOVE, *Computational Electrodynamics - The Finite-Difference Time-Domain Method*, Artech House, Boston, 1995.
[2] D. GOTTLIEB AND S.A. ORSZAG, *Numerical Analysis of Spectral Methods: Theory and Applications*, SIAM Publications, Philadelphia, 1977.
[3] J.S. HESTHAVEN, *A Stable Penalty Method for the Compressible Navier-Stokes Equations. III. Multidimensional Domain Decomposition Methods*, SIAM J. Sci. Comput. - accepted, 1996.
[4] P. FISCHER AND D. GOTTLIEB, *On the Optimal Number of Subdomains for Hyperbolic Problems on Parallel Computers*, J. Supercomput. Appl. - submitted, 1996.
[5] B. YANG, D. GOTTLIEB AND J. S. HESTHAVEN, *Spectral Simulations of Electromagnetic Wave Scattering*, J. Comp. Phys. - submitted, 1996.
[6] J. P. BERENGER, *A Perfectly Matched Layer for the Absorption of Electromagnetic Waves*, J. Comp. Phys. **114**(1994), pp. 185-200.
[7] S. ABARBANEL AND D. GOTTLIEB, *A Mathematical Analysis of the PML Method*, J. Comp. Phys. - submitted, 1996.
[8] S. ABARBANEL AND D. GOTTLIEB, *On the Construction and Analysis of Absorbing Layers in CEM* - this conference, 1997.
[9] L. ZHAO AND A. C. CANGELLARIS, *A General Approach for the Development of Unsplit-Field Time-Domain Implementations of Perfectly Matched Layers for FD-TD Grid Truncation*, IEEE Microwave Guided Wave Lett. **6**(1996), pp. 209-211.
[10] R. W. ZIOLKOWSKI, *Time-Derivative Lorentz-Material Model Based Absorbing Boundary Conditions* - preprint, 1996.
[11] P. PETROPOULOS. L. ZHAO AND A. C. CANGELLARIS, *A Reflectionless Sponge Layer Absorbing Boundary Condition for the Solution of Maxwell's Equations with High-Order Staggered Finite Difference Schemes*, J. Comp. Phys. - submitted, 1996.
[12] E.A. NAVARRO. C. WU, P.Y. CHUNG AND J. LITVA, *Application of PML Superabsorbing Boundary Condition to Non-Orthogonal FD-TD Method*, IEE Electron. Lett. **30**(1994), pp. 1654-1655.
[13] C. M. RAPPAPORT, *Perfectly Matched Absorbing Boundary Conditions Based on Anisotropic Lossy Mapping of Space*, IEEE Microwave Guid. Wave Lett. **5**(1995), pp. 94-96.

FVTD schemes using conformal hybrid meshes and a PML medium technique.

F. BONNET †- J.P. CIONI †- L. FEZOUI †- F. POUPAUD ‡
†INRIA Sophia-Antipolis, BP 93, 06 902 Sophia-Antipolis Cedex (France)
‡Laboratoire J.A. Dieudonné, Université de Nice, Parc Valrose, BP 71, 06108 Nice Cedex 02 (France).

Introduction

We are concerned here with the extension of the Bérenger PML method to finite-volume schemes for solving the time-domain Maxwell equations, using hybrid meshes.
To solve numerically exterior problems, one has to choose among the numerous absorbing boundary conditions that may be found in the literature. We refer the reader to [1] for a (non exhaustive) bibliography on the subject. We have chosen to use in the present work the PML method first introduced for grid based Yee schemes in [2]. The method consists in surrounding the computational domain with an artificial medium, called PML ("Perfectly Matched Layer"), in order to absorb outgoing electromagnetic waves. In this PML medium, the system written in conservative variables ${}^t(\mathbf{B},\mathbf{D})$ is no longer hyperbolic. This lack of hyberbolicity prevents us from using upwind centered schemes that are based on the splitting of the jacobian matrix according to the positive and negative parts of the eigenvalues. Despite this, we have suggested in [3] a way to circumvent this problem and to construct high-order upwind centered schemes using triangular meshes. However, this was achieved at a price of an extra cost in CPU time.
In order to improve the efficiency, we propose now a hybrid conformal structured-unstructured method. The region surrounding the body is still discretized using a finite element type mesh while the PML medium is discretized using a finite-difference type grid.
Some numerical results obtained with the PML method on hybrid meshes are presented and compared with classical FVTD scheme solutions on unstructured meshes [4]. Performance results are also presented.

1 Maxwell Equations

In vacuum, assuming no current and charge densities, the Maxwell equations can be written as :

$$\begin{cases} \mu_0 \dfrac{\partial \vec{H}}{\partial t} + rot(\vec{E}) = 0, \\ \\ \varepsilon_0 \dfrac{\partial \vec{E}}{\partial t} - rot(\vec{H}) = 0, \end{cases} \tag{1}$$

where $\vec{E} = \vec{E}(t,\vec{x})$ and $\vec{H} = \vec{H}(t,\vec{x})$ denote respectively the electric and magnetic fields, while μ_0 and ε_0 are the permeability and the permittivity of vacuum respectively.
These equations then lead via appropriate change of variables to the condensed conservative form in $\mathbb{R}^2$:

$$Q_\tau + \vec{\nabla}.\mathbf{F}(Q) = 0 \qquad (\vec{x},\tau) \in \Omega \times \mathbb{R}^+, \tag{2}$$

with $\mathbf{F}(Q) = {}^t(F(Q), G(Q))$. We note $Q = {}^t(H, E)$ (see [4] for more details).
Ω is a bounded domain of $\mathbb{R}^2$, whose boundary is denoted by $\Gamma = \Gamma_\infty \cup \Gamma_b$. Γ_∞ and Γ_b are the artificial and metallic boundaries respectively.

2 Numerical formulation

The computational domain Ω is split in two according to the characteristic length of the body (see fig.2). The neighbourhood of the body is discretized using P1 finite elements and the absorbing material zone is divided into

rectangles. Note that it is always possible to connect the two grids in a conformal way in the plane while it is impossible in 3-D space without introducing other element type at the grid interface.
Let $\mathcal{D}_T$ and $\mathcal{D}_R$ denote the triangular mesh and the structured grid respectively. A new partition (dual mesh) is now constructed by defining a cell denoted C_i around each node of the whole mesh as it is shown in the next figure.

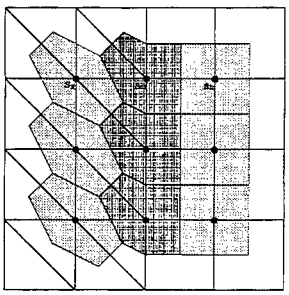

Figure 1: Finite volume cells

Integrating (2) on each cell and after a Green's formula, one gets :

$$Area(C_i)\,(Q_t)_i = -\sum_{j\in K(i)} \int_{\partial C_{ij}} \mathbf{F}(Q).\vec{\nu}_{ij}\,d\sigma - \int_{\partial C_i \cap \Gamma} \mathbf{F}(Q).\vec{n}\,d\sigma \tag{3}$$

where $\vec{\nu}_{ij}$ is the outward normal to the interface ∂C_{ij} and $K(i)$ is the set of nodes neighbouring the central node of C_i.
The term $\int_{\partial C_{ij}} \mathbf{F}(Q).\vec{\nu}_{ij}\,d\sigma$ is given by :

$$\mathbf{\Phi_{ij}} = \mathbf{F}_{ij}.\vec{\eta}_{ij},$$

where $\vec{\eta}_{ij} = {}^t(\eta_1, \eta_2) = \int_{\partial C_{ij}} \vec{\nu}_{ij}\,d\sigma$ and $\mathbf{F}_{ij}$ is some approximate value of $\mathbf{F}(Q)$.

We use different approximations for the flux integrals whether the $\mathcal{D}_\mathcal{T}$ domain or the PML medium $\mathcal{D}_\mathcal{R}$ is concerned. Let us recall briefly the method used in $\mathcal{D}_\mathcal{T}$ (see [4] for more details).

2.1 Approximation in $\mathcal{D}_\mathcal{T}$

First-order upwind flux :

We recall that for the linear systems with constant coefficients, such as the Maxwell equations in the vacuum, all first-order upwind fluxes reduce to the same. Thus a first-order flux may be written as follows :

$$\mathbf{\Phi_{ij}} = \Phi(Q_i, Q_j, \vec{\eta}_{ij}) = \frac{\mathcal{F}(Q_i, \vec{\eta}_{ij}) + \mathcal{F}(Q_j, \vec{\eta}_{ij})}{2} - \frac{\gamma}{2} \mid \mathcal{A}(\vec{\eta}_{ij}) \mid (Q_j - Q_i), \tag{4}$$

where $\mathcal{F}(Q, \vec{\eta}_{ij}) = \eta_1 F(Q) + \eta_2 G(Q)$ and $\mathcal{A}(\vec{\eta}_{ij})$ the Jacobian matrix of $\mathcal{F}(Q, \vec{\eta}_{ij})$.
The parameter γ is introduced in order to control the amount of residual viscosity.

High-order approximation :

The high-order approximation we use is based on the MUSCL (Monotonic Upwind Schemes for Conservative Laws) method introduced by B. Van Leer [5]. In a β-scheme formulation, the high order flux is written as follows:

$$\begin{cases} \mathbf{\Phi_{ij}} = \mathbf{\Phi_{ij}}(Q_{ij}, Q_{ji}, \vec{\eta}_{ij}), \\ Q_{ij} = Q_i + \frac{1}{2}\{(1-2\beta)(Q_j - Q_i) + 2\beta \overrightarrow{\nabla} Q_i . \mathbf{S_i S_j}\}, \end{cases} \tag{5}$$

The upwind parameter β will be equal to $\frac{1}{3}$ in the sequel.

The gradient of Q at each node i is evaluated as a mean of the linear interpolation gradients. It writes for each component k of the vector field Q:

$$\overrightarrow{\nabla} Q_i^k = \frac{1}{Area(C_i)} \sum_{i \in \mathcal{D}_T} \frac{Area(Triangle)}{3} (\overrightarrow{\nabla} Q)_T^k. \tag{6}$$

We note that at the interface of the two grids, the gradients are evaluated in the same way since we always may consider a rectangle as a union of two (fictitious) triangles.

2.2 Approximation in the absorbing material

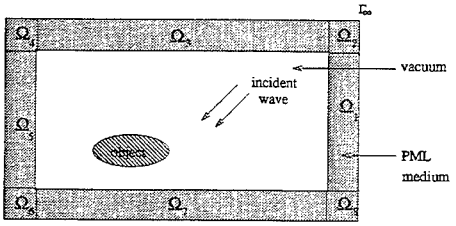

Figure 2: Computation domain with PML medium

In the artificial medium PML, the set of equations proposed by Bérenger can be rewritten in such a way that the classical Maxwell equations may emerge again. We write here this new formulation for the 2-D TM case :

$$\begin{cases} \dfrac{\partial H_x}{\partial t} + \dfrac{\partial E_z}{\partial y} + \sigma_y \, H_x = 0, \\ \dfrac{\partial H_y}{\partial t} - \dfrac{\partial E_z}{\partial x} + \sigma_x \, H_y = 0, \\ \dfrac{\partial E_z}{\partial t} + \dfrac{\partial H_x}{\partial y} - \dfrac{\partial H_y}{\partial x} + \sigma_x \, E_z + (\sigma_y - \sigma_x) \, E_{zy} = 0, \\ \dfrac{\partial E_{zy}}{\partial t} + \dfrac{\partial H_x}{\partial y} + \sigma_y \, E_{zy} = 0. \end{cases} \tag{7}$$

where E_{zy} is the new degree of freedom introduced by Bérenger. The matched conductivities σ_x and σ_y are decisive to get no reflection at the interface between $\mathcal{D}_\mathcal{T}$ and the PML medium [2].
If we look at the system (7) we observe that the first three equations are the Maxwell equations in free space with a source term. So, we decide to solve these equations using the same approximation described above but written now for a structured grid.

To solve the last equation, a Riemann problem is set at each interface between two neighbouring cells. Solving exactly this Riemann problem gives us the fourth numerical flux [3].

Boundary conditions :

We recall here the absorbing boundary condition and refer the reader to [4] for details on the approximation of the perfectly conducting boundary condition.
Instead of taking the artificial boundary Γ_∞ as a perfectly conducting boundary surface as suggested by Bérenger, we apply a first order absorbing condition through an upwinding. Since no informatiom is entering the computational domain, one gets in terms of scattered field :

$$\Phi_{i\infty} = \mathcal{A}^+(\vec{n}_{i\infty})Q_i^d.$$

where Q_i^d is the computed scattered field on Γ_∞ and $\mathcal{A}^+$ the positive part of $\mathcal{A}$.

Time integration :

We use the explicit Runge-Kutta scheme with three steps and low storage [4]. This scheme is third-order in time because the Maxwell system is linear.

3 Numerical Results

Metal cylinder :

We simulate the diffraction of an impulse (wave with compact support) on a metal cylinder. In order to improve the hybrid mesh, we propose to compare the hybrid results with ones abtained with an unstructured mesh (solution of reference). Here, we have just used an upwinding condition in order to avoid PML eventual interactions. We use the same discretization (i.e the same number of points). Figure 4 shows the time variation of the total electric field E_z. The good behavior of the solution with the hybrid mesh can be seen. In addition, no deterioration of the solution appears in the interface between the triangular part and the rectangular grid.

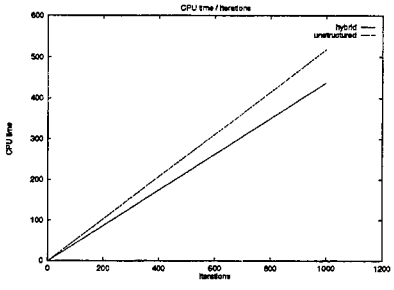

Figure 3: Performance in CPU time

We now describe the performance results obtained on a DEC ALPHA 400/233. The figure 3 shows the CPU time in seconds per iteration for both hybrid and unstructured meshes with the same number of points. The results show that the performance is faster with the hybrid mesh than with the unstructured one. The hybrid mesh allows us to win about 25% in time for gradients and 20% for the numerical fluxes calculations.

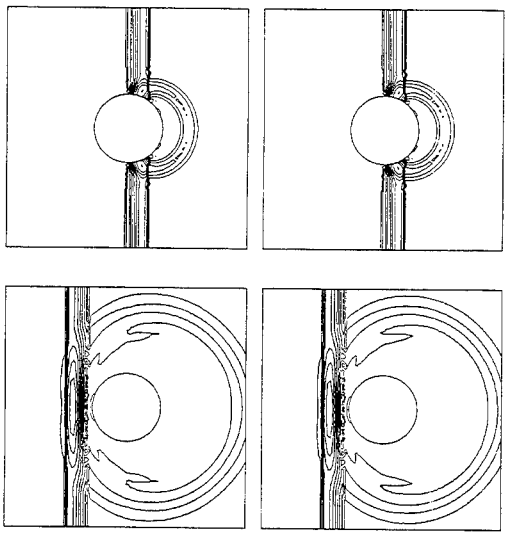

Figure 4: Time variation of the total field E_z
(left : unstructured mesh - right : hybrid mesh)

Airfoils :

A NACA0012 type metallic airfoil is illuminated by a harmonic TM wave at a frequency of 1.2 GHz with an angle of incidence of 90 degrees. The object is 4 wavelengths long and the number of points per wavelenght is approximately 15 in the neighborhood of the object. We use an hybrid mesh (fig. 5).
All the computations have been realised with a most favourable PML medium [3]. The table 1 shows that this technique allows us to spare both computational time and memory place.

Table 1: : Performance results for RCS to reach 10^{-3} L^2 RCS error

	PML + upwinding	Upwinding
location of the artificial boundary	λ	2λ
relative CPU time/iteration	1	2.5

Finally, figure 6 shows the RCS diagram. The RCS is compared in the same figure 6 with classical FVTD scheme solutions on unstructured grids [4]. We note an excellent agreement between the two solutions.

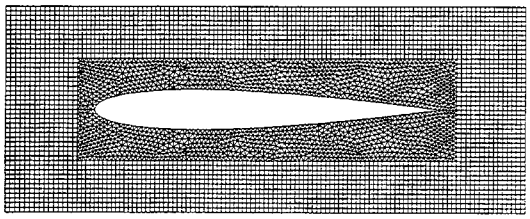

Figure 5: Airfoil hybrid mesh

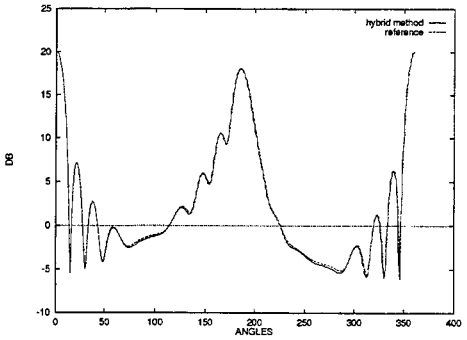

Figure 6: RCS with an incidence angle 90°

4 Conclusion

We have presented a hybrid method coupling the Bérenger equations approximated on a finite-difference type grid with a finite volume scheme written on a triangular mesh. We have shown that the use of an exact Riemann solver prevents from the apparition of spurious oscillations at the interface of the two grids.
This new method provides numerical solutions that compare well with the solutions obtained on 'uniform' unstructured meshes. Moreover, it allows us to spare both time and memory place without loss of accuracy.
These results are very encouraging to extend the method to the three dimensional case where the efficiency is more crucial. However, a mixing of more than two elements seems to be necessary for conformal meshes and good mesh generators have to be used.
Furthermore, the hybrid method seems to be well adapted to parallel architectures.

References

[1] F. Bonnet. Rapport bibliographique sur les conditions aux limites absorbantes pour la propagation d'onde. Technical Report 96-52, CERMICS, 1996.

[2] J.P. Berenger. Three-dimensional Perfectly Matched layer for the absorption of electromagnetic waves. *J. Comput. Physics*, 127:363–379, 1996.

[3] F. Bonnet and F. Poupaud. Condition aux limites de Bérenger avec un schéma temporel de type volumes finis en maillage triangulaire. Technical Report 96-53, CERMICS, March 1996. soumis a M2AN.

[4] J.P. Cioni, L. Fezoui, and H. Steve. A parallel time-domain Maxwell solver using upwind schemes and triangular meshes. *IMPACT in computing in science and engeenering*, (165), 1993.

[5] B. Van Leer. Flux vector splitting for the Euler equations. *Lecture Notes in Physics*, 170:405–512, 1982.

PML Study for FEM Modeling of Antennas and Microwave Circuits

Y. Botros, J. Gong and J.L. Volakis
Radiation Laboratory
Dept. of Electrical Engineering and Computer Science
University of Michigan
Ann Arbor, MI 48109-2122
Email: volakis@umich.edu
Fax: (313)647-2106

The perfectly matched layer(PML) [1], [2] has several attractive features. Among them, are superior absorptivity over a wide incident angles, implementation simplicity for frequency domain analysis, and high level of control on its absorption performance.

However, the design and implementation of the PML is still under research and development. One of the issues of concern is the deterioration of the system condition when introduced into the Finite Element solution. As a result, the resulting FEM solution may be unreliable. Another issue relates to the optimization of the PML [3] aimed at minimizing the layer thickness while attaining maximum absorption.

In this paper we will look at some three dimensional successful applications of the PML as a motivation for further investigation of the PML. We will then look at parameters which effect the condition of the overall finite element system and on methods for *a priori* prediction of the condition. The reduction of the PML region improves the condition of the system and techniques will be examined for modeling the PML region with the minimum number of elements and layer thickness. Algorithmic convergence improvements will be also presented along with applications to three dimensional antenna and microwave circuits.

References

[1] J.P. Berenger. "A perfectly matched layer for the absorption of electromagnetic waves ". *J. Comp. Physics*, vol. 114, pp. 185–200, 1994.

[2] Z.S. Sacks, D.M. Kingsland R. Lee, and J.F. Lee. "A perfectly matched anisotropic absorber for use as an absorbing boundary condition". *IEEE Trans. Antennas Propagat.*, vol. 43, pp. 1460–1463, 1995.

[3] S. Legault, T.B.A Senior, and J.L. Volakis. Design of planar absorbing layers for domain truncation in fem applications. *Electromagnetics*, vol. 16, No. 4, pp. 451-464, 1996.

SESSION 16:

FAST SOLVERS FOR ELECTROMAGNETIC SCATTERING PROBLEMS

Chairs: E. Michielssen and W. Chew

Least-Squares Based Far-Field Expansion in the Adaptive Integral Method (AIM)

E. Bleszynski[+], M. Bleszynski[++], and T. Jaroszewicz[+++]
[+]Boeing North American, Seal Beach, CA 90740-7644
[++] Science Center, Rockwell International Corporation
P.O. Box 1085, Thousand Oaks, CA 91360
[+++] Monopole Research, 2725 Glendon Ave, Los Angeles, CA 90064

Abstract

We discuss an improved version of the Adaptive Integral Method, which is based on a new approximation criterion in the far-field expansion of impedance matrix elements. We find that, compared to the previous method, the new expansion allows us to attain the same accuracy with a significantly reduced (by about the factor of 4) computational cost and storage requirements. Numerical examples illustrating the performance of the new algorithm for various electrically large objects will be presented.

The Adaptive Integral Method (AIM) [1, 2] is a fast iterative electromagnetic integral-equation solver with an impedance matrix compression and a fast matrix-vector multiplication method based on a specific decomposition of the impedance matrix into "near-" and "far-field" components. The near-field component is, by construction, a *sparse* matrix, computed as in the conventional Method of Moments (MoM), with arbitrary local-support basis functions, representing volume, surface, or line current elements. In the far-field component the original current elements are approximated by equivalent distributions of pointlike sources located at nodes of a three-dimensional Cartesian grid. Since the transformation between the original and the equivalent current distributions is given by a sparse matrix, and the Cartesian grid discretization of the Green's function results in a Toeplitz matrix, storage and matrix-vector multiplication complexity behave, up to logarithmic factors, as $O(N_C)$, where N_C is the required total number of Cartesian grid nodes. If N

is the number of unknowns, $N_C \sim N^{3/2}$ in surface problems, and $N_C \sim N$ in volumetric problems. Compared to the conventional MoM, with $O(N^2)$ storage and complexity, AIM provides a significant improvement already for problems with few thousand unknowns.

In the original implementation of the AIM algorithm, the equivalent Cartesian grid sources were determined by requiring that they reproduce the multipole moments of the original current element, up to a desired multipole order M. Here we describe an alternative algorithm, in which the equivalent currents are obtained based on a least-squares approximation to the angular distribution of the far-field radiated by the currents.

The AIM solver based on the approximation method described here has been fully implemented in both serial and parallel versions, and applied to a variety of large-scale three-dimensional scattering problems involving perfectly conducting and coated objects. Our theoretical analysis and numerical experience show that the new far-field expansion provides storage and computation time reduction by, typically, a factor of 3 or 4.

The far-field expansion of the AIM is applicable to any Galerkin matrix elements of the form

$$A_{\alpha\beta} = \int \mathrm{d}x_1 \, \mathrm{d}x_2 \, \psi_\alpha(\mathbf{x}_1) \, g(\mathbf{x}_1 - \mathbf{x}_2) \, \psi_\beta(\mathbf{x}_2) \equiv (\psi_\alpha, \, g \, \psi_\beta) \; , \tag{1}$$

where

$$g(\mathbf{x}) = \frac{\mathrm{e}^{\mathrm{i}\, k\, |\mathbf{x}|}}{4\pi |\mathbf{x}|} \tag{2}$$

is the Helmholtz equation Green's function with the wave number $k = 2\pi/\lambda$. The form (1) arises from discretization of all the integral operators appearing in Maxwell's equations with vector-valued electric and magnetic current elements; in that case the functions ψ_α and ψ_β are components of the original vectorial basis functions, or of their derivatives (divergences and curls).

In the far-field matrix elements the basis functions are approximated by linear combinations of Dirac delta-functions,

$$\psi_\alpha(\mathbf{x}) \simeq \widehat{\psi}_\alpha(\mathbf{x}) \equiv \sum_{\mathbf{u} \in C_\alpha} \Lambda_{\alpha \mathbf{u}} \, \delta^3(\mathbf{x} - \mathbf{u}) \; , \tag{3}$$

localized at some set C_α of grid nodes $\mathbf{u}$, depending on the basis function ψ_α. In the present implementation C_α is a cubic *expansion box* of $(M+1)^3$ nodes, whose center is nearest to the center of the support of ψ_α.

The the approximate far-field matrix elements obtained with the expansion (3) are

$$A^{\mathrm{Far}}_{\alpha\beta} \equiv (\widehat{\psi}_\alpha,\, g\,\widehat{\psi}_\beta) = \int \mathrm{d}x_1\,\mathrm{d}x_2\,\widehat{\psi}_\alpha(\mathbf{x}_1)\,g(\mathbf{x}_1-\mathbf{x}_2)\,\widehat{\psi}_\beta(\mathbf{x}_2)$$
$$= \sum_{\mathbf{u}\in C_\alpha}\sum_{\mathbf{v}\in C_\beta} \Lambda_{\alpha\mathbf{u}}\,g(\mathbf{u}-\mathbf{v})\,\Lambda_{\beta\mathbf{v}}\ , \tag{4}$$

i.e., the far-field component of the impedance matrix can be represented as

$$A^{\mathrm{Far}} = \Lambda\, g\, \Lambda^{\mathrm{T}}\ , \tag{5}$$

where Λ is, by construction, a *sparse* matrix, and $g = (g(\mathbf{u}-\mathbf{v}))$ is a (three-level) Toeplitz matrix, i.e., it depends only on the differences of the integer indices $(u_1 - v_1)$, $(u_2 - v_2)$, and $(u_3 - v_3)$, defined by the relation

$$\mathbf{u} = (a_1\,u_1,\, a_2\,u_2,\, a_3\,u_3) \tag{6}$$

(and similarly for $\mathbf{v}$), with Cartesian grid spacings a_1, a_2, a_3.

The full impedance matrix A is then approximated as

$$A \simeq A^{\mathrm{AIM}} \equiv A^{\mathrm{Near}} + A^{\mathrm{Far}}\ ; \tag{7}$$

here the matrix elements $A^{\mathrm{Near}}_{\alpha\beta}$ are defined, for distances smaller than a certain "near-field range", as $A_{\alpha\beta} - A^{\mathrm{Far}}_{\alpha\beta}$, and for larger distances are assumed to be zero (the near-field range is typically comparable to the wavelength). Thus, by construction, the matrix A^{Near} is sparse. Eqs. (7) and (5) provide then an approximation of the matrix A as a sum of a sparse matrix and a product of sparse and Toeplitz matrices (Eqs. (7) and (5)).

In the original far-field expansion method, the coefficients Λ were determined by requiring the equality of the set of $(M+1)^3$ the multipole moments (of orders 0 to M, in each of the three spatial directions) of the original basis function ψ_α and its approximation $\widehat{\psi}_\alpha$.

The error in the approximation (7) has been thoroughly discussed in Ref.[2] in the case of the original multipole-based expansion. We found there that the relative error in the matrix elements is proportional to $(a/\lambda)^{M+1}$, where a is the Cartesian grid spacing; in the typical case of the quadrupole expansion ($M = 2$), the grid spacing required to obtain a good far-field accuracy was $a \sim \lambda/10$. At the same time, storage and algorithm complexity also strongly depend on the grid spacing: they behave approximately as $(\lambda/a)^3$ (detailed estimates are given in Ref.[2]). Therefore, it is crucial for the performance of the algorithm to make the grid spacing as large as possible, while assuring that the error is

acceptably small. Such considerations have motivated the new far-field expansion method, which allows a larger grid spacing without deterioration of the accuracy.

The new expansion method is based on the least-squares approximation to the *far-field* generated by the considered basis function ψ_α; and since the far-field radiated by the current element ψ_α is, asymptotically, its Fourier transform, the new expansion method amounts to approximating Fourier transforms

$$\widetilde{\psi}_\alpha(\mathbf{k}) \equiv \int \mathrm{d}^3x\, \mathrm{e}^{\mathrm{i}\mathbf{k}\cdot\mathbf{x}}\, \psi_\alpha(\mathbf{x}) \tag{8}$$

by

$$\widetilde{\widehat{\psi}}_\alpha(\mathbf{k}) \equiv \int \mathrm{d}^3x\, \mathrm{e}^{\mathrm{i}\mathbf{k}\cdot\mathbf{x}}\, \widehat{\psi}_\alpha(\mathbf{x}) = \sum_{\mathbf{u}\in C_\alpha} \Lambda_{\alpha\mathbf{u}}\, \mathrm{e}^{\mathrm{i}\mathbf{k}\cdot\mathbf{u}} \ . \tag{9}$$

In its present form, the AIM algorithm utilizes the same far-field approximation of basis functions for all matrix elements. [1] Therefore, we define the far-field error as the directional average (over *all* directions $\hat{\mathbf{k}} \equiv \mathbf{k}/|\mathbf{k}|$) of the difference between the Fourier transform (8) and its approximation (9),

$$\Delta = \sum_{\hat{\mathbf{k}}} w_{\hat{\mathbf{k}}} \left| \widetilde{\psi}_\alpha(\mathbf{k}) - \sum_{\mathbf{u}\in C_\alpha} \Lambda_{\alpha\mathbf{u}}\, \mathrm{e}^{\mathrm{i}\mathbf{k}\cdot\mathbf{u}} \right|^2 , \tag{10}$$

where the sum runs over quadrature points on the unit sphere, and $w_{\hat{\mathbf{k}}}$ are quadrature weights.

Minimization of the error Δ constitutes a least-squares problem, and results in a system of linear equations for the coefficients $\Lambda_{\alpha\mathbf{u}}$,

$$\sum_{\mathbf{v}\in C_\alpha} L_{\mathbf{u}\mathbf{v}}\, \Lambda_{\alpha\mathbf{v}} = f_{\alpha\mathbf{u}} \qquad \text{for all } \mathbf{u} \in C_\alpha \ , \tag{11}$$

where

$$L_{\mathbf{u}\mathbf{v}} = \sum_{\hat{\mathbf{k}}} w_{\hat{\mathbf{k}}}\, \mathrm{e}^{\mathrm{i}\,\mathbf{k}\cdot\mathbf{u}}\, \mathrm{e}^{-\mathrm{i}\,\mathbf{k}\cdot\mathbf{v}} \equiv \sum_{\hat{\mathbf{k}}} w_{\hat{\mathbf{k}}}\, \cos(\mathbf{k}\cdot(\mathbf{u}-\mathbf{v})) \ , \tag{12}$$

and

$$f_{\alpha\mathbf{u}} = \sum_{\hat{\mathbf{k}}} w_{\hat{\mathbf{k}}}\, \cos(\mathbf{k}\cdot\mathbf{u})\, \widetilde{\psi}_\alpha(\mathbf{k}) \ . \tag{13}$$

---

[1] An alternative possibility is to use (in the context of domain decomposition) different far-field expansions for different pairs of domains.

We assumed here that every quadrature point $\hat{\mathbf{k}}$ has its antipodal $-\hat{\mathbf{k}}$, and that $w_{\hat{\mathbf{k}}} = w_{-\hat{\mathbf{k}}}$. We also assume that the basis functions ψ_α (and the coefficients $\Lambda_{\alpha \mathbf{u}}$) are real; therefore, all quantities appearing in Eq.(11) are real. The elements of the matrix L and of the vectors are labeled by multi-indices (u_1, u_2, u_3) and (v_1, v_2, v_3), defined as in Eq.(6).

According to Eq.(12), the matrix $L_{\mathbf{u}\,\mathbf{v}}$ is three-level Toeplitz, i.e., depends only on the differences of indices $(u_1 - v_1)$, $(u_2 - v_2)$, and $(u_3 - v_3)$ (similarly to the matrix g in Eqs. (7) and (5)). The first expression for L in Eq.(12) also shows that L can be written as a product of a matrix and its Hermitian conjugate (this follows from the positivity of the weights $w_{\hat{\mathbf{k}}}$). Therefore, in addition to being real symmetric, L is also positive-semidefinite.

In the numerical implementation of the algorithm we use the conventional Gauss-Legendre quadrature on the sphere, with the minimum number of quadrature points necessary to generate a nonsingular matrix L. Although L tends to have a large condition number (an effect related to the symmetry of the grid), stable numerical results are obtained by performing singular-value decomposition and discarding contributions of a few lowest singular values, usually separated by a noticeable gap from the remaining ones. [2] We note that the matrix L depends only on the wavelength, grid spacings, and the expansion order M, and is therefore universal for all basis functions.

We carried out an extensive numerical analysis of the errors in matrix elements for the Maxwell's equations case, using the conventional vectorial Rao-Wilton-Glisson [3] basis functions. As an example, we show in Fig. 1 the relative errors in the matrix elements $A_{\alpha\beta}$ of the electric-field operator, as a function of the distance r between the centers of the current elements α and β. We use here typical values of the parameters: $M = 2, 3$, $a = \lambda/8$, and the size of the current element (diameter of the basis function support) $b = 0.1\,\lambda$. In the considered example the current elements are positioned in the (x, y) plane, with the currents flowing, on the average, in the y-direction, and are separated by a distance r in the z-direction (this configuration is marked in Fig. 1 as a coupling of y-components of the currents, $\langle J_y\, J_y \rangle\,(z)$).

The curves in Fig. 1 show errors of the multipole-expansion-based far-field approximations of orders $M = 2$ and $M = 3$, and the least-squares approximation of order $M = 2$ (these curves exhibit characteristic periodic oscillations due to the error dependence on the location of the basis functions relative to the grid nodes). For comparison, we also plot the relative difference (marked "MoM") in the MoM matrix elements calculated using 12-point and 3-point two-dimensional Gaussian quadratures on triangles (the latter is the

[2] An alternative method of solving the least-squares problem as the "enhanced system" of equations is, in our case, numerically less reliable.

customary choice, especially for large problems, where the matrix fill is one of the most computationally intensive parts of the algorithm). This relative difference provides thus an estimate of the quadrature error inherent in all MoM computations.

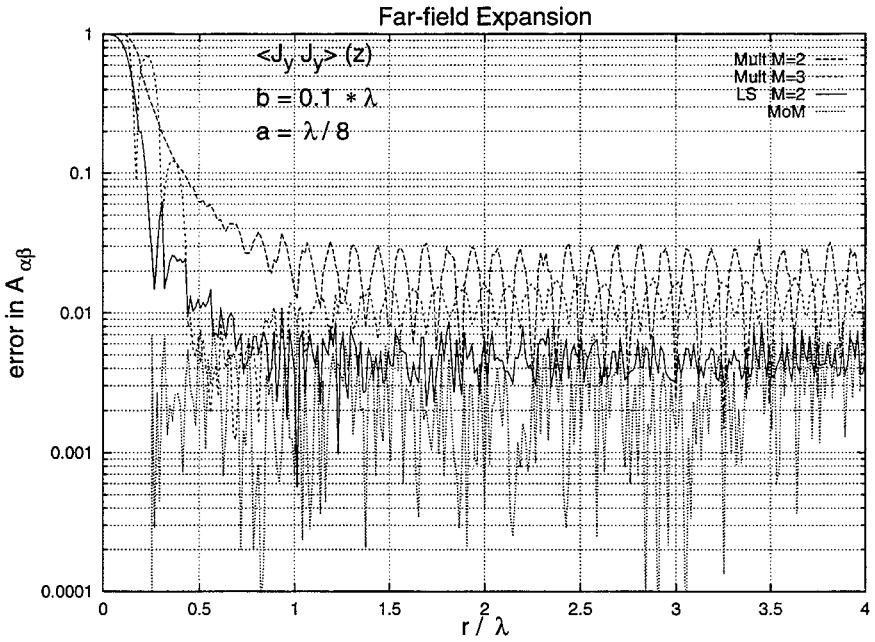

Fig. 1: Relative error in the matrix elements, due to various far-field approximations, compared with the quadrature error in the Method of Moments.

Fig. 1 shows that the $M = 2$ least-squares aproximation is significantly better than the multipole-based approximations of the same (quadrupole) order, as well as the octupole ($M = 3$) order. Actually, the least-squares far-field error is comparable to the MoM quadrature error, and thus it would be pointless to try to reduce it even further. As another interesting feature, we note that, although our least-squares approximation method is based only on the asymptotic far-field behavior, the resulting approximation is accurate already at distances smaller than the wavelength.

We summarize with the most important properties of the new far-field expansion, emerging from our theoretical analysis and extensive numerical experience with the AIM code:

1. The least-squares expansion provides a good accuracy (a 1% far-field error is entirely adeqate [2]) already for grid spacing $a \sim \lambda/7$ or larger, compared to $a \sim \lambda/10$ in the original method. Such an increase in grid spacing results in storage and computation time reduction by the factor $(10/7)^3 \simeq 3$.
2. It is applicable even at distances as small as $0.5\,\lambda$, typically smaller than the original expansion method, resulting in a more sparse near-field impedance matrix component.
3. Its accuracy is consistently good for a wide range of current element sizes, including sizes as small as, say, $\lambda/50$, which may occur in typical discretizations of geometrically complex objects. Compared to the original expansion, it is thus less sensitive to the discretization details and its possible anomalies.

As these features indicate, implementation of the least-squares far-field expansion method was a significant step towards further improvement of the performance and reliability of the AIM.

References

1. E. Bleszynski, M. Bleszynski, and T. Jaroszewicz, "A Fast Integral Equation Solver for Electromagnetic Scattering Problems", in *Proceedings of the 1994 IEEE APS International Symposium, Seattle, Washington*, pp. 417-420.
2. E. Bleszynski, M. Bleszynski, and T. Jaroszewicz, "AIM: Adaptive integral method for solving large-scale electromagnetic scattering and radiation problems", *Radio Science*, Vol. 31, pp. 1225-1251, 1996.
3. S.M. Rao, D.R. Wilton, and A.W. Glisson, "Electromagnetic Scattering by Surfaces of Arbitrary Shape", *IEEE Trans. on Antennas and Propagation*, Vol. AP-30, pp. 409-418, 1982.

Scattering of Electromagnetic Waves in Large-Scale Rough Surface Problems Based on the Sparse-Matrix Canonical-Grid Method

Kyung Pak*, Leung Tsang, Chi Hou Chan, Joel Johnson** and Qin Li
Electromagnetics and Remote Sensing Laboratory
Department of Electrical Engineering
Box 352500
University of Washington, Seattle, WA 98195-2500
*Jet Propulsion Laboratory, MS 300-235
California Institute of Technology
4800 Oak Grove Drive, Pasadena, CA 91109
**Department of Electrical Engineering
2015 Neil Ave., Columbus, OH 43210

Abstract Wave scattering from random rough surfaces is a large-scale computational electromagnetic problem because in order to simulate the wave scattering statistics, we need to calculate scattering from a large surface of many square wavelengths in extent. In this paper scattering of a 3-dimensional electromagnetic wave from random rough surfaces is studied with the sparse-matrix canonical grid method (SMCG). The key idea of SMCG is that interactions are decomposed into a near field which is represented by a sparse matrix and a non-near field which is Taylor expanded about a flat surface and subsequently calculated by FFT. The method is used for Monte-Carlo simulations of random rough surface problems of perfectly conducting surfaces and dielectric surfaces. Numerical examples are illustrated with up to 130,000 surface unknowns, surface areas up to 1024 square wavelengths, rms heights of up to one wavelength, and up to 1000 realizations. In the case of a perfectly conducting surface, comparisons with controlled laboratory experimental data show good agreement. For some cases, backscattering enhancement is observed in both co- and cross-polarization.

1 Introduction

The study of electromagnetic wave scattering by random rough surfaces is a topic of continuing interest due to its engineering and scientific applications. In mobile communications, the reflection of signals by rough terrain causes propagation loss. In remote sensing, backscattering coefficients from rough terrain are used to derive terrain media properties. In target detection problems, ground and ocean clutter can obscure scattering signals from the target. The electromagnetic wave scattering problem from random rough surfaces is a large-scale computational electromagnetic problem because in order to simulate the wave scattering statistics, we need (1) to solve Maxwell's equation for a large surface of, say, 20 wavelengths x 20 wavelengths = 400 square wavelengths in extent. Only such large surfaces have sufficient numbers of rough surface peaks and valleys to represent a statistical sample (a

realization), and (2) Maxwell's equations have to be solved for many realizations of rough surfaces in order to calculate the average scattered field, average scattered intensity, and covariance of electromagnetic fields. Realizations of rough surfaces refer to rough surfaces that have different height profiles and yet have the same statistics.

Three-dimensional electromagnetic wave scattering from a random rough surface is studied with Monte Carlo simulations [2,4-6]. The solution of the matrix equation is calculated using the sparse-matrix canonical grid method (SMCG). The method is applied to perfectly conducting [4,5] and dielectric surfaces [6]. The SMCG is the direct extension of the BMIA/CG [1] to three-dimensional scattering problems. Interactions are decomposed into near field which is represented by a sparse matrix and a non-near field which is Taylor expanded with a flat surface and subsequently calculated by FFT. Numerical examples are illustrated with up to 130,000 surface unknowns, surface areas up to 1024 square wavelengths, rms heights of up to one wavelength, and up to 1000 realizations. In the case of a perfectly conducting surface, comparisons with controlled laboratory experimental data show good agreement. We have also applied the method to ocean surface scattering.

In this paper the SMCG is formulated for the 3-D random rough surface scattering problem. The method is also applied to study backscattering enhancement from both 2-D perfectly conducting random rough surfaces and dielectric random rough surfaces. In the case of a perfectly conducting surface, Monte-Carlo simulation results are presented for an incident angle of 20° (measured from the normal to the mean surface plane), rms heights of 1.0 λ, rms slopes of 0.5 and 0.7, and a surface area of 1024 λ^2(up to 131,072 surface unknowns). The comparisons with controlled laboratory experimental data show good agreement. For a dielectric surface, Monte-Carlo simulation results are presented for an incident angle of 10°, moderate rms heights of 0.2 and 0.5 λ, rms slopes of 0.33 and 0.5, and a surface area of 256 λ^2(98,304 surface unknowns). Backscattering enhancement is observed in both co- and cross-polarization for an rms height of 0.5 λ and correlation length of 1.0 λ. However, in the case of rms height of 0.2 λ and correlation length of 0.6 λ, backscattering enhancement is observed only in cross-polarization.

2 Formulation and the Sparse-Matrix Canonical Grid Method

Consider a 3-D electromagnetic wave impinging on a rough surface with a random height profile z =f(x, y). Above the rough surface is a free space. The height function z =f(x, y) is a random process with zero mean. Using the Stratton-Chu surface integral equation formulation and the method of moment (MoM), the matrix equation is formed. The matrix equation is

$$\bar{\bar{Z}}\vec{x} = \vec{b} \qquad (1)$$

where $\bar{\bar{Z}}$ is the impedance matrix, $\vec{x}$ is surface unknowns, and $\vec{b}$ is the incident wave. The above equations can be solved using the matrix inversion method. However, for a large number of surface unknowns (e.g., 98,304 unknowns) the matrix inversion becomes computationally formidable. Thus, the SMCG method has been developed.

In the SMCG, the interaction between two points on the surface is distinguished as either a neighboring interaction (strong) or a non-neighboring interaction (weak). The parameter that

categorizes this neighborhood is the neighborhood distance r_d which defines the boundary between the weak and strong element of the impedance matrix $\overline{\overline{Z}}$ (for example, $r_d = 2\lambda$). Let $\rho_R = \sqrt{(x-x')^2+(y-y')^2}$ represent the horizontal separation between two points on the rough surface (x, y, f(x, y)) and (x', y', f(x', y')). Two types of interactions are defined, with two interacting points with $\rho_R < r_d$ distinguished as the near to intermediate field. Outside of this distance, the interaction is non-near field. Thus, The impedance matrix is decomposed into the sum of a strong and a non-near field matrix.

$$\overline{\overline{Z}} = \overline{\overline{Z}}^{(S)} + \overline{\overline{Z}}^{(W)} \qquad (2)$$

where $\overline{\overline{Z}}^{(S)}$ represents near-field interaction and $\overline{\overline{Z}}^{(W)}$ represents non-near field interaction. However, the non-near field elements, though smaller, can together contribute significantly. The strong matrix is a sparse matrix since r_d is much smaller than the overall dimensions of the rough surface. Thus, most interactions range outside of the neighborhood and are represented by the non-near field matrix elements. The choice of r_d depends on the rough surface statistics and the angle of incidence, but it is much less than L_x and L_y. Therefore, the number of non-zero entries in the non-near field matrix elements are much more numerous than the strong matrix elements.

Next, we note that, for the non-near field matrix elements, the separation of the two points is close to horizontal. Therefore, we expand the Green's function in a Taylor's series about the flat surface, f(x, y)=0. The expansion about f(x, y)=0 makes the flat surface plane a canonical grid. Truncation of the above series depends on the rough surface statistics and the size of r_d. For example, a bigger r_d requires fewer terms in the series. In this paper, we keep the expansion terms at 6 (M=5). Hence, the non-near field matrix equation can be written in following form

$$\overline{\overline{Z}}^{(W)} = \sum_{m=0}^{M} \overline{\overline{Z}}_m^{(W)} \qquad (3)$$

The zeroth term in (3) also called the flat surface contribution

$$\overline{\overline{Z}}^{(FS)} = \overline{\overline{Z}}_0^{(W)} \qquad (4)$$

Hence, equation (1) can be rewritten as

$$(\overline{\overline{Z}}^{S} + \overline{\overline{Z}}^{(FS)} + \sum_{m=1}^{M} \overline{\overline{Z}}_m^{(W)})\vec{x} = \vec{b}$$

The iterative matrix-solving procedure is, for the first-order and higher order solutions

$$(\overline{\overline{Z}}^{(S)} + \overline{\overline{Z}}^{(FS)})\vec{x}^{(1)} = \vec{b} \qquad (5)$$

$$(\overline{\overline{Z}}^{(S)} + \overline{\overline{Z}}^{(FS)})\vec{x}^{(n+1)} = \vec{b}^{(n+1)} \qquad (6)$$

$$\vec{b}^{(n+1)} = \vec{b} - \sum_{m=1}^{M} \overline{\overline{Z}}_m^{(W)} \vec{x}^{(n)} \qquad (7)$$

The new matrix equations (5) and (6) are solved using the conjugate gradient method (CGM). The flat surface matrix $\overline{\overline{Z}}^{(FS)}$ which represents the lowest order Taylor expansion term is on the left-hand side of the matrix equation. This is equivalent to the subtraction of the flat surface term on the right-hand side. This forces the non-near field matrix elements to be small. Without the flat-surface matrix on the

left-hand side, we have observed that the iteration does not converge for some moderately rough surfaces. Thus, the terms strong and weak refer to the magnitude of the matrix elements, instead of their overall contributions to the iterative matrix equation. Each individual non-near field matrix elements contributes little to the matrix equation. However, their combined effects are significant.

Since $\overline{\overline{Z}}^{(FS)}$ is a Toeplitz matrix, the product of $\overline{\overline{Z}}^{(FS)}$ with $\vec{x}$ can be computed using a 2-D fast FFT algorithm which makes conjugate gradient iteration efficient. $\overline{\overline{Z}}_m^{(W)}\vec{x}^{(n)}$ can be translated to canonical grid, so it is also quickly calculated using the FFT.

An additional advantage of the SMCG is that only the Taylor expanded coefficients need to be stored. For example, if the first 6 terms of the coefficients are retained, then 24 complex arrays of $2N_s$ x $2N_s$ are stored (where N_s is the surface dimension). This requires approximately 13 Mbytes of memory for N_s =128 sample points. The strong matrix elements are not stored, they are recalculated as needed.

With the number of Taylor series coefficient fixed at M=5, for a given rough surface the computational complexity will depend on the number of CGM iterations (equation (6)), SMCG iterations (equation (7)) and the neighborhood distance r_d. Dropping the pre- and post multiplication calculations and retaining only the dominant terms, the total number of operations (multiplication) is approximately

$$N_{CGM}[256r_d^2nN + 2N\log(N)m_{FFT}] + N_{SMCG}[72N\log(N)m_{FFT}] \quad (8)$$

where N_{CGM} and N_{SMCG} are the number of iterations in CGM matrix solver and the number of right-hand side updates, respectively, n is the number of sample points per λ^2 and N is the total number of sample points, and m_{FFT} is the total number of FFT's and inverse FFT's. Note that in the above equation, the total number of iterations required for convergence depends on r_d. As an example, consider a simulation with the following number of iterations N_{CGM} = 110 and N_{SMCG} =4, with sampling of n=64, r_d =2.5λ, N=16384 and m_{FFT}=120. The term containing the r_d dominates with 1.55 x 10^{11} computational steps. Therefore, SMCG is most effective for a moderate rms height so that the number of Taylor series expansion terms can be manageable and the neighborhood distance r_d can be much smaller than the surface length. The use of the FFT to fast-sum the computational steps of $\overline{\overline{Z}}_m^{(W)}\vec{x}^{(n)}$ and $\overline{\overline{Z}}^{(FS)}\vec{x}^{(n+1)}$ makes the SMCG efficient. The iteration is carried out until the error norm criterion

$$\sqrt{\frac{\left\|\overline{\overline{Z}}\vec{x}^{(n)} - \vec{b}\right\|}{\left\|\vec{b}\right\|}} < 1\% \quad (9)$$

is satisfied. In this paper, an error norm of 1% is used for all numerical simulations. This criteria has been found to work for the past 1-D and 2-D rough surface simulations.

3 Results and Discussion

We assume the rough surface has a Gaussian power spectrum given by

$$W(K_x,K_y)=\frac{l_x l_y h^2}{4\pi}\exp(-\frac{K_x^2 l_x^2}{4}-\frac{K_y^2 l_y^2}{4}) \qquad (10)$$

where l_x, l_y are the correlation lengths in x and y directions, respectively, K_x and K_y are the spatial frequency in x and y directions, respectively, and h is the surface rms height.

In past simulations, the SMCG method has been rigorously tested for both perfectly conducting 2-D rough surface problems [4,5] and 2-D dielectric rough surface [6]. In this section we describe various results.

In Figure 1 and 2, the Monte Carlo simulation results from perfectly conducting rough surfaces of both experimental and numerical results are given. The experimental data was obtained from the University of Washington electromagnetics and remote sensing laboratory. Both the Monte Carlo simulation and the experiment show backscattering enhancement for all co-polarized and cross-polarized components. The comparison is generally good in view of the fact that absolute values are compared and there are no adjustable parameters. In Figure 1, the average normalized bistatic scattering coefficients are plotted for up to 100 realizations. The surface is sampled at 64 points per λ^2 to give 131,072 surface unknowns. In Figure 2, the average normalized bistatic scattering coefficients are plotted for up to 600 realizations. The surface is sampled at 16 points per λ^2 to give 32768 surface unknowns.

In Figure 3 to Figure 5, the Monte Carlo simulation results from a dielectric rough surface are given. In figure 3, we carry out a power conservation test for a lossless dielectric rough surface. We can observe power conservation variation with respect to the second medium relative permittivity. A general decrease in power conservation from 99.8% to 98.9% is seen as relative permittivity increases from ε_r=3 to ε_r=7 . Thus, for a free space sampling rate of 64 points per λ^2, the maximum value that the second medium relative permittivity can be is 7 in order to satisfy energy conservation to within 1%. In Figure 4, the average normalized bistatic scattering coefficients are plotted for up to 300 realizations. The surface is sampled at 64 points per λ^2 to give 98,304 surface unknowns. Note that the sharp forward specular peak at 10° is present in the co-polarized scattering component. Unlike the co-polarized component, a peak in the backscattering direction can be seen. Backscattering enhancement is a result of higher order scattering. Analytically, they are the contributions of the cyclical scattering diagrams (maximally crossed Feynman diagrams) which start at the second-order. For co-polarization, the second-order terms can be obscured by the presence of first-order scattering. However, for cross-polarization, the first-order scattering is zero. Thus, the second-order backscattering enhancement can be more clearly exhibited for the cross-polarized case as seen in this example. It is informative to note that on the average approximately 25 CPU hours are required for one realization on a DEC Alpha workstation. The average number of iterations required for Figure 4 are N_{CGM}=105 and N_{CG}=4. With N=16384 and m_{FFT}=120, equation (8) gives approximately 2.5×10^{11} computational steps. A Monte Carlo simulation of the backscattering enhancement is illustrated for both co- and cross-polarization in Figure 5, for the case of larger rms height. The surface parameters of h=0.5 λ and l=1.0 λ are moderately rough with an incident angle of 10°.

REFERENCES

1. L. Tsang, C. H. Chan, K. Pak, and H. Sangani, ``A BMIA/FFT algorithm for the Monte-Carlo simulations of large scale random rough surface scattering: Application to grazing incidence," IEEE Antennas Propagat. Soc. Int. Symp., vol. 3, pp. 2028-2031, 1994.
2. L. Tsang, C. Chan, and K. Pak, ``Monte-Carlo simulation of a two-dimensional random rough surface using the sparse-matrix flat-surface iterative approach," Electron. Lett., vol. 29, pp. 1153-1154, 1993.
3. L. Tsang, C. H. Chan, K. Pak, and H. Sangani, ``Monte-Carlo simulations of large-scale problems of random rough surface scattering and applications to grazing incidence with the BMIA/Canonical grid method," IEEE Trans. Antennas Propagat. vol. 43, pp. 851-859, 1995.
4. K. Pak, L. Tsang, C. H. Chan, and J. T. Johnson, ``Backscattering enhancement of vector electromagnetic wave from two-dimensional perfectly conducting random rough surfaces based on Monte-Carlo simulations," J. Opt. Soc. Am. A, vol. 12, pp. 2491-2499, 1995.
5. J. T. Johnson, L. Tsang, R. Shin, K. Pak, C. Chan, A. Ishimaru, and Y. Kuga, ``Backscattering enhancement of electromagnetic waves from two-dimensional perfectly conducting random rough surfaces: a comparison of Monte-Carlo simulations with experimental data," IEEE Trans. Antennas Propagat., vol. 44, pp. 748-756, 1996.
6. K. Pak, ``Studies of large-scale random rough surface scattering problems based on Monte-Carlo simulations with efficient computational integral equation methods," Ph.D dissertation, Dept. of Electrical Engineering, Univ. of Washington, August, 1996.

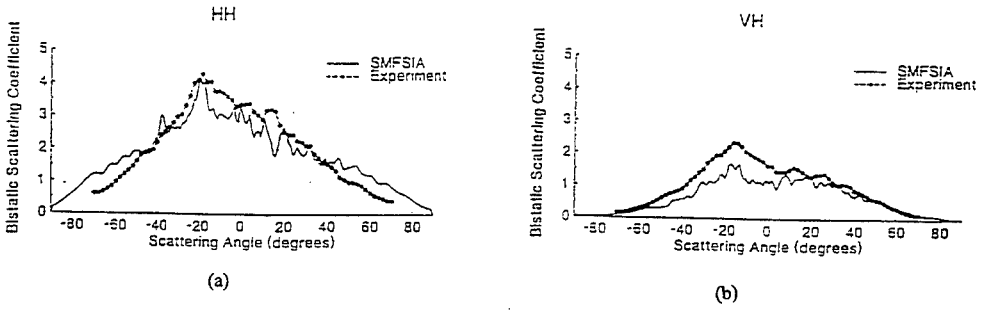

Fig. 1. Monte Carlo simulation comparison of the SMCG and the experimental data of backscattering enhancement. Rough surface parameters (Gaussian roughness spectrum) $L_x=L_y=32\lambda$, $h=1.0\lambda$, $l_x=l_y=1.41\lambda$; incident angles $\theta_i=20°$ and $\varphi_i=0°$; (a) co-polarized result (b) cross-polarized result. (Incident wave horizontally polarized)

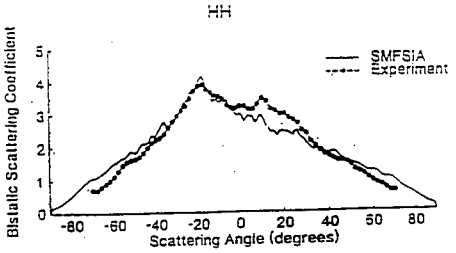

(a)

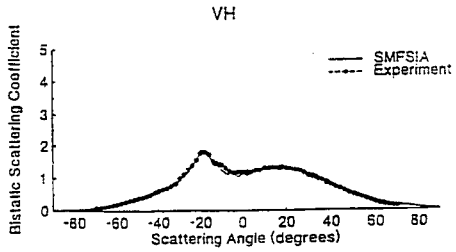

(b)

Fig. 2. Monte Carlo simulation comparison of the SMCG and the experimental data of backscattering enhancement. Rough surface parameters (Gaussian roughness spectrum) $L_x=L_y=32\lambda$, $h=1.0\lambda$, $l_x=l_y=2.0\lambda$; incident angles $\theta_i=20°$ and $\varphi_i=0°$; (a) result (b) cross-polarized result. (Incident wave horizontally polarized)

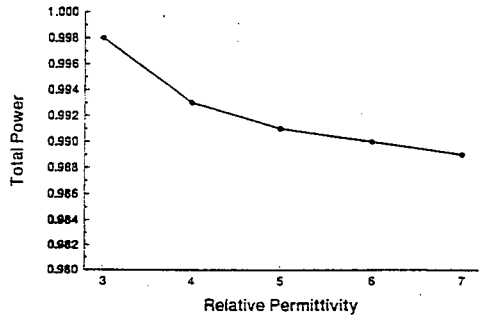

Fig. 3. Dependence of power conservation error on ε_r. $L_x=L_y=8.0\lambda$, $h=0.5\lambda$, $l_x=l_y=1.0\lambda$; $\theta_i=10°$ and $\varphi_i=0°$; $r_d=3.5\lambda$.

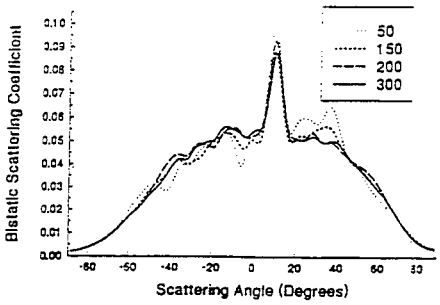

(a)

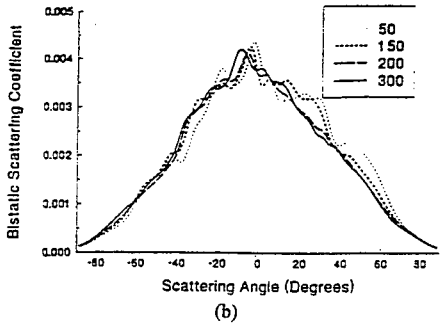

(b)

Fig. 4. Bistatic scattering coefficients for $L_x=L_y=16\lambda$, $h=0.2\lambda$, $l_x=l_y=0.6\lambda$; $\theta_i=10°$ and $\varphi_i=0°$; $\varepsilon_r=6.5+i1.0$; $r_d=3.0\lambda$. Result illustrates convergence with respect to the number of realizations. (a) co-polarized component (b) cross-polarized component

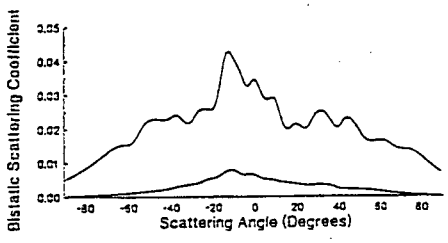

Fig. 5. Bistatic scattering coefficients for $L_x=L_y=8.0\lambda$, $h=0.5\lambda$, $l_x=l_y=1.0\lambda$; $\theta_i=10°$ and $\varphi_i=0°$; $\varepsilon_r=6.5+i1.0$; $r_d=3.5\lambda$. Result illustrates the backscattering enhancement.

Planar Structures Analysis with the Adaptive Integral Method (AIM)

Sunil S. Bindiganavale, John L. Volakis and Hristos Anastassiu
Radiation Laboratory
Department of Electrical Engineering and Computer Science
The University of Michigan
Ann Arbor, MI 48109-2122

Abstract

Fast integral equation algorithms provide for a reduction of the computational complexity of method of moments solutions of integral equations. The adaptive integral method (AIM) is one such algorithm and has been demonstrated to reduce memory down to $O(N^{1.5})$ and complexity down to $O(N^{1.5}\log N)$ for an N unknown surface problem while the corresponding figures for a N unknown volume problem are $O(N)$ and $O(N\log N)$. For flat bodies, the reduction is even further and in this paper we demonstrate the suitability of the AIM to model planar scatterers with intricate geometry details. It is shown that the AIM is extremely accurate while saving a significant amount of memory even for wavelength sized, highly tessellated bodies. The application of the 2D FFT eliminates the speed bottleneck encountered while employing the 3D FFT in the original AIM algorithm. Thus, it promises to be extremely useful in conjunction with the finite element method to handle highly irregular and composite material bodies.

1 Introduction

Research in integral equation techniques has been revitalized since the early 1990s with the introduction and development of techniques which accelerate the computation of matrix-vector products in iterative solutions of integral equations. The Adaptive Integral Method (AIM) [1] and the Fast Multipole Method (FMM) [2],[3],[4] belong to this class of techniques. While most of the initial applications of these techniques focussed on electromagnetic scattering from conducting bodies, they have recently also been used successfully in a hybrid environment [5],[6] to evaluate the scattering from composite structures. In this paper, we show that the AIM is particularly suitable for analysis of flat bodies. Unlike previous work in the literature, we examine the benefits of the AIM when the body is not electrically large, but has to be highly tessellated owing to its intricate construction, thus leading to a large number of unknowns.

2 Formulation

As in all fast integral equation algorithms based on iterative solvers, the integral equation is discretized using standard method of moments procedure. Thus, the equivalent electric current $\mathbf{J}$ on a body whose surface S is illuminated by an incident plane wave $\mathbf{E}^i$ is expanded in terms of basis functions $\mathbf{f}_q(\mathbf{r}')$ as

$$\mathbf{J}(\mathbf{r}') = \sum_q I_q \mathbf{f}_q(\mathbf{r}') \tag{1}$$

where I_q are unknown coefficients. Application of Galerkin's technique leads to the linear system

$$[Z]\{I\} = \{V\} \tag{2}$$

where the interaction matrix $[Z]$ is of the form

$$Z_{pq} = jkZ \int_S \int_S \mathbf{f}_p(\mathbf{r}) \cdot \overline{\overline{\mathbf{G}}}_e(\mathbf{r}, \mathbf{r}') \cdot \mathbf{f}_q(\mathbf{r}') \, dS dS' \tag{3}$$

and the excitation vector

$$V_p = \int_S \mathbf{E}^i \cdot \mathbf{f}_p(\mathbf{r}) dS \tag{4}$$

whereas $\{I\}$ is the vector of the unknown coefficients and $\overline{\overline{\mathbf{G}}}_e$ is the pertinent dyadic Green's function. To complete the discretization, we employ edge-based, divergenceless, linear basis functions first employed in [7]. Application of the AIM requires the whole geometry be enclosed in a regular rectangular grid. Each interior edge is expressed as a superposition of delta functions at the vertices of the square that surrounds its center. The new basis functions ψ_m corresponding to the m^{th} edge are given by

$$\psi_m = \sum_{q=1}^{M^2} \delta(x - x_{mq}) \delta(y - y_{mq}) [\Lambda^x_{mq} \hat{x} + \Lambda^y_{mq} \hat{y}] \tag{5}$$

where $\mathbf{r}_{mq}$ are locations of M^2 points on the square surrounding the center of the edge and $\Lambda^{x,y}_{mq}$ are suitable coefficients, chosen so that the new set of basis functions is equivalent to the initial basis. Equivalence is achieved by requiring the equality of the two sets of basis functions to the order M, thus determining the Λ coefficients. The approximate impedance matrix calculated via the auxiliary basis functions is given by

$$[Z]^{total}_{AIM} = \sum_{i=1}^{3} [\Lambda]_i [G] [\Lambda]^T_i \tag{6}$$

$[\Lambda]_i$ are sparse matrices and $[G]$, defined on the regular grid is Toeplitz. Based on a threshold distance, $[Z]^{total}_{AIM}$ can be split as

$$[Z]^{total}_{AIM} = [Z]^{near}_{AIM} + [Z]^{far}_{AIM} \tag{7}$$

On the same lines, the exact impedance matrix is

$$[Z] = [Z]^{near} + [Z]^{far} \tag{8}$$

and for the far field $[Z]^{far} \simeq [Z]^{far}_{AIM}$ thus giving

$$[Z] \simeq [Z]^{near} - [Z]^{near}_{AIM} + [Z]^{total}_{AIM} \tag{9}$$

The Toeplitz property of the Green' function, defined on the regular grid, enables the use of the FFT to accelerate the computation of the matrix-vector product. For the AIM with a 3D grid it can be shown that the memory and computation time are given by $O(N_g)$ and $O(N_g \log_2 N_g)$ where N_g is the number of grid points and for a scatterer which is a parallelepiped with sides a,b,c is given by

$$N_g \simeq \frac{abc}{8(ab + bc + ca)^{3/2}} N^{3/2} \tag{10}$$

where N is the number of original unknowns. From (10) the improvement in speed for a flat scatterer is apparent.

3 Results

When examining the merits of a fast integral algorithm such as AIM, of importance is the memory and CPU requirements, both contrasted to the delivered accuracy. The near-zone radius or threshold distance (the interactions between elements which are electrically closer than a set threshold distance are evaluated with the regular MoM) has a dramatic impact on the CPU requirements since it controls the non-zero element population of the system matrix. Moreover, in the case of AIM, because of the inherent mapping to a constant grid, we are highly interested in examining its suitability in modeling small and fine details embedded in much larger scale structures. In fact, the calculations for the six plate configurations given below are intended to address this issue by examining the method's performance in a number of representative and practical situations. All of the included results were generated using single precision arithmetic on an HP9000/C-110 workstation with a rated peak flop rate of 47 Mflops (level 4 optimization was also employed). Also, in all cases a third order (M=3) multipole expansion was used with a grid spacing of 0.05λ.

Figures 1-6 depict the $\hat{\theta}\hat{\theta}$ and $\hat{\phi}\hat{\phi}$ polarization radar cross section as calculated by the AIM method for the different threshold distances indicated. The pattern cuts are in the $\phi = 0^0$ principal plane of the plate structure. The first two plates (a rectangular and a circular) have no holes and were used to validate the method with the traditional MoM. From the pattern comparisons, it is clear that AIM recovers the exact result very well with only minor differences in the deep nulls of the RCS pattern. As given in Table 1, AIM achieves this with at least a factor of five less memory than the traditional MoM even though the geometries are still rather small to demonstrate the impact of AIM. Moreover, Table 1 shows that a near zone radius of 0.2λ is sufficient to maintain good accuracy (below one dB in RMS error [8]). To our surprise, the advantage of AIM is even more pronounced when holes are inserted into the plates surfaces. As depicted in Figures 3-6, AIM maintains its accuracy for the same threshold criterion even though the slots have a dominant effect on the RCS pattern as shown in Fig. 7. In the case of narrow slots (or thin ridges in the plates) of width 0.03λ, the memory requirements of the traditional MoM increase quickly due to the higher element density. However, in AIM we can still use a constant and uniform grid density of 0.05λ without accuracy deterioration, even though the cell width is larger than the smallest detail in the geometry. **The geometry in Figure 6 yields a saving in memory of 79% while the CPU time is cut by a factor of 12, retaining the accuracy to a tenth of a dB.** This is an important feature of AIM, because it demonstrates that the near zone threshold criterion is not affected by the specific geometrical details, leading to tremendous memory savings. Moreover, the accuracy of the results demonstrate that AIM can handle highly irregular and resonant (i.e. antenna) geometries as well as smooth scatterers.

4 Some Remarks

The performance is clearly much improved when using a 2D (rather than a 3D) FFT for calculating the RCS of flat complex scatterers. A memory reduction of 5 to 10 times over traditional MoM was observed without compromise in accuracy when using a threshold radius of 0.2λ. There was appreciable savings in CPU time for the geometry in Figure 6 and it can be reduced considerably by parallelization or by using optimized FFTs. However, it should be pointed out that the convergence rate of the iterative solver is affected by the use of AIM as seen in Figure 8.

References

[1] E. Bleszynski, M. Bleszynski, and T. Jaroszewicz. AIM: Adaptive integral method for solving large-scale electromagnetic scattering and radiation problems. *Radio Science*, 31(5):1225–1251,

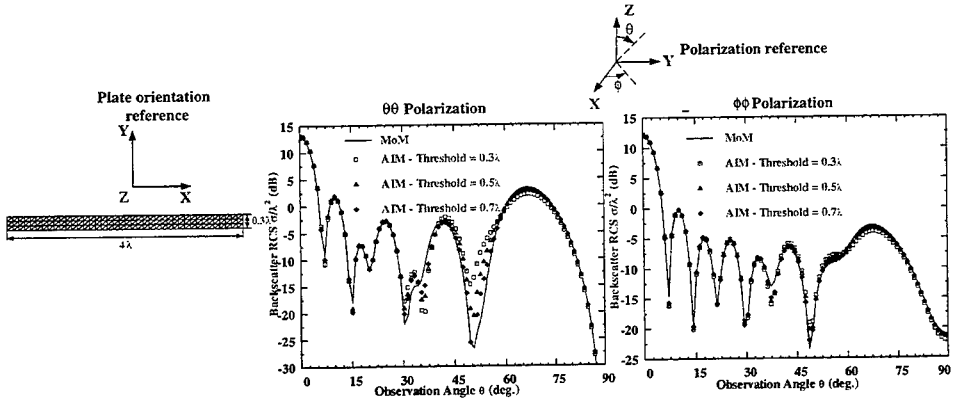

Figure 1: Monostatic RCS for a rectangular $4\lambda \times 0.3\lambda$ plate computed with standard MoM & AIM

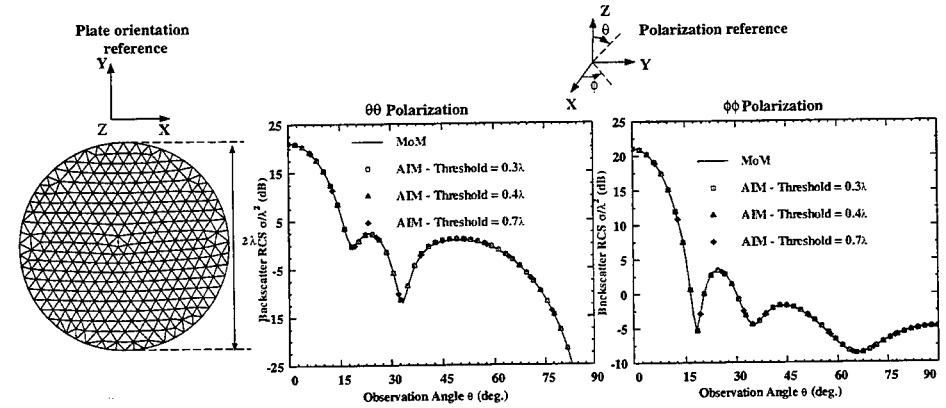

Figure 2: Monostatic RCS for a circular plate of diameter 2λ computed with standard MoM & AIM

Geometry	Discretization			MoM memory (MB)	MoM solution time $\hat{\theta}\hat{\theta}$ pol ($\theta = 0^0$ inc.)
	Facets	Edges	Unknowns		
Figure 1	240	403	317	0.76	6 secs
Figure 2	586	908	850	5.51	32 secs
Figure 3	710	1129	1001	7.64	1 min 32 secs
Figure 4	554	890	772	4.54	29 secs
Figure 5	1130	1806	1584	19.14	4 mins 50 secs
Figure 6	1036	1667	1441	15.84	4 mins

Geometry	AIM Data					
	Threshold (λ)	Non-Zeros in Near Z	Memory (MB)	Solution time $\hat{\theta}\hat{\theta}$ pol ($\theta = 0^0$ inc.)	RMS Error(dB) $\hat{\theta}\hat{\theta}$ pol	$\hat{\phi}\hat{\phi}$ pol
Figure 1	0.3	13724	0.15	6 secs	3.5815	0.9878
	0.5	22996	0.26	7.2 secs	2.2636	0.7070
	0.7	31720	0.36	7.5 secs	1.2806	0.4477
Figure 2	0.3	59928	0.68	23 secs	0.1718	0.0755
	0.4	100182	1.14	25 secs	0.1490	0.0693
	0.7	257390	2.94	28 secs	0.0728	0.0490
Figure 3	0.7	178664	2.04	1 min 17 secs	1.4654	0.7501
Figure 4	0.4	79030	0.9	21 secs	0.0728	0.0583
	0.6	157994	1.8	27 secs	0.0721	0.0520
Figure 5	0.7	283774	3.24	3 mins 32 secs	0.8017	0.5185
Figure 6	0.2	296250	3.39	20 secs	0.1063	0.0949
	0.4	649556	7.43	31 secs	0.0548	0.0632

Table 1: CPU Times and RMS error of AIM in comparison with standard MoM

Sept-Oct 1996.

[2] V. Rokhlin. Rapid solution of integral equations of scattering theory in two dimensions. *J. Comput. Phys.*, 86(2):414–439, 1990.

[3] R. Coifman, V. Rokhlin, and S. Wandzura. The fast multipole method for the wave equation: A pedestrian prescription. *IEEE Antennas and Propagat Mag.*, 35(3):7–12, 1993.

[4] J.M. Song and W.C. Chew. Multilevel fast multipole algorithm for soving combined field integral equation of electromagnetic scattering. *Micro. Opt. Tech. Lett.*, 10:14–19, 1995.

[5] S. S. Bindiganavale and J. L. Volakis. A hybrid FEM-FMM technique for electromagnetic scattering. *IEEE Trans. Antennas and Propagat.*, 45(1):180–181, January 1997.

[6] N. Lu and J. M. Jin. Application of the fast multipole method to finite element-boundary integral solution of scattering problems. *IEEE Trans. Antennas and Propagat.*, 44(6):781–786, 1996.

[7] S.M. Rao, D.R. Wilton, and A.W. Glisson. Electromagnetic scattering by surfaces of arbitrary shape. *IEEE Trans. Antennas and Propagat.*, 30(3):409–418, May 1982.

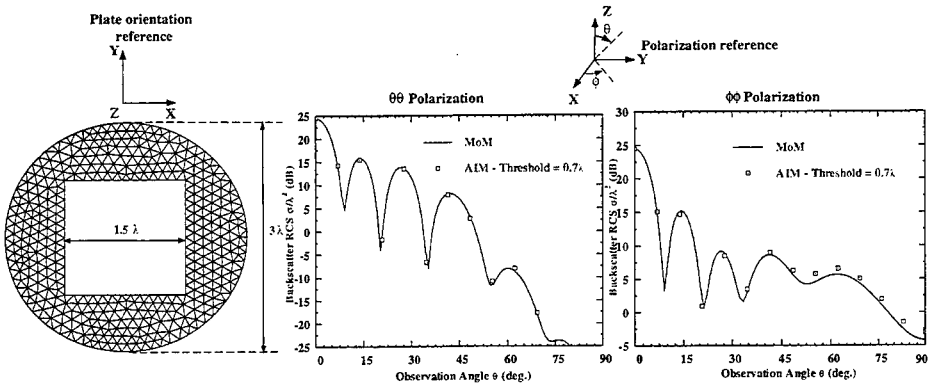

Figure 3: Monostatic RCS for a circular plate of diameter 3λ with a square hole of side 1.5λ computed with standard MoM & AIM

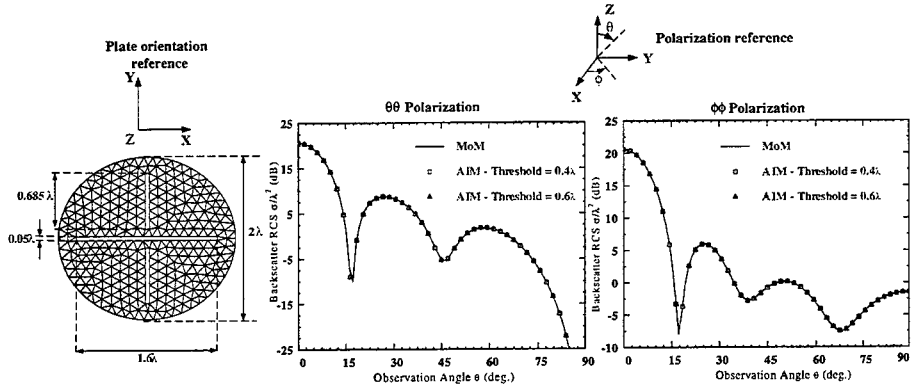

Figure 4: Monostatic RCS for a circular plate of diameter 2λ with three slots computed with standard MoM & AIM

[8] S. S. Bindiganavale and J. L. Volakis. Guidelines for using the fast multipole method to calculate the RCS of large objects. *Micro. Opt. Tech. Lett.*, 11(4):190–194, March 1996.

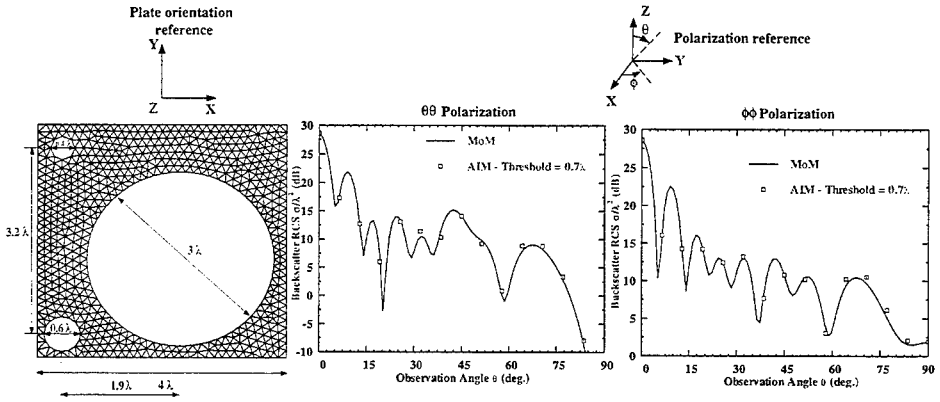

Figure 5: Monostatic RCS for a circular plate of diameter 3λ with three holes computed with standard MoM & AIM

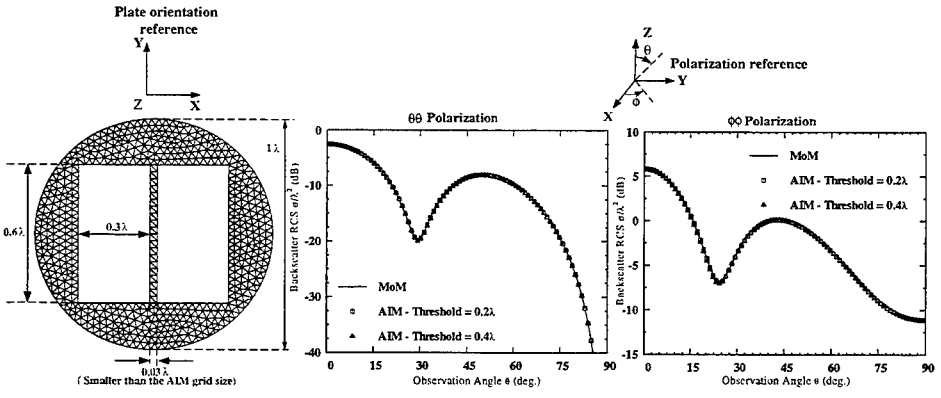

Figure 6: Monostatic RCS for a circular plate of diameter 1λ sampled at 0.03 λ (smaller than the AIM grid spacing) due to the narrow center ridge

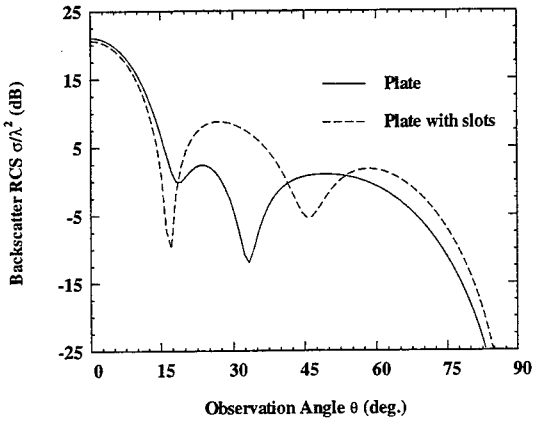

Figure 7: Effect of the narrow slots of Figure 4 on the Monostatic RCS of the 2λ diameter plate of Figure 2

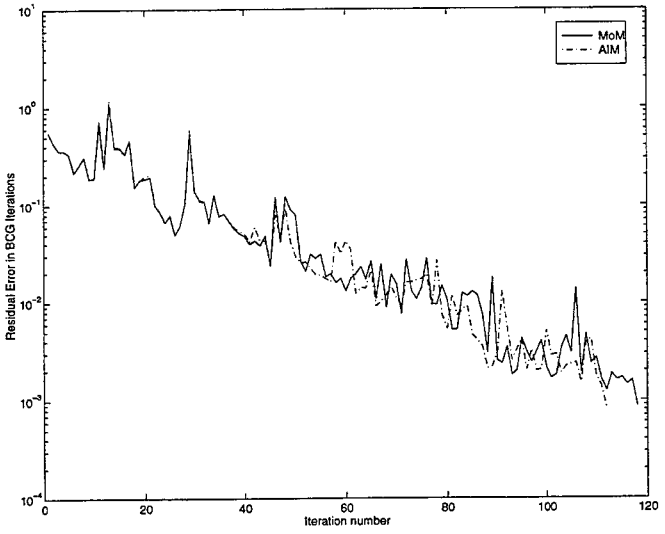

Figure 8: Biconjugate gradient solver convergence curves for the 2λ diameter circular plate at normal indcidence

FAST ILLINOIS SOLVER CODE (FISC) †

J. M. SONG[1,2], C. C. LU[1], W. C. CHEW[1], AND S. W. LEE[2]
[1]CENTER FOR COMPUTATIONAL ELECTROMAGNETICS
DEPARTMENT OF ELECTRICAL AND COMPUTER ENGINEERING
UNIVERSITY OF ILLINOIS, URBANA, IL 61801
[2]DEMACO, INC.
100 TRADE CENTRE DR., CHAMPAIGN, IL 61820

ABSTRACT— FISC (Fast Illinois Solver Code) is designed to compute RCS of a target described by a triangular facet file. The problem is formulated by the method of moments (MoM), where the RWG (Rao, Wilton, and Glisson) basis functions are used. The resultant matrix equation is solved iteratively by the conjugate gradient (CG) method. The multilevel fast multipole algorithm (MLFMA) is used to speed up the matrix-vector multiply in CG. Both complexities for the CPU time per iteration and memory requirements are of $O(N\log N)$, where N is the number of unknowns.

1. Introduction

The fast multipole method is an efficient way to perform matrix-vector multiplies whereby the field at each particle due to every other particle is calculated for all particles in an ensemble of N particles. Ordinarily, this would require $O(N^2)$ calculations. With the fast multipole method, this can be reduced to $O(N)$ or $O(N \log N)$ depending on the spatial distribution density of the particles and implementation. The fast multipole method for static problems has been of interest to astrophysicists for calculating Coulombic interaction between stars in galaxies. One of the first such algorithms is due to Barnes and Hut [1]. Later, Rokhlin and Greengard [2,3] described a more efficient method of performing fast multipole calculation for static problems.

Due to the oscillatory nature of dynamic fields, the original fast multipole algorithm for statics does not expedite matrix-vector multiplies for dynamic fields. This is because the number of multipoles needed to represent a field accurately depends on the size of the source distribution compared to the wavelength. The larger the size of the source distribution, the more the number of multipoles needed to approximate the field well, irrespective of the distance of the observation point from the sources.

Rokhlin [4] first suggested a diagonal form of the translation matrices in order to achieve reduction in computational complexity for surface scatterers. This was first demonstrated for acoustic problems. Then Lu and Chew [5] demonstrated the fast multipole concept for vector electromagnetic problems in two dimensions. Coifman, Rokhlin and Wandzura [6] furnished a lucid description of the fast multipole method for three dimensional electromagnetic problems. An implementation of the algorithm was later provided by Song and Chew [7] for 3D vector electromagnetic scattering problems.

Unlike static problems, the fast multipole method for dynamic problems cannot be easily

† This work was supported by the Office of Naval Research under grant N00014-95-1-0872, the National Science Foundation under grant NSF ECS 93-02145, and AFOSR under a MURI grant F49620-96-1-0025.

extended to the multilevel due to the oscillatory nature of the field. A method of treating the oscillatory field was suggested by Brandt [8] using interpolation and anterpolation. The idea of interpolation and anterpolation was later combined with the fast multipole method to arrive at a multilevel fast multipole algorithm (MLFMA) by Lu and Chew [9]. This was later generalized to three-dimensional vector electromagnetic problems by Song and Chew [10]. This results in an $O(N \log N)$ algorithm for performing matrix-vector multiplies for surface scatterers, and $O(N)$ algorithm for volumetric scatterers. Meanwhile, an $O(N \log^2 N)$ method of interpolation and smoothing for a multilevel fast multipole method using group-theoretic technique has been proposed by Dembart and Yip [11]. Another form of the multilevel algorithm has also been proposed by Michielssen and Boag albeit with $O(N \log^2 N)$ complexity [12].

Because the multilevel fast multipole algorithm (MLFMA) expedites matrix-vector multiplies, it can be used to speed up iterative solutions of scattering problems. We have combined MLFMA with the conjugate gradient (CG) and the biconjugate gradient (BCG) methods to arrive at efficient solvers for matrix equations arising from integral equation of scattering. The computational and memory-requirement complexities of this algorithm are both $O(N \log N)$ for surface scatterers. The total CPU time of the matrix solver is hence proportional to $N_{\text{iter}} N \log N$. Compared to traditional matrix solvers requiring $O(N^2)$ memory, and $N_{\text{iter}} N^2$ CPU time for iterative solvers, and $O(N^3)$ CPU time for LUD, this is a vast improvement, especially for large problems. Therefore, large problems that previously require the resources of a supercomputer to solve, can now be solved on a workstation-size computer.

FISC (Fast Illinois Solver Code) is designed to be an industrial-strength code using the most current technology from the method of moments (MoM) [13,14,15] and MLFMA. The method of moments is used carefully to develop a matrix equation from the integral equation. Both curvilinear quad-patch and tri-patch are used. Presently, the tri-patch is restricted to flat facets, but this restriction will be lifted in the future. Careful integrations are performed to account for singularities and near singularities in the evaluation for the matrix elements.

The code was first designed to model the scattering solution from a complex metallic target like an aircraft, so that its RCS (radar cross section) can be ascertained. Presently, impedance boundary conditions, thin dielectric sheets, and resistive boundary conditions can be modeled by the code. In the future, we hope to adapt the code to model material-coated targets as well as radiation of antennas from complex platforms like an aircraft and automobile.

2. Complexity and Accuracy

To test the complexity, we calculate the electromagnetic scattering from a conducting sphere solving the combined field integral equation (CFIE). The machine used is SGI Power Challenge with 4 processors (R8000) and 2 GB of memory. But only one processor is used for the simulations in this paper. The radius of the sphere is from 0.75 λ to 12 λ, number of unknowns (N) is from 2,352 to 602,112, and number of levels in MLFMA is from 3 to 7. The CPU time per iteration and memory requirement are plotted in Figure 1 as functions of the number of unknowns. Two curves, $8 \times 10^{-5} N \log N$ and $2.7 \times 10^{-3} N$, are also plotted on the same figure for comparison.

In Figure 2, we plot the $\theta\theta$ bistatic RCS of a conducting sphere of radius 1 m at 3.6 GHz (the diameter is 24 λ). A total of 602,112 unknowns with a seven-level MLFMA is used. It takes 12 hours on the Power Challenge using one processor [6 hours for set up (filling matrix and calculating plane wave expansions), 4 hours for 41 iterations to reach 0.001 normalized

residual error, and 2 hours for calculating 1,201 points of bistatic RCS]. A good agreement between our result and the Mie series solution is observed. The RMS error is 0.3 dB for all 1,201 points, and 0.08 dB for elevation angles from 90 to -30 degrees (θ is from 0 to 120 degrees, the incident angle is 0 degree).

Figure 3 shows the monostatic RCS for the aircraft (VFY 218) at 100 MHz as functions of azimuth angle in the horizontal plane using the Rockwell flat triangular patch model for HH polarization. The wings of the VFY 218 are on the x-y plane (horizontal plane). Zero degree corresponds to incidence angle on the nose. A five-level MLFMA is used. The measurement data are from H. T. G. Wang, M. L. Sanders, and A. Woo in Naval Air Warfare Center [16]. Good agreement between the numerical results and the measurements is observed. For this 9,747 unknown problem, FISC needs 102 MB of memory for this single-precision code and requires 3 hours of the CPU time on a DEC Alpha workstation for 181 incident angles. In contrast, the LUD solution is estimated to need 800 MB of memory and 10 hours of the CPU time for LUD, and $O(N^2)$ calculations for each incident angle. We estimate that only for 1,000 incident angles, FISC would need the same CPU time as the LUD solution. But it needs memory (102 MB) much less than the LUD solution (800 MB). The comparison is more in favor of FISC when N becomes larger.

3. Capabilities

3.1. Integral Equations

Three kinds of integral equations [17] are used in FISC: electric field integral equation (EFIE), magnetic field integral equation (MFIE), and combined field integral equation (CFIE). We implement Galerkin's method and line matching method in FISC. In Galerkin's method, the testing functions are the same as the basis functions, the RWG basis [13]. In line matching, the testing functions are constant along the line joining the centers of two adjacent patches.

3.2. Boundary Conditions

In addition to PEC, FISC can deal with impedance boundary conditions (IBC), resistive sheets (R-card) and thin dielectric sheet (TDS).

When the coating material has a large refractive index ($|\sqrt{\epsilon\mu/(\epsilon_0\mu_0)}|$, where ϵ and μ are the permittivity and permeability of the coating material), the wave inside the coating sheet propagates approximately in the direction normal to the sheet. Then, the incident angle dependence of the impedance can be neglected. If the material is lossy or the coating sheet is very thin, it can be modeled as IBC with

$$\eta_s = j\sqrt{\frac{\mu}{\epsilon}}\tan\left(\sqrt{\frac{\epsilon\mu}{\epsilon_0\mu_0}}k_0 d\right),$$

where k_0 is the wavenumber in the free space, and d is the thickness. IBC also can be used for lossy, electrically large scatterers, such as the earth and the ocean surface. The scatterer is modeled with IBC using

$$\eta_s = \sqrt{\frac{\mu}{\epsilon}}.$$

In Figure 4, we plot the bistatic RCS for a sphere with 1 m radius at 300 MHz as functions of elevation angle $(90-\theta)$. The impedance of impedance boundary condition is $100 + j37.7$

ohms. The sphere is described by 1,568 flat triangular facets, and three-level MLFMA is used. A good agreement between Mie series and numerical results by FISC is observed.

A thin dielectric sheet can be approximated by an impedance sheet

$$Z = \frac{1}{j\omega d\Delta\epsilon},$$

where d is its thickness, and $\Delta\epsilon = \epsilon - \epsilon_b$, where ϵ_b is the permittivity of the background.

3.3. Initial Guess

For iterative solutions of monostatic RCS, different incident angles require different iterative solutions. Since a small change in the incident angle corresponds to a small change in the current, we use the current solution from the previous angle with phase correction as the initial guess for the next angle. This technique reduces the number of iterations significantly. As an illustration, we calculate the monostatic RCS from the VFY218 at 100 MHz for VV polarization. Zero degree corresponds to incidence angle on the nose. In Figure 5, we plot the number of iterations for different incident angles using three kinds of initial guesses. The first case, which uses zero as the initial guess for all angles, needs about 85 iterations on the average for each angle. The second case, which uses the solution of the previous angle (2° step size) as the initial guess for the next angle, needs about 65 iterations per angle. The third case, which uses the phase-corrected solution of the previous angle as the initial guess for the next angle, needs only about 30 iterations per angle.

3.4. Approximation of Bistatic RCS to Monostatic RCS

For iterative solutions of monostatic RCS, different incident angles require different iterative solutions. Once the current distributions are found, calculating the RCS for one angle needs only $O(N)$ operations. Calculating the bistatic RCS is much less time-consuming than calculating the monostatic RCS. Thus, one advance feature in FISC is the calculation of the monostatic RCS using the bistatic RCS [18]. At 100 MHz, we need the monostatic RCS at 181 angles on the horizontal plane for the AZ angle from 0° to 180° for the VFY 218. We find the current distribution for 19 angles, and then use the approximation of bistatic RCS to monostatic RCS to calculate the monostatic RCS at all 181 points. In Figure 6, we plot the monostatic RCS of the VFY 218 at 100 MHz for HH polarization. The solid line is the monostatic RCS calculated using FISC without the approximation of bistatic RCS to monostatic RCS, the dashed line is the monostatic RCS calculated using FISC with the approximation, which needs only 1.5 hours on a DEC Alpha workstation.

4. Conclusions

FISC (Fast Illinois Solver Code) is designed to compute RCS of a target described by a triangular facet file. The MLFMA has been implemented to speed up the matrix-vector multiplies. Both the memory requirements and the CPU time per iteration are of $O(N\log N)$. Using a block diagonal preconditioner, near singularity extraction, phase corrected previous solution for the initial guess, and the approximation of bistatic RCS to monostatic RCS, we can solve for the electromagnetic scattering by large complex 3D objects like an aircraft (VFY 218) and automobiles on a small computer.

REFERENCES

[1] J. Barnes and P. Hut, "A hierachical $O(N \log N)$ force-calculation algorithm," *Nature,* vol. 324, pp. 446-449, Dec. 4, 1986.

[2] V. Rokhlin, "Rapid solution of integral equations of classical potential theory," *J. Comp. Phys.*, vol 60, pp. 187-207, Sept. 1985.

[3] L. Greengard and V. Rokhlin, "A fast algorithm for particle simulations," *J. Comp. Physics,* vol. 73, pp. 325-348, Dec. 1987.

[4] V. Rokhlin, "Rapid solution of integral equations of scattering theory in two dimensions," *J. Comput. Phys*, vol. 36, no. 2, pp. 414-439, Feb. 1990.

[5] C.C. Lu and W.C. Chew, "A fast algorithm for solving hybrid integral equation," *IEE Proceedings-H*, vol. 140, no. 6, pp. 455-460, Dec. 1993.

[6] R. Coifman, V. Rokhlin, and S. Wandzura, "The fast multipole method for the wave equation: A pedestrian prescription," *IEEE Antennas Propagat. Mag.*, vol. 35, no. 3, pp. 7-12, June 1993.

[7] J.M. Song and W.C. Chew, "Fast multipole method solution using parametric geometry," *Micro. Opt. Tech. Lett.*, vol. 7, no. 16, pp. 760-765, Nov. 1994.

[8] A. Brandt, "Multilevel computations of integral transforms and particle interactions with oscillatory kernels," *Comp. Phys. Comm.*, vol. 65, pp. 24-38, 1991.

[9] C.C. Lu and W.C. Chew, "A multilevel algorithm for solving boundary-value scattering," *Micro. Opt. Tech. Lett.*, vol. 7, no. 10, pp. 466-470, July 1994.

[10] J.M. Song and W.C. Chew, "Multilevel fast-multipole algorithm for solving combined field integral equations of electromagnetic scattering, " *Micro. Opt. Tech. Lett.*, vol. 10, no. 1, pp. 14-19, Sept. 1995.

[11] B. Dembart and E. Yip, "A 3D Fast Multipole Method for Electromagnetics with Multiple Level," *11th Annual Review of Progress in Applied Computational Electromagnetics*, vol. 1, pp. 621-628, Monterey, California, March 1995.

[12] E. Michielssen and A. Boag, "Multilevel evaluation of electromagnetic fields for the rapid solution of scattering problems," *Micro. Opt. Tech. Lett.*, vol. 7, no. 17, pp. 790-795, Dec. 1994.

[13] S.M. Rao, D.R. Wilton, and A.W. Glisson, "Electromagnetic scattering by surfaces of arbitrary shape," *IEEE Trans. Antennas Propagat.*, vol. 30, no. 3, pp. 409-418, May 1982.

[14] G. Antilla and N.G. Alexopoulos, "Scattering from complex three-dimensional geometries using a curvilinear hybrid finite-element-integral equation approach," *J. Optical Soc. America A*, vol. 11, no. 4, pp. 1445-1457, April 1994.

[15] R.D. Graglia, "On the numerical integration of the linear shape functions times the 3-D Green's function or its gradient on a plane triangle," *IEEE Trans. Antennas Propag.*, vol. 41, no. 10, pp. 1448-1455, Oct. 1993.

[16] H.T.G. Wang, M.L. Sanders, and A.C. Woo, "Radar cross section measurement data of the VFY 218 configuration," NAWCWPNS TM 7621, Jan. 1994.

[17] J.M. Song and W.C. Chew, "Fast multipole method solution of combined field integral equation," *11th Annual Review of Progress in Applied Computational Electromagnetics*, vol. 1, pp. 629-636, Monterey, California, March 1995.

[18] M.J. Schuh, A.C. Woo, and M.P. Simon, "The monostatic/bistatic approximation," *IEEE Antennas Propagat. Mag.*, vol. 36, no. 4, pp. 76-78, Aug. 1994.

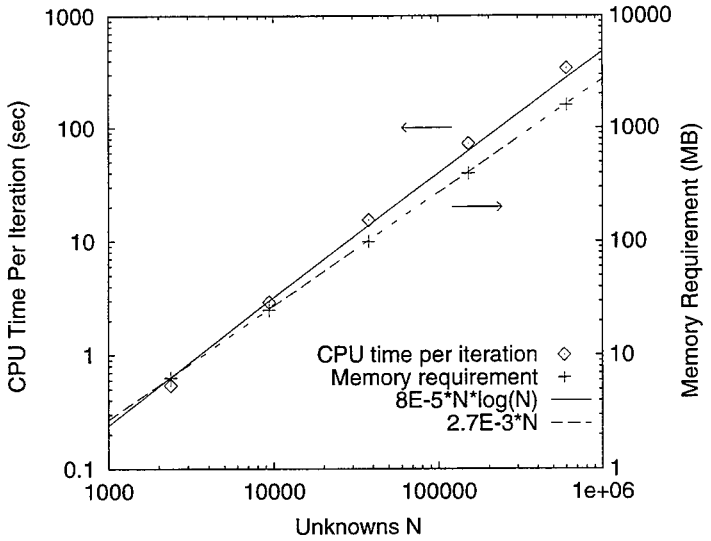

Figure 1. CPU time per iteration and memory requirements (points) as functions of number of unknowns for FISC. Two curves, $8 \times 10^{-5} N \log N$ and $2.7 \times 10^{-3} N$, are also plotted for comparison.

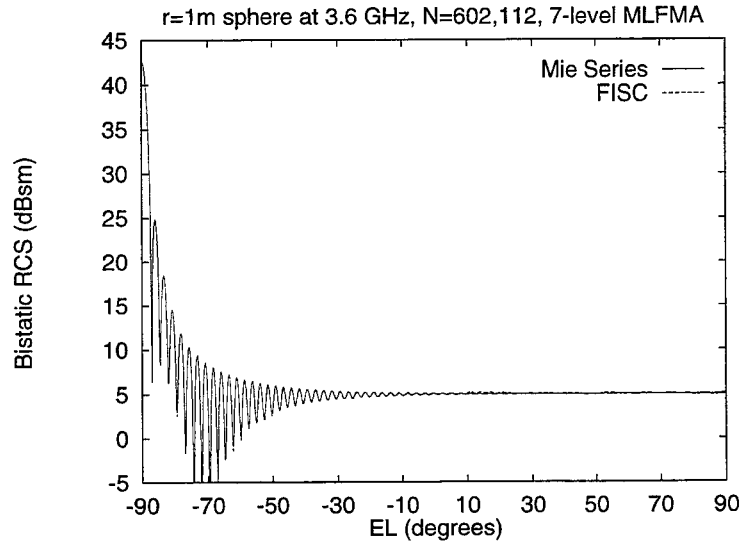

Figure 2. Validations of CFIE with MLFMA against the Mie series of the bistatic RCS of a metallic sphere of radius 1 m at 3.6 GHz for $\theta\theta$ polarization. A total of 602,112 unknowns with a seven-level MLFMA is used.

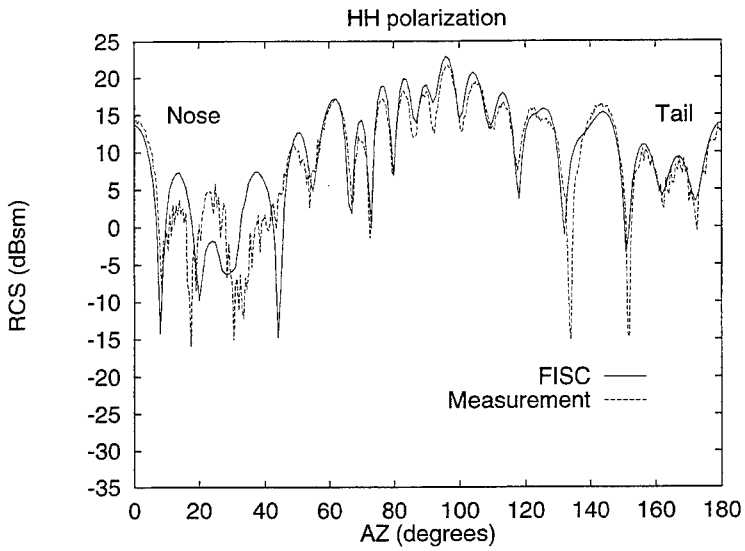

Figure 3. The monostatic RCS of the VFY 218 at 100 MHz. The measurement data are from Naval Air Warfare Center [20] (HH polarization).

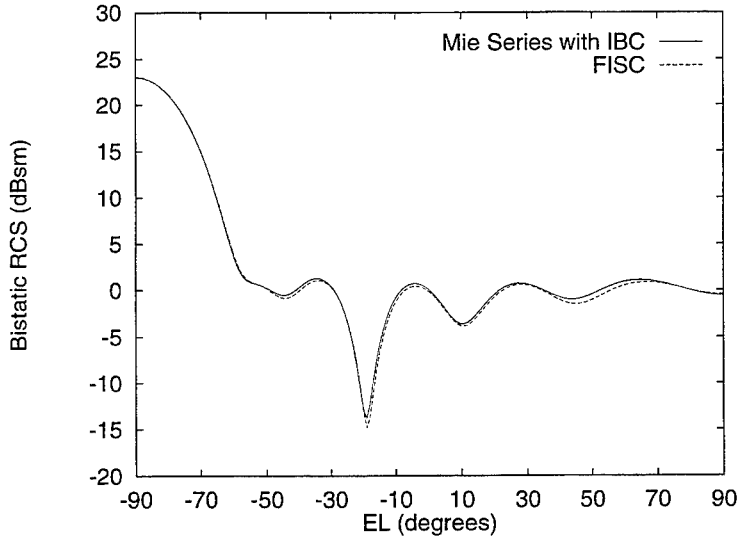

Figure 4. Bistatic RCS for a sphere with 1 m radius at 300 MHz as functions of elevation angle $(90 - \theta)$. The impedance of impedance boundary condition is $100 + j37.7$ ohms.

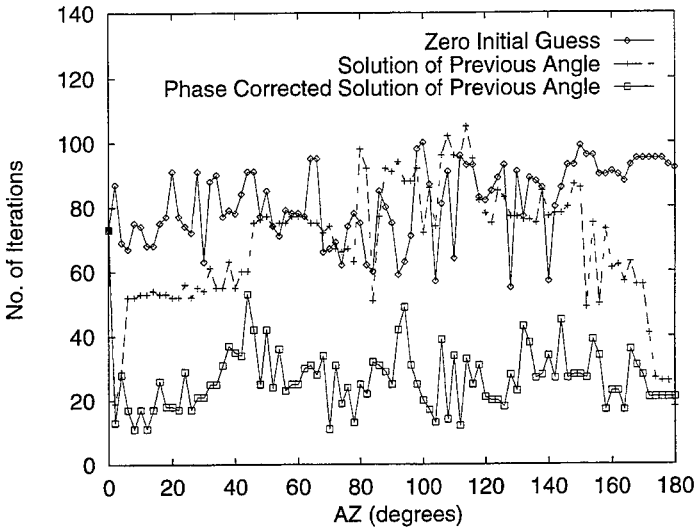

Figure 5. No. of iterations as functions of incident angles for different initial guesses: using zero initial guess for all angles, using the solution of the previous angle for the next angle with/without phase corrections.

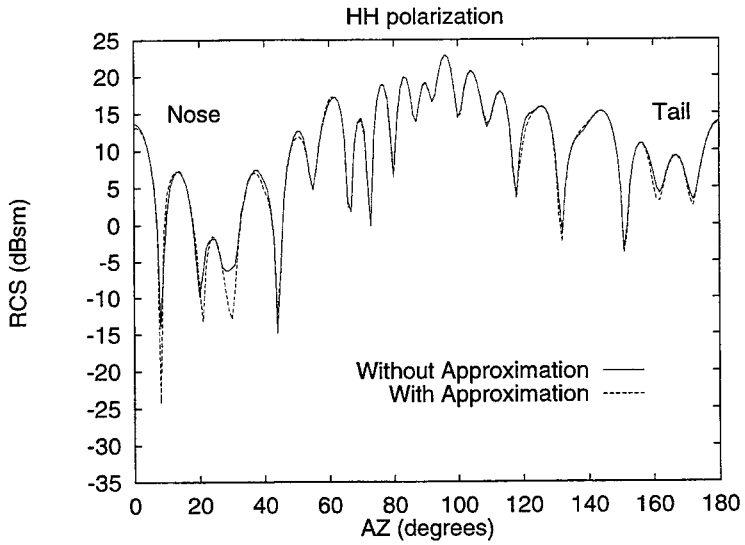

Figure 6. The monostatic RCS of the VFY 218 at 100 MHz. The numerical results with/without the approximation of bistatic RCS to monostatic RCS are calculated using FISC (HH polarization).

A Hybrid Fast Steepest Descent - Multipole Algorithm for Analyzing 3-D Scattering from Rough Surfaces

Vikram Jandhyala, Eric Michielssen, and Weng C. Chew
Center for Computational Electromagnetics
Department of Electrical and Computer Engineering
University of Illinois at Urbana-Champaign
1406 W. Green St., Urbana, IL 61801
Email: vikram@decwa.ece.uiuc.edu

Abstract

This paper describes a new multilevel algorithm for analyzing scattering from perfectly conducting 2-D rough surfaces. The proposed technique exhibits linear scaling in both CPU time and memory requirements. The method is based on a hybrid steepest descent-fast multipole formulation which takes advantage of the quasi-planar nature of random rough surfaces. An extremely efficient steepest descent integration is coupled with a multilevel fast multipole-like algorithm developed for inhomogeneous plane waves. It is rigorously shown that this method possesses linear computational complexity. Using this technique, very large surfaces can be analyzed in reasonable times. Comparisons with standard moment methods, Monte Carlo runs, and CPU times and memory requirements are presented.

1 Introduction

Electromagnetic scattering by rough surfaces [1] is an important topic in several diverse fields including remote sensing and physics of surfaces. Several analytical and numerical techniques have been developed for the efficient analysis of scattering by one- and two-dimensional rough surfaces, which constitute two- and three-dimensional scattering problems respectively. Of the numerical techniques utilized for this purpose, the Method of Moments (MoM) is probably the most popular. For large rough surfaces, solution of the MoM system using direct inversion is practically impossible due to CPU time and memory constraints. Moreover, the iterative solution of the MoM system arising from an integral equation formulation of the three-dimensional problem is a time consuming process, with both the number of operations per iteration and the memory to store the matrix scaling as $O\left(N^2\right)$, where N is the dimension of the system. Complexity reducing multilevel algorithms, such as the Fast Multipole Method (FMM), are necessary in order to minimize memory requirements and lower solution times. Two extremely efficient multilevel techniques tailored specifically towards rough surface analysis that use a Fast Fourier Transform (FFT) as part of their formulation are the Sparse-Matrix Flat Surface Iterative Algorithm (SMFSIA) [2] and the FMM-FFT [3]. These methods take advantage of the fact that rough surfaces are *quasi-planar* to alleviate the CPU time and memory burden. Both these techniques have $O(N \log N)$ computational complexity.

In this paper, a new technique, the Steepest Descent–Fast Multipole Method (SDFMM) is developed for the fast analysis of three-dimensional scattering from two-dimensional perfectly conducting rough surfaces. Advantage is taken of the fact that rough surfaces are quasi-planar in order to derive extremely efficient numerical integration rules for the steepest descent integration of the Sommerfeld integral representation of the free-space Green's function. Hankel functions arising in the integrand are evaluated efficiently using a multilevel FMM-like algorithm that is tailored towards rough surface analysis: the Green's function is expressed in terms of an inhomogeneous plane wave expansion. The proposed SDFMM has $O\left(N\right)$ CPU time and storage requirements. The technique is numerically rigorous and its accuracy can be controlled and traded off for computational efficiency.

This paper is organized as follows. Section 2 describes the formulation of the SDFMM technique. In Section 3, complexity estimates are computed for the SDFMM. Numerical results are presented in Section 4, and Section 5 contains our conclusions.

2 Formulation of the SDFMM

This paper focuses on scattering from Gaussian surfaces. These surfaces are chosen solely for illustration purposes as the proposed SDFMM technique is applicable to arbitrary quasi-planar scatterers. Random rough surfaces with

a Gaussian distribution are generated in a two-step process. An uncorrelated Gaussian distribution is obtained on a discrete two-dimensional regular grid and then filtered in the spectral domain using a Gaussian filter. The parameters associated with this process are the variance σ of the zero mean Gaussian generator and the correlation length l of the filter.

In order to analyze scattering from these Gaussian surfaces, a finite sample surface S of dimensions $L \times L$ centered at the origin is considered. It is necessary to avoid undesired edge effects when using finite surfaces to model essentially infinite ones. Therefore, in order that the illumination on the surface be spatially limited, a Gaussian-weighted sum of plane waves is utilized as the excitation.

An electric field integral equation (EFIE) is used to find the field scattered by the surface S when excited by the incident Gaussian beam. The standard MoM technique, with the Rao-Glisson-Wilton basis, is used to discretize the EFIE.

In the EFIE, the three-dimensional dynamic scalar Green's function

$$g(\mathbf{r},\mathbf{r}') = \frac{e^{ik_0|\mathbf{r}-\mathbf{r}'|}}{4\pi|\mathbf{r}-\mathbf{r}'|} , \tag{1}$$

where k_o is the free-space wavenumber, can be cast into a contour integral form using a Sommerfeld identity. An approximate Steepest Descent Path (SDP) can be derived for the integral based on the far field approximation to the Hankel function. The final form of the integral along the SDP is

$$\frac{e^{ik_0|\mathbf{r}-\mathbf{r}'|}}{4\pi|\mathbf{r}-\mathbf{r}'|} \cong \frac{k_0(1+i)}{8\pi\sqrt{2}} \int_{SDP} ds\ \cos\left(s\left\{\frac{1-i}{\sqrt{2}}\right\}\right) e^{ik_0(z-z')\sin\left(s\left\{\frac{1-i}{\sqrt{2}}\right\}\right)} H_0^{(1)}\left[k_0|\boldsymbol{\rho}-\boldsymbol{\rho}'|\cos\left(s\left\{\frac{1-i}{\sqrt{2}}\right\}\right)\right] . \tag{2}$$

where $z(z')$ and $\boldsymbol{\rho}(\boldsymbol{\rho}')$ are the cylindrical coordinate representation of $\mathbf{r}(\mathbf{r}')$, and the SDP near the origin is a straight line making an angle of $3\pi/4$ with the positive real axis. It can further be shown that the integrand decays exponentially along the SDP, thereby enabling the use of an efficient integration rule based on a small number of points. Therefore,

$$g(\mathbf{r},\mathbf{r}') \cong \frac{i}{8\pi} \sum_{j=1}^{n_{sd}} w_j\ k_\rho^{(j)}\ e^{ik_z^{(j)}(z-z')}\ H_0^{(1)}\left(k_\rho^{(j)}|\boldsymbol{\rho}-\boldsymbol{\rho}'|\right) , \tag{3a}$$

where

$$k_\rho^{(j)} = k_0\ \cos\alpha_j , \tag{3b}$$

and

$$k_z^{(j)} = k_0\ \sin\alpha_j , \tag{3c}$$

and α_j and w_j are the jth integration point and weight respectively (both complex) of the adopted numerical integration rule having n_{sd} points. Specific integration rules have been developed for the SDFMM, which work in conjunction with the multilevel FMM-like technique described next. The parameters associated with these rules include the rough surface variance and the FMM box size. The performance of these integration rules, as a function of rough surface height, are shown in Fig. 1, for FMM boxes of size $1\lambda \times 1\lambda$.

The Hankel function occuring in the SDP integral can be computed efficiently for several pairs of source and observation locations through a generalization of the free-space FMM by using the addition theorem and transforming to an inhomogeneous plane wave basis. The rough surface is divided hierarchically into blocks lying on a plane, by recursively dividing each block at a particular level into four smaller blocks at the finer level. The block at the coarser level is termed the *parent* and the derivative blocks are its *children*. At the finest level, sources lying in each block are represented by plane wave expansions located at the center of each block, irrespective of the particular z location of the source. The Hankel function can be expressed as:

$$H_0^{(1)}\left(k_\rho^{(j)}|\boldsymbol{\rho}-\boldsymbol{\rho}'|\right) \cong \frac{1}{2\pi}\int_0^{2\pi} d\phi\ e^{ik_\rho^{(j)}|\boldsymbol{\rho}-\boldsymbol{\rho}_c|\cdot\hat{\mathbf{s}}}\ \mathcal{T}\left(k_\rho^{(j)},\hat{\mathbf{s}},\boldsymbol{\rho}_c-\boldsymbol{\rho}_a\right) e^{ik_\rho^{(j)}|\boldsymbol{\rho}_a-\boldsymbol{\rho}'|\cdot\hat{\mathbf{s}}} , \tag{4a}$$

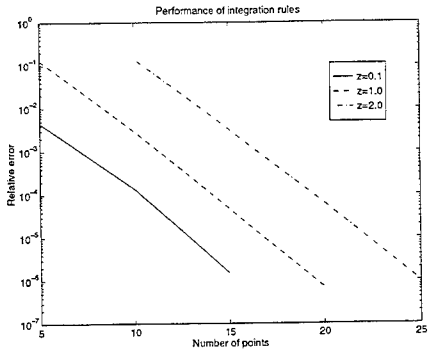

Figure 1: Performance of SDP integration rules

$$\mathcal{T}\left(k_\rho^{(j)}, \hat{\mathbf{s}}, \boldsymbol{\rho}_c - \boldsymbol{\rho}_a\right) = \sum_{p=-P}^{P} H_p^{(1)}(k_\rho^{(j)}|\boldsymbol{\rho}_c - \boldsymbol{\rho}_a|)\; e^{-ip[\theta-\phi-\pi/2]}\;, \tag{4b}$$

where the integral represents contributions from the entire plane wave spectrum, $\boldsymbol{\rho}_a$ and $\boldsymbol{\rho}_c$ are FMM box centers, and $\mathcal{T}$ is the translation operator which depends on the complex wavenumber, spectral angle, and the displacement between source and observation boxes. Also, $\hat{\mathbf{s}} = \hat{\mathbf{x}}\cos\phi + \hat{\mathbf{y}}\sin\phi$, and $\cos\,\theta = \hat{\mathbf{x}}\cdot(\boldsymbol{\rho}_c - \boldsymbol{\rho}_a)/|\boldsymbol{\rho}_c - \boldsymbol{\rho}_a|$. Finally, the dyadic Green's function $\bar{\mathbf{G}}(\mathbf{r},\mathbf{r}')$ appearing in the EFIE is represented in the SDFMM as

$$\bar{\mathbf{G}}(\mathbf{r},\mathbf{r}') \cong \frac{i}{16\pi^2}\sum_{j=1}^{n_{sd}} w_j e^{ik_z^{(j)}(z-z')}k_\rho^{(j)}\left(\bar{\mathbf{I}} - \frac{\mathbf{k}^{(j)}\mathbf{k}^{(j)}}{k_0^2}\right)\int_0^{2\pi} d\phi\; e^{ik_\rho^{(j)}(\boldsymbol{\rho}-\boldsymbol{\rho}_c)\cdot\hat{\mathbf{s}}}\;\mathcal{T}\left(k_\rho^{(j)}, \hat{\mathbf{s}}, \boldsymbol{\rho}_c - \boldsymbol{\rho}_a\right) e^{ik_\rho^{(j)}(\boldsymbol{\rho}_a-\boldsymbol{\rho}')\cdot\hat{\mathbf{s}}}\;, \tag{5a}$$

$$\mathbf{k}^{(j)} = k_\rho^{(j)}\hat{\boldsymbol{\rho}} + k_z^{(j)}\hat{\mathbf{z}}\;. \tag{5b}$$

The SDFMM implementation further utilizes a multilevel version of the FMM-like technique described above. In this case, plane wave expansions are shifted to centers of parent boxes, and incoming spectra are shifted to centers of child boxes, in addition to the use of translation operators at each FMM level. A specific bandlimited interpolation technique is used to window translation operators and also transfer plane wave spectra from one FMM level to another.

3 Complexity Estimates of the SDFMM

In order to analyze the computational complexity and memory requirements of SDMM, consider the following. Assume a rough surface of dimensions $L \times L\ \lambda^2$ with a maximum peak to peak height of z_{max}. Let this surface be modeled using N unknowns. Let the number of levels be f. At any intermediate level g, let the number of blocks be $b^{(g)}$, and the size of each block be $l^{(g)} \times l^{(g)}\ \lambda^2$. Furthermore, let the number of points used for the steepest descent integration be $n_{sd}^{(g)}$, and the number of spectral angles required by the FMM be $P^{(g)}$. Also, let (g-independent) constants be denoted by C_i where i is some integer. The following relations hold:

$$b^{(g)} = \lceil (L/l^{(g)})^2 \rceil\;, \tag{6a}$$

$$l^{(g-1)} = 2l^{(g)}\;, \tag{6b}$$

$$f = \lceil (\log_2(L/l^{(f)})) \rceil \tag{6c}$$

where $\lceil\ \rceil$ denotes the ceiling of the argument. The SDFMM proceeds by distinguishing between near-field and far-field interactions. At any level, let two blocks be considered to be in each other's far-field if they are removed by at least B_{di} blocks. This implies that the total number of direct interactions I_d is bounded from above by

$$I_d = (2\ B_{di} + 1)^2\ N^2\ (l^{(f)}/L)^2\ . \tag{7a}$$

Moreover, $L^2 = C_1\ N$ and, therefore,

$$I_d = (2\ B_{di} + 1)^2\ N\ (l^{(f)})^2/C_1\ . \tag{7b}$$

For the computation of the far-field contributions in the SDFMM, an initial step is the projection of sources which involves computing plane wave spectra at the centers of finest level boxes. The next step is the recursive generation of higher level spectra which involves spectrum interpolation and center translation. A dual step is the anterpolation of incoming spectra at finer levels and center translation. In-level translations using the diagonalized translation operator are also necessitated in order to obtain complete incoming wave spectra. At the finest level, plane wave spectra need to be back-projected to obtain actual field values. The overall far-field computation cost is calculated as follows. Let the number of points required for z- integration and for ϕ- interpolation at level g be given by $n_{sd}^{(g)}$ and $P^{(g)}$ respectively. The total cost of projection and back-projection I_p is given by

$$I_p = C_2\ n_{sd}^{(f)}\ P^{(f)}\ N\ . \tag{8}$$

The cost of all center-translations and interpolation/anterpolation $I_c^{(g)}$ at level g is:

$$I_c^{(g)} = C_3\ n_{sd}^{(g)}\ P^{(g)} b^{(g)}\ , \tag{9}$$

and the cost of in-level translations $I_t^{(g)}$ is given by

$$I_t^{(g)} = C_4\ n_{sd}^{(g)}\ P^{(g)}\ (2\ B_{di} + 1)^2\ b^{(g)}\ . \tag{10}$$

One can assume that $n_{sd}^{(g)}$ is independent of the level g and hence equals $n_{sd}^{(f)}$, and that $P^{(g)} = 2\ P^{(g+1)}$. The overall cost of the SDFMM I_{SDFMM} is therefore

$$I_{SDFMM} = I_d + I_p + \sum_{g=0}^{f} (I_c^{(g)} + I_t^{(g)})\ , \tag{11a}$$

$$I_{SDFMM} = (2\ B_{di} + 1)^2\ N\ (l^{(f)})^2/C_1 + C_2\ n_{sd}^{(f)}\ P^{(f)}\ N + C_4\ n_{sd}^{(f)}\ P^{(f)}\ N + C_5\ (2\ B_{di} + 1)^2\ n_{sd}^{(f)}\ P^{(f)}\ N\ , \tag{11b}$$

and, therefore,

$$I_{SDFMM} = O(N)\ . \tag{11c}$$

It is therefore evident that the cost of each matrix-vector product is O(N) and the total memory requirements (storing near field interactions and incoming and outgoing spectra at all levels) are also O(N).

4 Numerical Results

The SDFMM has been developed in this paper to analyze scattering from random rough surfaces although it is in principle applicable to a more general class of quasi-planar structures. In this section, the SDFMM is applied to solve scattering problems specifically involving Gaussian rough surfaces. RCS comparisons with the standard MoM, Monte-Carlo simulation results, and CPU-time and memory requirements are presented.

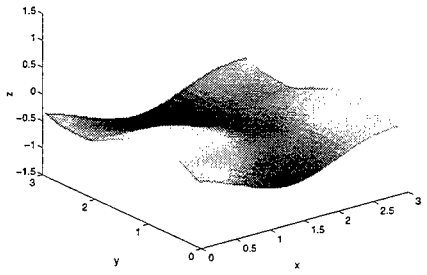

Figure 2: Sample rough surface. All dimensions in units of λ.

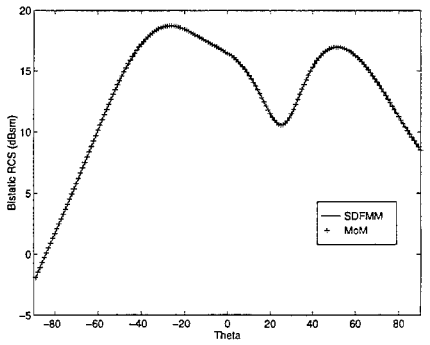

Figure 3: Bistatic RCS: SDFMM and MoM results. A Gaussian beam is incident at $\theta = -10°$.

To validate the approach, a comparison is made with results obtained by using the standard MoM technique. The rough surface used for this purpose is shown in Fig. 2. This surface has roughness $\sigma = 0.5\lambda$ and correlation length $l = 1.5\lambda$, and its size is $3.9\lambda \times 3.9\lambda$, where λ is the free-space wavelength. The surface is discretized using ten nodes per λ. Finest level blocks of size $0.5\lambda \times 0.5\lambda$ are used in the SDFMM. The residual error stopping criterion for the iterative solver is 10^{-2}. A Gaussian beam is used as the excitation. It lies in the x-z plane and has no amplitude variation in the y- direction. The beam is incident at an angle of 10° from the vertical with a positive x-component (i.e. $\theta = -10°$). The half-width of the beam is $W = L/4 = 0.975\lambda$. Its electric field vector is polarized in the x-z plane. The solution using the SDFMM produces a *current density* solution that is within 0.5% of that produced by solving the standard MoM. Figure 3 depicts the RCS results which are practically identical.

A Monte-Carlo simulation is carried out for an ensemble of 50 rough surfaces of size $5.9\lambda \times 5.9\lambda$ with $\sigma = 0.5\lambda$ and $l = 1.5\lambda$. The excitation field is a Gaussian beam similar to the one in the above problem, with $W = L/4 = 1.475\lambda$. The problem involves $N = 10325$ unknowns, and requires approximately 52 CPU hrs for the complete simulation on a 60 MFlop SGI Power Challenge. The non-coherent bistatic scattering coefficients for the cross- and co-polarized cases are depicted in Figs. 4 and 5. Backscattering enhancement (at $\theta = -10°$) is clearly observed for both cases.

To verify the $O(N)$ CPU time and memory estimates for the SDFMM, scaling tests are carried out using larger rough surfaces. The results of these tests are as follows. The CPU time for a matrix-vector product is shown in Fig. 6. For a 50,000 unknown case, the matrix-vector product requires 127 seconds. The scaling of memory requirements is seen in Fig. 7. Both CPU time and memory scale approximately linearly, as predicted by the

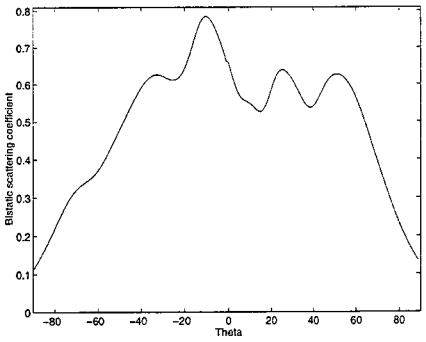

Figure 4: Monte Carlo simulation: Copolarized bistatic scattering coefficient. A Gaussian beam is incident at $\theta = -10°$.

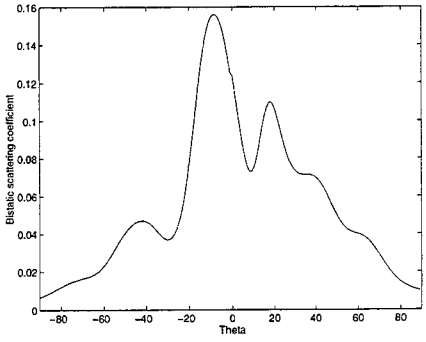

Figure 5: Monte Carlo simulation: Cross-polarized bistatic scattering coefficient. A Gaussian beam is incident at $\theta = -10°$.

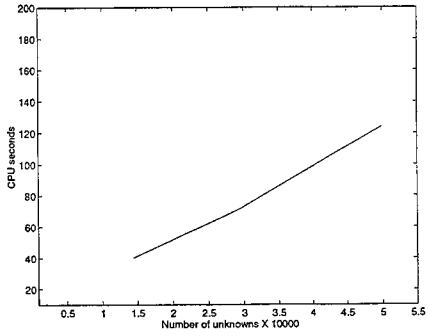

Figure 6: Matrix-vector product timings.

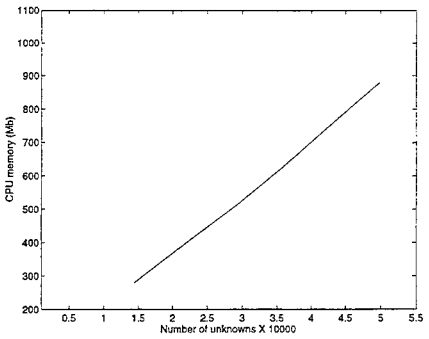

Figure 7: Total memory requirements.

complexity analysis in the previous section.

5 Conclusions

A new multilevel algorithm, the SDFMM, has been developed to efficiently analyze scattering from quasi-planar structures. Gaussian, perfectly conducting rough surfaces have been used for illustration purposes in this work. The proposed technique has $O(N)$ CPU time and memory requirements, and is rapid enough to permit Monte-Carlo simulations of large surfaces in reasonable times. The technique is "exact"; accuracy can be traded for efficiency by using integration and interpolation rules with different error characteristics. Further generalizations to the analysis of dielectric rough surfaces, anisotropic materials, and planar multilayered microwave circuits are currently under study. Efficient multilevel block-based preconditioners are also under development.

References

[1] A. Ishimaru, *Wave Propagation and Scattering in Random Media.* New York, NY: Academic Press, 1978.

[2] J. T. Johnson, L. Tsang, R. T. Shin, K. Pak, C. H. Chan, A. Ishimaru, and Y. Kuga, "Backscattering enhancement of electromagnetic waves from two-dimensional perfectly conducting random rough surfaces- a comparison of monte carlo simulations with experimental data," *IEEE Trans. Antennas Propagat.*, vol. 44, pp. 748–756, 1996.

[3] R. L. Wagner, J. Song, and W. Chew, "Monte carlo simulation of electromagnetic scattering from two-dimensional random rough surfaces," Tech. Rep. EM-WC-14-95, Center for Computational Electromagnetics, University of Illinois, Urbana-Champaign, 1995.

Fast Wavelet Packet Algorithm for the Combined Field Integral Equation

W. L. Golik
University of Missouri-St. Louis, St. Louis, MO 63121
D.-S. Wang
McDonnell Douglas Aerospace,St. Louis, MO 63166

Abstract

This paper considers the problem of wavelet sparsification of matrices arising in numerical solution of electromagnetic integral equations by the method of moments. Scattering of plane waves from two-dimensional cylinders is computed numerically using a constant number of test functions per wavelength. Discrete wavelet packet (DWP) similarity transformations and thresholding are applied to system matrices to obtain sparsity. If thresholds are selected to keep relative residual error constant the matrix sparsity is of order $O(N^{4/3})$. In addition, we study preconditioned BICGstab iterations comparing ILU preconditioning of DWP sparsified matrices with banded preconditioners full impedance matrix (of similar cost). The tests show that ILU preconditioners produce significantly fewer iterations than the banded preconditioners.

I. Introduction

Numerical solutions for electromagnetic integral equations describing scattering from electrically large, complex objects continues to be a challenging problem. The classical method of moments produces dense linear systems with N unknowns, where N grows with the electrical size of the scattering object. Since direct methods for dense systems have $O(N^3)$ complexity, they become impractical for large N and iterative methods must be used. The cost of one iteration for such methods is dominated by a a matrix-vector multiplication (MVM), which is of order $O(N^2)$ for dense matrices.

In recent years various approaches have been proposed to decrease the complexity of dense MVMs. In numerical solution of electromagnetic integral equations two avenues for fast MVM are available: algorithms that bypass the complete construction of the impedance matrix and matrix sparsification methods. Among the former is the fast multipole method (FMM) [2], [3], [4] and the adaptive integral method (AIM) [5]. The latter approaches include the impedance matrix localization method (IML) [6] and various wavelet transformation methods [7], [8], [9]. [1], [10]. The use of wavelet transformations was prompted by their success in numerical solutions of integral equations with non-oscillatory kernels [11]. The cited studies reported some sparsification of matrices, but only [1] studied the complexity of the MVM as the function of N. The study reported that matrix sparsification based on an orthogonal wavelet transform produced sparse matrices with βN^2 nonzero entries, where $0 < \beta < 1$. This compares unfavorably with the FMM, AIM, and IML methods, all of which reduce the complexity of MVM to $O(N^p)$ with $1 \leq p << 2$.

This paper is concerned with the question whether discrete wavelet packets are able to reduce the cost of MVM in numerical solution of electromagnetic integral equations to $O(N^p)$ with $1 \leq p << 2$. The investigations are restricted to the electromagnetic scattering from two-dimensional conducting cylinders with the combined field integral equation (CFIE) discretized by the method of moments. In the first section we formulate the CFIE, discuss its discretization with pulse basis functions, and introduce the idea of sparsifying transformations. The next section briefly discusses wavelet packets transforms and an an adaptive algorithm for the selection of the near best basis. Numerical examples illustrating $O(N^{4/3})$ sparsity of the transformed matrices and comparisons with other fast algorithms are given next. This is followed by a study of preconditioned BiCGstab iterations applied to the original and DWP transformed systems. The last section contains conclusions and suggestions for future research.

II. CFIE and Matrix Thresholding

Consider the problem of computing the scattering of a TM(E_z) polarized electromagnetic wave from a two-dimensional conducting cylinder with the boundary contour C. The far field scattering characteristics are obtained from the surface current J_z excited by an incident wave E_z^{inc}. In order to avoid problems with resonance the

surface current is computed from the combined field integral equation (CFIE)

$$(1+\tfrac{\partial}{\partial n_x})E_z^{inc}(\mathbf{x}) = \tfrac{\omega\mu_0}{4}(1+\tfrac{\partial}{\partial n_x})\int_C H_0^{(1)}(2\pi\lambda\mathbf{r})J(\mathbf{x}')dl(\mathbf{x}'), \tag{1}$$

where $H_0^{(1)}$ is the zero order Hankel function of the first kind, $\mathbf{r} = |\mathbf{x}-\mathbf{x}'|$, $\mathbf{x},\mathbf{x}'$ denote points on C, n_x is the outer unit normal at point $\mathbf{x}$, and λ is the excitation wavelength.

The integral equation is discretized in a standard way by subdividing contour C into N non-overlapping contour pieces of (roughly) equal length and applying point matching (collocation) of pulse functions. In practical computations N is proportional to the electric length of contour C. Discretization reduces the CFIE to the linear system

$$Zj = e, \tag{2}$$

where Z is a full non-symmetric complex nonsingular $N \times N$ matrix. Since the direct solution of the full system has a computational cost of $O(N^3)$, iterative methods must be used for large N. The cost of each iteration is dominated by a matrix-vector multiplication, an $O(N^2)$ operation for a full matrix. The idea of sparsifying transformations is to find nonsingular matrices T_1 and T_2, so that the matrix $Z' = T_1 Z T_2$ of the new system

$$Z'j' = e', \quad e' = T_1 e, \quad j = T_2 j', \tag{3}$$

has numerous very small elements which can be neglected (thresholded) without largely affecting the solution j'. Practical considerations require that matrices T_1, T_2 must satisfy the following design criteria:

1. the matrix $T_1 Z T_2$ must be (effectively) sparse,
2. matrices T_1, T_2 must be $O(N)$ sparse, so that matrix-matrix multiplications cost only $O(N^2)$,
3. the condition number of Z' is not much larger than that of Z.

III. Wavelet Packets Algorithm

The sparsifying transformations T_1, T_2 used in this paper are based on compactly supported, least asymmetric, periodized Daubechies wavelets [12] and $T_2 = T_1^t$. This choice was dictated by the desire to compare our results to those available in the literature [1], but other wavelet constructions may be used as well.

Recall that in the classical wavelet transformation only the slowly varying part of the vector is decomposed at each stage. This can be best illustrated by exhibiting its tree structure, shown in Fig. 1a. The tree corresponds to an orthogonal matrix transformation T, which depends only on the size N and the order of the Daubechies wavelets. The rows of T describe the new (wavelet) basis functions in terms of pulse functions. However, one can select a different tree, like the one shown in Fig. 1b. This tree indicates that at the second level both slow and fast modes are decomposed further. At the third level only the fast parts of both decomposed signals are transformed. The corresponding transformation matrix is also orthogonal. Its rows describe another set of basis functions (wavelet packets) in terms of pulse functions [13].

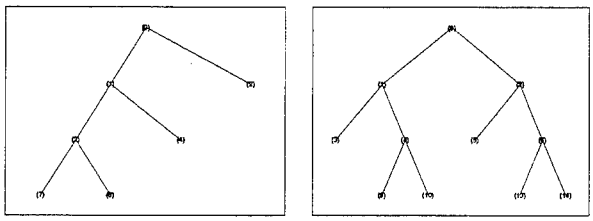

Fig. 1. Level 3 binary tree for a) the wavelet transform and b) a wavelet packet.

Clearly, a different tree gives rise to a different orthogonal transformation of the original vector (i.e. to a different wavelet packet). Our objective is to select a tree structure which would produce better sparsification of the impedance matrix Z. It turns out that this can be done with a simple algorithm which utilizes frequency and surface geometry information present in the right side of the system $Zj = e$. Starting with the incident wave vector e as the top node of the decomposition tree, a decision whether to continue decomposition at any

given node is based on a comparison of norms of vectors at the parent and children nodes. The information cost function used as a criterion is

$$C(x) = \sum_i |x_i|, \quad x = [x_1, \ldots, x_M]^t,$$

where x is a vector of decomposition coefficients related to the node, and $M = 2^r$ for some positive integer r. If the norm of the parent node vector is smaller than the norm of its two children, that part of the tree is not decomposed further. Once the tree structure has been determined, the orthogonal transformation T is known and it is applied to matrix Z to obtain $Z' = TZT^t$. The transformed matrix Z' is then thresholded and the resulting system solved for an approximation of the solution vector j'.

IV. Numerical Examples

In this section the results of a study of matrix sparsity as a function of the problem size are presented. Scattering of plane waves from two-dimensional cylinders is computed numerically using a constant number of test functions per wavelength. The surface currents induced on a two-dimensional conducting cylinder by planar waves are described by the integral equation (1). The incident waves are given by $E_z^{inc}(\mathbf{x}) = \exp(i\mathbf{k}\cdot\mathbf{x})$, $\mathbf{k} = 2\pi\mathbf{d}/\lambda$, where $\mathbf{d}$ is the incidence direction unit vector. Two different cylinder contours were considered: a circle and an L-shape (see Fig. 2 for the geometry of the latter contour).

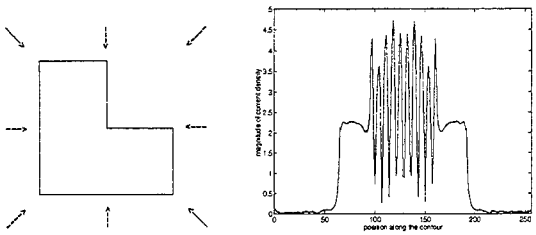

Fig. 2. L-shape contour with the incidence directions. Magnitude of the surface current density along the L-shaped contour induced by a plane wave incident at 45 degrees into the concave corner. The scatterer has length 25.6λ and is discretized with $N = 256$.

Equation (1) was discretized with pulse functions and point matching. The support of pulse functions was $\lambda/10$, throughout all experiments. For both contours we computed the scattering for increasing incident frequency (or equivalently, for the increasing electrical cylinder size), adjusting the threshold level τ to maintain the relative residual error $\|e' - Z'j'_{comp}\|/\|e'\|$ of $(1 \pm 0.01)\%$, where j'_{comp} is the solution computed using the thresholded sparse matrix Z'. This level of solution accuracy produces approximate solutions visually indistinguishable from those obtained from the full systems. We noted that τ had to be decreased as the problem size grew to maintain the accuracy of the solution of the sparse system. Fig. 2 shows the magnitude of the current density along the perimeter of the L-shape domain induced by the planar wave incident at 45 degrees (i.e. into the concave corner of the contour). Here the perimeter length is 25.6λ and the current was computed with the dense and the sparse matrices. The curves practically overlap.

The system sizes studied ranged from $N = 256$ (contour length of 25.6λ) to $N = 4096$ (contour length of 409.6λ). The sparsity results for the circular cylinder are presented in Fig. 3. The wavelet packet tree was computed from a single planar incident wave. It can be seen that the DWP produces much higher sparsity than does the DWT. Moreover, the sparsity of DWP transformed matrices does not level off for large N, but continues to decrease. Specifically, for the circular cylinder the DWT produced the sparsities ranging from 10.7% for $N = 256$ to 6.7% for $N = 4096$. The sparsities obtained from the DWP ranged from 7.4% for $N = 256$ to 1.1% for $N = 4096$.

Similar results were obtained for the L-shaped contour. In this case the wavelet packet tree for the L-shaped contour was computed from a block of 8 right hand side vectors obtained from planar waves with different incident angles as shown in Fig. 2. This was done to illustrate that the DWP produces good sparsification with many different excitation vectors. Note that since all excitations vectors play a role in the construction of the wavelet

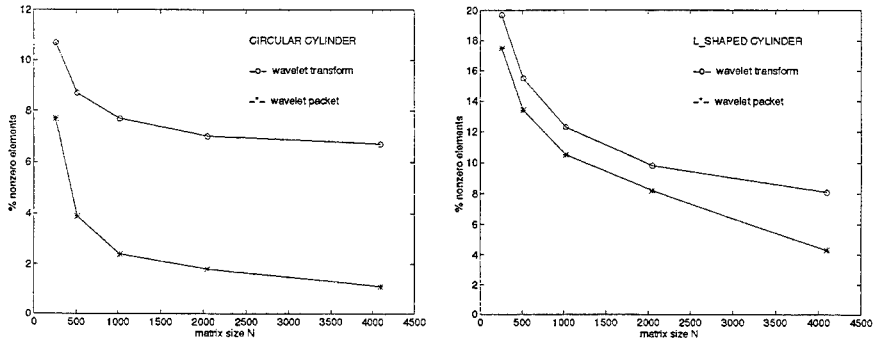

Fig. 3. Matrix sparsity as a function of size N for the circular and L-shaped cylinders. Periodic Daubechies wavelets of order 8 used. Threshold levels adjusted to maintain relative errors of $(1 \pm 0.01)\%$.

packet tree, the construction is based more on the geometry of the scatterer and less on the relation between the excitation and solution vectors.

The sparsity results for the L-shaped cylinder are presented in Fig. 3. As in the case of the circle the DWP produces higher sparsity than the DWT and the DWP-produced sparsity decreases faster as the problem scales. Specifically, the DWT sparsities range from 20.3% for $N = 256$ to 8.3% for $N = 4096$. The sparsities obtained from the DWP ranged from 17.7% for $N = 256$ to 4.2% for $N = 4096$. Since the relative importance of the contour corners diminishes with the increase of N, the sparsities will eventually approach those of the circular cylinder. This means that DWT-produced sparsities will level off (as suggested in [1], whereas the DWP-based sparsities will continue to decrease.

Figure 4 shows that the number of nonzero element in impedance matrices for circular and L-shaped cylinders sparsified by the DWP algorithm is roughly of order $O(N^{4/3})$ (the slopes are nearly parallel to a line with slope 4/3).

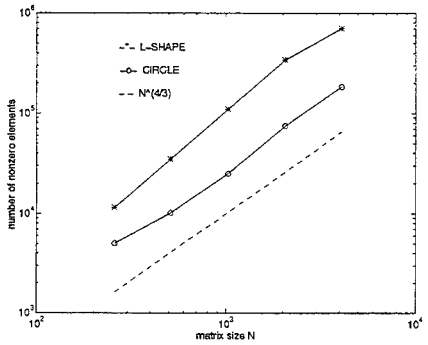

Fig. 4. Number of nonzero elements as a function of size N for circular and L-shaped cylinders. DWP sparsification. Threshold levels adjusted to maintain relative errors of $(1 \pm 0.01)\%$.

V. Iterative solution of DWP sparsified systems

In this section we study the efficiency of iterative solution of linear systems sparsified with the DWP. Specifically, we address the question whether an ILU preconditioning of DWP sparsified matrices gives rise to fewer iterations

than in the case of banded preconditioners applied to the full impedance matrix.

From among several conjugate-gradient-like solvers for systems with non-Hermitian matrices we selected the preconditioned biconjugate gradient stabilized algorithm (BiCGstab) [14]. Block-diagonally preconditioned BiCGstab with fast MVM based on a multilevel fast multipole algorithm (MLFM.\) has been reported in several papers [4]. The block-diagonal preconditioning is natural in conjunction with the fast multipole MVM, since the only explicitly evaluated elements of the impedance matrix are in blocks near the diagonal.

In the test below we compare the number of iterations for two kind of systems. Both describe scattering calculations from an L-shaped cylinder given in Fig. 2 with the contour length equal to $N\lambda/10$. The first system is given by equation (2) and the BICGstab iterations were performed with impedance matrix Z and banded preconditioners B with bandwidth p, where $B_{i,j} = 0, \quad i > j+p, j > i+p$. For each N the bandwidth was chosen to make the sparsity of B equal to the sparsity of the ILU preconditioners described below.

The second kind of systems considered here are described by equation (3), where Z' is the DWP-transformed and thresholded matrix. The BiCGstab iterations are preconditioned by a matrix S obtained from ILU factorization of matrix Z' (see [15]). The sparsity of incomplete factors is identical to the sparsity of Z' which varies with N and is given in Fig. 3.

The sparsity levels for banded and ILU preconditioners are selected so that the cost of their application is comparable. The cost of the complete LU factorization of a banded matrix with $O(N^p), 1 \leq p, 2$ nonzero elements is of order $O(N^{2p-1})$. The incomplete LU factorization of a general sparse matrix with $O(N^p)$ nonzero elements is of the same order. Once the sparse triangular factors with $O(N^p)$ nonzero elements are computed their application in the iterative loop adds only $O(N^p)$ floating point operations.

It is well known that iterative methods converge faster if the spectrum of the iteration matrix is clustered near the point $(1, 0)$ in the complex plane. Fig. 5 illustrates the eigenvalues of the original matrix Z (denoted by $+$), its preconditioned version $B^{-1}Z$ (denoted by $*$), and the ILU(0) preconditioned matrix Z'. Note that although most of the eigenvalues of Z are clustered near the point $(0, -2)$, a significant portion is scattered in a large "ring" around that point. Banded preconditioning improves the spectrum considerably: most of the $*$ eigenvalues are clustered near $(1, 0)$ with the remaining ones contained in a much smaller "ring". The ILU preconditioning is best: only very few x eigenvalues are visible outside the cluster at $(1, 0)$.

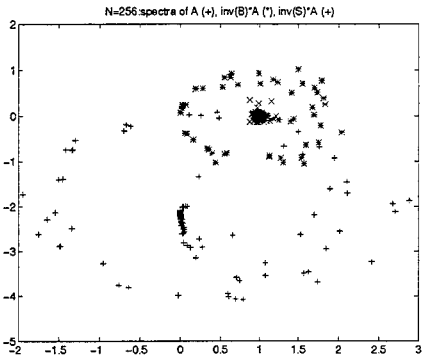

Fig. 5. Effect of preconditioning on the impedance matrix spectrum. $N = 256$. Eigenvalues of matrix Z with no preconditioning (+), matrix Z with banded preconditioning (band width 23) (*), and the DWP-sparsified and thresholded matrix Z' preconditioned by ILU. Both preconditioners have 17.7 % sparsity (x).

In Table 1 we list the number of preconditioned BiCGstab iterations to reduce the initial residual by a factor of 10^4. Note that the banded preconditioning has hardly any effect on reducing the number of iterations when compared with not preconditioned BiCGstab. On the other hand the ILU preconditioning of sparse matrices obtained from DWP transformations yields substantially fewer number of iterations.

TABLE I

NUMBER OF PRECONDITIONED BICGSTAB ITERATIONS FOR 10^4 RESIDUAL REDUCTION FOR THE L-SHAPED CYLINDER.

N	64	128	256	512	1024	2048
Z (no prec.)	10	16	28	62	130	>200
Z (banded prec.)	8	14	26	50	112	>200
Z' (with ILU)	3	3	3	16	24	83
prec. sparsity (%)	41.0	27.0	17.4	13.4	10.5	8.3

VI. CONCLUSIONS

In this paper we described an application of discrete wavelet packet (DWP) transformations which reduce the complexity of matrix-vector multiplications in iterative solutions of discretized electromagnetic integral equations roughly equal to $O(N^{4/3})$. This reduction of complexity is obtained assuming a fixed number of basis functions per incident wavelength. The order of the complexity is similar to that of the RPFMA method, but the DWP-based matrix-vector multiplication is much faster due to a smaller complexity constant.

In addition, preconditioned BiCGstab iterations applied to the original system $Zj = e$ and the DWP-transformed and thresholded system $Z'j' = e'$ were studied. The BiCGstab used a banded preconditioner in the case of $Zj = e$ and the ILU preconditioner in the case of $Z'j' = e'$. The cost of preconditioners was roughly the same. In all the tests banded preconditioners applied to the original matrix Z hardly improved convergence of the BICGstab. The use of ILU preconditioners with matrix Z' produced significant decrease in the number of iterations.

Many of the ideas presented here need further development, such as block sparsifications based on wavelets defined on intervals (instead of periodicised wavelets), extensions to integral equations on surfaces, construction of fast matrix fills prior to wavelet transformations, and design of preconditioners for iterative solvers for multiple right hand sides.

REFERENCES

[1] R.L. Wagner and W.C. Chew, "A study of wavelets for the solution of electromagnetic integral equations," *IEEE Trans. Antennas Propagat.*, vol. 43, no. 8, pp. 802–810, 1995.

[2] V. Rokhlin, "Rapid solution of integral equations of scattering theory in two dimensions," *J. Comp. Phys.*, vol. 86, no. 2, pp. 414–439, 1990.

[3] R.L. Wagner and W.C. Chew, "A ray-propagation fast multipole algorithm," *Micro. Opt. Tech. Lett.*, vol. 7, no. 10, pp. 435–438, 1994.

[4] C.-C. Lu and W.C. Chew, "A multilevel algorithm for solving boundary integral equation," *Micro. Opt. Tech. Lett.*, vol. 7, no. 10, pp. 466–470, July 1994.

[5] E. Bleszynski, M. Bleszynski, and T. Jaroszewicz, "Fast integral-equation solver for electromagnetic scattering problems," in *10th Annual Review of Progress in Applied Computational Electromagnetics*, Monterey CA, 1994, Naval Postgraduate School.

[6] F. X. Canning, "Sparse approximations for solving integral equations with oscillatory kernels," *SIAM J. Sci. Statist. Comput.*, vol. 13, no. 1, pp. 71–87, 1992.

[7] D.S.Wang and G.Welland, "Modelling of electromagnetic scattering using wavelet techniques for geometry modelling and expansion functions," *1993 URSI Radio Sci. Meet. Dig.*, p. 277, June 1992.

[8] H.Kim and H. Ling, "On the application of fast wavelet transform to integral equation solution of electromagnetic scattering problems," *Micro. Opt. Tech. Lett.*, vol. 6, no. 3, pp. 168–173, 1993.

[9] G. Wang, "A hybrid wavelet expansion and boundary element analysis of electromagnetic scattering from conducting objects," *IEEE Trans. Antennas Propagat.*, vol. 43, no. 2, pp. 170–178, 1995.

[10] Z. Baharav and Y. Leviatan, "Impedance matrix compression using adaptively constructed basis functions," *IEEE Trans. Antennas Propagat.*, vol. 44, no. 9, pp. 1231–1238, 1996.

[11] G. Beylkin, R. Coifman, and V. Rokhlin, "Fast wavelet transforms and numerical algorithms i," *Comm. Pure Appl. Math.*, vol. XLIV, pp. 141–183, 1991.

[12] I. Daubechies, *Ten Lectures on Wavelets*, vol. 61 of *CBMS Lecture Notes*, SIAM, 1992.

[13] M.V. Wickerhauser, *Adapted Wavelet Analysis from Theory to Software*, A.K. Peters, Boston, MA, 1994.

[14] R. Barrett et. al., *Templates for the Solution of Linear Systems: Building Blocks for Iterative Methods*, SIAM Publications, Philadelphia, 1993.

[15] Y. Saad, *Iterative Methods for Sparse Linear Systems*, PWS Publishing Co., Boston, 1996.

Matrix Assembly in FMM-MOM Codes

Elizabeth Yip and Ben Dembart
The Boeing Company, Seattle, WA

January 14, 1997

1 Introduction

We address the problem of assembling the matrix for a MOM/FMM code which admits a heterogeneous set of boundary conditions. Since the impedance matrix in a MOM/FMM code is not computed explicitly, it is important that the matrix equation be cast into the form:

$$(CZA + B)J = CV \tag{1}$$

with the matrices A, B and C capturing all the properties of the boundary conditions. We note this approach is taken by Putnam et. al. in Carlos-3D. We extend their approach to accommodate for the FMM structure and to include the case when an arbitrary number of surfaces with different boundary conditions meeting on a single edge. We refer to such edges as 'junction edges'.
The junction edges have been handled satisfactorily in classical MOM codes that deal with perfectly conducting or resistive surfaces in a single region. The elegant solution used in these codes does not apply directly when more than one region is involved. Our solution involves casting Kirchoff's current law as a homogeneous matrix system and finding the null vector of this system by singular value decomposition.
Each of our A and C matrices is the product of two matrices:

$$A = A_p A_j, \;\; C = C_j C_p.$$

A_p and C_p capture the boundary condition. A_j and C_j capture the junction information.
This approach simplifies programming and allows for easy extension of the capabilities of the code. If more boundary conditions are required, one just needs to modify the subroutine that generates the A_p, B and C_p matrix.
At present, our code handles twelve types of boundary conditions including dielectric interfaces, resistive surfaces and impedance boundaries.
In this paper, we present our extension of Putnam et. al.'s ABC approach in Carlos-3D and present the "junction edge" algorithm. We present examples of the A, B and C matrices of some of our boundary conditions in our code.
In order to extablish our notations, we present the fundamental equations in §2. In §3, we present our extention of the Carlos-3D approach. In §4, we present the theory of basis function for junction edges. In the Appendix A of [4], we present the list of boundary conditions and the corresponding A, B, C matrices in our code and address implementation issues.

2 Fundamental Equations

Consider a scatterer with a surface S iluminiated by a complex vector $(\vec{E}^{inc}, \vec{H}^{inc})$. The $\vec{E}$-field and $\vec{H}$-field integral equations are

$$\vec{E} = \vec{E}^{inc} - \left(j\omega\mu L(\vec{J}) - K(\vec{M})\right) \tag{2}$$

$$\vec{H} = \vec{H}^{inc} - \left(K(\vec{J}) + j\omega\epsilon L(\vec{M})\right). \tag{3}$$

The operators L and K are defined as:

$$L(\vec{X}) = \int_S \left[\Psi(\vec{p},\vec{q})\vec{X}(\vec{q}) + \frac{1}{k^2}\nabla_p\nabla_p\Psi(\vec{p},\vec{q})\vec{X}(\vec{q})\right] dq$$

$$K(\vec{X}) = \int_S \nabla_p\Psi(\vec{p},\vec{q}) \times \vec{X}(\vec{q})dq,$$

with $\Psi(\vec{p},\vec{q}) = \frac{\exp(-jkR)}{4\pi R}$ and $R = |\vec{p} - \vec{q}|$. $\vec{J}$ and $\vec{M}$ are the equivalent electric and magnetic surface currents and are defined as $\vec{J} = \hat{n} \times \vec{H}$ and $\vec{M} = \vec{E} \times \hat{n}$ with $\hat{n}$ as the surface normal. If the intgrals in equations (2) and (3) are taken as Cauchy principal values, then the K operator produces a jumped term : $\frac{1}{2}\hat{n} \times \vec{X}$.
Equations (2) and (3) become

$$\vec{E}_{tan} = \vec{E}^{inc}_{tan} - \left(j\omega\mu L(\vec{J}) - K(\vec{M})\right) + \frac{1}{2}\hat{n} \times \vec{M} \tag{4}$$

$$\vec{H}_{tan} = \vec{H}^{inc}_{tan} - \left(K(\vec{J}) + j\omega\epsilon L(\vec{M})\right) - \frac{1}{2}\hat{n} \times \vec{J}. \tag{5}$$

But

$$\frac{1}{2}\hat{n} \times \vec{M} = -\frac{1}{2}\hat{n} \times \hat{n} \times \vec{E} = \frac{1}{2}\vec{E}_{tan}$$

and

$$-\frac{1}{2}\hat{n} \times \vec{J} = -\frac{1}{2}\hat{n} \times \hat{n} \times \vec{H} = \frac{1}{2}\vec{H}_{tan}$$

Substituting these values into equations (4) and (5) and rearranging the terms, we obtain

$$j\omega\mu L(\vec{J}) - K(\vec{M}) + \frac{1}{2}\vec{E}_{tan} = \vec{E}^{inc}_{tan} \tag{6}$$

$$K(\vec{J}) + j\omega\epsilon L(\vec{M}) + \frac{1}{2}\vec{H}_{tan} = \vec{H}^{inc}_{tan} \tag{7}$$

We define the operators ${}_zL$ and ${}_zK$ to mean

$${}_zL(\vec{X}) = \hat{n} \times L(\vec{X})$$

and

$${}_zK(\vec{X}) = \hat{n} \times K(\vec{X}).$$

If we take the cross product of $\hat{n}$ with equations (6) and (7) on the left, we obtain

$$j\omega\mu\, {}_zL(\vec{J}) - {}_zK(\vec{M}) + \frac{1}{2}\hat{n} \times \vec{E}_{tan} = \hat{n} \times \vec{E}^{inc}_{tan}$$

$${}_zK(\vec{J}) + j\omega\epsilon\, {}_zL(\vec{M}) + \frac{1}{2}\hat{n} \times \vec{H}_{tan} = \hat{n} \times \vec{H}^{inc}_{tan}$$

Since $\hat{n} \times \vec{E}_{tan} = -\vec{M}$ and $\hat{n} \times \vec{H}_{tan} = \vec{J}$, the above equations can be written as:

$$j\omega\mu\, {}_zL(\vec{J}) - {}_zK(\vec{M}) - \frac{1}{2}\vec{M} = \hat{n} \times \vec{E}^{inc}_{tan} \tag{8}$$

$${}_zK(\vec{J}) + j\omega\epsilon\, {}_zL(\vec{M}) + \frac{1}{2}\vec{J} = \hat{n} \times \vec{H}^{inc}_{tan} \tag{9}$$

3 A_p, B, C_p Matrices Due to Boundary Conditions

Each surface is a boundary to two regions. We arbitrary call these the upper and lower regions of the surface. Up to four unknowns can be associated with each surface: electric current for the upper and lower surface, and magnetic current for the upper and lower surface. We denote these unknowns as $\vec{J}^+$, $\vec{J}^-$, $\vec{M}^+$, and $\vec{M}^-$ respectively. We also denote the electric field for the upper and lower surface as $\vec{E}^+$, $\vec{E}^-$, and the magnetic field for the upper and lower surface as $\vec{H}^+$, $\vec{H}^-$. Let $\mathcal{L}_+$, $\mathcal{K}_+$, ${}_z\mathcal{L}_+$, ${}_z\mathcal{K}_+$ be the matrix operators resulted from testing the L, K, ${}_zL$, ${}_zK$ operator for the upper region and $\mathcal{L}_-$, $\mathcal{K}_-$, ${}_z\mathcal{L}_-$, ${}_z\mathcal{K}_-$ be the matrix operators resulted from testing the L, K, ${}_zL$ and ${}_zK$ operators for the lower region. Up to eight equations can be used for each surface: equations (6),(7), (8), and (9) for the upper region, and the same four equations for the lower surface. Let X is the actual set of unknowns used. Let A_p be the matrix which relates the actual set of unknowns to the canonical set of unknowns $\vec{J}^+$, $\vec{J}^-$ $\vec{M}^+$, and $\vec{M}^-$. Let B model the "Ampere's - Ohm's" laws terms, which only affects the "self terms",i.e. when the source patch and the testing patch are the same. Further let C_p relates the boundary conditons to the fields $\vec{E}^+$, $\vec{E}^-$, $\vec{H}^+$, and $\vec{H}^-$. If only one region is involved, i.e. either one region is dark, or the upper and lower regions are the same, these assertions can be represented by the following matrix equation:

$$\left[C_p \left[\begin{array}{cc} j\omega\mu_+\mathcal{L}_+ & -\mathcal{K}_+ \\ \mathcal{K}_+ & j\omega\epsilon_+\mathcal{L}_+ \\ j\omega\mu_+ {}_z\mathcal{L}_+ & -{}_z\mathcal{K}_+ \\ {}_z\mathcal{K}_+ & j\omega\epsilon_+ {}_z\mathcal{L}_+ \end{array} \right] A_p + B \right] X = C_p V. \tag{10}$$

If n is the number of unknowns, then A_p is a $2 \times n$ matrix and C_p is a $n \times 4$ unknowns. If the two regions are distinct, the above assertions can be represented by the following matrix equation:

$$\left[\left[C_p \left[\begin{array}{cc} j\omega\mu_+\mathcal{L}_+ & -\mathcal{K}_+ \\ \mathcal{K}_+ & j\omega\epsilon_+\mathcal{L}_+ \\ j\omega\mu_+ {}_z\mathcal{L}_+ & -{}_z\mathcal{K}_+ \\ {}_z\mathcal{K}_+ & j\omega\epsilon_+ {}_z\mathcal{L}_+ \end{array} \right. \right. \right. \left. \left. \left. \begin{array}{cc} j\omega\mu_-\mathcal{L}_- & -\mathcal{K}_- \\ \mathcal{K}_- & j\omega\epsilon_-\mathcal{L}_- \\ j\omega\mu_- {}_z\mathcal{L}_- & -{}_z\mathcal{K}_- \\ {}_z\mathcal{K}_- & j\omega\epsilon_- {}_z\mathcal{L}_- \end{array} \right] A_p + B \right] X = C_p V. \tag{11}$$

If n is the number of unknowns, then A_p is a $4 \times n$ matrix and C_p is a $n \times 8$ unknowns. For each boundary condition, we generate its corresponding A_p, B and C_p matrix. The part of the matrix with testing patch having boundary condition p_t and source patch having boundary condition p_s involves the C_{p_t} and A_{p_s} matrices. This approach simplifies programming and debugging.
We illustrate our approach with two examples:, a perfectly conducting surface using the EFIE (Electric Field Integral Equation) and a dielectric interface.

3.1 Perfecting Conducting Surface Using EFIE

The boundary conditions for a perfect conductor is

$$\vec{E}_{tan} = 0,$$

this implies

$$\vec{M}^+ = \vec{M}^- = 0,$$

and only involves one region. We use equation (6). The unknowns are the $\vec{J}$'s. $\vec{J} = \vec{J}^+$ if the lower side is dark. $\vec{J} = \vec{J}^-$ if the upper side is dark. The A_p matrix is 2×1, B_p is a 1×1 zero matrix and C_p is a 1×4 matrix.

$$A_p = \left[\begin{array}{c} 1 \\ 0 \end{array} \right]; \qquad B = 0; \qquad C_p = \left[\begin{array}{cccc} 1 & 0 & 0 & 0 \end{array} \right]$$

3.2 R-card between Two Regions

Since $\vec{J} = \vec{J}^+ + \vec{J}^-$ and $\vec{M} = \vec{M}^+ + \vec{M}^-$, the boundary conditions for an R-card between regions become

$$\vec{E}_{tan} = Z(\vec{J}^+ + \vec{J}^-)$$

and

$$\vec{M}^+ = -\vec{M}^-.$$

Equations (6) and (7) are used. As indicated in the Carlos-3D document, these boundary conditions imply:

$$\vec{H}^+_{tan} = \hat{n} \times \vec{J}^+$$

$$\vec{H}^-_{tan} = \hat{n} \times \vec{J}^+ - Y\vec{M}^-$$

with $Y = 1/Z$. The unknowns are $\vec{J}^+$ and $\vec{J}^-$, $\vec{M}$. ($\vec{M} = \vec{M}^+$.)

$$A_p = \begin{bmatrix} 1 & 0 & 0 \\ 0 & 0 & 1 \\ 0 & 1 & 0 \\ 0 & 0 & -1 \end{bmatrix}; \qquad B = \begin{bmatrix} Z/2 & Z/2 & 0 \\ Z/2 & Z/2 & 0 \\ 0 & 0 & Y/2 \end{bmatrix}; \qquad C_p = \begin{bmatrix} 1 & 0 & 0 & 0 & 0 & 0 & 0 & 0 \\ 0 & 0 & 0 & 0 & 1 & 0 & 0 & 0 \\ 0 & 1 & 0 & 0 & 0 & -1 & 0 & 0 \end{bmatrix}$$

4 Basis Functions at Junctions

RWG basis functions are defined on two adjacent facets of a tessellation of the surface. These basis functions are defined as the difference of two RWG functions. An RWG function $\vec{F}$ is defined on a triangle with a distinguished edge, and the defining formula has been designed so that the fluence of $\vec{F}$ into the distinguished edge depends only on the geometry of the edge. Thus when two triangles share a common edge the fluence of $\vec{F}$ into that common edge will agree for both triangles. When these two RWG functions are subtracted to form the basis function the fluence *in* will match the fluence *out* (see Appendix B of [4]). Furthermore the RWG function on a triangle with a distinguished edge has the property that the fluence into the other two edges is zero. Thus the basis function defined as the difference of two RWG functions will satisfy a fluence matching condition (i.e. conservation of flow) at each edge of each of the two triangles. Experience has demonstrated that basis functions that satisfy fluence matching at every edge produce excellent results using the method of moments. The objective of this section is to generalize this definition of a basis function as the difference of two RWG functions to geometric situations where more than two facets come together at a common edge or two facets with different boundary conditions share a common edge. These geometric situations are called junctions. The approach is to define a basis function at the junction to be zero, one, or more linear combinations of RWG functions on the triangles sharing the junction edge. These linear combinations must satisfy the appropriate flow conservation laws. The next step is to write down these laws.

4.1 Conservation Laws

When viewed in the plane orthogonal to the common edge, the triangles sharing a common edge look like line segments sharing a common vertex (see figure 1.). Each of the triangles $T_1, T_2, T_3, \cdots$ has a surface normal $\hat{n}_1, \hat{n}_2, \hat{n}_3, \cdots$. The common edge has a common edge tangent $\hat{t}$, and each triangle has an edge normal $\hat{e}_1, \hat{e}_2, \hat{e}_3, \cdots$. The three unit vectors $\hat{n}_k, \hat{e}_k, \hat{t}$ are orthogonal, $k = 1, 2, 3, \cdots$. Each of the triangles T_k along with the common edge has an RWG function $\vec{F}_k$. The fluence of $\vec{F}_k$ into the junction is given by

$$fluence = \vec{F}_k \cdot \hat{e}_k$$

The other two RWG functions supported on T_k have zero fluence into the junction. Thus the only RWG function with non-zero fluence on T_k into the junction is $\vec{F}_k$. The RWG functions can be used for expanding electric current $\vec{J}$ and/or magnetic current $\vec{M}$. Expansions are required on the upper surface ($\hat{n}_k$ points to the upper surface of T_k) and the lower surface (-$\hat{n}_k$ points to the lower surface of T_k). We have

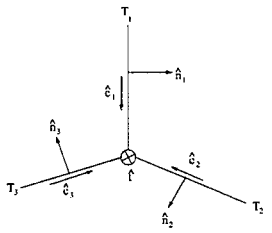

Figure 1: Geometry of RWG Basis Function

$$\vec{J}_k^+ = \hat{n} \times \vec{H}_k^+; \vec{H}_k^+ = \vec{H}_k \text{ on the upper surface of } T_k$$
$$\vec{J}_k^- = -\hat{n} \times \vec{H}_k^-; \vec{H}_k^- = \vec{H}_k \text{ on the lower surface of } T_k$$
$$\vec{M}_k^+ = -\hat{n} \times \vec{E}_k^+; \vec{E}_k^+ = \vec{E}_k \text{ on the upper surface of } T_k$$
$$\vec{J}_k^+ = \hat{n} \times \vec{E}_k^-; \vec{E}_k^- = \vec{E}_k \text{ on the lower surface of } T_k$$

The fluence into the junction is given by

$$\text{fluence}(\vec{J}_k^+) = \vec{e}_k \cdot \vec{J}_k^+ = \vec{e}_k \cdot \hat{n}_k \times \vec{H}_k^+ = -\hat{t} \cdot \vec{H}_k^+$$
$$\text{fluence}(\vec{J}_k^-) = \vec{e}_k \cdot \vec{J}_k^- = -\vec{e}_k \cdot \hat{n}_k \times \vec{H}_k^- = \hat{t} \cdot \vec{H}_k^-$$
$$\text{fluence}(\vec{M}_k^+) = \vec{e}_k \cdot \vec{M}_k^+ = -\vec{e}_k \cdot \hat{n}_k \times \vec{E}_k^+ = \hat{t} \cdot \vec{E}_k^+$$
$$\text{fluence}(\vec{M}_k^-) = \vec{e}_k \cdot \vec{M}_k^- = \vec{e}_k \cdot \hat{n}_k \times \vec{E}_k^- = -\hat{t} \cdot \vec{E}_k^+$$

Thus the fluence of $\vec{J}_k^+$ into the junction is the component of $\vec{H}$ parallel to the junction measured at the upper surface of T_k ($-\hat{t} \cdot \vec{H}_k^+$), and the fluence of $\vec{J}_{k+1}^-$ into the junction is the component of $\vec{H}$ parallel to the junction measured at the lower surface of T_{k+1} ($\hat{t} \cdot \vec{H}_{k+1}^-$). However, the upper surface of T_k and the lower surface of T_{k+1} bound the same region and $\vec{H}$ is continuous in a region. This leads to the conclusion

$$\text{fluence}(\vec{J}_k^+) + \text{fluence}(\vec{J}_{k+1}^-) = 0$$
$$\text{fluence}(\vec{M}_k^+) + \text{fluence}(\vec{M}_{k+1}^-) = 0$$

These equations can be integrated over the junction edge to get

$$\text{flux}(\vec{J}_k^+) + \text{flux}(\vec{J}_{k+1}^-) = 0$$
$$\text{flux}(\vec{M}_k^+) + \text{flux}(\vec{M}_{k+1}^-) = 0$$
$$\text{where flux} = \int_{\text{junction}} \text{fluence ds}$$

In Appendix B of [4] we have the result that $\int_{junction} \vec{F}_k \cdot \vec{e}_k ds = 1$ for RWG functions. This and the fact mentioned above that $\vec{F}_k$ is the only RWG function that contributes to flux($\vec{J}_k^+$) leads to the fact that when a basis function is expanded as a linear combination of the form $\sum_{k=1}^{N} (j_k^+ \vec{F}_k + j_k^- \vec{F}_k)$, where N is the number of facets at the junction, then the coefficient j_k^+ is flux($\vec{J}_k^+$). The flux conservation equation reduces to

$$j_k^+ + j_k^- = 0 \quad (12)$$
$$m_k^+ + m_k^- = 0 \quad (13)$$

This is the first conservation law.
Whenever the electrical parameters (ϵ, μ) of the volume above the surface are identical to the parameters of the volume below the surface, the following situation occurs. Each of the linear integral operators over the surface (upper surface + lower surface) has the form

$$I_+(\vec{J}^+) + I_-(\vec{J}^-) = I(\vec{J}^+ + \vec{J}^-)$$

$$I_+(\vec{M}^+) + I_-(\vec{M}^-) = I(\vec{M}^+ + \vec{M}^-)$$

where $I_\pm$ is either the L or the K operator, and $I_+ = I_- = I$. In this case $\vec{J}^+$, $\vec{J}^-$, $\vec{M}^+$, $\vec{M}^-$, are not the unknowns assigned to the surface. Instead $\vec{J} = \vec{J}^+ + \vec{J}_-$ and $\vec{M} = \vec{M}^+ + \vec{M}_-$, are taken as the unknowns (see Appendix A of [4]).

$$j_{k-1}^+ + j_k^- = 0$$

$$j_k^+ + j_{k+1}^- = 0$$

If T_k lies on a surface where $\vec{J}$ and/or $\vec{M}$ are the unknowns then the above equations are replaced by their sum

$$j_{k-1}^+ + j_k + j_{k+1}^- = 0 \tag{14}$$

where $j_k = j_k^- + j_k^+$. The same principle applies to $\vec{M}$.
A third principle is used for assigning basis functions to a junction edge. For a dielectric interface the tangential fields satisfy

$$\vec{H}_{tan}^+ = \vec{H}_{tan}^- \Rightarrow \vec{J}^+ = -\vec{J}^-$$

$$\vec{E}_{tan}^+ = \vec{E}_{tan}^- \Rightarrow \vec{M}^+ = -\vec{M}^-.$$

For an R-card between two regions we have

$$\vec{E}_{tan}^+ = \vec{E}_{tan}^- \Rightarrow \vec{M}^+ = -\vec{M}^-$$

In these cases there are additional constraints on the expansion coefficients

$$j_k^+ = -j_k^- \tag{15}$$

$$m_k^+ = -m_k^- \tag{16}$$

as required.
The final principle is that if a region in space is completely enclosed with impenetrable surfaces (perfect conductors and IBCs are impenetrable), the region is said to be dark. In a dark region all fields are zero. Thus if the region between T_k and T_{k+1} is dark then

$$j_k^+ = -j_{k+1}^- = 0 \tag{17}$$

$$m_k^+ = -m_{k+1}^- = 0 \tag{18}$$

these null coefficients must be removed from the basis function expansion.

4.2 Basis Function

In this section a method will be presented for finding basis functions for $\vec{J}$. The same method can be used for $\vec{M}$. A basis function is a sum of the form $\sum_{k=1}^{N}(j_k^+\vec{F}_k + j_k^-\vec{F}_k)$. The term $j_k^+\vec{F}_k$ is part of $\vec{J}_k^+$, and the term $j_k^-\vec{F}_k$ is part of $\vec{J}_k^-$. In the case where the second principle is used to replace j_k^+ and j_k^- with j_k , the term $(j_k^+\vec{F}_k + j_k^-\vec{F}_k)$ is replaced by $j_k\vec{F}_k$. All null coefficients must be removed. It is necessary that all the basis function for $\vec{J}$ be linearly independent so the number of coefficients ($(j_k^+$ and j_k^-) or j_k) is the number of degrees of freedom in the sum. Let M be this number. It is also necessary that each basis function satisfy all of the applicable conservation laws. These laws take the form

$$j_k^+ + j_{k+1}^- = 0$$

or

$$j_{k-1}^{+} + j_k + j_{k+1}^{-} = 0.$$

For dielectric interfaces we have the additional constraint

$$j_k^{+} + j_k^{-} = 0$$

All these constraint equations can be written in matrix form

$$K \cdot \vec{j} = \vec{0}$$

where $\vec{j}$ is the M vector $(j_1^{-}, j_1^{+}, \cdots, j_N^{+})^t$, and K is an L by M matrix (L is the number of constraints). A maximal set of linearly independent solutions to $K \cdot \vec{j} = \vec{0}$ is the set of basis functions for $\vec{J}$ at the junction. Such a set is a basis for the null space of K. One way to compute such a set is through a singular value decomposition (SVD) of K. The SVD of K is

$$K = \sum_{i=1}^{M} \sigma_i \vec{p}_i \vec{q}_i^{t}$$

where σ_i are the singular values, $\vec{p}_i$ are the orthogonal left singular vectors of dimension L, and $\vec{q}_i$ are the orthogonal right singular vector of dimension M. If $\sigma_\nu = 0$ then

$$K\vec{q}_\nu = \sigma_\nu \vec{p}_\nu = \vec{0}$$

Thus $\{\vec{q}_\nu : \sigma_\nu = 0\}$ is a basis for the null space of K, and therefore a set of basis functions for $\vec{J}$ at the junction.

4.3 The A_J Matrix

Each basis function is a vector function supported on the triangles adjacent to the junction edge. The basis function values contribute to $\vec{J}$, and $\vec{M}$ on upper and lower surface of each of these triangles. Associated with each basis function is a coefficient. The currents $\vec{J}$ and $\vec{M}$ are given as the sum of all the basis functions multiplied by their coefficients. When we want to evaluate the currents $\vec{J}$ and $\vec{M}$, given the basis function coefficients, we first must determine the coefficients $\vec{j} = (j_1^{-}, j_1^{+}, \cdots, j_N^{+})^t$ and $\vec{m} = (m_1^{-}, m_1^{+}, \cdots, m_N^{+})^t$. These coefficients are then multiplied by the appropriate RWG functions and contribute to $\vec{J}$ and $\vec{M}$ on upper and lower surface of each triangle. The A_J matrix is the mapping from the basis function coefficients to $\vec{j}$ and $\vec{m}$. The matrix is simply a matrix whose columns are $\{\vec{q}_\nu : \sigma_\nu = 0\}$ (i.e. the basis functions). The A_J matrix provides all the necessary information for defining basis functions on the junctions. It is most convenient to organize the rows of the A_J matrix by triangles.

4.4 Example 1: Perfect Conductors in one region

Consider three perfect electrical conductors (PEC) meeting at a junction. All surfaces in one region of space (see figure 1.). Magnetic current $\vec{M}$ is zero on a PEC so we need only consider $\vec{J}$. From the second principle we get

$$[1 \quad 1 \quad 1\,] \cdot \begin{bmatrix} j_1 \\ j_2 \\ j_3 \end{bmatrix} = [0]$$

An SVD of the matrix $K = [\ 1 \quad 1 \quad 1\ ]$ produces three singular values $\sigma = [\ 1.732 \quad 0 \quad 0\ ]$, and the right singular vectors corresponding to $\sigma = 0$ are

$$q_2 = \begin{bmatrix} -.816 \\ .408 \\ .408 \end{bmatrix}; q_3 = \begin{bmatrix} 0. \\ -.707 \\ .707 \end{bmatrix}$$

These are the two basis functions for $\vec{J}$ at the junction, and

$$A_J = \begin{bmatrix} -.816 & 0 \\ .408 & -.707 \\ .408 & .707 \end{bmatrix}$$

4.5 Example 2: Three R-cards in two regions

In this example we have T_2 is an R-card in region 1, while T_1 and T_3 are R-cards on the boundary between region 1 and region 2 (see figure 1.). First we derive basis functions for $\vec{J}$. From principle 2 we get $j_1^+ + j_2 + j_3^- = 0$, from principle 1 we get $j_3^+ + j_1^- = 0$. The matrix form is

$$\begin{bmatrix} 0 & 1 & 1 & 1 & 0 \\ 1 & 0 & 0 & 0 & 1 \end{bmatrix} \cdot \begin{bmatrix} j_1^- \\ j_1^+ \\ j_2 \\ j_3^- \\ j_3^+ \end{bmatrix} = \begin{bmatrix} 0 \\ 0 \end{bmatrix}$$

The basis functions for $\vec{J}$ from the SVD are

$$\vec{j} = \begin{bmatrix} j_1^- \\ j_1^+ \\ j_2 \\ j_3^- \\ j_3^+ \end{bmatrix} = \begin{bmatrix} 0 & 0 & -.5 \\ .408 & -.5 & 0 \\ -.816 & 0 & 0 \\ .408 & .5 & 0 \\ 0 & 0 & .5 \end{bmatrix} \cdot \begin{bmatrix} x_1 \\ x_2 \\ x_3 \end{bmatrix}$$

The constraint equation for $\vec{M}$ is $m_1 + m_3 = 0$. The matrix form is

$$[1 \quad 1\ ] \cdot \begin{bmatrix} m_1 \\ m_3 \end{bmatrix} = [0]$$

The basis functions for $\vec{M}$ from the SVD is

$$\begin{bmatrix} m_1 \\ m_3 \end{bmatrix} = \begin{bmatrix} -.707 \\ .707 \end{bmatrix} \cdot [x_4].$$

When the rows of A_J are organized by triangle we get four unknowns as follows:

$$= \begin{bmatrix} j_1^- \\ j_1^+ \\ m_1 \\ j_2 \\ j_3^- \\ j_3^+ \\ m_3 \end{bmatrix} = \begin{bmatrix} 0 & 0 & -.5 & 0 \\ .408 & -.5 & 0 & 0 \\ 0 & 0 & 0 & -.707 \\ -.816 & 0 & 0 & 0 \\ .408 & .5 & 0 & 0 \\ 0 & 0 & .5 & 0 \\ 0 & 0 & 0 & .707 \end{bmatrix} \cdot \begin{bmatrix} x_1 \\ x_2 \\ x_3 \\ x_4 \end{bmatrix}$$

References

[1] J.M. Putnam, L.N. Medgyesi-Mitchang and M.B. Gedera. Carlos-3D Three-Dimensional Method of Moments Code, Volume I Theory and Code manual, *Mcdonnell Douglas Corporation Report*, 10 December, 1992

[2] R. Coifman, V. Rokhlin and S. Wandzura. The Fast Mulitpole Method: A Pedestrian Prescription. *IEEE Antennas and Propogation Society Magazine*, 35(3):712, June 1993.

[3] B.C. Ahn, K. Mahadevan and A.W. Glisson. On the Applicability of Pulse Expansions and Point Matching in the Moment Method Solution of Three-Dimensional Electromagnetic Boundary-value Problems. *Proceedings of the 7-th Annual Review of Progress in Applied Computational Electromagnetics*. 265-277, March, 1991.

[4] E. Yip and B. Dembart. Matrix Assembly in FMM-MOM Codes *ISS Tech97-001*,January, 1997

A Near-resonance Decoupling Approach (NRDA) for Scattering Solution of Near Resonant Structures †

C. C. Lu and W. C. Chew

Center for Computational Electromagnetics
Electromagnetics Laboratory
Department of Electrical and Computer Engineering
University of Illinois
Urbana, IL 61801

1. Introduction

Recently, many fast algorithms [1-8] are developed to solve the integral equation of electromagnetic scattering. Most fast algorithms are developed to reduce the cost of the matrix-vector multiplications in the iterative solution of the matrix equations resulting from the integral equations. It is known that the dominant CPU time for iterative methods is the product of two factors: the time for each iteration, and the number of iteration required for a convergent result. The first factor can be significantly reduced by applying fast algorithms. The second factor usually depends on the problem geometry structures. In electromagnetic scattering problems, internal resonances, near resonances as in cavity modes, and multiple bounces of the waves will lead to large iteration numbers. The combined field integral equation (CFIE) can eliminate the slow convergence caused by the internal resonances. However, it does not rectify those caused by multiple bounces in open-ended cavities. Recently we conducted extensive calculations using MLFMA [8] for a model aircraft that contains an engine inlet. Above the frequency when the inlet supports one or more propagation modes, the iteration number for an iterative solver increases significantly compared to the same aircraft with the inlet sealed even though the number of unknowns for the cavity region is only a fraction of that for the entire problem. In high frequency methods, the multiple wave bounces are usually accounted for by ray expansion method and ray tracing method [9]. Even then, the inordinately large number of bounces in a cavity renders the use of ray-tracing method difficult for simulating waves in a cavity. Several hybrid methods [10-14] have also been reported for this problem in which low frequency methods are combined with a high frequency

† This work was supported by the Air Force Office of Scientific Research under Grant No. F49620-96-1-0025, the National Science Foundation under Grant No. NSF ECS93-02145, and the Office of Naval Research under Grant No. DAAH04-93-G-0430.

method to solve for the scattering solution from the cavity alone. No interior-exterior coupling was considered for these methods.

In this paper, we propose an algorithm that applies the equivalence principle and the method of moments to study the multiple wave bounces in an open-ended cavity, and to reduce the iteration number for an iterative solution of the problems. The idea is to apply the equivalence principle to separate the cavity region from the exterior region and solve the cavity problem by the method of moments with a direct solver. The interior and exterior solutions are coupled via a generalized admittance matrix called Y-matrix. As the cavity response is specified by the Y-matrix where multiple-bounce wave physics has already been incorporated, the iteration process for the exterior problem is free from having to account for multiple-bounce physics inside the cavity. Consequently, the iteration count for the exterior solution is greatly reduced. We call this method the near-resonant decoupling approach (NRDA) because it decouples the near-resonance in the cavity region from the exterior surface using the equivalence principle. It is a rigorous method and the only approximation is the result of the numerical implementation. In the following, we first introduce the formulation of this method for a general problem. Then we apply it to a two-dimensional problem.

2. General Formulation

The problem is to calculate electromagnetic scattering from a conducting object with an open-ended cavity due to an exterior incident field $\mathbf{E}^{inc}$. The boundary integral equation approach for this problem is to solve for the induced current distribution on the object surface (including the cavity wall and the exterior surface, see Figure 1) by solving the surface integral equation. For the problem in this paper, the object surface consists of two parts: (1) the interior surface (cavity wall), and (2) the exterior surface. The coupling between the interior and the exterior surface is through the aperture. Since the cavity interior structure gives rise to slow convergence of the entire problem due to multiple wave bounces, we decouple the cavity region from the rest of the object surface. To this end, we seal the aperture by a conducting sheet, and put electric and magnetic currents on both sides of the conducting sheet. Based on the equivalence principle, when the currents on the artificial conducting sheet are properly determined, the new configuration is exactly equivalent to the original one in that they give the same scattered field. As a result, the interior wall and the exterior surface are separated, and the original problem is converted into two problems: the interior problem, and the exterior problem. Two integral equations can be formulated for each problem.

The exterior equivalence problem is shown in Figure 1(b). In this case, the boundary integral equation is specified by

$$(\mathbf{E}^{sca} + \mathbf{E}^{inc}) \times \hat{n} = \mathbf{M}, \qquad \text{or} \qquad (\mathbf{E}^{sca} + \mathbf{E}^{inc})|_{\tan} = \hat{n} \times \mathbf{M}. \qquad (1)$$

where $\mathbf{M}$ is the magnetic current distribution. It is zero outside the aperture region.

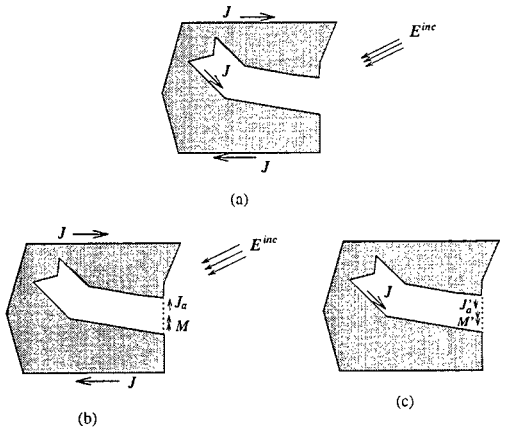

Figure 1. *(a) An open-ended cavity embedded in a conducting body. (b) External equivalence. (c) Interior equivalence.*

Equation (1) can be converted into matrix form using the method of moments,

$$\overline{\mathbf{G}}_{11} \cdot \mathbf{J} + \overline{\mathbf{G}}_{12} \cdot \mathbf{M} = \mathbf{V}. \tag{3}$$

where $\overline{\mathbf{G}}_{11}$ and $\overline{\mathbf{G}}_{12}$ are the matrix representation of the integral operators for $\mathbf{J}$ and $\mathbf{M}$, respectively, and $\mathbf{V}$ is the array calculated using the incident field $\mathbf{E}^{inc}$.

The integral equation for the interior equivalence problem can be formed in the similar manner, as shown in Figure 1(c). The electric and magnetic currents are $\mathbf{J}'$ and $\mathbf{M}'$ on the interior surface (now including the cavity wall and the aperture), respectively, with $\mathbf{M}' = 0$ on the cavity wall. A similar integral equation as (1) can be formed in terms of $\mathbf{J}'$ and $\mathbf{M}'$, and then converted into matrix form as

$$\overline{\mathbf{G}}'_{11} \cdot \mathbf{J}' + \overline{\mathbf{G}}'_{12} \cdot \mathbf{M}' = 0. \tag{4}$$

Equation (4) can be inverted to get $\mathbf{J}' = \overline{\mathbf{Y}} \cdot \mathbf{M}'$, where $\overline{\mathbf{Y}}$ is called generalized admittance matrix. It relates the aperture current $\mathbf{J}'$ in terms of $\mathbf{M}'$. Applying the continuity condition, we have

$$\mathbf{J}_a = \overline{\mathbf{Y}} \cdot \mathbf{M}. \tag{5}$$

where $\mathbf{J}_a$ and $\mathbf{M}$ are the aperture equivalent electric current and magnetic current on the external side of the aperture. Equation (5) can be combined

with Equation (3) to solve the induced current on the exterior surface of the target.

Since the multiple-bounce wave physics inside the cavity has been accounted for by direct matrix inversion, and the interaction information is contained in the Y-matrix, the iterative solution to Equation (6) is now free from the influence of the interior multiple wave bounces. Hence, the required iteration number essentially depends on the exterior structures. In addition, the equivalent exterior problem has less unknowns than the original integral equation for the entire object.

The algorithm introduced above applies to general problems. In the next section, we present two simulation results for two dimensional problems.

3. Two-Dimensional Applications

We have implemented the near-resonance decoupling algorithm (NRDA) for two dimensional problems. We use the method of moments with the pulse basis and point matching technique to discretize the integral equation. The code was implemented for arbitrary two-dimensional objects. The results presented here are based on the combined field integral equation.

The first object considered is shown in Figure 2(a). Figure 2(b) shows the RCS comparison between the algorithm in this paper (NRDA) and that of entire model solution. The entire model solution needs 156 iterations (64.8 sec. total CPU time on DEC workstation) to reduce the residue error to 5×10^{-3}, and NRDA require only 16 iterations (18.8 sec. total CPU time) to achieve the same residue error. To demonstrate the the iteration number reduction using NRDA, we conducted a simulation for a rectangular cavity as shown in Figure 3(a). In this simulation, the parameters $a = 2.0\lambda$ and $b = 0.5\lambda$ are fixed, and the depth parameter c is varying. Figure 3(b) shows the comparison of the iteration numbers. for the same problem and the same residual error in the conjugate gradient iteration, the iteration number required for NRDA is much smaller than that for the entire model solution. As is expected, as the cavity depth increases, the iteration number for the entire model solution also increases. On the contrary, the iteration number increases for NRDA is relatively small.

4. Conclusion

Equivalence principle method has been combined with the method of moments to calculate the scattering from conducting objects with near-resonant open-ended cavity. This method has successfully been applied to solve for the scattering solution from two-dimensional cavities. The numerical calculations show that this method has significantly reduced the iteration number in the iterative solution for problems that are plagued by multiple wave bounces and near-resonance in an open-ended cavity.

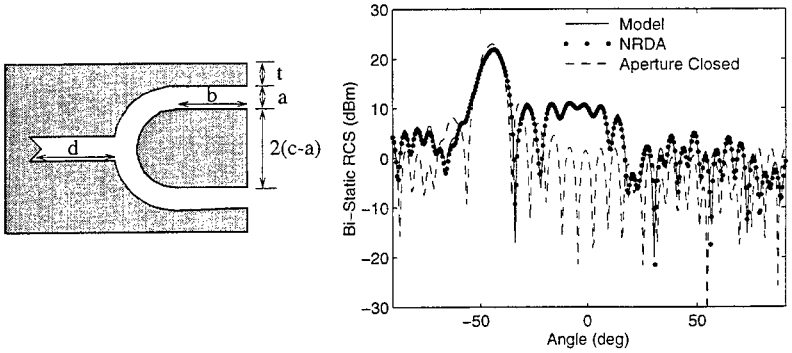

(a) (b)

Figure 2. *(a) An object a cavity and two apertures. the geometry parameters are: $a = 1\lambda$, $b = 1.6\lambda$, $c = 2.4\lambda$, $d = 3.6\lambda$, $t = 0.6\lambda$. (b) The RCS comparison of NRDA and entire model solution for TE wave incidence at 45°.*

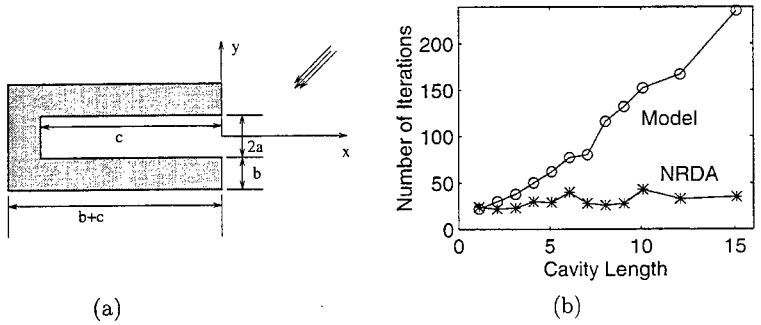

(a) (b)

Figure 3. *(a) A demonstration problem: The object is a 2D PEC cylinder with an open-ended cavity, defined by three parameters a, b, and c. The plane wave incident angle is 45° with a frequency of 300 MHz. (b) The iteration number comparison for the model solution and NRDA for the object shown in Figure 2. The parameters $a = 2\lambda$ and $b = 0.5\lambda$ are fixed, and c is varying. The result is for TM polarization.*

References

[1] V. Rokhlin, "Rapid solution of integral equations of scattering theory in two dimensions," *J. Comput. Phys.*, vol. 86, no. 2, pp. 414-439, February 1990.

[2] R. Coifman, V. Rokhlin, and S. Wandzura, "The fast multipole method for the wave equation: a pedestrian prescription," *IEEE Antennas Propagat. Mag.*, vol. 35, no. 3, pp. 7-12, June 1993.

[3] N. Engheta, W. D. Murphy, V. Rokhlin, and M. S. Vassiliou, "The fast multipole method (FMM) for electromagnetic scattering problems," *IEEE Trans. Antennas Propagat.*, vol. 40, no. 6, pp. 634-641, July 1992.

[4] B. Dembart and E. Yip, "A 3D moment method code based on fast multipole," *URSI Radio Sci. Meet. Dig.*, p. 23, 1994.

[5] E. Michielssen and A. Boag, "Multilevel evaluation of electromagnetic fields for the rapid solution of scattering problems," *Microwave Opt. Tech. Lett.*, vol. 7, no. 17, pp. 790-795, December 1994.

[6] E. Michielssen and A. Boag, "A multilevel matrix decomposition algorithm for analyzing scattering from large structures," *11th Annual Review of Progress in Applied Computational Electromagnetics*, pp. 614-620, 1995.

[7] C. C. Lu and W. C. Chew, "Fast algorithm for solving hybrid integral equations," *IEE Proceedings-H*, vol. 140, no. 6, pp. 455-460, Dec. 1993.

[8] J. M. Song and W. C. Chew, "Multilevel fast-multipole algorithm for solving combined field integral equations of electromagnetic scattering," *Microwave Opt. Tech. Lett.*, vol. 10, no. 1, pp. 15-19, September 1995.

[9] H. Ling, R. C. Chou, and S. W. Lee, "Shooting and bouncing rays: calculating the RCS of an arbitrary shaped cavity," *IEEE Trans. Antennas Propagat.*, vol. 37, no. 2, pp. 194-205, Feb. 1989.

[10] R. J. Burkholder and P. H. Pathak, "High-frequency electromagnetic scattering by open-ended waveguide cavities," *Radio Science*, vol. 26, no. 1, pp. 211-218, Jan.-Feb. 1991.

[11] D. C. Ross, J. L. Volakis, and H. T. Anastassiu, "Hybrid finite element-modal analysis of jet engine inlet scattering," *IEEE Trans. Antennas Propagat.*, vol. 43, no. 3, pp. 277-286, March 1995.

[12] R. F. Harrington and J. R. Mautz, "A generalized network formulation for aperture problems," *IEEE Trans. Antennas Propagat.*, vol. 24, no. 11, pp. 870-873, Nov. 1976.

[13] T. Wang, R. F. Harrington, and J. R. Mautz,"Electromagnetic scattering from and transmission through arbitrary apertures in conducting bodies," *IEEE Trans. Antennas Propagat.*, vol. 38, no. 11, pp. 1805-1814, Nov. 1990.

[14] T. -M. Wang and H. Ling, "Electromagnetic scattering from three-dimensional cavities via a connection scheme," *IEEE Trans. Antennas Propagat.*, vol. 39, no. 10, pp. 1505-1513, Oct. 1991.

Solution of Maxwell Equations Using Krylov Subspace From Inverse Powers Of Stiffness Matrix

Vladimir Druskin, Ping Lee
Schlumberger-Doll Research
Old Quarry Road
Ridgefield, CT 06877-4108, U.S.A.
and
Leonid Knizhnerman
Central Geophysical Expedition
Moscow, Russia

January 14, 1997

Abstract

We propose a new approach for solutions to Maxwell equations. The new method is based on Spectral Lanczos Decomposition Method (*SLDM*) with Krylov subspaces generated from the inverse powers of the Maxwell operator. This new approach speeds up significantly the convergence of standard *SLDM* for the solution of Maxwell equations and meanwhile retains the advantages of standard Krylov subspace technique such as the capability of solving for multiple frequencies and the ability of eliminating completely spurious modes. The cost of computing action of the inverse powers of the stiffness operator is effectively equivalent to the cost of solving a scalar DC equation. This is achieved by a decomposition of stiffness operator into the curl-free and divergence-free projections. The solution of the projections can be computed by discrete Fourier transforms (DFT) and preconditioned conjugate gradient (PCG) iterations. The convergence rate of the new method improves as frequency decreases which makes it more attractive for low frequency applications. We apply the new solution technique to model induction logging in geophysical prospecting applications, giving rise to more than an order of magnitude convergence improvement over the standard Krylov subspace approach. This makes it feasible to routinely use 3D modeling for model based interpretation, a breakthrough in induction logging and interpretation.

Key words. Spectral Lanczos decomposition, Krylov subspace, Maxwell equations.

1 Introduction

One exciting area where Krylov subspace techniques had enjoyed much success is in obtaining solution to three dimensional Maxwell equations for the applications in geophysical prospecting [2], [3]. It has been well documented that obtaining numerical solution to Maxwell equations using finite difference or finite element methods special care must be taken to prevent generation of spurious modes causes by the numerical inaccuracy in approximating divergence-free functions. Druskin and Knizhnerman [3] developed a spectral Lanczos decomposition (*SLDM*) method based Krylov subspace technique for solution of Maxwell equation that has the capability to completely remove numerical spurious modes. It also can, when implemented for computer simulations, compute solutions for multiple number of frequencies at the cost of a single frequency. As shown in [3], the convergence of *SLDM* depends on the conductivity contrast and frequency; in particular the convergence slows down for high contrast and for low frequencies. In addition, for low frequency problems, the finite difference grid (with large aspect ratios) used in discretization introduces ill-conditioning to the stiffness operator. Like all other Krylov subspace based methods, it is difficult to precondition the discretized equation.

In this paper, we introduce a alternative approach for solutions to Maxwell equations. The method is based on the *SLDM* (which we will refer to as the standard *SLDM*) but with Krylov subspaces generated from the inverse powers of the Maxwell operator. This new approach speeds up significantly the convergence of standard *SLDM* for the solution of Maxwell equations and meanwhile retains the advantages of standard Krylov subspace technique such as the capability of solving for multiple frequencies and the ability to eliminate spurious modes. The inverse powers of the stiffness operator are computed from a decomposition of the curl-free and divergence-free projections. The solution of the projections are computed by discrete Fourier transforms (DFT) and preconditioned conjugate gradient (PCG) iterations. As result, the cost of computing action of the inverse powers of the stiffness operator is effectively equivalent to the cost of solving a scalar DC equation. We show that the convergence rate of the new method improves as frequency decreases which makes it more attractive for low frequency applications. The new solution technique is applied to model induction logging in geophysical prospecting applications, giving rise to more than an order of magnitude convergence improvement over the standard Krylov subspace approach. This makes it feasible to routinely use 3D modeling for model based interpretation [1], a breakthrough in induction logging and interpretation.

The remainder of this paper is outlined as follows: In Section 2, we give a brief description of Maxwell equations and boundary condition. We will present some motivation in Section 3 for the use of Krylov subspaces generated from inverse of the stiffness operator. We show an efficient way of computing the action of the inverse operator in Section 4. Numerical results and performance speed-up are presented in Section 5.

2 Maxwell Equations

We consider the frequency domain problem for Maxwell's equations

$$\begin{aligned} \nabla \times \mathbf{E} + i\omega\mu\mathbf{H} &= 0 \\ \nabla \times \mathbf{H} - \sigma\mathbf{E} &= \mathbf{J}. \end{aligned} \tag{1}$$

The symbols $\sigma = \sigma(x, y, z)$ and μ_0 denote the conductivity coefficient and the permeability constant, respectively. Displacement current is assumed to be negligible. Substitutions of equation (1) lead to the equation expressed in terms of electric field $\mathbf{E}$,

$$\sigma^{-1}\mu^{-1}\nabla \times \nabla \times \mathbf{E} + i\omega\mathbf{E} = i\omega\sigma^{-1}\mathbf{J} \tag{2}$$

We define operator

$$A = \sigma^{-1}\mu^{-1}\nabla \times \nabla \times \tag{3}$$

and source function

$$\varphi = \sigma^{-1}\mathbf{J}$$

Then (2) becomes

$$(A + i\omega I)\mathbf{E} = i\omega\varphi, \tag{4}$$

For convenience, we assume the domain of interest $\Omega = \{(x, y, z) : x_{min} \leq x \leq x_{max},\ y_{min} \leq y \leq y_{max},\ z_{min} \leq z \leq z_{max}\}$. The boundary condition of equation (2) (or (4)) is given by

$$\mathbf{E} \times \mathbf{n}|_{\partial\Omega} = 0. \tag{5}$$

Note that Gauss Theorem implies the right hand side of equation (4) is orthogonal to the null-space of A, thus the boundary value problem (4) and (5) is well-posed. In this article we assume that the equation (2) is discretized by finite difference method on a staggered Yee grid and resulting a matrix equation of form (4) which we will use interchangeably, *i.e.*, we will use A to denote both the continuous operator defined in (3) and it discrete counterpart when there is no ambiguity.

3 Krylov Subspace Method

The solution method introduced in this paper is essentially based on the *SLDM* - Spectral Lanczos Decomposition Method. *SLDM* was first introduced by Druskin and Knizhnerman[2] for the solution of parabolic Maxwell equations in both time and frequency domain. The method can be extended to more general second order partial differential equations[3].

The motivation of our new method is based on the following observation. In view of (4), the matrix function $(A+i\omega I)^{-1}$ can be formally written as

$$(A+i\omega I)^{-1} = \sum_{k=0}^{\infty}(-1)^k(i\omega)^{-(k+1)}A^k \tag{6}$$

It is easy to see that the convergence of the truncated series depends on the value of ω. In particular, the convergence rate is slower for smaller frequency ω. We can also write $(A+i\omega I)^{-1}$ as

$$(A+i\omega I)^{-1} = -i\omega^{-1}(A^{-1}-i\omega^{-1}I)^{-1}A^{-1}$$

Again, we can write formally

$$(A^{-1}-i\omega^{-1}I)^{-1} = \sum_{k=0}^{\infty}(-1)^k(i\omega)^{k+1}A^{-k} \tag{7}$$

Compare (6) with (7) we see that the truncated series in (7) should converge faster than that of (6) when the frequency ω is small. This suggests that faster convergence rate can be obtained for small ω if we use *SLDM* with the Krylov subspace $\mathcal{K}^m(A^{-1},\varphi) = \text{span}\left\{\varphi, A^{-1}\varphi, \ldots, A^{-(m-1)}\varphi\right\}$. The solution of (4) can written as

$$\mathbf{E} = -i\omega^{-1}(A^{-1}-i\omega^{-1}I)^{-1}A^{-1}\varphi. \tag{8}$$

REMARK I: In induction logging applications, the logging tools typically have low operating frequencies (in the range of kilo Hertz). Therefore we can expect to obtain faster convergence when approximating the solution in the Krylov subspace spanned by the inverse powers of A.

REMARK II: One advantage of using spectral decomposition method for solving the Maxwell equation (2) is that one can pick and choose in the computed spectrum so that one can easily eliminate spurious modes generated by the numerical approximation of the operator defined in (3). The stability problem caused by numerical spurious mode has been well documented and is absolutely essential in obtaining accurate solutions to the Maxwell equations at low frequency.

4 Calculation of $\mathbf{A}^{-1}$

Computing the Krylov subspaces $\mathcal{K}^m(A^{-1},\varphi)$, originated from the operator A^{-1} requires computing the action of A^{-1} at each Lanczos step. More precisely, if ψ is the last Lanczos vector, then we need to compute $\mathcal{E} = A^{-1}\psi$. Recall the definition of A in (3), this translates to solving the equation

$$\nabla\times\nabla\times\mathcal{E} = \sigma\mu\psi, \tag{9}$$

subject to boundary condition

$$\mathcal{E} \times \mathbf{n} = 0. \tag{10}$$

By Gauss Theorem, we assume all Lanczos vectors $\mathcal{E}$ satisfy

$$\nabla \cdot \sigma\mathcal{E} = \nabla \cdot \sigma\varphi = 0, \tag{11}$$

where φ is the first Lanczos vector. We can decompose $\mathcal{E}$ into $\mathcal{E} = \mathcal{E}_0 + \nabla\Phi$, such that $\nabla \cdot \mathcal{E}_0 = 0$. Since $\mathcal{E}_1$ is curl-free, we have

$$\nabla \times \nabla \times \mathcal{E}_0 = \mu\sigma\psi.$$

Using the vector identity $\nabla \times \nabla \times = -\Delta + \nabla\nabla\cdot$ and the divergent free condition of $\mathcal{E}_0$, we arrive at

$$-\Delta\mathcal{E}_0 = \mu\sigma\psi. \tag{12}$$

The convergence free condition (11) gives rise to

$$-\nabla \cdot \sigma\nabla\Phi = \nabla \cdot \sigma\mathcal{E}_0, \tag{13}$$

From the above derivation, we see that the evaluation of $A^{-1}\psi$ can be reduced to the solutions of the vector Laplace equation (12) and the DC equation (13) with appropriate boundary conditions. The boundary condition (10) suggests that we can choose homogeneous Dirichlet boundary condition for the DC equation, *i.e.*,

$$\Phi|_{\partial\Omega} = 0, \tag{14}$$

and

$$\mathcal{E}_0 \times n|_{\partial\Omega} = 0. \tag{15}$$

The divergence condition condition $\nabla \cdot \mathcal{E}_0 = 0$ suggests the following complimentary normal flux boundary condition

$$\frac{\partial(\mathcal{E}_0 \cdot \mathbf{n})}{\partial n}|_{\partial\Omega} = 0. \tag{16}$$

For finite difference approximations of the vector Laplace equation (12) on the domain $\Omega = \{(x, y, z) : x_{min} \leq x \leq x_{max},\ y_{min} \leq y \leq y_{max},\ z_{min} \leq z \leq z_{max}\}$. The x-component of the equation (12) is

$$-\Delta\mathcal{E}_0^x = \mu\sigma\psi^x, \tag{17}$$

with boundary conditions

$$\mathcal{E}_0^x|_{y=y_{min}} = \mathcal{E}_0^x|_{y=y_{max}} = \mathcal{E}_0^x|_{z=z_{min}} = \mathcal{E}_0^x|_{z=z_{max}} = 0, \tag{18}$$

and

$$\frac{\partial \mathcal{E}_0^x}{\partial x}|_{x=x_{min}} = \frac{\partial \mathcal{E}_0^x}{\partial x}|_{x=x_{max}} = 0. \tag{19}$$

The equations and boundary conditions for $\mathcal{E}_0^y$ and $\mathcal{E}_0^z$ are defined in a similar fashion.

REMARK I: The key to the computational efficiency of our new solution scheme relies on whether we can efficiently evaluate the action of A^{-1} described in this section. To compute the action of A^{-1} we need to solve four scalar equations (three scalar Laplace equations and a DC equation). The solution to the finite difference equations for the boundary value problem (17), (18), and (19) can be obtained efficiently by either FFT or DFT. Similarly for the solution of $\mathcal{E}_0^y$ and $\mathcal{E}_0^z$. The solution to the DC equation can be obtained by preconditioned conjugate gradient iterations. The effectiveness of the preconditioner depends the characteristics of the underlying finite difference discretization. In our numerical experiments for induction logging simulations, preconditioning using the incomplete Cholesky factorization has proven to be very effective.

REMARK II: Strictly speaking, the equations (12) and (13) are uncoupled only if the domain of interest is the whole space. The coupling in bounded domains are enforced by boundary conditions.

5 Numerical Experiments

We have implemented the algorithm outlined in the previous sections for the solution of Maxwell equations to model induction logging in geophysical applications, which typically have operating frequency in the kHz range. The equations (4) are discretized by finite difference approximation on Yee grid [5]. The whole space is approximated by truncating the space into large rectangular box. To further reduce the number of grid points in the numerical approximation, the box is subdivided by variable size finite difference grid (exponentially increasing from the center of the box). This is made possible by the diminishing variation of the electromagnetic field away at relatively low frequency from the center of the box where sources and receivers are located. Material averaging are performed to allow arbitrary formation of earth structure, an important feature in our implementation (since most induction logging modeling codes to-date restrict to 1-D or 2D geometry).

For the sake of demonstration, we will use *SLDM* to refer to the standard Krylov subspace approach and *SLDMINV* to the new approach using the inverse powers. Table 1 compares the convergence rate of *SLDM* and *SLDMINV* for all three frequencies for a typical model (the convergence depends on the complexity of the model and conductivity contrasts). Figure 4 gives the comparison of convergence of one particular case. Table 2 shows the number of iterations required to reduce relative error to 10^{-6} as a function of frequency. The convergence improves as frequency decreases.

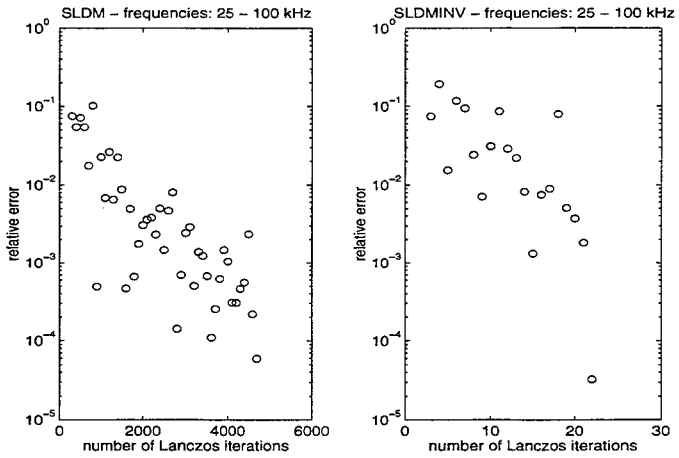

Figure 1: Comparison of convergence rate of *SLDM* and *SLDMINV*

	# Iteration	Time (min)[1]
SLDM	6,000	60
SLDMINV	35	3

Table 1. *convergence comparison of SLDM and SLDMINV*

Frequency (kHz)	# Iteration
105.300	31
52.650	23
26.325	20
1.000	7

Table 2. *number of iterations to convergence as function of frequency*

We also test the new method for different level of conductivity contrasts and deviations to formation layers. Table 3 and Table 4 show that the convergence of *SLDMINV* is insensitive to the conductivity contrast and deviation.

Contrast ($\sigma_B = 500$mS)	# Iteration
1	31
10	37
100	37

Table 3. *SLDMINV Convergence vs. Conductivity Contrast (4 ft. Bed)*

Contrast ($\sigma_B = 500$mS)	# Iteration
10	46
100	36

Table 4. *80 degree dip (4 ft. Bed)*

ACKNOWLEDGMENT: The authors wish to thank Drs. Barbara Anderson, Tarek Habashy and Michael Oristaglio for valuable discussions and support throughout the completion of this work.

References

[1] Anderson, B., Barber, T., Druskin, V., Dussan, E., Lee, P., Knizhnerman, L., and Davydycheva, S., q*The response of multiarray induction tools in highly dipping formations with invasion and in arbitrary 3D geometry, SPWLA Annual Conf.*, New Orleans, LA, June, 1996.

[2] Druskin, V. and Knizhnerman, L., *Two polynomial methods to compute functions of symmetric matrices*, Comput. Math. Math. Phys., Vol. 29, pp. 112-121, 1989.

[3] Druskin, V. and Knizhnerman, L., *Spectral approach to solving three-dimensional Maxwell's diffusion equations in the time and frequency domains*, Radio Science, Vol. 29, No. 4, pp. 937-953, 1994.

[4] Druskin, V. and Knizhnerman, L., *Extended Krylov subspaces approximations of matrix functions. Applications to computational electromagnetics*, Proceedings of Copper Mountain Conference on Iterative Methods, Copper Mountain, CO, April, 1996

[5] Yee, K. S., *Numerical solution of initial boundary value problems involving Maxwell's equations in isotropic media*, IEEE Trans. Antennas Prop., AP-14, pp. 302-307, 1966.

SESSION 17:

WAVE PROPAGATION

Chair: B. Weedon

WAVE PROPAGATION ON TWO DIMENSIONAL SLOW-WAVE STRUCTURES WITH SQUARE LATTICE

Ross A. Speciale

Redondo Beach, California

polytope@msn.com

1 - PRACTICAL APPLICATIONS.

Two dimensional slow-wave structures with square lattice, in the form of tightly-packed clusters of directly-coupled cavity resonators, have been theoretically analyzed in substantial depth [1 & 2], and experimentally evaluated as low-loss, wide-band signal-distribution networks for affordable, electronically steered phased arrays [2 & 3].

In this specific application, each of the mutually-coupled resonators in the structure feeds one of the array elements with the resultant vector-sum of the signals of a relatively small number of mutually-coherent sources [3 & 4].

This phased array configuration leads to large reductions in the required number of electronic beam-steering controls, and consequently in cost.

The aperture distributions, required for generating radiated beams in the specified pointing directions, are obtained as *complex linear combinations* of the component wave-fields of all the amplitude-, and phase-controlled sources used (in transmission, or of receiver front-ends in reception).

2 - THE NEW NETWORK ANALYSIS METHODS.

Such slow-wave structures that resemble egg-crates, have now been analyzed both formally as well as numerically, by applying new network-theory methods [1 & 2].

The ultimate objective of this study is the identification of the natural wave-propagation modes of egg-crate-like clusters of directly-coupled cavity resonators, and the characterization of these wave-modes in terms of their wave-impedance and propagation constants [5].

Characteristic wave-impedance matrices (the image-matrices Z_{I1} , and Z_{I2}), and transfer-function matrices (the scattering-matrix blocks S_2 , and S_3) have been both expressed in closed form, and evaluated numerically as functions of the experimentally determined impedance parameters $a = Z_{11}$, and $b = Z_{12}$ of a single four-port cavity resonator.

3 - THE BASIC BUILDING-BLOCKS OF AN EGG-CRATE STRUCTURE.

The outward-directed propagation of radial slow waves, emanating from a single multi-phase source inside any of the cavities, has been analyzed by considering the semi-infinite structure obtained by removing the cavity containing the source, and by considering the region

surrounding the resulting hole as a set of concentric, square tiers. Figure 1 shows a central patch, including the first three tiers of resonators surrounding the hole. The three tiers have been here progressively crosshatched for easy visual identification.

The central first tier, crosshatched at + 45° in figure 1, obviously exhibits the simplest network configuration (Figure 2), but plays nevertheless a very fundamental role as a) the basic prototype cell, and b) the first stepping-stone of the analysis process. Indeed, its equivalent circuit has a 4-port input-interface inside the hole, and a 12-port output-interface around its external boundary, for a total of 4 + 12 = 16 ports.

Simple arithmetic formulas express the number of resonators N_R , the number of input-interface ports n_p , the number of output-interface ports N_P , and the total number of ports P for the T^{th} resonator-tier, counting from the hole :

$$N_R = 8T \qquad (1) \qquad\qquad P = 16T \qquad (2)$$

$$n_p = 4\left[1+2(T-1)\right] \qquad (3)$$

$$N_P = 4\left[3+2(T-1)\right] \qquad (4)$$

4 - WAVE IMPEDANCES AND PROPAGATION CONSTANTS.

A closed-form expression has first been derived for the 16 × 16 impedance matrix of the first tier of resonators (Figure 2), by simply connecting eight mutually-identical resonators in a closed square ring. The interconnection was performed by writing the node-voltage (Kirchoff's) equations, and the corresponding node-current equations, for all eight internal nodes, thus eliminating the common-node voltages and currents.

This 16 × 16 impedance matrix, partitioned in a 4 × 4 leading block Z_1 , an 12 × 12 trailing block Z_4 , and two rectangular blocks Z_2 (4 × 12) , and Z_3 (12 × 4), exhibits very specific symmetries that are directly correlated to the rotation, and reflection symmetries of the first tier. Indeed, the 4 × 4 leading block Z_1 is *symmetric*, and *circulant* [6], the 12 × 12 trailing block Z_4 is *symmetric*, and *block-circulant* with *circulant* 3 × 3 *blocks* [6], and the rectangular blocks Z_2 , and Z_3 can be expressed as Kronecker Products of a *symmetric*, and *circulant* matrix Z_{21} by a 1 × 3 row-vector, and respectively a 3 × 1 column-vector, both having all elements equal to 1 (See enclosed Tables).

Further, closed-form expressions of the image-impedance matrices Z_{I1} , and Z_{I2} for the input-and output-interface of the first tier, and closed-form expressions of the transfer-function matrices S_2 , and S_3 have also been obtained, by applying the definitions given in Reference [2].

All the resonator-tiers beyond the first, can be similarly characterized, in a recursive process exploiting the *"a priori"* knowledge of the fact that the input-interface image-impedance matrix Z_{I1} of each tier is equal to the output-interface image-impedance matrix Z_{I2} of the preceding one it circumscribes.

5 - RESULTS.

The closed-form expressions of the four block Z_i of the impedance matrix Z_{24} of the first resonator-tier, are cast as functions of the *only two different* impedance parameters $a = Z_{11}$, and $b = Z_{12}$ of a single four-port cavity resonator.

Indeed, the impedance matrix of a *reciprocal*, and C_{4v}-*symmetric* four-port resonator can be expressed by [6] :

$$Z_6 = circ(a, b, b, b) \qquad (5)$$

6 - REFERENCES.

[1] Speciale R. A. ,"Advanced Design of Phased Array Beam-Forming Networks," Proceedings of the 12th Review of Progress in Applied Computational Electromagnetics, Monterey, California, March 18-22, 1996, pages 918-930.

[2] Speciale R. A. ,"Synthesis of Phased ArrayAperture Distributions," Proceedings of the 12th Review of Progress in Applied Computational Electromagnetics, Monterey, California, March 18-22, 1996, pages 898-913.

[3] Speciale R. A. , US Patent No. 5,347,287 Awarded September 13, 1994.

[4] Speciale R. A. , US Patent No. 5,512,906 Awarded April 30, 1996.

[5] Speciale R. A. ,"Mathematical Representation of Multiport Resonator Test Data," paper submitted to the 1997, 12th Review of Progress in Applied Computational Electromagnetics.

[6] Davis J. P. ,"Circulant Matrices," John Wiley & Sons, New York, 1979, Pure and Applied Mathematics Series, Chapter 3, pages 66-107, and Chapter 5, pages 155-191.

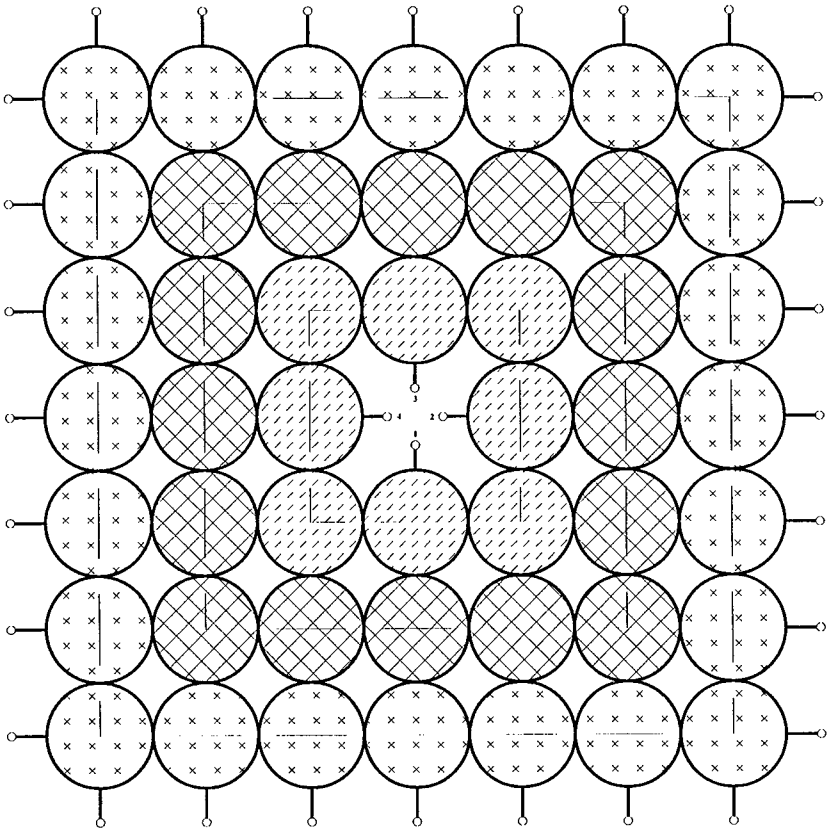

Figure 1 - This Two Dimensional Slow-Wave Structure with Square Lattice is a 3-Tier Cluster of Directly-Coupled Four-Port Cylindrical Resonators.

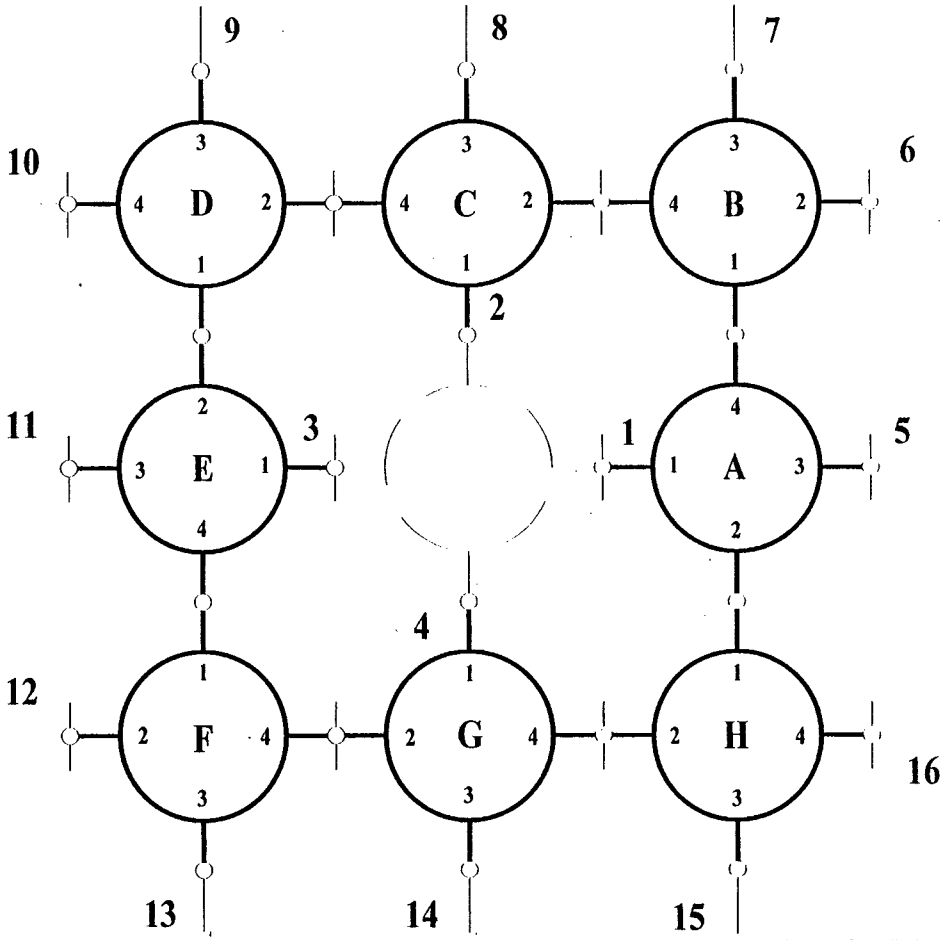

Figure 2 - Equivalent Circuit of the First Tier of Four-Port Cylindrical Resonators. This Prototype Eight-Resonator Set has a 4-Port Input and a 12-Port Output.

WAVE PROPAGATION ON TWO DIMENSIONAL SLOW-WAVE STRUCTURES WITH HEXAGONAL LATTICE

Ross A. Speciale

Redondo Beach, California

polytope@msn.com

1 - PRACTICAL APPLICATIONS.

Two dimensional slow-wave structures with hexagonal lattice, in the form of tightly-packed clusters of directly-coupled cavity resonators, have been theoretically analyzed in substantial depth [1 & 2], and experimentally evaluated as low-loss, wide-band signal-distribution networks for affordable, electronically steered phased arrays [2 & 3].

In this specific application, each of the mutually-coupled resonators in the structure feeds one of the array elements with the resultant vector-sum of the signals of a relatively small number of mutually-coherent sources [3 & 4].

This phased array configuration leads to large reductions in the required number of electronic beam-steering controls, and consequently in cost.

The aperture distributions, required for radiating beams in all the specified pointing directions, are obtained as *complex linear combinations* of the component wave-fields generated by all the amplitude-, and phase-controlled sources used (in transmission, or of receiver front-ends in reception).

2 - THE NEW NETWORK ANALYSIS METHODS.

Such slow-wave structures that resemble honeycombs, have now been analyzed both formally as well as numerically, by applying new network-theory methods [1 & 2].

The ultimate objective of this study is the identification of the natural wave-propagation modes of honeycomb-like clusters of directly-coupled cavity resonators, and the characterization of these wave-modes in terms of their wave-impedances and propagation constants [5].

Characteristic wave-impedance matrices (the image-matrices Z_{I1} , and Z_{I2}), and transfer-function matrices (the scattering-matrix blocks S_2 , and S_3) have been both expressed in closed form, and evaluated numerically as functions of the experimentally determined impedance parameters $a = Z_{11}$, and $b = Z_{12}$ of a single six-port cavity resonator.

3 - THE BASIC BUILDING-BLOCKS OF A HONEYCOMB STRUCTURE.

The outward-directed propagation of radial slow waves, emanating from a single multi-phase source inside any of the cavities, has been analyzed by considering the semi-infinite structure obtained by removing the cavity containing the source, and by

considering the region surrounding the resulting hole as a set of concentric, hexagonal tiers. Figure 1 shows a central patch, including the first four tiers of resonators surrounding the hole. The four tiers have been here progressively crosshatched for easy visual identification.

The central first tier, crosshatched at + 45° in figure 1, obviously exhibits the simplest network configuration (Figure 2), but plays nevertheless a very fundamental role as a) the basic prototype cell, and b) the first stepping-stone of the analysis process. Indeed, its equivalent circuit has a 6-port input-interface inside the hole, and an 18-port output-interface around its external boundary, for a total of 6 + 18 = 24 ports.

Simple arithmetic formulas express the number of resonators N_R , the number of input-interface ports n_p , the number of output-interface ports N_P , and the total number of ports P for the T^{th} resonator-tier, counting from the hole :

$$N_R = 6T \quad (1) \qquad P = 24T \quad (2)$$

$$n_p = 6\left[1+2(T-1)\right] \quad (3)$$

$$N_P = 6\left[3+2(T-1)\right] \quad (4)$$

4 - WAVE IMPEDANCES AND PROPAGATION CONSTANTS.

A closed-form expression has first been derived for the 24 × 24 impedance matrix of the first tier of resonators (Figure 2), by simply connecting six mutually-identical resonators in a closed hexagonal ring. The interconnection was performed by writing the node-voltage (Kirchoff's) equations, and the corresponding node-current equations, for all six internal nodes, thus eliminating the common-node voltages and currents.

This 24 × 24 impedance matrix, partitioned in a 6 × 6 leading block Z_1 , an 18 × 18 trailing block Z_4 , and two rectangular blocks Z_2 (6 × 18) , and Z_3 (18 × 6), exhibits very specific symmetries that are directly correlated to the rotation, and reflection symmetries of the first tier. Indeed, the 6 × 6 leading block Z_1 is *symmetric*, and *circulant* [6], the 18 × 18 trailing block Z_4 is *symmetric*, and *block-circulant* with *circulant* 3 × 3 *blocks* [6], and the rectangular blocks Z_2 , and Z_3 can be expressed as Kronecker Products of a *symmetric*, and *circulant* matrix Z_{21} by a 1 × 3 row-vector, and respectively a 3 × 1 column-vector, both having all elements equal to 1 (See enclosed Tables).

Further, closed-form expressions of the image-impedance matrices Z_{I1} , and Z_{I2} for the input-, and output-interface of the first tier, and closed-form expressions of the transfer-function matrices S_2 , and S_3 have also been obtained, by applying the definitions given in Reference [2].

All the resonator-tiers beyond the first, can be similarly characterized, in a recursive process exploiting the *"a priori"* knowledge of the fact that the input-interface image-impedance matrix Z_{I1} of each tier is equal to the output-interface image-impedance matrix Z_{I2} of the preceding one it circumscribes.

5 - RESULTS.

The enclosed tables show the closed-form expressions of the four block Z_i of the impedance matrix Z_{24} of the first resonator-tier, as functions of the *only two different* impedance parameters $a = Z_{11}$, and $b = Z_{12}$ of a single six-port cavity resonator.

Indeed, the impedance matrix of a *reciprocal*, and C_{6v}-*symmetric* six-port resonator can be expressed by [6] :

$$Z_6 \;=\; circ(\,a\,,b\,,b\,,b\,,b\,,b\,) \qquad (5)$$

Further, figure 3 shows a plot of the input-interface scalar image-impedance $Z_{II}(3)$ of the first tier, for the wave-mode with *equal amplitudes*, and *alternating phases* at the ports 1 through 6 (stepping by $e^{\,i\,m\,\varphi}$, with $m = 3$ and $\varphi = \pi / 6$) , and figure 4 shows a plot of the image phase-rotation φ_{IV} through the first tier for the same mode.

6 - REFERENCES.

[1] Speciale R. A. ,"Advanced Design of Phased Array Beam-Forming Networks," Proceedings of the 12th Review of Progress in Applied Computational Electromagnetics, Monterey, California, March 18-22, 1996, pages 918-930.

[2] Speciale R. A. ,"Synthesis of Phased ArrayAperture Distributions," Proceedings of the 12th Review of Progress in Applied Computational Electromagnetics, Monterey, California, March 18-22, 1996, pages 898-913.

[3] Speciale R. A. , US Patent No. 5,347,287 Awarded September 13, 1994.

[4] Speciale R. A. , US Patent No. 5,512,906 Awarded April 30, 1996.

[5] Speciale R. A. ,"Mathematical Representation of Multiport Resonator Test Data," paper submitted to the 1997, 12th Review of Progress in Applied Computational Electromagnetics.

[6] Davis J. P. ,"Circulant Matrices," John Wiley & Sons, New York, 1979, Pure and Applied Mathematics Series, Chapter 3, pages 66-107, and Chapter 5, pages 155-191.

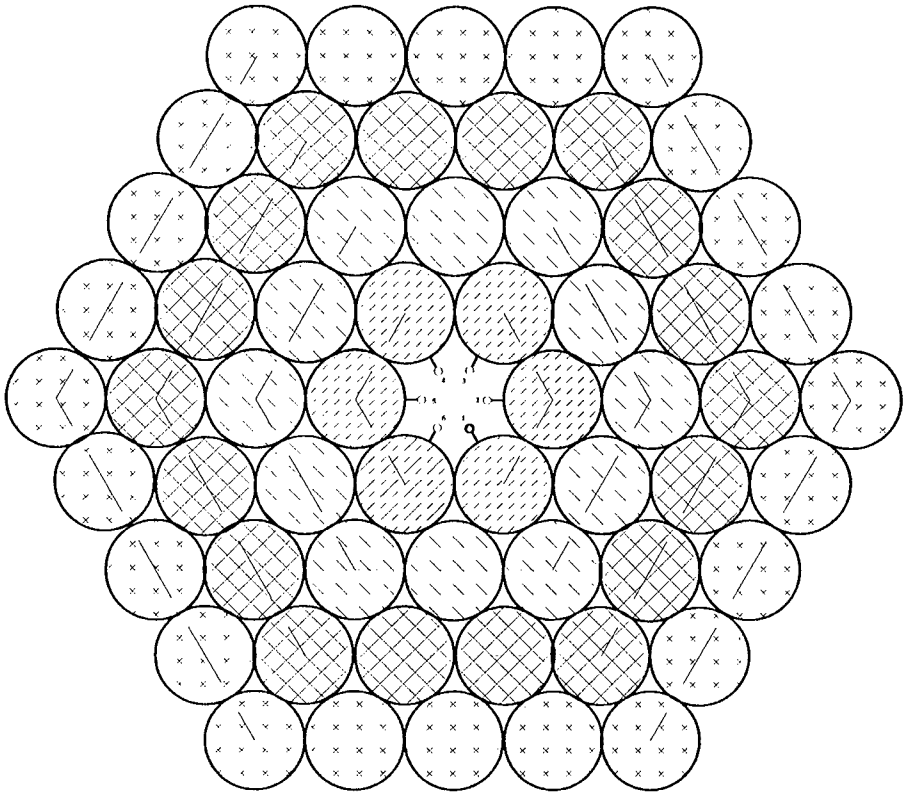

Figure 1 - This Two Dimensional Slow-Wave Structure with Hexagonal Lattice is a 4-Tier Cluster of Directly-Coupled Six-Port Cylindrical Resonators.

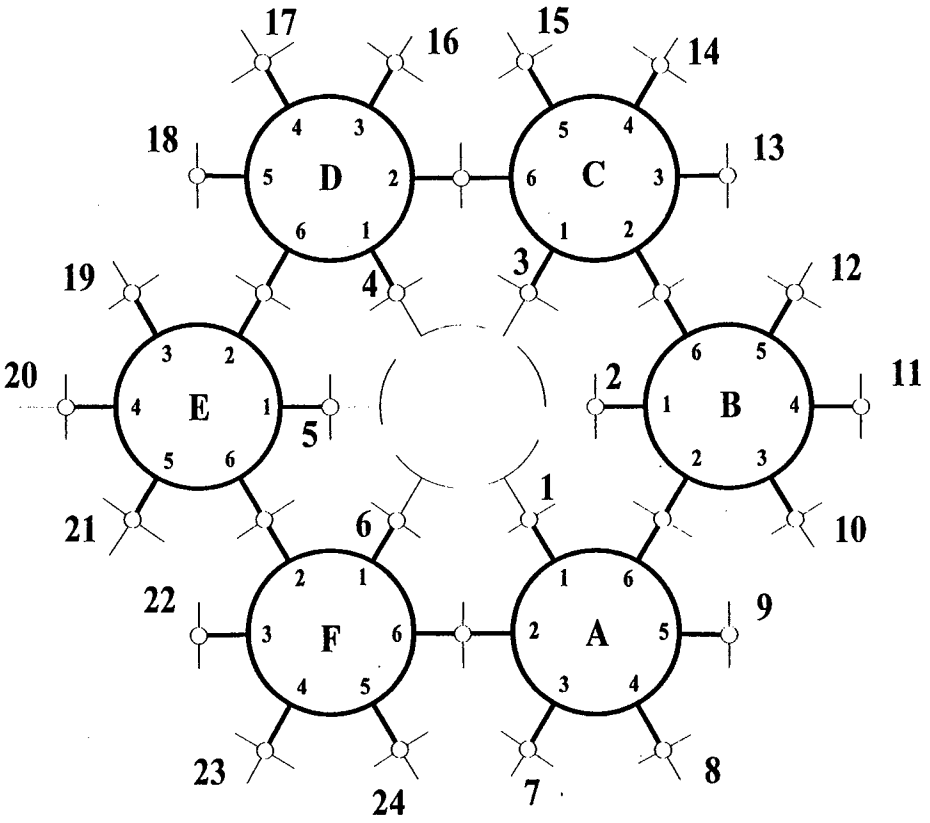

Figure 2 - Equivalent Circuit of the First Tier of Six-Port Cylindrical Resonators. This Prototype Six-Resonator Set has a 6-Port Input, and an 18-Port Output.

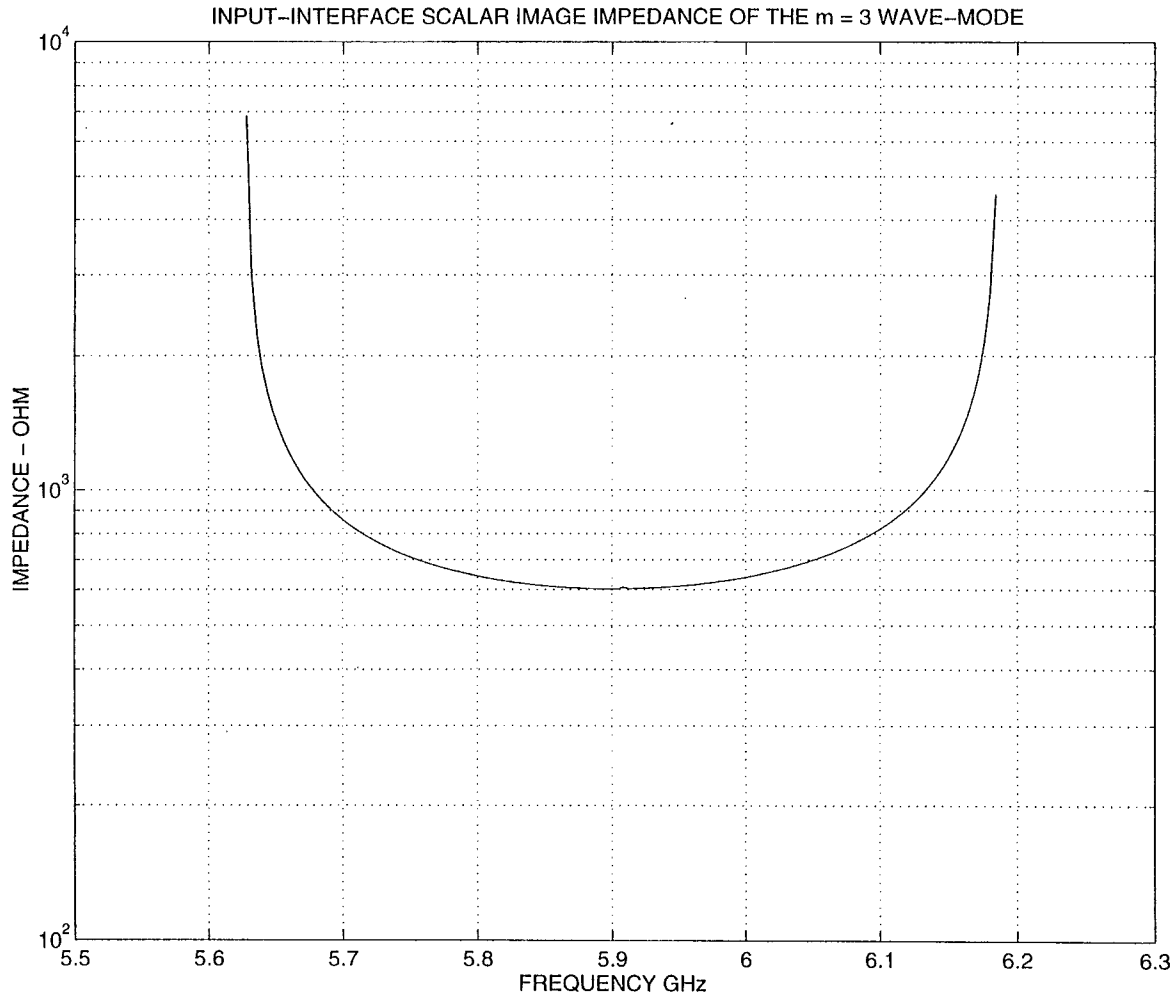
INPUT-INTERFACE SCALAR IMAGE IMPEDANCE OF THE m = 3 WAVE-MODE
IMPEDANCE - OHM
10^4
10^3
10^2
5.5
5.6
5.7
5.8
5.9
6
6.1
6.2
6.3
FREQUENCY GHz

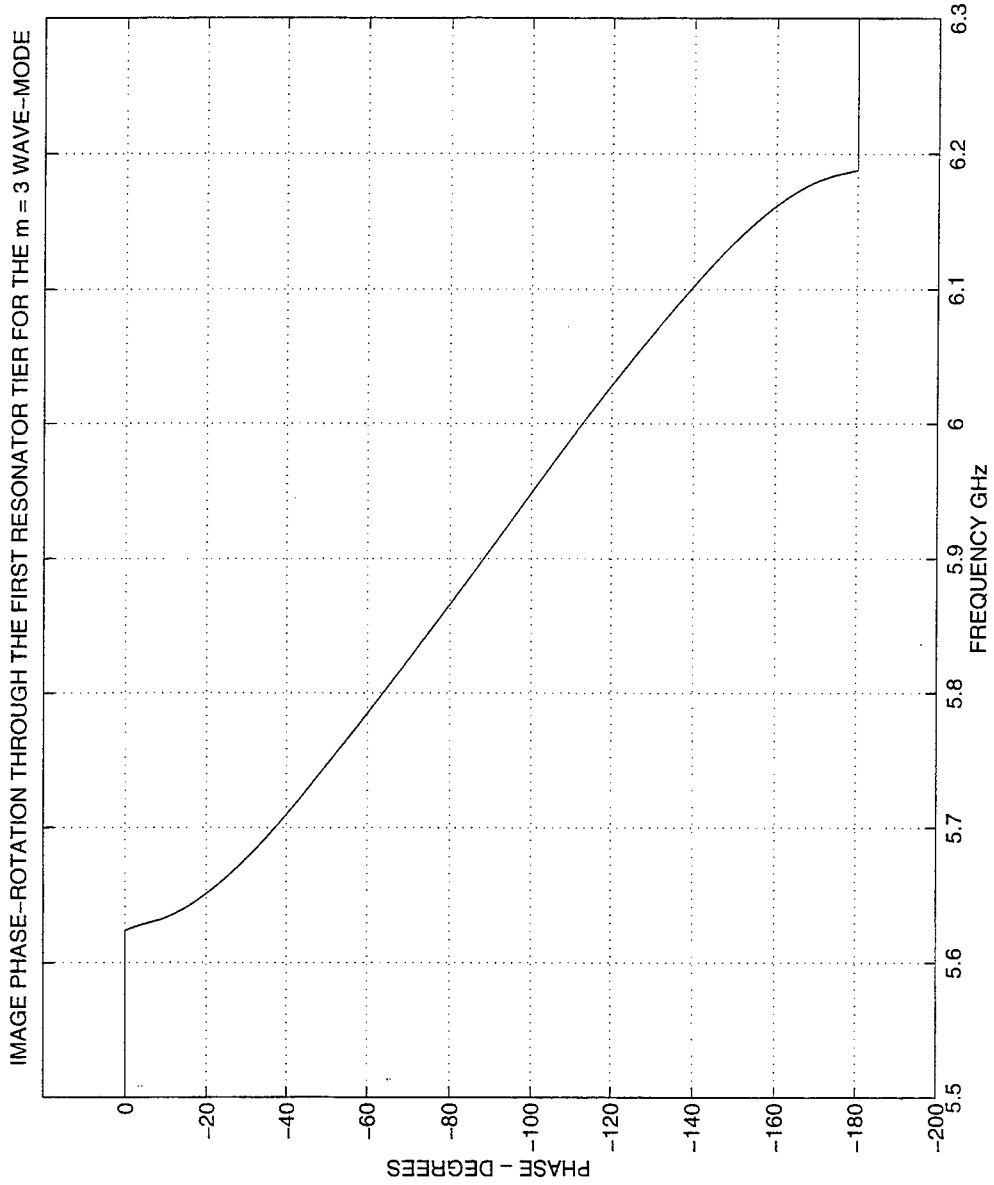
IMAGE PHASE-ROTATION THROUGH THE FIRST RESONATOR TIER FOR THE m = 3 WAVE-MODE
PHASE - DEGREES
0
-20
-40
-60
-80
-100
-120
-140
-160
-180
-200
5.5
5.6
5.7
5.8
5.9
6
6.1
6.2
6.3
FREQUENCY GHz

BLOCK STRUCTURE OF THE IMPEDANCE MATRIX Z_{24}

OF THE "EMPTY HEXAFOLIUM" CLUSTER

$$Z_{24} = \left|\begin{array}{c|c} Z_1 \quad 6 \times 6 & Z_2 \quad 6 \times 18 \\ \hline Z_3 \quad 18 \times 6 & Z_4 \quad 18 \times 18 \end{array}\right|$$

STRUCTURE OF THE 6 x 6 SYMMETRIC AND CIRCULANT BLOCK Z_1

$$Z_1 = \begin{vmatrix} A & B & C & D & C & B \\ B & A & B & C & D & C \\ C & B & A & B & C & D \\ D & C & B & A & B & C \\ C & D & C & B & A & B \\ B & C & D & C & B & A \end{vmatrix}$$

$$A = \frac{\left[(a+b)a - b^2\right](4a^2 - b^2) - 2ab^3}{(4a^2 - b^2)(a+b)} = a\,\frac{(1+\rho-\rho^2)(4-\rho^2) - 2\rho^2}{(4-\rho^2)(1+\rho)}$$

$$B = \frac{b^2(2a^2 - b^2)}{(4a^2 - b^2)(a+b)} = a\,\frac{\rho^2(2-\rho^2)}{(4-\rho^2)(1+\rho)}$$

$$C = \frac{ab^3}{(4a^2 - b^2)(a+b)} = a\,\frac{\rho^3}{(4-\rho^2)(1+\rho)} \qquad \left\{\rho = \frac{b}{a}\right\}$$

$$D = \frac{b^4}{(4a^2 - b^2)(a+b)} = a\,\frac{\rho^4}{(4-\rho^2)(1+\rho)}$$

SYMMETRY STRUCTURE OF THE 6 x 18 MATRIX-BLOCK Z_2

$$Z_2 = \left|\begin{array}{cccccc:cccccc:cccccc:cccccc:cccccc:cccccc}
E & E & E & B & B & B & C & C & C & D & D & D & C & C & C & B & B & B \\
B & B & B & E & E & E & B & B & B & C & C & C & D & D & D & C & C & C \\
C & C & C & B & B & B & E & E & E & B & B & B & C & C & C & D & D & D \\
D & D & D & C & C & C & B & B & B & E & E & E & B & B & B & C & C & C \\
C & C & C & D & D & D & C & C & C & B & B & B & E & E & E & B & B & B \\
B & B & B & C & C & C & D & D & D & C & C & C & B & B & B & E & E & E
\end{array}\right|$$

$$B = \frac{b^2\,(2a^2 - b^2)}{(4a^2 - b^2)(a+b)} \qquad C = \frac{a\,b^3}{(4a^2 - b^2)(a+b)}$$

$$D = \frac{b^4}{(4a^2 - b^2)(a+b)} \qquad E = \frac{a\,b\,(4a^2 - 3b^2)}{(4a^2 - b^2)(a+b)}$$

SYMMETRY STRUCTURE OF THE 18 x 18

MATRIX-BLOCK Z_4

$$Z_4 = \left|\begin{array}{ccc|ccc|ccc|ccc|ccc|ccc}
A & E & E & B & B & B & C & C & C & D & D & D & C & C & C & B & B & B \\
E & A & E & B & B & B & C & C & C & D & D & D & C & C & C & B & B & B \\
E & E & A & B & B & B & C & C & C & D & D & D & C & C & C & B & B & B \\
\hline
B & B & B & A & E & E & B & B & B & C & C & C & D & D & D & C & C & C \\
B & B & B & E & A & E & B & B & B & C & C & C & D & D & D & C & C & C \\
B & B & B & E & E & A & B & B & B & C & C & C & D & D & D & C & C & C \\
\hline
C & C & C & B & B & B & A & E & E & B & B & B & C & C & C & D & D & D \\
C & C & C & B & B & B & E & A & E & B & B & B & C & C & C & D & D & D \\
C & C & C & B & B & B & E & E & A & B & B & B & C & C & C & D & D & D \\
\hline
D & D & D & C & C & C & B & B & B & A & E & E & B & B & B & C & C & C \\
D & D & D & C & C & C & B & B & B & E & A & E & B & B & B & C & C & C \\
D & D & D & C & C & C & B & B & B & E & E & A & B & B & B & C & C & C \\
\hline
C & C & C & D & D & D & C & C & C & B & B & B & A & E & E & B & B & B \\
C & C & C & D & D & D & C & C & C & B & B & B & E & A & E & B & B & B \\
C & C & C & D & D & D & C & C & C & B & B & B & E & E & A & B & B & B \\
\hline
B & B & B & C & C & C & D & D & D & C & C & C & B & B & B & A & E & E \\
B & B & B & C & C & C & D & D & D & C & C & C & B & B & B & E & A & E \\
B & B & B & C & C & C & D & D & D & C & C & C & B & B & B & E & E & A
\end{array}\right|$$

EXPRESSION OF THE 6 x 18 BLOCK Z_2 IN THE FORM OF A KRONECKER PRODUCT

$$Z_2 = \left|\begin{array}{ccc:ccc} E & B & C & D & C & B \\ B & E & B & C & D & C \\ C & B & E & B & C & D \\ \hdashline D & C & B & E & B & C \\ C & D & C & B & E & B \\ B & C & D & C & B & E \end{array}\right| \otimes \left| 1 \,\vdots\, 1 \,\vdots\, 1 \right| = Z_{21} \otimes V_{1x3}$$

EXPRESSION OF THE 18 x 6 BLOCK Z_3 IN THE FORM OF A KRONECKER PRODUCT

$$Z_3 = \left|\begin{array}{cccccc} E & B & C & D & C & B \\ B & E & B & C & D & C \\ C & B & E & B & C & D \\ \hdashline D & C & B & E & B & C \\ C & D & C & B & E & B \\ B & C & D & C & B & E \end{array}\right| \otimes \left|\begin{array}{c} 1 \\ 1 \\ 1 \end{array}\right| = Z_{21} \otimes V_{3x1}$$

EXPRESSIONS OF THE FIVE DIFFERENT ELEMENTS OF THE 24×24

IMPEDANCE MATRIX Z_{24}

$$A = \frac{\left[(a+b)a - b^2\right](4a^2 - b^2) - 2ab^2}{(4a^2 - b^2)(a+b)} = a\frac{(1+\rho-\rho^2)(4-\rho^2) - 2\rho^2}{(4-\rho^2)(1+\rho)}$$

$$B = \frac{b^2(2a^2 - b^2)}{(4a^2 - b^2)(a+b)} = a\frac{\rho^2(2-\rho^2)}{(4-\rho^2)(1+\rho)}$$

$$C = \frac{ab^3}{(4a^2 - b^2)(a+b)} = a\frac{\rho^3}{(4-\rho^2)(1+\rho)}$$

$$D = \frac{b^4}{(4a^2 - b^2)(a+b)} = a\frac{\rho^4}{(4-\rho^2)(1+\rho)}$$

$$E = \frac{ab(4a^2 - 3b^2)}{(4a^2 - b^2)(a+b)} = a\frac{\rho(4-3\rho^2)}{(4-\rho^2)(1+\rho)}$$

WAVE PROPAGATION ON TWO-LEVEL TWIN-STACKED-HONEYCOMB STRUCTURES

Ross A. Speciale

Redondo Beach, California

polytope@msn.com

1 - A DIFFERENT TYPE OF SLOW-WAVE STRUCTURE.

A new type of two dimensional slow-wave structure, that combines two mutually-coupled layers of cylindrical cavity resonators, has been theoretically analyzed, and experimentally evaluated as low-loss, wide-band signal-distribution network for affordable, electronically steered phased arrays [1 & 2].

The cavity resonators of each layer are tightly packed in an hexagonal lattice, but are here *electrically uncoupled* from one another. Both layers exhibit the characteristic geometry of the same honeycomb, but the layers are stacked upon one another, with a *relative shift*, so that each top-level resonator *symmetrically overlaps* three bottom-level resonators (Figures 1 and 2).

Direct electromagnetic coupling is introduced, between the partially overlapping resonators of the two layers, by way of resonant irises cut out of the common shorting plane that separates the top level from the bottom level.

Indeed, each top-level resonator has three resonant irises cut out of its *bottom* shorting plane, at 120° azimuth around the resonator axis, while each bottom-level resonator has identical resonant irises cut out of its *top* shorting plane.

2 - THE MEANDERING WAVE-PROPAGATION PATH.

The geometrical *"shift"* of the top-level honeycomb, relative to the bottom-level honeycomb, is equal to the uniform spacing between resonator axes in the two honeycombs divided by $\sqrt{3}$, and oriented along one of the six azimuth directions that bisect the 60° angles between the reflection-symmetry planes of the structure.

Two-dimensional continuity of the wave-propagation path is attained because of each resonant iris being common to *one top-layer*, and *one bottom-layer* resonator, while each of the resonators in one level is *simultaneously coupled* to the *three* resonators of the other it symmetrically overlaps.

The wave-propagation properties of the two-level twin-honeycomb structure, *as seen from a single-layer viewpoint*, are clearly intrinsically different as the guided waves only couple and propagate *down*, from the *top* level to the *bottom* level, and *back up* to the top level, while there are *no coupling irises* between the resonators of each single level.

Because of the peculiar *up/down-meandering* geometry of the wave-propagation path, the two level stacked-honeycomb structure can be considered as the *two-dimensional counterpart* of the *"sinusoidally-folded"* slotted waveguide, used in some early, frequency-scanned, linear phased arrays.

The twin-honeycomb slow-wave structure also exhibits some similarity to the *"side-coupled-cavity"* accelerating structures, used in some charged-particle linear accelerators.

3 - PRACTICAL APPLICATIONS.

The described twin-stacked-honeycomb slow-wave structure has been theoretically analyzed, and experimentally evaluated for use as low-loss, wide-band signal-distribution network for affordable, electronically steered phased arrays.

In this specific application, *only* the resonators in the *top-layer* of the structure feed array elements, with the resultant vector-sum of the signals of a relatively small number of mutually-coherent sources [3 & 4]. As a consequence, the phase-shift between *adjacent* array elements is equal to *two times* the wave-propagation phase-shift *from the top layer to the bottom layer*. This means that the phase-shift between *adjacent* array elements can be set to 360° (which is obviously *equivalent* to 0°), as required for radiating a *broadside beam*.

This phased array configuration leads to large reductions in the required number of electronic beam-steering controls, and consequently in cost.

The aperture distributions, required for generating radiated beams in the specified pointing directions, are obtained as *complex linear combinations* of the component wave-fields of all the amplitude-, and phase-controlled sources used (in transmission, or of receiver front-ends in reception). The sources (or the receivers) may be here connected to resonators located in either the top layer, or in the bottom layer, or even simultaneously in both layers.

4 - THE NEW NETWORK ANALYSIS METHODS.

The described slow-wave structures, that resemble twin-stacked-honeycombs, have now been analyzed both formally as well as numerically, by applying new network-theory methods.

The ultimate objective of this study is the identification of *the natural wave-propagation modes* of coupled twin-honeycomb clusters of cavity resonators, and the characterization of these wave-modes in terms of their *wave-impedance* and *propagation constants* [5].

Characteristic wave-impedance matrices (the image-matrices Z_{I1} , and Z_{I2}), and transfer-function matrices (the scattering-matrix blocks S_2 , and S_3) have been both expressed in closed form, and evaluated numerically as functions of the experimentally determined impedance parameters $a = Z_{11}$, and $b = Z_{12}$ of a single *three-port* cavity resonator.

5 - THE BASIC BUILDING-BLOCKS OF A TWIN-HONEYCOMB STRUCTURE.

The outward-directed propagation of radial slow waves, emanating from a single multi-phase source inside any of the cavities, has been analyzed by considering the semi-

infinite structure obtained by removing the cavity containing the source, and by considering the region surrounding the resulting hole as a set of concentric, hexagonal tiers.

Figure 2 shows the central first tier of twelve resonators surrounding the hole, with six resonators in the top layer crosshatched at + 45°, and six in the bottom layer crosshatched at - 45° . The resonators of the two honeycombs have been crosshatched in Figure 2 for easy visual identification.

This central first tier exhibits obviously the simplest network configuration (Figure 3), but plays nevertheless a very fundamental role as a) the basic prototype cell, and b) the first stepping-stone of the analysis process. Indeed, its equivalent circuit has a 3-port input-interface inside the hole, and an 9-port output-interface around its external boundary, for a total of 3 + 9 = 12 ports.

Simple arithmetic formulas express the number of resonators N_R , the number of input-interface ports n_p , the number of output-interface ports N_P , and the total number of ports P for the T^{th} resonator-tier, counting from the hole :

$$N_R = 6(T+1) \quad (1) \qquad P = 6(3T-1) \quad (2)$$

$$n_p = 3\left[1+2(T-1)\right] \quad (3)$$

$$N_P = 3\left[3+4(T-1)\right] \quad (4)$$

6 - WAVE IMPEDANCES AND PROPAGATION CONSTANTS.

A closed-form expression has first been derived for the 12 × 12 impedance matrix of the first tier of resonators (Figure 3), by simply connecting twelve mutually-identical resonators in a closed ring. The interconnection was performed by writing the node-voltage (Kirchoff's) equations, and the corresponding node-current equations, for all twelve internal nodes, thus eliminating the common-node voltages and currents.

This 12 × 12 impedance matrix, partitioned in a 3 × 3 leading block Z_1, a 9 × 9 trailing block Z_4 , and two rectangular blocks Z_2 (3 × 9) , and Z_3 (9 × 3), exhibits very specific symmetries that are directly correlated to the rotation, and reflection symmetries of the first tier. Indeed, the 3 × 3 leading block Z_1 is *symmetric*, and *circulant* [6], the 9 × 9 trailing block Z_4 is *symmetric*, and *block-circulant* with *circulant* 3 × 3 *blocks* [6], and the rectangular blocks Z_2 , and Z_3 can be expressed as Kronecker Products of a *symmetric*, and *circulant* matrix Z_{21} by a 1 × 3 row-vector, and respectively a 3 × 1 column-vector, both having all elements equal to 1.

Further, closed-form expressions of the image-impedance matrices Z_{I1} , and Z_{I2} for the input-, and output-interface of the first tier, and closed-form expressions of the transfer-function matrices S_2 , and S_3 have also been obtained, by applying the definitions given in Reference [2].

All the resonator-tiers beyond the first, can be similarly characterized, in a recursive process exploiting the *"a priori"* knowledge of the fact that the input-interface image-impedance matrix Z_{I1} of each tier is equal to the output-interface image-impedance matrix Z_{I2} of the preceding one it circumscribes.

7 - RESULTS.

The closed-form expressions of the four block Z_i of the impedance matrix Z_{I2} of the first resonator-tier are cast as functions of the *only two different* impedance parameters $a = Z_{I1}$, and $b = Z_{I2}$ of a single three-port cavity resonator.

Indeed, the impedance matrix of a *reciprocal*, and C_{3V}*-symmetric* three-port resonator, with coupling irises at 120° azimuth around the axis, can be expressed by [6] :

$$Z_6 = circ(a, b, b) \qquad (5)$$

8 - REFERENCES.

[1] Speciale R. A. ,"Advanced Design of Phased Array Beam-Forming Networks," Proceedings of the 12th Review of Progress in Applied Computational Electromagnetics, Monterey, California, March 18-22, 1996, pages 918-930.

[2] Speciale R. A. ,"Synthesis of Phased ArrayAperture Distributions," Proceedings of the 12th Review of Progress in Applied Computational Electromagnetics, Monterey, California, March 18-22, 1996, pages 898-913.

[3] Speciale R. A. , US Patent No. 5,347,287 Awarded September 13, 1994.

[4] Speciale R. A. , US Patent No. 5,512,906 Awarded April 30, 1996.

[5] Speciale R. A. ,"Mathematical Representation of Multiport Resonator Test Data," paper submitted to the 1997, 12th Review of Progress in Applied Computational Electromagnetics.

[6] Davis J. P. ,"Circulant Matrices," John Wiley & Sons, New York, 1979, Pure and Applied Mathematics Series, Chapter 3, pages 66-107, and Chapter 5, pages 155-191.

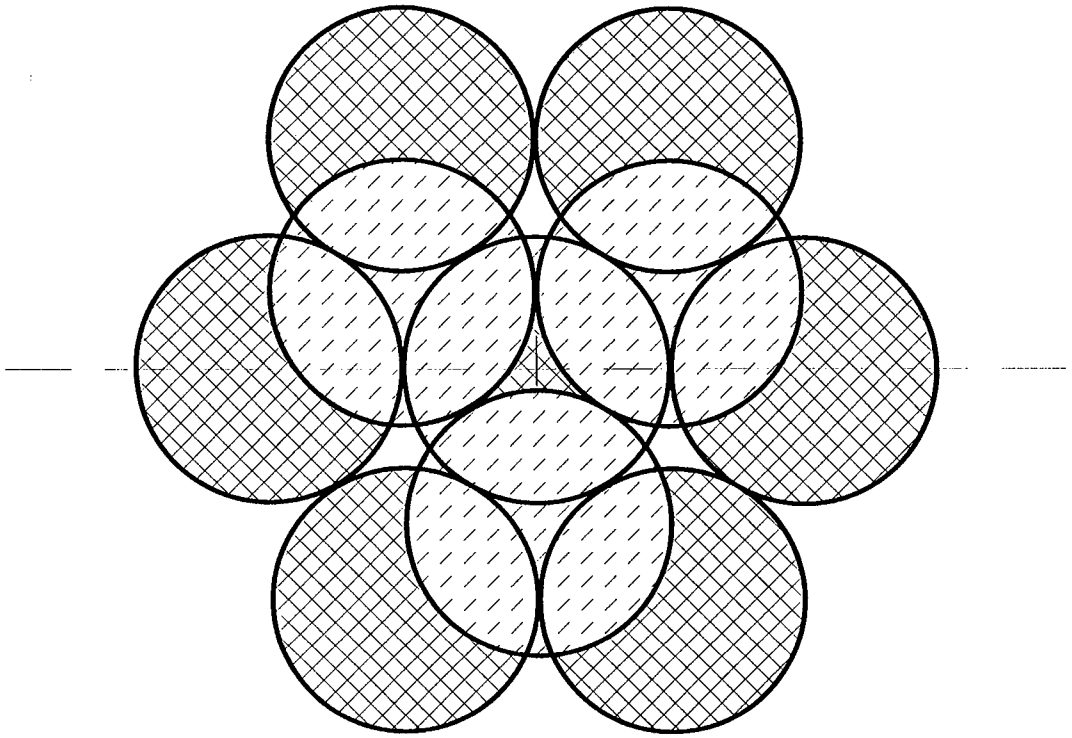

Figure 1 - Representative Geometry of a "Twin Stacked Honeycomb" Slow-Wave Structure. The Green Circles Represent here the Upper-Level Cylindrical Three-Port Resonators.

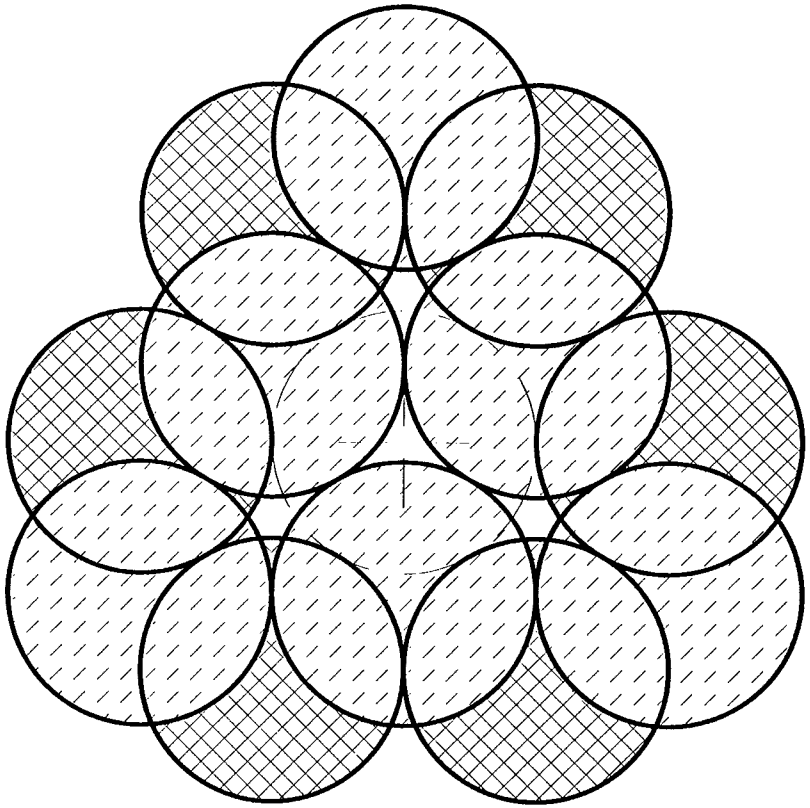

Figure 2 - Geometry of the First Twelve-Resonator Tier Surrounding the Central Hole. The Dashed Circle Marks the Location of the Bottom-Level Resonator Containing the Multi-Phase Source.

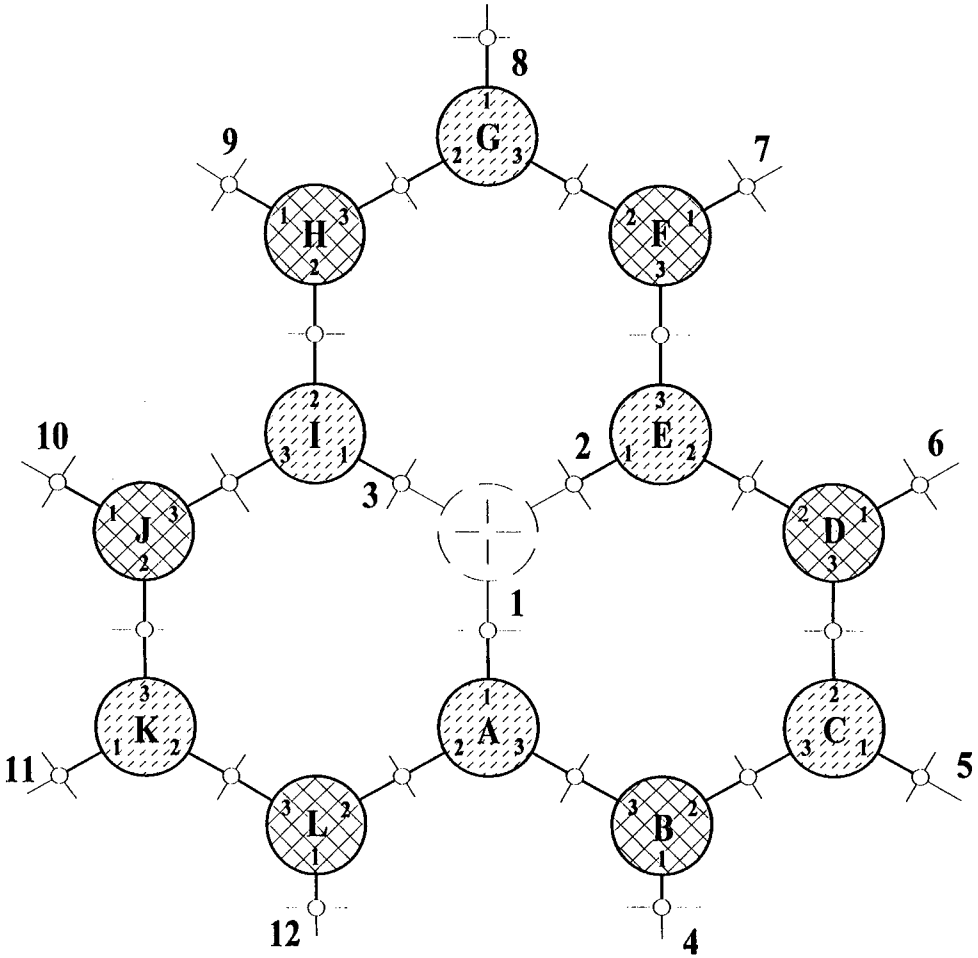

Figure 3 - Equivalent Circuit of the First 12-Resonator Tier of the Twin-Honeycomb. The Dashed Circle Marks the Resonator Containing a Multi-Phase Source.

Adiabatic Modes of Curved EM Waveguides of Arbitrary Cross Section

V. A. Baranov and A.V. Popov

Institute of Terrestrial Magnetism, Ionosphere and Radiowave Propagation, Troitsk, Moscow region, Russia

Theory of EM wave propagation in nonuniform waveguides has a number of applications in different branches of radiophisics and technics: microwave electronics, optoelectronics, mobile radio communication in tunnels etc. Since exact solutions of Maxwell's equations are available only for simple geometries, and straightforward numerical integration requires unproportionately great computational work, especially in the short-wave limit, alternative asymptotic approaches may be useful for practical problems.

In this paper, we consider short-wave EM propagation in smoothly curved waveguides of arbitrary cross section bounded by material walls. The Leontovich normal impedance is used to formulate the boundary conditions. In order to construct an approximate solution we use two small parameters inherent in typical problems of this class: (i) the wavelength is much smaller than the cross section characteristic scale; and (ii) relative curvature of the waveguide axis is small. A fairly simple solution can be found provided that the relation between these two parameters is similar to that assumed in classic Fock's study of diffraction behind a smooth convex body [1]. Namely: (ii) has the second order of magnitude compared with (i). Moreover, we confine ourselves with considering the low-order modes with small Brillouin angles, having minimum absorption in the waveguide walls.

Scaling the spatial variables by corresponding geometric scales (cross-section width and curvature radius) allows one to introduce the small parameter into Maxwell's equations, which reduces them to a singularly perturbed set of differential equations. Its solution is sought as an asymptotic expansion of the slowly varying 6-component vector amplitude of the propagating mode in powers of the small parameter. The solvability conditions of the arising recurrent linear algebraic equations determine longitudinal wavenumber and 2-component transversal eigenfunctions. To the zero-order approximation, they are nontrivial solutions of a boundary value problem for a 2D Schroedinger equation containing a term proportional to the waveguide local curvature. Therefore, the leading term of the asymptotic solution takes into account not only the cross section shape and material properties of the waveguide walls but also the effects of its curvature (penumbra and whispering gallery).

Let the waveguide axis be defined by the equation $\vec{r}_0(s) = (x_0(s), y_0(s), 0)$ where s is the arc length. We introduce an orthogonal coordinate set (s,q,z) with unit vectors

$\vec{t} = \vec{r}_0'(s)$, $\vec{n} = \rho(s)\vec{t}'(s)$, $\vec{k} = (0,0,1)$ (here $\rho(s)$ is local axis curvature radius):

$$\vec{r} = \vec{r}_0(s) + q\vec{n}(s) + z\vec{k} \tag{1}$$

Assuming that B is a reference waveguide width and L is a characteristic longitudinal scale, we introdice dimensionless variables $\xi = s/L$, $\eta = q/B$, $\varsigma = z/B$ and normalized curvature of the

waveguide axis $\kappa(\xi) = L/\rho(s)$. The following relations between the geometric parameters and the wavelength λ are implied: $\lambda/B = 0(\nu)$, $B/L = 0(\nu^2)$, $\nu << 1$. In the scaled variables (ξ, η, ς), Maxwell's equations can be written in the following form - cf. [2]:

$$\nu^3 \hat{L}\frac{\partial \vec{\Pi}}{\partial \xi} + \nu\left[(\hat{M}_0 + \nu^2\kappa\eta\hat{M}_1)\frac{\partial \vec{\Pi}}{\partial \eta} + (\hat{N}_0 + \nu^2\kappa\eta\hat{N}_1)\frac{\partial \vec{\Pi}}{\partial \varsigma}\right] = i\sigma h\hat{R}\vec{\Pi} \tag{2}$$

Here, $\vec{\Pi} = (hE_\xi, E_\eta, E_\varsigma, hH_\xi, H_\eta, H_\varsigma)^T$ is the 6-component EM field vector, $h = 1 - \nu^2\kappa(\xi)\eta$ is the Lame coefficient, $\sigma = \frac{2\pi}{\lambda}\sqrt{\frac{B^3}{L}} = 0(1)$ is a scaled wavenumber, and $\hat{L}, \hat{M}_0, \hat{M}_1, \hat{N}_0, \hat{N}_1, \hat{R}$ are constant block matrices:

$$\hat{L} = \begin{pmatrix} \hat{l} & 0 \\ 0 & -\hat{l} \end{pmatrix}, \quad \hat{l} = \begin{pmatrix} 0 & 0 & 0 \\ 0 & 0 & -1 \\ 0 & 1 & 0 \end{pmatrix}; \quad \hat{M}_0 = \begin{pmatrix} \hat{m}_0 & 0 \\ 0 & -\hat{m}_0 \end{pmatrix}, \quad \hat{m}_0 = \begin{pmatrix} 0 & 0 & 1 \\ 0 & 0 & 0 \\ -1 & 0 & 0 \end{pmatrix}$$

$$\hat{M}_1 = \begin{pmatrix} \hat{m}_1 & 0 \\ 0 & -\hat{m}_1 \end{pmatrix}, \quad \hat{m}_1 = \begin{pmatrix} 0 & 0 & -1 \\ 0 & 0 & 0 \\ 0 & 0 & 0 \end{pmatrix}; \quad \hat{N}_0 = \begin{pmatrix} \hat{n}_0 & 0 \\ 0 & -\hat{n}_0 \end{pmatrix}, \quad \hat{n}_0 = \begin{pmatrix} 0 & -1 & 0 \\ 1 & 0 & 0 \\ 0 & 0 & 0 \end{pmatrix} \tag{3}$$

$$\hat{N}_1 = \begin{pmatrix} \hat{n}_1 & 0 \\ 0 & -\hat{n}_1 \end{pmatrix}, \quad \hat{n}_1 = \begin{pmatrix} 0 & 1 & 0 \\ 0 & 0 & 0 \\ 0 & 0 & 0 \end{pmatrix}; \quad \hat{R} = \begin{pmatrix} 0 & \hat{I} \\ \hat{I} & 0 \end{pmatrix}, \quad \hat{I} = \begin{pmatrix} 1 & 0 & 0 \\ 0 & 1 & 0 \\ 0 & 0 & 1 \end{pmatrix}$$

Since Eq.(2) contains powers of the small parameter up to ν^3, its asymptotic solutions can be sought in the following form

$$\vec{\Pi}(\xi, \eta, \varsigma) = \vec{U}(\xi, \eta, \varsigma)\exp\left[i\frac{\sigma}{\nu^3}\Phi(\xi)\right] \tag{4}$$

where $\Phi(\xi) = \Phi_0(\xi) + \nu^2\Phi_1(\xi)$ is normalized phase and $\vec{U}$ is a slowly varying vector amplitude expanded in powers of ν:

$$\vec{U}(\xi, \eta, \varsigma) = \sum_{n=0}^{\infty} \nu^n \vec{U}_n(\xi, \eta, \varsigma) \tag{5}$$

(for the low order waveguide modes, all the derivatives of $\vec{U}_n$ are of order of unity). After substituting asymptotic series (5) into Eq.(2) we get a sequence of algebraic equations

$$\begin{aligned} \hat{S}\vec{U}_0 &= 0 \\ \hat{S}\vec{U}_n &= \vec{F}_n, \quad n = 1,2,\ldots \end{aligned} \tag{6}$$

with $\hat{S} = \hat{R} - \Phi_0'\hat{L}$ and

$$\begin{aligned} \vec{F}_n = \frac{1}{i\sigma}\left(\hat{M}_0\frac{\partial}{\partial \eta} + \hat{N}_0\frac{\partial}{\partial \varsigma}\right)\vec{U}_{n-1} + \left(\kappa\eta\hat{R} + \Phi_1'\hat{L}\right)\vec{U}_{n-2} + \\ + \frac{1}{i\sigma}\left[\hat{L}\frac{\partial}{\partial \varsigma} + \kappa\eta\left(\hat{M}_1\frac{\partial}{\partial \eta} + \hat{N}_1\frac{\partial}{\partial \varsigma}\right)\right]\vec{U}_{n-3} \end{aligned} \tag{7}$$

(here, $\vec{U}_n \equiv 0$ for negative n).

Evidently, nonzero solutions $\vec{U}_o$ exist only when matrix $\hat{S}$ degenerates:

$$\det \hat{S} = \left(\Phi_0'^2 - 1\right)^2 = 0 \tag{8}$$

Hence, the zero-order approximation for the phase function is $\Phi_0(\xi) = \xi$ which corresponds to the purely longitudinal propagation along the waveguide axis. The second-order correction $\Phi_1(\xi)$ will be found below.

It can be easily seen that, under condition (8), there exist two annuling eigenvectors

$$\vec{a} = (0,1,0,0,0,1)^T, \quad \vec{b} = (0,0,1,0,-1,0)^T \tag{9}$$

Therefore, the general solution to the zero-order amplitude equation (6) has the form

$$\vec{U}_0 = u_0 \vec{a} + \upsilon_0 \vec{b} \tag{10}$$

where $u_0(\xi,\eta,\varsigma)$ and $\upsilon_0(\xi,\eta,\varsigma)$ are scalar function to be determined in the process of constructing further approximations.

As matrix $\hat{S}$ degenerates, the right-hand sides of Eqs.(6) for $n = 1,2,3,\ldots$ must be orthogonal to the eigenvectors of the transposed matrix

$$\begin{gathered}\left(\vec{\alpha}\vec{F}_n\right) = \left(\vec{\beta}\vec{F}_n\right) = 0 \\ \vec{\alpha} = (0,0,1,0,1,0), \quad \vec{\beta} = (0,-1,0,0,0,1)\end{gathered} \tag{11}$$

in order to allow for a finite solution. Its general form is

$$\vec{U}_n = u_n \vec{a} + \upsilon_n \vec{b} + \hat{T}\vec{F}_n \tag{12}$$

where

$$\hat{T} = \begin{pmatrix} 0 & \hat{t} \\ \hat{t} & 0 \end{pmatrix}, \qquad \hat{t} = \begin{pmatrix} 1 & 0 & 0 \\ 0 & 1 & 0 \\ 0 & 0 & 0 \end{pmatrix}$$

and $u_n(\xi,\eta,\varsigma)$, $\upsilon_n(\xi,\eta,\varsigma)$ are arbitrary scalar functions. The orthogonality conditions (11) are those equations that determine step by step the unknown functions u_n, υ_n.

It can be easily shown that for $n = 1$ Eqs.(11) are fulifiled identically (with arbitrary u_0, υ_0). At the next step we have

$$\begin{aligned}\vec{\alpha}\vec{F}_2 &= 2(\Phi_1' + \kappa\eta)u_0 - \frac{1}{\sigma^2}\left(\frac{\partial^2 u_0}{\partial\eta^2} + \frac{\partial^2 u_0}{\partial\varsigma^2}\right) = 0 \\ \vec{\beta}\vec{F}_2 &= 2(\Phi_1' + \kappa\eta)\upsilon_0 - \frac{1}{\sigma^2}\left(\frac{\partial^2 \upsilon_0}{\partial\eta^2} + \frac{\partial^2 \upsilon_0}{\partial\varsigma^2}\right) = 0\end{aligned} \tag{13}$$

So the scalar amplitudes $u_0(\xi,\eta,\varsigma)$, $\upsilon_0(\xi,\eta,\varsigma)$ must be solutions of the two-dimensional Schroedinger equation

$$\frac{\partial^2 w}{\partial\eta^2} + \frac{\partial^2 w}{\partial\varsigma^2} - 2\sigma^2(\gamma + \kappa\eta)w = 0 \tag{14}$$

with coefficients $\kappa(\xi)$ and $\gamma(\xi)=\Phi_1'(\xi)$ depending on ξ as a parameter. Remember that the curvature $\kappa(\xi)$ is defined by the waveguide axis equation, and function $\gamma(\xi)$ (correction to the mode phase velocity) is to be found. In order to find it we have to supplement Eq.(14) with correspondent boundary conditions.

Let us go back to the initial problem formulation. Let the curvilinear waveguide wall equation be $\Gamma(s/L, q/B, z/B)=0$. In a general case, the vector normal to Γ is determined by the 3D gradient

$$\nabla_3\Gamma = \frac{1}{B}\left(\frac{\nu^2}{h}\frac{\partial\Gamma}{\partial\xi}\vec{t}+\frac{\partial\Gamma}{\partial\eta}\vec{n}+\frac{\partial\Gamma}{\partial\varsigma}\vec{k}\right) \tag{15}$$

However, in what follows we assume that the waveguide cross section shape is constant along the axis. Therefore, $\partial\Gamma/\partial\xi\equiv 0$, and the normal vector $\vec{\mu}$ lies in the (q,z) plane:

$$\vec{\mu} = \frac{\frac{\partial\Gamma}{\partial\eta}\vec{n}+\frac{\partial\Gamma}{\partial\varsigma}k}{\left[\left(\frac{\partial\Gamma}{\partial\eta}\right)^2+\left(\frac{\partial\Gamma}{\partial\varsigma}\right)^2\right]^{1/2}} \equiv \mu_\eta\vec{n}+\mu_\varsigma\vec{k} \tag{16}$$

As a basis in the tangent plane, it is natural to choose the longitudinal ort $\vec{t}=\vec{r}_0'(s)$ and the cross section tangent vector

$$\vec{\tau} = -\mu_\varsigma\vec{n}+\mu_\eta\vec{k} \tag{17}$$

orthogonal to $\vec{\mu}$ and $\vec{t}$.

In order to describe the electrical properties of the waveguide walls we use the Leontovich impedance boundary condition. In the local basis (16)-(17), it has the following form

$$E_\tau = ZH_\xi, \quad E_\xi = -ZH_\tau \tag{18}$$

or, using our 6-component vector notation,

$$\hat{G}\vec{\Pi}\big|_\Gamma = 0$$

$$\hat{G}=\hat{G}_0+\nu^2\hat{G}_2=\begin{pmatrix}0 & \mu_\varsigma h & -\mu_\eta h & Z & 0 & 0\\ 1 & 0 & 0 & 0 & -\mu_\varsigma Zh & \mu_\eta Zh\end{pmatrix} \tag{19}$$

Substitution of the asyptotic series (4)-(5) into boundary condition (19), after arranging in successive powers of the small parameter ν, yields

$$\hat{G}_0\vec{U}_0\big|_\Gamma = 0, \quad \hat{G}_0\vec{U}_1\big|_\Gamma = 0, \quad \left[\hat{G}_0\vec{U}_2+\vec{G}_2\vec{U}_0\right]_\Gamma = 0,\ldots \tag{20}$$

Making use of the general solution (12) we obtain an explicite form of the boundary conditions for scalar amplitudes u_0, v_0

$$\begin{aligned}\mu_\eta u_0+\mu_\varsigma v_0 &= 0\\ -\mu_\varsigma u_0+\mu_\eta v_0 &= 0\end{aligned} \tag{21}$$

and the first-order corrections u_1, v_1:

$$\begin{aligned}\mu_\eta u_1 + \mu_\varsigma \upsilon_1 &= \frac{1}{i\sigma Z}\left(\frac{\partial u_0}{\partial \eta} + \frac{\partial \upsilon_0}{\partial \varsigma}\right)\\ -\mu_\varsigma u_1 + \mu_\eta \upsilon_1 &= \frac{Z}{i\sigma}\left(\frac{\partial \upsilon_0}{\partial \eta} - \frac{\partial u_0}{\partial \varsigma}\right)\end{aligned} \tag{22}$$

Eqs.(21) have the trivial solution

$$u_0|_\Gamma = 0, \quad \upsilon_0|_\Gamma = 0 \tag{23}$$

and their differentiation along the cross section boundary Γ yields

$$\begin{aligned}\left[\frac{\partial u_0}{\partial \eta} + \frac{\partial \upsilon_0}{\partial \varsigma}\right]_\Gamma &= \left[\mu_\eta \frac{\partial u_0}{\partial m} + \mu_\varsigma \frac{\partial \upsilon_0}{\partial m}\right]_\Gamma\\ \left[\frac{\partial \upsilon_0}{\partial \eta} - \frac{\partial u_0}{\partial \varsigma}\right]_\Gamma &= \left[\mu_\eta \frac{\partial \upsilon_0}{\partial m} - \mu_\varsigma \frac{\partial u_0}{\partial m}\right]_\Gamma\end{aligned} \tag{24}$$

where $\frac{\partial}{\partial m} = \mu_\eta \frac{\partial}{\partial \eta} + \mu_\varsigma \frac{\partial}{\partial \varsigma}$ denotes the normal derivative in $\vec{\mu}$ direction. After substitution into the right-hand sides of Eqs. (22) and solving them with respect to u_1 and υ_1 we get finally

$$\begin{aligned}u_1|_\Gamma &= \frac{1}{i\sigma}\left[\left(\frac{\mu_\eta^2}{Z} + \mu_\varsigma^2 Z\right)\frac{\partial u_0}{\partial m} + \mu_\eta \mu_\varsigma \left(\frac{1}{Z} - Z\right)\frac{\partial \upsilon_0}{\partial m}\right]_\Gamma\\ \upsilon_1|_\Gamma &= \frac{1}{i\sigma}\left[\mu_\eta \mu_\varsigma \left(\frac{1}{Z} - Z\right)\frac{\partial u_0}{\partial m} + \left(\frac{\mu_\varsigma^2}{Z} + \mu_\eta^2 Z\right)\frac{\partial \upsilon_0}{\partial m}\right]_\Gamma\end{aligned} \tag{25}$$

As the zero-order amplitudes u_0 and υ_0 vanish on the boundary Γ, both of them are proportional to some eigenfunction of Eq. (14) satisfying the boundary condition

$$w|_\Gamma = 0 \tag{26}$$

(evidently, the eigenfunctions w_{mn} and the corresponding eigenvalues γ_{mn} of this boundary value problem are real):

$$\begin{aligned}u_0(\xi,\eta,\varsigma) &= A(\xi) w_{mn}(\xi,\eta,\varsigma)\\ \upsilon_0(\xi,\eta,\varsigma) &= B(\xi) w_{mn}(\xi,\eta,\varsigma)\end{aligned} \tag{27}$$

Thus, to the zero-order approximation, the asymptotyc solution of our problem is determined but for two normalizing factors $A(\xi)$, $B(\xi)$ being functions of the longitudinal variable ξ . Below it will be shown how they can be found from the solvability conditions of the boundary value problem for the first-order corrections u_1, υ_1.

The partial differential equations governing functions $u_1(\xi,\eta,\varsigma)$ and $\upsilon_1(\xi,\eta,\varsigma)$ follows from the orthogonality conditions (11) with n=3:

$$\begin{aligned}\frac{\partial^2 u_1}{\partial \eta^2} + \frac{\partial^2 u_1}{\partial \varsigma^2} - 2\sigma^2(\gamma + \kappa\eta)u_1 &= -2i\sigma \frac{\partial u_0}{\partial \xi}\\ \frac{\partial^2 \upsilon_1}{\partial \eta^2} + \frac{\partial^2 \upsilon_1}{\partial \varsigma^2} - 2\sigma^2(\gamma + \kappa\eta)\upsilon_1 &= -2i\sigma \frac{\partial \upsilon_0}{\partial \xi}\end{aligned} \tag{28}$$

The corresponding boundary values are determined by the formulae (25). Since $\gamma = \gamma_{mn}$ is an eigenvalue of the boundary value problem (14), (26), it is clear that the inhomogeneous equations (28)

may have a solution only under certain conditions imposed on their right-hand sides. Combining in a standart way Eqs. (28) with the corresponding equations of the zero-order approximation we obtain the following integral relationships

$$\frac{d}{d\xi}\iint_S u_0^2 dS = \frac{1}{i\sigma}\int_\Gamma \left(u_1 \frac{\partial u_0}{\partial m} - u_0 \frac{\partial u_1}{\partial m}\right) dl$$
$$\frac{d}{d\xi}\iint_S \upsilon_0^2 dS = \frac{1}{i\sigma}\int_\Gamma \left(\upsilon_1 \frac{\partial \upsilon_0}{\partial m} - \upsilon_0 \frac{\partial \upsilon_1}{\partial m}\right) dl \qquad (29)$$

Taking into consideration the boundary conditions (23), (25) and introducing normalization

$$\iint_S w_{mn}^2 dS = 1$$

we derive from Eqs. (27) and (29) a linear set of ordinary differential equations for the coefficients $A(\xi), B(\xi)$:

$$A' = P_{11}A + P_{12}B$$
$$B' = P_{12}A + P_{22}B \qquad (30)$$

where $P_{ij}(\xi)$ are weighted averages of the normal impedance $Z(\xi,l)$ and admittance $1/Z(\xi,l)$ over the cross section contour Γ:

$$P_{11}(\xi) = -\frac{1}{2\sigma^2}\int_\Gamma \left(\frac{\mu_\eta^2}{Z} + \mu_\varsigma^2 Z\right)\left(\frac{\partial w_{mn}}{\partial m}\right)^2 dl$$
$$P_{12}(\xi) = -\frac{1}{2\sigma^2}\int_\Gamma \mu_\eta \mu_\varsigma \left(\frac{1}{Z} - Z\right)\left(\frac{\partial w_{mn}}{\partial m}\right)^2 dl \qquad (31)$$
$$P_{22}(\xi) = -\frac{1}{2\sigma^2}\int_\Gamma \left(\frac{\mu_\varsigma^2}{Z} + \mu_\eta^2 Z\right)\left(\frac{\partial w_{mn}}{\partial m}\right)^2 dl$$

Since the transversal eigenfunction $w_{mn}(\xi,\eta,\varsigma)$ is constructed, coefficients $P_{ij}(\xi)$ can be calculated for arbitrary (uniform or nonuniform) distribution of the impedance $Z(\xi,l)$, and the solution $A(\xi)$, $B(\xi)$ can be easily found from Eqs. (30) by numerical methods. It determines attenuation and depolarization of the considered waveguide mode

$$\begin{pmatrix} u_0 \\ \upsilon_0 \end{pmatrix} = \begin{pmatrix} A \\ B \end{pmatrix} w_{mn} \qquad (32)$$

along the propagation path due to selective absorbtion in the waveguide walls.

The general solution to the considered propagation problem is a linear superposition of many adiabatic modes determined by the eigenfunctions (32) with constant excitation coefficients depending on the type and position of the radiation source. However, at large ranges one or few modes with minimum absorption dominate which simplities the propagation loss analysis.

References

1. V. A. Fock. *Electromagnetic Diffraction and Propagation Problems*, Pergamon, London, 1965
2. A. Baranov, A.V. Popov. Generalization of the Parabolic Equation for EM Waves in a Dielectric Layer of Nonuniform Thickness, *Wave Motion*, 17, pp. 337-347, 1993

GROUND CONDUCTIVITY EVALUATION METHOD BASED ON MEASUREMENTS OF RADIO WAVE PATH LOSS.

I.P. Zolotarev, V.A. Popov, V.P. Romanuk.
Institute of Terrestrial Magnetism, Ionosphere and Radio Wave Propagation (IZMIRAN), Troitsk, Moscow reg., 142092 RUSSIA.

1. Introduction.

Propagation of radio waves over terrain depends strongly on distribution of ground conductivity along path. Inhomogeneities of conductivity or buried objects can attenuate radio waves that propagate over ground or cause ground radio wave refraction. The last takes place when radio waves cross the boundary between areas of different conductivity such as, for a example, sea shore line. The effect of ground radio wave refraction results in navigation errors. To exclude these errors it is necessary to know distribution of conductivity and permittivity along path and simulate radio wave propagation.

The amplitude of receiving signal depends on the total distribution of ground parameters. Changes of ground conductivity along path can increase the amplitude of receiving signal with distance. Sometimes it is more profitable to move receiver at longer distance and place it over area with larger conductivity. The amplitude of receiving signal depends mainly on the distribution of ground parameters between transmitting and receiving points. But different areas between transmitter and receiver play different role in formation of receiving signal. More prominent role belongs to areas in vicinity of transmitter and receiver.

Investigation of radio wave propagation over inhomogeneous ground is rather complicated problem and has many aspects. Direct measurements of earth conductivity allow to create a map of ground permittivity and conductivity and then numerically solve problem of predicting of radio wave path loss. From other side, measurements of radio wave path loss allow to solve inverse problem and evaluate the distribution of conductivity along radio wave path. This can be very useful for many applied purposes and in particular for solving of mining problems. There exists several ground conductivity evaluation methods based on combination of experimental data analysis and numerical solutions. Below an implementation of conductivity evaluation method based on measurements of radio wave path loss and numerical solution of governing equation is discussed.

2. Ground Conductivity Evaluation Methods

Propagation of ground radio waves depends on the properties of thin surface ground layer. The thickness of this layer that is responsible for radio wave reflection, refraction and attenuation

depends on the frequency of radio waves and usually does not exceed several tens of meters. With increasing of radio frequency the thickness of active ground layer reduces. The electric and magnetic properties of layer depends on its composition, temperature, origination and wet content.

The most frequently used ground conductivity evaluation methods [1], [3], [2] are based on measurements of:

- active and reactive components of capacitor resistance (capacitor contains ground sample inside);
- voltage between two electrodes placed in ground;
- inductance coefficient between two wire loops on ground;
- polarization ellipse;
- radio wave attenuation along path;
- radio wave attenuation with depth;
- phase characteristics of radio wave along path;
- reflection coefficient;
- shape of whistlers (frequencies 0.1 - 25 kHz are used);
- surface ground impedance.

Some of methods require using of direct current measurements while others use radio frequency fields. The next step after measurements is to employ different mathematical methods to obtain ground parameters. For each of measurement method there exist several computational methods.

3. Evaluation of conductivity by measurements of radio wave attenuation

Dependence of radio wave electric field upon ground conductivity allows to use radio wave path loss data for evaluation of ground conductivity. In real conditions many factor such as diffraction, scattering, terrain profile influence on radio wave propagation. In some cases it is impossible to exclude these factors from experiment. So, evaluated conductivity for similar cases is effective conductivity for given radio wave path and radio wave frequency.

To evaluate ground conductivity using radio wave attenuation data there were developed several methods. One of them is based on comparison of calculated attenuation functions for uniform ground with experimental data. Corresponding best fit algorithm was developed by A.I. Smirnoff and L.D. Shoya [3]. This method is acceptable for many situations and allows to avoid many computational difficulties. More accurate for evaluation of ground conductivity is solving of equations governing radio wave propagation over the ground. Corresponding technique is described below. For evaluation of ground conductivity there were used data from recent experiment on radio wave attenuation.

3.1. Experiment

For measurements of radio wave path loss a special data acquisition system was elaborated. It consisted of portable transmitter working in pulse mode, receiver and a personal computer with 16 bit resolution DAC/ADC digital board inside it. Signals from transmitter were acquired into

personal computer, digitized and saved in binary format. For each record the information about gain of amplifiers and distance between transmitter and receiver were kept.

Special methods were undertaken to work with low level signals. At short distances the level of signal was far more than the level of noises. Received signal had almost pure sine form. The spectrum of received signal contained narrow central pick corresponding to useful signal. The width of pick was determined mainly by the length of transmitter pulses. The noise component grew with distance between transmitter and receiver. The larger distance the more was the relative amplitude of noise component in total signal. At very large distances noise component became compared with the amplitude of useful signal. Total form of received signal was significantly distorted and useful signal was masked by noise (Figure 1.a, c). Special steps were undertaken to extract useful signal from noise. Transmitter pulse frequency was specially chosen from range where industrial and natural noises were minimal. This allowed to extract useful signal from total signal using narrow band frequency filtering technique. Pulse structure of received signal can be seen in Figure 1.b. Although whole spectrum of received signal with noise component was very wide (Figure 2.a), it contained spectrum line corresponding to useful signal. This spectral component of useful signal was extracted using special hardware and software technique. Spectrum of filtered signal is depicted in Figure 2.b. Obtained data were statistically processed and average amplitude of useful signal was calculated.

4. Basic Equations

The time harmonic form of Maxwell's equations describing radio wave propagation in the space near the surface of the earth can be written as

$$rot\,\overrightarrow{E} = \frac{i\varpi}{c}\overrightarrow{H},\ rot\,\overrightarrow{H} = -\frac{i\varpi}{c}\varepsilon\overrightarrow{E}, \tag{4.1}$$

where $\varepsilon = \varepsilon' + i\varepsilon'' \equiv \varepsilon' + \frac{4\pi i\sigma}{\varpi}$ - complex dielectric permittivity and time dependence is taken in the form $-i\varpi t$.

For different grounds permittivity ε' varies from 4 to 30 and conductivity σ varies from $9*10^5$ to $9*10^7$ [2]. Very frequently earth conductivity changes along path in more than 10 times. We will assume that dielectric permittivity $\varepsilon = \varepsilon(x,y)$ is slow changing function in space. Let the source of radio waves is vertical electrical dipole at the point $(0,0,z_0)$. The electrical field E_z^0 in approximation of perfectly conducting earth in the plane $z=0$ for this case can be expressed by next formula [2]

$$E_z^0 = \frac{e^{ikD}}{D}\cos^2\psi, \quad D = \sqrt{x^2+y^2+z_0^2},\ \cos\psi = \frac{k_x}{k} \tag{4.2}$$

where $\overrightarrow{k}$ - is wave number. Influence of real earth on electric field can be taken into account by introducing an attenuation function W [2], [4].

$$E_z = E_z^0 W \tag{4.3}$$

In approach of slowly changing permittivity ε the attenuation function W satisfies to integral equation [2]

$$W(D) = 1 - \frac{ikD}{2\pi} \int \frac{W(x',y')}{\sqrt{\varepsilon^0(x',y')}} \frac{e^{ik(r+\rho)}}{r\rho} dS' \tag{4.4}$$

$$r = \sqrt{x'^2 + y'^2 + z_0^2}\,, \quad \rho = \sqrt{(x-x')^2 + (y-y')^2 + z^2}$$

where $dS' = dx'dy'$ and ε^0 is modified permittivity. Permittivity ε^0 allows to take into account the influence of the earth on reflection of radio waves with different wave numbers from the ground.

$$\sqrt{\varepsilon^0} = \sqrt{\frac{\varepsilon}{1 - \frac{\cos^2\psi}{\varepsilon}}} \tag{4.5}$$

For the case of $\varepsilon^0 = \varepsilon^0(x)$, and transmitter and receiver located immediately on the ground $z = 0$, $z_0 = 0$, it is possible to obtain from [4.4].

$$W(D) = 1 - \sqrt{\frac{ikD}{2\pi}} \int_0^D \frac{W(x')}{\sqrt{\varepsilon^0(x')}\sqrt{x'(D-x')}} dx' \tag{4.6}$$

Equation [4.6] is basic for investigation of many radio propagation problems. It can be used for predicting of radio wave attenuation along path provided ground permittivity and conductivity are known. Examples of calculated attenuation function W for complex paths over several areas with different permittivity are available in [2]. From other side, equation [4.6] allows to find out the distribution of ground permittivity and conductivity along path and make conclusions about ground properties using radio wave path loss data itself. Calculated distribution of ground parameters can be used then to correct navigation errors.

4.1. Evaluation of conductivity

During experiment amplitudes of signal at different distances from transmitter were recorded. These data were used for calculation of attenuation function $W(x_i)$ at points x_i of measurements. Behavior of received signal and attenuation function with distance is depicted in Figure 3.

Substituting $W(x_i)$ into [4.6] and assuming $W_0 = W(0) = 1$ it is possible to obtain for the case of n points of measurements

$$W_m = 1 - \sqrt{\frac{ikD}{2\pi}} \sum_{l=1}^{m} W_l \int_{x_{l-1}}^{x_l} \frac{dx'}{\sqrt{\varepsilon^0(x')}\sqrt{x'(D-x')}}, \quad m = 1..n \tag{4.7}$$

The system of n equations [4.7] determines ground parameters at points of measurements. This system was solved numerically. Resulted distribution of conductivity with running average is shown in Figure 4.

Obtained experimental data of received signal contain small oscillation component. This results in oscillations of calculated conductivity distribution. Apparently oscillations were caused by interference with secondary radio waves from ground inhomogeneities or remote objects. Smoothing of obtained data gives average distribution of conductivity along path.

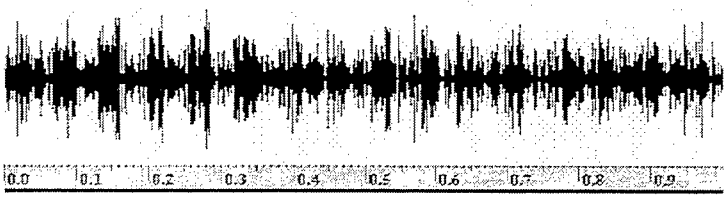

a) Signal with noise.

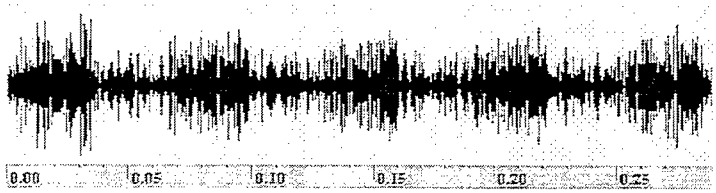

b) Pulse mode.

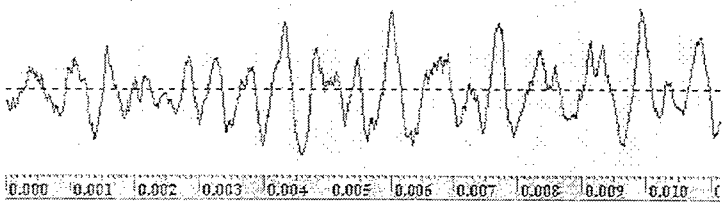

c) Detail structure.

Figure 1. Received signal.

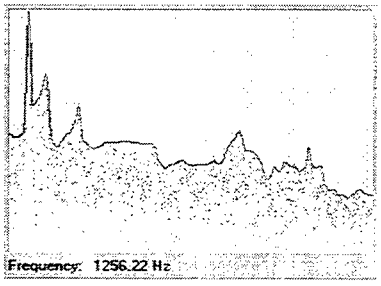

a) original

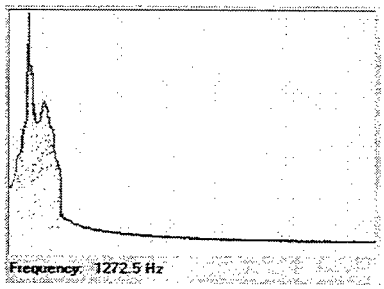

b) filtered

Figure 2. Spectra of received signal.

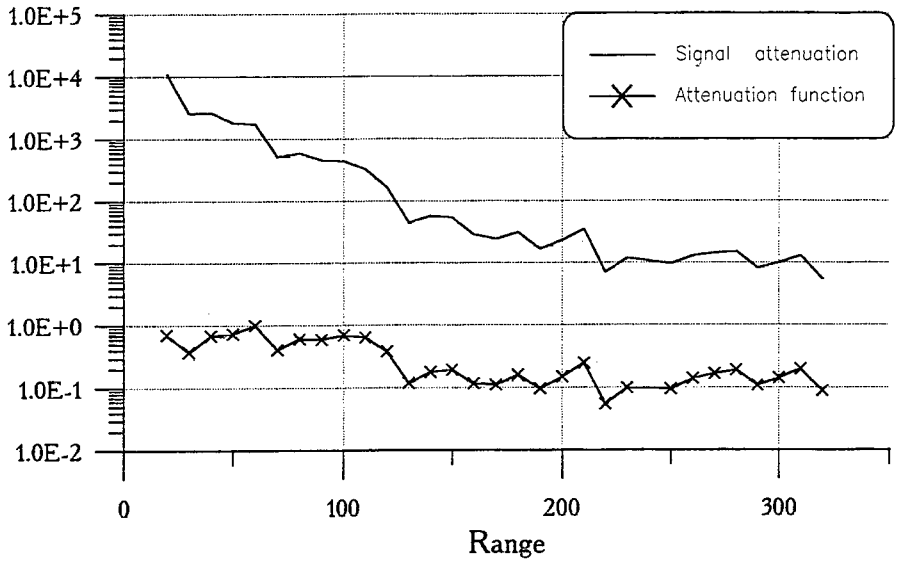

Figure 3. Attenuation of Radio Waves.

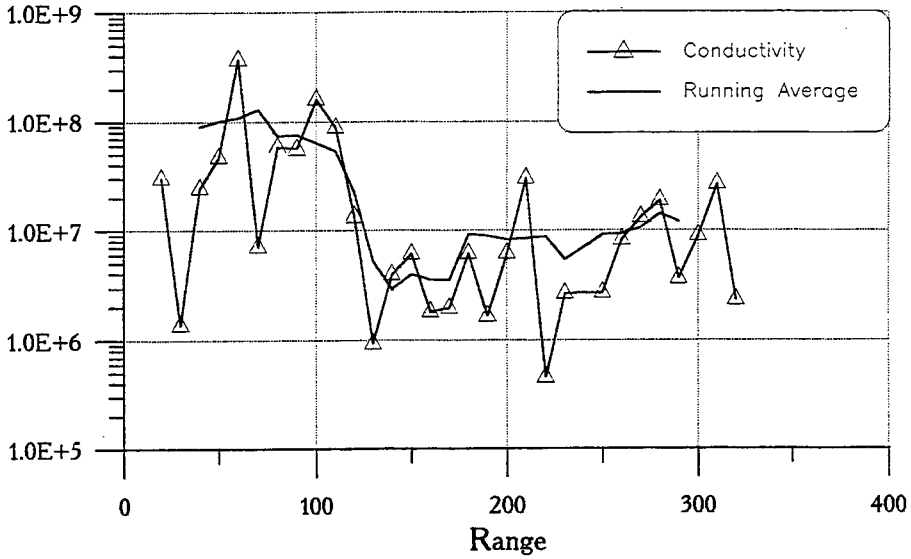

Figure 4. Distribution of conductivity.

5. Summary

Measurements of radio wave path loss provide convenient mechanism for gathering of information about ground surface layer properties. Obtained data can be used for calculation of ground permittivity and conductivity and for detection of buried objects or other purposes. Calculated permittivity and conductivity can be used then as input for evaluation of detail composition of ground layer. All results can be obtained in real time regime.

References

[1] F.B. Chernyj. Propagation of Radio Waves.Sovetskoe radio.1972.

[2] E.L. Feinberg. Radio wave propagation over terrain. 1961.

[3] V.E. Kashprovsky, F.A. Kuzubov. Propagation of short ground radio waves. Svyaz, Moscow 1971, 220.

[4] A.A. Semenov. Theory of electromagnetic waves. Moscow State University, 1968, 320.

Two-scale asymptotic description of radar pulse propagation in lossy subsurface medium.

V.A. Vinogradov
Moscow Institute of Physics and Technology
V.A.Baranov and A.V.Popov
Institute of Terrestrial Magnetism, Ionosphere and Radiowave Propagation, Troitsk, Russia

INTRODUCTION

Most of ground penetrating radars use short ultrawide-band EM pulses to acquire information on the geological features or buried objects. One of the difficulties arising in posing the inverse problem is the absence of adequate theory to describe propagation of such pulses in the background subsurface environment. Both analytical spectral approaches and straightforward numerical integration of Maxwell's equations requiring massive computation are often not handy for studying the qualitative behavior of the solution. In this respect, asymptotic techniques, being developed in the framework of the time-domain geometric optics, appear to be more useful. In this paper, we consider propagation of ultrawide-band transient pulses in weakly conducting nonuniform media. In such media, dispersion of the radar return pulse may be either accumulated along the whole propagation path, due to finite conductivity, or caused by the reflection at sharp interfaces between the layers characterized by different values of complex permittivity. To analize these effects, we use two-scale asymptotic expansion in the inherent small parameter of the problem: ratio of the radar pulse spatial length to the characteristic scale of the background nonuniformity.

We use scalar propagation model: damped wave equation containg static permittivity and electrical conductivity as parameters slowly varying in space. After introducing an additional fast variable (technique widely used in nonlinear mechanics) it takes the form admitting asymptotic expansion in powers of the above mentioned small parameter. As a leading term of this reccurent series, a time-space eikonal equation arises wich determines the geometric wavefronts (surfaces of constant phase). Further equations govern the zero-oder approximation to the true pulse waveform and subsequent corrections, all of them being functions both of the fast phase and slow time-space variables. An important feature of this approach is that all the equations can be solved explicitely with respect to the fast variable in terms of subsequent integrals of the initial waveform. The integration constants, as functions of slow time and spatial coordinates, are determined by the reguirement of removing secular (rapidly increasing) terms in the higher-order corrections to the leading term. The zero-order approximation corresponds to nondispersive pulse propagation along the geometric rays, modified only by the ray tube divergency and ohmic absorption. Dispertion effects arise in our approach as an additive correction depending on slow time and spatial variables and governed by a partial differential equation of Klein-Gordon type. In the simplest one-dimensional model, it can be solved analytically in terms of Bessel functions. For nonuniform 3D environments, the use of numerical integration is inevitable. However, the mesh steps can be chosen large compared witch the spatial scale of the initial pulse, wich ensures a radical gain in computational efficiency.

ANALYSIS

Consider scalar wave propagation in a lossy medium governed by the following model equation

$$c^2 \Delta E = \varepsilon \frac{\partial^2 E}{\partial t^2} + 4\pi\sigma \frac{\partial E}{\partial t}. \tag{1}$$

Here, c is light velocity, ε and σ are, respectively, permittivity and conductivity of a smoothly nonuniform subsurface medium. For monochromatic waves, a simple approximate theory (geometric optics) can be constructed if the wavelength λ is small compared to the characteristic scale L of the background nonuniformity. In the theory of transients, the spatial length of the propagating pulse Λ substitutes for the wavelength λ, and for $\Lambda << L$ a simple asymptotic solution can be expected too. In this case, the two-scale expansions [1] are adequate in order to separate fast and slow variables describing short pulse propagation over a long nonuniform path.

Let the initial pulse waveform be $f(t/T)$ where $T = \Lambda / c$ while function $f(s)$ is assumed to be equal to zero for $s < 0$, continous at $s = 0$ and have a finite integral (total impulse)

$$M = \int_0^\infty f(s)ds \tag{2}$$

We introduce scaled spatial variables $\vec{\rho}(\xi, \eta, \varsigma) = \vec{r} / L$ and seek an asymptotic solution to Eq. (1) in the following form

$$E\left(t, \vec{r}\right) = F\left[\frac{1}{\nu}\Phi\left(\tau, \vec{\rho}\right), \tau, \vec{\rho}\right]. \tag{3}$$

Here, $\nu = \Lambda / L << 1$ is the inherent small parameter, $\tau = ct / L$ is "slow time", and $s = \Phi\left(\tau, \vec{\rho}\right) / \nu$ is a fast variable normalized to the initial pulse duration. Substitution into Eq. (1) leads to a new wave equation in the extended space of indpendent variables $(s, \tau, \vec{\rho})$:

$$\begin{aligned} &\frac{1}{\nu^2}\left[V^2(\nabla\Phi)^2 - \Phi_\tau^2\right]F_{ss} + \frac{1}{\nu}[V^2(2\nabla\Phi\nabla F_s + F_s\nabla\Phi) - \\ &-(2\Phi_\tau F_{s\tau} + \Phi_{\tau\tau}F_s + 2q\Phi_\tau F_s)] + V^2\Delta F - (F_{\tau\tau} + 2qF_\tau) = 0 \end{aligned} \tag{4}$$

Here, $V\left(\vec{\rho}\right) = \varepsilon^{-1/2}$, $q\left(\vec{\rho}\right) = 2\pi\sigma L / (c\varepsilon)$ are, respectively, normalized phase velocity and conductivity as functions of slow spatial variables. The modified wave equation (4) contains the small parameter explicitely, which allows for constructing its solution in the form of asymptotic series in powers of ν:

$$F\left(s, \tau, \vec{\rho}\right) = \sum_{n=0}^{\infty} \nu^n F^{(n)}\left(s, \tau, \vec{\rho}\right). \tag{5}$$

Under the evident condition

$$(\nabla\Phi)^2 = \frac{1}{V^2}\Phi_\tau^2 \tag{6}$$

there arises a recurrent set of the partial differential equations for the functions $F^{(n)}(s, \tau, \vec{\rho})$:

$$\Phi_\tau F_{s\tau}^{(n)} + \left(\frac{1}{2}\Phi_{\tau\tau} + q\right)F_s^{(n)} - V^2\left(\nabla\Phi\nabla F_s^{(n)} + \frac{1}{2}\Delta\Phi F_s^{(n)}\right) = \\ = \frac{V^2}{2}\Delta F^{(n-1)} - \frac{1}{2}F_{\tau\tau}^{(n-1)}, \qquad n = 0,1,2,... \tag{7}$$

They can be explicitely integrated with respect to the fast variable s, and the integration "constans", being functions of the slow variables τ and $\vec{\rho}$, will be subject to the condition of eliminating secular (growing with s) terms in the asymptotic series (5). That will ensure the uniform applicability of the solution at spatial ranges $\left|\vec{r}\right| \sim L$.

Let us start constructing the solutions of Eqs. (6)-(7). By setting

$$\Phi\left(\tau,\vec{\rho}\right) = \tau - \Psi\left(\vec{\rho}\right) \tag{8}$$

we get for $\Psi\left(\vec{\rho}\right)$ an ordinary eikonal equation of geometric optics:

$$(\nabla\Psi)^2 = \frac{1}{V^2(\vec{\rho})} \tag{9}$$

Its solution has the form

$$\Psi\left(\vec{\rho}\right) = \int_{M_0}^{M}\frac{de}{V} + \Psi_0(\gamma_1,\gamma_2) \tag{10}$$

where integration is performed along the rays determined by the differential equation

$$\frac{d}{dl}\left(\frac{1}{V}\frac{d\vec{\rho}}{dl}\right) = \nabla\left(\frac{1}{V}\right) \tag{11}$$

with the initial conditions $\vec{\rho}\big|_{l=0} = \vec{\rho}_0(\gamma_1,\lambda_2)$, $\vec{\rho}'\big|_{l=0} = \vec{t}_0(\gamma_1,\gamma_2)$. In virtue of the well-known laws of geometric optics (see eg. [2])

$$\nabla\Psi = \frac{1}{V}\frac{d\vec{\rho}}{dl}, \quad \Delta\Psi = \frac{1}{J}\frac{d}{dl}\left(\frac{J}{V}\right) \tag{12}$$

where

$$J = \left|\frac{D(\xi,\eta,\varsigma)}{D(l,\gamma_1,\gamma_2)}\right| \tag{13}$$

is ray divergency, Eq. (7) can be rewritten in ray coordinates (l,γ_1,γ_2)

$$F_{s\tau}^{(n)} + qF_s^{(n)} + V\left[F_{sl}^{(n)} + \frac{V}{2J}\left(\frac{J}{V}\right)_l F_s^{(n)}\right] = \frac{V^2}{2}\Delta F^{(n-1)} - \frac{1}{2}F_{\tau\tau}^{(n-1)} - qF_\tau^{(n-1)} \tag{14}$$

The homogeneous zero-order equation can be easily integrated, and its general solution has the following form

$$F^{(0)}(s,\tau,\vec{\rho}) = A^{(0)}(s,\tau-\Psi,\gamma_1,\gamma_2)\sqrt{\frac{V}{J}}\exp\left(-\int_0^l\frac{q}{V}dl_1\right) + B^{(0)}(\tau,\vec{\rho}) \tag{15}$$

Here, $A^{(0)}$ and $B^{(0)}$ are arbitrary functions of their arguments. They will be found below from the boundary conditions and the reguirement of eliminating the secular terms.

The boundary values of the eikonal $\Psi(\vec{\rho})$ and amplitudes $F^{(n)}$ are determined by the radiation source. Here we assume that the wave field in the half-space $\varsigma > 0$ is generated by a short transient perturbation applied to the boundary plane $\varsigma = 0$:

$$E(\tau,\xi,\eta,0) = E_0(\xi,\eta) f\left[\frac{\tau - \tau_0(\xi,\eta)}{\nu}\right] \tag{16}$$

Here, $f(s)$ is the initial pulse waveform, $\tau_0(\xi,\eta)$ and $E_0(\xi,\eta)$ are its relative delay and initial amplitude in the given point (ξ,η) of the radiating surface.

By comparing the zero-order solution (15) with the boundary condition (16):

$$A^{(0)}\left(\frac{\tau-\Psi_0}{\nu}, \tau-\Psi_0, \gamma_1, \gamma_2\right)\sqrt{\frac{V_0}{J_0}} + B^{(0)}(\tau,\xi,\eta,0) = E_0(\xi,\eta) f\left(\frac{\tau-\tau_0}{\nu}\right) \tag{17}$$

one reveals that the boundary value of the eikonal Ψ_0 coincides with the radiation time delay:

$$\Psi_0(\xi_0,\eta_0) = \tau_0(\xi_0,\eta_0) \tag{18}$$

(we choose, as the ray parameters, the coordinates of the starting point (ξ_0,η_0)). This boundary condition determines a unique solution of the eikonal equation (9) and ray divergency $J(e,\xi_0,\eta_0)$. Furthermore, function $A^{(0)}$ can be chosen independent of the slow time τ:

$$A^{(0)}(s,\tau,\xi_0,\eta_0) = A^{(0)}(s,\xi_0,\eta_0) = A(\xi_0,\eta_0) f(s) \tag{19}$$

where

$$A(\xi_0,\eta_0) = E_0(\xi_0,\eta_0)\sqrt{\frac{J(0,\xi_0,\eta_0)}{V(\xi_0,\eta_0,0)}} \tag{20}$$

is the radiation pattern from the point $(\xi_0,\eta_0,0)$ in $\nabla\Psi(0,\xi_0,\eta_0)$ direction. In addition, to meet boundary condition (17), we impose

$$B^{(0)}(\tau,\xi,\eta,0) = 0 \tag{21}$$

Hence, we have constructed the leading term of the asymptotic series (5) but for a function of slow variables $B^{(0)}(\tau,\vec{\rho})$ whose boundary value is defined by Eq. (21). In order to find it along with the higher order corrections, one has to consider further recurrent equations.

After substituting into the right-hand side of Eq. (14) the function $F^{(0)}$ determined by Eqs. (15), (19) we get an inhomogeneous equation for the first correction $F^{(1)}(s,\tau,\vec{\rho})$:

$$\begin{aligned} &F^{(1)}_{s\tau} + qF^{(1)}_s + V\left[F^{(1)}_{sl} + \frac{V}{2J}\left(\frac{J}{V}\right)_l F^{(1)}_s\right] = \\ &= \frac{V^2}{2} f(s)\Delta\left[A\sqrt{\frac{V}{J}}\exp\left(-\int_0^l \frac{q}{V}dl_1\right)\right] + \frac{1}{2}\Re B^{(0)} \end{aligned} \tag{22}$$

with the differential operator $\Re$ defined below in Eq. (24). Integration with respect to s yields

$$F_\tau^{(1)} + qF^{(1)} + V\left[F_l^{(1)} + \frac{V}{2J}\left(\frac{J}{V}\right)_l F^{(1)}\right] =$$
$$= \frac{V^2}{2}\int_0^s f(s_1)ds_1\Delta\left[A\sqrt{\frac{V}{J}}\exp\left(-\int_0^l \frac{q}{V}dl_1\right)\right] + \frac{s}{2}\Re B^{(0)} + C^{(1)}\left(\tau,\vec{\rho}\right) \tag{23}$$

Since function $f(s)$ has bounded integral (2), the only secular term in Eq. (23) will be removed if

$$\Re B^{(0)} \equiv V^2\Delta B^{(0)} - B_{\tau\tau}^{(0)} - 2qB_\tau^{(0)} = 0 \tag{24}$$

This PDE must be supplemented by the boundary condition (21) and the initial condition

$$F^{(n)}\left(\frac{\tau-\Psi}{\nu},\tau,\vec{\rho}\right)\Big|_{\tau\le\Psi\left(\vec{\rho}\right)} = 0, \qquad n = 0,1,2,\ldots \tag{25}$$

(absence of the wave motion before the wave front). As $\tau = \Psi\left(\vec{\rho}\right)$ is a characteristic surface of Eq. (24), its solution is uniquely determined by Eq. (21) and single initial condition

$$B^{(0)}\left[\Psi\left(\vec{\rho}\right),\vec{\rho}\right] = 0 \tag{26}$$

following from Eqs. (15), (19) and (25). In virtue of homogeneity of these equations, $B^{(0)}\left(\tau,\vec{\rho}\right) \equiv 0$ and, consequently, to the zero-order approximation we obtain

$$F^{(0)}\left(s,\tau,\vec{\rho}\right) = E_0\left(\xi_0,\eta_0\right)f(s)\sqrt{\frac{J_0V}{JV_0}}\exp\left(-\int_0^l \frac{q}{V}dl_1\right) \tag{27}$$

This result describes undistorted pulse propagation along the rays (11) as well as its attenuation due to geometric divergency J and ohmic absorption q. In this approximation the pulse waveform $f(s)$ remains invariable. Therefore, accurate calculation of the dispersion effects reguires actual constructing the first-order correction $F^{(1)}\left(s,\tau,\vec{\rho}\right)$.

Taking into account Eq. (24) we can integrate the PDE (22):

$$F^{(1)}\left(s,\tau,\vec{\rho}\right) = [K\left(\vec{\rho}\right)\int_0^s f(s_1)ds_1 +$$
$$A^{(1)}\left(s,\tau-\Psi,\xi_0,\eta_0\right)]\sqrt{\frac{V}{J}}\exp\left(-\int_0^l \frac{q}{V}dl_1\right) + B^{(1)}\left(\tau,\vec{\rho}\right) \tag{28}$$

Here, the term

$$K(\vec{\rho}) = \frac{1}{2}\int_0^l \sqrt{VJ}\exp\left(\int_0^{l_1}\frac{q}{V}dl_2\right)\Delta\left[A\sqrt{\frac{V}{J}}\exp\left(-\int_0^{l_1}\frac{q}{V}dl_2\right)\right]dl_1 \tag{29}$$

determines a particular solution to Eq. (22) whereas $A^{(1)}$ and $B^{(1)}$ are arbitrary functions. Since the boundary condition (16) is already met due to the zero-order approximation, we can put

$$A^{(1)}\left(s,\tau,\vec{\rho}\right) \equiv 0, \quad B^{(1)}\left(\tau,\xi,\eta,0\right) = 0 \tag{30}$$

On the characteristic surface $\tau = \Psi\left(\vec{\rho}\right)$, the initial condition (25) is posed, whence

$$B^{(1)}\left[\Psi\left(\vec{\rho}\right),\vec{\rho}\right]=0 \tag{31}$$

The differential equation governing $B^{(1)}\left(\tau,\vec{\rho}\right)$ follows from the eliminating the terms linearly growing with s in the RHS of Eq. (14) with $n=2$:

$$V^2\Delta B^{(1)}-B^{(1)}_{\tau\tau}-2qB^{(1)}_{\tau}=-MV^2\Delta\left[K\sqrt{\frac{V}{J}}\exp\left(-\int_0^l\frac{q}{V}dl_1\right)\right]. \tag{32}$$

Here, M is the total impulse of the initial perturbation (2), and $K\left(\vec{\rho}\right)$ is the function defined by Eq. (29). Substitution

$$B^{(1)}=\bar{B}^{(1)}-MK\sqrt{\frac{V}{J}}\exp\left(-\int_0^l\frac{q}{V}dl_1\right) \tag{33}$$

reduces Eq. (32) to a homogeneous PDE whereas the boundary condition on the characteristic $\tau=\Psi\left(\vec{\rho}\right)$ becomes inhomogeneous:

$$\begin{gathered}V^2\Delta\bar{B}^{(1)}-\bar{B}^{(1)}_{\tau\tau}-2q\bar{B}^{(1)}_{\tau}=0\\ \bar{B}^{(1)}\left(\tau,\xi,\eta,0\right)=0\\ \bar{B}^{(1)}\left[\Psi\left(\vec{\rho}\right),\vec{\rho}\right]=MK\sqrt{\frac{V}{J}}\exp\left(-\int_0^l\frac{q}{V}dl_1\right)\end{gathered} \tag{34}$$

SIMPLE 1D EXAMPLE

In the case of constant coefficients V and q, an explicite solution of the problem (34) can be found via separation of variables or by Riemann's method [3]. For example, in the simplest one-dimensional case, substitution

$$\bar{B}^{(1)}\left(\tau,\varsigma\right)=H^{(1)}\left(\tau,\varsigma\right)e^{-q\tau} \tag{35}$$

yields the Klein-Gordon equation

$$V^2H^{(1)}_{\varsigma\varsigma}-H^{(1)}_{\tau\tau}+q^2H^{(1)}=0 \tag{36}$$

having the well-known Riemann function

$$R\left(\tau-\tau_0,\varsigma-\varsigma_0\right)=I_0\left[q\sqrt{\left(\tau-\tau_0\right)-\frac{1}{V^2}\left(\varsigma-\varsigma_0\right)^2}\right] \tag{37}$$

Here $I_0(z)$ is the zero-order modified Bessel function. After calculating the initial value at the characteristic line $\tau=\varsigma/V$ from Eq. (34)

$$h(\tau_0)=H^{(1)}\left(\tau_0,V\tau_0\right)=\frac{q^2}{2}E_0M\tau_0 \tag{38}$$

and making use of Riemann's formula

$$H^{(1)}(\tau,\varsigma)=\int_0^{\frac{1}{2}\left(\tau+\frac{\varsigma}{V}\right)}R(\tau-\tau_0,\varsigma-V\tau_0)h'(\tau_0)d\tau_0-$$
$$-\int_0^{\frac{1}{2}\left(\tau-\frac{\varsigma}{V}\right)}R(\tau-\tau_0,\varsigma+V\tau_0)h'(\tau_0)d\tau_0 \tag{39}$$

we obtain an explicite representation

$$H^{(1)}(\tau,\varsigma)=E_0M\frac{q\varsigma}{V\sqrt{\tau^2-\varsigma^2/V^2}}I_1\left(q\sqrt{\tau^2-\varsigma^2/V^2}\right) \tag{40}$$

Finally, the approximate solution to the primary equation (1), including the zero-order approximation (27) and the first correction (28) takes the form

$$E(t,z)\approx F^{(0)}(s,\tau,\varsigma)+\nu F^{(1)}(s,\tau,\varsigma)=E_0\left\{f(s)e^{-q\frac{\varsigma}{V}}-\right.$$
$$\left.-\nu q^2\frac{\varsigma}{2V}\left[e^{-q\frac{\varsigma}{V}}\int_s^{\infty}f(s_1)ds_1-2Me^{-q\tau}\frac{I_1\left(q\sqrt{\tau^2-\varsigma^2/V^2}\right)}{q\sqrt{\tau^2-\varsigma^2/V^2}}\right]\right\} \tag{41}$$

with $s=\frac{1}{V}(\tau-\varsigma/V)$. Below, in Figs. 1, 2 an example of transient pulse propagation with $f(s)=\sin as\exp bs$, $a=10^9\,s^{-1}$, $b=6\cdot10^8\,s^{-1}$ is shown. The material parameters of the medium are: relative permittivity $\varepsilon=9$ and conductivity $\sigma=10^{-2}\,S/m$. The depicted depth range is 0 to 10 meters in the temporal interval 15 ns from the wavefront.

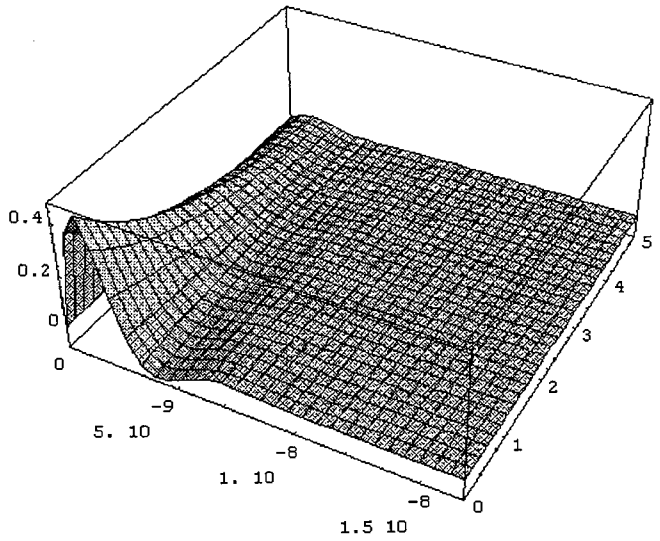

Fig.1. Initial waveform versus time and propagation depth

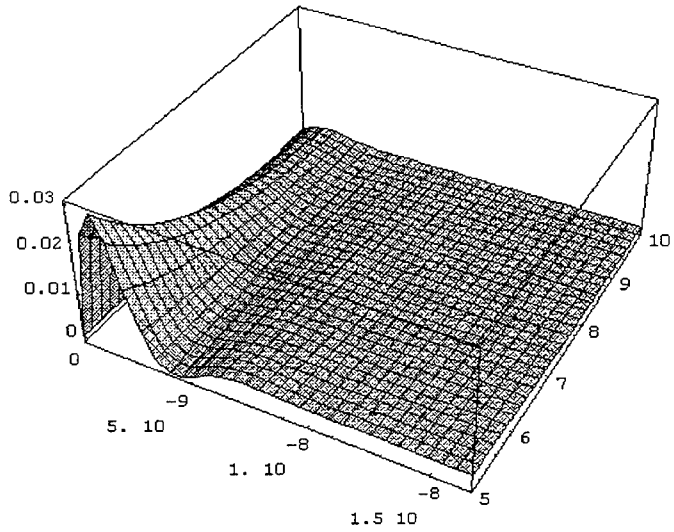

Fig.2. Distorted waveform versus time and propagation depth

Formula (41) reveals two kinds of effects causing distortion of the short ultrawide-band pulse in a conducting medium. The former one, proportional to the pulse length $\Lambda = \nu L$, propagation path $z = \varsigma L$ and the second power of conductivity, slightly modifies the initial pulse shape $f(s)$. The latter one, depending on the value of total impulse $M = \int_0^\infty f(s)ds$, generates a slowly varying "trace" of the passing transient. Contrary to the initial pulse, it dies down slowly $\left(\sim \tau^{-3/2}\right)$ and causes interfering artifacts in signal processing.

This work has been supported by the Russian Foundation for Basic Research, grant No 95-05-14027.

REFERENCES

1. J. D. Cole. Perturbation Methods in Applied Mathematics, Blaisdell Publishing Co, Waltham, MA. - Toronto - London, 1968
2. V. M. Babich, V. S. Buldyrev. Short-wavelength Diffraction Theory (asymptotic methods), Springer, New York, 1991
3. R. Courant. Partial Differential Equations, v.2, New York - London, 1962

SESSION 18:

EMI/EMC

Chairs:T. Hubing and J. Drewniak

Modeling of EMI Emissions from Microstrip Structures with Imperfect Reference Planes

Bruce Archambeault
SETH Corporation

Introduction

The EMI radiated emissions from most all commercial electronic products must be controlled to meet both US, European, and other regulatory requirements. Reducing product development and manufacturing costs are considered very important in order to remain competitive. Most engineers try to exercise some level of EMI control at the printed circuit board (PCB) level when ever possible to help reduce the costs associated with shielding etc. Since most high speed signals have better signal integrity and better EMI control with microstrip or stripline PCB structures, they are used extensively.

Proper design using a microstrip or stripline is fairly straightforward, as long as some well published guidelines are followed. Unfortunately, other design considerations often force a deviation from these typical design guidelines. In these cases, engineers are often at a loss to predict the severity of the effects caused by these design guideline deviations.

This paper briefly describes an effort to use numerical modeling tools to simulate a PCB with a microstrip and understand the effect of improper microstrip design. Measurement data is used to first validate the model, then various microstrip designs are implemented, and their effects noted. This effort was part of an effort to develop a set of internal microstrip design guidelines which went far beyond the normal guidelines.

Initial Model

The initial model was created using the Method of Moments (MoM). A wire frame ground reference plane was used with a single short microstrip. The ground reference plane mesh size was 5 mm near the microstrip, and 10 mm away for the microstrip. The microstrip itself was selected to be one inch long (centered on the reference plane), while the ground reference plane was 280 mm long by 120 mm wide. These dimensions were selected to allow comparisons to measured data by Dockey and German [1]. The microstrip was driven at one end, and terminated in a 50 ohm load at the far end. The entire structure was placed flat .8 meters above a ground plane.

Figure 1 shows the electric field levels at a distance of 3 meters over a ground plane for both the measured data and the results of the initial model. The receive location height was scanned from one to four meters, and rotated 360 degrees around the PC board. As can be seen in Figure 1, the modeled results agreed within 3-4 dB over most of the frequency range. This agreement was considered good.

Measured data also existed in the same reference for the same microstrip board structure, but with a 75 cm wire attached to either end of the board. This configuration was modeled, and the electric fields levels are shown in Figure 2. The modeled results agreed well except for predicting the resonant frequencies. The first resonant frequency for a 280 mm long structure with two 75 cm wires would normally be expected at about 85 MHz. The model predicts the first

Figure 1

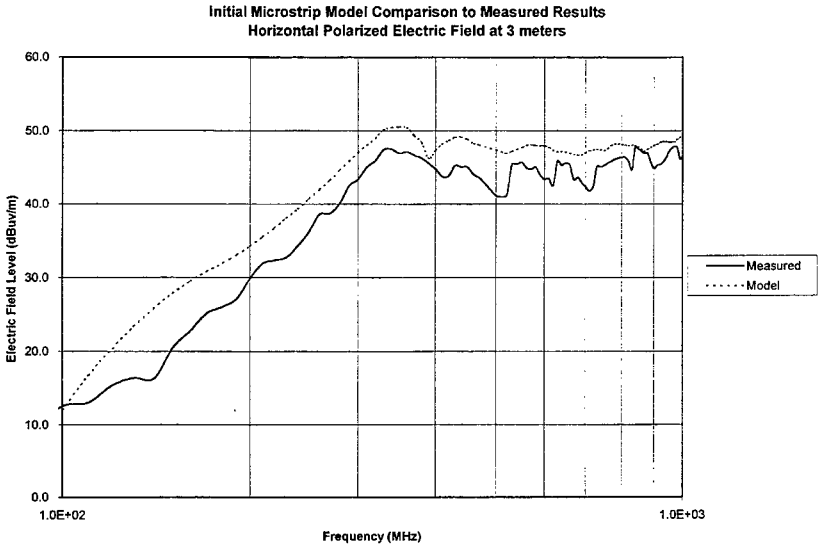

Figure 2

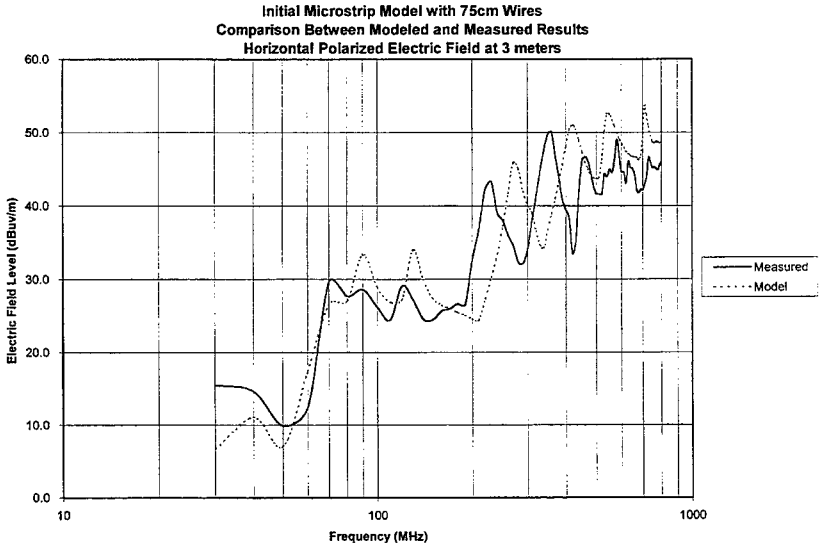

resonance at about 90 MHz, while the measured results show the first resonance at about 70 MHz. While the overall shape of the modeled and measured responses agree, the measured

results seem to consistently show a lower than expected resonant frequency. Since the main goal of this work is to compare the difference between different microstrip configurations, the difference in measured and modeled resonances are not important. So, again, the model was considered valid.

RF Current along the PCB Reference Plane Edge

One definite advantage of using modeling tools is there is extra information available that would be impossible to obtain through measurements. For example, since the MoM technique finds the currents every where on the structure being modeled in order to find the radiated fields, those currents are available for analysis. In this example, the current level in the ground reference plane along the edge of the PC board at 100 MHz is shown in Figure 3. The current distribution along the edge clearly resembles a dipole's current distribution. (Note the length of the PC board is shorter than ½ wavelength at 100 MHz.)

Figure 3

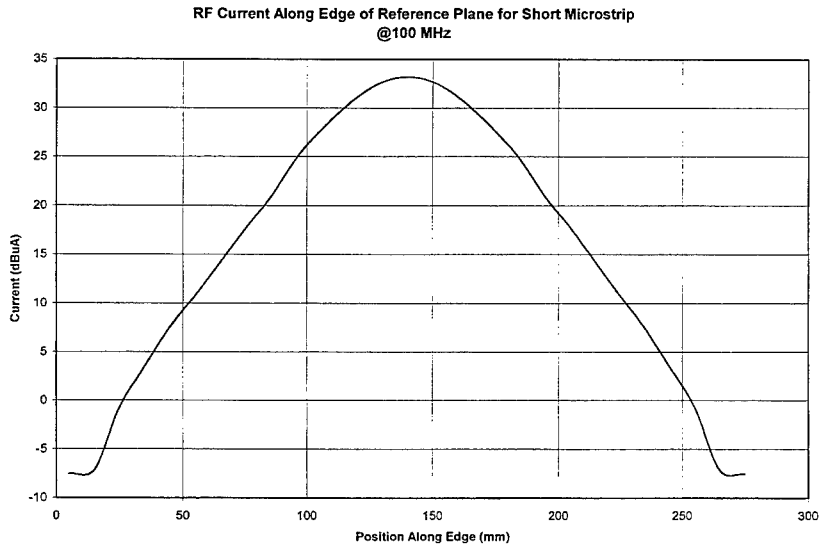

RF Current through the PC Board on the Reference Plane

The currents in the ground reference plane can be analyzed for all locations, of course. Figure 4 shows the current levels on the reference plane at 100 MHz for cuts through the PC board. Position #1 is through the center of the PC board, and includes the ground reference plane directly under the microstrip. Position #2 is about one-third of the way towards the end of the PC Board, and does not include the area under the microstrip.. Position #3 is near the end of the PC Board.

While it is expected that the currents under the microstrip would be highest, the currents 60 mm away at the edge of the PC Board are only about 45 dB less than the current directly under the microstrip. Since these currents on wide buss structures can be very significant (many amps of current all together), then this level along a PC Board edge can also be significant.

It is also interesting to note the shape of the current away from the microstrip area. The current was maximum in the center of the board, but was also very high along the edges.

Figure 4

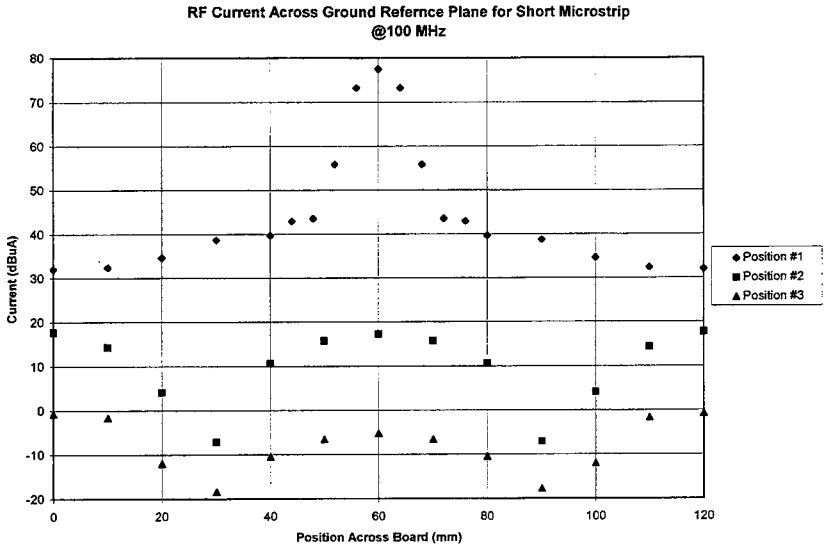

Non-Centered Microstrips

A series of models were used to compare the effect on the radiated fields when the microstrip was moved closer to the edge of the PC Board. Figure 5 shows the change in electric field levels for a case with two different microstrip positions. Position #1 was with the microstrip 35 mm from the edge of the board, and position #2 was with the microstrip 15 mm from the edge of the board. Since the microstrip was only 2 mm wide, a separation of 15 mm from the edge seemed to be sufficient. However, as Figure 5 shows, the radiated fields increased significantly with this close proximity position.

Voids in Ground Reference Planes

Although running a microstrip over a void in a ground reference plane is completely against all good EMI design practices, this practice occurs occasionally due to other design constraints that have an over-riding priority. When these reference plane voids occur, the currents can not return to their source directly under the microstrip, and must find other (longer) paths. Since it has already been shown that the currents along the edge of the reference plane are important and available from modeling tools, then such voids can be simulated easily by forcing a break in the wire mesh at the appropriate location, and analyzing the currents. Figure 6 shows the difference in the RF current along the edge of the ground reference plane at 100 MHz between the case of a normal reference plane and a reference plane with a split directly under the microstrip and extending an inch on either side. The amount of current increase was significant, and the shape of the current distribution changed from a single peak sine to a three peak distribution. This effectively places much more current in the corners of the board than might have been expected.

Figure 5

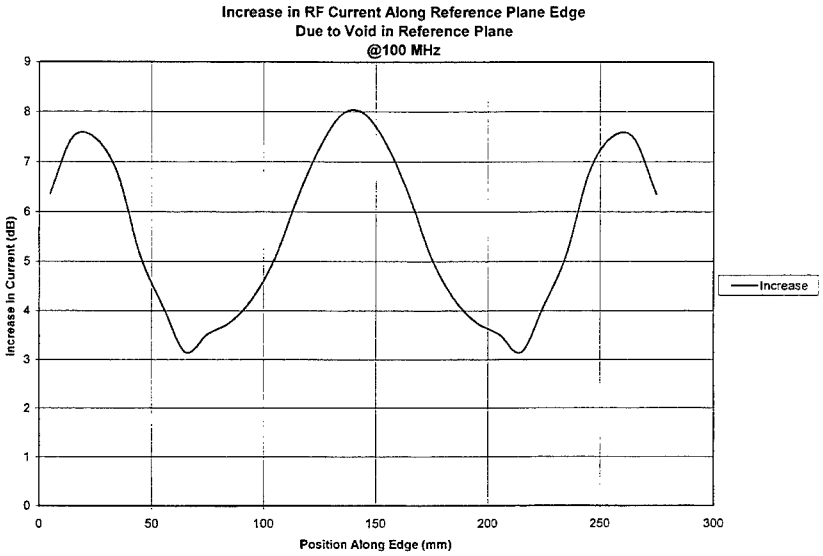

Figure 6

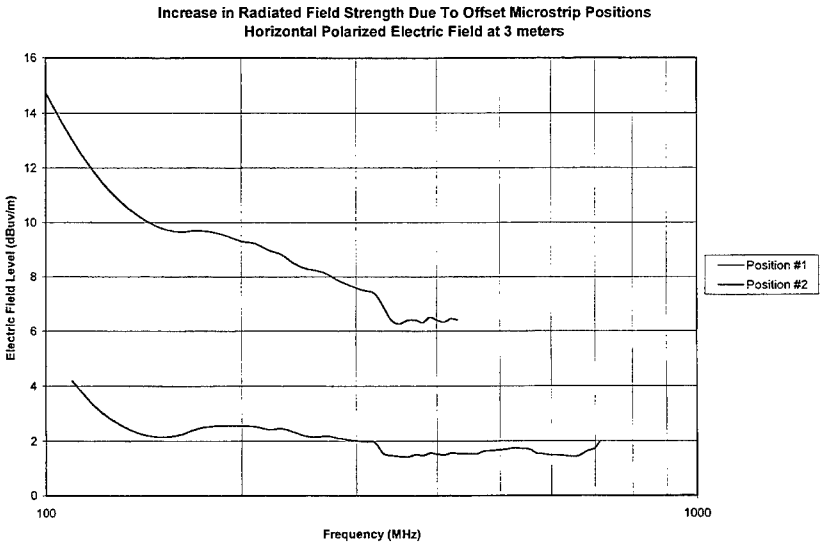

Summary

The use of modeling to simulate the performance of a microstrip printed circuit board structure has been shown to be accurate when compared to measured data. A number of different features, including location near an edge or void in the reference plane, were modeled and the results

compared to the 'normal' case. These types of analysis are much more convenient to perform than building a number of different PC boards and measuring all the different possible configurations. The test time costs to build a good series of cases would be extremely expensive, and the uncertainties associated with typical EMI testing could confuse the issue.

Once the general model is validated, the possible combinations of different cases are endless. Additional information present from the simulations (such as RF current distribution across a ground plane) provide the ability to better analyze the causes of the RF emissions. Once the causes are truly understood, then the appropriate design countermeasures can be implemented much more efficiently and accurately.

References

[1] "New Techniques for Reducing Printed Circuit Board Common-Mode Radiation," Robert W. Dockey and Robert F. German, 1993 IEEE International EMC Symposium, pp 334-339.

Pre-construction Evaluation Modeling of Open Area Test Sites (OATS)

Bruce Archambeault
SETH Corporation

Introduction

The construction of Open Area Test Sites (OATS) for commercial EMI testing for FCC and CE radiated emission requirements is at an all-time high. The demand for test facilities to meet the amount of testing required for computer, consumer, medical, and other products has forced many test laboratories to turn away business due to a lack of test capacity. Semi-anechoic rooms are sometimes used to perform radiated emissions testing, but these sites are very expensive and usually limited to large companies doing internal product testing. Therefore the construction of OATS facilities is rising to try and fulfill the test capacity demand.

The preferred location for an OATS is close to the product development areas, and yet in a wide open, RF quiet environment. These requirements are usually in conflict with each other, since a geographical location with a high concentration of product development activity tends to be located in close proximity to a highly developed area. Land prices are high, and the ability to have large open spaces around the OATS requires often excessive property purchases. As new OATS facilities are planned, the use of existing land is preferred, even if the CISPR-22 [1] recommended space and ground plane sizes are impossible.

Once a desired location is identified, and the ground plane size and near-by metal structures are identified, some determination must be made to see if the proposed test site will meet the CISPR site attenuation requirements. Since it's often desirable (or necessary) to violate the CISPR ground plane and open space recommendations, some way to give a high degree of confidence the OATS will be acceptable without extra expense after construction is needed. This paper discusses some OATS analysis using numerical modeling techniques (in this case, the Method of Moments). Comparison between various ground plane sizes and shapes, and near-by metal objects, are made to a perfect site.

The Perfect OATS

The definition of a perfect OATS would include an infinite ground plane with no other metal structures (fences, posts, power lines, etc.). Of course, it is impossible to achieve such a perfect OATS in real-life, but a perfect OATS can be simulated using numerical modeling techniques. For this work, both the Method of Moments (MoM) and the Finite-Difference Time-Domain techniques were used. A small dipole antenna was created (the length of the antenna was very short compared to the frequencies of interest, 30 MHz to 1GHz), and the receive location was scanned from a height of 1 to 4 meters, at a distance of 10 meters from the transmit antenna.

The case of a perfect (infinite) ground plane was first compared to the case of no ground plane for horizontal polarization. The deviation between perfect and no ground plane for the MoM case is shown in Figure 1. The comparison was repeated using FDTD with cell sizes of 100 millimeters (which should give reasonable results to 300 - 500 MHz). The FDTD comparison results are shown in Figure 2. In both cases, the distance between transmit and receive antennas was 10 meters, and the receive antenna was scanned over one to four meters for the maximum. As can be seen by comparing Figures 1 and 2, the two modeling techniques agreed to within one dB over the frequency range of 30 MHz to about 800 MHz.

Figure 1

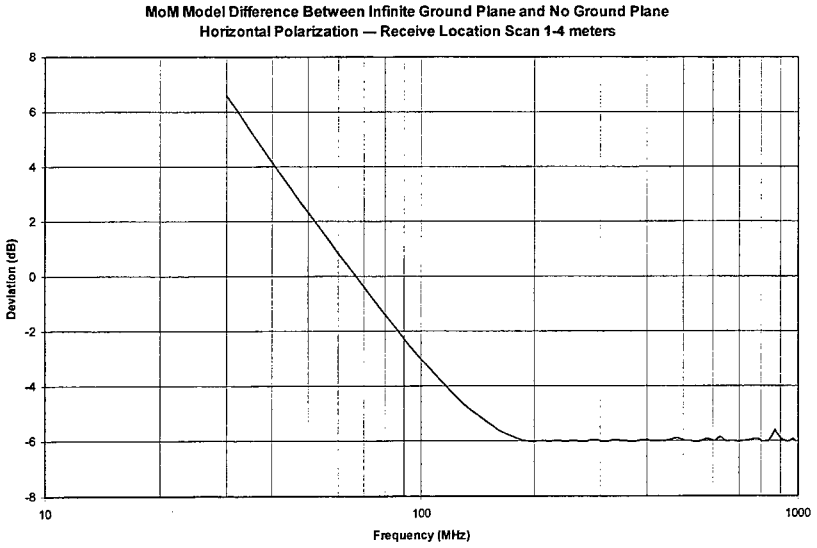

Figure 2

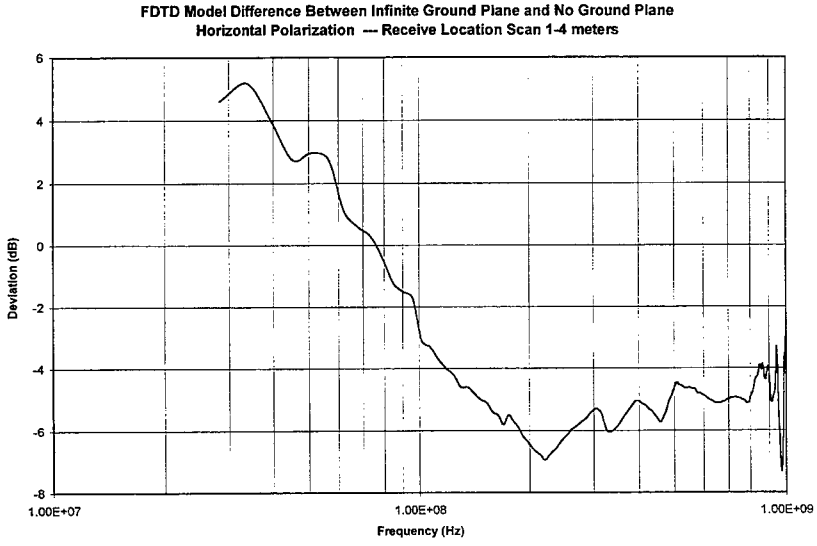

The perfect, infinite ground plane case became the normalized case. That is, all further results are shown as a deviation from this perfect OATS case. Although most of the results are shown

for the horizontal polarization, the vertical polarization can be analyzed just as easily (and is used for the near-by metal conductor examples).

MoM Ground Plane Mesh

The size of the CISPR recommended ground plane for a 10 meter site is 20 meters long by 17.3 meters wide. If the entire ground plane is to be enclosed in a weather proof enclosure, the size of the enclosure will be large, and therefore expensive. Space limitations will also sometimes require smaller ground planes.

Typically, an opening size of about $1/10^{th}$ wavelength (at the highest frequency) is used in wire mesh applications. In this case, at 1 GHz, the wavelength is .333 meters, resulting in a recommended mesh size of .033 meters. Such a mesh size over the full ground plane would result in approximately 650,000 wire segments; clearly too much for a typical MoM model to complete in a reasonable amount of time, even on a fast workstation. Therefore the initial analysis was performed with much larger mesh sizes, and the size reduced until the results converged reasonably well with the perfect OATS case. The final selected size was ½ meter meshes. This size is slightly larger than 10 times the typical MoM rule-of-thumb, but it was expected that any negative effects would only exist at high frequencies (and be obvious). Figure 3 shows the deviation between the perfect ground plane and various wire mesh ground planes. The mesh #6 case (1/2 meter) shows results easily within the +/- 4 dB allowed by the normalized site attenuation requirements.

Figure 3

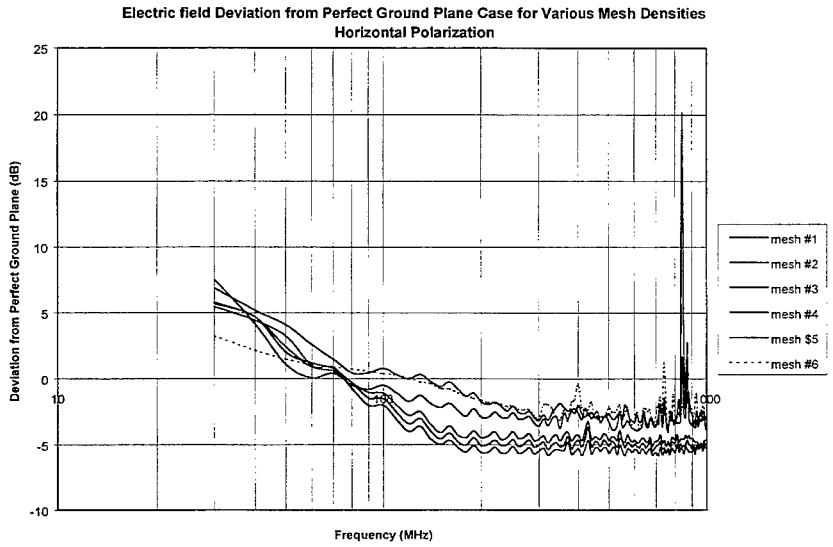

FDTD Modeling of Ground Plane Size

Although either MoM or FDTD could be used to model the reduced ground plane sizes, FDTD was considered more convenient to use. The deviation from a perfect ground plane for both the horizontal and vertical cases are shown in Figures 4 and 5 respectively.

Figure 4 FDTD Model with Various Ground Plane Sizes

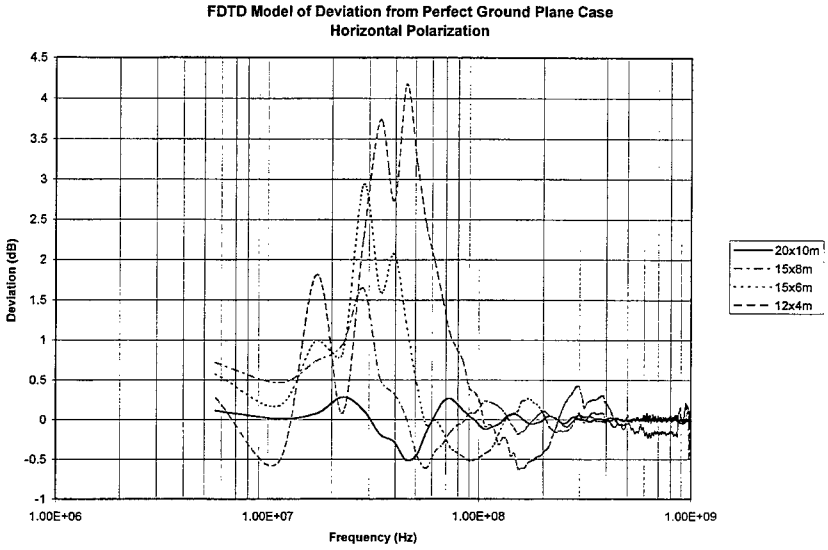

Near-by Conductors

The presence on metal conductors in the near-by vicinity of an OATS is sometimes a fact of life that is unavoidable. For example, a number of cases could be used to determine the effect of allowing a metal fence either alongside the OATS or behind the receive antenna at various distances. An example is shown here of a simulation of a metal light/utility post at two different distances from the EUT side of the OATS ground plane. As shown in Figure 6, the effects of the different set-back distances for the posts are clear.

Surrounding Walls

Since it is often desirable to put a weather-proof structure around an OATS to allow year-round use, the question of how much conductivity can be allowed in the walls often arises. The FDTD method is particularly useful for materials with limited conductivity or even a relative dielectric constant of other than one. Figure 7 shows the results of using FDTD to model an OATS with external walls that were partially conductive. As can be seen from this figure, the walls had a definite effect at lower frequencies.

Figure 5

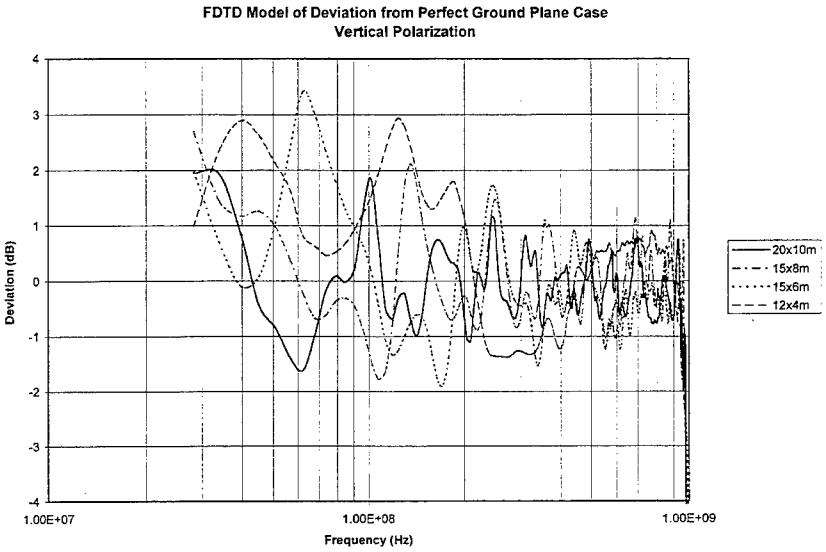

Figure 6

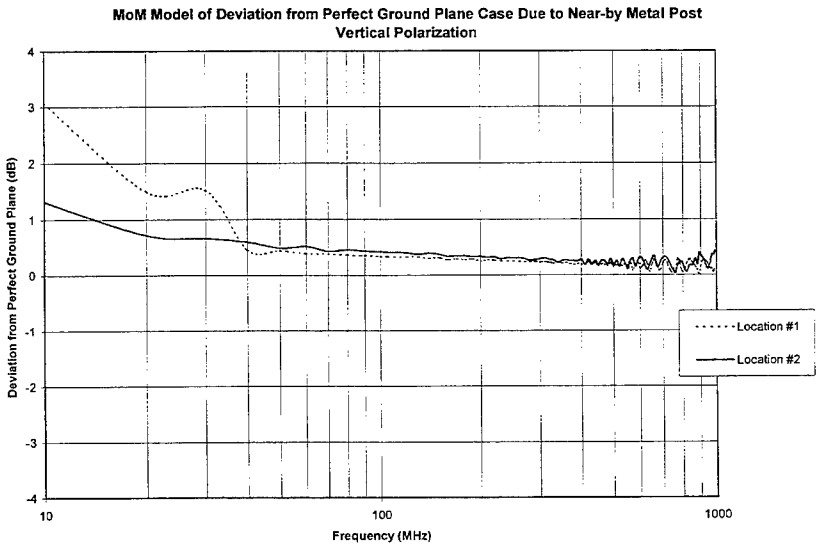

Figure 7

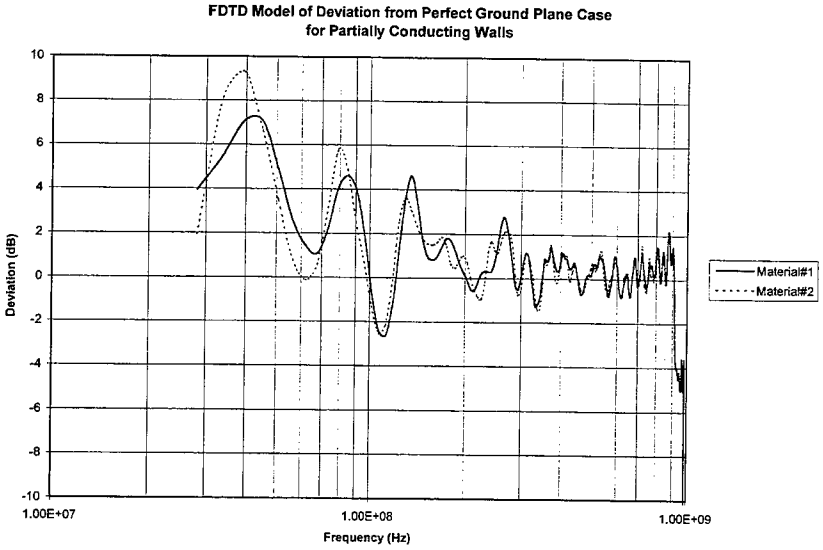

Summary

The design of OATS facilities sometimes require a deviation from the recommended ground plane sizes or near-by conductor spacing. Since such deviations can result in serious cost penalties if the OATS can not pass the normalized site attenuation certification tests after construction, normal practice is to avoid any deviation even though it will result in extra cost to the facility during construction.

However, numerical modeling techniques have been shown to be able to help analyze these non-standard OATS designs and provide engineers with a risk assessment in terms of expected normalized site attenuation error vs cost of design options. The various design parameters which can be analyzed include ground plane size, ground plane shape, and distance to near-by conductors, such as fences, metal poles, etc.

Both FDTD and MoM have been shown to be useful, depending upon the type of problem. MoM requires a wire frame mesh (or a surface patch plane) which must be fine enough to be useful at high frequencies. MoM is particularly useful for problems involving long wires, poles, etc. FDTD requires a fine grid, again for high frequency accuracy, and it is especially useful for problems involving partially conducting walls, intervening dielectrics, etc. Although the analysis shown here was limited in frequency to about 500 - 800 MHz, this could be easily extended by finer wire grids and cell sizes. Since practical OATS calibration has shown most of the problems due to site construction to be apparent at low frequencies rather than high frequencies, finer mesh models may not be necessary.

[1] CISPR-22 (1993) Limits and Methods of Measurement of Radio Disturbance Characteristics of Information Technology Equipment, IEC

Reducing EMI through shielding enclosure perforations employing lossy materials: FDTD modeling and experiments

M. Li, S. Radu, J. Nuebel*
J. L. Drewniak, T. H. Hubing, T. P. VanDoren
Electromagnetic Compatibility Laboratory
Department of Electrical Engineering
University of Missouri at Rolla
Rolla, MO 65409

* Sun Microsystems, Inc.
2550 Garcia Avenue
Mountain View, CA 94043-1100

Abstract

A lossy material is employed to reduce EMI from slots and apertures that results when interior sources couple to perforations in the shielding enclosure of a Sun S-1000 server. A specially designed rectangular enclosure with a slot is also studied experimentally and with finite-difference time-domain (FDTD) simulations. The results for both the S-1000 and the simple rectangular enclosure indicate that a lossy material can be effective in reducing the Qs of cavity mode resonances and resonances introduced by the slot, therefore reducing the radiation through the slots and apertures.

1 Introduction

The integrity of shielding enclosures is compromised by slots and apertures for heat dissipation, CD-ROMs, I/O cable penetration, and plate-covered unused connector ports, among other possibilities. Radiation from slots and apertures in conducting enclosures excited by interior sources is of great concern in meeting FCC radiated EMI limits. The radiation from enclosures through apertures has previously been studied numerically [1], though reported design approaches for reducing the radiation are limited.

Results presented in this paper indicate that numerical modeling of enclosure designs can aid in developing enclosure guidelines. The application of a lossy material in a simple rectangular enclosure fed with a wire probe was investigated. With appropriate modeling of the essential features such as the source, load, and loss, the FDTD simulated results of the delivered power agreed with the measurements. The simulated and measured results for the simple rectangular cavity show that the employment of a lossy material can reduce the Qs of the cavity mode resonances and resonances due to the slot. Two-port S-parameter measurements of the simple rectangular enclosure showed a lossy material bonded to one of the enclosure walls was effective in reducing EMI.

An S-1000 server was also investigated. Radiated EMI measurements on a functioning S-1000 showed that the lossy material could be effective in reducing EMI. However, the location of the lossy material and the EMI noise source at the PCB level is important to this effect. The potential for reducing EMI by putting lossy material on the enclosure walls is demonstrated herein through FDTD simulations and experiments. However, further work is necessary both in identifying and modeling the EMI noise source at the PCB to minimize cost in a practical design.

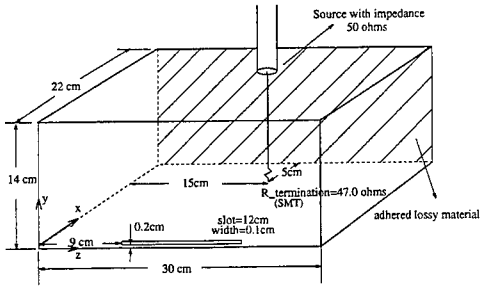

Figure 1: The geometry of the specially designed rectangular enclosure.

2 FDTD and Experimental Results

A rectangular enclosure with a thin slot near an edge was designed to study EMI through slots. The geometry of the experimental conducting enclosure is shown in Figure 1. The cavity was fed with a 50 Ω coaxial cable probe through a type-N bulkhead connector, which was peripherally bonded to the cavity. The center conductor of the probe was extended to span the width of the cavity with a 0.16 cm diameter wire, and terminated on the opposite cavity wall with a 1206 package size surface-mount (SMT) 47 Ω resistor stood on end and soldered to a $1.5'' \times 1.5''$ square of conductive adhesive copper tape. The feed probe was located at $x = 17$ cm, $y = 14$ cm, and $z = 15$ cm.

The cavity was constructed of 5 pieces of 0.635 cm thick aluminum, and one plate of 0.05 cm thick aluminum for the face containing the slot. A slot of width $w_s = 0.1$ cm ($\frac{w_s}{\delta y} = 0.2$) and length of 12 cm was located 0.25 $cm = \frac{1}{2}\delta y$ from the center of the slot to the bottom edge, where δy is the mesh dimension along the y-axis. The inside dimensions of the enclosure were 22 $cm \times 14$ $cm \times 30$ cm. One-inch copper tape with conductive adhesive was used to electromagnetically seal the seams. Two layers of lossy dielectric material with $R_\square = 1500\Omega/\square$ and thickness $d = 0.4$ cm (conductivity $\sigma = \frac{1}{R_\square d} = 0.00167$ S/cm) were employed on the interior wall $x = 22$ cm.

Two-port S-parameters were measured in a semi-anechoic chamber, where the enclosure under test was connected to Port 1 of a Wiltron 37247A network analyzer, and a horn antenna as the receiver was connected to Port 2 of the network analyzer. The network analyzer was placed outside the semi-anechoic room to measure the reflection coefficient $|S_{11}|$, from which the real power delivered by the source normalized to the source voltage was calculated as

$$P = \frac{1}{8Z_0}(1 - |S_{11}|^2). \quad (1)$$

The transmission coefficient $|S_{21}|$, which is related to the radiated power was also measured. The antenna factor of the receiving horn was not included in the calibration procedure, and the $|S_{21}|$ results were only relative measurements of improvements with the lossy material.

A cell size of 1.0 $cm \times 0.5$ $cm \times 1.0$ cm was employed in the FDTD simulations, where finer discretization along the y direction was used in order to better model the spatial extent of the SMT load resistor. The feed probe was modeled employing a quasi-static approach that modifies the magnetic field circling the wire [2]. The feed source was modeled by a simple gap voltage source V_s with a 50-Ω source resistance incorporated into a single cell at the feed point. The magnetic fields circling the source were modeled in the same fashion as a thin wire to give the cross-section of the source specified physical dimensions [3]. A magnetic frill type source, which may be more accurate in modeling the connector, was also investigated, but yielded little improvement over the wide gap type source [9]. The resistor was modeled as a lumped element using a subcellular algorithm [4]. The width of the SMT is approximately that of the feed probe diameter and the physical cross-section dimensions were modeled with the same diameter as that of the feed probe by modifying the magnetic field components circling the SMT in the same fashion as for the source. The slot was modeled with a capacitive thin-slot subcellular algorithm to avoid a small mesh dimension [5], and perfectly-matched-layer (PML) absorbing boundary conditions were employed for the 3D simulations [6]. The lossy material was simply

modeled by a one-cell layer of conducting material with conductivity $\sigma = 0.00167\ S/cm$. For the electric field components inside the conducting layer, the conductivity $\sigma = 0.00167\ S/cm$ was employed, while the conductivity $\sigma = \frac{0.00167}{2}\ S/cm$ was employed for the components in the interface of conducting layer and free space [7].

A sinusoidally modulated Gaussian pulse was employed as the excitation. The source voltage as a function of time t was

$$V_s(t) = e^{-\alpha^2(t-t_0)^2} cos[2\pi f_0(t-t_0)], \qquad (2)$$

where $f_0 = \frac{f_{upper}+f_{lower}}{2}$ is the center frequency (f_{lower} is the starting frequency and f_{upper} is the stopping frequency), and α and t_0 are

$$\alpha = \frac{\pi(f_{upper} - f_{lower})}{\sqrt{-ln(b_{BW})}}, \qquad (3)$$

$$t_0 = \frac{1}{\alpha}\sqrt{-ln(b_t)}, \qquad (4)$$

where b_{BW} is the minimum pulse level which is unaffected by computational noise, and b_t is the maximum allowable pulse level at $t = 0$. b_{BW} and b_t were set to be 0.0001 and 0.001, respectively, so that the temporal pulse was greater than two orders of magnitude below the maximum at the beginning and end of the pulse. A time step of 8.3333 ps was employed. The time-history of the voltage V_0 across the source and source impedance, and the current I_0 through the source were stored, and an FFT was employed to calculate frequency-domain quantities. A total of 20,000 time steps was required for a good resolution in the frequency domain. In simulations with frequency bands containing very high Q resonances, e.g., 1.36 GHz in Figure 2 for the case without the lossy material, an additional 20,000 time steps, or 40,000 total were required in order for the stored energy to decay and minimize ringing. The computed real power delivered by the source normalized to the source voltage was calculated as

$$P_{FDTD} = \frac{1}{2|V_s|^2} Re(\hat{V}_0 \times \hat{I}_0^*). \qquad (5)$$

The measured and simulated delivered power are shown in Figure 2 for the configuration in Figure 1 with the lossy material on the interior face $x = 22\ cm$, and without the lossy material. The available power from the source was 2.5 mW. The agreement between measurements and simulations is generally good. The measured and simulated results without the lossy material agree well over the entire frequency range considered. There is a slight discrepancy at 1.24 GHz which is the slot half-wave resonance. This shift to higher frequency for the FDTD results as compared to the measured results is due to the particular thin-slot subcellular algorithm employed. The agreement is nearly exact, to within measurement and simulation error if a more sophisticated thin-slot algorithm is used [9]. Since the feed probe was along the y direction, the y-component of the electric field was excited, while the y-component of the magnetic field was suppressed, i.e., only TM_y cavity modes were excited by the feed probe. For the configuration without the lossy material, the TM_y101 cavity mode is at 0.89 GHz. Resonances at 1.36 GHz and 1.44 GHz correspond to the TM_y111 and TM_y201 modes, respectively. The resonances at 1.12 GHz and 1.24 GHz are due to the slot. Measurements indicated that the resonance at 1.53 GHz was due to the slot as well. Calculations from the FDTD simulations of the power dissipated in the load resistor showed that most of the power delivered by source was radiated through slot at this resonance. The resonances at 1.12 GHz and 1.53 GHz result from interaction of the slot with the feed probe or cavity, and tuning of the reactance [8]. Calculations from FDTD simulations of the power dissipated in the load resistor and total power showed that 28%, 60%, and 89% of the delivered power was radiated through the slot at 1.12 GHz, 1.24 GHz, and 1.53 GHz, respectively. For the configuration with the lossy material, the TM_y101 cavity mode was virtually unaffected, and the feed probe TEM mode at 1.08 GHz [9] was shifted down by 2.5%. The resonances due to the slot at 1.12 GHz and 1.24 GHz were shifted with an increase in the radiated power at 1.20 GHz. The high-Q TM_y111 cavity mode at 1.36 GHz was greatly reduced, and the Q of the TM_y201 cavity mode at 1.44 GHz was also reduced. The significant discrepancy between the FDTD and measured results with the lossy material at the resonance at 1.53 GHz may be due

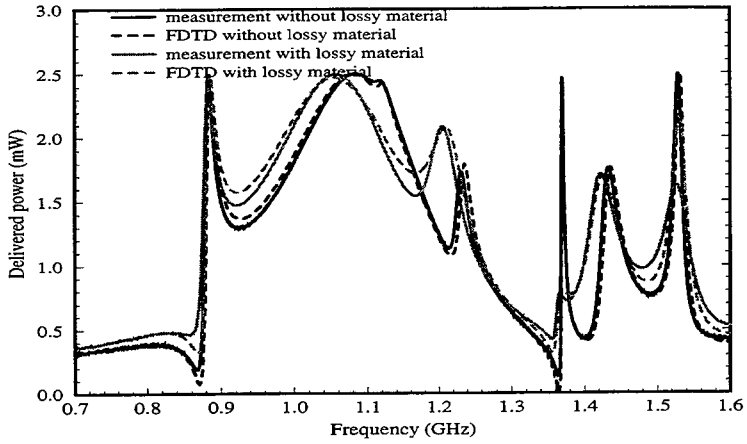

Figure 2: Measured and simulated delivered power to the specially designed rectangular enclosure with and without a lossy material.

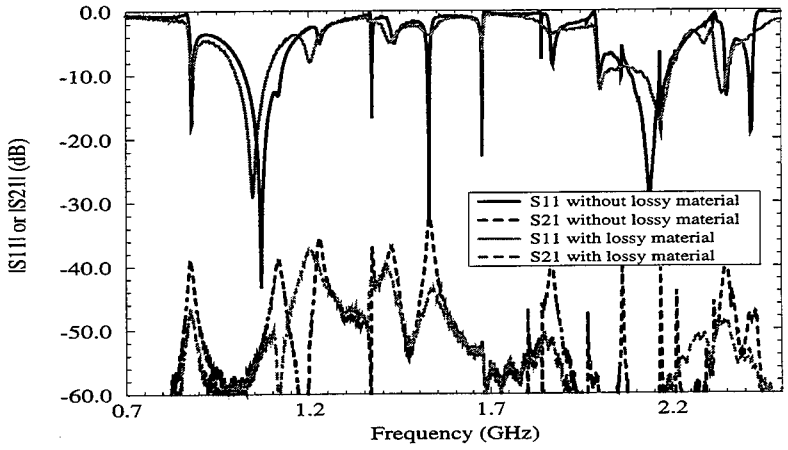

Figure 3: The two-port measured results for the simple rectangular enclosure with and without the lossy material.

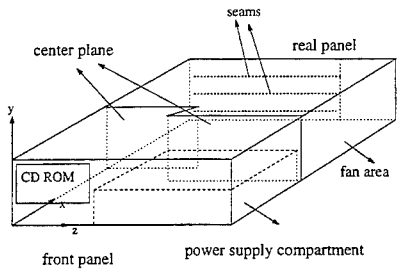

Figure 4: The geometry of the S-1000 enclosure.

to a frequency dependence in the conductivity of the lossy material.

Two-port measured results ($|S_{11}|$ and $|S_{21}|$) for the simple rectangular cavity with and without the lossy material are shown in Figure 3. The $|S_{11}|$ measurements were used for comparison with FDTD simulations in Figure 2. For the configuration without the lossy material, the radiation at the cavity modes is as significant as the radiation at the resonances due to the slot. The effect of the lossy material in decreasing the Qs of resonances is evident in the measured $|S_{11}|$, and reflected in reduced radiation in $|S_{21}|$, e.g., the TM_y101 at 0.89 GHz, the TM_y111 at 1.36 GHz, the TM_y201 at 1.44 GHz, and the resonance at 1.53 GHz. However, a resonance and a corresponding increase in radiation were measured at 1.20 GHz, where the two resonances due to the slot at 1.10 GHz and 1.24 GHz for the situation without the lossy material may have shifted and broadened to produce the resonance at 1.20 GHz.

The potential for reducing EMI through a judicious use of lossy material on enclosure walls was investigated in a functioning Sun S-1000 high-speed server design. A representation of the Sun S-1000 enclosure partitioned into front and back portions by a center plane is shown in Figure 4. One motherboard with a single CPU module was in the back portion, while a CD ROM, a controller card, and a power supply were in the front portion. Loss was introduced in the enclosure by adhering the lossy material to the interior top, bottom, and back faces, as well as the center plane. EMI from the functioning S-1000 production design was measured in a shielded room with a Tektronix 2712 Spectrum Analyzer, using a log periodical dipole array as the receiving antenna. The primary radiators for the design above 500 MHz were slots and apertures as determined from radiated measurements. The only attached cable during the measurement procedures was the power chord.

Radiated EMI measurements for a functioning S-1000 system with and without the lossy material on the previously indicated walls are shown in Figure 5. At frequencies above 500 MHz, the decrease in radiated EMI was $5 - 20$ dB for most CPU harmonics (60 MHz fundamental frequency), e.g., 5 dB at 900 MHz, 14 dB at 1320 MHz, and 20 dB at 1440 MHz, while at frequencies below 500 MHz, there was no significant effect. The radiation increased by $5dB$ at 600 MHz and 700 MHz. The position of the lossy material was also important and the employment of the lossy material on the center plane was most significant.

3 Summary and Conclusion

FDTD modeling of an interior-excited simple rectangular enclosure with a thin slot near an edge was compared with experimental results. The agreement was good for configurations with and without a lossy material on one enclosure wall. The lossy material was effective in reducing the Qs of the cavity mode resonances and resonances due to the slot, and reducing EMI through the slot. The potential of a lossy material in reducing EMI was also demonstrated in a functioning server system. However, further work is necessary in determing the optimal amount of loss in the material, the type of lossy material—dielectric or magnetic, and a method for selecting the optimum locations for loss The agreement between the simulated and measured results indicates that these issues can be explored relying on FDTD simulations, with fewer, more selective experiments for corroboration.

4 Acknowledgments

The authors gratefully acknowledge assistance from Yun Ji, and Wei Cui in portions of the measure-

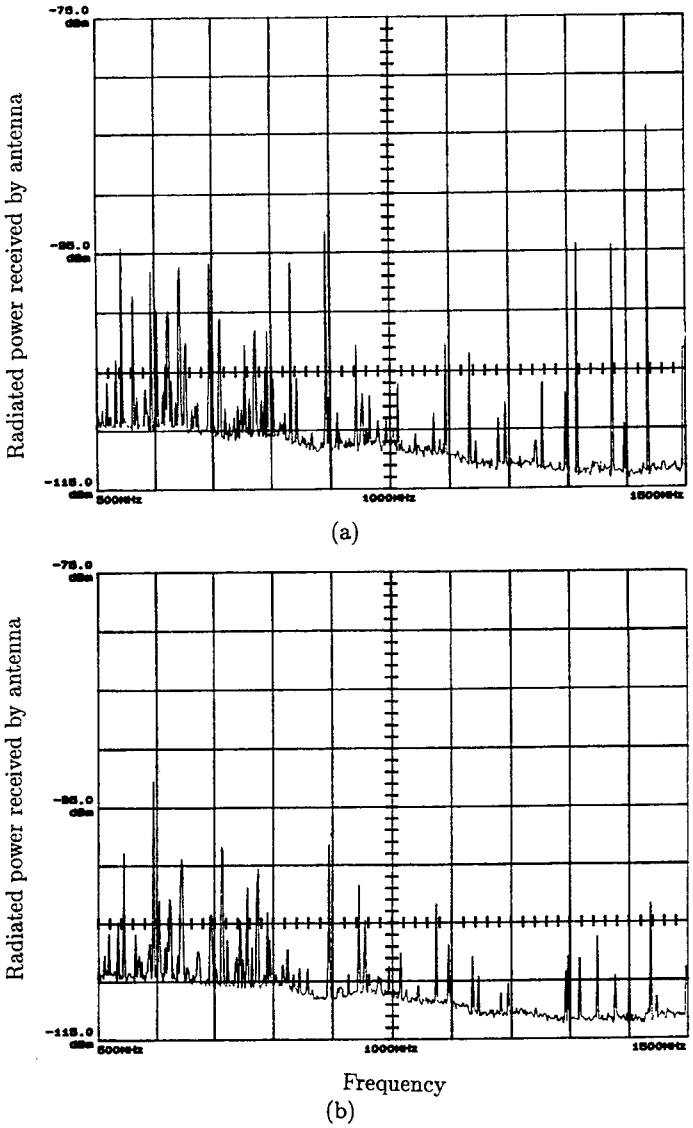

Figure 5: Radiated EMI measurements from a functioning S-1000 system (500 MHz — 1500 MHz) (a) without the lossy material, and (b) with lossy material.

ments.

References

[1] H. Moheb, L. Shafai and J. Shaker, "Numerical solution of radiation from single and multiple arbitrary apertures backed by a cavity", *IEEE Antennas and Propagat. Symposium, 1992 Digest*, vol. 1, pp. 61-64, 1992.

[2] A. Taflove, *Computational Electrodynamics.* Artech House; Boston, 1995.

[3] David M. Hockanson, James L. Drewinak, Todd H. Hubing and Thomas P. Van Doren, "FDTD modeling of common-mode radiation from cables," *IEEE Trans. Electromagn. Compat.*, vol. 38, pp. 376-387, August 1996.

[4] Yuh-Sheng Tsuei, A. C. Cangellaris and J. L. Prince, "Rigorous electromagnetic modeling of chip-to-package (first-level) interconnections," *IEEE Transactions on Components, Hybrids, and Manufacturing Technology,* vol. 16, pp.876-882, December 1993.

[5] J. Gilbert and R. Holland, "Implementation of the thin-slot formalism in the finite-difference EMP code THREDII," *IEEE Trans. Nuclear Sci.*, vol. NS-28, pp. 4269-4274, December 1981.

[6] J. P. Berenger, "Perfectly matched layer for the absorption of electromagnetic waves," *Journal of Computational Physics*, vol. 114, pp. 185-200, October 1994.

[7] D. M. Hockanson, *The Finite Difference Time Domain Method and Applications in Electromagnetic Compatibility*, M. S. Thesis, University of Missouri-Rolla, 1994.

[8] Chang-Hong Liang and D. K. Cheng, "Electromagnetic fields coupled into a cavity with a slot-aperture under resonant conditions," *IEEE Trans. Antennas Propagat.*, vol. AP-30, pp. 664-672, July 1982.

[9] M. Li, *Investigation of Electromagnetic Interference Through Slots in Shielding Enclosures: Finite-Difference Time-Domain Simulations and Experiments*, M. S. Thesis, University of Missouri-Rolla, 1996.

STATISTICAL DESCRIPTION OF CABLE CURRENT RESPONSE INSIDE A LEAKY ENCLOSURE

Richard Holland, Shield Rite, Inc., P. O. Box 8250, Albuquerque, NM 87198
(505)-343-1664 (W), (505)-842-0126 (H), (505)-344-6795 (FAX), (505)-238-4405 (M)

Richard St. John, Mission Research Corp., 1720 Randolph Rd., Albuquerque, NM 87106
(505)-768-7655 (W), (505)-293-2925 (H), (505)-768-7601 (FAX), rstjohn@mrcabq.com

ABSTRACT

A description is given of the statistics of EM fields and power fluxes inside a highly overmoded cavity which is driven through multiple small leaks. We have explored various combinations of chi square (with two and six degrees of freedom), normal, and log normal distributions. Convolution (in an unusual, logarithmic sense) of the two chi square models (with two and six degrees of freedom), to form the so-called Lehman distribution, has been demonstrated to provide the best match with observed power flux. Statistically generated field models based on this power-flux distribution are used as drivers of cable codes describing the wiring in a waveguide cavity resonator and in a Global Positioning Satellite (GPS) bus. Modeled and driven cable current cumulative distributions match within a factor of two, which is commensurate with the configuration and measurement uncertainty. We have empirically determined that the statistical distribution of the current squared on a cable or cable bundle inside an overmoded enclosure depends only on the separation of the cable from a ground plane in wavelengths, the mean power-flux density inside the enclosure, and very weakly on the cable radius. If the observer is within two wavelengths of the cable end, a dependence also exists on the cable termination.

THE LEHMAN DISTRIBUTION OF POWER FLUX

Within the past two years a new power-flux distribution model due to Lehman has been clearly demonstrated to match experimental results far better than any combination of conventional models such as normal, log normal, or chi square with two degrees of freedom.[1-4] This new model even shows excellent agreement between theory and observation on the upper tail of the distribution, which is where system-impairing effects will occur if they occur at all. While we are not sure just why this novel procedure should yield power-flux distributions which agree with the upper tail (as opposed to the midpoint, where most models seem to fit best, or, for that matter, as opposed to the lower tail), we remain most enthusiastic.

If an overmoded, high-Q enclosure is illuminated by an internal source, it is widely accepted that the internal power-flux distribution incident on a dipole antenna will be chi square with two degrees of freedom.[5-7] The Lehman model assumes that the power-flux density inside a leaky, externally illuminated enclosure should retain the physics leading to a power-flux distribution variate z_1, which is chi square with two degrees of freedom. However, a hypothesis is additionally put forward that, for an externally illuminated cavity, driving fields can come from

any of three directions, with either of two polarizations, and thus should result in inward aperture-drive power-leakage variate z_2 which is chi square with six degrees of freedom.[1] These assumptions imply the overall internal cavity response should have a power-flux distribution density which is the product of these two variates

$$z = z_1 z_2 \tag{1}$$

In terms of two variates, the power-flux distribution density projected on a dipole antenna axis thus becomes representable as

$$f_{\chi_2^2}(z_1) f_{\chi_6^2}(z_2)\, dz_1\, dz_2 \tag{2}$$

where this expression gives the probability that z_1 is between z_1 and $z_1 + dz_1$, while z_2 is between z_2 and $z_2 + dz_2$. However, z, z_1, and z_2 are not all independent variates. If (1) holds, the probability that z_1 is between z_1 and $z_1 + dz_1$, while z is between z and $z + dz$ is obtained from the variate transformation

$$\begin{aligned} z_1 &= z_1' \\ z_2 &= z'/z_1' \end{aligned} \tag{3}$$

The two-dimensional distribution density then becomes

$$f_{\chi_2^2}(z_1') f_{\chi_6^2}(z'/z_1') \frac{\partial(z_1, z_2)}{\partial(z_1', z')}\, dz_1'\, dz' \tag{4}$$

where

$$\frac{\partial(z_1, z_2)}{\partial(z_1', z')} = \begin{vmatrix} \partial z_1/\partial z_1' & \partial z_2/\partial z_1' \\ \partial z_1/\partial z' & \partial z_2/\partial z' \end{vmatrix} = \begin{vmatrix} 1 & -1/z_1'^2 \\ 0 & 1/z_1' \end{vmatrix} = 1/z_1' \tag{5}$$

is the Jacobian of the variate transformation. We now wish to find the probability that z is

---

[1] The energy density inside a chamber is the sum of the two phase-quadrature components squared and resummed over the three physical axes; i.e., it is the sum of six squares, and thus will have distribution characterizable as chi square with six degrees of freedom. It may seem that this energy distribution density is the origin of the χ_6^2 attribute of z in (1) (as opposed to its origin being a consequence of aperture physics). This viewpoint is demonstrably incorrect, however, as the power-flux density distribution for internal illumination z_1 also stems from an energy density distribution which is the sum of the same six squares. Yet z_1 has no χ_6^2 constituent.

between z and $z + dz$ regardless of z_1'. This 1D probability differential is obtained by summing all the 2D probability differentials of z_1' and z' over z_1' ; i.e., by integrating (4) over all possible z_1' [8]

$$f(z')dz' = \int_0^\infty f_{\chi_2^2}(z_1')\, f_{\chi_6^2}(z'/z_1')\, \frac{dz_1'\, dz'}{z_1'} = \int_0^\infty [\lambda e^{-\lambda z_1'}]\,[\gamma^3 (z'/z_1')^2\, e^{-\gamma z'/z_1'}]\, d(\ln z_1')\, dz' \quad (6)$$
$$= \Lambda_p^2\, z'\, K_2(2\sqrt{\Lambda_p z'})\, dz'$$

Here, λ, γ, and Λ_p are constants related by

$$\Lambda_p = \gamma\lambda \quad (7)$$

with Λ_p related to the mean power-flux density by

$$\Lambda_p = 3/\text{mean}[z] = 3/\mu_p \quad (8)$$

The top line of (6) is what we referred to in our abstract as a logarithmic convolution. Note that the power-dependent scale factors γ and λ are never explicitly required or evaluated.[2,4]

The cumulative distribution function associated with the Lehman distribution density is

$$\Phi(Z') = 1 - (\Lambda_p Z')^{3/2} K_3(\sqrt{\Lambda_p Z'}) \quad (9)$$

In these equations, K_2 and K_3 are the second- and third-order modified Bessel functions of the second kind.

The mean and standard deviation of the Lehman distribution are

$$\mu_p(\Lambda_p) = \frac{3}{\Lambda_p} \qquad \sigma_p(\Lambda_p) = \frac{\sqrt{15}}{\Lambda_p} \quad (10)$$

For a given external illumination, these relationships give us two formulas for determining the Lehman parameter Λ_p from simply measuring the μ_p or σ_p of a dipole antenna response inside the enclosure. In the past, we have published comparisons showing nice cumulative probability distribution agreements between the Lehman distribution, EMPTAC airframe data, and Celestron 8 satellite telescope data.[1]

It has been observed that the Lehman model somehow manages to accommodate otherwise troubling "trends" on power-flux data, and to give a correct upper-tail representation irrespective of the gross overall shape (including the trend) of the response distribution density. This

accomplishment is a major keystone in the successful representation of cable-driving fields; previously, we had no real idea how to insert "trend" effects into the model (other than using a log normal representation, which will fit anything to anything, but at the price of incorporating some very unacceptable upper tail characteristics).[9-11] The Lehman model thus provides something else that other models do not: a smooth, data-derived representation for the upper end of the distribution which does not require case-by-case tweaking.

The evaluation of the phase-quadrature field component distribution density associated with the Lehman power-flux distribution had, until recently, proved a major hurdle to us.[1] This difficulty is now resolved. Specifically, the quadrature-component field density distribution $l(u)$ corresponding to the Lehman distribution for power-flux density has been shown to be approximated by [4]

$$l(u,\Lambda_p) = \sqrt{\frac{\Lambda_p}{2\pi}} e^{-2\Lambda_p u^2} + u^2 \Lambda_p^{3/2} e^{-2\sqrt{\Lambda_p}|u|} \qquad -\infty < u < \infty \tag{11}$$

and the associated cumulative probability distribution has been shown to be approximated by

$$L(U,\Lambda_p) =$$

$$\frac{1}{2}\left\{\left[\frac{1}{2} + \frac{1}{\sqrt{\pi}} \int_0^{U\sqrt{2\Lambda_p}} e^{-u^2} du\right] + \left[\frac{1}{2} + \frac{U}{2|U|}\left(1 - e^{-\sqrt{\Lambda_p}|U|} \sum_{k=0}^{2} \frac{\left(2\sqrt{\Lambda_p}|U|\right)^k}{k!}\right)\right]\right\} \tag{12}$$

The deduction of the phase-quadrature field distribution associated with the Lehman power-flux distribution is an important accomplishment because it is necessary to have the phase-quadrature field distribution density to model the fields which actually couple to and drive the enclosure cabling. An attempt to obtain a canonical formula for the phase-quadrature field distribution density associated with the Lehman power-flux distribution density led to a jungle of modified Bessel and Whittaker [8,12] functions for the cable field drivers. Even approximations (11) and (12), obtained after all reasonable compromises have been made, are themselves far from simple or easy use.

COMPARISON WITH EXPERIMENT

Figure 1 illustrates some results we have obtained from an experimental setup involving external illumination of a leaky, resonant-waveguide chamber which we constructed to test Lehman statistics. This figure overlays the cumulative distribution of four typical measured, enclosure-contained cable currents with predictions obtained by driving a model of the enclosure cables with fields statistically distributed according to (12). The four computer-modeled cumulative distributions differ in generation only by altering the average of the power flux and by rerunning the random-number generator input to (12).

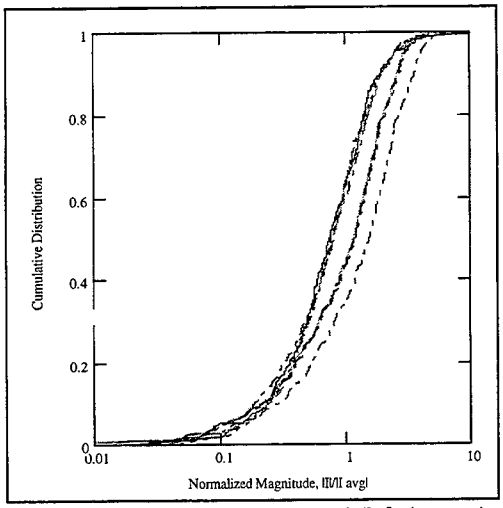

Figure 1. Comparison of measured (left 4 traces) and predicted (right 4 traces) cable currents in an externally illuminated, leaky waveguide enclosure.

It may be seen that the experimental and computed cable currents converge at the upper tail where a good model is of paramount importance. At no point do they differ by more than a factor of two. We note that, for these four tests, the model deviation always predicts greater-than-measured currents. In some other tests involving GPS cable bundle currents (discussed below), the deviation is in the other direction.

In our experimental work, frequency was swept from 0.3 to 3.0 GHz to obtain an experimental scatter. (This is a form of electronic mode-stirring.) The same scatter should be obtainable by either mechanical mode stirring or moving the probe.

Figures 2 and 3 show two cumulative probability distributions for the square of the measured E-field (power flux) projected on a dipole antenna, as compared to the cumulative probability distribution based on Lehman statistics. The agreement may be seen to be excellent. Corresponding current comparisons appear in Figures 4 and 5. Agreement here is not significantly different (factor of two) from that appearing in Figure 1. Figures 6-9 show corresponding comparisons for the cumulative power flux distribution and cumulative cable-bundle current distributions inside the GPS bus. Note that the cable bundle current in Figure 8 is underpredicted. (Figure 10 shows our test setup for illuminating the GPS bus.) The currents in Figures 7 and 8 are an order of magnitude less than those in Figures 4 and 5, even though the associated fields (Figures 2, 3, 6, 7) are similar because the cables carrying the currents of Figures 8 and 9 are much closer to the enclosure walls.

A CLOSING REMARK

Obviously, a simply shielded leaky enclosure is not the most complex topology which could be of concern. For example, we could have a leaky box nested inside the GPS satellite bus.

Using the above reasoning, for nested leaky chambers, the fields driving the apertures of the inner chamber should have a Lehman-distributed power flux driving their χ_6^2 physical attribute, and the inner chamber itself should have its own χ_2^2 property. This implies that, after working our way down through the topologies, we find the power-flux density distribution in the inner chamber to be the product of four variates,

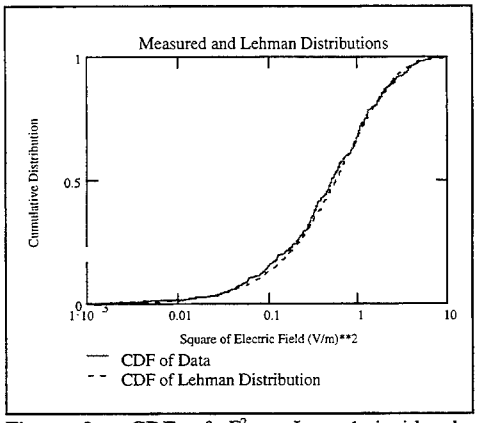

Figure 2. CDF of E^2 at Loc. 1 inside the waveguide chamber. Based on measured Λ_p = 2.986. (f9)

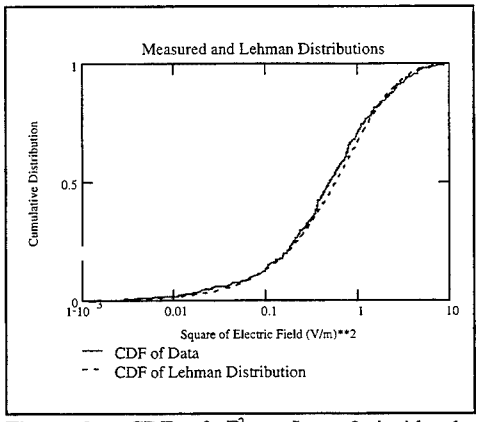

Figure 3. CDF of E^2 at Loc. 2 inside the waveguide chamber. Based on measured Λ_p = 2.954. (f10)

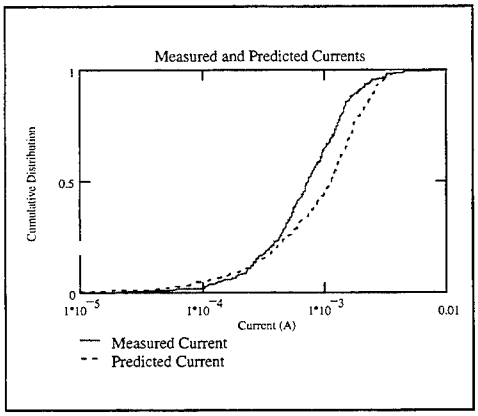

Figure 4. CDF of ABS(I) at Loc. 1 inside the waveguide chamber. Based on Lehman E-field distribution of Fig. 2. (f1 and f2)

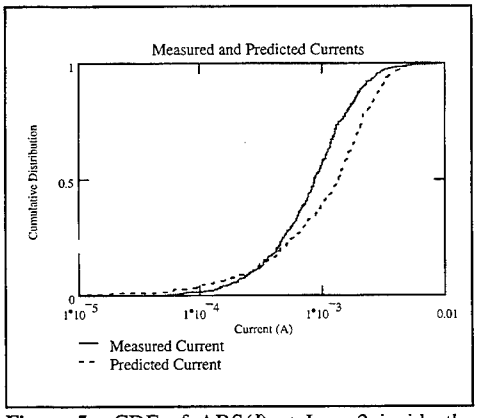

Figure 5. CDF of ABS(I) at Loc. 2 inside the waveguide chamber. Based on Lehman E-field distribution of Fig. 3. (f3 and f4)

$$z = z_1 z_2 z_3 z_4 \qquad \textbf{(13)}$$

where z_1 and z_3 are χ^2 with two degrees of freedom, while z_2 and z_4 are χ^2 with six degrees of freedom. This expression may be reorganized by seeing that the product of the z_1 and z_2 variates, z_{12}, is a variate with a Lehman distribution, as is the product of the z_3 and z_4 variates, z_{34}

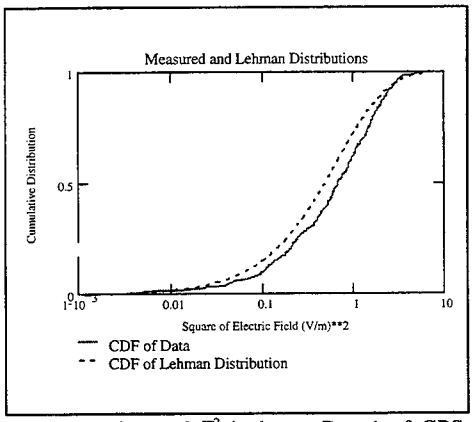

Figure 6. CDF of E^2 in lower Bay 1 of GPS. Based on measured $\Lambda_p = 3.486$. (f5)

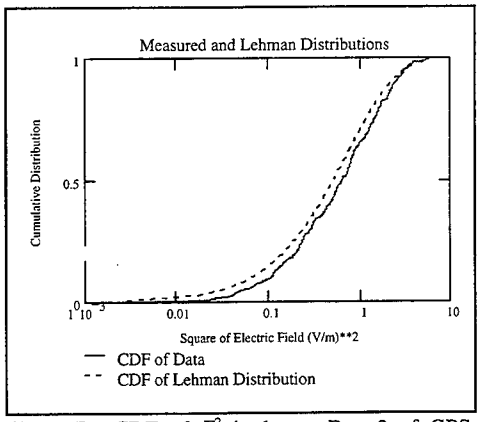

Figure 7. CDF of E^2 in lower Bay 2 of GPS. Based on measured $\Lambda_p = 3.344$. (f6)

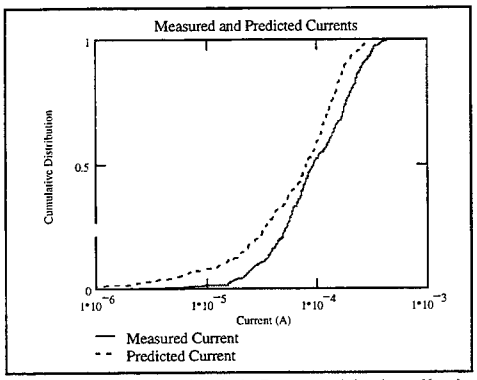

Figure 8. CDF of ABS(I) on cable bundle in lower Bay 1 inside the GPS. Based on Lehman E-field distribution of Fig. 6. (f7 and f8)

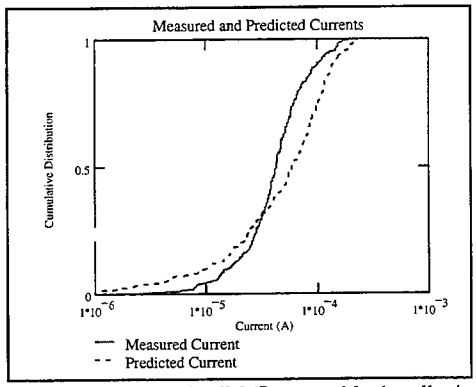

Figure 9. CDF of ABS(I) on cable bundle in lower Bay 2 inside the GPS. Based on Lehman E-field distribution of Fig. 7. (f11 and f12)

$$z = z_{12} z_{34} \tag{14}$$

The overall distribution density of the power flux in the inner chamber may thus be obtained in analogy with (6) as the logarithmic convolution of the inner and outer Lehman distributions:

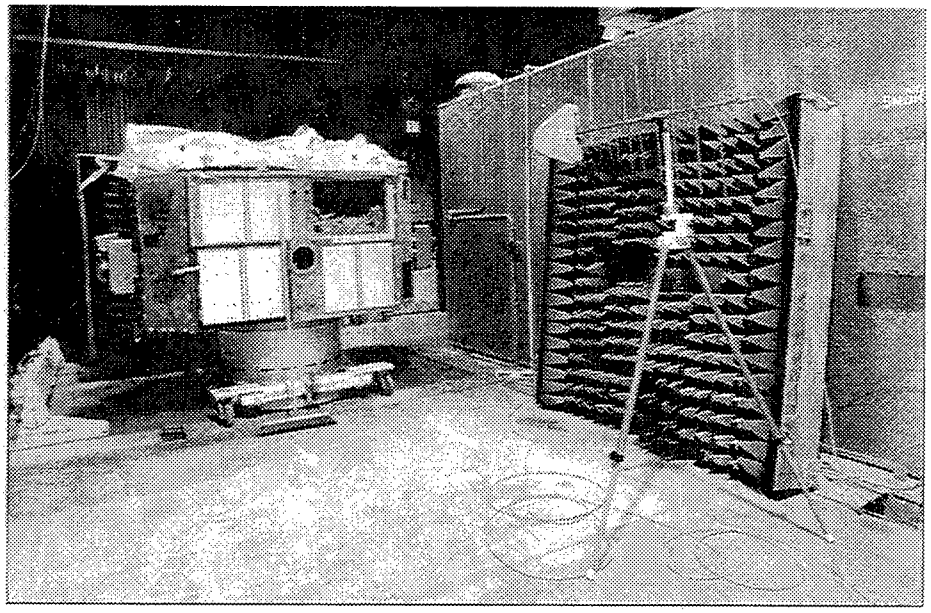

Figure 10. GPS bus (less antennas and solar panels) illuminated by log-periodic antenna (right). Note dust mop (in front of bus) to give size perception.

$$f_{\text{inner}}(z)\,dz = \int_0^\infty f_{l_{12}}(z'_{12}, \Lambda_{12}) f_{l_{34}}(z/z'_{12}, \Lambda_{34})\; d(\ln z'_{12})\,dz$$

$$= \int_0^\infty [\Lambda_{12}^2 z'_{12} K_2(2\sqrt{\Lambda_{12} z'_{12}})]\,[\Lambda_{34}^2 (z/z'_{12}) K_2(2\sqrt{\Lambda_{12} z/z'_{12}})]\,\frac{dz'_{12}\,dz}{z'_{12}} \qquad (15)$$

Work is currently in progress to study the implications of (15).

REFERENCES

[1] R. Holland and R. St. John, "Statistical coupling of EM fields to cables in an overmoded cavity," *Conference Proceedings*, Vol. 2, pp. 877-887, 12th Annual Review of Progress in Applied Computational Electromagnetics, Monterey, CA, 18-22 March 1996.

[2] T. H. Lehman and R. M. Marshall, "Application of statistical physics to derivation of stress and strength distributions," Ball Systems Engineering Division, Albuquerque, NM, September 26, 1991.

[3] T. H. Lehman, "A statistical theory of electromagnetic fields in complex cavities," Air Force Phillips Laboratory, Interaction Note 494, May 1993.

[4] R. St. John, "Approximate field-component statistics of the Lehman overmoded-cavity distribution," submitted to *IEEE Trans. Electromagn. Compat.*

[5] R. H. Price, H. T. Davis, and E. P. Wenaas, "Determination of the statistical distribution of electromagnetic-field amplitudes in complex cavities," *Phys. Rev. E*, Vol. 48, December 1993, pp. 4716-4729.

[6] R. H. Price, *et al.*, "Determination of the statistical distribution of electromagnetic field amplitudes in complex cavities," JAYCOR Rep. 88JAL129, June 1, 1988.

[7] R. Holland, "Statistical distribution of electromagnetic fields in complex cavities: penetration of the JAYCOR mystique," Shield Rite Rep., 13 February 1996.

[8] I. S. Gradshteyn and I. M. Ryzhik, *Tables of Integrals, Series, and Products*. New York: Academic Press, 1965, p. 307, Eq. 3.324.1 and p. 720, Eq. 6.643.3.

[9] R. Holland and R. St. John, "Statistical responses of enclosed systems to HPM environments," *Conference Proceedings*, Vol. 2, pp. 554-568, 10th Annual Review of Progress in Applied Computational Electromagnetics, Monterey, CA, 21-26 March 1994.

[10] R. Holland and R. St. John, "Statistical response of enclosed systems to HPM environments," PL-TR-94-1006, Air Force Phillips Laboratory, Kirtland Air Force Base, NM, 1994.

[11] R. Holland and R. St. John, "Statistical HPM satellite survivability modeling," PL-TR-96-2069, Air Force Phillips Laboratory, Kirtland Air Force Base, NM, December 1996.

[12] L. J. Slater, "Confluent hypergeometric functions," pp. 503-534, see especially Sec. 13.1, "Definitions of Kummer and Whittaker functions," pp. 504-505, Eqs. 13.1.1 to 13.1.34, in *Handbook of Mathematical Functions and Tables*, M. Abramowitz and I. Stegun, editors, National Bureau of Standards, Applied Mathematics Series, No. 55, Washington DC, June 1964.

Coupling into non-rectangular cavities: simulation and experiments

J. v. Hagen* D. Lecointe** J.-L. Lasserre+ J.-L. Lavergne+ W. Tabbara*

*Division Ondes, Laboratoire des Signaux et Systèmes/CNRS
**Service d'Electromagnétisme
*,**Supélec, Plateau de Moulon, F - 91192 Gif-sur-Yvette
+CEG, F - 46500 Gramat, France

1 Introduction

Coupling of electromagnetic energy into cavities through one or more holes in its walls is one major problem in the domain of electromagnetic compatibility. Investigations were conducted in this field by using both numerical simulations and experimentations. The numerical simulations in literature were based on several approaches, namely integral equations, the finite difference - time domain, and recently finite elements. We choose the Method of moments to solve the electric field integral equation using the Green's functions of the cavity. This approach allows us to make further investigations of the influence of different parts of the structure as aperture, objects, and the reaction of cavity and objects onto the aperture. This is not completely possible with commercially available codes based on finite elements or finite difference. Previous results in our field were the computation and the measurement of the coupling to wires in cavities, we now also consider three-dimensional metallic objects.

A typical cavity is shown in fig. 1. It is a rectangular cavity with an aperture centred in one wall. There is a plane wave attacking the structure from the front, interacting with the interior of the cavity. This is a monopole antenna attached to a network analyser to measure the current at the base of the antenna and, in the case shown, a large metallic plate hanging from the top of the cavity. Measurements of this configuration are shown further down.

The structure of this papers is as follows: first, we will describe the method used. We will focus especially on questions to reduce the computational effort, the choice of possible basis and testing functions, and we will shortly describe how to generate broad band data form only a few computations. Included are graphs of simulations. In the third part, we will show a comparison of computations and measurements. A short conclusion is at the end.

2 Method

Using the Green's function of the cavity, the electric field integral equation is solved by the means of a Method of Moments. The fact that we use the Green's functions of the cavity is reducing the number of unknowns needed in the Method of Moments considerably as only scatterers inside

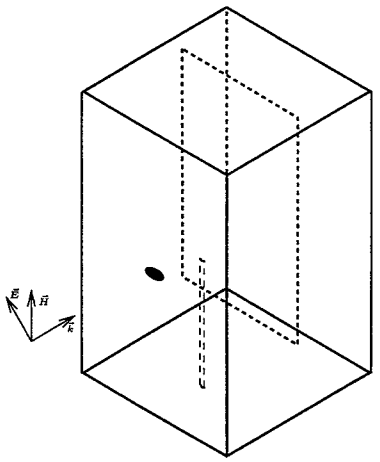

Figure 1: Typical cavity with monopole antenna and large plate

the cavity have to be discretized, the boundary conditions on the walls being already taken into account. It is though of no restriction to generality, as the shape of the initially rectangular cavity can be modified by including additional walls as scatterers. The method can be described in several steps: first to separate the exterior and the interior. Then to discretize the scatterers in the cavity with the appropriate set of functions, and finally to solve the linear equation. As in our case the matrices are only small (typically 200 × 200 lines), normal solution techniques like the Gauss elimination or the LU-decomposition can be used.

The first important step is to separate the exterior with its incident plane wave from the interior of the cavity. This is accomplished by replacing the aperture by one electric and one magnetic dipole as shown by among others Collin [1] and van Bladel [2] in the equivalent dipole principle. The values of the dipoles is computed by evaluating the difference of the electric and magnetic fields on both sides of the wall at the now metalized aperture. The dipoles are then sources of the field inside the cavity.

2.1 Reducing the computational effort

The Green's functions for the integral equation are written as a three-dimensional series of trigonometric functions. Collin showed that some series of trigonometric functions can be reduced to analytic expressions [1]. By applying this method to our series, it is always possible to reduce the three-dimensional series to two-dimensional ones. Now this series (supposing that we reduce the series in z) depends on the other two indexes combined in a factor of $exp\left(-\pi\sqrt{(l_x/A)^2+(l_y/B)^2}\,|z-z'|\right)$ (l_x and l_y are the indexes in x and y direction, A and B the dimension of the cavity in x and y). This sum will rapidly converge as already Seidel [3] pointed out if the argument of the exponential grows steadily. This can be done by ordering the terms in order of increasing argument with the

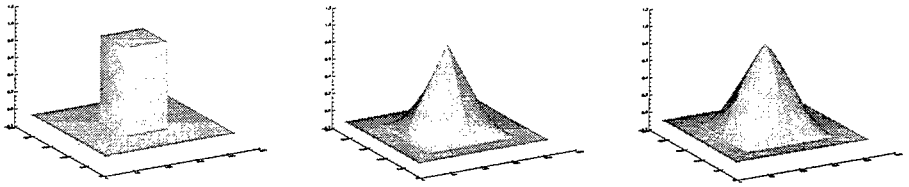

(a) Pulse (b) Triangle (c) Piecewise sinus.

Figure 2: Possible local functions: 2(a) pulse, 2(b) piecewise linear (triangle), 2(c) piecewise sinusoidal,

appropriate choice of the l_x and l_y. Typically only 100 to 150 terms of the double series are necessary for a convergence to a relative error of 10^{-6}.

2.2 Possible basis and testing functions

An interesting and important issue for all Method of Moments is the choice of the basis and testing functions. A wide range of functions was used for thin wire and 3D geometries. They involve ($x_N = \frac{x-x_0}{\Delta_x}$):

- point matching (the function is a Dirac pulse) $D(x) = \delta(x - x_0)$
- piecewise constant or pulse $CT(x) = 1$ for $|x_N| < 0.5$, 0 elsewhere
- piecewise linear or triangle $LI(x) = 1 - |x_N|$ for $|x_N| < 1$, 0 elsewhere
- piecewise sinusoidal $SI(x) = \frac{\sin k\Delta_x(1-|x_n|)}{\sin k\Delta_x}$ for $|x_N| < 1$, 0 elsewhere
- domain-range functions with local edge elements

The piecewise defined functions found a wide application not only in thin wire computations. Fig. 2 shows their graph for 3D plane conductors. Applied in our case of plane conductors in cavities, they offer the advantage that the integration of Green's function and basis/testing functions is feasible analytically. Furthermore, the piecewise linear and sinusoidal functions lead to expressions that decrease rapidly with the summation index. These two functions are also equivalent for fine discretizations.

Based on the reflections by Aksun [4], we will consider the following combinations of basis and testing functions (first is basis, second is testing function, abbreviations in parenthesis): pulse – triangle (CT – LI), pulse – sinusoidal (CT – SI), triangle – triangle (LI – LI), sinusoidal – sinusoidal (SI – SI). The latter two combinations are Galerkin solutions and offer therefore the possibility to compute only half of the matrix.

Another kind of functions are semi-global domain functions. We understand hereby functions constant over a certain width, and like sine or cosine functions according to the necessary boundary conditions in the direction of polarisation. To clarify this point, we use

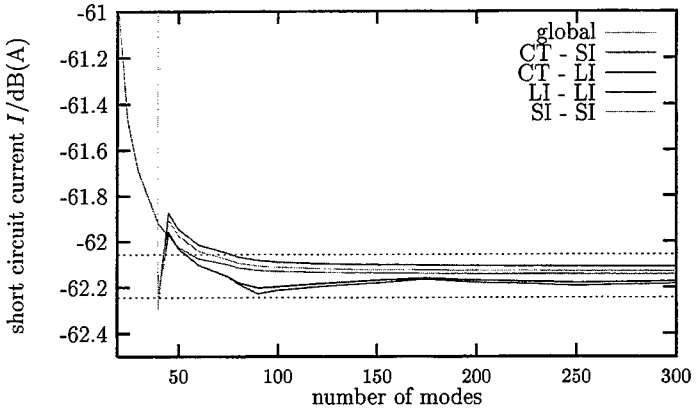

Figure 3: Convergence by number of modes

- pulse functions in the direction orthogonal to the polarisation of the current/field
- $\sin\left(\frac{m\pi}{2}\frac{x-x_{min}}{x_{max}-x_{min}}\right)$ for isolated conductors
- $\cos\left(\frac{2m+1}{2}\pi\frac{x-x_{min}}{x_{max}-x_{min}}\right)$ for conductors attached to others at $x = x_{min}$
- $\cos\left(\frac{2m+1}{2}\pi\frac{x_{max}-x}{x_{max}-x_{min}}\right)$ for conductors attached to others at $x = x_{max}$
- $\cos\left(m\pi\frac{x-x_{min}}{x_{max}-x_{min}}\right)$ for conductors attached to others at both ends.

These semi–global functions lead to smaller matrix systems compared to the local basis functions (only slightly smaller for the case of the plate we present further down). More interesting is the fact that the matrix elements not depend on the order of discretization. One can calculate a matrix for a given discretization, calculate the currents on the metallic objects, then increase the order of the discretization and calculate one more matrix column and line, recalculate the currents and stop this iterative process when the currents are sufficiently converged.

In fig. 3 we show the short circuit current I in dB(A) on the base of a rectangular plate of 0.0077m × 0.225m in a 0.297m × 0.297m × 0.498m cavity at 800 MHz as a function of the number of modes in one series. Discretization on the plate was 20 steps in longitudinal and two steps orthogonal to the polarisation of the current. For the semi-global functions we used only 8 functions. All solutions are at least after 100 modes in a small band of only ±0.15% of the mean. The pulse – pulse solution is not shown here as it leads to very slow converging wrong results, which is emphasising Aksun's guidelines, that the combined function set used for discretization should be piecewise differentiable. We do not however observe a faster convergence with smooth function sets as the half-width functions at the base of the plate which is necessary to account for the continuity of the current deteriorates this smoothness.

All results based on the different basis and testing functions converge to the same solution of the short circuit current. We can therefore chose our set of basis and testing functions with the ease of implementation in mind. This is especially necessary if one considers currents on plates which are not parallel to each other, where we tend to use a simple piecewise continuous — piecewise linear set. For smaller matrices and therefore faster computations we recommend nevertheless the use of the semi–global functions as they need less functions for a solution. As a matter of fact, for the same structure and a convergence to better than 0.1 % to the final solution we needed 14 functions for the CT – SI case, 12 functions for the LI – LI case and only 9 functions for the semi–global case.

2.3 Broadband data from small band simulations

For computations for several frequencies, the computation of the moment matrix can become very time consuming. For periodic free space configurations, a number of algorithms accelerating the actual computation of the matrix were treated in literature (see e.g. [5]). All these algorithms require however still the evaluation of the matrix at every point. Another method was proposed by Newman in 1988 [6] where he interpolates using a standard quadratic interpolation scheme the matrix elements on the frequency axis. By doing this he generates broad band data with almost no computational effort by increased storage need.

In the case of the Green's functions of the rectangular cavity, the matrix elements can show strong resonances at the resonances of the *empty* cavity. An interpolation which is not taking into account this resonant character does not well approximate the matrix elements and is therefore unsuitable for this case. However the interpolation with rational functions renders the approximation of resonances possible. An interpolation algorithm which computes recursively the interpolated value as well as an error estimate was found by Stoer in 1961 [7] (see also [8]). By using this algorithm we can interpolate the matrix elements between the resonances f_i^r and f_{i+1}^r of the empty cavity which are easily calculated. The match points are chosen either with an constant distance between the points (equidistant choice) or by a Chebyshev-law

$$f_k = \frac{f_i^r + f_{i+1}^r}{2} + \frac{f_i^r - f_{i+1}^r}{2} \cos\left(\frac{2k+1}{2n+2}\pi\right)$$

where k running index $0 \ldots n$ and $(n+1)$ number of match points. The latter is yielding a smaller error at the extremities of the interpolation interval [9]. We would like to stress that the choice of the match points is only based on the knowledge of the dimensions of the empty cavity. The points are the same for every possible structure inside the cavity.

For an example we choose again a cavity with dimensions 0.297m × 0.297m × 0.498m and a plate centred in the cavity with length 0.225m and width 0.0077m, loaded at the base with 50Ω. The current at the base of this plate using both interpolation schemes is given in fig. 4. The computation of the 324 elements in one matrix lasts about 7 s on a Sun Ultra 2, interpolation time is approx. 0.05 s. For 3 or 4 match points in a frequency band of 100 MHz to 1 GHz with 5 MHz spacing (200 points), the computation time for only computing the matrices is 23 min for exact evaluation. This time is reduced to 30*7 s + 170*0.05 s = 3.6 min in the case of 3 match points and to 40*7 s + 160*0.05 s = 4.8 min in the case of 4 match points. The 3 resonances between 700 MHz and 800 MHz at 711.9 MHz, 772.6 MHz and 783.5 MHz deteriorate the interpolation

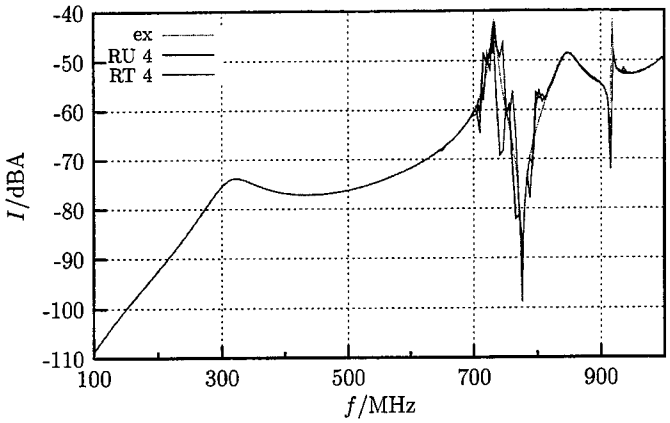

Figure 4: Broad band data by interpolation. *ex*: exact computations; *RU 4*: rational function, uniformly spaced, 4 match points; *RT 4*: rational function, Chebyshev-law, 4 match points

in the region of 700 to 800 MHz visible in fig. 4. In the other regions the interpolation is almost perfect.

3 Comparison measurements and computations

To compare our computations to measurements, an actual cavity was built. The cavity was then placed into the monoconic antenna of the SESAME measurement site at the Centre d'Etudes de Gramat. A sketch of this site is shown in fig. 5(a). The monoconic antenna is the source of the fields in the simulator and allows the creation of a plane wave over a large frequency range. We place a small monopole antenna into the cavity and measure the voltage at the base of this antenna by means of a network analyser which also drives the monoconic antenna. Earlier the measurements of a single monopole antenna in the cavity were presented [10], now we also present the comparison of two objects: the monopole antenna and a large metallic plate parallel to the antenna. The geometrical data are as follows: cavity size $0.3 \times 0.3 \times 0.5$ m^3, aperture diameter 20mm centred on on wall of the cavity. The monopole antenna has a radius of 2mm and a length of 225mm. It stands on the base of the cavity at 100mm from the aperture, also centred. The plate is covering almost all of the cavity section, at 75mm from the monopole and hanging from the ceiling of the cavity (height 400mm).

The data are shown in fig. 5(b). The data marked with 'noise' are measurements after closing the aperture by conducting tape. The level of this measurements is quite high due to the signal to noise ration of the network analyser and due to the fact that the tape is not an ideal means to provide for an perfect closing. More important is that we can see that at low frequencies the first resonance (due to the presence of the plate, cf. measurements in [10] without plate) is very well reconstructed. The second resonance ($\lambda/4$ resonance of the monopole antenna) is below the noise level and therefore not very well visible. The third resonance at 510 MHz is due to the

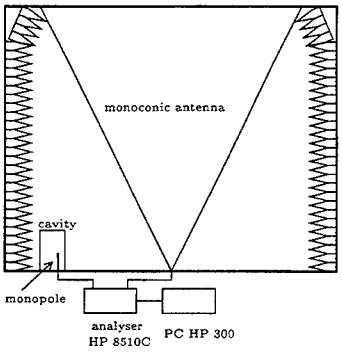

(a) The SESAME site

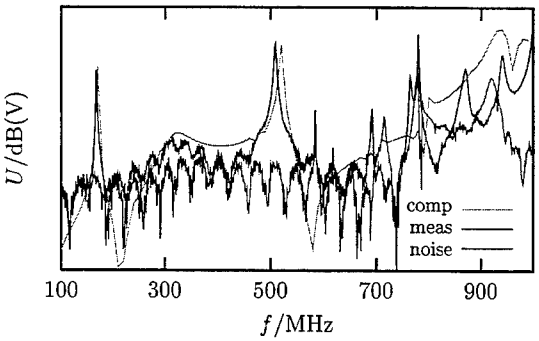

(b) Simulation and measurement with noise level for monopole antenna in presence of a plate

Figure 5: Measurements at CEG

cavity. For higher frequencies the noise level is to high for valid comparisons. Two things remain desirable: the consideration of the reaction of the cavity and the objects onto the aperture (an effect at higher frequencies as seen in [10]) and better measurements with a lower noise level.

4 Conclusion

We have presented a Method of Moment solution for the coupling of electromagnetic energy into cavities. It is based of the electric field integral equation, and separates interior form the exterior by the equivalent dipole method. By placing metallic plates into the cavity, it is possible to change the shape of the latter. Nevertheless the number of unknowns stays small, as the Green's functions of the rectangular cavity are used, so that only the scatterers are discretized. We have presented several sets of basis and testing functions, all of which show to yield the same result for the current supported on the conducting structures. There are however some particularities for each set of functions which recommend their use in one case or another.

By this method metallic objects can be placed into the cavity, the resulting currents be computed. This procedure is also valid for very large objects and objects behind metallic screens. As a matter of fact, computations not presented here have shown that the fields behind conducting walls are close to the numeric noise.

We have also presented an interpolation method which allows to produce wide band data from only a few simulations. This method is applicable for all structures with known resonances.

Comparisons of computations and simulations show the good agreement between the two. A high noise level in the measurements is nevertheless constricting the validation over a high frequency band.

In the future we direct our research to the reaction of the cavity and three–dimensional objects on the aperture.

Acknowledgements

The authors would like to express their thanks to the Centre d'Etudes de Gramat for having conducted the measurements to validate our computations.

References

[1] R. E. Collin, *Field Theory of Guided Waves.* New York, Toronto, London: McGraw-Hill, 1960.

[2] J. van Bladel, "Field penetration through small apertures: The first-order correction," *Radio Science*, vol. 14, pp. 319–331, March-April 1979.

[3] D. B. Seidel, "Aperture excitation of a wire in a cavity," PhD-thesis, University of Arizona, Arizona, 1977.

[4] M. Aksun and R. Mittra, "Choices of expansion and testing functions for the method of moments applied to a class of electromagnetic problems," *IEEE T-MTT*, vol. 41, pp. 503–509, Mar. 1993.

[5] S. Singh and R. Singh, "On the use of Levin's T-transform in accelerating the summation of series representing the free-space periodic Green's functions," *IEEE T-MTT*, vol. 41, pp. 884–886, May 1993.

[6] E. H. Newman, "Generation of wide-band data from the method of moments by interpolating the impedance matrix," *IEEE T-AP*, vol. 36, pp. 1820–1824, Dec. 1988.

[7] J. Stoer, "Über zwei Algorithmen zur Interpolation mit rationalen Funktionen," *Numerische Mathematik*, vol. 3, pp. 285–304, 1961.

[8] W. H. Press, S. A. Teukolsky, W. T. Vetterling, and B. P. Flannery, *Numerical Recipes in C.* Cambridge, New York and Melbourne: Cambridge University Press, 1992.

[9] R. Bulirsch and H. Rutishauser, "Interpolation und genäherte Quadratur," in *Mathematische Hilfsmittel des Ingenieurs* (R. Sauer and I. Szabó, eds.), no. H in Teil III, Berlin, Heildelberg: Springer–Verlag, 1968.

[10] D. Lecointe, W. Tabbara, and J. Lasserre, "Aperture coupling of electromagnetic energy to a wire inside a rectangular metallic cavity," *IEEE AP-S*, vol. 3, pp. 1571–1574, July 1992.

A Simple Computational Electromagnetic Analysis Example of Electromagnetic Coupling to Pyro Circuits.

Reinaldo Perez
Jet Propulsion Labaoratory
California Institute of Technology
Pasadena, California

Abstract

Analysis of electromagnetic coupling to pyro circuits with the objective of preventing adverse effects such as un-intentional firing, have been studied for many years using a variety of analytical approaches. It is proposed that a much simpler and faster approach, based on computational electromagnetic, can provide similar results. A portion of a pyro MOSFET circuit is first examined addressing failure modes within the design that can un-intentionally fire a pyro device if adverse electromagnetic fields of sufficient strength are present. The electrical conditions that will also contribute for the pyro circuits to fire un-intentionally are also discussed. Finally, the method of moments is used to address the field-to wire coupling scenario and to find if the necessary induced voltages within the pyro circuits are sufficient for a firing condition.

Introduction.

High current (5-15 amps) pyrotechnic devices (or pyros) are extensively used in many engineering applications requiring abrupt separation of functional stages in the course of a mission. For example, pyro devices are used in rockets for activating the separation of firts, second, and third propulsion stages when fuel and oxidizer are depleted and/or during insertion maneuvers. Most pyro devices are modeled after the NASA Standard Initiator (NSI) whose design was perfected over twenty years ago. All NSI are activated using a variety of pyro MOSFET initiator circuits which provide the needed current (5-7 amps average) in a period of a few microseconds. Most redundant pyro circuits perform the NSI activation simultaneously, others are synchronized to fire on a prescribed sequence. The design of pyro circuits have evolved over many years and more sophisticated designs are still being developed.

Statement of Problem

In this work the pyro circuits and accompanying NSI are used to release a series of parachutes during the initial stages of a high speed descend of a spacecraft over a planet surface. A portion of a pyro circuits and its associated NSI device is shown in Figure 1. The illustrated portion of the pyro circuit consists of a series of two HEXFET (MOSFET type) transistors (inhibit # 2 and inhibit # 3 in Figure 1). which serve as the "enable" and

"fire" switches to the NSI when commanded. The HEXFETs are pulled down by two NPN transistors which are themselves commanded by the buffered outputs of two field programmable gate arrays (FPGA). In the design of the FPGA it was discovered that an internal failure mode exists within the FPGA such that a latch-on-high condition could develop. The output high (about 7.5v) could easily switch ON both inhibits # 2 and # 3, which could then be followed by the firing of the NSI if the appropriate Vgs voltage for each HEXFET was present. Preventing this scenario from happening involves keeping the Vgs of the HEXFET to a low value of no more than 4V. In Figure 2 this is accomplished by the use of a battery enable plug that keeps battery power interrupted (Vgs = 0). The battery enable plug is for used at Launch Complex 17 (LC-17) at Kennedy Space Center (KSC) during final systems check out and testings. During flight, battery power is disabled through software means which de-activates several solid state powering switches (some of which are shown in Figure 1)..

Lacking battery power (or the means to activate such power) there is only one more source that could provide the needed Vgs=4V ---electromagnetic field coupling of known fields nearby LC-17. The coupling is unto pyro cabling, portions of which are shown in Figure 3. The pyro cabling of interest would be the one located between the battery enable plug and the first HEXFET (inhibit # 2) in Figures 1 or 2. Only that portion of the cabling will be considered in this work. The nearby electromagnetic fields of interest for the scenario in Figure 2 are those permanent fields located in LC-17. Figure 4 shows the worst case average electric field (W/m^2) at LC-17 from all known permanent sources. Figure 5 shows again the worst case emitters at LC-17 in terms of electric fields strengths of volts per meter (V/m). Finally, Figure 6 shows the "average" field strength (W/m^2) of LC-17 known emitters. The fields in Figure 6 are compared with the field strength needed to fire an NSI attached directly (i.e no pyro circuits of Figures 1 or 2 are present) to a hypothetical simple $\lambda/4$ perfectly conducting dipole antenna (maximum pick-up). In the figure this is known as the "99.9 % NO-fire line". Notice that with the effects of cable shielding no known emitter at LC-17 at KSC can even come close to the field strength needed to produce the 1A current for NSI firing. Therefore, as suggested by this work, the most realistic scenario of inadvertent pyro firing is through the activation of the HEXFET switches.

Once we have a good knowledge of the electromagnetic environment in LC-17, the question arises if any of such field strengths could induce enough current in the shielded cable between the battery enable plug and the "enable" HEXFET (inhibit # 2) so as to cause a Vgs = 4V or greater. From the EMC point of view this is a field-to-cable coupling scenario. Many of such analyses in the past have been done analytically for pyro circuits [1-4]. It is proposed that such analyses can also be done numerically using the method of moments (MOM). As shown in Figure 7, the critical cable layout of interest, which is inside a capsule, can be modeled using the method of moments where loads have been appropriately represented. The shielded cable (grounded at both ends to protect against high frequency coupling) which protects the enable line is modeled as a wire mesh [5]. The details of the modeling will be presented in the paper.

Modeling

The NEC code [6] used for thin wire modeling is the main software used for modeling. The center conductor and shield surrounding the main conductor shown in Figure xx. It is appropriate to use thin wire modeling. We are only interested in worst case coupling of an electric field to the center conductor and not in the accurate calculation of current distribution which could be better obtained using a surface patch modeling for the wire shield. The shield which is grounded at both ends (due to possible high frequency coupling) partially protects the electromagnetic wave from coupling directly into the conduction wire which could activate the HEXFET. With the presence of a shield only capacitive coupling will allow some of the induced current in the shield to couple into the conducting wire.

The segmentation of the inner conductor is done per NEC recommendations of $\lambda/10$. The shield is modeled as a thin wire mesh following the equal area rule given by the expression $d=2\pi a$ for the minimum wire radius a=1.0 mm. The mesh size is about $0.028\lambda^2$ and of rectangular shape. The term λ is the wavelength at each of the frequencies of interest. As in the inner conductor, the average length segments, where possible, are not longer than $\lambda/10$. However, the shortest and longest segments (in meters) in the wire mesh are given by

$$L_{SHORTEST} = \frac{12}{F_{\min}(MHz)} \qquad (1)$$

$$L_{LONGEST} = \frac{30}{F_{\max}(MHz)} \qquad (2)$$

For the F_{min}(MHz) of 1.6GHz and F_{max}(MHz) of 6.0 GHz the wire segment size will range between 7.5 mm and 5.0 mm. The limit on the wire thickness is given by

$$a_{MAX} = \frac{10}{F_{MAX}(MHz)} \qquad (3)$$

which provides a result of 1.6 mm and this is consistent with the wire radius previously chosen.

In principle there was only a need to look for a worst case electromagnetic coupling scenario. If for such scenario the induced coupled noise was significantly less than the needed Vgs=4.0V, there would be no need to pursue this issue any furhter from the safety point of view. The worst case analysis was envisioned by using the largest electric field magnitude recorded at LC-17, which corresponded to that of 222.5 V/M (5.692 GHz radar), and use this level as the incident plane wave across the frequency spectrum of

interest (1.6--6.0 GHz). The effects of apertures were also ignored for a worst case analysis. The calculated output voltage resulting from the field-to-wire coupling scenario on the HEXFET side will be equivalent to the input Vgs of the "enable" switch. The results of these noise voltages as a function of frequency are shown in Figure 8. The figure also shows the safety margin at the worst critical frequency.

Results of Analysis

The results show that: a) for this particular situation the induced noise voltage Vgs at the HEXFET input is very small to turn ON the enable switch, even if the FPGA failure (latch-to-high output) were to occur for both the "enable" and "fire" switches. Notice that the worst case scenario in Figure 7 is for a frequency that is not even one of the known emitters at LC-17, and b) computational electromagnetic can serve as a valuable tool in modeling pyro-initiation events triggered by electromagnetic field coupling.

References

[1] Baginski, Thomas A. "Hazard of low frequency electromagnetic coupling of overhead power transmission lines to electro-explosive devices, " IEEE Trans. on EMC, November 1989.

[2] Sabaroff, Samuel, "Worst Case analysis of squibs in an RF field," IEEE Trans. on EMC, December 1967.

[3] Hirsh R. Stanley, "RF Current induced in an ordnance circuit," IEEE International Symposium on EMC, August 1965.

[4] Lee, K.S, H.Marin, and Castillo, J.P. "Limitation on Wire Grid Modeling of a closed surface," IEEE Trans. EMC, No. 3, 1977.

[5] Ludwig, C. Arthur, "Wire Grid Modeling of Surfaces, IEEE Trans. AP, No. 9, September, 1987.

[6] Burke, Geral J. "The Numerical Electromagnetic Code-Method of Moments," UCRL-MA-109338, Jan. 1992, Lawrence Livermore National Labs.

FPGA & Telemetry power enable

- Simplified PIU circuit showing origin of FPGA and Telemetry power

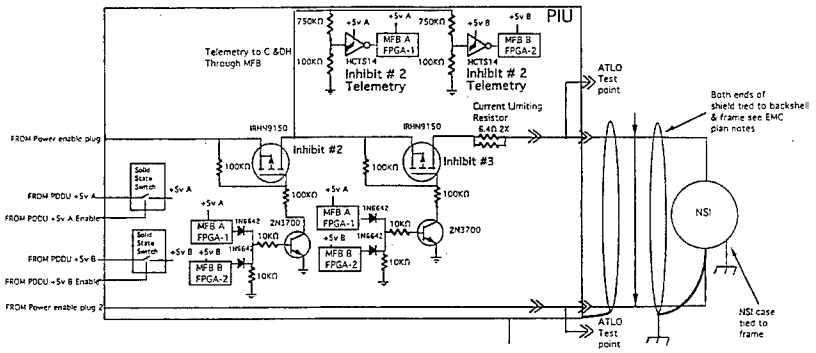

Figure 1. Pyro Crcuit within the Pyro Initiator Unit and its NSI connection

MSP Pyro Circuit

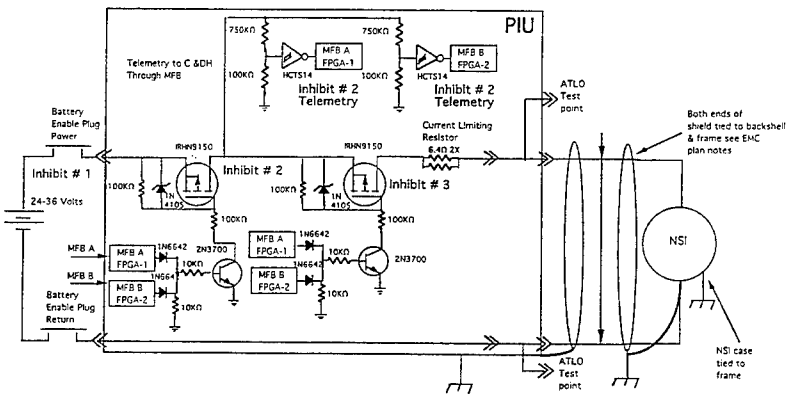

Two battery enable Plugs one on power and one on return breaks both 28v and 28v return paths for NSI

Entire circuit is inside Faraday cage when battery enable plug in place

Figure 2. Battery enable plugs configuration which prevents firing of NSI

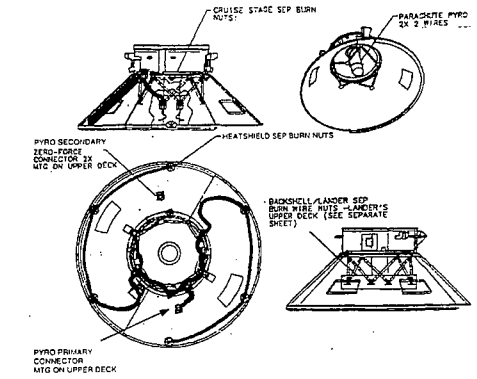

Figure 3. Cable layout of pyro initiator circuits

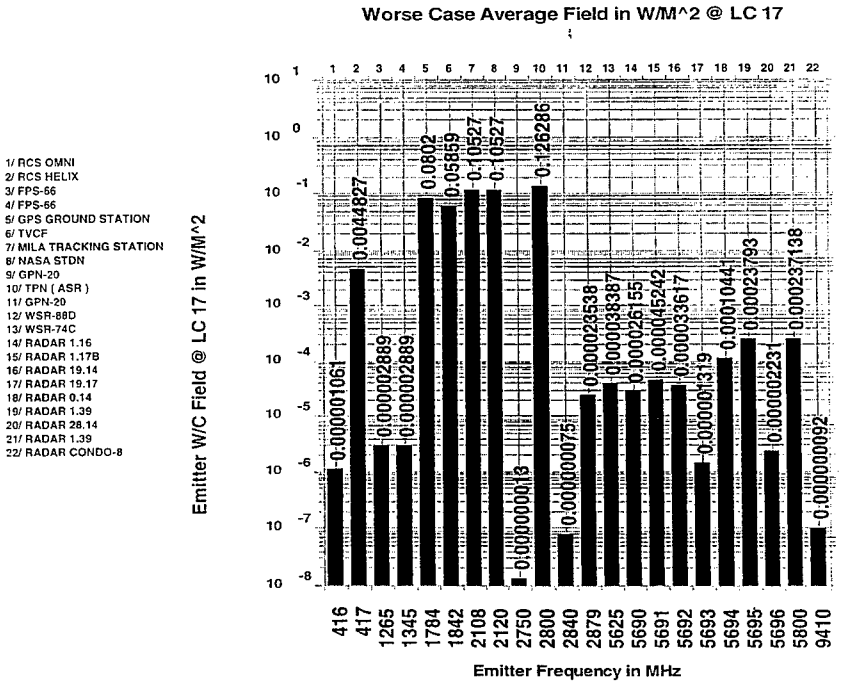

Figure 4. Known electromagnetic emitters at LC-17 at KSC and its worst case field strength in Watts/m^2.

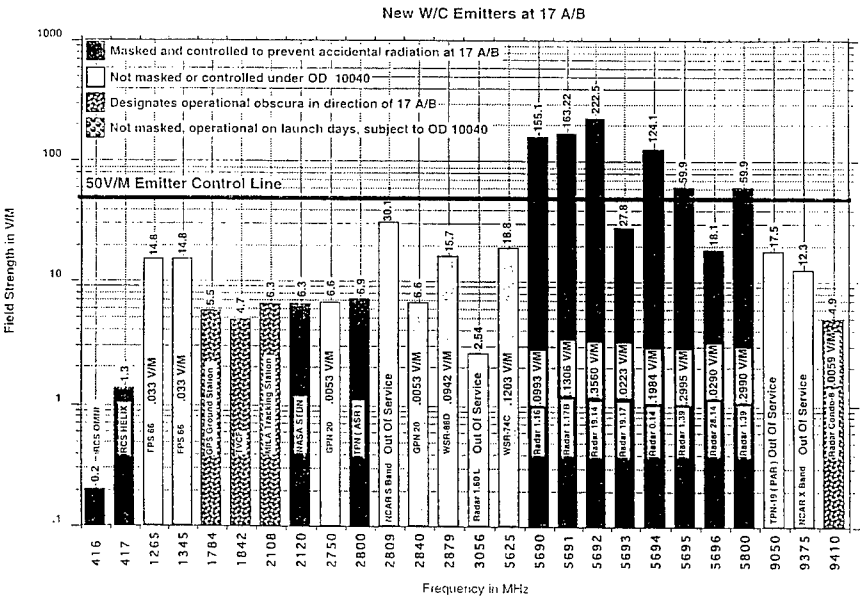

Figure 5. Known electromagnetic emitters at LC-17 at KSC and its worst case field strength in Volts/meter.

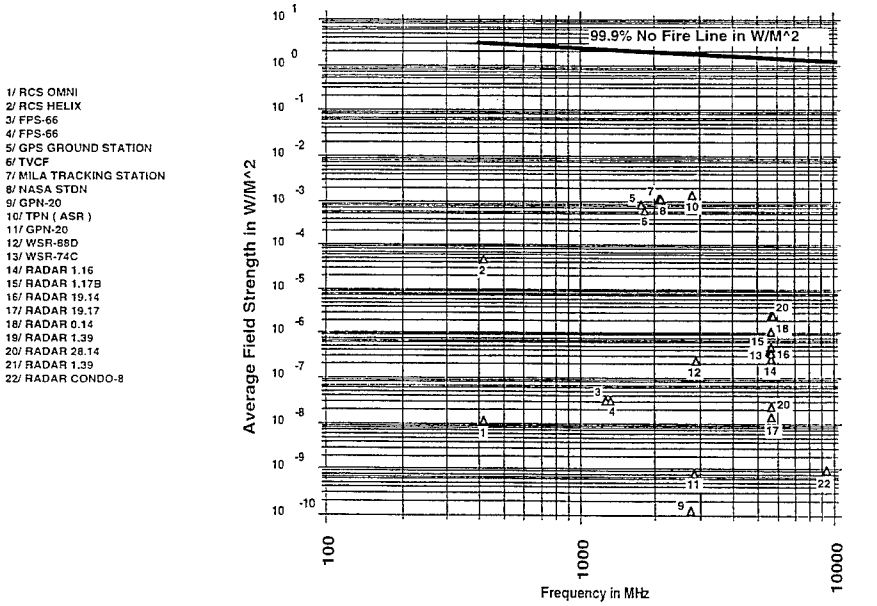

Figure 6. Average field strength (watts/m^2) of known emitters at LC-17 at KSC.

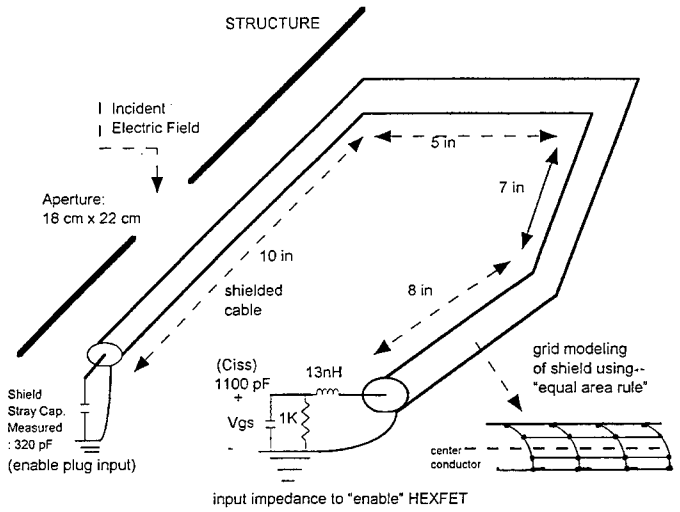

Figure 7. Method of Moments Modeling of Shielded Cable with Loads

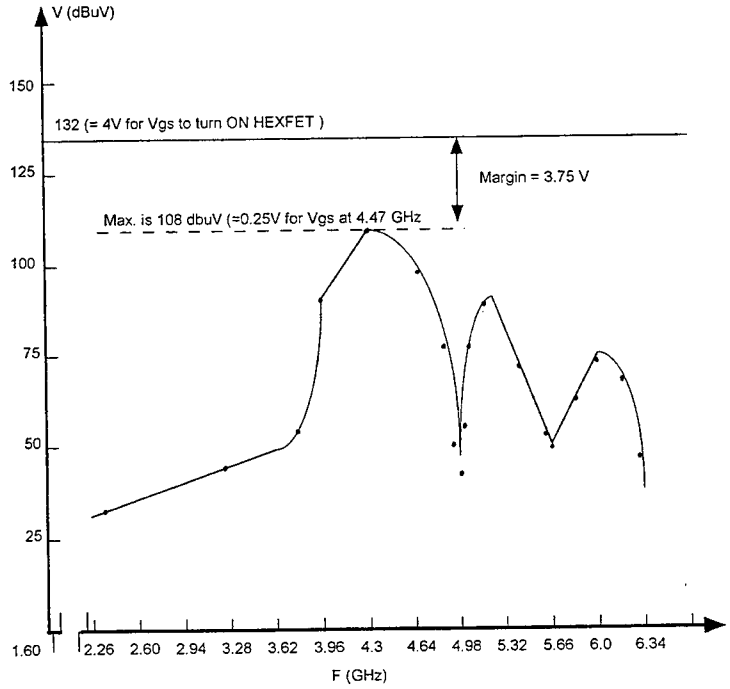

FIGURE 8. Induced Noise Voltage at input of "enable" HEXFET in pyro circuit for NSI Activation.

TRAK_RF - Simulation of Electromagnetic Fields and Particle Trajectories in High-power RF Devices

Stanley Humphries, Jr.
Department of Electrical and Computer Engineering
University of New Mexico
Albuquerque, New Mexico 87131

and

Daniel Rees
ATP Program
Los Alamos National Laboratory
Los Alamos, New Mexico 87545

A. Introduction

Trak_RF is an integrated finite-element software system to model charged particle trajectories in combined electrostatic, magnetostatic and electromagnetic fields. The program is an extension of the **Trak 3.0** gun design code[1]. New capabilities include frequency-domain calculations of electromagnetic fields in resonant cavities and open space and particle tracking in time-dependent fields. A unique feature is the ability to combine up to three independent numerical solutions for static electric and magnetic fields and RF modes. The current version is limited to two-dimensional static fields (planar or cylindrical geometries) and three-dimensional RF fields in two-dimensional structures. The latter case includes propagating modes in waveguides and modes of type TE_{mnp} or TM_{mnp} in cylindrical resonators.

The program has been developed to investigate contributions of multipactoring to breakdowns on RF windows in high-power accelerators. A cooperative program on Accelerator Production of Tritium to maintain the US nuclear weapons stockpile has recently been initiated at Los Alamos National Laboratory (LANL) and the Savannah River Site[2]. The goal is a continuously operating proton linac to generate a 1.3 GeV beam with an average current of 100 mA (130 MW beam power). The accelerator demands powerful RF systems with high reliability. A critical area of concern is the possibility of breakdowns on RF vacuum windows that must transmit MW power levels. To address the issue, an experimental and theoretical program of window testing and development has been initiated at LANL[3]. Starting in October 1996, the University of New Mexico has supported this effort through the development of particle and radiation diagnostics to warn of impending breakdowns and computer codes to help understand the role of stray electrons in window failure.

This paper reviews the status of the **Trak_RF** program. This computational tool has been completed and benchmark tested. We plan extensive studies of multipactoring and advanced window designs through Spring of 1997. Section B describes the conformal triangular meshes used in the program and the range of quasi-static field solutions that can be incorporated in orbit calculations. Section C reviews features of the finite-element methods used for frequency-domain RF solutions. The solver handles open and closed systems with frequency-dependent wall and material losses. Section D covers the particle tracking capabilities. The program can handle electron multiplication resulting from secondary emission with energy-dependent emission coefficients. Finally, Section E describes a benchmark test to demonstrate features of the code. The calculation follows electron orbits in a 700 kW coaxial feedthrough with a static magnetic mirror field to repel electrons from an alumina window.

B. Conformal meshes and static field computations.

All static and dynamic field calculations in **Trak_RF** are carried out on conformal meshes. As an example, Fig. 1 shows a mesh of triangular elements for the calculation of TEM waves in a high-power coaxial feedthrough. The advantage is apparent - the edges of elements conform closely to curved and angled material boundaries. As a result, each element can be uniquely associated with a material region. This is an important feature in a particle tracking code because it allows an accurate identification of particles striking material surfaces. Section D discusses some of the benefits of the finite element formulation for RF calculations. In static field solutions, there are three major advantages compared to finite-difference calculations: 1) the finite element method gives accurate field values near metal surfaces, 2) the technique represents field discontinuities at the boundaries of dielectrics and ferromagnetic materials, and 3) it is easy to implement Neumann conditions on angled and curved boundaries.

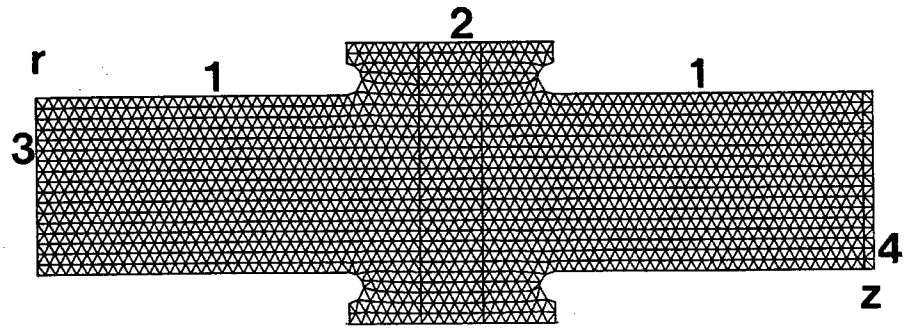

Figure 1. Conformal triangular mesh - TEM waves (H_θ) in a high-power coaxial feedthrough. r_{min}: 0.8", r_{max}: 3.3", z_{min}: -4.0", z_{max}: 4.0". Region 1: Vacuum with Neumann boundaries (metal wall). Region 2: Aluminum insulator. Region 3: Drive boundary (0° phase). Region 4: Resistive termination layer.

Trak_RF uses the standard mesh generator and static field solvers of the **TriComp** system[4]. This suite of finite-element programs runs on IBM standard personal computers under DOS, Windows 3.1 or Windows 95. Boundary information is entered through an interactive drafting program or from popular CAD software like Autocad. The basic electrostatic and magnetostatic programs **EStat** and **BStat** use the linear finite-element formulation of Ref. 5 with solutions by successive over-relaxation. The solvers analyze files of boundary and material information to produce output files of vertex coordinates and corresponding values of electrostatic or vector potential. Figure 2 shows an example, a magnetostatic field generated by a cylindrical coil. Note the use of variable mesh resolution for an efficient approximation of infinite space boundary conditions. There are several other quasi-static solvers in the **TriComp** series that create solution files compatible with **Trak_RF**. Two advanced electrostatic solvers were developed for medical applications of RF fields: **EStatA** handles non-linear and anisotropic dielectrics while **PAC** calculates harmonic field penetration into imperfect dielectrics. For magnetic fields, the **PerMag** program treats complex anisotropic materials, include permanent magnets with non-linear demagnetization curves. The **Pulse** program handles diffusion of magnetic fields created by pulsed coils with arbitrary current waveform and **Nelson** calculates harmonic field penetration into materials with eddy currents.

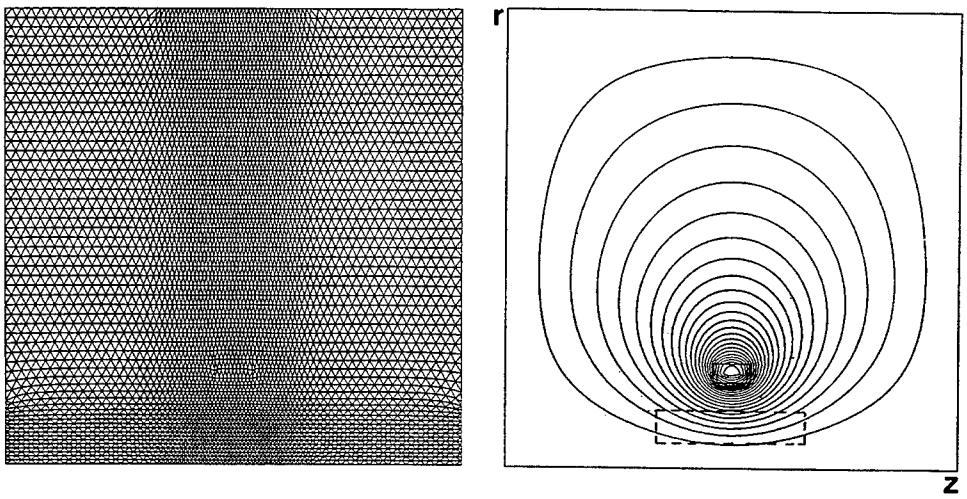

Figure 2. Field lines of a magnetostatic solution. Field from a single coil carrying current 2640 A. r_{min}: 0.0", r_{max}: 24.0", z_{min}: -12.0", z_{max}: 12.0". Dashed line shows approximate extent for the RF solution of Fig. 1.

C. RF field computations

The derivation of finite-element equations for two-dimensional frequency domain RF fields is reviewed in Ref. 6. As an example, consider the equations for a planar structure with no variation in z with electric field polarization E_z. The associated differential equation is

$$-\nabla\times\left(\frac{1}{\mu}\nabla\times\boldsymbol{E}\right) = -\epsilon\omega^2\boldsymbol{E} + j\omega\boldsymbol{J}_o \ . \tag{1}$$

The quantities μ and ϵ in Eq. 1 may have may have complex values to represent losses from resistivity or non-ideal materials. The current source $\mathbf{J}_o$ contains information on the amplitude and phase of drive regions. Figure 3 shows the geometry and indices of vertices and elements surrounding a test vertex. In the example, the mesh has a regular logic with six elements encompassing each vertex. The finite-element equation for wave propagation at the test vertex are determined by taking area integrals of Eq. 1 over the surface surrounded by the dashed line in Fig. 3. The result is

$$E_{zo}\left(-\sum_i W_i + \omega^2\sum_i\frac{\epsilon_i a_i}{3}\right) + \sum_i E_{zi} + = j\omega\sum_i\frac{J_i a_i}{3} \ . \tag{2}$$

In general, the quantities E_{zi} are complex numbers to represent amplitude and phase. The index *i* refers to the vertices surrounding the test vertex marked *o*. The quantities ϵ_i, μ_i and J_i are the material properties and current density of the elements shown in Fig. 3. The geometric coefficients are given by

$$W_i = \frac{\cot\theta_{bi+1}/\mu_{i+1} + \cot\theta_{ai}/\mu_i}{2} \ , \tag{3}$$

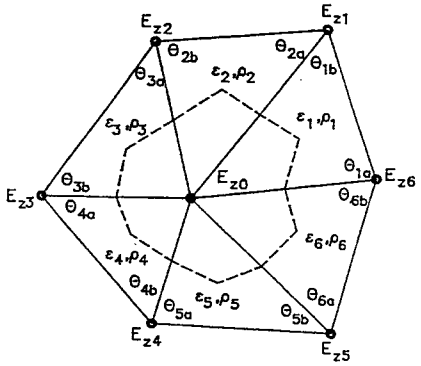

Figure 3. Geometry and labeling conventions for elements and vertices adjacent to a vertex of a finite element mesh with regular logic.

Equation 1 represents a large set of coupled linear equations, one for each mesh vertex. The set is solved in **Trak_RF** using matrix inversion with block decomposition methods. The complex values of E_{zi} gives the physical electric field at a given RF phase. Numerical derivatives give the magnetic field components B_x and B_y. For resonant type solutions in closed regions, we can use the current sources as coupling loops to create RF fields. The most convenient way to initiate fields in scattering solutions is with a drive boundary with a fixed complex value of E_z. In solutions with E_z polarization, a metal wall is represented by the fixed value $E_z = [0,0]$. The open circuit condition is the natural boundary of finite-element solutions. For waves with H_z polarization, the Neumann condition represents a metal wall. A significant advantage of the finite-element method is the ability to define absorbing layers of arbitrary shape to represent free-space boundary conditions. The procedure is to set up a thin layer of width δ on the outside of the solution volume. The imaginary part of the dielectric constant in the layer is assigned the value $\epsilon'' = -\sigma/\omega$, where the conductivity is matched to the impedance of the adjacent medium,

$$\sqrt{\frac{\mu}{\epsilon}} = \frac{1}{\sigma\delta} . \qquad (4)$$

The performance of absorbing layers equals or exceeds that of look-back techniques[7]. The advantages are that termination layers can have any shape or orientation and do not place restrictions on the time step in time-domain solutions. Furthermore, layers can be constructed with generalized reactive and resistive impedance components to represent imperfect matches to downstream devices.

To illustrate the method, Fig. 4 shows a benchmark test of a high power coaxial feedthrough using the mesh of Fig. 1. In the cylindrical geometry the finite-element equations are solved for H_θ to derive TEM type waves. The boundary on the left is a drive surface with the fixed stream function value $rH_\theta = [18.79, 0]$ to produce 700 kW of electromagnetic energy flux. The region on the right is an absorbing layer of thickness 0.1" (0.00254 m). The choice of material properties $\mu = \mu_o$ and $\epsilon = \epsilon_o(1 - 53.62)$ gives a termination matched to the impedance of free space. In time-domain tests, reflected energy from the termination is less than 1 part in 10^5. Figure 4 shows contours of rH_θ which lie along electric field lines. The magnitude of the electric field is proportional to the distance between lines divided by the relative dielectric constant. Note the accumulation of lines inside the alumina window with $\epsilon_r = 7.8$.

D. Charged-particle orbit calculations

Charged-particle orbit calculations in **Trak_RF** are straightforward. They involve Runge-Kutta integrations using numerically-calculated field components. The main challenge is organization of the broad range of possibilities. The program can handle three numerical field solutions on independent conformal meshes: electrostatic, magnetostatic, and electromagnetic. The motivation for this versatility is to model techniques for stray electron control near RF windows such as sweeping fields.

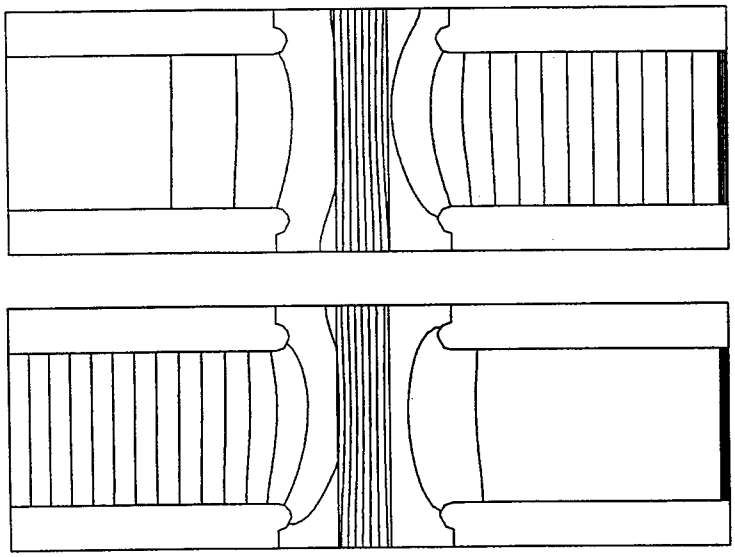

Figure 4. Field solution for the geometry of Fig. 1 at 350 MHz. Contours of rH_θ are parallel to electric field lines. a) Real part of rH_θ. b) Imaginary part of rH_θ.

Field geometries can be mixed in any combination. The quasi-static solutions may have either rectangular geometry (variations in x and y with infinite extent in z) or cylindrical (variations in r and z with azimuthal symmetry). There are four possibilities for electromagnetic fields: rectangular geometries with primary field components E_z or H_z or cylindrical systems with solutions for E_θ or H_θ. **Trak_RF** uses a reference three-dimensional Cartesian coordinate system and organizes interpolations of the numerical field solutions to derive total values of **E** and **B** at the position and elapsed time of the particle. The three field solutions can be assigned translations and rotations within the three-dimensional reference system.

The basic method to initiate particle orbits is through a parameter listing file generated by spreadsheets or user-written programs. The file specifies charge, mass, initial kinetic energy, position and direction cosines. When electromagnetic fields are present there is the option to assign reference phase. Each particle is initially assigned a multiplication factor of unity. **Trak_RF** can handle up to 1000 orbits in a run. The program also has the capability to generate a variety of particle distributions. Working from user-supplied numerical tables, **Trak_RF** can create arbitrary distributions in energy, position, and direction. The program has several options to stop orbits, including maximum distance and elapsed time. It is also possible to set up stopping planes along the Cartesian axes for high-accuracy interpolations of crossing particle parameters. An important feature for the multipactor application is stopping when a particle enters a material element. Element

characteristics are identified by the status of the corresponding mesh region. Regions can be individually set to one of three conditions: *Vacuum*, *Material* or *Secondary*. A particle stops if it enters a Material element on any of the three field meshes. For Secondary elements, the orbit is returned to its position before entering the surface and assigned a low momentum in the opposite direction. The particle multiplication factor is multiplied by the secondary emission coefficient of the material. This quantity is either a constant value or derived from a user-generated numerical function of the incident kinetic energy. Orbits that reach the end of their lifetime with multiplication factors much larger than unity indicate the possibility of multipactoring.

E. Benchmark calculation

The following example demonstrates the capabilities of **Trak_RF**. We shall consider electron orbits near the vacuum window of the system of Fig. 1 for a power level 700 kW. The solution incorporates the static solenoidal magnetic field of Fig. 2. The field is collinear with the transmission line with a maximum at the axial position of the window to repel electrons accelerated by the RF fields. To generate interesting orbits, the peak magnetic field value was set to 0.0125 tesla, the condition for electron cyclotron resonance at f = 350 MHZ. Figure 5 shows resulting orbits on the vacuum side projected in the reference x-y plane along with the inner and outer boundaries of the downstream transmission line. The increase of electron kinetic energy is clearly visible. There is also a simultaneous acceleration in z away from the window. Ultimately, the electrons strike the walls several inches from the window.

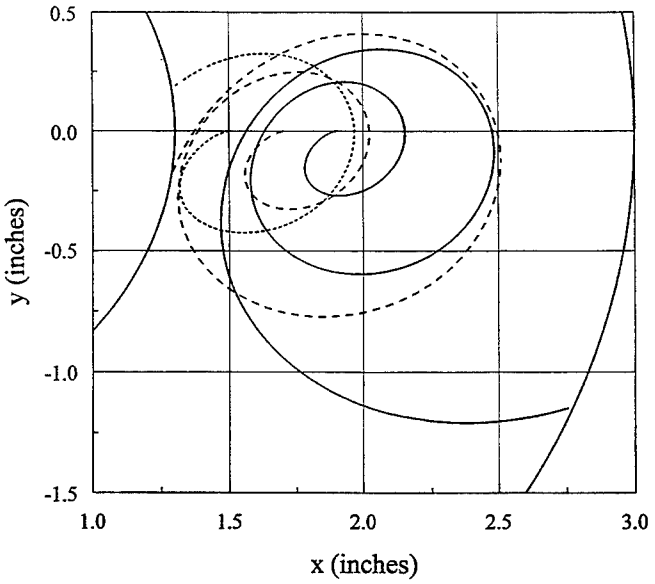

Figure 5. Electron orbits in combined fields of Fig. 3 and 4 - projection in the x-y plane.

References

1. S. Humphries, Jr., J. Comp. Phys. **125**, 488 (1996).
2. G. Lawrence, *et.al.*, *Conventional and Superconducting RF Linac Design for the APT Project* in **Proc. 1996 Int'l. Linear Acc. Conf.** (Geneva, 1996), to be published.
3. D. Rees, P.J. Tallerico and M. Lynch, IEEE Trans. Plasma Sci. **25**, 1033 (1996).
4. TriComp mesh generator and solution programs courtesy of Field Precision Company, Albuquerque, New Mexico.
5. See for instance, J.L. Warren, et.al. **Reference Manual for the Poisson/Superfish Group of Codes** (Los Alamos National Laboratory, LA-UR-87-126, 1987), unpublished.
6. S. Humphries, Jr., **Field Solutions on Computers** (CRC Press, Boca Raton, 1977), Chap. 14.
7. See, for instance, K.S. Kunz and R.J. Luebbers, The Finite Difference Time-Domain Method for Electromagnetics (CRC Press, Boca Raton, 1993), Chap. 18.

SESSION 19:

CEM ANALYSIS: THE APPROACH OF THE FUTURE

Chairs:K. Siarkiewicz and A. Drozd

APPLICATION OF THE RESEARCH AND ENGINEERING FRAMEWORK (REF) TO ANTENNA DESIGN AT RAYTHEON*

B. Hantman[§], J. LaBelle[§], Y. Chang[†], R. Abrams[‡]

Correspondence to:
Barry Hantman
Raytheon Company, Mailstop T3MR8
Tewksbury, MA 01876
Phone: (508) 858-5778
FAX: (508) 858-5976
Email: hantman@caesun.msd.ray.com

ABSTRACT

Scientific and engineering research and design codes are typically FORTRAN-based, having vastly different data structures and I/O, and unique and inconsistent user interfaces resulting in long learning curves and difficulties in usage. This is true of the codes implementing the various computational electromagnetics (CEM) and thermomechanics (TM) formulations. Manual manipulation of data from code to code is required to ensure validity of the input. Coupled with the difficulty of graphically viewing the geometry and translating it to an analysis model, the result is numerous opportunities for the introduction of human errors into the design process. This situation also adversely affects the cost (human and software/hardware) of maintaining and extending design capabilities as the theoretical foundation and design needs advance. The Research and Engineering Framework (REF) provides a coherent, integrated design environment which is the first step toward addressing the above problems. Although the REF was initially developed to address the problems of the U.S. power tube industry, the underlying framework is open; it can accommodate a broad range of scientific and engineering disciplines, including antenna design.

During the past year, Raytheon developed a prototype antenna design system based on the REF. While the framework had been used elsewhere for power tube design, this was the first usage in the antenna community. The prototype used a data dictionary developed by DSA (under contract from the Air Force Rome Laboratory) to integrate three regularly used analysis codes into the framework. These codes did not previously share data in an electronic manner nor was visualization of the code output an easy matter. The goal of the prototype was to use the REF to solve these problems and provide a basis for estimating the effort required for full integration of the antenna community's codes.

Earlier papers presented at ACES and IEE CEM conferences[1-6] and an article in the ACES Newsletter[7] provided an overview of how the REF could be applied to computational electromagnetics. This paper expands on that concept to provide the results of the first real application of the REF to antenna design at Raytheon Company.

* Work supported by the Naval Research Laboratory, Contract #N00014-94-C-2064, Raytheon's RESCAD IR&D Initiative and technical support from Mr. Kenneth Siarkiewicz, Rome Laboratory.
§ Permanent Address: Raytheon Co., 50 Apple Hill Dr. T3MR8, Tewksbury, MA 01876
† Permanent Address: Raytheon Co., 528 Boston Post Rd., Sudbury, MA 01776
‡ Permanent Address: Naval Research Lab., Code 6840, Washington, DC 20375-5347

BACKGROUND

The Research and Engineering Framework (REF) was developed as part of the DoD MMACE Program. The MMACE program has been underway for over four years and is now in its second phase. The first phase, which began in 1992, was an investigation phase. Four teams were put in place to study the problems of the Microwave Power Tube industry and develop roadmaps for the implementation of a framework to address those problems. The teams found an existing design environment that: was based largely on in-house developed software; was largely unsupported by commercial vendors; did not take advantage of the latest advances in CAD, visualization, database technology, and networking; was addressing technically difficult problems; contained a collection of tools that were not well integrated with each other; and was crucial to projects deemed important to the US government. While these items were true of the power tube industry, the same can be said of many specialized scientific disciplines including antenna design. The MMACE Program has now had its third major software release and will soon start its third phase which will focus on 3D design.

In 1994, the Air Force Rome Laboratory expressed interest in extending MMACE to accommodate the requirements of the antenna design community. The idea was to use the REF as the basis for an antenna design environment into which the various antenna codes can be inserted as shown in the following diagram.

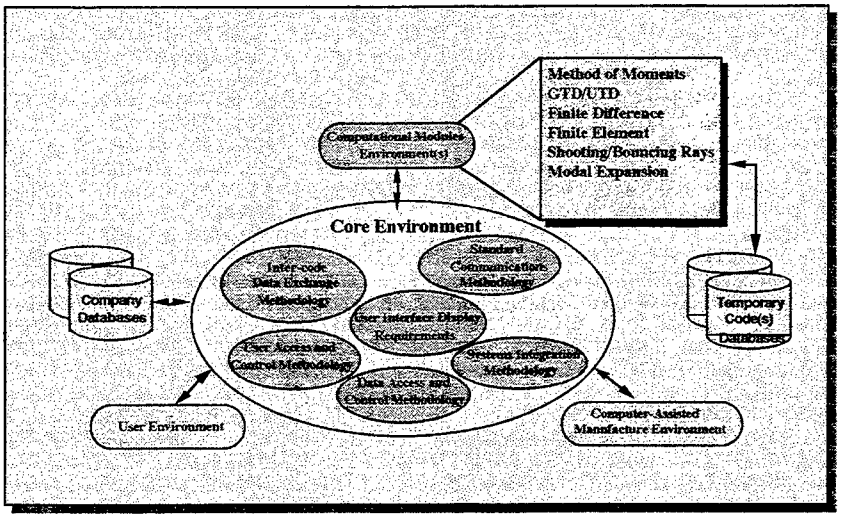

Source: EMCC Conference, 1995, K. Siarkiewicz, Rome Laboratory

While Rome Laboratory may at some point integrate many of the Air Force codes into the REF, they would not be integrating the specific, proprietary codes used within Raytheon. Therefore, Raytheon funded this activity themselves. A prototype was developed in 1996 and a full implementation is now underway.

REF ANTENNA ENVIRONMENT

Several steps were required in order to utilize the REF for antenna design. These steps were:

1. Instantiation of one antenna design flow into the MMACE control panel.
2. Development of a data dictionary for the codes to be integrated. This data dictionary was based on one developed by Rome Laboratory for antenna design.
3. Development of code wrappers.
4. Data visualization software to graphically view the output of an analysis.
5. Testing and validation.

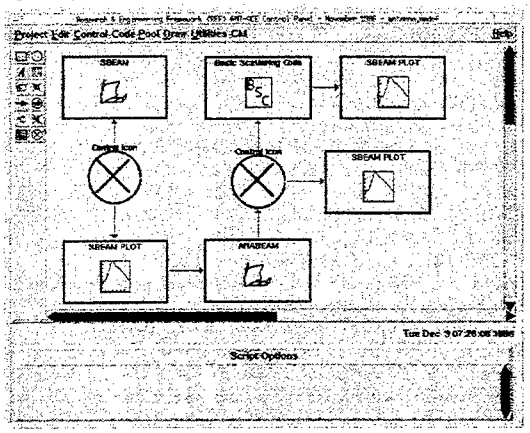

To instantiate the design flow into the REF Control Panel, Raytheon first needed to define its development process. Once this was complete, a subset of the process was selected for incorporation into the REF. The three tools selected were:

1. SHAPEBEAM & ANABEAM - A code for the synthesis and analysis of doubly-curved shaped beam antennas.
2. BSC - A basic scattering code
3. PMM - A code for the analysis of frequency selective surfaces using periodic moment method.

These three codes together are used regularly to perform antenna designs and analyses. When we started the REF prototype effort, these codes did not share data in an integrated manner. Icons were created to represent each of the design tools and these icons, and their associated visualization tool icons, were placed appropriately on the REF control panel canvas. This resulted in a screen similar to that shown in the figure above.

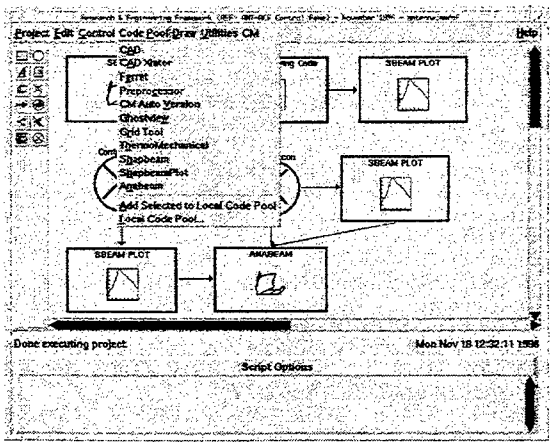

The circular icons containing the large "X" are control icons instructing the REF to execute several iterations of the code varying a certain set of input parameters until a set condition is reached. In order to make the selection and placement of tool icons easier, the control panel's "Code Pool" menu was modified so that the antenna design tools were listed. This is shown in the figure to the left.

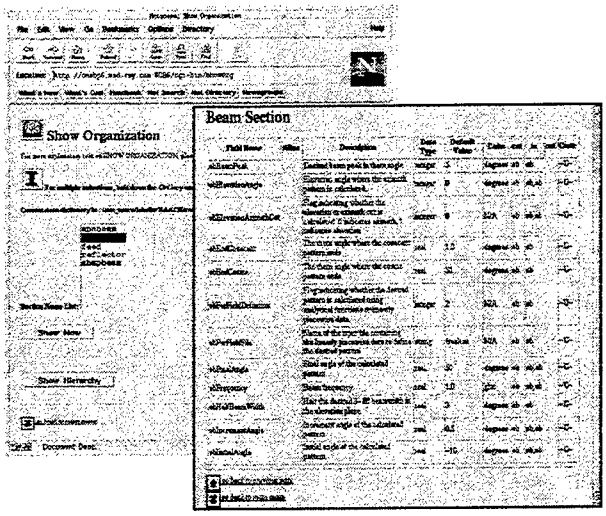

In order to link the codes together in an integrated manner, a data dictionary was needed. This dictionary defines the data attribute names, description, data type, constraints, etc. The dictionary provides a common understanding of the entities created and used by the various design tools. In essence, it defines the names of the entries in the REF database. To construct this dictionary, the REF Data Dictionary Support Software was utilized. This web-based software allows the information to be easily entered, viewed and modified. It can also automatically create the required tables in a relational database if desired. A fragment of the data dictionary that was created is shown in the figure above.

Once the data dictionary was complete, code wrappering could begin. The REF code wrappers are constructed in two parts. The first part, called GUIWRAP, extracts from the REF database all of the data attributes needed by a code and displays them for possible modification by the user. The person wrappering the code can easily specify the format that data should be displayed, the constraints on data input, and even the units used to display the data (even if those units differ from those used for the physical storage in the REF database). In addition, the person wrappering the code can specify that mathematical formulations of the data should be done before it is displayed. An example of a portion of the GUIWRAP display for the Anabeam code is shown in the figure to the right.

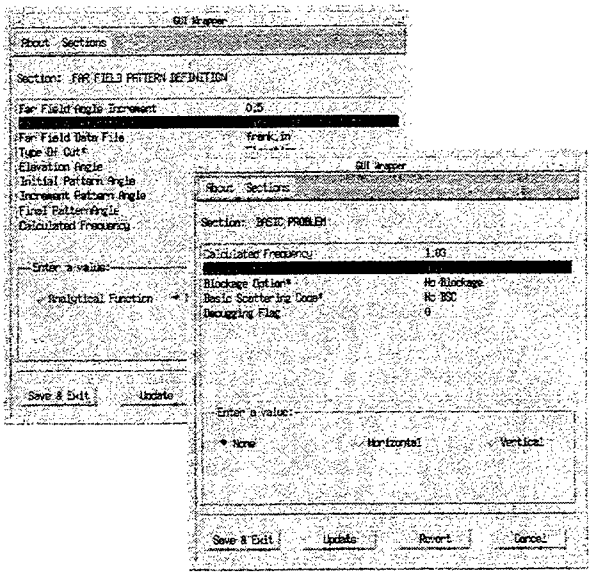

Once the user has validated the code's input parameters, the second portion of the wrapper, called FILEWRAP, is automatically executed. This portion of the wrapper extracts the data needed by the code from the REF database and constructs the code's input file in its native format (the opposite is done when the code completes). This requires a mapping of the code input and output files to the data dictionary. The diagram below illustrates how the Air Force planned to wrapper the GEMACS code. The codes wrappered under this task were wrappered in a similar manner.

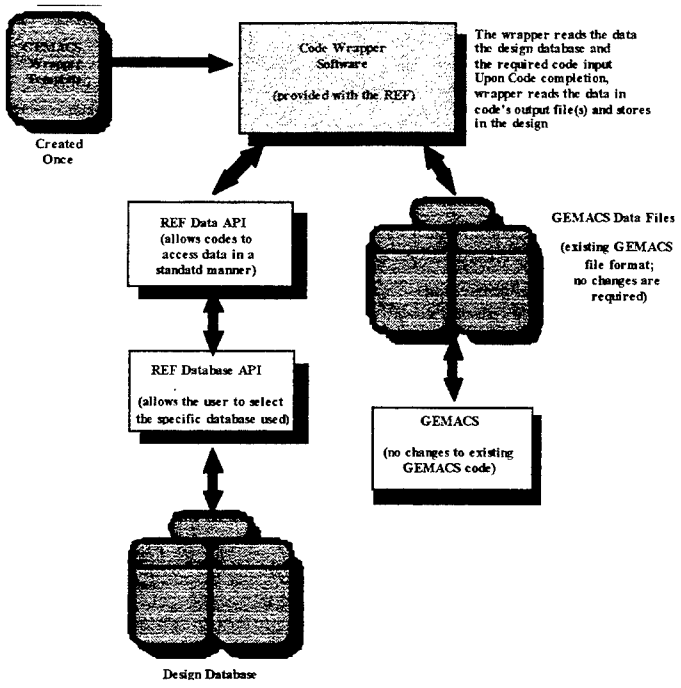

Once the codes were wrappered into the REF, Raytheon used the REF's standard visualization capabilities to display the code output. The REF includes a fairly sophisticated visualization tool, FERRET, which could easily render the data required by Raytheon's antenna designers. FERRET scripts were constructed to read the code output in its native format and display it in the desired manner. Previously, data visualization from these codes was done using DISSPLA. Designers found DISSPLA difficult to use, especially if one wanted to display the data in a slightly different format, overlay different plots, or add simple textual annotation. These limitations were easily overcome with FERRET. An example of the FERRET output generated by the codes is shown in the figure below.

SUMMARY

Raytheon has successfully integrated three antenna design tools into the REF with great success providing engineers with a cohesive design environment, data management facilities, data visualization utilities and a

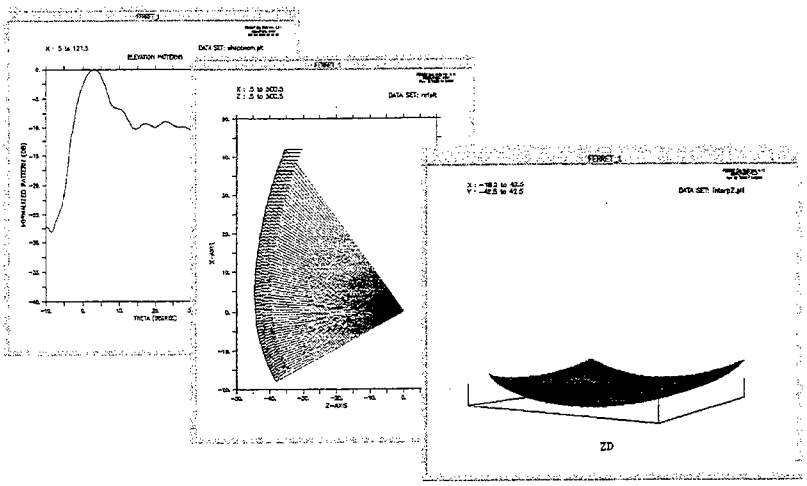

graphical view of the design process. This was the first use of the REF for a design discipline other than power tubes. The effort required to integrate the tools was straightforward and proceeded with very few problems encountered. The flexibility and utility of the REF was evident by the ability to integrate the three tools in a very short amount of time. Raytheon is now going ahead with a full implementation of the REF for use in the antenna design area and does not foresee any major obstacles.

REFERENCES

1. Siarkiewicz, K. "The Electromagnetic Modeling and Simulation Environment for Systems (EMSES)." *9th Annual Review of Progress in Applied Computational Electromagnetics Conference Proceedings*, March 1993, pages 114-121.
2. Siarkiewicz, K. "Further Considerations Regarding the Electromagnetic Modeling and Simulation Environment for Systems (EMSES)." *10th Annual Review of Progress in Applied Computational Electromagnetics Conference Proceedings*, Volume II, March 1994, pages 86-93.
3. Hantman, B et. al. "Research and Engineering Framework (REF) for Computational Electromagnetics." *11th Annual Review of Progress in Applied Computational Electromagnetics Conference Proceedings*, Volume I, March 1995, pages 118-125.
4. Woo, L. W. et. al. "Standardized Grid Generation for the Research and Engineering Framework." *11th Annual Review of Progress in Applied Computational Electromagnetics Conference Proceedings*, Volume I, March 1995, pages 135-142.
5. Woo, L. W. et. al. "Continuing Development of the Research and Engineering Framework (REF) for Computational Electromagnetics." *Proceedings of the IEE 3rd International Conference on Computation in Electromagnetics*, April 1996, pages 96-101.
6. Hantman, B. et. al. "Overview of the Research and Engineering Framework (REF) for Computational Electromagnetics." *12th Annual Review of Progress in Applied Computational Electromagnetics Conference Proceedings.*
7. Siarkiewicz, K. et. al. "Computational Electromagnetics Using the Research & Engineering Framework as a Backbone." *Applied Computational Electromagnetics Society Newsletter, Volume 10, Number 3*, November 1995.

AN ALGORITHM FOR SOLVING COUPLED THERMAL AND ELECTROMAGNETIC PROBLEMS

Harold A. Sabbagh, Lai Wan Woo, and Xun Yang*
Sabbagh Associates, Inc., 4635 Morningside Drive, Bloomington, IN 47408, USA
* Permanent address: Indiana University Cyclotron Facility

1. Introduction. The design of microwave components is driven by electromagnetic considerations, but these devices always fail because of thermomechanical weaknesses. Therefore, it is necessary to apply concurrent engineering principles early in the design phase to ensure that all aspects of the design are being met. This includes, of course, the underlying electromagnetic requirements, as well as thermomechanical considerations. In order to address the concurrent design process, we develop an algorithm that allows the solution of coupled thermal and electromagnetic problems using the finite-element technique, and demonstrate it on a canonical problem. The algorithm proceeds recursively, first solving an electromagnetic problem, and then a thermal problem. If the parameters vary with the field variables (that is the equations are nonlinear), as they are in the model problem that we solve, then it is necessary to interpolate data as a function of both thermal and electric fields during the iterations. We use two-dimensional non-uniform rational B-splines (NURBS) to accomplish this task. We have tested the convergence of the algorithm for two different problems, over a range of parameters, and have found that the algorithm behaves stably. The convergence may be slow for some purposes, so we introduce the theta-algorithm in order to accelerate the convergence. By using this algorithm we are able to quickly gain at least a two-orders of magnitude improvement in achieving the limit. We then discuss some interesting results that indicate that the grid requirements for the thermal and electrical problems may be distinctly different, based solely on the nature of the nonlinearity of the problem, rather than on the geometry or boundary conditions.

2. A Coupled CEM and Thermal Problem. This problem, which is shown in Figure 1, is a simplification of the problem studied in [1]. It is basically an 'infinite', parallel-plate, axisymmetric capacitor, whose dielectric is barium titanate $BaTiO_3$. The problem is nonlinear; the conductivity of $BaTiO_3$ is a function of temperature and electric field, as illustrated in Figure 2 [1].

The material constants are as follows:

Material Constants for Barium Titanate [1]

σ (S/m)	λ (W/mK)	$c\rho$ (J/m^3K)	a (W/m^2K)
—	4.5	3.00×10^6	20

The thermal boundary conditions shown in Figure 1 correspond to having having the top and bottom surfaces insulated, and the lateral surface cooled by convection, with the convective coefficient equal to a. The convection boundary condition is often referred to as a mixed boundary condition of the third kind. The condition at the radius, $r = 0$, is that there is no heat flux in the radial direction. The larger a is, the steeper will be the thermal gradient in the radial direction, and this will have an effect on the meshing requirements for the thermal problem, even though the electrical problem will have a rather uniform field. Homogeneous (Neumann) boundary conditions, in which the normal derivative is specified, indicate that the surface is insulated, in the case of a thermal problem, and that there is no electric current flowing through that surface, in the case of an electric problem.

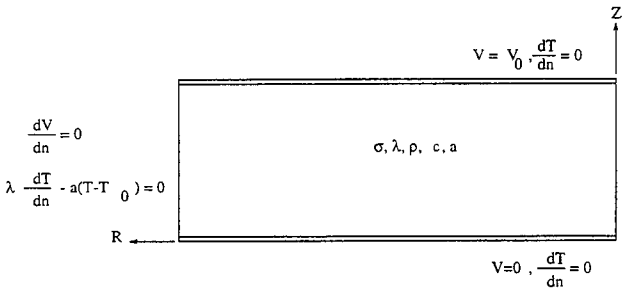

$$\nabla \cdot (\sigma \nabla V) = 0$$

$$\nabla \cdot (\lambda \nabla T) + \rho c \frac{dT}{dt} = \sigma (\nabla V)^2$$

$$\sigma = \sigma(T,E)$$

Figure 1: An axisymmetric coupled CEM and thermal problem. The electrical conductivity is a function of temperature and electric field, which makes the coupled problem nonlinear.

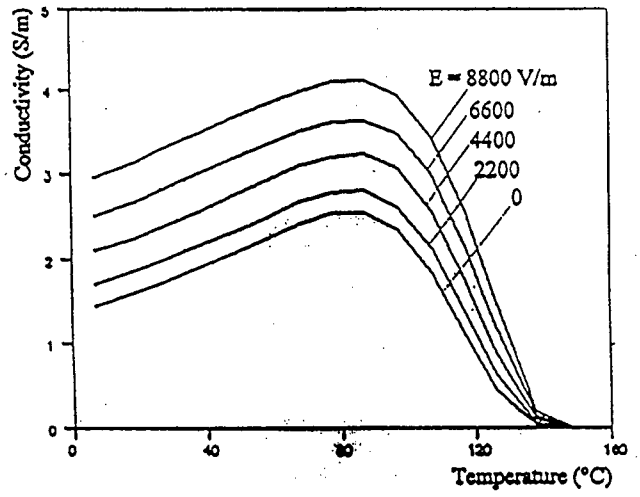

Figure 2: Electrical conductivity of Barium Titanate as a function of electric field and temperature [1].

This problem requires only a Poisson (or Laplace) solver to compute the electric and thermal fields; hence, we can use TOPAZ3D [2], a three-dimensional, implicit, finite-element code for solving thermal problems (or general Laplace-Poisson equations), to do the entire coupled problem.

3. An Algorithm for Solving Coupled Nonlinear Problems. An algorithm for solving the coupled nonlinear problems 2 and 3 is presented in Figure 3, and is explained by the following steps:

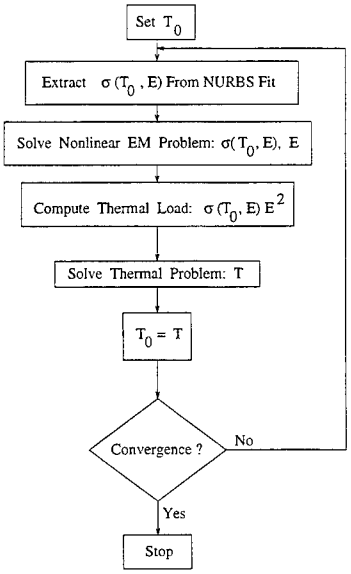

Figure 3: An algorithm for solving coupled nonlinear CEM/TM problems.

1. **Data Fitting:** Using a constant value of temperature, perform a NURBS (Non-uniform Rational B-Spline) fit to the conductivity data as a function of electric field.
2. **Electrical Problem:** Solve, $\nabla \cdot (\sigma \nabla V) = 0$, with a nonlinear conductivity, that depends only upon the electric field: $\sigma = \sigma(\mathbf{E})$.
3. **Thermal Problem:** Using $\sigma(\nabla V)^2$ as the distributed thermal load, compute the temperature, T. Use constant values for λ, ρc, and a, as given in the table of material constants.

4. Analysis of Nonlinear Coupled CEM and TM Problem. The coupled problem will be solved on the axisymmetric grid shown in Figure 4. The numbers to the left and below the figure label the rows and columns, whereas the other numbers label the nodes of the grid.

In applying the algorithm of Figure 3, we start with the trial temperature of 20° C, which from Figure 2 produces the following interpolated conductivity data:

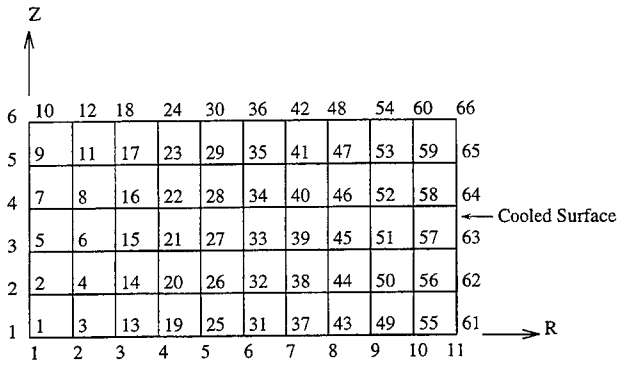

Figure 4: An axisymmetric grid for the coupled EM-TM problem.

$$\begin{aligned} \sigma &= 1.67 \quad \text{for } E = 0 \\ &= 1.85 \quad \text{for } E = 2200 \\ &= 2.3 \quad \text{for } E = 4400 \\ &= 2.72 \quad \text{for } E = 6600 \\ &= 3.2 \quad \text{for } E = 8800 \end{aligned}$$

The first two steps of the algorithm are illustrated next:

Step I: Solve $\nabla \cdot (\sigma \nabla V) = 0$ (A nonlinear EM problem)

$\sigma = \sigma(E, T)$ at $T = T_0 = 20°$ C

Let $T_i = 20°$ C, $T_a = 20°$ C, and $a = 20$, $V_0 = 1$ Volt

Result is $E = 6.6814 \times 10^2$ V/m, uniformally distributed throughout the material

$\sigma(T = 20°, E = 668.14) = 1.72$ (interpolated from graph)

Step II: Solve $\nabla \cdot (\lambda \nabla T) = \sigma(\nabla V)^2$ (A linear TM problem)

$T_i = 20°$ C, $T_a = 20°$ C, $a = 20$, $\lambda = 4.5$ (independent of T or E)

thermal load: $\sigma(\nabla V)^2 = 1.72 \times (668.14)^2 = 7.68 \times 10^5$ Watts/m^3

In order to proceed into the third step, which is another electrical problem, we must decompose the original body into ten parts, in order to accomodate TOPAZ3D. Each part corresponds to one of the columns of the grid.

Step III: Solve $\nabla \cdot (\sigma \nabla V) = 0$ (A nonlinear EM problem)

$\sigma = \sigma(E, T(r)) = \sigma(E, r)$ (electrically inhomogeneous body because of temperature variation)

The results of this step are then input to a fitting program that uses DT_NURBS [3] to interpolate the conductivity data, and produces the thermal load for the next thermal problem. The result after that cycle and the next few iterations follows:

Node No.	Temp	E(V/m)	Temp	E(V/m)	Temp	E(V/m)	Temp
1	44.665	823.22	46.197	833.215	45.761	830.415	46.034
3	44.560	823.02	46.090	832.815	45.649	830.015	45.924
13	44.316	822.02	45.839	831.616	45.389	828.815	45.667
19	43.920	820.02	45.433	829.616	44.967	826.615	45.250
25	43.370	817.02	44.869	826.616	44.382	823.416	44.672
31	42.667	813.02	44.151	822.416	43.637	819.215	43.935
37	41.812	808.22	43.279	817.415	42.734	814.015	43.043
43	40.807	802.42	42.259	811.615	41.677	807.815	41.991
49	39.655	795.62	41.096	804.615	40.472	800.619	40.808
55	38.358	787.82	39.794	796.815	39.123	792.615	39.477
61	36.922	783.62	38.360	792.819	37.638	788.415	38.011

5. Another Analysis of the Nonlinear Coupled CEM and TM Problem. We revisited the last problem, but with a new conductivity profile, in which the values shown in Figure 2 are all multiplied by 10. Furthermore, we raised the value of the convection coefficient, a, to be 200. Our interest is in seeing if there are significant changes in the way the algorithm of Figure 3 must be applied, or if there are significant changes in the solution for the electric and temperature fields.

When we applied the algorithm in the same manner as before, we found that the convergence was unaffected, and that the results, as shown in Table 1, were quite reasonable. The first row associated with each node corresponds to the temperature at that node, and the second row the electric field. Hence, we conclude that the algorithm performs stably over a wide range of material and physical parameters for this problem.

It is clear from these two examples that, though the algorithm converges, it does so slowly. To be sure, the results could be useful for some engineering design purposes after only two or three iterations, but it would be attractive to be able to estimate the limit of the sequence of iterations. There are a number of sequence-accelerating algorithms that exist in the mathematics literature, and one that we have applied to this problem is called the θ-algorithm [4], which is defined by:

$$\begin{aligned}
\theta_{2k+2}^{(n)} &= \theta_{2k}^{(n+1)} + \frac{\left[\theta_{2k}^{(n+2)} - \theta_{2k}^{(n+1)}\right]\left[\theta_{2k+1}^{(n+2)} - \theta_{2k+1}^{(n+1)}\right]}{\theta_{2k+1}^{(n+2)} - 2\theta_{2k+1}^{(n+1)} + \theta_{2k+1}^{(n)}} \\
\theta_{2k+1}^{(n)} &= \theta_{2k-1}^{(n+1)} + \frac{1}{\theta_{2k}^{(n+1)} - \theta_{2k}^{(n)}} \\
\theta_{-1}^{(n)} &= 0 \\
\theta_{0}^{(n)} &= S_n
\end{aligned}$$

In Table 2 we include the results of applying it to the iterations shown above for Node No. 1:

Note that the initial data, $\theta_0^{(n)}$, which are the results of the TOPAZ iterations, still differ by 0.2024 after twenty-two iterations. After fourteen stages of application of the theta algorithm, however, the difference between $\theta_{14}^{(0)}$ and $\theta_{12}^{(0)}$ in the top row[1] is only 0.13×10^{-2}, which means that we have reduced the error by more than two orders-of-magnitude. Because the theta algorithm is quite fast, we can recommend it for application to iterations of this sort. This algorithm has been applied to the computation of Green's function in electromagnetic problems [5].

[1] Convergence of the θ-algorithm is along this row.

Table 1: Results of Iterative Solution Algorithm.

	Iteration No.							
Node No.	1	2	3	4	5	···	21	22
1	23.2023	27.8183	23.6086	26.9054	23.9475	···	24.9543	25.1567
	68.80	71.72	69.08	71.16	69.28	···	70.08	69.92
3	23.1951	27.8122	23.6018	26.8993	23.9408	···	24.9479	25.1503
	68.80	71.72	69.08	71.16	69.28	···	70.08	69.92
13	23.1782	27.7981	23.5858	26.8850	23.9252	···	24.9330	25.1355
	68.80	71.72	69.06	71.14	69.28	···	70.06	69.92
19	23.1508	27.7751	23.5597	26.8617	23.8998	···	24.9087	25.1114
	68.80	71.70	69.04	71.12	69.26	···	70.04	69.92
25	23.1127	27.7431	23.5235	26.8294	23.8644	···	24.8750	25.0778
	68.78	71.68	69.02	71.12	69.24	···	70.02	69.88
31	23.0638	27.7021	23.4771	26.7879	23.8191	···	24.8317	25.0348
	68.74	71.66	69.00	71.10	69.22	···	70.00	69.86
37	23.0041	27.6521	23.4204	26.7373	23.7638	···	24.7789	24.9823
	68.70	71.64	68.98	71.06	69.18	···	69.98	69.82
43	22.9337	27.5631	23.3535	26.6776	23.6985	···	24.7165	24.9203
	68.66	71.60	68.94	71.02	69.14	···	69.94	69.78
49	22.8526	27.5250	23.2765	26.6088	23.6232	···	24.6447	24.8489
	68.62	71.56	68.90	70.98	69.10	···	69.90	69.74
55	22.7608	27.4480	23.1892	26.5309	23.5381	···	24.5634	24.7681
	68.56	71.52	68.84	70.94	69.06	···	69.86	69.70
61	22.6583	27.3621	23.0918	26.4440	23.4430	···	24.4726	24.6779
	68.52	71.48	68.80	70.92	69.04	···	69.84	69.68

6. A final analysis of the nonlinear coupled problem. In this final study, we attempt to force a condition that might require different grids to be used for the electrical and thermal analyses. That is, we seek conditions on the various parameters of the problem that would cause the gradient of one field to greatly exceed that of the other. Our approach is purely empirical, but it is guided by the guess that we will need to operate in that range of Figure 2 for which conductivity changes rapidly with temperature. This is above the knee, which is roughly 100°C. In this region of operation, a small change of temperature ought to produce a large change in electric field.

Our results are summarized as:

(a) In the range $0°C < T < 100°C$, for example when T is about 60 °C and E is about 1170 V/m, the largest change of temperature between two adjacent nodes is 2.7% and the largest change of electrical field is about 0.7%; there is no need to change the grid.

(b) In the range $100°C < T < 140°C$, for example, when T is about 120 °C and E is about a few hundred V/m, the largest change of temperature between two adjacent nodes is 3.4%, and the largest change of electrical field is about 20%. In this case, it may be necessary to use two different grids to solve the electrical problem and the thermal problem.

Now we consider the key parameters that may force one to use different grids. According to the results that are mentioned above, we know that when the temperature is above 100°C, a slight change of temperature will cause a large change of electric field, and this is due solely to the

Table 2: Result of θ-Algorithm Iterations.

n	$\theta_0^{(n)}$	$\theta_2^{(n)}$	$\theta_4^{(n)}$	$\theta_6^{(n)}$	$\theta_8^{(n)}$	$\theta_{10}^{(n)}$	$\theta_{12}^{(n)}$	$\theta_{14}^{(n)}$
1	23.2023	25.5301	25.1896	46.7976	25.2572	25.0773	25.0772	25.0785
2	27.8183	25.3972	26.3146	25.5808	25.0772	25.0773	25.0775	
3	23.6086	25.3042	25.1399	24.9870	25.0773	25.0778	24.8970	
4	26.9054	25.2375	24.7454	25.0774	25.0772	25.1448	25.0262	
5	23.9475	25.1883	25.0401	25.0772	24.9579	25.0097		
6	26.3346	25.1534	25.0753	25.0750	25.0154	25.0789		
7	24.2122	25.1282	25.0785	25.0218	25.0510	25.0604		
8	25.9539	25.1088	25.0601	25.0787	25.0801			
9	24.4269	25.0951	25.0741	25.0499	25.0694			
10	25.6894	25.0859	25.0794	25.0693	25.0638			
11	24.5870	25.0797	25.0700	25.0651				
12	25.5126	25.0759	25.0685	25.0638				
13	24.7083	25.0721	25.0643	25.0638				
14	25.3907	25.0678	25.0638					
15	24.8017	25.0649	25.0638					
16	25.2943	25.0638	25.0638					
17	24.8690	25.0638						
18	25.2291	25.0627						
19	24.9231	25.0618						
20	25.1837							
21	24.9543							
22	25.1567							

nonlinearity of the material. One must consider several factors in order to get the temperature above 100°C for this particular material, but the thermal load ($\sigma(E,T)*E^2$) is the most important one. The ambient temperature, initial temperature, and convection coefficient also play key roles in this problem.

For instance:

(a) When the thermal load is about 3.0×10^6 to 4.0×10^6, we need to consider using different grids. It doesn't matter what the ambient temperature is as long as the convection coefficient is small enough to keep the temperature in the range between 100°C and 140°C. For this particular type of material, if we rescale the electrical conductivity σ by a factor of 1.67, the thermal load will then be in the range of 3.0×10^6 to 4.0×10^6, and the results shown in the second table are obtained (a relatively big change in E-field and small change in T).

(b) If the ambient temperature is in the region of 100°C to 140°C, and if the convection coefficient is large enough to keep the temperature within the body close to the ambient temperature, then it may be necessary to use different grids for the T and E calculation. Ambient temperatures, however, are normally around 20°C, so that this case is rare.

(c) In conclusion, therefore, the question of whether or not to change the grid for the E and T calculation depends upon the nonlinearity of the material for a problem with a simple geometry, such as the one that we just solved. For problems with more complex geometries

or boundary conditions, however, the situation may be quite different and further studies should be done.

7. Acknowledgement. This work was supported by The U. S. Air Force (Rome Laboratory) under Contract No. F30602-95-C-0249. The final report [6] of that contract contains a greatly expanded version of the present paper.

References

[1] K. Preis, O. Biro, R. Dyczij-Edlinger, K. R. Richter, "Application of FEM to Coupled Electric, Thermal and Mechanical Problems," IEEE Trans. Magnetics, Vol. 30, No. 5, September 1994, pp. 3316-319. Also, Int. J. Applied Electromagnetics in Materials, Vol. 3, (1992), pp. 151-155.

[2] A. B. Shapiro, "TOPAZ3D–A Three-Dimensional Finite Element Heat Transfer Code," University of California, Lawrence Livermore National Laboratory Rept. UCID-20484 (1985).

[3] *dtnurbs: Spline Geometry Subprogram Library - Reference Manual*, Carderock Division, Naval Surface Warfare Center, Bethesda, MD 20084-5000, Version 3.1, CARDEROCKDIV-94/000, November 1995.

[4] J. Wimp, *Sequence Transformations and Their Applications.* New York:Academic Press, 1981.

[5] S. Singh and R. Singh, "A Convergence Procedure for Computing Slowly Converging Series," IEEE Trans. Microwave Theory and Techniques, Vol. 40, No. 1, January 1992, pp. 168-171.

[6] H. A. Sabbagh, Lai Wan Woo, and Xun Yang, "Algorithms and Software Requirements for Solving Coupled Microelectronics Problems," Final Report Contract No. F30602-95-C-0249, 7 October 1996.

Computational Electromagnetics' Future Database Architecture

Gerard T. Capraro, Capraro Technologies, Inc. 311 Turner Street-Suite 410 Utica, NY 13501 and
Kenneth Siarkiewicz, USAF/Rome Laboratory Rome, NY 13441

Abstract This paper provides an update to papers previously presented at earlier ACES symposia[1-4]. Those papers laid a foundation for the use of a Research and Engineering Framework (REF) for interfacing a number of computational electromagnetics (CEM) formulations and codes. This paper presents a process of implementation which can lead to the reality being proposed. Furthermore, this paper shows how the CEM analysis results can be integrated with the results of analyses performed by other engineering disciplines, all of which are needed to develop a system (e.g., the location of an antenna on an aircraft to maximize performance and minimize interference). The authors maintain that the paradigm of concurrent engineering is the way of the future, which is being driven by increasing system complexity and decreasing system development dollars.

Acknowledgments This paper describes work performed under Rome Laboratory Contract F30602-95-C-0109 and also supported by Rome Laboratory in-house funding. The REF is being developed under NRL contract N00014-94-C-2064 in support of the Tri-Service Vacuum Electronics Initiative.

1. Introduction The Integrated Computational Environment (ICE) is an approach for designing and modeling components, boards, boxes, line replaceable units (LRU), subsystems and systems for the USAF. The Department of Defense (DoD) is slowly moving towards the use of modeling and simulation techniques for fulfilling part of the functions that have been performed by military specifications and testing. The old approach was based upon the premise that if each component met the military's specifications then when the full system was integrated it would meet the military performance and environmental conditions. This approach in many cases led to over-designed components and increased costs because the commercial market did not require these designs and could not afford the extra quality. The trend of using commercial parts, when shown feasible through analysis, modeling and simulation, should bring the cost of military systems down by making use of less costly commercial off-the-shelf (COTS) hardware and software.

2. Overview The Rome Laboratory is developing technology to help design and build new or improved weapon systems with the highest reliability, compatibility, and maintainability while using commercial components and minimizing costs. The military acquisition process for purchasing systems with military specifications and standards will be changed over the next few years. Methods to integrate commercial components into military systems will rely heavily on computer modeling and simulation as opposed to standards and testing.

An approach to facilitate this transition to and use of computer modeling and simulation is to define a unified design and implementation of an Integrated Computational Environment (ICE). This computational framework will provide a consistent and obtainable database, describing an overall system, its components, and its environment, and will provide the capability of integrating Government and commercial data, modeling, and simulation tools. The ICE should be relatively transparent to the current tools and methods that are in practice. In addition, it will provide a compatible framework for integrating the different databases, tools, models, and simulation packages, such that well-defined interfaces can be established and controlled for a more efficient, timely, and accurate exchange of data. A conceptual vision of the ICE is shown in Figure 1.

The ICE will interface functional models, support models, and theater-level deployment models. Functional models are those models used to develop the components of a system to meet a system's primary performance requirements. The throughput of a computer, the sensitivity level of a communications receiver, and the radiated power of a radar are examples of system components' primary performance requirements. The support models are those models that are concerned with a component meeting a system's secondary set of requirements. These are usually related to environmental concerns such as mechanical, thermal, and electromagnetic. Theater-level deployment models are related to that process of evaluating new or unavailable components to determine their performance in actual and varied deployment environments. These models may be strictly digital simulations or they may be composed of a mixture of actual components, digital simulation models, and components which emulate other components. With the proliferation of computers within most military systems and the reduced DoD budget, it is becoming more common for the military to exercise theater-level simulation and/or emulation models to evaluate new or proposed military systems rather than building a prototype system.

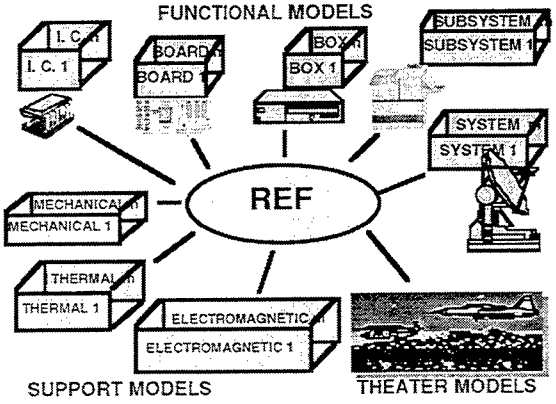

Figure 1. ICE Concept

The development and deployment process of a new system, e.g., radar, aircraft, or missile, is very complex and involves many people with varied capabilities and objectives. It usually requires a prime contractor and several subcontractors with many people at different locations. These people can be divided into three basic groups based upon their interests. Group 1 consists of those people interested in building a system's components, e.g., high power tubes, processors, amplifiers, sensors, power supplies. An example may be a sub-contractor or a component provider or supplier. Group 2 consists of those people interested by technology or support function, e.g., circuit design, thermal, electromagnetic, structural, signal processing, communications, radar, contracts, legal, accounting. Group 3 are those people interested in the system-level effects of integrating a system within the deployment environment; e.g., system simulations, system emulations, battlefield simulations/emulations. These three groups can be partitioned further by the data required of the computer applications or codes used in an individual's level or type of analysis, e.g., the CEM area is composed of codes like GEMACS, low frequency codes (e.g., NEC-MOM), high frequency codes (e.g., NEC-BSC), etc.

Consider the potential benefits gained if the data requirements of these different groups were consistent, computerized, secure, and instantly accessible anywhere throughout the world. Connection to a global database from any terminal with a modem would allow for the retrieval of the most detailed data instantly. This capability would reduce the cost and compress the schedule of system development, deployment, and maintenance throughout a system's life cycle, while enhancing performance and safety. The computer technology to accomplish this is here today; but the methods and tools for integrating the data among the three different groups is not in place. As an example consider Figure 2.

Figure 2 illustrates an approach for integrating a collection of heterogeneous databases from the bottom up. The bottom portion of the above diagram depicts each set of users partitioned by technology (i.e., Group 2). Each user within a technology would have a consistent database that represents any component of interest across all of the codes that are used in that technology over the life of the component. The different databases (thermal, CEM, design, etc.) would be integrated into another consistent database by the Global Database Management System (GDBMS). This allows all users access to the total database whether they are a technology modeler (Group 2), a sub-contractor (Group 1), or a Government agent assessing new technologies in a simulated battlefield environment (Group 3). Access to the data within the GDBMS can be obtained within any group given the need to know. The data can be stored at one location centrally located or across a distributed

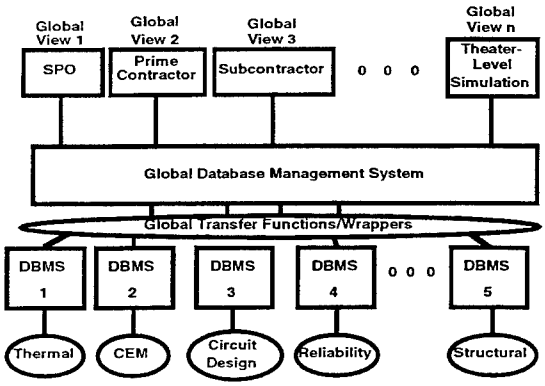

Figure 2. ICE Data Management

network of computers. Data can be obtained in "real-time" for analysis, meetings, inquires, and reporting at any location with a computer and a modem.

To obtain a consistent set of data that are available to many throughout the development and deployment of a weapon system, we must begin building a structure based upon existing data that are already being gathered by the respective groups. (See the bottom portion of Figure 2.) In modern-day systems the digitization of data usually takes place when people begin to design the system's components. They primarily use computer codes accepted by the community and/or company proprietary codes. However, it is the data, not the codes, that drive the requirements for an architecture like that shown in Figure 2. In many organizations the individual users are using their own codes and are not sharing data via a database management system. It is this level of the architecture that must be integrated first. To start the process by defining the data requirements from the users at the top level of the architecture (i.e. the global viewers at the top portion of Figure 2) would be too costly and more importantly would disrupt the current process.

The building of the architecture shown in Figure 2 begins by integrating data at the lowest of levels. How does one integrate data required by heterogeneous codes within the same technology and across multiple engineering disciplines? This area is being addressed in the Microwave/Millimeter-wave Advanced Computational Environment (MMACE) Research and Engineering Framework (REF) development program and will be discussed in the next section.

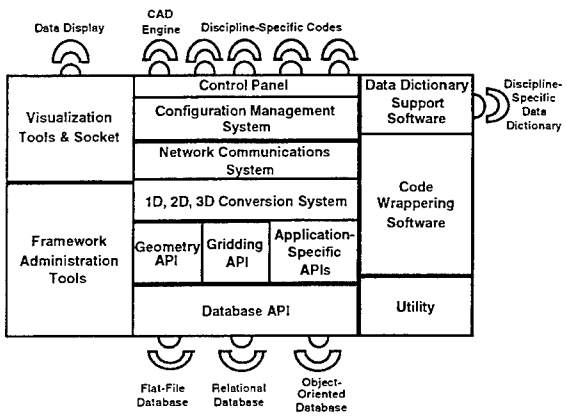

Figure 3. Framework Elements

3. Research and Engineering Framework (REF) The MMACE program is a Tri-Service and NASA initiative to improve the power tube design process. It is composed of two portions. One portion is composed of the vacuum electronics codes and tools that are used to perform the design and analysis of power tubes. The second portion is the REF which contains the programming interfaces, standards, and utilities to aid in the integration of the codes and tools. A diagram of the elements of REF is shown in Figure 3.

The REF requires a discipline-specific Data Dictionary (DD) which maintains a list of the attributes within the database. Such a data dictionary for CEM applications has been developed[5]. A DD within a DBMS stores meta data and authorization information, such as key constraints and user privileges; and it is the direct interface to the database. (Meta

data are those data about the data, e.g., an attribute's name, field type, and size of the field.) The DD within the REF only performs a bookkeeping function that allows one to query which attributes are in the database, but it is not capable of searching the database for the values of these attributes. The DD is as up-to-date as the practitioners of the discipline manually maintain its contents. This is an important issue since adding new data to the database is easy. However, changes to the database affect the DD and all wrappers interfacing codes to the database. The users must manually update the wrappers and the DD when one adds, deletes, or changes the database schema or design. This manual process could be simplified if the DD and the database were implemented with a DBMS. This would provide data independence from the application tools and the wrappers and would minimize the cost for maintaining the system. Data independence allows one to change the database design and contents while minimizing the effect to the application tools and wrappers.

Furthermore, integrating a DBMS within the REF will enhance its capabilities, reduce its maintenance cost, and increase its robustness and growth potential. Areas within the REF that can take advantage of a full DBMS are shown in Figure 4. The shaded portions indicate those areas where modifications to the REF can be performed. A portion of this integration process will be re-hosting pieces of REF on a DBMS and using commercial software tools to help integrate databases. The REF Control Panel can be enhanced allowing the user access to forms for user-friendly building of queries and reports from the DBMS. These forms would add to the current capability for executing jobs within the REF. The Data Dictionary Support Software and Discipline Specific Data Dictionary functions can utilize the DBMS's imbedded data dictionary capability, e.g., its software algorithms for defining data, setting priorities, defining key words, access control, and integrating the different data definitions within domains and between domains. Database APIs are those tools that allow for report generation and query support for the casual user and for the domain specific database administrator. The Framework Administration Tools help in maintaining data integrity and concurrent engineering functions required by the different domains. Some tools within the chosen DBMS can replace current REF tools and/or work in concert with them and add functionality.

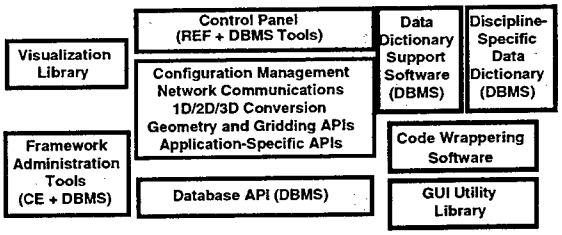

Figure 4. DBMS-Aided Elements

4. An Integrating REF Structure The previous section provided an overview and proposed a DBMS extension to the REF software architecture. This extended REF will allow it to be the foundation for integrating data from many engineering domains. This section will describe the process of how this can be accomplished.

The process of determining which attributes the codes share and how to describe them to build a common database definition requires domain-knowledgeable and database-knowledgeable people. The REF design and implementation process can be used as a foundation for a "bottom up" building of an integrated tool set and database for each technology domain. For example, the process that was developed for the vacuum electronics industry can be applied to the CEM domain. The process and the framework tools would be the same; but the individual translators, the data model, some of the utilities, and the database schemas would be different.

Consider the first step in applying the REF development process for the CEM community. This is to integrate the data from the different codes into a consistent relational DBMS (RDBMS). This will require evaluating the different codes within the technology and defining its integrated domain database. Once completed it will provide the database for CEM as shown in Figure 5.

An architecture can be developed for the CEM community by replicating the development process used by the vacuum electronics industry and by utilizing a large majority of their developed software. The user interface software, IGES standard format tools, CAD IGES translator software, and database tool suite for translators and wrappers can be used and/or modified to meet the CEM environment's specifications. The first step is to define

a homogeneous database from a collection of heterogeneous codes with varying data attributes, parameters, fields, names, etc. This process is labor-intensive and requires both domain-knowledgeable and database-knowledgeable people. The resultant effort will create a unified data dictionary definition of the data attributes used by the CEM community. Through this process the requirements for the translators will also be defined. Depending upon the codes used, the resultant Venn diagram will be similar to the one shown in Figure 6.

Once the data requirements for the CEM codes are developed, then the first portion of building a consistent data dictionary for the RDBMS will have been accomplished. The next steps will be to develop an entity relationship model for the use of the data and to complete building the data dictionary and schemas. These steps are followed by building the interface tools to read the input and output files of these codes and convert them to the definitions of the database data dictionary. Some of the tools written for the REF can be used along with commercial tools to perform these functions. These tools, translators and wrappers will help provide the consistent databases required for the RDBMS. These elements and their interrelationships are shown in Figure 7.

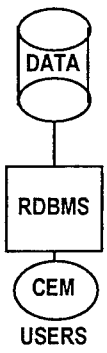

Figure 5. Integrated Database Build

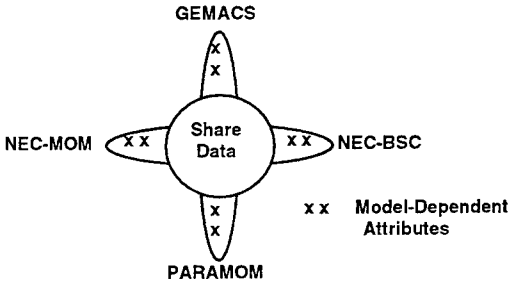

Figure 6. CEM Code Data Relationships

The integration of code data is of primary importance to ICE. It is the consistent and accurate representation of the entity under investigation that is of concern. The input/output files shown coming to/from the above codes represent the entity description data (or input data to the individual codes) and the chosen output (or analysis data). These input and output data have merit as input to other codes or for comparison with the results from other codes.

The File Translators are those codes that understand the format of the data for each of the codes and are able to select and convert each data field that has been chosen to enter into the integrated database. They are capable of converting those selected fields within each code to an intermediate standard format that can then be integrated within the database of choice. For the IGES-generated codes the translators map the different representations to a uniform IGES representation.

The Database & Tool Suite Translator/Wrapper is a set of tools to help build the data dictionary and directory for the integrated database. The term wrapper is used because it "wraps" the code in software and performs the transfer function or the data translation to and from the different databases. These are the tools that, for example, will convert the inches to centimeters, help resolve the issues as to which attributes are synonyms and homonyms, help resolve the binary variable representation, convert integers to floating point formats and load the files in the database. These tools will also help design the integrated database system and help manage the database and its meta data. Once the data are made compatible and loaded into the RDBMS, then users can obtain access to the data via the RDBMS directly. They can then perform general queries, generate reports, maintain different code representations of the entity under study as a local technology user, and they can access the Global DBMS as a Global user.

This same procedure would be applied in developing each of the engineering domains (e.g., thermal, structural). This provides the different domains with a consistent set of data within their own RDBMS.

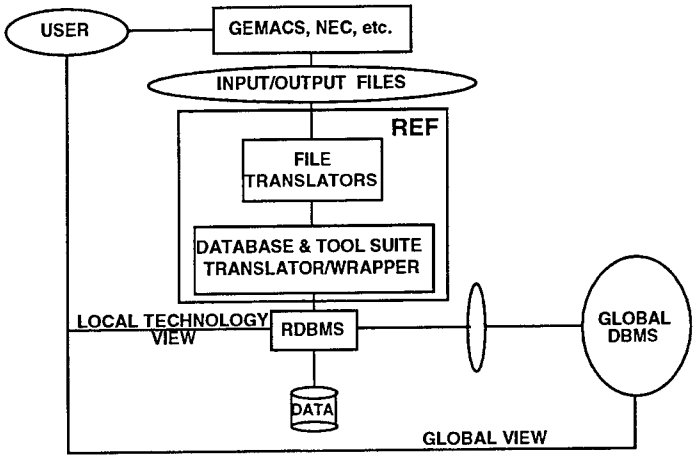

Figure 7. The REF Structure and CEM Integrated Databases

5. Integration of Multiple Domain-Specific Relational DBMSs The previous section describes how the vacuum electronics industry's REF development tools and processes can be used as a model for integrating heterogeneous databases within the CEM domain. The REF and the process described above can also be used to integrate many different technologies, as shown in Figure 8, in which the CEM and structural analysis domains are integrated.

To integrate these two domains is a matter of integrating two databases with well defined schemas and data dictionaries. Since both are assumed to be built with RDBMS SQL-compliant systems, their integration should be relatively straightforward. Data definitions, synonyms, homonyms, formats and subtle data coding differences will need to be determined and repaired based upon data and meta data intersections between the two databases. The resultant solutions will be incorporated with the global transfer functions and wrappers in a manner similar to what was described for the integration of data within the CEM domain.

6. Conclusions The implementation of an integrated architecture of distributed heterogeneous databases as discussed above has many benefits. It allows users to obtain information based upon controlled and accurate data and knowledge. It should reduce cost through the reduction in the number of databases that will be maintained. It will also increase the number of accurate knowledge bases with an inherent low maintenance cost because of its distribution and coherency. It will also provide more timely, consistent, and accurate data, knowledge, and intelligence which will be accessible by different global users. In addition it provides information lineage, in that there is a direct linkage to intelligence, knowledge, and data. One will know or can derive where and how a result was obtained.

In the future antenna engineers and system designers will need to play electromagnetic and structural considerations against each other. The aircraft manufacturer will put an antenna in one place because it minimizes drag and the location is available. The antenna designer will disagree because of blockage, diffraction, or some other electromagnetic phenomenon which decreases performance or causes unacceptable levels of interference. A counter-location will be suggested, which might be located immediately above a structural member which cannot be weakened. The trade-off discussions continue. The availability and consistency of the integrated databases and means of access will facilitate the discussion and reduce the

opportunities for continuing down a fruitless design path. Concurrent engineering is the way of the future, and the design considerations presented here will provide a means to accomplish this optimum design procedure.

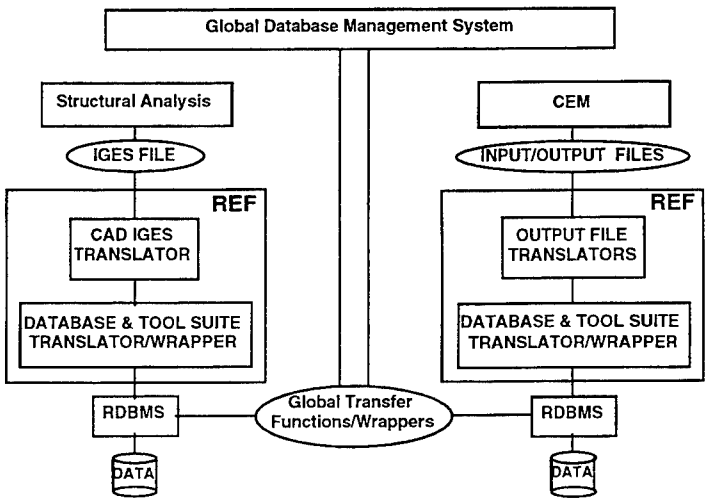

Figure 8. The REF Structure and the Integration of Two Different Database Domains

References

1. Siarkiewicz, K. "The Electromagnetic Modeling and Simulation Environment for Systems EMSES)." *9th Annual Review of Progress in Applied Computational Electromagnetics Conference Proceedings*, March 1993, pages 114-121.
2. Siarkiewicz, K. "Further Considerations Regarding the Electromagnetic Modeling and Simulation Environment for Systems (EMSES)." *10th Annual Review of Progress in Applied Computational Electromagnetics Conference Proceedings*, Volume II, March 1994, pages 86-93.
3. Hantman, B et. al. "Research and Engineering Framework (REF) for Computational Electromagnetics." *11th Annual Review of Progress in Applied Computational Electromagnetics Conference Proceedings*, Volume I, March 1995, pages 118-125.
4. Siarkiewicz, K. et. al. "Computational Electromagnetics Using the Research & Engineering Framework As a Backbone." *Applied Computational Electromagnetics Society* Newsletter, Volume 10, Number 3, November 1995.
5. Evans, J., "Research & Engineering Framework (REF) Data Dictionary Specification for Computational Electromagnetics," *12th Annual Review of Progress in Applied Computational Electromagnetics Conference Proceedings*, Volume I, March 1996, pages 340-346.

AN EXPERT SYSTEM TOOL TO AID CEM MODEL GENERATION

Andrew L.S. Drozd*
Timothy W. Blocher†
Kenneth R. Siarkiewicz§
Victor K. C. Choo*

1.0 INTRODUCTION

This paper presents an update of ongoing research and development to apply Artificial Intelligence (AI) methodologies and Expert System (ES) software technologies in the design of a smart pre-processor for government, university, and industry Computational Electromagnetics (CEM) codes. The pre-processor is called the Intelligent Computational Electromagnetics Expert System (ICEMES). Its purpose is to enhance the analyst's efficiency in generating complex CEM models and in choosing appropriate electromagnetic physics and solution techniques within the constraints of selected codes. This ongoing effort builds upon the original research and findings previously reported on in the ACES literature.[1,2] Work in progress is being funded under the DoD SBIR Program, Contract F30602-96-C-0163, Phase II for the USAF Rome Laboratory.

The intelligent pre-processor invokes modeling rules-of-thumb based on an array of CEM physics formalisms and numerical solution techniques, and, in turn generates electromagnetic structure models for corresponding CEM codes and user modeling scenarios. Discussed in this technology update is the evolution of the pre-processor design, refinements to its framework and functionality, and particularly, how it will benefit the CEM code user community at large.

1.1 Background

For all practical purposes, the "resident electromagnetics expert" is the one relied upon to undertake complex CEM modeling and analyses tasks for his/her organization on behalf of a product or customer. At times however, even the "expert" can be overwhelmed by the complexity of a given problem let alone how to best approach the electromagnetics problem-solving task. An added complication arises when the analyst finds that his/her arsenal of tools may not be well suited to the task and/or may require a great deal of proficiency. This dilemma begs for a solution, one that assures the availability of a "resident expert" and a readily usable set of tools to address CEM requirements.

Recently, there has been a great deal of interest in identifying and implementing new, effective procedures for automating CEM modeling and analyses tasks to assess antenna performance and radiation scattering in the presence of complex structures, radar cross section (RCS), intrasystem Electromagnetic Compatibility (EMC), and so on. Techniques range from the use of simplified, graphical user interfaces to highly robust, software pre-processor frameworks employing expert system engines and rule-based methods. These approaches are intended to ease burdensome modeling tasks, assist in more rapidly generating valid CEM structure models and performing complex system analyses, and reduce associated modeling/analysis uncertainties.

This paper focuses on an approach using AI/ES technologies and knowledge/rule-basing techniques to develop a state-of-the-art pre-processor that automates the CEM modeling/analysis task, and, in turn assists the novice-to-experienced engineer in efficiently addressing CEM problems. The evolving, cutting-edge capability is discussed in terms of recent architecture design and functionality enhancements, and its application to CEM problem solving by way of illustration.

*ANDRO Consulting Services, P.O. Box 543, Rome, NY 13442-0543, andro1@aol.com
†Rome Laboratory/ERST, 525 Brooks Road, Rome, NY 13441-4505, blochert@rl.af.mil
§Rome Laboratory/ERST, 525 Brooks Road, Rome, NY 13441-4505, kens@rl.af.mil
*c/o ANDRO Consulting Services, P.O. Box 543, Rome, NY 13442-0543, vchoo@mail.edgenet.net

1.2 Intelligent Pre-processing Environment

The modular, flexible framework currently under construction will readily allow a number of CEM formalisms (MoM, GTD, SBR/PO/PTD, hybrids), software codes (GEMACS, NEC-MOM, NEC-BSC, CARLOS-3D, APATCH, XPATCH, etc.), and associated constraints to be "plugged-in" or linked to the system in either a loosely- or tightly-coupled manner, as appropriate. The ability to accommodate a range of CEM physics is highly dependent upon properly generating a hierarchical and interlinked set of generic knowledge base reference objects. These consist of superior (parent) class objects, subordinate (child) class objects or items, nth-generation entities, and so on. These objects embody the essential "general" knowledge (characteristics, attributes, and parameters) common to all CEM formalisms, as well as code/data-specific knowledge (i.e., characteristics and constraints that are unique to selected CEM codes and Computer Aided Design or CAD data). Common attributes and relationships are established to "share" characteristics and eliminate superfluous parameter definitions within the knowledge base. Examples of common attributes include frequency, physical dimensions, electrical properties (conductivity, permitivitty, etc.), and a specified range of observable quantities. Fundamentally these parameters, variables, and quantities are applicable to all CEM formalisms and analysis methodologies.

2.0 ENHANCED SYSTEM FRAMEWORK AND FUNCTIONALITY

Refinements have been made to the baseline ICEMES architecture design to further enhance its modularity and functionality. These enhancements affect the configuration and integration of the following key components of the system: the CEM Knowledge Base (KB), its partitioned structure and associated rule sets; interactive geometry modeling and visualization packages; graphical user interfaces (GUIs); file/database management systems; discipline-specific data dictionary; CAD engine interface and built-in translators operating on shared, reusable data for a select range of CAD data types/formats; and other Commercial Off-the-Shelf/Non-Development Item (COTS/NDI) software used to support the system's functionality.

At the heart of the current ICEMES framework is a high-end, commercial Expert System and an Intelligent Manager operational and accessible through an interactive GUI. The Intelligent Manager provides the central link to/from all other essential components of the system. These include:

- Interactive Geometry Modeler (IGM) providing 3-D, color-rendered visualization and the ability to manipulate generated CEM structure models;
- CAD Engine Interface Translator to convert a subset of popular CAD package data formats into equivalent KB and corresponding CEM models;
- Relational Database Manager working with a discipline-specific Data Dictionary[3] to capture and store geometric as well as electromagnetic properties of a physical system; and
- File System and Support Utilities which support overall functionality, seamless data transactions and other data storage management operations.

The overall ICEMES framework showing its constituent components is illustrated in Figure 1. This figure also shows that the system can automatically launch the execution of external CEM codes, at the operator's request, under the control of the Intelligent Manager. These codes may be resident in parallelized form on a massively parallel processor or High Performance Computer (HPC, e.g., multi-node Paragon), or accessed from within a configuration of distributed workstations communicating through a central server. It is noted that ICEMES itself is being hosted on a platform running Windows NT 4.0.

The modularized design based on an Intelligent Manager allows the system functions that do not require the expert system to be performed by FORTRAN, PASCAL, C, and C++ programs. This includes a number of house-keeping functions such as user interface management, identifying authorized users, loading user profiles, object and data storage, data translation, on-line help systems, software interfacing, and calls to the various module calls. This allows the expert system to focus on tasks and functions that require the use of its inferencing/reasoning engine. This approach also limits the number of direct links between the expert system and external programs which in general alleviates potential "bottle necks" which would slow down system performance.

Further, the Intelligent Manager acts as the main controller for the entire system. It is being coded in C and C++ to maximize functionality and performance. The flexibility and portability of C/C++ enables the main controller to communicate with the GUI, Expert System Module, the IGM as well as any other C, FORTRAN or PASCAL programs. For example, it will work closely with the Expert System and GUI to develop "user profiles" whereby the system would

collect statistics and information about an operator over time, establish a profile, and interact with the user in a highly meaningful way based on his/her level of expertise. Effectively, the expert system will "learn" from the operator how he/she typically approaches CEM modeling and analysis tasks, making the overall process more efficient and user friendly.

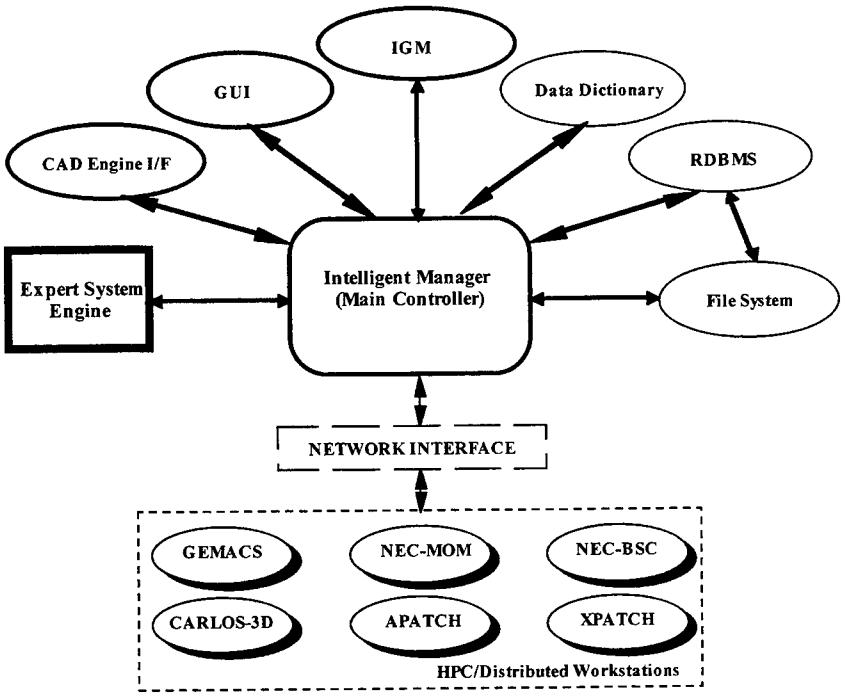

Figure 1. ICEMES Configuration Illustrating Component Framework and External CEM Code Communications

Next, consider the role of the IGM. Assuring the IGM's seamless interplay with the rest of the system is crucial to demonstrating ICEMES' full potential and utility for CEM modeling tasks. The present IGM design, based on a virtual reality visualization approach, is anticipated to provide two important capabilities to the operator: (1) allow the user to graphically display interim and final versions of the CEM structure model in 3-D space, and (2) permit the user to manipulate or institute modifications to the model (add, modify, delete, zoom in/out, or select regions of the overall structure model) and intelligently re-evaluate the impact of any changes through the expert engine. Modifications made interactively by the user to a baseline model via the IGM would be automatically reasoned upon, assessed for validity, and archived to establish a series of system-project files. These would be stored with the aid of the Relational Database Manager working in conjunction and in conformance with the Data Dictionary structure.

In order to facilitate rapid development and demonstration of the system, the current approach involves integrating a cost-effective commercial database package (e.g., MiniSQL, Microsoft Access) and implementing SQL-compatible calls, data transfers, and scripts that permit other modules to communicate with this database component. Sufficient flexibility is being instituted in the design and configuration management process to accommodate the insertion of any SQL-based data management package such as Oracle, Sybase, FoxPro, etc. with a minimum number of software interface modifications.

With regard to the CAD Engine component, current research and applications of CAD data are focusing on methods to read, parse, strip, and translate 3-D facet files; finite element data; subsets of the IGES (superset) standard; and associated spline functions and parameters. Research to investigate the possible translation of the STEP data standard is also anticipated as part of the capability's future expansion.

As in the prototype design previously reported upon, ICEMES will convert input data, whether CAD geometry or CEM, into a set of generic CEM objects in order to maximize the applicability of its inherent knowledge across the various CEM formalisms. Generic objects contained within the KB structure are intended to represent the basic building blocks that can be combined to form complex CEM geometries. The generic CEM objects include points, wires, plates, and cylinders as well as geometric variations on these. The generic CEM components permit the analyst to perform a number of data manipulations prior to selecting the analysis code or formalism type. This approach also provides a convenient method of sharing input data sets among CEM codes.

Figure 2 illustrates how the above functions work in unison to produce a valid CEM input model. This figure shows the general method of reading in all or a portion of a CAD model; converting the CAD data into an equivalent KB representation that conforms to the Data Dictionary definitions and structure; generating the CEM model; and performing (iterative) validations to arrive at the final model.

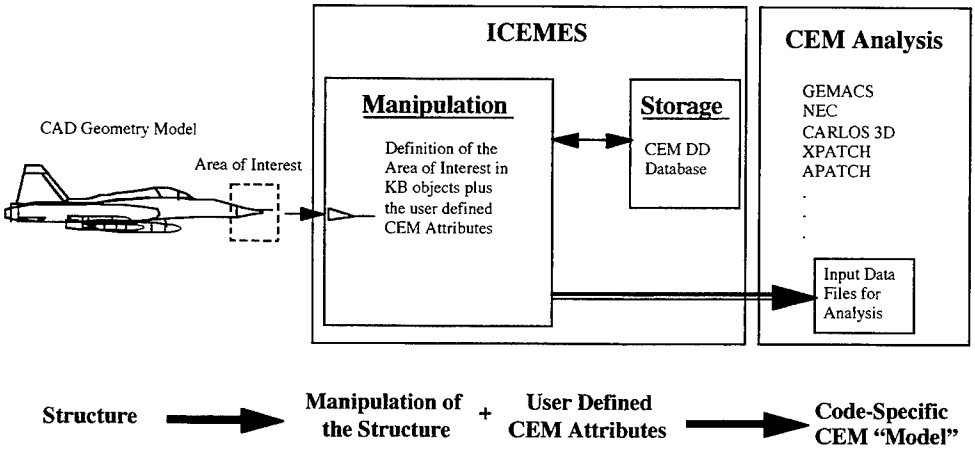

Figure 2. ICEMES and CEM Data Dictionary Functional Connection for CEM Input Model Generation

Per the original concept, the present ICEMES design and framework development approach will allow the individual software modules to be maintained and upgraded independently of each other. This means that the linking process does not fix the design to operate with a single version of any one of the components. Also, the use of Application Program Interfaces (APIs) simplifies the incorporation of additional tools as the system continues to grow in the future.

It is pointed out that a separate, Air Force sponsored research and development effort is anticipated to establish a Data Dictionary capability that is compliant with the government's Research and Engineering Framework (REF) technical requirements[3,4]. This will involve implementing an RDBMS and File System approach that is generally consistent with the methods and applications outlined above for ICEMES. This independent effort is expected to result in a capability that will complement the ICEMES concept and approach, and assist in enhancing its overall utility and functionality.

2.1 Knowledge Base Environment

In the present design, a "Master Knowledge Base" is established which consists of a series of separate, but interlinked KB partitions. The separate KBs are used to incorporate the knowledge and interfaces required for individual or unique CEM formalisms and processes, respective software packages, CEM codes, etc. Since each of these KBs shares the

same basic structure, they can easily be duplicated and updated to accommodate new capabilities, including individual CEM formalisms and CEM code-specific modeling constraints. With this approach the end-user is not required to have all the modules or analysis programs in order to operate the system. The knowledge is incorporated into the partitioned KBs via objects, rules, procedures, and relations.

The updated block diagram of Figure 3 illustrates the individual, hierarchical nature of the internal KB partitions and their purpose. Specifically, the block diagram shows the partitioning of knowledge first as a function of CEM formalism (i.e., "general" knowledge), and then by individual CEM codes and their peculiar modeling constraints (i.e., "specific" knowledge). This approach supports modularity, portability, and expansion to include other formalisms and code constraints.

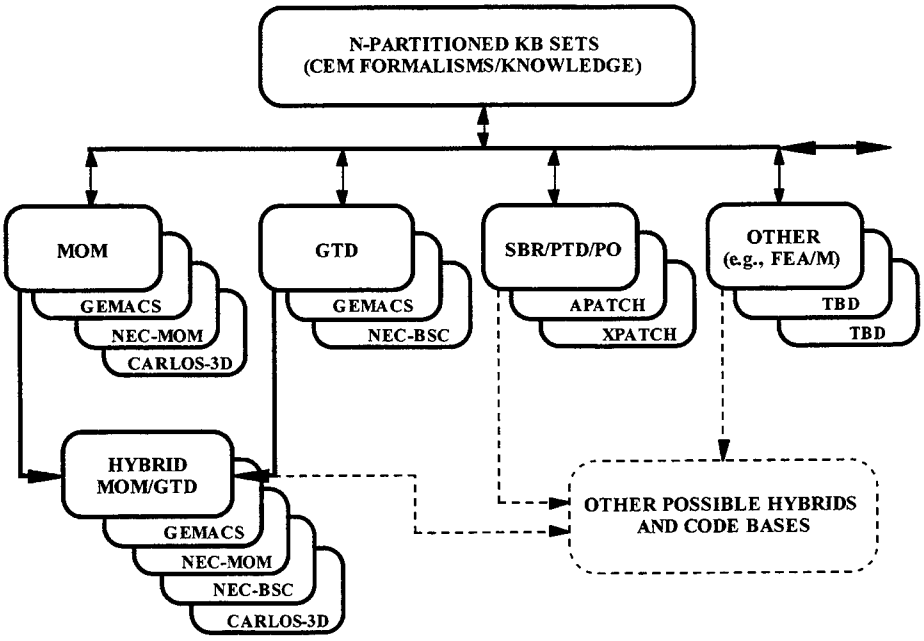

Figure 3. Hierarchical Knowledge Base Structure

3.0 MODELING METHOD AND USER SCENARIO

The reader may recall from previously published literature on this subject that a viable user interface which facilitates automated CEM structure model generation was initially developed and demonstrated[1,2]. This was defined in the technical literature as the "User Modeling Scenario" or UMS. The UMS is a methodology or roadmap which describes the general procedures involved in a typical ICEMES model development session, with the GUI as its infrastructure. At the time of this writing, a fairly comprehensive query-response system was in the initial stages of detailed design. This system will eventually provide varying degrees of user interaction depending upon the analyst's modeling and simulation goals, and CEM domain expertise.

The analyst will have the option of using a standard set of pull-down menus, tool bars, and an automated Assistant to navigate through the system during a modeling session. The Assistant consists of menus that lead the analyst through each step of the modeling task, and it provides recommendations along the way regarding the use of various modeling parameters as requested by the user or as determined by ICEMES' internal inferencing/reasoning engine.

3.1 Example Illustration

Consider the generalized system geometry illustrated in Figure 4. A "typical" albeit simplified modeling scenario may involve a situation in which the analyst is interested in (a) performing antenna siting on a complex structure such as the aircraft system of Figure 4 and (b) generating a corresponding CEM structure model as a function of antenna location, frequency and some observable quantity (e.g., electric field). Let us also assume that the analyst is attempting to concentrate his/her investigation on a "local" region (e.g., forward conical radome) of the total geometry based on some performance or safety-critical criterion. Finally, assume that the analyst is also looking for ways to achieve a simplified, yet valid CEM structure model, i.e., one which does not require significant computational resources or time to analyze.

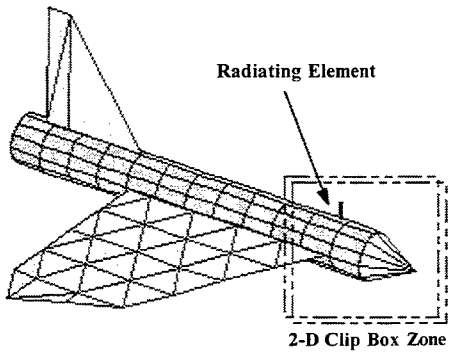

Figure 4. Generalized System Geometry Illustrating Interactive Display and Region Selection

In this case, the analyst may display the complete model via the IGM and interactively select a region to be emphasized for which a corresponding CEM structure model will be generated. This is shown via the 2-D "clip box" centered about the nose cone geometry of Figure 4. The result will be the generation of a complete, valid CEM structure model which exhibits high fidelity or which is more accurately defined in the subregion of interest (e.g., using a series of contiguous, discrete patches or wire gridded surface), and less detail (e.g., properly-sized GTD objects) beyond some $n\lambda$ boundary limit possibly dictated by the extent of the clip box area where λ is the wavelength of interest. The region of interest is highlighted in Figure 5.

The method of successfully accomplishing the above is currently under detailed investigation and initial implementation. The validity of this highlighting method is dependent upon the following: the manner in which selected objects (subregions) are grouped or tagged; determining the 2-D to 3-D transfer function or extent to which the 2-D clip box area relates to a 3-D volume; and assuring valid boundary conditions at the interface between the higher- and lower-fidelity regions of a model.

It is reiterated that the ICEMES model validation and correction measures ultimately act upon the generic CEM objects resident in the KB. Any size adjustments, position changes, connectivity modifications, etc. are applied directly to the generic CEM model components.

Also, other validations that will be performed during the model generation process include: finite-element resizing (plate sizing), connectivity/misalignment checking (MoM wire segments to GTD objects, GTD plates to GTD cylinder), incomplete definitions, and MoM element sizing and connection angles. Again, each of these validations is based upon assessing the relevant electromagnetic conditions and "physical" parameters defined for the given problem such as: frequency, object dimensions, relative location of source(s) with respect to the system geometry, specified observables (e.g., field points, wire currents, patch current densities, etc.), and any specified accuracy constraints.

Once the geometry model complies with the set of applicable CEM rules, it passes through a "filter" for the application code selected; and the filter converts the generic parameters into a specific format required by the CEM code.

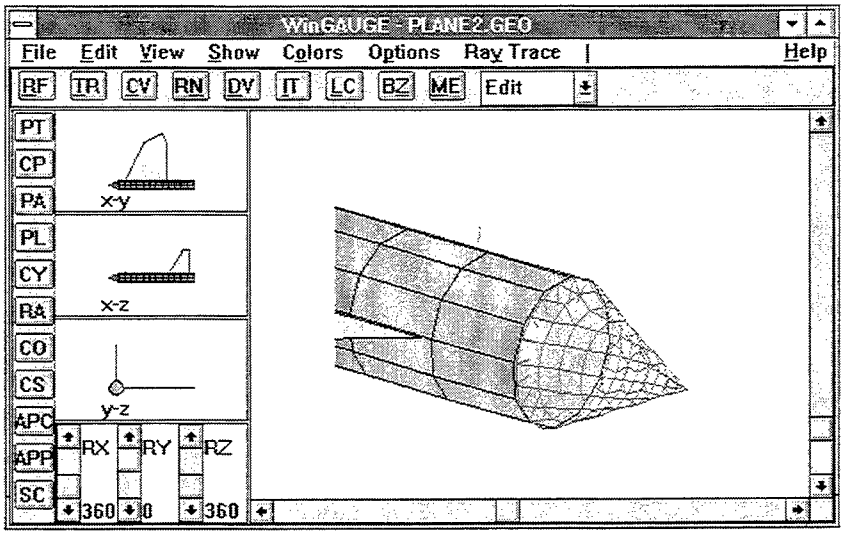

Figure 5. View of Aircraft Nose Cone Region of Interest Using WinGAUGE

4.0 CONCLUSIONS AND FUTURE DIRECTIONS

The evolving ICEMES capability is an innovative, significant step forward in the successful adaptation and integration of next-generation software technologies with existing CEM codes. The present stage in ICEMES' development cycle is focusing on expanding its framework to encompass additional CEM formalisms, codes and associated data formats, and algorithms. Ancillary features and capabilities are also being adapted to ICEMES' architecture. These include a database management system, CEM model libraries and data dictionary, interactive geometry modeling and visualization tools, and tailored graphical user interfaces.

ICEMES exhibits the potential to support the goals and objectives of broader modeling and simulation computational engineering environments. One example is the Air Force's Integrated Computational Environment/Research and Engineering Framework (ICE/REF)[4] which stresses Concurrent Engineering applications, the use of common-type data, and a "global" modeling/simulation environment. The current ICEMES concept and design continues to be generally in conformance with architectural and functional features of the ICE/REF that include code wrappers, Applications Program Interface (API) routines, CAD file data extraction, library structures generated via database managers, and use of the CEM Data Dictionary.

The ICEMES capability continues to offer opportunities for government and commercial sectors to benefit from advanced AI/ES-based tools for product value added. It is expected to also benefit academia by providing a learning tool for student and journeyman-level engineers who may be tasked with investigating CEM concerns in the professional job market.

Eventually, the AI/ES approach discussed herein is expected to support synthesis modeling whereby an item (e.g., antenna radiator) can effectively be "built" from a pallet library of "standard" elements and characteristics of commercially-manufactured hardware, and integrated with the host system using an incremental or building block approach. The synthesis method would be driven by operational, electrical and physical characteristics in conjunction with user-specific options all under the control of an expert engine.

REFERENCES

[1] A. Drozd, T. Blocher, et. al., "The Intelligent Computational Electromagnetics Expert System (ICEMES)", Conference Proceedings of the 12th Annual Review of Progress in Applied Computational Electromagnetics at the Naval Postgraduate School, Monterey, CA, 18-22 March 1996, pp. 1158-1165 (Research and Development sponsored under the DoD SBIR Program, Contract No. F30602-95-C-0198, Phase I for the US Air Force Rome Laboratory).

[2] A. Drozd, T. Blocher, et. al., "The Intelligent Computational Electromagnetics Expert System (ICEMES)", Applied Computational Electromagnetics Society Newsletter, Vol. 11, No. 2, ISSN 1056-9170, July 1996, pp. 28-40.

[3] J. Evans, "Research and Engineering Framework (REF) Data Dictionary Specification for Computational Electromagnetics", Conference Proceedings of the 12th Annual Review of Progress in Applied Computational Electromagnetics at the Naval Postgraduate School, Monterey, CA, 18-22 March 1996, pp. 340-346.

[4] L.W. Woo,. B. Hantman, et. al., "Continuing Development of the Research and Engineering Framework (REF) for Computational Electromagnetics", Conference Proceedings of the 12th Annual Review of Progress in Applied Computational Electromagnetics at the Naval Postgraduate School, Monterey, CA, 18-22 March 1996, pp. 383-390.

ACKNOWLEDGMENTS

The authors wish to acknowledge the ongoing support and contributions made on behalf of the ICEMES development program by Clifford E. Carroll, Jr. of ANDRO, Dr. Edgar L. Coffey III of Advanced Electromagnetics, Dr. Ronald J. Marhefka of The Ohio State University, Jeffrey A. Evans of Decision-Science Applications, Inc., and James B. McCreary of Innovation Strategy Group, Inc.

ABOUT THE AUTHORS

Andrew L. S. Drozd is President of and Chief Research Engineer for ANDRO Consulting Services. He has nearly 20 years of experience in the field of Electromagnetic Environmental Effects (E^3), Electromagnetic Compatibility (EMC) and Computational Electromagnetics (CEM). He holds a B.S. in Physics and Mathematics (1977) and an M.S. in Electrical Engineering (1983), both from Syracuse University. In recent years, he has focused his research on applying AI and expert systems to CEM applications. Mr. Drozd is also a Senior Member of the IEEE and is currently a Member of the IEEE EMC Society Board of Directors.

Timothy W. Blocher also conducts CEM research at the Rome Laboratory. He holds a B.S. in Physics and Electrical Engineering from the State University of New York and Clarkson University, respectively, and an M.S. in Electrical Engineering from Syracuse University.

Kenneth R. Siarkiewicz has over 30 years experience in the field of CEM at the Rome Laboratory. He holds a B.S. and M.S. in Electrical Engineering, respectively, from the University of Detroit and the University of Michigan. Mr. Siarkiewicz is a Rome Laboratory Fellow for his work in CEM, and he has been named IEEE Fellow for his work in developing and promoting computational models.

Victor K.C. Choo, an Associate Senior Scientist, provides part-time technical support to ANDRO Consulting Services on behalf of the ICEMES project. Mr. Choo is also currently a full-time staff member of the Naval Undersea Warfare Center (NUWC) in Newport, RI working in the area of systems EMC.

Web-Based High Performance Computational Electromagnetics Servers

Donald M. Leskiw*, Grant S. Ingersoll, and Thomas J. Vidoni of The Ultra Corporation
Geoffrey C. Fox and Kivanc Dincer of NPAC at Syracuse University

Abstract

We present results from a project for migrating a large-scale computational electromagnetics system onto parallel processors and to enable interactive, simulation-on-demand for remote users. The legacy system is the Air Force's General Electromagnetic Model for the Analysis of Complex Systems (GEMACS). Its geometric theory of diffraction and method of moments modules are paralleized and hosted on the Rome Laboratory Paragon. The Input/Output modules are being modified for Web-browser data entry and visualization. We include examples of speedup from parallel processing and show how use of Internet Web technology expedites results visualization and archiving. This new technology enables simulations such as high performance computational electromagnetics to be conveniently accessed via the Internet.

I. Introduction

Background

The military and the commercial sectors require accurate and fast codes for calculating reliable internal and external fields for electromagnetic compatibility analyses. The benefits of using high performance computing (HPC) for complex simulations is well established [1], [2] and [3]. Problems that previously were intractible because they required large computing time can now be solved with even greater modeling complexity and precision. Also, beyond providing faster speed, developments in computing technologies together with advancements in Internet technologies allows work to be distributed to locations where expertise or knowledge-bases reside. This enables practical integrated manufacturing and design, or multidisciplinary analysis, such as coupling physical, electromagnetic, aerodynamic, structural, and theromechanical characteristics of a structure[4] and [5]. Integration among multidisciplinary tools, however, increases requirements for interactivity of simulations. This provides further motivation for an interactive and "on-demand" computational electromagnetics capability.

GEMACS Architecture

The General Electromagnetic Model for the Analysis of Complex Systems (GEMACS) is a tool designed by Rome Laboratory of the Air Force to solve non-trivial problems[6]. Radiation and scattering problems for the exterior and interior of a structure are treated. It provides techniques for analyzing any phase of system engineering: design, development, production, or maintenance. The analyst is provided with low, high, and hybrid frequency techniques -- method of moments (MOM) for low and geometric

*Principal Author

theory of diffraction (GTD) for high. GEMACS is an evolving computer simulation system intended to provide sophisticated analysis of electromagnetic fields associated with radiating or scattering Air Force systems[7]. New developments in physics, math and engineering are constantly being added to GEMACS upgrades. The modular structure of GEMACS is illustrated below in Figure 1.

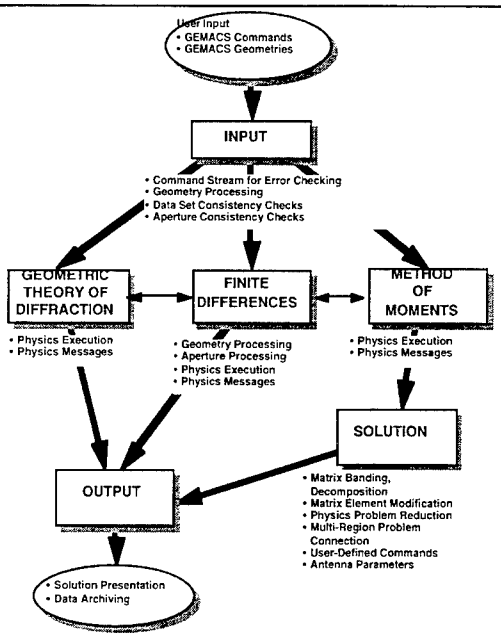

Fig. 1 GEMACS Architecture

II. HPC and GEMACS

High Performance GTD

The Caltech Concurrent Computation Program (C3P)[8] effectively demonstrated the practical use of parallel computing for both scientific and engineering applications[9],[10] and [11]. High Performance Computing (HPC) technology brings new life to the GEMACS system by offering a dramatic speed-up for large simulations and thereby allowing higher fidelity models of the physics. At present, we are applying parallel processing to the GTD, MOM, and SOLVE modules of GEMACS. Initial results are provided below in figures 2 (speed-up for GTD) and 3 (runtime for MOM). For GTD we distribute the high frequency interaction points evenly among the separate procesors. We employ a ray-tracing algorithm where each subsequent bounce is handled by the processor responsible for the first bounce.

Having all "first-bounce" calculation evenly distributed by a uniform assignment of interaction points to processors, the computational load is thereby balanced.[12] The speed-up is quite linear since this is an "embarasingly parallel", i.e., little or no communication among the processing nodes. This algorithm scales well with increasing order of GTD interactions, i.e., multi-bounce.

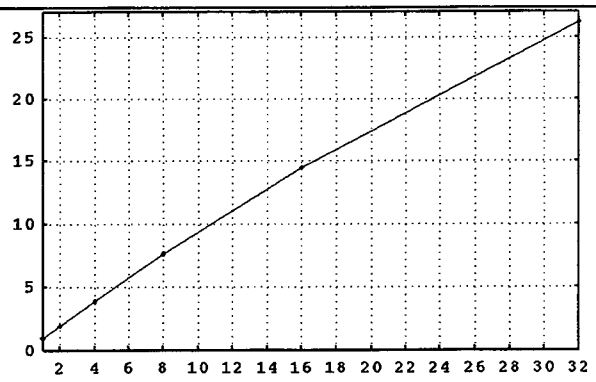

Figure 2 GTD Speed-up Versus Number of Processors

High Performance MOM

For MOM the situation is more complicated. We distribute the calculation of elements in the interaction and Green's function matrices. A parallel linear algebra solution library (e.g., ScaLAPACK) is also needed to solve for the unknowns. Unfortunately, with MOM we are faced with Amdahl's Law: as a given problem is parallelized and the number of processors increased, any residual serial portion will eventually dominate. Thus, if the total time of computation is T_{total} then

$$T_{total} = T_{serial} + T_{parallel}/N$$

where T_{serial} and $T_{parallel}$, respectively, are the times spent in the serial and parallel portions, and N is the number of processors. As the number of processors is increased T_{total} approaches T_{serial}. GEMACS MOM consists of serial and parallel parts, and so Amdahl's law applies. Figure 3 demonstrates this phenomina. There we have instrumented the MOM module to provide internal measurements of runtime as a function of parallelization. The $P + S$ curves provide the runtimes for the code comprising the parallel and the serial residue of unparallelizable code that surrounds the parallel portion. The P curves represents the time consumed by the parallel portion of GTD alone. The S curves are the difference between the $P + S$ and P values. Note that these figures are not "pure" in that the act of instrumenting the software containates the measured values.

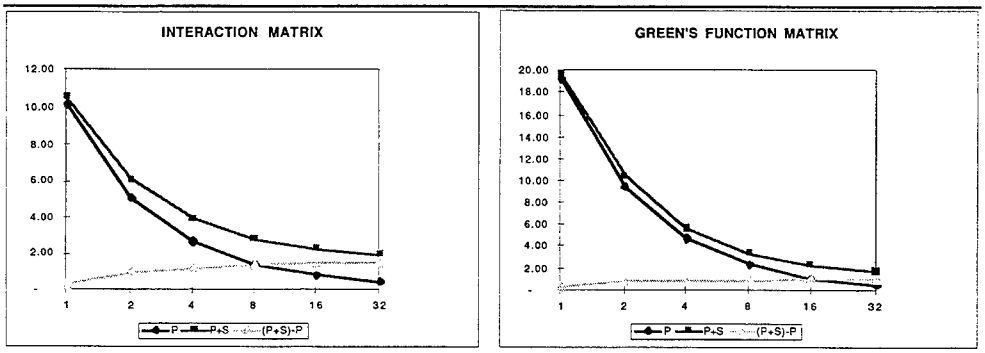

Figure 3 MOM Runtime Versus Number of Processors

The antidote to Amdahl's Law is to increase the size of the problem. A parallel algorithm has good overall efficency if the runtime is constant when we double the size of the problem and simultaneously double the number of processors. In principal, T_{serial} is constant with respect to problem size. With a sufficiently large problem size, however, T_{serial} will pale in comparison with $T_{parallel}$. But we can only increase the size of the problem untill we run out of memory. At that point a previously missing computational overhead is introduced: communication from having to use out-of-core memory. This destroys any gains made by overcoming Amdahl's Law earlier and leads to requiring efficient parallel input/output runtime libraries.

The Scalable Input/Output (SIO) Initiative has developed a runtime library for parallel I/O on the Paragon.[13] The goal of that group is to examine parallel, scalable I/O issues and develop a system application programming interface (API) called LLAPI, for Low Level API. It has five goals: portability, flexibility, high performance, limited number of functions, and extensibility. LLAPI is meant to be used by a higher level library (such as MPI, described below), not by the actual application programmer. LLAPI supports reading and writing with scatter/gather capabilities for memory and file ranges as well as: asynchronous operations, client control over client caching, file access and layout hints, fast file copy and batching collective I/O operations. Most important for our current work: there is a version of LLAPI for the Paragon which tests have shown to give speed-up over Intel's Parallel File System. We have started to use that library to obtain better results for large out-of-core MOM problems.

GEMACS HPC Portability Issues

A primary concern in parallel computing has been the volatility of the hardware market. No sooner is a code parallelized for a given machine than the vendor discontinues that product line or goes bankrupt. To perform parallel computation the work (functions, data, or both) must be partitioned, executed in parallel, and recombined. These steps require system overheads of initializing, communicating and

coordinating, and finally terminating the parallel activities. The Message Passing Interface (MPI) forum has address the portability issue by defining a standard runtime library for these system calls. The MPI forum involves a group of over 40 participants, including Government, Academia, and Industry. They have produced MPI 1.0, a very capable, efficient system library for parallel processing. The application programmer need only call MPI; MPI in turn calls the native system software for a given hardware installation. MPI is available on every noteworthy parallel machine and is free. We have installed MPI on: Rome Paragon, networks of Workstations, and networks of Windows NT/95 and Linux PCs. Our experience with parallel GEMACS on the Paragon shows no discernible difference between the native Intel libraries (NX) and MPI. Also, by only recompiling the MPI version of GEMACS, the code runs on networks of PCs (or other MPI-based parallel/distributed system).

III. Web Client/Server Architecture for GEMACS

The goal here is to provide a standard, Internet capable user interface for world-wide accessible Simulation-on-Demand (SoD), using a the HPC GEMACS as a test case demonstration. The ability to run complex simulations using Web-browsers user interface from anywhere in the world offers a plethora of opportunities for researchers, educators and students. Furthermore, the marriage of HPC, with its high speed networking capabilities and runtime speed-up, to the client/server approach leads to interactive and dynamic simulations. Other benefits from using Web-based Internet technologies for client/server infrastructures are the inherent multimedia standards and technologies for exchanging data and publishing results. Thus we further distribute GEMACS using a client/server architecture with the input and output user interfaces (client) hosted on Web-based PC browsers and the computation of fields (server) hosted on a parallel processors (e.g., the Rome Laboratory Paragon or a network of PCs).

Implementation

As of this writing, a prototype implementation of the client/server architecture is available using a standard Web browser running on a PC. The SoD interface relies on Common Gateway Interface (CGI) scripts written in Perl to parse user input submitted through HTML (with Javascript or VBscript) forms to build a GEMACS input file. The geometry in the input file is then converted to the Virtual Reality Markup Language (VRML) and displayed in a VRML browser where it may be manipulated and viewed. The input file is then submitted to the HPC resource through a scripting system developed for GEMACS. Upon completion (the user is notified via email), another script is run to display the results. Figure 4 provide an example in which the electromagnetic field and scattering geometry (a Cessna) are displayed in a Netscape browser using a VRML viewer.

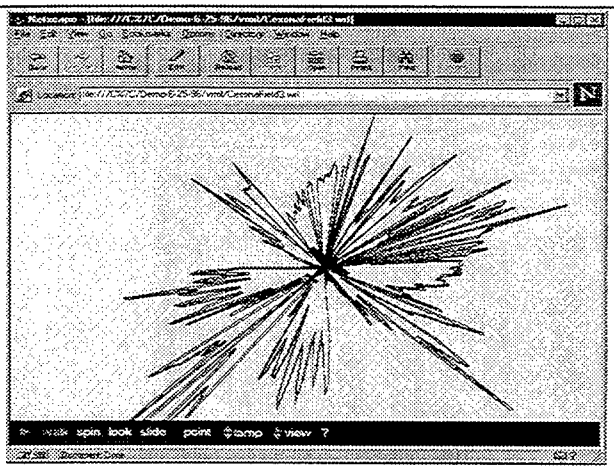

Figure 5 Client-Side Viewing of Input Geometry and Results

In any serious electromagnetic compatibility assessment project, many simulation runs are required with a variety of parametric changes. We thus also provide Web-based data archiving, browsing, and display. The results of GEMACS are stored in a standard output file together with a key-word header. These may be visually displayed and inspected, manipulated, printed, etc. according to the user's needs. Figure 5 gives an example of a graphical/text view of a segment of outlput sets.

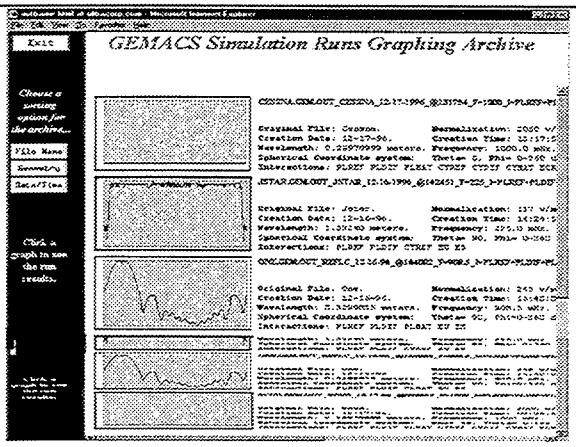

Figure 6 Web Browsing of Visual Output Archive

Next Steps in Simulation-on-Demand

Current and future developments in the client/server design are focusing on creating an intuitive, easy-to-use user interface. After analyzing the advantages and disadvantages of various programming languages, several changes and improvements for the user interface are in development. With new web technologies emerging almost daily from various web vendors, the GUI will be developed to run as plug-ins for Netscape and Microsoft web browsers taking advantage of C++ and it's large collection of libraries; a future version written in Java will take advantage of Java's platform-independent nature and the capability to embed applets into web pages. Currently, however, Java does not have the properties required to offer a full-featured integrated interface, but this is expected to change in the near future as more libraries are developed and security issues are solved.

Moreover, future developments look to require less specific expert knowledge of GEMACS. Implementations of wizards, or small helper applications, will step the user through the process of creating, submitting and analyzing simulations. As is always the case in software, the SoD framework will continue to evolve and expand to meet the simulation demands of the future; additionally, with efforts to increase the speed of computers and the networks they communicate on, Simulation-on-Demand will become a valuable, integrated, fully interactive tool embedded into many powerful applications.

IV Disclaimer and Acknowledgments

The work described here was supported in part by the Air Force Material Command under Ultra contract F30602-95-C-0221 with Rome Laboratory, Rome, NY, Syracuse University contract F19628-94-C-0057 with the Electronics Systems Center, Hanscom AFB, MA, and by the Ballistic Missile Defense Organization under Ultra contract DASG60-92-C-0155 with US Army Missile Defense and Space Technology Center, Huntsville, AL. The views and conclusions contained herein are those of the authors and should not be interpreted as necessarily representing the official policies, either expressed or implied, of the Air Force or the US Government. The authors address are: Leskiw, Ingersoll, Vidoni at The Ultra Corporation, University Station, PO Box 50, 1004 E. Adams St. Syracuse, NY 13210; Fox and Dincer at Northeast Parallel Architectures Center of Syracuse University, 111 College Place, Syracuse, NY 13244

V. References

[1] Matzner, R., *Binary Black Holes Grand Challenge Alliance*: Internet WWW page, at URL: <http://www.npac.syr.edu/projects/bh> (version current at July 15, 1996).

[2] Bernholdt, D., *Computational Chemistry*: Internet WWW page, at URL: <http:/ /www.npac.syr.edu /users /bernhold/ comp_chem/index.html> (version current at July 15, 1996).

[3] Blocher, T., Leskiw, D. and Tyman, P., "High Performance Computing for C3I Computational Electromagnetics Applications", Final Technical Report, The Ultra Corporation, Syracuse, NY, March 17, 1994.

[4] Fox, Geoffrey C. and Bogucz, Edward A., " Planning for Industry Interaction in High-Performance Computing for Multidisciplinary Design in Computational aerosciences," Final Technical Report for Grant: NAG2-821, NPAC at Syracuse University, Syracuse, NY, 1996.

[5] Lettes, T., "Flexible Computer Integrated Manufacturing and the Ability to Compete in Global Markets," Office of the Assistant Secretary for Technology Policy, DoC, December 1991.

[6] RADC-TR-90-360, "General Electromagnetic Model for the Analysis of Complex Systems (GEMACS) — Version 5," RL/ERPT, Griffiss AFB.

[7] Siarkiewicz, K. R., "GEMACS — An Executive Summary," *Proceedings of the 1985 International Symposium on Electromagnetic Compatibility*, Wakefield, MA, August 1985, pp. 75-81.

[8] Angus, I., Fox, G., Kim, J., Walker, D., *Solving Problems on Concurrent Processors Volume II: Software for Concurrent Processors*, Englewood Cliffs, Prentice Hall, 1990.

[9] Fox, G., Leskiw, D., et al, "Impact of Grand Challenge Applications on HPCC Software and Tools," report of the Applications Working Group of the *Workshop on Systems Software and Tools for High Performance Computing Environments,* NASA/JPL April 1992.

[10] Rome Laboratory, The Ultra Corporation, et al, "Appendix A: Strategic Plan" of the *Cooperative Research and Development Agreement (CRDA) for Parallel Software Engineering,* AFMC/RL August 1992.

[11] Fox, G., Johnson, M., Lyzenga, G., Otto, S., Salmon, J., Walker, D., *Solving Problems on Concurrent Processors Volume I: General Techniques and Regular Problems*, Englewood Cliffs, Prentice Hall, 1988.

[12] Li, P. P. and Curkendall, D. W., "Parallel Three Dimensional Perspective Rendering," Internal JPL Report, available from the authors, at NASA/JPL.

[13] Demetrio, C; "The Scalable I/O Low-Level API: A Portable Programming Interface for Parallel File Systems" An online set of slides residing at www.pdl.cs.cmu.edu

Graphical User Interface for Computational Electromagnetics Software

Bob Joseph
Armand Paboojian
Stan Woolf
Ed Cohen
ARCON Corporation
260 Bear Hill Rd.
Waltham, MA 02154

ABSTRACT

There are many scientific codes that over the years have established themselves as standards of their fields. Although these codes have well established their scientific validity, their lack of a user-friendly interface restricts their use from being as wide as possible.

We demonstrate the use of a software product, ArconViz, that will facilitate the use of software packages such as GEMACS and NEC. This product will provide a Graphical User Interface which will assist the user in the specification of the conditions of the calculation containing context-sensitive on-line help. Since these codes require the specification of the problem geometry situation to be modeled, ArconViz will provide an interface between the user's CAD package and the modeling software. ArconViz will also provide a means to immediately visualize the output of the calculation.

ArconViz will also interface with other scientific software codes, such as SINDA/G for heat transfer. The software is being developed for both IBM-PC platforms, using Microsoft Windows95 or WindowsNT and UNIX platforms, using X-Windows.

INTRODUCTION

In June 1994, ARCON Corp. embarked on an SBIR Phase I project entitled "Visualization for Computational Electromagnetics"[1]. The purpose of this project was to determine the feasibility of developing a commercial product that would facilitate the use of a number of popular scientific modeling codes. The need for such a product becomes apparent when one realizes that these codes were developed in the days of the computer punch card or perhaps the text-based computer terminal such as the VT100. Today a new generation of computer consoles provide the user additional input facilities, and graphics displays which are capable of displaying 3-D graphics.

The purpose of our product is to provide these modeling codes a Graphical User Interface, allowing the user to navigate through the creation of an input deck using a mouse. In addition, our product will provide a mechanism for the visualization of the large volume of output data that these codes generate. We have chosen to facilitate the use of a number of modeling codes, such as GEMACS, NEC2 and others, that all share the feature that they can incorporate fairly complicated geometric models. To further facilitate the preparation of the input deck our product will allow the

user to design the geometric situation in question using a CAD program, import the CAD file and translate it into the format required by the modeling software.

The outcome of Phase I was the development of a working prototype of our product. Though primitive, it demonstrated many of the features that we want to incorporate into our final product. We made a presentation on the product at the March 1995 meeting of the Applied Computational Electromagnetics Society[2]. We are now three-quarters of the way through Phase II of our project. We will show our product, ArconViz, as it will ultimately be by the end of Phase II.

DEVELOPMENT

It is our intention to have multiple versions of our product, for UNIX workstations and for the PC. To that end we are pursuing two parallel development programs.

For the UNIX platform, we are using an SGI Indigo^2 running IRIX 5.3. Programming is in C/C++. The Graphical User Interface on the X-Windows platform is being programmed using Motif.

An important feature of our product is its ability to visualize both the input geometric situation and the output from the modeling program. Probably one of the most important aspects about our product development is the use of the OpenGL 3-D graphics library[3]. OpenGL was originally developed by Silicon Graphics Incorporated for their high performance graphics workstations, but in the spirit of "open computing" has been transferred to the OpenGL Architecture Review Board whose members include Silicon Graphics, IBM, DEC, and Microsoft among others. This has made OpenGL available on a wide range of X-Workstations and now most recently, PCs running WindowsNT and Windows 95. OpenGL is a platform independent application programming interface providing about 120 distinct 2-D and 3-D graphics functions, including transformations, color, lighting, and drawing objects as simple as a point and as complex as a non-rational B-spline surface.

For the PC platform, we are currently using Windows NT 3.51, and Visual C++ v.4.02.

The CAD packages that we have been interfacing around include ACAD, AutoCAD, DesignCAD and TurboCAD. The scientific modeling codes include GEMACS, NEC, SINDA/G, SPICE, and ITS among others.

PROGRAM FUNCTION

To show our product, we will demonstrate its use in the analysis of an electromagnetics problem. We will apply GEMACS to the following situation: A dipole antenna above a metal hut. The hut is 4 m wide x 8 m long x 4 m high. The antenna is 2/3 m long, radiating at a frequency of 225 MHz. We follow the analysis beginning with the creation of the geometry using a CAD program, importing the geometry into ArconViz, and then setting the calculational parameters through the ArconViz Graphical User Interface.

1. Geometry Design.

Figure 1 shows the geometry that we are going to model using GEMACS. The CAD program that we are using here is a PC program called DesignCAD 3-D. The particular CAD program used is not important, as long as it has some facility for outputting the geometry information in some commonly-used exchange format. We are programming around two exchange formats, Initial Graphics Exchange Specification (IGES)[4] and the AutoCAD Drawing Exchange Format (*dxf*)[5]. There are other formats that we may add later. ArconViz does have the ability to call the user's CAD program while remaining in the background.

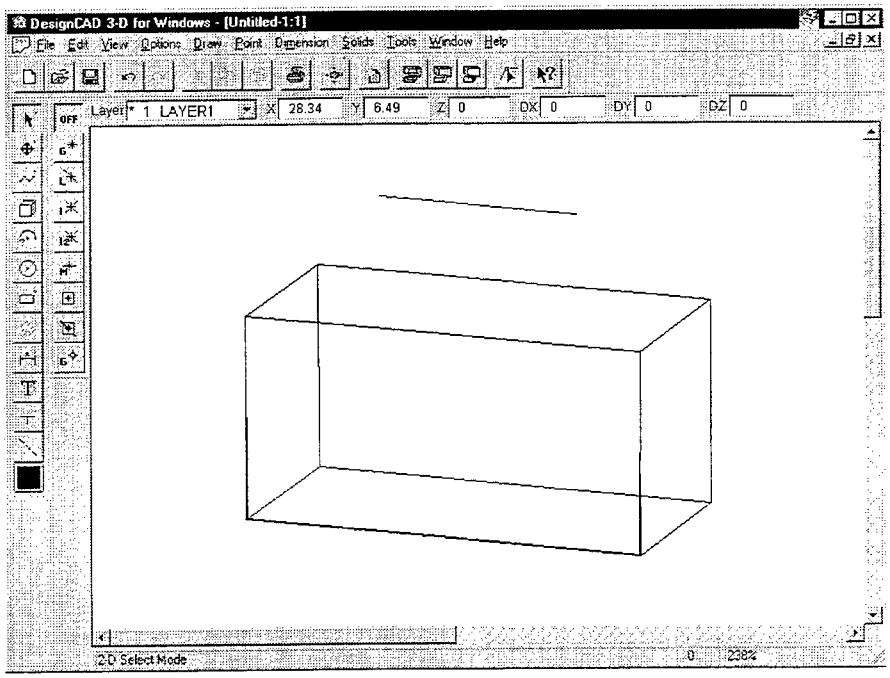

Figure 1. Geometry to be modeled being designed using DesignCAD.

2. Setting Program Parameters

Figure 2 shows the first dialog box presented to the user on choosing GEMACS analysis. ArconViz provides access to every parameter required for a GEMACS run. The numerous parameters are divided into various related sets and are presented in the various dialog boxes. For instance, Figure 3 shows the dialog box which allows the user to set the points in space where the field is calculated.

Figure 4 shows the ArconViz input visualization screen. This facility allows the user to rotate the drawing, pan horizontally and vertically, and zoom in and out, but it allows for more than the simple review of the input geometry. The user is able to select with the mouse a part of the drawing, the wire on top of the shed for instance, and a dialog box, shown in Figure 5, will pop-up allowing the user a convenient method for setting properties such as excitation.

After setting all the pertinent parameters the user may then run GEMACS. Note that the user may save all the parameter values in an ArconViz project file, which will hold the values for all the parameters for all the different types of analysis available. This allows for situations where an engineer or scientist may perform several types of analysis at the same time.

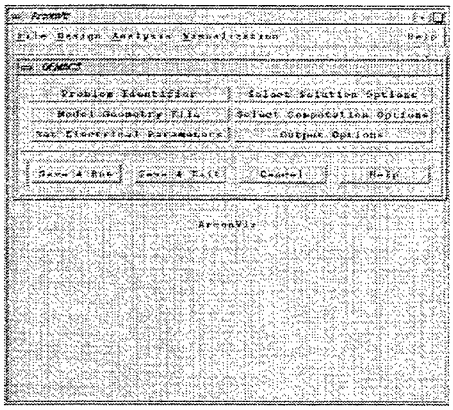

Figure 2. Top of the GEMACS parameter selection tree.

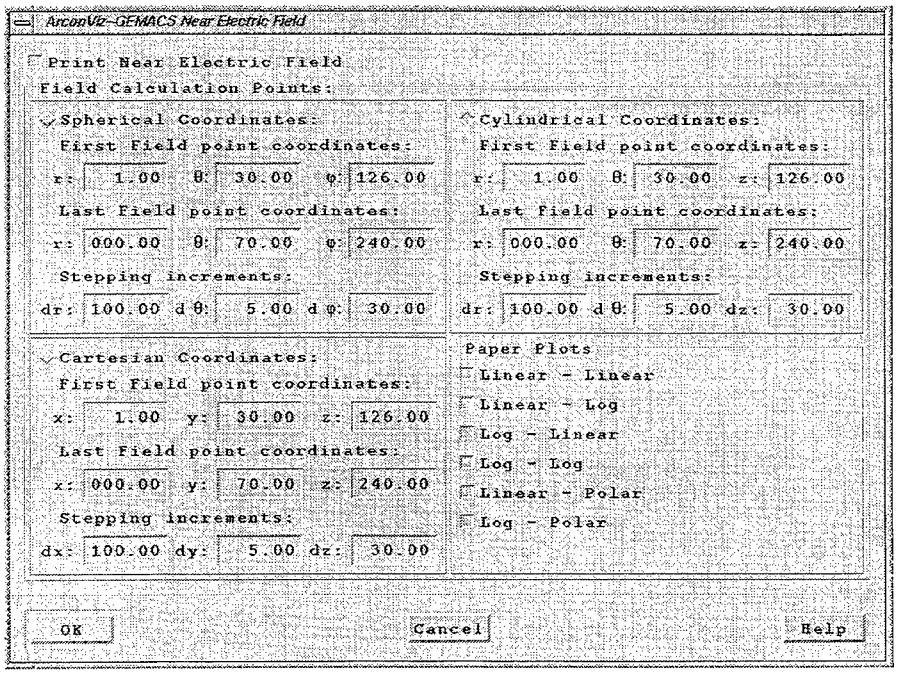

Figure 3. Dialog box for setting field points.

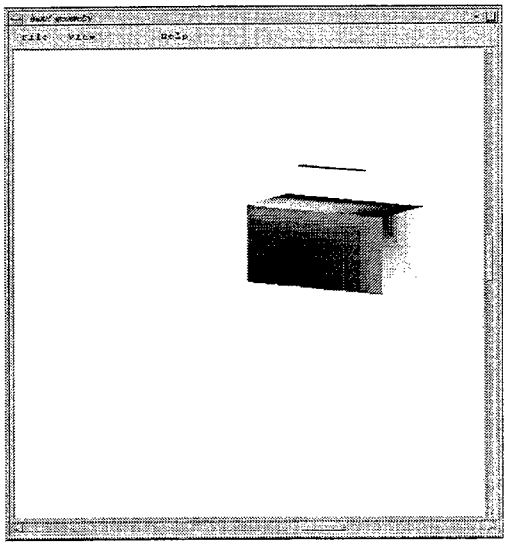

Figure 4. ArconViz input visualization screen.

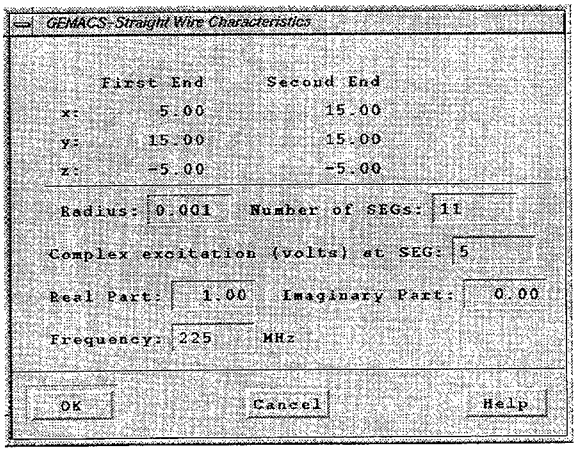

Figure 5. Set characteristics dialog box.

In addition to input geometry visualization, ArconViz will have many facilities for the visualization of the program output data giving the scientific modeling code user immediate feedback without having to transfer the data to some other plotting software.

CONCLUSION

We have made a great deal of progress on our project to produce a software product which will greatly facilitate use of scientific modeling codes such as GEMACS and NEC2 and we have every reason to believe that we will be able to bring this product to market by the end of this year. We envision having versions for both PC and UNIX workstations, and we will also have a version for academic environments. We will also have special interest versions which may concentrate on particular software modeling codes.

REFERENCES

[1] R.A. Joseph, W.F. Bellew and S. Woolf, "Visualization for Computational Electromagnetics", ARCON Corporation Final Technical Report ERST RL-TR-95-102, ERST, Grifiss AFB, NY, June 19995.

[2] R.A. Joseph, "Visualization Toolkit for Computational Electromagnetics", 11th Annual Review of Progress in Applied Computational Electromagnetics, March 1995, pp 151-154.

[3] J. Neider, T. Davis, and M. Woo, OpenGL Programming Guide, Addison-Wesley Publishing Co., Reading, MA, June, 1993.

[4] IGES - Initial Graphics Exchange Specification (Ver. 5.2), US PRO/IPO-100, U.S. Product Data Association, Fairfax, VA, January 1993.

[5] Autodesk, Inc., 111 McInnis Parkway, San Rafael, CA 94903.

SESSION 20:

FDTD APPLICATIONS

Chairs:J.H. Beggs and S. Blocher

IMPLEMENTATION OF A TWO DIMENSIONAL PLANE WAVE FDTD USING ONE DIMENSIONAL FDTD ON THE LATTICE EDGES

Scott C. Winton and Carey M. Rappaport
Center for Electromagnetics Research
Northeastern University
Boston, MA 02115

Abstract **Development and testing of angle independent absorbing boundary conditions (ABCs) can be improved by simulating waves incident on the ABC at a single angle. By using one-dimensional Finite Difference Time Domain (FDTD) as the lattice side edge condition, the creation and numerical propagation of a two dimensional plane wave with arbitrary incident angle is possible. The application and extent of usefulness of the method are examined and extensions to increase the range of usefulness are introduced.**

I. INTRODUCTION

Until recently, the use of the FDTD method for numerical solutions of electromagnetic scattering problems was severely hampered by the poor performance of absorbing boundary conditions used to prevent reflections of EM waves at the lattice edges. With the advent of the Berenger Perfectly Matched Layer[1], this problem has been significantly reduced and the computational efficiency of FDTD problems has been significantly improved.

Understandably, this has created considerable interest in improving and optimizing the PML and angle-independent ABCs as a whole. But this effort has been impaired by the fact that commonly used excitations, such as point or line sources, generate waves incident on the ABC at all angles. This complicates the analysis of the performance of the ABC and impairs design optimization. The problem is ameliorated by introducing plane wave sources incident on the ABC at a single angle. With such an excitation, the performance of the ABC is clearly defined. However, because of the difficulty in dealing with propagation on the lattice edge ,the creating and propagating such a wave is difficult.

For a two-dimensional FDTD simulation using the standard Yee cell formulation[2], the update of a given spatial grid point requires data from the four adjacent grid points. Clearly this creates a problem at the lattice edges. Typically, in scattering simulations, a Mur total/scattered field region separation avoids the need to calculate incident waves on the edges[3]. However, to test ABCs, the incident wave must be a uniform plane wave without deformations along the edge. ABCs cannot be used at these edges since they fail for plane waves propagating at steep grazing angles. Furthermore, the values on the edges must not be specified analytically because the numerical values of the fields inside the discretized ABC under test are not known.

II. INTEGRATION OF ONE-DIMENSIONAL EDGE FDTD WITH A TWO-DIMENSIONAL GRID

For the following discussion, consider a two-dimensional grid on which a boundary value FDTD simulation will be run. The "front" of the grid is the source boundary value while the ABC to be tested is positioned at the "back". What is desired is the create a plane wave with a phase front at an angle θ with respect to the front wall. For this discussion a transverse electric (TE) wave is considered. The x directions is front to back and the y direction is left to right as shown in Figure 1.

Instead of ABCs at the "left" and "right" edges, 1-D FDTD is used. The update of each spatial point on these edges will require data from only the grid points preceding and succeeding it. At each time step, information from this 1-D FDTD is passed to the larger 2-D FDTD to update spatial points adjacent to the left and right edges. If the wave is normally incident on the ABC, the formulation of the plane wave is quite simple. In this case, H_x is zero and both E_z and H_y are uniform left to right. Therefore, no information is obtained from the transverse difference and the calculations along each grid line running front to back reduces to as a 1-D FDTD algorithm. To illustrate this, consider the time harmonic Maxwell's curl equations for TE waves in lossless media:

$$\frac{\partial E_z}{\partial y} = -j\omega\mu H_x \tag{1a}$$

$$\frac{\partial E_z}{\partial x} = j\omega\mu H_y \tag{1b}$$

$$\frac{\partial H_y}{\partial x} + \frac{\partial H_x}{\partial y} = j\omega\epsilon E_z \tag{1c}$$

These have the familiar (forward propagating) solutions:

$$E_z = E_o e^{-jk(x\cos\theta + y\sin\theta)} \tag{2a}$$

$$H_y = -\cos\theta \frac{E_o}{\eta} e^{-jk(x\cos\theta + y\sin\theta)} \tag{2b}$$

$$H_x = -\sin\theta \frac{E_o}{\eta} e^{-jk(x\cos\theta + y\sin\theta)} \tag{2c}$$

It is clear that for normal incidence, ($\theta = 0$), this becomes a TEM wave with no y dependence. Equations (1a) and (2c) become unnecessary and the 1-D FDTD and the 2-D FDTD calculations are identical.

The situation is more complicated when θ is nonzero. Now H_x is nonzero and the 1-D wave is no longer identical to the 2-D wave. In order for the 1-D FDTD simulation to supply the correct data to the 2-D grid, the 1-D wave must propagate with a velocity that keeps pace with the 2-D wave. This velocity is simply the phase velocity of the 2-D wave in the x direction, *i.e.* $v_{1D} = v_o/cos\theta$, where v_o is the velocity of the 2-D wave in the direction θ. This is analogous to taking a slice along the right (or left) edge of the grid, of an infinite 2-D plane wave. Clearly this "slice" must travel along the edge with greater velocity than the the wave traveling an angle θ. Since the velocity, v_{1D} of this wave is given as $v_{1D} = \frac{\omega}{k_x}$, we can write Eq. (2) for the 1-D wave at $y = 0$ as:

$$E_{z_{1D}} = E_o e^{-jkx\cos\theta} \tag{3}$$

$$H_{y_{1D}} = -\cos\theta \frac{E_o}{\eta} e^{-jkx\cos\theta}$$

The solution in Eq.(3) does not satisfy Maxwell's curl equations. This problem can be addressed by modifying Ampere's Law. By taking the partial derivative of Eq.(2c) at $y = 0$ one obtains:

$$\frac{\partial H_x}{\partial y} = jk\sin^2\theta \frac{E_o}{\eta} e^{-jkx\cos\theta},$$

which, using Eq.(2b) becomes

$$\frac{\partial H_x}{\partial y} = \frac{(1-\cos^2\theta)\frac{\partial H_y}{\partial x}}{\cos^2\theta}.$$

Thus,

$$\frac{\partial H_y}{\partial x} + \frac{\partial H_x}{\partial y} = \frac{1}{\cos^2\theta}\frac{\partial H_y}{\partial x}$$

Now Eq.(1), for the 1-D wave will become:

$$\frac{\partial E_{z_{1D}}}{\partial x} = j\omega\mu H_{y_{1D}} \tag{4}$$

$$\frac{1}{\cos^2\theta}\frac{\partial H_{y_{1D}}}{\partial x} = j\omega\epsilon E_{z_{1D}}$$

Having described the changes to Maxwell's equations needed to integrate the 1-D FDTD into the 2-D grid, it is worthwhile examining the discretization of the modified 1D curl equations.

III. DISCRETIZATION OF MODIFIED EQUATIONS AND STABILITY CONSIDERATIONS

Through a straight forward discretization process[4], the discretized 1-D modified Maxwell's curl equations for lossless media become;

$$E_i^{n+\frac{1}{2}} = E_i^{n-\frac{1}{2}} + \frac{R}{\cos^2\theta}\eta(H^n{}_{i+\frac{1}{2}} - H^n{}_{i-\frac{1}{2}}) \tag{5}$$

$$H^{n+1}{}_{i+\frac{1}{2}} = H^n{}_{i+\frac{1}{2}} + \frac{R}{\eta}(E_{i+1}^{n+\frac{1}{2}} - E_i^{n+\frac{1}{2}})$$

where n is the time index, i is the space index and $R = v_o\Delta t/\Delta x$ is the Courant Number, and the vector component designations has been suppressed. Note that the velocity of the modified 1-D wave is $v_{1D} = \frac{v_o}{\cos\theta}$ as is apparent in the discretized wave equation based on Eq.(5).

Of particular importance is the Courant Number, R. Stability analysis indicates that for a FDTD simulation to be stable $R \leq 1$. For Equation (5), a new Courant number $R_{1D} = \frac{R}{\cos\theta}$ must be used instead. Since $R_{1D} \leq 1$, the usefulness of this method is limited to smaller angles. For example, let R_g be the Courant Number of the 2-D FDTD simulation. If R_g is chosen to be 0.5, then the largest angle that may be used is 60°. Clearly larger angles may be used if R_g is chosen to be smaller. However, since R_g is also a measure of how fast the wave moves through the grid, choosing it too small increases computational expense for the entire 2-D grid.

IV. LARGE ANGLE SOLUTIONS

For applicability with large propagation angles without decreasing R_g, changes must be made to the method. This is done by adjusting the Courant Number of the 1-D FDTD edge simulation. A smaller Courant number $R'_{1D} = v_o\Delta t'/\Delta x\cos\theta$ may be chosen such that $R'_{1D} \leq R_{1D}$. Since Δx remains the same, two simulations using R'_{1D} and R_{1D} would be spatially similar at the same physical time t, whenever $n'\Delta t' = n\Delta t$ for some different number of new time steps. The the stability condition is now $R'_{1D} \leq 1$ and thus θ may be increased.

Some care must be exercised in order to insure that the correct data is being passed to the 2-D grid. Let $m = \Delta t/\Delta t'$. If m is an integer($= n'/n$), then the m^{th} iteration of the 1-D FDTD is used to update the 2-D interior of the grid. If m is not an integer, then the correct value of E_z on the

edge of the lattice must be interpolated with respect to time from two or more iterations of the 1-D FDTD and **then** supplied to the 2-D grid.

The interpolation process is quite straight forward, with emphasis given to insuring the correct timing. Assume the 1-D FDTD simulation has a time sample interval of $\Delta t'$ and the 2-D simulation has a time sample interval of Δt. To meet the above criteria, $\Delta t' \leq \Delta t$. In order to insure that interpolation, and not extrapolation, is being performed, the 1-D simulation must be performed until $n'\Delta t' \geq n\Delta t$. The number of previous time values that must be stored in order to perform the interpolation is equal to the order of interpolation desired. Increasing the order will increase accuracy, but since previous values must be stored for **every** point on the 1-D grid, the order should be kept as low as possible.

Once the values needed for interpolation have been identified and calculated, any standard interpolation algorithm, such as Lagrange Interpolation, can be used. After the interpolated edge E_z values have been calculated, they can then be supplied to the 2-D grid. The edge H_y values need not be interpolated.

V. FDTD SIMULATION RESULTS

Several experiments were performed using the methods described above using a variety of parameters. Excellent results were obtained for angles ranging from 0 to 85 degrees. The general method of each experiment was the same. A Gaussian pulse plane wave was created along the initial boundary at $x = 0$ with time variation corresponding to various propagation angles and with various values of R_g. In each of these experiments, the plane wave encounters a PML ABC at the back of the grid. The ABC in question is from [5] with 8 PML layers and conductivity profile $\sigma_i = \sigma_f(i/8)^{3.7}$. Figure 2a shows a 50×50 view sampled from a 200×200 grid. The propagation angle is 45° degrees and the Courant Number R_g is 0.5. Note that the wave propagates without edge distortion. Figure 2b is the same wave 200 time steps later. The wave has encountered the ABC and no reflection is visible, even in the lattice corner, where the 1-D FDTD accurately extends the 2-D ABC interaction calculation to the edge. In the scattered field view 2c, which is at the same time step as 2b, the magnification has been increased by 5 orders of magnitude and the incident field has been removed. The features to note are that the scattered wave satisfies Snell's law and that the scattered wave is uniform along the 45° angle, *i.e.*, the introduction of the 1-D FDTD on the right edge of the grid has not introduced any additional reflection artifacts. Figure 3a is once again a 50×50 view of a 200×200 grid. Here the Gaussian pulse plane wave is incident on the ABC at 70°. Once again R_g is 0.5 but now $R_s{}' = 0.25/\cos\theta$. The 1-D wave is traveling at one-half the velocity needed to keep pace with the 2-D wave, so only every second time sample is passed to the 2-D grid. Figure 3b is the same wave 150 time steps later. As with 45° wave, the interaction with the ABC has produced no visible reflection. Once again it may be noticed that the scattered wave, Figure 3c, obeys Snell's law and is uniform along the Snell angle. Clearly the visible reflection is due solely to the plane wave interacting with the ABC, which is the desired information.

VI. CONCLUSIONS

A method for testing angle-independent ABCs has been described. By using a one-dimensional FDTD simulation on the left and right edges of a two-dimensional grid, a plane wave incident on a ABC at the back edge of the grid at a single angle can be created and propagated. This method will greatly simplify the analysis of angle-independent ABC performance. The method has been tested using a Gaussian pulse plane wave with a variety of parameters and has been shown to give excellent results. Finally, since all of the desired information is found in the 1-D simulations, it can be concluded that the analysis of angle-independent ABCs may be carried out using only 1-D simulations.

REFERENCES

[1] Berenger, J., "A Perfectly Matched Layer for the Absorption of Electromagnetic Waves", *Journal of Computational Physics*, Vol. 114, No. 1, pp. 185–200, October 1994.

[2] Yee K.S., "Numerical Solution of Initial Boundary-Value Problems Involving Maxwell's Equations in Isotropic Media", *IEEE Trans. Ant. Prop.*, Vol. AP-14, No. 1, pp. 302–307, May 1966.

[3] Mur, G., "Absorbing Boundary Conditions for the Finite-Difference Approximation of the Time-Domain Electromagnetic-Field Equations", *IEEE Transactions on Electromagnetic Compatibility*, Vol. EMC-23, No. 4, pp. 377–382, November 1981.

[4] Sadiku, M.N.O, "Numerical Techniques in Electromagnetics", pp. 139–144, CRC Press, Boca Raton, 1992.

[5] Rappaport, C., "Interpreting and Improving the PML Absorbing Boundary Condition Using Ansitropic Lossy Mapping of Space", *IEEE Trans. on Magnetics*, pp. 968–974, May 1996.

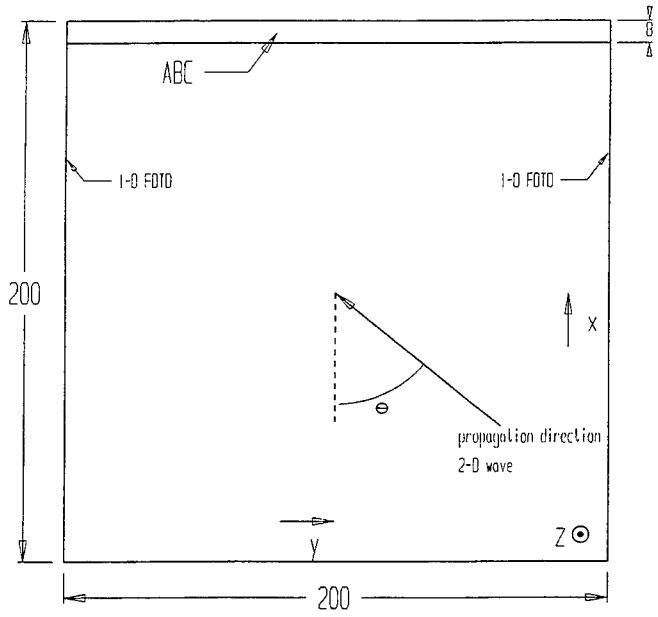

Figure 1
Geometry of grid.

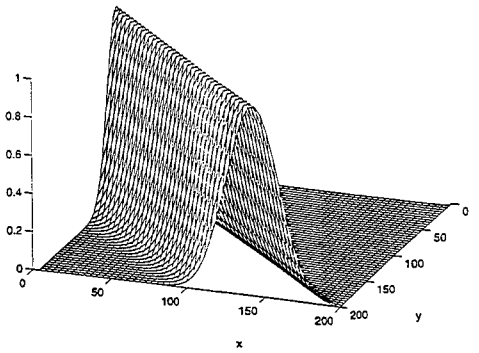

Figure 2a Gaussian pulse plane wave generated at $x = 0$ incident on the ABC at 45°. After 500 time steps, the 1-D FDTD simulation at $y = 200$ aligns perfectly with the 2-D FDTD simulation throughout the grid. ABC exists for $192 \leq x \leq 199$.

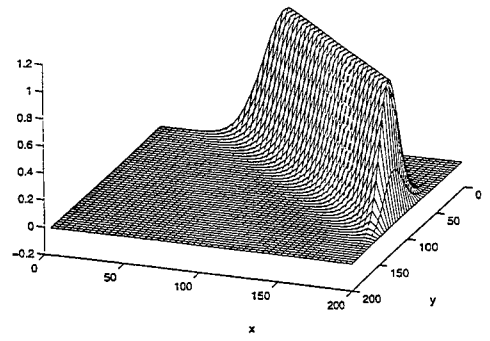

Figure 2b Gaussian pulse of Figure 2a, 200 time steps later: total field. The pulse has encountered the ABC, and is almost completely absorbed.

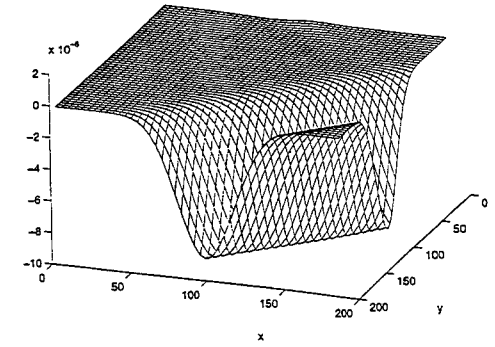

Figure 2c Scattered field at the same time of Figure 2b showing the residual reflection of the ABC.

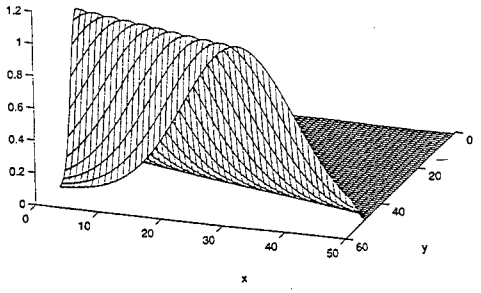

Figure 3a Gaussian pulse plane wave generated at $x = 0$ incident on the ABC at 70°. After 375 time steps, the 1-D FDTD simulation at $y = 200$ aligns perfectly with the 2-D FDTD simulation throughout the grid. ABC exists for $192 \leq x \leq 199$.

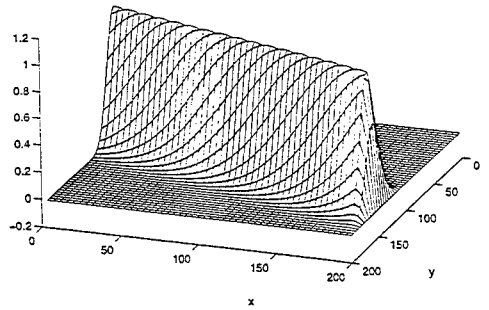

Figure 3b Gaussian pulse of Figure 3a 150 time steps later: total field.The pulse has encountered the ABC and is almost completely absorbed.

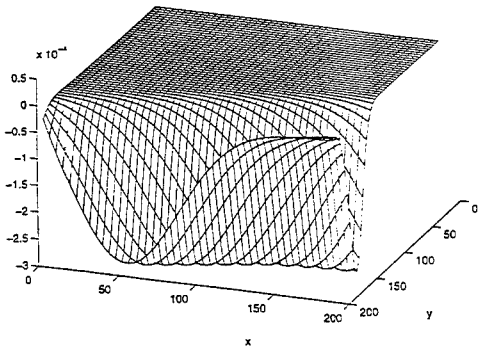

Figure 3c Scattered field at the same time of Figure 3b showing the residual reflection of the ABC.

Numerical Modeling of Light-Trapping in Solar Cells

T. Marshall and M. Piket-May
Department of Electrical and Computing Engineering
University of Colorado at Boulder
Boulder CO 80309-0425

Abstract

The light-trapping of a solar cell is controlled and enhanced by surface textures and anti-reflection coatings. Two numerical models used to study light-trapping. The first model is based on geometrical optics (ray-trace analysis). This analysis is inherently limited to thick solar cells. The second model is based on a Kane Yee's finite-difference time-domain algorithm (full-wave analysis) which allows accurate predictions of light-trapping in thin solar cells. The full-wave model is designed for solar cells with characteristic dimensions on the order of the wavelength of light. The full-wave model is a new method to study light-trapping in thin solar cells. Both models treat the solar cell as an infinite periodic structure illuminated by sunlight. Both models allow many different solar cell geometries to be analyzed. The geometry of the solar cell is defined in general terms so future light-trapping designs can be studied with the present models. Sunlight is defined by its polarization and irradiance spectrum. The output from both models is the absorption spectrum of the solar cell and the maximum achievable current density under a given irradiance spectrum. The irradiance spectrum used for terrestrial applications is the Air Mass 1.5 spectrum. For space-based applications, the Air Mass 0 spectrum can be used.

Both models predict a significant improvement of light-trapping when surface textures and anti-reflection coatings are used. Thin solar cells offer the promise of being efficient and inexpensive. When the ray-trace model is applied to thin solar cells, the light-trapping predictions are shown to be inaccurate. The full-wave model is more accurate than the ray-trace model. The full-wave model is used to predict the light-trapping capacity of various thin solar cell designs.

Introduction

Solar cells are semiconductor devices designed to convert light into electrical power. In order to be cost effective they must be as efficient as possible. Solar cell efficiency is related to the percent of the incident sunlight converted into electrical power. The goal in the design of solar cell devices is to trap and absorb as much light as possible inside the semiconductor. In the language of the solar cell community, the goal is to maximize light-trapping.

One effective way to maximize light-trapping is to coat the semiconductor with a thin film which reduces reflection. This anti-reflective coating ensures a higher percentage of light enters the cell so more light is absorbed. A second effective approach to increase light-trapping is to

texture the surface of the solar cell. The texture creates multiple reflections which will lead to increased light-trapping. The specific design of the textures is critical to maximize light-trapping. All commercial solar cell designs include encapsulation to protect the solar cell from nature. The effect of encapsulation on light-trapping is poorly understood. Encapsulation is assumed to be detrimental to light-trapping. The integration of the anti-reflection coating, encapsulation, and texture into the solar cell design determines the overall light-trapping capacity of a solar cell.

Historically, the solar cell industry has not had a means to effectively and accurately predict the light-trapping of a given solar cell geometry. Each solar cell was manufactured and then its efficiency was measured. This is expensive and time consuming. This research fills the need of the solar cell community by quantifying and predicting the light-trapping of a given solar cell design with the aid of numerical models. The result of this research is two numerical solar cell models which provide industry a means to quantify the light-trapping capability of many different three-dimensional solar cell designs. By modeling light-trapping, the expensive and time consuming step of fabrication is streamlined. Only the promising designs need to be fabricated and tested. This, in turn, frees valuable resources which can be utilized to design more efficient solar cells.

Maxwell's Equations

The interaction between sunlight and the solar cell is an interaction between light and matter. Maxwell's equations, therefore, are the fundamental governing equations. The types of materials found in solar cells are lossy. Solar cells absorb energy from light and convert it into electrical current. The absorption of light is included in Maxwell's equations by defining the loss via an electric current density, $\vec{J}_e = \sigma\vec{E}$. Hence, Maxwell's equations governing the physics of light-trapping are

$$\frac{\partial \vec{E}}{\partial t} = \frac{1}{\epsilon}\nabla \times \vec{H} - \frac{\sigma}{\epsilon}\vec{E} \tag{1}$$

$$\frac{\partial \vec{H}}{\partial t} = -\frac{1}{\mu}\nabla \times \vec{E} \tag{2}$$

where the permittivity, ϵ, and conductivity, σ, completely describe the optical properties of the solar cell. The solution to Maxwell's equations gives the electric and magnetic fields in space as a function of time. The fields then define the instantaneous power absorbed within the solar cell as

$$P_a(t) = \sigma \int_V \vec{E}(\vec{r}, t) \cdot \vec{E}(\vec{r}, t)\, dv \tag{3}$$

The amount of light that is converted to electrical current is determined partially by $P_a(t)$. The more absorbed power the better the light-trapping in the solar cell. Hence, the absorbed power, $P_a(t)$, is directly related to light-trapping in solar cells.

Maxwell's equations do not have a closed analytical solution except the most simple cases. This presents an immense challenge to solving problems in design and engineering, including the design of efficient solar cells. The difficulties of solving Maxwell's equations lie at the core of this research and are overcome by applying numerical methods.

A Measure of Light-Trapping

How is light converted to electrical power by a solar cell? The answer to this question provides the measure of light-trapping used in this research. The front side of the cell receives the incident sunlight and has some ohmic "fingers" to collect the carriers of current. The finger shape allows light to enter the solar cell. The back surface is a solid ohmic contact. The back side of the cell, for simplicity of discussion, is far enough away from the front surface to guarantee that no light reaches the back surface. The intensity of light decreases exponentially as a function of depth within the solar cell.

J_p is the current density collected at the front side and J_n is the current density collected at the back side of the solar cell. Overall, the total photocurrent as a function of wavelength is

$$J(\lambda) = J_p(\lambda) + J_n(\lambda) + J_{dr}(\lambda) \tag{4}$$

If the diffusion length is much larger than the solar cell thickness, most of the absorbed photons will be collected and contribute to the current.

The internal spectral response of the solar cell is defined as

$$SR(\lambda) = \frac{J_p(\lambda) + J_n(\lambda) + J_{dr}(\lambda)}{qF(\lambda)[1 - R(\lambda)]} \tag{5}$$

The total fraction of incident power absorbed by the solar cell is $1 - R(\lambda)$. The denominator, $qF(\lambda)[1-R(\lambda)]$, is the maximum current density possible when every absorbed photon contributes to the net current. The internal spectral response, therefore, describes the fraction of absorbed photons which contribute to the net current of the solar cell. In the ideal case, $SR(\lambda) = 1$ when the photon's energy is greater than the bandgap energy and $SR(\lambda) = 0$ otherwise. In general, the internal spectral response depends on the quality of the solar cell material and the specific device configuration. For instance, the internal spectral response may have a large dependence on the surface recombination velocity. Other parameters, like diffusion length and solar cell thickness, also affect the internal spectral response.

The total photocurrent density in the solar cell, J_L, is

$$J_L = q \int_0^\infty F(\lambda)A(\lambda)SR(\lambda)\, d\lambda \tag{6}$$

where q is the charge of an electron, $SR(\lambda)$ is the internal spectral response of the solar cell, $F(\lambda)$ is the solar spectrum (usually AM1.5 for terrestrial applications) of the incident light, and $A(\lambda)$ is the total fraction of light absorbed in the semiconductor.

The solar spectrum and electrical properties of the solar cell are ignored if only $A(\lambda)$ is used to quantify light-trapping. For this reason, the Maximum Achievable Current Density (MACD) of a solar cell is introduced. The MACD takes into account both absorption and the incident solar spectrum by counting the maximum number of photons that can be converted into current. The MACD is based on the assumption that every absorbed photon in the semiconductor creates an electron-hole pair which, in turn, contributes to the net electric current. The MACD is based on the assumption of an ideal internal spectral response. The MACD, J_{sc}, is defined by

$$J_{sc} = q \int_0^{\lambda_m} F(\lambda)A(\lambda)\, d\lambda \tag{7}$$

where q is the charge of an electron, $F(\lambda)$ is the solar spectrum (usually AM1.5) of the incident light, and $A(\lambda)$ comes from the solution to Maxwell's equations. The ideal internal spectral response makes it possible to study light-trapping without reference to any specific semiconductor material used in the solar cell. In this way, silicon as well as any other semiconductor can be studied based solely on optical considerations.

Both the absorption, $A(\lambda)$, and the MACD are used to quantify light-trapping. In the strict sense, absorption is the pure measure of light-trapping. Absorption quantifies how the incident light is absorbed as a function of wavelength but ignores the spectral content of the sunlight. On the other hand, the MACD integrates the effects of both the absorption and solar spectrum into a single quantity, J_{sc}. The MACD gives a more telling characterization of the real operational solar cell than absorption, without limiting itself to any particular semiconductor.

Ray Trace Light-Trapping Analysis

The effect of various front and rear surface geometry combinations on light-trapping is explored in this section. Eight different solar cell designs are modeled and compared based on the maximum achievable current density they can produce under AM1.5 solar illumination. The solar cells differ from the simple planar solar cell in their use of surface textures and anti-reflection films to enhance light-trapping. The front surface of the solar cell is textured with a periodic V-groove surface or a randomized surface. The V-groove has a peak angle of 70.4° corresponding to the crystalline structure of silicon. The random surface texture is modeled by choosing a set of random peak angles and heights. All of the front surfaces are coated with a two layer anti-reflection coating consisting of Si_3N_4 (0.0710 μm thick) and SiO_2 (0.0100 μm thick). The rear surface of the silicon is also textured with a periodic or random surface. A planar-polished back surface is also modeled. The rear surface is coated with aluminum in half the models. The aluminum ensures all light which reaches the back surface is reflected back into the solar cell. In all cases, the front surface texture type was the dominating design criterion. The periodic front texture is more effective than the randomized front surface at light-trapping. This is due to the reduced front reflection and increased optical path length. The periodic front surface allows greater control of the light-trapping effect. The random surface allows some fraction of the incident rays to experience only one bounce unlike the periodic surface. Some of the incident rays lead to a net reflection of R_1 unlike the desired reflection of R_1R_2 in the periodic texture which explains the better performance of the periodic front surface. The second dominant factor in light-trapping is the aluminum coating on the back surface. Independent of the type of rear surface texture, the aluminum coating achieved the higher current densities. The rear surface with an aluminum coating minimizes the amount of light transmitted out the back surface. The less light transmitted out the back surface leads to more light reflected back into the solar cell where it can be absorbed. Finally, a solar cell with a textured rear surface is better than the solar cell with a polished rear surface. The back surface texture must enhance the optical path length by further increasing the relative angle of the light rays.

Solar cells as thin as 0.75 μm have been proposed for their radiation hardness. Also, thin solar cells can be made inexpensive by using short diffusion length materials. The surfaces of the solar cell are polished flat. The thickness is 0.75 μm. As the wavelength increases, the ray-trace model begins to deviate from the exact model. The low extinction coefficient at the higher wavelengths allows light that is reflected from the back surface to set up interference. The exact model takes

into account the interference of light but the ray-trace model does not. As a result, the ray-trace model is not a good model to study light-trapping in thin solar cells.

Discussion

In this paper, two computer models are used to analyze solar cell light-trapping. The characteristic size of the solar cell determines which model is useful. The ray-trace model is based on the laws of geometrical optics. For this reason, the ray-trace model is limited to thick solar cells. The ray-trace model is inaccurate when applied to the thin 0.75 μm thick planar solar cell. The ray-trace model ignores the wave nature of light and interference effects within the solar cell. The Finite-Difference Time-Domain model is based on solving Maxwell's equations directly. The FDTD model accounts for the wave nature of light. The FDTD model accurately predicts the absorption spectrum for the thin, 0.75 μm, planar solar cell. The FDTD model is applicable to thin solar cells where the characteristic dimension is on the order of the wavelength of light.

Based on the ray-trace analysis, a good light-trapping design will incorporate a periodic front surface texture with an AR coating and a mirrored rear surface. Of the solar cell designs, the ray-trace model predicts the perpendicular slat design is the best at enhancing light-trapping. The ray-trace model shows that most of the photons are absorbed within 20 μm of the front surface of a textured solar cell. Therefore, the solar cell does not need to be thicker than 20 μm. The increased photon density due to texturing may increase the negative effects of surface recombination.

Thin solar cells, a few microns thick, promise to be efficient and inexpensive. The FDTD technique was used to model thin solar cells. A planar solar cell 0.75 μm thick has a maximum achievable current density of 10 mA/cm^2. The MACD is increased by 74% to 18.1 mA/cm^2 by texturing the front surface of the solar cell with pyramids. The perpendicular slat solar cell configuration increased the MACD by only 66%. The absorption density in the thin solar cell is more complicated than the standard exponential decay seen in thick planar solar cells. The absorption density in a textured solar cell can be larger at the back surface than at the front surface. Surface recombination may be most important at the back side of a thin solar cell. Overall, the FDTD model demonstrates texturing has a large effect on light-trapping in thin solar cells.

acknowledgments

The authors thank Cray Research for supercomputing grants. They also acknowledge the support of Associated Western Universities, Inc. for a Thesis Parts Fellowship. The ray-trace work was supported by the US Department of Energy under contract DOE DE-AC02-83CH10093 and the National Renewable EnergyLaboratory under two contracts; CT-2-12285-1 and CAT-4-13527-01.

Numerical Modeling of a Clock Distribution Network for a Superconducting Multichip Module

P. Vichot, J. Mix, Z. Schoenborn, J. Dunn, M. Piket-May
University of Colorado at Boulder
Campus Box 425
Boulder, CO 80309-0425
Fax:(303) 492-2758

January 3, 1997

Abstract

As supercomputers continue to move towards more powerful processors and parallelization, fast switching structures to route data signals between processors and shared memory become essential, and in fact, may be a primary limiting factor in overall computational throughput. The fast switching network under consideration in this paper is a crossbar switch employing superconducting Josephson Junction (JJ) and Multichip Module (MCM) technologies. This paper focuses on the design and simulation of the clock distribution network, located within the MCM, that will provide the necessary timing mechanism for data signals traveling through the crossbar switch.

1 Background

With the advent of Multichip Module technology, the adverse effects of a system's packaging on electrical performance have been substantially reduced. Higher IC packaging efficiencies, which are made possible by MCM's, allow for a significant increase in circuit densities, thereby reducing the effects of the interconnects. For computer applications, this means a significant reduction in the percentage of cycle time attributable to packaging delays. As clock speeds continue to increase, MCM packaging technology will play an essential role in the system architecture.

2 Introduction

A new, highly efficient switching network comprised of Josephson Junction Integrated Circuits (JJ IC's) has been developed for use as part of a massively parallel, shared memory computer architecture. The switching network is comprised of an array of switch chips which sit atop a Multichip module. This network serves to route data signals between the processors and memories which are both located off of the MCM. The Multichip module that provides the interconnection

for the switch chips in this network possesses the feature of combining superconducting and nonsuperconducting technologies (Figure 1).

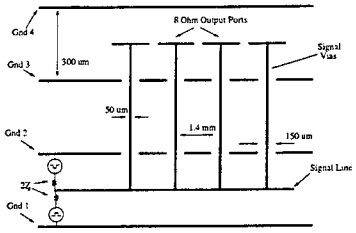

Figure 1: Multichip Module profile.

This research has focused on modeling the electromagnetics of the circuitry which distributes the clock signal to the inputs of the switch chips. This circuitry has originally been allocated to the second Tungsten metalization layer (W2) of the MCM. The 2.5 Gbit/sec clock signal enters this W2 layer of the MCM on a 50Ω stripline. The function of the circuitry is to then distribute this signal to several of the JJ IC's in parallel at the top of the MCM. The effective input impedance of each JJ IC is 8Ω. Several formidable electromagnetic issues must be addressed in the design of the clock:

- Broadband performance (preserve the harmonic content of the digital signal)
- Impedance transform from 50Ω to several 8Ω loads in parallel
- Maintain relative delay between the signals at successive output ports
- Compact design ($\approx 10mm \times 20mm$ footprint)

Though it is not possible to perfectly transform this severe impedance differential over such a broad range of frequencies within the footprint size, the goal of this project is to procure a clock design whose performance is successful in preserving an acceptable level of signal integrity at the inputs of the JJ IC's. The absolute amplitudes of each signal must be the same for each JJ IC. Signal magnitude variations (overshoot) of about $\pm$ 30% from the steady state value are permitted: anything larger than this may erroneously trigger a false logic state in the JJ IC's. There must be a 6 picosecond time-delay of the clock signal between the inputs of successive JJ IC's to correspond to propagation delays incurred within the switching network as signals pass from processors to memories. In addition, any reflection of the incident clock signal on the distribution network will be circulated and dissipated outside of the MCM.

The electromagnetic modeling for the clock structures detailed in the following sections makes use of frequency-domain and time-domain methods in tandem. Full-wave frequency-domain analysis is implemented through the use of a packaged Finite-Element code (HP High Frequency Structure Simulator), while the time-domain analysis employs the Finite-Difference Time-Domain method.

3 Clock Simulations

Our initial work focused on fanout structures and serial feed designs. Given modifications to our original design specifications and the limitations encountered in the fanout and serial feed designs we investigated a sectoral feed design.

Instead of sixteen 8Ω outputs, the clock now must distribute the signal to only four 8Ω outputs. This was done in order to reduce the significant impedance mismatch between the 50Ω input and the multiple 8Ω outputs.

3.1 Sectoral Design

The results for the Serial feed indicate that there are high frequency effects inherent to the MCM signal line/via structure that need to be taken into consideration. Therefore the new class of structures currently being simulated are Sectoral power dividers first introduced by K.C. Gupta and M.D. Abouzahra [1] which naturally account for the signal wave propagation and higher frequency effects. The reported transmission parameters for the Sectoral power divider are very broadband(from 1 to 15 Ghz) which should translate into a preservation of the signal integrity of the clock signal. A representative schematic of this power divider is shown in Figure 2. The principal behind the sectoral structure is to obtain equi-amplitude and equi-phase signal

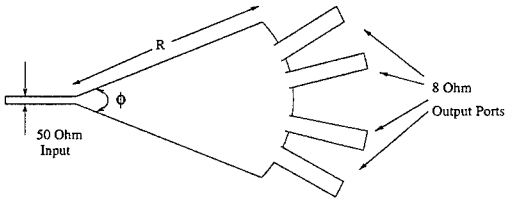

Figure 2: Sectoral power divider geometry.

distribution among the four output ports. By then varying the length of signal lines between these ports and the vias, proper phase delay may be achieved. Different designs are obtained by changing the angle ϕ and the radius R of the sectoral structure. The angle is chosen such that there is sufficient amount of pitch between output lines to provide the desired amount of isolation. The radius is chosen to be $\frac{\lambda}{2}$ at the design frequency. The first design considered is on a polyimide substrate ($\epsilon = 5.2$) with a radius of 13.51 mm, a ϕ of 72 degrees, and a height between groundplanes of $300\mu m$. The input line is $125\mu m$ wide to provide the 50Ω input impedance and the output vias are placed directly on the sector and extend through the upper ground layer to 8Ω output lines which are then terminated. The results for the sectoral power divider are given in Figure 3 where Port 1 is the input port to the sector, Port 2 is one of the outer ports, and Port 3 is an inner port. The structure is resonant at 12.5Ghz as shown by the trace of S_{11}. The transmission parameters were not as broadband as those reported for the planar structure presented in [1], as evidenced from the plots of S_{21} and S_{31}. This decrease in bandwidth may accounted for by the two primary modifications from the structure reported in [1]. First, the

impedance of the output ports have been reduced from 50 to 8Ω for this modified model. The second difference is the incorporation of via effects on propagation as the signal travels vertically through the MCM. The resulting signal distortion produces a final time domain signal (as shown in Figure 3 d) with a 30% overshoot. Although this signal is on the edge of the design requirements for overshoot, the signal does not stabilize and its use as a clock is questionable.

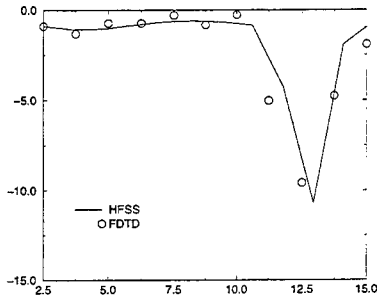

(a) S11

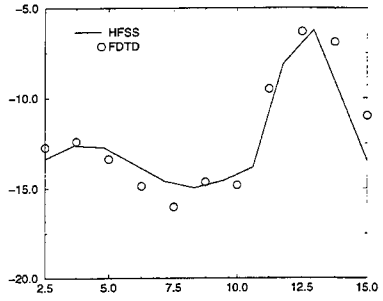

(b) S21

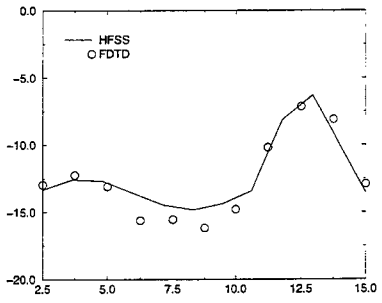

(c) S31

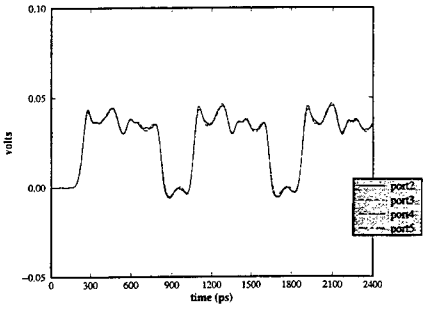

(d) Time-Domain Results

Figure 3: Sectoral power divider simulation results

3.2 Cross Feed

Recently, the possibility of allocating space for the clock distribution network on one of the Niobium layers has been investigated. The placement of the clock circuitry on this thin film layer, where the $6\mu m$ substrate height reduces the widths of the 8Ω output lines from 1.285mm to 25um, allows for the implementation of a new set of rudimentary designs.

The design presented here is shown in Figure 4. The signal is incident on a 50Ω line in one of the lower, thick film layers. It then vias up through multiple layers ultimately distributing the signal to the four 8Ω output lines on the Niobium layer. These lines then via directly up to the 8Ω inputs of the switch chips. The variation in line lengths achieve the necessary delays of 12ps between successive outputs.

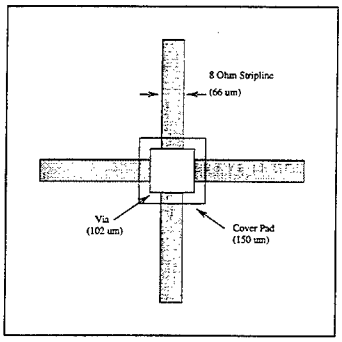

Figure 4: Cross design for implementation on thin film layer of MCM.

As expected, the majority of the power is reflected ($S_{11} \approx -0.6$) due to the impedance mismatch between the 50Ω input and the four 8Ω outputs in parallel. Though the return loss is significant, this reflected power may be circulated out of the system. More importantly, the power levels transmitted to the outputs are uniform and invariant over the frequency range of interest.

The corresponding voltages measured at the four outputs of the Cross design for the specified digital signal show no loss of signal integrity and the relative delay of 12ps between successive outputs is preserved.

4 Conclusions

We have presented both frequency and time-domain simulation results obtained for the sectoral design. The primary design criteria for this 2.5Gbit/s clock is that it must maintain skew and signal integrity while transforming from a 50Ω input to several 8Ω outputs.

If placement of the clock on one of the upper, Niobium thin-film layers is possible, then the design of the clock becomes relatively straightforward due to the significant shrinkage of the

circuitry. The Cross design presented in the previous section indicates that ideal performance for this application may be obtained: both signal integrity and skew are preserved.

Placement of the clock on one of the lower, ceramic layers complicates the design considerably. This is due primarily to the intractably large widths of 8Ω lines on this layer, which eliminate the use of the Cross design. If it is necessary to have the clock on the ceramic layer the Sectoral design shows promise in satisfying the necessary system requirements.

5 Work in Progress

5.1 Test MCM

To aid in the design of the final clock network, a test MCM has been fabricated with numerous variations on the designs presented in this paper. Measurements are currently generated for this test MCM. This will establish baseline models for comparison with simulation data. This data can then be used to validate and, where necessary, improve the simulation models. Comparison of the simulated and measured results will be presented in the future.

Acknowledgments

The authors would like to acknowledge the sponsor of this project, Dr. F. Bedard of the U.S government and other project team members including Tektronix, JHU/APL, Kyocera, TRW, and IBM.

References

[1] K.C. Gupta and M.D. Abouzahra, Eds., *Analysis and Design of Planar Microwave Components*, IEEE Press, New York, 1994.

Computational Evaluation of an Optical Sensor using the Finite Difference Time Domain Method

Ronald R. DeLyser, University of Denver, Denver, CO

1 Introduction

TEMAC3D [1] is a FDTD code developed by John H. Beggs of Mississippi State University for use in modeling High Power Microwave antennas, ulta-wideband antennas and for electromagnetic coupling calculations. It is a FORTRAN code which is based on the three dimensional implementation of the FDTD method [2] and has the following capabilities: (1) treatment of perfectly conducting, lossy dielectric, and lossy magnetic materials; (2) second order Liao outer radiation boundary condition; (3) transient near to far field transformation capability to obtain scattered far fields at multiple scattering angles; (4) band limited, Gaussian, hyperbolic secant, unit step, hyperbolic cosine unit step and ramped sinusoid incident pulses with arbitrary incidence directions and polarization; (5) custom pulse or raw time-domain data excitation; (6) plane wave or point source incident excitation; (7) near field sampling anywhere within the computational domain; (8) diagnostic output files; (9) standardized input deck for reading simulation variables; (10) field sampling specified by character strings; (11) benchmark problems; (12) C-preprocessor capability; and (13) steady state antenna calculations, including a steady state near to far field transformation.

A suite of peripheral software is needed to generate solid models, generate the Finite Difference mesh, view the mesh for consistency, generate the problem name list and header files, and view the results of the analysis. The solid model geometry file is generated by BRL-CAD version 4.4 which is available from Ballistics Research Laboratory, Aberdeen proving Ground, MD. The geometry file is then used as input to ANASTASIA, a component of TSAR (Temporal Scattering And Response) from Lawrence Livermore National Laboratory, CA. ANASTASIA generates a mesh given the number of "pad" cells[1] and the size of the cell. IMAGE (another component of TSAR) is used to view the mesh (a few examples will be given below) to be sure that the FD mesh is really the desired mesh. This mesh file is then an input for XTEAR (X-window Temporal Electromagnetic Analysis and Response) [1] which is a graphical user interface designed for input of all relevant parameters for the FDTD simulations using TEMAC3D. Since XTEAR was written using the scripting language, TCL/TK, these software packages (version 7.3 of TCL and version 3.6 of TK) have to be installed on the same computer that runs XTEAR. Finally, software is needed to view output fields as a function of time, frequency and/or position, to generate far-field scattering and/or radiation plots, and to do Fast Fourier Transforms (FFTs) in order to determine the frequency response. FORTRAN programs were provided by John Beggs for far zone processing and radiation plots. I used DeltaGraph Pro 3.5 [4] for radiation plots, and Mathcad 6.0 [3] for doing the FFTs, and spatial, temporal and frequency dependent field visualization.

TCL/TK, TEMAC3D and XTEAR[2] were installed and run at the University of Denver (DU) on an IBM RS6000 model 570 Powerstation with 512 MBytes of RAM and 6.5 GBytes of disk space. I was

[1] Pad cells occupy the space between the outermost cells of the modeled object and the outermost cells of the problem space which implement the absorbing boundary conditions.

[2] These installations were not straight forward. Information on porting this software to the IBM RS6000 is available from the author or from Capt. Tim Fromm, PL/WSTS, Kirtland AFB, NM 87117-5776.

unable to install BRL-CAD at DU and therefore, could not install TSAR (BRL-CAD is necessary for TSAR.) I therefore used BRL-CAD, ANASTASIA and IMAGE on a SUN Workstation at the Satellite Assessment Center at Phillips Laboratory, Kirtland AFB, NM. Mesh files generated at Phillips Lab were then sent to DU for processing by XTEAR and numerical analysis by TEMAC3D.

2 The Sensor Model

A drawing of the cross-section of a sensor from a satellite is shown in Figure 1. The detail of this drawing cannot be captured with a reasonably sized mesh[3] so some further simplifications were made: (1) Rounded corners have been squared. This makes drawing the model with BRL/CAD a reasonable task. The meshing process will do this in the long run anyway. (2) The short, narrow gap between the central cavity region and the lower cavity region remains. This is because some significant amount of energy may propagate through this gap due to its shortness. (3) The long narrow gap between the lower outside cavity regions has been closed. I view this gap as a waveguide below cutoff and little if no energy will propagate through it due to its length. This assumption allows us to fill the large "T" shaped region with metal. (4) Short, narrow gaps in the cavity areas are filled with metal. These areas add little volume to the cavity and are so narrow as to prevent energy propagation.

The layered area in the center of the drawing contains the filter area which is composed of a metal frame and 8 filters and detectors in an octagonal configuration. Below the filters is an air gap and below that is a layer of Mylar upon which the Bismuth/Tellurium thermopile detectors are mounted. Since the resolution of the mesh will be 1 mm and the filter, air gap and Mylar lie in slanted regions, I decided to make the Mylar and air regions 1.5 mm thick and the filter region 2 mm thick. This will prevent the regions from touching each other during the meshing process.

A view of the center cross-section of the mesh is shown in Figure 2. Note that the large metal areas below the sensor are hollowed out. This ultimately results in a much smaller mesh file since the background, which is free space, does not get specified in the file. The numbered locations are where the total electric fields will be reported.

3 Results for the Sensor

The sequence of anaysis is to do the scattering problem first to identify frequencies of interest. The radiation problem follows at those frequencies in order to identify angles of interest. The scattering problem can then be repeated at those angles.

3.1 The Scattering Problem

The sensor model was illuminated from the top with a y-polarized plane wave with the following Gaussian characteristics: (1) rise time = 70.3 psec, (2) half-power pulse width = 69.4 psec, (3) truncation pulse width = 476.5 psec, (4) time offset = 238.2 psec, (5) 80 dB frequency limit = 16.39 GHz, (6) upper frequency limit = 30 GHz, and (7) time step = 1.925 psec.

Figures 3 - 4 show the y components of the electric field at the locations 1 and 2. A comparison of Figures 3 and 4 shows that the fields in the larger upper cavity (location 2) are much larger than the fields at the detector location (location 1). This is reasonable since the detector is located below the Germanium filter. The fields in the smaller cavity regions (locations 3 and 4), which are accessible from

[3]The lens and filters are made of Germanium with a dielectric constant of 14. A 1 mm mesh size then will be good for frequencies up to ~8 GHz and require ~180 MBytes of RAM. A model with a 0.66 mm mesh size will be good to ~12.6 GHz and take ~500 MBytes of RAM.

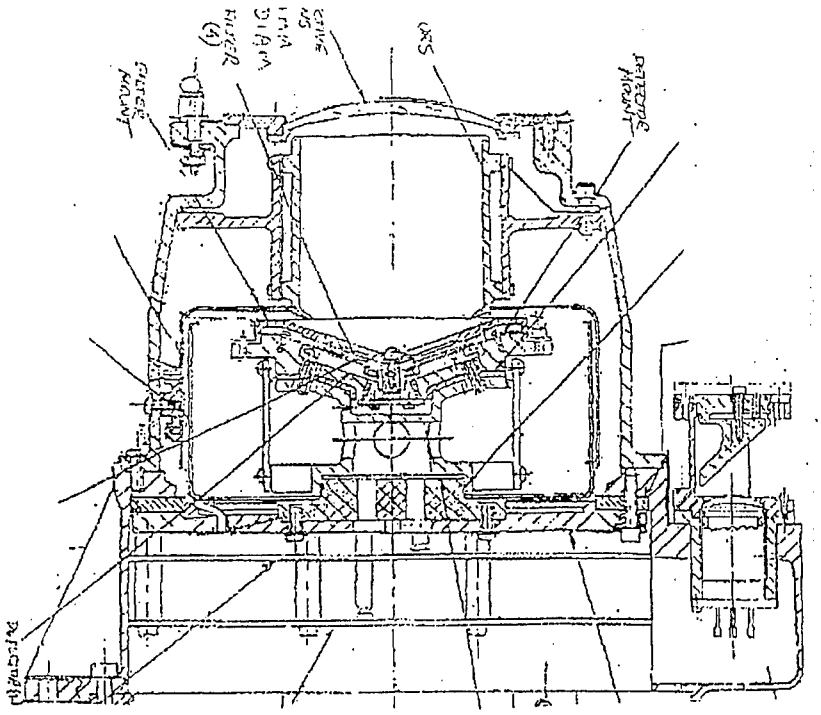

Figure 1: A sketch of the satellite sensor.

the larger cavity through narrow slotted regions, are much smaller and are dominated by the incident field.

This mesh is good for frequencies up to ~8 GHz based upon the fact that the cell size (1 mm) should be no larger than 0.1 λ at the highest frequency of interest in the material with the highest dielectric constant (the Germanium for this case.) Since the regions of Germanium are rather small, I felt that the high frequency content of this source signal is sufficiently attenuated for this model. Figure 5 shows the FFTs of the dominant components (y in this case) of the electric fields at locations 1 and 2 normalized to the incident field. The other components (x and z) were 20 - 40 dB lower than the y components.

Some observations concerning resonances can be made. A sharp resonance at ~3.58 GHz at location 2 also shows up at a much lower level at location 1. The resonances in the outer cavity regions are at an even lower level and at different frequencies which reflect their different geometries (toroidal as opposed to cylindrical) and volumes. If a closed cylindrical cavity of the dimensions of the large central cavity is postulated, the resonance frequencies of the TE_{111} and TM_{111} modes is calculated to be 3.59 GHz and 6.44 GHz respectively. There are two resonances at location 2 corresponding to these frequencies, 3.58 GHz and 6.47 GHz. Field plots of the transverse modes for cylindrical waveguides in [5] show that the TE_{11n}, TM_{11n}, TE_{12n}, TM_{12n}, TE_{13n}, and TM_{13n} will have non-zero fields in the center of the cavity. If we want to look at other modes in the upper cavity, we need to place sensors in locations away from the

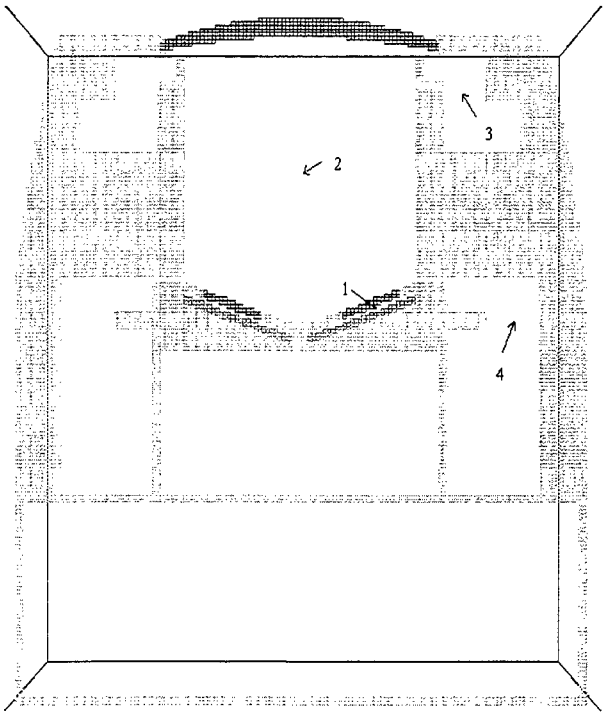

Figure 2: FDTD mesh of the sensor showing locations a electric field calculations.

center and in directions tangential to the field quantity to be calculated. While this would be instructive from an academic point of view, the fields at location 1 are of primary interest and will include all modes excited at that location given the particular characteristics of the source.

3.2 The Radiation Problem

The resonances determined from the scattering problem, 3.58 GHz, 4.82 GHz and 6.47 GHz, where chosen for the radiation problem. The source, positioned at location 1 of Figure 2, is now a sine wave at the appropriate frequency which is ramped to full amplitude in 10 cycles. The simulations ran for 16,384 time steps to ensure that the fields inside the sensor reached steady state. Figures 6 - 8 show the radiation plots generated for these three frequencies with x and y polarized excitations. Since the sensor is in the $\phi = 0°$ plane, the radiation plots for the $\phi = 90°$ plane should be symmetrical, as they are.

We must also take note of the fact that, in reality, the sensor is mounted on a larger structure that could be modeled by a ground plane. This ground plane would have a significant effect on the radiation plot of the lower half sphere where $90° < \theta < 270°$, and to a lesser extent, on the radiation from

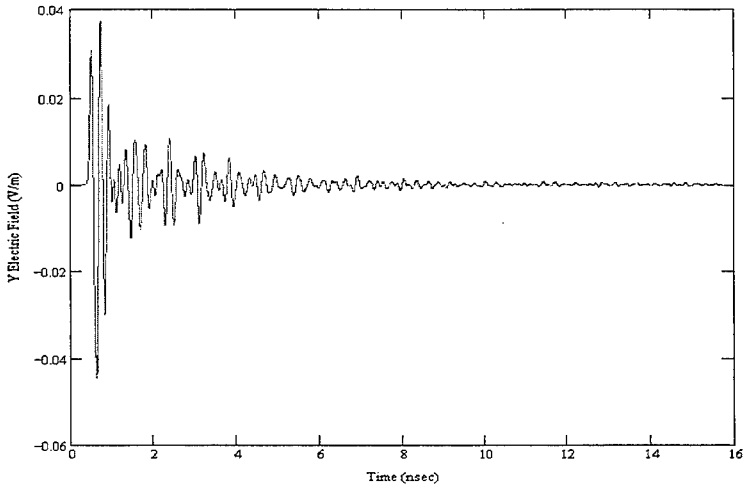

Figure 3: Electric field at location 1.

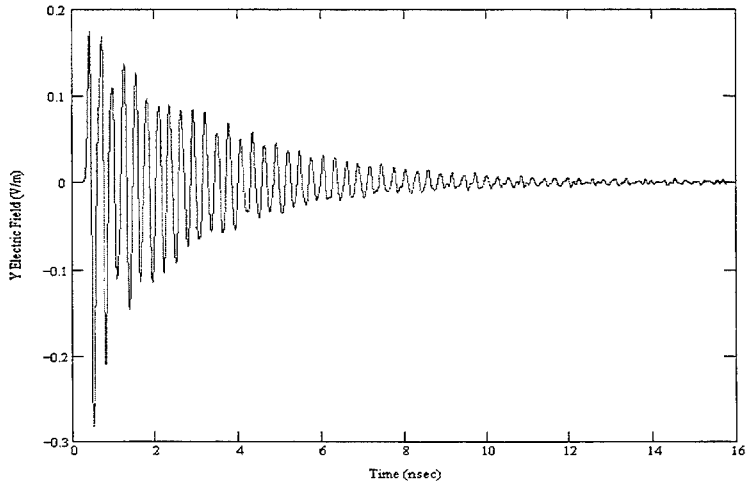

Figure 4: Electric field at location 2.

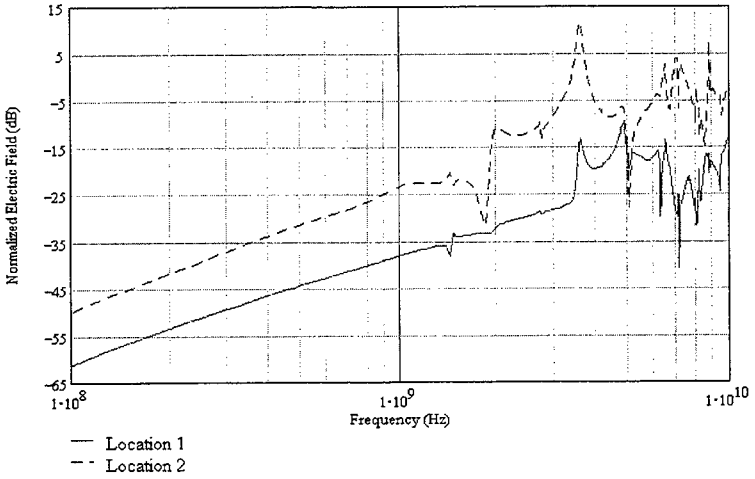

Figure 5: FFT of the electric field at locations 1 and 2.

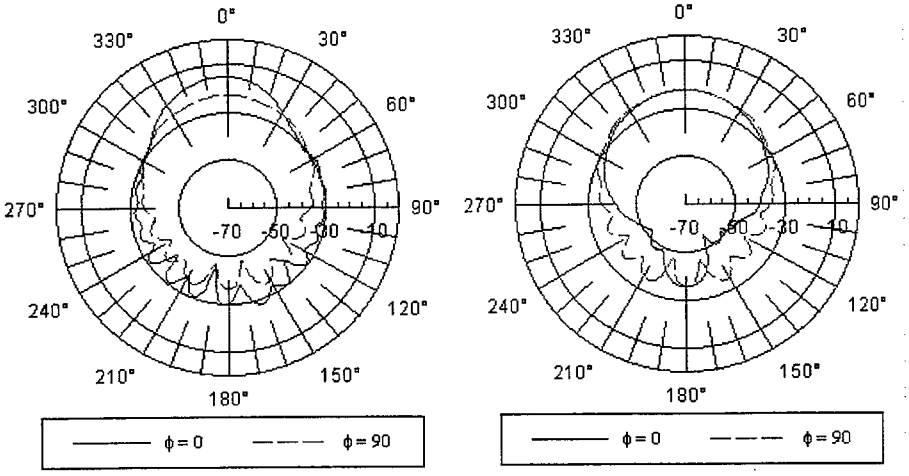

Figure 6: Sensor gain for x and y polarizations at 3.58 GHz.

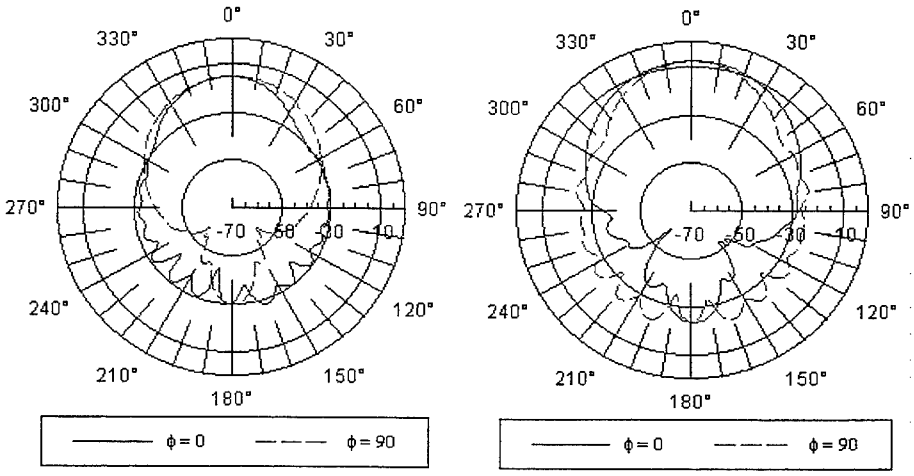

Figure 7: Sensor gain for x and y polarizations at 4.82 GHz.

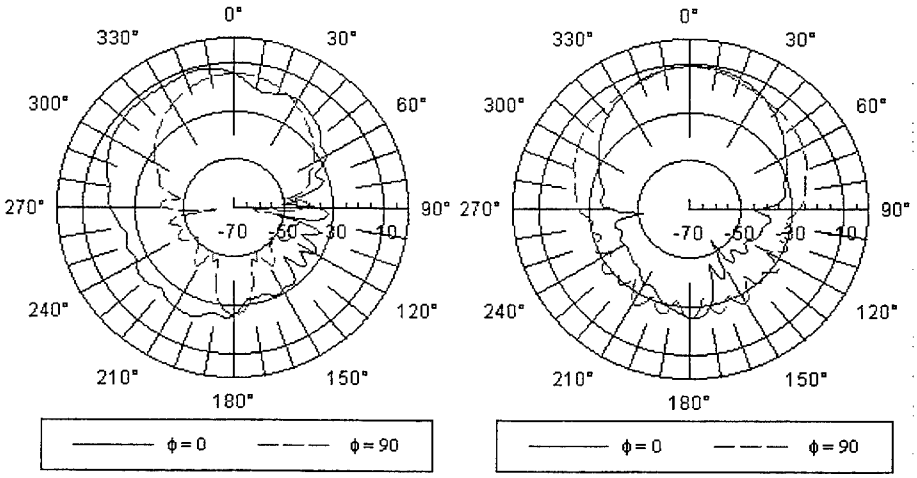

Figure 8: Sensor gain for x and y polarizations at 6.47 GHz.

the upper half sphere. Unfortunately, ground planes cannot be directly modeled with TEMAC3D. To effectively take the ground plane into account in TEMAC3D, we would have to take advantage of Image Theory [5] and mirror the mesh shown in Figure 2 through the xy plane (the bottom plane of the mesh). This would double the problem space, and therefore reduce the usable upper frequency limit. While this procedure is probably not necessary for the scattering problem, it would be useful for comparison purposes to do it for the radiation problem.

4 Conclusions

The preliminary results reported here show that TEMAC3D is an effective tool for analysis of complex cavities. It can be used to treat a cavity as a scatterer in order to find frequency response of a particular field location inside the cavity. Once frequencies of interest are identified, TEMAC3D can be used to analyze the cavity as a radiator (antenna with a specified point source internal to the cavity) in order to find angles of incidence that are particularly sensitive. Once these are found, the frequency response can be repeated at these angles.

TEMAC3D results, while not verified by independent calculations or testing, are reasonable. Future work should continue on this optical system using TEMAC3D with plane wave excitation using a narrower pulse, producing a wider frequency response, and using meshes with smaller cells. Models that will require ~500 MBytes of RAM have been generated which will be good to $\sim$ 12.6 GHz.

TEMAC3D is capable of doing every step in the process of generating a frequency response at points of interest inside the cavity, followed by radiation models at the most sensitive frequencies, followed by frequency response models at the sensitive angles. Where possible, this information should be used to define test parameters for future experiments on the sensor.

Some improvements to TEMAC3D could be made: (1) Implementation of perfect magnetic and perfect electric boundaries would allow the user to specify ground planes or apply symmetry to problems, thus reducing computational requirements. This capability would also allow the modeling of the sensor on a ground plane. (2) Adapting the program for parallel processing would speed up the simulation significantly.

Acknowledgments: The author thanks John Beggs and Sydney Blocher for many productive discussions, and Phillips Laboratory, WSTS, for funding this project.

References

[1] John H. Beggs, James D. Letterio and Sydney A. Blocher, Jr., *User Manual for XTEAR and TEMAC3D Computational Electromagnetic Time-Domain Codes*, available from Sydney A. Blocher, Jr., Phillips Laboratory/WSM, 3550 Aberdeen Ave. SE, Kirtland AFB, NM 87117.

[2] K. S. Kuntz and R. J. Luebbers, "The Finite Difference Time Domain Method for Electromagnetics," CRC Press, Boca Raton, FL, 1993.

[3] Mathcad Plus 6.0, MathSoft, Inc., 101 Main St., Cambridge, MA 02142, 1995.

[4] DeltaGraph Pro 3.5, DeltaPoint, Inc., 2 Harris Court Suite B-1, Monterey, CA 93940, 1995.

[5] Constantine A. Balanis, "Advanced Engineering Electromagnetics," John Wiley & Sons, New York, 1989.

Applications of the Hybrid Dynamic-Static Finite Difference Approach on 3D-MMIC Structures

Stefan Lindenmeier, Peter Russer and Wolfgang Heinrich*

Technische Universität München, Lehrstuhl für Hochfrequenztechnik, Munich, Germany
*Ferdinand-Braun-Institut für Höchstfrequenztechnik, Berlin, Germany

ABSTRACT

The Hybrid Dynamic-Static Finite Difference approach combines numerical solutions of the static fields with a Finite Difference full wave analysis in frequency domain. The static fields are calculated in a fast way by Finite Difference methods using a dense discretization of the given structure. They contain the accurate information of the structure details. After incorporating the information of the static field into the Finite Difference full wave analysis, the field dynamics are considered too. The full wave analysis can now be done by using a coarse mesh while the information about the structures details is kept. This yields a considerable increase in efficiency of the Finite Difference method in Frequency domain. In this contribution the hybrid Finite-Difference approach is extended to be applicable in threedimensional MMIC-structures. In examples of a microstrip bend and a coplanar double discontinuity the high efficiency of the method is shown.

INTRODUCTION

For the design of micro- and millimeter-wave integrated circuits, flexible and efficient CAD tools are required The trend towards higher packaging density and the necessity to include housing effects demands for a highly flexible numerical field solver as given for example by the Finite Difference Method [1]. One restriction to the efficiency of the method is, that high spatial resolution is required for the description of structure details of small dimension which causes high numerical effort. On the other hand there is a quasi static field behaviour at structure details of small dimension [2]. With that, the static field solutions in these areas can be used as a priori information for the full wave analysis in the FDFD-method.

In [3] we presented a hybrid Dynamic-Static Finite Difference approach in frequency domain for the numerical modeling of MMIC-circuits in the micro- and millimeter wave range. This approach represents an highly efficient combination of static field solutions and the full wave analysis. The geometrical details are treated by a fast static approach using a fine mesh and the dynamic problem is solved only on a relatively coarse grid. By using the static field solutions for the consideration of the structures details, the discretization of the full wave analysis is only restricted for the lengths of each elementary cell to be far below the wavelength. The incorporation of static field data into the finite difference algorithm for the simulation of the dynamic field is done by weighting factors. They are multiplied with the integral approximations of the Finite difference formulation to improve the accuracy of the integral modeling. The weighting factors are the relation between the corresponding integral of the static field and its Finite Difference approximation For each electric and magnetic field component in the structure there exist weighting factors for the corresponding line integrals and also for the surface integrals. The efficiency of the method was shown for several examples of twodimensional structures.

In this contribution we extend the hybrid Finite-Difference approach to be applicable in threedimensional MMIC-multiport structures for the calculation of the scattering coefficients. In the threedimensional case the efficient calculation of the magneto-static field is done by using the PPS-method [4,5], which makes possible the Finite Difference calculation of a scalar magnetic potential. As we will show, also in the threedimensional case, the approach yields a high reduction in computational effort, compared with the conventional Finite Difference method. The CPU-time can be reduced to less than one tenth, the storage to one third. Additionally, using the hybrid approach, there is no essential increase in CPU-time for the consideration of more frequencies. The method is applicable in structures with details of dimensions far below the wavelength. The incorporation of the static field data into the Finite-Difference algorithm doesn't change the structure of the algorithm.

FOUNDATION OF THE METHOD

The hybrid FD scheme consists of the following two-step procedure (Fig.1 illustrates the different levels of discretization):

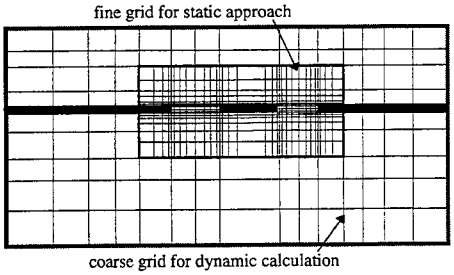

Fig.1: The different levels of discretization for the static and the dynamic field description in a CPW structure

The structure (or only critical subregions) is analyzed by a static FD method with high resolution, i.e., a dense mesh. The numerical expense is much lower than for the corresponding full-wave solution. Additionally, in the lossless case, the static data do not change with frequency. Thereby, when varying the frequency, this part of the analysis needs to be calculated only once. The static results are incorporated into the dynamic FDFD analysis by means of weighting factors for the integrals over the elementary cells. Then the complete problem is solved on a coarse mesh.

Our approach is based on the integral formulation of the Finite-Difference frequency domain (FDFD) method [1], [6]. Maxwells equations are written in the form of integrals over the edges and surfaces of the elementary cells. The principal of our hybrid approach is that we use the static information (or any other a-priori knowledge of the field behavior) to improve the integral approximation.In the conventional scheme, the integrals are calculated simply by multiplying the field value in the center with the respective cell length. This approximation yields the discretization error δ_d, e.g. for the line integral of E_x:

$$\int_{x_m}^{x_m+\Delta x_m} E_x(x)\cdot dx = E_x(x_m+\Delta x_m/2)\cdot\Delta x_m\cdot(1+\delta_d) \qquad (1)$$

It is clear that the resulting error in the integral approximation can be eliminated if the true mean value is applied in eqn.1 instead of the cell-center value $E_x(x_m+\Delta x_m/2)$. In many cases however, the mean value can be determined with good accuracy by a static analysis.

The static fields have to be calculated in an efficient way for 3D-structures with high complexity and nearly arbitrary geometry. This can be done in an efficient and flexible way by calculating scalar potentials of the fields in a Finite Difference-scheme. The potentials are defined on the vertexis of the mesh cells. For the numerical calculation of the magneto-static field by a scalar potential, the method of Potential Partitioning Surfaces (PPS) is used, which is presented in [4,5].

For example, a weigthing factor Λ^{ex} is generated from the static field distribution $E_{xs}(x)$

$$\Lambda_m^{ex} = \frac{\int_{x_m}^{x_m+\Delta x_m} E_{xs}(x)\cdot dx}{E_x(x_m+\Delta x_m/2)\cdot \Delta x_m} = (1+\delta_{ds}) \tag{2}$$

and its discretization error δ_{ds} respectively. The improved description of the integral in eqn.1 then reads

$$\int_{x_m}^{x_m+\Delta x_m} E_x(x)\cdot dx = \Lambda_m^{ex}\cdot E_x(x_m+\Delta x_m/2)\cdot \Delta x_m\cdot(1+\delta_r) \tag{3}$$

with the residual error δ_r:

$$\delta_r = \frac{\delta_d - \delta_{ds}}{1+\delta_{ds}} \tag{4}$$

Due to the fact that the relative dynamic and static field distributions approach in critical subregions, such as metallic edges, the difference δ_d-δ_{ds} and hence the resulting error δ_r remains small. In this way, weighting factors Λ for all line integrals and Φ for all surface integrals are introduced in the dynamic FD approach. This leads to a substitution of the field values in the FD-algorithm:

$$\boldsymbol{E} \rightarrow \left[\Lambda^e\right]\cdot\boldsymbol{E} = \tilde{\boldsymbol{E}}\ ; \quad \boldsymbol{B} \rightarrow \left[\Phi^b\right]\cdot\boldsymbol{B} = \tilde{\boldsymbol{B}} \tag{5}$$

Now the electric field values are interpreted as line integrals, while the magnetic field values are interpreted as surface integrals. The local averages of the tensors of ε and μ are also substituted.

$$\begin{aligned} [\bar{\varepsilon}] &\rightarrow \left[\Phi^e\right]\cdot\left[\Lambda^e\right]^{-1}\cdot[\bar{\varepsilon}] = [\tilde{\varepsilon}]; \\ [\bar{\mu}] &\rightarrow \left[\Lambda^b\right]\cdot\left[\Phi^b\right]^{-1}\cdot[\bar{\mu}] = [\tilde{\mu}] \end{aligned} \tag{6}$$

Thus the discretization errors of a FD simulation using a coarse mesh are compensated by artificial anisotropic material parameters. While the type of weighting factor formulation is related to [7,8] we now have an uniform two-grid-level FD approach with both static and dynamic data derived by the FD scheme. Furthermore, the static field information is utilized not only in the edge regions but over subsections or even the entire structure. This enables one, for instance, to discretize the slot of a MMIC coplanar waveguide with only one step in the dynamic solution without sacrificing accuracy. It should be pointed out that the inclusion of the weighting factors as

described above preserves consistency of the FD approach. Therefore, mode orthogonality, energy conservation, and similar theorems are fullfilled for the discretized system within numerical accuracy, as in the conventional FD approach. This feature is important, for instance, with regard to S-parameter extraction.

NUMERICAL RESULTS

The new formulation was implemented as a FORTRAN code to investigate efficiency and numerical properties. In order to evaluate the improvement against the conventional approach the propagation characteristics for typical MMIC geometries are studied. We investigated the threedimensional realization of our hybrid approach for the field analysis in several multiport structures. For example we consider a microstrip bend on Gallium Arsenide substrate with low resolution for the dynamic field. The high resolution for the static field is also used for the full wave analysis to produce accurate reference solutions. This resolution is five times higher (Fig 2).

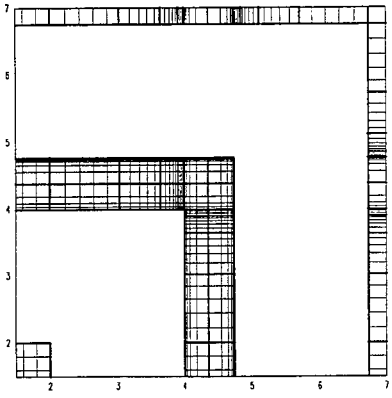

Fig.2: microstrip bend on Gallium Arsenide substrate with low resolution for the dynamic field (bold lines). The high resolution for the static field is also used for the full wave analysis to produce accurate reference solutions (fine lines). Lengths: 1:100µm. (grid shows only the metallic surfaces)

Fig.3 shows the relative deviations of the magnitude of the reflexion-S-parameter to the accurate reference solutions (using a fine mesh of 169000 cells). The results of the hybrid approach are compared with the results of the conventional Finite Difference method, using the same coarse mesh for the full wave analysis (1352 cells). One can see, that the deviations by use of the hybrid approach are more than ten times lower than those by using of the conventional method. The minimum at 13 GHz exists due to a change in sign in the deviation of the hybrid-solutions. For higher frequencies we can see an increase in the deviation of the hybrid approach. This is because of the increasing difference between the static and the dynamic field. In the threedimensional application of the hybrid approach a local average of static field values has to be done. With this a resting error of 0,6 % can be seen in the hybrid-solutions even for low frequencies. This effect can be reduced by increasing the discretization density of the static fields. So, a higher resolution for the static field and the accurate reference solutions will also improve the results.

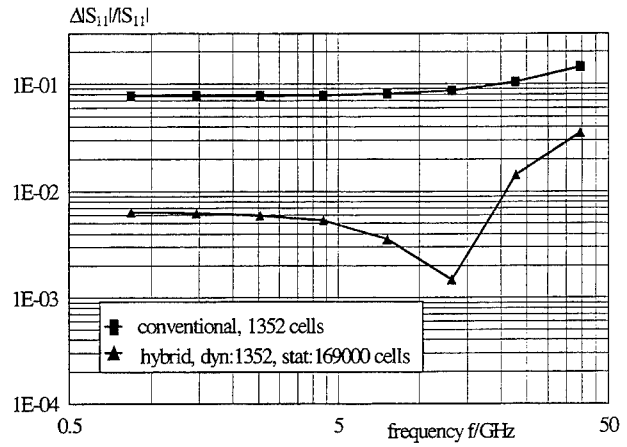

Fig.3: Comparison of solutions of hybrid and conventional method at a microstrip bend: Deviations in absolute values of the reflexion-S-parameter using a coarse mesh (1352 cells) related to accurate reference solutions of the conventional FD-method using a fine mesh (169000 cells)

Also the Deviations in Phase of the S-Parameter are in case of the hybrid approach considerably below that of the conventional method (Fig.4). The results approximate in the higher frequency range. This results from the wave length, which approach the order of magnitude of the coars mesh cells. If choosing a higher resolution for the full wave analysis, this effect disappears.

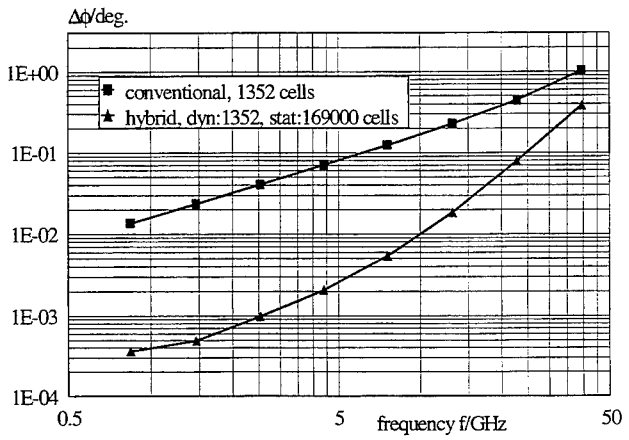

Fig.4: Comparison of solutions of hybrid and conventional method at a microstrip bend: Deviations in phase of the reflexion-S-parameter using a coarse mesh (1352 cells) related to accurate reference solutions of the conventional FD-method using a fine mesh (169000 cells)

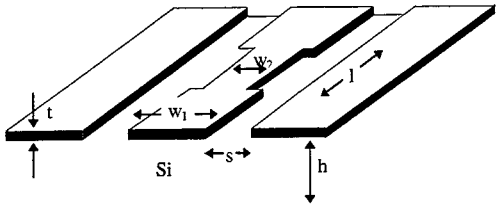

Fig.5: Double-step-discontinuity of a coplanar waveguide, t=3μ, s=15μ, l=100μ, w_1=20μ, w_2=8μ, h=520μ

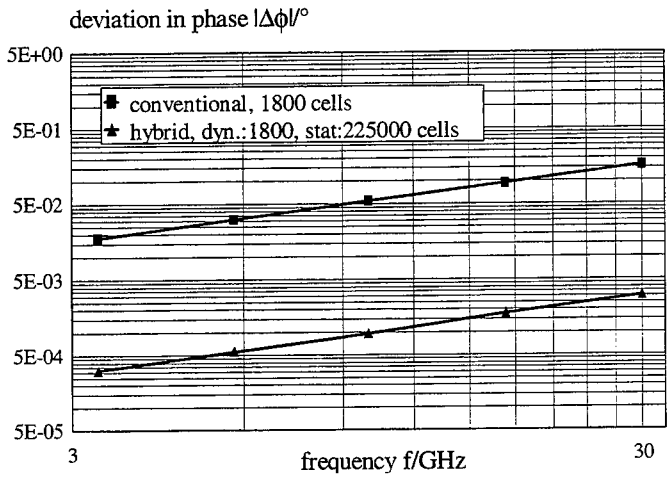

Fig.6: Comparison of solutions of hybrid and conventional method at a CPW-double-step-discontinuity: Deviations in phase of the reflexion-S-parameter using a coarse mesh (1800 cells) related to accurate reference solutions of the conventional FD-method using a fine mesh (225000 cells)

In coplanar structures The static fields and the dynamic field have a similar distribution for higher frequencies than in the case of microstrip structures [3]. With that an even better result of the hybrid method can be estimated in the case of a coplanar structure. As Fig.6 shows, the deviation in phase can be reduced to 1/60 by using the hybrid method, compared to the conventional FDFD-method in the frequency range of more than 30 GHz.

For estimating the efficiency of our hybrid method we compare the computation time, required for the hybrid method with the computation time, which is required for the conventional Finite Difference method withnthe same discretization of the given structure. Fig. 7 shows the CPU-time of the methods in dependence of the number of cells, which were used for the simulations. for the discretization of full wave analysis in the hybrid method we used only n_{coarse}=805 elementary cells. The CPU-time of the hybrid method is the sum of the CPU-time for this full wave analysis, multiplied by the number of considered frequencies and the CPU-time for the calculation of the static fields, using n elementary cells. For high numbers n of cells, the main part of the CPU-

time is required for the static field simulations. It is lower and increasing more slowly than the CPU-time which is required for the conventional full wave analysis. For the calculation of a number of frequencies there is no essential increase in CPU-time. When we use the conventional method, the CPU-time increases linearly with this number.

The comparison of the hybrid method with the conventional FDFD-method shows that with the efficiency of the hybrid method is considerably higher due to the high reduction in computation time. Due to local averaging of the magneto-static potential there is a little additional averaging error but this is small in relation to the discretization error of the Finite Difference method. When we choose a high discretization density for the static calculations, the averaging error will even approximate zero. With this the solutions of the hybrid method approximate the solution of the conventional method. As we see in Fig. 7, the CPU-time of the hybrid method is in this case several decades lower than the one of the conventional method. This means that the efficiency of the hybrid increases with the demanded accuracy of the solutions and with the number of considered frequency points.

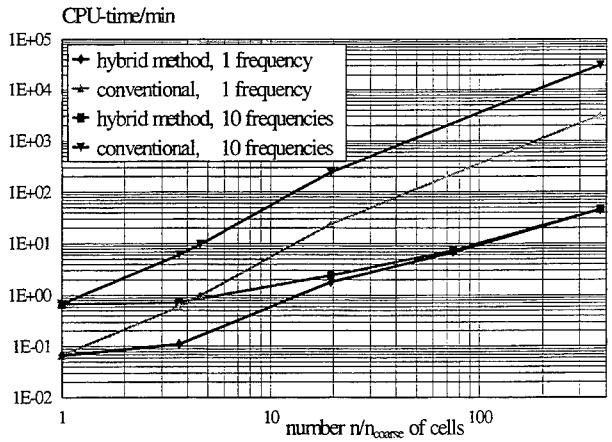

Fig. 7: CPU-time of the hybrid and conventional method in dependence of the number n of cells, which were used for the simulations. Discretization of full wave analysis in the hybrid method: n_{coarse}=805 elementary cells.*(Data produced at a DEC 3000/800 Alpha workstation).*

As can be seen, considerable savings in CPU time are obtained. This is true also for the storage which is related to the mesh size *n*. Because of sparsity the matrix size of both conventional and hybrid approach grows linearly with *n*. Due to the simplified mathematics in the static case, however, this type of analysis consumes only 30% of the corresponding full-wave problem. Furthermore, only the critical subregions of a structure need refinement. This further increases the efficiency of the hybrid approach.

ACKNOWLEDGEMENTS

This work is supported by the Deutsche Forschungsgemeinschaft (DFG) under contract He-1676/12.

CONCLUSIONS

We presented an efficient hybrid Finite Difference approach for the numerical modeling and the calculation of the scattering coefficients of 3D-MMIC-circuits in the micro- and millimeter wave range. The approach yields high reduction in computational effort in comparison with the conventional Finite Difference method. The CPU-time can be reduced to less than one tenth, the storage to one third. Using the conventional method the CPU-time increases linearly with the number of frequencies. Using the hybrid approach there is no essential increase in CPU-time for more frequencies. The hybrid approach preserves the consistency of the Finite Difference-scheme thus maintaining properties such as mode orthogonality and energy conservation.

REFERENCES

[1] K. S. Yee, „ Numerical solution of initial boundary value problems involving Maxwell's equations in isotropic media," *IEEE Trans. Ant. Prop.*, Vol. 14, pp. 302-307, may 1956

[2] W. Heinrich, „Quasi TEM description of MMIC coplanar lines including conductor loss effects", *IEEE Trans. Microwave Theory Tech.*, Vol. 41, NO. 9, pp. 1534-1537, 1993

[3] S. Lindenmeier, P. Russer, W. Heinrich, "Hybrid dynamic-static Finite-Difference approach for MMIC design," *IEEE MTT-S Digest*, Vol. 1, pp. 197-200, June 1996

[4] S. Lindenmeier, W. Heinrich, P. Russer, "A fast magneto-static field simulation for the incorporation into a hybrid dynamic static finite-integral algorithm," Prague, Europ. Microwave Symposium Digest, Vol. 1, pp. 447-451, Sep. 1996

[5] S. Lindenmeier, P. Russer, „The PPS-method for the FD-calculation of inductances of unrestricted lossless 3D-structures using a scalar magnetic potential", to be presented in *Progress in Electromagnetics Research Symposium PIERS.*, Hongkong, UK., January 1997

[6] T. Weiland, "On the numerical solution of Maxwellian eigenvalue problems in three dimensions," Particle Accelerators, Vol. 17, pp. 227-242, 1985.

[7] D.B. Shorthouse, C. J. Railton, „The incorporation of static field solution into the finite-difference time-domain algorithm", *IEEE Trans. Microwave Theory Tech.*, Vol. 40, pp. 986-994, ,may 1992

[8] K. Beilenhoff, W. Heinrich, "Treatment of field singularities in the Finite-Difference approximation," 1993 International Microwave Symposium Digest, Vol. 2, pp. 979-982.

Application of FD-TD Methods to Planetary and Geological Remote Surface Sensing

J. E. Baron, G. L. Tyler, and R. A. Simpson
Center for Radar Astronomy, Stanford University, Stanford, CA, 94305-9515

Abstract

Several features of the finite-difference time-domain (FD-TD) method make it an attractive option for studying the interaction of electromagnetic waves with geophysical surfaces: i) surface and scattering structures of arbitrary shape and composition can be modeled with relative ease; ii) outgoing waves in the presence of a material discontinuity can be readily handled using perfectly matched layer techniques; iii) wideband far-field results for transient incident waves can be obtained efficiently, given suitable Green's functions; and iv) code implementation of a Cartesian-grid FD-TD model is relatively straightforward. Expanding on previous efforts in two dimensions, we describe a three-dimensional FD-TD model for calculating scattering from objects resting on or buried partially or fully within a lossless dielectric half-space. In a radar remote sensing context, such a tool is useful for studying the effects of discrete wavelength-scale surface and subsurface heterogeneities, such as rocks, which interact strongly with the incident radiation but are difficult to incorporate into theoretical models. We present results for scattering from spheres and from models of real rocks whose shapes were digitized using a three-dimensional laser scanner.

1 Introduction

Extreme distances and constraints on observing geometries have historically limited interpretation of planetary radar remote sensing data to quasi-specular models (e.g., [1]). New data sets from orbiting spacecraft such as Magellan [2] require development of more diverse analysis tools appropriate for high incidence angles, where wavelength-scale surface and subsurface structure—rocks, fractures, pits, *etc.*—is almost entirely responsible for the returned signal and the quasi-specular models are hopelessly inadequate. Because this "diffuse" component of the radar echo is difficult to incorporate into a theoretical framework, we investigate the problem numerically.

Although a traditional application of finite-difference time-domain (FD-TD) techniques has been to scattering from objects in free space, recent attention has been devoted to a variety of remote sensing problems, including calibration of sea ice dielectric constant measurements [3], ground penetrating radars (*e.g.*, [4, 5]), scattering from random rough surfaces [6, 7], and scattering from buried objects in stratified media [8, 9]. Using a two-dimensional (2-D) Cartesian-grid FD-TD model [10], we have explored the scattering behavior of cylinders resting on or buried partially or fully within a homogenous dielectric half-space [11]. In the following section we discuss the extension of the 2-D model to three dimensions (3-D). In Section 3 we give representative results for scattering from spheres for a range of sizes and depths. We also calculate the cross section of a terrestrial rock whose shape was digitized using a 3-D laser scanner.

2 Methodology

Figure 1 illustrates a "total field" FD-TD implementation of the scattering problem for objects in the vicinity of the interface between free space and a dielectric half-space. Most of the details of our 3-D model are straightforward extensions of the 2-D "3-wave" model described in Wong *et al.* [10], such as the implementation of the composite driving source consisting of the incident, reflected, and transmitted waves. In the transition, we have improved the capabilities of the code to include both single-frequency and broadband excitation. Although we used the Mur absorbing boundary [12] in our 2-D code, we use the Berenger perfectly matched layer (PML) [13] in 3-D because it is well-suited to problems involving an interface between two or more lossless dielectric media and can be extended to include lossy and dispersive media [14].

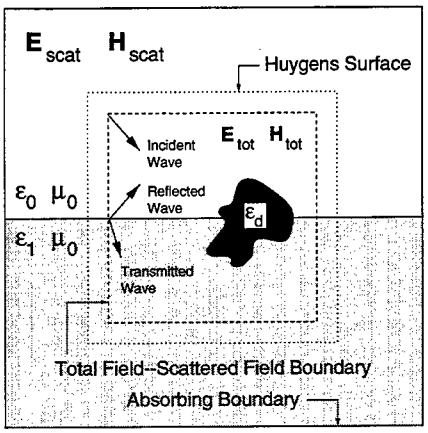

Figure 1: Division of Computation Space. The total field is the sum of a composite source field and the scattered field; the composite source consists of the incident, reflected, and transmitted waves for a plane surface in the absence of a scatterer. Equivalent electric and magnetic currents are evaluated on a Huygens surface surrounding the total-field region. Integration over the Huygens surface using appropriate Green's functions gives the far-field scattering cross section.

Both the permittivity of the soil, ϵ_1 in Fig. 1, and the scattering object, ϵ_d, are complex in general. For our calculations here, however, we take ϵ_1 to be real. The regoliths of most planets and satellites, with the notable exception of wet soil on Earth, are thought to be low-loss; in high loss media, only the upper few wavelengths of the regolith are sensed by the radar, and penetration depth factors can be introduced to normalize the results of our calculations. The assumption of a lossless regolith also simplifies the code implementation for broadband incident waves. For some applications, such as the detection of buried drums in stratified media, loss is a necessary part of the model, and additional steps must be taken to include transient sources [8].

The most notable difference between the 2-D and 3-D codes is the near- to far-field transformation, due to the differing nature of the Green's functions. The Green's functions for both electric

and magnetic dipoles in the vicinity of a conducting half-space have been rigorously quantified [15]. However, because such research typically is applied to radio wave propagation over ground, the Green's functions generally are not available in a form that is suitable for geometries employed by imaging radars, except in limited cases [16]. In Table 1 we detail the time-harmonic Green's functions in a form that is easily implemented in an FD-TD code.

Sources in Free Space		
	E_θ	E_ϕ
J_x	$-\kappa\eta_0 \cos\theta \cos\phi(e^{jkh\cos\theta} - R_v e^{-jkh\cos\theta})$	$\kappa\eta_0 \sin\phi(e^{jkh\cos\theta} + R_h e^{-jkh\cos\theta})$
J_z	$\kappa\eta_0 \sin\theta(e^{jkh\cos\theta} + R_v e^{-jkh\cos\theta})$	0
M_x	$\kappa \sin\phi(e^{jkh\cos\theta} + R_v e^{-jkh\cos\theta})$	$\kappa \cos\theta \cos\phi(e^{jkh\cos\theta} - R_h e^{-jkh\cos\theta})$
M_z	0	$-\kappa \sin\theta(e^{jkh\cos\theta} + R_h e^{-jkh\cos\theta})$
Buried Sources		
	E_θ	E_ϕ
J_x	$-\kappa\eta_0 \cos\theta \cos\phi(1 - R_v)e^{-jkh(\epsilon_r - \sin^2\theta)^{1/2}}$	$\kappa\eta_0 \sin\phi(1 + R_h)e^{-jkh(\epsilon_r - \sin^2\theta)^{1/2}}$
J_z	$\frac{\kappa\eta_0 \sin\theta(1 + R_v)}{\epsilon_r} e^{-jkh(\epsilon_r - \sin^2\theta)^{1/2}}$	0
M_x	$\kappa \sin\phi(1 + R_v)e^{-jkh(\epsilon_r - \sin^2\theta)^{1/2}}$	$\kappa \cos\theta \cos\phi(1 - R_h)e^{-jkh(\epsilon_r - \sin^2\theta)^{1/2}}$
M_z	0	$-\kappa \sin\theta(1 + R_h)e^{-jkh(\epsilon_r - \sin^2\theta)^{1/2}}$

Table 1: Green's functions for horizontal and vertical components of equivalent currents, $\mathbf{J} = \mathbf{n} \times \mathbf{H}$ and $\mathbf{M} = \mathbf{E} \times \mathbf{n}$, located a distance h ($h > 0$) above or below the interface between the two media; $\mathbf{n}$ is the outward normal to the Huygens surface. The scale factor in the expressions above is $\kappa = jke^{-jkR}/(4\pi R)$, where $k = 2\pi/\lambda$ is the free space wave number and R is the distance from the observation point to the coordinate system origin.

The expressions given in the table are the polar and azimuthal components, (E_θ, E_ϕ), of the the free-space electric far-field due to equivalent electric and magnetic dipole current sources at location ($x = 0, y = 0, z = \pm h$), where h is the distance above or below the interface between the two media. The terms R_h and R_v are the Fresnel reflection coefficients for horizontal and vertical polarization, respectively, and are given by

$$R_h = \frac{\cos\theta - (\epsilon_r - \sin^2\theta)^{1/2}}{\cos\theta + (\epsilon_r - \sin^2\theta)^{1/2}}. \tag{1}$$

and

$$R_v = \frac{\epsilon_r \cos\theta - (\epsilon_r - \sin^2\theta)^{1/2}}{\epsilon_r \cos\theta + (\epsilon_r - \sin^2\theta)^{1/2}} \tag{2}$$

The expressions are valid for complex dielectric contrast $\epsilon_r = \epsilon_1/\epsilon_0$, except in the limit $\theta \to 90°$, where surface waves become important. Note that the response for y-directed sources can be

obtained by replacing $\sin\phi$ with $-\cos\phi$ and $\cos\phi$ with $\sin\phi$ in the expressions for the x-directed sources. The total far-field response is calculated by integrating the equivalent currents, weighted by the appropriate Green's functions, over the entire Huygens surface for each frequency of interest.

Except in certain limiting cases, analytic scattering solutions for the geometries we have considered are difficult, if not impossible, to obtain. In addition, to our knowledge no comparable 3-D method of moments code exists. In order to validate our code, then, we resorted to indirect methods: i) in the limit where $\epsilon_1 \to \epsilon_0$, correct free space results are obtained for scattering from canonical shapes; ii) calculations for buried spheres match theoretical predictions in the long wavelength limit; and iii) results for long cylinders of moderate diameter match those of our previously validated 2-D code, after appropriate scaling factors are included.

3 Scattering Examples

When modeling diffuse scattering from rocky surfaces such as Mars or the Moon, planetary scientists often use spheres as representative rocks. In the simplest models, the spheres are assumed to scatter in proportion to the product of their projected area and their Fresnel reflectivity [17]. A more sophisticated model uses Mie theory to estimate the cross section of surface rocks, with appropriate scaling factors for buried rocks to account for Fresnel transmission effects and loss within the regolith [18, 19]. Note that any depolarization in backscatter predicted by the latter model is due solely to the Fresnel factors, since spheres in free space do not depolarize in backscatter. We can investigate the validity of these approximations using our 3-D FD-TD code.

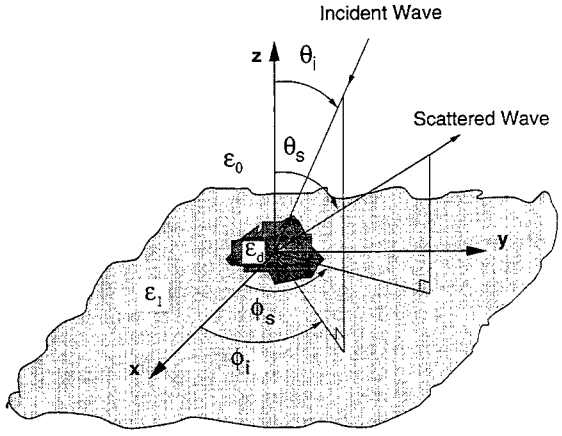

Figure 2: Bistatic Geometry for Scattering Calculations.

Figure 2 shows the general bistatic scattering geometry for our FD-TD calculations. For the cases shown in this paper we use $\epsilon_1 = 2.56\epsilon_0$ and $\epsilon_d = 4\epsilon_0$, values appropriate for the Moon and some regions of Mars, and $(\theta_s, \phi_s) = (\theta_i, \phi_i)$, *i.e.*, backscatter. In Fig. 3 we show the cross section of a sphere versus radius for three depths and two incident polarizations. As expected,

surface spheres scatter much more strongly than buried spheres, and at an amplitude comparable to spheres in free space. While the scattering behavior of partially buried spheres is difficult to quantify, the offset between the results for fully buried spheres and the thick dashed Mie solution can be almost exactly compensated by Fresnel coefficient scaling. In this respect, then, the simple scattering model discussed previously does appear to be valid.

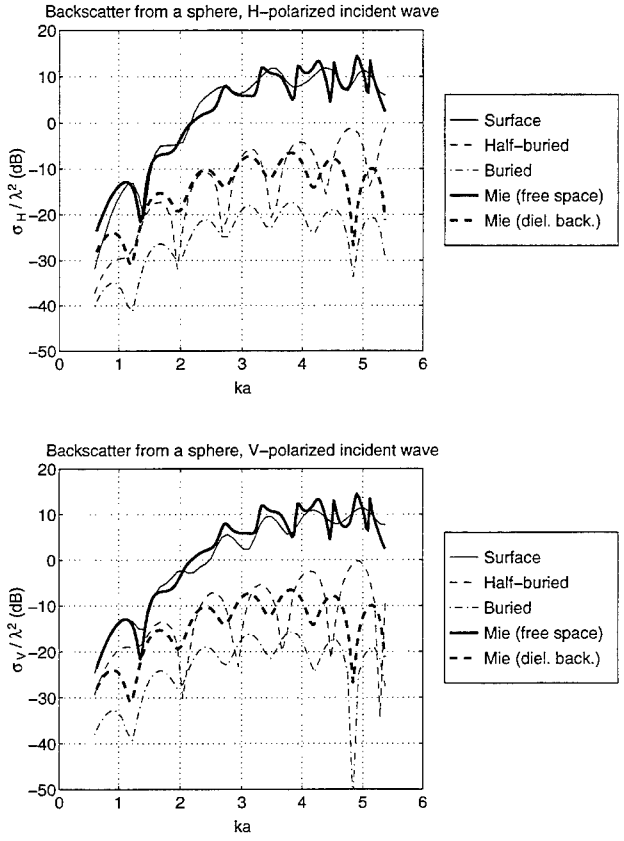

Figure 3: Backscatter Cross Section of a Sphere vs. Size. The backscatter cross section of a sphere over a range of sizes $ka = 2\pi a/\lambda$, where a is the sphere radius, is shown for three different depths: resting on the surface, half-buried, and tangentially buried beneath the surface. The top figure corresponds to a horizontally polarized wave incident at $\theta_i = 60°$; the bottom figure, vertically polarized. The thick solid line in each figure is the Mie solution in free space; the thick dashed line is the Mie solution for the same object immersed in an infinite background medium of permittivity 2.56.

Of course, very few naturally-occurring rocks have spherical shapes, so we would also like to examine the scattering behavior of more realistic rock models. Fortunately, one of the strengths of the FD-TD technique is the relative ease with which objects of arbitrary shape can be gridded. Based on rock population data from the Mars Viking Lander sites [20], we have calculated that typical axial ratios for Martian rocks at these sites are 1 (length) : 0.7 (width) : 0.5 (height). Using a laser scanner, we have produced 3-D digitized models of terrestrial rocks, including several whose axial ratios correspond to those above. We show one such model in Fig. 4.

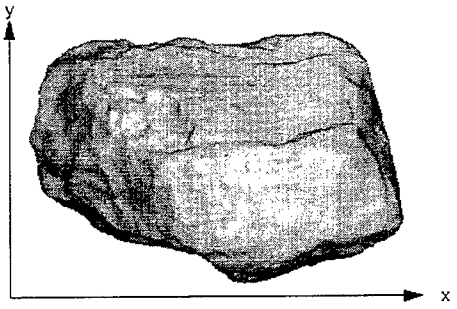

Figure 4: Digitized model of terrestrial rock sample. The shape of a sample of serpentine rock was parameterized using a 3-D laser scanner, courtesy of the Stanford Computer Graphics Lab. Approximate rock dimensions are 11 cm in x, 7 cm in y, and 6 cm in z; scanner precision is on the order of tens of microns.

The FD-TD calculation provides both magnitude and phase information at each far-field observation point. After running simulations using both vertically and horizontally polarized incident waves, arbitrary transmitter/receiver polarization states, such as right/left circular polarization, can be synthesized. In Fig. 5 we calculate the circular polarization ratio, $\mu_c = \sigma_{sc}/\sigma_{oc}$, for the rock model given in Fig. 4; μ_c is the cross section ratio of the same ("unexpected") sense of circular polarization to the opposite ("expected") sense and is considered a measure of small-scale roughness. In order to smooth the results we have averaged over azimuth before calculating the ratio. Interestingly, the surface rock depolarizes more strongly than the partially or fully buried rock, a feature which could not be predicted by the simple scattering models described earlier.

4 Conclusion

Three-dimensional FD-TD models can be used to calculate scattering from discrete wavelength-scale surface and sub-surface structures. Such a tool is useful, among other applications, for studying the diffuse component of planetary radar echoes. We are currently applying the results of our calculations to estimate scattering cross sections for Martian rock fields.

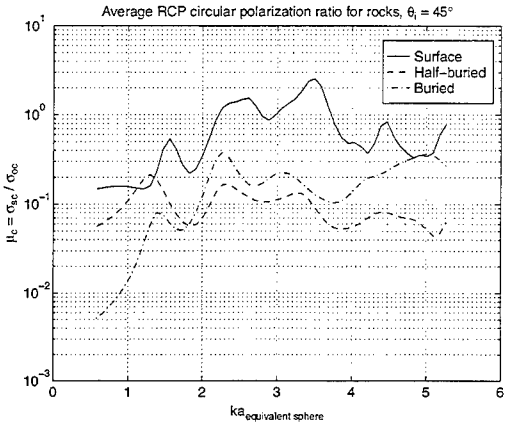

Figure 5: Circular Polarization Ratio of a Rock vs. Size. Results are shown for three burial depths, and have been averaged over azimuth. The abscissa is the size parameter, ka, of the equivalent-volume sphere. The incidence angle in this case is 45°.

References

[1] T. Hagfors, "Backscattering from an undulating surface with applications to radar returns from the Moon," *Journal of Geophysical Research*, vol. 69, no. 18, pp. 3779–3784, 1964.

[2] R.S. Saunders, A.J. Spear, P.C. Allin, R.S. Austin, A.L. Berman, R.C. Chandlee, J. Clark, A.V. deCharon, E.M. De Jong, D.G. Griffith, J.M. Gunn, S. Hensley, W.T.K. Johnson, C.E. Kirby, K.S. Leung, D.T. Lyons, G.A. Michaels, J. Miller, R.B. Morris, A.D. Morrison, R.G. Piereson, J.F. Scott, S.J. Shaffer, J.P. Slonski, E.R. Stofan, T.W. Thompson, and S.D. Wall, "Magellan mission summary," *Journal of Geophysical Research*, vol. 97, no. E8, 1992.

[3] E. Nassar, R. Lee, K. Jezek, and J. Young, "In-situ measurement of the complex dielectric constant of sea ice from 1 to 10 GHz," in *International Geoscience and Remote Sensing Symposium*, 1996, pp. 118–120.

[4] B.J. Zook, "FDTD modeling of ground-penetrating radar antennas," in *11th Annual Review of Progress in Applied Computational Electromagnetics*, 1995, pp. 740–747.

[5] J.M. Bourgeois and G.S. Smith, "A full three-dimensional simulation of a ground-penetrating radar: FDTD theory compared with experiment," *IEEE Transactions on Geoscience and Remote Sensing*, vol. 34, no. 1, pp. 36–44, 1996.

[6] A. K. Fung, M. R. Shah, and S. Tjuatja, "Numerical simulation of scattering from three-dimensional randomly rough surfaces," *IEEE Transactions on Geoscience and Remote Sensing*, vol. 32, pp. 986–994, 1994.

[7] F. D. Hastings, J. B. Schneider, and S. L. Broschat, "A Monte-Carlo FDTD technique for rough surface scattering," *IEEE Transactions on Antennas and Propagation*, vol. 43, no. 11, pp. 1183–1191, 1995.

[8] K. Demarest, R. Plumb, and Z. Huang, "FDTD modeling of scatterers in stratified media," *IEEE Transactions on Antennas and Propagation*, vol. 43, no. 10, pp. 1164–1168, 1995.

[9] K. Demarest, Z. Huang, and R. Plumb, "An FDTD near- to far-zone transformation for scatterers buried in stratified grounds," *IEEE Transactions on Antennas and Propagation*, vol. 44, no. 8, pp. 1150–1157, 1996.

[10] P. B. Wong, G. L. Tyler, J. E. Baron, E. M. Gurrola, and R. A. Simpson, "A three-wave FDTD approach to surface scattering with application to remote sensing of geophysical surfaces," *IEEE Transactions on Antennas and Propagation*, vol. 44, no. 4, pp. 504–514, 1996.

[11] J. E. Baron, R. A. Simpson, and G. L. Tyler, "Radiowave scattering from surface and subsurface heterogeneities," *Icarus*, vol. 122, no. 2, pp. 383–396, 1996.

[12] G. Mur, "Absorbing boundary conditions for the finite-difference apprximation of the time-domain electromagnetic field equations," *IEEE Transactions on Electromagnetic Compatibility*, vol. 23, pp. 377–382, 1981.

[13] J. P. Berenger, "A perfectly matched layer for the absorption of electromagnetic waves," *Journal of Computational Physics*, vol. 114, pp. 185–200, 1994.

[14] S.D. Gedney, "An anisotropic PML absorbing media for the FDTD simulation of fields in lossy and dispersive media," *Electromagnetics*, vol. 16, no. 4, pp. 399–415, 1996.

[15] A. Baños, Jr., *Dipole Radiation in the Presence of a Conducting Half-Space*, vol. 9 of *International Series of Monographs in Electromagnetic Waves*, Pergamon Press, 1966.

[16] N. Engheta, C.H. Pappas, and C. Elachi, "Radiation patterns of interfacial dipole antennas," *Radio Science*, vol. 17, no. 6, pp. 1557–1566, 1982.

[17] W. M. Calvin, B. A. Jakosky, and P. R. Christensen, "A model of diffuse radar scattering from Martian surface rocks," *Icarus*, vol. 76, pp. 513–524, 1988.

[18] T. W. Thompson, J. B. Pollack, M. J. Campbell, and B. T. O'Leary, "Radar maps of the Moon at 70-cm wavelength and their interpretation," *Radio Science*, vol. 5, no. 2, pp. 253–262, 1970.

[19] J. K. Harmon and S. J. Ostro, "Mars: Dual-polarization radar observations with extended coverage," *Icarus*, vol. 62, pp. 110–128, 1985.

[20] H. J. Moore and J. M. Keller, "Surface-material maps of Viking landing sites on Mars," *Reports of the Planetary Geology and Geophysics Program*, vol. NASA TM-4300, pp. 160–162, 1991.

INCORPORATION OF ACTIVE DEVICES USING DIGITAL NETWORKS IN FDTD METHOD

Chien-Nan Kuo and Tatsuo Itoh

Department of Electrical Engineering
University of California, Los Angeles
Los Angeles, CA 90095-1595

Abstract

This paper presents an alternative approach for incorporating active devices into the FDTD algorithm using a mathematical model, which describes the device characteristics and device-wave interaction. The Laguerre network is employed to realize this model. This approach is applied to the analysis of different microwave active circuits.

1 Introduction

For those MMIC-based systems located in complicated environments where electromagnetic effects cannot be ignored, the insufficiency of simple circuit theory approach in circuit design necessitates the increasing demand of electromagnetic simulation of the entire system. To this end, electromagnetic simulators require appropriate modeling of the interaction between active devices and electromagnetic waves to realize comprehensive simulation of microwave active circuits. Thus, recent development of full-wave techniques has been focused on the inclusion of active devices.

In literature, the FDTD method has shown its versatility in the modeling of sophisticated structures and its extension has been capable of incorporating lumped elements [1]. On the three-dimensional modeling of device incorporation, a complete full-wave approach characterizes the device by applying semiconductor transport equations for carrier transport phenomena and Maxwell's equations for electromagnetic wave propagation [2]. This approach requires the knowledge of the fabrication process and inconveniences the spatial meshing as it is applied to a practical microwave circuit, where it is necessary to use much finer meshes in the device region as compared to those in other passive structures. Recognizing that the size of an active device is much smaller than the wavelength, the other approach treats the device as a lumped element, which lumped circuit model is employed to characterize the device-wave interaction [3-6]. The device model typically originates from the physical structure of the specific device. Different devices call for different circuit models.

This paper presents an alternative approach for incorporating active devices. The approach adopts a mathematical model by applying the device S-parameters, which are directly obtainable from measurements. The model, including the device characteristics as well as the device-wave interaction, is realized by a digital network.

2 Mathematical Model of Device Incorporation

The approach used in this paper is applicable to devices with sizes electrically much smaller than the wavelength. Following the principle of using equivalent sources [4, 5], the formulation begins with the placement of equivalent sources in the device region to substitute for the device. If equivalent current sources are used, the formulation applies Ampere's equation and yields the integral form of the equation into a finite difference equation,

$$I_{total}^{n-\frac{1}{2}} = \frac{C}{\Delta t}(V_{dev}^{n} - V_{dev}^{n-1}) + I_{dev}^{n-\frac{1}{2}}, \tag{1}$$

where I_{total} comes from the integration of H fields in the region, C is the space capacitance of a FDTD cell, and V_{dev} and I_{dev} are the device voltage and current, respectively. The device voltage and current are related by the S-parameter rather than the device circuit model as in [4, 5]. Taking the Z-transform of Eq. (1) to obtain the response on the unit circle gives the mathematical model,

$$V_{dev}(\omega) = G_I(\omega) I_{total}(\omega) = \left[\frac{1 - e^{-j\omega}}{\Delta t} C + e^{-j\frac{\omega}{2}} Y\right]^{-1} I_{total}(\omega), \tag{2}$$

where Y is the admittance of the device and $G_I(\omega)$ is the system function of the model. Note that the notation of the total current $I_{total}(\omega)$ corresponds to the time sequence sampled at half integral time steps. The total current acts as the input of the model to evaluate the device voltage, and to update the field components in the device region. Similarly, according to Faraday's equation, the formulation of using equivalent voltage sources leads to

$$I_{dev}(\omega) = G_V(\omega) V_{total}(\omega) = -\left[\frac{1 - e^{-j\omega}}{\Delta t} L + e^{-j\frac{\omega}{2}} Z\right]^{-1} V_{total}(\omega), \tag{3}$$

where L is the space inductance of a FDTD cell, and Z is the impedance of the device. The formulation can also be generalized to devices of multiple ports.

Since the admittance and impedance, derived from the S-parameters, are only available in a limited frequency range the implementation of the model by time-convolution technique is formidable. The model yet can be represented by a digital network with a system response designed to match with $G_I(\omega)$ or $G_V(\omega)$ in the frequency range of interest. This technique has been applied to the implementation of the absorbing boundary condition [7].

There are different forms of digital networks. In this paper, the discrete-time Laguerre network is employed [8]. The Laguerre network benefits in that it is numerically stable and the time-domain finite-difference equations of the network can be formulated quite in a straightforward manner. The network consists of a complete set of the Laguerre functions, which expands the system function based on the optimization procedure of the least-square error [9]. The expression in the Z-domain is

$$G(\omega) = \sum C_k L_k(\omega, b), \tag{4}$$

where

$$L_k(z, b) = \frac{\sqrt{1 - b^2}}{1 - bz^{-1}} \left[\frac{z^{-1} - b}{1 - bz^{-1}}\right]^k. \tag{5}$$

3 Results

The approach is first applied to the case as shown in Fig. 1(a), where a one-port device, modeled as a series connection of a resistor and a capacitor, is fixed to a microstrip line of 50-Ω at 6 GHz. Theoretically, the reflection coefficient looking at the device is calculated by

$$\Gamma = \frac{R + j\omega C - Z_o}{R + j\omega C + Z_o}. \tag{6}$$

The FDTD simulation applies equivalent current sources. A fifth-order Laguerre network, with the pole chosen as b=0.85, is used to match the system function $G_I(\omega)$, as shown in Fig 1(b),(c). The coefficients are optimized as C_0 = 8.9105898e+00, C_1=-1.1634694e+01, C_2=9.9901254e+00, C_3= -4.7279116e+00, and C_4= 9.4770895e-01. The reflection coefficient calculated by the FDTD simulation is plotted in Fig. 1(d). In comparison to the theoretical value, the deviation at 6 GHz is 0.2 dB, while the discrepancy become larger at the other frequencies without taking into account the frequency dispersion of a microstrip line in the calculation of Eq. (6).

The second case is a MESFET, a two-port device, in a microwave amplifier as in [10]. The circuit includes biasing circuits and matching circuits. There are four Laguerre networks used for the device, each for the implementation of a matrix element in the system function. Respectively, the number of the order and the pole for $G_{I,11}$ are chosen as 12 and 0.97; for $G_{I,12}$, 6 and 0.9; for $G_{I,21}$, 16 and 0.98; for $G_{I,22}$, 6 and 0.9. The S-parameters can be reconstructed from the optimized network by Eq. (2). Fig. 2 illustrates the calculated S-parameters. These networks are applied to the analysis of the amplifier. Results are shown in Fig. 3. Compared to the results of [10], the matching dip occurs 1.7 GHz higher in frequency, while the curves have good agreement in the out-of-band frequency. This error apparently comes from mismatching of the circuit. If higher orders of the Laguerre network are chosen to improve accuracy, it has been found that numerical oscillation occurs. Since the network is optimized for a limited frequency range, its value at very high frequency might be unreasonable and cause the system unstable.

4 Conclusion

An alternative approach for device incorporation is realized by utilizing a mathematical model to characterize the device and device-wave interaction. The model is represented by a digital network with a system function expanded into the discrete-time Laguerre functions by the optimization procedure of the least-square error. As applied to a one-port device, this method shows good results. In doing linear analysis, this approach is more general and applicable for different devices.

5 Acknowledgments

This work was supported by Hughes Micro, JSEP contract F49620-92-C-0055, and Army Research Office contract DAAH04-93-G-0068.

References

[1] W. Sui, D. A. Christensen and C. H. Durney, "Extending the two-dimensional FD-TD method to hybrid electromagnetic systems with active and passive lumped elements," *IEEE Trans. Microwave Theory Tech.*, vol. 40, pp. 724-730, Apr. 1992.

[2] M. A. Alsunaidi, S. M. Sohel Imtiaz, and S. M. El-Ghazaly, "Electromagnetic wave effects on microwave transistors using a full-wave time-domain model," *IEEE Trans. on Microwave Theory Tech.*, vol. 44, no. 6, pp. 799-808, June 1996.

[3] B. Toland, B. Houshmand, and T. Itoh, "Modeling of nonlinear active regions with the FDTD method," *IEEE Microwave and Guided Wave Lett.*, vol. 3, no. 9, pp. 333-335, Sep. 1993.

[4] V. A. Thomas, M. E. Jones, M. Piket-May, A. Taflove, and E. Harrigan, "The use of SPICE lumped circuits as sub-grid models for FDTD analysis," *IEEE Microwave and Guided Wave Lett.*, vol. 4, no. 5, pp. 141-143, May 1994.

[5] C.-N. Kuo, R.-B. Wu, B. Houshmand and T. Itoh, "Modeling of microwave active devices using the FDTD analysis based on the voltage-source approach," *IEEE Microwave and Guided Wave Lett.*, vol. 6, no. 5, pp. 199-201, May 1996.

[6] P. Ciampolini, L. Roselli, and G. Stopponi, "Integrated FDTD and solid-state device simulation," *IEEE Microwave and Guided Wave Lett.*, vol. 6, no. 11, pp. 419-421, Nov. 1996.

[7] M. Mrosowski, M. Niedźwiecki, and P. Suchomski, "A fast recursive highly dispersive absorbing boundary condition using time domain diakoptics and Laguerre polynomials," *IEEE Miocrwave and Guided Wave Lett.*, vol. 5, no. 6, pp. 183-185, June. 1995.

[8] M. A. Masnadi-Shirazi and M. Ghasemi, "Laguerre digital filter design," *1995 International Conference on Acoustics, Speech, and Signal Processing Conference Proceeding*, pp. 1284-1287, New York, NY.

[9] E. C. Levy, "Complex-curve fitting," *IRE Trans. on Automatic Control*, vol. AC-4, pp. 37-43, May 1959.

[10] C.-N. Kuo, V. A. Thomas, S. T. Chew, B. Houshmand, and T. Itoh, "Small signal analysis of active circuits using FDTD algorithm," *IEEE Microwave and Guided Wave Lett.*, vol. 5, no. 7, pp. 216-218, July 1995.

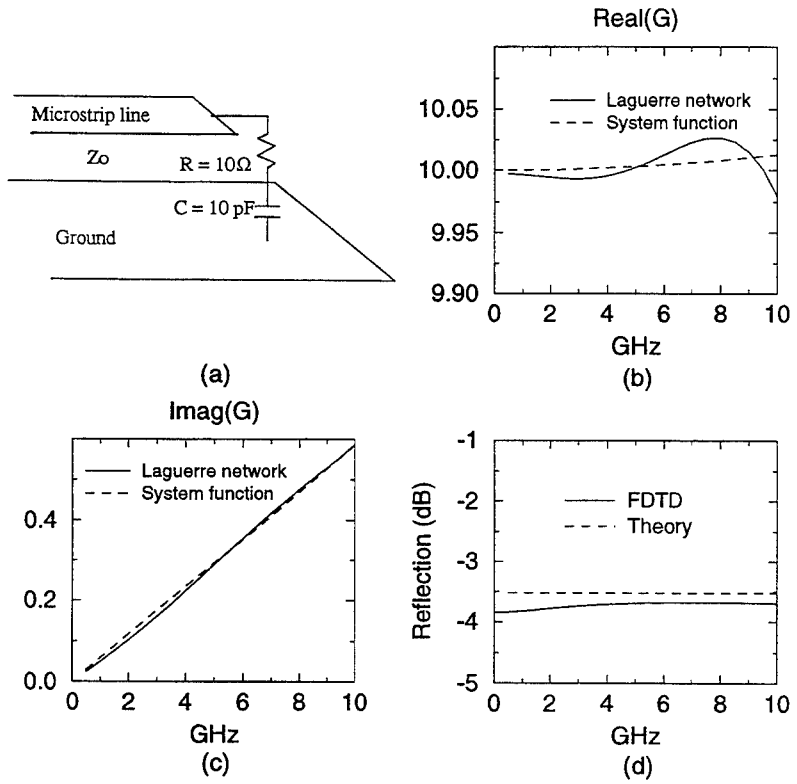

Figure 1: Application to a one-port device, modeled as a series connection of a resistor and a capacitor (order=5, pole=0.85). (a) The circuit, (b) the real part of the system function, (c) the imaginary part of the system function, and (d) the reflection coefficient.

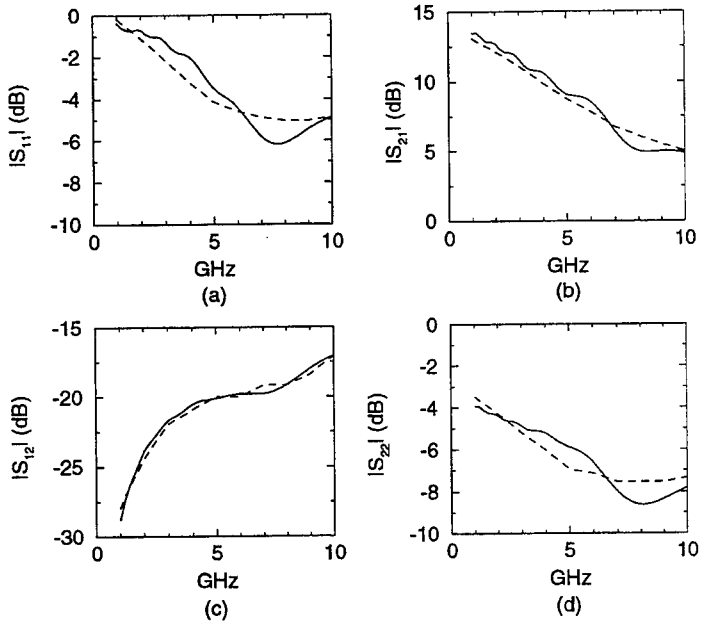

Figure 2: The S-parameters of a MESFET. Solid lines are results of the Laguerre network; dashed lines are those of the two-port device.

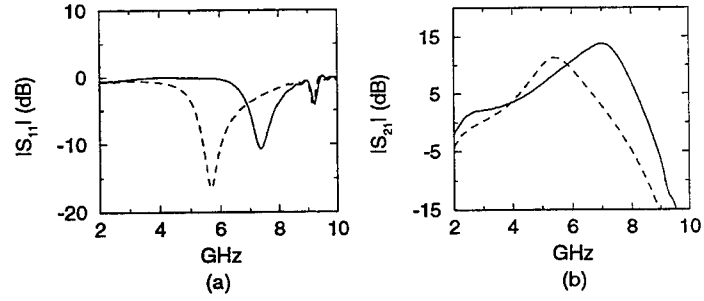

Figure 3: The calculated S-parameters of a small-signal amplifier. Solid lines are results of the Laguerre network; dashed curves are those of [10].

FDTD Calculations of Energy Absorption in an Anatomically Realistic Model of the Human Body

P J Dimbylow

National Radiological Protection Board, Chilton,
Didcot, Oxon OX11 0RQ, Great Britain

1 Introduction

This paper reports Finite-Difference Time-Domain (FDTD) calculations in an anatomically correct voxel (volume pixel) model of a human male body. Their purpose is to define the link between external fields and/or source configurations which can be measured to internal dose quantities in the body which are difficult to measure. These dose quantities such as current density and specific energy absorption rate, SAR are related to possible biological effects.

2 Voxel Model of the Body

The raw MRI data were taken from a series of continuous partial body scans of a single subject. These blocks of data were conjoined by rescaling, translation and rotation to form an entire body. The greyscale data of the medical images were interpreted into tissue types, a process known as segmentation. Each ~ 2 mm cube voxel has a tag which identifies the discrete tissue type of that particular voxel. The phantom consists of ~ 9 million voxels and is segmented into 37 tissue types. The exact dimensions of the voxel were scaled so that the height (1.76 m) and the mass (73 kg) would agree with the 'reference man' suggested by the International Commission on Radiological Protection. Hence the phantom is known as NORMAN (NORmalised MAN). The height fixes the vertical voxel dimension and the horizontal dimensions are then fixed by the mass. The total domain of the phantom and adjacent air is a 3D array of 148 voxels from front to back, 277 from side to side and 871 voxels high.

An evaluated review of the dielectric properties of all the tissue types in NORMAN was performed by Gabriel (1995, 1996). A 4-Cole-Cole dispersion model was fitted to the data for each tissue type to parameterise the conductivity and permittivity as a function of frequency.

Figure 1 shows an illuminated, rendered 3D image of NORMAN produced using the code Voxel View (1993). Each voxel greyscale has an associated opacity which can be varied to make specific tissues more transparent so that you can "look through" the body. In this case only the skin, skeleton and digestive system are shown, all the other organs have been made totally transparent. The opacity of the skin and bones has been set to 0.5 (an opacity of 0.0 makes the tissues transparent, 1.0 makes them solid).

3 FDTD Implementation

A domain enclosing the target and a boundary condition on the surface of the domain must be chosen to mimic numerically the unbounded region outside the domain by absorbing the outgoing scattered waves. Previously, the main method available was the second order one-way wave equation condition proposed by Mur (1981). However, it was found that when the body

was near resonance, ~ 30-40 MHz the boundaries had to be placed up to 2 m from the body when using this condition. This makes the computational domain very large and necessitates a coarse resolution. The new perfectly matcher layer (pml) based boundary conditions of Berenger (1994, 1996) can produce, with an optimised grading of the layer, a reflection that is orders of magnitude less than for the Mur condition. The method is also easily implemented and computationally efficient by reducing the number of cells to the boundary.

A Huygens surface (Merewether, 1980) was implemented in the FDTD code to allow the description of arbitrary incident fields, to separate the scattered field that is required for the boundary conditions from the total field required for the FDTD formulation and also to connect the pml layers to the inner region of the domain. Electric and "magnetic" currents are defined on the Huygens surface which produce the correct total fields inside the surface but just the scattered fields outside the surface.

It is not computationally tractable to perform FDTD calculations directly at a cell size of 2 mm. Therefore, the phantom was rescaled to produce 6 mm, 1 cm and 2 cm models with the properties of the rescaled cells being taken as the volume average of the basic component voxels. As the frequency increases smaller cell sizes are required so that an adequate sampling of the waveform is performed. The usual criterion is that the cell size should be less than a tenth of the wavelength in the particular medium. The period of the wave is proportional to the inverse of the frequency and so at the lower frequencies more time steps are required. Therefore, 2 cm resolution was used at the lowest frequencies whilst 6 mm was used at the highest and 1 cm at intermediate frequencies. At 2 cm there are 35,700 cells in the domain but at 1 cm and 6 mm this number increases to 3×10^5 and 1.4×10^6, respectively. The computational effort required is proportional to the reciprocal of the 4th power of the cell size, eg. if you double the resolution the number of cells is increased by 2^3 and you also need to decrease the time step by a factor of 2. Surrounding the domain there were 16, 12 and 8 layers of pml for the 2 cm, 1 cm and 6 mm resolutions, respectively. The program size for the 6 mm resolution is 220 MBytes of which 80 MBytes are required for the description of NORMAN.

4 SAR Calculations

The specific energy absorption rate is defined by

$$\mathrm{SAR} = \frac{\sigma |\mathbf{E}|^2}{\rho}$$

where σ is the conductivity, $\mathbf{E}$ is the r.m.s. electric field and ρ the density.

Figure 2 shows an anatomical horizontal slice through the chest and a corresponding histogram of the power absorbed in each voxel for this slice. The irradiation is a plane wave incident on the front of the body at 120 MHz for grounded conditions. The front of the section faces the top right-hand corner. There is not an exact correspondence between the images because the anatomy slice has the 2 mm voxel resolution whilst the calculations were performed at 6 mm. Energy is preferentially absorbed in the high conductivity tissues such as in muscle, the cerebrospinal fluid and the blood in the heart. Conversely, low conductivity tissues tend to have a lower SAR and you can clearly see the lungs and the breast-bone in the histogram.

Figure 3 shows the whole-body averaged SAR as a function of frequency when the phantom is grounded through the feet and when the phantom is isolated in air. The whole body

resonance can clearly be seen. When the phantom is isolated in air this occurs when the height of the phantom is ~$\lambda/2$, where λ is the wavelength in air. When the phantom is grounded, the reflection in the ground plane halves the resonant frequency, ie the height ~$\lambda/4$. However, the body is quite a 'fat', irregularly shaped antenna and the distribution of SAR in the body depends also on the anatomy and frequency dependent dielectric properties and so the above conditions are approximate guidelines. The effect of wearing shows was investigated for the grounded adult phantom by placing a 2 cm layer of rubber below the feet. The values of the SAR - frequency curve were slightly reduced and displaced to a resonant frequency of 40 MHz.

A complete description of the voxel phantom development and its application to the calculation of the whole body averaged SAR for an adult phantom and for scaled 10-, 5- and 1-year old models from 1 MHz to 1 GHz for plane wave exposure is given in Dimbylow (1997).

5 Conclusion

The fine-scaled, 2 mm resolution model of the body, NORMAN linked with the FDTD method provides a powerful tool for the comprehensive dosimetry of electromagnetic fields above 1 MHz. The incorporation of the Huygens surface enables the description of heterogeneous incident fields. Alternatively closely-coupled sources, such as communication equipment, can be inclusively modelled within the domain.

References

Berenger, J P, 1994. A perfectly matched layer for the absorption of electromagnetic waves. J. Comp. Phys., 114, 185-200.

Berenger, J P, 1996. Perfectly matched layer for the FDTD solution of wave-structure interaction problems. IEEE Trans. Antennas and Propagat. 44 (1), 110-117.

Dimbylow, P J, 1997. FDTD calculations of the whole-body averaged SAR in an anatomically realistic voxel model of the human body from 1 MHz to 1 GHz. Phys. Med. Biol. in press.

Gabriel, C, 1995. Compilation of the dielectric properties of body tissues at RF and microwave frequencies. Report prepared for the NRPB by Microwave Consultants Ltd.

Gabriel, C et al. 1996. The dielectric properties of biological tissues. Phys. Med. Biol. 41 (11) 2231-2294.

Merewether, D E, Fisher, R and Smith, F W, 1980. On implementing a numeric Huygens source scheme in a finite differences program to illuminate scattering bodies. IEEE Trans. Nucl. Sci. NS-27, 1829-33.

Mur, G, 1981. Absorbing boundary conditions for the finite-difference approximation of the time domain electromagnetic fields equations. IEEE Trans. Electromag. Compat., EMC-23, 377-82.

Voxel View, 1993, Vital Images Inc., Fairfield, Iowa.

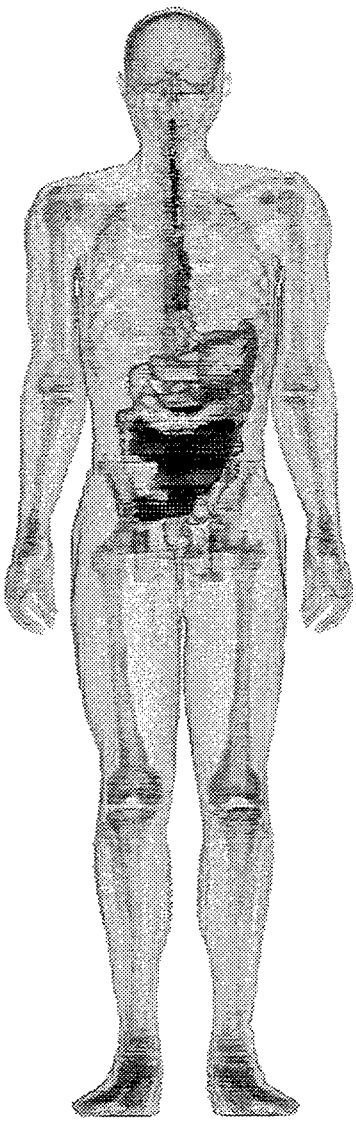

Figure 1 3D rendered image of NORMAN

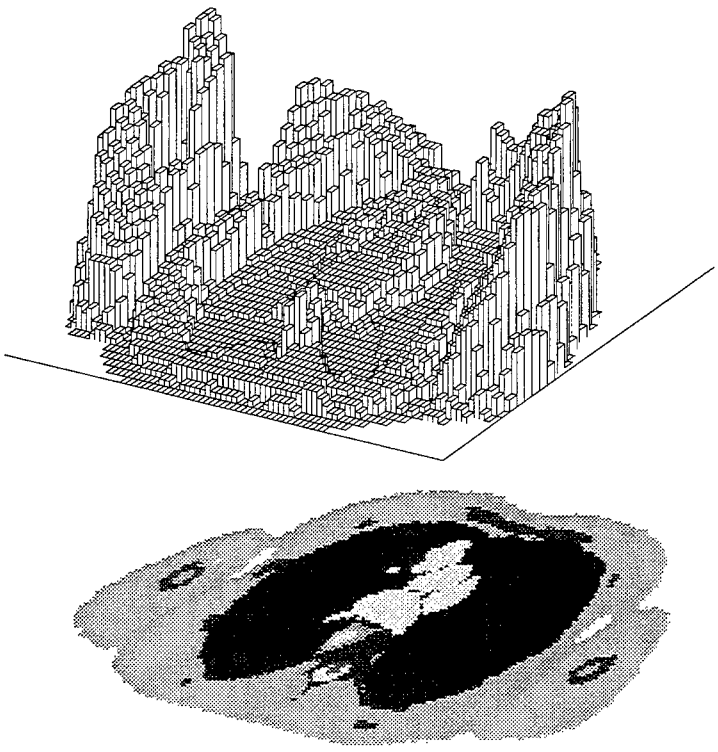

Figure 2 **Horizontal slice anatomy through the chest and a corresponding histogram of the power absorbed for AP plane wave irradiation at 120 MHz**

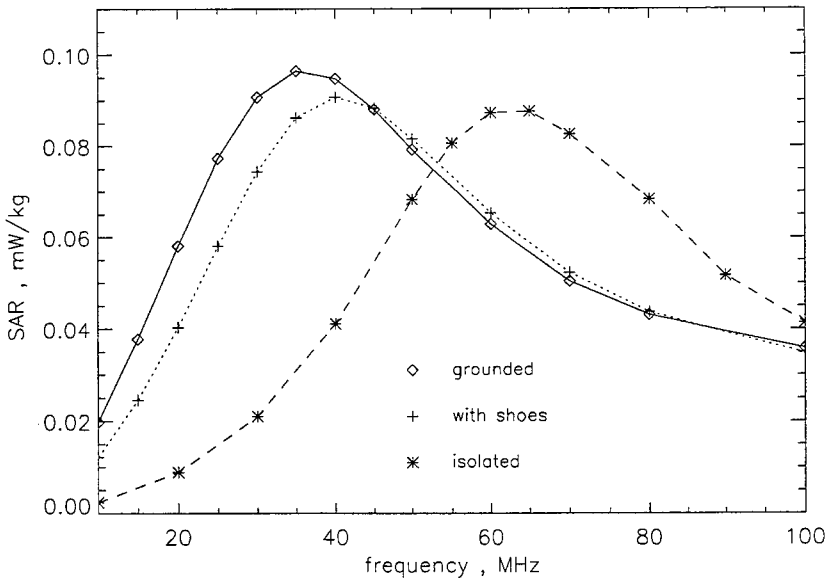

Figure 3 Whole-body averaged SAR. The incident electric field is 1 Vm^{-1}

SESSION 21:

PLANAR ANTENNAS AND CIRCUITS

Chairs: G. Vandenbosch and N. Fache

PLANAR ANTENNAS: OVERVIEW OF THE MODELING EFFORTS IN EUROPE

Guy A. E. Vandenbosch
Departement Elektrotechniek
Katholieke Universiteit Leuven
Kardinaal Mercierlaan 94
3001 Leuven, Belgium

Abstract - In Europe, a lot of research labs are involved, already for many years, in the modeling, design, measurement and application of planar antennas. In this paper, an overview is given of the work done and being done by some important European labs within the field of planar antenna modeling. Although the emphasis is on planar antennas, labs with a planar circuit or other background recently starting to do work on antennas will also be addressed. Since it is impossible to give a complete and detailed overview within the context of this one paper, it has to be clear that the labs discussed only form a representative selection. The fact that a lab is referred to or not referred to is by no means a statement about the quality of the work done by this lab. I also wish to point out that the comparison of European work with work done in the U.S., Japan, and the rest of the world is not a scope of this paper.

Introduction

The early development of planar printed circuits at microwave frequencies was mainly driven by the need of low-cost microwave circuits. Considering the radiation loss of these structures, the microstrip antenna concept was introduced in 1953 by Deschamps [1]. However, it was only in the early 1970s that the antenna community started focusing on making use of the radiation loss of planar circuits. Since then, planar antennas have been considered for a wide variety of applications (aircraft antennas, missiles and telemetry, missile guidance, adaptive antennas, mobile radio, reflector feeds, remote sensing, biomedical applications, personal communication, ...).
From manufacturers' standpoint today however, there is still a lack of ready-to-use design models, and hence reliable CAD packages. This situation is due to several reasons: the mathematical difficulties associated with practical geometry's, the many varieties of planar antennas, and the increasing system requirements. Horn, wire and other conventional antennas can be analyzed to a high accuracy with well-established models. This is also true for electrically larger apertures, such as the reflector antenna. In contrast to these homogeneous electromagnetic systems, the modeling complexity of planar array antennas arises from the presence of several elements in a multilayered structure, where each element consists of different components. Mutual coupling, surface wave effects, and feed radiation are small effects but they quickly take charge of sidelobe and cross-polarization levels as the number of elements increases.
In my view, it can clearly be stated that even after ca. 25 years of modeling research on planar antennas, there are still a number of big challenges for the future. The modeling of planar antennas is still a very useful research field.
In this paper, the European contribution in the field of modeling planar antennas is discussed: the contribution established in the past, the current research in Europe, and the research planned for the future are considered. This is done by looking at the activities of a representative choice of

European research labs active in this field, and by putting these activities within the framework of the European COST actions on antennas, taking into account the very active role of ESTEC (**E**uropean **S**pace Agency's **Te**chnology **C**entre).

The European COST actions on antennas

In my view, the role of the European antenna COST actions is crucial in the research field considered. COST means "European **CO**operation in the field of **S**cientific and **T**echnical research". The COST framework is an open and flexible framework for R&D cooperation. The COST actions involve pre-competitive or basic research, or activities of public utility. In contrast to much other European Union research, this form of collaboration does not require an agreed overall research policy. It is characterized by a large research freedom for the labs and companies involved. The scope of the work includes collaborative projects, technical meetings, and visits to European research institutes.
In the antenna field there have been five COST actions since 1973. COST 25/1, COST 204, 213 and 223 are completed and COST 245 currently is being finished. The planned successor of COST 245 is COST 260. The topic of modeling antennas always has been considered of importance in the antenna COST actions. Within the framework of COST 223, it was considered so important that since then a separate working group is devoted to it.
This paper is partially based on the information I acquired during the last four years leading working group 1 within the European COST 245 action on "Active phased arrays and array fed antennas". This action gathers the most important university and industry labs of 16 European countries and Turkey and the antenna research group of ESTEC (European Space Agency) in a unique forum. The goal is to study the needs within the European antenna community, to take action in areas where this is necessary (for example modeling and analysis) and to study and design new antenna concepts. The working group 1 addresses the topic "Modelling and Analysis" (working group 2 concerns "Radiating elements", and working group 3 "Architecture, Circuits, Components and Measurement").
The research groups known to me as being active within working group 1 were contacted and asked to give a brief overview of their planar antenna modeling activities and about their plans for the near future. The result of this inquiry is embedded within this paper.

Planar antenna modeling in Europe: past (1973-1990)

In 1976, Derneryd (Sweden) published an equivalent network for rectangular microstrip elements [2], and in 1978 a theoretical investigation of the rectangular microstrip antenna [3]. The topic of the second paper is the description of an approach to model mutual coupling in the antenna. This research clearly can be considered part of the "transmission line model" research.
In 1979, P. Hammer et al. (Belgium) published a model for calculating the radiation field of microstrip antennas [4]. The paper is related to [2] and [3] and establishes several basic ideas used within the transmission line type of models. The original extremely simple model of this research group continuously improved over the years and due to the refinement of the original approximations and the extension to more general configurations, it became sufficiently accurate and general to be implemented in a software package installed at ESTEC [5].
A most significant set of publications, with the results of one decade of research, is gathered in the special edition of the IEEE Transactions on Antennas and Propagation of January 1981. There are two European contributions to this issue: [6] by James et al. (U. K.), and [7] by Derneryd and Karlsson (Sweden). Concerning modeling, in these papers only very basic modeling is used.

Modeling was not really seen as a specific research goal, but rather as a help to designers to construct good planar antennas. Considering the references mentioned in [6] and [7], it is seen that the authors of both papers already had been very active in the field.
In 1983, an important lab came into the European picture. In [8], Mosig and Gardiol (Switzerland) made a first step towards a rigorous integral equation model by considering techniques concerning Green's functions. In 1985 this work was completed and they published their first integral equation model [9]. In [10], this model was extended to be able to analyze stacked patches. Another paper using the integral equation technique is [11] (Germany).
I refer also to a paper about the finiteness of the ground plate [12] (Norway), a paper describing basic research on the spectral dyadic Green's functions [13] (Italy), two papers involving conjugate gradients [14] (The Netherlands) and [15] (Spain), and a paper about a transient-frequency mixed analysis [16] (France).
Overlooking all the papers referred to in this section, it is clear that in the period between 1973 and 1990, in Europe the research on planar antennas clearly involved the transmission line model for rectangular microstrip antennas, and the integral equation model for more general structures. Concerning the transmission line model there was an important activity in Sweden and in Belgium, concerning the integral equation model there was an important activity in Switzerland.

Planar antenna modeling: "present" (1991-1995)

Although in the period 1991-1995, in Europe the transmission line type of model was considerably improved [17], more general network models were developed [18], and there was further activity based on the cavity method [19], the integral equation type of model became the hot topic in the field of planar antenna modeling. There are two reasons for this. The first one is the fact that, due to the lack of fundamental theoretical approximations, this type of model is able to analyze almost any configuration with an inherent high accuracy. The second one is the fact that the vast need of calculation capacity became less restrictive due to the increasing calculation speed of computer systems. Many research groups became active in the field and most of them kept in close contact through the actions COST 223 and COST 245.
A first group which became very active is the antenna research group at the Katholieke Universiteit Leuven (Belgium). Although this group had build a considerable background concerning the transmission line model, Vandenbosch contributed considerably to the further development of the integral equation model in Europe. He implemented a variant of the integral equation model developed by Mosig et al. [20], and combined it with several new techniques: the use of **S**ubsectional **E**dge **E**xpansion **F**unctions (SEEFs) [21], and the use of a highly efficient new coaxial feed model [22, 23]. He also implemented a new expansion scheme, the so-called mixed expansion [24]. In this technique entire domain expansion is used but the entire domain expansion functions are constructed as fixed combinations of subsectional expansion functions. This was a first step towards a solution for the problem of the large number of unknowns in planar arrays.
The same problem was also studied by the research group of Mosig at the Swiss Federal Institute of Technology in Lausanne (Switzerland). They tackled the problem by using an infinite-array approach with Fourier windowing and fast iterative techniques [25, 26]. They also made a study on the finiteness of the ground plane [27].
The labs in Leuven and Lausanne clearly define the modeling of general planar antennas as a long-term job they perform to serve European antenna industry. This means that the modeling does not need to be linked to a specific antenna design to be made for industry or ESTEC, but is rather a goal in itself. In many cases the work is performed within the framework of an ESTEC project. This explains why configurations suitable for space application are always kept in mind. There are

many other groups in Europe which were also active between 1991 and 1995 in the modeling of planar antennas, but more in combination with the construction of specific antennas to perform specific jobs. The University of Karlsruhe (Germany) was involved in the modeling of SAR antennas based on the technology of Dornier GmbH [28]. At Ericsson Microwave Systems (Sweden), in-house developed programs dedicated to particular problems within large planar arrays were used to design radar and communication systems. In France, there were activities at the universities of Nice and Rennes in cooperation with the French telecom industry, in Norway at the Norwegian Institute of Technology and at SINTEF DELAB in Trondheim, in Portugal at the University of Lisbon, etc..

Planar antenna modeling: future (1996-...)

"While it is probably true that the beginner will have little problem with a simple microstrip element or array, the number and range of design variables involved with more complex elements or larger arrays quickly become formidable enough to make a successful conclusion unlikely unless the designer is able to use CAD software tools in conjunction with his or her own experience and understanding of the problem. And at this point in time, fully versatile and accurate CAD tools for microstrip antenna and array design are not available." (D. M. Pozar, COST 245 ESA Workshop on Active Antennas, 27-28 June 1996).

In August 1994, there was a unique meeting at the ESTEC premises in Noordwijk, The Netherlands, concerning "Planar Antenna Design Tool Development". Representatives from all important European companies and universities, in many cases also members of COST 245, were present. The goal was to have two days of discussion on 1. which planar antenna structures a good design tool should be able to cope with, and 2. how a good design tool for planar antennas should look like.
Concerning the second item, very soon it became obvious that what European industry wants is a user-friendly, one-pass design tool, which is able to make the analysis of a certain structure in a few seconds or minutes. The software tools already available at that time could only be considered a first step in this direction. These tools in fact are analysis tools with large calculation times in case of complex structures or large arrays. It was understood that in order to be able to create such a tool, model tuning in some cases should be allowed. It was also understood that in order to be the most efficient, the planar antenna design tool to be developed should be integrated within the Antenna Design Framework [29]. This framework has been conceived by ESTEC to make modern computational technologies available to antenna and electromagnetic engineers. It has been designed to be a single hub around which new modeling tools can be developed using these technologies.
Concerning the first item, it was stated that the topics of immediate importance that were not covered in a satisfactory manner at that time were: 1. the modeling of the finiteness of the layer structure, 2. the modeling of coplanar line configurations within the antenna structure, 3. the modeling of cavities and/or walls within an antenna structure and the finite thicknesses of ground plates, and 4. the efficient modeling of large arrays.
Since August 1994, the first European contributions to the one-pass design tool already have been made. In Lausanne, (Switzerland) the study on efficient iterative schemes for array analysis is continuing [30]. In Lyngby (Denmark), the development of fast coarse models for specific antenna geometry's is going on. In Trondheim (Norway), a study of cavity backed structures has started [31], in cooperation with VTT (Finland). At Chalmers University (Sweden), the research on the S2DS technique [32] was recently directed also towards planar antennas and, in cooperation with

Zagreb (Croatia), research on symmetry in planar antennas is going on [33]. In Leuven, the mixed expansion scheme was upgraded to the Expansion Wave Concept (EWC) [34, 35], to my knowledge a completely new, very general and fast technique to model mutual coupling in larger planar (antenna) structures, and a framework was designed for the analysis of arbitrary planar structures [36, 37]. Out of Europe, but within the context of the COST 245 action, efficient moment method techniques were developed in Ankara (Turkey) [38].
Another important factor is HP-momentum, the software package of Hewlett-Packard for the analysis of planar microwave circuits. Although the analysis of planar antennas was not one of the original scopes of this package, recently the group that developed this software (Ghent, Belgium) got interested in the antenna market.
In my view, the optimal way to reach the ultimate goal of a one-pass design tool is to establish a close cooperation between the (European) labs active in this field. University labs could be mainly involved in the theoretical modeling, and research labs of companies and/or institutes could work on validation and application and give feedback to the univerities. The work could be done under the supervision of ESTEC and COST 260, the planned successor of COST 245.

Conclusions

In this paper, the past, present and future of planar antenna research in Europe has been discussed. The ultimate goal in Europe is to establish a one-pass design tool for planar antennas. Both universities and companies cooperate towards this goal, within the unique forum of the COST actions, and with ESTEC as a prime partner.

Acknowledgment

The author would like to thank the members and experts of COST 245 for the information they provided.

References

[1] G. A. Deschamps, "Microstrip microwave antennas", 3rd USAF Symposium on Antennas, 1953.
[2] A. G. Derneryd, "Linearly polarized microstrip antennas", IEEE Trans. Antennas Propagat., pp. 846-851, Nov. 1976.
[3] A. G. Derneryd, "A theoretical investigation of the rectangular microstrip antenna element", IEEE Trans. Antennas Propagat., vol. 26, pp. 532-535, Jul. 1978.
[4] P. Hammer et al., "A model for calculating the radiation field of microstrip antennas", IEEE Trans. Antennas Propagat., vol. 27, pp. 267-270, Mar. 1979.
[5] B. Nauwelaers and A. Van de Capelle, "A transmission line model for arrays of rectangular microstrip antennas", Annales des Télécommunications, vol. 44, pp. 549-554, Sept.-Oct. 1989.
[6] J. R. James et al., "Some recent developments in microstrip antenna design", IEEE Trans. Antennas Propagat., vol. 29, pp. 124-128, Jan. 1981.
[7] A. G. Derneryd and I. Karlsson, "Broadband microstrip antenna element and array", IEEE Trans. Antennas Propagat., vol. 29, pp. 140-141, Jan. 1981.
[8] J. R. Mosig and F. E. Gardiol, "Analytical and numerical techniques in the Green's function treatment of microstrip antennas and scatterers", Proc. IEE, pt. H, vol. 130, pp. 175-182, Mar. 1983.

[9] J. R. Mosig and F. E. Gardiol, "General integral equation formulation for microstrip antennas and scatterers", Proc. IEE, pt. H, vol. 132, pp. 424-432, Dec. 1985.
[10] L. Barlatey et al., "Analysis of stacked microstrip patches with a mixed potential integral equation", IEEE Trans. Antennas Propagat., vol. 38, pp. 608-615, May 1990.
[11] G. Splitt and M. Davidovitz, "Guidelines for design of electromagnetically coupled microstrip patch antennas on two-layer substrates", IEEE Trans. Antennas Propagat., vol. 38, pp. 1136-1140, Jul. 1990.
[12] E. Lier and K. R. Jakobsen, "Rectangular microstrip patch antennas with infinite and finite ground plane dimensions", IEEE Trans. Antennas Propagat., vol. 31, pp. 978-984, Nov. 1983.
[13] L. Vegni et al., "Spectral dyadic Green's function formulation for planar integrated structures", IEEE Trans. Antennas Propagat., vol. 36, pp. 1057-1065, Aug. 1988.
[14] P. van den Berg and R. E. Kleinman, "The conjugate gradient spectral iterative technique for planar structures", IEEE Trans. Antennas Propagat., vol. 36, pp. 1418-1423, Oct. 1988.
[15] M. F. Catedra and E. Gago, "Spectral domain analysis of conducting patches of arbitrary geometry in multiylayer media using the CG-FFT method", IEEE Trans. Antennas Propagat., vol. 38, pp. 1530-1536, Oct. 1990.
[16] J. Herault et al., "A new approach to microstrip antennas using a mixed analysis: transient - frequency", IEEE Trans. Antennas Propagat., vol. 38, pp. 1166-1175, Aug. 1990.
[17] F. J. Demuynck and A. R. Van de Capelle, "Higher order modes in microstrip antenna design via the transmission line model", Electron. Lett., vol. 28, pp. 1732-1734, Aug. 1992.
[18] M. Dich, A. Ostergaard, and U. Gothelf, "A network model for the aperture coupled microstrip patch", Int. Journal of Microwave and Millimeter Wave Computer Aided Eng., vol. 3, pp. 326-339, 1993.
[19] D. Thouroude, M. Himdi, and J. P. Daniel, "CAD-oriented cavity model for rectangular patches", Electr. Lett., vol. 26, pp. 842-844, June 1990.
[20] G. A. E. Vandenbosch and A. R. Van de Capelle, "Mixed-potential integral expression formulation of the electric field in a stratified dielectric medium - application to the case of a probe current source", IEEE Trans. Antennas Propagat., vol. 40, pp. 806-817, July 1992.
[21] G. A. E. Vandenbosch and A. R. Van de Capelle, "Use of subsectional edge expansion functions (SEEFs) to analyse rectangular microstrip antennas with the method of moments", Proc. IEE, pt. H, vol. 139, pp. 159-164, Apr. 1992.
[22] G. A. E. Vandenbosch and A. R. Van de Capelle, "Reduction of coaxial feed between two parallel conductors into finite number of voltage sources", Electron. Lett., vol. 27, pp. 2387-2389, Dec. 1991.
[23] G. A. E. Vandenbosch and A. R. Van de Capelle, "Admittance of coaxial feed between two finite parallel conductors", Electron. Lett., vol. 28, pp. 1780-1781, Sept. 1992.
[24] G. A. E. Vandenbosch and A. R. Van de Capelle, "Use of a combined expansion scheme to analyze microstrip antennas with the method of moments", Radio Science, vol. 27, pp. 911-916, Nov-Dec. 1992.
[25] A. K. Skrivervic and J. R. Mosig, "Finite phased array of microstrip patch antennas: The infinite array approach", IEEE Trans. Antennas Propagat., vol. 40, pp. 579-582, May 1992.
[26] A. K. Skrivervic and J. R. Mosig, "Analysis of finite phased arrays of microstrip patches", IEEE Trans. Antennas Propagat., vol. 41, pp. 1105-1114, Aug. 1993.
[27] S. A. Bokhari, J. R. Mosig, and F. E. Gardiol, "Radiation pattern computation of microstrip antennas on finite size ground planes", Proc. IEE, pt. H, vol. 139, pp. 278-286, June 1992.
[28] F. Rostan and W. Wiesbeck, "Design considerations for dual polarized aperture-coupled microstrip patch antennas", Proc. IEEE International Antennas and Propagat. Symp., Newport Beach, California, pp. 2086- 2089, June 18-23, 1995.

[29] "The Antenna Design Framework - An overview", ESA-ESTEC report XEA/023.94, 1994.
[30] Y. Brand, A. K. Skrivervik, and J. R. Mosig, "An iterative scheme for array analysis", Journées Internationales de Nice sur les Antennes JINA 96, pp. 683-686, Nice, France, Nov. 1996.
[31] H. Thonstad, "Analysis of cavity-backed planar antennas", COST 245 ESA Workshop on Active Antennas, pp. 27-30, Noordwijk, The Netherlands, June 1996.
[32] K. Fooroghi, P.-S. Kildal, and S. Rengarajan, "Admittance of an isolated waveguide slot radiating between baffles using a spectrum of two-dimensional solutions", IEEE Trans. Antennas Propagat., vol. 41, pp. 422-428, Apr. 1993.
[33] Z. Sipus, J. Bartolic, and D. Bonefacic, "Symmetries in microstrip array analysis", COST 245 ESA Workshop on Active Antennas, pp. 133-138, Noordwijk, The Netherlands, June 1996.
[34] F. J. Demuynck, G. A. E. Vandenbosch and A. R. Van de Capelle, "The expansion wave concept, part I: efficient calculation of spatial Green's functions in a stratified dielectric medium", accepted for publication in IEEE Trans. Antennas Propagat..
[35] G. A. E. Vandenbosch and F. J. Demuynck, "The expansion wave concept, part II: a new way to model mutual coupling in microstrip antennas", accepted for publication in IEEE Trans. Antennas Propagat..
[36] B. L. A. Van Thielen and G. A. E. Vandenbosch, "Magmas: present status", COST 245 ESA Workshop on Active Antennas, pp. 149-158, Noordwijk, The Netherlands, June 1996.
[37] G. A. E. Vandenbosch, "Planned developments of the MAGMAS framework", COST 245 ESA Workshop on Active Antennas, pp. 43-50, Noordwijk, The Netherlands, June 1996.
[38] L. Alatan, M. I. Aksun, and M. T. Birand, "Use of computationally efficient spatial-domain method of moments in CAD of microstrip antennas", COST 245 ESA Workshop on Active Antennas, pp. 13-15, Noordwijk, The Netherlands, June 1996.

MICROSTRIP PATCH ANTENNA RESEARCH ACTIVITIES AT THE TECHNICAL UNIVERSITY OF LISBON

Custódio Peixeiro
IT/DEEC - Instituto Superior Técnico
Technical University of Lisbon
Av. Rovisco Pais, 1 1096 Lisboa Codex Portugal
e-mail: ecpeixe@beta.ist.utl.pt

Abstract
This paper presents an overview of the patch antenna research activities carried out at Instituto de Telecomunicações and Instituto Superior Técnico - Technical University of Lisbon. Research in this area has began almost then years ago. A small group of people has been involved.

1. Introduction

Microstrip patch antennas have been found increasing application in the microwave and millimetre wave bands. Their success us due to, mainly, some physical characteristics, such as, being planar but can also be conformal, small size, low profile and lightweight. They can be used as single element radiator or grouped in arrays providing many interesting electrical characteristics, for instance, a wide range of possible gains, electronic beam steering and beam shaping. Moreover direct integration with active devices can be achieved using MMIC technologies. However microstrip antennas present some drawbacks the most important being inherent narrow band. To overcome this and other disadvantages and to present innovative configurations intensive R&D activities have been pursued and reported in the specialised literature and in the many related conferences taking place each year around the world.
Microstrip patch antenna work has began almost ten years ago at the Instituto Superior Técnico (which is the engineering school of the Technical University of Lisbon). A small group of people has been involved namely two academic staff two technicians and some graduation and post-graduation students. This paper presents a brief description of the most important topics and for the sake of simplicity they are grouped in five separate sections.

2. Anisotropy in Microwave Substrates

With the aim of evaluating the importance of anisotropy in microwave plastic substrates extensive permittivity measurements were carried out. A very simple cavity small perturbation method was used to obtain the elements of the permittivity diagonal tensor $\underline{\underline{\varepsilon}}$ [1].

$$\underline{\underline{\varepsilon}}=\varepsilon_o\begin{bmatrix}\varepsilon_{rx} & 0 & 0\\ 0 & \varepsilon_{ry} & 0\\ 0 & 0 & \varepsilon_{rz}\end{bmatrix}$$

Results were obtained, at the X band, for some substrates commonly used in microwave applications. The cavity used in the experiments is shown in figure 1. Some results are contained in table 1.

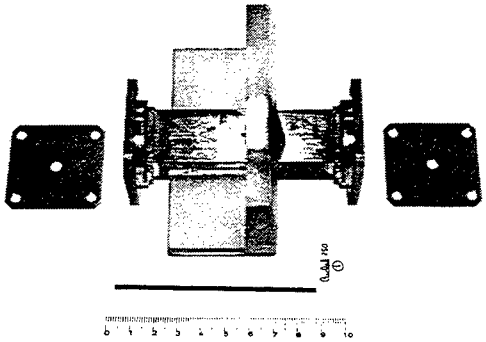

Figure 1: X band resonant cavity used in the experiments.

Substrate	ε_{rx}	ε_{ry}	ε_{rz}	A. R.
Cuflon	1.979±0.022	1.970±0.022	1.971±0.022	1.002±0.022
Cuclad 217	2.163±0.026	2.166±0.027	2.063±0.027	1.049±0.027
TLY 5A	2.129±0.039	2.119±0.037	2.077±0.039	1.023±0.038
Duroid 5880	2.195±0.028	2.189±0.027	2.122±0.028	1.033±0.027
Cuclad 250	2.690±0.037	2.688±0.038	2.472±0.038	1.088±0.032
Ultralam 2000	2.785±0.040	2.704±0.038	2.468±0.040	1.112±0.034
Duroid 6006	6.949±0.263	6.927±0.262	6.077±0.263	1.142±0.093
Epsilam 10	11.280±0.315	10.797±0.299	10.411±0.315	1.030±0.061
Duroid 6010	10.926±0.424	10.689±0.412	10.660±0.424	1.014±0.080

Table 1: Relative dielectric constant at 10 GHz.

The anisotropy ratio (A. R.) is given by $$A.R.=\frac{\varepsilon_{rx}}{\varepsilon_{rz}}\cong\frac{\varepsilon_{ry}}{\varepsilon_{rz}}$$

It can be concluded that specially the woven laminate Ultralam 2000 exhibits a non-negligible amount of uniaxial anisotropy. If accurate results are required anisotropy has to be taken into account.

3. Modelling of Microstrip Patch Antennas

This is a generic topic whose long term goal was the development of a software package to be used in the CAD of microstrip antennas. A block structure has been chosen so that new features could be easily included in the numerical simulation tool. A current integral equation has been deduced and solved by a moment method. A spectral approach has been used to obtain the Green's functions. It uses complex

wave theory taken into consideration both surface wave and leaky wave modes [2]. An accurate model of thick coaxial probe feeds has been included [3]. Uniaxial anisotropic substrates have been considered [2,3]. As a first application circular patches have been considered [4]. The effects of uniaxial anisotropy on the circular patch performance has been determined. The effect of the A.R. on the resonance frequency and input impedance of a centre-fed circular patch are shown in figures 2 and 3, respectively. The results correspond to a patch with 4 cm diameter, a substrate thickness of 4 mm and $\varepsilon_{rz} = 2.468$.

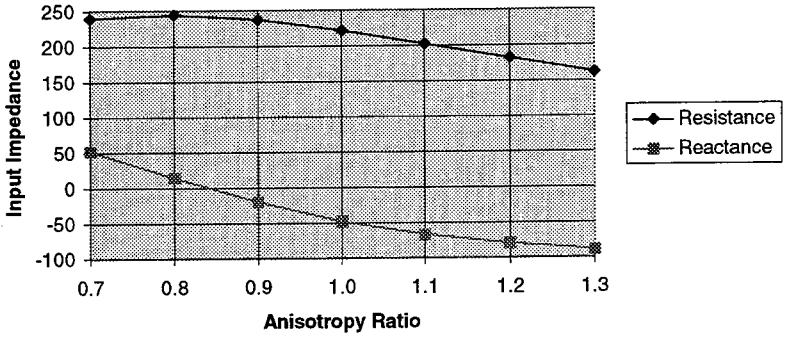

Figure 2: Effect of uniaxial anisotropy on input impedance.

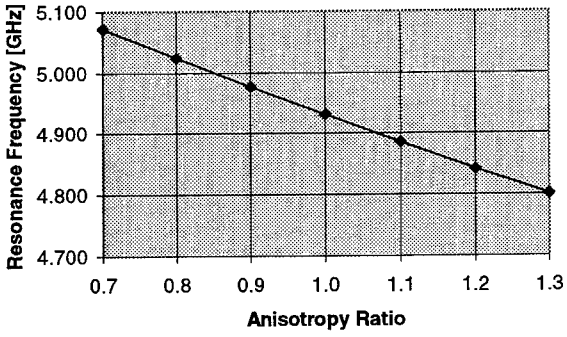

Figure 3: Effect of uniaxial anisotropy on resonance frequency.

For Ultralam 2000 substrate (A. R. = 1.112) the change in the resonance frequency relative to the isotropic case (1%) is comparable to the typical bandwidth.

Ten years ago, no accurate software was available commercially for the modelling of microstrip patch antennas. For that reason it was important, at that time, to develop our own software. However in ten years the situation changed completely. Nowadays many software packages for the accurate modelling of microstrip antennas are available. Just to mention a few; ENSEMBLE, THESADE, MAGMAS, SONNET, IE3D, MOMENTUM, and MAFIA. Some of them run on a PC and are not very expensive.

It is hard to compete with the large teams of experts, not only in antennas but also in software engineering, mainly in terms of computer efficiency, user friendship, and flexibility. As a consequence in our small group of people modelling is not a priority at the moment.

4. Microstrip Patch Antennas for a Mobile Communication System at 60 GHz

The work on this topic was carried out, with the collaboration of French partners (CNET and Thomson), in the frame of RACE project Mobile Broadband System (MBS) partially funded by the European Union. The goal was to proof that microstrip patch antennas can be an alternative to conventional antennas, such as horns and lenses, in millimetre wave mobile communication systems. Two switchable series-fed linear arrays of four microstrip patches, mounted back to back, were selected for the base station [5,6]. The geometry and test fixture of the array are shown in figures 4 and 5, respectively.

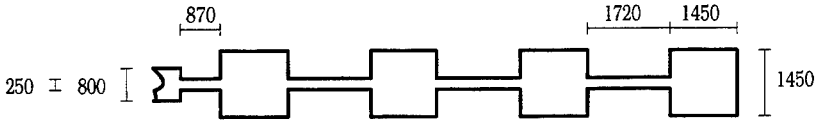

Figure 4: Geometry of the series fed linear array (dimensions in μm).

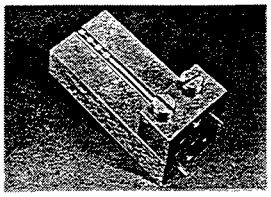

Figure 5: Array mounted on the test fixture.

	ENSEMBLE	Experimental
|S11| minimum frequency [GHz]	65.3	64.4
Bandwidth (|S11| ≤ -10 dB) [GHz]	0.5	1.5
Gain at 62.5 GHz [dBi]	14.3	10.8
E plane half-power beamwidth [Degree]	17	16
H plane half-power beamwidth [Degree]	80	71
Side lobe level [dB]	-9.4	-5.8
E plane cross-polar radiation level [dB]	< - 50	≤ - 20
H plane cross-polar radiation level [dB]	< - 22	< - 20

Table 2: Comparison of array theoretical and experimental results.

Array theoretical and experimental results are summarised in table 2. ENSEMBLE [7] software has been used to obtain the theoretical predictions. E and H plane radiation patterns are shown in figures 6 and 7. A good agreement has been obtained between theory and experiments allowing the validation of the design/fabrication procedure.

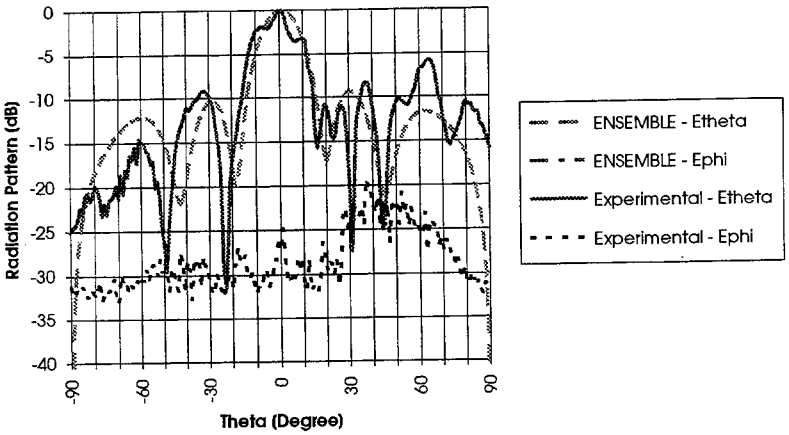

Figure 6: E plane radiation pattern of the array.

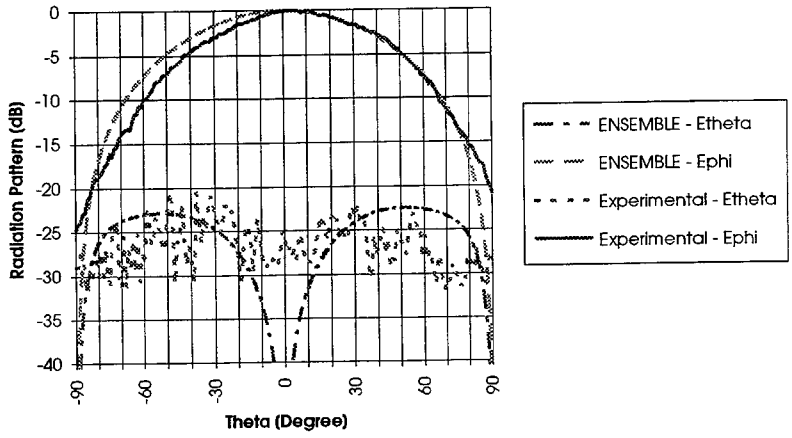

Figure 7: H plane radiation pattern of the array.

5. Active Integrated Microstrip Patch Antennas

The work on this topic was carried out also in the frame of project MBS. The goal was to evaluate feasibility and performance of active integrated microstrip patch antennas at 60 GHz. Single element active receive and transmit antennas were designed, fabricated and tested. Philips Microwave D02AH Gallium Arsenide technology was used [8,9]. This process was developed specifically for microwave and millimetre wave applications up to 70 GHz.

In the layout of the active integrated patch antenna, shown in figure 8, the rectangular microstrip patch and the two stage amplifier can be easily identified.

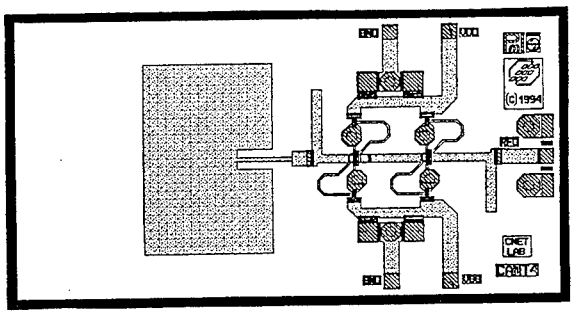

Figure 8: Layout of the active integrated patch antenna (2.85×1.5 mm).

The input return loss of the antenna has been measured on wafer. The experimental results show a good agreement with the ENSEMBLE predictions (figure 9).

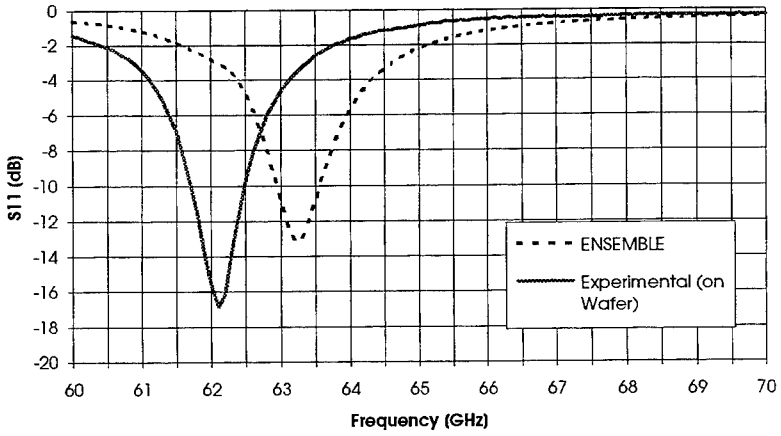

Figure 9: Return loss of the passive antenna.

6. Microstrip Patch Antennas for a Mobile Communication System at 2 GHz

The work described on this topic has been carried out in the frame of research project ITCOM partially funded by the National (Portuguese) Research Council. Microstrip patch antennas have been selected both for the base station (BS) and the mobile terminal (MT) of a mobile communication system at 2 GHz. The antennas have been designed with a shaped beam in the vertical plane. Two arrays of four elements are used. The BS array is linear [10] whereas the four elements of the MT array are mounted on the side walls of a pyramid to allow an almost omnidirectional radiation pattern [11]. Two electromagnetically coupled rectangular patches printed on a Duroid 5880 substrate, separated by an air gap, are used as the basic element of the arrays. BS array geometry and input return loss are shown in figures 10 and 11, respectively.

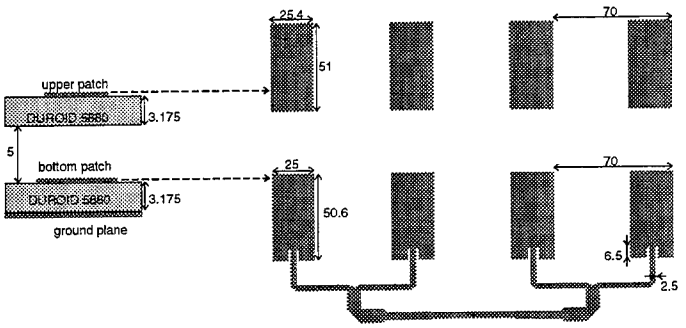

Figure 10: BS array configuration (dimensions in mm).

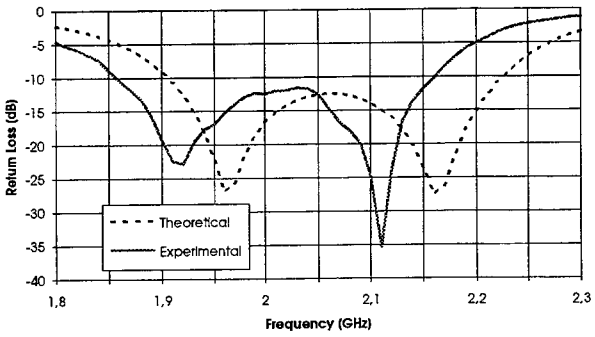

Figure 11: BS array input return loss.

A reasonable agreement has been obtained between ENSEMBLE theoretical and experimental results. The required dual-band behaviour has been obtained. However additional fine tuning is required.

7. Conclusion

An overview of the microstrip patch antenna research activities carried out at the Instituto de Telecomunicações and Instituto Superior Técnico - Technical University of Lisbon has been presented. Special attention has been paid in the past to accurate modelling with emphasis on thick substrates, uniaxial dielectrics and coaxial probes. Nowadays priority has been given to applications in the field of mobile communication systems and active integrated antennas.

Acknowledgements

The author wishes to acknowledge all the people (included in the references) and partners whose collaboration was essential to the fulfilment of the objectives of the work described in this paper. The author wishes also to acknowledge the National (Portuguese) Research Council and the European Union for the partial funding of some of the research activities.

References

1. Peixeiro, C. and A. M. Barbosa, "Measurement of Anisotropy in Microwave Substrates", (Abstract) *Proc. PIERS'93*, p. 50, Pasadena, California, U.S.A, July 1993.
2. Peixeiro, C. and A. M. Barbosa, "Leaky and Surface Waves in Anisotropic Printed Antenna Structures", *IEEE Trans. Ant. Propagation*, vol. 40, n. 5, pp. 566-569, May 1992.
3. Peixeiro, C. and A. M. Barbosa, "Rigorous Modelling of Coaxial Probes on Anisotropic Mulilayered Structures", *Journal of Electromagnetic Waves and Applications*, vol. 7, n. 2, pp. 285-300, February 1993.
4. Peixeiro, C. and A. M. Barbosa, "Analysis of Circular Patch Antennas Printed on Multilayered Anisotropic Structures", *Proc. JINA'94*, pp. 131-134, Nice, France, November 1994.
5. Peixeiro, C., "Modelling of Microstrip Patch Antennas at 60 GHz", *Proc. COST 245/ESA Workshop on Active Antennas*, pp. 117-122, ESTEC, Noordwijk, The Netherlands, June 1996.
6. Peixeiro, C., P. Dufrane, Y. Guillerme, "Microstrip Patch Antennas for a Mobile Communication System at 60 GHz", *Proc. IEEE/APS Int. Symposium*, pp.78-81, Baltimore, Maryland, U.S.A, July 1996.
7. ENSEMBLE, Design & Review User's Guide, Version 4.0, Boulder Microwave Technologies, Inc., February 1996.
8. Peixeiro, C., P. Dufrane, Y. Guillerme, A. Boulouard, E. Delhaye, B. Byzery, "Microstrip Patch Antennas at 60 GHz for Race Project MBS", *Proc. 26th European Microwave Conference*, pp.933-937, Prague, Czech Republic, September 1996.
9. Cordeiro, J., C. Peixeiro, E. Delhaye, B. Byzery, A. Boulouard, "Modelling of Millimetre Wave Active Integrated Microstrip Patch Antennas", *Proc. JINA'96*, pp. 649-652, Nice, France, November 1996.
10. Armogida, A., and C. Peixeiro, "Microstrip Patch Antenna Array for a Mobile Communication System Base Station", submitted to the *1997 IEEE AP-S Int. Symposium*, Montreal, Canada, July 1997.
11. Rutkowski, T. and C. Peixeiro, "Microstrip Patch Array for the Mobile Terminal Omnidirectional Antenna of a Mobile Communication System", submitted to the *27th European Microwave Conference*, Jerusalem, Israel, September 1997.

A FULL-WAVE ELECTROMAGNETIC SIMULATION TECHNOLOGY FOR THE ANALYSIS OF PLANAR CIRCUITS

Niels Faché, Hewlett Packard,

HP EEsof division, Lammerstraat, 20 9000 Ghent - Belgium

Abstract

Traditional circuit simulators have proven to be of insufficient accuracy for the successful virtual prototyping of high frequency circuits. The circuit decomposition into independent components as the basis of any circuit simulator along with the limited accuracy of component models result in inherent limitations. Electromagnetic (EM) simulators address those limitations by simulating complete subcircuits or circuits through the solution of first principle equations. The combination of circuit and EM simulators yields a powerful simulation vehicle that can tackle the challenges posed by contemporary high frequency design.

This paper presents a full-wave EM simulation technology for the analysis of planar circuits such as *Monolithic Microwave Integrated Circuits* (MMICs), *RF Integrated circuits* (RFICs), *Printed Circuit Boards* (PCBs) and antennas. The first section defines planar circuits in the context of this work. Next, the mixed potential integral equations governing the electromagnetic behaviour of a hybrid strip-slot-via planar circuit are presented. The third section reviews the solution technique and discusses some innovative technological contributions such as the edge mesh and adaptive frequency sampling in more detail. Two examples in the fourth section illustrate the role em simulations play in the design of high frequency circuits.

The EM simulation technology discussed in this paper is implemented in the commercial planar EM simulator HP Momentum [1].

1. Planar Circuits

The physical layout model of a general planar circuit is shown in Figure 1. The multilayered substrate in which the circuit is embedded consists of an arbitrary number of homogeneous layers. The substrate layers extend to infinity and the substrate is open (no ground planes), semi-open (one semi-infinite layer and at least one ground plane) or closed (multiple ground planes). Each layer has a complex permittivity ε_r and a complex permeability μ_r. Frequency dependent behavior such as found in FR4 (real, frequency dependent ε_r) and Silicon (substrate conductivity) is included in the physical layout model.

A general planar circuit embedded in a multilayered substrate is a combination of strips, slots and vias. The strip and slot circuits are parallel to the substrate layers while the vias connect strip layers and ground planes. Each strip or slot circuit has an arbitrary polygonal shape. Strip and via conductor losses are modelled by a surface impedance Z_s. A planar circuit can be excited by a variety of sources such as single or coupled transmission lines, bond wire feeds, surface mount device feeds, coaxial ports and others.

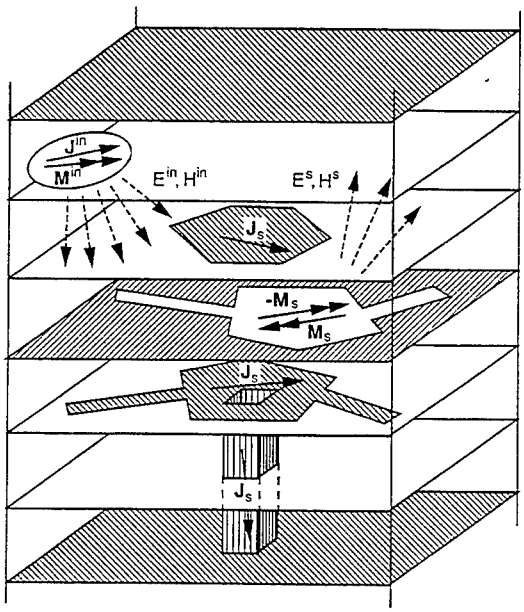

Figure 1 : A general planar circuit consisting of strip, slot and via levels embedded in a multilayered substrate

2. Mixed Potential Integral Equations (MPIE)

To obtain an electrical model of a planar circuit, several simulation techniques can be used such as finite elements, method of lines or method of moments. In this work a method of moments technique is applied to the mixed potential integral equations (MPIE) which govern the electromagnetic behavior of planar circuits. The MPIE are derived from Maxwell's field equations and express the boundary conditions at the strips, slots and vias. The specific formulation used in this work yields three coupled integral equations, each one expressing a boundary condition at the strip, slot and via surfaces [2-4] :

microstrip boundary condition ($E_t - Z_s J_{s,t} = E_t^{in}$)

$$\iint_{S'_m} dS' \left[G^A_{mm}(\rho) \boldsymbol{J}_s(\boldsymbol{r}') - \nabla_t (G^V_{mm}(\rho) \nabla'_t \cdot \boldsymbol{J}_s(\boldsymbol{r}')) \right] +$$

$$\iint_{S'_s} dS' \left[G^A_{ms}(\rho) (\boldsymbol{u}_z x \boldsymbol{M}_s(\boldsymbol{r}')) - \nabla_t (G^V_{ms}(\rho) \nabla'_t \cdot (\boldsymbol{u}_z x \boldsymbol{M}_s(\boldsymbol{r}')) \right] +$$

$$\iint_{S'_v} dS' \left[-\nabla_t G^A_{mv}(\rho, z') J_{s,z}(\boldsymbol{r}') - \nabla_t (G^V_{mv}(\rho, z') \frac{\partial J_{s,z}}{\partial z'}(\boldsymbol{r}')) \right] - Z_s \boldsymbol{J}_s(\boldsymbol{r}) = -\boldsymbol{E}_t^{in}(\boldsymbol{r})$$

slot boundary condition ($\Delta H_t = \Delta H_t^{in}$)

$$\iint_{S'_s} dS' \left[G^A_{ss}(\rho) \boldsymbol{M}_s(\boldsymbol{r}') - \nabla_t (G^V_{ss}(\rho) \nabla'_t \cdot \boldsymbol{M}_s(\boldsymbol{r}')) \right] -$$

$$\boldsymbol{u}_z \times \iint_{S'_m} dS' \left[G^A_{sm}(\rho) \boldsymbol{J}_s(\boldsymbol{r}') - \nabla_t (G^V_{sm}(\rho) \nabla'_t \cdot \boldsymbol{J}_s(\boldsymbol{r}')) \right] +$$

$$\boldsymbol{u}_z \times \iint_{S'_v} dS' \left[\nabla_t G^A_{sv}(\rho, z') J_{s,z}(\boldsymbol{r}') + \nabla_t (G^V_{sv}(\rho, z') \frac{\partial J_{s,z}}{\partial z'}(\boldsymbol{r}')) \right] = -\Delta \boldsymbol{H}_t^{in}(\boldsymbol{r})$$

via boundary condition ($E_z - Z_s J_{s,z} = E_z^{in}$)

$$\boldsymbol{u}_z \iint_{S'_m} dS' \left[G^A_{vm}(\rho, z) \nabla'_t \cdot \boldsymbol{J}_s(\boldsymbol{r}') - \frac{\partial}{\partial z} (G^V_{vm}(\rho, z) \nabla'_t \cdot \boldsymbol{J}_s(\boldsymbol{r}')) \right] +$$

$$\boldsymbol{u}_z \iint_{S'_s} dS' \left[G^A_{vs}(\rho, z) \nabla'_t \cdot (\boldsymbol{u}_z x \boldsymbol{M}_s(\boldsymbol{r}')) - \frac{\partial}{\partial z} (G^V_{vs}(\rho, z) \nabla'_t \cdot (\boldsymbol{u}_z x \boldsymbol{M}_s(\boldsymbol{r}'))) \right.$$

$$\boldsymbol{u}_z \iint_{S'_v} dS' \; G^A_{vv}(\rho, z, z') J_{s,z}(\boldsymbol{r}') - \frac{\partial}{\partial z} \left[G^V_{vv}(\rho, z, z') \frac{\partial J_{s,z}}{\partial z'}(\boldsymbol{r}') \right] - Z_s \boldsymbol{J}_{s,z}(\boldsymbol{r}) = -\boldsymbol{E}_z^{in}(\boldsymbol{r})$$

where t and z are the transverse direction and the direction perpendicular to the layers, respectively. The subscripts m, s and v refer to microstrips, slots and vias. The integrals are convolutions of Green function kernels and sources taken over the strip, slot and via surfaces. The unknowns are the strip and via electrical currents $\mathbf{J}_s$ and the magnetic slot currents $\mathbf{M}_s$. The formulation assumes that the vias carry only a vertical current $J_{s,z}$ and no horizontal current $\mathbf{J}_{s,t}$. An incoming electric field at the strip and via interfaces and a jump in the magnetic field at the slot interface at the right hand side of the above equations act as the excitations of the planar circuit.

3. Solution Technique

3.1. Method of Galerkin

In order to solve the MPIE for the unknown currents $\mathbf{J}_s$ and $\mathbf{M}_s$ the equations are discretized using the method of Galerkin. In this method the unknown currents are expanded into a finite sum of independent rooftop basis functions. The expansion is substituted in the MPIE. To find the unknown expansion coefficients the MPIE are tested with the basis functions. The solution of the resulting interaction matrix equation yields the expansion coefficients. Once those coefficients are known, the currents on the planar circuit can be found. From the surface currents other physical quantities such as the S-parameters and near and far fields can be calculated. More details on the calculation technique can be found in [2-4].

3.2. Rooftop Basis Functions : Mesher

In order to generate the rooftop basis functions, the surface of the planar circuit is meshed with small rectangles and triangles. Figure 2 provides a simple illustration of a uniform mesh for a strip-via transition. A rooftop is defined over each pair of cells. At the strip-via interface the continuity of the current is incorporated in the rooftop expansion (see Figure 2).

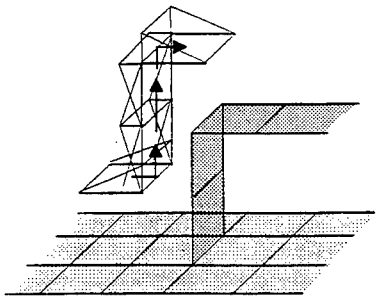

Figure 2 : Rooftop functions used to model the surface currents in a planar circuit

There is an important relationship between the mesh of rectangles and triangles used to define the rooftop expansion functions and the accuracy of an EM simulation. In order to perform accurate simulations using moderate compute requirements several novel techniques have been implemented to improve the efficiency of the mesh. Firstly, pattern recognition techniques maximize the regularity of the mesh while reducing the number of cells. Secondly, an edge mesh creates small edge cells which are needed to model the current confinement at the edges. These two mesh features are illustrated in Figure 3. Figure 3 shows the mesh of a slanted bandpass filter. The mesher applies an edge mesh along the border of the circuit to accurately model the current with a mininal

number of cells in the transverse direction of the transmission lines. Triangular cells which are less computationally efficient are limited to the corners. This is achieved by recognizing the different transmission line segments in the circuit. The simulation results of this circuit will be presented in the next section.

3.3. High Resolution S-Parameters : Adaptive Frequency Sampling

Very often designers want high resolution representations of S-parameters over given frequency bands. Traditionally, high resolution representations are obtained by simulating many frequency sample points and using straight line data interpolation. Although acceptable for fast circuit simulations, this approach is very time consuming for EM simulations which require orders of magnitude more compute resource requirements than circuit simulations.

In HP Momentum a novel interpolation technique was introduced for the efficient calculation of high resolution S-parameter data. The technique is called Adaptive Frequency Sampling. Instead of using straight line interpolation, rational function fits are employed to represent the S-parameters of a circuit. The simulation starts with the calculation of a few (typically four) frequency sample points. A rational fitting model is built for each S-parameter. In order to refine the fitting model, error functions are estimated for the rational function fits. These error functions indicate the location of the next frequency sample. Each new frequency sample refines the fitting models until convergence is reached. The resulting rational fitting models are derived from a minimal number of frequency samples and give accurate results for the S-parameters in each frequency point of the band, even if one or multiple resonances occur in the frequency band.

4. Illustrations

In this section the EM simulation technique will be illustrated for two examples. The first example is a slanted bandpass filter. The second example is a spiral inductor above a hole in a ground plane.

4.1 Slanted Bandpass Filter

Figure 3 shows the substrate and the mesh used in the EM simulation. The structure was simulated over a frequency band from 2.5 Ghz to 50 Ghz. The frequency samples were selected by AFS. A total of 10 samples was needed for the accurate representation of the S-parameters over the whole frequency range.

The results in Figure 4 show that the simulated data (Momentum) agree well with the measurements. Note that the resonance is predicted very accurately although no frequency sample was taken at that frequency. The resonance is captured by the rational fitting model used to represent the S-parameters.

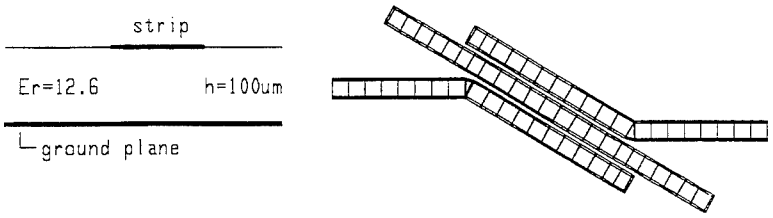

Figure 3 : Slanted band pass filter substrate and mesh

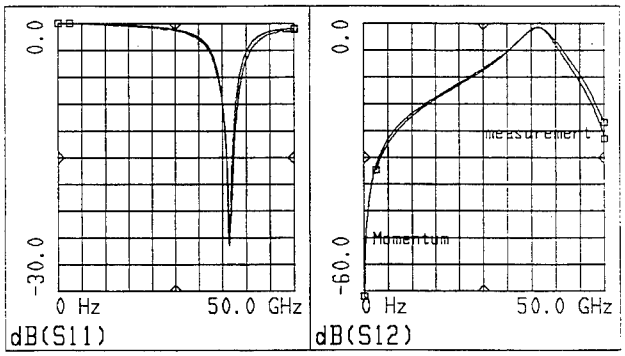

Figure 4 : Simulation versus measurement for the slanted filter of Figure 3

4.2. Spiral Inductor

The spiral inductor substrate and the mesh on the slot, spiral and airbridge (via-airstrip-via) are shown on Figure 5. The spiral inductor has two ports, one of which is connected to the middle of the spiral through a via-airstrip-via (model for a bondwire). This circuit is an example of a hybrid strip-slot-via circuit. The hole in the ground plane reduces the capacitance to ground and increases the self resonance frequency of the spiral inductor. The location of the resonance along with the inductance value can be calculated using an EM simulator.

The results in Figure 6 indicate that the self resonance occurs at around 3 Ghz while the inductance value is flat in the 1-2 Ghz frequency range (linear phase of S_{12}). Other

values for the inductances can be obtained by changing the number of spiral turns. Such what-if experiments can easily be done with EM simulators.

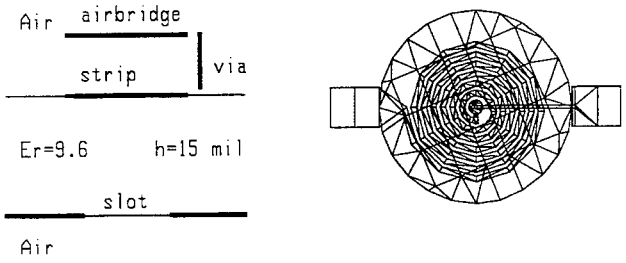

Figure 5 : Spiral inductor substrate and mesh

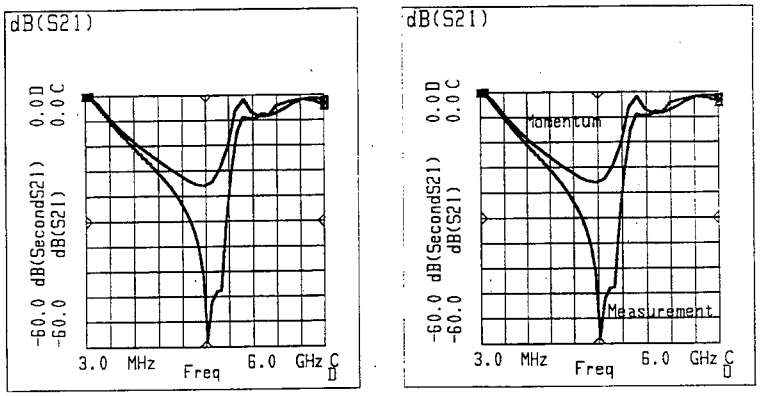

Figure 6 : Simulation versus measurement for the spiral inductor of Figure 5

5. Acknowledgments

HP Momentum is developed by the planar EM team of HP EEsof (Hewlett Packard). The team is based in Gent, Belgium.

References

[1] HP Momentum, Hewlett Packard, HP EEsof Division, 1400 Fountaingrove Parkway, Santa Rosa 95403, CA.

[2] K. Biomme, J. Van Hese, L. Vandormael, N. Faché and D. De Zutter, " Analysis of Strip-Slot Coupled Circuits in a Multilayered Medium using a new Calculation Technique for the Green Functions", 23rd EuMC, pp. 685-686.

[3] J. Sercu, N. Faché, F. Libbrecht and P. Lagasse, "Mixed Potential Integral Equation Technique for Hybrid Microstrip-Slotline Multilayered Circuits using a Mixed Rectangular-Triangular Mesh", IEEE-MTT, No 5, pp. 1162-1172, May 1995

[4] J. Sercu, J. Van Hese, N. Faché and Daniel De Zutter, "Improved Calculation of the Inductive and Capacitive Interactions of Vertical Sheet Currents in a Multilayered Medium", 26th EuMC, pp. 533-536

Analysis of Metal Patches, Strips and Corrugations Inside Cylindrical Multilayer Structures by Using G1DMULTc

Zvonimir Šipuš, Per-Simon Kildal and Silvia Raffaelli
Department of Microwave Technology
Chalmers University of Technology
S-412 96 Göteborg, Sweden
Fax (+46 31) 16 45 13, Phone (+46 31) 772 50 51, E-mail: zvonimir@nt.chalmers.se

ABSTRACT We have previously introduced an algorithm for calculating the Green's functions of general multilayer structures in the spectral domain. This has been developed into a Fortran subroutine G1DMULT for planar multilayer structures, as described in a companion paper. In the present paper we describe a subroutine which applies to coaxially layered cylindrical structures. The subroutine has been built into main programs for computing the input impedance of a microstrip patch and a dipole in a multilayer cylindrical structure and for calculating scattering from a multilayer cylinder loaded with a periodic grid of metal patches. The subroutine can also handle a structure in which there is an anisotropic layer. Thereby, we are able to easily analyze corrugations and metal strips inside the multilayer structure.

1. Introduction

Antennas on singly curved ground planes or substrates find many applications in communication and radar systems. Periodic elements on the curved surfaces can be used as frequency or polarization selective subreflectors in reflector antenna systems or as radomes. When the curvature of the structure is small, such antennas can be analyzed by assuming a planar structure. If this is not the case, more precise methods should be used. We will describe a Fortran subroutine for analyzing microstrip antennas and frequency selective surfaces in coaxially layered cylindrical structures.

We have previously presented a general methodology and common terminology by which planar, cylindrical and spherical multilayer structures can be respectively analyzed and described. We refer to this approach as analysis by using a spectrum of one-dimensional solutions (S1DS) [1]. The methodology has been reduced to an algorithm and implemented in a Fortran subroutine G1DMULT for calculating Green's functions of planar multilayer structures [2]. In the present paper we describe how G1DMULT is modified to G1DMULTc for calculating the Green's functions of cylindrical multilayer objects. The Green's functions are determined in the cylindrical spectral domain. They are applicable for analyzing e.g. microstrip antennas on cylindrical structures and singly curved frequency selective surfaces by using the method of moments.

We will also describe how layers with corrugations and strips are included in G1DMULTc,

provided their periods are small compared to the wavelength. By this we are able to analyze soft and hard surfaces [3]. The rigorous analysis of antennas which contain corrugations or metal strips is usually complex and time consuming. The analysis can be simplified by using asymptotic boundary conditions for strips (ASBC) and corrugations (ACBC) [4]-[6], in which we consider strips or corrugations as if their periodicity is approaching zero. The periodicities of corrugations and strips are normally around $0.1 - 0.3\ \lambda_0$, which is sufficiently small for ASBC and ACBC. In order to validate the ASBC we developed a complete Floquet mode solution (based on G1DMULTc as well) for circumferential strips.

Both G1DMULT and G1DMULTc are available free of cost under certain conditions from the authors.

2. Description of G1DMULTc

The structure of the S1DS method for multilayer cylinders is shown in Fig. 1. It is similar to the approach for planar multilayer problems [2]. The original 3D problem (Fig. 1.a) is transformed to the spectral domain by performing the cylindrical-Fourier transformation

$$\tilde{\mathbf{J}}(\rho, n, k_z) = \int_{-\pi}^{\pi} \int_{-\infty}^{\infty} \mathbf{J}(\rho, \phi, z) e^{jn\phi} e^{jk_z z} dz d\phi \tag{1}$$

The spectral domain problem can be interpreted in space as radiation from a harmonic current tube in the presence of the multilayer structure (Fig. 1.b). This is in space referred as a harmonic 1D field problem, and it is solved by the routine G1DMULTc. The algorithm behind G1DMULTc is based on Figures 1.c and 1.d. The harmonic 1D problem is divided into several equivalent subproblems, one for each cylindrical layer. The unknowns in the programs are two orthogonal components of the electric and magnetic fields at each interface. The two basic subroutines in G1DMULTc determine the electromagnetic fields due to electric and magnetic current tubes in homogeneous media (Fig. 1.e). The rest of G1DMULT organizes the results of these two subroutines in a linear system of $4n_i$ equations (with the same number of unknowns) where n_i is the number of layer interfaces. After determining the values of the fields at the interfaces, the Green's function is obtained as the values of the fields at desired locations within the structure.

The main differences compared to the routine for the planar case are the two basic subroutines for determining the electromagnetic fields due to electric and magnetic current tubes with given harmonic variations in ϕ and z. In the planar case the subroutines calculate the fields due to plane electric and magnetic current sheets with harmonic $x-$ and $y-$variation. The other differences have numerical reasons. The two subroutines for the cylindrical case contain Bessel and Hankel functions, and we have chosen to tabulate the values of these functions in order to improve computational efficiency. The reason is that an nth order Bessel/Hankel function in most commercial function libraries is calculated by evaluating all Bessel/Hankel functions from 0th to nth order, which is not very time efficient unless storing and reusing intermediate results like we do.

Previously multilayer coaxial structures have been analyzed by writing the field quantities within each region as the superposition of a forward and a backward traveling cylindrical wave, and solving for the unknown coefficients of these waves by enforcing the continuity of the tangential field components at each interface [8], [7]. Although in our approach we also

(a) 3-D problem

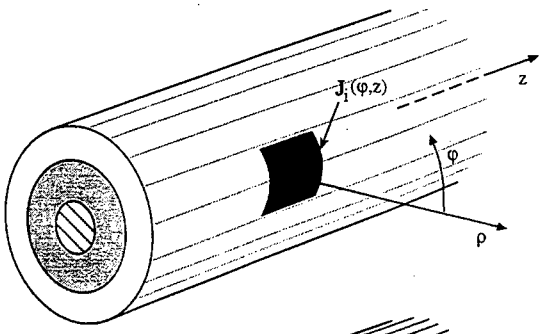

(b) Harmonic 1-D problem

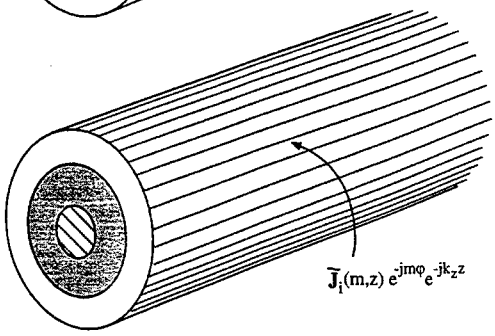

(c) Definition of material boundaries and regions
Region 4 (Nregion) extend to infinity

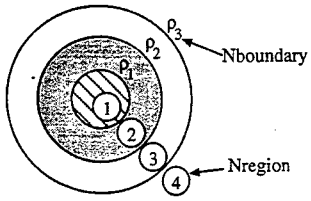

(d) Equivalent problem of region j
Equivalent currents are:

$$\tilde{\mathbf{J}} = \mathbf{n} \times \tilde{\mathbf{H}}_{\text{boundary}}$$

$$\tilde{\mathbf{M}} = -\mathbf{n} \times \tilde{\mathbf{E}}_{\text{boundary}}$$

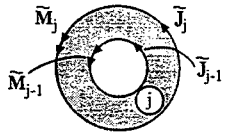

(e) The basic homogeneous harmonic 1-D field problem

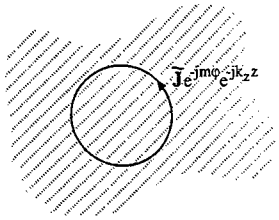

Figure 1. Structuring of a 3D field problem with a cylindrical layered structure into a harmonic 1D problem and its subproblems. The G1DMULTc subroutine solves the harmonic 1D problem.

consider traveling cylindrical waves, the way of determining the tangential field components at the interfaces is different. The particular advantage of our approach is that it is easy to modify it. E.g., the ASBC and ACBC were simply implemented in it for analyzing respectively strips and corrugations inside the multilayer cylindrical geometry.

3. Asymptotic boundary conditions

We have included an inner corrugated layer by using an anisotropic surface impedance which is different for different $e^{jn\phi}$ and k_z variations, i.e. which varies with angular dependence and direction of incidence. E.g., for corrugations that are transverse to the z-axis, the z component of the spectral surface admittance is

$$Y_z(n,k_z) = -\frac{\tilde{H}_\phi}{\tilde{E}_z} = \frac{j}{\eta}\frac{p}{w}\frac{J_n'(k\rho_t)H_n^{(2)}(k\rho_b) - J_n(k\rho_b)H_n'^{(2)}(k\rho_t)}{J_n(k\rho_t)H_n^{(2)}(k\rho_b) - J_n(k\rho_b)H_n^{(2)}(k\rho_t)} \tag{2}$$

where ρ_b and ρ_t are the value of the radial coordinate ρ at the bottom and the top of corrugations, p and w are the periodicity and width of the grooves, $k^2 = \omega^2\mu\epsilon$ and $\eta = \sqrt{\mu/\epsilon}$ with μ and ϵ the permeability and permittivity of the media inside the corrugations. Equation (2) is obtained by considering a parallel plate waveguide where only the dominant cylindrical mode is propagating [5]. This surface impedance is simply implemented into the algorithm by relating H_ϕ to E_z at the corrugation boundary, and therefore reducing the number of unknown equivalent currents by one. A corresponding surface impedance has been implemented for longitudinal corrugations.

Metal strip grids can be modeled asymptotically by enforcing the ASBC which are for transverse strips

$$E_\phi^b = 0, \qquad E_\phi^t = 0, \qquad E_z^b = E_z^t, \qquad H_\phi^b = H_\phi^t \tag{3}$$

where superscripts b and t means the bottom and top of the strips. This boundary condition is easely implemented into the algorithm by forcing the component of the electric field which is parallel to the strips to be zero at the bottom and the top of strips, and by setting the width of the layer which contains the strips equal to zero.

4. Numerical results

Patch impedance: We have used the routine to analyze input impedance and radiation pattern from cylindrical microstrip patches and dipoles, and to analyze scattering from corrugated and strip-loaded cylinders. Table 1 shows the comparison between measured and calculated resonance frequencies and resistances of a coaxially fed cylindrical-rectangular patch antenna. The resonant frequency is defined as the frequency where the real part of the input impedance has a maximum. The antennas are produced on a single-layer dielectric substrate with $\epsilon_r = 2.32$ and thickness 0.08 cm, and they are excited in the TM_{01} mode (i.e. the patch current is mainly z-oriented). The ground plane has radius $\rho_{GND} = 5$ cm. The length and width of the patches are: $L_1 = L_2 = 6.5\,cm$, $L_3 = 3\,cm$, $W_1 = 8\,cm$, $W_2 = 11\,cm$, $W_3 = 4\,cm$. More details about the measurements can be found in [9]. We have modeled the patch current with 7 entire-domain basis functions, and the probe by a constant current distribution. To

avoid surface wave poles in the k_z integral, the integration contour has been deformed appropriately in the first quadrant of the complex plane. The convergence of ϕ modes was checked for every calculated antenna. The agreement between the measured and calculated results is good. We have also tested the program for the case when the patch antenna is printed on a two-layer substrate [10].

Dipole impedance: The input impedance of the half-wavelength axially-oriented dipole is shown in Fig. 2. The dipole is radiating in the presence of a dielectric cylinder with $\epsilon_r = 20 - j5$. The frequency is $f = 1.8\ GHz$. The radius of the cylinder and the height of the dipole over the cylinder are taken as parameters. In order to reduce the needed computer time we have only calculated the change of the input impedance due to the presence of the cylinder and added this to the free-space impedance. The reason is that the free space impedance is faster to calculate directly in the free space. Thereby fewer phi modes are needed and the k_z integral is converging much faster. The results show that by enlarging the radius of the cylinder the input impedance approaches the planar case, i.e. radiation in the presence of a dielectric half-space, which is a good test for our program.

antenna	1	2	3
f_{res} meas.	1.499 GHz	1.497 GHz	3.166 GHz
f_{res} cal.	1.498 GHz	1.495 GHz	3.199 GHz
R_{in} meas.	52.5 Ω	36.7 Ω	119.1 Ω
R_{in} cal.	63.0 Ω	41.6 Ω	114.0 Ω

Table 1 Comparison of resonance frequencies and resonant resistances for cylindrical-rectangular microstrip antenna. The measured results are from [9].

Scattering from circumferential strips: In order to evaluate the accuracy of the ASBC and ACBC, we have also developed a program for analyzing a grid of circumferential strips by using a rigorous Floquet-mode approach. This program also uses the G1DMULTc subroutine. The two approaches are compared in Fig. 3 for normal incidence. The shown scattered fields are normalized to $E_i\sqrt{2j/\pi k\rho}\ exp(-jk\rho)$. The dielectric cylinder has $\epsilon_r = 2.1$, radius $\rho = 1.27\ cm$, and the strips are located at the dielectric-air interface. The frequency is $10\ GHz$, and the period and width of the strips are $0.8\ cm$ and $0.3\ cm$, i.e $0.27\lambda_0$ and $0.1\lambda_0$, respectively. In the rigorous Floquet-modes approach four basis functions are used in the moment method procedure, which is sufficient for this strip width [11]. Results show that the ASBC give accurate results for the periodicities and widths of strips which are used in practice. For corrugations the comparison of the ACBC results with the rigorous result can be found in [5]. Multilayer substrates give the same agreement.

4. Conclusion

We have developed a routine called G1DMULTc for calculating the Green's functions of general coaxially layered cylindrical structures in the cylindrical spectral domain. The routine has the same structure as the G1DMULT routine for planar multilayer structures. The advantage of the algorithm upon which G1DMULT and G1DMULTc are based is its

simplicity. E.g., it was easy to implement an anisotropic spectral surface impedance, which we have used for implementing the asymptotic boundary conditions for analyzing corrugations and metal strips inside the multilayer structure. This approach save a lot of computer time since the rigorous analysis of corrugations and strips is complex and time consuming. We have shown that the concept of the asymptotic boundary conditions is accurate for strips and corrugations with small periodicity in comparison with the wavelength, which is common in practice. We have also used G1DMULT for analyzing the input impedance of microstrip patches and dipoles.

References

[1] P-S. Kildal, J. Sanford, "Analysis of conformal antennas by using spectral domain techniques for curved structures," COST 245 - ESA workshop on active antennas, Noordwijk, The Netherlands, 1996, pp. 17-26.

[2] P-S. Kildal, M. Johansson, and Z. Šipuš, "G1DMULT - a numerical algorithm for computing Green's function of multilayer objects," to appear at the 1997 ACES Symposium, Monterey.

[3] P-S. Kildal, "Artificially soft and hard surfaces in electromagnetics," IEEE Trans. Antennas Propagat., Vol 38, pp. 1537-1544, Oct. 1990.

[4] P-S. Kildal, A. A. Kishk, and Z. Šipuš, "Asymptotic boundary conditions for strip-loaded and corrugated surfaces," Accepted for publication in Microwave Opt. Technol. Lett.

[5] A. A. Kishk, P-S. Kildal, G. Manara, and A. Monorchio, "An asymptotic boundary condition for corrugated surfaces and its application to calculate scattering from circular cylinders with dielectric filled corrugations," Submitted to IEE Proceedings, part H.

[6] A. A. Kishk, P-S. Kildal, "Asymptotic boundary conditions for strip-loaded scatters applied to cylinders under oblique incidence," Accepted for publication in IEEE Trans. Antennas Propagat.

[7] A. Nakatani, N. G. Alexopoulos, "Microstrip elements on cylindrical substrates - general algorithm and numerical results," Electromagnetics, Vol. 9, pp. 405-426, 1989.

[8] W. C. Chew, "Waves and fields in inhomogeneous media," IEEE Press, New York, 1995.

[9] W. Y. Tam, A. K. Y. Lai, and K. M. Luk, "Mutual coupling between cylindrical rectangular microstrip antennas," IEEE Trans. Antennas Propagat., Vol. AP-43, pp. 897-899, Aug. 1995.

[10] N. Herscovici, Z. Šipuš, P-S. Kildal, "The cylindrical omnidirectional patch antenna," Submitted to the 1997 IEEE AP-S Symposium, Montreal.

[11] T. K. Wu, "Fast convergent integral equation solution of strip gratings on dielectric substrate," IEEE Trans. Antennas Propagat., Vol. AP-35, pp. 205-207, Feb. 1987.

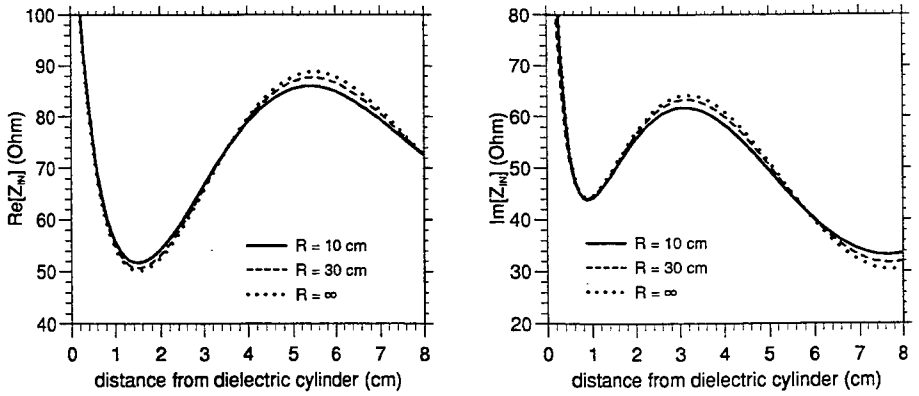

Figure 2. Input impedance of a half-wavelength dipole near a dielectric cylinder. The radius R of the dielectric cylinder is parameter. Frequency is 1.8 GHz. The cases of finite R are calculated by using G1DMULTc, the case of infinite R is calculated by using G1DMULT.

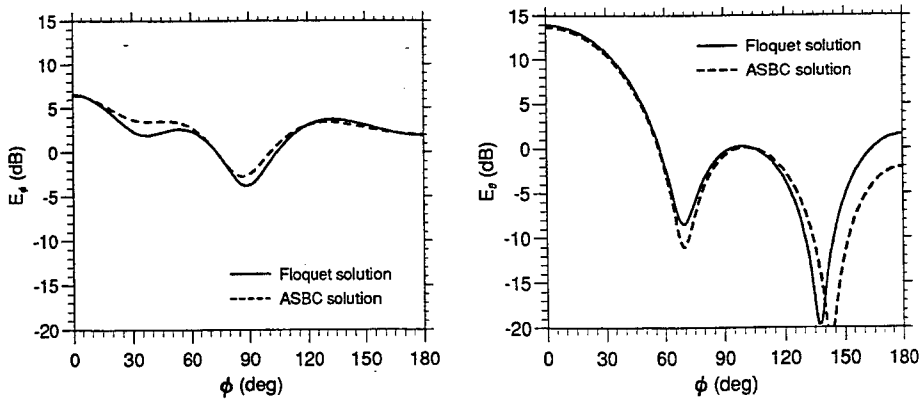

Figure 3. Scattered field from a dielectric cylinder loaded with periodic circumferential strips. (a) TE_z polarized normal incident field, (b) TM_z polarized normal incident field.

A Numerical Algorithm G1DMULT for Computing Green's Functions of Multilayer Objects

Per-Simon Kildal, Zvonimir Sipus and Martin Johansson,
Chalmers University of Technology, Department of Microwave Technology,
S-412 96 Gothenburg, Sweden
e-mail: martinjo@nt.chalmers.se
Fax: +46 31 7721740

1. Introduction

Several papers have been written on deriving Green's functions of planar layered structures for analysis of microstrip antennas and frequency selective surfaces. The Green's functions are often derived in the spectral domain and they are in some way inverse Fourier transformed to space before or after the weighting and testing needed in a moment method application. The spectral domain Green's function can be interpreted in space as plane waves originating from equivalent current sheets. We prefer to refer to the spectral domain approach as a solution in terms of a spectrum of one dimensional (or plane wave) solutions (S1DS) [1].

The purpose of the present paper is to introduce a general numerical algorithm G1DMULT for computing such Green's functions in the spectral domain. The algorithm different from previous approaches. It is analytically simple, and it is applicable to any multilayer structure of planar, coaxial cylindrical or concentric spherical types. The lay-out of the algorithm is shown in Figure 1 and the flow chart of its software implementation in Figure 2. The lay-out is pedagogical as well as easy to modify if additional features are to be included such as e.g. metal corrugations or strip loaded layers. The basic mathematical formulas are those of the plane waves radiated by current sheets as given in [1, Section 4.6]. The rest of the algorithm is simply a programming of the logical layout of the algorithm.

The terminology as well as the similarities between the planar, coaxial and concentric layer geometries are described in more detail in [1]. We will in the present paper concentrate on the application of G1DMULT to planar multilayer structures.

The algorithm is implemented for multilayer planar structures as subroutines called G1DMULT in both FORTRAN and Matlab. We have also developed an almost identical FORTRAN subroutine G1DMULTc for multilayer coaxial structures. The two first codes are available free of cost from the authors under certain conditions. The G1DMULTc routine is described in detail in [2] where also examples of use are given. The extension to spherical multilayer structures remains to be done.

The software implementation of G1DMULT is general and can be used for any number of structure layers. The materials can have complex permittivities and permeabilities, and the components k_x and k_y of the wave numbers (i.e. the variables in the spectral domain) may be complex. The latter allows us to perform the inverse Fourier transformation in the complex plane in order to avoid surface wave poles for real k_x and k_y.

Both G1DMULT and G1DMULTc has been extensively tested against results published by others for single-layer planar and cylindrical substrates which may or may not be grounded. They have also been validated for multilayer cases.

In the following we will document G1DMULT and explain how to use it. Finally, we will describe five examples which were solved by FORTRAN or Matlab programming using

G1DMULT. The examples were actually given as students exercises in a graduate course. Each of the students solved one problem, and they were able to get numerical results after typically 3 weeks of work.

2. Solving field problems using a spectrum of 1D solutions (S1DS) and the G1DMULT algorithm

We will here explain how to use the S1DS method and the G1DMULT algorithm in a moment mehod solution for an antenna on a multilayer planar structure (Figure 1). The original field problem consists of a planar multilayer structure with one or more radiating elements such as e.g. metal patches (Fig. 1a). The multilayer structure has boundaries only in z-direction and is therefore 1D. The radiating elements are three-dimensional (3D) with finite extents in x and y. They may also be called spectral excitation elements, as they excite the spectral distribution of the fields.

We replace the 3D elements by equivalent sources. We Fourier transform the basis functions in the x- and y-directions. The Fourier transformed currents can be interpreted in space as thin 1D current sheets with harmonic $e^{-jk_x x}$ and $e^{-jk_y y}$ variations (Fig. 1b). The original 3D current is reconstructed as an inverse Fourier transform corresponding to a superposition of the harmonic current sheets over continuous spectral variables $\infty < k_x < -\infty$, $\infty < k_y < -\infty$. The multilayer field problem with the harmonic 1D source is here referred to as the harmonic 1D field problem. It corresponds in more conventional terminology to the spectral domain problem.

The G1DMULT routine solves the harmonic 1D field problem as illustrated in Figure 1c-e. The problem is divided in one equivalent problem per layer (Fig. 1c), where the field in each region is formulated as the field radiated by electric and magnetic currents at the layer boundaries. These currents are also interpreted in space as current sheets with harmonic variations in the x- and y-directions. The boundary conditions between the layers give 4 linear equations per boundary. The basic mathematical formulas are those of the plane waves radiated by such current sheets in a homogeneous region (Fig. 1e) [1, Section 4.6], see also Appendix A.

The G1DMULT FORTRAN and Matlab routines are simply a programming of the flow chart in Figure 2. G1DMULT has 3 subroutines which are called a number of times. These are:

EQHOMO which calculates the E- and H-fields at a certain z-location in a given layer by using the tangential E- and H-field components at the boundary of the layer (region) by using the infinite homogeneous region equivalent.
G1DJ calculates the E- and H-fields from an electric current sheet in an infinite homogeneous region.
G1DM calculates the E- and H-fields from a magnetic current sheet in an infinite homogeneous region.

In a moment method (MM) procedure for calculating the 3D excitation currents we need to expand them in basis functions. The spectral Green's functions (i.e. E- and H-fields due to point sources) must be calculated at the location of the 3D elements from G1DMULT over the full spectrum of k_x and k_y (though discretized and truncated) by using a unit excitation current sheet as input, as this corresponds to a point source in the spectral domain. These fields must then be multiplied with the Fourier transforms of the basis and the test functions used in the moment method approach and inverse transformed. (This procedure is known as using MM in the spectral domain.) The result is a set of equations to determine the expansion coefficients of the 3D currents and thereby the currents themselves. When the

(a) 3-D problem

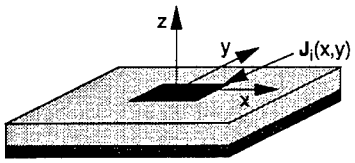

(b) Harmonic 1-D problem

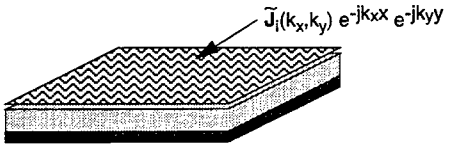

(c) Definition of material boundaries and regions
Regions 1 and 4 (Nregion) extend to $-/+\infty$, respectively

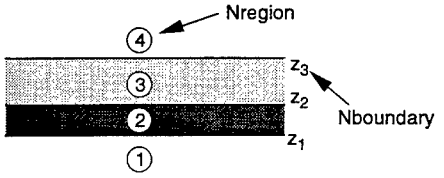

(d) Equivalent problem of region j
Boundary fields: $\mathbf{E}_j^b$ and $\mathbf{H}_j^b$

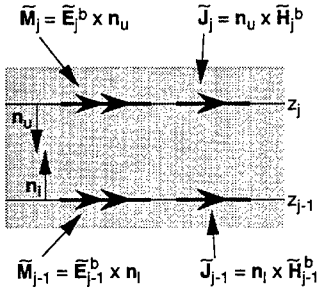

(e) The basic homogeneous harmonic 1-D field problem

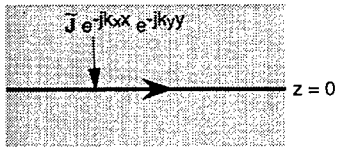

Figure 1. Structuring of a 3D field problem with a planar layered structure into a harmonic 1D field problem (or spectral domain problem) and its sub problems. The G1DMULT algorithm solves the harmonic 1D field problem.

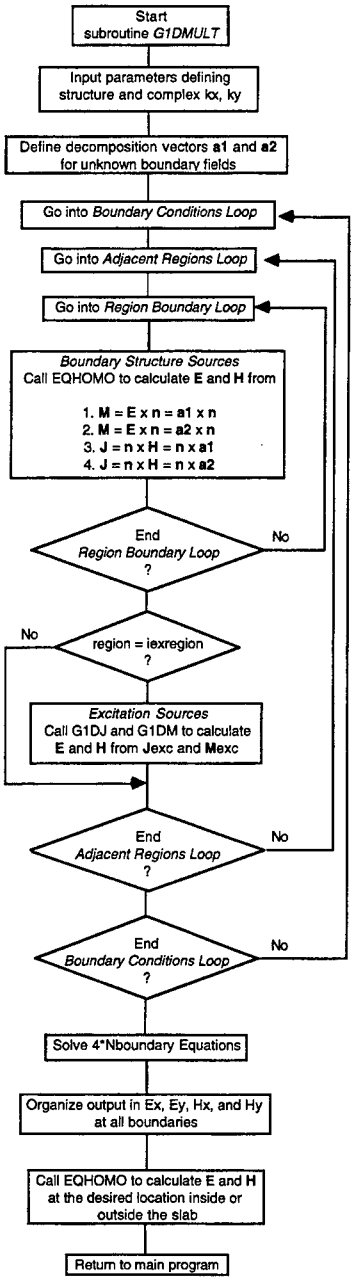

Figure 2. Flow chart of subroutine G1DMULT for solving the harmonic 1D field problem.

currents and their Fourier transforms are known, the field can be evaluated anywhere (e.g. in the far field) by using G1DMULT as well. If the near field is needed, e.g. for calculating the source impedance, an inverse Fourier transform of the spectral domain field must be evaluated. The inverse transform may be difficult to solve due to surface wave poles for real k_x and k_y. These can be avoided by integration in the complex plane around the singularities in the same way as others do, by using complex k_x and k_y.

3. Documentation of G1DMULT

G1DMULT is implemented both as a FORTRAN subroutine and as a Matlab Mex-file subroutine. G1DMULT solves the multilayer planar harmonic 1D field problem. In more conventional terminology, it calculates the spectral domain Green's functions of a multilayer planar structure. More specifically, it calculates the E- and H-fields at desired locations due to a given electric or magnetic current sheet with harmonic x- and y-variations in a multilayer planar structure.

Input parameters: The spectral variables k_x and k_y are in the program called *akx* and aky. They are complex. The multilayer structure has *Nboundary* material interfaces. These are located at the z-positions *Zboundary(iboundary)* for *iboundary*=1,2,....*Nboundary* where *Zboundary(iboundary+1)* for all *iboundary* must be larger than or equal to *Zboundary(iboundary)*. There are Nboundary+1 material regions. Region number 1 is below the first boundary. If the input parameter *IPEC=1*, region 1 contains a perfect electric conductor. If *IPEC=0* the material is specified by the values of Ak(1) and *Etar(1)*. *Ak(iregion)* is complex and equal to the wave number in region number *iregion*. *Etar(iregion)* is complex and equal to the wave impedance in region *iregion*. Region number *Nboundary+1* is by default taken to be free space. We also specify on input a real vector *A1(3)* in the xy-plane which defines one of two orthogonal directions into which we want to decompose the unknown tangential E- and H-fields at the structure boundaries. This can conveniently be chosen *A1(1)=1., A1(2)=0.* and *A1(3)=0.*. We also define on input a total of *Nexci* excitation current sheets. Current sheet number *iexci* is located at *Zexci(iexci)* and consists of an electric part with a complex amplitude *Curjs1d(i,iexci)* with i=1,2 for the x- and y-components, respectively, and a magnetic part with a complex amplitude *Curms1d(i,iexci)* with i=1,2 for the x- and y-components, respectively. We must specify which material region these current sheets are in by the value of the integer *Iexregion(iexci)*. When the current sheet is at material interface number *Iboundary*, we can choose *Iexregion* equal to either the lower region *iregion=Iexregion* or the upper region *iregion=Iexregion+1*. We can evaluate the field at *Nfield* different z-locations. These are specified by the z-values stored in Zfield(ifield). We must also specify on input which region number *Ifregion(ifield)* the field points are in. This is of importance when evaluating the fields at material boundaries, because the z-component is discontinuous there. The integer values of *Iexregion(iexci)* and *Ifregion(ifield)* must be carefully and correctly chosen in order to avoid errors.

Output parameters: The output parameters are the complex E- and H-fields at the locations *Zfield(ifield)*. These E- and H-fields are stored in *Eresult(i,iexci,ifield)* and *Hresult(i,iexci,ifield)* where i=1,2,3 for the x,y,z-components, *iexci* is the excitation current sheet number and *ifield* is the field point number.. *Eresult* and *Hresult* contains the total field, except if the field point is located in the excitation region, i.e. if *Ifregion=Iexregion*, for which *Eresult* and *Hresult* contain only the scattered field from the structure and not the field due to the source current sheet. To get the total field we need to add the field due to the source current sheet by using G1DJ or G1DM.

G1DMULT is written in such a way that it gives correct results both if the input wave impedances in *Etar* and the currents in *Curjs1d* are normalized or when they have actual values. In the first case, *Etar* must contain the wave impedances in the different layers normalized to a value of unity in free space, and *Curjs1d* must contain a normalized value representing the product of the free space wave impedance and the actual spectral current. The outputs are the spectral E- and the H-fields, with the latter normalized to become equal to the E-field for a plane wave in free space. In the latter case *Etar* must contain the unnormalized wave impedances in the different layers and *Curjs1d* must contain the actual spectral current value, and the outputs are the actual values of the spectral E- and H-fields unnormalized.

4. Five examples of using G1DMULT

G1DMULT has been used to solve the following field problems:

1) Impedance of dipole over a multilayer lossy ground. The radiation efficiency (including losses in the ground and mismatch losses) compared to a matched dipole in free space was calculated.

2) Scattering from dipole over a multilayer lossy ground. The radar cross section of a horizontal dipole over lossy multilayer ground was calculated. The problem was solved for a dipole of finite thickness. The results where validated towards previous results available in the research group for a single layer lossy ground [4].

3) Corrugated ground plane under multilayer slab. The asymptotic corrugation boundary condition for corrugated surfaces [3] was implemented inside G1DMULT and the field solutions were studied for cases when we expected the boundary conditions to be soft or hard. Special care was taken to treat the surface waves. The results were validated towards numerical Green's functions calculated previously in the research group by using complete analytical formulas for single layer substrates with metal corrugations [5]. The agreement was very good. Both studies show special surface waves following the corrugations.

3) Strip-loaded multilayer slab. The asymptotic strip boundary condition for strip-loaded surfaces [3] was implemented inside G1DMULT, and the field solutions were studied for cases when we expected the boundary conditions to be soft or hard. The results were validated towards numerical Green's functions calculated previously in the research group by using complete analytical formulas for single layer substrates with metal strip gratings [5]. The agreement was very good. Both studies show special surface waves following the strips. We are also in the process of studying this for complete Floquet mode expansion of the fields and using G1DMULT. The first result including validation of the asymptotic strip boundary condition is given in [6].

4) Impedance of rectangular microstrip patch. The impedance of a rectangular patch on a multilayer substrate was calculated. The results were validated towards results published elsewhere by others. The results could have agreed better. We believe the disagreement to be due to our choice if integration path in the inverse Fourier transform. We plan to improve this work later.

5) Frequency selective surfaces. The reflection and transmission coefficients of frequency selective surface realized as a double periodic grid of rectangular patches on a multilayer structure were calculated. The results were validated towards results published elsewhere by others. The agreement was good [7].

5. Conclusion

We have developed a general subroutine for numerical calculation of the Green's functions of multilayer structures. The subroutine has been used to analyze several different field problems and validated towards other results. The validation has shown that G1DMULT is accurate and easy to modify and use. G1DMULT has been developed in order to be easy to use and modify. This may mean that it is numerically slower than other algorithms and subroutines. We have not yet investigated this.

Appendix A. Green's functions of homogeneous harmonic 1D field problem.

These Green's functions are the fields radiated by current sheets. The expressions for the spectral E- and H-fields become

$$\tilde{\boldsymbol{E}} = \begin{cases} -\frac{k}{2k_z}\left[\eta\tilde{\boldsymbol{J}} - \left(\eta\tilde{\boldsymbol{J}}\cdot\hat{\boldsymbol{k}}^+\right)\hat{\boldsymbol{k}}^+\right]e^{-jk_z z} & z>0 \\ -\frac{k}{2k_z}\left[\eta\tilde{\boldsymbol{J}} - \left(\eta\tilde{\boldsymbol{J}}\cdot\hat{\boldsymbol{k}}^-\right)\hat{\boldsymbol{k}}^-\right]e^{jk_z z} & z<0 \end{cases} ; \quad \eta\tilde{\boldsymbol{H}} = \begin{cases} \frac{k}{2k_z}\left(\eta\tilde{\boldsymbol{J}}\times\hat{\boldsymbol{k}}^+\right)e^{-jk_z z} & z>0 \\ \frac{k}{2k_z}\left(\eta\tilde{\boldsymbol{J}}\times\hat{\boldsymbol{k}}^-\right)e^{jk_z z} & z<0 \end{cases}$$

where $\tilde{\boldsymbol{J}}$ is the spectral domain current at z=0 (or corresponding spatial current sheet with the harmonic x- and y-variations suppressed),

$$\hat{\boldsymbol{k}}^+ = \left(k_x\hat{x} + k_y\hat{y} + k_z\hat{z}\right)/k \text{ and } \hat{\boldsymbol{k}}^- = \left(k_x\hat{x} + k_y\hat{y} - k_z\hat{z}\right)/k,$$
$$k_z = \sqrt{k^2 - k_x^2 - k_y^2} \text{ when } k_x^2 + k_y^2 < k^2, \text{ and}$$
$$k_z = -j\sqrt{k_x^2 + k_y^2 - k^2} \text{ when } k_x^2 + k_y^2 > k^2.$$
$$k^2 = kk = k_0^2\varepsilon_r\mu_r \text{ and } \eta = \eta_0\sqrt{\mu_r/\varepsilon_r}$$

with k_0 and η_0 respectively the wave number and wave impedance in free space. The above fields have discontinuities at z=0. Therefore, if we need to evaluate the E- of H-fields at z=0, we must specify whether to evaluate it above ($z=0^+$) or below ($z=0^-$) the current sheet The E- and H-fields resulting from magnetic current sheets are given by the dual equations. It is most easy to interpret these E- and H-fields in the spatial domain. Including the harmonic dependencies in x- and y-directions we get for the E-field

$$\tilde{\boldsymbol{E}}e^{-jk_x x}e^{-jk_y y} = \begin{cases} -\frac{k}{2k_z}\left[\eta\tilde{\boldsymbol{J}} - \left(\eta\tilde{\boldsymbol{J}}\cdot\hat{\boldsymbol{k}}^+\right)\hat{\boldsymbol{k}}^+\right]e^{-jk\hat{\boldsymbol{k}}^+\cdot\vec{r}} & z>0 \\ -\frac{k}{2k_z}\left[\eta\tilde{\boldsymbol{J}} - \left(\eta\tilde{\boldsymbol{J}}\cdot\hat{\boldsymbol{k}}^-\right)\hat{\boldsymbol{k}}^-\right]e^{jk\hat{\boldsymbol{k}}^-\cdot\vec{r}} & z<0 \end{cases}$$

and correspondingly for the H-field. This equation represents two plane waves which both originate at the current sheet, one propagating in the direction $\hat{k}^+$ in the half space above the current sheet and the other propagating in the direction $\hat{k}^-$ in the half space below the current sheet. Both the E- and H-fields are orthogonal to the directions of propagation, and orthogonal to each other.

References

[1] P-S. Kildal and J. Sanford, "Analysis of conformal antennas by using spectral domain techniques for curved structures", COST 245/ESTEC Workshop on Active Antennas, June 1996.

[2] Z. Sipus, P-S. Kildal and Silvia Raffaelli, "Analysis of Metal Strips and Corrugations Inside Cylindrical Multilayer Structures by Using G1DMULT", companion paper at present 1997 ACES Symposium, Monterey.

[3] P-S. Kildal and A. Kishk, "Asymptotic boundary conditions for strip-loaded and corrugated surfaces", to appear in Microwave and Optical Technology Letters, Feb 97. See also A. Kishk et al, "Validation of the asymptotic corrugation.." submitted to IEEE AP-S Symposium in Montreal, July 1997.

[4] L. M. H. Ulander and Z. Sipus, "RCS of dipoles used for SAR calibration", presented at EUSAR'961996, Königswinter, Germany, Proceedings , 1996. (L.M.H. Ulander is with National Defence Research Establishment (FOA))

[5] Z. Sipus, H. Merkel, and P.-S. Kildal, "Green's functions for planar soft and hard surfaces derived by asymptotic boundary conditions", submitted to IEE Proceedings Part H, 1996.

[6] S. Raffaelli, Z. Sipus, P-S. Kildal, M. Johansson, "Comparison of accurate and asymptotic analysis of an infinte array of metal strip gratings using G1DMULT", submitted IEEE AP-S Symposium in Montreal, July 1997.

[7] A. Budillon, B. Lindmark and P-S. Kildal, "Scattering from an infinite planar array of rectangular patches over a multilayer structure using G1DMULT", submitted IEEE AP-S Symposium in Montreal, July 1997.

FAST MOMENT METHOD ALGORITHM FOR ELECTROMAGNETIC SCATTERING BY FINITE STRIP ARRAY ON DIELECTRIC SLAB

Borislav Popovski [1], Boris Spasenovski [1], Juraj Bartolic [2]

[1] University of Skopje, Electrotechnical Faculty
Department of telecommunications
Karpos, Skopje
Republic of Macedonia

[2] University of Zagreb, Faculty of Electrical Engineering and Computing
Department of Radiocommunications and Microwave Engineering
Unska 3, HR-10000 Zagreb
Croatia

ABSTRACT

In this paper a fast moment method algorithm is developed to compute the scattering properties of large but finite strip array on a dielectric slab. Exact spectral Green's function is used to derive electric field integral equation (EFIE) for the field on the strips. In the solution process closed form asymptotic expressions are derived for mutual coupling terms for strips separated by 0.1 free-space wavelengths or more. This, coupled with the interpolation technique used for the impedance self terms drastically improves the computational speed and efficiency of the moment method solution for the strip current density. To validate the developed algorithm, extensive tests have been done for both, TE and TM incident polarization, for strips loaded with dielectric slab with or without ground plane or placed in the free space. Obtained results are in a very good agreement with the data in the open literature. Since this algorithm is very fast compared to other conventional methods, it can be used to analyze very large strip arrays in the Ultra-Wideband (UWB) frequency range.

1. INTRODUCTION

The wave scattering by strip arrays finds applications in a number of areas like frequency selective surface, antenna arrays, slow-wave structures, leaky-wave antennas and microstrip arrays. For instance, frequency selective properties of these screens are exploited to use as components in reflector antenna systems or to reduce Radar Cross Section (RCS).

Recent advances in short pulse signal generation and processing have stimulated interest in impulse or Ultra-WideBand (UWB) radar in applications pertaining the target identification and classification, to detection of targets, to remote sensing of terrain, etc., because of the resulting enriched data base when compared with narrow-band information.
Hence, wave scattering from strip arrays has been investigated by many authors [1,2,5]. However, the most part of works is limited to infinite periodic gratings in free space, when the problem reduces to much simpler investigation of scattering from a single unit cell. For practical applications, the strip arrays are electrically large but finite and are usually supported by a dielectric slab.

In this paper an efficient algorithm is developed for numerical calculation of wide-band scattering from large but finite strip array supported by a dielectric slab, with or without ground plane. This technique is further extended to analyse more complicated structures involving lossy dielectrics and resistive strips.
In order to provide rigorous theoretical treatment, in Section 2 the scattering problem was formulated in the spectral domain using exact spectral Green's function for the dielectric slab. Moment method (MM) solution of the Electric

Field Integral Equation (EFIE) based on the full wave approach includes all the mutual coupling effects which are neglected by most of the approximate analysis. Closed form asymptotic expressions are developed in Section 3.1 for mutual coupling integrals that contain expansion and testing functions separated by 0.1 free-space wavelength or more. For the evaluation of these asymptotic expressions virtually no CPU time is needed. The time-consuming part of the algorithm involves the computation of the self terms, where expansions and testing functions occupy the same strip. Realizing, however, that these integrals vary slowly with frequency, the self terms are efficiently computed using interpolation. This, coupled with asymptotic expressions for mutual coupling impedance terms, drastically improves the computational speed and efficiency of the moment method solution for the strip current density.
In the MM analysis complete domain sine basis functions are used, which do not satisfy the edge condition for TE incident polarization. By inclusion of two basis edge modes in the current expansion, defined in terms of Chebyshev functions, the convergence of the MM solution for TE microstrip case is highly improved and the speed of the entire algorithm is preserved. This is presented in Section 3.2.

Efficiency, accuracy and versatility of the developed method is demonstrated in calculating RCS in UWB frequency range for large array of Perfectly Electric Conducting (PEC) and resistive strips on dielectric slab, for different strip widths and different characteristics of the dielectric slab. Numerical results are presented in Section 4. The information gathered from these explorations may find use in the interpretation of UWB radar data from large periodic and quasi-periodic multiscale environments, such as ocean waves.

2. MOMENT METHOD SOLUTION OF THE EFIE

Referring to Fig.1, the surfaces of the strips are assumed to be perpendicular to $\vec{z}$, located at z=0 on dielectric slab with thickness d. Strip width is W, separation of the strip edges is D, and the fields in this two-dimensional problem are assumed to be independent of y.

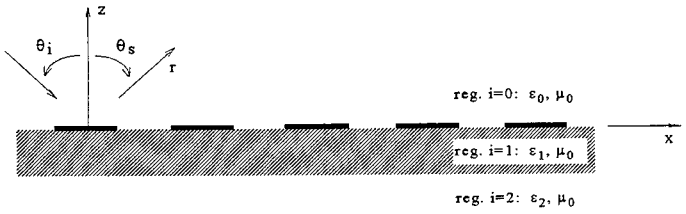

Fig. 1. The geometry of the finite strip array supported by a dielectric slab.

For a plane wave incident at an angle θ_i measured from the z axis as shown in Fig.1, the EFIE to be solved is a statement of the boundary condition that the total tangential electric field must vanish on the perfect conductors,

$$E^t_{tan}(x,z) = E^{exc}_{tan}(x,z) + E^s_{tan}(x,z) = 0 \ , \qquad \text{x, z on strips,} \tag{1}$$

where $E^t_{tan}(x,z)$ is the total tangential electric field given as a sum of $E^{exc}_{tan}(x,z)$, the excitation tangential field at the strips location due to an incident plane wave and $E^s_{tan}(x,z)$, the scattered field produced by the electric surface current density $J(x',z')$ induced on the strips.
The scattered field can be expressed in terms of the dyadic Green's function and surface current density, $\underline{\tilde{G}}$ and $\tilde{J}$, respectively, in the k_x spectral wave number domain [4].
When the boundary condition (1) is applied on the surface of each strip for tangential components one obtains (an $e^{j\omega t}$ time-dependence is assumed and suppressed henceforth) :

$$-E^{exc}(x,z)=\frac{1}{2\pi}\int_C \underline{\tilde{G}}(k_x,z\,;z')\cdot\tilde{J}(k_x,z')\,e^{-jk_x x}\,dk_x \qquad , \qquad \text{x , z on strips.} \tag{2}$$

Equation (2) is the electric field integral equation (EFIE) for the investigated structure with the appropriate Green's function, and it can be used to find the unknown current density $J(x',z')$.

Because the problem is two-dimensional, only a single component of surface current density (longitudinal or transverse) is induced for a given polarisation (TE or TM to $\vec{z}$, respectively). Therefore, only a single component of the dyadic Green's function is required for given incident polarisation. For a three layered structure for sources located at interface plane z = 0, and observation points in region i=0 (z≥0), TE and TM components of the spectral dyadic Green's function are given with:

$$\tilde{G}_0^{e,h}(k_x,z;z'=0)=-\frac{Z_0^{e,h}Z_1^{e,h}\left[Z_2^{e,h}+Z_1^{e,h}\,th(\gamma_1 d)\right]}{Z_0^{e,h}\left[Z_1^{e,h}+Z_2^{e,h}\,th(\gamma_1 d)\right]+Z_1^{e,h}\left[Z_2^{e,h}+Z_1^{e,h}\,th(\gamma_1 d)\right]}\;e^{-\gamma_0 z} \quad , \tag{3a}$$

where:

$$Z_i^e(k_x)=\frac{j\omega\mu_i}{\gamma_i(k_x)} \;,\; Z_i^h(k_x)=\frac{\gamma_i(k_x)}{j\omega\varepsilon_i} \;,\; \gamma_i=\sqrt{k_x^2-k_i^2} \;,\; k_i^2=\omega^2\varepsilon_i\mu_i \;,\; i=0,\,1,\,2\,., \tag{3b}$$

and the superscripts e, h stand for TE and TM case, respectively. For grounded dielectric (i.e. microstrip configuration) components of the spectral Green's function are obtained setting $Z_2 \equiv 0$ in (3a).

When Moment Method is used to solve (2), by expanding the unknown strip current densities into a set of N_b basis function with unknown coefficients a_k,

$$J(x')=\sum_{k=1}^{N_b} a_k f_k(x') \quad , \tag{4}$$

and applying a Galerkin testing procedure to EFIE, one ends with a system of linear algebraic equations written in matrix form $\underline{Z}\cdot I=V$, where the elements of the impedance matrix are given with:

$$Z_{mk}=\frac{1}{2\pi}\int_c \tilde{f}_m^*(k_x)\cdot\underline{\tilde{G}}(k_x)\cdot\tilde{f}_k(k_x)e^{-jk_x(x_m-x_k)}dk_x \quad . \tag{5}$$

In (5) $\tilde{f}_k$ is the Fourier transform of the expansion mode k, and x_m and x_k locate the position on the x axis of the testing function m and expansion function k, respectively. Entire domain cavity mode basis functions are chosen, which do not explicitly enforce the edge condition [1]. The spectral domain representation of $f_k(x)$ is $\tilde{f}_k(k_x)=j\,sin(k_x W/2)\,s_k(k_x)$, for k even, and $\tilde{f}_k(k_x)=cos\,(k_x W/2)\,s_k(k_x)$, for k odd, with $s_k(k_x)$ defined as:

$$s_k(k_x)=\frac{1}{k_x-\dfrac{k\pi(-1)^k}{W}}-\frac{1}{k_x+\dfrac{k\pi(-1)^k}{W}} \quad . \tag{6}$$

The spectral representation of the basis function therefore consists of a trigonometric function which, in general, varies rapidly with respect to the remaining algebraic expression s_k.

Main difficulty in the MM solution is calculating Z matrix elements. Integrals (5) involves infinite integration of the slowly convergent integrand which can be highly oscillatory when the basis function spacing is large. Moreover, when this integrals are calculated over the ultra wide bandwidth, the efficiency of such integration's determines the ultimate speed of the algorithm. To avoid this difficulty, in the present study, Z matrix integrals are approximated with only few asymptotic terms over the steepest descent path (SDP) of integration. It is found that this analytical closed form asymptotic expressions remain accurate for strip separation as small as 0.1 λ_0 . The elements of the excitation vector **V** can be calculated without integration using reciprocity theorem.

When basis function defined with (6) are substituted in (5), after decomposition, Z_{mk} can be expressed as a sum of integrals of the form:

$$K_{mk}^{e,h} = \int_c \tilde{G}^{e,h}(k_x)\, s_m(k_x)\, s_k(k_x)\, e^{-jk_x\Delta_x}\, e^{k_x nW} dk_x \quad , \tag{7}$$

for TE and TM incidence. In (7), n is either 0, 1 or -1, $\Delta_x = x_m - x_k$ and function s_k is the slowly varying part of the Fourier transformed basis function.

3.1 ASYMPTOTIC CLOSED FORM OF MUTUAL COUPLING INTEGRALS

In the asymptotic development first with the change of variables: $\xi = k_0 \sin w$, $d\xi = k_0 \cos w\, dw$, $\sqrt{\xi^2 - k_0^2} = j\, k_0 \cos w$, $\Delta_x - nW = r\sin\theta$, the integral (7) takes the form:

$$K_{mk}^{e,h} = \int_{c'} F^{e,h}(w) e^{\Omega q(w)} dw \quad , \tag{8}$$

being $q(w) = -j\cos(w-\theta)$ and $\Omega = k_0 r$ with r denoting the spherical radial coordinate and θ is measured as shown on Fig.1. These integrals are evaluated most efficiently along the SDP with saddle point found from $q'(w_{sd}) = 0$ and $q''(w_{sd}) \neq 0$ (first order saddle point). For expansion and testing functions on the same plane, on the interface z=0, saddle point is located at $w_{sd} = \theta = \pi/2$ [2, 3]. First, the contour of integration C' is deformed to the SDP and then is mapped onto a contour along the real axis, in the new s-plane with the change:

$$q(w) = \tau(s) = q(w_{sd}) - s^2 ; \qquad \cos(w-\theta) = 1 - js^2 ; \qquad \frac{dw}{ds} = \frac{2js}{|s|\sqrt{1-js^2}} \tag{9}$$

The saddle point is, now, mapped to s=0. With this two transformations closed asymptotic form of the integral (7) is obtained:

$$K_{mk}^{e,h} = \sum_{n=0}^{\infty} \frac{c_{2n}\Gamma(n+\frac{1}{2})}{(k_0 r)^{n+1/2}} - j2\pi \left[\sum_{sr} R[F^{e,h}(w_{sr})]\, e^{\Omega q(w_{sr})} + \sum_{\lambda} R[F^{e,h}(w_\lambda)]\, e^{\Omega q(w_\lambda)} - \kappa(s_p) \sum_{p} R[Q^{e,h}(s_p)]\, e^{k_0 r s_p^2} \right] \tag{10}$$

where: $$Q^{e,h}(s) = 2jk_0 s\, e^{-jk_0 r}\, \tilde{G}^{e,h}(k_x) s_m(k_x) s_k(k_x)\Big|_{k_x = k_0(1-js^2)} \quad ,$$

Γ is the gamma function and R[ ] denotes residues at the poles. Coefficients c_n are obtained by Taylor series expansion of $Q^{e,h}$ (s) near the saddle point. For a good accuracy it is sufficient to take only the first few terms of the series expansion.

In (10) s_p are poles of the function $Q^{e,h}$ (s) in the s-plane (surface wave as well as leaky wave poles), while w_{sr} and w_λ are surface and leaky wave poles in the w-plane. Coefficient κ depends on s_p poles location, with possible values +1, -1 and 0 [3]. This poles are simply related to the poles k_{xp} of the Green's function $\widetilde{G}^{e,h}(k_x)$ in the k_x- plane. Coefficient k depends on s_p poles location, with possible values +1, -1, 0.
When the poles are near the saddle point, the contributions of the saddle point and of the poles cannot be separated and modified saddle point method must be used [3].

It is important to note that derived formulas are general and valid when configuration and structure of the substrate are changed. Thus, when the substrate is without ground plane or grounded, or when the substrate is isotropic or has complex structure (anisotropic, bianisotropic), or is multilayered, only the appropriate Green's function will have to be employed. Moreover, for the evaluation of the asymptotic expressions of mutual coupling impedance terms virtually no CPU time is needed.

3.2 INCLUSION OF THE BASIS EDGE MODE IN THE TE CASE TO SPEED UP CONVERGENCE

Success in developing the closed asymptotic form of the mutual coupling integrals in the impedance matrix is dictated in the large part by the specific choice of basis functions. In the MM analysis complete domain basis functions are used [1], which do not satisfy the edge condition for TE incident polarization. Although, for TE case, a large number of basis functions is required to obtain adequate convergence for the currents, it has been determined that 12 basis functions per strip are sufficient to obtain convergence for the scattered far fields (better than 1 per cent), when strips are loaded with ungrounded dielectric slab (or are placed in the free space). In the case of TE microstrip array configuration (dielectric slab with the ground plane), it is found that even more than 24 basis functions per strip are not sufficient to obtain adequate convergence for the scattered far fields. Use of such large number of basis functions will make analysis of TE microstrip array configuration inefficient. To avoid this difficulty, two edge modes are included in the basis function expansion of the current of each strip. Assuming that number of basis function per strip N_s is even number, unknown surface current density on each strip is expanded in the following way:

$$J(x') = \sum_{k=1}^{N_s-2} a_k f_k(x') + a_{N_s-1} T_0\left(\frac{x'}{W/2}\right) \Big/ \sqrt{1-\left(\frac{x'}{W/2}\right)^2} + a_{N_s} T_1\left(\frac{x'}{W/2}\right) \Big/ \sqrt{1-\left(\frac{x'}{W/2}\right)^2} \qquad (11)$$

In (11) a_k , k=1,2,... N_s are unknown coefficients, N_s is the number of the basis functions per strip and $f_k(x')$ are sine basis functions. Two added edge modes are defined in terms of Chebyshev polynomials of the first kind T_0 and T_1. It is important to note that edge mode functions have closed spectral domain representation in term of Bessel functions, which in turn obey the same even and odd properties as original sine basis functions, so number of the redundant integrals in the Z impedance matrix are very high. When edge mode basis functions are included, Z matrix will not be symmetrical (in the set of testing functions no edge mode is included), but only about 10 per cent new integrals will have to be calculated compared to the symmetrical one. Mutual coupling integrals Z_{mk} that contain edge mode basis function again can be expressed as a sum of integrals similar to (7) that can be solved in the closed analytical form using asymptotic technique outlined in section 3.1.
By inclusion of the basis edge modes the convergence of the MM solution for TE microstrip case is highly improved so that accurate solution (within 1 per cent error) for the scattered far-field is obtained using 10 basis functions per strip.

4. NUMERICAL RESULTS AND DISCUSSION

In order to test the validity of the algorithm based on MM and asymptotic solution of the mutual coupling integrals, extensive tests have been done for different array arrangements and incident polarization.
Fig.2 shows calculated RCS versus frequency in the reflected direction for a uniform array of 10 strips on a slab without a ground plane for TE incident plane wave at angle $\theta_i = -30^o$. Variation of the RCS with frequency are obtained by calculating impedance matrix every 200 MHz in the UWB frequency range, and than matrix elements are interpolated to obtain scattered field every 10 MHz. In the case of Fig.2, variation of the RCS is compared with the results obtained by numerical integration of the Singular Integral Equation. Also, results are compared with [5], where fast recursive algorithm has been used. In both cases agreement is very good.

Fig.3 shows comparisons of the bistatic RCS versus scattering angle of the ten strip array, when calculations are done with and without inclusion of edge mode basis functions. Strips are placed on slab without a ground plane and polarization of the incident plane wave is TE to z. As it can be noted from Figure differences in the RCS are very small for the entire range of the scattering angle. Convergence of the induced surface current densities on the first and the last strip (from left to right) for the same example is presented on Fig.4. As stated in Section 3.2, 12 basis function are sufficient to obtain convergence for the scattered far fields for strips in free space or loaded with dielectric without ground plane.
In the case of microstrip configuration, 10 basis functions have been used with the two edge modes included to speed up the convergence. Fig.5 shows comparisons of monostatic RCS of PEC strips array with resistive strips, placed on grounded dielectric slab for TE incident polarization. From Fig.5 one can note that strips with constant surface resistance of 377 Ω show similar scattering patterns as that of tapered strips, with the expected decrease in amplitude.

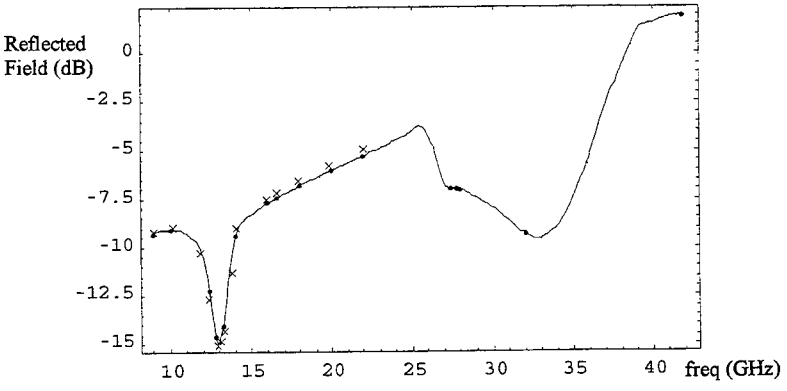

Fig.2. RCS versus frequency for a uniform array of 10 strips on a ungrounded dielectric slab for TE incident plane wave at $\theta_i = -60^o$ ($\varepsilon_r = 2.57$, $d = 0.171\ \lambda_0$, W=D=0.75 cm),

— *this work,*
• *Numerical Singular Integral Equation (SIE),*
x *Recursive algorithm [5].*

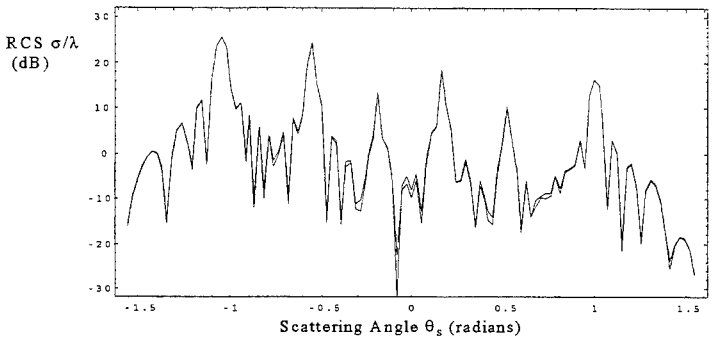

a)

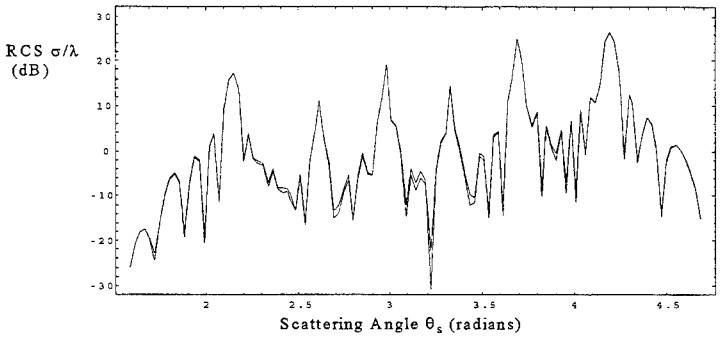

b)

Fig.3. Comparisons of the bistatic RCS for the uniform array of 10 strips on a slab without a ground plane, TE incident plane wave at $\theta_i = -60^o$ (freq.=12 GHz, $\varepsilon_r = 2.17$, loss tan. = 0.001, d = 0.158 cm, W = 3.66 cm, D = W);
— 12 basis function; ····· 10 basis function with two edge modes;
a) $\theta_S \in [-\pi/2;\pi/2]$, b) $\theta_S \in [\pi/2; 3\pi/2]$.

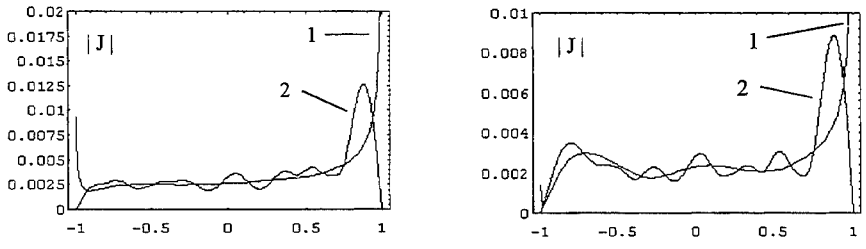

a) b)

Fig.4. Comparisons of the induced surface currents with (curve 1) and without (curve 2) edge modes inclusion, for the case of Fig.7; a) strip number 1; b) strip number 10.

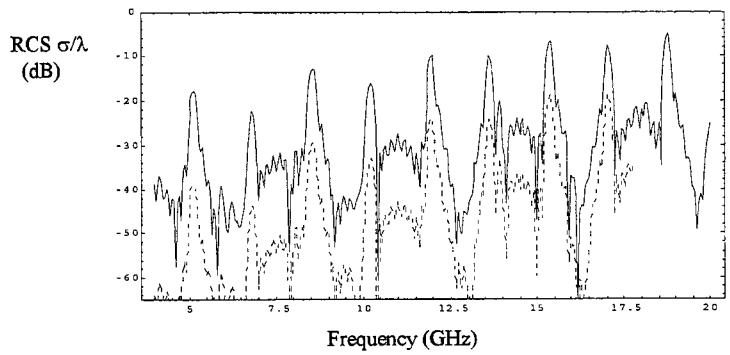

Fig.5. Comparison of monostatic RCS as a function of frequency for ten strip array on grounded dielectric slab, TE incidence (W=5.08 cm, D=W, d=0.078 cm, ε_r=2.33, loss tangent=0.001, θ_i= − 60.0^o , θ_s=60.0^o);
—PEC, ···· 377 Ω .

REFERENCES

[1] L.Carin and L.B.Felsen, "Efficient analytical-numerical modelling of ultra-wideband pulsed plane wave scattering from a large strip grating" Int. Jour. of Numerical Modelling: elec. netw.,devices and fields", Vol 6, pp.3-17, 1993.
[2] B. Popovski, B. Spasenovski, "Efficient Moment method for Ultra-wideband scattering from finite array of perfectly conducting and resistive strips on grounded dielectric slab", IEEE AP-S International Antennas and Propagation Symposium, July, 21-26, 1996, Baltimor, USA.
[3] B.Popovski, A.Toscano and L.Vegni, "Radial and Asymptotic Closed Form Representation of the Spatial Microstrip Dyadic Green's Function", Journal of Electromag. Waves and Appl. vol 9, pp. 97-126, No.1/2, 1995.
[4] L.Vegni, R.Cicchetti and P.Capece, "Spectral Dyadic Green's Function Formulation for Planar Integrated Structures", IEEE Trans. Antennas Propagat., vol. 36, pp. 1057-1065, August 1988.
[5] Cheng Lu and Cho Chew, "Electromagnetic Scattering of Finite Strip Array on a Dielectric Slab", IEEE Trans. Antennas Propagat., vol. 41, pp. 97-100, January 1993.

OPTIMIZATION OF VARIOUS PRINTED ANTENNAS USING GENETIC ALGORITHM. APPLICATIONS AND EXAMPLES

M. Himdi, J.P. Daniel
University of Rennes I, Laboratory Antennes & Array, URA CNRS 834
35042 Rennes Cedex France
Tel : (33) 2 99 28 62 19; Fax : (33) 2 99 28 62 19; Email : Jean-Pierre.Daniel@univ-rennes1.fr

Introduction :

In this paper, we present an original applications of the genetic algorithm. It concerns, the optimization of printed dipoles geometries in order to obtain : reduced size antenna, shaping of printed filar antennas with impedance matching or increase of directivity, dual polarized and large bandwidth printed antenna.

The first problem is to developp a model of antenna which is precise enough while not too much time consuming. In order to satisfy this requirement integral equation for printed filar structures were used assuming a simple expression of polarisation current effects, or transmission line model for antennas with a larger surface. The second problem is to use an efficient algorithm which avoids the local minimum when many variables are considered. In this way the genetic is well suited.

In each application the main difficulty comes from the large number of parameters (lengths and widths of dipoles, angles between wires, lengths of parasitic dipoles, distances between dipoles...). The number of combinations is too large and an exhaustive research is impractical.

For the reduced size antenna, the application concern the printed monopole. Differents shapes have been analyzed and gives a notable reduction of the antenna length. The optimum lengths and widths have been obtained through a genetic algorithm. The shape of a dipole has been also considered to get either a good matching or a directional property . Finally dual polarization with large bandwidth dipoles antennas have been investigated taking into account all the mutual coupling between the different dipoles.Other kinds of antennas have been also optimized successfully using the genetic algorithm such as patches, slot fed patches...

1 - Presentation of methods

Two methods have been experimented: the equivalent transmission line and the reaction equation integral equation.

a) equivalent transmission line

Fig. 1 shows a printed monopole antenna mounted over a ground plane and excited by a 50 Ω coaxial line. It is considered as a lossy line. A simple analysis based on the transmission line model offers the possibility to calculate more complicated structures, as shown in Figure2-a, a printed monopole antenna with one step change of the width, and Figure2-b, a printed triangular monopole as approximate as succession of more step change.

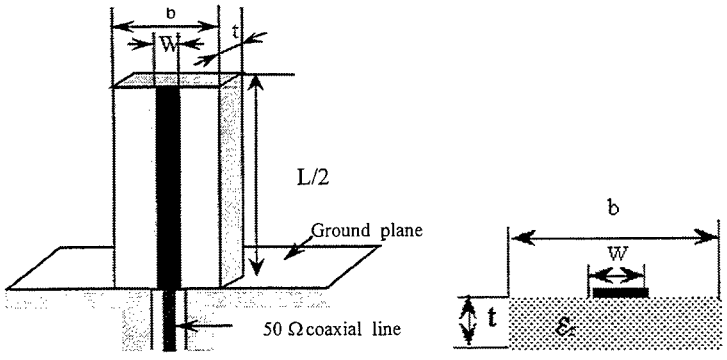

Figure 1: geometry of a printed monopole

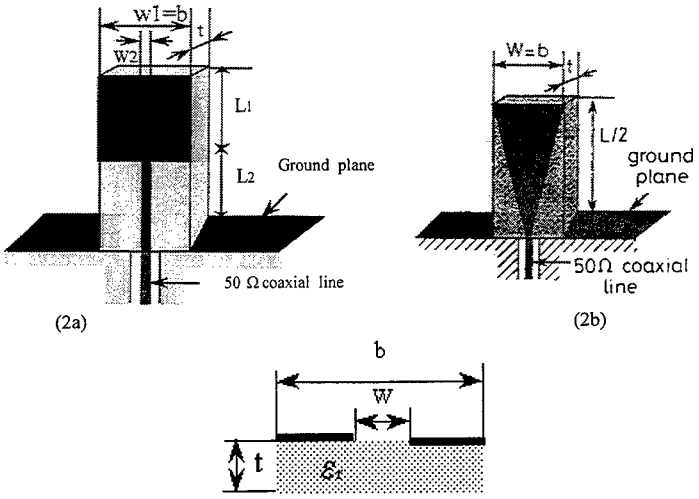

Figure 2: Printed monopoles of various shapes

The method of calculating is the same as previously described in [1]. Indeed, the transmission line model considered this structure as succession of two or more lossy lines with proper characteristics impedance Zcdi (i=1,2, ...) and waves number Γdi. The expression of the input impedance for the first printed open loss line of length L1 and width W1, is given by:

$$Zd_1 = Zcd_1 \times \coth(\Gamma d_1 L_1)$$

where $\Gamma_{d1} = \alpha_{d1} + j\beta_{d1}$ propagation coefficient and Zcd1: characteristic impedance for printed line 1.

Then the expression of the input impedance for the other printed load lossy lines of length Li and width Wi is:

$$Zd_i = Zcd_i \times \frac{Zcd_{i-1} + Zcd_i \times th(\Gamma d_i L_i)}{Zcd_i + Zcd_{i-1} \times th(\Gamma d_i L_i)} \qquad (i=2,3,...)$$

where $\Gamma_{di} = \alpha_{di} + j\beta_{di}$ propagation coefficient and Zcdi: characteristic impedance for printed line i.

The characteristic impedances Zcdi , the effective permittivity ε_{effi}, and the attenuations α_{di} for an equivalent loss line are first calculated for the dual slot line.

First, the Babinet principle allows Zcdi to be obtained from the following formulas:

$$Z_{cdi} \times Z_{csi} = Z_o^2/4\varepsilon effi \qquad (i=1,2, ...)$$

Where Z_{csi} is the characteristic impedance of printed slot line figure 2c, and the ε_{effi} is assumed to be the same for both structures (printed line and slot line). Z_{csi} and ε_{effi} are determined using COHN'S method [2].

Next, the calculation of α_{di} is the same as described in reference [1,3]. In addition, α_{di} are determined for the total length L/2 of the monopole antenna.

b) reaction integral equation

Printed filar structure are analysed using basically the same procedure developped in [5]. It performs a frequency domain analysis of thin wire antennas. A sleeve antenna is presented on figure 3. On figure 4 is represented the monopole with an arbitrary shape.

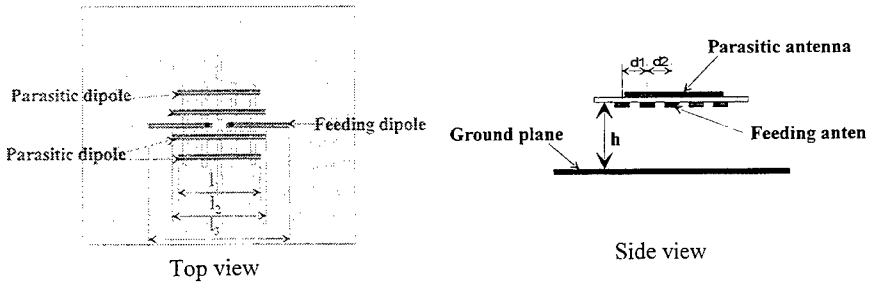

Figure 3 : Configuration of the dual polarized antenna

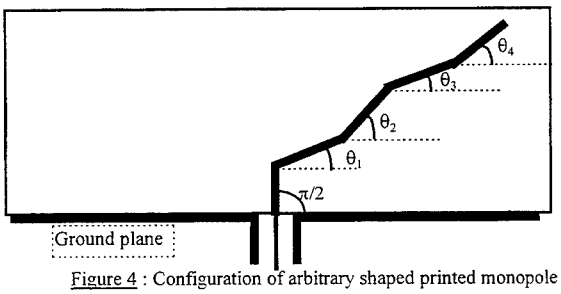

Figure 4 : Configuration of arbitrary shaped printed monopole

Integral equations for conducting wire structures are written in order to satisfy boundary condition on the wire. The resolution of the integral equation is based on the reaction concept and the well known method of moment. As in [5], the dielectric effect is taken via the polarization current Jp which yields a supplementary term ΔZ_{mn} added to the generalised impedance term Z_{mn} . In our case, a basis function as a piecewise sinusoidal is selected and with the Galerking method, we obtain the linear equation :

$$[V_m]=[Z_{mn} + \Delta Z_{mn}].[I_n] \qquad (1)$$

Using the concept of equivalent radius of thin cylindrical antenna, the method described by Richmond [5] can be used for printed antenna. The polarisation current $\bar{J}_p = j\omega\varepsilon_o(\varepsilon_r - 1)\bar{E}$ depends on the knowledge of the field distribution.

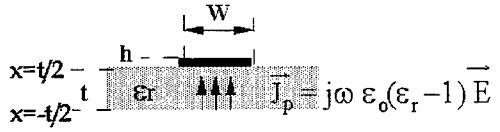

Figure. 5 : Dielectric modelisation with polarisation current Jp due to E field

The first assumption of a uniform E field distribution under the metallic strip yields a simple mathematical relation which needs some refinement in order to take into account the fringing fields. An empiric formula $f(\varepsilon_r)$ has been established for ε_r =1 to ε_r =10.2.
The polarisation current becomes :

$$J_p = \frac{(\varepsilon_{r1} - \varepsilon_{r0})}{\varepsilon_{r1}} \frac{1}{2W} \frac{\partial I}{\partial l} f(\varepsilon_r)$$

where :

$$f(\varepsilon_r) = \frac{1}{7.27 - 3.06\varepsilon_r + 0.75\varepsilon_r^2 - 9.44.10^{-2}\varepsilon_r^3 + 5.935.10^{-3}\varepsilon_r^4 - 1.48.10^{-4}\varepsilon_r^5}$$

Thanks to this simple expression of Jp, simple expression of ΔZ_{mn} were obtained and we save a lot of computation time.

2-Optimization procedure

The genetic algorithm has been recently chosen because it is a robust stochastic search method which operates on a group of solutions (population) using encoded parameters rather the parameters themselves [6], [7], [8].
The Fig.6 summarizes the optimization technique which associates a genetic algorithm and the electromagnetic analysis. Various reproduction schemes have been tested.

We introduce here the optimization technique named genetic algorithm which uses the well known sequences (Initialisation of the population, Selection, crossover and mutation).
Population : A set of trial solutions is assembled as a population. The parameter set (I_1, I_2, I_3..., d_1, d_2...) representing each trial solution is first coded using binary code (also name chromosome).

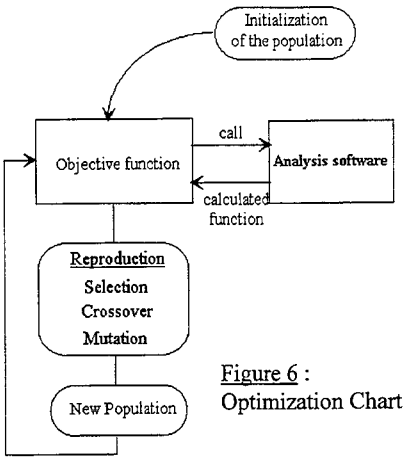

Figure 6 : Optimization Chart

Reproduction : As shown on figure 6, this step follows a first initialization random process. then a selection scheme occurs which uses a probability for each individual; the probability is proportionnal to the individual's relative fitness. Following the choice of the two chromosomes, children are then generated using two main stochastic operators : crossover and mutation.
Crossover involves the random selection of a crossover site (binomial process) and the combination of the two parent's genetic information included in a chromosome. Mutation is a mechanism for introducing new, unexplored points into the genetic algorithm optimizer's search domain.

Objective function : In this case, the objective function is the mean value $|\Gamma_t|$ of the return loss over the total bandwidth (evaluated numerically by the analysis method) or the difference value between a specified pattern and the calculated one .over a given angle $|\Delta_t|$

$$|\Gamma_t| = \frac{1}{N}\sum_{i=1}^{N}|\Gamma_i| \qquad |\Delta_t| = \frac{1}{N}\sum_{i=1}^{N}\left\|D_i| - |D_{ri}\right\|$$

Where Γ_t, Γ_i, are respectively the average return loss, the return loss for the considered frequency , D_i , D_{ri} the calculated and the specified normalized amplitude patterns in the direction θ_i and N the number of frequencies considered on the bandwidth or the numbers of directions. To optimize both the return loss and the pattern it is possible to combine them with proper weights and define a global objective function E :

$$E = W_1|\Gamma_t| + W_2|\Delta_t|$$

It must be noticed that the ranges of variation of the parameters are defined and are very important constraints which need a previous physical knowledge from the designer.
Finally the algorithm determines the parameters (within the range mentioned) of the antenna which provide an optimal solution (minimum value of the objective function).

3- Applications

a) size reduction

The first example (Figure.7) shows the good agreement between the measurement values and the theoretical impedance (normalized to 50 Ω) for the monopole antenna (Figure.2-a) with one step change width, printed on the Duroid substrate with dielectric constant εr = 2,2±0,02 and thickness t = (0,8±0,02) mm in the range 100 - 700 Mhz.

It must be noted that this structure offers a reduction of size (ρ = 48%). The size reduction ρ ($\rho = \frac{\lambda_g/4 - L_t}{\lambda_g/4} * 100$) versus $L_1/(L_1+L_2)$ is presented for various ratio W_1/W_2 on figure 8 [4]. The maximum of ρ appears for $W_1/W_2 = 0.5$.

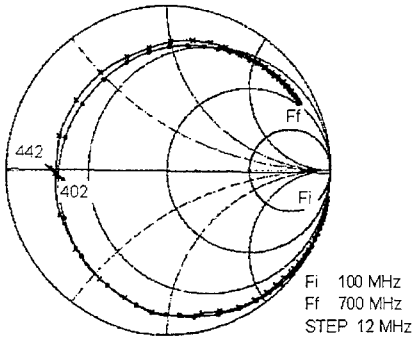

Figure 7: variation of input impedance
antenna of fig 2a xx measured
oo theory
(W_1=50 mm, W_2=0.4 mm
L_1= 40.67mm, L_2= 40.67 mm)

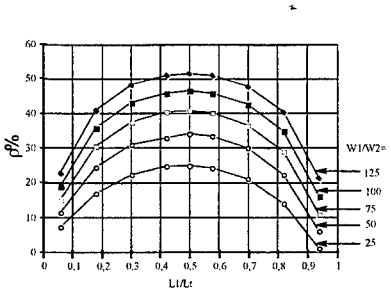

Figure 8: shortening ratio ρ versus L_1/L_2 with W_1/W_2 as parameter.

Optimisation

In order to find the proper geometries of dipoles under constraints of size reduction different examples have been tested. The geometry shown on Fig.2a has been analysed first for different kinds of substrates and frequency bands. *The objective function is the reflection coefficient (with a normalization resistance* R_0 *as variable) for a given size reduction ratio at one frequency.*
The optimum lengths and widths have been obtained through a genetic algorithm. The results are given below:

Given datas:	example1	-frequency= 420 Mhz - ε_r substrate= 2.2 -L = L_1 + L_2 = 81.34 mm - W_1= 50 mm - W_2= 0.4 mm	Results: -L_1= 39.78 mm -L_2= 41.56 mm - R_0= 10.75 Ω
	example2	-frequency= 1.84 Ghz - ε_r substrate= 2.2 -L = L_1 + L_2 = 25.1 mm - W_1= 6.8 mm - W_2= 0.4 mm	Results: -L_1= 7.45 mm -L_2= 17.65 mm - R_0= 20.9 Ω

b- Optimization of impedance or radiation pattern by varying the shape of printed monopole.

Popovic [9] had shown that an inclined monopole could be perfectly matched and also could exhibit a directive pattern in the horizontal plane. A more sophisticated structure is represented on figure 4. More flexibility is obtained when more than two segment wires are considered . A proper choice of the angles of the different segments offers the possibility to get simultaneously a good matching and a given pattern.

The five segments have the same lenght here ($\lambda_g/6$ = 52.38 mm) and the angles can vary from 0 up to 180°. The first step was to check the result of Popovic for one segment.(one variable) The objectives was to match the monopole at 0.964 Ghz (objective function on Γ): The curve plotted on figure 9e are in good agreement with the previous results.

The second step was to take into account the angular positions of the 3 or 4 wire segments as variables and search for the best match. As seen on figure 9b and 9c the shapes are not straight, and a perfect match is obtained.

The last step was to search for a prescribed directive pattern (with a front to back ratio equals - 20 dB in H plane) .On figure 10 and 9d are given both the patterns and the shape which have been found. The input impedance

exhibits a resistance near 50 Ω but also a reactance (fig. 9f) which can be compensated with a proper inductance (see return loss of case D on figure 9e). The table 1 shows the angles which were obtained for optimization minimizing the return loss (Examples A,B,C) or synthesizing a prescribed pattern with a minimum return loss (example D).The directive pattern is plotted on figure 10 for E and H plane pattern at 0.964 Ghz.

case A	case B	case C	case D
1 variable (θ_1)	3 variables (θ_2, θ_3, θ_4)	4 variables (θ_1, θ_2, θ_3, θ_4)	5 variables (pattern and Γ) (θ_1, θ_2, θ_3, θ_4,inductance)
L1=20 mm, seg=52.38 mm	L1=20 mm, seg=52.38 mm	L1=20 mm, seg=52.38 mm	L1=18.36 mm seg=48.087 mm
no inductance	no inductance	no inductance	inductance =12.5 nH
90°	90°	90°	90°
60°	62°	**27.7°**	**68.7°**
60°	**55.5°**	**29.07°**	**68.7°**
60°	**64.6°**	**34.6°**	**12.8°**
60°	**53.9°**	**21.66°**	**11.94°**

Table 1: results of optimizations (value of angles written in dark)

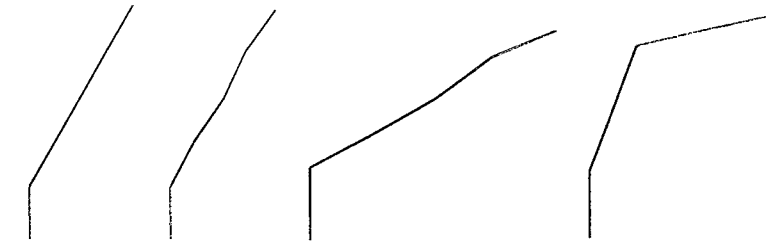

9-a 9-b 9-c 9-d

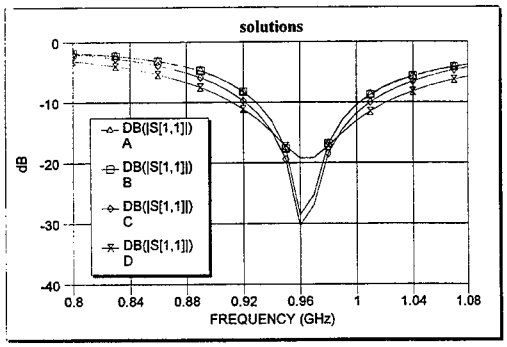

9-e

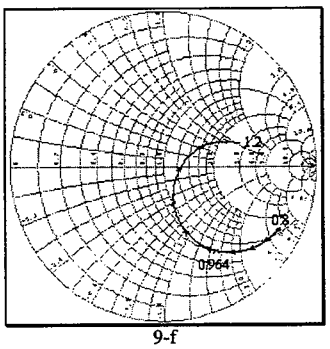

9-f

Figure 9: Examples of shapes return loss of printed monopoles for different number of variables
9-a example of Popovic [9] (case A)
9-b example with 3 variables (objective function on Γ) (case B)
9-c example with 4 variables (objective function on Γ) (case C)
9-d example with 4 variables (objective function on pattern and Γ) (case D with additional inductance)
9-e variation of the return loss for the above examples.
9-f input impedance of monopole D without additional inductance

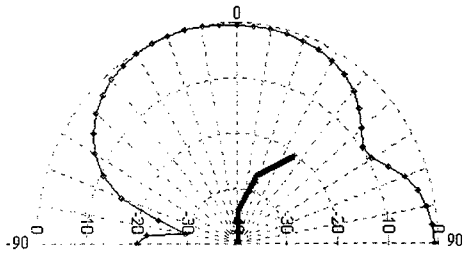

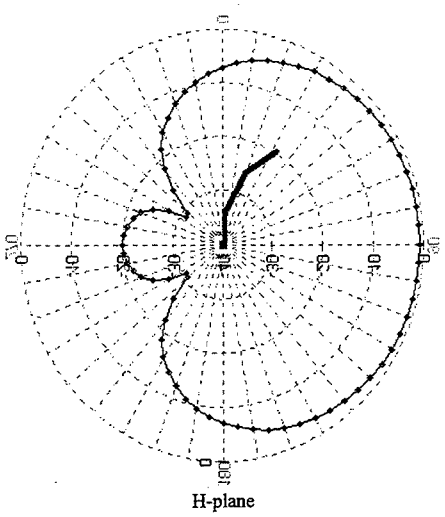

Figure 10 : pattern of monopole D with inductance (case D at 0.964 GHz)

c- Dual polarized and large bandwidth printed antenna

The printed sleeve antenna is presented on fig.3. Thanks to the printed technology the idea was to get two orthogonal large bandwidth dipoles antennas (one per polarization , each on one side) The analysis solved coupled integral equations using the well known method of moment.Mutual coupling effects are very strongs and all the radiating elements must be considered.

In this case, the objective function is the mean value $|\Gamma_t|$ *of the return loss over the total bandwidth for a given normalization impedance.*

The optimization algorithm presented above has been applied first to the design of a broadband antenna linearly polarized (impedance results on fig. 11a). Keeping the dimensions previously obtained and taking into account a second orthogonal dipole antenna one finds a new input impedance plotted on figure 11b. The results which are plotted on fig.11-a give a loop between 5 to 8 GHz around 100 Ω correspond to a relative bandwidth of 46 %. The substrate is a DUROID sheet of thickness 0.78 mm and a dielectric constant = 2.2. The dimensions are : l_1=14.74mm, l_2=15.426mm, l_3=26.49mm, d_1=4.99mm, d_2=1.39mm, h=12.3 mm. The curve given on fig. 11-b shows the new impedance curve of the dual polarized structure of figure 5 and the reduction of the relative bandwidth to 33% near 6 GHz

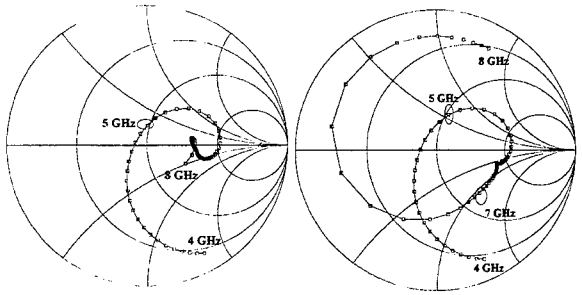

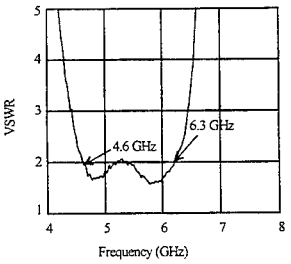

Fig11-a Fig. 11-b Fig. 11-c

Figure. 11 : Theoretical input impedances and VSWR

Some experiments were carried out on this dual polarized antenna which is fed through a 100 Ω printed bifilar transmission line orthogonally located toward the dielectric sheet and followed by a printed balun. Fig. 11-c shows the measured VSWR and relative bandwidth of 30%. The experimental E and H plane radiation patterns at the central frequency 5.3 Ghz. show a cross polarization lower than -23 dB.

Unfortunately, the mutual coupling between the two orthogonal structures (fig. 3-b) has a strong effect and a global electromagnetic analysis must be performed for the optimization. The new dimensions are:

l_1= 15.16 mm, l_2= 14.83 mm, l_3= 26.59 mm, d_1= 1.37 mm, d_2= 3.3 mm, , h=12.3 mm.

After optimization a new input impedance with a loop around 100 Ω is obtained and plotted on figure 12-a. More over the isolation between the two ports remains lower than -15 dB (figure 12-b).

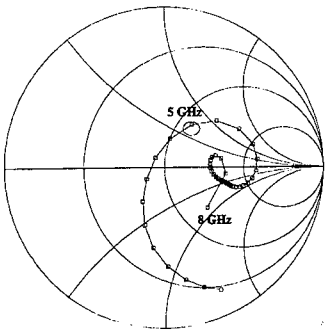

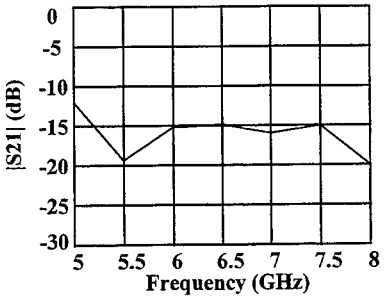

Fig. 12-a Fig. 12-b

Figure. 12 : Final results after optimization (all mutual coupling included)
12-a : S_{11} of the fed element
12-b: S_{12} between the two elements

Conclusion :

In this paper, we have presented some applications of the genetic algorithm associated with printed antenna analysis methods. The optimisation process has been used to determine the dimensions of reduced size printed antennas, the shape of printed monopole and the parameters of a broadband dual polarized sleeve antenna. The same process is under developpment to synthesize the geometries of printed patches working on two or three frequencies with proper slots located on the patch ; in this case the algorithm gives the position and size of the slots for given resonant frequencies.

References:

[1] H.Lebbar, M. Himdi and J. P. Daniel,, "Transmission line analysis of printed monopole", ELECTRONICS LETTERS , 1992. Vol . 28 , No . 14 , pp. 1326 - 1327.

[2] S. B. Cohn, "Slot line on dielectric substrate", I.E.E.E, Vol. 17, N°10, OCTOBER 1969, pp. 768 - 778.

[3] M. Himdi and J. P. Daniel, "Analysis of Microstrip Linear slot antenna using lossy transmission line model", ELECTRONICS LETTERS, 1992. Vol. 28, No. 6, pp. 598 - 600.

[4] H.Lebbar, M. Himdi and J. P. Daniel, "Analysis and Optimization of reduced printed monopole", 1993 IEEE/AP-S. SYMPOSIUM AND URSI MEETING , MICHIGAN.

[5] J.H. Richmond, E.H Newman : "Dielectric coated wire antennas" Radio Science, vol 11, n°1, pp13-20, jan. 1976.

[6] D.E. Goldberg : "Genetic Algorithms " Addison-Wesley France, USA, 1991

[7] R.L. Haupt : " An introduction to genetic algorihms for electromagnetics" I.E.E.E. Antennas and Propagation Magazine.vol 37, n°2, April 1995

[8] E. Michielsen, S. Ranjithan, R. Mittra : "Optimal multilayer filter design using real coded genetic algoritms" I.E.E Proceedings J, Vol 139, n0 6, December 1992

[9] B.D Popovic, M.B. Dragovic, A.R. Djordjevic : "Analysis and Synthesis of Wire Antennas" Electronic & Electrical Engineering Research Studies , Antennas Series, Series Editor: Professor J.R. James. Research Studies Press , Division of John Wiley & Sons LTD, 1982.

[10] F. COLOMBEL :" Antennes à double polarisation et large bande. Application aux réseaux" Thèse de l'Université de Rennes I,janvier 1996.

CHARACTERIZATION OF ASYMMETRIC MICROSTRIP TRANSMISSION LINES ON MULTILAYERS WITH FR-4 COMPOSITE OVERLAY

Magda El-Shenawee and Hai-Young Lee*
Pacific States University
College of Electrical Engineering and Computer Science
E.mail: eerdeom@engunx.unl.edu

*Ajou University
School of Electrical and Electronics Engineering
Suwon, South Korea

Abstract:
The method of lines (MoL) is used in this work to analyze two coupled asymmetric microstrip lines with an overlay. The material of the overlay is chosen to be FR-4 composite with relative permittivity of 4.3. The FR-4 composite is assumed to be lossless is this work. The height and the width of the overlay are varied to investigate their effect on the effective dielectric constants of the coupled microstrip lines. The normalized phase velocities of the dominant modes (c and π-modes) are shown as functions of the frequency up to 100GHz.

Formulation of the Problem

The detailed analysis of applying the method of lines (MoL) to the microstrip lines is given in [1]-[2]. In this work, the MoL is used to characterize two asymmetric coupled microstrip lines on dielectric multilayers with an overlay on the metallic strips, see Fig. 1. The method of lines is adapted to analyze inhomogeneous dielectric layers [1]-[2]. The procedure of the hybrid-mode analysis starts by solving the Helmholtz equation and the Sturm-Liouville differential equation [1]. The wave field can be determined from the two vector potentials Π_e and Π_h which have only one component in the x-direction. The wave is assumed to propagate in the z-direction, see Fig. 1. Thus the fields are given by [1]:

$$E = \frac{\nabla \times \nabla \times \Pi_e}{\varepsilon_r(x)} - jk_o \nabla \times \Pi_h \tag{1a}$$

and

$$\eta_o H = jk_o \nabla \times \Pi_e + \nabla \times \nabla \times \Pi_h \tag{1b}$$

where $k_o = \omega\sqrt{\mu_o \varepsilon_o}$ and $\eta_o = \sqrt{\mu_o / \varepsilon_o}$. The vector potential for the LSM modes is given by:

$$\Pi_e = \psi_e \frac{\exp(-jk_z z)}{k_o^2} a_x \tag{2a}$$

and for the LSE modes is given by

$$\Pi_h = \psi_h \frac{\exp(-jk_z z)}{k_o^2} a_x \tag{2b}$$

where a_x is unit vector in the x-direction. The propagation constant is given by k_z. The scalar potentials ψ_h and ψ_e must fulfill the Helmholtz equation and the Sturm-Liouville differential equation, respectively, [1] as:

$$\frac{\partial^2 \psi_h}{\partial x^2} + \frac{\partial^2 \psi_h}{\partial y^2} + \left(\varepsilon_r(x) k_o^2 - k_z^2\right)\psi_h = 0 \tag{3a}$$

and

$$\varepsilon_r(x) \frac{\partial}{\partial x}\left(\frac{1}{\varepsilon_r(x)} \frac{\partial \psi_e}{\partial x}\right) + \frac{\partial^2 \psi_e}{\partial y^2} + \left(\varepsilon_r(x) k_o^2 - k_z^2\right)\psi_e = 0 \tag{3b}$$

A comprehensive description and detailed formulation of the technique is given in [1]. The effective dielectric constants of the dominant modes are obtained by solving the following equation:

$$[Z][J] = [0] \tag{4}$$

in which the elements of the matrix [Z] are functions of the frequency, the propagation constant k_z, and the characteristics of the different dielectric layers. The vector [J] contains the current densities on the metallic strips (J_{xm} and J_{zm}). The effective dielectric constant (ε_{re}) is varied until the determinant of the system matrix (4) vanishes. The eigenvectors of system (4) (for each eigenvalue ε_{re}) are the current densities on the strips for each mode. All the electric and magnetic field components can be calculated [1].

Numerical Results

The configuration of the two asymmetric coupled microstrip lines is given in Fig.1. The metallic strips are assumed to have zero thickness. The total height of the substrate is H=1.3mm and the relative permittivity is ε_r=10.5 (DI-CLAD 810 [3]). The widths of the metallic strips are W1=1.2mm and W2=2.0mm. The separation between the strips is S=1.0mm. The normalized propagation constants of the dominant modes (c and π-modes) are plotted versus the frequency in Fig.2. The total number of magnetic lines is 51, the number of magnetic lines on the strips are 5 and 8, and the discretization distance is h=0.266666mm. The results obtained using the MoL are compared with those obtained using the Spectral Domain Approach (Fig.3 in [3]). The results in Fig.2 show good agreement between the MoL and the SDA [3]. An overlay made of FR-4 composite is put on the two asymmetric microstrip lines, see Fig.1. The dielectric constant of the FR-4 is ε_{r3}=4.3 and it is assumed to be lossless [4]. The width of the overlay is chosen to be T=4.5333mm. The height of the overlay (H3) is varied from zero (no overlay) to 2H, (H=1.3 mm). The effect of varying the overlay height on the effective dielectric constants of the dominant modes at f=1GHz is shown in Fig.3. The results show that the effective dielectric constants of the dominant modes slightly change as the height of the overlay is about 2H. The normalized phase velocities of the dominant modes are plotted versus the frequency in Fig.4, where the height of the overlay is chosen to be H3=0.65mm. The difference between the phase velocities of the dominant modes is smaller when an overlay is used as shown in Fig.4. This difference is expected to get smaller as the height of the overlay is larger than the total height of the substrate H (H=1.3mm), see Fig.3. The width of the overlay is varied from zero (no overlay) to full layer of FR-4 composite with H3=0.65mm. In Fig.5, the effective dielectric constants of the dominant modes are plotted versus the width of the overlay at f=1GHz. The results show that the effective dielectric constants slightly change as the width of the overlay is about 30h, see Fig.5.

Conclusions

The overlay has significant impact on the phase velocities of the dominant modes of the two asymmetric coupled microstrip lines. The FR-4 composite is chosen as an overlay for its low cost. The results show that the difference between the phase velocities of the c and π-modes is smaller when an overlay is used. This phenomena can be used to decrease pulse distortion in the coupled microstrip lines.

Acknowledgment

This work is supported by the Korean Science and Engineering Foundation (KOSEF) under a fellowship program. It is conducted in the Microwave Applications Laboratory, School of Electrical and Electronics Engineering, Ajou University, Suwon, Korea.

References

[1] R. Pregla and W. Pascher, "The Method of Lines," in Numerical Techniques for Microwave and Millimeter Wave Passive Structures, T. Itoh, Ed. New York: Wiley, pp.381-446, 1989.

[2] R. Pregla, M. Koch, and W. Pascher, "Analysis of Hybrid Waveguide Structures consisting of Microstrips and Dielectric Waveguides," Proceedings 17th European Microwave Conference, pp. 927-932, 1987.

[3] Y. Qian and E. Yamashita, "Characterization of Picosecond Pulse Crosstalk Between Coupled Microstrip Lines with Arbitrary Conductor Width," IEEE Trans. on Microwave Theory and Tech., Vol. MTT-41, pp. 1011-1016, No.6/7, June/July, 1993.

[4] B. C. Wadell, Transmission Line Design Handbook, Chapter 9, pp. 431-451, Artech House, Inc., 1991.

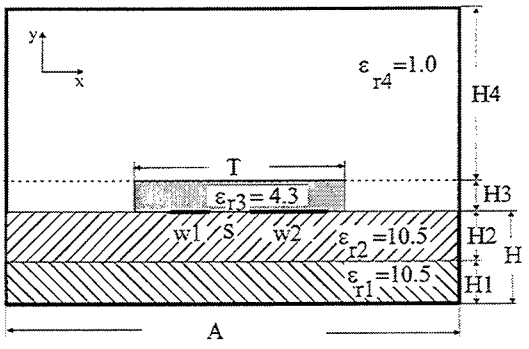

Fig. 1. Two asymmetric coupled microstrip lines with an overlay, W1 = 1.2 mm, W2 = 2.0 mm, S = 1.0 mm, H = H1+H2 = 1.3 mm, H4 = 20.0 mm, and A = 13.8666 mm.

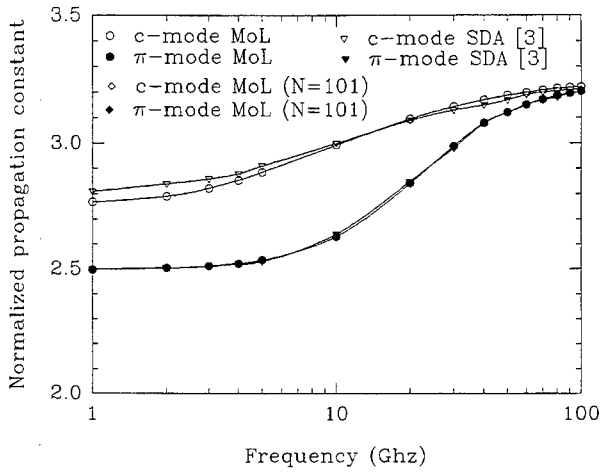

Fig. 2. The normalized propagation constants of the c and π-modes versus the frequency using the MoL (this work) and the SDA [3], W1=1.2mm, W2=2.0mm, S=1.0mm, H=H1+H2=1.3mm, $\varepsilon_{r1}=\varepsilon_{r2}=10.5$ (DI-CLAD 810), H3=0.0 (no overlay), and H4=20.0mm.

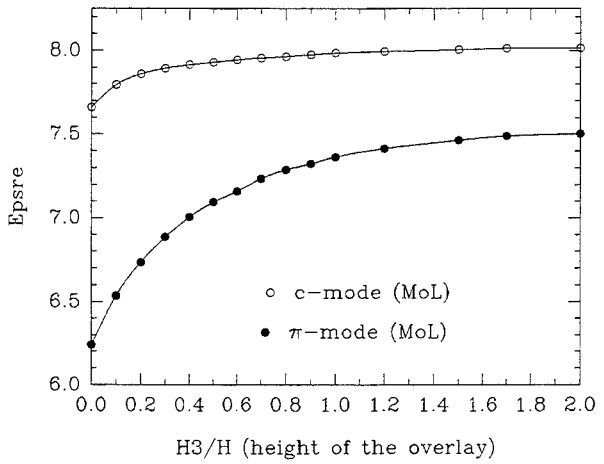

Fig. 3. The effective dielectric constants versus the height of the FR-4 overlay (H3), W1=1.2mm, W2=2.0mm, S=1.0mm, H=H1+H2=1.3mm, $\varepsilon_{r1}=\varepsilon_{r2}=10.5$ (DI-CLAD 810), T=4.5333mm, $\varepsilon_{r3}=4.3$ (FR-4 composite), H4=20.0mm, and f=1GHz.

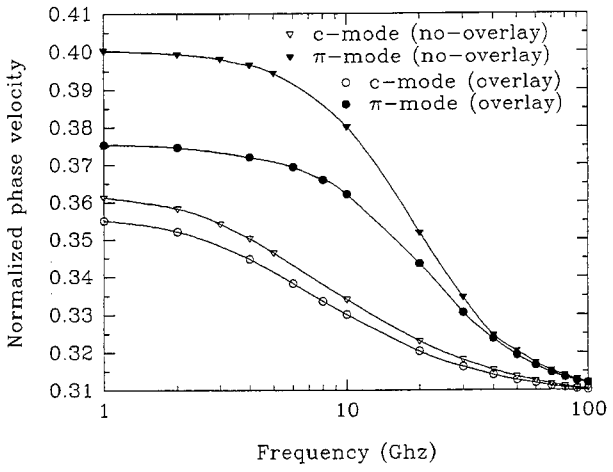

Fig. 4. The normalized phase velocities versus the frequency, W1=1.2 mm, W2=2.0mm, S=1.0mm, H=H1+H2=1.3mm, $\varepsilon_{r1}=\varepsilon_{r2}=10.5$ (DI-CLAD 810), H3=0.65mm, T=4.5333mm, $\varepsilon_{r3}=4.3$ (FR-4 composite), and H4=20.0mm.

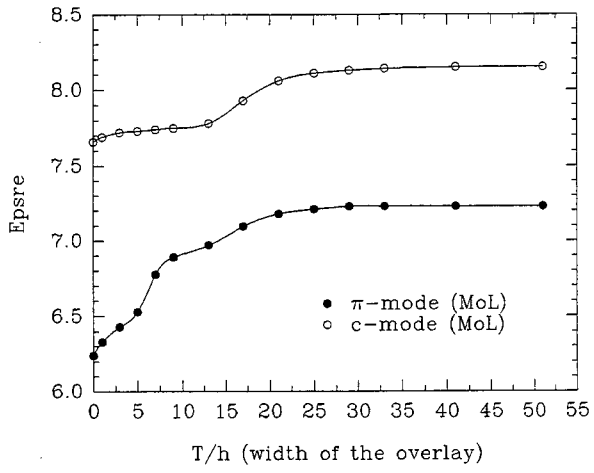

Fig. 5. The effective dielectric constants versus the width of the FR-4 overlay (T), h=0.266666mm (discretization distance), W1=1.2mm, W2=2.0mm, S=1.0mm, H=H1+H2=1.3mm, $\varepsilon_{r1}=\varepsilon_{r2}=10.5$ (DI-CLAD 810), H3=0.65mm, $\varepsilon_{r3}=4.3$ (FR-4 composite), H4=20.0mm, and f=1GHz.

SESSION 22:

SCATTERING

Chairs: J. Jin and A. Elsherbeni

RCS and Antenna Modeling with MOM Using Hybrid Meshes

J.M. Putnam
McDonnell Douglas Corporation
J.D. Kotulski
Sandia National Laboratories

Abstract

During the last decade, the method of moments(MOM) has become a robust technique for solving electromagnetic problems for arbitrary three-dimensional geometries. There are several reasons why the MOM technique has become so widely used. First, modeling fully three-dimensional geometries has been facilitated by the development of robust basis functions, such as the roof-top functions introduced by Rao-Wilton-Glisson(RWG) for triangular meshes. Secondly, complex boundary conditions can be readily incorporated into the formulation. These boundary conditions, for example, can include conducting, dielectric, resistive, magnetically conducting, and the impedance boundary condition. Finally, the advent of modern fast parallel and vector computer architectures has permitted the solutions of larger and more complex problems.

In this presentation, we will investigate the use of hybrid meshes for modeling RCS and antenna problems in three dimensions. We will consider two classes of hybrid basis functions. These include combinations of quadrilateral and triangular meshes for arbitrary 3D geometries, and combinations of axisymmetric body-of-revolution (BOR) basis functions and triangular facets. In particular, we will focus on the problem of enforcing current continuity between two surfaces which are represented by different types of surface discretizations and unknown basis function representations. We will illustrate the use of an operator-based code architecture for the implementation of these formulations, and how it facilitates the incorporation of the various types of boundary conditions in the code. Both serial and parallel code implementation issues for the formulations will be discussed.

Results will be presented for both scattering and antenna problems. The emphasis will be on accuracy, and robustness of the techniques. Comparisons of accuracy between triangularly meshed and quadrilateral meshed geometries will be shown. The use of hybrid meshes for modeling BORs with attached appendages will also be presented.

Introduction

The method of moments has been used to solve many electromagnetic problems over the years since its inception. With the advent of massively parallel architectures, large complex problems have been solved. To further extend the class of problems that can be solved hybrid techniques can be incorporated. These hybrid techniques can be other MOM formulations coupled together, or MOM combined with high-frequency asymptotic techniques. In this paper alternate MOM formulations will be presented and incorporated within the CARLOS-3D code which has been ported to massively parallel architectures and uses the MOM technique to solve Stratton-Chu integral equations. The different hybrid formulations will be presented, discussed, and tested.

Quadrilateral Patch Formulation

Basis functions can be defined on a surface which is arbitrarily meshed with quadrilateral patches in a manner which is analogous to the RWG basis functions [1] on a triangularly meshed surface. Use of these linear quad roof-top basis functions on large smooth surfaces has been shown to reduce the number of unknowns required. In addition, wire structures can be simply represented as a thin quadrilateral patched surface, with the current being axially directed along the wire. These quad basis functions are edge based and possess all of the important properties of the edge based RWG triangular basis functions, which make them well suited for modeling surfaces of arbitrary shape. Namely, the component of current normal to each interior edge is continuous across the edge,

line charges do not exist along the boundary of the two quad patches which define the edge, and the symmetric form of the scalar potential term in the MOM implementation can be used. Also, since the linear quad basis functions are edge based, the modifications to a RWG based code are straightforward [2,3].

On a surface which is represented by a quadrilateral mesh, linear roof-top basis functions are defined on pairs of adjacent quads which define each interior edge. Junction edges between surfaces are handled using half basis functions which are equated to enforce current continuity between surfaces. An edge formed by a pair of quad patches is illustrated in Figure 1. Each patch is represented as a local parametric bi-linear surface formed by four vertex points, in terms of the parametric coordinates u and v.

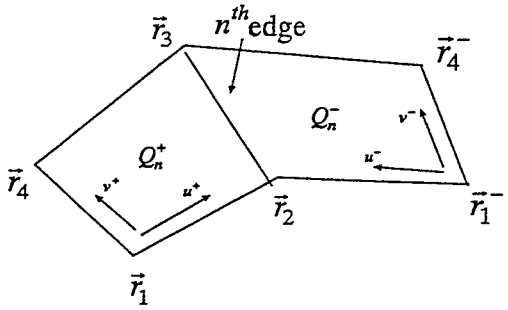

Figure 1. Quad-patch geometry.

The basis function for the n-th edge is defined in terms of the parametric variables u, v $(0 \le u \le 1, 0 \le v \le 1)$ as

$$\vec{f}_n(u,v) = \begin{cases} \dfrac{l_n u \vec{u}}{\sqrt{g(u,v)}} & , \quad \vec{r} \in Q_n^+ \\ \dfrac{-l_n u \vec{u}}{\sqrt{g(u,v)}} & , \quad \vec{r} \in Q_n^- \end{cases}$$

where l_n is the length of the n-th edge, and for a point (u,v) on the positive side(Q_n^+) of the edge, we have

$$\vec{r}(u,v) = \vec{r}_1 + u(\vec{r}_2 - \vec{r}_1) + v(\vec{r}_4 - \vec{r}_1) + uv(\vec{r}_1 - \vec{r}_2 + \vec{r}_3 - \vec{r}_4) \quad ,$$

$$\vec{u} = \frac{\partial \vec{r}}{\partial u} = (\vec{r}_2 - \vec{r}_1) + v(\vec{r}_1 - \vec{r}_2 + \vec{r}_3 - \vec{r}_4) \quad ,$$

$$\sqrt{g(u,v)} = \left| \vec{u} \times \vec{v} \right| \quad \text{and} \quad \iint ds = \iint \sqrt{g(u,v)}\, du dv \quad .$$

Similar expressions are obtained for the negative side (Q_n^-).

In addition, the surface divergence of the basis function is given by

$$\nabla \cdot \vec{f}_n(u,v) = \begin{cases} \dfrac{l_n}{\sqrt{g(u,v)}} & , \quad \vec{r} \in Q_n^+ \\ \dfrac{-l_n}{\sqrt{g(u,v)}} & , \quad \vec{r} \in Q_n^- \end{cases} .$$

The current is expanded in terms of these basis functions, and then substituted into a surface integral equation formulation and solved using the Galerkin method of moments technique. The surface integral equation formulation used depends on the boundary conditions that need to be satisfied. Each of the formulations is implemented in terms of an operator structure which is independent of the form of the basis function. The resulting matrix elements can be computed in a manner analogous to the RWG case using a combination of analytic and numerical procedures to compute the self and non-self terms.

Hybrid Quad/Triangle Patch Formulation

When modeling a complex geometry, it is often advantageous to have the freedom to generate hybrid meshes containing both triangular and quadrilateral patches, where quads are used for the large smooth parts and triangles are used for the fine detailed parts of the geometry. The forms of the edge based linear quad and RWG roof-top basis functions allow them to be combined at edges formed by adjacent quads and triangles as illustrated in Figure 2.

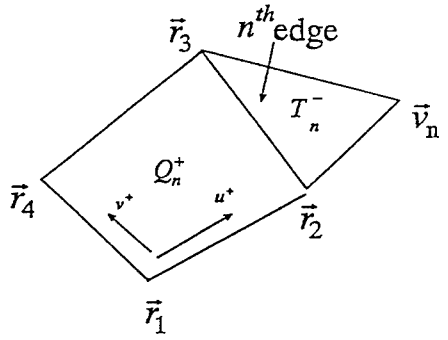

Figure 2. Hybrid Quad/Triangle Geometry.

Continuity of the normal component of current across hybrid edges is preserved, where these hybrid basis functions are defined as

$$\vec{f}_n(u,v) = \begin{cases} \dfrac{l_n u \vec{u}}{\sqrt{g(u,v)}} & , \quad \vec{r} \in Q_n^+ \\ \dfrac{-l_n(\vec{r} - \vec{v}_n^-)}{2A_n^-} & , \quad \vec{r} \in T_n^- \end{cases}$$

where A_n^- is the area of the triangle.

Hybrid BOR/Patch Formulation

For a BOR geometry, the surface is parameterized in terms of (t, φ), where t is the distance along the generating curve defining the BOR, and $\varphi (0 \le \varphi \le 2\pi)$ is the circumferential variable. A point on the surface is given by $(x,y,z) = (\rho(t)\cos\varphi, \rho(t)\sin\varphi, z(t))$, where $\rho(t)$ is the distance from the z axis to a point on the generating curve. For the BOR/Patch formulation, the currents on the 3D meshed part of the geometry are represented by the basis functions defined above, and the currents on the BOR part are represented using overlapping triangle functions for the t variation of the current and an entire-domain Fourier series representation for the φ variation

[4]. The BOR basis functions and current expansion in terms of the orthogonal tangent vectors $\hat{t}$ and $\hat{\varphi}$ on the surface are given by

$$\bar{J}(t,\varphi) = \sum_{n,k} (a^t_{nk}\bar{f}^t_{nk} - a^{\varphi}_{nk}\bar{f}^{\varphi}_{nk}) \quad ,$$

where

$$\bar{f}^{\alpha}_{nk}(t,\varphi) = \hat{\alpha}\frac{T_k(t)}{\rho(t)}e^{jn\varphi}$$

and $T_k(t)$ is the k-th overlapping triangle function of the surface.

When combinations of BOR and patch basis functions are substituted into a surface integral equation formulation and solved using the MOM technique, the Fourier mode interactions between test and source functions on the BOR surfaces decouple and the resulting matrix equation has the form

$$\begin{bmatrix} Z^{pp} & Z^{ps}_0 & Z^{ps}_{-1} & Z^{ps}_1 & \cdots & Z^{ps}_n \\ Z^{sp}_0 & Z^{ss}_0 & 0 & 0 & 0 & 0 \\ Z^{sp}_{-1} & 0 & Z^{ss}_{-1} & 0 & 0 & 0 \\ Z^{sp}_1 & 0 & 0 & Z^{ss}_1 & 0 & 0 \\ \vdots & 0 & 0 & 0 & \ddots & 0 \\ Z^{sp}_n & 0 & 0 & 0 & 0 & Z^{ss}_n \end{bmatrix} \begin{bmatrix} I^p \\ I^s_0 \\ I^s_{-1} \\ I^s_1 \\ \vdots \\ I^s_n \end{bmatrix} = \begin{bmatrix} V^p \\ V^s_0 \\ V^s_{-1} \\ V^s_1 \\ \vdots \\ V^s_n \end{bmatrix}$$

where the superscripts s (BOR) and p (patch) specify the surface on which the test (1st superscript) and source (2nd superscript) functions reside, and the subscript gives the Fourier mode number. The submatrices are given by Z, and the column vectors I and V represent the unknown coefficients and known source voltages, respectively. The variable n specifies the largest positive and negative Fourier mode numbers used in the current expansion. The sparse form of this matrix equation can be exploited to more efficiently solve the system of equations. In addition, the matrix sub-blocks possess certain symmetries which can be taken advantage of during the matrix fill process.

Current Continuity Between Hybrid Surface Representations

When dealing with hybrid surface representations which intersect, surface current continuity between the different representations must be maintained. For the combination of triangular patched and quadrilateral patched surfaces, this is a simple matter since both representations are edge based, and the functional form of the two types of basis functions allows them to be connected at each hybrid edge. For the case of the BOR/Patch formulation, it is not a simple procedure to match the unknowns in order to explicitly enforce current continuity. In fact, for certain classes of intersecting surfaces, such as the intersection between a circular cylinder and a plate, strict enforcement of the junction condition would result in coupling of the Fourier modes on the BOR surface. This would destroy the primary advantage of a BOR formulation.

The simplest procedure for allowing current continuity between intersecting BOR and patched surfaces involves overlapping of the intersecting surfaces. This amounts to extending the patched surface so that it overlaps onto the rotationally symmetric BOR surface. Typically, the overlap should be on the order of a half basis function, although it can be larger. If the overlap region is too small, then the current variation in the intersecting region will be overly constrained, and result in a poor representation for the actual current. This procedure is analogous to overlapping wires in order to form a junction without explicitly implementing the Kirchhoff junction condition. This procedure of overlapping intersecting surfaces simply results in regions of the surface which are represented by two different types of current expansions. From the theoretical point, this procedure is perfectly valid, however, the numerical implementation requires care due to the singularity in the Green's function in the overlapping region. A robust implementation should use a singularity extraction procedure to handle this case, however, we have found that the equivalent distance approximation used by Mautz and Harrington[5] in their BOR formulation

is adequate. Results will be presented which validate this procedure for both 3D patched surfaces and intersecting BOR/patch surfaces.

Parallel Implementation

The parallel implementation of the quad patch version and the quad/triangle patch version uses the previous parallelization effort on CARLOS 3D v2.0 [6]. The code was originally structured to run on either a workstation or Intel Paragon. By incorporating the parallel message passing protocol MPI (Message Passing Interface) it can now be run on a workstation, workstation cluster, or a massively parallel machine that supports MPI.

In the parallel version of the code all the input that specifies the type of problem to be solved is read by one node. This node processes the information then sends it to the rest of the nodes. The next step requires the matrix fill procedure and is partitioned among the different nodes. The solution technique to solve the matrix equation depends on the matrix description. For the quad/triangle hybrid formulation the resulting matrix is dense and LU decomposition optimized for parallel platforms can be used. For this case the matrix solve consists of n^3 operations which dominates the total solution time. For this reason the block matrix fill algorithm, that realizes optimal load balancing, is prescribed by the solver. The two parallel dense solvers used are the Intel Prosolver-DES package for out-of core solutions and the Sandia in-core solver. The Sandia in-core solver has also been configured to run under the MPI protocol. The BOR/Patch hybrid formulation yields a sparse matrix so using an LU decomposition optimized for a dense matrix would be inefficient in time and memory management. Two alternatives would be a sparse LU solver or an iterative solver. These possibilities have not been exercised on parallel platforms for this problem. Once the solution is obtained the scattering cross section or scattered fields are computed on separate nodes and then accumulated to one node to write to an output file.

Results

The RCS for the one meter NASA almond was computed for three different patch representations: quad, triangular, and quad/triangular patch descriptions. The spatial resolution of the different grids are 106 facets/λ^2 and 215 facets/λ^2 for the quad and triangular patches, respectively. The hybrid grid is shown in Figure 3 where triangular facets are used from the tip to 0.2m from the tip. The RCS was calculated at 2 GHz and is shown in Figure 4.

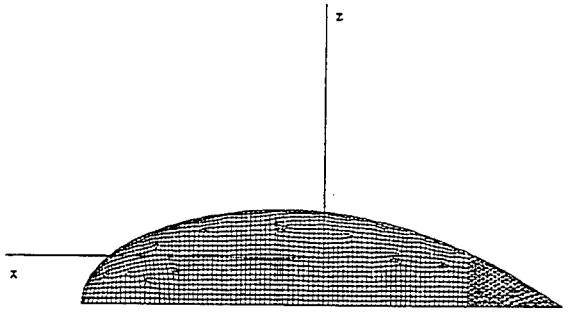

Figure 3. Hybrid quad and triangular patch grid for the NASA 1 m. almond.

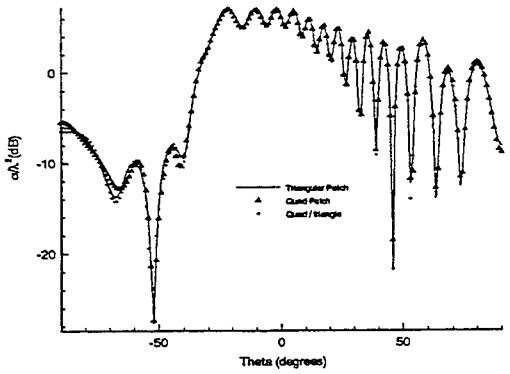

Figure 4. Monostatic RCS of a one meter almond at 2 GHz ($\hat{\theta}$-pol, $\varphi = 0$).

The results show good agreement with minor variations in the tip region.

Another problem to consider is the modeling of a wire by using the quad-patch representation. Two wires each 0.75m long separated by 0.75m were modeled using a dense triangular patch mesh and a coarse quad mesh. The triangular patch mesh models the thickness of the antenna (0.0375m) while the quad mesh does not. The quad and triangular patch models for this configuration are shown in Figure 5. The monostatic RCS of this configuration is shown in Figure 6.

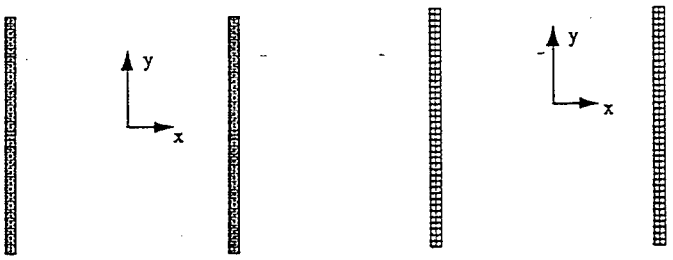

a) Triangular patch b)Quad patch

Figure 5. Quad and triangular patch models for the two antenna configuration.

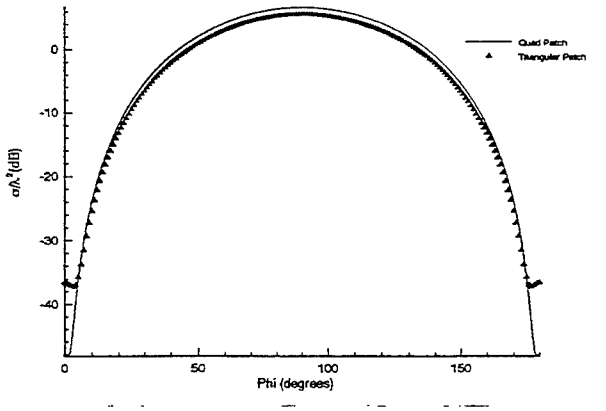

Figure 6. Monostatic RCS for wire configuration at 200MHz ($\vec{\theta}$ - pol, $\vec{\theta} = 0$).

Again excellent agreement is seen except in the region where the thickness of the antenna is important. For modeling of thin wires the quad basis function is more natural since the current is decomposed into axially and circumferentially directed currents.

The final example is the BOR/Patch hybrid model for a cone which is 2λ long with a base radius of $.5\lambda$. The monostatic RCS is shown in Figure 7 for a BOR model and a BOR/Patch model with overlap. The overlap region was chosen to be a half triangle function on the BOR surface.

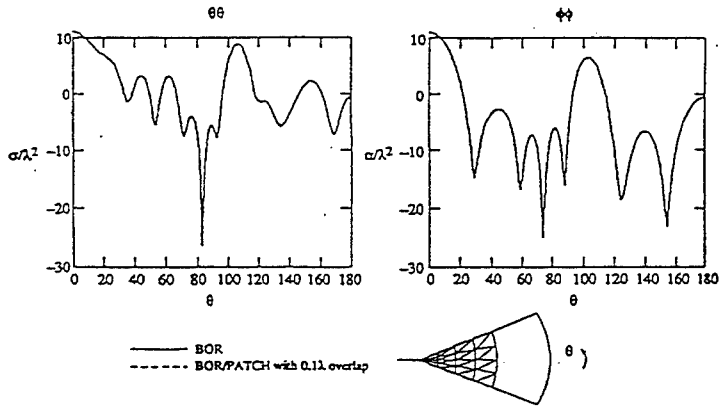

Figure 7. Monostatic RCS comparisons for a 2λ cone - BOR and hybrid BOR/Patch.

Conclusions

A number of different hybrid schemes have been presented and tested. The methods considered in this paper were incorporated into the CARLOS-3D code which has been ported to massively parallel systems and uses a modular operator formulation so that only a few routines needed to be added. The use of these hybrid schemes extends the range of problems that can be solved using the method of moments by modeling the geometry of interest more efficiently.

References

[1] S.M. Rao, D.R. Wilton, and A.W. Glisson, "Electromagnetic Scattering by Surfaces of Arbitrary Shape", IEEE Trans. Ant. Prop.,AP-30,3,pp.409-418,1982.

[2] J.M. Putnam and M.B. Gedera, "CARLOS-3D: A General-Purpose Three-Dimensional Method-of-Moments Scattering Code", IEEE Antennas & Propagation Magazine, April, 1993.

[3] J.M. Putnam and J.D. Kotulski, "Parallel CARLOS-3D Code Development", Proceedings of the 12th Annual Review of Progress in Applied Computational Electromagnetics, Monterey,CA, March 1996.

[4] L.N. Medgyesi-Mitschang and J.M. Putnam, "Electromagnetic Scattering from Axially Inhomogeneous Bodies of Revolution",IEEE Trans. Ant. Prop. AP-32,8,pp.797-806,1984.

[5]J.R. Mautz and R.F. Harrington, "H-field, E-field, and Combined Field Solutions for Bodies of Revolution", Tech. Rep. RADC-TR-77-109, Rome Air Development Center, Griffiss Air Force Base, NY, March 1977.

[6] J.M. Putnam, D.D. Car, and J.D. Kotulski, "Parallel CARLOS-3D - An Electromagnetic Boundary Integral Method for Parallel Platforms", Submitted to Engineering Analysis with Boundary Elements, June 1996.

APPLICATION OF MOMENT METHOD SOLUTIONS TO RCS MEASUREMENT ERROR MITIGATION

John Stach <stach@erim.org>
Environmental Research Institute of Michigan (ERIM), http://erim.org
P.O. Box 134001
Ann Arbor, MI 48113-4001

ABSTRACT

For several years, ERIM has been studying RCS measurement error sources and processing methods by which these errors can be reduced. Typical errors that can affect RCS measurements include near-field effects, multipath contamination, and target support interactions. In this paper we will discuss the use of network models and moment method solutions to mitigate these RCS error sources, describe some of the advantages and limitations of the network model approach, and provide some examples that demonstrate the use of moment method solutions for multipath applications.

1.0 INTRODUCTION

Scattering measurements are typically contaminated by one or more of several error sources that are dependent on the measurement range and the desired data. Typical contamination sources that will be addressed in this paper are near-field effects, multipath contamination, and target support interactions. Many techniques exist to mitigate these error sources, but for many measurements situations, they cannot be applied due to data or phenomenology limitations [5].

For example, range gating and image editing (2-D range-crossrange gating [1,2,3]) have been successfully used to remove target supports such as pylons or foam columns. However, these image-based approaches require that (1) significant target scattering mechanisms do not lie near the target support in the image, (2) the interactions between the target and the support are negligible, and (3) a user is able to determine the appropriate regions of the image to edit. These approaches fail when the bandwidth of the measurement is too small to separate undesired scattering from target scattering, and when interactions become significant. The network model (NM) is derived from a moment method (MM) solution so that it takes into account interactions even for single frequencies. In addition, the network model approach does not require the use of imagery.

Another example of measurement error mitigation is the use of target translation to reduce multipath effects. The performance of a translation approach is limited by the amount of translation available in a facility and the type of multipath. An advantage of the NM approach is that it can be applied using conventional angular measurements as well as translations. In fact, the network model approach can be used to exploit any measurement which can be reasonably modeled with a MM code including bistatic and near field measurements.

2.0 NETWORK MODEL OVERVIEW

Figure 2-1 shows a block diagram of the NM concept applied to target scattering. The incident basis functions couple the radar transmitter to the target geometry, the target couples inbound and outbound basis functions, and the outbound modes couple the target geometry to the radar receiver. Note that the center block which couples the inbound and outbound basis functions (typically an admittance matrix) is independent of the measurement geometry which is entirely contained in the left and right blocks. This means that the basis function coupling due to the target is independent of angles, polarization and whether measurements are made in the near or far field. This fact serves as the foundation for the NM error mitigation. In the NM approach, we esti-

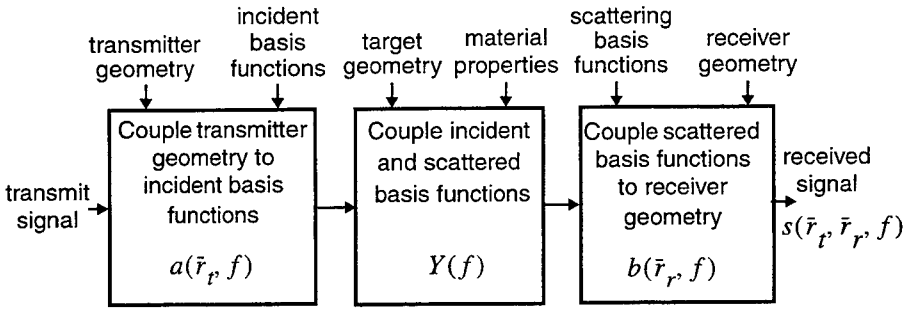

FIGURE 2-1. Block Diagram of the Network Model Representation for Target Scattering

mate an interaction matrix from a given set of measurements, then use the estimated interaction matrix and appropriate radar coupling terms to predict data that could not be measured.

The NM is based on the same bilinear form that is typical of MM codes [6, p107]. A measurement at a single frequency can be described by the combination of the three coupling mechanisms described above.

$$s(r,t) = \sum_{i}^{N}\sum_{j}^{N} a_i(r) b_j(t) y_{ij}, \qquad \text{(Eq 1)}$$

where s is the measured scattering value, t and r represent the transmitted and receive geometries (e.g., polarization, angle) for the radar respectively, a_i describes the coupling of the transmitter to the ith basis function, b_j describes the coupling of the receiver to the jth basis function, and y_{ij} describes the coupling between the ith and jth basis function due to the target geometry. Recall that y_{ij} is independent of the transmitter or receiver geometry.

A MM solution can be used to initialize the NM terms in Eq. 1 for a particular set of scattering measurements where the MM model includes the contamination effects to be mitigated. The y_{ij} terms of the NM are then perturbed so that the NM correctly predicts the measurements within a specified error to account for noise and sensitivity. Finally, the perturbed NM is used to predict scattering measurements in the absence of error sources. In a MM solution, the y terms of Eq 1 would be the self and mutual admittances found by inverting the computed impedance matrix. Likewise, a and b would represent the coupling of the MM basis functions to the modeled receiver and transmitter (typically a plane wave for far-field computations). Although the basis functions for MM codes typically consists of wires, plates, or other physical elements, the NM is not restricted to these bases and more general orthogonal basis functions such as spherical modes have also been used.

Due to the similar nature of MM and NM models, the limitations of the NM error mitigation approach parallel those of the MM modeling limitations. The electrical target size and bandwidth must be small enough to compute a MM solution, and to perform the NM mitigation computation which have similar computational complexity.

2.2 NETWORK MODEL PERTURBATION

Equation 1 describes a single noiseless measurement in terms of a model. Since there are errors in the measurement as well as in the model, we can introduce a perturbation of the admittance values that forces the

model to match a given set of measurements to within a specified residual. If we enumerate all combinations of i and j in a new variable, n, we can rewrite Eq 1 for the kth measurement as

$$s_k(r,t) = \sum_{n}^{N^2} g_{kn}(r,t)(y_n + \Delta y_n) \ , \qquad \text{(Eq 2)}$$

where $g_{kn}(r,t) = a_{ki}(r)b_{kj}(t)$ describes the geometry for the N^2 combinations of i and j, and Δy_n is a perturbation of the admittance matrix that satisfies the equality to a specified level. This equation can be further simplified in matrix form to

$$s = G(y_o + \Delta y) = G\Delta y + s_o \ , \qquad \text{(Eq 3)}$$

where $\boldsymbol{G}$ is the geometry matrix whose rows represent the kn geometry terms for each measurement, and $\boldsymbol{s}$ and $\boldsymbol{s_o}$ represent vectors of measurements and model predictions respectively. $\boldsymbol{Gy_o = s_o}$ is the initial model prediction. The perturbation can be computed in the minimum norm sense [7, p409] from

$$\Delta y = G^H(GG^H + \lambda I)^{-1}(s - s_o) \ , \qquad \text{(Eq 4)}$$

where superscript H denotes conjugate transpose, and $\lambda\boldsymbol{I}$ imposes a constraint on the norm of the Δy due to noise or poorly conditioned matrices [5]. The uniqueness of the minimum norm solution for this underdetermined equation (the number of basis functions *squared* will almost certainly be much larger than the number of measurements) comes from finding the smallest perturbation in the least squares sense. The constrained normal equation solution is used so that the perturbation can be computed efficiently for large problems.

3.0 NETWORK MODEL MEASUREMENT ERROR MITIGATION

Given the method of section 2.2 for perturbing the model to match measurements, there are many error mitigation problems that can be addressed including target editing and field corrections. Target editing deals with model modifications such as target support removal and target configuration changes. Field corrections alter the measurement geometry such as in near-field to far-field corrections and multipath removal. All of these errors can be handled simultaneously with the NM approach.

The error mitigation process is shown in Figure 2-1. The MM code is used to extract the NM parameters based on the target and measurement geometry information. The NM is then perturbed to match measurements within constraints determined by noise and model sensitivity estimates. If needed, the perturbed NM is then edited, e.g., to remove a target support. Finally, the desired measurement geometry from the MM model is used to estimate the desired measurement.

Note that we could also use the perturbed model to provide information about model errors, i.e., reasons why a MM model do not match measurements. We are currently investigating the use of the NM to correct/design MM models based on measurements and other simulations. We expect to publish details and results of this work in 1998.

3.2 MITIGATION OF TARGET ERRORS

Target errors that are typical of measurement facilities are (1) target supports, and (2) target configurations. For target support removal, the model of the target with support is perturbed to match the corresponding measurements. Then the support is numerically removed from the model and the scattering is predicted. A recent study showed that for a simple cylinder and attached wire to represent a support, the wire-free measurement

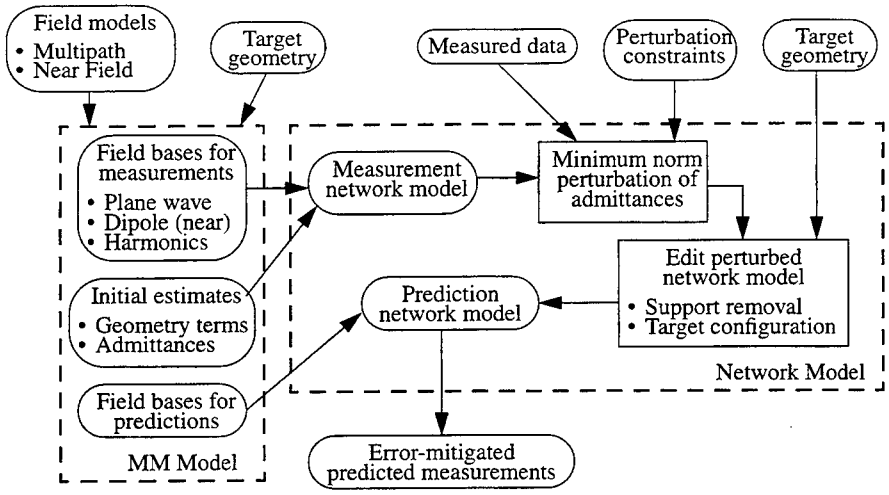

FIGURE 3-1. Block diagram of network model error mitigation process

could be predicted to within the noise floor of the measurement facility [4]. The same approach applies to target configuration. However, there are additional issues to contend with if things are added to the model rather than removed.

The NM editing must be done in the impedance domain. After perturbing the admittances so that the model matches measurements using

$$\Delta y = G^{+}(s - s_o)\,, \qquad \text{(Eq 5)}$$

we invert $y_o + \Delta y$ to get the impedance matrix. The removal of model elements is accomplished by setting the diagonal elements of the impedance matrix that correspond to elements that are to be removed to a large value. The new admittance matrix found from the inverse of the "edited" impedance matrix is then used to predict a support-free measurement.

$$s_e = G y_e, \qquad \text{(Eq 6)}$$

where s_e are the support-free predictions found from perturbed and "edited" y_e.

3.3 MITIGATION OF FIELD ERRORS

Field errors are due to the arrangement of radar and target in the measurement facility. These errors are primarily near field effects and multipath. For these errors, the NM is perturbed and then the measurement geometry is altered to estimate the desired measurements.

3.3.1 NEAR FIELD ERROR MITIGATION

For the near-field problem, we can perturb the model with near-field geometry terms to fit measured near-field

data and then use far-field geometry terms to predict far-fields. The estimated desired measurements, s_f, can be summarized as

$$s_f = G_f(y_o + G_n^{+}(s_n - s_{on})), \quad \text{(Eq 7)}$$

where subscripts n and f indicate near and far-fields respectively, and

$$G^{+} = G^{H}(GG^{H} + \lambda I)^{-1} \quad \text{(Eq 8)}$$

is the minimum norm pseudoinverse. Note that the admittance matrix, y, is independent of the near or far field geometry. This requires that the MM code used to extract the NM support both near and far field computations using the same basis functions.

3.3.2 MULTIPATH MITIGATION

If we include a sum of multipath terms for the measurement configuration, Eq 2 becomes

$$s_k = \sum_{(r,t)}^{M} \sum_{n}^{N^2} g_{kn}(r,t)(y_n + \Delta y) \ , \quad \text{(Eq 9)}$$

where various combinations of r and t form the M multipath geometries. However, it is not necessarily a sum over all combinations of r and t because for pulsed measurement ranges not all combinations of bistatic multipath are included in any given range gate.

We can reverse the order of summation to get

$$s_k = \sum_{n}^{N^2} \left(\sum_{r,t}^{M} g_{kn}(r,t) \right) (y_n + \Delta y) \ , \quad \text{(Eq 10)}$$

where the summation in parenthesis is a row of a multipath geometry matrix with the same form as in Eq 3. Once the admittance matrix is perturbed to match the multipath-contaminated measurements via Eq 4, the perturbed admittance is then used with a multipath-free geometry matrix to predict the desired scattering.

The multipath models are typically computed from a probe of the target zone [8] and are assumed to be independent of the target.

4.0 MULTIPATH MITIGATION EXAMPLES

In these examples, we showed that we can significantly reduce the multipath errors using a simulated measurement of monostatic target scattering. Figure 4-1 shows the MM wire models used for the simulated measurements and for the NM mitigation. In lieu of real measurements, the mitigation model is sparse to demonstrate the robustness of the approach with respect to model fidelity,i.e., we use the dense model to generate measurements and the sparse model to remove multipath (without using knowledge about the measurement source.) We used the NEC scattering code for the measurement simulations and for the initialization of the NM.

The multipath diagrams and levels are shown in Figure 4-2. They correspond to a simple model of an assumed compact range with modest absorber performance and multiple floor and ceiling reflections due to feed effects. The baseline multipath levels are shown in Figure 4-3 along with a plot of the NM errors before perturbation. In all plots, the solid lines represent scattering data and the dashed lines represent coherent differ-

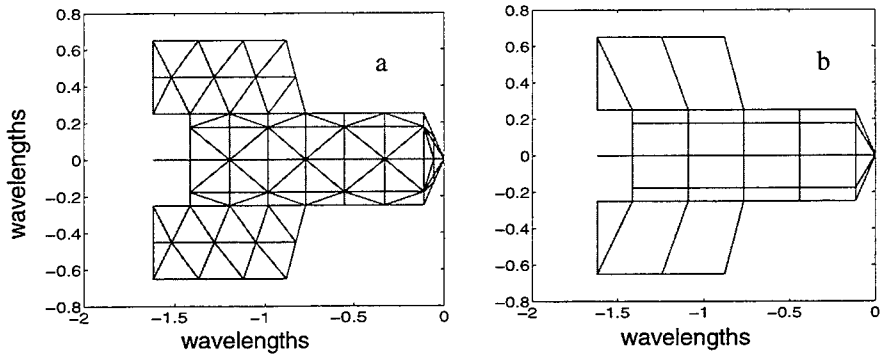

FIGURE 4-1. The MM model used to simulate measurements (a) has a much higher wire density than that used as the basis for network model mitigation (b) in which some wires are nearly 0.5 wavelengths long.

Multipath Component	True RCS Component	Measured RCS Component			
		VV	VH	HV	HH
Direct Scatter	VV	0 dB	-30	-0	-60
	VH	-30	0	-60	-30
	HV	-30	-60	0	-30
	HH	-60	-30	-30	0
Ceiling and Floor (30 degees from boresight)	VV	-35	-65	-65	-95
	VH	-65	-35	-95	-65
	HV	-65	-95	-35	-65
	HH	-95	-65	-65	-35
Ceiling and Floor (50 degees from boresight)	VV	-30	-60	-60	-90
	VH	-60	-30	-90	-60
	HV	-60	-90	-30	-60
	HH	-90	-60	-60	-30
Left and Right Walls (50 degees from boresight)	VV	-45	-75	-75	-105
	VH	-75	-45	-105	-75
	HV	-75	-105	-45	-75
	HH	-105	-75	-75	-45

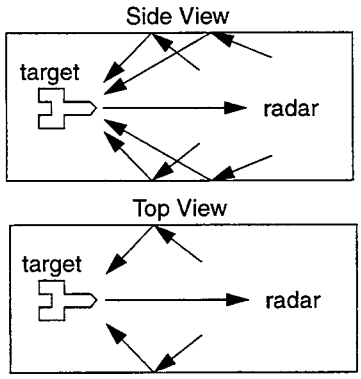

FIGURE 4-2. Multipath diagrams and levels for the example

ences, i.e., errors. Note that the cross-pol multipath in the figure is at about the same level as the co-pol multipath. This is typical because of the cross-polarization effects of the target with respect to the radar, especially at the bistatic multipath angles. However, in these cases, the co-pol multipath terms were still the largest, even after mitigation.

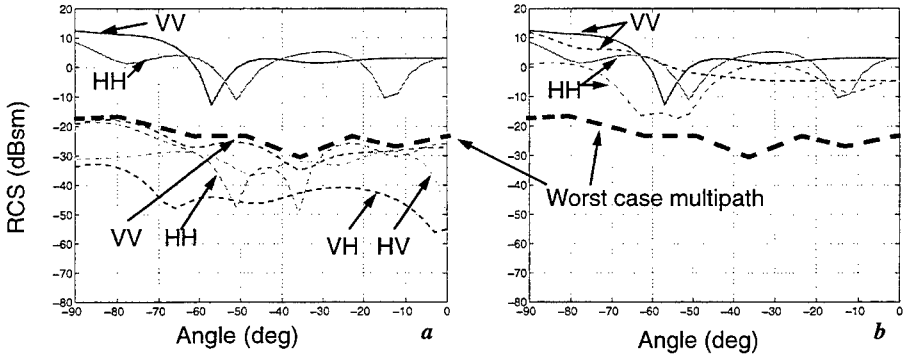

FIGURE 4-3. The simulated measurements multipath error levels shown as dashed lines in plot (a) are significantly smaller than the corresponding errors due to model sparsity shown as dashed lines in plot (b). The thick dashed line shows the worst case multipath.

Two examples of multipath mitigation are shown in Figure 4-4. The angles have been shifted in plot (a) to

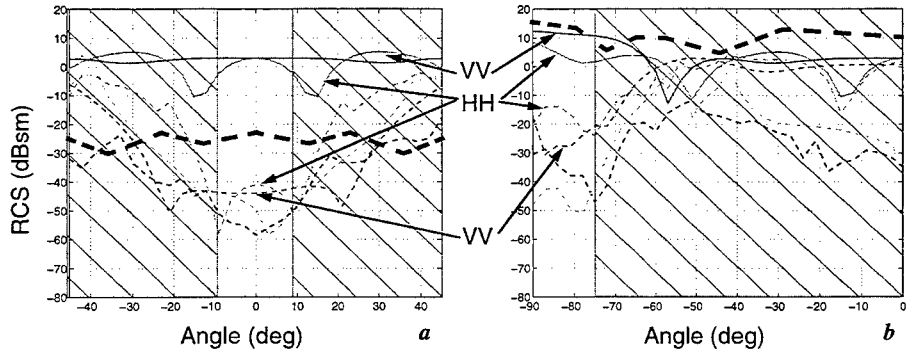

FIGURE 4-4. In plot (a), the multipath error was reduced by about 15 dB over the 7 waterline angles. The hatched areas were outside the fit region and were treated separately. For case (a), the measurements included the waterline plus 4 elevations patterns for a total of 140 simulated measurements for the perturbation. In plot (b), the multipath was increased to the level shown in the thick dashed line. This time the 7 waterline angles plus 4 translations were used to reduce the multipath error levels by more than 15 dB.

address a symmetric case. The results are typical of that seen at all angles. The perturbation in each case was limited to a waterline span of 7 angles spaced 3 degrees apart. This angular span is close to the Nyquist sampling rate which has proven to provide reasonable performance. These cases were used to show different forms of measurement diversity, specifically elevation patterns and translations. Other diversity such as bistatic angles could also have been used.

In the first case (a) of Figure 4-4, the multipath levels from Figure 4-2 were used along with elevation patterns

to add some measurement diversity to the perturbation. The result was about 15 dB of reduction in the multipath levels over the region of perturbation. We also verified that similar reductions were seen at the other elevations. The shaded portions of the plots are outside the region of measurements and were used to determine the sensitivity of the process. We found in this study that the variations in errors outside the region of perturbation measurements can be used to optimize the constraints on the perturbation.

In the second case (b) of Figure 4-4, the multipath levels were increased to the level shown by the thick dashed line. Also, translation was used to achieve similar performance (>15 dB reduction) to that found by using elevation angles.

These cases provide a snapshot of an ongoing effort to characterize the process and performance of the NM approach to measurement error mitigation. In other work, we have shown similar performance where the RCS patterns had a high dynamic range so that the multipath from a high RCS angular region completely masked a low RCS angular region.

5.0 SUMMARY

We have shown how a network model, derived from moment method simulations, can be used to reduce RCS measurement errors. These errors can be field errors such as near fields and multipath, or target errors such as the target support. We also showed a simple example of multipath mitigation to demonstrate the robustness of the technique with respect to model fidelity. Other studies have consistently shown that we can typically reduce the measurement errors to the level of the unmodeled noise which includes nonstationary clutter, radar system noise, and unmodeled field or target variations.

6.0 REFERENCES

[1] I.J. LaHaie, E.I. LeBaron, C.J. Roussi, and K. Quinlan, "Processing Techniques for Removal of Target Support Contamination," *1993 IEEE AP-S Intl. Symp. Digest.*

[2] J. Stach and E.I. LeBaron, "Enhanced Image Editing by Peak Region Segmentation," *AMTA Proceedings*, September-October 1996.

[3] S.R. DeGraaf, "ISAR RCS Editing via Modern Spectral Estimation Methods," *AMTA Proceedings*, November 1995.

[4] J. Stach and L. Heck, "RCS Extrapolation Using Network Models," *Proceedings of the URSI Radio Science Meeting*, Ann Arbor, MI., June 1993.

[5] J. Stach, "Numerical Methods for Measurement Error Mitigation," *AMTA Proceedings*, November 1995.

[6] R.F. Harrington, *Field computations by moment methods*, Robert E. Krieger Publishing Co, Malabar, FL

[7] G.H. Golub and C.F. Van Loan, *Matrix Computations*, The Johns Hopkins University Press, Baltimore, Maryland, 1985.

[8] J. Stach, I. LaHaie, and E. LeBaron, "Multipath Mitigation in Compact RCS Ranges Using the Network Model and 2-D PML Spectral Estimation Techniques," submitted to 1997 IEEE APS/URSI Conference, Montreal, July 1997.

Scattering From Arbitrarily Shaped Cylinders by Use of Characteristic Modes

G. Amendola, G. Angiulli, G. Di Massa

Dipartimento di Elettronica, Informatica e Sistemistica
Università della Calabria, 87036 Rende (Cs), Italy
Phone +39.984.494700 Fax +39.984.494713 E-Mail DiMassa@Na.INFN.It

Abstract - The scattering of electromagnetic waves from several metallic objects is formulated as an electric field integral equation for the induced current on the bodies. The characteristic modes are used as basis function in the moment method solution of the problem. It is shown that only a small number of them are required for the current reconstruction and consequently large dimension problems are solvable.

I. INTRODUCTION

The electromagnetic scattering by multiple objects has many applications such as simulation of complex structures, prediction of radiation by antennas, etc.. The usual approach for resolving these problems consists in solving the integral equation for the electric surface current density on the metallic surfaces of the bodies by the method of moment. Moment's method solutions compare favourably with measured results, but requires a large amount of computational effort. One important point affecting the performances of the method is the choice of the basis functions. Theoretically, there are infinitely many possible basis sets. In practice two types of expansion functions are considered: entire domain basis functions and subdomain functions. Usually, the first choice assumes a resonant behaviour of the unknown current, so that only one term is retained when expanding the current of a single element of an array antenna or scatterers. When subdomain functions are considered, the unknown current is discretized by the expansion function. They may be used without a priori knowledge of the nature of functions to be represented. However, due to much larger number of unknowns, the required computational time can become unacceptable. In this work the characteristic modes of the single scattterer are proposed as a choice for the basis functions in the analysis of scattering and mutual coupling between similar metallic bodies. The theory of characteristic modes for conducting bodies has been developed by Garbacz [1] and by alternative approach by Harrington and Mautz [2]. Due to the resonant behaviour of such modes, only a small number of them are required for an accurate representation of the current distribution even in presence of mutual coupling [3]. In what follows a concise account of the theory is given and then some significant result of numerical simulations is presented and commented.

II. THEORY

A. Basic Formulation and Summary of Characteristic Mode Theory.

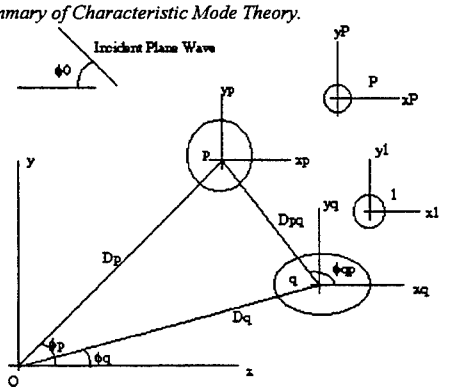

Fig. 1 Geometry for scattering of a plane wave by a configuration of many objects.

Figure 1 shows the general arrangement of similar scattering cylinders. Let us consider the cylinders supposed to be perfectly conducting and infinitely long, with their axes in the z-direction. We consider the scattering due to an incident plane wave transverse magnetic with respect the z axis

$$\overline{E}^{inc} = \mathbf{z}E_0 e^{jkp\cos(\phi-\phi_0)} \tag{1}$$

where $k=2\pi/\lambda$ is the free space wavenumber, λ is the wavelength and ϕ_0 is the angle of incidence of the plane wave with respect to the x direction The problem of the two dimensional scattering from conducting cylinders under an impressed electric E polarized field leads to a Fredholm integral equation of first kind for the induced current J

$$\left(\frac{Z_0 k}{4}\oint_{C_1\cup\ldots\cup C_P} H_0^2\left(k|\mathbf{r}-\mathbf{r}'|\right)\mathbf{J}(\mathbf{r}')dC\right)_{Tan} = E_{Tan}^{inc} \tag{2}$$

whose support is the union of the curves $C_1,\ldots,C_P$ covered by P cylinders. In equation (2) H_0^2 is the Hankel function of second kind and zero order and Z_0 is the free space impedance. Relation (2) can be expressed as an operator equation

$$\left(L(\mathbf{J}) - E^{inc}\right)_{Tan} = 0 \tag{3}$$

Following [2], we consider the eigenvalue equation

$$X(\mathbf{J}_n) = \lambda_n R(\mathbf{J}_n) \tag{4}$$

where R and X are real and imaginary parts of the operator

$$Z(\mathbf{J}) = \left[L(\mathbf{J})\right]_{Tan} \tag{5}$$

Both R and X are real symmetric operator. Hence all eigenvalue and eigenfunction are real. The eigenfunction diagonalize Z, i.e.

$$\langle \mathbf{J}_n | Z\mathbf{J}_m \rangle = (1+j\lambda_n)\delta_{nm} \tag{6}$$

where δ_{mn} is the Kronecker delta and the symmetric product of two vectors functions on S is defined as

$$\langle \mathbf{A}|\mathbf{B}\rangle = \oint_S \mathbf{A}\cdot\mathbf{B}dS \tag{7}$$

These $\mathbf{J}_n$ are called characteristic modes of the conducting body defined by S. A modal solution for the current J on the metallic object can be obtained using eigenfunctions both as expansion and testing functions in the moment method. The current J is expanded as a linear superposition of the modal currents

$$\mathbf{J} = \sum_k \alpha_k \mathbf{J}_k \tag{8}$$

Applying (6) to the operator equation for the scattering problem (3) we get the modal solution for the current J

$$\mathbf{J} = \sum_k \frac{V_k^i \mathbf{J}_k}{1+j\lambda_k} \tag{9}$$

where

$$V_k^i = \langle \mathbf{J}_k | \mathbf{E}_{Tan}^{inc} \rangle \tag{10}$$

is the modal excitation coefficient. The electric field $\mathbf{E}_n$ and the magnetic field $\mathbf{H}_n$ produced by an eigencurrent $\mathbf{J}_n$ on S will be called the characteristic fields or eigenfields corresponding to $\mathbf{J}_n$. The set of $\mathbf{E}_n$ or $\mathbf{H}_n$ form a Hilbert space of all fields throughout space produced by currents on S [2]. The fields are linearly related to the currents, and hence can also be expressed in modal form

$$\mathbf{E} = \sum_k \frac{V_k^i \mathbf{E}_k}{1 + j\lambda_k} \tag{11}$$

$$\mathbf{H} = \sum_k \frac{V_k^i \mathbf{H}_k}{1 + j\lambda_k} \tag{12}$$

where $\mathbf{E}$ and $\mathbf{H}$ are the fields from $\mathbf{J}$ everywhere in space.

B. Computation of Characteristic Modes and Moment Method Solution.

The reduction of the operator equation (4) to matrix equation can be effected in the usual way by the moment method. Substitution of the expansion of $\mathbf{J}_n$

$$\mathbf{J}_n = \sum_k I_k \mathbf{T}_k \tag{13}$$

where I_k are coefficients to be determined, give the matrix eigenvalue equation

$$[R][I] = \lambda[X][I] \tag{14}$$

where

$$[R] = \left[\left\langle T_i \middle| RT_j \right\rangle\right] \tag{15}$$

$$[X] = \left[\left\langle T_i \middle| XT_j \right\rangle\right] \tag{16}$$

In order to solve the (14) the Singular Value Decomposition of the matrix [R] is performed

$$[R] = [U][W][V]^T \tag{17}$$

where [U] and [V] are orthogonal square matrix, and [W] is a diagonal matrix with positive or zero elements. Using (17) and the properties of orthogonal square matrices (14) becomes

$$\left[U^T XV\right]\left[V^T I\right] = \lambda\left[W\right]\left[V^T I\right] \tag{18}$$

Equation (18) is ordered according the decreasing values of [W] and partitioned picking up the first n values of [W]. The matrix involved in (18) are partitioned according to

$$[W] = \begin{bmatrix} [W_{11}] & 0 \\ 0 & 0 \end{bmatrix} \tag{19}$$

$$[X] = \left[V^T I\right] = \begin{bmatrix} [X_1] \\ [X_2] \end{bmatrix} \tag{20}$$

$$[A]=\left[U^T XV\right]=\begin{bmatrix}[A_{11}] & [A_{12}]\\ [A_{21}] & [A_{22}]\end{bmatrix} \tag{21}$$

Substituting (19-21) in (18) we obtain the system of matrix equations

$$[A_{11}][X_1]+[A_{12}][X_2]=\lambda[W_{11}][X_2] \tag{22}$$

$$[A_{21}][X_1]+[A_{22}][X_2]=0 \tag{23}$$

Substituing $[X_2]$ from the (23) in the (22) we obtain the real eigenvalue equation

$$[B][Y]=\lambda[Y] \tag{24}$$

where

$$[B]=\left[W_{11}^{-1/2}\right]\left[A_{11}-A_{12}A_{22}^{-1}A_{21}\right]\left[W_{11}^{-1/2}\right] \tag{25}$$

$$[Y]=\left[W_{11}^{1/2}X_1\right] \tag{26}$$

Eigenvalues of (24) are the smaller eigenvalues of (4) and eigenvectors of (24) give the corresponding eigenvectors of (4). Let us consider the case of P similar conducting objects depicted in fig. 1. In order to apply the moment method, the unknown surface current density **J** in equation (2) is expanded in a set of N characteristic modes relevant to the single object

$$\mathbf{J}=\sum_{k=0}^{k=P}\sum_{h=0}^{h=N}\alpha_h^k \mathbf{J}_h^k \tag{27}$$

where α_h^k are coefficients to be determinate. Galerkin method give the following discretized version of (2)

$$\begin{bmatrix}[B^{11}] & \cdots & [B^{1P}]\\ [B^{p1}] & [B^{pq}] & [B^{pP}]\\ [B^{P1}] & \cdots & [B^{PP}]\end{bmatrix}\cdot\begin{pmatrix}\overline{\alpha}^1\\ \overline{\alpha}^p\\ \overline{\alpha}^P\end{pmatrix}=\begin{pmatrix}[V^1]\\ [V^p]\\ [V^P]\end{pmatrix} \tag{28}$$

in which the submatrices are given by

$$[B^{pp}]=\begin{bmatrix}1+j\lambda_1^p & \cdots & 0\\ 0 & 1+j\lambda_i^p & 0\\ 0 & \cdots & 1+j\lambda_N^p\end{bmatrix} \tag{29}$$

$$[B^{pq}]=\begin{bmatrix}\left\langle \mathbf{J}_1^p \middle| \mathbf{Z}\left(\mathbf{J}_1^q\right)\right\rangle & \cdots & \left\langle \mathbf{J}_1^p \middle| \mathbf{Z}\left(\mathbf{J}_N^q\right)\right\rangle\\ \cdots & \cdots & \cdots\\ \left\langle \mathbf{J}_N^p \middle| \mathbf{Z}\left(\mathbf{J}_1^q\right)\right\rangle & \cdots & \left\langle \mathbf{J}_N^p \middle| \mathbf{Z}\left(\mathbf{J}_N^q\right)\right\rangle\end{bmatrix} \tag{30}$$

$$\left\langle J_i^p \left| Z\left(J_j^q\right)\right.\right\rangle = \oint_{CpCq}\oint J_i^p H_0^2\left(|r-r'|\right) J_j^q dC_q dC_p \tag{31}$$

$$\left[V^p\right] = \begin{pmatrix} \left\langle J_1^p \left| E_{Tan}^{inc}\right.\right\rangle \\ \cdots \\ \left\langle J_N^p \left| E_{Tan}^{inc}\right.\right\rangle \end{pmatrix} \tag{32}$$

$$n,m \in \{1,2,...,N\} \qquad p,q \in \{1,2,...,P\}$$

The (29), (30,31), (32) are the self interaction block terms, the mutual interaction block terms and modal excitation vectors respectively.

III. RESULTS AND CONCLUSION

In order to investigate the convenience of using the characteristic modes of a single arbitrarily shaped cylinder as entire domain expansion functions, some simple considerations about the computational costs can be done. It is well known that the conventional moment of methods applied to a system of M identical scatterer leads to a discretized problem with $N_s = n_s M$ unknowns, where n_s is the number of subsections used on the single scatterer. The storage and computational costs for such a problem are of the order of $O(N_s^2)$ and $O(N_s^3)$ respectively and become prohibitive if the number or the size of scatterers increase too much. When the characteristic modes are used the size of the problem reduces to $N_c = n_c M$ where n_c is the number of modes used to expand the current. The storage and computational costs are now $O(N_c^2)+O(n_s^2)$ and $O(N_c^3)+O(n_s^3)$ where the term added in the expressions accounts for the computation of the characterstic modes on a single scatterer. The advantages of the method is quite evident if we consider that $n_c << n_s$. In all the cases that will be shown in the remaining part of the paper the ratio n_s/n_c will be always greater then 15.

In the following, results of the application of characteristic modes to linear arrays of arbitrarily shaped cylinders are presented, in all the cases shown the incidence of the plane wave is $\phi_0 = \pi/2$. In fig. 2 the scattering pattern of a linear array of three circular cylinders has been computed and it is in agreement with the one published in [5]. Fig. 3 shows the normalized echo width $\sqrt{\sigma/\lambda}$ for a linear array of five large strips (2λ wide) spaced of 4λ. In figs 4,5 and 6 results for the scattering of square cylinders are presented. Figs. 4 and 5 show the current and the polar plot of the normalized echo width for an array of two cylinders with side λ and spaced λ. Fig. 6 is relative to the scattering from an array of 10 square cylinders with side λ and spacing 4λ.

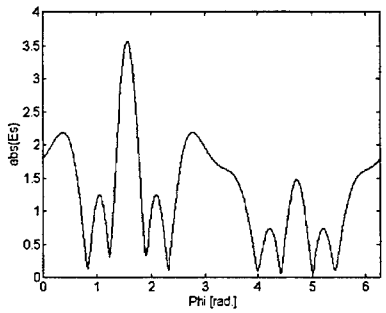

Fig. 2. Scattering pattern by a linear array of three cylinders with radius 0.12λ and spacing λ [5].

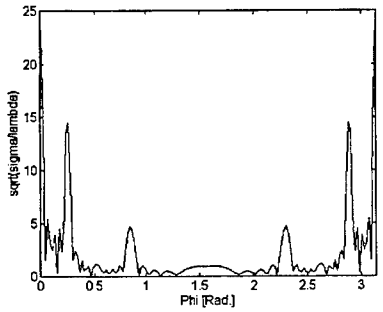

Fig. 3. Normalized echo width for a scattering by a linear array of five identical strips with width 2λ and spaced by 4λ.

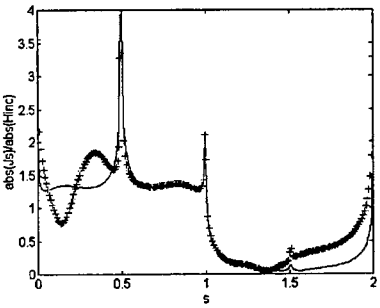

Fig.4. Current for the scattering by two identical square cylinders of side λ (line with crosses) and by a single square cylinder (cont. line).

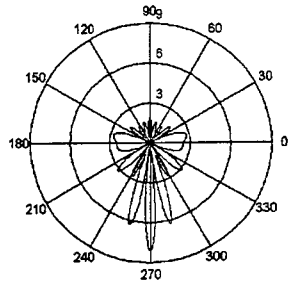

Fig 5. Polar plot of the normalized echo width for the scattering by two square cylinders as in fig.4.

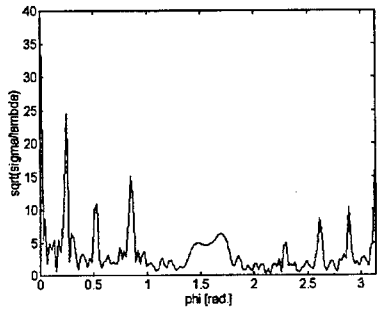

Fig. 6 Normalized echo width for the scattering from a linear array of ten square cylinders with side λ and spaced 4λ.

In conclusion it can be stated that the problem of analyzing the scattering by similar metallic bodies can be treated by use of characteristic modes for the single scatterer as basis functions in the moment method solution. This approach combines the precision of the moment method with numerical efficiency due to the fact that only a small number of basis functions are required for an accurate representation of the induced current, because of the resonant character of these modes.

REFERENCES

[1] R. Garbacz, "Modal Expansions for Resonance Scattering Phenomena", Proc. IEEE, vol.53 pp.856-864, 1965

[2] R. Harrington, J. Mautz, "Theory of Characteristic Modes for Conducting Bodies" IEEE Trans. Antennas Propag., vol.19, pp.622-628, 1971

[3] R. Harrington, J. Mautz, "Computation of Characterisic Modes for Conducting Bodies" IEEE Trans. Antennas Propag., vol.19, pp.629-639, 1971

[4] O.M. Bucci, G. Di Massa, "Use of Characteristic Modes in Multiple Scattering Problems" J. Phys. D: Appl. Phys. Vol.28 , pp.2235-2244, 1995

[5] H. Ragheb, M. Hamid, "Scattering by N parallel conducting circular cylinders" Int. J. Electro., vol. 59, pp.407-421 1985

A high order solver for problems of scattering by heterogeneous bodies

OSCAR P. BRUNO AND ALAIN SEI

Applied Mathematics, Caltech, Pasadena, CA 91125

Abstract

We present a high order integral algorithm for the solution of problems of scattering by heterogeneous bodies. Here a scatterer is represented by a variable refractive index $n(x)$ within a two-dimensional bounded region Ω; solutions of the associated Helmholtz equation under given incident fields are then obtained by high-order inversion of the Lippmann-Schwinger integral equation. A basic element in our method is the use of truncated Fourier expansions of the Green function of the problem. The logarithmic point-singularities of the Green function manifest themselves, in the finite Fourier approximations, as singular curves inside the integration domain. As we shall show, such singularity distributions allow for computation of two dimensional integrals by means of one-dimensional *high-order* integrators. The sum of the Fourier expansions of the (smoothly varying) integrals, finally, delivers the desired high order accuracy. As we demonstrate in a number of cases, our algorithms can produce very accurate solutions in fast runs on desktop computers.

1 Introduction

The calculation of electromagnetic scattering from electrically large two-dimensional surfaces remains one of the most important and challenging problems in computational science. Roughly, these problems present difficulties as they require accurate descriptions and manipulation of highly oscillatory functions. Scattering problems involving one dimensional integrals have been efficiently treated by means of high order integrators (most notably the exponentially accurate trapezoidal-type rules [10, 3]), which reduce dramatically the complexity necessary to meet a given accuracy requirement. In problems involving two-dimensional singular integrals, such as those we consider here, the need for high-order methods is even more pressing; yet, few high-order algorithms have been proposed in this context, and limited success has thereby been achieved.

In this paper we present a new high-order integral approach. For simplicity, we do not consider here the two dimensional integrals arising in scattering from three dimensional objects. Instead, we restrict ourselves to the simplest electromagnetics problem in which two-dimensional singular integrals occur: scattering by a two-dimensional heterogeneous body. A basic element in our method is the use of truncated Fourier expansions of the Green function of the problem. The logarithmic point-singularities of the Green function manifest themselves, in the finite Fourier approximations, as singular arcs inside the integration domain. As we shall show, such singularity distributions allow for computation of two dimensional integrals by means of simple one-dimensional *high-order* integrators. The sum of the Fourier expansions of the integrals together with preconditioners based on "mode-by-mode" approximate inversions and the GMRES matrix iterative solver, finally, deliver the desired high order accuracy. In some nontrivial problems our method has produced full double precision solutions in five-second desktop computations.

In problems containing very large obstacles, or obstacles consisting of a large number connected components, the complexity of our problem could be reduced by means of fast summation methods [11, 6, 12]. These methods take advantage of expansions of the integral kernels to organize the summations involved in the evaluation of multidimensional integrals. They can reduce the complexity of two dimensional integral evaluations by up to an order of magnitude, from $\mathcal{O}(N^2)$ to slightly above $\mathcal{O}(N)$, where $N \approx m^2$ is the number of discretization points in the two-dimensional domain. (The improvement is observed for sufficiently large problems, substantially larger than the explicit examples we present in this paper, since the constant in the complexity count above is itself large.) Yet, even an $\mathcal{O}(N)$ complexity is not enough to produce accurate results, unless a method of sufficiently high order is used. Indeed, a first order fast summation method requires an increase in complexity by a factor of

$100 = 10^2$ to produce a single additional digit of accuracy. In the specific examples presented below, in contrast, up to four additional digits of accuracy result from a complexity factor of $16 = 2^4$. Thus, asymptotically a high order method is faster than a low-order fast-summation method. Fortunately, algorithms which take advantage of both high order and fast summation can be devised. For large configurations such compound algorithms hold the best promise.

As we said, high order methods have often been used in problems involving one dimensional integrals [10, 3]; combinations of high-order one-dimensional integrators with fast summation techniques are given, for example, in [12, 5]. As for higher order methods considered earlier for problems related to two-dimensional singular integrals we mention [8, 1, 9, 7]. The approaches in the first two of these papers rely in some form of refinement around the singular point. The technique of [1], for example, uses a hierarchy of approximations of various orders to obtain, from a coarse grid calculation, results equivalent to those given by a low-order fine grid. This interesting approach exhibits excellent numerical properties for smooth kernels, and calculations with errors of order of $10^{(-9)}$ were reported in some cases. The accuracy of this algorithm is limited for singular integrals, however, as its discretizations do not resolve the kernel singularities to high order. As a result, applications of the method to singular problems exhibit the singularity enhancement associated with direct use of high order approximation; for two-dimensional singular integrals errors of the order of $10^{(-4)}$ were reported.

The method of [8], on the other hand, is based on Galerkin approximations using polynomial elements of high degree. This approach, which has not been implemented numerically, would use a large number of quadrature points inside the interpolation elements. Further, the number of quadrature points would be made to increase with the distance to the singularity, as a means to resolve the singular behavior, and the overall complexity of this algorithm seems quite large. A related approximating strategy was presented in [9] in connection with a method for two-dimensional scattering which couples finite-elements to a boundary integral equation on an artificial boundary. The one-dimensional integral equation enforces the condition of radiation at infinity, and the volume problem does not require use of volume Green functions. In an example considered in [9] results with errors of the order of $10^{(-3)}$ were obtained.

In [7], finally, the authors completely avoid explicit two-dimensional integrations. Instead, restricting themselves to calculation of solutions of Poisson's equation in a square (which can indeed be computed by means of a two-dimensional singular integral), they propose an algorithm which proceeds by finding solutions in small square elements as linear combinations of tensor products of Chebyshev polynomials. These basic elements are then pieced together to form a continuous solution on the square domain by means of fast multipole calculation of appropriate one-dimensional integrals. This method is extremely accurate, and it has produced full double precision solutions in fast desktop computations. The approach does rely heavily on the *surface* differential equation solved by the integral to be calculated, which is generally not available, and it does not seem to extend easily either to integrations involving general singular kernels or to integration in general domains.

In sum, general high order algorithms for problems associated with two-dimensional singular integrals have consistently found difficulties in the resolution of the high-order components of singularities and boundaries. Our approach addresses these difficulties through consideration of truncated Fourier expansions of the Green function of the problem. Such truncated expansions have the effect of re-distributing the Green's function singularity into arcs inside the integration domain. This allows for computation of the associated two dimensional integrals by means of iterated one dimensional high-order integrators. The singularity in the one dimensional integrals can be resolved analytically, and it is therefore not necessary to refine the integrators near the singular points.

Although the Fourier series of the Green function converge slowly around the logarithmic singular points, use of truncated series as explained above does lead to accurate computations. Indeed, the integrated quantities are smooth. Thus, a low order Fourier approximation of the kernel, which produces a Fourier approximation of the integral of the same order, can provide a very good approximation of the integrated quantity. The order of the expansion, therefore, needs only to account for the oscillations in the incoming wave and those of the scatterer itself, as a rather interesting cancellation of errors produces good approximation for the integrals from poor approximations for the kernel. Finally, and most importantly, our method incorporates "single mode" approximate solutions as preconditioners for the associated matrix equations.

Because of its high order nature, our approach can produce accurate results with limited requirements of

storage and computing time. For example, far field results with full double precision accuracy were obtained using only 500 discretization points (for a circle of radius = 1 with wavenumber $k = 1$ and rather sharp variations in refractive index). For more challenging configurations we consider, engineering accuracies can be obtained from our algorithms in short computing times, and improved solutions can be obtained with reasonable additional effort. Extensions of our approach to three dimensional volume and surface scatterers are envisioned.

2 Numerical Method

In this section we describe some of the main elements of our approach. The present discussion assumes a scatterer Ω whose boundary admits a polar coordinate representation

$$r = R(\theta) \tag{1}$$

with a smooth function $R(\theta)$ and, further, a smoothly varying refractive index $n(x)$. Our algorithms can easily be extended to treat piecewise smooth obstacles, and even assemblages of such, making up a general body with a piecewise smooth refractive index [2].

Letting u^{inc} denote the incident field, we seek the total field u (equal to the sum of the incident and scattered fields) as a solution of the equation

$$\Delta u + k^2 n(x) u = 0 \tag{2}$$

in the plane with conditions of radiation at infinity. As is known [3], u can be found as a solution to the Lippmann-Schwinger integral equation

$$u(x) = u^{inc}(x) - \frac{ik^2}{4} \int_\Omega H_0^1(k|x-y|) m(y) u(y) dy \tag{3}$$

where $m(y) = 1 - n(y)$ and where H_0^1 is the Hankel function. We will solve this equation by an iterative technique. The accuracy of the calculation will be determined by that of the computation of the integral on the right hand side of (3), however, thus our focus on high-order quadrature rules for such singular integrals.

Using polar coordinates (a, ψ) and (r, θ)

$$x = ae^{i\psi} \qquad y = re^{i\theta},$$

and defining

$$v(a,\psi) = u^{inc}(a,\psi) - \frac{ik^2}{4} \int_0^{2\pi} d\theta \int_0^{R(\theta)} H_0^1(k|ae^{i\psi} - re^{i\theta}|) m(r,\theta) u(r,\theta) r dr, \tag{4}$$

our equation (3) becomes $u(a,\psi) = v(a,\psi)$. An iterative solver for this equation requires repeated evaluations of the quantity $v(a,\psi)$ for given inputs $u(r,\theta)$. To obtain these quantities we introduce the Fourier expansion of u^{inc}

$$u^{inc}(a,\psi) = \sum_{\ell=-\infty}^{\infty} u_\ell^{inc}(a) e^{i\ell\psi} \tag{5}$$

and, for a given input u, that of v

$$v(a,\psi) = \sum_{\ell=-\infty}^{\infty} v_\ell(a) e^{i\ell\psi}. \tag{6}$$

In view of the addition theorem for the Hankel function (cf. [4, p. 266])

$$H_0^1(k|ae^{i\psi} - re^{i\theta}|) = \sum_{l=-\infty}^{+\infty} \mathcal{J}_\ell(a,r)e^{i\ell(\psi-\theta)}$$

$$\mathcal{J}_\ell(a,r) = J_\ell(k\min(a,r))H_\ell^1(k\max(a,r))$$

we have

$$v_\ell(a) = u_\ell^{inc}(a) - \frac{ik^2}{4}\int_0^{2\pi} e^{-i\ell\theta}d\theta \int_0^{R(\theta)} \mathcal{J}_\ell(a,r)m(r,\theta)u(r,\theta)rdr. \tag{7}$$

Once the coefficients v_ℓ are known, the function v is obtained by summation of the Fourier series (6). Thus, the task of computing v for a given input u reduces to evaluating the integrals on the right hand side of (7). The following narrative describes the high order integrator we devised for this purpose. A complete description and analysis is forthcoming [2].

Considering first the integration in r, we note that the *type* of the singularity in the corresponding integrand does not change with θ. Indeed, for all θ the kernel $\mathcal{J}_\ell$ in the r integral

$$I(a,\theta) = \int_0^{R(\theta)} \mathcal{J}_\ell(a,r)m(r,\theta)u(r,\theta)dr$$

is singular at $r = a$ (its first derivative is discontinuous there), and, further, the Hankel factor in $\mathcal{J}_\ell$ has a logarithmic point at $r = 0$. Also, the point (a,θ) corresponding to a singularity (a,ψ) is not necessarily a discretization point on a given θ radius. Finally, singularities in the Fourier coefficients $v_\ell = v_\ell(r)$ occur at values of r for which the circle of radius r is tangent to the boundary of the scatterer. To circumvent these problems we devised a one dimensional high-order integrator based on interpolations for the discretized values of the (smooth) function $m(r,\theta)u(r,\theta)$. The integration interval is divided in a number N_s of subintervals, in each one of which an interpolation of order N_p is used; an arbitrarily large number N_s of subintervals may be considered. For very large values of N_p the interpolation problem becomes ill-conditioned, however, but our experiments indicate that interpolation degrees as large as $N_p = 13$ can be used with negligible ill conditioning effects. The integrator, finally, results by analytical calculations of moments of the Hankel and Bessel functions in intervals which do not contain discontinuities for the first derivative of $\mathcal{J}_\ell$. The v_ℓ singularities mentioned above are dealt with by an appropriate change of variables.

The θ integration is also challenging since, for a given θ, the singularity (a,ψ) may lie inside or outside the interval $0 \le r \le R(\theta)$. This represents a difficulty, as it is seen by consideration of the representation

$$I(a,\theta) = H_\ell^1(ka)\int_0^{\min(a,R(\theta))} J_\ell(kr)m(r,\theta)u(r,\theta)dr + J_\ell(ka)\int_{\min(a,R(\theta))}^{R(\theta)} H_\ell^1(kr)m(r,\theta)u(r,\theta)dr.$$

which shows that, for every a, the values of θ for which $R(\theta) = a$ are singular points for the θ-integration. This problem can be resolved by consideration of smooth extensions $\tilde{I}_1$ and $\tilde{I}_2$, e.g.

$$\tilde{I}_2(a,\theta) = J_\ell(ka)\int_a^{R(\theta)} H_\ell^1(kr)m(r,\theta)u(r,\theta)dr$$

which are computed even for $a > R(\theta)$. The actual θ integrals are then obtained by means of appropriate polynomial interpolations and moment calculations. For circular scatterers it is possible and advantageous to perform the θ integrations by means of Gaussian quadrature rules.

3 Numerical Results

We begin with numerical results for a radially symmetric configuration considered in [9], for which the scatterer is the unit disk. The refractive index in the scatterer is given by $n(x) = 1 + (1 - |x|^4)^2$, while outside the disk $n(x) = 1$. It can be seen [9] that for such an axisymmetric scatterer our problem reduces to a decoupled system of one-dimensional integral equations. Our calculations below do not make any use of this fact, of course. In Table 1 we give the errors and computing times in our calculations of far field patterns for this problem. Note that in the case $k = 2$, which was considered in [9], our discretization with approximately 6000 points in the two-dimensional domain produced results with full double precision accuracy.

(The values N_r and N_θ in these tables represent the number of discretization points in the r and θ variables respectively. Here and in what follows the θ integrals were computed by means of Gaussian quadratures, while the r integrations were performed by an integrator of order 13, as mentioned in the previous section. Errors were obtained by comparison with a larger computation: 31 modes, $N_r = 145$, $N_\theta = 81$. This method of error computation was satisfactorily checked for a circular scatterer with a constant refractive index in a circle, for which exact solutions are known. All computations were performed on a Silicon Graphics R-10000 workstation.)

$k = 1$

# Modes	$N_r - N_\theta$	Error
5	13-11	(-04)
7	25-21	(-08)
11	25-21	(-15)
21		
25		

$k = 2$

# Modes	$N_r - N_\theta$	Error
5	13-11	(-02)
7	13-11	(-03)
11	25-21	(-07)
21	145-41	(-15)
25		

$k = 4$

# Modes	$N_r - N_\theta$	Error
5	13-11	(-00)
7	13-11	(-00)
11	25-21	(-02)
21	49-41	(-08)
25	97-41	(-11)

# Modes	$N_r - N_\theta$	t/Iter (sec)
5	13-11	0.17
7	25-21	0.7
11	25-21	1.05
21	49-41	12
25	97-41	55

Table 1: Errors and computing times for far field pattern calculations: $n(x) = 1 + (1 - |x|^4)^2$ and various wavenumbers k.

Our second example, presented in Table 2, is non-axisymmetric: the refractive index in the circular scatterer Ω is given by $n(x) = 1 + (1 - x_1^4)^2$, and it equals one outside Ω. Thus, $n(x)$ is discontinuous at the scattering boundary. Unlike the configuration of the previous example, the present one couples all the Fourier modes of the solution u. As a result, several additional Fourier modes are significant in the present problem for a given error tolerance. The resolution of these higher order oscillations to a given accuracy requires an increased computational effort, compare Tables 1 and 2. Still, a very good performance of our algorithm is observed.

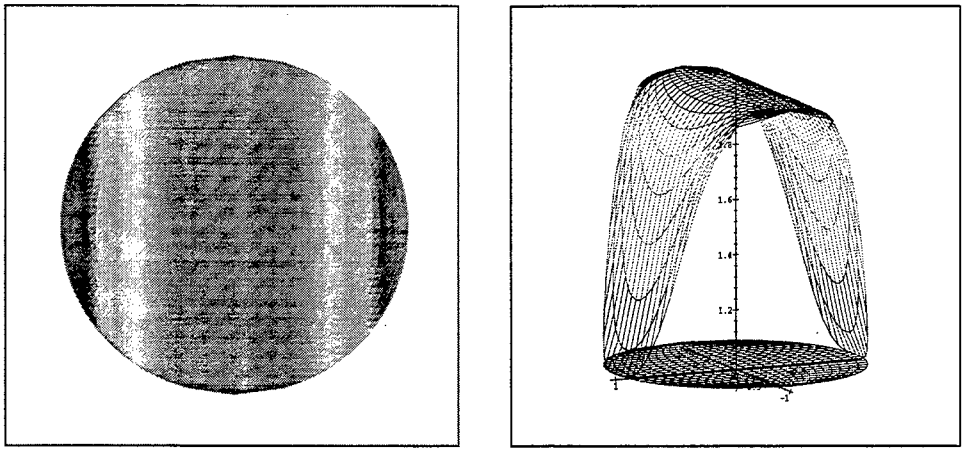

Figure 1: The refractive index $n(x) = 1 + (1 - x_1^4)^2$ for the scatterer in Table 2.
Left, contour plot; right, 3-d graph.

$k = 1$

# Modes	$N_r - N_\theta$	# Iter	Error
5	13-11	1	(-03)
7	25-21	3	(-05)
11	25-21	4	(-07)
21	49-41	8	(-12)
25	97-41	9	(-14)

$k = 2$

# Modes	$N_r - N_\theta$	# Iter	Error
5	13-11	1	(-02)
7	25-21	2	(-03)
11	25-21	4	(-05)
21	49-41	15	(-09)
25	97-41	11	(-12)

$k = 4$

# Modes	$N_r - N_\theta$	# Iter	Error
5	13-11	1	(-00)
7	13-21	1	(-00)
11	25-21	3	(-02)
21	49-41	6	(-05)
25	97-41	14	(-07)

# Modes	$N_r - N_\theta$	t/Iter (sec)
5	13-11	0.17
7	25-21	0.7
11	25-21	1.05
21	49-41	12
25	97-41	55

Table 2: Errors and computing times for far field pattern calculations:
$n(x) = 1 + (1 - x_1^4)^2$ and various wavenumbers k.

Acknowledgements: The authors gratefully acknowledge support from the AFOSR through contract No. F49620-96-1-0008). OB gratefully acknowledges support from NSF (through an NYI award and through contracts No. DMS-9200002 and DMS-9523292), from the Sloan Foundation (through the fellowships program), and from the Powell Research Foundation.

Acknowledgement and Disclaimer: Effort sponsored by the Air Force Office of Scientific Research, Air Force Materials Command, USAF, under grant number F49620-96-1-0008. The US Government is authorized to reproduce and distribute reprints for governmental purposes notwithstanding any copyright notation thereon. The views and conclusions contained herein are those of the authors and should not be interpreted as necessarily representing the official policies or endorsements, either expressed or implied, of the Air Force Office of Scientific Research or the US Government.

References

[1] A. Brandt and A. A. Lubrecht, *Multilevel matrix multiplication and fast solution of integral equations,* J. Comp. Phys. 90, 348-370, 1990

[2] O. Bruno and A. Sei, in preparation

[3] D. Colton and R. Kress, *Inverse acoustic and electromagnetic scattering theory,* Springer-Verlag, 1992

[4] L. Eyges, *The Classical electromagnetic field,* Addison-Wesley Publishing Company, 1972

[5] A. Greenbaum, L. Greengard and G. McFadden, *Laplace equation and the Dirichlet-Neumann map in multiply connected domains,* J. Comp. Phys. 105, 267-278, 1993

[6] L. Greengard and V. Rokhlin, *A fast algorithm for particle simulations,* J. Comp. Phys. 73, 325-348, 1987

[7] L. Greengard and J. Lee, *A direct adaptive Poisson solver of arbitrary order accuracy,* J. Comp. Phys. 125, 415-424, 1996

[8] C. L. Johnson and L. R. Scott, *An analysis of quadrature errors in second-kind integral methods,* SIAM J. Numer. Anal. 26, 1356-1382, 1989

[9] A. Kirsch and P. Monk, *An analysis of the coupling of finite-element and Nyström methods in acoustic scattering,* IMA J. Numer. Anal. 14, 523-544, 1994

[10] E. Martensen, *Über eine methode zum räumlichen Neumannschen problem mit einer anwendung für torusartige berandungen,* Acta Math. 109, 75-135, 1963

[11] V. Rokhlin, *Rapid solution of integral equations of classical potential theory,* J. Comp. Phys. 60, 187-207, 1985

[12] V. Rokhlin, *Rapid solution of integral equations of scattering theory in two dimensions,* J. Comp. Phys. 86, 414-439, 1990

Electromagnetic Scattering from Eccentric Cylinders at Oblique Incidence

Hashim A. Yousif
Natural Sciences Division
University of Pittsburgh
Bradford, Pa 16701
E-mail: yousif+@pitt.edu

Atef Z. Elsherbeni
Electrical Engineering Department
University of Mississippi
University, MS 38677
atef@olemiss.edu

Abstract

This paper provides an outline of an analytical solution for the scattering of electromagnetic plane waves from infinitely long eccentric cylinders. The cylinders are made of homogeneous isotropic dielectric materials with circular cross sections. The method of solution starts by expressing the incident, scattered, and internal fields in cylindrical harmonic functions with eight sets of unknown coefficients. The application of the appropriate boundary conditions along with the additional theorem of Bessel functions were utilized to derive eight coupled equations for the unknown scattering and internal coefficients. These exact equations are then solved numerically by truncating the infinite sets of coefficients into finite sets. The electric and magnetic fields can be found from these coefficients. The developed computer program is tested against several special cases and excellent agreement is obtained in every case. Numerical calculations for the backscattering and extinction cross sections are presented. These calculations show that the eccentricity parameter enhances the backscattering and extinction cross sections.

1. Introduction

The scattering of electromagnetic plane waves from eccentric cylinders at normal incidence with small eccentricity parameter with respect to the cylinders radii have been investigated by Roumeliotis, et al [1] , Roumeliotis and Kopidis [2], and Roumeliotis and Kakogiannos [3]. Parrikar, et al [4] derived expressions for the scattering cross sections of a normally incident plane wave and also for an incident cylindrical wave with no restrictions on the eccentricity parameter. They have also extended their method to include the problem of multilayered eccentric cylinder in [5]. Ragheb and Hassan [6] have introduced some other related aspects of the two layered eccentric cylinder. All of the previous studies of the eccentric cylinders have investigated the special case of normal incidence, i.e., the incident ray is perpendicular to the axis of the cylinder. Wenyan [7] investigated the scattering of the incident TM plane waves by bianisotropic eccentric cylinders at oblique incidence. However, numerical calculations are presented for the normal incidence case only. In this article, we will describe a method to find an exact analytical solution of the scattering of plane waves from infinitely long eccentric cylinders of circular cross sections and of arbitrary materials at oblique incidence with no restrictions.

Numerical examples will be presented to illustrate the scattering characteristics of the eccentric cylinders at oblique incidence.

2. The Geometry of the Problem

The geometry of the problem shown in Fig. 1 includes two infinitely long non-concentric cylinders of radii r_1 and r_2. Each cylinder is defined in its own cylindrical coordinate system, i.e., (ρ_1, ϕ_1, z_1) and (ρ_2, ϕ_2, z_2). The axes of the cylinders are separated by a distance d. Region 0 (j=0), the space outside the outer cylinder ($\rho_1 \geq r_1$), is a lossless dielectric with $\sigma_0 = 0$. Region 1 (j=1) is the space occupied by the region between the cylinders, while region 2 (j=2) is the space occupied by the inner cylindrical core, $0 \leq \rho_2 \leq r_2$. The permittivity, conductivity, and permeability of each region are denoted by ε_j, σ_j and μ_j, respectively. The propagation vector of the incident wave makes an angle θ_0 with the negative z axes and its projection makes an angle ϕ_o with the negative x axes (x_1 and x_2).

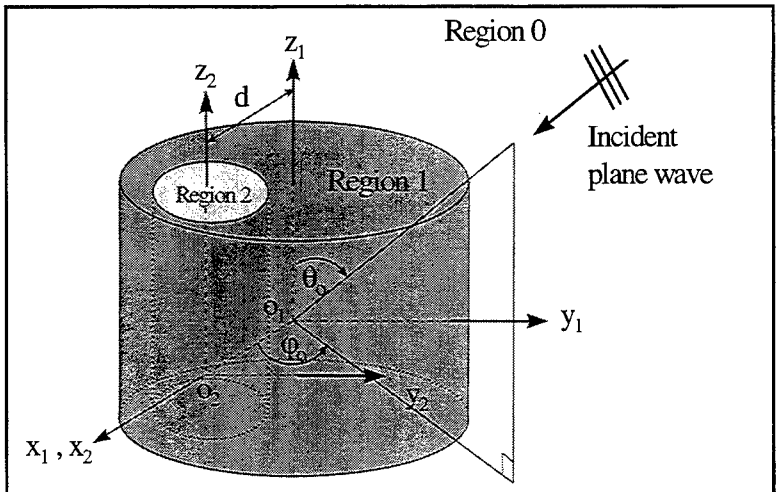

Figure 1 The geometry of the problem.

3. Solution Outline and Basic Formulation

In order to find a complete solution for this problem, two independent polarizations of the incident wave as the TM_z and TE_z should be considered. Assuming $e^{i\omega t}$ for the time dependence factor, the z-component of the incident electric field expressed in terms of the coordinates of O_1 is given by

$$E_z^{inc}(\rho_1, \phi_1, z) = E_0 \sin\theta_0 \; e^{ik_0 z \cos\theta_0} \sum_{n=-\infty}^{\infty} i^n J_n(\lambda_0 \rho_1) e^{-in(\phi_1 - \phi_0)}, \qquad (1)$$

where E_0 is the amplitude of the incident electric field which is parallel to the incident plane. Furthermore, $k_0 = \sqrt{\varepsilon_0 \mu_0}\,\omega$ is the wave number in the medium outside the cylinders and ω is the angular frequency of the incident wave. J_n is the Bessel function of the first kind of the integral order and $\lambda_0 = k_0 \sin\theta_0$.

The z-component of the scattered electric field must satisfy the wave equation. This field can be expressed in terms of the coordinates of O_1 as:

$$E_z^{sca}(\rho_1,\phi_1,z) = e^{ik_0 z\cos\theta_0} \sum_{n=-\infty}^{\infty} a_n^{(0)} H_n^{(2)}(\lambda_0\rho_1) e^{-in(\phi_1 - \phi_0)} . \quad (2)$$

The z-component of the scattered magnetic field in terms of the coordinates of O_1, which must also satisfy the wave equation, is of the form

$$H_z^{sca}(\rho_1,\phi_1,z) = e^{ik_0 z\cos\theta_0} \sum_{n=-\infty}^{\infty} b_n^{(0)} H_n^{(2)}(\lambda_0\rho_1) e^{-in(\phi_1 - \phi_0)} . \quad (3)$$

In equations (2) and (3), $H_n^{(2)}$ is the Hankel function of the second kind, and $a_n^{(0)}$ and $b_n^{(0)}$ are the unknown scattering coefficients.

Similar expressions of the field components can be written in region 1 and region 2. Appropriate boundary conditions are then applied (continuity of the tangential components of the electric and magnetic fields) at the boundaries between different regions and utilizing the translational addition theorem of Bessel functions. A system of eight set of coupled equations with eight unknown coefficients is resulted and has been solved numerically. Expressions for the scattering and internal coefficients, scattered fields, backscattering cross section, and extinction cross section can then be derived. Expressions for the backscattering and extinction cross sections for the incident TM waves are

$$\sigma_{ba}^{TM} = \frac{4}{\lambda_0 \sin\theta_0 E_0^{\,2}} \left(\left| \sum_{n=-\infty}^{n=\infty} i^n a_n^{(0)} \right|^2 + \left| \sum_{n=-\infty}^{n=\infty} i^n \beta b_n^{(0)} \right|^2 \right), \quad (4)$$

$$\sigma_{ext}^{TM} = \sum_{n=-\infty}^{n=\infty} (-i)^n \frac{a_n^{(0)}}{E_0 \sin\theta_0}, \quad (5)$$

where $\beta = \dfrac{\mu_0 \omega}{k_0}$.

4. Numerical Calculations

Figure 2 shows the extinction and backscattering cross sections (σ_{ext} and σ_{ba}) for the incident TM and TE waves as a function of ϕ_0. The solid line is for d=0 (coaxial cylinders), the dashed line is for $d=0.2\lambda_0$, and the dotted solid line is $d=0.4\lambda_0$, where λ_0 is the wavelength of the incident wave. The

radii of the cylinders are λ_0 and $0.5\lambda_0$, respectively. The relative permittivity of the outer cylinder $\varepsilon_1/\varepsilon_0$, and the inner one $\varepsilon_2/\varepsilon_0$, are 1.69 and 4.0, respectively, and the tilt angle θ_0=45°. It should be pointed out that the backscattering cross section is independent of the angle of incidence ϕ_0 for coaxial cylinders. As shown from the figure, the extinction cross section is symmetric with respect to ϕ_0 =90° as expected. It can be seen clearly from the diagram that as the eccentricity parameter d increases, both the backscattering and the extinction cross sections show significant sensitivity to this parameter.

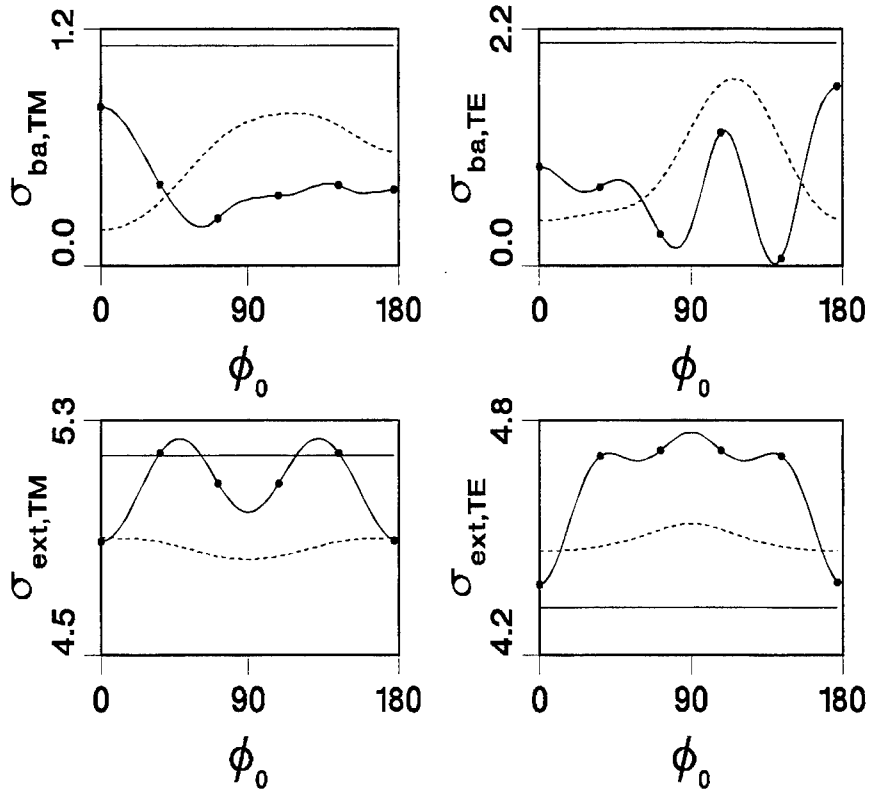

Figure 2 The back scattering and extinction cross sections per unit length (σ_{ba} and σ_{ext}) for the incident TM and TE waves as functions of the angle of incidence ϕ_0. $\varepsilon_1/\varepsilon_0$=1.69, $\varepsilon_2/\varepsilon_0$=4.0, $r_1=2r_2=\lambda_0$, θ_0=45°. The solid line is for d=0, dashed line is for d=0.2λ_0 , and dotted solid line is for d=0.4λ_0.

Also, the effect of the inner cylinder on the scattering and extinction cross sections were studied. Figure 3 shows the backscattering and extinction cross sections per unit length (σ_{ba} and σ_{ext}) for the incident TM and TE waves as functions of the size parameter of the inner cylinder k_0r_2 at normal incidence. The relative premittivities $\varepsilon_1/\varepsilon_0$ and $\varepsilon_2/\varepsilon_0$ are 1.69 and 4, respectively. The radius r_1 and the eccentricity parameter d are λ_0 and $0.25\lambda_0$, respectively. The solid line is for ϕ_0=0° and the dashed one is for ϕ_0= 90°. Both the backscattering and extinction cross sections can be used to distinguish the two cases of the incident angle (ϕ_0= 0° and 90°), however, the backscattering cross section shows more sensitivity to this parameter.

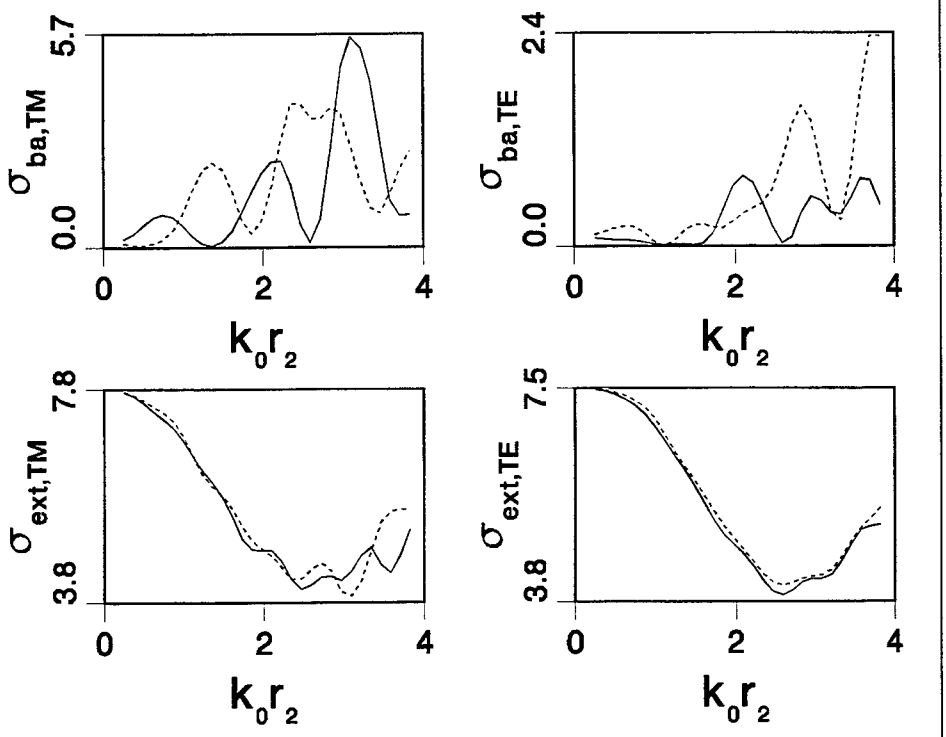

Figure 3 The back scattering and extinction cross sections per unit length (σ_{ba} and σ_{ext}) for the incident TM and TE waves as functions of the size parameter of the inner cylinder (k_0r_2). $\varepsilon_1/\varepsilon_0$=1.69, $\varepsilon_2/\varepsilon_0$=4, $r_1=\lambda_0$, θ_0=90°. The solid line is for ϕ_0=0 and the dashed line is for ϕ_0= 90°. d=0.25λ_0.

The effect of the material of the inner cylinder on the scattering patters has been studied too. Figure 4 shows the backscattering and extinction cross sections as functions of the size parameter of the inner cylinder. This cylinder is perfectly conducting cylinder. The other parameters of the figure are the same as those of figure 3. By comparing figures 3 and 4, it reveals the sensitivity of the backscattering cross section for this case.

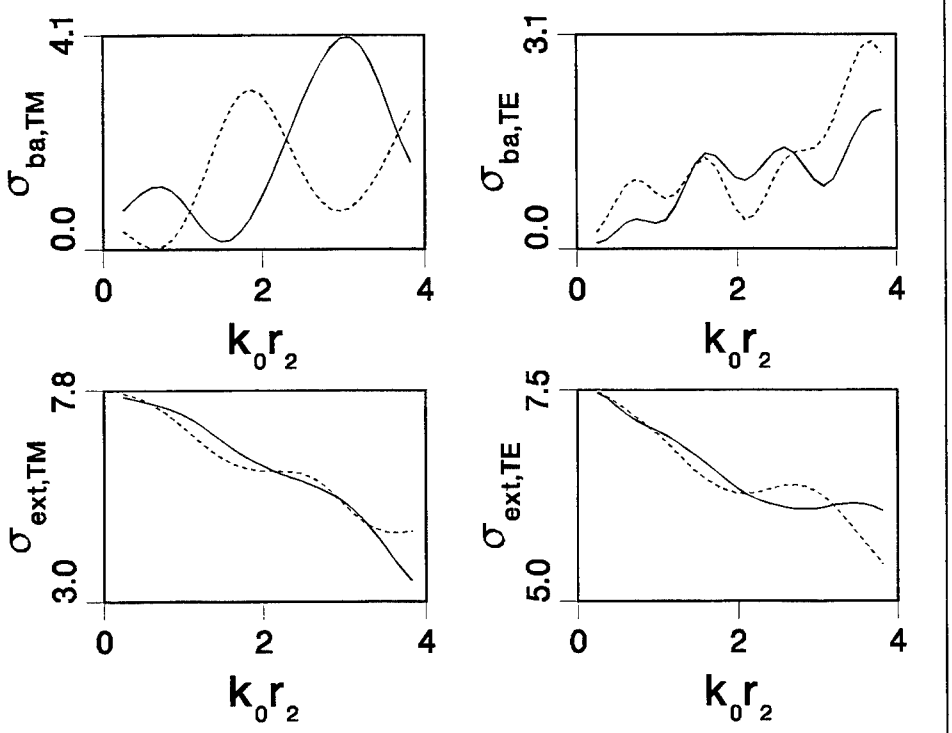

Figure 4 The backscattering and extinction cross section as functions of the size parameter of the inner cylinder. The inner cylinder is perfectly conducting. The other parameters are the same as those for figure 3.

5. Conclusion

An outline of the analytical solution of the electromagnetic scattering from two eccentric cylinders at oblique incidence was presented. The cylinders are infinitely long, penetrable, and of circular cross

sections. The numerical solution is found by inverting a truncated complex matrix. Numerical examples are presented and they indicate that the eccentric cylinder arrangement is distinguishable from that of the coaxial cylinders.

References

[1] J. A. Roumeliotis, J. G. Fikioris, and G. P. Gounaris, " Electromagnetic scattering from an eccentrically coated infinite metallic cylinder, *J. Appl. Phys.*, vol. 51, no. 8, pp. 4488-4493, 1980.

[2] J. A. Roumeliotis and P. D. Kopidis, "Scattering of plane electromagnetic waves from an eccentrically coated infinite dielectric cylinder," in *ICAP 83*, pp. 186-188.

[3] J. A. Roumeliotis and N. B. Kakogiannos, "Scattering from an infinite cylinder of small radius embedded into a dielectric one," *IEEE Trans. Antennas Propagat.*, vol. AP-42, no. 3, pp. 463-470, 1994.

[4] R. P. Parrikar, A. A. Kishk, and A. Z. Elsherbeni, " Scattering from an impedance cylinder embedded in nonconcentric dielectric cylinder," *Proc. IEE*, pt. H, vol. 138, pp.169-175, 1991.

[5] A. A. Kishk , R. P. Parrikar, and A. Z. Elsherbeni, " Electromagnetic scattering from an eccentric multilayered circular cylinder," *IEEE Trans. Antennas Propagat.*, vol. AP-40, no. 3, pp. 295-303, 1992.

[6] H. A. Ragheb and E. E. Hassan, "Radiation Characteristic of slots on conducting circular cylinder covered by eccentric dielectric cylinder," *IEE Proc. Microw. Antennas Propag.*, vol. 142, no. 2, pp. 168-172, 1995.

[7] Y. Wenyan, "Electromagnetic scattering by some composite bianisotropic eccentric cylinders," *Microwave Opt. Technol. Lett.*, vol. 10, no. 3, pp. 177-182, 1995.

ITERATIVE TECHNIQUE FOR SCATTERING AND PROPAGATION OVER ARBITRARY ENVIRONMENTS

Olga M. Conde, M.Felipe Cátedra

Grupo de Sistemas y Radio. Departamento de Ingeniería de Comunicaciones.
E.T.S.I.I. Telecomunicación. Universidad de Cantabria
Avda. Los Castros s/n. 39005 Santander
Tel: +34 42 201391 (ext.21), FAX: +34 42 201873, e-mail: felipe@gsr.unican.es

ABSTRACT

A technique based on a hybrid-iterative scheme has been developed to analyze propagation and scattering over arbitrary structures and environments. The aim of the method is to analyze, with an integral procedure, electrically large structures with an extensive reduction of time and memory requirements. Different iterative processes have been compared in order to see which one presents the best convergence in the minimum time.

1. INTRODUCTION

Nowadays, the capability to develop a tool able to estimate the influence of arbitrary structures on antenna radiation patterns is a great advantage when aspects such as time and money saving are considered. In on-board antennas design and cellular network planning, it should not have to make costly measurements. It will be useful to have a software tool to find out which is the interaction between the structure and the antenna in the first application or, which are the best locations for base stations due to propagation effects in network planning problems.

In recent applications, frequencies are going higher to avoid spectral saturation. This fact causes structure dimensions to become greater in terms of wavelengths. If we want to find the exact environment behaviour with a Low-Frequency Technique (MoM, FEM, CG-FFT) this task will be limited by computer requirements. On the other hand, with High-Frequency Methods (GO-UTD,PTD), some propagation features are still not solved. Thus, the necessity of a novel technique capable of obtaining results as exact as low-frequency methods with the computer requirements (low CPU times and memory) of the high-frequency ones is obvious.

Literature shows different hybrid methods based on integral formulations to solve problems as those previously exposed. These methods include the combination of MoM with GO-GTD [1]-[3] and with PO [4], combination of MFIE and MoM [5], or directly implementing the MFIE with an iteration procedure [6]. The developed work follows this last tendency but with the peculiarity of introducing approximation techniques to speed-up the MFIE calculations.

Basically, the method consists of finding out, after an iterative process, the electrically induced current on a perfectly conducting structure. Different iterative processes have been implemented in order to find which one gets the best convergence with the lowest CPU time consumed.

The structure is modeled in 3D and can be completely arbitrary. This degree of flexibility can be obtained with the representation of the environment in terms of parametric surfaces denominated NURBS (Non-Uniform Rational B-Spline) frequently used in the CAGD (Computer Aided Geometric Design) field.

2. ENVIRONMENT, ANTENNA AND CURRENT MODELING

This work is focused on three main facts:

- geometric representation of the environment
- antenna characterization
- hybrid-iterative method to obtain the induced current on the body surface

2.1. Environment and Antenna Description

An important aspect in this kind of tools is how to manage the geometry of the environment to be studied with the aim of being sufficiently accurate and without the need for forbidden computer requirements. This has been solved by using special parametric surfaces named NURBS (Non-Uniform Rational B-Spline) [7]. Due to the high flexibility of this representation, it is possible to model realistic geometries with a small set of data and therefore, spending low CPU processing times.

The model created to design the structure is directly used in the electromagnetic analysis. This fact represents a clear advantage because it can be understood that when one is working with the real model, accuracy is not lost as much as when the arbitrary model is translated into a piecewise-flat model. Another point to highlight is that flat and canonic surfaces are a special kind of NURBS.

On the other hand, the antennas will be modeled with a combination of infinitesimal electric dipoles *IED* and infinitesimal magnetic dipoles *IMD* [8]. After an empirical process the number and kind of dipoles, their locations and their dipolar moments can be determined in such a manner that the selected dipoles set is able to generate a radiation pattern equivalent to any commercial antenna.

2.2. Current Discretization

As in low frequency methods (MoM,CGM), current is described as a combination of basis functions sampling the electric current density over the surface of the structure. The basis functions used are those developed in [9]. These functions are a generalization of Glisson's planar rooftops but with the peculiarity of being directly defined over the parametric subpatches resulting from the automatic subdivision of surfaces. Each rooftop is defined between two subpatches, as shown in figure 1, keeping in mind that the size of each one does not exceed the typical limit of $\lambda/8$-$\lambda/10$.

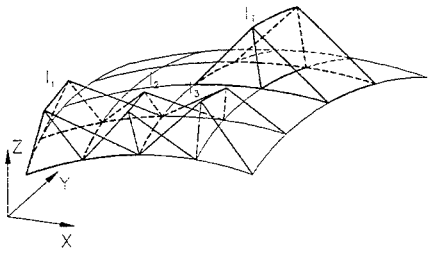

Fig. 1.- Current discretization.

The goal of the method, as in the MoM, is to determine the coefficients I_i of each basis function. These coefficients represent the electric current carried by each rooftop. Once the current is characterized, it can be determined how the environment affects the transmission-reception and thus one will be able to describe completely the radio-channel.

3. METHOD DESCRIPTION

The developed method is denominated 'iterative' because the induced current is calculated after successive iterations, each one modifying the previous solution. Also it is denominated 'hybrid' because the initial solution is PO, after this, PO is modified with the coupling information among different current rooftops.

3.1. Current Calculation

The induced current on a specific rooftop is calculated following *Amper's Law* [10] as a function of the total magnetic field radiated on that surface point:

$$I_i^{(K)} = \oint \vec{H}_i^{(K)} \cdot d\vec{l}$$

where $I_i^{(K)}$ represent the amperes in rooftop i after the iteration $^{(K)}$, and $\vec{H}_i^{(K)}$ is the total magnetic field induced by the antenna $\vec{H}^{imp}$, its own current $\vec{H}_{ii}$ and the rest of the surface currents $\vec{H}_{ij}$.

$$\vec{H}_i^{(K)} = \vec{H}^{imp} + H_{ii}^{(K-1)} + \sum_{j=1}^{n^{o}rooftops-1} H_{ij}^{(K-1)}$$

The different terms are defined as follows:

$$\vec{H}_{ii}^{(K-1)} = \frac{1}{2}\,\vec{J}_i^{(K-1)} \times \hat{n}_i$$

$$\vec{H}_{ij}^{(K-1)} = \frac{1}{4\pi}\int_{S_j'} \nabla G(\vec{r}_i - \vec{r}_j') \times \vec{J}_j^{(K-1)}\, ds'$$

where $\hat{n}_i$ is the unit normal to surface at the center point of the rooftop, $\vec{J}_i^{(K-1)}$ the previous iteration current density at the observation rooftop i, $\vec{J}_j^{(K-1)}$ the previous iteration current density at the rooftop source of the coupling and, $\nabla G(\vec{r}_i - \vec{r}_j')$, the gradient of Green's function in free space between observation and source rooftops:

$$G(\vec{r}_i - \vec{r}_j) = \frac{e^{-j\beta|\vec{r}_i - \vec{r}_j|}}{|\vec{r}_i - \vec{r}_j|} \qquad \nabla G(\vec{r}_i - \vec{r}_j) = -\frac{1 + j\beta|\vec{r}_i - \vec{r}_j|}{|\vec{r}_i - \vec{r}_j|^3}\, e^{-j\beta|\vec{r}_i - \vec{r}_j|}\,(\vec{r}_i - \vec{r}_j)$$

With the idea of minimizing CPU time, a formulation based on a previous work has been chosen [11]. This formulation states that each current rooftop can be characterized by two parameters: its electric dipolar moment $\vec{p}$ and its magnetic dipolar moment $\vec{m}$. The goal of this approximation is to make the magnetic field calculation $\vec{H}_{ij}(\vec{J})$ independent of the frequency analysis and of Green's function application point. The dipolar moments $\vec{p}$ are calculated once at the beginning of the program and after that, they are directly utilized. The effect of this formulation is to translate the integration of $\vec{H}_{ij}$ into a simple curl product and therefore get the desired time saving.

3.2. PO Approximation

The initial solution for the iterative process is PO approximation: we have current only on the illuminated area of the structure and leaving the rest of the surface with zero current, as figure 2 shows.

$$\vec{H}^{(0)} = \begin{cases} \vec{H}^{imp} & S_{illuminated} \\ 0 & S_{shadowed} \end{cases}$$

Results have been obtained where this approximation is enough to account for body scattering. It is obvious that the dimensions of the structure must be reasonably large. The main advantage of this formulation is its minimum CPU time.

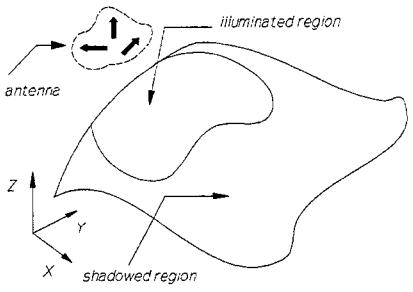

Fig. 2.- PO Approximation.

3.3. Iterative Process

A study of different iterative schemes has been made in order to see which one provides the best convergence in the lowest time. The developed methods differ in how the current is modified after each iteration. Really, the four methods developed are grouped into two sets: one with an iterative process following the *CGM* (Conjugate Gradient Method), and the other in the line of [6].

The CGM iteration process is based on the minimization of a functional. The minimization functional comes from the fact that the magnetic field inside a PEC is zero.

$$\vec{H}^{\,imp} + \vec{H}^{\,scatt} = 0 \qquad \vec{H}^{\,scatt} = -\vec{H}^{\,imp}$$

So, the algorithm minimizes the functional

$$F(\vec{J}\,) = \langle \vec{r},\vec{r}\,\rangle = \|\vec{r}\,\|^2 \quad \Rightarrow \quad \vec{r} = \vec{H}^{\,scatt} - \vec{H}^{\,imp} = L[\vec{J}^{\,i}] - \vec{H}^{\,imp}$$

where $\vec{J}^{\,i}$ is the approximate solution for the induced electric current density on the body surface and L is the operator that accounts for the coupling among current rooftops. For the algorithm implementation it has to be developed both, L as its adjoint L^{adj}.

The algorithm parts from the initial solution $\vec{J}_0$ that is always zero. After that, it progresses following [12] until the required error is obtained, the error is defined as:

$$\varepsilon_r = \frac{\| L[\vec{J}^{\,i}] - \vec{H}^{\,imp} \|}{\| \vec{H}^{\,imp} \|}$$

Depending on the impressed field chosen, $\vec{H}^{\,imp}$, two variants of the method are obtained that give rise to methods 1 and 2.

In the other set of methods the induced current is calculated after a refinement process. Beginning with the PO current, at each iteration the current is modified following the MFIE. The condition to stop the iterations is that the difference between two successive iterations will be less than a specific value. The 'error' after the iteration $^{(K)}$ is defined as:

$$\varepsilon_r^{(K)} = \frac{\| \vec{J}^{\,(K)} - \vec{J}^{\,(K-1)} \|}{\| \vec{J}_{PO} \|}$$

Also, relying on the parts of the surface that interact with each other, two different methods have been obtained.

Method 1. CGM#1.

Here, the impressed field is the field radiated by the dipoles that constitute the antenna model. The current obtained at the end of the iterative process is the current induced on the structure.

$$\vec{H}^{\,imp} = \vec{H}^{\,dip}$$
$$\vec{J}_{TOTAL} = \vec{J}_{CGM}$$

Method 2. CGM#2.

In this method, the impressed field $\vec{H}^{imp}$ is generated by the sum of the antenna field and the magnetic field radiated by the rooftops with PO current. The current after the iterative process is a residual current that enhances the current from the PO approximation.

$$\vec{H}^{imp} = \vec{H}^{dip} + \vec{H}(\vec{J}_{PO})$$
$$\vec{J}_{TOTAL} = \vec{J}_{PO} + \vec{J}_{CGM}$$

Method 3. $S^{illuminated}$ treated equal as $S^{shadowed}$

In this process, the current at the illuminated area of the structure, from the viewpoint of the antenna, is calculated taking into account the current of rooftops located in the shadowed part of the structure.

$$\vec{H}_i^{(K)} = \vec{H}^{dip} + H_{ij}^{(K-1)}(\vec{J}_j^{illum}) + \vec{H}^{(K-1)}(\vec{J}_j^{shad}) \qquad i \in S$$

Method 4. $S^{illuminated}$ treated isolated from $S^{shadowed}$

This method is based on the supposition that the current in the shadowed part of the structure is smaller than the current in the illuminated part so its coupling effect can be removed. With this assumption, the illuminated current $\vec{J}^{illum}$ could be calculated in a first step and afterwards, with $\vec{J}^{illum}$ properly defined, calculate the current in the shadowed part of the geometry $\vec{J}^{shad}$.

$$\vec{H}_i^{(K)} = \begin{cases} \vec{H}^{dip} + H_{ij}^{(K-1)}(\vec{J}_j^{illum}) & i \in S^{illum} \\ \vec{H}^{dip} + H_{ij}^{(K-1)}(\vec{J}_j^{illum}) + \vec{H}^{(K-1)}(\vec{J}_j^{shad}) & i \in S^{shad} \end{cases}$$

4. RESULTS

A comparative study among the four different techniques has been made showing their behaviour in time and convergence. They are compared with a classic Method of Moments (*MoM*) [9]. The table shows problem dimensions for the analyzed structures with 8 basis/λ (curves) and 10 basis/λ (flat).

CUBE → Side=1m, f=0.3 GHz, horizontal infinitesimal electric dipole centered over the cube at 1 λ
SPHERE → Radius=1m, f=0.3 GHz, horizontal infinitesimal electric dipole above a pole at 1.5 λ

	No.basis functions	*Memory - MoM*	*Memory - our appr.*
CUBE - 1 λ	1452	49.2 Mbytes	1.2 Mbytes
SPHERE - 1 λ	2652	152.2 Mbytes	1.4 Mbytes

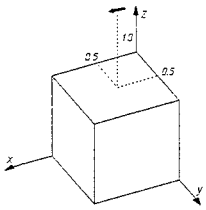

Fig. 3.- *Cube of side 1 λ.*

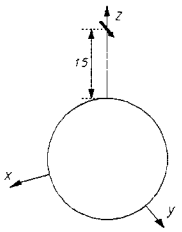

Fig. 4.- *Sphere of radius 1 λ.*

These geometries have been analyzed and radiation patterns have been obtained. Figure 5 shows cut $\phi = 0°$ for the cube and figure 6 displays cut $\phi = 90°$ for the sphere.

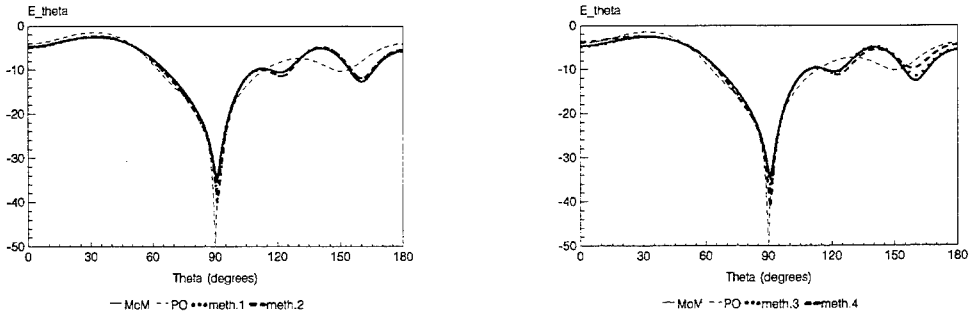

Fig. 5.- *Cut $\phi=0°$ for the CUBE - 1 λ.*

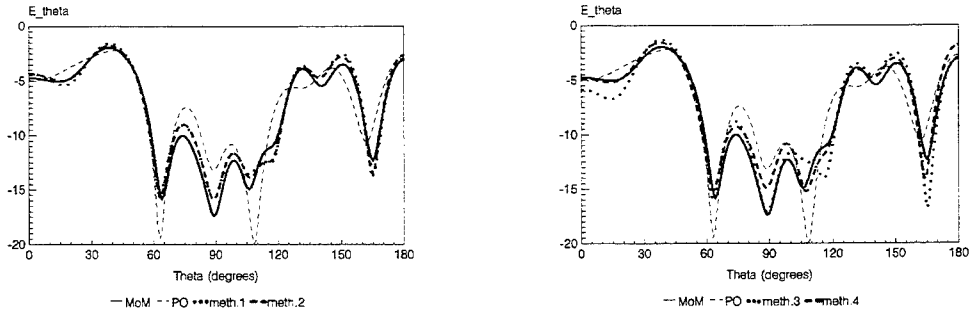

Fig. 6.- *Cut $\phi=90°$ for the SPHERE - 1 λ.*

The maximum error allowed for all the methods is 0.01. The machine utilized is *Silicon Graphics - PowerChallenge L* and next table shows the execution times for all the simulations in this computer (peak 387.5 MFlops).

With respect to the results, it has to be noted that the methods derived from the CGM present the best behaviour although they take the longest time, but always lower than the MoM.

Methods 3 and 4 also show reasonably good agreement with MoM, and they enhance the PO solution for the shadowed area. Other results make us think that these methods will be favourable when the electrical size of the structures increases. Even for this kind of environments, PO solution will be enough to analyze the scattering.

	CUBE - 1 λ	*SPHERE - 1 λ*
MoM	00:11:58	00:48:31
PO	00:00:03	00:00:12
meth.1	00:05:38	00:24:17
meth.2	00:06:33	00:25:58
meth.3	00:03:40	no convergence
meth.4	00:01:14	00:02:41

5. CONCLUSIONS

Various iterative methods have been developed to solve the MFIE. The goal of the methods is the study of electromagnetic scattering and propagation over arbitrary structures modeled in 3D using parametric surfaces denominated NURBS. Results have been shown that state good behaviour in time and memory requirements when they are compared with classic methods like, for instance, the MoM.

The application area of all these methods is the analysis of electrically large structures, where the MoM cannot operate because of restrictions in memory and CPU time.

REFERENCES

[1] G.A.Thiele, T.H.Newhouse, "A Hybrid Technique for Combining Moment Methods with the Geometrical Theory of Diffraction", *IEEE Trans. on Antennas and Propagation*, vol.23, pp.62-69, January 1975.

[2] L.W.Henderson, G.A.Thiele, "A Hybrid MM-Geometrical Optics Technique for the Treatment of Wire Antennas Mounted on a Curved Surface", *IEEE Trans. on Antennas and Propagation*, vol.30, pp.1257-1261, November 1982.

[3] L.Valle,F.Rivas,M.F.Cátedra,"A Hybrid MM-GTD Technique for the Analysis of Antennas Mounted on Arbitrary Bodies Modeled by NURBS Surfaces", *International Symposium on Electromagnetic Compatibility*, Rome, 13-16 September 1994.

[4] U.Jakobus, F.M.Landstorfer, "Current-Based Hybrid Moment Method Analysis of Electromagnetic Radiation and Scattering Problems", *ACES Journal: Special Issue on Advances in the Application of the Moment Method to Electromagnetic Radiation and Scattering Problems*, vol.10, No.3, pp.38-46, 1995.

[5] T.J.Kim, G.A.Thiele, "A Hybrid Diffraction Technique: General Theory and Applications", *IEEE Trans. on Antennas and Propagation*, vol.30, No.5, pp.888-897, September 1982.

[6] M.Kaye, P.K.Murthy, G.A.Thiele, "An Iterative Method for Solving Scattering Problems", *IEEE Trans. on Antennas and Propagation*, vol.33, No.11, pp.1272-1279, November 1985.

[7] G.Farin, *'Curves and Surfaces for Computer Aided Geometric Design'*, Academic Press, Cambridge, 1988.

[8] M.Domingo, P.Díaz, R.P.Torres, "Simple Numerical Models for On Board Antennas", *PIERS'94*, ESA, Noordwijk, Netherlands, July 1994.

[9] L.Valle, F.Rivas,M.F.Cátedra, "Combining the Moment Method with Geometrical Modeling by NURBS Surfaces and Bézier Patches", *IEEE Trans. on Antennas and Propagation*, vol.42, pp.373-381, March 1994.

[10] C.Balanis, *'Advanced Engineering Electromagnetics'*, John Wiley & Sons, New York, 1989.

[11] S.Piedra, J.E.Fernández, J.Basterrechea, M.F.Cátedra, "A Quasi-Static Tool for the EMI/EMC Analysis of Analog Circuits: PET+SEP", *submitted to IEEE Trans. on EMC*, November 1996.

[12] M.F.Cátedra, J.G.Cuevas, L.Nuño,"Scheme to Analyze Conducting Plates of Resonant Size Using the Conjugate-Gradient Method and the Fast Fourier Transform", *IEEE Trans. on AP*, Vol.36, pp.1744-1753, December 1988.

A NEW APPROACH FOR SOLVING SCATTERING PROBLEMS IN STRATIFIED CONDUCTIVE MEDIA IN TIME DOMAIN

Michael Weber and Karl Reiß

Institut für Theoretische Elektrotechnik und Meßtechnik
Universität Karlsruhe, D-76128 Karlsruhe, Germany
E-mail: weber@tem.etec.uni-karlsruhe.de

Abstract

The transient scattering of arbitrary one-dimensional stratified conductive homogeneous media for arbitrary incident wave form functions is studied in the time domain applying analytic time domain solutions. Neither discretizations as required by FDTD methods nor laplace or fourier transforms are necessary for the presented method. The computation of scattered fields is performed by solving integral equations at the boundaries between two different media and controlled by a sequential timing algorithm which backtraces the multiple scattering events for every single scattered wave. The presented impulse response for arbitrary locations allows a very fast time domain convolution for fixed geometries and varying incident wave form functions. EMI/EMC related examples are presented and discussed in detail.

1 Introduction

Scattering problems in stratified media are usually solved by matrix methods in the frequency domain. With transmission-matrices modelling the boundaries and propagation-matrices modelling the propagation between the boundaries the scattering problem can be solved, but only for harmonic wave form functions.

Calculating the scattering of *transient pulses* of arbitrary wave form functions in frequency domain leads to numerical problems due to fourier-transform, its inverse and the limited bandwidth.

To avoid fourier-transforms and limiting bandwidth, we decided to solve the transient scattering problem in the time domain applying analytic time domain solutions of Maxwell's equations.

Several analytic approaches for solving Maxwell's equations in homogeneous conductive media for one dimensional wave propagation have been published. They use the fourier-transform [1] or the laplace-transform [2, 3] solving Cauchy initial value problems. Besides the approach in [4, 5] which has been discussed very controversially, in [6] the Riemann method has been proposed, but again, only for Cauchy data.

Scattering problems usually don't have initial Cauchy data as transmission line problems do. The incident wave form function of a scattering problem is preferably modelled as a *characteristic initial value problem.* In [7] solutions for the electric *and* magnetic fields using the Riemann's integration method with a characteristic initial value problem have been introduced and applicated in [8]. The characteristic wave form function determines the wave form directly on the characteristics of the wave equation.

2 Time Domain Solutions in Conducting Homogeneous Media

The Time Domain solution of Maxwell's equations for homogeneous Conductive media (TDC) with constant material parameters ε, σ, μ for homogeneous plane TEM-waves [7] starting the propagating in $\pm z$-direction at $z = \zeta$ is given by

$$\mathbf{E}(\mathbf{r},t) = E(z,t)\,\mathbf{e}_x\,,\quad \mathbf{H}(\mathbf{r},t) = H(z,t)\,\mathbf{e}_y \tag{1}$$

using normalized time and space variables,

$$t' = \frac{t}{t_0}, \quad z' = \frac{z-\zeta}{vt_0} \text{ with } v = \frac{1}{\sqrt{\mu\varepsilon}} \text{ and } Z = \sqrt{\frac{\mu}{\varepsilon}}, \; t_0 = \frac{2\varepsilon}{\sigma} \tag{2}$$

and the real amplitude E_0, the TDC yields

$$E(t,z,\zeta) = E_+(t,z,\zeta) + E_-(t,z,\zeta) = E_0\,[+A_+ + B_+ + C_+ + A_- + B_- + C_-]\,, \tag{3}$$

$$H(t,z,\zeta) = H_+(t,z,\zeta) + H_-(t,z,\zeta) = \frac{E_0}{Z}\,[-A_+ + B_+ + C_+ + A_- - B_- - C_-]\,, \tag{4}$$

where I_n is the modified Bessel function, $w_\pm(t,z,\zeta) = \sqrt{(t' \pm z')\,(t' \mp z' - \xi)}$, $C_\pm(t,z,\zeta) = \mathrm{e}^{-t'} F_\pm\,(t' \mp z')$,

$$A_\pm(t,z,\zeta) = -\frac{1}{2}\mathrm{e}^{-t'} \int_{\xi=0}^{t' \mp z'} \mathrm{I}_0\,(w_\pm)\,F_\pm\,(\xi)\;\mathrm{d}\xi\,, \quad B_\pm(t,z,\zeta) = +\frac{1}{2}\mathrm{e}^{-t'} \int_{\xi=0}^{t' \mp z'} (t' \pm z')\,\frac{\mathrm{I}_1\,(w_\pm)}{w_\pm} F_\pm\,(\xi)\;\mathrm{d}\xi\,. \tag{5}$$

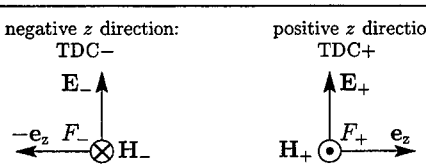

Figure 1: The TDC are separated into TDC+ and TDC− to model the propagation into $\pm z$-direction. The TDC+ and TDC− have different characteristic wave form function F_+ and F_-.

Fig. 1 shows the two different parts of the TDC propagating in $+z$ and $-z$ direction. They were calculated using Riemann's method as a characteristic initial value problem in order to get analytic solutions which can be separated into 'positive' and 'negative' parts. We want to distinguish the main part of the wave, $C_\pm$, with determined direction of propagation, and the diffusive part of the wave, $A_\pm, B_\pm$ always propagating into both directions. As the two characteristic wave form functions $F_\pm$ are the only degree of freedom besides the material parameters, they completely determine the electric (3) and magnetic (4) fields in conductive media and can be assumed arbitrary functions. Thus, the propagation of any arbitrary wave form function can be modelled.

3 Time Domain Propagation Modelling in Stratified Media

Fig. 2 shows the geometry for the scattering problem to be solved. Between the two half-spaces $z < z_1$ and $z > z_{n-1}$ there are $(n-2)$ conductive slabs, enumerated from 2 to $(n-1)$. The n different media are described by the constant material parameters $\varepsilon_k, \mu_k, \sigma_k$ with $k = 1, 2, \ldots, n$. The left half-space (medium 1) is assumed non-conductive to determine an arbitrary given incident wave

$$E_{1+}(t,z,\zeta) = E_0 \cdot F_{1+}\left(t - \frac{z}{c_1}\right) \quad , \quad H_{1+}(t,z,\zeta) = \frac{E_0}{Z_1} \cdot F_{1+}\left(t - \frac{z}{c_1}\right) \tag{6}$$

propagating towards the left boundary $z = z_1$. During the scattering process waves have to be modelled by one TDC+ and one TDC− for each slab. The waves reflected into the left non-conductive half-space are modelled by a simple wave form function whereas the wave transmitted into the right conductive half-space has to be modelled by one TDC+ .

4 Local Two Media Scattering Problems

First, we focus on an arbitrary boundary $z = z_k$ between two slabs k and $l = k+1$. Fig. 2 shows the ansatz of the TDC+ and TDC− for each slab. The TDC already simulates the propagation of the waves, thus we have only

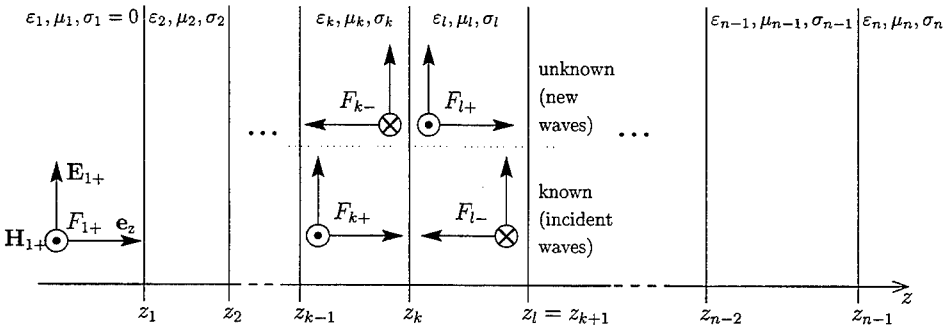

Figure 2: Stratified geometry with $k = 1, 2, \ldots, n$: $(n-2)$ conductive slabs between two half-spaces.

to enforce the boudary conditions for the tangential field components at $z = z_k$ for $k = 1, 2, \ldots, (n-1)$

$$E_{k+}(t, z_k, z_{k-1}) + E_{k-}(t, z_k, z_k) = E_{l+}(t, z_k, z_k) + E_{l-}(t, z_k, z_l)\,, \tag{7}$$

$$H_{k+}(t, z_k, z_{k-1}) + H_{k-}(t, z_k, z_k) = H_{l+}(t, z_k, z_k) + H_{l-}(t, z_k, z_l)\,. \tag{8}$$

Eq. (7) and (8) yield a coupled system of two Volterra Integral Equations of second kind (VIEQ) for the unknown characteristic wave form functions F_{k-} and F_{l+}

$$\begin{pmatrix} F_{l+}(t) \\ F_{k-}(t) \end{pmatrix} = \int_{\xi=0}^{t} \begin{pmatrix} O_k & P_k \\ Q_k & R_k \end{pmatrix} \begin{pmatrix} F_{l+}(\xi) \\ F_{k-}(\xi) \end{pmatrix} \mathrm{d}\xi + \begin{pmatrix} e^{\alpha_l t} S_{l+} \\ e^{\alpha_k t} S_{k-} \end{pmatrix} \tag{9}$$

with $w_{i\pm}(0) = |\gamma_i| \sqrt{t(t-\xi)}$, $\alpha_i = \gamma_i = \frac{\sigma_i}{2\varepsilon_i}$ the kernel yield

$$O_k := r_{kl} \frac{\gamma_l}{2} \mathrm{I}_0(w_{l+}(0)) - \frac{\gamma_l^2}{2} t \frac{\mathrm{I}_1(w_{l+}(0))}{w_{l+}(0)}\,, \quad P_k := -e^{(\alpha_l - \alpha_k)t} d_{kl} \frac{\gamma_k}{2} \mathrm{I}_0(w_{k-}(0))\,,$$

$$Q_k := -e^{(\alpha_k - \alpha_l)t} d_{lk} \frac{\gamma_l}{2} \mathrm{I}_0(w_{l+}(0))\,, \qquad R_k := r_{lk} \frac{\gamma_k}{2} \mathrm{I}_0(w_{k-}(0)) - \frac{\gamma_k^2}{2} t \frac{\mathrm{I}_1(w_{k-}(0))}{w_{k-}(0)}\,,$$

and

$$S_{l+}(t) := d_{kl} \left[B_{k+}(t, z_k, z_{k-1}) + C_{k+}(t, z_k, z_{k-1})\right] - A_{l-}(t, z_k, z_{k+1}) - r_{kl} \left[B_{l-}(t, z_k, z_{k+1}) + C_{l-}(t, z_k, z_{k+1})\right]\,,$$

$$S_{k-}(t) := d_{lk} \left[B_{l-}(t, z_k, z_{k+1}) + C_{l-}(t, z_k, z_{k+1})\right] - A_{k+}(t, z_k, z_{k-1}) - r_{lk} \left[B_{k+}(t, z_k, z_{k-1}) + C_{k+}(t, z_k, z_{k-1})\right]\,,$$

using eq. (5) and the real Fresnel coefficients for perpendicular incidence

$$r_{kl} = \frac{Z_l - Z_k}{Z_k + Z_l} \quad , \quad d_{kl} = \frac{2\,Z_l}{Z_k + Z_l}\,. \tag{10}$$

For numerical evaluation the integration is replaced by summation using the trapezoidal rule. Evaluating eq. (9) the characteristic wave form functions F_{l+} and F_{k-} are given and by integrating eq. (3) and (4) we get the electric and magnetic fields for both slabs k and $l = k+1$. Fig. 3 shows local two media problems for $n = 4$.

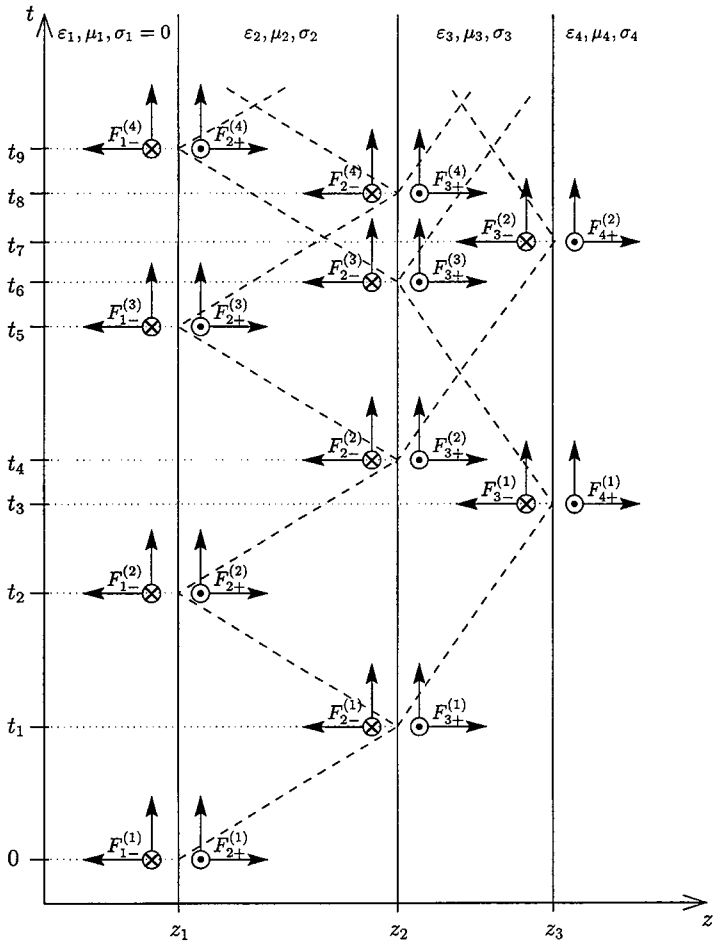

Figure 3: For $n = 4$ different media the scattered waves are shown in a (z,t)-graph. Their (z,t)-trajectories are outlined by dashed lines with the slope proportional to the inverse of the velocity of propagation. The upper index of the characteristic wave form function (F) enumerates the multiple scattered waves in the same medium with the same direction of propagation. In [8] was shown that all $F_{k\pm}^{(i)}$ can be summed up to one common characteristic wave form function $F_{k\pm} = \sum_i F_{k\pm}^{(i)}$. Thus, only one TDC+ and TDC− for each medium is required.

5 Impulse Excitation

We assume $F_{1+} = \delta(t)$ in eq. (6) an incident dirac impulse. Therefore the characteristic wave form functions have to be separated into an ordinary function part $F^{<N>}$ and dirac impulse part $F^{<\delta>}$. Eq. (9) then yields

$$\begin{pmatrix} F_{l+}^{<N>} + F_{l+}^{<\delta>} \\ F_{k-}^{<N>} + F_{k-}^{<\delta>} \end{pmatrix} = \int_{\xi=0}^{t} \begin{pmatrix} O_k & P_k \\ Q_k & R_k \end{pmatrix} \begin{pmatrix} F_{l+}^{<N>} + F_{l+}^{<\delta>} \\ F_{k-}^{<N>} + F_{k-}^{<\delta>} \end{pmatrix} \mathrm{d}\xi + \begin{pmatrix} e^{\alpha_l t}\left[S_{l+}^{<N>} + S_{l+}^{<\delta>}\right] \\ e^{\alpha_k t}\left[S_{k-}^{<N>} + S_{k-}^{<\delta>}\right] \end{pmatrix} \qquad (11)$$

and yields two equations

$$\begin{pmatrix} F_{l+}^{<\delta>} \\ F_{k-}^{<\delta>} \end{pmatrix} = \begin{pmatrix} e^{\alpha_l t} S_{l+}^{<\delta>} \\ e^{\alpha_k t} S_{k-}^{<\delta>} \end{pmatrix}, \quad \begin{pmatrix} F_{l+}^{<N>} \\ F_{k-}^{<N>} \end{pmatrix} = \int_{\xi=0}^{t} \begin{pmatrix} O_k & P_k \\ Q_k & R_k \end{pmatrix} \begin{pmatrix} F_{l+}^{<N>} + F_{l+}^{<\delta>} \\ F_{k-}^{<N>} + F_{k-}^{<\delta>} \end{pmatrix} \mathrm{d}\xi + \begin{pmatrix} e^{\alpha_l t} S_{l+}^{<N>} \\ e^{\alpha_k t} S_{k-}^{<N>} \end{pmatrix}$$

for the Dirac impulses and the normal function parts, respectively.

6 Sequential Timing Algorithm for Multiple Scattering

The Sequential Timing Algorithm builds up the sequence and time intervals during which the local two media problems have to be iterated and composed to the entire solution. The following rules have to be considered (see fig. 2):

- the computation of the unknown F_{k-}, F_{l+} is only possible while the incident F_{k+}, F_{l-} are known, so they have to be computed first.
- to avoid computations of zero incidence, the iterations at z_k begin after the time of first incidence $\tau_k = 0 + \sum_{i=1}^{k-1} T_{i \to i+1}$ with $T_{i \to i+1}$ as the propagation time from $z = z_i$ to $z = z_{i+1}$.
- the entire scattering problem is solved as soon as every local two media problem at $z = z_k$ has reached maximum computation time for the whole scattering calculation.

Fig. 4 shows the flow chart of the algorithm. In the beginning the algorithm sets all `done[k]=-1` to the first incidence time τ_k. Then, if the right incidence is unknown for the next time interval the algorithm steps one boundary to the right (`k++`) until `right[k=n]`$=\infty$ (no wave incident from the right half-space). If the incident waves (`myt:=min(left[k],right[k])`) are known longer than the iteration for $z = z_k$ has been performed (`done[k]<myt`), the iteration of the local two media problem for $z = z_k$ is performed until `done[i]=myt`. If the left incidence is unknown for the next time interval, the algorithm steps one boundary to the left (`k--`).

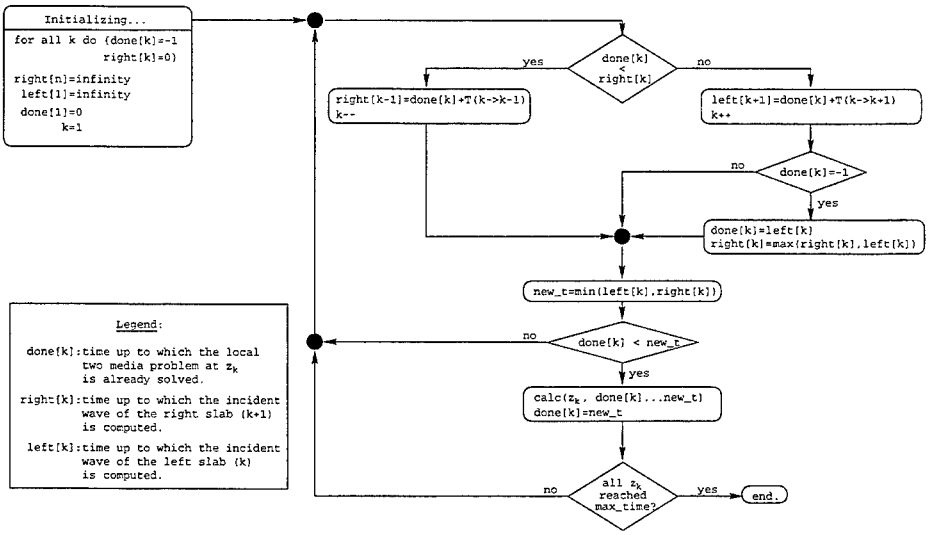

Figure 4: Flow chart of the sequential timing algorithm which controls the iteration of the $(n-1)$ VIEQs (9).

7 Time Discretization for Numerical Evaluation

For the numerical evaluation of the VIEQs at the boundaries $z = z_k$ we have to use a common time discretization as the computed characteristic wave form functions are excitations to all the other boundaries.

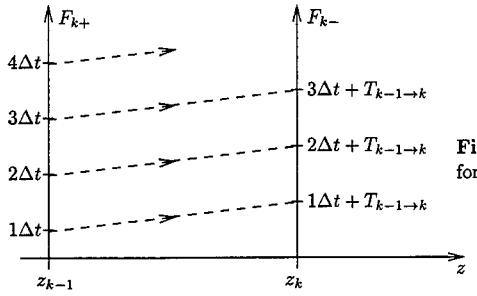

Figure 5: Considering the propagation time for time discretization.

In Fig. 2 we assume F_{k+} as a function of Δt

$$F_{k+} = \{F_{k+}(1 \cdot \Delta t),\, F_{k+}(2 \cdot \Delta t),\, \ldots,\, F_{k+}(i \cdot \Delta t),\, \ldots\} \tag{12}$$

and incident to $z = z_k$ after the propagation time from z_{k-1} to z_k

$$T_{k-1\to k} = \frac{z_k - z_{k-1}}{c_k} \tag{13}$$

(see fig. 5) and get

$$F_{k-} = \{F_{k-}(T_{k-1\to k} + 1 \cdot \Delta t),\, F_{k-}(T_{k-1\to k} + 2 \cdot \Delta t),\, \ldots,\, F_{k-}(T_{k-1\to k} + i \cdot \Delta t),\, \ldots\} \tag{14}$$

with the same time steps Δt but displaced by the propagation time $T_{k-1\to k}$. F_{k-} is again incident to $z = z_{k-1}$ after $2 \cdot T_{k-1\to k}$ and has to be considered in the numerical evaluation in eq. (9). Therefore, we have to enforce

$$T_{k-1\to k} = m \cdot \Delta t\ , m = 0, 1, 2, \ldots\ . \tag{15}$$

In order to save computation time and memory we have to determine the maximum possible Δt as the *greatest common divisor* for rational numbers of all $T_{k-1\to k}$ with $k = 2, 3, \ldots, (n-1)$.

8 Simulations

As an EMC application for the presented method we discuss the shielding properties of two parallel conductive slabs shown in fig. 6 which may enclose an electronic device between them. Therefore, we calculate the impulse response ($F_{1+} = \delta(t)$ in eq. (6)) for $z = 1.0cm$ shown in fig. 9 and for $z > 2.0cm$ shown in fig. 7 in order to get the electromagnetic field impulse responses.

Then, applying an incident gaussian pulse, we get the electromagnetic fields for $z = 1.0cm$ shown in fig. 10 and for $z > 2.0cm$ shown in fig. 8 by a very fast convolution with the incident gaussian pulse. For any arbitrary incident wave form function it is possible to calculate the electromagnetic fields easily by convolution with the incident electromagnetic fields in eq. (6). Fig. 11 and fig. 12 show the electric fields for $z = 1.0cm$ for an incident triangular and rectangular pulse of the same pulse width as the gaussian pulse.

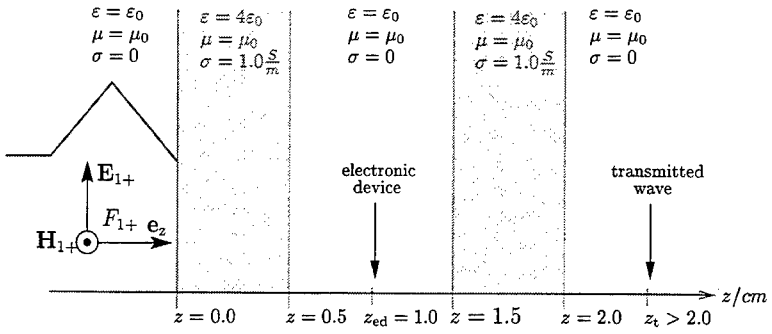

Figure 6: Shielding problem with two conductive slabs. We observe the electromagnetic field in the middle of the slabs $z = z_{ed}$ and the right outside of the geometry z_t. For $t = 0$ the incident pulse just arrived at the most left boundary shown here for a triangular pulse.

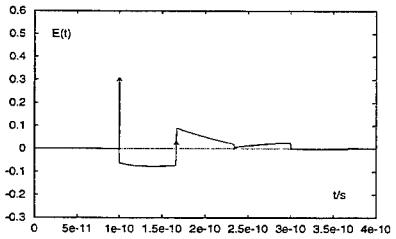

Figure 7: Impulse response for the transmitted electric field at $z = z_t$.

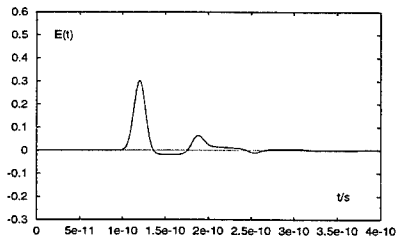

Figure 8: Transmitted gaussian pulse with $t_\sigma = 3.33 \cdot 10^{-12} s$ at $z = z_t$.

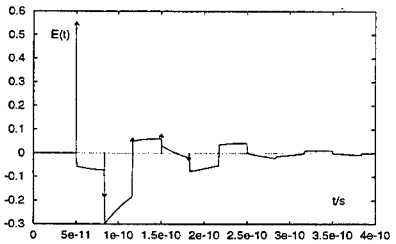

Figure 9: Impulse response for the electric field at $z = z_{ed}$.

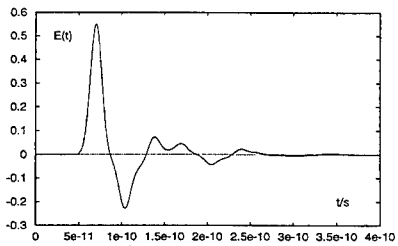

Figure 10: Electric field at $z = z_{ed}$ caused by an incident gaussian pulse. The negative amplitude for $t = 1.1 \cdot 10^{-10}$ is caused by the right slab. The further signal is caused by the multipe reflection inside and between the slabs.

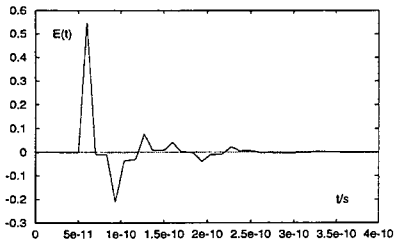

Figure 11: Electric field at $z = z_{\text{ed}}$ caused by an incident triangular pulse of pulse width $t_{\text{PW}} = 2.0 \cdot 10^{-11} s$.

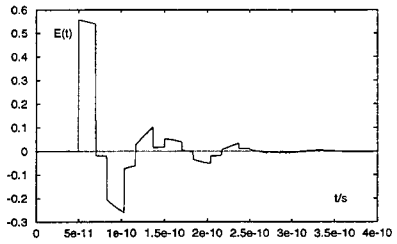

Figure 12: Electric field at $z = z_{\text{ed}}$ caused by an incident rectangular pulse of pulse width $t_{\text{PW}} = 2.0 \cdot 10^{-11} s$.

9 Conclusion

The presented method is particular applicable for studying the scattering of arbitrary wave form functions in stratified media with constant material parameters. Being able to compute the impulse response for the electric and magnetic fields for arbitrary locations, electromagnetic fields can easily be computed by convolution in time domain just in seconds. Thus, it is a powerful tool for studying stratified homogeneous shielding geometries for particular signal forms.

Due to the flexibility of the analytic time domain solutions, the transmission line problem with piecewise constant R', L', C', G' can be solved with the same approach.

References

[1] J.A. Stratton. *Electromagnetic Theory.* McGraw-Hill, New York, 1941.

[2] P. I. Richards. Transients in conducting media. *IEEE Trans. on Antennas and Propagation*, 6:178–182, April 1958.

[3] G. Lehner and H. Maisch. Green's functions for transient plane waves in finite and infinite lossy media. *Archiv für Elektrotechnik*, 78:345–363, 1995.

[4] H. F. Harmuth. Correction of Maxwell's equations for signals I. *IEEE Trans. on Electromagnetic Compatibility*, 28:250–258, November 1986.

[5] H. F. Harmuth. Correction of Maxwell's equations for signals II. *IEEE Trans. on Electromagnetic Compatibility*, 28:259–266, November 1986.

[6] O. R. Asfar. Riemann-Green function solution of transient electromagnetic plane waves in lossy media. *IEEE Trans. on Electromagnetic Compatibility*, 32:228–231, August 1990.

[7] M. Schinke and K. Reiß. A new method for solving scattering problems with conducting media in the time domain. In *11th Annual Review of Progress in Applied Computational Electromagnetics (ACES 95)*, volume I, pages 37–44, March 20–25 1995, Monterey, CA, USA.

[8] M. Weber, M. Schinke and K. Reiß. Reflection and transmission properties of a conductive slab in time domain. In *IEEE International Symposium of Antennas and Propagation and URSI Radio Science Meeting*, volume 3, pages 2072–2075, July 21–26 1996, Baltimore, MD, USA.

Effects of Multiple Scattering in Photon Correlation Spectroscopy*

V. I. Ovod*,*, D. W. Mackowski**, D.F. Nicoli***, R. Finsy******

* Department of Chemistry, University of California, Santa Barbara, CA 93106
** Department of Mechanical Engineering, Auburn University, AL 36849
*** Particle Sizing Systems, 75 Aero Camino, Suite B, Santa Barbara, CA 93117
**** Department of Theoretical Physical Chemistry, Vrije Universiteit Brussel, Pleinlaan 2, B-1050 Brussel, Belgium

Abstract

A numerical technique to model the effect of multiple scattering by concentrated interacting particles on a time autocorrelation function (ACF) of the scattered light is developed. Systematic error of the modeling of the particle dynamics and the error of the ACF estimation was investigated for Brownian free particles. It has been shown that the systematic error and a decreasing of the dynamic range of the ACF exponential behavior for free particles are caused by the low and the high frequency oscillations of terms, averaged in the ACF estimator.

An optimization of the numerical model has been carried out in order to reach a required magnitude of the systematic error and a maximum of the dynamic range by a minimum of calculation expenditures. The dynamics of an ensemble of particles was generated by a stochastic technique. Influence of the multiple scattering by interacting spheres on the ACF depending on the diameter of spheres and on their concentration was investigated by using a rigorous multiple scattering technique developed by D. W. Mackowski. Results are in a good agreement with experimental data reported by H. Wiese and D. Horn. The model can be used to further develop photon correlation spectroscopy for the characterization of particles in concentrated and turbid media.

1 Introduction

Photon correlation spectroscopy (PCS) is a promising technique for particle sizing in turbid colloidal systems [1]. Application of optical fibers in PCS in principle simplifies measurements of high concentrated dispersed media [2]. The problem of an optimal fiber optical sensor for turbid media is multiple scattering of light by particles, which affects the exponential behavior of the time autocorrelation function (ACF). The ACF is the main measured property of PCS [3], which can be estimated by the following average

$$g_e^{(1)}(\tau) = \frac{\langle \mathbf{E}(t+\tau)\, \mathbf{E}^*(t) \rangle}{\langle \mathbf{E}(t)\, \mathbf{E}^*(t) \rangle}$$

* Correspondence should be addressed to:
V. I. Ovod, Particle Sizing Systems, 75 Aero Camino, Suite B, Santa Barbara, CA 93117. Phone: (805) 968 14 97. Fax: (805) 968 03 61. E-mail: PSS@worldnet.att.net

where $\mathbf{E}(t)$ is the electric vector of the scattered field, t is the measurement time, τ is the delay time. In fact, the problem is that most of the known theoretical models for PCS work without any rigorous computation of multiple light scattering (MLS) by the ensemble of moving particles[1,3]. To predict the effect of multiple scattering in PCS measurements, a numerical method is derived. As shown in Fig. 1, the model involves a generator of clusters, a simulator of multiple scattering in a cluster, an averaging scheme for the ACF estimation and a model for the ACF presentation.

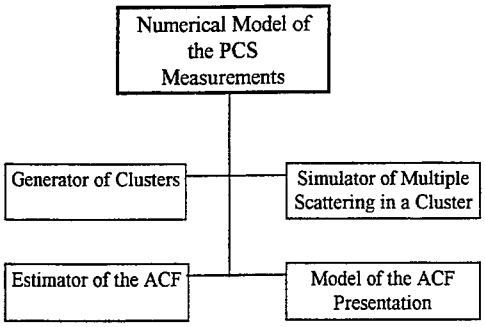

Fig. 1. Numerical model of the PCS measurements involving four separate modules.

For the generation of the dynamics of interacting particles a stochastic technique is used. According to this technique, a time set of clusters is generated in order to model the motion of particles. At each discrete time interval, a corresponding cluster is characterized by the new positions of the interacting particles.

The multiple scattering is calculated using the rigorous algorithm of D. W. Mackowski [4]. Most calculation "expenditures" (run times) are related to the calculations of multiple scattering in a cluster. The expenditures strongly depend on the number of particles N_p in a cluster and on the number of clusters N_c [4]. Hence, to model the PCS measurements in a reasonable length of time, the number of particles and the number of clusters should be limited.

This limitation causes a decrease in the calculation accuracy of the model. The model accuracy involves two components: the generating accuracy of the particle dynamics and the accuracy of the ACF estimator (see Fig. 1). Accuracy of the ACF estimator depends on the scheme chosen for the average of the time-dependent electrical vector of scattered light. Hence, to be sure that the change of the simulated ACF is caused by MLS, the above mentioned components of the accuracy should be negligible. Two criteria for the simple case of Brownian non-interacting particles were used to check the calculation accuracy: the relative mean-squared displacement of particles should be closed to unity, and the ACF should have an exponential behavior.

An effective scheme is used for the quickly averaging the scattered electric field. A set of optimal parameters of this scheme is found, taking into account the minimization of the particle number N_p and cluster number N_c for a given required ACF accuracy.

After the above mentioned optimization, the effect of multiple scattering on the ACF was modeled and compared with experimental data.

2 Numerical Model

2.1 Particle Dynamics: Generator of Clusters

As mentioned above, instead of a dispersed media characterized by volume fraction φ, only N_p particles in a cubic scattering volume are taken with the same φ. The length of the cube is given by

$$l = d_p \sqrt[3]{\frac{\pi N_p}{6\varphi}}$$

where d_p is the diameter of monodispersed spherical particles.

Hence, a set of clusters is generated in order to model the motion of particles at discrete observation times. Let $\Delta\tau$ be a discrete time interval.

In order to provide the minimization of terms averaged in the ACF estimator, the following assumption of the discrete motion of particles is used

$$\left|\Delta \mathbf{X}\right|^2 = \left\langle \left|\Delta \mathbf{X}(\Delta\tau)\right|^2 \right\rangle$$

where $|\Delta\mathbf{X}|$ is the magnitude of any modeled unit displacement of any particle in the cubic scattering volume after the time interval $\Delta\tau$ and $\langle|\Delta\mathbf{X}(\Delta\tau)|^2\rangle$ is the 3-D mean squared displacement characterizing the real motion of particles.

Free Particle Diffusion

In the proposed model, the 3-D mean-squared displacement of a free particle after time $\Delta\tau$ is given by

$$\left\langle \left|\Delta \mathbf{X}\left(\Delta\tau, \varphi \to 0\right)\right|^2 \right\rangle = \left(\frac{f}{q}\right)^2$$

where f is the non-dimensional parameter of the particle displacement, q is the magnitude of the scattered wave vector $\mathbf{q} = \mathbf{k}_i - \mathbf{k}_s$, $\mathbf{k}_i$ is the incident wave-vector and $\mathbf{k}_s$ is the scattering vector. Hence,

$$\left|\Delta \mathbf{X}_d\right| = \frac{f}{q}$$

is the modeled unit discrete displacement of any free particle.

The initial position $\mathbf{X}(j=1,p)$ of each p-th particle and a new position $\mathbf{X}(j,p)$ after the j-th step of motion (j-th cluster) are chosen randomly without checking whether the new space is already occupied by another particle and without a space limitation on the particle motion. Motion of any p-th particle is described by

$$\mathbf{X}\left(j,p\right) = \mathbf{X}\left(j-1,p\right) + \mathbf{s}\left|\Delta \mathbf{X}\right|, \text{ for } j \geq 2$$

where

$$\mathbf{s} = s_x\mathbf{x} + s_y\mathbf{y} + s_z\mathbf{z}$$

is the unit random vector. To generate the unit random vector, the function ran2(idum) is borrowed from [5]. This function is recommended [5,p.272] for generating more than

100,000,000 random numbers in a single calculation. The parameter idum (defined in [5]) is used for initialization of the generator. A new magnitude of this parameter is responsible for a new "history" of generated clusters.

Motion of Interacting Spheres

Discrete motion of interacting spheres is modeled by checking whether a new space is already occupied by another particle. The motion of each sphere is limited also by a cubic scattering volume. Thus, any attempt of a particle to leave the scattering volume is changed by another random attempt, which fits the above mentioned limitations.

The effect of many-body hydrodynamic interactions between an arbitrary number of spheres on the short-time diffusion coefficient was investigated by C.W.J. Beenakker and P. Mazur [6]. In order to take into account this effect, the unit discrete displacement is taken depending on the volume faction, as shown in Table 1 (the data are borrowed from [6, p.362]).

Table 1. Dependence of the square of the relative unit discrete displacement on the volume fraction of a dispersed media (data are borrowed from [6, p.362]).

φ	0	0.5	0.1	0.15	0.2	0.25	0.3	0.35	0.4	0.45
$(<\|\Delta\mathbf{X}\|>/<\|\Delta\mathbf{X}_o\|>)^2$	1	0.9	0.79	0.69	0.6	0.51	0.44	0.38	0.33	0.33

2.2 Measured Properties of PCS in a Time Discrete Scale

As mentioned above, the time autocorrelation function is the main property of PCS. For free particle diffusion, the estimation of the time ACF of the electric field scattered into the far zone can be simplified by averaging only phase factors [1,3]

$$g_e^{(1)}(\tau) = \left\langle \exp\left(i\,\mathbf{q}\left(\mathbf{X}(\tau) - \mathbf{X}(0)\right)\right)\right\rangle$$

where $\mathbf{X}(\tau)$ is the position vector of a particle at delay time τ. It is well known that the exact averaging in the last equation gives an exponentially decaying function

$$g^{(1)}(\tau) = \exp\left(-\frac{\tau}{\tau^*}\right)$$

where

$$\tau^* = \frac{1}{D_o q^2}$$

is the decay time and D_0 is the free particle diffusion coefficient.

Let the discrete scale of time be characterized by the set of integers {k,j}, so that

$$\tau = k\,\Delta\tau$$

$$t = j\Delta\tau$$

and

$$D_0 = \frac{|\Delta\mathbf{X}_o|^2}{6\,\Delta\tau}$$

Then the above equations for the ACF can be presented in the discrete scale of time in the following form:

$$g_e^{(1)}(k) = \frac{\langle \mathbf{E}\,(j+k)\ \mathbf{E}^*(j) \rangle}{\langle \mathbf{E}\,(j)\ \mathbf{E}^*(j) \rangle}$$

for interacting particles;

$$g_e^{(1)}(k) = \left\langle \exp\left(i\ \mathbf{q}\ (\mathbf{X}(k) - \mathbf{X}(0))\right)\right\rangle$$

and

$$g^{(1)}(k) = \exp\left(-\frac{k}{k^*}\right)$$

for free particle diffusion, where

$$k^* = \frac{6}{f^2}$$

is the non-dimensional decay time.

Other kinds of the PCS measured properties can be described by the relative diffusion coefficient (RDC)

$$RDC\,(k,\varphi) = \frac{D(k)}{D_o} = \frac{\ln\left(g_e^{(1)}(k)\right)}{\ln\left(g^{(1)}(k)\right)} = -\frac{\ln\left(g_e^{(1)}(k)\right)}{k/k^*}$$

or by the relative mean diffusion coefficient (RMDC)

$$RMDC\,(k_d,\varphi) = \frac{\left\langle D(k)\right\rangle}{D_o} = -\frac{\left\langle \ln\left(g_e^{(1)}(k)\right)\right\rangle}{k/k^*}$$

where k_d is the dynamic range over which the last average is provided and D(k) is the diffusion coefficient at the k-th discrete time.

2.3 Averaging Schemes for ACF Estimation

Scheme Taking Into Account Rigorous Simulation of Multiple Scattering by Particles

The time autocorrelation function of the electric field (multiple scattered by interacting particles) can be estimated by simple averaging scheme

$$g_e^{(1)}(k) = \frac{1}{N_q}\sum_{h=x,y,z}\left|\frac{\sum_j^b \left(\mathbf{E}\,(j+k)\,\mathbf{E}^*(j)\right)}{\sum_j^b \left(\mathbf{E}\,(j)\,\mathbf{E}^*(j)\right)}\right|$$

where N_q denotes the number of different h-th directions of the incident wave-vector over which an additional average is provided. This additional average allows an increase in the efficiency of the calculation of the multiple scattering by rotation of clusters. The rotation is a very important advantage realized in the code of D. W. Mackowski [4]. Only three orientations $N_q = 3$ of scattered wave-vector (along the axes X,Y and Z of the cluster's coordinate system) are used below.

Two Schemes Based on "Hindered Self-Diffusion" and "Collective" Assumptions

For the specific case of a single scattering by Brownian non-interacting particles, the above average can be simplified by using a so called "hindered self-diffusion" assumption:

$$g_e^{(1)}(k) = \frac{1}{N_q} \sum_{h=x,y,z} \left| \frac{1}{bN_p} \sum_{j=1}^{b} \sum_{p=1}^{N_p} \exp\left(i\, q\, \left(h(j,k,p)\right)\right) \right|$$

where

$$h(j,k,p) = h(j+k,p) - h(j,p)$$

h(j+k,p) denotes the x,y, or z coordinate of the p-th particle in the (j+k)-th cluster. The hindered self-diffusion assumption is equal to the self-dynamic structure factor for slow-interacting Brownian particles discussed in [3].

The "collective diffusion" assumption

$$g_e^{(1)}(k) = \frac{1}{N_q} \sum_{h=x,y,z} \left| \frac{1}{bN_p} \sum_{j=1}^{b} \sum_{p=1}^{N_p} \sum_{u=1}^{N_p} \exp\left(i\, q\, \left(h(j,k,p,u)\right)\right) \right|$$

is equal to the coherent or full dynamic structure factor [3], where

$$h(j,k,p,u) = h(j+k,p) - h(j,u)$$

describes the cross term between the p-th and the u-th particles. It is not difficult to show that the "hindered self-diffusion" and "collective diffusion" assumptions don't depend on the scattered vector.

2.4 Linear Scheme of the ACF Presentation

Let $k_{max} = \max\{k\}$ and $c = k_{max}/k^*$ be, respectively, the upper range and the relative upper range of the investigated interval of non-dimensional discrete delay time. To economize the computation expenditures without decreasing the calculation accuracy, a linear scheme of the ACF presentation is used. The idea of the scheme is that the ACF is presented (simulated) by N_t points instead of k_{max} ($N_t \le k_{max}$), uniformly located along the k/k^*-th axis.

For this scheme, the expression for the discrete delay time corresponding to the m-th presentation point is given by

$$k = n\, m$$

where

$$n = c\, \frac{k^*}{N_t}$$

is a constant and m=1,2,... N_t ;

$$k_{max} = nN_t$$

The total number of clusters is defined by

$$N_c^* = k_{max} + b$$

where

$$b = M\, N_t$$

is the upper averaging range and M is an integer.

To economize the computation time, a "rare" scheme is used. According to this scheme, each n-th cluster is only taken for the simulation of ACF. Hence, the number of clusters, saved for the further simulation, is reduced:

$$N_c = N_c^*/n$$

To summarize, the numerical model of the PCS measurements can be defined by the following set of parameters {f, M, n, N_p, N_q, N_t, idum}.

3 Optimization of the Numerical Model

3.1 Accuracy Criteria of the Numerical Model

Before the beginning of an investigation of MLS effects on the measurement properties in PCS, the calculation errors of the numerical model should be suppressed. There are two main sources of calculation errors: the generator of clusters and the estimator of ACF. These errors, caused by the limitation of the number of particles and the number of clusters, can be estimated in the regime of free particle diffusion when the effect of multiple scattering is negligible.

The error ε_d of the modeled free particle diffusion ($\varphi \to 0$) at any discrete time k can be estimated by

$$\varepsilon_d(k) = RMSD\left(k, \varphi \to 0\right) - 1$$

where

$$RMSD\left(k, \varphi\right) = \frac{\left\langle \left|\Delta \mathbf{X}(k)\right|^2 \right\rangle_m}{\left\langle \left|\Delta \mathbf{X}_o(k)\right|^2 \right\rangle_t}$$

is the relative mean squared displacement (RMSD) of spheres. Two averages are provided over N_p spheres. The subscript m denotes that the mean-squared displacement (MSD) $\langle|\Delta\mathbf{X}(k)|^2\rangle_m$ is calculated by taking into account the *modeled* dynamics of interacting spheres. Here, $\Delta\mathbf{X}(k) = \mathbf{X}(k) - \mathbf{X}(0)$ is the displacement of a sphere from its initial position after a discrete time k. The *theoretical* MSD of free Brownian spheres after a discrete time k is simulated by the well known equation

$$\left\langle \left|\Delta \mathbf{X}_o(k)\right|^2 \right\rangle_t = 6D_o k\Delta\tau = \left|\Delta \mathbf{X}_o\right|^2 k$$

If $\varepsilon_d(k=k_d)$ is negligible, then RMSD reflects the self diffusion of interacting spheres. Hence, RMSD can be used to compare different numerical models of the particle dynamics [7,8].

The systematic error of the ACF modeling is given by

$$\varepsilon_a(k) = RDC\left(k, \varphi \to 0\right) - 1 \quad ,$$

or by

$$\langle \varepsilon_a \rangle = RMDC\left(k_d, \varphi \to 0\right) - 1 \quad ,$$

where the relative diffusion coefficient RDC and the relative mean diffusion coefficient are defined in Section 2.2.

3.2 Optimization Criteria of the Numerical Model

In general, the main parameters of the numerical model {f, M, n, N_t} must be optimized. For a given calculation error ε and a number of particles in each cluster, the following optimization criteria are taken

$$\min\left\{\varepsilon_a\left(\frac{k}{k^*}=\frac{2}{3}\right)\right\}$$

$$\max\left\{\langle k_{dm}\rangle\right\}$$

and

$$\min\left\{N_c\right\}$$

Here $\varepsilon_a(k/k^*=2/3)$ is the systematic error of the ACF modeling at the discrete delay time of $k/k^*=2/3$; k_{dm} is the maximum dynamic range of the exponential behavior of a modeled ACF relative to the above mentioned time, over which the below expression is valid

$$\left|\frac{RDC\left(\frac{k_{dm}}{k^*},\ \varphi\to 0\right)}{RDC\left(\frac{k}{k^*}=\frac{2}{3},\ \varphi\to 0\right)}-1\right|\le\varepsilon$$

where ε is the calculation error of the numerical model.

3.3 Optimization of the Displacement Parameter

The dependence of the systematic error and the maximum dynamic range for ε=0.1 on the squared displacement parameter are given in Fig. 2 and Fig. 3, respectively. Calculations are carried out for the parameters listed in Table 2. Only one numerical generator, ran(idum), is taken for the generation of all random parameters.

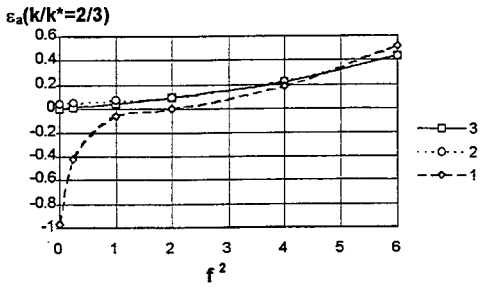

Fig. 2. Dependence of the systematic error of the numerical technique for the ACF modeling on the squared displacement parameter. N_q is equal to 3 for all calculations.
1 - corresponds to {N_p=1, b=80}; 2 - {N_p=10, b=800}; 3 - {N_p=100, b=8000}.

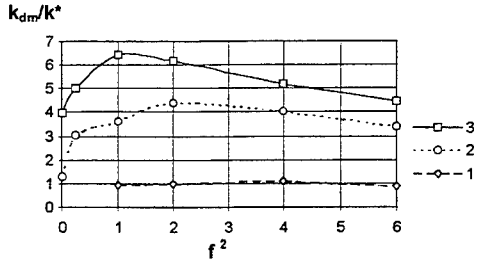

Fig. 3. Dynamic range of the numerical technique for the ACF modeling vs. the squared displacement parameter. The error ε of the estimation of the maximum dynamic range is equal to 0.1. N_q=3. 1 - corresponds to {N_p=1, b=80}; 2 - {N_p=10, b=800}; 3 - {N_p=100, b=8000}.

Table 2. Parameters taken for the analysis of the systematic error and the maximum dynamic range of the numerical technique for the ACF modeling.

f^2	k^*	N_t	n
0.01	600	8	400
0.025	24	8	16
1	6	8	4
2	3	8	2
4	1.5	8	1
6	1	6	1

The systematic error and the reduction of the dynamic range are caused, in general, by the influence of the oscillations of the averaged cos(h(j,k,l)) and sin(h(j,k,l)) functions on the numerical accuracy of the averaging scheme. As follows from the analysis of the above functions presented in Fig. 4 and Fig. 5 for a single moving particle, the period of the low frequency oscillations is approx. k for f=0.1 and is several times k for f=1.

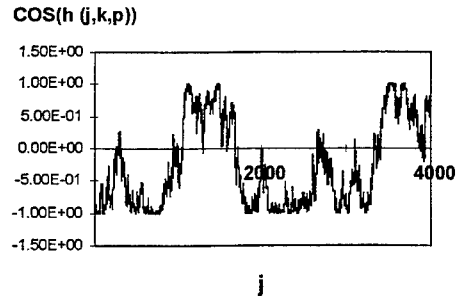

Fig. 4. An averaged function vs. the discrete time j for the displacement parameter f=0.1. n=400, m=7 (k=2800), N_p=1 (p=1), s_x=1.

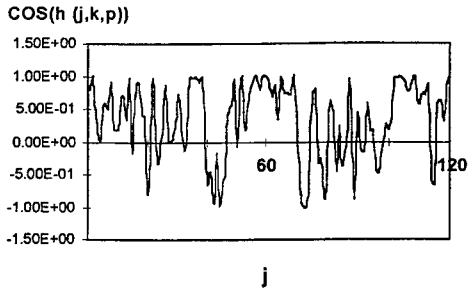

Fig. 5. An averaged function vs. the discrete time j for the displacement parameter f=1. n=4, m=7 (k=28), N_p=1 (p=1), s_x=1.

Hence for a single moving particle, an acceptable calculation accuracy can be achieved if the upper range, b, of the average interval is larger than the period of the low frequency oscillations mentioned above. An insufficient magnitude of the upper range leads to incorrect results (see Fig. 2, Fig. 3 curve 1 at f<0.5).

The period of high oscillations is 5-10 for f=0.1 - 1 and their amplitude increases relative to the low frequency amplitude with an increase of the displacement parameter f. These kinds of oscillations cause an increase in the systematic error (especially, for $f^2 > 2$) and a decrease of the dynamic range for greater values of f.

Curve 3 in Fig. 2, obtained for a large number of averaged terms, can be used to estimate the limiting systematic error of the model, caused in general by the oscillations discussed.

Analysis of Fig. 2 and Fig. 3 shows that the range $0.8 < f^2 < 1.5$ fits first two criteria of the optimization. For further investigations, f = 1 is chosen as an optimal displacement parameter.

3.4 Optimization of M, n and N_t Parameters

Additional investigations were performed in order to optimize other parameters of the model. It was found that by decreasing the number of clusters up to N_c=216, the set {M=25, n=2, N_t=16} satisfies well all three of the above mentioned optimization criteria.

Thus, the numerical model, characterized by optimized parameters {f=1, M=25, n=2, N_t=16}, is prepared for the investigation of the MLS effect. Fig. 6 and Fig. 7 illustrate the systematic errors of the model, which arise at the stage of the generation of the particle dynamics and at the stage of the ACF estimation, respectively. An additional average over idum = -3, -5, -7 is used. A further increase in accuracy was achieved by applying a set of new random numerical generations (an individual generator for each random parameter of the model in Fig. 6 and Fig. 7, instead of one generator for all random parameters, as in Fig. 2 and Fig. 3).

Fig. 6 and Fig. 7 show that by generation of only N_c = 216 clusters and N_p = 5 (or more) particles, the proposed technique allows the modeling of the dynamics of free particles and estimation of the ACF of the light scattered by these particles with error less than 4 - 6 % in the range of delay time $k/k^* < 5$.

The model can be used for the estimation of the effect of multiple scattering, even if the number of spheres in a cluster is limited by N_p=3, when both errors are less than 4 %, if $k/k^* \leq 1$.

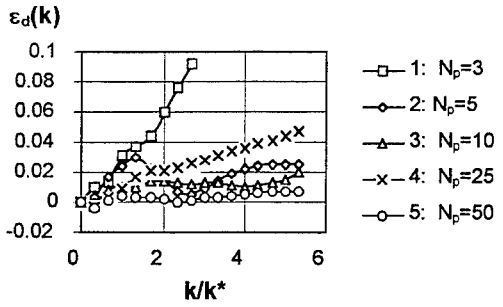

Fig. 6. Error of the free particle motion depending on the relative discrete time for the different number of particles in clusters. An additional average is provided over three different "histories" of cluster motion (idum = {-3,-5,-7}). M = 25, n = 2, N_t = 16.

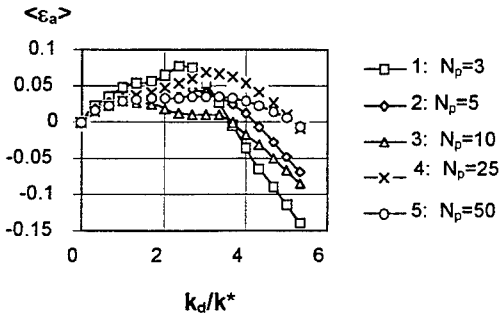

Fig. 7. Mean error of the ACF estimator vs. the relative average interval k_d for different number of particles in clusters. An additional average is provided over three different "histories" of cluster motion (idum = {-3,-5,-7}). M = 25, n = 2, N_t = 16.

4 Modeling of the Effect of Multiple Scattering on the ACF

Some calculation results are presented below to show the practical application of the numerical model which has been developed. The model and obtained results appear to be in the ground breaking rigorous theoretical investigations of the influence of multiple scattering by interacting particles on the measurement properties of highly concentrated systems in photon correlation spectroscopy (PCS).

Calculations are provided for the back-scattering scheme of a fiber-optic sensor for PCS (FOPCS). This scheme is chosen because comprehensive experiments were reported by Wiese and Horn [3]. Other main parameters of the numerical model are {M=25, n=2, N_t=16, f=1, idum= - 3}. The complex refractive index of spheres is 1.59 - i0, the refractive index of the solvent (water) is 1.33 - i0.

The modeling of the effect of multiple scattering on the ACF as function of the diameter of the spherical particles is given in Fig. 8 and Fig. 9 for the volume fraction of suspended spheres 0.05 and 0.45, respectively. The magnitudes 326 ,199, 115, 63 and 41 nm of the diameter of spheres

are taken to be identical to the diameters of particles investigated experimentally [3]. In the figures, the ACF is defined by ACF = $\ln g^{(1)}(k)$.

The lines, plotted in Fig. 8 and Fig. 9, reflect an exponential behavior of the autocorrelation function of the light scattered by an ideal Brownian system. The second curve marked by □ corresponds to the hindered self-diffusion assumption for a set of five Brownian particles. Deviation of this curve from the line is caused by the calculation error because the average is performed over the small number of Brownian particles (N_p=5). The error $\varepsilon_a(k)$ of the ACF estimation is negligible (less than 1.35 %) for the range of the relative discrete delay time $k/k^* <$ 1.4. Deviations of other curves in the same range $k/k^* < 1.4$ demonstrate the contribution of the multiple scattering by five interacting spheres on the ACF. As may be seen from Fig. 8 and Fig. 9, the numerical model allows for the prediction of the contribution of multiple scattering (MLS) as a function of the sphere's diameter and the volume fraction.

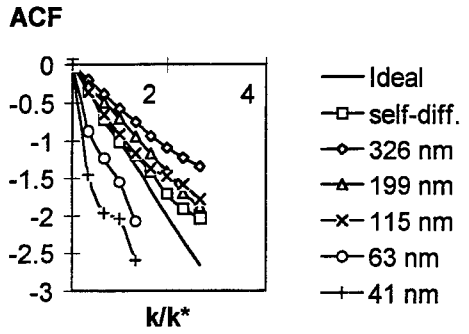

Fig. 8. Modeling of the influence of multiple scattering on the ACF vs. diameter of five interacting spheres. Volume fraction $\varphi = 0.05$.

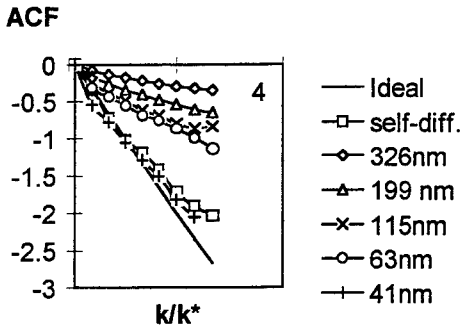

Fig. 9. Modeling of the influence of multiple scattering on the ACF vs. the diameter of five interacting spheres. Volume fraction $\varphi = 0.45$.

Dependence of the relative diffusion coefficient (RMDC) $\langle D \rangle / D_o$ measured in FOPCS on the volume fraction is of large interest to investigators [3]. Modeled $\langle D \rangle / D_o$ is presented in Fig.10 vs. the volume fraction for three interacting spheres only. Averaging of $\langle \ln g^{(1)}(k) \rangle$ is provided over the dynamic range $k_d/k^* = 1 (k_d \leq k_{dm})$, where the numerical error is less than 4% for Brownian free particles (see also Fig. 8, curve 1). Calculation results are reproducible: an additional averaging over idum= - 3, idum= - 5 and idum= - 7 (in other words, - over three sets of clusters with different "histories" of motion) was performed for part of the simulated data only.

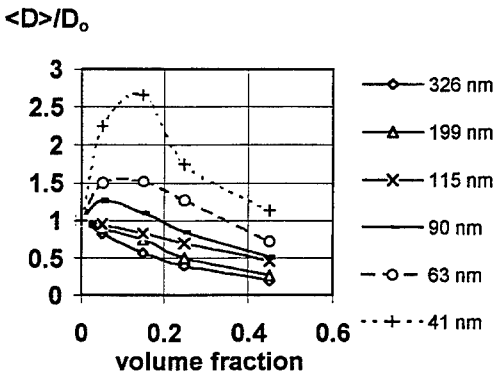

Fig. 10. Modeling of the contribution of the multiple scattering by three interacting spheres on the measurement results of FOPCS depending on the volume fraction and on the diameter of spheres. The range of averaging is $k_d/k^* = 1$.

Experimental data reported by Wiese and Horn [3] are borrowed and presented in Fig. 11 for comparison with the theoretical results shown in Fig. 10.

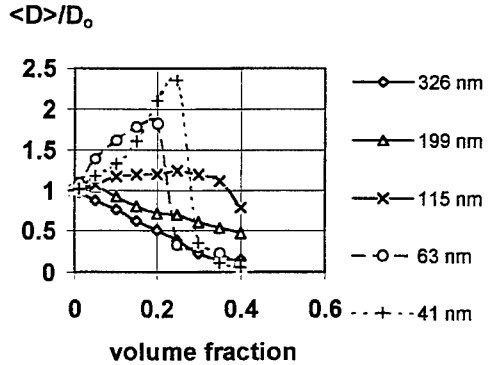

Fig. 11. Experimental data reported by Wiese and Horn [3]. The data are borrowed for the comparison with the theoretical results presented in Fig. 10.

A detailed explanation of experimental results is given by Wiese and Horn. Here we want to show that the theoretical results compare well with their experimental data even if the dynamics and the multiple scattering are modeled by a small number of interacting particles (N_p=3). What's more, the numerical model created here can be used for the first time for the prediction of the results of highly concentrated systems in PCS. To decrease the differences between the theoretical results and the experimental data, the non-plane wave approximation [9] of the model should be used, and the number of averaged spheres should be increased, especially for a sphere diameter smaller than 60 nm.

Another advantage of the proposed numerical model is that the model allows for the separate investigation of the effect of multiple scattering and the effect of dynamics on the ACF. Fig. 12 and Fig. 13, prepared for the volume fraction 0.05 and the sphere diameters 326 nm and 41 nm respectively, are a good illustration of this advantage.

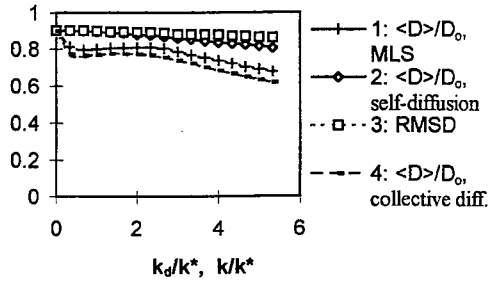

Fig. 12. Contribution of the multiple scattering and the dynamics of twenty five interacting spheres to the measured diffusion coefficient vs. the range of the averaging k_d/k^*. The sphere diameter is 326 nm. Volume fraction $\varphi = 0.05$.

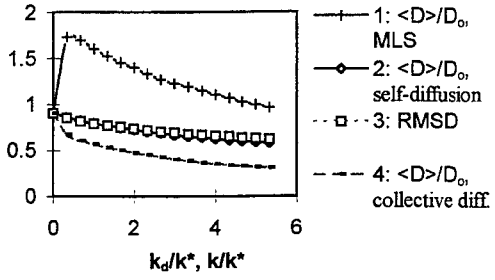

Fig. 13. Contribution of the multiple scattering and the dynamics of twenty five interacting spheres to the measured diffusion coefficient vs. the range of the averaging k_d/k^*. The sphere diameter is 41 nm. Volume fraction $\varphi = 0.05$.

The relative mean-squared displacement (RMSD) of twenty five interacting spheres vs. the relative discrete time of motion k/k^* are presented by curves 3. As mentioned in Section 3.1, the RMSD reflects the influence of the particle's interaction on the ACF. Comparison of the curves 3 in Fig. 12 and Fig. 13 shows that the greater steepness of the RMSD's curve (curve 3, Fig. 13) corresponds to the greater effect of the particle's interaction on the changing of the ACF from the exponential behavior.

In fact, the estimation of $<D>/D_o$ using the hindered self-diffusion assumption for interacting particles (curve 2) gives results identical to those for the RMSD algorithm (curve 3). Differences between curves 2 and 3 are caused by an additional calculation error in the assumption discussed in Section 2.3. Hence, the hindered self-diffusion assumption can be used for estimation of the dynamics of interacting particles only, and it cannot be used for estimation of the measurement results of turbid media in PCS.

Calculations of $<D>/D_o$, provided by the multiple light scattering algorithm reflect the real measurement results in PCS (curve 1, Fig. 12 for particle's diameter 326 nm; curve 1, Fig. 13 for the particle's diameter 41nm). As it follows from the analysis of Fig. 12 and Fig. 13, the collective diffusion assumption (curve 4) can be used for rough estimation of the measurement results (curve 1) of large particles only (Fig. 12).

The numerical model also provides a useful check on the estimation of the "long-time" diffusion coefficient [3]. The number of interacting particles should be increased for this purpose to suppress the calculation errors in the range of large delay time. For the "long-time" investigations, the generator of clusters should be improved by using a more rigorous algorithm of the particle's dynamics [8].

5 Conclusions

A numerical model is proposed as a tool for the study of multiple scattering effects in PCS. A limitation on the number of particles in a cluster and on the number of clusters used to model the motion of particles is necessary to create an effective code. These limitations lead to a decrease in the accuracy of any numerical technique. In this work, the accuracy of the proposed technique, characterized by systematic error and by dynamic range, is investigated for Brownian free particles. A "rare" algorithm and a linear scheme of the ACF presentation is used for the purpose of economizing the computation time. It is shown that the systematic error of the ACF estimator and the reduction of the dynamic range are caused by the low and the high frequency oscillations of the averaged functions.

For a single moving particle, an acceptable calculation accuracy can be accomplished if the upper range b of the averaging interval is larger than the period of the low frequency oscillations. The period of the low frequency oscillations is about equal to the delay time k for the displacement parameter $f=0.1$ and is roughly several times k for $f=1$. An insufficient upper range magnitude leads to incorrect results (see Fig. 2, Fig. 3 curve 1 at $f<0.5$). The high frequency oscillations cause a decrease in the dynamic range and an increase in the systematic error for larger values of f (especially, for $f^2 > 2$).

In the optimized numerical model, characterized by a set of parameters {f = 1, M = 25, n = 2, N_t =16}, the maximum calculation error of the ACF estimator is suppressed up to 4 % for the limited number of clusters N_c =216 and the number of particles N_p =3 if $k/k^* \leq 1$. Hence, even in the case for the strong limitations (N_c =216, N_p =3), the numerical model allows for the prediction of an MLS contribution of 4 % (and more) to the PCS results. What's more, the MLS contribution of less than 4 % can also be predicted, if the signs of the MLS contribution and the calculation error are opposite.

The results obtained for the theoretical investigations of the multiple scattering by three interacting spheres are in a good agreement with experimental data, reported [3] for the back scattering scheme of a PCS fiber sensor. Separate calculations of the effects of MLS and dynamics on the ACF (see Fig. 12 and Fig. 13) give a tool for the quantitative investigation of the processes of collective motion and self-diffusion, including long-time self-diffusion [3].

6 Acknowledgments

The assistance of M. Weckx in administrative support, of Luc Deriemaekeris in the engineering support and of Y. De Smet in comprehensive discussions is greatly appreciated. V. I. Ovod is grateful to the Brussels-Capital Region and the Ministry of Economic Affairs, Belgium, for the financial support of this work.

7 References

1. *R. Finsy:* Particle sizing by Quasi-Elastic Light Scattering. Advances in Colloid and Interface Science. 52 (1994) 79-143.
2. *D. S. Horne:* Particle Size Measurement in Concentrated Latex Suspensions Using Fiber-Optic Photon Correlation Spectroscopy. J. Phys. D: Appl. Phys. 22 (1989) 1257-1265.
3. *H. Wiese, D. Horn:* Single-Mode Fibers in Fiber-Optic Quasielastic Light Scattering: A Study of the Dynamics of Concentrated Latex Dispersions. J. Chem. Phys. 94 (1991) 6429-6443
4. *D. W. Mackowski:* Calculation of Total Cross Sections of Multiple-Sphere Clusters. J. Opt. Soc. Am. A. 11 (1994) 2851-2861.
5. *W. H. Press, S. A. Teukolsky, W. T. Vetterling, B. P. Flannery:* Numerical Recipes in FORTRAN. The art of scientific computing. Cambridge university press, 1992, pp. 272,276.
6. *C. W. J. Beenakker, P. Mazur:* Diffusion of spheres in a concentrated suspension ||. Physica 126A (1984) 349-370.
7. *R. W. Hockney, J. W. Eastwood:* Computer Simulation Using particles. Inst. of Physics Publishing. Bristol and Philadelphia, 1988, p. 485.
8. *M. P. Allen, D. J. Tildesley:* Computer Simulation of Liquids. The Ipswich Book Co Ltd, 1993.
9. *V. I. Ovod:* Characterization of Particles and Particulate Polluants in Concentrated and Turbid Media by Photon Correlation Spectroscopy. Scientific Report. Department of Theoretical Physical Chemistry. Vrije Universiteit Brussel. August 1996.

Fictitious Domain Method for Calculating the Radar Cross Section

F. Millot[1] F. Collino[1,2]

1: CERFACS, 42 avenue G. Coriolis 31057 Toulouse
2: INRIA, Domaine de Rocquencourt 78153 Le Chesnay

Abstract

The finite-difference time domain method (FDTD) has been used extensively to calculate scattering from perfectly conducting objets. An improvement of this method is presented in this paper. We propose to use the fictitious domain method (FD) to compute the near-field. This method appears as a slight perturbation of the FDTD method. First results show a superiority in terms of accuracy of this method over the method that consists in using a staircase like approximation of the boundary. We analyze this improvement on the computation of the Radar Cross Section (RCS). Pulsed excitations are used. RCS calculations in two dimensions are presented. At a given precision, the fictitious domain method minimizes the storage required and the computation time.

1 Introduction

The finite-difference time domain method (FDTD) has been used extensively to compute scattering from perfectly conducting objets. The electromagnetic field is defined on a regular grid and an explicit scheme is used for the time integration, providing a very efficient tool from the computation point of view [2]. However, its main drawback is to create numerical diffractions when the obstacle does not match the grid exactly.

Recently, we have proposed to adapt the fictitious domain method (noted below the FD method) to improve the computation of electromagnetic scattering for obstacles of complicated shapes ([5],[6]). The idea of this method consists in extending artificially the sought solution inside the conductor in the solution of Maxwell's equations constrainted by the perfectly conductor condition. This constraint gives rise to a Lagrange multiplier which is nothing else than the induced surface current. Thus we have to determine the solution in a computational domain which may have now a very simple shape (typically a rectangle in 2D) and to compute a Lagrange multiplier defined on the boundary. The main advantage of the FD method is that the solution may be discretized on a mesh which may be chosen independently of the geometry of the obstacle and may even be a uniform grid, which guarantees the efficiency of the method. Indeed a source term has been created in Maxwell's equations and the final scheme appears as a slight perturbation of the FDTD equations. First results ([5],[6]) show a superiority in terms of accuracy of this method over the method that consists in using a staircase like approximation of the boundary (noted below the ST method).

The purpose of this article is to analyze this improvement on the computation of the Radar Cross Section (RCS). In section 2, we briefly present the FD method with a Dirichlet boundary condition.

The discretization of this method is also described. The scheme appears to be a slight perturbation of the Yee scheme. Some numerical results are discussed in section 3. RCS calculations in the 2D case are presented.

2 Description of the fictitious domain method

The fictitious domain method is a numerical method to solve scattering problems by perfectly conductor obstacles. We refer to ([5],[6]) for an exhaustive description of the method and we only give here a short review of the method.

2.1 Presentation of the new method

The electromagnetic scattering by a perfectly conducting obstacle Ω_{obs} included in an embedded domain Ω is described by Maxwell's equations

$$(1) \qquad \begin{cases} \dfrac{d^2E}{dt^2} + curl\, curl\, E = s & \text{in } \Omega - \Omega_{obs} \\ (E \times n) \times n = 0 & \text{on } \Gamma_{obs} = \partial\Omega_{obs}, \end{cases}$$

with the initial conditions

$$(2) \qquad E(0) = E_0 \text{ and } \frac{dE}{dt}(0) = E_1.$$

For the presentation, a Dirichlet boundary condition is assumed on the exterior boundary of $\partial\Omega$. The main idea of the fictitious domain method is to extend the electric field inside the perfect conductor Ω_{obs}. The electric field E is now defined in Ω. We introduce a new unknown j defined on the surface Γ_{obs}, and we look for (E, j) which verifies

$$(3) \qquad \begin{cases} \left(\dfrac{d^2E}{dt^2}, F\right) + a(E,F) + b(F,j) = (s,F) & \forall F \in H(curl,\Omega) \\ b(E(t), j_S) = 0 & \forall j_S \in M, \end{cases}$$

with the two initial conditions (2). In (3), the following notations have been used

$$(4) \qquad \begin{cases} (E,F) = & \displaystyle\int_\Omega E.F\, dx \\ a(E,F) = & \displaystyle\int_\Omega curl\, E.curl\, F\, dx \\ b(E,j) = & \displaystyle\int_{\Gamma_{obs}} ((E \times n) \times n).j\, d\gamma. \end{cases}$$

and

$$(5) \qquad \begin{cases} M = H^{-1/2}(div_\gamma, \Gamma_{obs}) & \text{in 3D} \\ M = H_T^{1/2}(\Gamma_{obs}) & \text{in 2D} \end{cases}$$

(see [7] for the definitions of the spaces)

The new unknown j is a lagrangian multiplier, and can be interpreted as the time derivative of an induced surface electric current. This current is chosen so that it forces the trace of the tangential component of the electric field on the surface $(E \times n) \times n|_{\Gamma_{obs}}$ to be equal to 0. In conclusion, we have two unknowns to be determined: the surface current j defined on the obstacle and the electromagnetic field E defined in the whole space. Let us remark that the mesh of the solution E may now be chosen independently of the geometry of the obstacle.

2.2 Discretisation

In order to take advantage of the fictitious domain method, we use regular grids for discretizing the domain Ω. In the 2D (resp 3D) case, we use rectangles (resp cubes). We consider for simplicity the lowest order Nédelec elements of the space $H(curl)$[14]. In the 2D case, the Lagrange multiplier belongs to $H_t^{1/2}(\Gamma_{obs})$. We can approximate the boundary Γ_{obs} by segments and choose the piecewize linear elements for the approximation of the Lagrange multiplier. In the 3D case, the Lagrange multiplier belongs to $H^{-1/2}(div_\gamma, \Gamma_{obs})$. The boundary which is now a surface, can be approximated by triangles and the lowest order Raviart-Thomas elements for the discretization of j [15] are retained.

Let X_h be the finite element space of the lowest order Nedelec elements associated to the cubic mesh of Ω, and let M_h be the finite elements space of the piecewize linear elements in 2D case (resp. of the lowest order Raviart-Thomas elements in the 3D case) associated to the mesh of Γ_{obs}. We note p and q the dimensions of the vector spaces X_h and M_h. Let $(N_i)_{i\leq p}$ a basis of X_h and $(\eta_j)_{j\leq q}$ a basis of M_h. We use the standard finite difference scheme for the time derivatives. The problem to be solved is

$$(6) \qquad \begin{cases} E_h^{n+1} - 2E_h^n + E_h^{n-1} = \Delta t^2 s_h^n - \Delta t^2 M_h^{-1} K_h E_h^n - \Delta t^2 M_h^{-1} B_h^t \lambda_h^n & (1) \\ B_h E_h^n = 0, & (2) \end{cases}$$

where E_h (resp λ_h is the colum vector corresponding to the decomposition of E (resp. j) on the basis N_i (resp. η_i)

and where

- $M_h = [(N_i, N_j)]$ is the mass matrix,
- $K_h = [a(N_i, N_j)]$ is the stiffness matrix;
- $B_h = [b(N_i, \eta_j)]$ is a $p \times q$ rectangular matrix and B_h^t its transpose.

The matrix B_h couples the electric field and the surface current. The cœfficient $b(N_i, \eta_j)$ vanishes if and only if the supports of N_i and η_j do not intersect each other. So B_h is a very sparse matrix. Its computation requires to compute the intersection of the two meshes. In (6), the Lagrange multiplier is given in an implicit way. To derive an equation involving λ^n, we apply B_h to the equation providing E_h^{n+1}. As $B_h E_h^{n+1} = 0$, we get the equivalent system

$$(7) \qquad \begin{cases} E_h^{n+1} = 2E_h^n - E_h^{n-1} + \Delta t^2 M_h^{-1} s_h^n - \Delta t^2 M_h^{-1} K_h E_h^n - \Delta t^2 M_h^{-1} B_h^t \lambda_h^n & (1) \\ \lambda_h^n = (B_h M_h^{-1} B_h^t)^{-1} B_h M_h^{-1} (s_h^n - K_h E_h^n), & (2) \end{cases}$$

Remark: without the obstacle, the previous first equation of system (7) is the classic equation of the Finite Difference Time Domain Method. The effect of the FD method is to introduce only a source term in the FDTD equations. So it can be interpreted as a perturbation of the FDTD method [2].

In order to compute the current density j, we have to solve the second equation of ((2) -7) which is a linear system with the matrix $Q_h = B_h M_h^{-1} B_h^t$. The symmetrical positive matrix $B_h M_h^{-1} B_h^t$ is non singular if we have the following condition, named the discrete inf-sup condition [3]:

$$\exists C_h > 0, \quad \inf_{j_h \in M_h} \sup_{F_h \in X_h} \frac{b(F_h, j_h)}{\|F_h\| . \|j_h\|} \geq C_h$$

Moreover, if the previous inequality is true with a constant C independent of h, then the solution of the scheme tends to the solution of (3) when h vanishes ([5],[6]). We don't have establish this condition yet but it has been obtained for an elliptic Dirichlet problem when the ratio of the step

sizes of the two meshes is bounded [9]. Thanks to mass lumping, the matrix M_h is diagonal which implies that $B_h M_h^{-1} B_h^t$ is not equal to zero when the volumic elements intersected by the supports η_i are distinct. This implies a very sparse structure for the matrix which can be inverted once using the Cholesky method for example.
However to modelize outgoing waves, we can replace this condition by some absorbing boundary conditions. We have retained the Joly-Mercier's conditions [10]. Let us recall that these conditions imply first order derivative operators for second order accuracy (i.e an accuracy equivalent to the one of Mur conditions [12]).
Calculation of the RCS requires the computation of the frequency response of the obstacle. A separate Fourier transformation on the pulse waveform response is performed. This method provides the complete frequency response from a single run. In order to obtain the scattered amplitude, an transformation near-field -far field [2] is then used.

3 Numerical results

In order to validate the feasibility of the method to analyze electromagnetic scattering, two dimensional structures are studied. The plane wave excitation is TE polarized with field components E_y , H_z and propagates in the $-x$ direction. The pulse is the derivative of a gaussian with frequency equal to 37.5 MHz. The minimum wavelength of the incident pulse is of order $\lambda_{min} = 4m$. In order to simplify the notations, we define by h_v the space increment, by h_s the space increment used for the discretization of the boundary of the obstacle. We note also nw the number per wavelength $nw = \frac{\lambda_{min}}{h_v}$. Convergence is determined when the wave almost vanishes at all points of the computational domain. Both near fields and scattered field patterns are thus obtained and they are compared with results obtained from a ST method.

3.1 Circular cylinder

In this case, analytical results are calculated from the Bessel expansion of the field around the cylinder [11]. The boundary of the cylinder is approximated by a polyhedral whose sides have a length of order $h_s = \frac{3h_v}{2}$ for the FD method. The radius of the cylinder is noted a and is equal to λ_{min}. Results are shown in figure 1 for the backscattered RCS as a function of the frequency ($k = 2\pi\frac{F}{c}$) and of the radius of the cylinder a. The average deviation between analytical results and those obtained with the FD method is of order 10% for $nw = 10$ and 5 % when $nw = 20$. In accordance with [8], the average deviation between analytical results and those obtained with the ST method is of order 30% for $nw = 10$ and 10 % when $nw = 20$ and 5 % when $nw = 40$. For the fixed point number per wavelength, the relative error for the ST method has increased about a factor 2 or 3.
In conclusion, appropriate space increments to model the RCS within 10% error are found to be of order $\frac{\lambda_{min}}{10}$ for the FD and of order $\frac{\lambda_{min}}{20}$ for the ST method. The fictitious method allows us to use the minimum space increment. It also minimizes the storage required in order to maximize the size of the obstacle which can be modeled.
The results are also compared with those obtained from a boundary edge elements method noted the MM method ([1],[4],[13]). They agrees very well with the MM method where 80 points are used for the discretization. The error is less than 5%. The MM method always provides better results in terms of accuracy than those obtained by the FD method. But this method requires a run for every frequency of interest.
In the next section, the MM method is used as the benchmark for comparison of results.

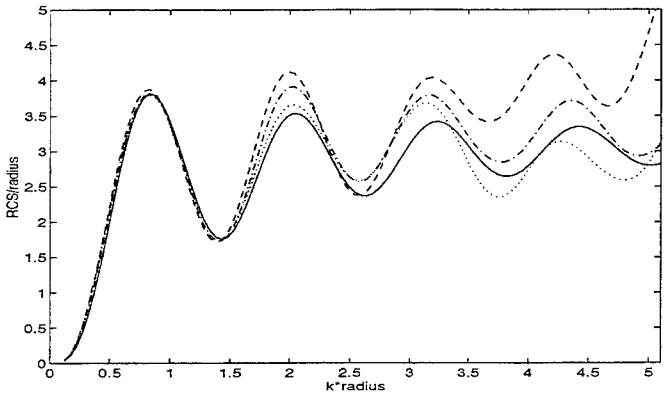

FIG. 1. *Backscattered RCS of a circular cylinder (-:analytical. ... :FD method nw = 10, - -: ST method nw = 10 , -.:ST method nw = 20)*

3.2 Open structures

In this section, we want to analyse the scattering of open structures in which the electromagnetic energy can be retained. We begin to study the structure of an half circular cylinder. It is illuminated by the same incident pulse. Its boundary is approximated by a polyhedral whose sides have a length of order $\frac{3h_v}{2}$ for the FD method. Results can be shown in figure 2 for the RCS as a function of the frequency and the radius of the half circular cylinder. The same remarks observed for the circular cylinder are also available for open structures. The FD method presents results superior in terms in accuracy than those obtained from the ST method. For example, the average deviation between the reference results (obtained from the MM method) and results obtained from the FD method is of order 12% when $\frac{\lambda_{min}}{h_v}$ is equal to 10. Note that the average deviation for the results obtained from the ST method is of order 20 % for the same space discretisation.

4 Conclusion

We have analyzed the computation of the RCS using the fictitious domain method (noted the FD method). The FD method is superior in terms of accuracy of the method using the staircase like approximation of the boundary. In fact, for a fixed number per wavelength, the FD method provides better results than those obtained with the ST method using a staircase approximation for the boundary. For various configurations studied here, the error has been decreased by a factor 2-3. This improvement has been demonstrated on both near and far fields. Finally a space step of order $\frac{\lambda_{min}}{10}$ and a time step $\frac{\lambda_{min}}{10\sqrt{2}}$ is sufficient to obtain a good accuracy. The FD method allows us to use the minimum space increment and by consequence the time step.

References

[1] A.Bendali and M. Souilah. Consistency estimates for a double layer potential and application to the numerical analysis of the boundary element approximation of acoustic scattering by a penetrable object. *Meth. of Comp.*, 62:65–91, 1994.

[2] A.Taflove. *Computational Electrodynamics, The Finite-Difference Time Domain method.* Artech House, London, 1995.

[3] H. Brezis. *Analyse fonctionnelle, Théorie et applications.* Masson, Paris, 1993.

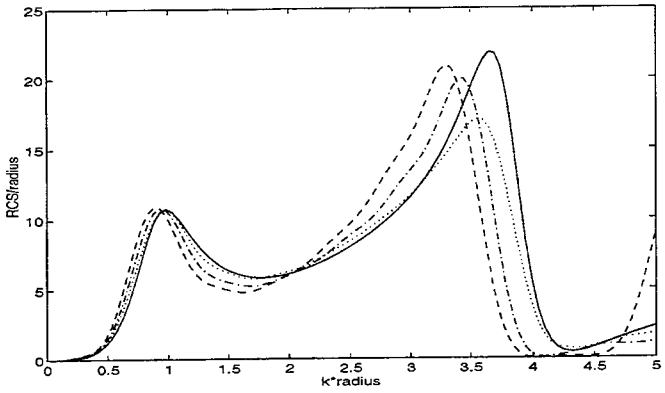

FIG. 2. *Backscattered RCS of a half circular cylinder (-:reference, ... : FD method nw = 10, - -: ST method nw = 10 , -.: ST method nw = 20)*

[4] Y. Chang and R.F Harrington. A surface formulation for characteristic modes of bodies. Technical Report 2 AD/A 000 285 NTIS, U.S. departement of commerce, 1974.

[5] F. Collino, P. Joly, and F. Millot. Fictitious domain method for unsteady problems: application to electromagnetic scattering. *Third International Conference on mathematical and numerical aspects of wave propagation*, 1995.

[6] F. Collino, P. Joly, and F. Millot. Fictitious domain method for unsteady problems: application to electromagnetic scattering. Technical Report CERFACS REPORT TR/EM/96/32, CERFACS, *42,av G Coriolis, 31057 Toulouse, France*, 1996.

[7] R. Dautray and J.L Lions. *Analyse mathématique et calcul numérique pour les sciences et les techniques*. Masson-Paris, 1988.

[8] C. Furse, S. Mathur, and OM P. Gandhi. Inprovement to the Finite Difference Time Domain method for calculating the Radar Cross section of a perfectky conducting target. *IEEE trans. on microwave theory and techniques.*, 38(7):919–927, Jul. 1990.

[9] V. Girault and R. Glowinski. Error analysis of a fictitious domain method applied to a Dirichlet problem. *Japan J. Indust. Appl. Math.*, 12(3):487–514, 1995.

[10] P. Joly and B. Mercier. Une nouvelle condition transparente d'ordre 2 pour les équations de maxwell en dimension 3. Technical Report 1047, I.N.R.I.A., Domaine de de Voluceau Rocquencourt, B.P.105, 78153, Le Chesnay Cedex France, Juin 1989.

[11] N.N Lebedev. *Special functions and their applications*. Dover Publications, New-York, 1972.

[12] G. Mur. Absorbing boundary conditions for the finite-difference approximation of the time-domain electromagnetic-field equations. *IEEE trans. on Electromagnetic compatibility*, 23(4):377–382, November 1981.

[13] J.C. Nedelec. Integral equations with non-integrable kernels. *Integral Equations Operator theory*, 5:561–572, 1982.

[14] J.C. Nedelec. Mixed finite elements in R^3. *Num. Math.*, 142:79–95, 1984.

[15] P.A Raviart and J.M Thomas. *Introduction à l'analyse numérique des équations aux dérivées partielles*. Masson, Paris, 1983.

SESSION 23:

OPTIMIZATION TECHNIQUES FOR ELECTROMAGNETICS

Chairs: J. Volakis and E. Michielssen

Optimization of Wire Antennas Using Genetic Algorithms and Simulated Annealing

Benjamin Kemp, Stuart J Porter, John F Dawson
Department of Electronics
University of York
York YO1 5DD, UK

Abstract

The antenna synthesis problem is essentially a problem of non-linear optimization. Therefore, a convenient real function is constructed which has a minimum when the desired antenna properties are reached. This function is referred to as the optimization function. Since the antenna properties depend on the antenna parameters, the optimization function is a function of these parameters. A convenient optimization method is then used to minimize the optimization function.

Evolutionary optimization methods take a standpoint between weak and strong optimization methods – they are said to be moderate. Moderate methods may be competitive under circumstances wherein both weak and strong methods are likely to fail. For instance, when a calculation model is increasingly complex, strong methods will increasingly fail as the assumptions they are based on collapse. When, in addition, the problem dimensionality is high, weak optimization methods may require too much time, given practical time constraints. Under such real-world circumstances, moderate methods typically become attractive choices.

Introduction

Genetic algorithms [1] and simulated annealing [2] fit within a broader methodological context – a paradigm called natural computing. Natural computing refers to all problem solving methods that are founded upon a natural system or process. As the resemblance between such a system or process and the method derived from it is very loose, there is virtually no limit to the number of method configurations that might be useful in practice.

There is an important unifying notion behind natural computing. The information about the natural system or process that is mimicked by such a method is stored in an ensemble of identical units – neurons in artificial neural networks, strings in simulated evolution methods, chemicals in artificial chemical reaction systems, lymphocytes in artificial immune networks. Each unit in the ensemble possesses simple information processing capabilities owing to a small number of properties. The properties comprise a means for mutual interactions between the units. These interactions are controlled by a finite set of comparatively simple computation rules that are, effectively, applied massively in parallel in each time step. Due to the nonlinear impact of the interactions, properties at the level of ensemble units will collectively transform into novel, or emergent, properties at the global level, wherein computational power is hidden. The emergence of structure in the system is a spontaneous complex-dynamic process, essentially without any central supervising agent for the manipulation of data representations. The system is therefore said to be capable of self-organization (learning).

Optimizing a 6-element Yagi-Uda Antenna

The optimization function sets out which parameters are to be optimized and with what priority. Proper formulation of the optimization function specification is important when a number of the properties which are to be optimized are in contention. For example, the optimum antenna gain and the optimum match to a 50Ω load can not be achieved simultaneously in many cases. Furthermore, a rigid insistence on one of these properties being as near optimal as possible will surely lead the optimization algorithm to produce an unacceptably poor value for the other property. Similarly, radiated power which is not contained within the main lobe of the antenna's radiation pattern should be minimized, but can never be reduced to zero. It is imperative that the calculation of the optimization function should acknowledge this and not simply reward lower and lower values of back radiation *ad infinitum*, as this would have the effect of rendering the algorithm blind to any other considerations.

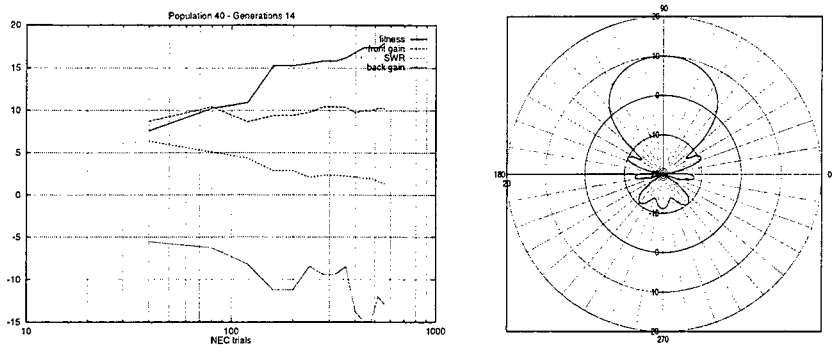

Figure 1: (a) results for 40/30 genetic algorithm and (b) associated radiation pattern.

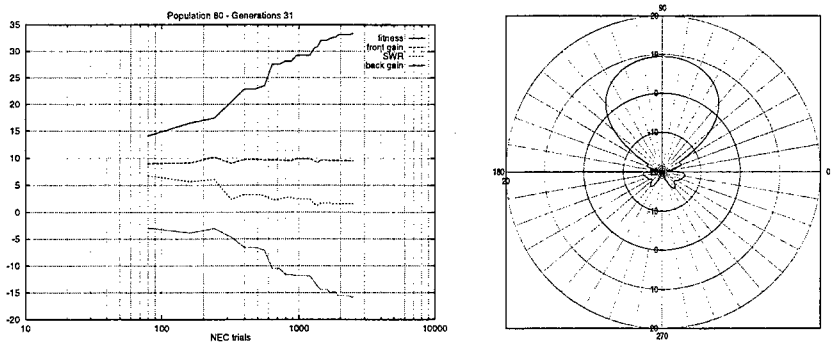

Figure 2: (a) results for 'worst case' optimization function and (b) associated radiation pattern.

Using a NEC model the back radiation from a 6-element Yagi-Uda antenna was assessed at 67.5, 90, 112.5, 135, 157.5, and 180 degrees from the forward direction. An increasing penalty was imposed if the gain rose above -10dB at any of these points, but there was no further reward for a lower gain. Had a simple linear scale been used, as is successful for forward gain, then a rogue result with back gain far lower than is really necessary (a null) would have been allowed to dominate. This is the case because gain in any one direction may be reduced to $-\infty$. Similarly, the reactance may take on values between $-\infty$ and $+\infty$, but it is the narrow range of values around $50j0\Omega$ which is of interest.

The highest gain which can be achieved from a 6 element Yagi antenna is of the order of 11dB, but this is accompanied by a poor radiation pattern and poor match to 50Ω. Also the requirement for no lobe, except the main lobe, to have a gain higher than -10dB is no mean feat—a front to back ratio of 15dB may typically be considered good for a 6 element Yagi antenna. The termination criteria were front gain $>$ 10dB, back gain < -10dB, SWR < 1.5.

Genetic Algorithm

The genetic algorithm required typically between 2000 and 3000 NEC trials (a few hours) to produce a good solution. Good solutions were obtained with 500 NEC trials, but with this minimal number of trials the control parameters must be properly matched to the objective function. The minimum number of NEC trials typically was required with a population/generation ratio of 40/30 (1200 NEC trials). The same results were achieved with 80/30 (2400 NEC trials) and 160/30 (4800 NEC trials), indicating that 30 generations are required to optimally solve the problem and the population size is less important. However, outside these limits the algorithm failed to find good solutions so easily. A lower population/generation ratio lead to premature convergence due to lack of diversity in the small population. A higher population/generation ratio lead

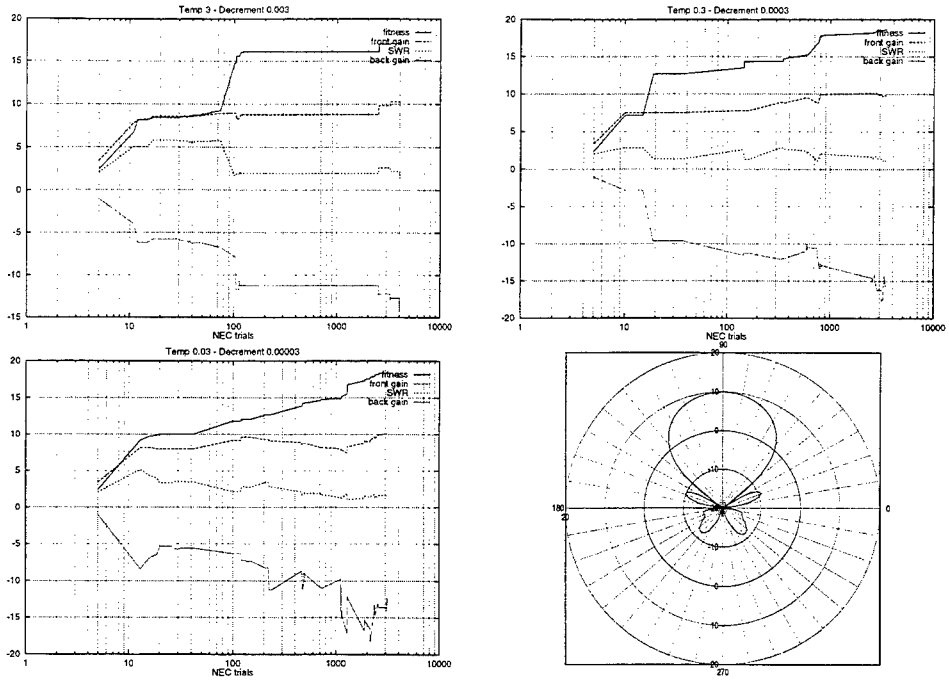

Figure 3: results for (a) 3/0.003, (b) 0.3/0.0003, and (c) 0.03/0.00003 simulated annealing, and (d) a radiation pattern.

to failure as the large population could not converge in a small number of generations. A mutation rate of 0.1 was found to be best. This corresponds to a bit mutation rate of just under 1 percent. Higher (0.5) and lower (0.05) mutation rates were found to give longer convergence times and premature convergence respectively. A typical plot of performance for the algorithm is shown in Figure 1(a) and the associated radiation pattern is given in Figure 1(b).

In the above examples, the optimization function was based on the average back radiation over 6 points. The function was calculated so as not to encourage individual values of back radiation below -10dB as this would be to the detriment of the other parameters. A different means of calculating the optimization function was also used in which the algorithm switches its attention from one point to another in such a way that the optimization function is calculated in a different manner each time. The highest individual value of back radiation is always chosen each time from the 6 points available. This has the effect of squeezing the back radiation at its worst point so as to fill in the nulls and allow a much smaller worst-case back radiation. A slightly lower front gain (about 9.5dB as opposed to 10) has to be accepted, but worst-case back gain figures of -15dB and better were achieved. Typical results are shown in Figure 2(a) and the associated radiation pattern is given in Figure 2(b). It can be seen by comparing Figures 1(b) and 2(b) that the worst-case optimization function changes a lobes-and-nulls radiation pattern into one where there are only two nulls - one at each side - and the remaining single rear lobe is much smaller.

Simulated Annealing

A Nelder-Mead simplex [3, 4] driven simulated annealing algorithm was used so as to combine the search accuracy of simulated annealing with the search precision of a conventional technique. The performance of the simulated annealing algorithm and genetic algorithm were similar. Simulated annealing required between 3000 and 4000 NEC trials to produce a good solution, whereas genetic algorithms required between 2000 and 3000 or less. In the three examples, these termination criteria are met in different ways. Figure 3(a) shows the effect of a high starting temperature and a large temperature

decrement. Looking at the 'fitness' curve, a period of time can be clearly seen, approximately between 100 and 2000 NEC trials, where there is no improvement. This can be attributed to the algorithm accepting jumps into areas of the search space with lower fitness. This is analogous to exploration in the genetic algorithm, and too much of it will result in the flat line continuing indefinitely and the algorithm not converging in reasonable time. Failure occurred in this manner at (start temperature / temperature decrement) 30/0.03 and higher. Figure 3(b) illustrates the effect of an intermediate starting temperature and temperature decrement. No such period of non-improvement can be seen, although improvement in the 'fitness' curve does come in fits and starts. Figure 3(c) has a lower starting temperature and a smaller temperature decrement. The 'fitness' curve is smoother and less erratic. This is analogous to exploitation in the genetic algorithm. Improvement is gradual with no prolonged periods of fruitless exploration. If this trend were continued, the danger would be that the curve would continue to become more smooth and shallow, much like the opposite extreme just described. The algorithm began to fail in this way at (start temperature / temperature decrement) 0.0003/0.0000003 and lower. However, the low temperature extreme effectively becomes a simplex-driven monte carlo algorithm and should in principle be capable of finding a good solution – given enough time. The radiation pattern for the second example is shown in Figure 3(d).

Monte Carlo

Because of practical constraints, the monte carlo method was not allowed more than $1,000,000$ NEC trials, which requires several weeks of run time on a SPARC 20-61. In comparison, the 3000 NEC trials of the other two methods require a few hours of run time. The Monte Carlo technique was not successful in meeting any of the termination criteria within the 1,000,000 NEC trials allocated. All criteria must be met simultaneously for termination.

These results show that, for this problem, simulated annealing and genetic algorithms are capable of reducing the apparent problem size by some factor greater than 300 (greater than $2,000$ in the case of genetic algorithms with properly chosen control parameters). Two important observations can be made about the problem which was being optimized. Firstly, this is not a particularly large problem, so the reduction in apparent problem dimensionality is not as great as could be expected for a larger problem. The exact size of the problem space was chosen somewhat arbitrarily from an approximate knowledge of what a Yagi-Uda antenna looks like. The problem size would have been increased by allowing more unconventional candidate solutions, but it is unlikely that they would have been accepted by the algorithm, so no benefit would have been gained. Similarly, the problem size could have been reduced by constraining the parameters more tightly to allow only the more conventional candidate solutions, but this carries the increasing risk of excluding good solutions. Secondly, the problem was highly multimodal and exhibited a high degree of interaction. This is likely to be the case in all antenna optimization problems, and it presents a challenge to any optimization method which attempts to improve on blind or naive search heuristics such as monte carlo or cartesian grid search.

It should be noted that, just as there are many varied and successful designs of Yagi-Uda type antenna on the market, an optimization algorithm may produce any number of good solutions, with very little to choose between them. For this reason, it may be said that the multimodality of the problem is such that there is no single optimal solution, although this will, of course, be true only in a practical sense. One interesting feature of these low-sidelobe designs is that the reflector element is often shorter than a half wavelength, and shorter than the driven element. This was also found to be the case by Kajfez [5, 6] who used a Fletcher-Reeves conjugate-gradient method to minimize the sidelobes of a 6-element Yagi antenna [7, 8]. This is an exception to the general rule that the reflector should usually be longer than the driven element.

Extending the Bandwidth

As a step toward a truly broadband antenna, the Yagi antenna was modeled at three frequencies; 430 MHz, 435 MHz, and 440 MHz representing the lower, centre, and upper frequencies of a 10 MHz bandwidth (the UK 70cm amateur band). The 'worst case' algorithm was adapted so that the poorest value of front gain and SWR was always chosen from the 3 available values. The poorest back gain was chosen from the 6 available angles, and from the 3 available frequencies – a total of 18 possible values. In this way, the algorithm switched its attention so that the optimization function was calculated in a different way each time. The effect of this was to push the frequency response of the antenna into line by always selecting the poorest point for improvement. The results, which were very successful and required hardly any more NEC trials than for a single frequency, are shown below. The termination criteria were front gain > 9.5dB, back gain < -10.5dB, SWR < 2.5. Note that the front-gain figure has had to be reduced by 0.5dB, but the back-gain figure was reduced accordingly in order to maintain a 20dB front-to-back ratio. The SWR figure has been increased from 1.5 to 2.5, corresponding to an increase in reflected power from 0.2dB to 1dB.

Genetic Algorithm

Solutions were obtained with typically between 3000 and 4000 NEC trials and are shown in Figure 4. The algorithm was successful with 80/30 and 160/30 (population/generations) indicating, as with the single frequency antenna, that 30

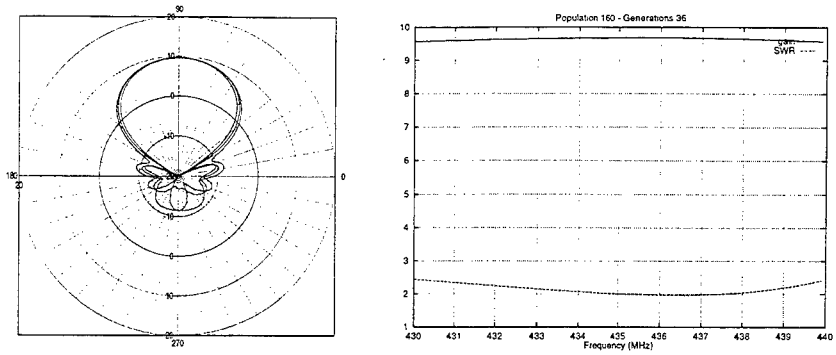

Figure 4: (a) patterns at 430, 435, and 440 MHz and (b) gain & SWR for genetic algorithm on broadband antenna.

generations are required and the population size is less important. The algorithm failed for population sizes of 40 and less, and for populations of 160 and greater, for the same reasons as previously (premature convergence due to lack of diversity and slow convergence, respectively). As was shown previously, the effect of the worst-case algorithm is to create uniformity. This can be seen in Figure 4(b) where front-gain and SWR are plotted against frequency. Gain hardly varies from 9.5dB over the 10MHz bandwidth, and SWR is always between 2.5 and 2.

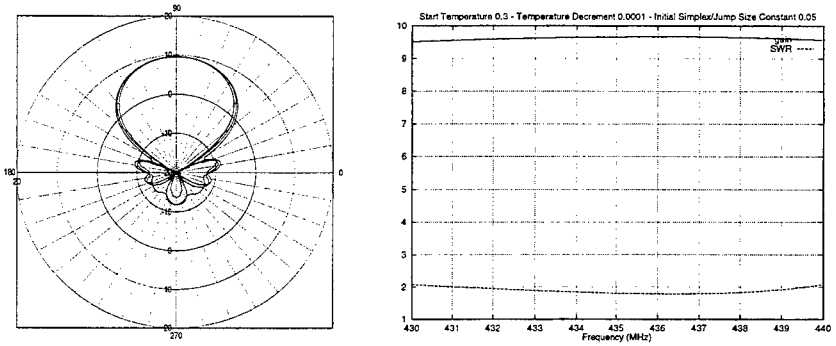

Figure 5: (a) patterns at 430, 435, and 440 MHz and (b) gain & SWR for simulated annealing on broadband antenna.

Simulated Annealing

The performance of simulated annealing as shown in Figure 5 and genetic algorithms were similar. Solutions were obtained with typically between 4000 and 5000 NEC trials, compared with 3000 to 4000 for genetic algorithms. The SWR was better (2 compared with 2.5) than for genetic algorithms, and this can be attributed to the method noise associated with genetic algorithms which, as was seen earlier, effects SWR results due to the relatively large gradients seen at impedance optima. The algorithm was successful with 0.3/0.0001 (starting temperature / temperature decrement), but not with 1/0.0003 and higher or with 0.1/0.00003 and lower. This represents quite a critical dependency on the configuration of the cooling schedule. Furthermore, the initial size of allowed step across the search space, and the initial size of the simplex were also critical at 0.05 of the total size of the search space (although it made little difference whether these parameters were constant, or under the control of the cooling schedule). Values of 0.1 and higher were not successful, and neither were values of 0.01 and lower, no matter how many trials were allocated. Such a critical dependency on configurational parameters requires a long experimental stage in which to find an optimal configuration. If, in addition, this optimal configuration turns out to be

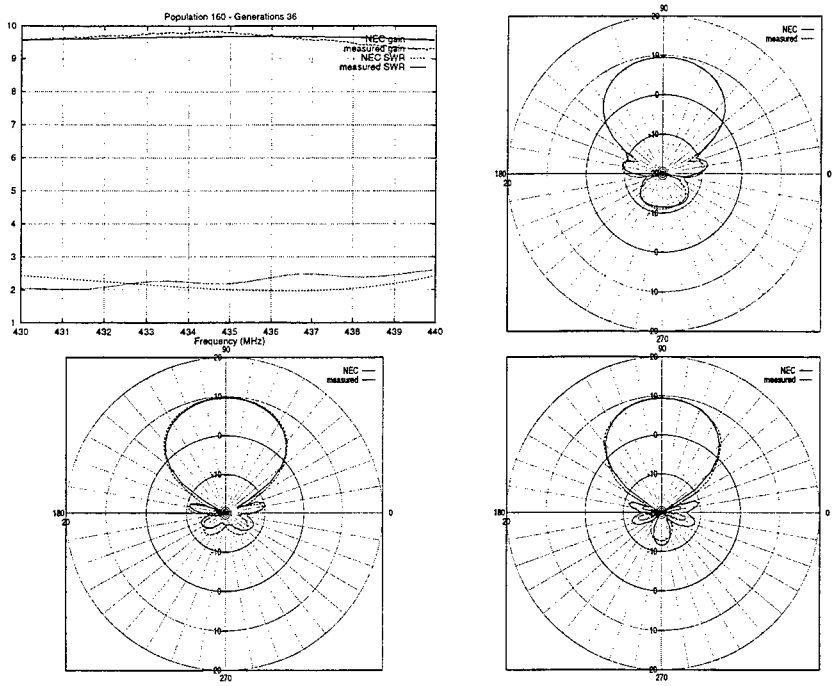

Figure 6: (a) measured gain & SWR, and measured radiation patterns at
(b) 430MHz, (c) 435MHz, and (d) 440MHz for broadband antenna designed using genetic algorithms.

highly problem-dependent then it can only be concluded that the time spent is not worthwhile, when one considers that the performance of genetic algorithms is less critically dependent on configurational parameters and less problem-dependent. The radiation pattern is shown in figure 5(a) and the gain and SWR in figure 5(b). Note that the E-plane pattern is never optimized, but *in all cases* it meets the convergence criteria provided that the H-plane pattern does.

Confirming the Results by Measurement

In order to verify that the NEC models produce genuine solutions, a series of models were built and tested. This is important because the optimization methods will not just optimize the physical and electrical properties of the antenna, but will also optimize any inaccuracy in the NEC model. That is to say, the techniques will maximize any inaccuracies in the NEC model which lead to an over-optimistic solution. The situation is to be avoided where an apparently good solution is obtained by manipulating these inaccuracies, which may be seen as an easy target by the optimization techniques.

Genetic Algorithm

The measured SWR of the antenna was contained within the same bounds (2dB < SWR < 2.5dB) as the NEC SWR, but the actual shapes of the curves differ slightly. The measured gain was very similar to the NEC gain, remaining within 0.3dB across the band. The results are shown in Figure 6. The gain seen around the back 180 degrees on the radiation patterns is within the −10dB design specification, and is actually better than the NEC model at the top of the frequency band.

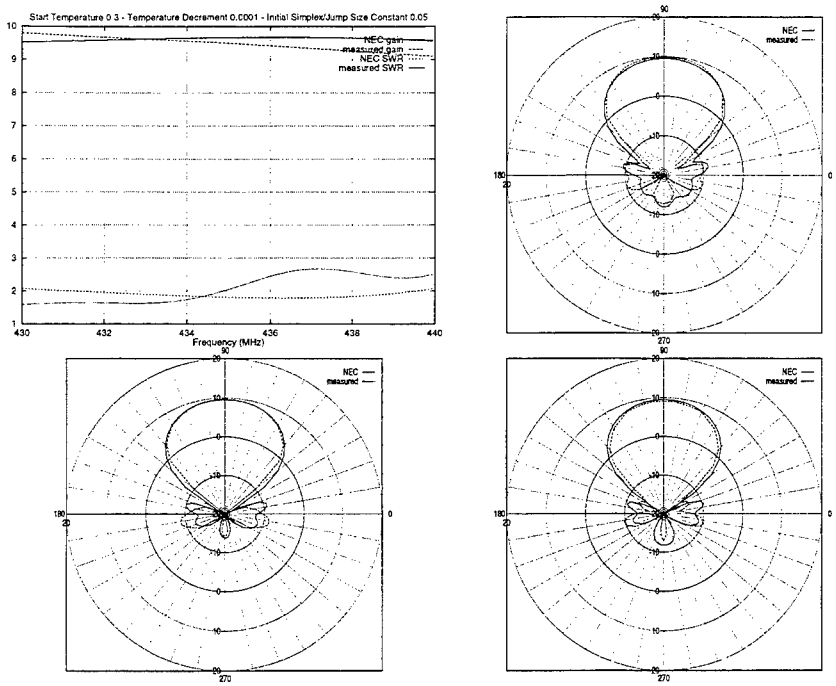

Figure 7: (a) measured gain & SWR, and measured radiation patterns at (b) 430MHz, (c) 435MHz, and (d) 440MHz for broadband antenna designed using simulated annealing.

Simulated Annealing

It was assumed that this antenna would be more critical to build and should therefore give a poorer agreement between modeled and measured results compared with the genetic algorithm method due to construction (or modeling) inaccuracies. Because of the method noise associated with the genetic algorithm method, it should be unlikely to produce highly critical antenna designs, whereas the simulated annealing method is able to find the 'deep well' type of optima just as readily as it finds broader and less critical optima, thus increasing the chance of producing a critical design.

The measured SWR of the antenna was slightly lower than expected at the bottom end of the frequency band, and higher than expected at the top end. This was also the case for the antenna designed using genetic algorithms. The measured gain was lower than expected at the top end of the band, due to the unexpected impedance mismatch. The results are shown in Figure 7. The measured radiation patterns differ somewhat from the NEC models in the sidelobe region. This may be due to reflections from local obstructions (cars) which were irradiated by the main lobe of the antenna while the sidelobes were being measured, this effect was certainly observed while measuring the genetic algorithm antenna, but it may be due to the simulated annealing algorithm producing more critical designs than the genetic algorithm. Certainly the expected values of SWR were not obtained, and it is difficult to attribute this to anything other than construction inaccuracies in the model.

Conclusion

The evolutionary techniques were found to be very efficient and capable of producing designs which are better, when a number of factors are considered over a wide frequency bandwidth, than those which are commercially available. Genetic algorithms are preferred over simulated annealing for several reasons. The efficiency of the genetic algorithms was better, and their performance was less critically dependent on the configurational control parameters and less problem-dependent

than was the case for simulated annealing. The configurational flexibility in genetic algorithm methodology is an attractive feature. The configurational space of a genetic algorithm is large and there is no standard methodology available to find an optimum working point in this space. Because they can not be determined independently, the choice of the control parameters itself can be a complex nonlinear optimization problem. Further, it is evident that the optimal control parameters critically dependent on the nature of the objective function. However, with a reasonable understanding of genetic algorithm mechanics it is possible to make an educated guess at a productive working point and, even if a non-optimal working point is chosen, the global optimum can be found ultimately, although more time steps will be required typically. Therefore, genetic algorithms are configurationally robust. Results were more repeatable for genetic algorithms and they were more intuitive to use - it is usually easy to see why a genetic algorithm fails and what changes to the configurational control parameters are necessary. Also, direct analogies with genetics are helpful in understanding the operation of genetic algorithms. In fact there appears to be more scope for improvement of the basic genetic algorithm, compared with simulated annealing, by incorporating all manner of more advanced features found in biological genetics, many of which are discussed in Goldberg's book [9].

Genetic algorithms are also robust in another sense. They tend to approach the global solution quite independently from the starting population in the search space. Thus, genetic algorithms are characterized by a good search accuracy. On the other hand, genetic algorithms exhibit a poor search precision. The spread can be ascribed to the stochastic search heuristics used by genetic algorithms, and it may be indicated as method noise. Opposite properties - good search precision and poor search accuracy - often apply to traditional optimization techniques. Therefore, better performance might be attained in a sequential combination, where the genetic algorithm generates a starting point for subsequent refinement by a local technique.

Acknowledgement

This work was funded by the Engineering and Physical Sciences Research Council (EPSRC).

References

[1] R.L. Haupt, *An introduction to genetic algorithms for electromagnetics*, IEEE Antennas and Propogation Magazine, 37(2):7-15, April 1995.

[2] S. Kirkpatrick, C.D. Gelatt, and M.P. Vecchi, *Optimization by simulated annealing*, Science, 220(4598):671-680, May 1983.

[3] J.A. Nelder and R. Mead, *A simplex method for function minimization*, Computer Journal, 7:308-313, 1965.

[4] D.M. Olsson and L.S. Nelson, *The Nelder-Mead simplex procedure for function minimization*, Technometrics, 17(1):45-51, 1975.

[5] D. Kajfez, *Nonlinear optimization reduces the sidelobes of Yagi antenna*, IEEE Transactions on Antennas and Propogation, 21:714-715, 1973.

[6] D. Kajfez, *Nonlinear optimization extends the bandwidth of Yagi antenna*, IEEE Transactions on Antennas and Propogation, 23:287-289, 1975.

[7] D.K. Cheng and C.A. Chen, *Optimum element spacing for Yagi-Uda arrays*, IEEE Transaction on Antennas and Propogation, 21, 1973.

[8] C.A. Chen and D.K. Cheng, *Optimum element lengths for Yagi-Uda arrays*, IEEE Transactions on Antennas and Propogation, 23:8-15, 1975.

[9] D.E. Goldberg, *Genetic algorithms in search, optimization, and machine learning*, Addison-Wesley Publishing Company, Inc., 1989.

AUTOMATED ELECTROMAGNETIC OPTIMIZATION OF MICROWAVE CIRCUITS

J.W. Bandler, R.M. Biernacki and S.H. Chen

Optimization Systems Associates Inc.
P.O. Box 8083, Dundas, Ontario, Canada L9H 5E7

email: osa@osacad.com
Tel 905 628 8228
Fax 905 628 8225

Abstract

The focus of this paper is automated electromagnetic (EM) optimization of microwave circuits and structures. We address the challenges in EM optimization in general and applications to microwave circuit design in particular. We describe an efficient Datapipe connection between an optimization driver and several EM field solvers. Advanced interpolation and database techniques are integrated in order to reduce the number of EM field analyses. We describe the Geometry Capture technique for parameterizing arbitrary geometrical structures. The novel concept of Space Mapping is also reviewed. The technique is employed to carry out the bulk of computations using a coarse (fast) model while the fine model (accurate but CPU intensive EM simulations) is used to align the coarse model and guide the optimization process. Practical industrial applications illustrate the effectiveness of our approach. The examples include a planar microstrip circuit suitable for a commercial method-of-moments solver, and a waveguide structure which is analyzed by a 3D finite-element solver.

INTRODUCTION

The most significant features of EM simulators (the finite element method FEM, the integral equation/boundary element method IE/BEM, the transmission-line method TLM, the finite difference time-domain method FDTD, the mode matching method MM, the method of moments MoM) [1-9] include their unsurpassed accuracy, extended validity ranges, and the capability of handling fairly arbitrary geometrical structures. In order to take full advantage of these features the structures may need to be simulated in their entirety. Decomposition into substructures, which might be desired from the point of view of computational efficiency, should be considered only if no significant couplings are neglected. This means that increasingly more complex structures need to be accurately simulated. Therefore, the efficiency of CAD techniques employing EM simulators is of utmost importance.

EM simulators will not realize their full potential to the designer unless they are optimizer-driven to automatically adjust designable parameters [10-13]. To this end we have made several Datapipe connections between our optimization engine OSA90 [14], which features state-of-the-art direct search, gradient based and simulated annealing algorithms, and EM field solvers including MoM, FEM, TLM and mode-matching codes. Advanced interpolation and database techniques are integrated within the optimization driver to reduce the number of EM field analyses required as well as to facilitate gradient calculations within a fixed grid meshing scheme.

We have developed a Geometry Capture technique for parameterizing planar and solid models in arbitrary formats. A parametric abstraction is derived from a set of incremental models, accommodating not only parameters representing linear dimensions, but also material parameters and composite geometrical evolutions.

We also describe the novel concept of Space Mapping [15,16]. A coarse model is employed to carry out the bulk of computations in the optimization process. The coarse model can be an empirical model, an equivalent circuit model or an EM model with a coarse resolution. A fine model is used to align the coarse model and guide the optimization process. We have developed an aggressive strategy incorporating the Broyden update to establish a mapping between the coarse and fine models.

To illustrate our approach a planar microstrip frequency doubler is analyzed by a commercial MoM solver and a waveguide structure is simulated by a 3D FEM commercial solver. Both circuits are optimized using the techniques described in this paper.

DATAPIPE ARCHITECTURE

The open architecture of our optimization engine OSA90 [14] is based on the Datapipe technology. It allows the users to create fully optimizable interconnections of components, subcircuits, simulators and mathematical functions, supported by fully integrated expression processing capabilities. Several Datapipe protocols are available for connecting external programs through UNIX interprocess pipes. This facilitates high-speed data connections to external *executable* programs, even across networks.

Datapipes are flexibly defined in the input file. The user specifies a set of inputs from OSA90 to the external program and defines outputs to be returned. The external programs are run in separate processes and communicate with OSA90 in a manner similar to subroutine calls. Specialized Datapipe-based interfaces exist for a number of applications, including the popular analog circuit simulator SPICE and several electromagnetic simulators, both commercial and academic:

(1) Empipe [14] interface to ***em*** [5] - an efficient full-wave MoM field solver for predominantly planar circuits; with full accuracy up to millimeter-wave frequencies, ***em*** simulates arbitrary geometries accounting for dispersion, coupling, surface waves, radiation, metallization and dielectric losses,

(2) Empipe3D [14] interface to Maxwell Eminence [6] and HFSS [7] - FEM based solvers for full-wave EM field analysis of three-dimensional passive structures; Maxwell Eminence and HFSS are capable of computing the S-parameter responses, EM field distributions and radiative effects at microwave frequencies,

(3) interfaces to 2d-tlm and 3d-tlm [2,17] - 2D and 3D time-domain TLM based EM solvers,

(4) interfaces to rwgmm - Fritz Arndt library of fast and accurate waveguide building blocks [4] - MM solvers for fast EM simulations of waveguide discontinuities,

(5) interfaces to MM solvers developed at the University of Perugia [12].

Our optimization engine features powerful and robust gradient-based optimizers: ℓ_1, ℓ_2, Huber, minimax, quasi-Newton, conjugate gradient, as well as non-gradient simplex, random and simulated annealing optimizers. Optimization variables can include circuit parameters, bias voltages, input power levels, Datapipe inputs and abstract variables. The responses that can be optimized include built-in and user-defined circuit responses, Datapipe outputs and abstract error functions.

The Datapipe technology allows the users to enhance their own software with OSA90's friendly user interface, graphics, expression parser, optimization and statistical features. By linking several separate programs through OSA90 the users can form their own functionally integrated CAE systems. OSA90 can invoke itself through Datapipe to create a simulation/optimization hierarchy of virtually unlimited depth.

INTERPOLATION AND DATABASE TECHNIQUES

Interpolation and database techniques are integrated within the optimization driver to reduce the number of EM field analyses required as well as to facilitate gradient calculations. Interpolation may be necessitated by an EM simulator if the particular solver used employs a fixed grid meshing scheme, for example *em*. If not enforced by the solver, interpolation is still a highly desirable feature.

If interpolation is employed, EM simulations are performed at on-grid points only. For off-grid points, user-selectable linear or quadratic interpolation schemes have been adopted. Also selectable by the user are the parameters to be interpolated: S, Y or Z, in either rectangular or polar form. For example, in the case of linear interpolation we have [18]

$$R(\boldsymbol{\phi}) = R_{EM}(\boldsymbol{\phi}^c) + \boldsymbol{\theta}^T \,\mathrm{sign}\boldsymbol{\Theta}\, \Delta\boldsymbol{R}_{EM}(\boldsymbol{B}) \tag{1}$$

where

$$\Delta\boldsymbol{R}_{EM}(\boldsymbol{B}) = [\; R_{EM}(\boldsymbol{\phi}^1)-R_{EM}(\boldsymbol{\phi}^c) \quad R_{EM}(\boldsymbol{\phi}^2)-R_{EM}(\boldsymbol{\phi}^c) \quad \ldots \quad R_{EM}(\boldsymbol{\phi}^n)-R_{EM}(\boldsymbol{\phi}^c) \;]^T \tag{2}$$

R_{EM} denotes the response being interpolated, $\boldsymbol{\phi}^c$ is the center (on-grid) base point, and $\boldsymbol{\phi}^1$, $\boldsymbol{\phi}^2$, ..., $\boldsymbol{\phi}^n$ are n (also on-grid) base points obtained by perturbing each parameter ϕ_i by its (plus or minus) discretization step d_i, one at a time. $\boldsymbol{\theta}$ and $\boldsymbol{\Theta}$ represent the relative (w.r.t. the discretization step) deviation of the off-grid point $\boldsymbol{\phi}$ from $\boldsymbol{\phi}^c$, arranged in a vector or a diagonal matrix form, respectively. The gradient of (1), which is the function actually seen by the optimizer, is also readily available as

$$\frac{\partial R(\boldsymbol{\phi})}{\partial \boldsymbol{\phi}} = \boldsymbol{D}^{-1} \,\mathrm{sign}\boldsymbol{\Theta}\, \Delta\boldsymbol{R}_{EM}(\boldsymbol{B}) \tag{3}$$

where $\boldsymbol{D} = \mathrm{diag}\{d_i\}$.

The results of on-grid simulations are stored in a database system for efficient re-use during subsequent interpolations at other off-grid points for which some or all of the base points may have already been simulated.

GEOMETRY CAPTURE

This section addresses the critical issue [19,20] of parameterization of geometrical structures for the purpose of layout-based design, in particular automated EM optimization. As the optimization process proceeds, revised structures must be automatically generated. Moreover, each such structure must be physically meaningful and should follow the designer's intention w.r.t. allowable modifications and possible limits. It is of utmost importance to leave the parameterization process to the user. In our earlier work (*Empipe Version 1.1, 1992*) we created a library of predefined elements (lines, junctions, bends, gaps, etc.), that were already parameterized and ready for optimization. The applicability of that approach is, however, limited to structures that are decomposable into the available library elements. Moreover, even a comprehensive library would not satisfy all microwave designers, simply because of their creativity in devising new structures. Furthermore, the library approach inherently omits possible proximity couplings between the elements since they are individually simulated by an EM solver and connected by a circuit-level simulator.

Geometry Capture facilitates user parameterization of arbitrary structures by processing the native files of the respective EM simulators. In Empipe, designable parameters and optimization variables are automatically captured from a set of "geo" files created using *xgeom*. In Empipe3D the optimization variables are captured from a set of Maxwell Eminence or HFSS projects. These projects, or "geo" files reflect the structure evolution in response to parameter changes. The user's graphical inputs are

processed to define optimizable variables. Once a structure is captured, the modified project files are automatically generated, and then the field solver is invoked to display and optimize, for instance, the S-parameter responses. The captured structures are as easy to use as conventional circuit elements. In addition to geometrical dimensions, dielectric and other material parameters can also be selected for optimization.

The Geometry Capture technique is illustrated in Fig. 1. An example of the Empipe3D's Geometry Capture form editor is shown in Fig. 2.

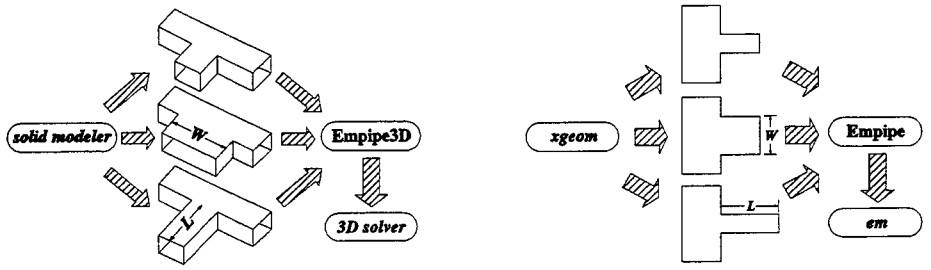

Fig. 1. The process of Geometry Capture for (a) 3D, and (b) planar structures.

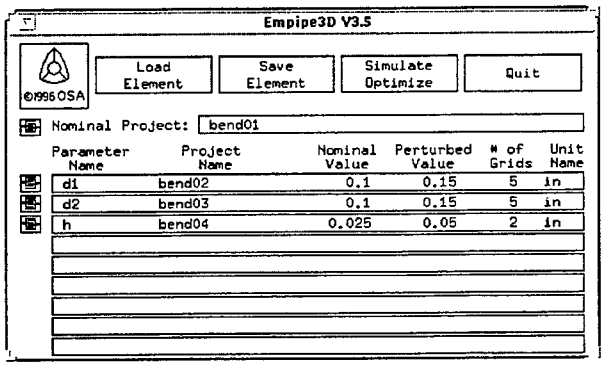

Fig. 2. The Geometry Capture form editor.

SPACE MAPPING OPTIMIZATION

We consider models in two distinct spaces, namely the optimization space denoted by X_{OS}, and the EM space denoted by X_{EM}. We assume that the X_{OS} model is much faster to evaluate but less accurate than the X_{EM} model. The X_{OS} model can be an empirical model or a coarse-resolution EM

model. We wish to find a mapping P between these two spaces, i.e., a function that maps the parameters of one model onto the parameters of the other model:

$$x_{OS} = P(x_{EM}) \tag{4}$$

such that

$$R_{OS}(P(x_{EM})) \approx R_{EM}(x_{EM}) \tag{5}$$

where $R_{OS}(x_{OS})$ and $R_{EM}(x_{EM})$ denote the model responses in the respective spaces.

The purpose of Space Mapping (SM) is to avoid direct optimization in the computationally expensive X_{EM} space. We perform optimization in X_{OS} to obtain the optimal design x_{OS}^* and then use SM to find the mapped solution in X_{EM} as

$$\bar{x}_{EM} = P^{-1}(x_{OS}^*) \tag{6}$$

P is found by an iterative process starting from $x_{EM}^1 = x_{OS}^*$. At the ith step, the X_{EM} model is simulated at x_{EM}^i, i.e., the current parameter values. If the X_{EM} model does not produce the desired responses we perform parameter extraction of the X_{OS} model to find x_{OS}^i which minimizes

$$\| R_{OS}(x_{OS}^i) - R_{EM}(x_{EM}^i) \| \tag{7}$$

where $\|\cdot\|$ denotes a suitable norm. In the aggressive SM strategy the next iterate is found by a quasi-Newton step

$$x_{EM}^{i+1} = x_{EM}^i + (B^i)^{-1}(x_{OS}^* - x_{OS}^i) \tag{8}$$

which employs an approximate Jacobian matrix B^i. The matrix B^i is subsequently updated using the Broyden formula [21].

In a number of applications, the aggressive Space Mapping strategy has enabled us to achieve optimal or near-optimal results after very few fine model EM simulations. Furthermore, the mapping established at the solution can be utilized for efficient statistical analysis of manufacturing tolerances.

EXAMPLES

Harmonic Balance Simulation and Optimization of a Frequency Doubler

We perform EM based simulation and optimization of a class B frequency doubler shown in Fig. 3 [22]. The doubler consists of a single FET (NE71000) and a number of distributed microstrip elements including two radial stubs and two large bias pads.

Significant couplings between the distributed microstrip elements exist in the doubler, e.g., between the radial stubs and the bias pads. In order to take them into account the entire structure between the two capacitors is parameterized and considered as a whole to be simulated by ***em***. Ten parameters denoted as $\phi_1, \phi_2, \ldots, \phi_{10}$ are selected as design variables. The ***em*** results are directly returned to OSA90/hope through Empipe for harmonic balance simulation and optimization. For the active device we use the built-in Curtice and Ettenberg FET model.

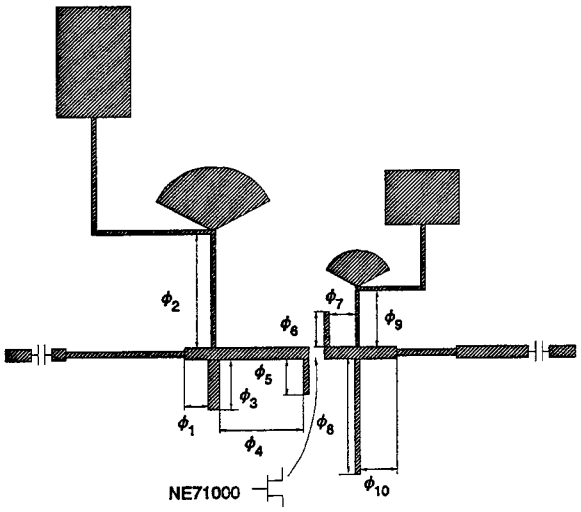

Fig. 3. Circuit structure of the class B frequency doubler.

The design specifications imposed on the doubler responses included conversion gain ≥ 3 dB and spectral purity ≥ 20 dB at 7 GHz and 10 dBm input power. Fig. 4 shows the conversion gain versus input power before and after minimax optimization. Significant improvement of the circuit performance is obtained and all specifications are satisfied after optimization.

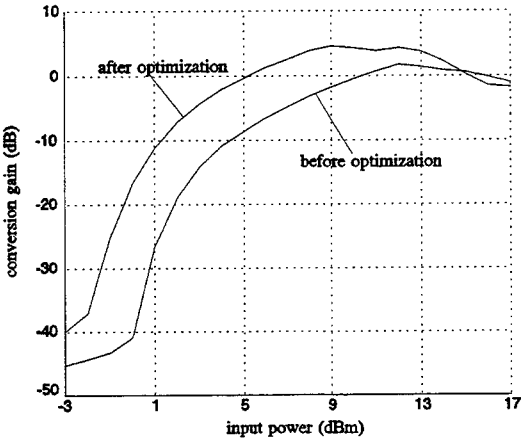

Fig. 4. Conversion gain of the frequency doubler versus input power before and after optimization.

Design of an Optimal Mitered Waveguide Bend

To illustrate fully 3D EM optimization we apply Empipe3D to design a single-section mitered waveguide bend sketched in Fig. 5. Just one parameter controls the location of the 45 degree bend. We use the distance d between the edge of the miter and the edge of the non-mitered bend (d = 0 corresponds to the non-mitered bend). The design specification is set for the return loss $\geq$ 30 dB over the full bandwidth of $9 \leq f \leq 15$ GHz.

A standard gradient-based minimax optimization has been performed. The starting value is set to d = 0.1 inch and the bounds are set to 0 and 0.375 inch. The solution, d_{opt} = 0.2897 inch is reached after 14 iterations. The total CPU time of a Sun SPARCstation 10 with 32 Mb RAM is about 23 hours. It is important to note that only 9 Maxwell Eminence simulations were needed because of time saving offered by the integrated database/interpolation feature of Empipe3D. The response of the optimized structure achieved the return loss of about 29 dB.

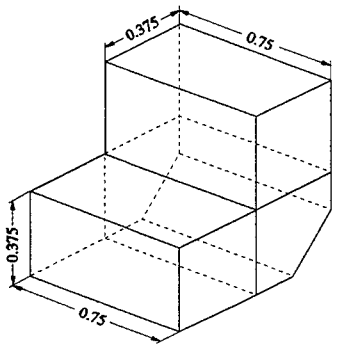

Fig. 5. Geometry of the optimized WR-75 mitered bend.

CONCLUSIONS

The increasing computing power of modern workstations and PCs and advances in computational electromagnetics, including a rapidly growing number of available field solvers, direct exploitation of EM simulation techniques in circuit design optimization becomes both tempting and tractable. Nevertheless, slowness of such solvers, particularly when practical industrial are to be effectively solved, requires sophisticated approaches which can reduce the number of EM simulations needed to successfully complete optimization.

In this context we have reviewed a number of recent developments in the area of automated EM optimization of microwave circuits and structures. First, the Datapipe technology has been found to be an effective and efficient tool to drive a variety of disjoint EM simulators. Particularly useful in reducing the number of EM simulations is the interpolation approach integrated with a database system of simulated results. We have also presented the Geometry Capture technique for user parameterization of geometrical, structures, a key to design optimization of arbitrary structures. Finally, the Space Mapping technique is a very promising approach to design optimization when extremely CPU intensive simulators are used. It combines the speed of circuit-level optimization with the accuracy of EM simulations.

REFERENCES

[1] J.C. Rautio and R.F. Harrington, "An electromagnetic time-harmonic analysis of arbitrary microstrip circuits," *IEEE Trans. Microwave Theory Tech.*, vol. 35, 1987, pp. 726-730.

[2] W.J.R. Hoefer, "Time domain electromagnetic simulation for microwave CAD applications," *IEEE Trans. Microwave Theory Tech.*, vol. 40, 1992, pp. 1517-1527.

[3] R.H. Jansen and P. Pogatzki, "A hierarchically structured, comprehensive CAD system for field theory-based linear and nonlinear MIC/MMIC design," *1992 2nd Int. Workshop of the German IEEE MTT/AP Joint Chapter on Integrated Nonlinear Microwave and Millimeterwave Circuits Dig.* (Duisburg, Germany), 1992, pp. 333-341.

[4] T. Sieverding, U. Papziner, T. Wolf and F. Arndt, "New mode-matching building blocks for common circuit CAD programs," *Microwave Journal*, vol. 36, July 1993, pp. 66-79.

[5] ***em***™ and ***xgeom***™, Sonnet Software, Inc., 1020 Seventh North Street, Suite 210, Liverpool, NY 13088.

[6] *Maxwell*™ *Eminence*, Ansoft Corporation, Four Station Square, Suite 660, Pittsburgh, PA 15219.

[7] *HFSS*, HP-EEsof, 1400 Fountaingrove Parkway, Santa Rosa, CA 95401.

[8] *IE3D*™, Zeland Software, Inc., 39120 Argonaut Way, Suite 499, Fremont, CA 94538.

[9] *LINMIC+*, Jansen Microwave GmbH, Kackert Str. 16-18, D-52072 Aachen, Germany.

[10] J.W. Bandler, R.M. Biernacki, S.H. Chen, P.A. Grobelny and S. Ye, "Yield-driven electromagnetic optimization via multilevel multidimensional models," *IEEE Trans. Microwave Theory Tech.*, vol. 41, 1993, pp. 2269-2278.

[11] J.W. Bandler, R.M. Biernacki, S.H. Chen, D.G. Swanson, Jr., and S. Ye, "Microstrip filter design using direct EM field simulation," *IEEE Trans. Microwave Theory Tech.*, vol. 42, 1994, pp. 1353-1359.

[12] F. Alessandri, M. Dionigi, R. Sorrentino and M. Mongiardo, "A fullwave CAD tool of waveguide components using a high speed direct optimizer," *IEEE MTT-S Int. Microwave Symp. Dig.* (San Diego, CA), 1994, pp. 1539-1542.

[13] Workshop WMFE, *Automated Circuit Design using Electromagnetic Simulators*. 1995 IEEE MTT-S Int. Microwave Symposium (Orlando, FL), 1995.

[14] *OSA90*™, *OSA90/hope*™, *Empipe*™ and *Empipe3D*™, Optimization Systems Associates Inc., P.O. Box 8083, Dundas, Ontario, Canada L9H 5E7.

[15] J.W. Bandler, R.M. Biernacki, S.H. Chen, P.A. Grobelny and R.H. Hemmers, "Space mapping technique for electromagnetic optimization," *IEEE Trans. Microwave Theory Tech.*, vol. 42, 1994, pp. 2536-2544.

[16] J.W. Bandler, R.M. Biernacki, S.H. Chen, R.H. Hemmers and K. Madsen, "Electromagnetic optimization exploiting aggressive space mapping," *IEEE Trans. Microwave Theory Tech.*, vol. 43, 1995, pp. 2874-2882.

[17] P.P.M. So, W.J.R. Hoefer, J.W. Bandler, R.M. Biernacki and S.H. Chen, "Hybrid frequency/time domain field theory based CAD of microwave circuits," *Proc. 23rd European Microwave Conf.* (Madrid, Spain), 1993, pp. 218-219.

[18] J.W. Bandler, R.M. Biernacki, S.H. Chen, L.W. Hendrick and D. Omeragić, "Electromagnetic optimization of 3D structures," *IEEE Trans. Microwave Theory Tech.*, vol. 45, May 1997.

[19] M.A. Schamberger and A.K. Sharma, "A generalized electromagnetic optimization procedure for the design of complex interacting structures in hybrid and monolithic microwave integrated circuits," *IEEE MTT-S Int. Microwave Symp. Dig.* (Orlando, FL), 1995, pp. 1191-1194.

[20] J.W. Bandler, R.M. Biernacki, Q. Cai, S.H. Chen and P.A. Grobelny, "Integrated harmonic balance and electromagnetic optimization with Geometry Capture," *IEEE MTT-S Int. Microwave Symp. Dig.* (Orlando, FL), 1995, pp. 793-796.

[21] C.G. Broyden, "A class of methods for solving nonlinear simultaneous equations," *Math. of Comp.*, vol. 19, 1965, pp. 577-593.

[22] "CAD review: the 7GHz doubler circuit," *Microwave Engineering Europe*, May 1994, pp. 43-53.

Design Optimization of Patch Antennas Using the Sequential Quadratic Programming Method

Z. Li+, P.Y. Papalambros* and J. Volakis+
+Dept. of Electrical Engineering and Computer Science
*Dept. of Mechanical Engineering and Applied Mechanics
University of Michigan
Ann Arbor, MI 48109-2122

Abstract

Over the past several years a variety of sophisticated computer codes has been developed for antenna analysis based on the popular integral equation and PDE methods. The utility of these codes is greatly enhanced if they can be used for design, a situation which typically involves iterative optimization algorithms. Recently, genetic algorithms (GAs) have been examined for array design and absorber optimization. However, in these applications the response function was available in analytic form and required little computation time. In contrast, antenna simulations rely on complex and computationally expensive integral equation, finite element or finite difference codes, making the use of GAs less desirable. A more attractive alternative is gradient-based algorithms developed for solving nonlinear programming (NLP) problems. In this paper, we examine the performance of a general sequential quadratic programming (SQP) optimization algorithm for designing patch antennas in conjunction with a finite element-boundary integral code. The algorithm has been applied to determine the antenna geometrical parameters (patch size, substrate thickness, loads, stacked patch spacing, etc.) to achieve pre-specified resonance and bandwidth characteristics. We will present results for some specific examples and discuss the potential for more complex antenna configurations.

1. Introduction

Antenna design is a topic of great importance to electromagnetics and involves the selection of antenna physical parameters to achieve optimal gain, pattern performance, VSWR, bandwidth and so on, subject to specified constraints. Over the past 10 years, several sophisticated computer codes have been developed for antenna analysis [1-3] based on a variety of popular methods. The utility of these codes is greatly enhanced if they provide the user with a design capability. To date, codes have not been extended to include design capabilities primarily because of their complexity and non-linearity with respect to the physical properties of the antenna (material constants, dimensions, feed location and type, etc.). Some design algorithms have been proposed but these are only applicable to specialized antenna shapes and do not address the general antenna optimization problem[4].

Recently, genetic algorithms (GAs) have been examined for array design and absorber optimization [5-7]. However, in these cases the response function was available in analytic form and required little computation time. This is consistent with the nature of GAs which, although robust, require a large number of function evaluations to complete the optimization study. Also GAs are more suitable for discrete variable problems. In contrast, antenna simulations rely on complex, computationally intensive integral equation or finite element codes, which generate continuous functions. It may therefore be impractical to generate a sufficiently large sample space for carrying out an optimization study using GAs, and NLP algorithms should be more appropriate.

Such an alternative optimization algorithm is Sequential Quadratic Programming (SQP) suitable for continuous nonlinear objective functions such as the input impedance, gain, pattern shape and so on, with both equality and inequality constraints. Convergence is typically achieved in a few iterations, and therefore their interface with rigorous (but expensive) numerical antenna analysis codes is much more practical. SQP and other similar algorithms are routinely used for large structural design problems involving finite element analysis [8].

In this paper, we examine the performance of a general SQP code [9] for designing patch antennas in conjunction with a finite element-boundary integral code [10]. Both are rigorous general purpose codes. The main point of the paper is to examine the suitability of SQP for antenna parameter optimization to achieve the design objectives subject to constraints. We will illustrate the performance of the optimizer using a few illustrative examples from simple to more complex.

2. SQP (Sequential Quadratic Programming) Algorithm

SQP is a gradient-based class of methods that became prominent in the late 1970s [11]. They are considered the most efficient general purpose nonlinear programming algorithms today. The basic principle of sequential approximations is to replace the given nonlinear problem by a sequence of quadratic subproblems that are easier to solve.

Algorithm Description

Consider the equality constrained problem:

$$\begin{aligned} &\min\ f(\mathbf{x}) \\ &\text{subject to } \mathbf{h}(\mathbf{x}) = \mathbf{0} \end{aligned} \tag{1}$$

where $\mathbf{x}$ is the design variable vector, $f(\mathbf{x})$ is the objective function, and $\mathbf{h}(\mathbf{x})$ is the vector of equality constraints. Using a Lagrange-Newton method described in most optimization books [see e.g. 11], at kth iteration, we have

$$\begin{bmatrix} \mathbf{W}_k & \mathbf{A}_k^T \\ \mathbf{A}_k & \mathbf{0} \end{bmatrix} \begin{bmatrix} \mathbf{s}_k \\ \lambda_{k+1} \end{bmatrix} = \begin{bmatrix} -\nabla f_k^T \\ -\mathbf{h}_k \end{bmatrix} \tag{2}$$

where $\mathbf{W} = \nabla^2 f + \lambda^T \nabla^2 \mathbf{h}$, $\mathbf{A} = \nabla \mathbf{h}$, and λ is the vector of Lagrange multipliers. Solving the above equations iteratively, we obtain the iterates $\mathbf{x}_{k+1} = \mathbf{x}_k + \mathbf{s}_k$ and λ_{k+1} which should eventually approach $\underset{\sim}{\mathbf{x}}$ and $\underset{\sim}{\lambda}$, the optimal values. When formulated in this way, any method can be referred to as a Lagrange-Newton method for solving the contrained problem (1).

Alternatively, we observe that the above equation can be viewed as the first order optimality (Karush-Kuhn-Tucker) conditions for the quadratic model:

$$\begin{aligned} &\min\ q(\mathbf{s}_k) = f_k + \nabla_{\mathbf{x}} L_k \mathbf{s}_k + \frac{1}{2} \mathbf{s}_k^T \mathbf{W}_k \mathbf{s}_k \\ &\text{subject to } \mathbf{A}_k \mathbf{s}_k + \mathbf{h}_k = \mathbf{0} \end{aligned} \tag{3}$$

where $\nabla_{\mathbf{x}} L_k = \nabla f_k + \lambda_k^T \nabla \mathbf{h}_k$. Solving the quadratic programming subproblem (3) gives the same $\mathbf{s}_k$ and λ_{k+1} as solving equation (2) and thus the two formulations are equivalent. In the second formulation, the values of $\underset{\sim}{\mathbf{x}}$ and $\underset{\sim}{\lambda}$ will be obtained from solving a sequence of quadratic programming (QP) subproblems, hence the name SQP methods for the relevant algorithms.

Proper convergence properties are achieved with some modifications on this basic SQP algorithm. We may view $\mathbf{s}_k$ as a search direction and define the iteration as $\mathbf{x}_{k+1} = \mathbf{x}_k + \alpha_k \mathbf{s}_k$, where the step size α_k is

introduced and computed by minimizing an appropriate merit function along the search direction. The merit function measures how good $\mathbf{x}_k$ and λ_k are. in terms of minimizing the original objective function as well as any infeasibilities that may exist at the current iteration. The QP subproblem can be solved efficiently by well-developed QP solvers, for example, based on projection or augmented Lagrangian methods. Using an active set strategy, problems with both equality and inequality constraints can be solved.

In summary, SQP algorithms have the following steps:
1. Initialize.
2. Solve the QP subproblem to determine a search direction $\mathbf{s}_k$.
3. Minimize a merit function along $\mathbf{s}_k$ by performing a line search to determine the step length α_k.
4. Set $\mathbf{x}_{k+1} = \mathbf{x}_k + \alpha_k \mathbf{s}_k$
5. Check for termination, go to step 2 if not satisfied.

Inexact Line Search

The line search determines a value of α_k that ensures an acceptable objective function decrease from $\mathbf{x}_k$ to $\mathbf{x}_{k+1}$. It is usually unnecessary and computationally expensive to perform a line search with perfect accuracy. Therefore, an inexact line search is typically used, where a suitable step size rather than the optimal one is found. With a suitable step size a sufficient decrease in f_k is realized. The most common conditions in inexact line search are the Armijo-Goldstein criteria [12-13]. The importance of using an inexact line search is that the number of function evaluations needed in step 3 above is substantially reduced.

Finite Differences

Finite differences can be used when the derivatives of a function must be approximated using information only from function values. Forward or central differences can be used for this purpose. However, in engineering problems where the cost of function evaluations is high, it is usually recommended to use forward differences.

3. Combining SQP with the Finite Element Method (FEM)

In the next section we give two examples of microstrip antenna optimization using SQP algorithms. For the calculation of the objective function, a hybrid finite element algorithm is used to compute electromagnetic scattering and radiation by an open three-dimensional rectangular cavity recessed in an infinite ground plane [10]. The cavity may support microstrip patch or slot antennas and may be filled with layered dielectric material. The problem is formulated using the finite element method and boundary integral equation and the resulting system of equations is solved via the biconjugate gradient method. Besides different layers of dielectrics, the cavity may also have lumped loads, probe feeds, and short circuit pins. The flow chart of the whole process is shown on the next page.

In accordance with the flow chart, the FEM code first computes the values of initial point which are used by the optimizer to determine the new search direction and step size. The process is repeated until convergence within the given tolerance is achieved.

4. Example Applications

(1) Optimization of Patch Antenna with Finite Dielectric Substrate

Wide use of patch antennas for mobile communications (e.g. cellular telephones, pagers, GPS, LAN) makes it necessary to study antennas with finite substrates. The finite element method is ideally suited for the calculation of antenna characteristic parameters. Our interest is to find the optimal width for this kind of antenna at

resonance frequency. Consider the configuration shown in Figure 1. The initial rectangular patch is 2 cm wide. and is placed on a finite dielectric substrate. For simplicity, we set the width of the substrate to be the same as that of the patch. As shown in the figure, the patch is recessed in a $5.25cm \times 4cm$ rectangular metallic cavity which is $0.0787cm$ deep.

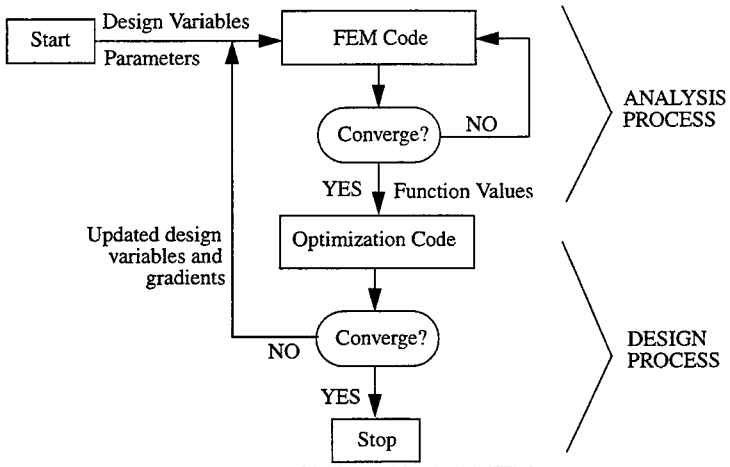

Flow chart of SQP combined with FEM.

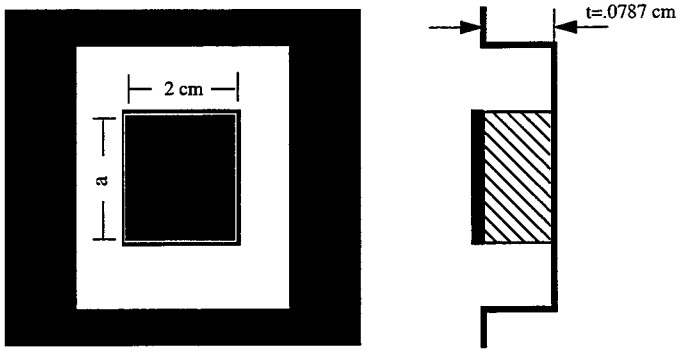

Figure 1: Geometry of the patch antenna with finite dielectric substrate.

At 1.575 GHz and starting with a length of 2.7 cm, the resonant length was found after 7 iterations, involving a total of 60 calls to the antenna code. The optimum patch length value was a = 3.3 cm and Figure 2 gives the iteration history of the design variable (patch length) and objective function. We note that the finite dielectric substrate had the effect of shifting the resonant length from 2.7 cm to 3.3 cm. The performance of the finite

substrate patch at the resonant length is given in Figure 3. The expected narrowband behavior is clearly evident and it would be difficult to precisely determine the resonant length using random search.

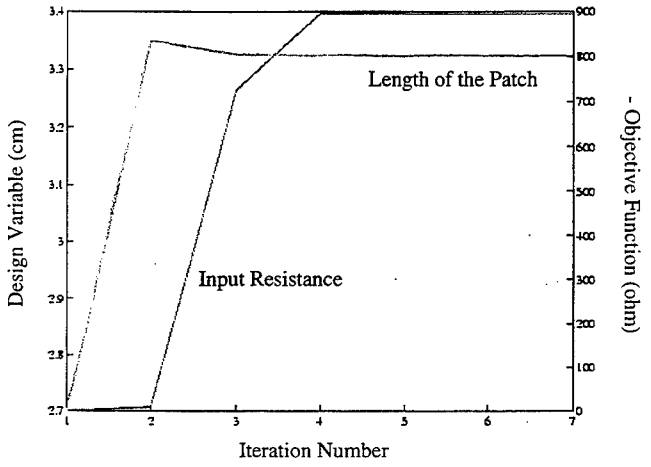

Figure 2: Iteration history for the optimization of a patch antenna with finite dielectric substrate.

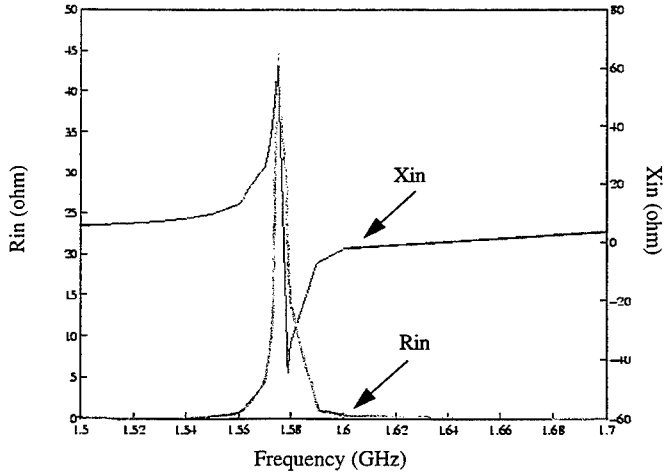

Figure 3: Performance of the optimal patch antenna with finite dielectric substrate.

(2) Increasing the Bandwidth of a Dual Patch Antenna

Microstrip patch antennas have many attractive features such as conformality, lightweight, and ease of fabrication. One of their principal limitations is their narrow bandwidth which is on the order of only a few percent. A number of techniques have been suggested and implemented to improve the bandwidth of the microstrip patch antenna. One of them is stacking patches horizontally or vertically [14].

Figure 4 illustrates the configuration of the stacked antenna under investigation. The top and lower substrates have a dielectric constant of $\varepsilon_r = 2.2$ and thickness h = 1.59mm, and the driven patch is designed to operate at 1.53 GHz. The middle substrate has a relative permittivity of $\varepsilon_r = 1.1$. We wish to find the optimum length, width and separation of the patches to achieve a 15% bandwidth. As a starting point in the optimizer, we use the values from the cavity model [15], i.e., L = 5.73 cm and W = 6.60 cm, respectively. The bottom patch is probe-fed and the top patch is parasitically coupled to the driven patch. The top patch has the same dimensions.

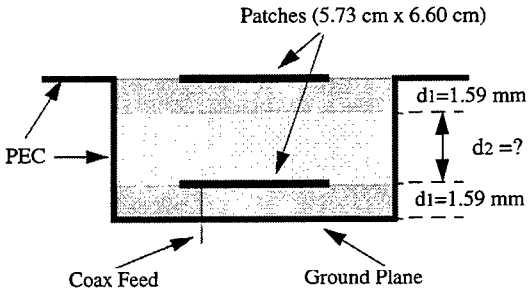

Figure 4: Geometry of the dual patch antenna.

Keeping the patch lengths and widths at L = 5.73 cm and W = 6.60 cm, respectively, the problem statement is simply, min R_{in}/R_0.

After 9 iterations of the optimizer, a value of $d_2 = 14.25mm$ was determined which delivers a bandwidth of 15%. The VSWR is less than 2.09, within the entire bandwidth. This is a great improvement from the original single patch. The center frequency is 1.53 GHz, if the patch size is $5.73cm \times 6.6cm$. Figure 5 gives the iteration history for the dual patch optimization, and Figure 6 shows the performance of the optimal patch configuration.

5. Conclusions

The advantages of the SQP algorithm are fast convergence and reduced number of function evaluations. This is attractive when expensive computations are needed within the optimization loop. SQP achieves its speed by restricting its search in a more narrow range (local optimization) than genetic algorithms, and making use of gradient information. This is suitable for a large class of antennas where a limited range of parameter values is sufficient for good performance. Apart from the differences among optimizers, there are other important issues related to the interface of the antenna simulation and optimization algorithms. True optimization requires full variability of the antenna parameters but numerical analyses are often too restrictive to allow for free parameter variations. This can only lead to local optimizations and it restricts the achievement of innovative designs which may deviate from the known classes of antennas. FEM codes are less restrictive. Nevertheless, greater flexibility

in analyses algorithms is needed to exploit and realize the true value of optimization techniques.

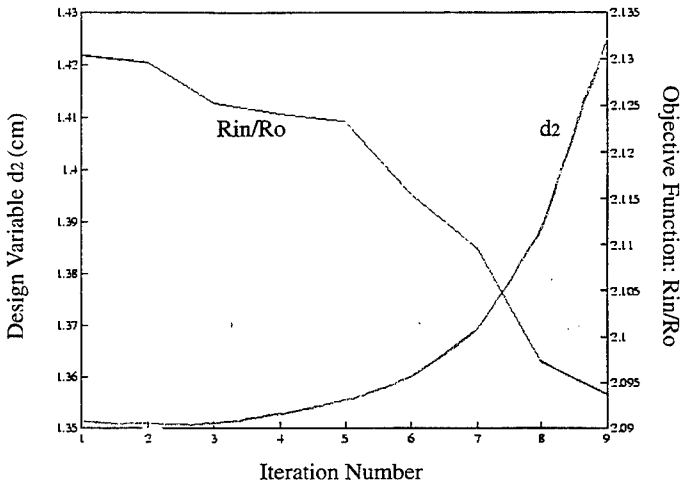

Figure 5: Iteration history for the optimization of the dual patch antenna.

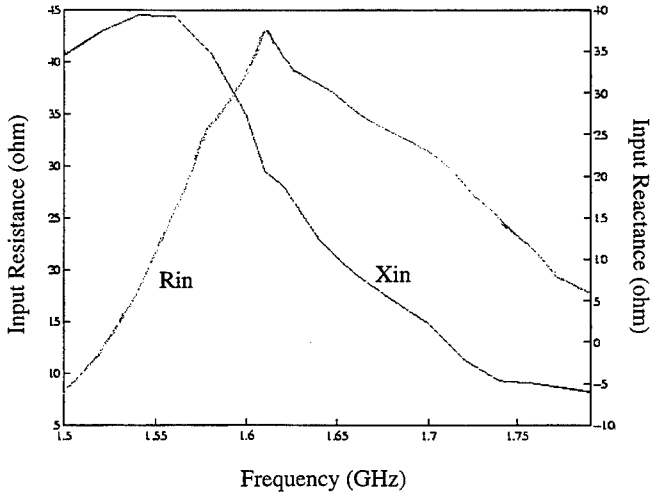

Figure 6: Performance of the optimized dual patch antenna.

6. References

[1] Pozar, D.M. and Schaubert, D.H., *Microstrip Antennas*, IEEE Press (reprints volume), New York, 1995.

[2] Volakis, J.L., Gong, J. and Ozdemir, T., "Application of the FEM to conformed antennas," in *Finite Element Software for Microwave Engineering*, Itoh et. al., (ed.), pp. 313-345, Wiley, New York, 1996.

[3] Penny, C. and Luebbers, R.J. "Radiation and scattering of a square archimedean spiral antenna using FDTD", *Electromagnetics*, vol. 14, no. 1, pp. 87-98, 1994.

[4] Haupt, R.L., "Introduction to genetic algorithms for electromagnetics," *IEEE Antennas & Propagation Magazine*, vol. 37, no. 2, Apr. 1995, pp. 7-15, 1995.

[5] Haupt, R.L., "Thinned arrays using genetic algorithms," *IEEE Transactions on Antennas and Propagation*, vol. 42, no. 7, pp. 993-999, 1994.

[6] Weile, D.S., Michielssen, E. and Goldberg, D.E., "Genetic algorithm design of Pareto optimal broadband microwave absorbers", *IEEE Transactions on Electromagnetic Compatibility*, vol. 38, pp. 518-525, 1996.

[7] Michielssen, E., Sajer, J.M., Ranjithant, S. and Mittra, R., "Design of lightweight, broad-band microwave absorbers using genetic algorithms," *IEEE Transactions on Microwave Theory and Techniques*, vol 41, no. 6-7, pp. 1024-1030, 1993.

[8] Olhoff, N. and Rozvany, G.I.N., (eds.), *Structural and Multidisciplinary Optimization*, Pergamon-Elsevier, Oxford, 1995.

[9] Crane, R.L., Hillstrom, K.E., and Minkoff, M., *Solution of the General Nonlinear Programming Problems with Subroutine VMCON*, Argonne National Labs, 1990.

[10] Volakis, J.L., Gong, J. and Alexanian, A., "A finite element-boundary integral method for antenna RCS analysis," *Electromagnetics*, vol. 14, no. 1, pp. 63-85, 1994.

[11] Papalambros, P.Y. and Wilde, D. J., *Principles of Optimal Design*, Cambridge University Press, New York, 1988.

[12] Armijo, L., "Minimization of functions having Lipschitz continuous first partial derivatives," *Pacific Journal of Mathematics*, vol. 16, no. 1, pp.1-3, 1966.

[13] Goldstein, A.A., "On steepest descent," *SIAM J. on Control*, vol.3, pp. 147-51, 1965.

[14] Dahele, J.S., Tung, S.H. and Lee, K.F., "Normal and Inverted Configurations of the broadband Electromagnetically Coupled Microstrip Antennas," *IEEE AP-S Int. Symp. Digest*, 1986, pp. 841-844.

[15] James, J.R. and Hall, P.S., "Handbook of Microstrip Antenna," *IEE Electromagnetic Waves, Series 28*, Peter Peregrunus, London, 1989.

A Novel Integration of Genetic Algorithms and Method of Moments (GA/MoM) for Antenna Design

J. Michael Johnson[1] and Yahya Rahmat-Samii[2]
Department of Electrical Engineering
University of California, Los Angeles
405 Hilgard Ave
Los Angeles, CA 90095-1594
[1]johnson@ee.ucla.edu, [2]rahmat@ee.ucla.edu

Abstract—This paper introduces a novel technique for efficiently integrating Genetic Algorithms (GAs) with Method of Moments (MoM) for antenna design and related electromagnetic problems through the application of direct Z-matrix manipulation (DMM). In the DMM approach to GA and Method of Moments (GA/MoM), a "mother" impedance or Z-matrix is filled only once at the beginning of the GA process, and then the GA optimizer operates on subsets of the original "mother" Z-Matrix to perform the optimization. Application of DMM for GA/MoM significantly reduces the total optimization time by eliminating multiple Z-matrix fill operations. DMM also facilitates the use of matrix partitioning and pre-solving to further reduce the optimization time in many practical cases. The design of a broadband patch antenna using GA/MoM with DMM is detailed by way of example.

INTRODUCTION

As wireless systems find wider acceptance, performance and cost constraints on the antennas that are essential for these new wireless systems become more difficult to meet. To address the new requirements, new innovative antenna designs will be required. To date, most wireless system antenna designs have been derived by extending canonical designs such as the monopole or the ½ and ¼ wavelength patch antennas. Generally, new designs, especially those featuring wide bandwidth are arrived at by applying engineering judgment and/or through serendipitous discovery [1]. Either way, the development of new designs can be slow. What is needed is a new approach that allows the designer to specify some design goals and generate a candidate structure with little or no engineering expertise. One approach that holds much promise is the coupling of full wave electromagnetic modeling codes with optimization methods.

Recently, several investigators have reported encouraging results coupling a relatively new form of optimization known as the Genetic Algorithm (GA) with Method of Moments (MoM) [2-4]. In particular [2] reported the design of compact microwave filters using GA coupled with a 2.5D method of moments analysis technique and [3,4] reported some interesting results of applying the well known NEC code and GA to the design of circularly polarized wire antennas with broad angular coverage. In both of these cases the results obtained from the GA optimization exhibited excellent performance for the selected optimization parameters. These examples also resulted in entirely unconventional and non-intuitive physical results.

A novel integration of GA and MoM is introduced here that utilizes direct manipulation of the Z-matrix (DMM) which results in significant computational time savings in the optimization process.

The use of matrix partitioning and pre-solving along with DMM to reduce the solve time for some problems is also presented. Finally, some results of successful GA optimization of a broadband patch antenna design are detailed.

GENETIC ALGORITHMS

Genetic Algorithms (GAs) are a class of robust optimization methods modeled on the concepts of natural selection and evolution. As optimizers, GAs are adept at handling complex, multi-modal optimization problems, especially those that are naturally combinatorial. Unlike more familiar gradient methods, GA optimizers tend to yield results that are near global maxima even in high dimensional, multi-modal function domains and the results are achieved in a near optimal manner. GA optimizers do not require object functions that are differentiable or even continuous, again unlike the more familiar gradient methods. Genetic Algorithms are classified as global optimizers while more familiar techniques such as conjugate gradient and the quasi-Newton methods are generally classified as local optimizers.

The concepts of computer based Genetic Algorithms were first introduced and later formalized by Holland in [5]. Around the same time, the application of GAs was extended to functional optimization by De Jong [6]. The first application of GAs to an electromagnetic problem was by Michielssen et. al. [7] in the design of broadband multilayer absorbers. GAs differ from more conventional techniques in that 1) they operate on a group (or *population*) of trial solutions in parallel, 2) they normally operate on a coding of the function parameters (*chromosome*) rather than on the parameters themselves, and 3) they use simple, stochastic operators (*selection*, *crossover*, and *mutation*) to explore the solution domain in search of an optimal solution.

In a simple Genetic Algorithm (GA) optimizer, a set of trial solutions is caused to evolve toward an optimal solution under the selective pressure of the fitness function. The trial solutions are represented by a string of parameters, generally encoded in some form such as binary. The trial solutions or individuals, form a population. Operators called selection, crossover and mutation act on the population of trial solutions to produce a new generation from the current generation. The optimization objectives are used to influence the constitution of the new generation through evaluation of the fitness function that assigns a numerical value to each individual.

A block diagram of a simple GA optimizer is illustrated in Figure 1. After an initial population is formed and fitness values are assigned to each member of the population, a reproductive loop, consisting of the operations selection, crossover and mutation, is performed until enough new individuals are generated to fill the new generation. When a new generation has been completely filled, the new generation replaces the old generation and if the termination criteria has not been met, a new round of selection, crossover, and mutation begin. Details of the implementation of a GA optimizer, and the various operators involved are covered in [8]. EM applications of GAs along with many relevant references are presented in [9].

METHOD OF MOMENTS

Since the goal in this paper is the development of wideband antennas using optimization methods such as GA, evaluation of the performance of antenna structures that are developed in an optimization design effort must be carefully considered. In GA the fitness function provides the only link between

the optimization algorithm and the problem under consideration. In particular, evaluation methods must be capable of accurately accounting for local interactions such as mutual coupling and parasitic coupling. This usually implies a form of full wave analysis such as FDTD or Method of Moments (MoM). Since the majority of antenna structures can be reasonably well described by a set of wires, sources, and metal plates, an Electric Field Integral Equation (EFIE) based MoM provides considerable flexibility. We will concentrate here on EFIE MoM as the performance evaluation engine for the optimization process.

EFIE MoM is a well-established full wave method for evaluating the performance of arbitrarily shaped electromagnetic structures consisting of wires and electrically thin metal plates. The method involves sub-dividing the metal surfaces and wires in the modeled structures. A basis function representing an expansion of the unknown currents is applied to the discretization and a testing function is applied to resulting integral equations to produce a set of linear equations from which the solution in terms of surface currents on the wires and metal surfaces. This allows the general problem to be reduced to the solution of a set of linear equations of the form of equation (1),

$$ZI = V \tag{1}$$

where Z is the so called Z-matrix or impedance matrix that specifies the relationship between the various surface patches and wire segments in the problem, V is a vector accounting for voltage sources, and I is a vector containing the unknown currents that are to be found.

Although a number of basis function sets and testing functions have been applied to this type of problem, an excellent choice of testing and basis functions is to use point matching or a delta function for the testing function and to use the RWG basis function set developed in [10]. The Rao, Wilton, Glisson (RWG) basis function set has the advantage of not requiring different basis functions for boundary elements and interior elements and is designed to be used with triangular surface patches. Triangular patches are much better suited to the modeling of arbitrary surfaces than rectangular patches. The wire elements are well modeled by triangular basis functions [11]. An important modification, especially important in small structures, involves the balancing of currents at any wire/surface junctions to ensure continuity of current as required by Kirchoff's current law. In addition, a straight forward modification of the Green's function in the EFIE enables the inclusion of infinite ground planes. Having established the discretization and chosen a testing and basis function, a Z-matrix can be constructed. This construction, in the case of the RWG basis with point matching, essentially reduces down to the successive evaluation of three integrals for each pair of patches in the modeled structure. This is often referred to as the "filling" operation. Once a Z-matrix is constructed, the desired solution in terms of surface currents is obtained by solving the linear equations of (1).

GA/MoM Methodology

Now, consider the situation where some of the metal of the original structure is absent. In this case, the currents for these patches are identically zero. Since the solution of (1) should be unique, zeros in the solution vector are assumed to correspond to zero rows and columns in the Z-matrix. In practice, these zero rows and columns cause problems in solving (1) and are simply not included when a Z-matrix is constructed for the case with missing patches of metal.

We can, therefore, consider an optimization methodology as depicted in Figure 2. In this methodology, a *mother* Z-matrix is constructed that includes the presence of metal everywhere that we might allow metal to be. All possible structures that can be constructed from this *mother* configuration then become subsets of this *mother* configuration. The Z-matrices of these subset configurations likewise are realized to be sub matrices of the *mother* Z-matrix. Put simply, the Z-matrix of any substructure can be derived from that of the *mother* structure by simply removing the rows and columns of the matrix corresponding to the pieces of metal that are being removed. The other matrix elements are unchanged by this removal of elements. An exception to this rule is that the matrix elements that are formed by junctions between wire segments and metal patches. In these cases, the entries in the Z-matrix are dependent on other rows and columns due to the application of Kirchoff's current law to relate the surface currents in the surface patches and the wire attached thereto. However, excluding these rows and columns, all substructures can be formed by simply removing rows and columns from the *mother* Z-matrix, voltage vector and current vectors of equation (1). A solution methodology is then apparent that allows for the exploration of a large number of potential configurations without the need for costly re-execution of the Z-matrix filling operations.

The chromosome in this case is simply a string of ones and zeros, one bit for each subsection in the *mother* structure. A zero represents the absence of metal while a one represents the presence of metal. The fitness function involves solving a $ZI = V$ equation for a sub-matrix derived from the original, *mother* Z-matrix and then extracting the appropriate parameters from the results to compare with the optimization goals.

Referring to Figure 2, a sub-matrix, $\tilde{Z}$, is created from the *mother* Z-matrix by removing the rows and columns corresponding to a mapping of the zeros in the chromosome to metal regions in the model. The $\tilde{Z}\tilde{I} = \tilde{V}$ equation is then solved and the resulting current vector is used to extract the desired parameters such as input impedance or antenna pattern.

This method avoids the cost of refilling the Z-matrix at each re-evaluation of the fitness function that can be substantial. Figure 3 shows the times involved in filling and subsequently solving a typical MoM problem relative to the number of unknowns involved. For the typical problem with less than about 200 unknowns, fill time is on the order of the solve time. This time savings can be particularly important when considering an optimization problem that may involve a large number of successive MoM evaluations. If we consider a problem involving 100 unknowns, and where we might use a population of 100 individuals and 100 generations, the total time saved by not refilling the matrix as outlined above amounts to 133 minutes on a 200 MHz Pentium Pro running LINUX. In other words, with the DMM methodology proposed above, a total optimization time of approximately 50 minutes results as opposed to 183 minutes without the application of DMM.

Having adopted the DMM approach we can exploit a second computational cost saving methodology by using matrix partitioning. Many problems involve portions of a given modeled structure that are modified during optimization along with portions that are not modified. This characteristic can be exploited to achieve further execution time savings by partitioning the matrix equation and "pre-solving" a portion of the equation associated with the elements that are not changed [12]. If we partition the problem such that the elements that do not change, or are always present, are

always located in the lower right corner of the matrix, we can solve the equation as outlined in equations (2)-(5). With partitioning, equation (1) becomes

$$\begin{bmatrix} Z_{mm} & Z_{cm} \\ Z_{mc} & Z_{cc} \end{bmatrix} \begin{bmatrix} I_m \\ I_c \end{bmatrix} = \begin{bmatrix} V_m \\ V_c \end{bmatrix} \tag{2}$$

where the subscript m refers to elements that may be modified (removed) during optimization and c refers to elements that are constant during optimization. After partitioning, the matrix equations can be solved for I_c as given in equations (3) and (4).

$$I_c = Y_{cc} \cdot \{V_c - Z_{mc} I_m\} \tag{3}$$

$$Y_{cc} = Z_{cc}^{-1} \tag{4}$$

Then substituting this result back into (2) and solving for I_c we get, after some simple algebra, equations (5) and (6).

$$Y_{mm} = \{Z_{mm} - Z_{cm} Y_{cc} Z_{mc}\}^{-1} \tag{5}$$

$$I_m = Y_{mm} \{V_m - Z_{cm} Y_{cc} V_c\} \tag{6}$$

If we count the number of complex multiplication operations necessary to repeatedly solve the system represented by the original matrix equation (2) vs the result of pre-solving for I_c using equation (3) and (4) followed by (5) and (6) we find that when *the number of elements that are modfied* is less than or equal to *number of elements that are held constant*, the application of matrix partitioning and pre-solving can yield significant savings in computation time.

WIDEBAND PATCH ANTENNA DESIGN EXAMPLE

The GA/MoM method described above has been applied to several antenna optimization problems involving plates and wires. In these cases the optimization goals were to be met through the modification of the plates by the removal of patches of metal.

Consider the design of a broadband patch antenna. Usually broadband patch designs are achieved by adding passive resonating elements to a basic design leading to antennas that are usually much larger and/or more complicated to build and tune. The goal here was to produce a patch antenna that has an acceptable, 2:1 VSWR, match over a 20% bandwidth centered at 3 GHz. As can be seen in Figure 4, the initial match, as indicated by a dotted line, has a bandwidth of approximately 6%. The original patch design consists of a 0.48 x 0.48 cm patch suspended 0.048 cm above an infinite ground plane. The feed consists of a wire with a voltage source at the ground plane/wire interface and located 0.24 x 0.12 cm from the corner of the patch. The original patch structure including the triangularization used is shown in Figure 5.

A *mother* matrix for the original design was formed and GA optimization was performed by removing square metal from the patch region as outlined above. The population size was 100 individuals and 100 generations were produced. Probability of crossover was set at 0.7 while the probability of mutation was equal to 0.02. Elitism and roulette wheel selection [9] were used. The goal was to minimize the maximum S11 magnitude at three frequencies, 2.7 GHz, 3 GHz and 3.3 GHz. The fitness function in this case is given by equation (9),

$$fitness = \min_{\forall n}(S11_n) \tag{9}$$

where the subscript n refers to sample points in the S11 vs frequency function.

The results of the best individual from the GA/MoM optimization in terms of magnitude S11 are shown in Figure 4 as a solid line. As can be seen, an acceptable 2:1 match has been achieved over the entire 2.7-3.3 GHz band. The resulting structure is shown in Figure 6. While not an intuitive result, the design is readily realizable by standard printed circuit board techniques.

It is reasonable to ask whether or not the MoM model represented by the structure of Figure 5 is still valid. To test whether the result after GA optimization still represents a converged solution, the structure of Figure 6 was analyzed using MoM for a discretization having twice the density. The calculated S11 results for both the single and double density discretization are plotted in Figure 8. Very little change is observed in either the original square patch performance or that of the optimized patch so we can conclude that the result in the optimized case is representative of the true performance of the design within the limitations of MoM.

As an aside, we might consider approaching these designs through an exhaustive manual trial and error method. In the first case we had 72 triangular patches grouped into 36 square patches. There are 2^{36} or 68.7×10^9 possible combinations of this design. The GA approach required less than 3×10^3 solutions of the ZI=V equation to find a good result. For the patch antenna case we again had 36 square patches and three frequencies or 206.2×10^9 possible configurations of patches and frequencies. Again GA/MoM found a good result after only 10×10^3 trials.

CONCLUSION

The goal of this paper was to present a method of combining GAs with MoM involving direct matrix manipulation (DMM) that yields significant reductions in analysis cost by eliminating the multiple re-filling of the Z-matrix. In addition, a technique for achieving computational cost savings from matrix partitioning and pre-solving of portions of the problem was described. As was true with earlier investigators, the current investigation found that GAs coupled with method of moments can yield some surprising, high performance designs for antennas. In particular, compact broadband patch antennas were developed using this technique. The use of GAs for the design of compact antennas combining metal patches and wires has been demonstrated. There is much promise for this technique.

Acknowledgments– This work was supported in part by DARPA Contract number JFBI94-222/J4C942220

REFERENCES

[1] Johnson, J. M. and Y. Rahmat-Samii, "The TabMonopole," *IEEE Trans. Antennas and Propagat.*, vol. 45, no. 1, January 1997.

[2] John, a and R. H. Jansen, "Evolutionary Generation of (M)MIC Component Shapes using 2.5D EM Simulation and Discrete Genetic Optimization," *1996 MTT-S Digest*, pp. 745-748.

[3] Linden, D. S. and E. E. Altshuler, "Automating Wire Antenna Design using Genetic Algorithms," *Microwave Journal*, vol. 39, March 1996, pp. 74-86.

[4] Linden, D. S., and E. E. Altshuler, "The design ofYagi antennas using a genetic algorithm,"*Proceedings of the USNC/URSI Radio Science Meeting,* Baltimore, MD, July 1996, pp. 283.

[5] Holland, J. H., *Adaptation in Natural and Artificial Systems.* Ann Arbor, MI: University of Michigan Press, 1975.

[6] De Jong, K. A., "An Analysis of the Behavior of a Class of Genetic Adaptive Systems," (Doctoral dissertation, University of Michigan). *Dissertation Abstracts International*36(10), 5140B. (University Microfilms No. 76-9381), 1975.

[7] Michielssen, E., J. Sajer, S. Ranjithan, and R. Mittra, "Design of Lightweight, Broad-band Microwave Absorbers Using Genetic Algorithms, *IEEE Trans. Microwave Theory and Tech.*, vol. 41, no. 6/7, June/July 1993, pp. 1024-1031.

[8] Goldberg, D. E., *Genetic Algorithms in Search, Optimization and Machine Learning* Addison-Wesley, 1989.

[9] Johnson, J. M. and Y. Rahmat-Samii, "Genetic Algorithms in Engineering Electromagnetics," submitted for publication in the*AP Magazine.*

[10] Rao, S. M., D. R. Wilton and A. W. Glisson, "Electromagnetic Scattering by Surfaces of Arbitrary Shape," *IEEE Trans. Antennas Propagat.*, vol AP-30, no. 3, pp. 409-418, May 1982.

[11] Hodges, R.E., and Y. Rahmat-Samii, "An Iterative Current-Based Hybrid Method for Complex Structures," *IEEE Trans. Antennas and Propagat.*, vol. 45, no. 2, February 1997.

[12] Parhami, P., Y. Rahmat-Samii and R. Mitra, "Technique for Calculating the Radiation and Scattering Characteristics of Antennas Mounted on a Finite Ground Plane," *Proc. IEE*, vol. 124, no. 11, November 1977, pp. 1009-1016.

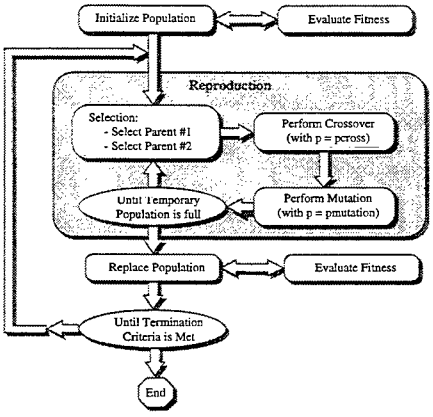

Figure 1: Block diagram of a simple genetic algorithm optimization.

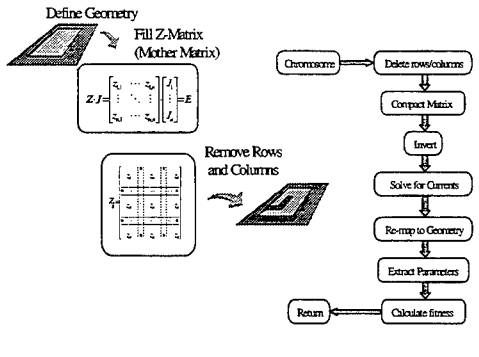

Figure 2: Block diagram of GA/MoM Direct Matrix Manipulation approach.

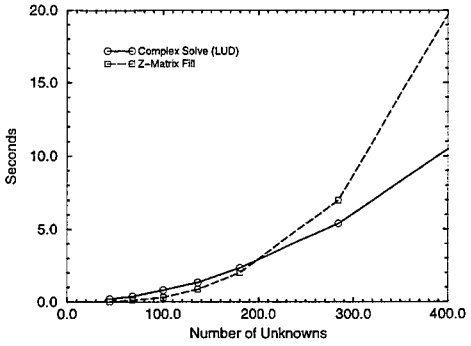

Figure 3: Matrix fill time and matrix inversion time comparison.

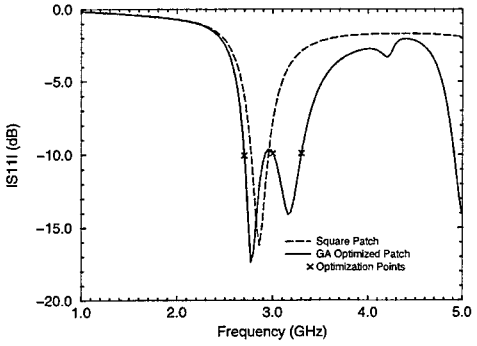

Figure 4: Calculated S11 for patch antenna before and after GA/MoM optimization.

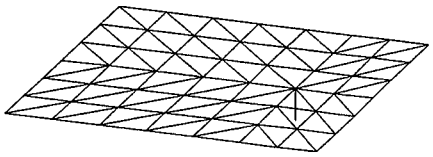

Figure 5: Original patch above an infinite ground plane (not shown) structure showing triangular discretization used in MoM analysis.

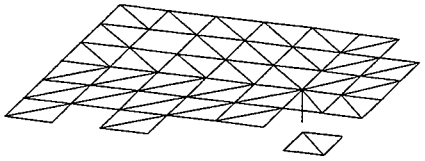

Figure 6: GA/MoM optimized patch antenna above an infinite ground plane (not shown).

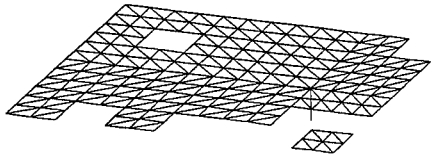

Figure 7: Optimized patch structure above an infinite ground plane (not shown) showing double density discretization.

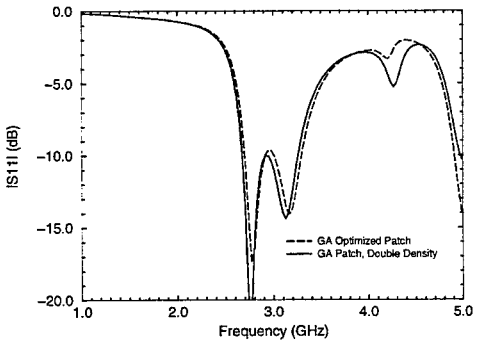

Figure 8: Calculated S11 of optimized patch at original discretization density and with doubled density discretization.

The Application of Novel Genetic Algorithms to Electromagnetic Problems

Daniel Treyer, Daniel S. Weile, and Eric Michielssen
Center for Computational Electromagnetics
University of Illinois at Urbana-Champaign
1406 W. Green Street
Urbana, IL 61801

Abstract

Two novel genetic algorithms called the Gene Expression Messy Genetic Algorithm and the Community Genetic Algorithm are applied to problems of electromagnetics. These algorithms have been devised to enhance their convergence properties, as well as the quality of the resulting solution when compared to standard genetic algorithms. The Gene Expression Messy Genetic Algorithm is applied to the problem of thinning an array of isotropic radiators to lower their sidelobes, while the Community Genetic Algorithm is applied to the synthesis of doubly periodic frequency selective surface. Results for both algorithms are presented.

1. Introduction

Based on Darwin's Theory of Descent with Modification by Natural Selection, Genetic Algorithms (GAs) have become an increasingly popular tool for the optimization of electromagnetic devices [1]. Because of their empirical robustness and resistance to convergence to poor optima, they have been applied to problems ranging from antenna array synthesis [2] to optical filters [3] and microwave absorbers[4]. Unfortunately, as stochastic optimization routines GAs can converge quite slowly, requiring many thousands of objective function evaluations before settling on an acceptable optimum. To address this deficiency, this paper introduces two novel algorithms for optimizing electromagnetic devices: the Gene Expression Messy GA (GEMGA) [5] and the Community Genetic Algorithm (CGA).

First, the GEMGA is applied to the thinning of linear arrays of isotropic elements to lower the maximum sidelobe level radiated by the array. The GEMGA is a modified GA which uses information about the local behavior of the objective function in its search for building blocks of the optimal solution. Because it combines candidate solutions to the problem using information about the fitness of constituents of their genetic material, the GEMGA has been shown to be a more robust algorithm than the standard GA for many difficult problems [5].

Second, a CGA is applied to the design of Frequency Selective Surfaces (FSSs). The CGA uses a community structure to both enhance the convergence of the algorithm and accelerate the analysis of the devices which is very computationally intensive. Though community structures are not uncommon in the GA literature, the CGA described here is specially designed for the optimization of stratified electromagnetic devices.

The remainder of this paper will proceed as follows. Section 2 will describe both the GEMGA and the CGAs, as well as the specific problems to which they will be applied. Section 3 will present the results of the applying each algorithm to its respective problem, and compare the results with available results from the literature and standard algorithms.

2. Formulation

2.1 The Gene Expression Messy Genetic Algorithm and Array Thinning

In this section, we demonstrate the design of a linear antenna array consisting of an even number of isotropic radiators, spaced a half wavelength apart. The array excitation is symmetric with respect to the array center and the feed current for each element can either be 1 or 0 (on or off, all in phase). The GEMGA then searches for the element excitation which minimizes the maximum relative sidelobe level (MSLL) of the array in the far-field.

Like a standard GA, the GEMGA begins with a population of binary strings called chromosomes describing a subset of all potential design candidates initialized at random. Also like a standard GA, all design parameters (i.e. the excitation states of each element) are binary encoded and concatenated to form a chromosome. Unlike the standard GA, however, each bit in each chromosome also has an associated weight, which will serve as an indicator of the quality of the corresponding gene in the context of its chromosome. Once the population is initialized, the GEMGA enters the primordial phase where the weights are determined, and then begins the juxtapositional phase where he actual optimization process takes place.

The primordial phase begins by finding the objective function value of each chromosome. To determine the weights, a transcription operator is applied to each gene in each chromosome as follows. The value of the gene under consideration is temporarily negated and the change of fitness of the corresponding chromosome is observed. If the fitness increases, the weight will be set to zero, since the original value is not such that fitness is maximized. Conversely, if the fitness decreases, the original bit is locally optimal and the weight will be assigned the absolute value of change in fitness.

After all of the weights have been allotted, the juxtapositional phase begins to isolate and reproduce superior building blocks (bit combinations), using selection and crossover. The two selection operators used, fitness selection and class selection, work with the fitness values and weights respectively. The fitness selection operator is similar to that in the standard GA. Two chromosomes are chosen from the population without replacement. With probability P_{fit}, the superior chromosome is allotted two spaces in the subsequent generation, and with probability $1-P_{fit}$ the two chosen chromosomes are grafted into the next population unchanged. Contrary to fitness selection, the class selection operator works on individual genes rather than on whole chromosomes. Two chromosomes are picked at random for the application of class selection with probability P_{class}. If class selection is to be applied to the pair, the weights of bits at equal positions in the chromosomes are compared with each other. A bit with higher weight will overwrite the corresponding gene with lower weight in the other chromosome. Pairs to which class selection is not applied are copied unmodified into the next generation.

Crossover in the GEMGA is also effected in concert with the weights. Again, two chromosomes are picked at random to undergo recombination with probability P_{recomb}. The weights of bits in the same positions in each chromosome are compared with each other. The chromosomes are then hybridized such that one chromosome receives all the bits with lower weights, and the other chromosome obtains all the bits with higher weights. Again, pairs not crossed are inserted into the next generation unchanged. Fitness, class selection and recombination are then iteratively applied to the population in this orderuntil some termination criteria is met.

2.2 The Community Genetic Algorithm and Frequency Selective Surface Design

We now describe a procedure for the design of FSSs using the CGA. FSSs are composed of layers of dielectric material whose electromagnetic filtering properties are enhanced by the inclusion of periodic metallization between the dielectric slabs (Figure 1). The design of an FSS therefore entails finding the dielectric constants and thicknesses of the slab layers, and choosing the shape size and period of the intervening metallization to match a desired filter response. All of this information may be encoded into a binary chromosome, with the shape and dielectric picked from a database of useful shapes and available dielectrics, and the other real parameters decoded between two limiting values using the method described in [4]. Unfortunately, unlike the antenna array problem above which is computationally simple, the analysis of FSSs uses a spectral Galerkin technique [6] which is computationally expensive, rendering most general optimization algorithms ineffective. Thus the algorithm we present here is specifically designed to accelerate both the analysis of groups of FSSs and the convergence of the GA.

Specifically, CGAs are two tiered algorithms which operate on groups of similar designs as well as the designs themselves to speed the convergence of the algorithm. In each algorithm, the design descriptions have two parts: a community part which describes everything but the thicknesses of the dielectric slabs, and an individual part which only describes the slab thicknesses. Each community part is associated with several individual parts. The algorithm uses the evolutionary operators first to optimize the communities themselves, and then to optimize the individuals within each community. The process is thus a completely straightforward application of a standard GA on two levels, except for the problem of assigning objective function values to communities. This can easily be accomplished, however, by taking a weighted average of the best member in each community and each community's average values as the community objective function value.

The community structure of algorithm speeds both the analysis of the communities and the algorithm's convergence. The speedup in analysis is due to the observation that even though calculating the scattering from a single layer of periodic metallization involves the inclusion of hundreds of Floquet modes, very few propagate to other layers. The scattering contribution of these modes may be calculated quickly due to their local nature, and may be their contribution may be reused for an entire community. Community GAs also often allow a more parallel search, enhancing the convergence of a typical GA.

3. Numerical Results

To demonstrate the application of the GEMGA, an 80 element linear thinned antenna array was optimized. The settings of the GEMGA were as follows: chromosome length = 40 (by symmetry), P_{fit}=0.4, P_{class}=0, and P_{recomb}=1.0. Five different population sizes n were chosen: n=512, 1024, 2048, 4096, 8192. For each population size, five independent GEMGA runs were performed. The juxtapositional phase termination criteria were: the fitness of the best chromosome exceeds 21 dB, the number of objective function evaluations exceeds two million, 30 generations lapses without improvement in the best chromosome, or the number of juxtapositional generations exceeds 50. The GEMGA performance in these trials is graphed in Figure 2, with the radiation pattern of the optimal individual in Figure 3. Figure 2 shows that the minimum MSLL achieved is -20.5dB. As the algorithm repeatedly converged to the same design, this design is likely the global optimum. The design shown is also superior to that found for the same problem in [2].

The CGA was applied to the design of a twist polarizer which reflects incident Transverse Electric (TE) waves as Transverse Magnetic (TM) waves. The polarizer was designed with two sheets of periodic metallization and two dielectric slabs. To ensure full reflection the entire device was backed by a conducting sheet. The algorithm used 70 communities of 10 members each, with mutation probabilities varying between 0.001 and 0.1 and a crossover probability of 0.9. The algorithm ran with 10 community generations with two intervening individual iterations. The TM reflectance of the screens is shown in Figure 4.

4. Conclusions

Two novel genetic algorithms, the GEMGA and the CGA, have been introduced for the genetic optimization of electromagnetic devices. The GEMGA, which introduces more intelligent crossover and selection operators into genetic optimization, has been applied to the problem of thinned linear antenna array synthesis with results better than those published previously in the literature. The CGA was applied to the problem of FSS twist polarizers, also yeilding very good results. As the problems to which GAs are applied get more and more difficult, we expect that such novel approaches will be indispensable to electromagnetic design by evolutionary optimization.

References

[1] D. E. Goldberg, *Genetic Algorithms in Search, Optimization and Machine Learning*. Reading, MA: Addison-Wesley, 1989.

[2] D. S. Weile and E. Michielssen, "Integer coded Pareto genetic algorithm design of antenna arrays," *Electronics Letters*, vol. 32, no. 19, pp. 1744-1745, 1996.

[3] E. Michielssen, S. Ranjithan and R. Mittra, "Optimal multilayer filter design using real coded genetic algorithms," *IEE Proceedings-J*, vol. 139, no. 12, pp. 413-420, 1992.

[4] D. S. Weile, E. Michielssen and D. E. Goldberg, "Genetic algorithm design of Pareto optimal broad band microwave absorbers," *IEEE Transactions on Electromagnetic Compatibility*, vol. 38, no. 4, pp. 518-524, 1996.

[5] H. Kargupta, *SEARCH, Evolution, and the Gene Expression Messy Genetic Algorithm*, Technical Report LA-UR-96-60, Los Alamos National Laboratory, 1996.

[6] R. Mittra, C. H. Chan and T. Cwik, "Techniques for analyzing frequency selective surfaces-A review," *Proceedings of the IEEE*, vol. 76, no. 12, pp. 1593-1615, 1988.

Figures

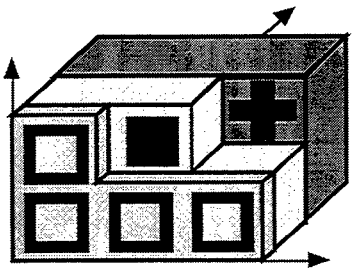

Figure 1. A typical FSS with three metallized layers and three dielectric slabs.

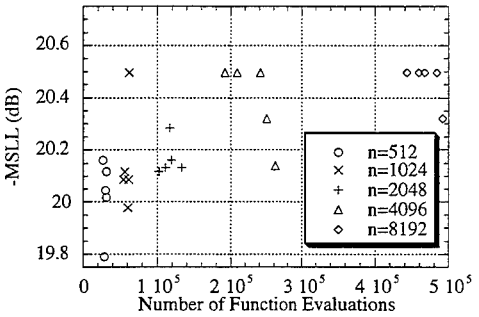

Figure 2. GEMGA performance on the thinned array problem with population size n.

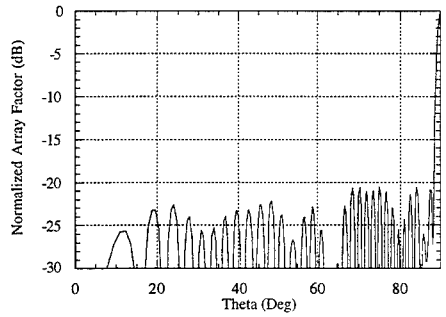

Figure 3. Optimal array pattern found by the GEMGA.

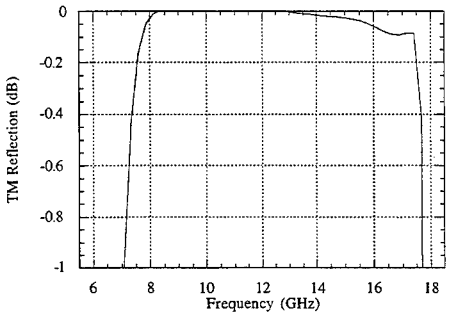

Figure 4. Response of a twist polarizer designed by the CGA.

Continuous Parameter vs. Binary Genetic Algorithms

Randy L. Haupt
HQ USAFA/DFEE
2354 Fairchild Dr, Suite 2F6
USAF Academy, CO 80840
and
Sue Ellen Haupt
HQ USAFA/DFP
2354 Fairchild Dr, Suite 2A6
USAF Academy, CO 80840

Abstract: This paper introduces the continuous parameter genetic algorithm and compares its performance with a binary genetic algorithm for reducing the sidelobe levels of an antenna array.

I. Introduction

Engineers use many advanced computational electromagnetics models to optimize antenna and RCS designs. Conventional numerical optimization relies upon so called "hill-climbing" methods, such as conjugate gradient and Powell's method. These algorithms are based on their analytical calculus ancestors that follow the steepest path up the closest hill. Genetic algorithms have the ability to break away from the hill-climbing mentality. Thus, the genetic algorithm is often a logical choice for optimizing an extremely complex cost function.

There is often a mistaken impression that the genetic algorithm can't optimize with continuous parameters (or at least parameters that are represented to machine precision). This allegation is simply not true, and the goal of this paper is to present a continuous parameter version of the genetic algorithm and explain when it is appropriate to use. In particular, the crossover and mutation operators are quite different from the binary genetic algorithm. Several alternatives to these operators will be presented. Some examples will be shown and a comparison made with the binary genetic algorithm.

II. Components of the Continuous Parameter Genetic Algorithm

The flow chart in Figure 3.1 provides a "big picture" overview of a continuous genetic algorithm. This genetic algorithm is very similar to the binary genetic algorithm. The primary difference is the fact

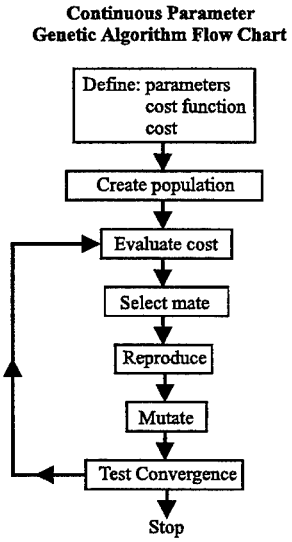

Figure 1:

that parameters are no longer represented by bits of zeros and ones, but instead by real numbers over whatever range is deemed appropriate. However, this simple fact adds some nuances to the application of the technique that must be carefully considered. In particular, we will carefully reconsider how to apply our crossover and mutation operators.

The population is a matrix in which each row of the matrix is a chromosome, an array of parameter values to be optimized. If the chromosome has N_{par} parameters (an N-dimensional optimization problem) given by p_1, p_2,...,$p_{N_{par}}$ then the chromosome is written as an array with $1 \times N_{par}$ elements so that

$$chromosome = \left[p_1,\ p_2,\ p_3, \cdots p_{N_{par}}\right] \tag{1}$$

In this case, the parameters are each represented as floating point numbers. Each chromosome has a cost found by evaluating the cost function, f, at the parameters p_1, p_2,...,$p_{N_{par}}$.

$$c = f\left(chromosome\right) = f(p_1, p_2, ..., p_{Npar}) \tag{2}$$

Equations (1) and (2) along with applicable constraints constitute the problem to be solved.

Since the genetic algorithm is a search technique, it must be limited to exploring a reasonable region of parameter space. Thus, constraints must be placed on the parameters. If one does not know the initial search region, there must be enough diversity in the initial population to explore a reasonable sized parameter space before focusing on the most promising regions.

To begin the genetic algorithm, we define an initial population of random chromosomes. A matrix represents the population with each row in the matrix being a $1 \times N_{par}$ array (chromosome) of continuous parameter values. This society of chromosomes is not a democracy: the individual chromosomes are not all created equal. Each one's worth may be assessed by the cost function. So at this point, the parameters are passed to the cost function for evaluation.

Now is the time to decide which chromosomes in the initial population are fit enough to survive and possibly reproduce offspring in the next generation. The costs and associated chromosomes are ranked from lowest cost to highest cost. We only retain the best members of the population for the next iteration of the algorithm. The rest die off. This process of natural selection must occur at each iteration of the algorithm to allow the population of chromosomes to evolve over the generations to the most fit members as defined by the cost function.

Not all of the survivors are deemed fit enough to mate. Only a subset of the best chromosomes mate to produce offspring to replace the discarded chromosomes. There are various methods of selecting parents, most of which are based on random selections with the best chromosomes weighted the most.

As for the binary algorithm, once the parents have been chosen, we must find a way to combine their information to produce offspring. The primary operator for doing this is the crossover in which the information between the two is exchanged. Many different approaches have been tried for crossing over in continuous parameter genetic algorithms. Adewuya [1] reviews some of the current methods thoroughly. Several interesting methods are demonstrated by Michalewicz [4] . The simplest methods choose one or more points in the chromosome to mark as the crossover points. Then the parameters between these points are merely swapped between the two parents. The extreme case is selecting N_{par} points and randomly choosing which of the two parents will contribute its parameter at each position. Thus, one goes down the line of the chromosome and at each parameter, randomly chooses whether or not to swap information between the two parameters. This method is called uniform crossover. The problem with these point cross-over methods is that no new information is introduced: each continuous parameter value that was randomly initiated in the initial population is propagated to the next generation, just in different combinations. Although this strategy worked fine for binary representations, now there is a continuum of values of which we are merely interchanging two data points.

The blending methods remedy this problem by finding ways to combine the information from the two parents into the offspring. The new offspring parameter value, p_{new}, is some combination of

$$p_{new} = \beta p_{parent1} + (1 - \beta) p_{parent2} \tag{3}$$

where β is a random number on the interval $[0, 1]$ [5] . The second offspring is merely the complement of the first (i.e.. replacing β by $1 - \beta$). If $\beta = 1$, then p_{parent} is propagated. The opposite occurs for $\beta = 0$. When $\beta = 0.5$ [2] , the result is an average of the parameters of the two parents. This method is demonstrated to work well on several interesting problems by Michalewicz [4] . Choosing which parameters to blend is the next issue. Sometimes, this linear combination process is done for all parameters to the right or to the left of some cross-over point. Any number of points can be chosen to blend, up to N_{par} values where all parameters are linear combinations of those of the two parents. The parameters can be blended by using the same β for each parameter or by choosing different β's for each parameter. These blending methods effectively combine the information from the two parents and choose values of the parameters between the values bracketed by the parents; however, they do not allow introduction of values beyond the extremes already represented in the population. To do this requires one of the extrapolating methods. The simplest of these methods is linear crossover [6] . In this case, three offspring are generated from the two parents by

$$p_{new1} = 0.5 p_{parent1} + 0.5 p_{parent2} \tag{4}$$

$$p_{new2} = 1.5 p_{parent1} - 0.5 p_{parent2} \tag{5}$$

$$p_{new3} = -0.5 p_{parent1} + 1.5 p_{parent2} \tag{6}$$

Any parameter outside the bounds is discarded in favor of the other two. Then the two best of the

offspring are chosen to propagate. Of course, the factor 0.5 is not the only one that can be used in such a method. Heuristic crossover [4] is a variation where some random number, β, is chosen on the interval $\beta \in [0, 1]$ and the parameters of the offspring are defined by

$$p_{new} = \beta(p_{parent1} - p_{parent2}) + p_{parent1} \tag{7}$$

Variations on this theme include choosing any number of parameters to modify and generating different β for each parameter. Note that this method allows generation of offspring outside of the bounds. If this happens the offspring is discarded and the algorithm tries another β. The BLX-α (blend crossover) method [3] begins by choosing some parameter α that determines the distance outside the bounds of the two parent parameters the offspring parameter may lie. This method allows new values outside of the range of the parents without letting the algorithm stray too far. Many codes combine the various methods to use the strengths of each. New methods, such as quadratic crossover [1] , do a numerical fit to the fitness function. Three parents are necessary to perform a quadratic fit.

We can sometimes find our method working a bit too well. If care is not taken, the genetic algorithm converges too quickly into one region of the cost surface. If this area is in the region of the global minimum, that is good. However, some functions, such as the one we are modeling, have many local minima. If we do nothing to solve this tendency to converge quickly, we could end up in a local rather than a global minimum. To avoid this problem of overly fast convergence, we force the routine to explore other areas of the cost surface by randomly introducing changes, or mutations, in some of the parameters. For the binary algorithm, this amounted to just changing a bit from a 0 to a 1 or vice versa. The process for the real valued genetic algorithm the basic method of mutation is not much more complicated (although more complicated methods exist [4]).

To introduce mutations to a real valued chromosome, we must first decide an appropriate mutation rate. This percentage is not cast in stone, but must be determined on a problem by problem basis. However, a bit of hand-waving guidance suggests that a percentage similar to that used for a binary genetic algorithm is most appropriate (1 to 5%). Next we need to randomly determine which parameter of which chromosome mutates. This is most easily done by simply choosing random locations in the chromosome parameter matrix. Then a new random parameter is generated.

III. Example.

The linear array model has an even number of point sources lying along the x-axis. Its mathematical formulation when the main beam points at broadside is given by

$$AF(\phi) = 2\sum_{n=1}^{N} a_n \cos\left[(n - .5)\Psi\right] \tag{8}$$

where

$2N$ = number of elements
$\Psi = kd\cos\phi$
a_n = array weight at element n
$k = \frac{2\pi}{\lambda}$
λ = wavelength
d = spacing between elements
ϕ = angle of incidence of electromagnetic plane wave

The objective is to minimize the maximum sidelobe level of the array factor of a 42 element array. An analytical solution already exists in the form of the binomial amplitude taper which has no sidelobes.

Figure 2 shows the convergence of the binary genetic algorithm that represents the amplitude weights with ten bit accuracy. This version of the algorithm only worked with a population of 16 chromosomes.

Figure 3 shows the convergence of the continuous parameter genetic algorithm. In this case, the amplitude weights are represented to machine precision (double precision on a PC). The continuous parameter genetic algorithm did not perform as well as the binary genetic algorithm.

So, why use the continuous parameter genetic algorithm? One reason is that you don't have to worry about how many bits are needed to appropriately represent a parameter. If we used only five bits to represent the amplitude weights, the binary genetic algorithm arrives at a worse solution than the continuous parameter genetic algorithm (only a -130 dB sidelobe level). Another reason is the parameters may assume a finite number of values that is not divisible by 2. Thus, the parameter encoding is inefficient. Finally, the parameters might have to be represented to machine precision.

We tried optimizing the amplitude weights using the Nelder Mead Downhill Simplex algorithm. This algorithm failed to converge after 4000 iterations with a random starting point.

IV. Conclusions.

Both the binary and continuous parameter genetic algorithms quickly found a reasonable approximation of the binomial array amplitude taper. The Nelder Mead Downhill Simplex algorithm could not find a solution due to the large number of parameters. Thus, the continuous parameter genetic algorithm is an acceptable alternative to the binary genetic algorithm in many applications.

References

[1] A.A. Adewuya, *New Methods in Genetic Search with Real-Valued Chromosomes*, Master's Thesis, Massachusetts Institute of Technology, 1996.

[2] L.Davis, "Hybridization and Numerical Representation," in L.Davis (Ed.), *The Handbook of Genetic Algorithms*, Van Nostrand Reinhold (pp. 61-71), New York, 1991.

[3] L.J. Eshelman and D.J. Shaffer, "Real-coded Genetic Algorithms and Interval-Schemata," in Whitley, D.L. (Ed.), *Foundations of Genetic Algorithms 2* (pp.187-202), Morgan Kaufman, California, 1993.

[4] Z. Michalewicz, *Genetic Algorithms+Data Structures=Evolution Programs*, 2nd ed., Springer-Verlag, New York, 1994.

[5] N.J. Radcliff, "Forma Analysis and Random Respectful Recombination," in *Proceedings of the Fourth International Conference on Genetic Algorithms*, Morgan Kauffman, California, 1991.

[6] A. Wright, "Genetic Algorithms for Real Parameter Optimization," in Rawlins, G.J.E. (Ed.), *Foundations of Genetic Algorithms* (pp. 205-218), Morgan Kaufmann, California, 1991.

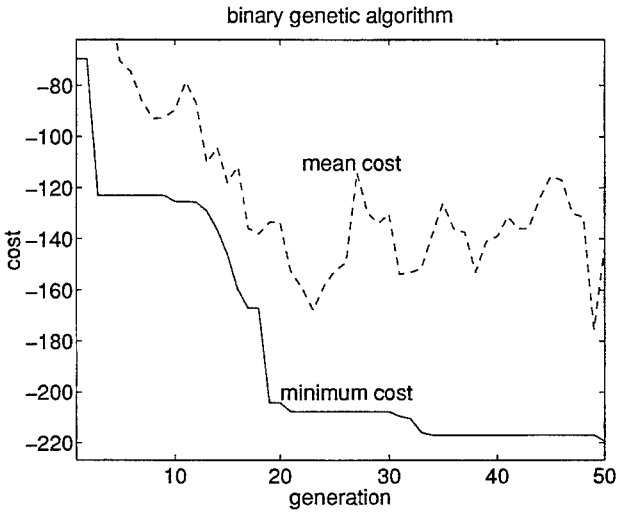

Figure 2: Convergence of the binary genetic algorithm.

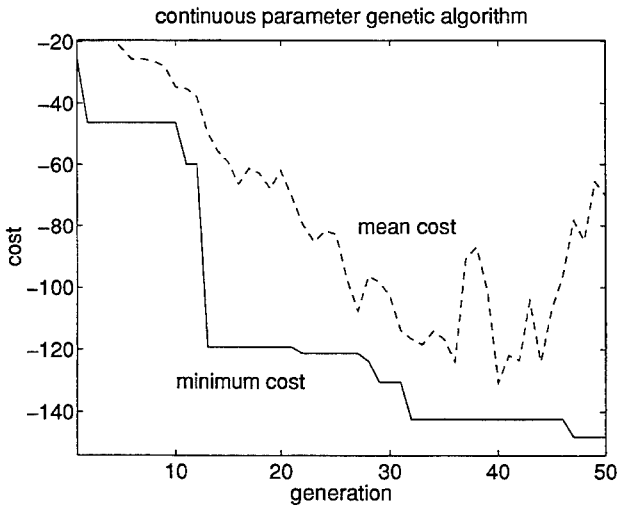

Figure 3: Convergence of the continuous parameter genetic algorithm.

COMPLEX PLANE ARRAY PATTERN CONTROL USING A GENETIC ALGORITHM

R J Mitchell, B Chambers and A P Anderson
University of Sheffield, UK

INTRODUCTION

Genetic algorithms (GAs) use the Darwinian notion of "survival of the fittest" to solve a problem by operation on a population of possible solutions [1]. GAs can require large amounts of computation, but they are robust and often outperform other optimisation methods where analytic techniques cannot be used due, for example, to discontinuous or non-differentiable functions, or where a problem has multiple objectives. Several authors have recently applied GAs to problems in electromagnetics [2-5]. Here, a GA is used to find the necessary complex weights for null steering adaptation of linear array antennas with performance constraints, taking advantage of the benefits of operating on the complex roots of the array polynomial.

ARRAY ANTENNAS

The array polynomial of a linear N-element antenna array excited by currents I_n may be written

$$E_\theta = I_0 + I_1 e^{j\psi} + I_2 e^{j2\psi} + \ldots + I_{(N-1)} e^{j(N-1)\psi} \qquad (1)$$

where

$$\psi = kd\cos\theta + \alpha \qquad (2)$$

k is the wave number ($2\pi/\lambda$), d is the element spacing, and α is the progressive phase shift applied to each element.

If we assume that $I_0 = 1$ and set $z = e^{j\psi}$, the array factor in a direction θ may be written as

$$E_\theta = (z - z_1)(z - z_2)\ldots(z - z_{N-1}) \qquad (3)$$

If there is no requirement for filled nulls in the antenna radiation pattern, we can assume that each root z_n of the array polynomial lies on the unit circle in the complex plane [6]. Each root may therefore be represented simply by its angle from 0°, thus reducing the problem search space. The speed of the function evaluation is also increased due to the terms in equation (3) involving multiplication rather than exponentiation.

SOLUTION CONSTRAINTS

Steering the nulls of an antenna is relatively simple, but it can often result in array excitations that are inefficient or in radiation patterns with undesirably high sidelobes. To avoid these problems, it is necessary to apply extra constraints to the optimisation. Firstly, we apply a pattern envelope constraint, which fixes the maximum value of the radiation pattern in each direction of interest. It can be of arbitrary shape (here we simply follow a uniform array envelope) except that it is modified by the null steering requirements. The GA minimises the number of angles at which the calculated array factor violates the pattern envelope constraint; hence a satisfactory solution has no violations. This also prevents unwanted beam steering and ensures that sidelobe levels do not rise, although some main beam broadening is allowed.

The second constraint is the efficiency of the antenna excitation, which is maximised. The efficiency of an N-element array antenna excited with currents I_n may be expressed as

$$\eta = \frac{\left|\sum_{n=0}^{N-1} I_n^2\right|}{N\sum_{n=0}^{N-1}\left|I_n^2\right|} \times 100\% \qquad (4)$$

This quantity is maximised by the GA until it exceeds a specified value. Since (4) is effectively the efficiency index of the array it is a measure of the tolerance of the latter to errors in the excitation coefficients [7] and hence operates to minimise the sensitivity of the solution. The obtainable efficiency depends upon the difficulty of the required nulling constraints, and is currently set arbitrarily. If a single null is required, efficiencies of over 90% are easily obtainable, but for more complicated constraints it is sometimes necessary to reduce the efficiency requirement to 75 or 80%, although higher efficiencies may be achieved given longer run-times.

GENETIC ALGORITHM IMPLEMENTATION

The genetic algorithm is applied to a population of 50 potential solutions. Each solution is a vector of N-1 floating-point numbers representing the root angles in the complex plane. We choose to operate on the real-valued root positions rather than using the more popular binary coded representation to avoid loss of precision due to discretisation and time-consuming conversion between number formats for function evaluation.

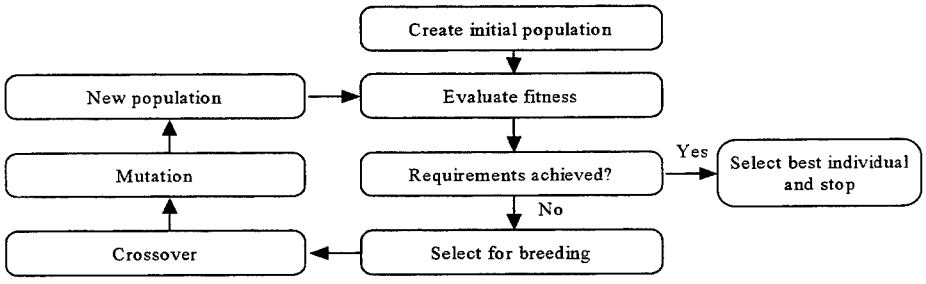

Figure 1: Flow chart of a genetic algorithm

A technique known as *pareto ranking* [8] is used to determine the rank of each potential solution within the population (this method is useful for multiple-objective GAs, especially where the objectives conflict, as is the case here). The highest-ranked solutions are then combined using the genetic operators of *crossover* and *mutation* to produce better solutions.

SOLUTION QUALITY

We are interested in dealing with some issues relating to the practical implementation of an adaptive array antenna, such as the frequency tolerance of a solution. We are also investigating the sensitivity of the solutions to perturbations in the amplitude and phase of the currents applied to the elements, bearing in mind that most implementations use digital amplitude and phase control, whereas our GA operates on real-valued root positions. Since we have access to an 8-element adaptive waveguide array antenna with 6-bit amplitude and phase control, we will limit our discussion to the 8-element broadside case. To simulate this antenna, we assume that the elements are spaced at 2.76cm intervals and have a setting accuracy of ±0.25 dB in amplitude and ±2.8° in phase. Mutual coupling is neglected, and because of the presence of a ground plane, the element pattern is assumed to be isotropic over the range 0° to 180°.

Since the problem is closely specified, it is possible to tailor the operation of the GA to it. Single-point crossover [1] was chosen because each solution contains only 7 values. After trying out several ways of pairing "parent" solutions (such as the commonly used roulette wheel method), a pairing-by-rank scheme was adopted, where the best two individuals are paired, then the 3rd and 4th-ranked individuals, etc. Also, because it is more difficult for a broadside array to conform to the pattern envelope than to achieve the required efficiency (the reverse is true for endfire arrays) a two-stage implementation was devised. First the GA optimises solely with regard to the pattern envelope constraint, until 20 of the 50 solutions in the population satisfy this criterion. After this, the efficiency constraint is introduced, and the GA continues optimising until a solution is found which satisfies both criteria. This has been found to be faster than optimising for both criteria from the start.

FREQUENCY SENSITIVITY

For an antenna with fixed element spacing, the nulls in the radiation pattern change position with frequency, tracking in towards the main beam as the frequency is increased. Therefore, if a null is required at a fixed angle over a range of frequencies, it can be specified simply by making the null wide (a "notch") at the centre frequency. Since the width of the required notch is calculable, we can evaluate the antenna radiation pattern at a single frequency during the optimisation process, making a great saving in CPU time.
Figure 2 shows a typical result. The GA was required to produce a notch null of -30dB between 43° and 55° at the centre frequency of 5.43 GHz so as to ensure a null of -30dB at 51° over the frequency range 4.9-6.3 GHz. (At 5.43 GHz the element spacing of 2.76 cm is equal to half the wavelength.) This choice of frequencies was governed by the operating range of the real antenna. The minimum acceptable efficiency was set to 90%. The uniform array factor is shown for comparison, as is the pattern envelope applied. Figures 3 and 4 show the radiation patterns produced by the same element excitations at 4.9 and 6.3 GHz, demonstrating that the null at 51° is indeed maintained over this range. The dotted lines on the graphs are the radiation patterns of the same antenna uniformly excited at each frequency. Table 1 gives the element excitations of this solution, which has 92.6% efficiency and a directivity of 8.70 dBi (compared to 9.03 dBi for the uniform case). It was found after 28 generations of the GA, taking 12 seconds on a 133MHz Pentium PC.

AMPLITUDE AND PHASE SENSITIVITY

Many electromagnetic applications of genetic algorithms concentrate on design problems. However, we are also interested in the case of adaptive antennas, where the element positions and patterns are fixed but the currents in them are varied by some means. In practise, it may not be possible to apply any arbitrary set of currents due to physical limitations, quantisation, or noise in the system. We are therefore interested in the sensitivity of the GA's solutions to small variations in the element currents. The tolerance of the result shown in Figure 2 (element amplitudes and phases given in Table 1) was tested by randomly perturbing the amplitudes and/or phases 1000 times. The perturbations were set according to a normal distribution, with mean zero and standard deviation 0.125dB for the amplitude case. For the phase variation case, the mean was zero and the standard deviation was 1.4°. Figure 5 shows the maximum and minimum values of the array factor at each angle for variations in the element amplitudes, Figure 6 shows the envelopes for phase variations, and Figure 7 shows the envelopes for variations in both amplitude and phase. All three graphs show the pattern envelope constraint, for comparison. They show that the notch null is fairly insensitive to perturbations in the amplitude and/or phase. Solutions with narrower nulls or lower efficiencies are often much more sensitive than the result given here.

MUTUAL COUPLING AND INDIVIDUAL ELEMENT PATTERNS

The effects of both mutual coupling and individual element patterns have been ignored in the above analysis. However, these effects should not be ignored when attempting to apply this algorithm to an actual antenna. It is relatively easy to include the element patterns, as this merely involves a suitable modification of equation (1) or (3). Mutuals are more difficult to include, but may play an important role, especially in cases where the solution is sensitive to amplitude and/or phase perturbations in the element currents.
We intend to include both these factors in later developments of this work.

ROOTS OFF THE UNIT CIRCLE

There are many radiation patterns which cannot be achieved with the roots of the array polynomial constrained to lie on the unit circle. However, allowing the roots to take on any position in the complex plane greatly enlarges the search space and lengthens the computational time necessary to find a good solution. We are therefore investigating the performance of a GA which allows a limited freedom by placing each root on one of three "rings" in the complex plane. One ring is the unit circle; the other two have radii 0.8 and 1.25, respectively. We hope that this will provide the flexibility necessary to give a wider range of radiation patterns. If a shaped pattern with filled nulls were to be required, it would be possible to include an additional constraint in the GA to ensure that the peaks did not drop below a certain level. At the time of writing, this investigation is still in the preliminary stages.

CONCLUSIONS

A genetic algorithm has been applied to the problem of adaptive array antennas. Operating on the roots of the array polynomial offsets the reduction in performance caused by the application of constraints on the shape of the radiation pattern and the efficiency of the antenna excitation. A frequency-insensitive solution (broadband null) may be achieved by requiring the algorithm to produce a notch in the range of angles to be nulled. A high efficiency index constraint implies a solution which is less sensitive to perturbations in the amplitude and/or phase of the element currents. Further investigations into the effects of mutual coupling, individual element patterns, and moving roots off the unit circle are in progress.

ACKNOWLEDGEMENTS

We are grateful to GEC Marconi Research, Baddow, UK, for access to a digital phased array antenna system.

REFERENCES

[1] Goldberg D E, 1989, "Genetic Algorithms in Search, Optimisation and Machine Learning", Addison-Wesley

[2] Michielssen E, Ranithan S and Mittra R, 1992, "Optimal multilayer filter design using real coded genetic algorithms", Proc. IEE pt. J, 139, 413-420

[3] Tennant A, Dawoud M M and Anderson A P, 1994, "Array pattern nulling by element position perturbations using a genetic algorithm," Electron. Lett., 30, 174-176

[4] Haupt R L, "Thinned Arrays using Genetic Algorithms," 1994, IEEE Trans., AP-42, 993-999

[5] Mitchell R J, Chambers B and Anderson A P, 1996, "Array pattern synthesis in the complex plane optimised by a genetic algorithm", Electron. Lett., 32, 1843-1845

[6] Schelkunoff S A, 1943, "A mathematical theory of linear arrays," Bell Syst. Tech. J., 22, 80-107

[7] Collin and Zucker, 1969, "Antenna Theory, Part 1," McGraw-Hill (chapter 5)

[8] Horn J, Nafpliotis N, and Goldberg, D E, 1994, "A niched pareto genetic algorithm for multiobjective optimization, 1st Int. Conf. Evolutionary Computation, 82-87

TABLE 1 - Element Excitations

Element	Amplitude (abs)	Amplitude (dB)	Phase (radians)	Phase (degrees)
1	0.5430	-7.0299	0	0
2	1.0781	-1.0730	0.1739	9.9636
3	1.1590	-0.4450	0.1372	7.8606
4	1.2199	0	0.0567	3.2513
5	1.2199	0	0.2601	14.9035
6	1.1590	-0.4450	0.1797	10.2942
7	1.0781	-1.0730	0.1430	8.1912
8	0.5430	-7.0299	0.3169	18.1548

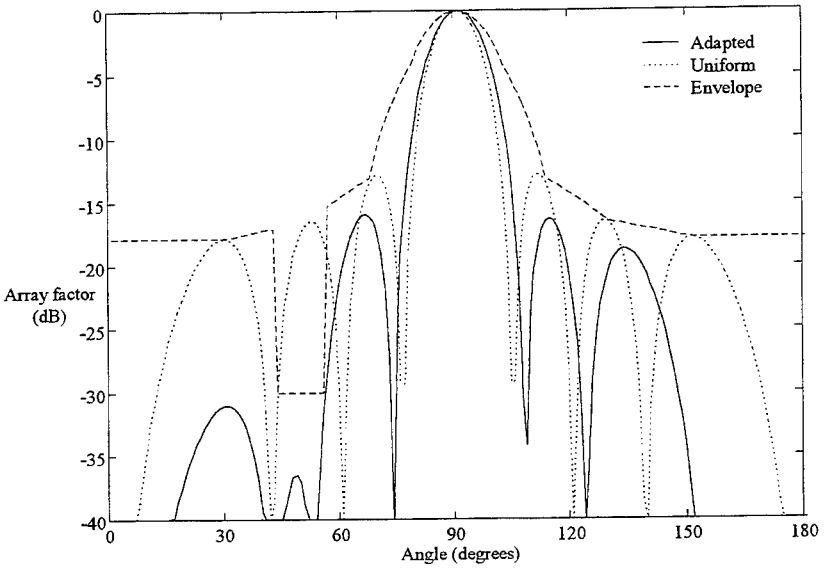

Figure 2: Radiation pattern of an 8-element array with a -30dB notch from 43° to 55° at 5.43 GHz

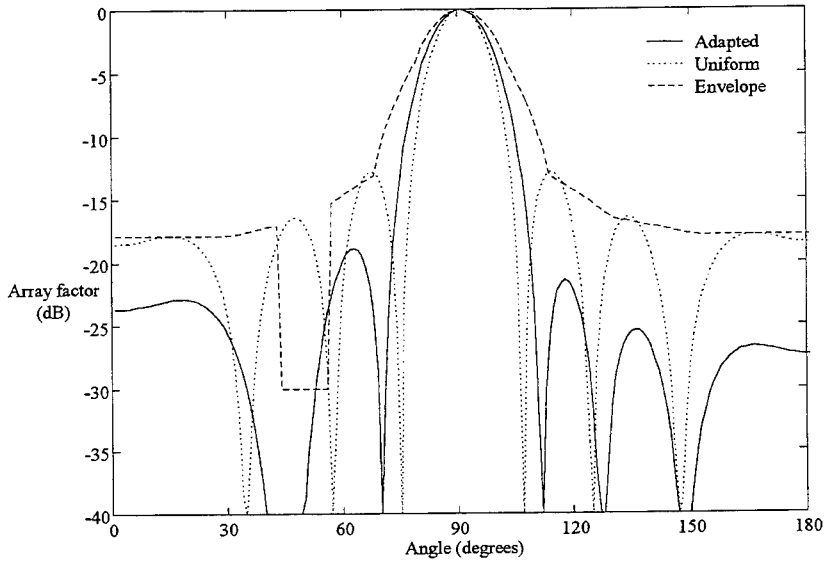

Figure 3: Radiation pattern of an 8-element array at 4.9 GHz

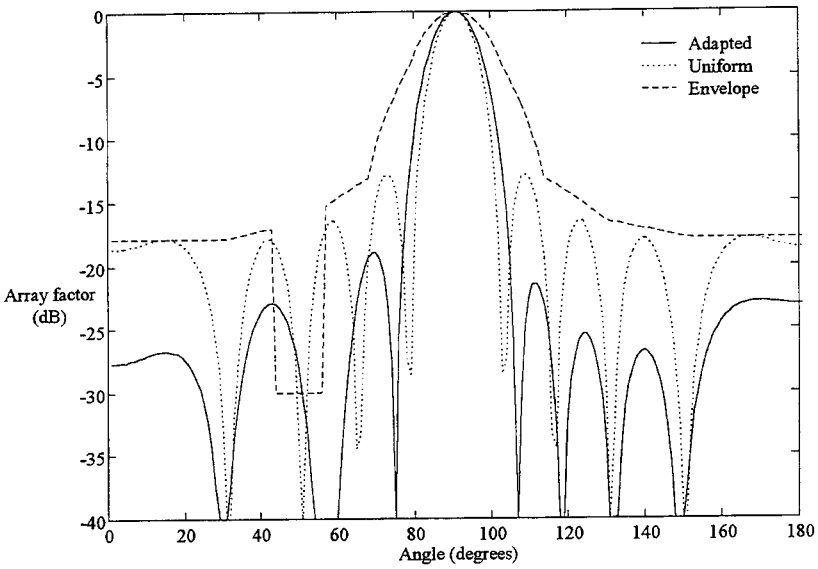

Figure 4: Radiation pattern of an 8-element array at 6.3 GHz

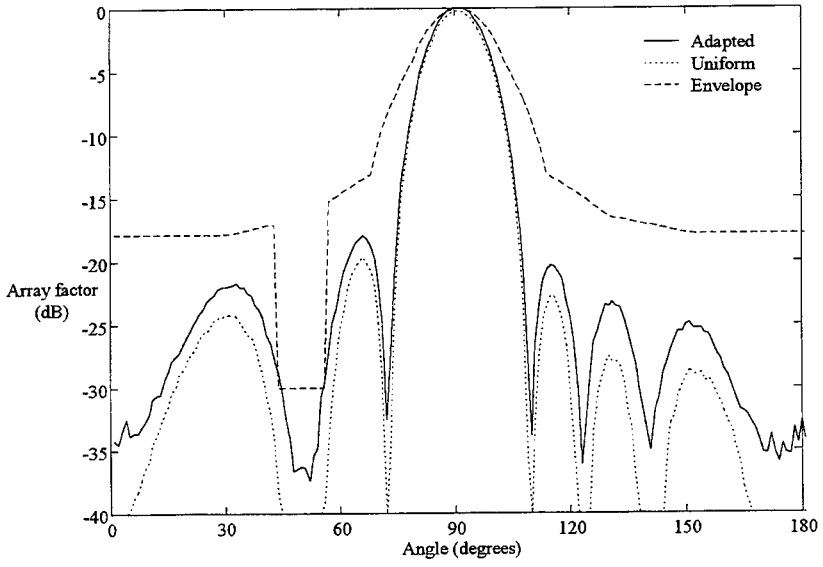

Figure 5: Amplitude sensitivity envelope at 5.43 GHz

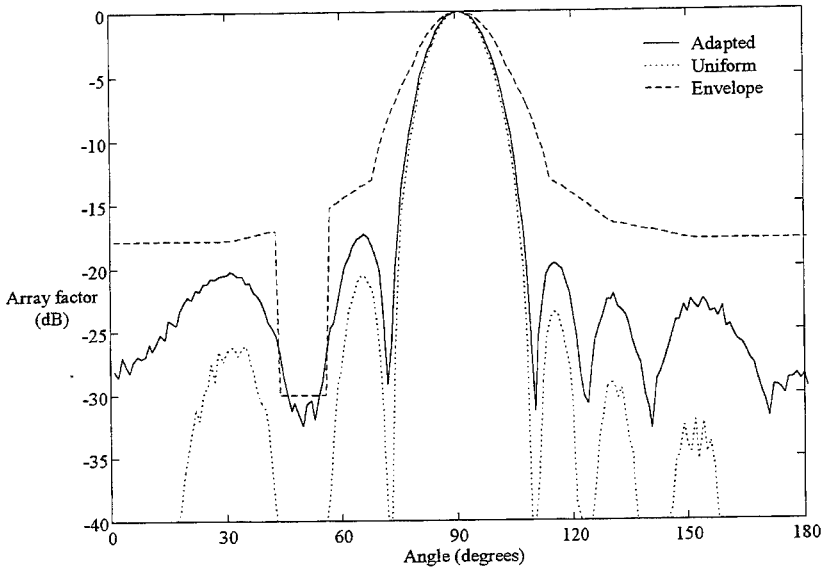

Figure 6: Phase sensitivity envelope at 5.43 GHz

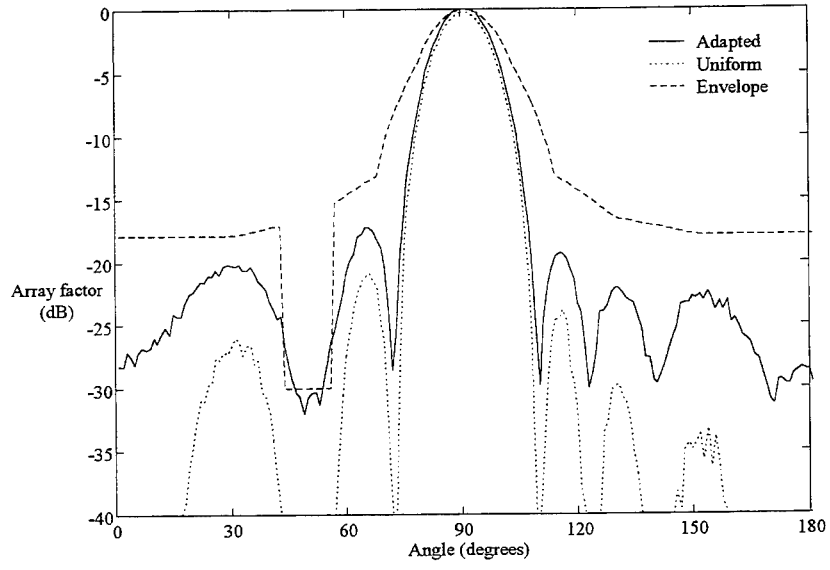

Figure 7: Sensitivity envelope for variations in both amplitude and phase at 5.43 GHz

SESSION 24:

ADVANCES IN TRANSMISSION LINE MATRIX (TLM) MODELING II

Chairs: W. Hoefer and P. Russer

CHARACTERISTICS OF THE OPTIMIZATION PROBLEM FOR ANALYSIS OF TIME SERIES' OBTAINED FROM TLM OR 2D-FDTD HOMOGENEOUS WAVEGUIDE SIMULATIONS

by

Ulf Müller, Manuel M. Rodriguez, Marc Walter and Adalbert Beyer
Department of Electrical Engineering, Duisburg University, Bismarckstr. 81,
47057 Duisburg, Germany Tel.: ++49/203/379-4217, Fax: ++49/203/379-3218
Email: a.beyer@uni-duisburg.de

1 ABSTRACT

It has been shown during the last few years, that the simulation of homogeneous waveguides can be efficiently carried out by either the TLM- or the 2D-FDTD method. Rigorous mathematical treatment of the problem leads to time series of the sinusoidal type as simulation results. Since these simulations require a very fine waveguide even the corresponding time step is very small. Hence, the calculation of several periods necessary for Fourier transformation lead to unacceptable computation times.

An optimization based method of parameter extraction for these simulation results of the sinusoidal type has already been presented and applied to several structures successfully. In this paper this optimization based method will be discussed concerning its characteristics and its sensitivity to the initially guessed parameters.

2 INTRODUCTION

The transmission line matrix (TLM) method is a widely established numerical tool for the full-wave analysis of wave-propagation in the free-space as well as along guiding structures [3]. There exist several strategies for the analysis of the structure under consideration as there are the eigenvalue formulation [4,5], the transient analysis [3] and special formulations for longitudinally homogeneous [6,7,8] and longitudinally periodic [9] structures. Applying the later special methods of analysis it can be shown analytically that the obtained time series are of the sinusoidal type (10).

3 THEORETICAL BACKGROUND

It has been shown in [1] and [2] that the calculation of the frequency from the obtained sinusoidal type time series lead to unacceptable computer requirements as long as a discrete Fourier transformation is used. This is due to the fact that the Fourier transformation needs at least several periods of the sinusoidal type signal to carry out the transformation with significant accuracy.

A method to overcome this problem was first introduced by Hofschen et al. [1,2]. The basic idea is that, if the time series contains only a sinusoidal function of one frequency, the missing parameter of the function can be determined by fitting an analytical description to the time series in the sense of least-squares via an optimization process.

3.1 DEFINITION OF THE PROBLEM

Considering the above mentioned time series *f(t)* of a single frequency sinusoidal function, the function under consideration is of the analytical type

$$\tilde{f}(t) = a \sin\left(\frac{2\pi}{T}\, t + \varphi\right) \cdot \mathrm{e}^{-\alpha t} + d .$$

The unknown parameters are the amplitude a, the period T, the phase-shift φ, the damping α and the offset d. The optimization process to be carried out has to be applied to the error function

$$e = e(\vec{p}) = \frac{1}{t_{\max}} \int_0^{t_{\max}} \left(\tilde{f}(t) - f(t)\right)^2 \mathrm{d}t$$

with the parameter vector

$$\vec{p} = (a, T, \varphi, \alpha, d)$$

and has to yield the condition

$$e \xrightarrow[\vec{p} \to \vec{p}_{opt}]{} 0 ,$$

if $\vec{p}_{opt}$ denotes the optimum vector of parameters. Hofschen et al. [1] proposed a Fletcher-Powell optimizer to work quiet well, but for application reasons the condition has to be reduced to

$$e \xrightarrow[\vec{p} \to \vec{p}_{opt}]{} \min .$$

This method for the evaluation of the unknown parameters should be discussed concerning its sensitivity to the initially guessed values. Therefore, in the following subsection an estimation algorithm for initial parameters will be described. Afterwards, the sensitivity of the optimization process will be shown for an analytical example.

3.2 INITIAL VALUE ESTIMATION

As mentioned in the previous subsection it is necessary to estimate initial values for the optimization parameters. Therefore, we take a look at the analytical description

$$\tilde{f}(t) = a \sin\left(\frac{2\pi}{T}\, t + \varphi\right) \cdot \mathrm{e}^{-\alpha t} + d$$

with the amplitude a, the period T, the phase φ, the damping α and the offset d as parameters. If losses are not taken into account (α=0), we can decompose $\tilde{f}(t)$ easily into

$$\tilde{g}(t) = \tilde{a} \cos(\omega t) + \tilde{b} \sin(\omega t) + d$$

and transfer the problem from the unknowns

a, T, φ and d

into the unknowns

$$\tilde{a},\ \tilde{b},\ \omega = 2\pi/T \text{ and } d.$$

Assume now $\tilde{g}(t)$ known at four equidistant times (time distance δ):

$$g_1 = \tilde{g}(0) \quad g_2 = \tilde{g}(\delta)$$
$$g_3 = \tilde{g}(2\delta) \quad g_4 = \tilde{g}(3\delta)$$

the values of the function $\tilde{g}(t)$ at the sampling points can be expressed by

$$g_1 = \tilde{a} + d$$
$$g_2 = \tilde{a}\cos(\omega\delta) + \tilde{b}\sin(\omega\delta) + d$$
$$g_3 = \tilde{a}\left(\cos^2(\omega\delta) - \sin^2(\omega\delta)\right) + 2\tilde{b}\sin(\omega\delta)\cos(\omega\delta) + d$$
$$g_4 = \tilde{a}\cos(\omega\delta)\left(4\cos^2(\omega\delta) - 3\right) + \tilde{b}\sin(\omega\delta)\left(3 - 4\sin^2(\omega\delta)\right) + d$$
$$1 = \cos^2(\omega\delta) + \sin^2(\omega\delta).$$

Calculating $\tilde{a}$, $\tilde{b}$, $\cos(\omega\delta)$ and $\sin(\omega\delta)$ from the equations g_1 to g_4 lead to

$$\cos(\omega\delta) = \frac{g_2 - g_1 + g_4 - g_3}{2(g_3 - g_2)}$$
$$\sin(\omega\delta) = \sqrt{1 - \cos^2(\omega\delta)}$$
$$\tilde{b} = \frac{2g_2 - g_1 - g_3 + 2\cos(\omega\delta)(g_2 - g_1)}{2\sin(\omega\delta)}$$
$$\tilde{a} = \frac{g_2 - g_1 - \tilde{b}\sin(\omega\delta)}{1 - \cos(\omega\delta)}$$
$$d = g_1 - \tilde{a},$$

where $0 < \omega\delta < \pi\ (\cos(\omega\delta) \neq 0, \cos(\omega\delta) \neq 1, \sin(\omega\delta) > 0)$ and $g_2 \neq g_3$ must be required.
The comparison with the function

$$\tilde{f}(t) = a\sin\left(\frac{2\pi}{T}\, t + \varphi\right) + d$$

leads to the estimated parameters

$$a = \sqrt{\tilde{a}^2 + \tilde{b}^2}$$

$$T = \frac{2\pi\delta}{\arccos\left(\frac{g_2 - g_1 + g_4 - g_3}{2(g_3 - g_2)}\right)}$$

$$\varphi = \arctan\left(\frac{\tilde{a}}{\tilde{b}}\right)$$

$$d = g_1 - \tilde{a}$$

as estimated initial values.

4 RESULTS

Apply now the above mentioned definition for the error function to an analytically known function

$$f(t) = 5\sin\left(\frac{2\pi}{5}\, t \div \frac{\pi}{3}\right).$$

Hence, the optimum vector for the parameters is (offset d=0)

$$\vec{p}_{opt} = (a, T, \varphi) = \left(5{,}5, \frac{\pi}{3}\right).$$

To estimate the sensitivity of the optimization process we consider the error function with two free variables and the third parameter set to its optimum value.

Therefore, three experiments can be made leading to the results as shown in Fig. 1, Fig. 2 and Fig. 3. In the first experiment amplitude and period are taken as variables, while the phase is given exactly. Fig. 1 shows the error function e versus the free variables. The optimum value for the amplitude can easily be reached, but the optimum value for the period lies in a long smooth valley. The second experiment shows the sensitivity of the error function for the change in amplitude and phase with fixed period. The plots in Fig. 2 show that both the amplitude and the phase can be determined with less effort, if the period is known exactly. In Fig. 3 for the third experiment it can once again be seen that the period can hardly be determined without any good initial guess (long smooth valley), while the phase exhibits no problems (high gradients).

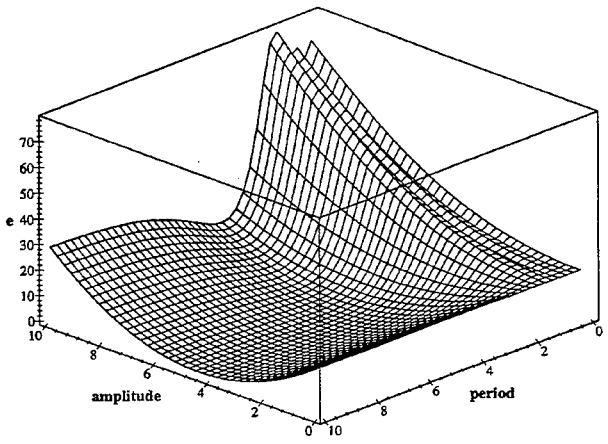

a)

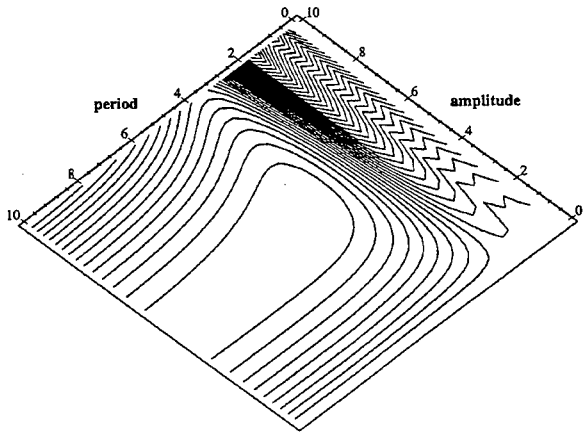

b)

Figure 1: *Error function e plotted versus amplitude and period (phase is given exactly): a) surface plot and b) contour plot.*

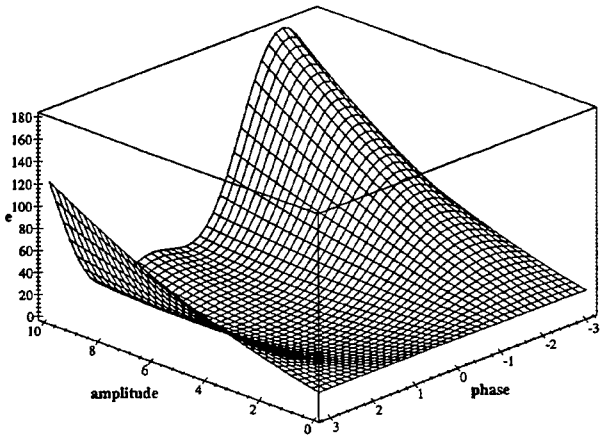

a)

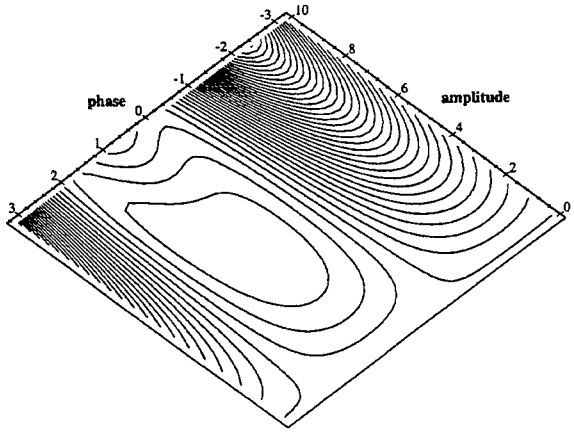

b)

Figure 2: *Error function e plotted versus amplitude and phase (period is given exactly): a) surface plot and b) contour plot.*

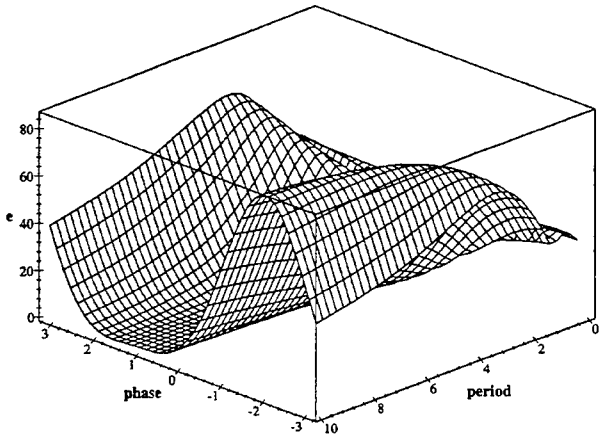

a)

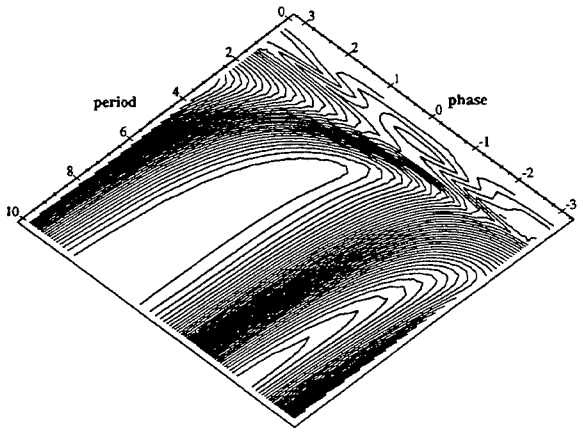

b)

Figure 3: *Error function e plotted versus phase and period (amplitude is given exactly): a) surface plot and b) contour plot.*

5 CONCLUSION

In this paper the conditions of exact parameter extraction for time series of the sinusoidal type has been discussed extensively. Therefore, an optimization process has been analyzed concerning its sensitivity to initially guessed parameters. A method for estimating the initial values has been proposed. The optimization problem has been studies as a function of these initial values by defining an error function in the sense of least square. It could be seen, that the main problem is to have a good initial guess for the period of the signal.

6 REFERENCES

[1] **Hofschen, S.; Wolff, I.:** "Improvements of the 2-D-FDTD method for the simulation of small CPW" on GaAs using time series analysis", *1994 IEEE MTT-S Int. Microwave Symp. Dig.*, San Diego, CA, May 1994, pp. 39-42.

[2] **Hofschen, S.; Wolff, I.:** "Simulation of an elevated coplanar waveguide using 2-D-FDTD", *IEEE Microwave and Guided Wave Letters*, vol. 6, no. 1, pp. 28-30, January 1996.

[3] **Hoefer, W.J.R.:** "The transmission line matrix (TLM) method ", in T. Itoh, *"Numerical techniques for microwave and millimeter-wave passive structures"*, pp. 496-591, J. Wiley & Sons, New York, 1989.

[4] **Akhtarzad, S.:** "Analysis of lossy microwave structures and microstrip resonators by the TLM method", Ph.D. Dissertation, University of Nottingham, England, July 1975.

[5] **Johns, P.B.:** "Application of the transmission line matrix method to homogeneous waveguides of arbitrary cross-section", *Proc. Inst. Electr. Eng.*, vol. 119, pp. 1086-1091, August 1972.

[6] **Jin, H.; Vahldieck, R.; Xiao, S.:** "An improved TLM full-wave analysis using a two dimensional mesh", *1991 IEEE MTT-S Int. Microwave Symp. Dig.*, Boston, Mass., June 1991, pp. 675-677.

[7] **Jin, H.; Vahldieck, R.; Xiao, S.:** "Full wave analysis of guiding structures using a 2-D array of 3-D TLM nodes", *IEEE Trans. Microwave Theory Tech.*, vol. MTT-41, pp. 472-477, March 1993.

[8] **Celuch-Marcysiak, M.; Gwarek, W.K.:** "A transformed symmetrical condensed node for the effective TLM analysis of guided wave problems", *IEEE Trans. Microwave Theory Tech.*, vol. MTT-41, pp. 820-823, May 1993.

[9] **Celuch-Marcysiak, M.; Gwarek, W.K.:** "Effective timed domain analysis of periodic structures", *Proceedings of the 23rd European Microwave Conference*, pp. 293-295, September 1993.

[10] **Walter, M.:** "Untersuchungen zur Simulation der Methodik der TLM-Simulation für längshomogene Leitungsstrukturen" (in german), Gerhard-Mercator-Universität -Gesamthochschule- Duisburg, Department of Electrical Engineering, undergraduate thesis, 1995.

[11] **Rodriguez, M.M.:** "Untersuchung der Konditionierung des Optimierungsproblems zur Analyse von Zeitfunktionen aus TLM Simulationen längshomogener Leitungsstrukturen" (in german), Gerhard-Mercator-Universität - Gesamthochschule- Duisburg, Department of Electrical Engineering, undergraduate thesis, 1995.

Acknowledgment:

The author would like to thank Dipl.-Ing. Stefan Hofschen for many discussions on these topics and for the helpful suggestions during the preparation of this paper.

Comparison of 3D TLM Meshing Techniques for Modeling Microwave Components

J. L. Herring and W. J. R. Hoefer

NSERC/MPR Teltech Research Chair in RF Engineering,
Department of Electrical & Computer Engineering, University of Victoria,
P. O. Box 3055, Victoria, B. C., V8W 3P6, Canada.

Abstract

The application of graded mesh and multigrid techniques to the modeling of microwave components in 3-dimensions with the TLM method are discussed. Comparisons are made for graded mesh and multigrid interfaces in a waveguide, for a non-touching axial strip placed in a waveguide, and for a microstrip impedance step. The issues of appropriate excitation and absorbing boundary conditions are addressed. It is shown that multigrid techniques provide an effective means of reducing the mesh resolution away from discontinuities.

Introduction

The transmission-line matrix (TLM) method of numerical electromagnetic analysis with the symmetrical condensed node (SCN) [1] is well established. To increase the flexibility in which a problem can be meshed, two main techniques have been proposed: graded mesh and multigrid mesh. In this paper, graded and multigrid techniques will be applied to simple waveguide and microstrip examples, and the relative efficiency and accuracy will be compared.

Graded Mesh

A graded mesh is defined by the cell dimensions along each of the coordinate axes. A feature of graded meshes is that fine mesh regions cannot be completely isolated from the rest of the mesh. In the original approach, the link-line impedances were kept constant and stubs were added at the nodes (the *stub-loaded* node). However, if the nodes are far from being cubic, this imposes an unreasonable limit on the timestep. The *hybrid* node [2] offers a more favorable limit on the timestep and also has superior dispersion characteristics.

Multigrid Schemes

Multigrid techniques allow connection between two disjoint meshes. These meshes can be uniform (with cubic or cuboid nodes) or they can be graded. At least three multigrid schemes have been proposed and these will be referred to as methods *A*, *B* and *C* in this paper.

In method *A*, the average field is maintained across the fine/coarse mesh interface (this is equivalent to conserving charge) and the coarse→fine and fine→coarse conversions are dealt with separately [3]. The coarse and fine mesh timesteps can be equal but it is more useful to run the fine mesh with a smaller timestep. For example, if both meshes are uniform and cubic, the standard 12-port node can be used for both meshes and each mesh can be run with the maximum timestep of $\Delta l/2c$. In situations where the fine and coarse mesh timesteps are not equal, it is essential that the calculation is ordered such that an axial TEM wave will propagate perfectly. The standard 12-port node is the most efficient SCN formulation and it is also the most accurate for axial propagation. If a node is used in which the link-line impedance can vary over the interface, then appropriate reflection and transmission coefficients may need to be applied before the conversion takes place [4]. For the hybrid node, this must be done if the ratio of the timestep and the normal node dimension are not the same in both the fine and coarse meshes. The main disadvantage of method *A* is that there is a loss of energy in the fine→coarse conversion.

In method *B*, the fine/coarse mesh interface is implemented as an electrical connection [5]. Energy is conserved in the conversion procedure but it does require that both fine and coarse meshes are run with the same timestep. This means that the standard 12-port node cannot be used for the coarse mesh (e.g. stub-loaded or hybrid nodes must be used), resulting in longer run-times and a higher memory requirement. The fine→coarse conversion is identical to that in method *A*. For the coarse→fine conversion, for the case when the incident fine mesh pulses are not equal, the extra degrees of freedom needed

to enforce both charge and energy conservation, are accommodated by modifying the reflected fine mesh pulses. There is a choice in whether to connect the fine mesh link-lines by row first or by column first, although in practice there appears to be little difference between the two.

In method *C*, the interface is implemented by fitting a two-dimensional spline to the pulses incident upon the interface and then calculating the transmitted pulses by interpolation [6]. This method allows greater flexibility in both spatial and temporal discretization, for example, a non-integer number of link-lines from the fine mesh can be connected to a non-integer number of link-lines from the coarse mesh. However, the procedure does not enforce conservation of energy and, in contrast to method *A*, there can be a gain of energy, as well as a loss. There is also the problem of trying to fit a spline in the presence of spurious modes with a high spatial frequency. Such modes can be predicted theoretically [7] and, in practice, are often observed close to excitation points. Spurious modes do not present a problem to methods *A* and *B*, and since these methods usually provide adequate options for meshing, they will be concentrated on in this paper.

Meshing Methodology

Both graded mesh and multigrid methods have been used as mesh refinement techniques, so that a uniform fine mesh does not have to be used throughout the entire problem space. However, for certain discontinuities, mesh refinement may not give a significant improvement. Normally, TLM is expected to be second order accurate but in the presence of, for example, a knife-edge discontinuity, the accuracy is reduced to first order [8,9]. When such discontinuities are present, the only practical solution is to make use of local mesh modification techniques. These techniques can be based on analytical formulations [10], or on correction factors obtained from an optimization procedure [11]. Special nodes are also available for wires and slots [12,13], where the features are much smaller than the cell size.

Mesh grading can be used to fit the mesh to the exact physical dimensions of the structure under study. However, since the cell dimensions must be constant along each of the axes, this means that unless the features of the structure are aligned, then small cells must be introduced. This will have a detrimental affect on the timestep. Alternatively, the size of cells adjacent to short or open-circuit boundaries can be varied continuously by altering the link-line impedance [14]. For the SCN, the arm length can be reduced to one half of the standard value (the presence of the side arms means that the length cannot be reduced below this), or the length can be increased arbitrarily. This procedure works well for normal incidence.

The most appropriate use of multigrid techniques is to reduce the resolution away from discontinuities. For example, by increasing the distance to absorbing boundary conditions (ABC's), the effect of higher order modes is reduced and better absorption is obtained. Multigridding can also be used to connect disjoint graded meshes for structures with features which are not aligned.

Interface Between Two Meshes in a Waveguide

Following the example of *Wlodarczyk* [5], the accuracy of multigrid schemes can be assessed by calculating the S-parameters of the interface in a section of waveguide. The ends of the waveguides can be terminated with modal diakoptic boundaries [15,16]. For a uniform mesh, the reflection from these ABC's is close to the limit of numerical precision (-120dB single precision, -300dB double precision) and so they will not distort the results. There are no resonance elements present, so the simulation will be short and the discrete Green's function does not need to be truncated. To avoid problems with sampling the field at a single point in meshes of different resolution, a modal decomposition is performed over the cross-section to extract the mode amplitude.

Fig. 1 shows the reflection and transmission coefficients for multigrid interfaces between a 16x8 coarse mesh and a 32x16 fine mesh, for methods *A* and *B*. The nodes are cubic in all cases. Two cases are considered for method *B*: stub-loaded coarse mesh and hybrid node coarse mesh. The standard 12-port node is used for all other meshes. For method *B*, the reflection coefficients are the same for both coarse→fine and fine→coarse conversions. Also, the transmission coefficients are symmetrical about unity. Smaller reflections are obtained with the hybrid node coarse mesh. For method *A*, the fine→coarse conversion works better than the coarse→fine conversion. The reflection coefficient for the fine→coarse conversion is better than for method *B*. Both transmission coefficients are much less frequency dispersive, particularly the fine→coarse conversion. This means that if it is only the fine→coarse conversion which is of interest (e.g. the region of interest is contained in the fine mesh and the coarse mesh is only used to increase the distance to ABC's), method *A* can give superior results. However, if the system contains resonant elements, and if the oscillation occurs across the interface, then the loss of energy will be a problem and method *B* will be more appropriate.

The magnitudes of the reflection and transmission coefficients for a multigrid interface are similar to those observed with a straightforward graded mesh interface. Fig. 2 shows curves for an interface between cubic nodes and nodes with normal

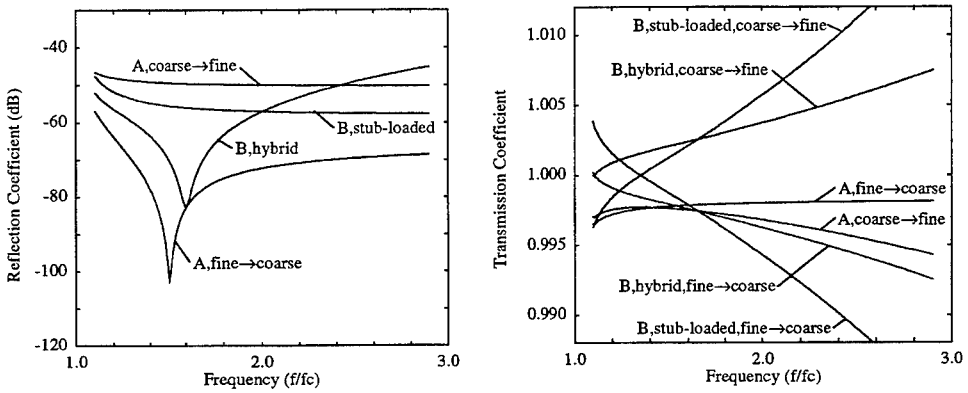

Fig. 1 – Reflection and transmission coefficients for multigrid interface between 16x8 coarse mesh and 32x16 fine mesh

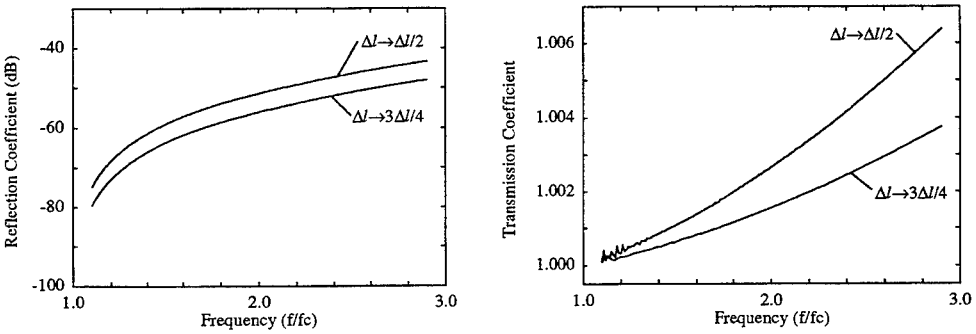

Fig. 2 – Reflection and transmission coefficients for hybrid node graded mesh, 16x8 node cross-section

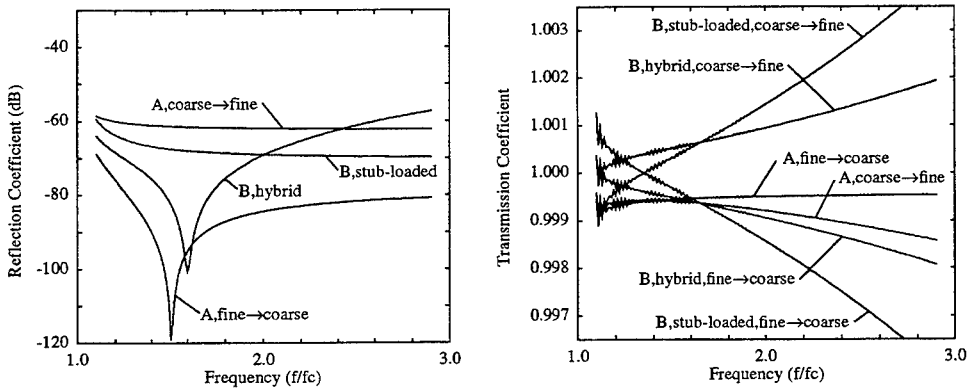

Fig. 3 – Reflection and transmission coefficients for multigrid interface between 32x16 coarse mesh and 64x32 fine mesh

dimensions of $\Delta l/2$ and $3\Delta l/4$, modeled with the hybrid node. The curves are functions only of the initial and final node dimensions; the same results are obtained if the node dimensions are changed in one step or if they are changed gradually.

The performance of multigrid interfaces improves as the mesh resolution is increased. Fig. 3 is the same as Fig. 1 except that both coarse and fine meshes are doubled in resolution. The trends observed are the same as in the previous case.

Non-touching Axial Strip in a Waveguide

A simple three-dimensional discontinuity consisting of a non-touching axial strip placed in a waveguide, as shown in Fig. 4, has been modeled. The dimensions of the strip are such that for Δl=0.1185mm, the strip is exactly 3x16 nodes and the waveguide cross-section is 60x30 nodes. Symmetry can be exploited about the strip. The size of this strip presents a challenge to the modeler: if the strip was very small compared to the mesh size, a special node (similar to a wire node) would have to be used; if the strip was much larger, then a straightforward TLM description would probably be sufficient. Here, an edge correction is applied around the strip to reduce the coarseness error [11]. The correction factors were obtained from a systematic optimization for a single finned waveguide, and if the correct result is obtained for this structure, it will give a measure of the generality of the method and of the correction factors.

To allow comparison between different meshing schemes, the strip is described in a uniform fine mesh 13 nodes in length, as shown in Fig. 5. The output planes are taken three nodes from the edge of the strip (the edge correction extends over nodes 5 and 9). Since the output planes are close to the strip, a modal decomposition must be performed over the cross-section to extract the dominant mode amplitude. This is done from the *Hz* field component. In the general case, where it is necessary to distinguish between TE and TM modes of the same order, it is more convenient to work with *Hz* and *Ez* rather than with the voltage pulses. This is in contrast to the usual implementation of modal diakoptic ABC's, which work directly on the voltage pulses [16]. For the excitation, *Ey* is introduced with the spatial distribution of the dominant mode, on the same plane as the first port output. Special care must be taken when calculating the field at the same point as the excitation since the usual condition, that the incident charge before scattering is the same as the reflected charge, does not hold. In this case, *Hz* must be calculated from both incident and reflected voltage pulses. The pulses needed to produce the required excitation waveform are obtained from a reference structure containing hard voltage sources [17]. This reference structure is only a single cell in length and is terminated with dominant mode diakoptic ABC's.

Given that the strip is adequately described in the fine mesh, the main decision to be made is on the waveguide terminations. Some of the available options are shown in Fig. 6. The waveguide can be terminated close to the strip, which requires an ABC that will adequately absorb higher order modes. The termination can be moved a short distance away, to reduce the number of modes to be absorbed, or, the termination can be moved far away, so that only the dominant mode needs to be considered. Single mode diakoptic ABC's and one-way equation ABC's [18] can be used in the last case. Multi-mode diakoptic ABC's can be used in the other cases, provided the modes are known in advance. The Berenger perfectly matched layer (PML) is also a possibility [19,20], although the PML must be of a certain thickness, which increases the computation effort. Multigridding provides an efficient way to distance ABC's by adding coarse mesh regions.

The results obtained with a uniform fine mesh (30x30x96 nodes) and dominant mode diakoptic ABC's are shown in Fig. 7, along with independent results [21,22]. There is very good agreement considering the small number of nodes describing the strip. The effect of adding a coarse mesh to the original 13 node fine mesh is shown in Fig. 8, for lengths of 20 and 5 coarse mesh nodes, and for no coarse mesh, again for dominant mode ABC's. The 20 node coarse mesh gives results almost identical to the uniform fine mesh but with much reduced computing resources. To provide good terminations with multi-mode ABC's, modes up to 5,4 must be considered with no coarse mesh, and modes up to 3,2 with a 5 node coarse mesh. Placing modal diakoptic boundaries in a coarse mesh has the advantage that the modal decomposition can be performed more efficiently because there are fewer nodes in the cross-section. In a practical simulation, the output planes could be placed on the waveguide terminations, where the dominant mode amplitudes can be obtained directly from the ABC's.

For the previous results, a band-limited (modulated Gaussian) excitation was used. An impulse excitation (still with the spatial distribution of the dominant mode) could also be used. The only disadvantage is that energy is introduced at the waveguide cutoff frequency, causing a ringing effect which does not decay. The magnitude of the dominant mode at the input port is shown for the two cases in Fig. 9. The extraction of frequency domain characteristics in the second case is more challenging since the required signal is much smaller than the ringing. One possibility is to apply a window function before taking the Fourier transform. The point illustrated here is that the simulation remains perfectly stable with an impulse excitation, for both multigrid methods tested (*A* and *B*) with modal diakoptic ABC's. In practice, it is better to avoid exciting the waveguide cutoff and impulse excitation must be avoided altogether when certain elements are present, e.g. one-way equation ABC's.

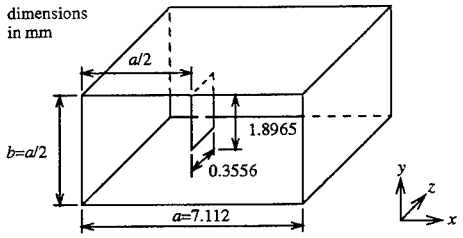

Fig. 4 – Geometry of non-touching axial strip

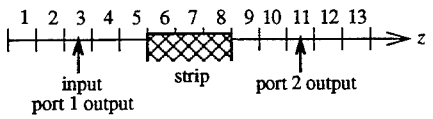

Fig. 5 – Discretization along the length of the waveguide

Fig. 6 – Meshing Schemes

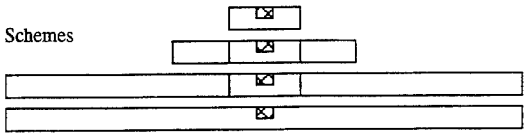

30x30x13 fine
30x30x13 fine, 2 15x15x5 coarse
30x30x13 fine, 2 15x15x20 coarse
30x30x96 fine

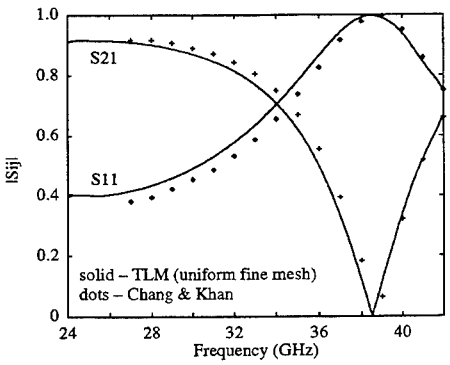

Fig. 7 – Non-touching strip: TLM and independent results

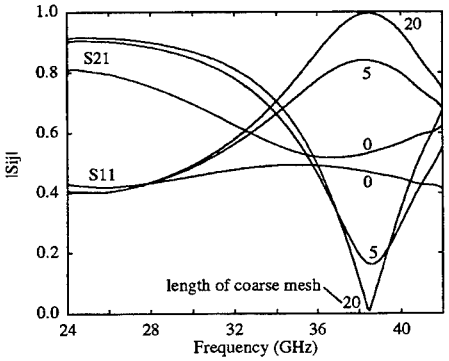

Fig. 8 – Non-touching strip: varying length of coarse mesh

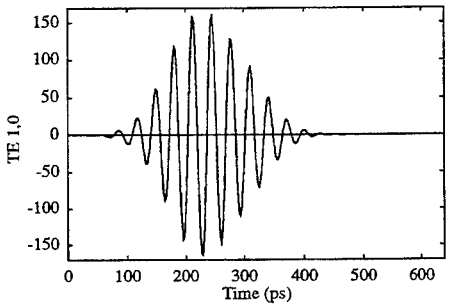

(*a*) band-limited (modulated Gaussian) excitation

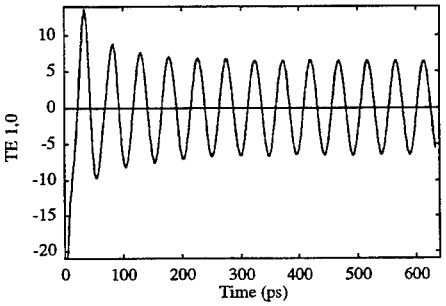

(*b*) impulse excitation

Fig. 9 – Non-touching strip: magnitude of the dominant mode taken from the total field at the input port

A comparison of the results obtained with different multigrid schemes is shown in Fig. 10. These curves show the difference (x0.001) between the multigrid results and the results from the long uniform fine mesh. The result from method *B* is much closer to the fine mesh result than method *A* and, interestingly, at higher frequencies, the stub-loaded coarse mesh is better than the hybrid node coarse mesh. However, the error introduced by any of these schemes is likely to be much less than the other errors involved.

A comparison of the run-times on a 100MHz HP 735 workstation is given below. 2000 fine mesh timesteps were performed in all cases. Runs marked with an asterisk gave poor results and are only included to give an indication of the computational effort. The best solution is to use multigridding to distance the ABC's. Method *A* runs in the shortest time but a slightly better result can be obtained with method *B*. Multi-mode ABC's are expensive compared to adding a coarse mesh region. It should be noted that these figures are very implementation dependant (for example, execution speed could be increased at the expense of an increase in storage requirement), so they should only be taken as a rough indication of the efficiencies of different meshing schemes.

Mesh	ABC	Run-time (sec.)
uniform fine 30x30x96	dominant mode diakoptics	1228
uniform fine 30x30x13	dominant mode diakoptics	422 *
uniform fine 30x30x13	multi-mode diakoptics, to order 3,2	886 *
uniform fine 30x30x13	multi-mode diakoptics, to order 5,4	1694
method A, 30x30x13 fine, 2 15x15x5 coarse	dominant mode diakoptics	430 *
method A, 30x30x13 fine, 2 15x15x5 coarse	multi-mode diakoptics, to order 3,2	514
method A, 30x30x13 fine, 2 15x15x20 coarse	dominant mode diakoptics	459
method B, 30x30x13 fine, 2 15x15x20 stub-loaded coarse	dominant mode diakoptics	582
method B, 30x30x13 fine, 2 15x15x20 hybrid coarse	dominant mode diakoptics	691

Microstrip Impedance Step

To accurately describe microstrips, a reasonable number of nodes must be taken across the width of the metallization and in the height of the substrate. A suitable ABC must be selected to terminate the microstrip. One-way equation ABC's can be used, in which the coefficients are based upon the effective dielectric constant of the microstrip [18]. In this example, simple matched boundaries (giving a reflection coefficient of zero) are used. Here, matched boundaries give adequate performance and some tuning of the coefficients would be required to get a superior performance from one-way equation ABC's. The side and top boundaries are also modeled with matched boundaries. These boundaries must be placed sufficiently far from the microstrip so that they do not disturb its operation. Adding a coarse mesh around the microstrip is an efficient method of increasing the distance to these boundaries. Excitation of microstrips must be done carefully. One possibility is to excite the vertical component of the E-field uniformly under the strip and to allow a certain distance for the correct field distribution to establish itself. Here, a complete plane is excited spatially with the d.c. E-field distribution and temporally with a Gaussian pulse. The d.c. field distribution is obtained from a 2-dimensional slice of TLM nodes, excited with a raised cosine voltage source placed between the ground plane and the strip. To encourage the decay of transients, all metallic surfaces are replaced with matched boundaries, since these will form an equipotential in the steady-state.

The example of an impedance step resulting from a 1:2 change in width is considered here. The dimensions, and details of the multigrid scheme are shown in Fig. 11. The results obtained from a uniform fine mesh with a cross-section of 72x48 nodes, and a mesh of 30x12 nodes (the same as that used in the multigrid schemes) are shown in Fig. 12. The S-parameters were calculated from the strip voltage, and to account for the different impedances of the input and output ports, a factor $\sqrt{Z_{01}+Z_{02}}$ was included in the S21 calculation. The large fine mesh result agrees well with independent results [23]. The proximity of the ABC's in the small fine mesh causes a significant distortion to the results. Multigrid (method *A* and method *B* with both stub-loaded and hybrid nodes) and graded mesh (hybrid node) schemes are compared in Fig. 13. The graded mesh has the same cell dimensions in the cross-section as the multigrid schemes and the same longitudinal dimensions as the fine mesh. The result from the graded mesh is identical to the uniform fine mesh. The 51x30 uniform fine mesh actually gives slightly better agreement than multigrid method *A*. However, all multigrid schemes have half as many nodes in the longitudinal direction in the coarse mesh. Of the multigrid schemes, method *B* with the hybrid node gives the best agreement. It should be noted that there are still errors present in the simulation, in that the curves should be much flatter in the frequency range. In summary, the graded mesh gives the most accurate result but multigrid method *A* runs the fastest.

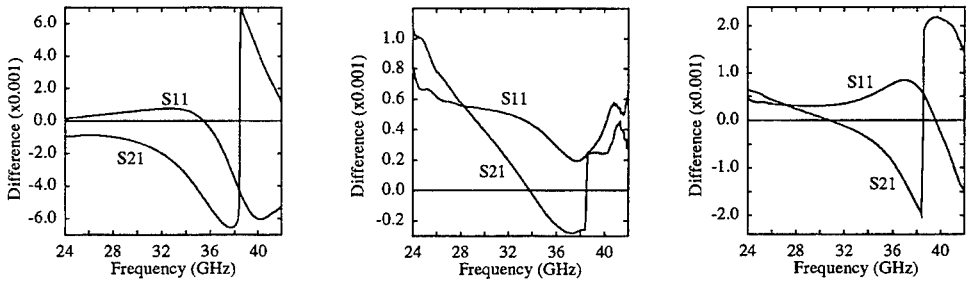

(*a*) method *A* (*b*) method *B*, stub-loaded node (*c*) method *B*, hybrid node

Fig. 10 – Non-touching strip: difference in S-parameters obtained with different multigrid schemes

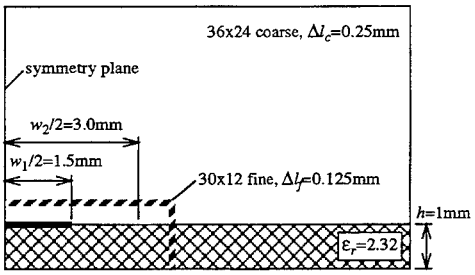

Fig. 11 – Multigrid mesh for microstrip impedance step

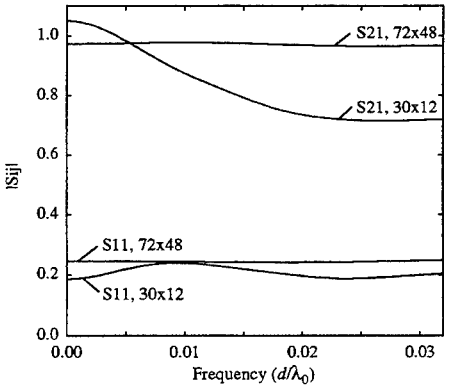

Fig. 12 – Impedance step: uniform fine mesh

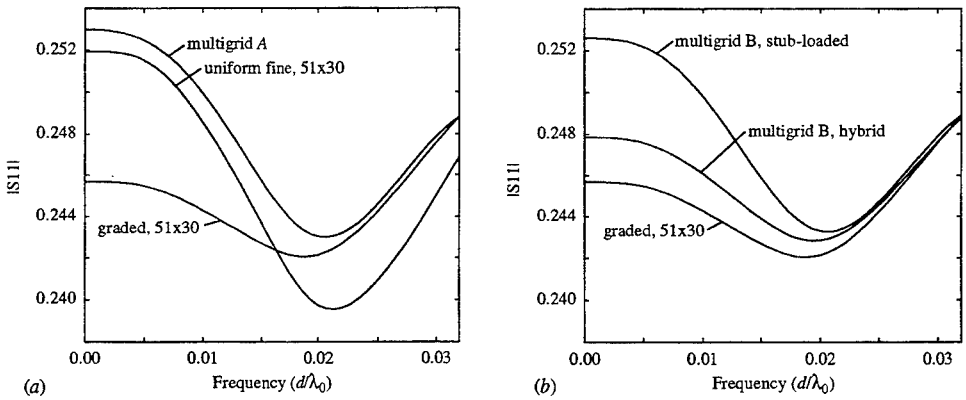

(*a*) (*b*)

Fig. 13 – Impedance step: comparison of graded mesh and multigrid schemes

Conclusions

Multigrid techniques provide an effective means of reducing the mesh resolution away from discontinuities. For the examples considered, method *B* gives better results than method *A*. However, for certain classes of problems, method *A* can give results more quickly without a significant reduction in accuracy. Graded meshes can be more accurate but require greater computer resources.

References

[1] P. B. Johns, "A symmetrical condensed node for the TLM method", *IEEE Trans. MTT*, vol. 35, no. 4, pp 370–377, Apr. 1987.

[2] R. Scaramuzza and A. J. Lowery, "Hybrid symmetrical condensed node for the TLM method", *Electronics Letters*, vol. 26, no. 23, pp 1947–1949, Nov. 1990.

[3] J. L. Herring and C. Christopoulos, "Multigrid TLM method for solving EM field problems", *Electronics Letters*, vol. 28, no. 20, pp 1794–1795, Sept. 1991.

[4] J. L. Herring and C. Christopoulos, "Solving electromagnetic field problems using a multiple grid transmission-line modeling method", *IEEE Trans. AP*, vol. 42, no. 12, pp 1654–1658, Dec. 1994.

[5] J. Wlodarczyk, "New multigrid interface for the TLM method", *Electronics Letters*, vol. 32, no. 12, pp 1111–1112, June 1996.

[6] M. I. Sobhy, M. H. Abd El-Azeem and K. W. Royer, "A new multi-grid 3-D TLM algorithm for simulation of microwave FSS", *IEEE MTT-S Symposium*, June 16-21 1996, San Francisco, CA, USA, pp 439–442.

[7] J. S. Nielsen and W. J. R. Hoefer, "Generalised dispersion analysis and spurious modes of 2-D TLM and 3-D TLM formulations", *IEEE Trans. MTT*, vol. 41, no. 8, pp 1375–1384.

[8] L. de Menezes and W. J. R. Hoefer, "Accuracy of TLM solutions of Maxwell's equations", *IEEE MTT-S Symposium*, June 16–21 1996, San Francisco, CA, USA, pp 1019–1022.

[9] L. de Menezes, C. Eswarappa and W. J. R. Hoefer, "A comparative study of dispersion errors and performance of absorbing boundary conditions in SCN-TLM and FDTD", *13th Annual Review of Progress in Applied Electromagnetics (ACES)*, 17–21 March 1997, Monterey, CA, USA, *this proceedings*.

[10] L. Cascio, G. Tardioli, T. Rozzi and W. J. R. Hoefer, "A quasi-static modification of TLM at knife edge and 90° wedge singularities", *IEEE MTT-S Symposium*, June 16–21 1996, San Francisco, CA, USA, pp 443–446.

[11] J. L. Herring and W. J. R. Hoefer, "Compensation of coarseness error in TLM modeling of microwave structures with the symmetrical condensed node", *IEEE MTT-S Symposium*, May 16–20 1995, Orlando, Florida, USA, pp 23–26.

[12] J. A. Porti, J. A. Morente, M. Khallad and A. Callego, "Comparison of thin-wire models for TLM method", *Electronics Letters*, vol. 28, pp 1910–1911.

[13] A. Mallik, D. P. Johns and A. J. Wlodarczyk, "TLM modelling of wires and slots", *10th International Zurich Symposium on Electromagnetic Compatibility*, 9–11 March 1993, pp 515–520.

[14] F. J. German, "Infinitesimally adjustable boundaries in symmetrical condensed node TLM simulations", *9th Annual Review of Progress in Applied Electromagnetics (ACES)*, 22–26 March 1993, Monterey, CA, USA, pp 482–490.

[15] Eswarappa, G. I. Costache and W. J. R. Hoefer, "Transmission line matrix modeling of dispersive wide-band absorbing boundaries with time-domain diakoptics for S-parameter extraction", *IEEE Trans. MTT*, vol. 38, no. 4, pp 379–386, Apr. 1990.

[16] M. Righi and W. J. R. Hoefer, "Efficient 3D-SCN-TLM diakoptics for waveguide components", *IEEE Trans. MTT*, vol. 42, no. 12, pp 2381–2385, Dec. 1994.

[17] J. L. Herring and W. J. R. Hoefer, "Improved excitation of 3D SCN TLM based on voltage sources," *IEEE MTT-S Symposium*, June 16–21 1996, San Francisco, CA, USA, pp 1019–1022.

[18] C. Eswarappa and W. J. R. Hoefer, "One-way equation absorbing boundary conditions for 3-D TLM analysis of planar and quasi-planar structures", *IEEE Trans. MTT*, vol. 42, no. 9, pp 1669–1677, Sept. 1994.

[19] C. Eswarappa and W. J. R. Hoefer, "Implementation of Berenger absorbing boundary conditions in TLM by interfacing FDTD perfectly matched layers", *Electronics Letters*, vol. 31, no. 15, pp 1264–1266, July 1995.

[20] N. Pena and M. M. Ney, "A new TLM node for Berenger's perfectly matched layer", *IEEE Microwave and Guided Wave Letters*, vol. 6, no. 11, pp 410–412, Nov. 1996.

[21] Eswrappa and W. J. R. Hoefer, "Diakoptics and wideband dispersive absorbing boundaries in the 3D TLM method with symmetrical condensed nodes", *IEICE Trans.*, vol. E 74, no. 5, pp 1242–1250, May 1991.

[22] K. Chang and P. J. Khan, "Equivalent circuit of a narrow axial strip in waveguide", *IEEE Trans. MTT*, vol. 24, no. 9, pp 611–615, Sept. 1976.

[23] N. H. L. Koster and R. H. Jansen, "The microstrip step discontinuity: a revised description", *IEEE Trans. MTT*, vol. 34, no. 2, pp 213–223, Feb. 1986.

Acknowledgments

This work has been funded by the Natural Sciences and Engineering Research Council of Canada, the Science Council of British Columbia, MPR Teltech Inc. of Burnaby, B.C., and the University of Victoria.

A Comparison of Commercially Available Transmission Line Modeling (TLM) and Finite Element Method (FEM) 3-D Field Solvers

Fred J. German and John A. Svigelj
Texas Instruments, Inc.
2501 W. University, MS 8019
McKinney, TX 75070
Tel: (972) 952-3723
FAX: (972) 952-3773
f-german@ti.com

INTRODUCTION

In the past several years microwave and antenna design engineers have been able to reap the rewards of decades of research and development in the field of computational electromagnetics through the availability of commercial EM field solvers for the characterization of complex three-dimensional structures. The ability to accurately predict performance in the design stage without resorting to costly hardware design iterations has led to lower development cost, reduced design cycle time, and designs with better performance. These tools are invaluable when used within their limitations and potentially disastrous when applied inappropriately.

In very general terms there are two widely available types of EM solvers on the market today. The first is concerned with the class of predominantly planar problems such as printed microwave circuits and are based on integral equation solution techniques. The second type is the more general 3-D field solvers based on volumetric meshing. In this paper we investigate two popular software packages employing volumetric meshing for general 3-D structure analysis. The programs used in this study are Ansoft's "Maxwell Eminence" [1] and KCC's "Micro-Stripes" [2]. While both programs provide a full 3-D field solution for arbitrary geometries, they are based on very different methods. "Maxwell Eminence" employs the frequency domain finite element method (FEM) to arrive at a solution while "Micro-Stripes" uses a time domain transmission line modeling (TLM) technique. These particular software packages were chosen for this study due to availability and to enable the comparison of solvers based on entirely different numerical methods.

When using these simulation tools in a real design environment the performance of the devices being modeled are not known a priori so there is no benchmark answer to "tweak" the model to. We have approached this comparison from the viewpoint of a practical design engineer: once the benchmark problems were chosen the geometries were meshed and run with minimal "tuning" of the models to improve agreement with the benchmark data. Thus, the results presented should not be viewed as providing information on the accuracy that can be obtained from the FEM or TLM, but rather as first pass results from models assembled by design engineers that are reasonably familiar with the modeling tools and the microwave devices being modeled.

When comparing analysis packages there are many factors that should be taken into account such as accuracy, ease of use, computational burden, etc. Due to space limitations only the simulation results will be presented in this paper along with some modeling issues. Further information concerning computational requirements and ease of use will be addressed in our presentation.

RESULTS

We have chosen to present results from two different problems which display distinctly differing characteristics. One is a bounded three-dimensional waveguide discontinuity problem and the other is an antenna problem which involves radiation. These two problems provide a good test for the analysis packages in two differing environments (bounded and radiative) and reliable benchmarks exist in the form of measurements for the waveguide problem and the method of moments (MoM) results for the antenna structure.

Waveguide Discontinuity - The geometry for the waveguide discontinuity consisting of cascaded E- and H-plane bends separated by a waveguide section of length L is shown in Figure 1. The details of the geometry for the optimum miters is available in [3] as well as measured data for the structure. The discontinuity was analyzed with values of L equal to 0 and 10.16 mm. A comparison of the magnitude of S_{11} is shown in Figure 2. The agreement with the measurements is reasonable for the most part with Micro-Stripes showing the better overall

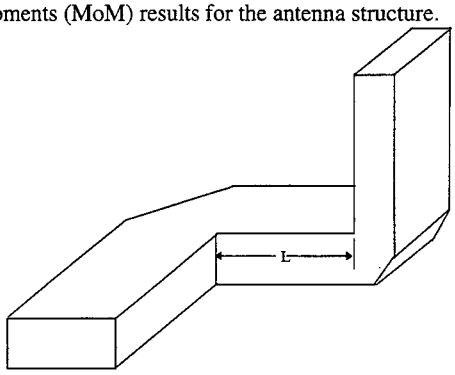

Figure 1. geometry of optimum mitered 90 degree cascaded E- and H-plane bends in WR90 waveguide.

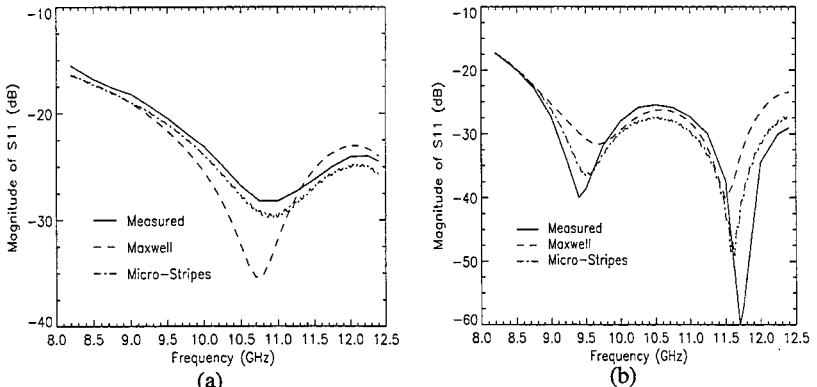

Figure 2. Reflection of waveguide discontinuity shown in Figure 1 (a) L = 0 and (b) L = 10.16 mm.

accuracy for L=0. The Micro-Stripes model also does a slightly better job of predicting the location of the minima for the L=10.16 mm case. There is a slight ripple in the results calculated with Micro-Stripes which results from the necessity of truncating the time domain impulse response. This ripple can be reduced if desired by running the simulation for more time steps at the cost of increased computing time. Conversely, the computing time can be reduced if more ripple is tolerable in the results. It should be noted that the complete frequency response for the structure is obtained from Micro-Stripes in a single simulation while the Maxwell Eminence results are computed at each discrete frequency. Depending on the number of frequency samples required, there is a trade-off that can be made in computational time when deciding between a frequency domain method such as Maxwell Eminence or a time domain method like Micro-Stripes. This issue will be addressed in more depth in the presentation.

Maxwell Eminence has a feature called "fast frequency sweep." It is claimed that this can be used to obtain results over a broad bandwidth by performing the full solution at a single frequency and then using an asymptotic wave expansion (AWE) to extrapolate data at other frequencies. The results for Maxwell Eminence in Figure 2 were computed by performing the full solution at each frequency point. Figure 3 shows the result when the fast frequency sweep is applied to the waveguide bend for the L=10.16 mm case. For this simulation the full solution was performed at the center of the band of interest, 10.3 GHz, and the rest of the frequency response obtained from the fast frequency sweep feature in Maxwell Eminence. Clearly the answer obtained from the fast frequency sweep is unacceptable in this case. In other cases that we have run, as we will demonstrate in the next problem, the fast frequency sweep provides accurate results compared to the full solution. Our experience indicates that the accuracy of the fast frequency sweep is unpredictable and its use should be approached with extreme caution in a real design environment.

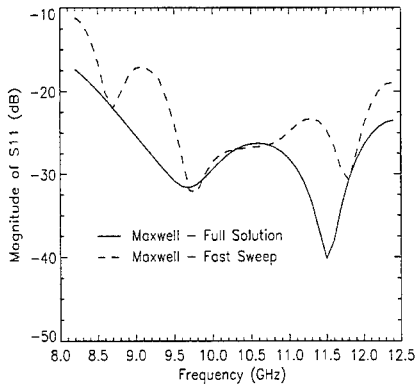

Figure 3. Reflection for the waveguide bend (L = 10.16 mm) calculated with Maxwell Eminence full solution and fast frequency sweep.

The Micro-Stripes software uses rectangular cells for the discretization of problems and so any structure that contains boundaries which do not fall on the faces of these cells requires some degree of approximation. In the waveguide problem this results in the mitered corners being modeled using a "Staircase" approximation. In Micro-Stripes the mesh is defined entirely by the user and very accurate modeling is obtained by careful choice of mesh placement at the miter to insure that the sloped boundary intersects the cell walls at the halfway point for all cells along the boundary. However, if care is not taken in the meshing, severe inaccuracies can result. The Micro-Stripes results in Figure 2 were

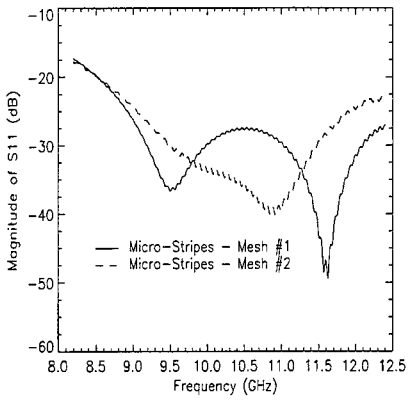

Figure 4. Reflection for the waveguide bend (L = 1.16 mm) for two different Micro-Stripe meshes.

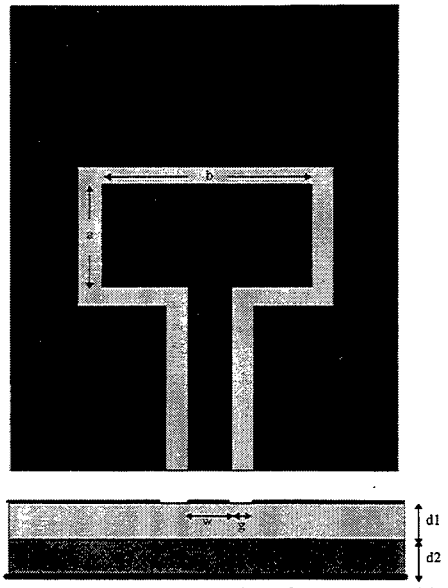

Figure 5. Geometry of coplanar waveguide fed slot loop antenna. (a = 5.22mm, b = 6.69mm, w = 1.74mm, g = 3.48mm, d1 = 0.787mm, d2 = 0.635mm, e1 = 2.2, e2 = 1.0)

obtained from a mesh that was designed by the analyst to accurately model the sloped wall. If the same cell size is used but the location of the cell face is shifted by as little as a half cell severe inaccuracies can result as shown in Figure 4. Further investigation revealed that the E-plane bend was more sensitive than the H-plane bend to this discretization error due to the way the currents distribute themselves on the waveguide walls. Thus, caution must be exercised when meshing such problems. Guidelines for building the Micro-Stripes mesh in these cases require some degree of experience and knowledge of the TLM method.

Coplanar Waveguide Fed Antenna - The next problem that was investigated was a slot loop antenna with a coplanar waveguide feed [4]. The geometry of the structure is shown in Figure 5. In order to simulate an infinite ground plane the problem space in the computational models was approximately (3a)x(3b) in the plane of the antenna and the antenna structure extended all the way to the edges of the computational domain. Appropriate boundary conditions were used to allow the antenna to radiate into an infinite half-space. Initially only half of the structure was meshed and a symmetry plane was used in the models. The results for the reflection coefficient magnitude are shown in Figure 6. The Maxwell Eminence and Micro-Stripes results are compared to data from an MoM integral solution of the structure. Both methods predict the resonant frequency with reasonable accuracy but the Maxwell Eminence solution does not predict as deep a null as the MoM or Micro-Stripes solutions. The Maxwell Eminence solution shown in Figure 6 represents a full solution at each frequency point.

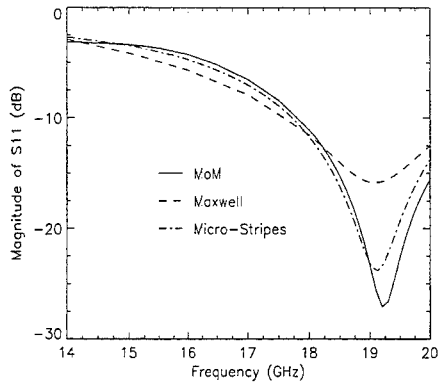

Figure 6. Reflection for slot loop antenna with coplanar waveguide feed shown in Figure 5.

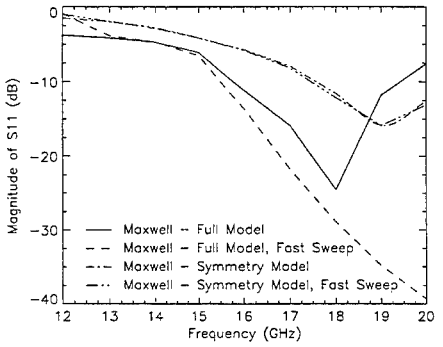

Figure 7. Reflection for slot loop antenna with coplanar waveguide feed for various Maxwell Eminence simulation situations.

Next, the entire problem was solved without the use of the symmetry boundary. Naturally, the same answer is expected and indeed the Micro-Stripes solutions with and without the symmetry boundary are indistinguishable. It is disconcerting, however, that Maxwell Eminence yields significantly differing solutions with and without the symmetry, as shown in Figure 7. Also included in this figure are the results obtained using the fast frequency sweep option in Maxwell Eminence. The unpredictability of the fast frequency sweep is further demonstrated here. For the symmetry model the fast frequency sweep solution agrees well with the solution obtained by simulating the structure at each frequency while for the model without symmetry the agreement with the full solution is quite poor. At this time we feel that the differing solutions with and without symmetry are due to differences in the port solutions used to excite the feedline in the two cases - further investigation is warranted.

In the Micro-Stripes model the conductors were modeled with zero thickness. Since the conducting surfaces are placed on cell faces and the excitation is located at cell centers, it was necessary to take great care to excite the model using a divergenceless source so that excess charge did not accumulate at the port. This was accomplished quite easily by placing small one cell "tabs" at the input port to excite the initial voltage across. While conceptually easy to understand and implement, serious errors in the results would be present if a user was unaware of the necessity to implement the source in this fashion. As mentioned previously all of these results have been obtained without any attempt to optimize the model for best accuracy. One factor to consider for an optimized model would be the distance from the antenna to the absorbing boundaries as well as the size of the ground plane.

CONCLUSIONS

In this paper we have compared two commercially available 3-D electromagnetic field solvers. Our approach to evaluating and comparing the two packages has been from a design engineer's point of view. We assumed we had a device to analyze and we meshed and solved the problem. We have presented the first pass analysis results and no significant effort was made to optimize the models or solutions. In this way we hope to yield some information on the performance of these analysis tools in practical design scenarios.

Table 1 summarizes some of our key conclusions regarding the two packages.

TABLE 1

	Micro-Stripes	**Maxwell Eminence**
Meshing	• Manual • Rectangular Bricks • Requires some experience	• Automatic • Tetrahedra • Limited control of mesh (seeding)
Solution Domain	Time Domain • Yields broadband response	Frequency Domain • Solution at single frequencies
Accuracy	• Accuracy is very good on problems in this paper • Results can be sensitive to "staircased" meshing	• Different results with symmetry boundaries • Fast frequency sweep yields unpredictable results

An important aspect that has not been addressed is the computational requirements of the packages. This will be covered in our presentation. There are many factors that need to be considered when comparing computational resources. A fast solution of questionable accuracy is totally useless. A broadband solution that provides thousands of frequency samples but takes a long time to run may be a waste of computer resources if data is only required over a few frequency points.

We do not draw any conclusions as to the "best" analysis tool as this would be subjective opinion at best. Ultimately the best tool is dependent on the characteristics of the specific problem to be solved and just as importantly on the analyst's experience and familiarity with the tool.

ACKNOWLEDGMENTS

We would like to thank Dr. Jon Veihl for providing the MoM data used for comparison in this paper.

REFERENCES

[1] Maxwell Eminence User's Manual, Ansoft Corporation, Pittsburgh, PA.

[2] Micro-Stripes User's Manual, Version 2.3, Kimberley Communications Consultants (KCC), Nottingham, UK

[3] J.M. Reiter and F. Arndt, "Rigorous analysis of arbitrarily shaped H- and E-Plane discontinuities in rectangular waveguides by a full-wave boundary contour mode-matching method," IEEE Trans. Microwave Theory Tech., vol. MTT-43, no. 4, pp. 796-801, April 1995.

[4] H.C. Liu, T.S. Horng and N.G. Alexopoulos, "Radiation of printed antennas with a coplanar waveguide feed," IEEE Trans. Ant. Prop., vol. AP-43, no. 10, pp. 1143-1148, October 1995.

Validation of Transmission Line Matrix, Finite-Integration Technique, and Finite-Difference Time-Domain Simulations of a Multi-Segment Dielectric Resonator Antenna

Neil R. S. Simons[1], Aldo Petosa[1], Michel Cuhaci[1], Apisak Ittipiboon[1],
Riaz Siushansian[2], Joe LoVetri[2], and Stefan Gutschling[3]

[1]Directorate of Antennas and Integrated Electronics
Communications Research Centre
3701 Carling Avenue, P.O. Box 11490, Station H
Ottawa, Ontario, Canada, K2H 8S2

[2]Department of Electrical Engineering
The University of Western Ontario
London, Ontario, Canada, N6A 5B9

[3]Technische Hochschule Darmstadt
Fachbereich 18, Fachgebiet Theorie Elektromagnetischer Felder,
Schlossgartenstr. 8, D-64289, Darmstadt, Germany

Abstract: A multi-segment dielectric resonator antenna (MSDRA) and various single element dielectric resonator antennas (DRAs) were analyzed using three different differential equation based electromagnetic analysis programs. The three programs are based on the Finite-Integration Technique (FIT) [1], the Yee Finite-Difference Time-Domain (FD-TD) algorithm [2], and the symmetric-condensed Transmission Line Matrix (TLM) method [3]. The methods were applied to compute the scattering parameters of the MSDRA, which are compared with measurements. None of the methods accurately analyzed the MSDRA, and therefore simpler single element DRAs were considered. The methods are capable of accurately analyzing the single DRA elements with relative permittivities less than 40.

I: Multi-Segment Dielectric Resonator Antennas

The geometry of the MSDRA is shown in Figure 1, and for this particular investigation the MSDRA is proximity coupled with a microstrip line [4]. Over the past few years some research has been focused on dielectric resonators as radiating elements. Low loss dielectric resonators have been used for many years as energy storage devices in microwave circuits such as oscillators and filters, where the resonators are enclosed in metal shields to prevent radiation. Only in the last decade or so has research been initiated to investigate the radiation characteristics of open dielectric resonators. Much of this research has been focused on the characterization of individual resonators as antenna elements. Studies have been carried out on dielectric resonator antennas (DRAs) of various shapes such as rectangular, cylindrical, ring, semi-spheres, and crosses. A variety of feeding mechanisms have been used including probes, apertures, co-planar waveguides, microstrip lines, and dielectric image guides. This research has demonstrated that DRAs offer several attractive features including wide impedance bandwidth, high radiation efficiency, and compact size. DRAs are currently being investigated as elements in linear and planar arrays.

The ability to accurately characterize DRAs would facilitate their use in larger more complex designs. Cavity models provide reasonable accuracy in the prediction of resonant frequency and

bandwidth, but are not capable of including feed structures [5]. In [6], the FD-TD method is applied to compute the radar-cross-section of single element DRAs as well as their resonant frequency and Q-factor. Differential equation based numerical techniques are ideally suited for solving heterogeneous electromagnetic field problems, such as the MSDRA and DRA.

The dimensions of the problem are: L=10.0mm, W=4.0mm, H=6.5mm, and T=1.0mm. The relative permittivity of the inserted segment is 40, while the relative permittivity of the dielectric resonator antenna is 10. The 50Ω microstrip line is printed onto a 0.75mm substrate of permittivity 3.0, and has a line width of 1.75mm. The microstrip line is matched at both ends, and the element is centered on the microstrip line.

Several aspects of the DRAs make their analyses challenging. These include the high relative permittivity of the dielectric resonator antenna elements (up to 100), which also indicate a potentially high Q factor. As well, there is a large range in relative geometrical sizes within the MSDRA. For elements operating around 10GHz, the thickness of the microstrip line substrate and height of the dielectric inserts is typically less than 1.0mm, while the length and height of the resonator is on the order of several mm.

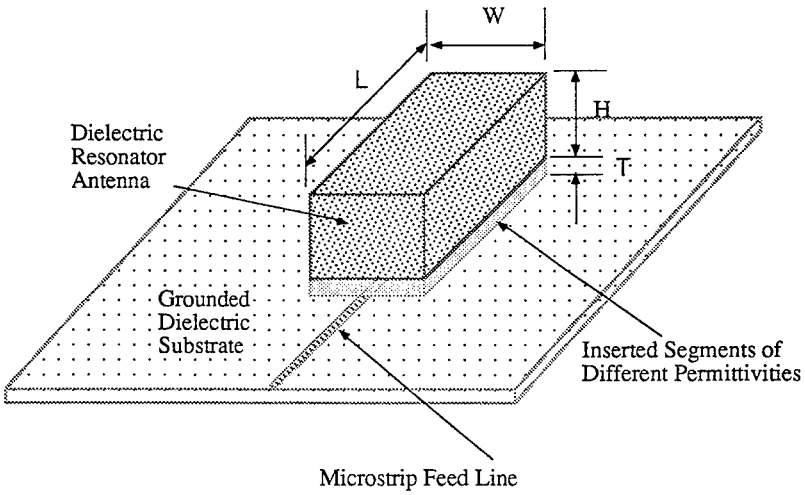

Figure 1: A multi-segment dielectric resonator antenna (MSDRA) proximity coupled to a microstrip line.

II: The Computational Methods

The Finite-Integration Technique as implemented within the MAFIA CAE tool is based on a integral form of Maxwell's equations [1]. The analytic formulation is discretized using two grids, which are orthogonal to each other. Static, time-harmonic, and time-dependent problems can be analyzed with the formulation. For the present investigation, computations are performed in the time domain. A *waveguide* absorbing boundary condition is used to match the exterior boundaries, which utilizes mode patterns of the microstrip line. The mode patterns are determined using a two-dimensional eigenvalue solver. A graded mesh is used to improve the discretization of the problem near the microstrip line and dielectric insert. The mesh size ranges from Δ=0.16mm to Δ=1.0mm. The

symmetry of the MSDRA is exploited such that only one half of the structure was modelled (a magnetic wall was used).

Details regarding the FD-TD simulation program can be found in [2]. To briefly summarize, it is based on Yee's formulation and utilizes first-order Mur absorbing boundary conditions. A Gaussian pulse is launched on the microstrip line using a matched Thevenin equivalent voltage source. The program is capable of using a graded mesh, although this capability has not yet been utilized. The geometry is discretized using $\Delta x=\Delta y=\Delta z=0.25$mm, within a mesh of size Nx=85, Ny=200, Nz=70.

The TLM simulation program is based on the symmetric-condensed (SCN) TLM node, and is described in [3]. A Gaussian pulse is launched on the microstrip line using an idealized TEM source. The *match termination for normal incidence* absorbing boundary condition is applied, which usually provides performance superior to first-order, but inferior to second-order absorbing boundary conditions. The geometry is discretized using $\Delta x=\Delta y=\Delta z=0.25$mm, within a mesh of size Nx=96, Ny=120, Nz=71.

The simulations were performed for the same amount of physical time, which corresponds to approximately 5000 TLM time steps. For all three simulation programs, convergence tests were performed with respect to the number of time steps, and the distance from the antenna to the outer boundary condition. All three programs have been previously validated through application to a wide variety problems.

III: Comparison with Measured Data

We first present results for the complete MSDRA structure as described in Section I, Fig. 1. In Fig. 2, the FIT and FD-TD numerical results for S_{21} are compared to the measured data. The FIT and FD-TD numerical results agree well with each other, but not with measured data. The agreement between the FIT and FD-TD numerical results is remarkable considering the considerable differences in the simulation programs noted above and the different meshing applied with each. In Fig. 3, the TLM numerical results for S_{21} are compared with the measured data. Once again numerical results do not agree well with measured data. Examining the behavior between 6 and 12 GHz, the numerical results fit the general triple-resonance shape of the measured data, but there exists a significant frequency shift of 1 GHz. The FIT and FD-TD data fit the general shape of the measurements better than the TLM results. Only S_{21} data is displayed for conciseness. The trends for S_{11} were similar to that for S_{21}.

In order to examine the possible problems with the numerical results, we have considered simpler structures. The first involves removing the MSDRA completely, and analyzing a metallic block with physical dimensions L=4.0mm, W=10.0mm, H=1.0mm. The FD-TD and TLM predictions for the magnitude of S_{21} are compared to measured data in Fig. 4. The measured resonance which appears just under 15GHz is slightly shifted down in the FD-TD and TLM predictions. Agreement with the measured data (and between the FD-TD and TLM results) is superior to that observed with the MSDRA structure.

In addition to the metal block described above, we have considered the analysis of single element DRAs (i.e., without the high permittivity insert). In Figs. 5, 6, and 7, FD-TD and TLM predictions for S_{21} are compared to measured data for the following cases: ε_r=10, L=10.0mm, W=4.0mm, H=6.5mm; ε_r=25, L=8.0mm, W=4.0mm, H=5.0mm; and ε_r=40, L=10.0mm, W=4.0mm, H=1.0mm. The results of Figs. 5-7 indicate decreasing agreement with increasing permittivity of the DRA. Several other sized resonators with ε_r=40 were considered. The same general trend of the FD-TD and TLM results diverging from each other and from the measured data was observed. In addition, a case with ε_r=100, was examined in which extremely poor results were obtained from the numerical simulations.

As noted in Section II, the discretization used in the TLM and FD-TD simulations was 0.25mm. At 10GHz, this discretization corresponds to $37.9\Delta l/\lambda$ in ε_r=10, $19.0\Delta l/\lambda$ in ε_r=40, and $12.0\Delta l/\lambda$ in ε_r=100. Following [7] this discretization is sufficient for all cases, except for the ε_r=100 case, where it is marginal, but still acceptable.

The single element DRA comparisons indicate the inaccuracy in both the TLM and FD-TD methods with increased permittivity of the DRA. A possible explanation for the inaccuracy, despite sufficient discretization, is in the lack of strong enforcement of normal field boundary conditions. The coupling of energy from the microstrip line to the DRA elements is through the electric field component normal to the dielectric interface. The discontinuity in this normal electric field component is not satisfied directly by the Yee FD-TD or SCN TLM algorithms. This effect has been investigated with respect to edge and nodal finite-element formulations [8]. We are currently investigating simple cavity problems to determine if this is the source of the inaccuracies.

The measurements were reconfirmed on different occasions. Care was taken to ensure that the presence of glue (used to bond the MSDRA sections together as well as bond the MSDRA to the microstrip line) had a negligible effect. The only concern regarding the measured data is that of a very small air gap existing between the MSDRA element and the substrate (due to the finite-thickness of the metalization of the microstrip line. It was observed that if the MSDRA was not bonded tightly to the microstrip line, the resonances in the S_{21} data were shifted up in frequency by about 1GHz. Since the simulations do not take into account this small gap, this can perhaps account for some of the frequency shift in the MSDRA simulations.

IV: Conclusions

A multi-segment dielectric resonator antenna (MSDRA) and various single element dielectric resonator antennas (DRAs) were analyzed using three different differential equation based electromagnetic analysis programs (FIT, FD-TD, and TLM). None of the simulation programs accurately characterized the MSDRA. The FD-TD and FIT numerical results are in good agreement with each other. The FD-TD and TLM methods are capable of accurately analyzing single DRA elements with relative permittivities less than 40. Possible causes for the discrepancies include, a very small air gap existing between the antenna elements and the microstrip substrate, and the lack of strong enforcement of normal field boundary conditions at dielectric interfaces within all three numerical methods.

---

[1] T. Weiland, "Time-Domain Electromagnetic Field Computation With Finite Difference Methods", *International Journal of Numerical Modelling: Electronic Networks, Devices and Fields*, vol. 9, pp. 295-319, 1996

[2] M. Rizvi, and J. LoVetri, "Modelling and Reduction of Crosstalk on Coupled Microstrip Line Structures and Multichip Modules: An FDTD Approach", *Int. Journal on Microwave and Millimeter-Wave Computer-Aided Eng. (special issue on Time Domain Modeling for Microwave Components)*, vol. 6, No. 1, pp. 58-68, 1996.

[3] N. R. S. Simons, A. Sebak, and A. Ittipiboon, "Analysis of Aperture-Coupled Microstrip Antenna and Circuit Structures Using the Transmission Line Matrix Method", *IEEE Antennas and Propagation Magazine*, vol. 37, no. 4, pp. 27-37, August 1995.

[4] A. Petosa, A. Ittipiboon, M. Cuhaci, R. Larose, "Low Profile Phased Array of Dielectric Resonator Antennas", *IEEE International Symposium Phased Array Systems and Technology* , Oct. 1996.

[5] R. K. Mongia, "Theoretical and experimental resonant frequencies of rectangular resonators", IEE Proceedings-H, vol. 139, no. 1, pp. 98-104, February 1992.

[6] C. W. Trueman, S. R. Mishra, C. L. Larose, and R. K. Mongia, "Resonant Frequencies and Q Factors of Dielectric Parallelpipeds", *IEEE Transactions on Instrumentation and Measurement,* vol. 44, no. 2, pp. 322-325, April 1995.

[7] K. S. Kunz and R. J. Luebbers, **The Finite Difference Time Domain Method for Electromagnetics**, CRC Press, 1993.

[8] X. Yuan, D. R. Lynch, and K. Paulsen, "Importance of Normal Field Continuity in Inhomogeneous Scattering Calculations", *IEEE Transactions on Microwave Theory and Techniques* vol. 39, no. 4, pp. 638-642, 1991.

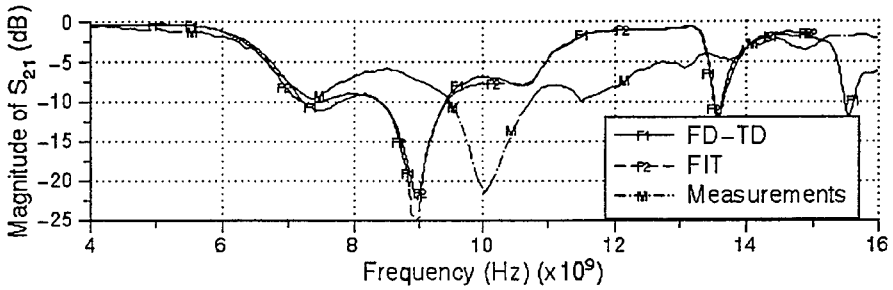

Figure 2: Analysis of the MSDRA structure: FIT and FD-TD numerical results for the magnitude of S_{21} are compared with measured data. The FD-TD and FIT numerical results agree well with each other, but not with measured data.

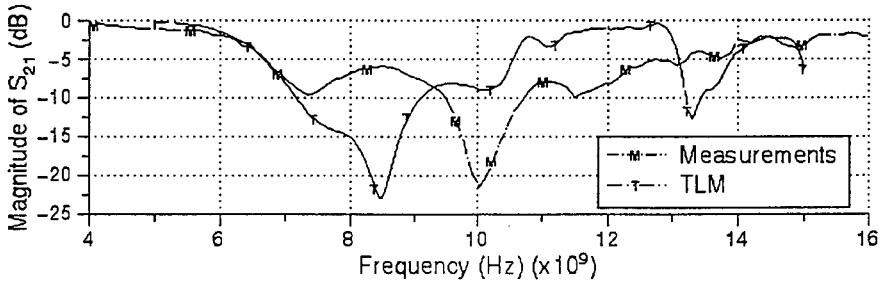

Figure 3: Analysis of the MSDRA structure: TLM numerical results for the magnitude of S_{21} are compared with measured data. The TLM numerical results do not agree well with the measured data.

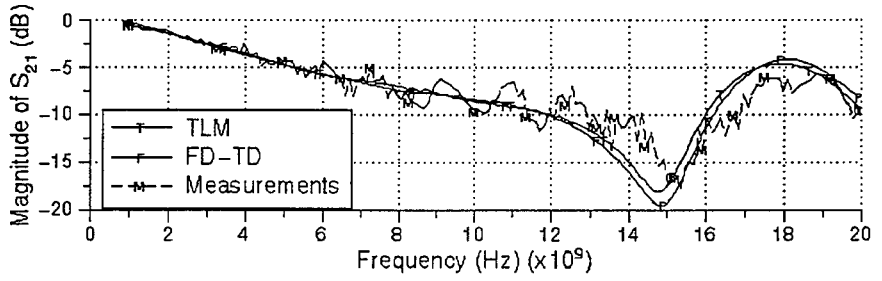

Figure 4: Metal block: FD-TD and TLM numerical results for the magnitude of S_{21} are compared with measured data. Good agreement is obtained.

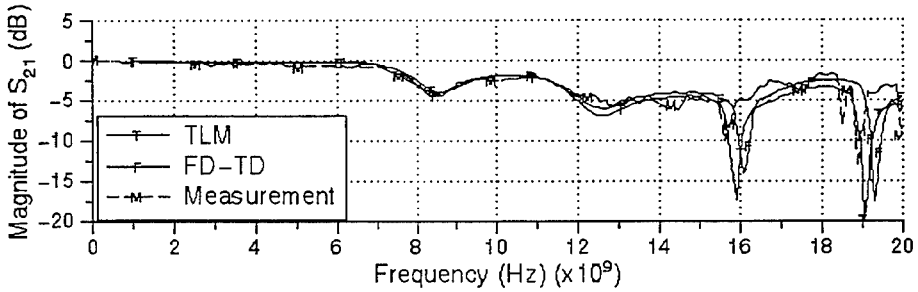

Figure 5: Single DRA element with ε_r=10, L=10.0mm, W=4.0mm, H=6.5mm: FD-TD and TLM numerical results for the magnitude of S_{21} are compared with measured data. Good agreement is obtained. A frequency shift of approximately 0.3GHz is observed from 16 to 20GHz.

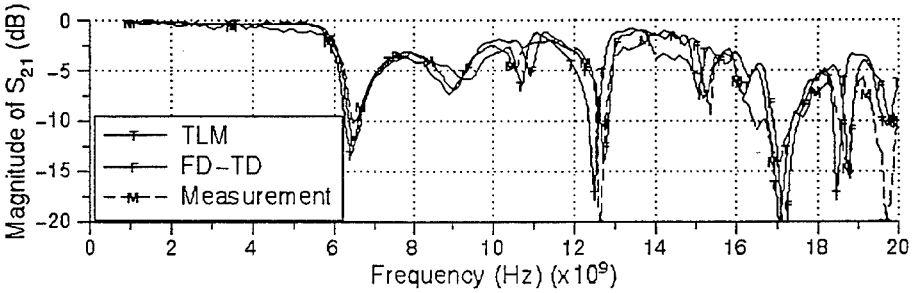

Figure 6: Single DRA element with ε_r=25, L=8.0mm, W=4.0mm, H=5.0mm: FD-TD and TLM numerical results for the magnitude of S_{21} are compared with measured data. Good agreement is obtained. A frequency shift of approximately 0.3GHz is observed in the resonance at 17GHz.

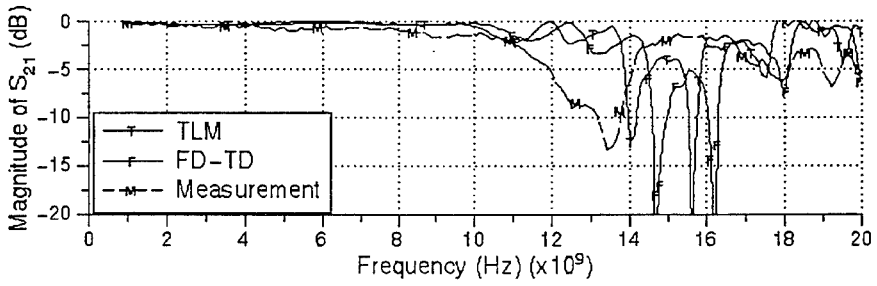

Figure 7: Single DRA element with ε_r=40, L=10.0mm, W=4.0mm, H=1.0mm: FD-TD and TLM numerical results for the magnitude of S_{21} are compared with measured data. Numerical results do not agree with measured data.

Microstrip antenna characterization using TLM and Berenger's Perfectly Matched Layers (PML).

J.L.DUBARD, D.POMPEI

Electronic, Antennas and Telecommunications Laboratory
Nice Sophia Antipolis University
CNRS, Bat 4, 250 rue A EINSTEIN, 06560 Valbonne, France
Tel : (33) 4 92 94 28 00 , Fax (33) 4 92 94 28 12,
email : pompei@alto.unice.fr

Abstract : The characterization of complex microstrip antennas, with spatial discretisation methods, needs the simulation of infinite space of propagation. We propose in this paper the results given by a new 3D-TLM scattering matrix describing the Berenger's Perfectly Matched Layers (PML). Comparisons of efficiencies between absorbing boundary conditions, the Higdon's conditions and the Berenger's one, are proposed. The effects on the electromagnetic far fields are compared with experimental results giving informations for the characterization of microstrip antennas. We show also the improvements considering the computation time and memory space used.

Characterization of microstrip antennas : Studies in the temporal domain of printed antennas allow wide frequency band investigations, while minimising computation time. For this work, we have used the Transmission line matrix method, and a massively parallel computer, the Connection Machine, CM5. The transmission line matrix method simulates a temporal electromagnetic wave propagation in any medium. For our problems, the TLM mesh is larger than the physical dimensions of the antenna and then we take especially into account the effects of the finite dielectric substrate and the finite ground plane. This last point is very important and it's one of the reasons to use TLM. We use the variable mesh with the three dimensional condensed nodes [1].
About the radiation patterns, we have used the equivalence principle. It consists in giving the electromagnetic far fields $\vec{E}$ and $\vec{H}$, outside a closed surface S, from the $\vec{E}$ and $\vec{H}$ distribution on this surface S (figure 1). We note $\vec{E}_S$ and $\vec{H}_S$ the field components tangential to the closed surface S around the radiating element, $\vec{n}$ is the unit vector perpendicular to the surface, $\vec{u}$ the unit vector along the direction of propagation. The surface S is the support of secondary sources $\vec{J_s}$ and $\vec{M_s}$. k is the propagation constant, r being the distance to the point M of observation, P the point on the surface, $\eta = 377\ \Omega$, the vacuum impedance.These sources create far fields of potentiel vectors $\vec{A}$ and $\vec{F}$ which give the electric far field. Then knowing of the magnitudes and phases of E_ϕ and E_θ gives the polarisation and the radiating pattern of the antenna.

About the input impedance, we compute it from the standing waves, established in the microstrip feed line. Using the Prony Pisarenko Method (PPM) [2], both in time domain and in spatial domain, we get out the stationnary waves, at each frequency, and we compute then the modulus, and the phase of the reflection coefficient. But our present purpose remains the following specific problem : the characterization of complex microstrip antennas with spatial discretisation methods needs the simulation of infinite space of propagation. Many solutions have been recently proposed in order to improve the simulation of absorbing layers [3].

Absorbing boundary conditions : About the boundary conditions, we have used in a first time the matched terminations at the end of the meshlines, on the boundaries of the computed structure. In this case, the absorbing boundary conditions were established to provide a perfect absorption for plane

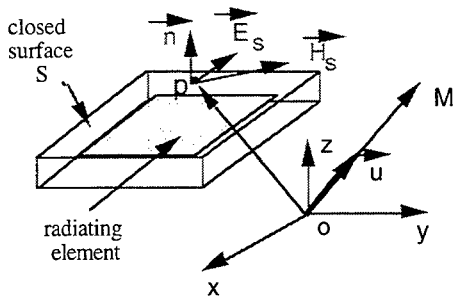

$$\vec{J}_S = \vec{n} \wedge \vec{H}_S \qquad \vec{M}_S = -\vec{n} \wedge \vec{E}_S$$

$$\vec{A} = \int_S \vec{J}_S \frac{e^{-ikr}}{4\pi r} e^{ik(\vec{OP}.\vec{u})} dS$$

$$\vec{F} = \int_S \vec{M}_S \frac{e^{-ikr}}{4\pi r} e^{ik(\vec{OP}.\vec{u})} dS$$

$$\vec{E} = -ik\eta \left[(\vec{A} \wedge \vec{u}) \wedge \vec{u} - \frac{1}{\eta} \vec{F} \wedge \vec{u} \right]$$

Figure 1 : Equivalence principle

waves travelling at incidence angle 0°. About other incidences, this technique may not appear very correct. The matched termination absorbing boundaries affect mainly the input impedance computation particularly if the excitation point is close to the absorbing walls. About radiation patterns, this effect is considerably reduced if the end of the TLM network above the patch is sufficiently far away (about 0.8λ). We have made tests using the boundary condition proposed by Higdon[4], rectifying the reflections at incidence angles ± 45°. To clarify our use of Higdon's conditions, we recall the boundary relations for outgoing waves in x-direction,

$$BE = \prod_{i=1}^{P} B_i E = \prod_{i=1}^{P} \left(\frac{\partial}{\partial x} + \frac{\cos\theta_i}{(c)} \frac{\partial}{\partial t} + \varepsilon_i \right) E = 0$$

$$B_i = \frac{I - D^{-1}}{\Delta x} \left((1-a)I + aK^{-1} \right) + \frac{\cos\theta_i}{(c)} \left(\frac{I - K^{-1}}{\Delta t} \right) \left((1-b)I + bD^{-1} \right) + \varepsilon_i$$

B represents the boundary operator which ensures a total absorption for any linear combinations of plane waves travelling with incidence angles ± θ_i. The damping factors ε_i allow to absorb DC and low frequency components. E represents the tangential electric field on the considered wall while c is the velocity of light. Taking difference approximations for both $\frac{\delta}{\delta x}$ and $\frac{\delta}{\delta t}$, the B coefficients become B_i. I, K and D are the shift operators defined in [4]. We have limited our model to a second order and we have chosen a total absorption for $\theta_1 = 0°$ and $\theta_2 = \pm 45°$. Then, the coefficients a and b, respectively the weighted time and space averages of the space and time differences, are equal to 0.25 while $\varepsilon_1 = 0.15/\Delta l$ (Δl : TLM cell size) and $\varepsilon_2 = 0$. Finally, we have applied the recommendations given in [2] about the numbers of TLM cells between the boundaries and the excitation point to avoid instabilities.

Another approach is possible with the solution proposed by Berenger [5] and we have applied this solution directly on TLM mesh. We propose (and we suggest to refer) a description of this new TLM scattering matrix, applying the Perfect Matched Layers, in another communication [6]. To valid the modified SCN, the scattering problem [7] of figure 2 was considered. The scatterer is a cube of side $10\Delta l$ with Δl=50mm. It is illuminated by a gaussian plane wave travelling in the +x direction. A reference solution was obtained with the usual SCN in a large domain (N_X=N_Y=N_Z=150). The first 150 samples of the Ez field component are exact values since no reflections from boundaries reach the output point below this time step. The performance of the conditions will be quantitavely stated by evaluating the error parameter e_r (Fig 2).

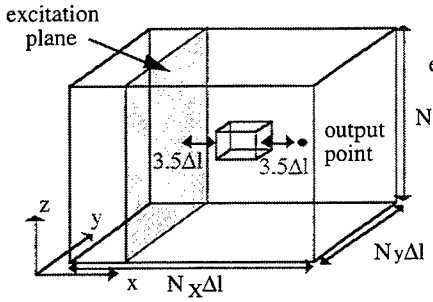

$$\text{error}(n) = e_r = \sqrt{\sum_{i=1}^{n} \left(E_z(i) - E_{z\,ref}(i)\right)^2}$$

Figure 2

Results obtained with the usual SCN in a restricted domain ($N_X=N_Y=N_Z=40$) using matched terminations and Higdon's conditions are plotted in figure 3. The error is respectively -4dB and -15dB. Note that the difference between matched terminations and Higdon's conditions, which is the most important point in comparison of different absorbing boundary conditions, is approximately 10dB as in [7].

We have also plotted in figure 3 the results obtained using the modified SCN with PML layers set only two cells from the scatterer and adjacent to the excitation plane and to the output point. We performed several tests to study the effect of varying the conductivity profile, the layer thickness and the theoretical reflection factor R(0) [5]. It seems that a geometric progression, with a ratio of 1.5, is an optimal conductivity profile in TLM simulation. The efficiency of the PML increases when the thickness grows up and when R(0) decreases. PML layers with 13 cells and $R(0)=10^{-6}$ provide 34dB more accurate solution than Higdon's conditions and 45dB more accurate than matched terminations for approximately the same computational domain ($N_X=44$, $N_Y=N_Z=40$). Reducing R(0) do not improve the results. Furthermore, instabilities appear at time step 3000 approximately except for $R(0)\geq 10^{-4}$. A 13 cells PML layer with $R(0)=10^{-4}$ provides a stable solution and seems to be a good trade-off between efficiency and stability.

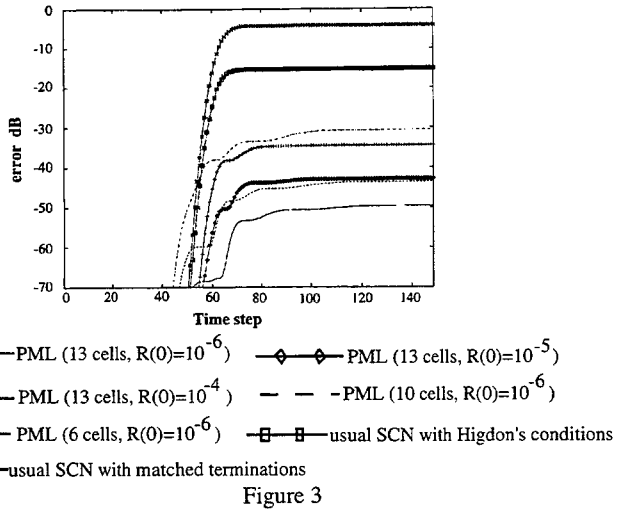

Figure 3

Effect analysis : Finally, we have applied these techniques to antenna characterisations.

Input impedances : The comparisons of input impedances have been made considering the reference square printed antenna fed by coupling through a slot (figure 4) studied by Croq [8].

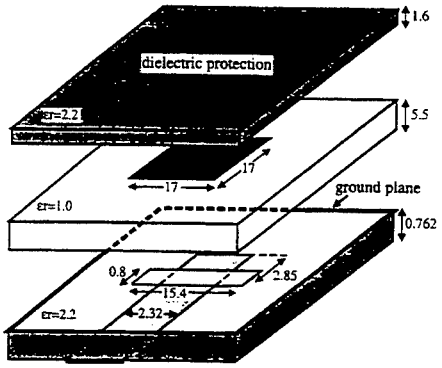

Figure 4
(dimensions in mm)

We have used the same computational domain (46x27x78 cells) for all TLM simulations. With this configuration, PML layers with 6 cells were set 2 cells from the excitation. As observed on the input impedance loci shown in figure 5, the differences between the absorbing boundaries are not sensitive and all the results are in good agreement with the calculed and mesured loci given by Crocq.

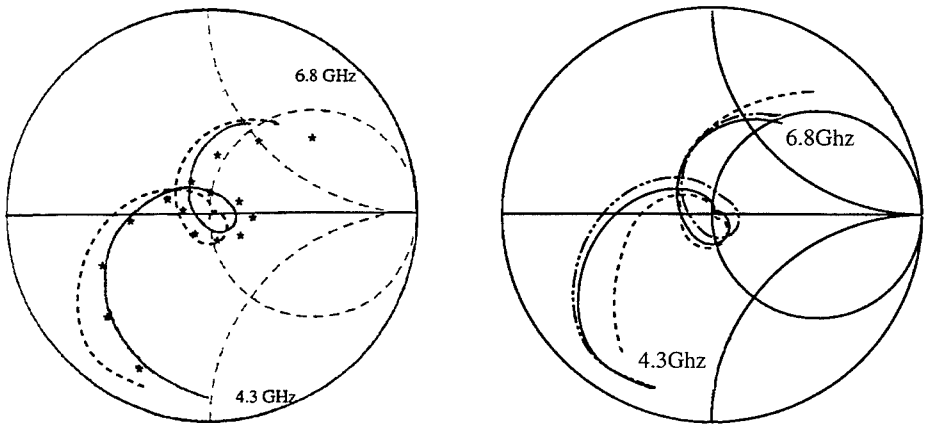

Figure 5 : Input impedance of the antenna shown on figure 4

Radiation patterns : We propose here comparisons about the radiation patterns of a classical microstrip antenna studied by Bokhari in [9]. As observed on figure 6, results obtained with TLM using 6 cells PML layers set 3 cells from the antenna are very closed to Bokhari experiment. These good results can be obtained using the same computational domain (57x24x56 cells) with Higdon's conditions but not with matched termination.

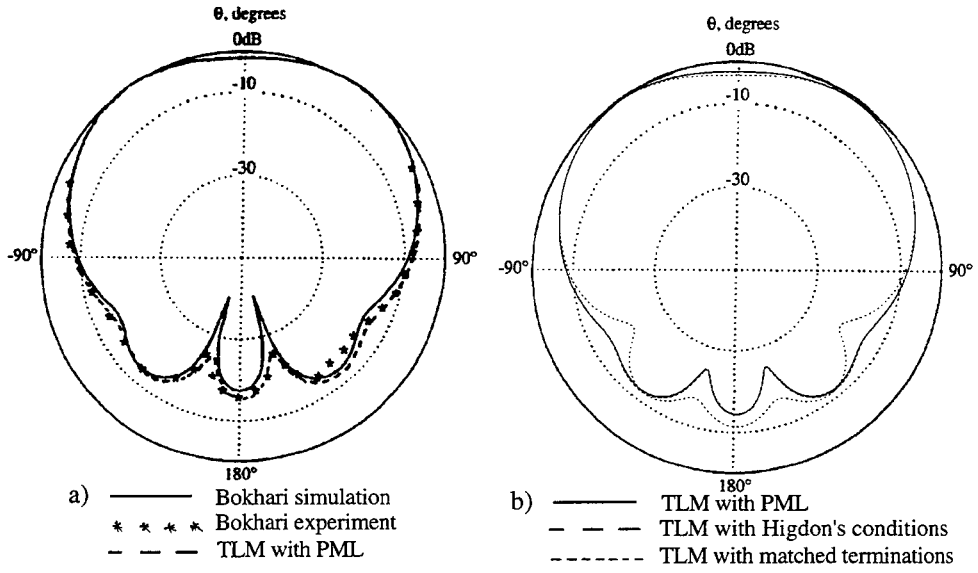

Figure 6 : Radiation pattern (E_θ field) of microstrip patch antenna on $1.5\lambda_0 x 1.5\lambda_0$ ground plane [9]

V. CONCLUSION

A new variable mesh 3D-TLM condensed node, allowing direct implementation of Berenger's PML in TLM method, has been used for the characterization of microstrip antennas. Although it was proved that PML is more accurate than Higdon's conditions, it seems that antenna's simulation can be achieved successfully with both of these two techniques. However, TLM simulations with Higdon's conditions need 1.5 more cpu time than TLM with PML for approximately the same memory space.

V. ACKNOWLEDGMENT

Computational ressources were supported by the Connection Machine 5 of the Centre National de Calcul Parallele en Sciences de la Terre, Paris, France.

VI. REFERENCES

[1] C.CHRISTOPOULOS : "The Transmission-line Modeling Method TLM" *Oxford. IEEE Press1995*

[2] J.L.DUBARD, D.POMPEI, J.LE ROUX, A.PAPIERNIK : Characterization of microstrip antennas using the TLM simulation associated with a Prony Pisarenko Method. *International Journal of Numerical Modelling (1990) , 3, n°4, pp269-285*

[3] Z.CHEN, M.M.NEY, W.J.R.HOEFER : Absorbing and connecting boundary conditions for the TLM method *IEEE Trans on MTT(1993), 41, n°11, pp 2016-2024*

[4] C.ESWARAPPA,, W.J.R.HOEFER : *One way equation absorbing boundary conditions for the 3-D TLM analysis of planar and quasi-planar structures , IEEE Trans MTT (1994) ,42, n°9,pp 1669-1677*

[5] J.P.BERENGER : Perfectly matched layer for the FDTD solution of wave-structure interaction problems, *IEEE Transactions on Antennas and Propagation*, 1996, 44, (1), pp. 110-117.

[6] J.L. DUBARD, D.POMPEI : A modified 3D-TLM variable node for the Berenger's Perfectly matched Layer implementation. *ACES Symposium,1997 Monterey*

[7] J.A.MORENTE, J.A.PORTI, M.KHALLADI : Absorbing boundary conditions for the TLM method. *IEEE Transactions on Microwave Theory and Techniques, 1992, 40, (11), pp. 2095-2099.*

[8] F.CROQ,A.PAPIERNIK : Large bandwidth aperture-coupled microstrip antenna. *Electronics letters (1990), 26, n°16, pp.1293-1294*

[9] S.A. BOKHARI, J.R. MOSIG, F.E GARDIOL : Radiation pattern computation of microstrip antennas on finite ground plane. *IEE Proc. H, microwave, antennas and propagation, 1992, vol. 139, n°3, pp. 278-286.*

Parallelization of a 3D-TLM-Algorithm on a Workstation Cluster

Christoph Fuchs[1], Peter Fischer[2] and Adolf J. Schwab[2]

1) Siemens AG, Semiconductors, D-81617 Munich, Germany

2) Institute of Electric Energy Systems and High-Voltage Technology, University of Karlsruhe, Kaiserstrasse 12, 76128 Karlsruhe, Germany

1 Introduction

The TLM Method has proved as a powerful tool for analyzing electromagnetic time domain problems. Due to the limited memory of Neumann computers, problems are limited in size. To overcome these restrictions, parallel and distributed computing techniques become increasingly important, particularly, with respect to time-domain techniques like FDTD and TLM. The highly localized nature of the TLM algorithm - any change in the state of a TLM node affects only its immediate neighbours at the next computational step - is perfectly suited for parallel processing. Different parallel implementations can be used, depending on the development of parallel software and available hardware. This paper presents the parallelization of a 3D-TLM code using a workstation cluster connected by Ethernet and operated by the PVM (Parallel Virtual Machine) software package. Workstation cluster can be readily composed into a virtual parallel computer and require no additional investment.

2 Introduction to Parallelism and Multiprocessor Computing

A wide range of multiprocessor computer architectures have been developed [1, 2]. One key of classification is in the mode by which memory is accessed, i.e. shared and distributed memory. In shared memory architectures processors address a globally accessible memory bank, whereas in distributed memory computers the memory is distributed among all processors. Only local memory is physically addressed and communication between processor-memory units can be done using message passing subroutines.

Distributed memory architectures can be further categorized in single-instruction multiple-data (SIMD) and multiple-instruction multiple-data (MIMD) computers. SIMD computers perform the same operation with different data simultaneously. MIMD computers can perform multiple operations with different data concurrently while interacting through message passing (e.g. master slave principle). The message passing programming method supports explicit communication only and has the advantage that programs can be readily ported to other parallel computers.

Independent workstations interconnected by a local area network, referred as a workstation cluster, represent a loosely coupled MIMD architecture. The main difference to real parallel computers are the higher latencies from the communication network, e.g. the Ethernet. The software system PVM allows to define a heterogeneous network consisting of serial, parallel and vector computers working as one large computer [3].

Advantages of PVM:

- public domain product
- use of existing hardware, no extra expenses for parallel computing
- many parallel computer producers support PVM
- de facto standard, ideal for portability

Disadvantages of PVM:

- reduced communication performance

Using PVM, the following procedure is necessary for data transmission:
PVM sends a message by first initializing a send buffer. Subsequently, data are added to the buffer by pack functions and, finally, the message is transmitted.
For reduced computation time data packing should be very efficient. This leads to an improved connect algorithm for the TLM method, which will be introduced in Section 4.

3 Parallelization of the 3D-TLM Algorithm

For parallelization the 3D-TLM mesh is uniformly divided to the number of available workstations along the z-axis of the coordinate system. In order to compute the scattering in the TLM mesh a single program, multiple data (SPMD) computing model is used. This model uses a copy of the same TLM program on each processor and arranges the communication of each processor with adjacent processors.

The partitioning will be demonstrated for a shielding case and a workstation cluster of p=10 processors, Figure 1.

Example: Planes: n=36
Processors: p=10
Processors 1 to 6 will be assigned to 4 planes
Processors 6 to 10 will be assigned to 3 planes

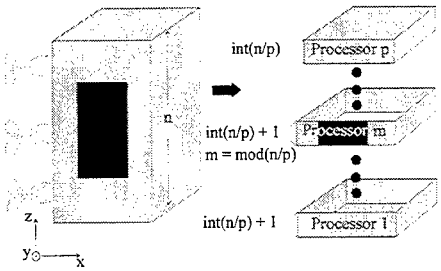

Figure 1. Partitioning of a shielding case among p processors.

Each processor will be assigned a subdomain of the mesh with dimensions **int(n/p)**. For most applications, these ratios are noninteger values and the sizes of the subdomains will be slightly uneven. Therefore, processors 1 to **m** will be assigned to subdomains with dimensions **int(n/p)+1**, with **m=mod(n/p)**.

In partitioning of the mesh, the so-called "double boundaries", the TLM boundaries or surfaces shared by subdomains/processors, require a special treatment. These boundaries, as well as the excitation and output points, are mapped to the adjacent processors q and q+1.

Efficient interprocessor communication is the key to powerful parallel processing [4]. Interprocessor communication becomes necessary when remote processors need to exchange data. Using the TLM algorithm, electromagnetic fields are modeled by the field domain with a network of transmission lines. This renders the problem discrete in space and time. Pulses launched on the network scatter from point to point in space in fixed time steps [5]. Outgoing pulses of one node become incident pulses of the neighbouring nodes. After determining the scattering at the nodes, processor q sends (receives) data to (from) the processors q+1 and q-1. This interprocessor communication results in additional CPU time and determines the efficiency of the parallelization/calculation. Calculating the communication overhead (part of communication versus calculation time) it can be shown, that $n>8^3=512$ nodes are necessary for efficient parallelization.

4 Improved Connect Algorithm

For the exchange of data between adjacent processors, PVM adds the TLM data (pulses of the nodes) to a send buffer by pack functions. The required time to pack the communication packets can be reduced by writing all TLM (Send) data automatically in one array. Then, only one pack function must be called.
Before introducing the new connect algorithm, which means the data transfer between adjacent nodes, the commonly used algorithm will be described, Figure 2.

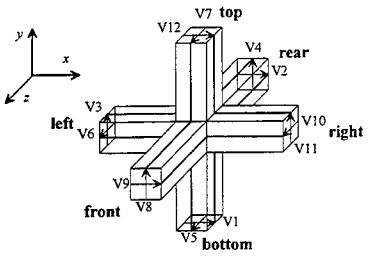

Figure 2. Symmetrical Condensed Node (SCN) with new port description.

After determining the scattering at the nodes, the pulses between adjacent nodes must be exchanged ("connected").
Thus, a typical ANSI-C subroutine for the data exchange in z-direction would be:

```
helpz1 = node (i, j, (k+1))->v[2];
helpz2 = node (i, j, (k+1)->v[4];
node (i, j, (k+1))->v[2] = p->v[9];
node (i, j, (k+1))->v[4] = p->v[8];
p->v[9] = helpz1;
p->v[8] = helpz2;
```

Six instructions for each of the coordinate-direction will be necessary to exchange the data for one node. This implies 18n instructions for the total mesh, with n being the number of nodes of the mesh. Using the new algorithm 6 pointers determine the directions top, bottom, right, left, front and rear of the SCN, Figure 2. These pointers will be assigned to special parts of the memory which contain all data of the TLM mesh.

According to Figure 2 pointer "rear" determines the part of memory containing values V2 and V4 of all mesh nodes, pointer "front" values V8 and V9, etc.

Example:
Figures 3 and 4 illustrate the new connect algorithm. A small, but complete TLM mesh is used.

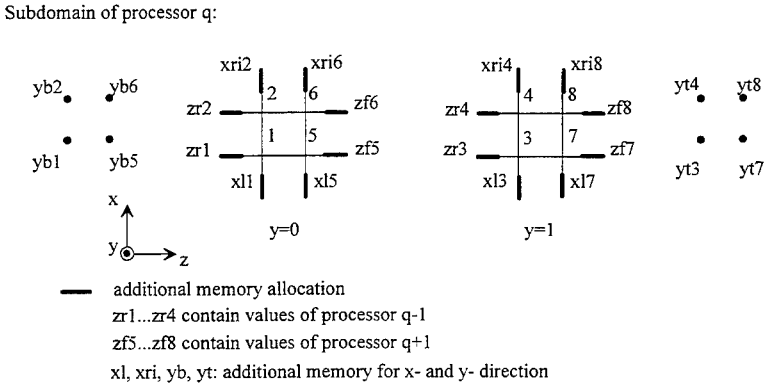

Figure 3. Node numbers and additional nodes of the improved connect algorithm.

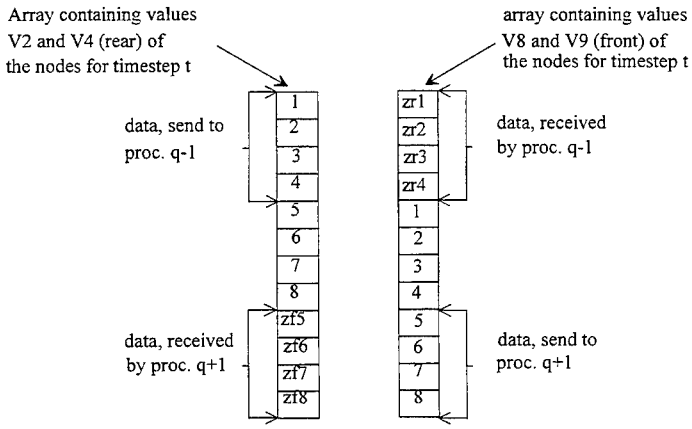

Figure 4. Array in z-direction.

While the commonly used connect algorithm needs 18n instructions for data exchange, the new algorithm changes the **entire mesh data** between adjacent nodes by just **six instructions**. This, by simple exchanging the pointer's memory address "rear" and "front" (figure 4), "right" and "left" and "top" and "bottom".
This new connect algorithm is also suited for sequential TLM programs and reduces the computing time by an additional factor of two!

5 Simulation Results

The following examples demonstrate the parallel efficiency of the TLM algorithm.
Existing hardware:

- 7 HP 715 workstations at the Institute of Electric Energy Systems and High Voltage Technology (IEH).
- 10 IBM RS6000 workstations at the Computing Center (CC) of the University of Karlsruhe.

All available workstations are connected via Ethernet. The two geographically separated networks at the IEH and the Computing Center were connected via FDDI, Figure 5.

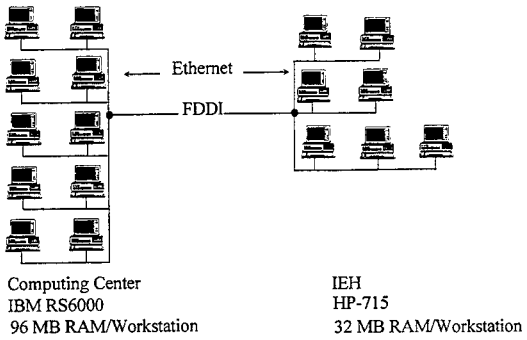

Figure 5. Existing hardware and networks.

The overall efficiency of the parallelization is determined by evaluating the speed-up factor

$$\text{Speedup } S = \frac{T_{sequential}}{T_{parallel}}$$

Figure 6 shows the speed-up factor as a function of the number of processors for the computation of a shielding case with:

- 145.088 mesh nodes
- 18 MB memory
- Timesteps: 1024
- $T_{sequential}$: 55 min

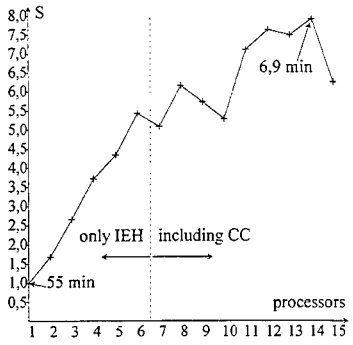

Figure 6. Speed-up factor depending on number of processors.

This Figure illustrates, that increasing the number of processors significantly reduces the simulation time. The negative slope of the speed-up factor with increasing number of processors is due temporary overloaded workstations. Using a workstation cluster, the efficiency of the calculation is determined by the network transmission rates because the workstations as well as the Ethernet are shared by different users. The speed-up factor and the computing time depends on the day and the time of the day. Therefore occasionally, the exact forecasting of the speed-up factor is difficult.

It should be noted, that in a workstation cluster, the total computation time needed to complete a global task is equal to the time required by the slowest workstation to compute its local task.
Numerical field calculation involves a large amount of main memory. Insufficient available memory results in a paging problem increasing the simulation time. Figure 7 illustrates the paging problem and the capabilities of parallel processing.

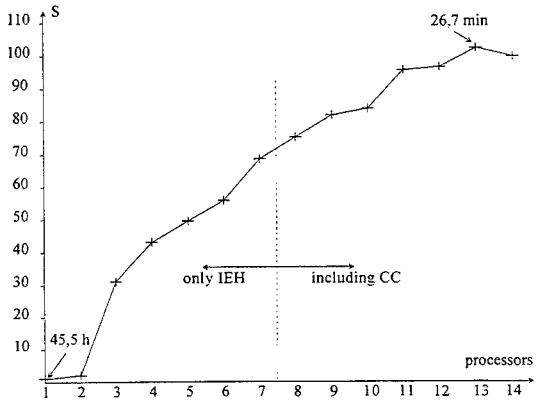

Figure 7. Speed-up depending on number of processors (Size of problem: 62 MB, $T_{sequential}$: 45.5 h).

The given problem size was 62 MB versus the computer's memory of only 32 MB. A minimum of three processors was necessary to avoid paging and reduce the computing time. Using 13 workstations the calculation time can be reduced by a factor of 102.
This figures indicate that the speed-up is nonlinear. For a given problem size, the ratio of communication and calculation per processor increases with increasing number of processors. The impact of the communication overhead becomes more apparent.

5 Conclusion

This paper described the creation and formulation of a parallel 3D-TLM algorithm [6]. Its implementation on a workstation cluster not only decreases the computing time but also increases the amount of available memory. Furthermore, no additional investment is required and the developed implementation can be rapidly ported to other distributed memory architectures assuring its relevance also for future applications.

6 References

[1] A. Taflove, Chapter 16 in *Computational Electrodynamics: The Finite-Difference Time-Domain Method,* Artech House, Norwood, 1995
[2] International Journal of Numerical Modelling, *Special Issue on Parallel and Distributed Processing Techniques for Electromagnetic Field Solution,* J. Wiley, May-August 1995
[3] A. Geist, A. Beguelin, J. Dongarra, W. Jiang, R. Manchek, V. Sunderman, *PVM: Parallel Virtual Machine User's Guide and Reference Manual,* Oak Ridge National Laboratory, September 1994
[4] B.P. Lester, *The Art of Parallel Programming,* Prentice Hall, Englewood Cliffs, New Jersey, 1993
[5] P.B. Johns, *"New Symmetrical Condensed Node for Three-Dimensional Solution of Electromagnetic-Wave Problems by TLM"*, Electronics Letters, Januar 1986
[6] C. Fuchs, *Effiziente Modellierung leitfähiger Schirme im Zeitbereich,* Ph.D. Thesis, University of Karlsruhe, Germany

A comparison of the TLM and finite-difference excitation schemes for diffusion and wave equations

Ciarán Kenny, Richard Harvey and Donard de Cogan
{cpk, rwh, ddc}@sys.uea.ac.uk
School of Information Systems, University of East Anglia, Norwich, NR4 7TJ, UK.

Abstract

The relationship between the shunt TLM algorithm and simple explicit finite difference schemes for solving the scalar wave- and diffusion equations is explored. A general TLM algorithm is presented and an algebraic comparison of this and finite-difference schemes is performed. It is shown how some TLM schemes undergo the same iteration as explicit finite-difference and visa versa.

The treatment of initial conditions is then considered for the two schemes: an area that has received little attention in the TLM literature. The circumstances under which the two schemes provide identical discretisations of the initial conditions are examined and some guidelines for the correct excitation are presented.

1 Introduction

In the development of finite-difference time-domain (FDTD) techniques the analysis of errors is said to be of paramount importance (see [1] for example). The transmission line matrix (TLM) method [2], although it too is a finite-difference time-domain technique, originates from models of physical components and the analysis or errors is given less prominence. For example, Christopoulos [3] writes "the nature and significance of errors can, in most cases, be intuitively assessed". The aim of this paper is to test this claim by means of algebraic comparisons between certain configurations of shunt TLM and explicit finite-difference algorithms. In particular we will concentrate on algorithms for the numerical solution of the scalar wave equation [4].

The TLM configuration considered here is shown in Figure 1, namely a two-dimensional network with a stub line. For this type of mesh the TLM algorithm may be written as

$$\Phi_k(x,y) = \frac{2\left(R_s+Z_s\right)}{R_l+Z_l+4\left(R_s+Z_s\right)}\sum_{l=1}^{4} V_{k,l}^{i}(x,y) + \frac{2\left(R_l+Z_l\right)}{R_l+Z_l+4\left(R_s+Z_s\right)} V_{k,5}^{i}(x,y) \tag{1}$$

where R_s and Z_s are the resistance and impedance of the stub and R_l and Z_l are the resistance and impedance of the connecting lines. $\Phi_k(x,y)$ is the potential at the kth iteration at node x, y and $V_{k,l}^{i}(x,y)$ is the pulse incident

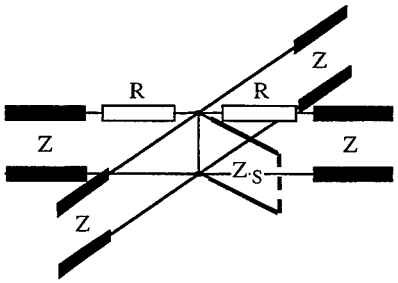

Figure 1: A TLM node with a stub line

at node x, y at the kth iteration on the lth line. The connecting lines are denoted by $l = 1 \cdots 4$ and the stub line by $l = 5$.

The scatter equations give the relationship between the reflected pulses $V^r_{k,l}(x,y)$ and the incident ones.

$$V^r_{k,l}(x,y) = \Phi_k(x,y) - V^i_{k,l}(x,y), \qquad l = 1, \cdots, 4 \tag{2}$$

and

$$V^r_{k,5}(x,y) = \frac{Z_s}{R_s + Z_s}\Phi_k(x,y) + \frac{R_s - Z_s}{R_s + Z_s}V^i_{k,5}(x,y) \tag{3}$$

At each iteration the pulses reflected from each node become incident pulses on adjacent nodes via the connection equations.

$$\begin{aligned} V^i_{k,1}(x,y) &= V^r_{k-1,3}(x-1,y) \\ V^i_{k,2}(x,y) &= V^r_{k-1,4}(x,y+1) \\ V^i_{k,3}(x,y) &= V^r_{k-1,1}(x+1,y) \\ V^i_{k,4}(x,y) &= V^r_{k-1,2}(x,y-1) \\ V^i_{k,5}(x,y) &= V^r_{k-1,5}(x,y) \end{aligned} \tag{4}$$

The algorithm described by Figure 1 and equations (1) to (4) provides a solution to the telegrapher's equation

$$\nabla^2\Phi = \frac{1}{c^2}\Phi_{tt} + \frac{1}{D}\Phi_t \tag{5}$$

By choosing R_s, Z_s, R_l and Z_l appropriately, TLM practitioners seek to provide solutions to the wave equation ($D = \infty$), approximate solutions to the diffusion equation ($c = \infty$) or, less commonly, solutions to the telegrapher's equation.

2 Conditions for equivalence

The shunt TLM system for two-dimensional scalar potential problems described in Section 1 may be expressed as [5]

$$\Phi_k(x,y) = A\sum_{l=1}^{4} V^i_{k,l}(x,y) + BV^i_{k,5}(x,y) \tag{6}$$

$$V^r_{k,l}(x,y) = a\Phi_k(x,y) + bV_{k,l}(x,y), \qquad l = 1 \ldots 4 \tag{7}$$

$$V^r_{k,5}(x,y) = c\Phi_k(x,y) + dV_{k,5}(x,y) \tag{8}$$

and

$$\begin{aligned} V^i_{k,1}(x,y) &= V^r_{k-1,3}(x,y) \\ V^i_{k,2}(x,y) &= V^r_{k-1,4}(x,y) \\ V^i_{k,3}(x,y) &= V^r_{k-1,1}(x,y) \\ V^i_{k,4}(x,y) &= V^r_{k-1,2}(x,y) \\ V^i_{k,5}(x,y) &= V^r_{k-1,5}(x,y) \end{aligned} \tag{9}$$

where the coefficients A, B, a, b, c and d are chosen to solve the diffusion, wave or telegrapher's equation.

Explicit finite-difference schemes for diffusion and wave equations are well known (see [1] or [6] for example). For the wave equation the usual FDTD scheme is

$$\begin{aligned} \Phi_{k+1}(x,y) &= r\left(\Phi_k(x-1,y) + \Phi_k(x,y+1) + \Phi_k(x+1,y) + \Phi_k(x,y-1)\right) \\ &\quad + 2(1-2r)\Phi_k(x,y) - \Phi_{k-1}(x,y) \end{aligned} \tag{10}$$

where $r = \left(\frac{c\Delta t}{\Delta l}\right)^2$ is known as the *aspect ratio* or *discretisation parameter*. The routine is stable provided $r \leq 1/2$.

Equations (6), (7), (8) and (9) are not comparable with FDTD (10) as they involve the intermediate quantities $V^i_{k,l}$ and $V^r_{k,l}$ which do not feature in the explicit finite-difference routine. However, after a little re-arrangement of (6)–(9), it is possible to write an expression for the potential at time $k+1$ in the TLM formulation as

$$\begin{aligned}\Phi_{k+1}(x,y) &= Aa\left(\Phi_k(x-1,y)+\Phi_k(x,y+1)+\Phi_k(x+1,y)+\Phi_k(x,y-1)\right)\\ &\quad + Bc\Phi_k(x,y)+\Phi_{k-1}(x,y)\left(4Aab+Bcd\right)+Ab^2\sum_{l=1}^{4}V^i_{k-1,l}(x,y)+Bd^2V^i_{k-1,5}(x,y)\end{aligned} \tag{11}$$

This is a two-step routine like the finite-difference time-domain scheme but, unlike the finite-difference method, it contains potentials and pulses. Requiring that $b^2 = d^2$ allows (11) to be written as

$$\begin{aligned}\Phi_{k+1}(x,y) &= Aa\left(\Phi_k(x-1,y)+\Phi_k(x,y+1)+\Phi_k(x+1,y)+\Phi_k(x,y-1)\right)\\ &\quad + Bc\Phi_k(x,y)+\left(4Aab+Bcd+b^2\right)\Phi_{k-1}(x,y)\end{aligned} \tag{12}$$

in which the pulses do not appear.

Comparing coefficients between (10) and (12) gives a set of equations,

$$\begin{aligned}Aa &= r\\ Bc &= 2(1-2r) \qquad (13)\\ 4Aab+Bcd+b^2 &= -1\\ b^2 &= d^2 \qquad (14)\end{aligned}$$

that, if satisfied, would make TLM and explicit finite-difference equivalent. Ignoring the solution $b = -d$, as this leads to complex solutions, gives $b = d = -1$. In this case the TLM method is identical to the FDTD procedure. Choosing the TLM components as

$$\begin{aligned}Z_l &= 1\\ R_l &= R_s = 0 \qquad (15)\\ Z_s &= \frac{r}{2(1-2r)} \qquad (16)\end{aligned}$$

satisfies the equivalence conditions (13). Thus, if the TLM components are chosen in the conventional manner, TLM and FDTD give the same iteration equations. If $r = 1/2$, the finite-difference scheme is operated on the limit of its stability and, equivalently, $Z_s = \infty$. The stub line is dispensed with.

Similar results are available for the diffusion equation and telegrapher's equation [5].

3 Excitation

The previous section showed that the TLM shunt mesh, in its usual configuration, and conventional explicit FDTD provide identical discretisations. However for the two methods to provide identical solutions they must treat the initial conditions in a similar manner. The treatment of initial conditions is a standard topic in finite-difference theory but, so far, has received little attention in the TLM literature. Considering, for example, a set of conventional initial conditions (a Cauchy problem)

$$\Phi_0(x,y) = f(x,y) \tag{17}$$

$$\left.\frac{\partial\Phi(x,y)}{\partial t}\right|_{t=0} = 0 \tag{18}$$

the usual approach in finite-difference theory is to approximate (18) using a central difference approximation and hence seed the finite difference scheme

$$\Phi_1(x,y) = \frac{r}{2}\left(f(x+1,y)+f(x-1,y)+f(x,y+1)+f(x,y-1)\right)+(1-2r)\,f(x,y) \tag{19}$$

$\Phi_0(x,y)$ is specified in (17) and $\Phi_1(x,y)$ is computed in (19) so the FDTD iteration may now proceed.

Using the the TLM algorithm, (11), $\Phi_1(x,y)$ may be written as

$$\begin{aligned}\Phi_1(x,y) &= Aa\left(f(x+1,y)+f(x-1,y)+f(x,y+1)+f(x,y-1)\right)+f(x,y)Bc \\ &\quad + Ab\left(V^i_{0,1}(x+1,y)+V^i_{0,2}(x-1,y)+V^i_{0,3}(x,y+1)+V^i_{0,4}(x,y-1)\right)+BdV^i_{0,5}(x,y) \qquad (20)\end{aligned}$$

Requiring that the pulses applied at iteration zero should sum to the initial potential $f(x,y)$ gives

$$\Phi_0(x,y) = f(x,y) = A\sum_{l=1}^{4} V^i_{0,l}(x,y) + V^i_{0,5}(x,y) \qquad (21)$$

For (20) to be equivalent to (19) the excitation pulses in (21) must be chosen properly for which there are two possibilities. If $r = 1/2$ there is no stub line and one may choose the excitation as

$$V^i_{0,l}(x,y) = \frac{f(x,y)}{4A} \qquad l = 1\cdots 4 \qquad (22)$$

$$V^i_{0,5}(x,y) = 0 \qquad (23)$$

If stub lines are present, and stub lines are needed if the wave speed is not constant, then the choice

$$V^i_{0,l} = \frac{f(x,y)}{4A+B} \qquad l = 1\cdots 5 \qquad (24)$$

gives equivalence. Equations (22), (23) and (24) are useful because they give firm guidance as to how to excite a TLM mesh when solving wave propagation problems.

This analysis of the initial conditions has been repeated for the diffusion and telegrapher's equation and in one and two dimensions [5].

4 Discussion

It is a stated advantage of TLM that it is possible to derive a computational model by an analysis of the physical process [7]. However there are many applications, particularly in image and signal processing, where the sole definition is algebraic. In these cases the isomorphisms between TLM and FDTD developed in Section 2 allow an existing finite-difference discretisation to be converted into a computationally identical TLM routine. This approach has been used to solve anisotropic diffusion problems [8].

For the scalar wave equation in two dimensions reported here, it would appear that the standard configurations of TLM are identical to explicit finite difference. Since both methods use the same discretisation it is simple to compare their computational efficiencies. For the limiting case $r = 1/2$ the TLM iterations become

$$\Phi_k(x,y) = \frac{1}{2}\sum_{l=1}^{4} V^i_{k,l}(x,y) \qquad (25)$$

$$V^r_{k,l} = \Phi_k(x,y) - V^i_{k,l}(x,y) \qquad l = 1\cdots 4 \qquad (26)$$

plus the connection equations (9). Computation of these equations may be achieved with eight additions and one multiplication per node per iteration. Furthermore the multiplication is by a power of two and so may be implemented particularly efficiently on binary computers. The FDTD case with $r = 1/2$ gives

$$\Phi_{k+1}(x,y) = \frac{1}{2}\left(\Phi_k(x-1,y)+\Phi_k(x,y+1)+\Phi_k(x+1,y)+\Phi_k(x,y-1)\right) - \Phi_{k-1}(x,y) \qquad (27)$$

which requires five additions and one, power-of-two, multiplication per node per iteration. So, in this configuration, FDTD requires less computation than TLM. However FDTD a slightly less modular algorithm as it has to store two time-steps compared to TLM which is a single-step algorithm.

For the case $r \neq 1/2$ the TLM routine described by (1), (2), (3) and (4) requires ten additions and four multiplications per node per iteration whereas FDTD, (10), requires six multiplications and two multiplications. Again FDTD is quicker to compute than TLM but provides the same solution.

From the evidence presented here it appears that TLM is an unattractive option for solving the scalar wave equation in two dimensions (see [9] or [4] for an example of its use acoustics). It provides no better convergence

than FDTD and requires more computation. However, this analysis has ignored the implementation of boundaries. At first sight TLM may be more convenient for the implementation of boundaries since it is a single step algorithm. If this proves to be the case then TLM should be used only at the boundaries since FDTD is more efficient in free-space.

So far the discussion has been restricted to the solution of two-dimensional wave equations using shunt TLM and explicit finite-difference. It is easy to specialise the results to include the one-dimensional wave equation and the choice

$$R_l = R_s = 0$$

$$Z_l = 1 \tag{28}$$

$$Z_s = \frac{r}{2(1-r)} \tag{29}$$

produces an identical routine to the one-dimensional finite-difference scheme

$$\Phi_{k+1}(x) = r\left(\Phi_k(x+1) + \Phi_k(x-1)\right) + 2(1-r)\,\Phi_k(x) - \Phi_{k-1}(x) \tag{30}$$

where $r = \left(\frac{c\Delta t}{\Delta x}\right)^2$ which is stable for $r \leq 1$.

The work described here would extend naturally to three-dimensions but more effort is required to examine the usefulness of TLM for solving the vector wave equations that occur in vibration and electromagnetics and this work is ongoing. Since TLM is based on electromagnetic analogues it may be that it is only in this field that it is truly useful but, at this stage, what can be stated is that TLM is not a natural choice for solving propagation problems involving a scalar potential.

References

[1] W.F.Ames. *Numerical methods for partial differential equations.* Academic Press, 1977.

[2] P.B.Johns and R.L.Beurle. Numerical solution of 2-dimensional scattering problems using a scattering matrix. *Proceedings of the IEE*, 188:1203–1208, 1971.

[3] C. Christopoulos. The historical development of TLM. In *IEE Colloquium on Transmission Line Matrix modelling*, volume 1991/157, pages 1/1–1/4, Oct. 1991.

[4] P.A.Willison. *Underwater acoustic modelling using TLM.* PhD thesis, School of Information Systems, University of East Anglia, 1991.

[5] C.P.Kenny. *TLM and finite difference: a comparison.* PhD thesis, School of Information Systems, University of East Anglia, 1997.

[6] R.D.Richtmyer. *Difference methods for initial value problems.* Wiley, 1962.

[7] P.B.Johns. Simple explicit and unconditionally stable numerical routine for the solution of the diffusion equation. *International Journal of Numerical of Modelling*, 11:1307–1328, 1977.

[8] R.Harvey and C.P.Kenny. TLM for vision systems. In *First international workshop on transmission line matrix modelling-thoery and applications*, pages 187–190, 1995.

[9] A.H.M.Saleh and P.Blanchfield. Analysis of acoustic radiation patterns of array transducers using the TLM method. *International Journal of Numerical modelling*, 3:39–56, 1990.

Drift-diffusion using transmission line matrix modelling

Abhimanyu Chakrabarti (106456.2356@compuserve.com)
RADIONICS Europe N.V., Gentesteenweg 40, B-9230 Wetteren, Belgium

Donard de Cogan (ddc@sys.uea.ac.uk)
School of Information Systems, University of East Anglia, Norwich NR4 7TJ (UK)

Introduction

The development of transmission line matrix (TLM) algorithms to model the motion of charged particles under the influence of electric and magnetic fields has been relatively slow. In 1988 Allen and Clark [1] considered the field distribution in a rising-sun magnetron structure, but their work was restricted to cold operation. Recently, Al-Asadi et al [2] have developed a technique which embeds charged particle motion within a TLM field code which allows the investigation of field-particle interactions. But this development was predated by work of Al-Zeben et al [3] on the drift-diffusion modelling of charged particles in semiconductor devices. However, when this technique was applied to the motion of carriers in the presence of high field gradients the algorithms became unstable. This was contrary to the expectation based on the unconditional stability tenet attributed to TLM. This paper describes the ensuing investigation, and provides an insight into the underlying mechanisms of TLM as well as the limitations of application to drift-diffusion problems. After a brief introduction to the Al-Zeben approach we determine which difference equation is satisfied by the TLM drift-diffusion algorithm. This will then be checked for consistency and stability and compared with conventional finite difference methods. The paper will conclude with some results to demonstrate our findings.

The TLM drift-diffusion formulation

The concentration of minority charge carriers (p) diffusing in the presence of and externally applied electric field can be represented by the drift-Diffusion Equation

$$\frac{\partial p}{\partial t} = D\frac{\partial^2 p}{\partial x^2} - \mu E\frac{\partial p}{\partial x} \tag{1}$$

(p is concentration cm^{-3}, D is diffusion constant and μ is the carrier mobility)

The response to an initial delta input, $p_0(x)$, has an analytic solution [4]

$$p(x,t) = \frac{p_0(x)}{A\sqrt{4\pi Dt}} exp\left(-\frac{(x-\mu Et)^2}{4Dt}\right) \qquad (A \text{ is sample area}) \tag{2}$$

The TLM drift-diffusion model

Figure 1 shows the network used by Al Zeben et al [3] to model eqn (1) as:

$$\frac{\partial V(x,t)}{\partial t} = \frac{1}{R_d C_d}\frac{\partial^2 V(x,t)}{\partial x^2} + \frac{g_m}{C_d}\frac{\partial V(x,t)}{\partial x} \tag{3}$$

The generator is given by $g_m \Delta V_x$, where g_m is the transconductance and ΔV_x is the average voltage difference at adjacent nodes. For normalised impedance the analysis gives :

$$D = \frac{1}{R_d C_d} \qquad p = V(x,t) \qquad -\mu E = \frac{g_m}{C_d} \tag{4}$$

and hence

$$R = \frac{\Delta x^2}{2D\Delta t} \qquad g_m Z = \frac{-\mu E}{\left(\frac{\Delta x}{\Delta t}\right)} \tag{5}$$

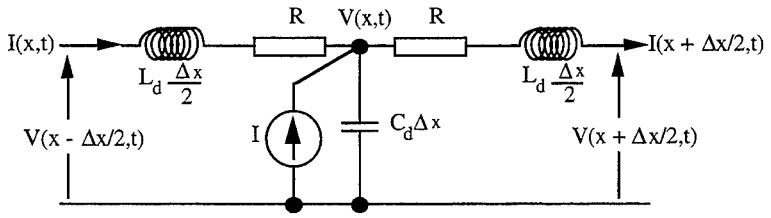

Figure 1 Electrical circuit for modelling drift-diffusion equation

Explicit TLM

The explicit TLM method models the drift-diffusion equation by applying the three stages shown below:

1. It calculates the nodal voltage

$$ {}_k\phi(x) = {}_kV_L^i(x) + {}_kV_R^i(x) + \tfrac{1}{2}\, {}_k I(m)[R + Z] \tag{6}$$

(where ${}_k I(x) = \frac{1}{2} g_m [\, {}_{k-1}\phi(x+1) - {}_{k-1}\phi(x-1)]$)

Therefore, ${}_k\phi(x) = {}_kV_L^i(x) + {}_kV_R^i(x) + B\,[{}_{k-1}\phi(x+1) - {}_{k-1}\phi(x-1)]$ (where $B = g_m \frac{R+Z}{4}$) (7)

2. It calculates the reflected voltages, ${}_kV_L(x)$ and ${}_kV_R(x)$, using the **scattering** process:

$$ {}_kV_L(x) = \rho\, {}_kV_L^i(x) + (\rho - \tau)\, {}_k\phi(x), \qquad {}_kV_R(x) = \rho\, {}_kV_R^i(x) + (\rho - \tau)\, {}_k\phi(x), \tag{8}$$

where $\rho = \frac{R}{R+Z}$ is the reflection coefficient and $\tau = \frac{Z}{R+Z}$ is the transmission coefficient.

3. Finally, it calculates the new incident voltages, ${}_{k+1}V_L^i(m)$, ${}_{k+1}V_R^i(m)$, using the **connect** process:

$$ {}_{k+1}V_L^i(x) = {}_kV_R(x-1), \qquad {}_{k+1}V_R^i(x) = {}_kV_L(x+1). \tag{9}$$

Semi-Implicit TLM

As a variation to explicit TLM, a semi-implicit algorithm was implemented. Here, the current source depended on an iterative determination of the potentials of adjacent nodes at the same time-step i.e.:

$$ {}_k\phi(x) = {}_kV_L^i(x) + {}_kV_R^i(x) + B\,[{}_k\phi(x+1) - {}_k\phi(x-1)] \tag{10}$$

All other steps in the algorithm were kept exactly the same.

Difference Equation of the TLM Algorithms

To see what difference equation is satisfied by the TLM algorithm, the whole process is written in terms of nodal potentials ϕ. To do this, the incident voltage terms from eqn. (7) are eliminated in successive stages by substitution. This gives the full difference equation of the explicit TLM model in terms of ${}_{k+1}\phi(x)$ as an expression which depends on the three previous time-steps.

$$ {}_{k+1}\phi(x) = (\rho - \tau)\,{}_{k-1}\phi(x) + B(1-4\rho\tau)\,\{{}_{k-2}\phi(x-1) - {}_{k-2}\phi(x+1)\} + \tau\{{}_{k}\phi(x+1) + {}_{k}\phi(x-1)\} $$
$$ + B\{{}_{k}\phi(x+1) - {}_{k}\phi(x-1)\}. \qquad (11) $$

The difference equation satisfied by the semi-implicit algorithm is:

$$ {}_{k+1}\phi(x) = (\rho - \tau)\,{}_{k-1}\phi(x) + B(1-4\rho\tau)\,\{{}_{k-1}\phi(x-1) - {}_{k-1}\phi(x+1)\} + \tau\{{}_{k}\phi(x+1) + {}_{k}\phi(x-1)\} $$
$$ + B\{{}_{k+1}\phi(x+1) - {}_{k+1}\phi(x-1)\} \qquad (12) $$

Finite Difference

In the forward-time centred-space (FTCS) finite difference method [5] the difference equation for the drift-diffusion case is derived directly from the differential equation (the same spatial and temporal notations have been used in TLM and the FTCS analyses; the dependent variable in the FTCS case has been assigned the letter u as opposed to ϕ in TLM):

$$ {}_{k+1}u(x) = {}_{k}u(x) - \frac{\mu E \Delta t}{2\Delta x}\,[{}_{k}u(x+1) - {}_{k}u(x-1)] + \frac{D\Delta t}{\Delta x^2}\,[{}_{k}u(x+1) + {}_{k}u(x-1) - 2\,{}_{k}u(x)]. \qquad (13) $$

Truncation Errors

Both the TLM and finite difference techniques suffer from truncation errors since the calculations cannot contain all the terms in the Taylor's series. The truncation errors introduce artefacts in the model such as extra diffusion and/or dispersion. These have been termed *implicit numerical diffusion* and *implicit numerical dispersion*. All even ordered spatial derivatives in the truncation error creates implicit numerical diffusion whilst the odd ordered spatial derivatives gives rise to dispersion.

For a numerical approximation to be consistent with the PDE it is solving, the truncation errors must go to zero as the discretisation parameters, Δx and Δt, go to zero *independently*. Each term is expanded using Taylor's series. The base point taken is the grid point, x, and temporal point k. These have been omitted below for clarity. For the FTCS method the zero-order derivatives have been written as u; the first-order derivatives as u_x and u_t; the second-order as u_{xx} and u_{tt} etc.; whilst for the TLM methods the variables are ϕ, ϕ_x, ϕ_{xx}, ϕ_t, ϕ_{tt} etc.

Explicit TLM

To find the truncation errors, eqn. (11) is expanded using Taylor's series and manipulated to give:

$$ \phi_t = \phi_x\left\{\frac{4B\,\tau\,\Delta x}{\Delta t}\right\} + \phi_{xx}\left\{\frac{\tau\,\Delta x^2}{2\rho\,\Delta t}\right\} + \phi_{xt}\left\{\frac{4B\,(\rho-\tau)^2\Delta x}{2\rho\Delta t}\right\} + \phi_{tt}\left\{-\frac{\Delta t\,\tau}{2\rho}\right\} \qquad (14) $$

The TLM coefficients are then substituted by their physical equivalents reducing eqn. (14) to:

$$ \phi_t = -\mu E\phi_x + D\phi_{xx} + \mu E\Delta t - \mu E D\frac{\Delta t^2}{\Delta x^2} - \frac{\mu E}{4D}\,\Delta x^2\,\phi_{xt} - D\,\frac{\Delta t^2}{\Delta x^2}\,\phi_{tt} + \cdots. \qquad (15) $$

The truncation errors disappear as $\Delta x, \Delta t \rightarrow 0$. However, the two discretisation terms cannot act independently to cancel out these terms owing to the presence of the $\Delta t^2/\Delta x^2$ ratios. If $\Delta x \rightarrow 0$ faster than Δt the ϕ_{xt} and ϕ_{tt} derivatives become indeterminate rather than zero. Therefore, the explicit TLM method is <u>not</u> consistent with the drift-diffusion equation.

To distinguish the nature of the error terms, they are expressed only in terms of spatial derivatives. This is done by repeated differentiation of eqn. (14). So, the partial differential equation satisfied by the TLM difference equation (showing only the most significant error terms) is:

$$ \phi_t = -\mu E\phi_x + D\phi_{xx} + (\mu E)^2\left(\frac{\Delta x^2}{4D} - \Delta t\right)\phi_{xx} + \mu E\left(D\Delta t - \frac{\Delta x^2}{4}\right)\phi_{xxx} + \cdots \quad . \qquad (16) $$

The PDE in eqn.(16) is the drift diffusion equation, with truncation error terms. Of these, ϕ_{xx} creates implicit numerical diffusion and ϕ_{xxx} creates implicit numerical dispersion.

Semi-Implicit TLM

Taylor's expansion and manipulation for the semi-implicit case gives the PDE to be:

$$\phi_t = -\mu E\phi_x + D\phi_{xx} - \left[\frac{\mu E\Delta x}{4D} + \mu E D\,\frac{\Delta t^2}{\Delta x^2}\right]\phi_{xt} - \left[D\,\frac{\Delta t^2}{\Delta x^2}\right]\phi_{tt} + \cdots \quad . \tag{17}$$

Yet again, the TLM method, albeit a semi-implicit variation, does not produce a consistent difference equation because of the $\Delta t^2/\Delta x^2$ terms that exist in the error terms. Elimination of the time derivatives from eqn. (17) gives:

$$\phi_t = -\mu E\phi_x + D\phi_{xx} + \left[\frac{(\mu E)^2\,\Delta x^2}{4D}\right]\phi_{xx} + \left[\frac{\mu E\,\Delta x^2}{4}\right]\phi_{xxx} + \cdots \quad . \tag{18}$$

The errors are influenced by Δx and μE. Unlike the explicit case, Δt, has no affect on them.

Finite Difference

Taylor's series expansion of eqn. (12) gives the PDE of the FTCS difference equation to be:

$$u_t = -\mu E\,u_x + Du_{xx} - (1/2)u_{tt}\Delta t - (1/6)\,u_{ttt}\,\Delta t^2 - \cdots - (1/6)\,\mu E\,u_{xxx}\Delta x^2 - \cdots + (1/12)\,Du_{xxxx}\Delta x^4 + \tag{19}$$

Unlike TLM, the FTCS method is consistent because as Δx, $\Delta t \rightarrow 0$, truncation errors also disappear. Once again, the error is represented in terms of spatial derivatives:

$$u_t = -\mu E\,u_x + D\,u_{xx} - (1/2)(\mu E)^2\,\Delta t\,u_{xx} + [(-1/6)\mu E\,\Delta x^2 + \mu E D\,\Delta t - (1/3)(\mu E)^3\,\Delta t^3\,]\,u_{xxx} + \tag{20}$$

The absolute values of the errors vary with the discretisation numbers, Δx, Δt and the physical parameters of D, μE etc. The discretisation numbers are related by a ratio, called the *diffusion number*, r, where:

$$r = \frac{D\Delta t}{\Delta x^2} \text{ in FTCS and } r = \frac{Z}{2R} \text{ for the TLM models.} \tag{21}$$

Similarly, the electric field is also represented as a ratio of the discretisation parameters, called the *convection number*, s, where:

$$s = \frac{\mu E\Delta t}{\Delta x} \text{ in FTCS and } s = g_m = \frac{\mu E\Delta t}{\Delta x} \text{ (transconductance) for the TLM models.} \tag{22}$$

All three models show that the errors are directly proportional to the electric field. In the case of the two explicit methods, a further factor affects the errors - the time-step, Δt, in the guise of the diffusion number, r. By increasing r as well as the electric field, the diffusion and dispersion errors of the explicit TLM and FTCS must also vary. This is shown graphically by plotting eqns. (16), (18) and (20). Since the two types of errors affect the solution differently - diffusion error affects the amplitude, dispersion the frequency - they have been plotted separately.

The diffusion errors of the three methods are shown in figures 2a, 2b; while the corresponding dispersion errors are shown in figures 3a and 3b. The diffusion number, r, has been increased in steps of 0.05, and they have been indicated on the graph. The x-axis is the convection number (g_m for TLM and s for FTCS) and the y-axis is the error. Since the maximum limit of r for the FTCS case is 0.5, the error is plotted for each of the models for the values of r between 0.05 and 0.45. The numerical parameters are: D = 50 cm^2 s^{-1}, μ = 2000 cm^2 V^{-1} s^{-1}, Δx = 0.001cm. The others parameters such as Δt and E, depend on the diffusion and convection numbers.

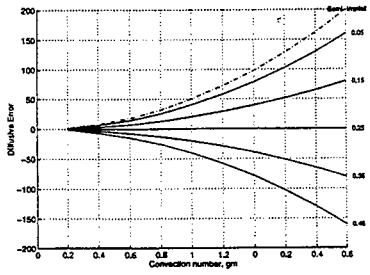

Figure 2a: Diffusion errors of the two TLM solutions.

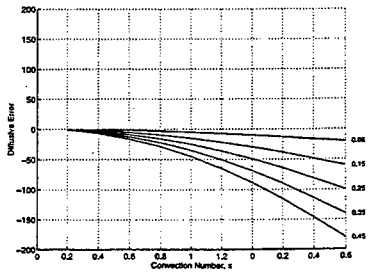

Figure 2b: Diffusion errors of the FTCS solution

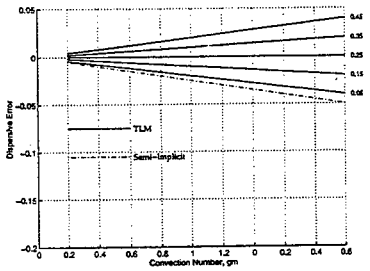

Figure 3a: Dispersion errors of the two TLM solutions

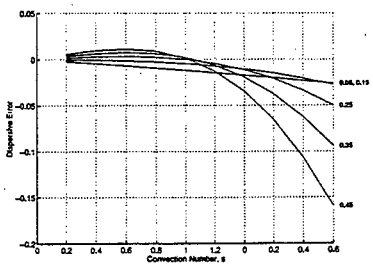

Figure 3b: Dispersion errors of the FTCS solution

The single most distinguishing feature between the two sets of graphs is how the inconsistency affects the TLM solutions. Whereas the FTCS solutions become more accurate as $r \rightarrow 0$, the explicit TLM solution shows least error as $r \rightarrow 0.25$. The semi-implicit method is only affected by the convection number, g_m. In all the cases implicit numerical diffusion dominates the errors. Dispersion is minimal, but not non-existent. One error cannot mask the other since their respective influences affect the solution differently. Having established the various consistency features, the next step was to compare the respective stability limits of the three methods. As the boundaries do not play a part in the area of interest, von Neumann stability testing provides a good indicator of the stability limits of the models.

Stability

A numerical approximation of a bounded problem is only stable if its solution is also bounded. It is unstable if its solution is unbounded. The von Neumann stability analysis, also known as the Fourier analysis, represents the initial condition as a series of Fourier modes, and checks whether the solution remains bounded - in the case of any diffusion-type equations the initial distribution of the dependent variable decays with the passing of time[6,7]. If that is not the case, then the solution is said to be unbounded. In notational terms, for a numerical method giving the solution at an arbitrary time N to be stable, the condition: ${}_{k=N}\phi(m) = \xi^N {}_0\phi(m)$ has to be bounded, i.e. $|\xi| \leq 1$ has to be satisfied. The initial condition, ${}_0\phi(m)$ is expressed as a complex Fourier series ${}_0\phi(m) = e^{j\lambda_m \Delta_x}$, where λ is the *wave number* and ξ is the *amplification factor* [5].

Explicit TLM

Substituting for ${}_k\phi(m)$ in eqn. (11) gives:

$$e^{i\lambda_m\Delta_x}\,\xi^{k+1} = \rho\,(\rho + 2\tau)e^{i\lambda_m\Delta_x}\,\xi^{k-1} + B\rho^2\,\xi^{k-2}\,\{\,e^{i\lambda_{(m-1)}\Delta_x} - e^{i\lambda_{(m+1)}\Delta_x}\,\}$$
$$+ \tau\,\xi^k\,\{\,e^{i\lambda_{(m+1)}\Delta_x} + e^{i\lambda_{(m-1)}\Delta_x}\,\} + B\xi^k\,\{\,e^{i\lambda_{(m+1)}\Delta_x} - e^{i\lambda_{(m-1)}\Delta_x}\,\}. \qquad (23)$$

By dividing eqn.(23) by $e^{i\lambda_m\Delta_x}\,\xi^k$ and replacing the exponential terms with their trigonometric equivalents the polynomial of the explicit TLM model to be satisfied is:

$$\xi^3 - 2\xi^2[\,\tau\cos\lambda\Delta x + iB\sin\lambda\Delta x\,] - \rho\,(\rho + 2\tau)\xi + 2iB\rho^2\sin\lambda\Delta x = 0. \qquad (24)$$

Semi-Implicit TLM

Similarly the semi-implicit stability criterion is ascertained by the equation:

$$\xi^2[1 - i2B\sin\lambda\Delta x] - \xi\,2\tau\cos\lambda\Delta x - [\rho\,(\rho + 2\tau - i2B\rho\sin\lambda\Delta x)] = 0. \qquad (25)$$

Finite Difference

The stability criterion is determined from: $\xi = 2r\cos\lambda\Delta x - is\sin\lambda\Delta x + \{1-2r\}$ (26)

In all the cases we must have $|\xi| < 1$ for stability

The finite difference stability limits of the *convection-diffusion* equation are well known. They are:

1) If there is no drift, the condition for stability $1-2r \le 1$ has to be true, i.e. $\frac{D\Delta t}{\Delta x^2} \le \frac{1}{2}$.

2) If $r = 0$, $s \le 1$, i.e. $\frac{\mu E\Delta t}{\Delta x} \le 1$. (The *Courant-Friedrichs-Lewy* stability criterion [8]).

3) If r and s are both present then $s^2 \le 2r$, i.e. $\left(\frac{\mu E\Delta t}{\Delta x}\right)^2 \le 2\frac{D\Delta t}{\Delta x^2}$.

The combination of the three conditions gives: $s^2 \le 2r \le 1$. (27)

The stability criteria for the three models are plotted in Figs. 4a, 4b and 4c.

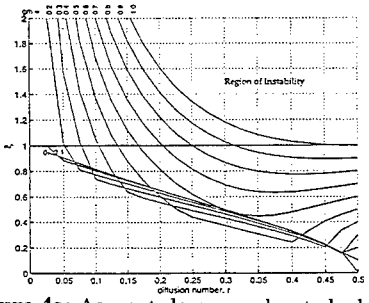

Figure 4a: As r gets larger, g_m has to be kept small to have a stable solution. The numbers on the graph show the different values of the TLM convection number g_m. ($r = 0.25$, $r = 0.333$ shown in graph)

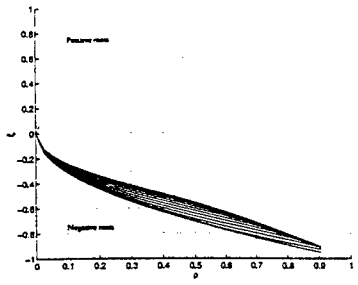

Figure 4b: Complete stability for semi-implicit TLM for $g_m = 0$ to 1

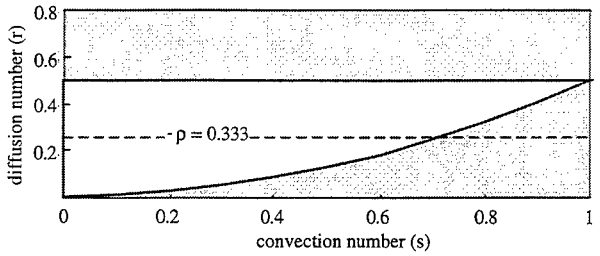

Figure 4c: Stability region of the FTCS method. Only the unshaded region is stable. The reflection coefficient corresponding to r = 0.25 is shown

Validity

Now that the limits of the methods have been established, it is possible to select particular values of diffusion and convection numbers and predict the behaviour of the model. For this final check, the explicit TLM has been used as the demonstration model since it highlights a peculiar idiosyncrasy owing to its minimum error point occurring when the diffusion number r equals 0.25. Because the stability is offset, the signs of the diffusive errors also vary. In Fig. 2a, if $r < 0.25$, then the diffusive error of the explicit TLM is positive. If $r > 0.25$, the error is negative (the semi-implicit diffusive error is positive regardless of r). In the FTCS case, the error is always negative. From the truncation error equations of the two explicit methods eqns. (16) and (20), we can infer that a positive diffusive error *adds* extra implicit diffusion, whilst negative diffusive error *subtracts* diffusive behaviour or adds *infusion*.

To test this hypothesis, two experiments were conducted using the two explicit methods, the initial condition being that the semiconductor sample was injected with an excess carrier concentration of $1000cm^{-3}$ at some arbitrary time at the midpoint of the mesh $x = 0.5cm$. The diffusion number r was varied (consequently, different r's), but the results were taken after the same absolute time - $5\ 10^{-7}$ seconds. For both the cases, the convection number, g_m, was kept at 0.5 (from Figs. 4a and c, the values lie within the stability limit of FTCS and TLM), and the space discretisation Δx was 0.001cm.

1) $r = 0.35$ so that $\Delta t = r\Delta x^2/D = 7\ 10^{-9}$s. Therefore, the results were calculated after a total number of iterations of 71. The external electric field corresponding to $g_m = 0.5$ is $E = -35.7 Vcm^{-1}$.
2) $r = 0.15$, so that $\Delta t = 3\ 10^{-9}$s i.e. 166 iterations and field for $g_m = 0.5$ is $E = -83.3 Vcm^{-1}$.

The results are plotted in Figs. 5a and 5b.

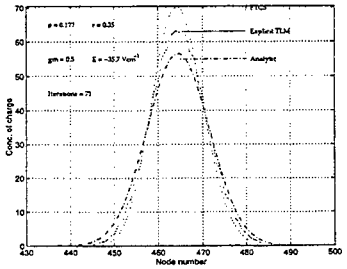

Figure 5a: Infusion for both explicit TLM and FTCS

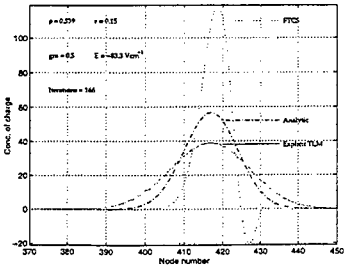

Fig 5b: Extra diffusion for explicit TLM, infusion for FTCS

Conclusions

The aim of the work was to investigate the limits of the drift-diffusion model as proposed by Al-Zeben et al[1], to extend the investigation to semi-implicit TLM and to undertake comparisons with the more established FTCS method. Since the drift-diffusion model falls within the generic convection-diffusion equation, this work is also of importance for the treatment of electromagnetic models involving moving charges.

The investigation shows that neither of the two TLM methods are numerically consistent. Owing to the extra wave terms the TLM models show least error when the diffusion number $r \rightarrow 0.25$. As a result of this, the diffusive error affects the explicit TLM solutions in two ways. If $r < 0.25$, implicit numerical diffusion adds diffusive behaviour to the model. If $r > 0.25$, diffusive behaviour is subtracted.

The drift term sets a limit which compares favourably with the FTCS method. Yet, despite its versatility, it cannot encompass an unlimited range of electric field. It would appear to be unsuitable for situations where there are significant field gradients.

The semi-implicit TLM aproach does not look promising so far as truncation errors are concerned. Like the explicit scheme, it is not numerically consistent. In common with the FTCS method the errors do not reduce as the diffusion number is varied from 0 to 1 However, for the convection number range 0 - 1, it is unconditionally stable.

References

1. R. Allen and M.J. Clark, *Application of the symmetrized transmission line matrix method to the cold modelling of magnetrons.* International Journal of Numerical Modelling **1** (1988) 61-70.

2. M. Al-Asadi, T.M. Benson and C. Christopoulos, *A method for incorporating charged particle motion within a 2-D TLM field code.* International Journal of Numerical Modelling **9** (1996) 201-214.

3. M.Y. Al-Zeben, A.H.M. Saleh and M.A. Al-Omar, *TLM modelling of diffusion, drift and recombination of charge carriers in semiconductors.* International Journal of Numerical Modelling **5** (1992) 219 - 225

4. S. M. Sze, *Physics of Semiconductor Devices,* (2nd Ed)., John Wiley & Sons, Inc., USA, 1981.

5. J. D. Hoffman , Numerical Methods for Engineers and Scientists, McGraw-Hill Inc., Singapore, 1993.

6. W. F. Ames, *Numerical Methods for Partial Differential Equations,* (2nd Ed)., Academic Press Inc., USA, 1977.

7. K. W. Morton and D. F. Mayers, *Numerical Solution of Partial Differential Equations,* Cambridge University Press, UK, 1994.

8. R. Courant, K. Friedrichs, and H. Lewy, *On the Partial Difference Equations of Mathematical Physics,* IBM Journal (1967), 215-234.

FULL WAVE CHARACTERISTICS OF A TWO CONDUCTOR MULTILAYER MICROSTRIP TRANSMISSION LINE USING THE METHOD OF LINES

Magda El-Shenawee
Pacific States University
College of Electrical Engineering and
Computer Science
Los Angeles, CA 90006
eerdeom@engunx.unl.edu

Atef Z. Elsherbeni
The University of Mississippi
School of Engineering
Department of Electrical Engineering
University, MS 38677
atef@olemiss.edu

Abstract:

In this paper, a full wave approach is used to analyze a coupled symmetric microstrip transmission line. The purpose of this analysis is to extend the validity of previously reported quasi-static techniques to higher frequencies for applications in the millimeter wave frequency range. The objective is to reduce the distortion of a transmission line that consists of two parallel microstrip lines on two dielectric substrates with a notch and a dielectric overlay. The distortion in such a transmission line is produced due to the difference in the phase velocities of the even and odd dominant modes. Techniques based on controlling the dielectric constant, height and width of the notch and the overlay are used to reduce distortion. The method of lines (MoL) technique is applied here to solve for the normalized phase velocities of the dominant even and odd modes for the planar microstrip transmission line. The numerical results reported in this paper provide a detailed analysis of the transmission line controlling parameters for frequencies up to 100GHz.

INTRODUCTION

One of the major problems in designing closely placed interconnections is the distortion due to the difference between the propagation phase velocities of the dominant modes. This phenomenon can be explored by considering parallel microstrip transmission lines. The transmission line being investigated here consists of two symmetric thin perfectly conducting strips with a rectangular notch between the strips, two layers of dielectric substrate, and a dielectric overlay as proposed in [1]. Several techniques were presented to overcome the distortion that arises due to the difference between the propagating phase velocities of the even and odd modes using a quasi-static method of moment approach [1]-[3]. These techniques are based on controlling the dielectric constant of the notch, the height and width of the notch, dielectric substrate, and overlay materials. Although the reported data are useful in reducing the distortion, it's application is limited due to the quasi-static solution which provides a valid data for the lower band (DC to 3GHz) of frequency of interest.

FORMULATION

The transmission line geometry investigated here is basically the same as that was investigated before using quasi-static method of moment approach [1] as shown in Fig. 1. The only difference is that in this analysis a PEC boundary is placed around the geometry. The dimensions of the metallic box are chosen large enough such that they do not affect the performance of the original open structure transmission line.

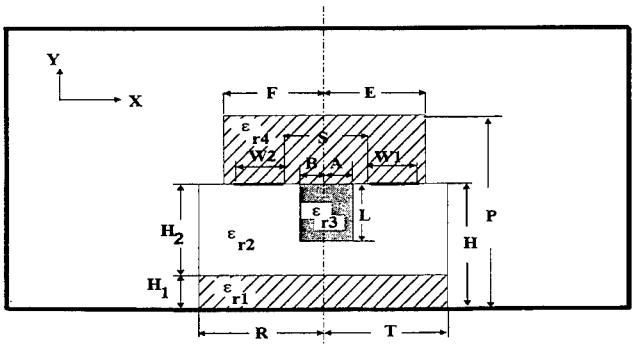

Fig. 1, Geometrical model of the two conductor microstrip transmission line enclosed in a metallic box.

The semi-analytical technique, method of lines (MoL) [4], will be used to investigate this transmission line geometry. The method of lines has been found suitable to analyze planar microstrip lines on dielectric multilayers [4] and [5]. Each dielectric layer can be inhomogeneous in one direction [5]. Since the transmission line geometry is enclosed in a perfectly conducting box as shown in Fig.1, all dielectric layers are partially filled with air, thus they are inhomogeneous dielectric layers in the x-direction. The details of the numerical (MoL) technique are given in [4] and they will be mentioned briefly here.

Due to the inhomogeneity of the transmission line structure, the procedure of this full wave analysis requires solving the Helmholtz and the Sturm-Liouville partial differential equations [4]. They are given, respectively, as follows:

$$\frac{\partial^2 \psi_h}{\partial x^2} + \frac{\partial^2 \psi_h}{\partial y^2} + \left[\varepsilon_r(x) k_o^2 - k_z^2\right]\psi_h = 0 \tag{1a}$$

$$\varepsilon_r(x)\frac{\partial}{\partial x}\left(\frac{1}{\varepsilon_r(x)}\frac{\partial \psi_e}{\partial x}\right) + \frac{\partial^2 \psi_e}{\partial y^2} + \left[\varepsilon_r(x) k_o^2 - k_z^2\right]\psi_e = 0 \tag{1b}$$

where ψ_h and ψ_e are the scalar magnetic and electric potentials, respectively. The wave is assumed to propagate in the z-direction with propagation constant k_z. The free space wave number is $k_0 = \sqrt{\mu_0 \varepsilon_0}$. The relative dielectric constant $\varepsilon_r(x)$ in each horizontal layer is inhomogeneous in the

x-direction which is obvious from Fig. 1. The magnetic and electric scalar potentials should fulfill the boundary conditions [4]:

On electric walls: $$\psi_h = 0, \quad \frac{\partial \psi_e}{\partial x} = 0 \tag{2a}$$

On magnetic walls: $$\psi_e = 0, \quad \frac{\partial \psi_h}{\partial x} = 0 \tag{2b}$$

Upon applying the MoL technique, the x-dimension of the geometry is divided into a number of electric and magnetic lines parallel to the y-direction with discretization distance h. The electric lines are shifted from the magnetic lines by $h/2$. The first order forward finite difference approximation is used to replace the first and the second derivatives with respect to the x-variable as follows:

$$h\frac{\partial \psi_h}{\partial x} \approx D\psi_h, \text{ and} \qquad h^2\frac{\partial^2 \psi_h}{\partial x^2} \approx -D'D\psi_h \tag{3a}$$

$$h\frac{\partial \psi_e}{\partial x} \approx -D'\psi_e, \text{ and} \qquad h^2\varepsilon_r(x)\frac{\partial}{\partial x}\left(\frac{1}{\varepsilon_r(x)}\frac{\partial \psi_e}{\partial x}\right) \approx -\varepsilon_e D\varepsilon_h^{-1}D'D\psi_e \tag{3b}$$

where D is a difference operator in the matrix form that takes into account the boundary conditions of the scalar electric and magnetic potentials given in Eqs. (2). The matrix D' is the transpose of the matrix D. Thus the partial differential equations (1) are converted to ordinary differential equations in the y-variable which can be solved analytically for ψ_h and ψ_e [4].

Due to the symmetry of the configuration shown in Fig. 1, only half of the cross section will be considered. The x-dimension will be divided into a number of electric and magnetic lines, N1 and N, respectively. For the even mode, the line of symmetry is a magnetic wall, thus the boundary conditions of the configuration will be Dirichlet-Neuman. But for the odd mode, the line of symmetry is an electric wall, thus the boundary conditions of the configuration will be Dirichlet-Dirichlet. Thus, for the even and odd modes, the matrices $[D]_{even}$ and $[D]_{odd}$ are given by:

$$[D]_{even} = \begin{bmatrix} 1 & 0 & 0 & \cdots & 0 \\ -1 & 1 & \ddots & \ddots & \vdots \\ 0 & \ddots & \ddots & \ddots & 0 \\ \vdots & \ddots & \ddots & 1 & 0 \\ 0 & \cdots & 0 & -1 & 1 \end{bmatrix}_{N\times N}, \quad [D]_{odd} = \begin{bmatrix} 1 & 0 & 0 & \cdots & 0 \\ -1 & 1 & \ddots & \ddots & \vdots \\ 0 & -1 & 1 & \ddots & 0 \\ 0 & \ddots & -1 & 1 & 0 \\ \vdots & \ddots & \ddots & -1 & 1 \\ 0 & \cdots & 0 & 0 & -1 \end{bmatrix}_{N1\times N} \tag{4}$$

where for the even mode, N is the number of magnetic lines or the number of electric lines (in this case they are equal), while for the odd mode, N1 is the number of electric lines and N is the number of the

magnetic lines (in this case N1=N+1). It is obvious that using the symmetry reduces the order of the matrix operator D and consequently the order of all matrices that are involved in the calculations. The configurations of the even and the odd mode cases are shown in Fig. 2.

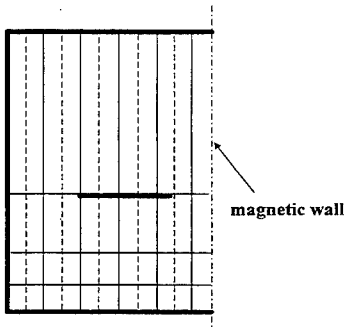

Fig. 2a, Geometrical model for even mode.
number of electric lines (dashed)=5,
number of magnetic lines (solid)=5

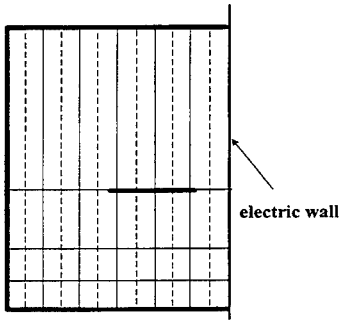

Fig. 2b, Geometrical model for odd mode.
number of electric lines (dashed)=6,
number of magnetic lines (solid)=5

After some algebraic manipulations, a system of equations is obtained as:

$$[Z][J]=[E] \tag{5a}$$

in which each of the matrix [Z], the vector [J], and the vector [E] is of order (N1+N). The elements of the vector [J] are the tangential (x and z-direction) current densities at each electric and magnetic line on the interface that has the metallic strip. The elements of the vector [E] are the tangential electric field on each electric and magnetic line on that interface. Upon applying the boundary conditions on the dielectric interfaces and the metallic strip, the system of equations (5a) can be reduced and given by:

$$[z]_{red.}[J]_{red.}=[0] \tag{5b}$$

in which $[J]_{red.}$ contains the tangential current densities on each electric and magnetic line only on the metallic strip. The order of the matrix $[Z]_{red.}$ is (M_e+M_m), where M_e and M_m are the number of the electric and magnetic lines, respectively, on the metallic strip. The elements of the matrix $[Z]_{red.}$ are functions of frequency, the propagation constant, and the characteristics of every dielectric layer in the geometry (dielectric constant and dimensions). The eigenvalues of Eq. (5b) are the propagation constants (k_z) of the modes and their eigenvectors are the associated tangential current densities (J_x and J_z) on the metallic strip.

NUMERICAL RESULTS

The developed MoL computer code is verified by comparing the numerical results with the previously reported data for a simpler transmission line geometry [6]. The configuration chosen from [6] to

compare the results with, consists of two symmetric microstrip lines located on two dielectric substrates. The width of the metallic strips are W1=W2=1.5mm, the separation between the strips is S=3.0mm, the height of the lower substrate is H1 and its dielectric constant is $\varepsilon_{r1} = 2.2$, the height of the second substrate from below is H2 and its dielectric constant is $\varepsilon_{r2} = 9.7$, and the total height of the two substrates is H=H1+H2=1.5mm. For the even mode, the number of magnetic lines is N=50, the discretization distance is h=0.2mm, the number of electric lines on the strip is M_e=7, and the number of magnetic lines on the strip is M_m=8. A comparison between our results and the results obtained in [6] is shown in Fig. 3. The effective dielectric constants of the even and the odd modes are plotted as functions of the relative height of the lower substrate H1/H at f=10GHz. Good agreement between our results and those reported in [6] is observed in Fig. 3. The calculations are repeated for the same configuration but at f=1GHz. The results are plotted in Fig.4a, and are compared with the results obtained in [1] using the quasi-static moment method technique. The results in Fig. 4a show good agreement between the MoL and the results published in [1] at f=1GHz. From Fig. 4a, at H1/H=0.3, the effective dielectric constants of the even and odd modes are equal at f=1GHz. In Fig. 4b, the relative height of the lower substrate is fixed at H1/H=0.3, and the effective dielectric constants of the even and odd modes are plotted as functions of frequency from 1GHz to 100GHz. The results in Fig. 4b show that the effective dielectric constants of the even and odd modes are almost equal at all frequencies from f=1GHz up to f=100GHz. In Fig. 5a, the normalized phase velocities of the even and odd modes are plotted as functions of the relative dielectric constant of the overlay (ε_{r4}) at f=1GHz for the configuration shown in Fig. 1. The dimensions used to produce the results in Fig. 5a are W1=W2=1mm, H=1mm, S=2mm, P=1.5mm, H1=0.7mm, T=R=5mm, E=F=3mm, A=B=0.99mm, L=0.25mm, $\varepsilon_{r1} = 9.7$, $\varepsilon_{r2} = 2.2$, and $\varepsilon_{r3} = 1.0$. The number of the magnetic lines is N=50, the discretization distance is h=0.18mm, the number of electric lines on the strip is M_e=5, and the number of magnetic lines on the strip is M_m=6. The results based on the MoL technique are compared with those obtained by the quasi static moment method [1]. The comparison in Fig. 5a shows reasonable agreement at f=1GHz. As the dielectric constant of the overlay is equal to $\varepsilon_{r4} = 7.2$, the normalized phase velocities of the even and odd modes are equal at f=1GHz. In Fig. 5b, the normalized phase velocities of the even and odd modes are plotted as functions of frequency with $\varepsilon_{r4} = 7.2$. The results show that the difference between the normalized phase velocities of the even and odd modes is not significant as the frequency increases from 1GHz up to 100GHz. The effect of the geometrical and electrical parameters of the notch will be discussed during the presentation.

CONCLUSIONS

The numerical results reported in this paper provided a detailed analysis of the transmission line controlling parameters for frequencies up to 100GHz. Equal phase velocities of the even and odd modes can be controlled by changing the height of the substrate or the overlay dielectric constant. The numerical results show that the controlling parameters which are obtained at DC frequency can be used at higher frequencies producing low distortion microstrip transmission line.

ACKNOWLEDGEMENT

This research was partially supported by the Army Research office under grant No. DAAH04-94-G-0355.

REFERENCES

[1] Elsherbeni, A. Z., Smith, C. E., Golestanian, H., and He, S., "Quasi-static characteristics of a two-conductor multilayer microstrip transmission line with dielectric overlay and a notch between the strips," Journal of Electromagnetic Waves and Applications, Vol. 7, pp. 769-789, 1993.

[2] Smith, C. E., and Chang, R. S., "Microstrip transmission lines with finite-width dielectrci," IEEE Trans., Microwave Theory Tech., Vol. MTT-28, No. 2, pp. 90-94, 1980.

[3] He, S., Elsherbeni A. Z., and Smith, C. E., "Decoupling between two conductor microstrip transmission line," IEEE Trans., Microwave Theory Tech., Vol. MTT-41, No. 1, pp. 53-61, 1993.

[4] Pregla, R., Pascher, W., Numerical Techniques for Microwave and Millimeter Wave Passive Structures, edited by: T. Itoh, (chapter 6), New York, Wiley, 1989.

[5] El-Shenawee, M., "Effect of inhomogeneous dielectric layers on dispersion of microstrip lines using MoL," IEEE-APS Proceedings, Baltimore, pp. 2206-2209, 1996.

[6] Gilb, J. P., and Balanis, C. A., "Pulse distortion on multilayer coupled microstrip lines," IEEE Trans., Microwave Theory Tech, Vol. MTT-37, No. 10, pp. 1620-1627, 1989.

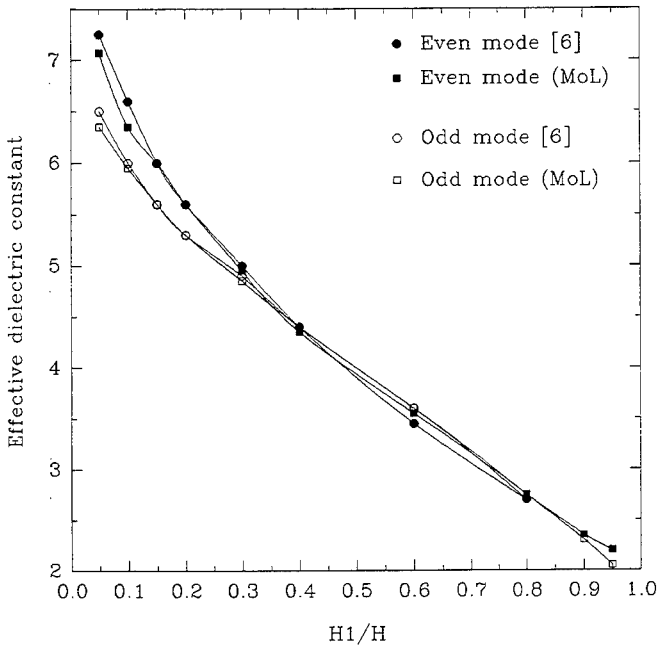

Fig. 3. Effective dielectric constant versus H1/H with W1=W2=1.5mm, S=3.0mm, H=1.5mm, ϵ_{r1} =2.2, ϵ_{r2} =9.7, and f=10GHz.

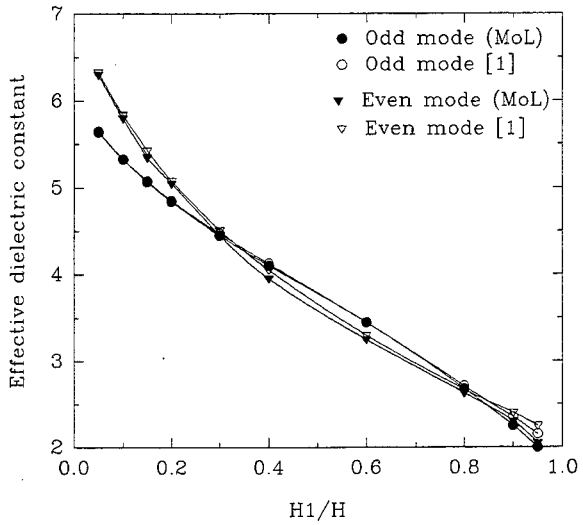

Fig. 4a. Effective dielectric constant versus H1/H with W1=W2=1.5mm, S=3.0mm, H=1.5mm, ϵ_{r1}=2.2, ϵ_{r2}=9.7, and f=1GHz.

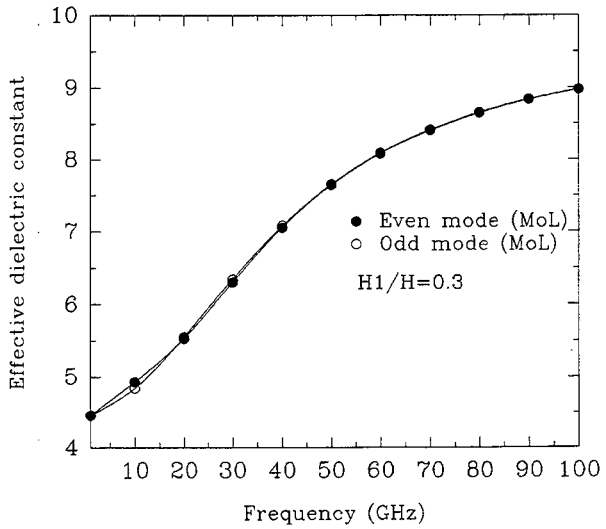

Fig. 4b. Effective dielectric constant versus frequency with H1/H=0.3 and the same dimensions for Fig. 4a.

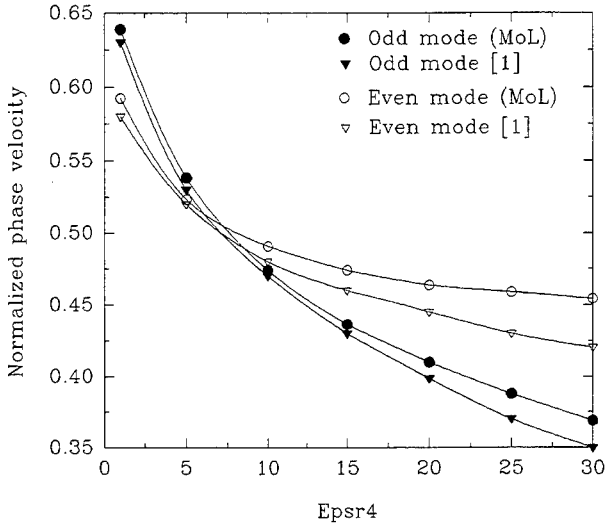

Fig. 5a. The normalized phase velocity versus ϵ_{r4} with W1=W2=1.0mm, S=2.0mm, H=1.0mm, P=1.5mm, H1=0.7mm, T=R=5mm, E=F=3.0mm, A=B=0.99mm, L=0.25mm, ϵ_{r1}=9.7, ϵ_{r2}=2.2, ϵ_{r3}=1.0, and f=1GHz.

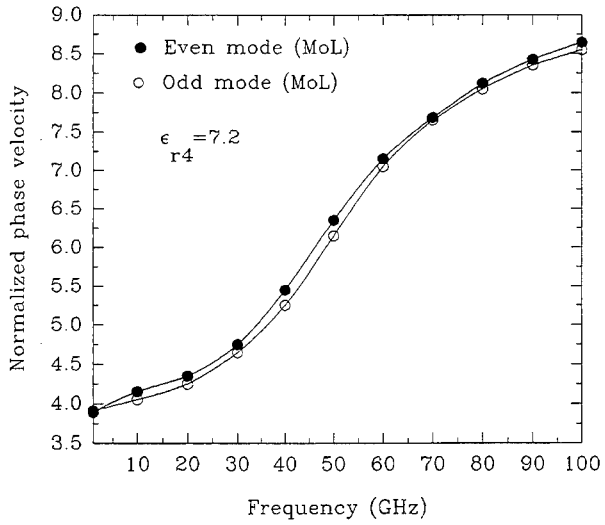

Fig. 5b. The normalized phase velocity versus frequency with ϵ_{r4}=7.2 and the same dimensions for Fig. 5a.

Sources of Error within Lattice Gas Automata Simulation of Electromagnetic Field Problems

Neil Simons[1], Greg Bridges[2], Dino Cule[2], Ming Zhang[2], Michel Cuhaci[1]

[1]Directorate of Antennas and Integrated Electronics
Communications Research Centre
Ottawa, Canada, K2H 8S2

[2]Department of Electrical and Computer Engineering
University of Manitoba
Winnipeg, Canada, R3T 2N2

Abstract: The application of lattice gas automata (LGA), along with special purpose computational hardware to the solution of electromagnetic field problems is presented. The sources of error within the LGA simulations are identified and compared with errors found within traditional differential-equation based numerical methods. Benchmark problems which allow for the quantification of the errors are the prediction of resonant frequencies in cavities, the modelling of field distributions in the vicinity of metallic edges, and electromagnetic interaction with heterogeneous scatterers. Significant reduction in unwanted numerical viscosity has been realized through the use of a 4-bit integer LGA.

I: Introduction

In this paper we present a new computational technique based on the lattice gas automata for the solution of electromagnetic field problems. Lattice gas automata are an alternative to the traditional differential equation based numerical methods now widely used in computational electromagnetics. A lattice gas automaton (LGA) is an extremely large regular lattice of interconnected cells [1]. The cells are very simple, usually only a few bits being used to define all possible states. All cells are updated in synchronism according to the same deterministic rule which is local in space and time. LGAs have received the most attention in the modelling of fluid dynamics, where the individual bits of the lattice cells mimic interacting particles. In the small perturbation limit, a fluid will behave according to the linear wave equation, and thus making an analogy between fluid and field parameters. We have utilized this simple particle interaction paradigm as a tool for computational electromagnetics. We have previously shown how LGA algorithms are capable of simulating a variety of electromagnetic propagation and scattering problems [2]. The main disadvantage with this approach is the presence of a viscosity term within the LGA dynamics [1]. In Section V we demonstrate a viscosity reduction technique which significantly reduces this error. The use of a single bit or small integer (at most 4 bits) representation of variables requires a fine mesh to statistical converge to the appropriate dynamic behavior. A benefit of this fine discretization is a reduction in stair-casing errors, as discussed in Section IV.

One of the main motivations for our investigation of LGA is that they are inherently simple parallel systems. The unit computational cell requires only a few bits of memory and simple logical operations for evaluation. This makes LGA ideally suited for implementation on fine-grained parallel architectures, unlike their difference equation counterparts which require floating point processors. Furthermore, special purpose computing architectures, referred to as cellular automata machines, already exist. The algorithms in this paper have been implemented on a special purpose cellular automata hardware accelerator, CAM-8, constructed by the Information Mechanics group at MIT [3]. It is capable of analyzing computational spaces of up to 32M cells at a rate of 200M cell updates per

second. Each cell contains up to 16 bits. The machine uses a look-up table style computational process.

II: Background

In Fig. 1, a small portion of an HPP LGA is shown [4]. This LGA is constructed on a rectangular lattice with only 4 bits per cell. Each bit represents a particle in the lattice constrained to the x and y directions. The lattice operates in two phases; a collision phase where the particles interact and the state of each cell is updated, and an advection phase where particles are passed to adjacent cells. Particle directions are noted in the top left cell of Fig. 1(a). The collision/advection rules are derived directly from Newtonian mechanics where only conservation of particle mass and momentum suffice to describe the microdynamics of the system. The examples of collisions shown in the HPP LGA of Fig. 1 satisfy these conservation rules.

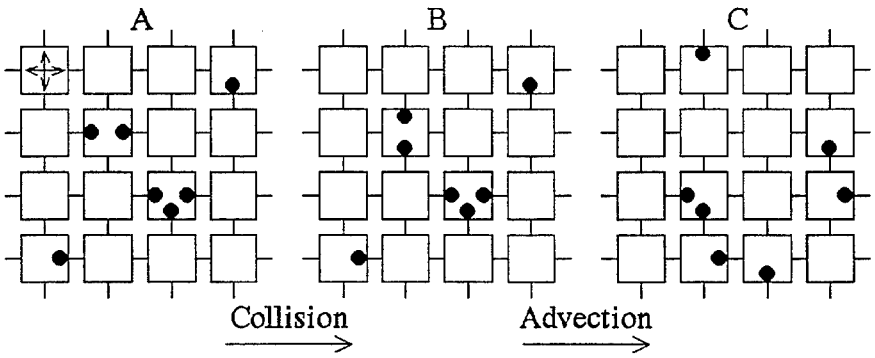

Figure 1: Operation of the HPP lattice gas automaton over a single time step. In (a), the particles are traveling toward the center of the cells. In (b) the state of the lattice is shown after the collisions have taken place. In (c), the particles have been transferred to adjacent cells. Typical simulations employ lattices consisting of millions of cells.

To calculate macroscopic quantities, such as densities and fluxes, a statistical average over a group of cells in a local region is performed. The collective behaviour of the lattice gas on a macroscopic scale can be determined by assuming the lattice is uniform and infinite, and then determining the equilibrium and transport equations using a perturbation analysis [5]. It has been shown [4] that the simple four particle LGA described above approximates the incompressible form of the Navier-Stokes and conservation of mass differential equations describing the dynamics of a fluid.

In electromagnetics applications we are only concerned with modelling the linear wave equation. Linear wave dynamics can be obtained from the more general fluid equations by operating the LGA near an equilibrium state (a uniform background distribution of particles with no initial flow) and then observing small density and flow velocity perturbations to this equilibrium. By making an analogy between density and flow perturbations and electric and magnetic fields we can use the LGA paradigm for computational electromagnetics. With the inclusion of appropriate boundary conditions, we have previously used LGA to model two-dimensional TE or TM field problems involving PEC and simple dielectric scatterers [2].

III: Modelling Heterogeneous Media

The addition of rest particles can be used to model heterogeneous media within LGA simulations [1]. One of many possible rest particle models is shown in Fig. 2, where a stack of rest particles of various masses can be created [6]. For example, a rest particle of mass 4 is created when four unit mass moving particles collide and initially there is no mass 4 rest particle. Alternatively, if a mass 4 rest particle already exists at a site and there are no initial moving particles, four moving particles will be created after the collision phase and the rest particle will be annihilated. All the collision rules still obey the microscopic conservation laws and thus linear wave behaviour is maintained. The rest particles enable mass (energy) to be stored for a short period of time at each cell which results in a decrease of the average speed of propagation, c_s, of the perturbations in the lattice. By specifying regions of the lattice to have different rest particle numbers and masses, lattices with inhomogeneous propagation speeds (dielectric constant) can be modelled. Extensions of this principle which involve spatial grading of the rest particle rules or through the incorporation of stochastic rules (probabilistic events allowing rest particles to be created or annihilated) enable a wide range of dielectric constants to be modelled. The theoretical dielectric constant for the model shown in Fig. 2 with 4 moving particles of unit mass and allowing up to M_r rest particles of mass m_k to be placed at a lattice site with probability p_k is

$$\varepsilon_r = \frac{\left[4f_m(1-f_m) + \sum_{1}^{M_r} m_k^2 p_k f_k (1-f_k)\right]}{[4f_m(1-f_m)]},$$

where f_m and f_k are the average background densities of the moving and rest particles, respectively. The relationship between the particle populations, f_m and f_k can be determined for equilibrium conditions and assuming Fermi-Dirac distributions for the particle populations [1],[5],[7].

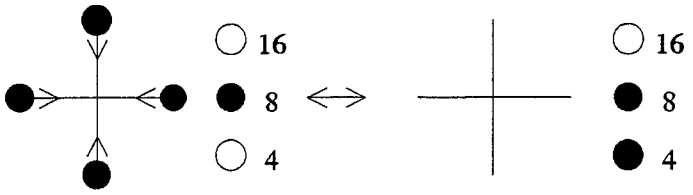

Figure 2: LGA rule with three binary weighted rest particles.

Using only three rest particles of mass 4, 8, and 16, within the dielectric regions, we have been able to model dielectric media with relative dielectric constant ranging from ε_r=1 to ε_r=85. This range is obtained with the addition of only three extra bits per computational cell, and is sufficient for most practical problems. We have performed various validations of the rest particle model including comparison of the theoretical relative permittivity to numerical values via propagation speed measurements.

The transient response at an observation location in front of a dielectric ring is provided in Fig. 4. The ring was created using a single uniform rest particle with mass 4, and was embedded in a lattice of size 2048 by 4096. The outer diameter of the ring is r_{out}=100Δl. The transient response are provided in Fig. 4 for inner diameters of a) r_{inner}=0.5r_{out}, and b) r_{inner}=0.8r_{out}. The ε_r=5 material is located between the inner and outer rings. The results obtained using a transmission-line-matrix numerical approach are given for comparison [8]. Good agreement between the two transient responses is observed. We have also applied the LGA to the analysis of more challenging

heterogeneous electromagnetic field problems. In [6], a demonstration of wave interaction with a human body cross-section model is provided. The extensions for heterogeneous media are directly applicable to our three-dimensional field models, which are described in the following section.

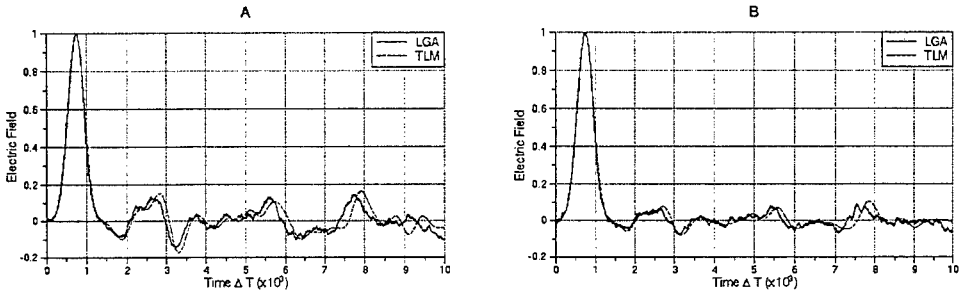

Figure 3: Time-domain electric field intensities in front of a ε_r=5 dielectric ring with a) $r_{inner}=0.5r_{out}$ and b) $r_{inner}=0.8r_{out}$. Comparison is made to the results obtained using the TLM method. Good agreement between the two transient responses is observed.

IV: Three-Dimensional Problems

The lattice gas rules described above for two dimensions, and all current LGA models, are based on the interaction of scalar particles. The particles have the properties of mass and momentum only and thus can not be used to model vector fields. The vector model we have developed is based on the interaction of particles having the properties of mass, momentum, as well as polarization. The three-dimensional model was validated through the simultaneous simulation of both TE and TM modes within conducting cavities. Accurate predictions of resonant frequencies were obtained.

Using this three-dimensional vector LGA we have been able to compute the cut-off frequencies of several cavity resonators, for which analytical comparison have been made. One such problem is a short cylindrical perfectly conducting cavity. This problem requires stair-stepped discretization of the cylindrical surface which was embedded within an LGA space of 128 by 128 by 8 cells. In [9], we compare the percent error in the calculated cut-off frequency of the TE_{110} dominant mode computed using the LGA and a stair-stepped FD-TD algorithm. The percent error within the LGA computations ranged from 0.29 to 0.76 percent, whereas the percent error within the FD-TD computations ranged from 1.95 to 4.36 percent even though the spatial cell size used with the LGA was only 1/5 that used with FD-TD. This shows that the LGA approach is capable of modelling fine geometrical details, without increasing the complexity of the LGA algorithm or lattice. In addition, for the spatial discretizations utilized in [9], the LGA technique does not exhibit numerical dispersion inherent with difference equation approximations. It does, however, exhibit dissipative effects due to the presence of viscosity within the dynamics [1].

V: Integer Lattice Gases

The LGA algorithms we have previously demonstrated for two-dimensional field problems utilize only 4 bits per cell on a rectangular lattice (one bit per direction). For the two-dimensional homogeneous model, a simple 16 (2^4) state transition table is required to update a cell, making it extremely efficient for implementation within computing architectures such as CAM-8. However, one of the drawbacks of this binary variable approach is that statistical averaging over a group of cells is necessary to obtain macroscopic field quantities with a reasonable dynamic range. Thus, a finer mesh

(more cells for a given spatial dimension) is required than when using floating-point variables as in the differential equation methods. Numerical experiments presented in [9] indicate that (depending on the specific problem) the increased mesh density is on the order of 5-30 per dimension for lattice gases with single bits per direction. The low end of this estimate (5 per dimension) is for problems with smoothly varying field distributions such as the cylindrical cavity problem described above. The high end (30 per dimension) is for problems with rapidly varying field distributions, such as those containing sharp metallic edges [10]. The viscous terms within the LGA dynamics tend to dissipate rapidly varying field distributions, causing significant errors in the modelling of the field distributions. The increased mesh density becomes a severe limitation for three-dimensional problems, since the number of lattice gas cells required per unit three-dimensional floating point (TLM or FD-TD) cell becomes 125 to 27,000 (5^3 to 30^3).

To reduce the two problems identified above, we have investigated integer LGA (ILGA) [11]. ILGA utilize small integers rather than single bits. Our investigations have thus far utilized up to 4 bits per lattice direction. Even though the number of bits is increased it is still amenable to implementation on CAM-8. The variables are allowed up to only 16 states (for the 4 bit case). The collision rules are selected such that they maintain the appropriate conservation laws.

Significant reduction in viscosity is achieved through the use of ILGA. In Fig. 4, we observe the unphysical decay of a TE_{10} mode in a rectangular waveguide cross section modelling using a space of 128 by 64 LGA cells. This unwanted decay is caused by the viscous damping of the LGA. The transient response consisting of 10,000 time steps obtained from the single bit LGA is significantly damped, while that obtained from the 4-bit ILGA is negligibly damped. Based on the significant reduction in viscosity observed in Fig. 4, we have re-examined structures which possess sharp metallic edges. These structures are relevant to the analysis of typical electronic or microwave circuit components [10]. Analysis of a fin-line cross-section, indicated an initial estimate of the LGA to TLM (or FD-TD) discretization ratio is in the range of 30:1 [9]. Results presented in Fig. 5 indicate a 4-bit ILGA to TLM (or FD-TD) discretization ratio of about 3:1. This represents a significant improvement in the computational efficiency of LGA with only a minimal increase in computational complexity.

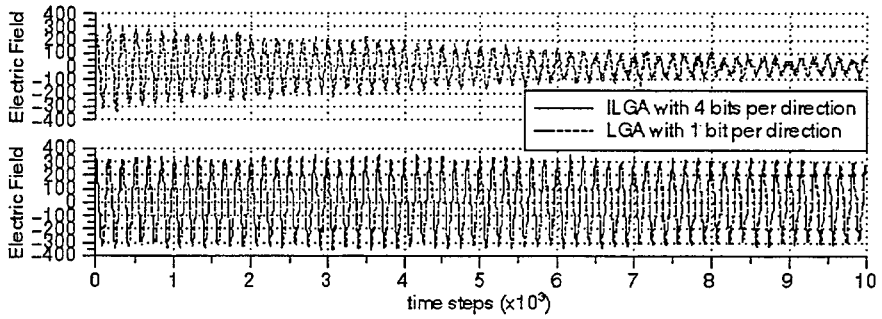

Figure 4: Comparison of the unwanted physical decay observed in the transient response of a TE_{10} mode over 10,000 time steps as predicted by a single bit LGA and a 4 bit ILGA. The 4-bit ILGA significantly reduces the damping.

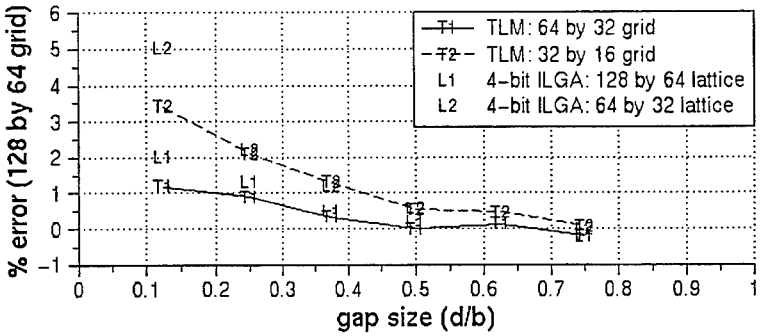

Figure 5: Comparison of percent error in predicted resonant frequency versus gap length for the finned waveguide problem (geometrical details available in [9], [10]). Use of a 4-bit ILGA reduces the discretization ratio (as compared to SCN-TLM simulations) to approximately 3:1. A previous estimate of this ratio obtained from single bit LGA simulations was 30:1 [9].

VI: Conclusions

In this paper we have discussed the application of lattice gas automata (LGA) to the solution of electromagnetic field problems. Increased mesh density was found to decrease errors associated with stair-stepping curved surfaces. For the discretizations considered in this paper, the LGA technique does not exhibit the numerical dispersion inherent with difference equation approximations. It does, however, exhibit dissipative effects due to the presence of viscosity within the dynamics. Significant reduction of this unwanted viscosity has been realized through the use of a 4-bit integer LGA.

Acknowledgment: We gratefully acknowledge the assistance of Dr. Norman Margolus (Laboratory for Computer Science, MIT), with the ILGA implementation.

[1] G. Doolen (ed.), **Lattice Gas Methods for Partial Differential Equations**, Santa Fe Inst. (Addison-Wesley), 1990.

[2] N. R. S. Simons, N. Adnani, G. Bridges, M. Cuhaci,"On the Potential Use of Cellular Automata Machine for Electromagnetic Field Solution", *International Journal for Numerical Modelling*, vol. 8, pp. 301, 1995.

[3] N. Margolus, "CAM-8: a computer architecture based on cellular automata", in: **Pattern Formation and Lattice Gas Automata**, (ed: R. Kapral, A. Lawniczak) American Mathematics Society (Fields Institute Series), 1995.

[4] J. Hardy, O. de Pazzis, and Y. Pomeau, "Molecular Dynamics of a Classical Lattice Gas: Transport Properties and Time Correlation Functions", *Phys. Rev. A*, vol. 13, pp. 1949-1961, 1976.

[5] U. Frisch, D. d'Humieres, B. Hasslacher, P. Lallemand, Y. Pomeau, and J-P. Rivet, "Lattice Gas Hydrodynamics in Two and Three Dimensions", *Complex Systems*, vol. 1, pp. 649-707, 1987.

[6] G. E. Bridges, N. R. S. Simons, D. Cule, M. Zhang, M. Cuhaci, "Application of the Lattice Gas Automata Technique to Modelling Wave Interaction with Biological Media", *IEE Tenth International Conference on Antennas and Propagation*, Edinburgh, UK, April, 1997.

[7] N. Adnani, "Cellular Automata Models for the Two Dimensional Scalar Wave Equation", M.Sc. Thesis, University of Manitoba, 1996.

[8] N. R. S. Simons, A. Sebak and A. Ittipiboon, "Analysis of Aperture-Coupled Microstrip Antenna and Circuit Structures Using the TLM Method", *IEEE APS Magazine*, vol. 37, pp. 27, August 1995.

[9] D. Cule, N. R. S. Simons, G. E. Bridges, M. Cuhaci, and J. LoVetri, "Investigation of Geometrically Small Features within Numerical Solutions to Electromagnetic Field Problems", ANTEM'96, Montreal, Quebec, 1996.

[10] J. L. Herring, W. J. R. Hoefer, "Accurate Modelling of Zero Thickness Septa with the Symmetric Condensed Node", *First International Workshop on Transmission Line Matrix (TLM) Modelling*, pp. 237-240, 1995.

[11] B. M. Boghosian, J. Yepez, F. J. Alexander, N. H. Margolus, "Integer Lattice Gases", submitted to: *Phys Rev E*, 1996.

SESSION 25:

PLANAR AND CONFORMAL ANTENNAS AND CIRCUITS

Chair: G. Vecchi

Transmission line approach for the study of planar periodic structures

R.Orta, P.Savi, R.Tascone, R.Zich

CESPA (C.N.R.), Dipartimento di Elettronica, Politecnico di Torino,
Corso Duca degli Abruzzi 24, 10129 TORINO (Italy)
Tel.(+)39-11-564-4074, FAX (+)39-11-564-4089, e-mail: savi@polito.it

ABSTRACT – The transmission line technique for the study of the scattering problem from planar periodic structures is described. Both passive arrays of metallic patches and perforated screens in a stratified dielectric support are considered. The method yields the Generalized Scattering Matrix (GSM) of an array in its dielectric enviroment. The behaviour of multiple array configurations can be predicted by cascading the GSM of each array. The frequency response of a millimeter-wave diplexer is shown as an example.

1 Introduction

In the last two decades planar periodic structures have aroused a growing interest in the electromagnetic community and many investigators have given their contribution for improving the techniques of analysis and design of these structures. Planar periodic structures also known as Frequency Selective Surfaces (FSS) find application as free-space diplexers, subreflectors for multifrequency antenna systems, spatial filters and polarizers [1]-[8].

FSS may be basically of two types, those that at low frequency are transparent (capacitive FSS) and those that are reflecting (inductive FSS). The behaviour at the resonance frequency is complementary. Capacitive FSS consist of an array of metal patches embedded in a stratified dielectric structure, which has mainly the purpose of providing mechanical support. Inductive FSS are in the form of perforated screens and, if the metal is sufficiently thick, the dielectric support structure may be absent. However, for generality, we will take them always into account. At first sight, capacitive and inductive FSS seem to be completely different structures: it is clear, however, that if the metallic patches of a capacitive array are large enough to touch each other and to ensure electric continuity, a perforated screen is obtained, with complementary frequency response. This fundamental identity is apparent also from the point of view of the analysis, since both types of structures can be analyzed by a unified formulation.

The frequency response of an FSS of the types described above does not in general satisfy the stringent specifications posed by the applications in diplexers and antenna subreflectors. Satisfactory results can be obtained by stacking several arrays or screens to give rise to a multiple array configuration.

FSS of practical interest have such geometries that analytical techniques cannot be applied to solve the relevant scattering problem. Among the numerical techniques we may cite the Method of Moments in the spatial or spectral domain, the Mode Matching technique, iterative techniques, the Conjugate Gradient method and the Finite Element Method. In our opinion, spectral techniques are the most appropriate for FSS, specially when complicated dielectric supports are present. In fact, also in this case, the spectral representation of the Green function is known in analytical form.

In this paper an arbitrary planar array of patches or apertures is considered and the spectral formulation of the scattering problem is presented. This formulation allows the introduction of a vector transmission line representation, where voltages and currents are the two-dimensional Fourier transforms of the transversal electric and magnetic fields, respectively. Two solution approaches are discussed, the *patch approach*, where the unknown is the current induced on the metallic region, and the *aperture approach*, where the aperture electric field is chosen as unknown. Subsequently, the Generalized Scattering Matrix in the Floquet mode base is derived. Multiple array configurations are analyzed by a cascading procedure.

2 Analysis

Let us consider an arbitrary planar distribution of zero thickness patches, placed at $z = 0$ and embedded in a stratified dielectric medium (see fig.1). This class of structures can be interpreted as a transversal discontinuity in an open waveguide with homogeneous cross section and, therefore, the scattering problem can be attacked by modal techniques. The mode eigenfunctions are exponentials which constitute a continuous spectrum of plane waves. As a consequence, the modal voltages and currents in free space [9] can be seen as polar components of the Fourier transform of the transverse (to $\hat{z}$) electric and magnetic fields. It will be shown that the scattering problem can be solved directly in the spectral domain.

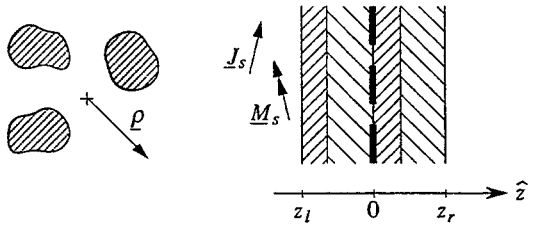

Figure 1: Geometry of a general FSS consisting of a planar distribution of metallic patches embedded in a stratified dielectric medium.

We use a vector formulation, so that TE and TM modes with the same eigenvalue are treated jointly. In particular, the vector voltage and current at a generic section z are defined as

$$\underline{V}(\underline{k},z) = \frac{1}{2\pi}\int \underline{E}_t(\underline{\rho},z)\, e^{j\underline{k}\cdot\underline{\rho}}\; d\underline{\rho} \quad , \quad \underline{I}(\underline{k},z) = \frac{1}{2\pi}\int \underline{H}_t(\underline{\rho},z)\times\hat{z}\, e^{j\underline{k}\cdot\underline{\rho}}\; d\underline{\rho} \tag{1}$$

where the vector $\underline{\rho}$ and $\underline{k}$ lie in the plane transverse to the z-axis.

The modal free-space impedance, with this formulation, is defined by the dyadic operator

$$\underline{\underline{Z}}_0(\underline{k}) = \frac{\beta}{\omega\epsilon_0}\,\hat{k}\hat{k} + \frac{\omega\mu_0}{\beta}\,(\hat{k}\times\hat{z})(\hat{k}\times\hat{z}) \tag{2}$$

where $\beta = \sqrt{k_0^2 - |\underline{k}|^2}$ and $\hat{k} = \underline{k}/|\underline{k}|$. By defining $\underline{I}$ to be the Fourier transform of $\underline{H}_t \times \hat{z}$, the modal impedance matrix is diagonal in the polar basis $\{\hat{k};\hat{k}\times\hat{z}\}$. Moreover, transverse distributions of electric ($\underline{J}(\underline{\rho},z)$) and magnetic ($\underline{M}(\underline{\rho},z)$) currents are represented in circuit terms by vector current and voltage generators with strength given by [9]:

$$\underline{i}(\underline{k},z) = \frac{1}{2\pi}\int \underline{J}(\underline{\rho},z)\, e^{j\underline{k}\cdot\underline{\rho}}\; d\underline{\rho} \quad , \quad \underline{v}(\underline{k},z) = \frac{1}{2\pi}\int \underline{M}(\underline{\rho},z)\times\hat{z}\, e^{j\underline{k}\cdot\underline{\rho}}\; d\underline{\rho}\,. \tag{3}$$

By applying the Equivalence Theorem to the closed region defined by the two plane surfaces $z = 0^-$ and $z = 0^+$, the conducting elements are substituted with an unknown distribution of electric current defined by:

$$\underline{J}(\underline{\rho}, 0) = [\underline{H}_t(\underline{\rho}, 0^-) - \underline{H}_t(\underline{\rho}, 0^+)] \times \hat{z} \ . \tag{4}$$

Assuming an arbitrary field incident from the left side of the structure, we obtain, by the transmission line formalism [9], the equivalent circuit of fig.2 corresponding to a generic value of the spectral variable $\underline{k}$. The voltage generator has strength $2\check{\underline{V}}^i$ where $\check{\underline{V}}^i(\underline{k})$ is the Fourier transform of the incident

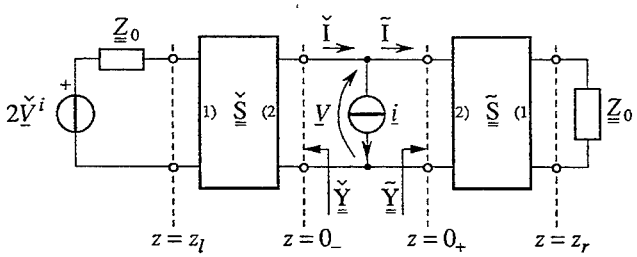

Figure 2: Modal vector equivalent circuit of the structure of fig.1 for a generic value of the spectral variable $\underline{k}$.

electric field at the section $z = z_l$. The current generator at the section $z = 0$ has strength $\underline{i}(\underline{k})$ equal to the Fourier transform of the sum of the electric currents induced on both sides of the patches $\underline{J}(\underline{\rho})$. $\underline{V}(\underline{k})$ is the Fourier transform of transversal electric field at $z = 0$. The stratifications of the dielectric media on the left and right side of the conductors are characterized by their 2×2 scattering matrices $\check{\underline{S}}(\underline{k})$ and $\tilde{\underline{S}}(\underline{k})$, respectively, whose elements are dyadic operators. These matrices can be computed according to usual transmission line techniques. We use the symbols $\check{}$ and $\tilde{}$ to denote quantities relative to the left and right region with respect to the section $z = 0$, respectively. It is convenient to define as port 2 of both the scattering matrices $\check{\underline{S}}(\underline{k})$ and $\tilde{\underline{S}}(\underline{k})$ the ports adjacent to the patches. Moreover, even if the dielectric layers are directly adjacent to the conductors, it is convenient to use the free-space modal impedance as reference for these scattering matrices. This choice will allow us to use the free-space modal description, i.e. the usual TE and TM modes, also in the case of anysotropic dielectrics.

Both the total voltage at $z = 0$, $\underline{V}(\underline{k})$, and the impressed current, $\underline{i}(\underline{k})$, are unknown and satisfy the following equation which can be easily obtained from the circuit of fig.2:

$$-[\check{\underline{Y}}(\underline{k}) + \tilde{\underline{Y}}(\underline{k})]^{-1} \cdot \underline{i}(\underline{k}) + \check{\underline{T}}^v(\underline{k}) \cdot \check{\underline{V}}^i(\underline{k}) = \underline{V}(\underline{k}) \ . \tag{5}$$

$\check{\underline{Y}}(\underline{k})$ and $\tilde{\underline{Y}}(\underline{k})$ are the load admittances seen by the current generator looking to the left and to the right, respectively.

Eq.(5) describes completely the scattering problem even if it contains two unknowns. This is due to the analytical properties of $\underline{V}(\underline{k})$ and $\underline{i}(\underline{k})$ that are transforms of functions with complementary supports: $\underline{E}_t(\underline{\rho})$ vanishes on the conductors whereas $\underline{J}(\underline{\rho})$ vanishes on the apertures.

We introduce the following definitions. A generic function $\underline{f}(\underline{k})$ will be called a *patch function* (*aperture function*) if its inverse Fourier transform has support on the metallic patches (on the apertures) only and is identically zero on the apertures (on the patches). Therefore, $\underline{V}(\underline{k})$ is an aperture function and $\underline{i}(\underline{k})$ is a patch function. Obviously, any patch function is orthogonal to any aperture function. We see that these definitions generalize the concepts of *plus functions* and *minus functions*

typical of the Wiener-Hopf technique; in that case, the complementary regions, where the two types of functions have support, are semiinfinite. This fact implies certain regularity properties for their Fourier transforms [10], which are exploited to solve the relevant functional equation by a factorization method. In the present case the scattering problem is three-dimensional and this technique is not applicable. However, we will use the concepts of aperture and patch functions in order to solve eq.(5) by the Galerkin Method of Moments according to two alternative approaches, based on the choice of the unknown function to be expanded, either $\underline{i}(\underline{k})$ (*patch approach*) or $\underline{V}(\underline{k})$ (*aperture approach*).

Patch approach

Let us introduce a set of vector patch basis functions $\{\underline{f}_n(\underline{k})\}$ in order to expand the unknown $\underline{i}(\underline{k})$:

$$\underline{i}(\underline{k}) = \sum_n I_n \, \underline{f}_n(\underline{k}) \ . \tag{6}$$

According to the general formalism of the Galerkin Moment Method, this expansion is substituted into eq.(5) and subsequently the projections of $\underline{V}(\underline{k})$ on the same set $\{\underline{f}_n(\underline{k})\}$ are equated to zero in order to ensure that $\underline{V}(\underline{k})$ is an aperture function. In virtue of Parseval theorem, this step translates, in the spectral domain, the enforcement of the boundary conditions, i.e. it corresponds to imposing $\underline{E}_t(\underline{\rho}) = 0$ on the patches. In this way, eq.(5) is turned into a matrix equation in the unknown coefficients $\{I_n\}$:

$$\mathbf{A\,I = B} \tag{7}$$

where

$$\begin{aligned} A_{mn} &= \int \underline{f}_m^*(\underline{k}) \cdot [\underline{\tilde{Y}}(\underline{k}) + \underline{\tilde{Y}}(\underline{k})]^{-1} \cdot \underline{f}_n(\underline{k}) \, d\underline{k} \ , \\ B_m &= \int \underline{f}_m^*(\underline{k}) \cdot \underline{\tilde{T}}^v(\underline{k}) \cdot \underline{\tilde{V}}^i(\underline{k}) \, d\underline{k} \ . \end{aligned} \tag{8}$$

Once the system (7) is solved, it is easy to obtain the solution of the scattering problem by expressing the scattered voltages at the sections $z = z_l$ and $z = z_r$, by means of the circuit of fig.2:

$$\underline{\tilde{V}}^s(\underline{k}) = \underline{\tilde{S}}_{11}(\underline{k}) \cdot \underline{\tilde{V}}^i(\underline{k}) - \underline{\tilde{T}}(\underline{k}) \cdot [\underline{\tilde{Y}}(\underline{k}) + \underline{\tilde{Y}}(\underline{k})]^{-1} \cdot \underline{i}(\underline{k}) \ , \tag{9}$$

$$\underline{\tilde{V}}^s(\underline{k}) = \underline{\tilde{S}}_{21}(\underline{k}) \cdot \underline{\tilde{V}}^i(\underline{k}) - \underline{\tilde{T}}(\underline{k}) \cdot [\underline{\tilde{Y}}(\underline{k}) + \underline{\tilde{Y}}(\underline{k})]^{-1} \cdot \underline{i}(\underline{k}) \tag{10}$$

where $\underline{\tilde{S}}_{11}(\underline{k})$ and $\underline{\tilde{S}}_{21}(\underline{k})$ are the reflection and transmission operators of the scattering matrix of the whole dielectric structure between sections z_l and z_r. $\underline{\tilde{T}}(\underline{k})$ ($\underline{\tilde{T}}(\underline{k})$) is the transmission coefficient which connects the total voltage at section $z = 0$ to the scattered voltage at $z = z_l$ ($z = z_r$).

Aperture approach

In certain cases it may be difficult to find an appropriate expansion function set for the induced currents because the metallic region have a complicated shape (for instance in the case of a perforated screen). If, in such cases, the geometry of the apertures is simple (rectangular or circular holes, etc.) and thus it is possible to find an expansion function set for the aperture fields, the scattering problem is still solved by the Moment Method. The corresponding functional equation in the spectral domain can be obtained very easily with this formulation by solving eq.(5) with respect to $\underline{i}(\underline{k})$:

$$-[\underline{\tilde{Y}}(\underline{k}) + \underline{\tilde{Y}}(\underline{k})] \cdot \underline{V}(\underline{k}) + [\underline{\tilde{Y}}(\underline{k}) + \underline{\tilde{Y}}(\underline{k})] \cdot \underline{\tilde{T}}^v(\underline{k}) \cdot \underline{\tilde{V}}^i(\underline{k}) = \underline{i}(\underline{k}). \tag{11}$$

Incidentally, it is interesting to note that this equation can also be derived by using the Equivalence Theorem in a different form, by replacing the patches with a solid metallic plate on the left and right

side of which two distributions of equivalent magnetic current of value $\underline{E} \times (-\hat{z})$ and $\underline{E} \times \hat{z}$ respectively are present in place of the apertures [11]. In this way, it is immediate to observe that the operator acting on the incident voltage in eq.(11) is a trans-admittance operator linking the short circuit current at $z = 0$ to the incident voltage:

$$\underline{\underline{\check{Y}}}_t(\underline{k}) = [\underline{\underline{\check{Y}}}(\underline{k}) + \underline{\underline{\tilde{Y}}}(\underline{k})] \cdot \underline{\underline{\check{T}}}^v(\underline{k}) \ . \tag{12}$$

To solve eq.(11) by the Galerkin Method of Moments, we introduce a set of vector basis functions $\{\underline{g}_n(\underline{k})\}$ to expand the Fourier transform of the aperture electric field as follows:

$$\underline{V}(\underline{k}) = \sum_n V_n \, \underline{g}_n(\underline{k}) \ . \tag{13}$$

Then, we equate to zero the projections of the unknown function $\underline{i}(\underline{k})$ given by eq.(11) on the same set $\{\underline{g}_n(\underline{k})\}$. The problem is reduced to the solution of a linear system of equations in the unknown coefficients $\{V_n\}$:

$$\mathbf{A}\,\mathbf{V} = \mathbf{B} \tag{14}$$

where, now

$$\begin{aligned} A_{mn} &= \int \underline{g}_m^*(\underline{k}) \cdot [\underline{\underline{\check{Y}}}(\underline{k}) + \underline{\underline{\tilde{Y}}}(\underline{k})] \cdot \underline{g}_n(\underline{k}) \, d\underline{k} \ , \\ B_m &= \int \underline{g}_m^*(\underline{k}) \cdot \underline{\underline{\check{Y}}}_t(\underline{k}) \cdot \underline{\check{V}}^i(\underline{k}) \, d\underline{k} \ . \end{aligned} \tag{15}$$

After solving the linear system (14), the total voltage $\underline{V}(\underline{k})$ at section $z = 0$ is known and the scattered voltages on both sides of the structure, at $z = z_l$ and $z = z_r$, can be computed by circuit considerations as:

$$\begin{aligned} \underline{\check{V}}^s(\underline{k}) &= \underline{\underline{\check{\Gamma}}}_c(\underline{k}) \cdot \underline{\check{V}}^i(\underline{k}) - \underline{\underline{\check{T}}}(\underline{k}) \cdot \underline{V}(\underline{k}) \ , \\ \underline{\tilde{V}}^s(\underline{k}) &= \underline{\underline{\tilde{T}}}(\underline{k}) \cdot \underline{V}(\underline{k}) \end{aligned} \tag{16}$$

where $\underline{\underline{\check{\Gamma}}}_c(\underline{k})$ is the dyadic reflection coefficient of the complete structure looking from the left side when the perforated screen is substituted with a solid plate.

Periodic structure

When the metallic patches are arranged in a periodical lattice defined by the basis vectors $\underline{d}_1, \underline{d}_2$ and the incident field is a plane wave with a transverse wave vector $\underline{k}_t$, the structure excites a discrete spectrum of plane waves, characterized by the transverse wavevector $\underline{k}_{pq}$ (Floquet modes):

$$\underline{k}_{pq} = \underline{k}_t + p\,\underline{k}_1 + q\,\underline{k}_2 \tag{17}$$

where $\underline{k}_1$ and $\underline{k}_2$ are the basis vectors of the reciprocal lattice. Thus the integrals of eq.(8) are converted into summations on the indices p, q, and the coefficients of the system (7) are expressed as double infinite summations over the points of the reciprocal lattice (p, q):

$$\begin{aligned} A_{mn} &= \sum_{pq} \underline{f}_m^*(\underline{k}_{pq}) \cdot \underline{\underline{Z}}(\underline{k}_{pq}) \cdot \underline{f}_n(\underline{k}_{pq}) \ , \\ B_m &= \sum_{pq} \underline{f}_m^* \cdot \underline{\underline{\check{T}}}^v(\underline{k}_{pq}) \cdot \underline{V}^i(\underline{k}) \ . \end{aligned} \tag{18}$$

where $\underline{\underline{Z}}(\underline{k}_{pq}) = [\underline{\underline{\check{Y}}}(\underline{k}_{pq}) + \underline{\underline{\tilde{Y}}}(\underline{k}_{pq})]^{-1}$ is the total load impedance seen by the current generator. Analogous expressions hold for the aperture approach.

In order to obtain a numerical solution, the number of expansion functions is fixed to N_f and the number of points of the reciprocal lattice to N_l; these two numbers are not independent because of the phenomenon of relative convergence.

The behaviour of the structure consisting of an array embedded in a dielectric stratification between the sections $z = z_l$ and $z = z_r$ can be completely specified by its Generalized Scattering Matrix (GSM), which can be derived from (9) and (10). It has the form:

$$\begin{bmatrix} \underline{\tilde{V}}^s \\ \underline{\check{V}}^s \end{bmatrix} = \begin{bmatrix} \underline{\underline{S}}^d_{11} - \underline{\underline{\tilde{T}}} \cdot \underline{\underline{Z}} \cdot \underline{\underline{W}} \cdot \underline{\underline{\check{T}}}^v & \underline{\underline{S}}^d_{12} - \underline{\underline{\tilde{T}}} \cdot \underline{\underline{Z}} \cdot \underline{\underline{W}} \cdot \underline{\underline{\tilde{T}}}^v \\ \underline{\underline{S}}^d_{21} - \underline{\underline{\check{T}}} \cdot \underline{\underline{Z}} \cdot \underline{\underline{W}} \cdot \underline{\underline{\check{T}}}^v & \underline{\underline{S}}^d_{22} - \underline{\underline{\check{T}}} \cdot \underline{\underline{Z}} \cdot \underline{\underline{W}} \cdot \underline{\underline{\tilde{T}}}^v \end{bmatrix} \begin{bmatrix} \underline{\check{V}}^i \\ \underline{\tilde{V}}^i \end{bmatrix} \tag{19}$$

The ports to which this GSM refers are the N_l Floquet modes. This matrix can be decomposed into the sum of two matrices. The first:

$$\underline{\underline{S}}_d = \begin{bmatrix} \underline{\underline{S}}^d_{11} & \underline{\underline{S}}^d_{12} \\ \underline{\underline{S}}^d_{21} & \underline{\underline{S}}^d_{22} \end{bmatrix} , \tag{20}$$

defines the GSM of the dielectric support structure with the metallic discontinuity removed. $\underline{\underline{S}}^d_{ij}$ are $(N_l \times N_l)$ abstract diagonal matrices representing, in the Floquet mode basis, the reflection and transmission coefficients of the whole dielectric structure between sections z_l and z_r. The second matrix takes into account the radiation of the electric currents induced on the metallic patches, in presence of the dielectric stratification. Consider, for example, the term $\underline{\underline{\tilde{T}}} \cdot \underline{\underline{Z}} \cdot \underline{\underline{W}} \cdot \underline{\underline{\check{T}}}^v$. The matrices $\underline{\underline{\tilde{T}}}, \underline{\underline{Z}}, \underline{\underline{\check{T}}}^v$ refer to the dielectric stratification only and, hence, are diagonal matrices. $\underline{\underline{W}}$ is a full matrix and takes into account the metallic discontinuity. In particular, the dielectric transmission coefficient $\underline{\underline{\check{T}}}^v$ ($\underline{\underline{\tilde{T}}}^v$) gives the electric field in the array section when the metallic patches are removed in terms of the electric field incident on the section z_l (z_r). $\underline{\underline{W}}$ represents an admittance type Green function, relating the magnetic field jump at the discontinuity to a couple of opposite magnetic current distributions placed on the faces of the array. The matrix $\underline{\underline{Z}}$ is the impedance type Green function of the dielectric layers, relative to the discontinuity section. Finally, the dielectric transmission coefficient $\underline{\underline{\tilde{T}}}$ ($\underline{\underline{\check{T}}}$) gives the scattered electric field in z_l (z_r). All the quantities pertaining to the dielectric stratification are easily obtained by the transmission line technique. The matrix $\underline{\underline{W}}$ is

$$\underline{\underline{W}} = \underline{\underline{Q}} \cdot (\underline{\underline{Q}}^+ \cdot \underline{\underline{Z}} \cdot \underline{\underline{Q}})^{-1} \cdot \underline{\underline{Q}}^+ \tag{21}$$

where $\underline{\underline{Q}}$ is the projection matrix whose element Q_{mn} is the n-th vector basis function $\underline{f}_n(\underline{k})$ evaluated in the m-th point of the reciprocal lattice (m stays for the indices p, q and $+$ indicates the hermitian adjoint).

The form of the GSM shown in eq.(19) is typical of the patch approach, where the patches are seen as perturbation of a reference structure consisting of the dielectric stratification alone.

If we now consider a perforated screen, for which the aperture approach is more natural, the GSM, according to eq.(16), takes the form:

$$\begin{bmatrix} \underline{\tilde{V}}^s \\ \underline{\check{V}}^s \end{bmatrix} = \begin{bmatrix} \underline{\underline{\tilde{\Gamma}}}^d_c + \underline{\underline{\tilde{T}}} \cdot \underline{\underline{W}} \cdot \underline{\underline{\check{Y}}}_t & \underline{\underline{\tilde{T}}} \cdot \underline{\underline{W}} \cdot \underline{\underline{\tilde{Y}}}_t \\ \underline{\underline{\check{T}}} \cdot \underline{\underline{W}} \cdot \underline{\underline{\check{Y}}}_t & \underline{\underline{\check{\Gamma}}}^d_c + \underline{\underline{\check{T}}} \cdot \underline{\underline{W}} \cdot \underline{\underline{\tilde{Y}}}_t \end{bmatrix} \begin{bmatrix} \underline{\check{V}}^i \\ \underline{\tilde{V}}^i \end{bmatrix} . \tag{22}$$

Also this GSM can be decomposed into the sum of two matrices. The first,

$$\underline{\underline{S}}^d_c = \begin{bmatrix} \underline{\underline{\check{\Gamma}}}^d_c & \underline{\underline{0}} \\ \underline{\underline{0}} & \underline{\underline{\tilde{\Gamma}}}^d_c \end{bmatrix} \tag{23}$$

defines the GSM of the reference structure, consisting of the dielectric support structure with the perforated screen substituted with a solid one. The second matrix takes into account the presence

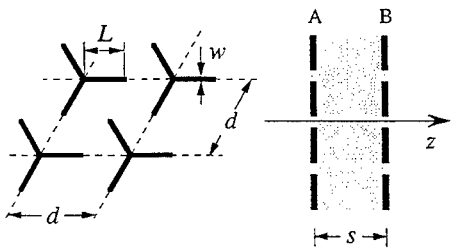

Figure 3: Transversal and longitudinal view of the double array of tripole patches.

of the apertures and is related to the radiation of the magnetic currents placed on the solid metallic plate, in presence of the dielectric stratification.

Furthermore, the full matrix $\underline{\underline{W}}$ has here the meaning of an impedance type Green's function relating the electric field on the screen to a distribution of electric current placed in the same plane. Its expression is

$$\underline{\underline{W}} = \underline{\underline{Q}} \cdot (\underline{\underline{Q}}^{+} \cdot \underline{\underline{Z}}^{-1} \cdot \underline{\underline{Q}})^{-1} \cdot \underline{\underline{Q}}^{+} \tag{24}$$

where now, $\underline{\underline{Q}}$ contains the values of the functions $\underline{g}_n(\underline{k})$ in the points of the reciprocal lattice. As far as the multiple array structures are concerned, the relevant GSM can be obtained by a cascade procedure of the GSM of each substructure consisting of the array with its adjacent dielectric layers.

3 Example of Results

As an example, consider a 45°-incidence diplexer with the following specifications: two 0.5 dB transmission bands at (90 ± 3) GHz and at (157 ± 1.5) GHz and 0.5 dB reflection band at (183 ± 8) GHz. These requirements were satisfied by a double array configurations as shown in fig.3. In particular, the two transmission bands are obtained by selecting the array spacing in order to realize an impedance matching at those frequency bands for both TE and TM polarizations. The tripole elements are arranged on an equilateral triangular lattice and printed on the two side of a fused quartz slab with $\epsilon_r = 3.78$. The geometry is the following: lattice dimension $d = 500$ μm, arm length $L = 265$ μm, arm width $w = 20$ μm, dielectric thickness $s = 785$ μm.

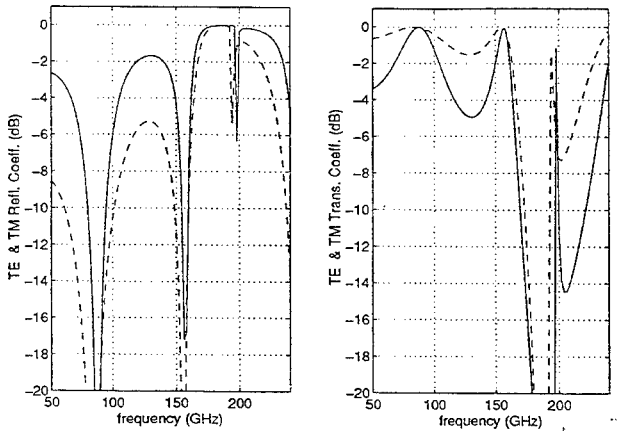

Figure 4: TE (solid line) and TM (dashed line) reflection and transmission coefficients of the double array configuration. 45° incidence in a symmetry plane.

The frequency response of this structure (see fig.4) was obtained with 10 sinusoidal expansion functions for each tripole arm (vanishing at the arm ends) and 439 points of the reciprocal lattice. The coupling between the two substructures has been computed through the first Floquet modes with a nominal attenuation less than 30 dB. The transmission spike at about 200 GHz, for both polarizations, is due to the filtering properties of the whole structure which acts as a Fabry-Perot interferometer. In fact, at that frequency, the distance between the two arrays is about one guided wavelength and the arrays are highly reflecting.

References

[1] F. S. Johansson, L. R. Lagerholm, and P. S. Kildal, "Frequency-scanned reflection gratings with integrated polarizer", *IEEE Trans. Antennas Propagat.*, vol. 40, pp. 331-334, March 1992.

[2] J.C. Vardaxoglou, A. Hossainzadeh, A. Stylianou, "Scattering from two-layer FSS with dissimilar lattice geometries", *IEE Proceedings-H*, vol. 140, pp. 59-61, Feb. 1993.

[3] Y. Rahmat-Samii, A.N. Tulintseff, "Diffraction Analysis of Frequency Selective Reflector Antennas", *IEEE Trans. Antennas Propagat.*, vol. 41, pp. 476-487, April 1993.

[4] P.W.B. Au, E.A. Parker, R.J. Langley, "Wideband filters employing multilayer gratings", *IEE Proceedings-H*, vol. 140, pp. 292-296, Aug. 1993.

[5] D.B. Webb, E. Michielssen, R. Mittra, "Single and Double square-loop Frequency-Selective Surfaces with thick metallization", *Microwave and Optical Technology Letters*, vol. 6 , pp. 875-879, Dec. 1993.

[6] T.K. Wu, W.P. Shillue, "Dichroic design for the orbiting VLBI station antenna", *IEEE Trans. Antennas Propagat.*, vol. 141, pp. 181-184, June 1994.

[7] R.A. Hill, B. Munk, "The effect of perturbating a Frequency-Selective Surface and its relation to the design of a dual-band surface", *IEEE Trans. Antennas Propagat.*, vol. 44, pp. 368-374, March 1996.

[8] R.Orta, P.Savi, R.Tascone, "Numerical Green's Function technique for the analysis of screens perforated by multiply connected apertures", *IEEE Trans. Antennas Propagat.*, vol. 44, pp. 765-776, June 1996.

[9] L. B. Felsen and N. Marcuvitz, *Radiation and Scattering of Waves*, Englewood Cliffs, NJ Prentice-Hall, pp. 183-217, 1973.

[10] R. Mittra and S. W. Lee, *Analytical techiques in the theory of guided waves*, New York, The Macmillan Co., 1971.

[11] R. Orta, R. Tascone and R. Zich, "Multiple dielectric loaded perforated screen as frequency selective surfaces", *IEE Proc.H., Microwaves, Opt. & Antennas*, vol. 135, no. 2, pp. 75-82, Apr. 1988.

ANALYSIS OF ARRAYS OF ELEMENTS OVER SURFACES WHICH CAN BE CONFORMED TO A BODY OF REVOLUTION

Salvadora Piedra, José Basterrechea, M. Felipe Cátedra
Grupo de Sistemas y Radio. Dpto. Ingeniería de Comunicaciones
Universidad de Cantabria
39005 Santander. SPAIN
fax: +34 42 201873. E-mail: felipe@gsr.unican.es

ABSTRACT

A method that allows the analysis of arrays of apertures or patches conformed to a Body of Revolution (BOR) is presented. The method uses the here called combined-convolution technique to discretize the Mixed Potentials Integral Equation (MPIE) using a CG-FFT scheme. It does not require a uniform discretization along the generatrix of the BOR enabling a better geometrical modelling. Results are successfully compared with measurements.

INTRODUCTION

Many practical problems in applied electromagnetics are involved with arrays of elements over planes or conformed to curved surfaces. In the first case the arrays usually have a periodic nature in one or two directions whereas in the case of arrays conformed to curved surfaces generated by the revolution of a generatrix curve around an axis, the structure is intrinsically periodic in the revolution direction. Examples of these structures are:

a) Plane or volumetric elements, uniformly distributed over the nodes of a periodic mesh which extends over a strip. In this case, the periodicity is only along the strip axis.

b) Plane or volumetric elements uniformly located over the nodes of a plane periodic mesh. Now the problem is periodic along the two plane directions.

c) Arrays of elements which can be conformed to a body with symmetry of revolution. In this case, the elements are periodic with the revolution coordinate.

All these problems are well suited for their study with Integral Equation (IE) techniques. In fact, an iterative method, the Conjugate-Gradient Fast Fourier Transform (CG-FFT) method is considered here as solver. Due to the periodic nature in some coordinates of these structures, convolutions in the IE can be computed with the Discrete Fourier Transform and hence can be computed very efficiently by using the FFT. Convolutions for the non-periodic directions can be computed by constructing an equivalent cyclic problem as shown in [1,2] and using the FFT for all coordinates. This technique is used in [1,2] for structures of type a) and b). The use of the FFT for all directions for these structures requires a uniform discretization along all directions and implies building new periodic Green's functions of at least twice the size of the problem along non-periodic directions. It also implies the use of new periodic source functions which are obtained

by padding with zeroes the original ones until reaching the same period as the new Green's functions. That ensures obtaining correct results for the original problem in the region not padded with zeroes and allows computing convolutions in all directions as cyclic ones using the FFT. That constitutes the robustness of the CG-FFT technique and, at the same time, its weakness because it restricts the possibility of representing arbitrary geometries unless a very fine discretization is carried out. However, many usual structures in electromagnetics have regular enough shapes so as to be properly characterized using these techniques.

As an alternative, convolutions in the IE can be computed by using the FFT for the periodic coordinate and the real-space domain for the non-cyclic ones. This last technique is more appropriate for the analysis of arrays conformed to BOR's because it allows a non-uniform discretization of the generatrix curve and as a consequence a better geometrical modelling.

COMBINED CONVOLUTION OPERATOR FOR THE STATIC CASE

In order to show the process followed to obtain the operators, an electrostatic general case is considered. The extension of the technique used here to the electrodynamic case is straightforward with small differences due to the vectorial nature of the problem and the existence of derivatives in the integral equations. These derivatives can be computed as differences. The shift property of the Fourier Transform can also be helpful to simplify expressions.

Consider an arbitrary BOR whose surface is represented using a Dupin coordinate system (ϕ: azimuth, t: tangent to the generatrix, n: outgoing normal to the surface). The geometry of the BOR is represented by using a power of two uniformly distributed subintervals ($N_\phi+1$) in the ϕ-direction (distance: $\Delta\phi$) and an arbitrary number, N_t+1, of subintervals along the t-direction. The latter can be obtained by selecting arbitrary points along the generatrix and connecting them with straight segments of length Δt_j. The ϕt plane mesh generated in this way, which is shown in Figure 1 is used to model the BOR geometry.

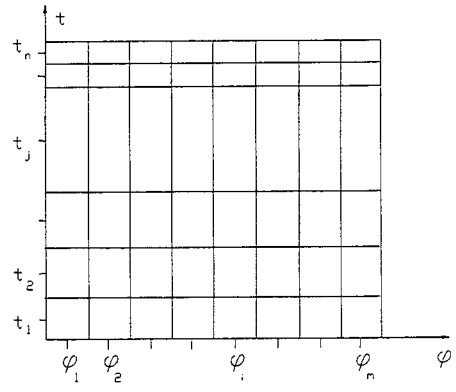

Figure 1.- ϕt plane representation of geometry.

The potential at any point of the surface produced by an arbitrary surface charge distribution comes given by:

$$V(\phi,t) = \frac{1}{4\pi\epsilon}\int_{S'}\rho(\phi',t')\,G(\phi,\phi',t,t')\,ds' \qquad (1)$$

where G represents the Green's function, given by:

$$G(\phi,\phi',t,t') = \left(\rho^2+\rho'^2-2\rho\rho'\cos(\phi-\phi')+(z-z')^2\right)^{-1/2} \qquad (2)$$

Expression (1) has the generic form:

$$V = L\,\rho \tag{3}$$

It seems evident from these equations that due to the periodicity along ϕ-direction, convolution in ϕ is cyclic in nature.

To obtain a discrete representation of this operator, the current density is expanded in terms of a set of pulse functions which extends over the subdomains defined by the ϕt mesh and centred at the points (ϕ_i, t_j) as shown in (4). These points, which coincide with the centres of the subdomains will be used to discretize the operator in the following.

$$\rho(\phi,t) = \sum_{i=1}^{N_t+1}\sum_{j=1}^{N_\phi+1} P_{ij}(\phi,t)$$

$$with \quad P_{ij}(\phi,t) = P_j(\phi,t) \tag{4}$$

$$and\ P_j(\phi,t) = \begin{cases} 1 & |\phi| \le \dfrac{\Delta\phi}{2}\ ;\ 0 \le t \le \Delta t_j \\ 0 & otherwise \end{cases}$$

By substituting (4) in (1), the following expression is obtained:

$$V(\phi,t) = \frac{1}{4\pi\epsilon}\int_{S'}\sum_{i'=1}^{N_\phi+1}\sum_{j'=1}^{N_t+1} P_{i'j'}(\phi,t)\ G(\phi-\phi',t,t')\ ds' \tag{5}$$

Keeping in mind that basis functions extend over only one subdomain, and have discrete amplitudes ρ[i,j] to be determined, the last expression can be written for the discretization points (ϕ_i,t_j) as:

$$V[i,j] = \frac{1}{4\pi\epsilon}\sum_{i'=1}^{N_\phi+1}\sum_{j'=1}^{N_t+1}\rho[i',j']\int_{\phi'_i-\frac{\Delta\phi}{2}}^{\phi'_i+\frac{\Delta\phi}{2}}\int_{t'_j-\frac{\Delta t'_j}{2}}^{t'_j+\frac{\Delta t'_j}{2}} G(\phi_i-\phi',t_j,t')\ \rho'\ d\phi'\ dt' \tag{6}$$

or in simplified form

$$V[i,j] = \frac{1}{4\pi\epsilon}\sum_{i'=1}^{N_\phi+1}\sum_{j'=1}^{N_t+1}\rho[i',j']\ G[i-i',j,j'] \tag{7}$$

Then convolution along ϕ coordinate can be easily computed by using the FFT and the transform domain potential will appear as:

$$\tilde{V}[m,j] = \frac{1}{4\pi\epsilon}\sum_{j'=1}^{N_t+1}\tilde{\rho}[m,j']\ \tilde{G}[m,j,j'] \tag{8}$$

where the tilde indicates transform magnitudes with respect to the ϕ coordinate.

The operator then will appear as follows:

$$L[i,j,j'] = FFT^{-1}\left[\frac{1}{4\pi\epsilon}\sum_{j'=1}^{N_t+1}\tilde{G}[m,j,j']\right] \tag{9}$$

Following a similar scheme to the one described here, the general operators for the electromagnetic case can be obtained. Their final expressions are summarized in next section.

COMBINED-CONVOLUTION OPERATOR FOR BOR's

Consider an arbitrary conducting surface S that conforms to a BOR. Let $\boldsymbol{E}^{inc}$ denote the impressed field on this surface. This field induces a current distribution $\boldsymbol{J}^{ind}$ which generates a scattering field $\boldsymbol{E}(\boldsymbol{J}^{ind})$. Applying the superposition principle, we can write the total electric field as

$$\boldsymbol{E} = \boldsymbol{E}^{inc} + \boldsymbol{E}(\boldsymbol{J}^{ind}) \tag{10}$$

Taking into account that on the conducting surface,

$$\boldsymbol{n} \times \boldsymbol{E} = 0 \tag{11}$$

where $\boldsymbol{n}$ is an outgoing normal vector, the following expression states the IE for the problem:

$$\boldsymbol{n} \times \boldsymbol{E}^{inc} = -\boldsymbol{n} \times \boldsymbol{E}(\boldsymbol{J}^{ind}) \tag{12}$$

where the field produced by a current distribution can be written

$$\begin{aligned} \boldsymbol{E}(\boldsymbol{J}) = & -k^c \int\int_{S'} \boldsymbol{J}(\boldsymbol{r}')\, G(\boldsymbol{r}, \boldsymbol{r}')\, ds' \\ & -k^q \nabla \int\int_{S'} \nabla' \boldsymbol{J}(\boldsymbol{r}')\, G(\boldsymbol{r}, \boldsymbol{r}')\, ds' \end{aligned} \tag{13}$$

which has the generic form

$$\boldsymbol{E} = L\,\boldsymbol{J} \tag{14}$$

Two sets of basis functions (rooftops) are distributed over each contiguous couple of rectangles in each direction (ϕ and t) of this mesh to represent the current density along ϕ (J_ϕ) and the total current flowing along t ($I_t = 2\pi\rho J_t$).

After expressing (13) in the Dupin coordinate system, expanding the current distributions in terms of the basis functions and testing with razor-blade functions, the discrete operator in the real-space domain is obtained. This operator involves the computation of several convolutions for ϕ and t components. Taking into account the cyclic nature of the problem for the ϕ direction, the advantage of using the FFT to compute convolutions for this component is again evident. Convolutions in t-direction are directly computed in the real-space domain under this combined-convolution technique as explained earlier.

Following a scheme similar to the one described in previous section, the final operator expression can be written in the following form:

$$\begin{bmatrix} V_\phi^{inc} \\ V_t^{inc} \end{bmatrix} = FFT^{-1} \left(\begin{bmatrix} \tilde{L}_{\phi\phi} & \tilde{L}_{\phi t} \\ \tilde{L}_{t\phi} & \tilde{L}_{tt} \end{bmatrix} \begin{bmatrix} \tilde{J}_\phi \\ \tilde{I}_t \end{bmatrix} \right) \tag{15}$$

where the symbol FFT indicates a Fast Fourier Transform applied to the ϕ-direction (index i), and

$$\tilde{J}_\phi[m, j] = FFT\left[J_\phi[i, j]\right] \tag{16}$$

$$\tilde{I}_t[m, j] = FFT\left[I_t[i, j]\right] \tag{17}$$

The terms in the transform domain operator are as follows:

$$\tilde{L}_{\phi\phi}[m,j,j'] = \left[\frac{\rho_j + \rho_{j-1}}{2} \Delta\phi\, k^c\, \tilde{G}_{11}[m,j,j'] + \frac{k^q}{\Delta\phi}(F_\phi - 1)\left(1 - F_\phi^*\right)\tilde{G}_d[m,j,j'] \right] \tag{18}$$

$$\tilde{L}_{\phi t}[m,j,j'] = \left[-\frac{k^c}{2\pi}\frac{\rho_j + \rho_{j-1}}{2}\Delta\phi\, \tilde{G}_{12}[m,j,j'] + \frac{k^q}{2\pi}(F_\phi - 1)\left[\frac{\tilde{G}_d[m,j,j']}{\Delta t_{j'}} - \frac{\tilde{G}_d[m,j,j'+1]}{\Delta t_{j'+1}} \right] \right] \tag{19}$$

$$\tilde{L}_{t\phi}[m,j,j'] = \left[\frac{\Delta t_j + \Delta t_{j+1}}{2} k^c \sin\gamma_j^t\, \tilde{G}_{21}[m,j,j'] + \frac{k^q}{\Delta\phi}\left(1 - F_\phi^*\right)\left(\tilde{G}_d[m,j+1,j'] - \tilde{G}_d[m,j,j']\right) \right] \tag{20}$$

$$\tilde{L}_{tt}[m,j,j'] = \frac{k^c}{2\pi}\frac{\Delta t_j + \Delta t_{j+1}}{2}\left(\sin\gamma_j^t\, \tilde{G}_{22}[m,j,j'] + \cos\gamma_j^t\, \tilde{G}_{05}[m,j,j']\right) + \frac{k^q}{2\pi}\left[\frac{\tilde{G}_d[m,j+1,j'] - \tilde{G}_d[m,j,j']}{\Delta t_{j'}} - \frac{\tilde{G}_d[m,j+1,j'+1] - \tilde{G}_d[m,j,j'+1]}{\Delta t_{j'+1}} \right] \tag{21}$$

where the tilde denotes transform quantities and the asterisk indicates the complex conjugate. Two different parts can be observed in these terms. The first one introduces the transforms of the quantities G_{ij}. These quantities are obtained after approaching the basis functions (rooftops) by pulses with the same dipolar moment and basically consist of integrals, extended to the source approached basis functions with observation points in the discretization points, of the free space Green's function multiplied by the sine or cosine of the angular ϕ distance when the sources are directed along the cyclic coordinate and by it and by the sine or cosine of the angle formed by the revolution axis and the t direction when the sources are directed along t. Hence they correspond to the current contribution to the operator or inductive term. The second part will represent the charge contribution to the operator or capacitive term. In this case, the transform of the quantity G_d appears in a repetitive way due to the intrinsic representation of charge by pulses when using rooftops as basis functions. Two derivatives appears in the charge term of the field in (13), one for the source and another for observation domains, that can be computed as differences. These differences in the transform domain are computed with the help of the shifting property of the Fourier Transform ($F_\phi = \exp(j2\pi m/(N_\phi+1))$ for the cyclic coordinate.

The adjoint operator used in the CG algorithm is obtained from the elements of $\tilde{L}_{\alpha\beta}$ by taking $(\tilde{L}_{\beta\alpha})^*$ (the transpose and complex conjugate) and interchanging the indexes j and j'.

RESULTS

As an example, the circular shortcircuited TTC antenna with apertures whose geometry is sketched in Figure 2 has been analyzed and the results compared with measurements. To achieve the main objective of TTC antennas, the omnidirectionality, 8 equiespaced apertures 1 mm wide in the metallic wall have been considered. The goal of the skirt in the geometry is to reduce radiation in back zones. The design has been done for a frequency of 10.7 GHz.

For the simulation, the antenna has been fed with two crossed dipoles with a phase shift of $\pi/2$ placed $\lambda/4$ from a shortcircuit in the back side of the waveguide. This feeding system has been placed far enough away from the front side of the waveguide so as to avoid spurious modes reaching the apertures (the waveguide supports circularly polarized TE_{11} mode).

Figure 3 shows results for three different simulations of the antenna in Figure 2. The dash-dotted line is the computed pattern when the geometry is modelled with a double wall, in such a way that the real width of the metallization has been taken into account. The other two curves are the results obtained when a single wall is considered: the continuous line is for a waveguide diameter of 20mm and the dashed line corresponds to a simulation of an antenna with a waveguide diameter of 22 mm. It has to be pointed out variations in the waveguide diameter do not imply significative differences in the resulting patterns, whereas including single o double wall in the antenna model produces significant modifications in the radiation pattern.

In Figure 4 a comparison between measurements and simulation for both copolar and crosspolar patterns is shown. The continuous line corresponds to the computed copolar pattern, while dashed line corresponds to the measured one. The dash-dotted and dotted lines represent simulated and measured crosspolar patterns respectively. The double wall simulation as been considered has better solution for two reasons: it gives a more realistic representation of the geometry and modifies in a significative way the results compared to the single wall simulations. It can be observed that there is a very good agreement between simulation and measurements.

Additional work is being carried out at this moment to include the connectivity between the two walls through the apertures which is expected to enlarge the range of validity of the method as well as to improve the results for the crosspolar pattern.

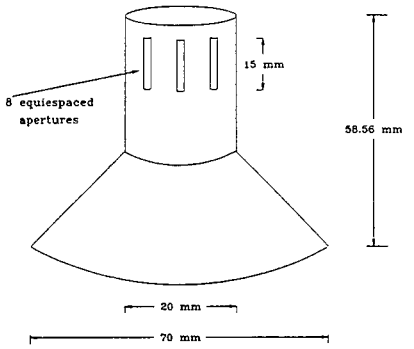

Figure 2.- TTC antenna for validation of the method.
Frequency = 10.7 GHz

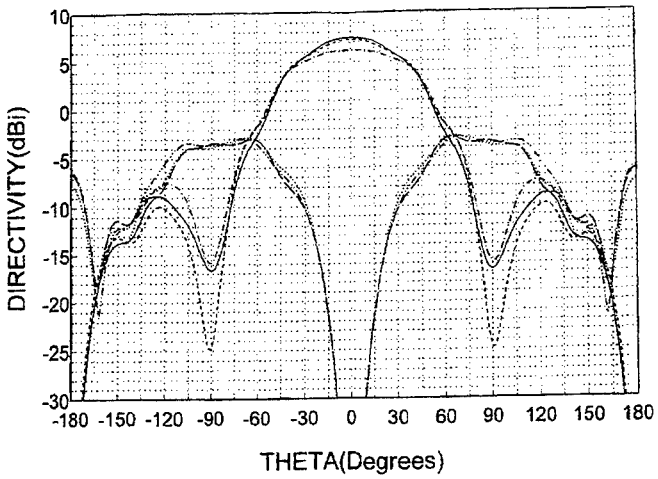

Figure 3.- Simulation results for the TTC antenna of Figure 2. Characteristics of each simulation are described in the text. Frequency: 10.7GHz.

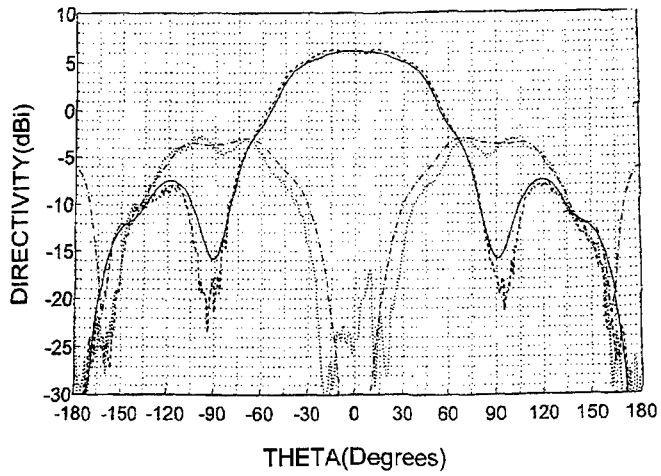

Figure 4.- Comparison between measured and simulated radiation pattern for the TTC antenna of Figure 2. Frequency: 10.7GHz.

CONCLUSIONS

An efficient approach for the analysis and design of arrays of apertures conformed to a BOR has been presented. The approach results have been successfully compared with measurements of radiating slots in circular waveguide. The efficiency of the approach comes given by the memory storage and CPU requirements which are proportional to $N_t N_t N_\phi$ and $(N_t N_t N_\phi)^2$, respectively, N_t being the number of samples in the BOR generating-arc coordinate and N_ϕ the number of samples in the revolution one. In that way, problems of arrays of apertures conformed to BORs with sizes of tens of wavelengths in both the maximum value of diameter and length of the generating arc can be affordable with latest generation of personal computers.

ACKNOWLEDGEMENTS

The authors wish to thank the INTA (Instituto Nacional de Técnicas Aeroespaciales) in SPAIN for providing the measurements for the TTC antenna.

REFERENCES

[1] M. F. Cátedra, R. P. Torres, J. Basterrechea, E. Gago: "The CG-FFT Method. Application of Signal Processing Techniques to Electromagnetics". Artech House Inc., 1995.

[2] E. Gago, J. Basterrechea, M. F. Cátedra: "2-D Validation of a Formulation for the Analysis of 3-D Bodies which are Periodic in One Direction and Finite Sized in the Others". IEEE Trans. on Antennas and Propagation, Vol. 42, No. 4, pp. 713-721, April 1994.

Computational Aspects of Finite and Curved Frequency Selective Surfaces

John Vardaxoglou

Department of Electronic and Electrical Engineering,
Loughborough University, Loughborough
Leicestershire, LE11 3TU
United Kingdom

Abstract
The convergence behaviour of several iterative schemes applied to finite Frequency Selective Surfaces (FSSs) is reviewed. In addition, the transmission coefficient is compared with the MoM solution. A brief description is given of the steps required to produce the scattered fields from a curved surface, representing an FSS radome. The boresight frequency response of a frequency selective conical horn antenna of loaded dipoles is shown using a finite array analysis.

Introduction
It has long been established that moment methods are powerful tools for solving integro-differential equations which arise from many electromagnetic scattering problems. Their use has also been extended to predict scattering from single or multilayer Frequency Selective Surfaces (FSSs) of infinite extent. Although this has been relatively successful, it does not readily provide information with regard to size or curvature. In general the finite array analysis is an element by element approach and therefore provides information about surface current distribution and edge scattering. The computation of scattering from finite and curved FSSs will be the theme in this presentation. In particular a overview will be given of predicting the array currents using the method of moments and an iterative conjugate gradient technique. The latter may suffer from convergence problems if a suitable preconditioning operator is not chosen. Several iterative schemes are reviewed, by looking at their efficiency and accuracy. Computed copolar fields will be compared with some measured data. Some results will also be given when the array is backed by a dielectric substrate.
The second part of the paper will outline two methods of computing the fields through a curved FSS. The first concentrates on structures, where the curvature is expected to be gentle. It is therefore assumed that the surface is locally (a few unit cells wide) flat. The second method is practically applicable to 'smaller' curved FSSs. It uses a finite array analysis, whereby the curvature is introduced by positioning the elements in a three dimensional space. This of course allows an arbitrary curvature to be modelled, but results from conical structures will be shown. In addition dielectric element loading and its effect on the scattered fields will be discussed.

Planar Finite FSS
The iterative method used here is developed by viewing the problem as that of minimising an error which assesses the deviation of the numerical solution from the exact one. This means that the approximation is improved at a steady rate throughout the process, and in the absence of round off errors, a solution may be obtained in a finite number of steps. It is then combined with the Fourier transform, whereby the convolution theorem is employed. The cumbersome computation of the convolution integral is reduced to simple algebraic manipulations in the spectral domain. Owing to speed of convergence and memory savings, we implement the conjugate gradient method. Since prior to the application of the scheme on a computer, the (Fourier) transformed operator equation has to be expressed in a discrete form, attention must be paid to sampling techniques. The finite FSS is shown in Fig. 1, where its size is determined by the number of elements. Here, we assume a periodic array of rectangular lattice with arbitrary element geometry. The analysis however can be

applied to non-periodic elements. The local element area is A' and the overall conducting area is D. The array is excited by a incident plane wave whose wave vector is $\underline{k}^i$. The EFIE involves a convolution type integral which is conveniently reduced to a simple multiplication in the spectral domain.

$$\frac{j}{\omega\varepsilon}F^{-1}\left(\begin{bmatrix} k^2-k_x^2 & -k_xk_y \\ -k_yk_x & k^2-k_y^2 \end{bmatrix}\tilde{G}(k_x,k_y)F\left(\chi_d\underline{J}(x,y)\right)\right)=\begin{bmatrix} E_{0x}e^{-j(k_x^ix+k_y^iy)} \\ E_{0y}e^{-j(k_x^ix+k_y^iy)} \end{bmatrix} \quad (1)$$

where F and F^{-1} denote the forward and inverse Fourier transforms respectively. χ_d is a truncation function on the conducting elements, k_x and k_y are the Fourier variables and $\tilde{G}(k_x,k_y)$ is the spectrum of the free space Green's function. Eqn. 1 can alternatively be written in an operator equation form as $F^{-1}(\tilde{\Lambda}F(\chi_d\underline{J}))=\underline{E}^{inc}$. We also solve this equation using the MoM, where a set of subdomain pulse bases have been used to develop a matrix system. The iterative method is applied to the above equation in a discrete form. A number of variants have been examined and compared here. The Conjugate Contrast Source Truncation technique (CCST3), the Conjugate Gradient-Fast Fourier Transform (CG-FFT) and the Conjugate Gradient-Discrete Fourier Transform (CG-DFT). Details of these can be found in [1], where the main differences lie in the choice of the preconditioner. CCST3 uses the inverse of the operator Λ, whereas the rest use its conjugate transpose. Several dipole and crossed dipole arrays are examined using the CCST3 and the CG-FFT iterative methods, both employing the delta basis and testing procedure [1]. The latter scheme is also developed with the rooftop basis and pulse testing functions, ECG-FFT method [2]. These schemes were applied to several dipole arrays shown in Table 1.

Array	*No. of dipoles*	*Area*	*FFT size*	*Samples on the array area*
1	3x3	18xl8	128xl28	33x33
2	5x5	30x30	128xl28	55x55
3	7x7	42x42	256x256	77x77
4	9x9	54x54	256x256	99x99
5	9x5	27x30	128xl28	63x55

Table 1. Array size and number of samples.

The distance separating the elements for each of the arrays 1-4 was 6 mm, in both the x and y directions, and the sampling interval was set at 6/11 mm. For array 5, the dipoles were separated in the x direction by 3mm with a sampling rate equal to 3/7 mm. The length of each element was represented by 7 samples whereas its width by one. In Table 1 the size of the FFT employed in the computations for the CCST3 and CG-FFT schemes is also shown. It was chosen to be equal to the first power of two greater than twice the number of samples on the arrays' area, since an FFT padding with zero elements had to be included in the computations. That is, for array 2 the size of the FFT was 128x128 points since 55x55 samples were needed to represent the 30x30 mm^2 array area. For the CG-DFT method, however, since the cyclic convolution is employed in its formulation, the size of the FFT for the analysis of the same array was only 110x110 points. At the onset of the iteration loop the current was set to zero and the criterion for terminating the iteration process was based upon attaining a pre-assigned value for the root mean square error

The convergence behaviour of the iterative schemes for array 2 is shown in Fig. 2. The number of iterations needed to meet an rms error of 0.01 are plotted against frequency. For all states of incidence the CG-FFT method requires almost twice the number of iterations to converge when compared with the other two schemes, reaching a maximum of 120 for TE:45^0 at 29GHz. The CG-DFT method provides a better convergence rate for the high frequencies (>33GHz) than the CCST3 scheme. Similar comments could be made for the convergence rates of the schemes when applied to the other size dipole arrays. However, it was found that the convergence was affected primarily by the array geometry and to a lesser extent by the number of elements comprising the array. The narrow spacing between the dipoles of array 5 resulted in a slow convergence rate. A maximum of 45 iterations were required to meet the target error at 30GHz. On the other hand, for the analysis of array 1 (3x3 elements) the scheme required only a maximum of 10 iterations to converge at 34GHz. Differences in the transmission performance have been found when compared with the infinite array one. The resonance from finite arrays at oblique angles of incidence is more shallow.

Table 2 summarises the number of iterations and computational time required by each of the iterative schemes CCST3, CG-FFT, CG-DFT to reach a 0.05 target error for normal incidence. In the same Table the number of unknowns needed to be evaluated by each method is also shown. Although the MoM solution is faster, it had to solve for less number of unknowns. This means that, if in the case of array 4 a 1134x1134 element matrix were had to be inverted, 1168 ms would be required by the MoM. The changes in the size of the FFT employed had a marked effect on the computational time.

Array	1	2	3	4	5
Number of unknowns					
MOM	63	175	343	567	315
Iterative schemes	126	350	686	1134	630
Number of iterations 30GHz (34GHz)					
CCST3	8 (11)	10 (21)	17 (18)	10 (20)	45 (21)
CG-FFT	36 (30)	30 (54)	27 (62)	39 (58)	81 (56)
CG-DFT	18 (21)	23 (16)	30 (21)	23 (18)	45 (22)
Computational Time, ms 30GHz (34GHz)					
MOM	0.2 (0.2)	4 (4)	32 (32)	146 (146)	25 (25)
CCST3	14 (20)	18 (39)	136 (144)	81 (163)	90 (42)
CG-FFT	63 (52)	53 (96)	215 (493)	311 (462)	159 (110)
CG-DFT	11 (13)	41 (29)	178 (55)	131 (103)	85 (42)

Table 2. Computational time comparison between the schemes for dipole arrays.

For example, for arrays 1, 2 and 5 (128x128 point FFT) about 1.82ms/iteration were required by the CCST3 whereas for arrays 3, 4 (256x256 point FFT) the time was increased to 8.07ms/iteration. The low computational time required by the CG-DFT is due to the changes in the FFT size rather than its fast converging behaviour. For array 1, where a 66x66 point FFT was employed, 0.61 ms required per iteration. This is in contrast to 1.75ms/iteration needed by the CG-FFT using a 128x128 point FFT.

With regards to arrays with a thin dielectric backing, an approximation was used in the computations. The operator was modified by altering the spectral Green's function, in a similar way to the infinite array case. The characteristics of the 5x5 element arrays were chosen here by varying their width to the length ratio. The element spacing was 6 mm for arrays 1-3, and 5 mm for array. The sampling rate for the arrays 1-3 was set at 6/11 mm whereas for the array 4 at 5/11 mm. A 128x128 point FFT was employed in the computations. In Table 3 the computational time required by the iterative schemes to attain a 0. 05 rms target error for normal incidence at 30GHz and 32GHz is shown. As can be seen, the solution from array 1 is faster obtained by employing the CCST3 than the other two iterative schemes. This is due to the low number of iterations required for convergence, but the CCST3 requires more computational time per iteration since an incomplete orthogonalisation procedure is employed. It was found that 1.87ms/iteration were required by the CCST3 whereas only 1.79ms/iteration were needed by the other two schemes. For arrays 2-4 the CCST3 was not satisfactory, suffering from stagnation and slow convergence. On the contrary, the ECG-FFT produced fast convergence behaviour resulting from the use of the rooftop basis and pulse testing functions. This makes the scheme a superior choice for the analysis of more complicated element geometries. For array 2 less time, by about a factor of seven, was required when compared with the conventional CG-FFT.

Finally, the inclusion of the dielectric support of the arrays in the computations, had little affect on the required computational time per iteration. An increase by only 0.0lms/iteration had occurred for the CCST3 and CG-FFT schemes when applied to the 5x5 dipole array backed with the dielectric. In Fig. 3 the predictions for the array 1 are compared with the measured results for TM:30^0 incidence at 31.5GHz. The theoretical results, despite minor discrepancies, compare well with the measurements, predicting the position as well as the normalised level of the main and first sidelobe. The crosspolar component of the scattered field was low for the normal incidence but there was a noticeable increase (about -26dB) for oblique angles of incidence.

Array	1	2	3	4
Element type	*Dipole*	*Dipole*	*Crossed Dipole*	*Crossed Dipole*
w/L	0.06	0.42	0.06	0.054
Number of iterations 30GHz (32GHz)				
CCST3	13 (17)			
CG-FFT	53 (54)	196 (401)	57 (74)	128 (90)
ECG-FFT	43 (48)	43 (41)	52 (61)	97 (83)
Computational Time, ms 30GHz (34GHz)				
CCST3	24 (32)	-	-	-
CG-FFT	95 (97)	292 (802)	120 (155)	273 (192)
ECG-DFT	77 (86)	86 (128)	109 (128)	206 (177)

Table 3. Computational time required for normal incidence.

Curved FSS

To begin to analyse the behaviour of a curved FSS one may consider flat arrays using the physical optics approximation. The inclusion of the illuminating feed fields can then be utilised so that a more realistic pattern scan be obtained. The leading assumption to all of these is that each element under consideration is part of a tangential infinite array, locally planar approximation. Irrespective of the above assumption, an important aspect in the design of curved FSSs is the insensitivity of the frequency response to a wide range of incident angles representing the feed illumination. A superposition of point sources has been adopted for modelling the near and far fields of the feed. Both electric and magnetic surface currents have been used to obtain the fields transmitted through the surface. Use of the modal analysis method has been made for the calculation of these currents. In both cases the illumination was provided by a corrugated horn.

The first approach given here utilises the infinite array modal analysis by assuming that each local element is part of a large array tangential at that locality, [3]. For large surfaces and/or gentle curvatures this approximation will hold. At the present time these assumptions are best quantified by concentrating on the type of application and the specified accuracy. However, one can make most of information provided by the modal analysis by including both electric and magnetic currents in each cell. In addition the fields produced by the feed illuminating the curved surface needs to be properly taken into account. Here we have used a superposition of point sources approach whereby the source fields can be computed at any point on the surface. Lastly the interaction between the feed and the surface is accounted for by integrating over a path enclosing both the feed and the curved FSS. Fig. 4 shows a curved FSS section and feed position in relation to it. The position vectors on the surface and the observation (arbitrary) point Q are also shown. The feed orientation may be allowed to vary and its origin may be at a fixed distance away form the surface's origin, O. At point Q a probe acting either as a transmitter or receiver can be placed. With the aid of Ludwig's vectors, the patterns can be computed and compared with measured data. Usage of the plane wave computer model is made in conjunction with modelling of the illuminating feed. Fig. 5 shows the measured and predicted copolar radiation patterns of the conical FSS using the SPS feed model at 15 GHz. A triangular lattice of ring slot elements was used. The array was initially designed to produce a passband at a frequency near 15 GHz. The initial design was based on the results of a modal analysis of an infinite planar wave illumination at an angle of incidence of 45^0 and can only be taken as a guide to the likely passband of the FSS cone.

The cone height was 554 mm and inner base radius was 110 mm. In total there were 3,794 elements on and the inner surface was illuminated by a corrugated feed horn with a circular aperture of diameter 96 mm and a semiflare angle of 6^0. The feed was designed to operate over the band 12-18 GHz. The FSS cone and feed horn were mounted on an azimuth turntable which provided the necessary angular scan for far field radiation pattern measurements. A fixed pyramidal horn antenna was used as a receive antenna at a distance of 1.6 metres from the origin. It can be observed that there is good agreement between measured and predicted patterns out to angles of about $\pm 20^0$. At larger pattern angles the overall envelope of the sidelobe structure is fairly well predicted by the model, with some discrepancies in the fine structure. of the measured sidelobe levels. The rapid oscillation of the sidelobe levels in this region is thought to be due to constructive and destructive interference between the transmitted fields and those reflected by the inner cone wall. In addition, multiple reflections may have been present between the FSS cone and the feed. This is to be expected since outside the centre of the transmission band the FSS becomes reflective and gives rise to internal reflections within the conical cavity.

The radiation performance of a conical horn frequency selective antenna, [4], with dipole elements is discussed next. The analysis considers a finite array of linear conducting elements coated with an arbitrary material. This may be dielectric or ferrite. Here we focus on the dielectric effects of the in band frequency shift. Fig. 6 shows a sketch of the frequency selective horn (FSH) antenna as well as the geometry of the dipole and its coat. The horn is fed with a cylindrical waveguide carrying the TE_{11} mode. This in turn has been modelled using a superposition of point sources at each element (segment) position, in a similar fashion to the corrugated feed model for the FSS radome above. The EFIE with an arbitrary coating, of relative permeability and permitivity ε_r and μ_r respectively, takes the following form:

$$\underline{E}^i(r) = \frac{j\omega\mu_o}{4\pi}\left[\int_{-L/2}^{L/2} \mu_r\, I\hat{u}\, G(r-r_a)du_a - \int_{-L/2}^{L/2}(\mu_r - 1) I\hat{u}\, G(r-r_b)du_b\right] + \frac{1}{4\pi\varepsilon_o}\left[\int_{-L/2}^{L/2}\frac{1}{\varepsilon_r}\left(\frac{-1}{j\omega}\frac{dI}{du_a}\right)\nabla G(r-r_a)du_a\right. \quad (2)$$

$$\left. + \left(1-\frac{1}{\varepsilon_r}\right)\int_{-L/2}^{L/2}\left(\frac{-1}{j\omega}\frac{dI}{du_b}\right)\nabla G(r-r_b)du_b\right]$$

where I is the current flowing on the dipole of length L, G is the Green's function and E^i is the incident electric field. r_a and r_b denote vectors regarding the inner and outer radii of the cylindrical layer of the coating. The EFIE is transformed into a matrix system having segmented the elements. This system has been solved by a conjugate gradient iterative method and an elimination technique. Due to element segmentation, the matrix size is large and poses storage as well as running problems. Structure symmetry helps up to a point with regards to the calculation of the matrix elements. Varying the dielectric thickness has shifted the in band (resonance) of the antenna as well as altered the bandwidth. This is depicted in Fig. 7, where it can be observed that the gain is also affected. A 15.7 cm long horn with a 13^0 semiflare angle was used. A total of 254 elements (spaced 9.65 mm apart) were placed on the horn, resulting in a matrix of order 1270. Each element had a length of 7.65 mm, radius of 0.175 mm and the computing time per frequency was 4 minutes.

The element geometry has a noticeable influence on the gain and bandwidth of the frequency selective horn. Whereas dipole elements have narrow bandwidths, circular elements and square loops produce wider bandwidths associated with a gain increase. Cross dipoles offer dual band performance, where the low band is dominated by a surface wave. The bandwidth increase is related to the sensitivity of the internal reflections to the incident angles.

Closing comments

It has been shown that the computing time of scattering from finite FSS depends on the type of iterative scheme used. Whereas for thin elements the CCST3 provides a rapid convergence, the ECG-FFT is recommended for wide range of geometries. The presence of a 0.037 mm thick dielectric substrate did not seem to affect the convergence.

Bandpass FSS radomes can be modelled with an approximate procedure which is based on the surface being locally planar. In band losses and radiation patterns agree reasonably well with measured data. Out of band internal reflections degrade the radiation pattern. A finite array analysis can be used for predicting the radiation performance of frequency selective horns. The dielectric loading has indicated a frequency shift and gain increase.

References

[1] Vardaxoglou, J.C. and Stylianou, A.: 'Finite and multi-layer FSS responses using iterative techniques', Report ELJK3, Loughborough University, Loughborough, UK, 1992.

[2] Stylianou, A. and Vardaxoglou, J.C: 'Moderate Conjugate Gradient FFT Method for Rapid Convergence in Analysing Finite FSSs', Electron. Lett., 1992, Vol.28, pp.506-508.

[3] Vardaxoglou, J.C.: 'Frequency selective surfaces: analysis and design', to appear, Chapter 5, Research Studies Press Ltd, UK.

[4] Vardaxoglou, J.C., Robinson, A.J. and Seager, R.D. : 'Towards a new class of waveguiding structures and lightweight horn antennas using passive arrays', Proc. IEEE International Conference in Electromagnetics on Aerospace Applications, ICEAA, 1993, Torino, Italy, pp.343-346.

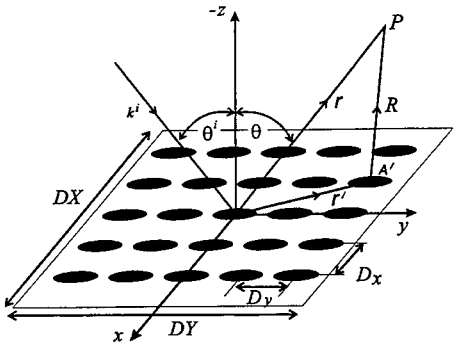

Fig. 1 Finite size FSS of conducting elements.

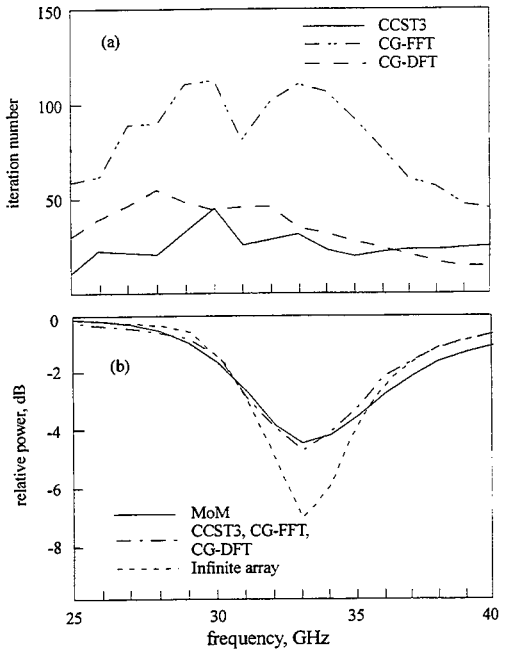

Fig. 2. (a) Iteration and (b) transmission responses for TM:45^0.

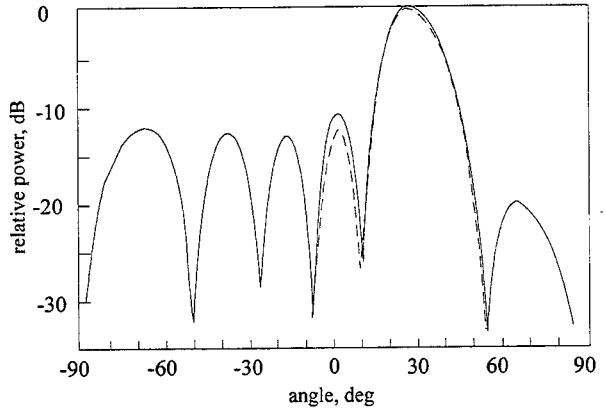

Fig. 3. Radiation pattern in reflection for TM:30^0.
– – – – Measured data

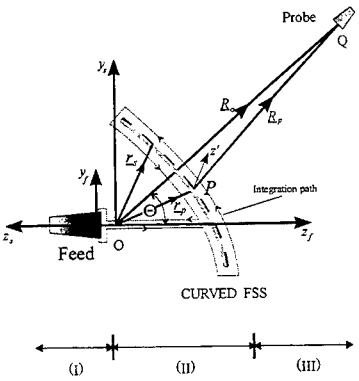

Fig. 4. Cross section of part of a curved FSS and its feed.

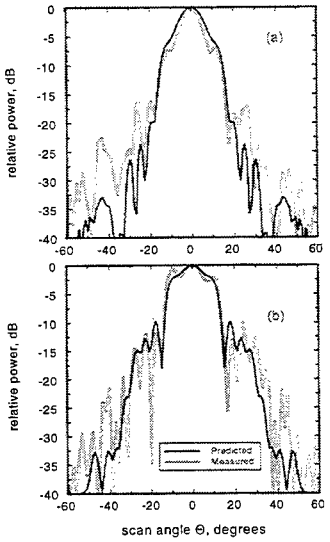

Fig. 5. Copolar pattern of conical FSS radome (ring apertures) at 15 GHz. (a) 0^0 plane, (b) 90^0 plane.

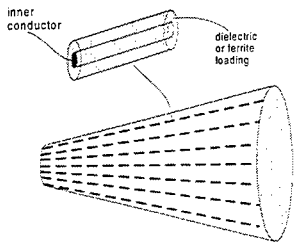

Fig. 6. Geometry of FSS horn antenna.

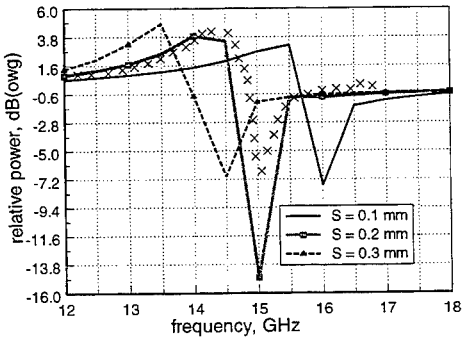

Fig. 7. Effect of dielectric on the frequency and gain level. Crosses show measured data.

COMPUTATIONALLY EFFICIENT MOM AND ITS APPLICATIONS

L. Alatan[1], N. Kınayman[2], M. I. Aksun[2], K. Leblebicioğlu[1], M. T. Birand[1]

1 Dept. of Electrical & Electronics Eng., Middle East Technical University, 06531 Ankara,Turkey.
2 Dept. of Electrical & Electronics Eng., Bilkent University, 06533 Ankara, Turkey.

1 Introduction

Numerical modeling of microstrip antennas and printed structures in multilayer media can be performed rigorously via the method of moments (MoM). In the analysis of moderate-size printed geometries (spanning several wavelengths in two dimensions), the computational efficiency of the MoM is determined by the time used to calculate the entries of the MoM matrix, namely the matrix-fill time.

Application of the spatial-domain MoM to the solution of mixed-potential integral equation, results in a matrix equation whose entries contain two-dimensional (2-D) integrals over finite domains. These integrals involve spatial-domain vector and scalar type Green's functions which can be obtained from their spectral-domain counterparts via Hankel transformation, also called Sommerfeld integral. Numerical implementation of the Hankel transform is the computational bottleneck of the spatial-domain MoM due to highly oscillatory and slow convergent nature of the kernel of the transformation. Hence, the matrix-fill time in the application of the spatial-domain MoM is mainly determined by two processes : i) calculation of the spatial-domain Green's functions and ii) evaluation of the 2-D integrals. The problems pertaining to the former process are eliminated by the use of the closed-form Green's functions method in which the spectral-domain Green's functions are approximated by complex exponentials and their spatial-domain counterparts are cast into a form of complex exponentials, via the Sommerfeld identity. The method was first developed for the Green's functions corresponding to a horizantal electric dipole on a single thick substrate [1]. Then, the approach was generalized to cover multilayer geometries with arbitrary thicknesses and with arbitrary source types, horizantal and/or vertical electric and/or magnetic dipoles [2]. The efficiency and the robustness of the method has been significantly improved with the use of a multi-level approximation scheme whose details were described in [3]. The 2-D integrals involved in the calculation of the matrix entries, which is the second process that contributes to matrix-fill time, can be performed analytically with the use of Taylor's series expansions of the complex exponentials that appear in the closed-form represantation of the spatial-domain Green's functions [4]. Thus, the computational efficiency of the spatial-domain MoM is improved significantly. The efficiency is further improved by using Taylor's series expansion in the calculation of the self-terms and a polynomial approximation in the calculation of the other entries.

The formulation of the computationally efficient MoM is extended to planar geometries (in the x-y plane) with vertical connections (in z-direction). The introduction of the vertical connections requires some modifications in the formulation, because the spectral-domain Green's functions are functions of the source and observation locations (z' and z, respectively), while the closed-form Green's functions are approximated for constant z and z' values. To account for vertical connections with different lengths, two different modifications are proposed [5]. If the vertical connection is short, the integrals with respect to z and z' variables are performed in the spectral domain and then the approximation is carried out in the same way as before. On the other hand, if the vertical connection is long, the variation of the Green's functions with respect to z and z' are factored out and the coefficients of these terms are approximated.

In the design and optimization of printed antennas, the computationally efficient MoM is used in conjuction with the Order Recursive Gaussian Elimination (ORGE) method [6], which is developed to improve the efficiency of solving the matrix equations for modified geometries. An inset-fed and a circularly polarized patch antennas

are designed. The closed-form Green's functions method is detailed in Section 2, the analytical evaluation of the MoM matrix entries is summarized in Section 3 and the formulation for geometries with vertical connections is presented in Section 4. The results of the computationally efficient MoM are compared to those obtained from a commercially available software called *em* from SONNET. The results are discussed in Section 5 and followed by a conclusion in Section 6.

2 Closed-Form Green's Functions

It is well-known that the spectral-domain Green's functions for the vector and scalar potentials are represented analytically in a multilayer medium, and their spatial domain counterparts are obtained simply by the Hankel transform of the spectral domain Green's functions,

$$G = \frac{1}{4\pi} \int_{SIP} dk_\rho k_\rho H_o^{(2)}(k_\rho \rho) \tilde{G}(k_\rho) \tag{1}$$

where $k_\rho^2 = k_x^2 + k_y^2$, ρ is the variable in cylindrical coordinate system, G and $\tilde{G}$ are the Green's functions in the spatial and spectral domains, respectively, $H_o^{(2)}$ is the Hankel function of the second kind and SIP is the Sommerfeld integration path. Note that this integral, also called the Sommerfeld integral, can not be evaluated analytically for the spectral domain Green's functions $\tilde{G}$. If the spectral domain Green's function $\tilde{G}$ is approximated by exponentials, the Sommerfeld integral (1) can be evaluated analytically using the well-known Sommerfeld identity;

$$\frac{e^{-jk_s r}}{r} = -\frac{j}{2} \int_{SIP} dk_\rho k_\rho H_o^{(2)}(k_\rho \rho) \frac{e^{-jk_z |z|}}{k_z}. \tag{2}$$

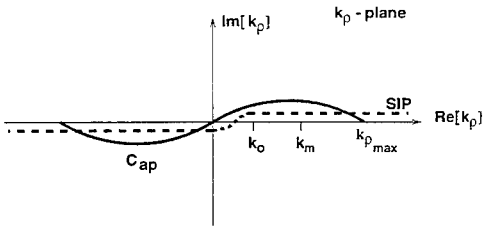

Figure 1: Integration path for single-level approximation

The approximation of the spectral-domain Green's functions with the complex exponentials is carried out by using the generalized pencil of function (GPOF) method [7], which is a more robust and a less noise sensitive scheme when compared to the other approximation algorithms, such as Prony's and least square Prony's methods. Since this approximation technique requires uniform sampling of a complex-valued function along a real variable, one could choose to sample along the k_ρ variable which results in exponentials in terms of k_ρ. However, our aim is to obtain exponentials in terms of k_z so that the Sommerfeld identity can be utilized. Hence, a deformed path on k_ρ plane, denoted by C_{ap} in Fig.1, is defined as a mapping of a real variable t onto the complex k_z plane by

$$k_z = k_s \left[-jt + (1 - \frac{t}{T_0}) \right], \qquad 0 \le t \le T_0 \tag{3}$$

where k_z and k_s are defined in the source layer. The Green's functions are sampled uniformly on $t \in [0, T_0]$, which maps onto the path C_{ap} with $k_{\rho_{max}} = k[1 + T_0^2]^{1/2}$ in the k_ρ-plane. Hence they are approximated in terms of exponentials of t which can easily be transformed into a form of exponentials of k_z. It is of utmost importance to judiciously choose the approximation parameters; T_0 and the number of samples, for the success of the approach. The number of samples should be large enough to capture abrupt changes that could occur for small values of

k_ρ and T_0 must be large enough to capture the asymptotic behaviour of the spectral-domain Green's functions. However, this results in a reduntant oversampling at large values of k_ρ, where the approximated function is slowly varying and well-behaved. To circumvent this problem, a two-level approximation scheme is developed. The first part of the approximation is performed along the path C_{ap1} while the second part is done along the path C_{ap2}, as shown in Fig.2. In the first part of the approximation, the asymptotic behaviour of the approximated function is extracted and the fine features of the remaing function are easily captured in the second part of the approximation by using a small number of sampling points. This approach can be easily extended to multi-level approximation schemes, as it could be necessary for the analysis of planar geoemtries with vertical connections, where a three-level approach is used.

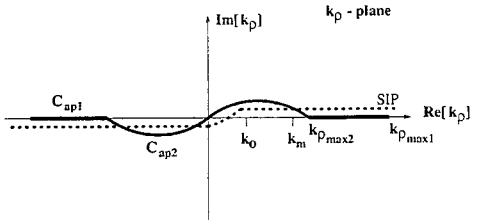

Figure 2: Integration path for two-level approximation

After approximating the spectral-domain Green's functions and using the Sommerfeld identity, the spatial domain Green's functions can be cast into a form of

$$\tilde{G} \cong \frac{1}{j2k_z} \sum_{n=1}^{N} a_n e^{-k_z a_n} \Rightarrow G \cong \sum_{n=1}^{N} a_n \frac{e^{-jk_s r_n}}{r_n} \tag{4}$$

where $r_n = \sqrt{x^2 + y^2 - \alpha_n^2}$ is a complex distance and k_s is the wave number in the source medium.

3 Analytical Evaluation of the Matrix Entries

The electric field for a planar printed geometry due the surface current density $\mathbf{J}$ can be written in terms of the mixed-potential integral equation as

$$\mathbf{E} = -j\omega \mathbf{G}^A * \mathbf{J} + \frac{1}{j\omega} G_q * \nabla . \mathbf{J} \tag{5}$$

where $\mathbf{G^A}$ and G_q are the Green's functions of vector and scalar type, respectively and $*$ denotes convolution.With the use of the well-known MoM procedure, the integral equation given in (5) is transformed into the following matrix equation

$$\begin{bmatrix} Z_{xx}^{mn} & Z_{xy}^{mn} \\ Z_{yx}^{mn} & Z_{yy}^{mn} \end{bmatrix} \begin{bmatrix} A_n \\ B_n \end{bmatrix} = \begin{bmatrix} V_x^m \\ V_y^m \end{bmatrix} \tag{6}$$

where Zs denote the mutual impedances between the testing and basis functions, Vs represent the excitation voltages due to the current source(s), and A_n's and B_n's are the coefficients of x-directed and y-directed basis functions, respectively.

For the sake of brevity, the formulation is explained for a typical matrix entry, given as

$$Z_{xx}^{mn} = < T_{xm}, G_{xx}^A * B_{xn} > + \frac{1}{\omega^2} < T_{xm}, \frac{\partial}{\partial x} \left(G_q * \frac{\partial}{\partial x} B_{xn} \right) > \tag{7}$$

where $<,>$ denotes inner product, and T_{xm}, B_{xn} are the testing and basis functions, respectively. The testing and basis functions are chosen to be rooftop functions which are triangular in the longitudinal direction and

constant in the transverse direction. The sources are modeled as current filaments, therefore half-rooftop basis functions are used at the source terminals. The first inner product of (7) is written explicitly as

$$< T_{xm}, G^A_{xx} * B_{xn} >= \int_{D_T}\int dxdy T_{xm}(x,y) \int_{D_B}\int dx'dy' G^A_{xx}(x-x', y-y') B_{xn}(x',y') \tag{8}$$

By changing the order of integration and substituting the closed-form Green's functions given in (4), the inner product takes the form of

$$\begin{aligned} < T_{xm}, G^A_{xx} * B_{xn} > &= \int\int dudv G^A_{xx}(u,v) \int\int dxdy T_{xm}(x,y) B_{xn}(x-u, y-v) \\ &= \sum_{n=1}^{N} a_n \int\int dudv \frac{e^{-jk_s r_n}}{r_n} T_{xm} \otimes B_{xn} \end{aligned} \tag{9}$$

where $\otimes$ denotes correlation function which can be evaluated analytically.

It has been shown that the 2-D integrals given in (9) can be evaluated analytically by replacing the exponential term appearing in (9) with its Taylor's series expansion. The center of expansion is chosen to be the mid point of each integration region and the number of terms in the expansion are chosen to be five. For these choices, the amount of error introduced by the use of Taylor's series expansion is limited by 10^{-4}. The elimination of the numerical integrals reduces the computation time approximately by a factor of 40.

Although, the matrix-fill time has been significantly reduced with this approach, there is still possibility for improvement. This is recognized from the fact that the Taylor's series expansion is applied for every exponential function in the closed-form Green's function expression and the analytic integration is performed for every exponential. To avoid this repetation, the overall summation is approximated in the least square sense by a polynomial as

$$\sum_{n=1}^{N} a_n \frac{e^{-jk_s r_n}}{r_n} \cong \frac{\beta_0}{R} + \beta_1 + \beta_2 R + \beta_3 R^2 + \beta_4 R^3 + \beta_5 R^4 \tag{10}$$

where $R = \sqrt{x^2+y^2}$. As the resultant polynomial is a function of R only, the analytical integrations are performed only once. Since the polynamial approximation can not be applied for the matrix entries which contain singularities, it is used in the calculation of all the matrix entries except for the self and adjacent terms. The improvement obtained in the matrix fill time is approximately 10-15 times as compared to the Taylor's series approximation method.

A similar formulation as summarized in this section can be applied for the second inner product term in (7), after transfering the differentiation on the convolution integral onto the testing function with the use of integration by parts.

4 Analysis of Planar Structures with Vertical Connections

With the introduction of a vertical connection to the planar geometry, z-directed basis currents (B_z) are used in addition to x- and y- directed basis currents, all of which are chosen to be rooftop functions in this study. At the sink terminals where the shorting pins or via holes are terminated in the gorund plane, half-rooftop functions are used as in the case of source terminals. At the intersection of vertical and horizontal conductors, half-rooftop and saw-tooth basis functions are employed on the vertical and horizontal conductors, respectively, whose amplitudes are related to satisfy the conservation of charges, Fig. 3.

As additional basis functions are used, the impedance matrix given in (6) is augmented and the additional entries are denoted by Z_{xz}, Z_{yz} and Z_{zz}. The entries corresponding to Z_{zz} can be calculated by using the tactics given in the previous section. Since Z_{xz} and Z_{yz} contain similar expressions, the difficulties encountered in the formulation of vertical connections will be presented by using the expression of Z_{xz} only, which is given as

$$Z^{mn}_{xz} = \frac{1}{j\omega} \left\langle T_{xm}, \frac{\partial}{\partial x} \left[G^q_z * \frac{\partial B_{zn}}{\partial z} \right] \right\rangle \tag{11}$$

where the Green's function of the scalar potential due to the vertical electric dipole is denoted by G^q_z.

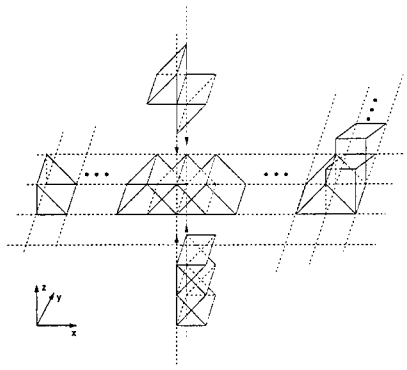

Figure 3: Rooftop basis functions

In the application of the exponential approximation method explained in section 2, the parameters, z and z', should be fixed, in order to be able to sample the function over the range of approximation. Although fixing z and z' does not pose a problem for the analysis of horizantal conductors, the evaluations of the MoM matrix entries corresponding to the vertical metalizations are problematic as they involve convolution integrals and inner-product integrals which are to be integrated over z and/or z'. This difficulty can be eliminated by recognizing that the amplitudes of the up- and down-going waves in the spectral-domain Green's functions are the exponential functions of z and z' that can be factored out. As an example, $\tilde{G}_z^q$ can be written as

$$\begin{aligned}\tilde{G}_z^q \;\propto\; & [e^{-jk_z|z-z'|} + A(k_\rho)(e^{-jk_z(z+z')} + B(k_\rho)e^{-jk_z(z-z'+2d_i)}) \\ + \; & C(k_\rho)(e^{-jk_z(2d_i-z-z')} + D(k_\rho)e^{-jk_z(z'-z+2d_i)})] \end{aligned} \tag{12}$$

where A, B, C and D are the coefficients which are not functions of z and z', d_i is the thickness of the source layer. There are two different approaches to handle the difficulty associated with the z and z' variations. If the vertical connection is short enough to be approximated by a single basis function, the integration over z and z' is performed analytically in the spectral domain, then the exponential approximation is employed. In addition to the basis function on the vertical connection, there is a half-rooftop function at the sink terminal. Hence, the integration on z and z', and the approximation should be performed three times for the evaluation of each inner product. The exponential approximation of the integrated spectral-domain Green's functions with the GPOF method should be performed with care, because it has been observed that the functions obtained after evaluating z and z' integrals may contain peaks for intermediate values of k_ρ. Therefore, to capture such behaviours efficiently, the two-level approximation scheme is extended to three-levels for these terms.

On the other hand if the vertical connection is long, the exponential approximation is applied to each coefficient A,B,C and D to obtain z and z' explicitly in the approximation. The cost of this approach is to apply the GPOF method three times more as compared to approximating the Green's function as a whole.

5 Results and Discussions

In this section, application of the formulation presented in this paper is demonstrated on some practical geometries and the results are compared with those obtained from a commercial EM analysis program *em*, version 3.0 (SONNET Software Inc.). First example is a coupled-line band-pass filter whose geometry and layer informations are given in Fig. 4.a. The analysis of this filter is performed by using the method described here and by the *em* software, the results are in perfect agreement as shown in Fig. 4.b.

As a second example, a geometry with a vertical connection is chosen and a square-spiral MMIC inductor terminated in a short circuit as shown in Fig.5.a is analyzed. The input impedance of the inductor at the reference plane (P1) is plotted in Fig. 5.b.

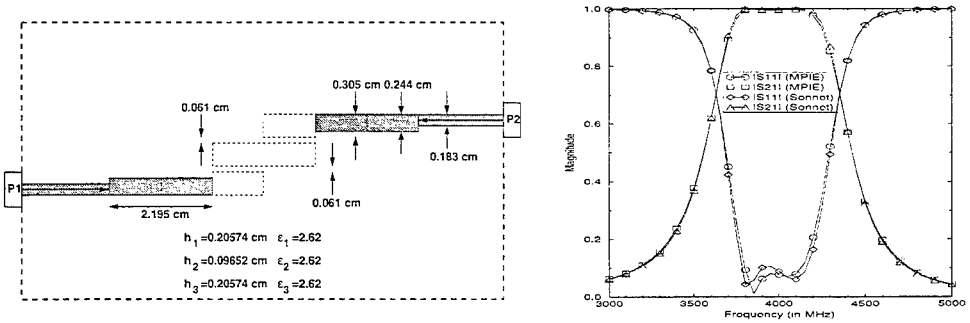

(a) Numbering of the layers is from ground plane to free-space (b)

Figure 4: Coupled line band-pass filter a) geometry, b) frequency characteristic

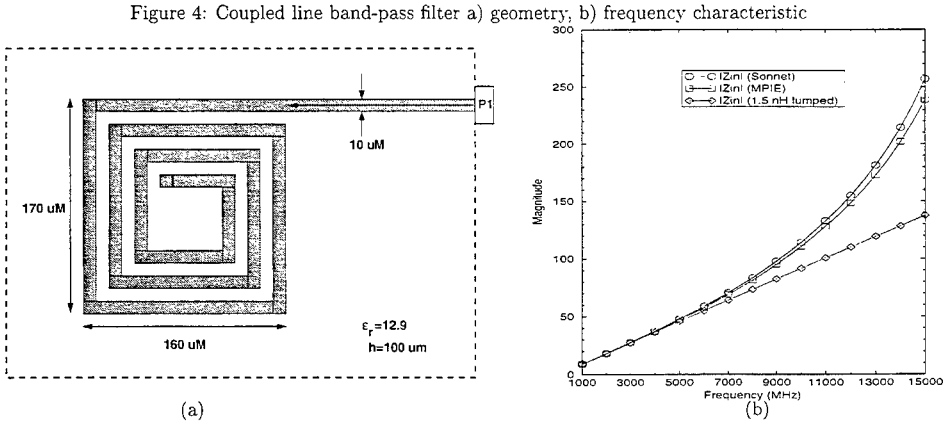

(a) (b)

Figure 5: Square-spiral inductor a) geometry, b) input impedance

The use of the closed-form Green's functions method and the analytical evaluation of the matrix entries improves the matrix-fill time significantly. However, this alone is not enough for a useful CAD design tool, in addition matrix solution time has to be improved as well. One simple strategy for speeding up the computation is to recognize that in interactive design or optimization, typically the entire geometry of the circuit or antenna is not changed at each iteration, but that only a small part of it is either deleted or augmented. Thus, at each iteration step, only a few rows and columns are added to, or deleted from, the matrix system utilized in the previous iteration step. For such iterative design problems ORGE method, which constructs the solution of the modified matrix equation by utilizing the one generated in the previous iteration, can be employed efficiently. Hence, a region to be optimized at the beginning of the process is selected and the remainder of the structure, which will remain unaltered, is designated as the "main structure". Next, the entire structure is divided into cells, the corresponding spatial-domain MoM matrix is filled and the matrix thus computed is stored. The matrix entries corresponding to the main structure are selected from the stored matrix, and the LU decomposed form of the matrix is obtained by using the Gaussian elimination method. Next, the matrix entries corresponding to the "region to be modified" are selected and appended to the end of the LU decomposed matrix. Finally, the contribution of the modified region is calculated by using the ORGE method.

With the incorporation of the schemes of improving the matrix fill and solution times in the MoM procudure, we obtain a very efficient analysis technique that can be used in conjunction with an optimization procedure

very efficiently. It should be recognized, however, that different optimization algorithms may be employed for different applications to fit the characteristics of the problem. In one of the applications, Genetic Algorithms (GA) [8] is used to optimize the geometrical properties of a printed circuit configuration. In this method, the shape of the metallic etch that needs to be optimized is divided into subregions (cells) and GAs are applied to determine whether or not a particular cell is to be metalized. The encoding process of this problem is very easy as the code of each cell in the modified region is set equal to 1 if it is metalized, and 0 otherwise.

GAs are applied to obtain a circularly polarized antenna by removing some portions of the metalization from the opposite corners of a square patch antenna. In center-fed square patch antennas, circular polarization can be achieved by exciting two diagonal modes in such a way that the resonant frequency of one of them will be higher than that of the other. This can be achieved by disturbing the field variation of one of the diagonal modes [9].This disturbance can be obtained either by placing a diagonal slot at the center or by perturbing the opposite corners of the patch. The frequency of operation should be adjusted such that the two diagonal modes are excited in phase quadrature.

A center-fed square patch antenna with parameters, ϵ_r=2.56, d=0.3175 cm, L=W=6.12cm is divided into 21×21 cells. The state of the two 5×5 cells, which are located at the opposite corners of the antenna are chosen as the parameters to be optimized. The best result (axial ratio=1.09) at 1.48 GHz is obtained for the geometry shown in Fig.6.a. The polarization pattern of the antenna is measured by rotating the test antenna opposite to a linearly polarized antenna. The measured polarization pattern is plotted in Fig.6.b and the measured axial ratio is found to be 1.15, which is in good agreement with the simulation results.

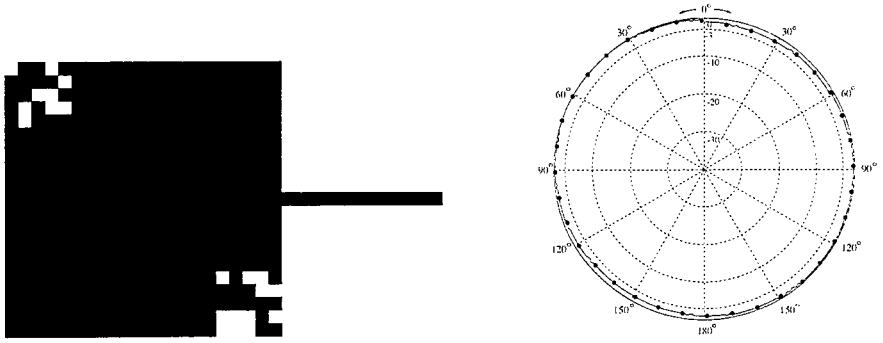

(a) (b)

Figure 6: Circulary polarizied antenna a) geometry, b) polarization pattern

In a different type of application, the dimensions of the geometry are optimized by using a directional (gradient) search algorithm. The use of a uniform meshing for this problem leads to a relatively large number of unknowns if one desires to observe the effects of small changes in the dimensions of the structure. Hence, to eliminate this problem, we use non-uniform meshing and optimize the width of the non-uniform sections. Steepest descent method is used to optimize the dimensions of an inset-fed antenna shown in Fig.7.a. As shown in Fig.7b, the widths of the two sections are chosen to be the variables and are optimized to obtain a good matching condition. An inset-fed patch antenna with parameters ϵ_r=2.33, d=1.5748 mm, W=7.62 mm is optimized and it is found that a perfect match at 11 GHz is obtained when the length of the patch is 8.12 mm and the depth of the notch is 1.88 mm.

6 Conclusion

It is demonstrated that the efficient and robust derivation of the closed-from Green's functions in the spatial-domain has improved the computational efficiency of the MoM for planar geoemtries in multi-layer media.

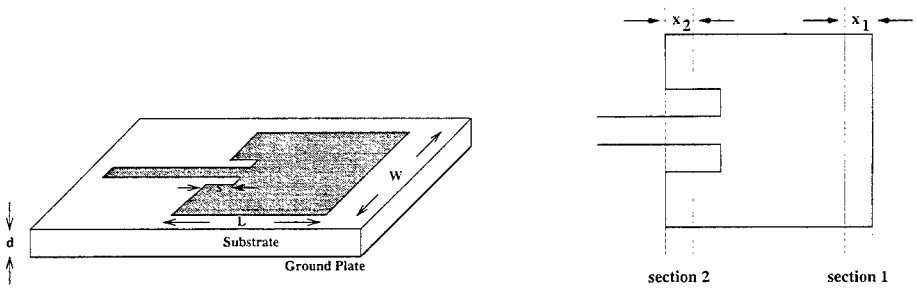

(a) (b)

Figure 7: Inset-fed antenna geometry

Moreover, the difficulties in the use of these closed-form Green's functions in the analysis of geometries with vertical metalizations are eliminated with the use of the tactics discussed in this paper. Further improvement on the computational efficiency of the spatial-domain MoM is obtained by the analytical evaluation of the MoM matrix entries. The formulation is applied to some realistic geometries, for which the scattering parameters and relevant circuit parameters are extracted and compared to those obtained from a well-known commercial software, em from SONNET. A natural extension of the above effort was to incorporate this analysis technique into an optimization algorithm and to asses its potential as a CAD tool. With this background in mind, we have employed the Gradient search and Genetic algorithms, in conjunction with the EM simulation technique, to a representative examples of interest.

References

[1] Y. L. Chow, J. J. Yang, and D. F. Fang and G. E. Howard, "Closed form spatial Green's function for the thick substrate," *IEEE Trans. Microwave Theory Tech.*, vol. MTT-39, no. 3, pp. 588-592, Mar. 1991.

[2] G. Dural and M. I. Aksun, "Closed-form Green's functions for general sources and stratified media," *IEEE Trans. Microwave Theory Tech.*, vol. MTT 43, No. 7,pp. 1545-1552, July 1995.

[3] M. I. Aksun, " A robust approach for the derivation of the closed-form Green's functions," *IEEE Trans. Microwave Theory Tech.*, Vol. MTT-45, No. 5,pp. 651-658, May 1996.

[4] L. Alatan, M. I. Aksun, K. Mahadevan, and M. T. Birand, " Analytical evaluation of the MoM matrix elements, " *IEEE Trans. Microwave Theory Tech.*, Vol. MTT-44, pp. 519-525, April 1996.

[5] N. Kınayman, M. I. Aksun, " Efficient use of closed-form Green's functions for the nalysis of planar geometries with vertical connections ", accepted to be published in *IEEE Trans. Microwave Theory Tech.*.

[6] K. Naishadham, and P. Misra, " Order recursive Gaussian elimination and efficient CAD of microwave circuits," *Proceedings of IEEE MTT-S International Microwave Symposium*, vol. 3, pp. 1435-1438, Orlando, May 16-20, 1995.

[7] Y. Hua and T. K. Sarkar, " Generalized pencil-of-function method for extracting poles of an EM system from its transient response,"*IEEE Trans. Antennas Propagat.*, vol. AP-37, pp. 229-234, Feb. 1989.

[8] L. Davis, Ed., *Handbook of Genetic Algorithms*, New York: van Nostrand Reinhold, 1991.

[9] P. C. Sharma, and K. C. Gupta, " Analysis and optimized design of single feed circularly polarized microstrip antennas, " *IEEE Trans. Antennas and Prop.*, vol. AP-31, pp. 949-955, Nov. 1983.

Analysis and synthesis of conformal microstrip antennas with a fast and accurate algorithm using new symbolic objects.

by Jean-Pierre Damiano, Jean-Marc Ribero, Martine Scotto

Laboratoire d'Electronique, Antennes et Télécommunications, Université de Nice-Sophia Antipolis
CNRS, Bât.4, 250 rue Albert Einstein, 06560 Valbonne, France, tel: +33.4.92.94.28.00, fax: +33.4.92.94.28.12

Abstract

Conformal microstrip antennas on arbitrary curved surfaces are recently used for mobile communications. Analysis and simulation are always a critical task. The complexity of the electromagnetic equations and the cost of real experiment plead in favour of new kinds of simulations. This paper presents a fast and accurate symbolic algorithm allowing the analysis and the synthesis of conformal microstrip antennas. Some examples are considered.

Introduction

The rigorous models or investigations (full wave method, moment method, modal expansion, etc.) are time consuming and are not easily included in C.A.D. package. Here we propose an original algebraic tool to determine the resonance frequency of some conformal antennas. We have developed some symbolic objects whose aim is to generate analytical solution of various Helmholtz equations in different coordinate systems taking into account boundary and continuity conditions. A special family of objects helps us to evaluate the scalar Green's function and the charge distribution adapted to compute the dynamic permittivity necessary to obtain the expression of the resonance frequency. For it, we use an efficient Computer Algebra System (C.A.S.).

A C.A.S. consists of automatically transforming mathematical formulas. Its initial principle consists of changing expressions into polynomial form, so that both algebraic and arithmetic concepts are used [1,2]. We give in appendix 1 some details on C.A.S. We have chosen MAPLE, because of its ability to handle very large expressions using a reasonable amount of storage space while maintaining good runtime performances.

A symbolic algorithm is built differently from a purely numerical algorithm. A complex problem must be broken down into several well thought-out stages [3]. Defining the equations to be solved, the solution techniques, the choice of their solutions must be done rigorously. This is the price to pay if one expects, for example, accurate expressions of the zeros of equations or exact algebraic evaluation of Green's functions. We show in the next section how are built the symbolic objects corresponding to the data of the theoretical problem.

A last step consists of the coding of all the used objects in Visual Basic on personal computers for numerical simulations.

The symbolic objects

In figure 1, we present the philosophy of our symbolic algorithm. The originality consists to solve analytically all the basis equations with the boundary and continuity conditions verified by the electric field or the scalar potential [1]. The radiocharacteristics of the antenna are expressed in polynomial form that allows to be included in C.A.D. systems and to work very quickly.

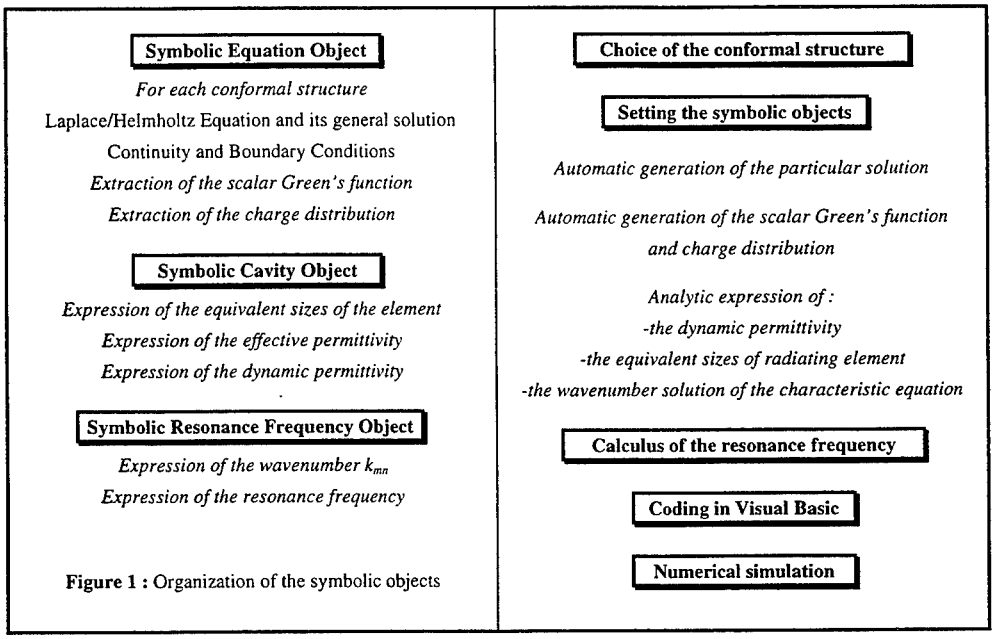

Figure 1 : Organization of the symbolic objects

Equation Objects

The aim is the automatic generation of the basis equations, Helmholtz type for example, for various conformal antenna and the deduction of their general solution. By the imposition of the continuity and boundary conditions, we obtain the algebraic expression of the scalar potential or the electric field.

For a conical structure, the Helmholtz equation is satisfied by E_θ :

$$\frac{1}{r^2}\frac{\partial}{\partial r}\left(r^2\frac{\partial E_\theta}{\partial r}\right)+\frac{1}{r^2\sin\theta}\frac{\partial}{\partial\theta}\left(\sin\theta\frac{\partial E_\theta}{\partial\theta}\right)+\frac{1}{r^2\sin^2\theta}\frac{\partial^2 E_\theta}{\partial\Phi^2}+k^2E_\theta=0 \qquad (1)$$

The general solution is :

$$E_\theta(r,\theta,\phi)=[A_\lambda j_\lambda(k_{nm}r)+B_\lambda n_\lambda(k_{nm}r)]\,[P^m{}_\lambda(\cos\theta)+Y_\lambda Q^m{}_\lambda(\cos\theta)]\,[C_m\sin(m\phi)+D_m\cos(m\phi)] \qquad (2)$$

where $j_\lambda(x)$ and $n_\lambda(x)$ are the spherical Bessel functions of first and second kind. $P^m{}_\lambda(x)$ and $Q^m{}_\lambda(x)$ are the associated Legendre functions of first and second kind. All the constants are calculated from the boundary conditions given by the following relations :

Electric wall (TM_{mn} mode)

$$\left|\frac{d}{d\theta}\left(P_\lambda^m(\cos\theta)\right)\right|_{\theta=\theta_0}=0$$

Magnetic wall,

$$j_\lambda'(k_{mn}r_b)\,n_\lambda'(k_{mn}r_a)-j_\lambda'(k_{mn}r_a)\,n_\lambda'(k_{mn}r_b)=0 \qquad (3)$$

For a spherical structure, the scalar potential distribution verifies a Laplace equation in spherical coordinates. The symbolic object generates the algebraic expression of the solution which is :

$$\Phi(r,\theta,\phi)=\sum_{m=0}^{\infty}\sum_{n=0}^{\infty}\left[Ar^{n}+Br^{-(n+1)}\right]P_{n}^{m}(\cos\theta)e^{jm\varphi} \tag{4}$$

where $P_n^m(\cos\theta)$ are the associated Legendre functions, that satisfy the condition of finite field for $\theta=0,\pi$. In the case of the TM_{0n} (azimuthal symmetry), these functions are reduced to Legendre polynoms, and the solution becomes :

$$\Phi(r,\theta)=\sum_{n=0}^{\infty}\left[Ar^{n}+Br^{-(n+1)}\right]P_{n}(\cos\theta) \tag{5}$$

All the field quantities (potential, charge density distribution on the patch $\rho(r,\theta,\phi)$) are expressed in the form of Legendre series, and the following transform is used :

$$\tilde{F}(n)=\frac{(2n+1)(n-m)!}{2(n+m)!}\int_{0}^{\pi}F(\theta)P_{n}^{m}(\cos\theta)\sin\theta d\theta \tag{6}$$

Each term of the sum (4) is therefore written in the spectral domain as :

$$\tilde{\Phi}(r,n)=\left[Ar^{n}+Br^{-(n+1)}\right] \tag{7}$$

where we have suppressed the term $e^{jm\phi}$.

The symbolic object generates automatically the expression of the scalar Green's function $\tilde{g}(n)$ and the charge distribution. The structure is presented in figure 4. The expression of $\tilde{g}(n)$ is given below :

$$\tilde{g}(n)=\frac{\left[1-r_0^{2n+1}r_1^{-(2n+1)}\right]r_1}{(n+1)+n\varepsilon_r+r_0^{2n+1}r_1^{-(2n+1)}(n+1)(\varepsilon_r-1)} \tag{8}$$

Cavity Model Object

Our theoretical study is based on a modified cavity model which we have adjusted to the treatment of the conformal structure. We associate the boundary conditions of electrical and magnetic walls to the concept of dynamic permittivity [1,4] to take into account physical and geometrical parameters and fringing effects. Assuming that the thickness of the dielectric substrate h is relatively small with the dielectric wavelength, only one component of the electric field is predominant. In addition, for the small curvature radius, this component satisfies the Helmholtz equation, for example in the case of the cone.

This object gives a general expression of the dynamic permittivity ε_{dyn} in which we replace the unknown quantities (scalar Green's function, charge distribution, etc.) by that calculated by the Equation Object.

Resonance Frequency Object

From the modified cavity model [1,4], the resonance frequency depends upon :

-the dynamic permittivity ε_{dyn} for which it is necessary to know the effective permittivity ε_{eff}. Considering the radiating element as an open microstrip line, the variational expression of the capacitance allows us to take into account the layers of dielectric substrates with the scalar Green's

functions and the shape of the element with the charge distribution. We then obtain the effective permittivity and the equivalent dimensions of the patch and then, the dynamic permittivity.

-the expressions of the zeros k_{mn} of the characteristic equation.

-the equivalent sizes of the radiating element.

This object returns a algebaric expression of the resonance frequency taking into account all the previous analytical results of the other objects.

Thus, the analysis as well as the synthesis of conformal printed antennas are available.

Simulations

Conical structure

The Equation Object allows us to obtain an analytical polynomial expression of the zeros of the characteristic equation and the analytical relations between the order λ of the spherical Bessel functions and the half angle θ_0 of the cone (figure 2) versus geometrical parameters [1]. For example, after symbolic solving, we have a polynomial relation between the product $k_{mn}\ r_{aeq}$ and the ratio $R_{eq}=r_{beq}/r_{aeq}$ available for $1.2 < R_{eq} < 2.6$. k_{mn} represents the wave number of the equivalent cavity.

$$k_{mn}\ r_{aeq} = 1.841183781 + 44315.82028195981\ Req^{-31} - 153336.59705194\ Req^{-29} + 186046.0794919215\ Req^{-27} - 63977.3011547717\ Req^{-25} - 22949.8078072233\ Req^{-23} - 44680.04679851\ Req^{-21} + 116321.3981495437\ Req^{-19} - 79167.105854849\ Req^{-17} + 7642.63160633189\ Req^{-15} + 19526.48111883166\ Req^{-13} - 12472.84193728154\ Req^{-11} + 3077.68157834161\ Req^{-9} + 8.Req^{-7} - 196.9348317052172\ Req^{-5} + 64.380990152\ Req^{-3} - 5.28361693137724\ Req^{-1} \quad (9)$$

The figure 3 shows the evolution of the ratio R_{eq} versus the impressed resonance frequency. We compare our theoretical model working in synthesis with the experiments and some published theoretical results [5]. A very good agreement is observed.

Spherical structure

In order to speed up the evaluation of the effective permittivity, we have derived, the asymptotic behavior of $\tilde{g}(n)$, given by :

$$\tilde{g}_{asympt}(n) = \frac{0.00305}{0.055(\varepsilon_r+1)n} - \frac{0.000166375}{(0.055(\varepsilon_r+1)n)^2} \quad (10)$$

As it is not distinguishable from the exact for n>=20 (see figure 5), it can be substituted at this last in the sum, at least when n>20, yielding a drastical reduction of the computational time, in the numerical phase.

Conclusion

We have presented a algebraic approach to study conformal microstrip antennas. The originality is the availability to work in analysis and synthesis that is very useful for design's engineer in microstrip antennas. With the help of Computer Algebra Systems, it is possible to solve more easily and analytically complex electromagnetic equations.

Acknowledgments

We wish to thank Paola Pirinoli, at Dipartimento di Elettronica, Politecnico di Torino, Italy, for the advice, availability and interest with which she accompanied a part of this study.

References

1 J.P. Damiano, M. Scotto, J.M. Ribero, «New application of an algebraic tool to fast analysis and synthesis of conformal printed antennas », Electronics Letters, 1996, vol.32, n°22, pp.2033-2035.

2 J.P. Damiano, M. Scotto, J.M. Ribero, « The computer algebra systems and the electromagnetic problems », IEEE-AP Magazine, 1996, December.

3 J.P. Damiano, M. Scotto, J.M.Ribero, P. Nicotra, « Fast and accurate algebraic tool for C.A.D. applied to the analysis and synthesis of printed antennas on conical and spherical surfaces », Journées Internationales de Nice sur les Antennes, JINA, Nice, F., 1996, 12-14 nov., pp.691-694.

4 J.P. Damiano, J.M. Ribero, R.Staraj, "Original simple and accurate model for elliptical microstrip antennas", Electronics Letters, 1995, vol. 31, n° 13, pp. 1023-1024.

5 R. Descardeci, A.J. Giarola, « Microstrip antennas on a conical surface », IEEE Trans., 1992, vol.AP-40, n°4, pp.460-463.

Appendix 1 : *The Computer Algebra System*

Using a computer algebra system can be of great help to the programmer. The characteristics are presented in table 1.

Manipulative operations in Arithmetic, Analysis, Polynomial/Matrix Algebra, *etc* Simplification, substitution, factorisation	**Some other characteristics** 3D powerful visualization, Simulation language Coding in Fortran/C, Results in Postscript/Tex form
Advantages Exact arithmetic, Speedy, efficient tools Large library of mathematical functions	**Interested fields** Mechanical / Electrical Engineering Mathematics, Physics, Electromagnetics, *etc.*

Table 1. *The Computer Algebra Systems*

To be attractive and helpful from an engineer's point of view, a package must combine a very good symbolic calculus system, an efficient numerical calculus module and a powerful 3D graphical interface. However the feasibility of calculus is often difficult to demonstrate. It is difficult to anticipate the computation time and the amount of memory resources required when solving a given problem. The simplification of the rough expressions obtained from the system is an important stage. The numerical phase consists of C, Fortran or Visual Basic coding.

The next tables 2 and 3 offer various sources of information on C.A.S. :

alt.algebra.help	de.sci.mathematik	sci.math.research
comp.soft-sys.math.mathematica	sys.matlab	sci.math.stat
comp.soft-sys.matlab	sci.math	sci.math.symbolic

Table 2. *Some newgroups on Internet*

Axiom 2.0	http://www.nag.co.uk:80/symbolic/AX.html
Derive 3.0	http://www.derive.com/
Macsyma 2.1	http://www.macsyma.com/
Maple V.4	http://www.maplesoft.com/
MathCad 6.0	http://www.mathsoft.com/
Matlab 5	http://www.mathworks.com/
Mathematica 3.0	http://mathsource.wri.com/
MuPad 1.3.0	http://math-www.uni-paderborn.de/MuPAD/
Reduce 3.6	http://www.rrz.uni-koeln.de/REDUCE/, http://ufer.zib-berlin.de/Symbolik/reduce/
Theorist	http://www.maplesoft.com/

Table 3. *SomeWorld Wide Web servers of various C.A.S. on Internet*

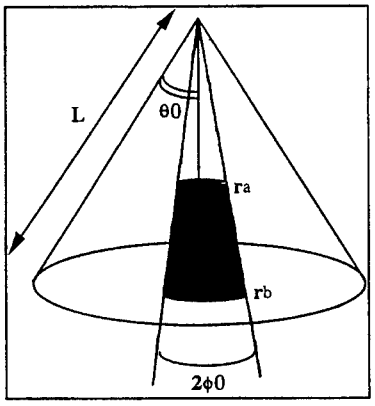

Figure 2 : Geometry of the conical antenna
θ_0 : half angle of the cone
r_a : inside radius, r_b : outside radius, L : cone length
$2\,\phi_0$: azimuthal length of the patch

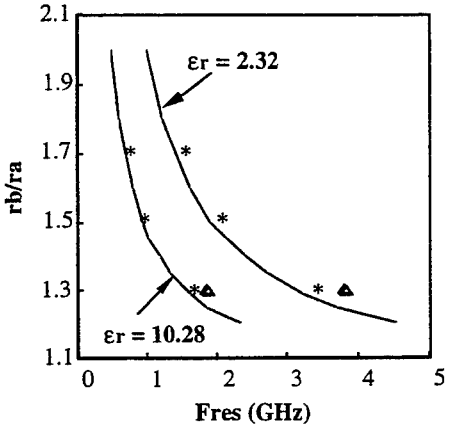

Figure 3 : Synthesis in TM_{01} mode
h = 1.14 mm, ra = 10 cm, $\theta_0 = 33.88°$, $\phi_0 = 9.17°$
—— Our Model ▲ Theory [5], * Our experiments

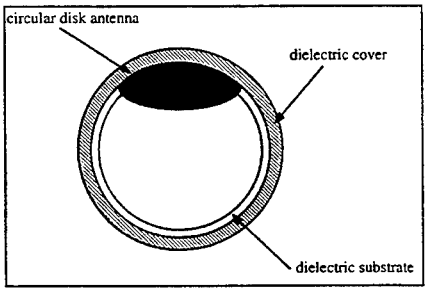

Figure 4: Spherical microstrip antennas
r_0 is the radius of the sphere
$r_1 = r_0 + h$ *(substrate thickness)*

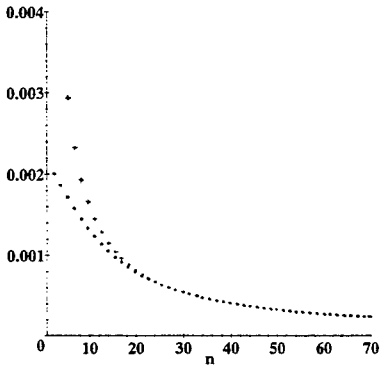

Figure 5 : Exact (o) and asymptotic (+) scalar Green's function versus the n order. r_0=5 cm, h=5 mm, εr=2.33
(no dielectric cover)

Space/Time Adaptive Meshing and Multiresolution Time Domain Method (MRTD)

Emmanouil Tentzeris[1], Andreas Cangellaris[2], Linda P.B. Katehi[1]
[1]Radiation Laboratory, EECS Department, University of Michigan,
Ann Arbor, MI 48109-2122, USA
[2]University of Arizona, Tucson, AZ, USA

I Introduction

Recently the principles of the Multiresolution Analysis have been successfully applied [1, 2] to the time-domain numerical techniques used for the analysis of a variety of microwave problems. New techniques have been derived by the use of scaling and wavelet functions for the discretization of the time-domain Maxwell's equations. The multiresolution time domain technique (MRTD) based on Battle Lemarie functions has been used for the simulations of planar circuits and resonating structures. The conventional FDTD absorbers (e.g. PML) have been generalized in order to analyze open planar structures. MRTD has demonstrated unparalleled savings in execution time and memory requirements (2 orders of magnitude for 3D problems). In addition to time and memory, MRTD technique can provide space- and time- adaptive meshing without the problems that the conventional FDTD variable grids are encountering (e.g. reflections between dense-coarse regions). This unique feature stems from the use of two separate sets of basis functions, the scaling and wavelets. Due to the excellent conditioning of the formulated mathematical problem, MRTD offers the capability to threshold the wavelet field coefficients. This advantage of the MRTD Technique is demonstrated herein by performing a space-/time-adaptive meshing.

In this paper, a space-/time- adaptive meshing algorithm based on the MRTD scheme is proposed and validated for a specific waveguide problem. Wavelets up to the second resolution are placed only at locations where the EM fields have significant values. These locations are changing with the time as the pulse is propagating inside the waveguide and with the space as the pulse is approaching regions of discontinuities. The proposed algorithm offers the opportunity of a space-/time- adaptive mesh with variable resolution of the field representation. In this way, significant memory and execution time savings can be achieved in comparison to the conventional variable-mesh FDTD algorithms.

II MRTD Formulation

Without loss of generality, the 2D-MRTD scheme for the TM_z modes will be described herein. To derive the scheme equations, the field components are represented by a series of cubic spline Battle-Lemarie scaling and 1-order wavelet functions along the z-direction, while pulses are used for the time representation. Wavelets of higher-order can be included in a similar way. After inserting these series expansions in Maxwell's equations and sampling them with pulse functions in time and scaling/wavelet functions in space domain, we derive the following equations for the electric field:

$$\frac{1}{\Delta t}({}_{k+1}D^{\phi x}_{l+1/2,m} - {}_{k}D^{\phi x}_{l+1/2,m}) = -\frac{1}{\Delta z}(\sum_{i=m-m_2}^{m+m_1} a(i)_{k+1/2}\, H^{\phi y}_{l+1/2,i+1/2} + \sum_{i=m-m_4}^{m+m_3} b(i)_{k+1/2}\, H^{\psi y}_{l+1/2,i+1/2})$$

$$\frac{1}{\Delta t}({}_{k+1}D^{\psi x}_{l+1/2,m} - {}_{k}D^{\psi x}_{l+1/2,m}) = -\frac{1}{\Delta z}(\sum_{i=m-m_4}^{m+m_3} b(i)_{k+1/2}\, H^{\phi y}_{l+1/2,i+1/2} + \sum_{i=m-m_6}^{m+m_5} c(i)_{k+1/2}\, H^{\psi y}_{l+1/2,i+1/2})$$

$$\frac{1}{\Delta t}({}_{k+1}D^{\phi z}_{l,m+1/2} - {}_{k}D^{\phi z}_{l,m+1/2}) = \frac{1}{\Delta x}(\sum_{i=l-l_2}^{l+l_1} a(i)_{k+1/2}\, H^{\phi y}_{i+1/2,m+1/2}) \quad ,$$

$$\frac{1}{\Delta t}({}_{k+1}D^{\psi z}_{l,m+1/2} - {}_{k}D^{\psi z}_{l,m+1/2}) = \frac{1}{\Delta x}(\sum_{i=l-l_4}^{l+l_3} c(i)_{k+1/2}\, H^{\psi y}_{i+1/2,l+1/2}) \quad ,$$

where ${}_{k}D^{\xi x}_{l,m}$, ${}_{k}E^{\xi x}_{l,m}$ and ${}_{k}H^{\xi y}_{l,m}$ with ξ=ϕ (scaling),ψ (wavelets) are the coefficients for the electric flux, electric and magnetic field expansions. The indices l, m and k are the discrete space and time indices, which are related to the space and time coordinates via $x = l\Delta x$,$z = m\Delta z$ and $t = k\Delta t$, where Δx,Δz are the space discretization intervals in x- and z-direction and Δt is the time discretization interval. The coefficients $a(i), b(i), c(i)$ are derived and given in [1]. For an accuracy of 0.1% the values $m_1 = m_5 = 8$, $m_2 = m_3 = m_4 = m_6 = 9$ have been used. The indices l_i have to take similar values to achieve tha same accuracy in the summations.

The use of non-localized basis functions in the 2D-MRTD scheme causes significant effects. Localized boundary conditions are impossible to be implemented, so the perfect electric boundary conditions are modelled by use of the image principle in a generic way. The implementation of the image theory is performed automatically for any number of PEC, PMC boundaries. The material discontinuities are represented in terms of scaling and wavelet functions resulting into a linear matrix equation as explained in [1, 3] where this technique was used in the modeling of anisotropic dielectric media. In addition, the total value of a field component at a specific point of the mesh is a summation of the contributions from the neighbooring non-localized scaling and wavelet functions. The field values at the neighbooring cells can be combined appropriately by adjusting the scaling and wavelet function values and by applying the image principle.

The demand for the simulation of open structures led to the generalization of the perfectly matched layer (PML) technique [4], so as it can be used in the MRTD simulations. The conductivity is expanded in terms of scaling functions instead of pulse functions with respect to

space. The amplitudes of the expansion scaling functions follow the PML spatial conductivity distribution. In our simulations, the parabolic distribution was used, though the realization of other distributions (linear, cubic, ...) is straightforward. For example, if we assume that the PML absorbing material $(\epsilon, \mu, \sigma^E)$ extends to the z-direction, substituting

$$D^{(i)x,z}(x,z,t) = \tilde{D}^{(i)x,z}(x,z,t)e^{-\sigma^E_{(z)}t/\epsilon} \tag{1}$$

and

$$H^{(i)y}(x,z,t) = \tilde{H}^{(i)y}(x,z,t)e^{-\sigma^H_{(z)}t/\mu} \tag{2}$$

for i=ϕ, ψ, leads to the following equation:

$$\frac{\partial \tilde{D}^x}{\partial t} = -\frac{\partial \tilde{H}^y}{\partial y} \quad . \tag{3}$$

Following a procedure similar to the one used for the derivation of the non-PML region equations, we get for D_x components

$$\begin{aligned} {}_{k+1}D^{\phi x}_{l+1/2,m} &= e^{-\sigma^E_{(m\Delta z)}\Delta t/\epsilon}\, {}_kD^{\phi x}_{l+1/2,m} \\ &- \frac{\Delta t}{\Delta z} e^{-\sigma^E_{(m\Delta z)}0.5\Delta t/\epsilon} \Big(\sum_{i=m-m_2}^{m+m_1} a(i)_{k+1/2}\, H^{\phi y}_{l+1/2,i+1/2} + \sum_{i=m-m_4}^{m+m_3} b(i)_{k+1/2}\, H^{\psi y}_{l+1/2,i+1/2} \Big) \quad , \end{aligned}$$

$$\begin{aligned} {}_{k+1}D^{\psi x}_{l+1/2,m} &= e^{-\sigma^E_{(m\Delta z)}\Delta t/\epsilon}\, {}_kD^{\psi x}_{l+1/2,m} \\ &- \frac{\Delta t}{\Delta z} e^{-\sigma^E_{(m\Delta z)}0.5\Delta t/\epsilon} \Big(\sum_{i=m-m_4}^{m+m_3} b(i)_{k+1/2}\, H^{\phi y}_{l+1/2,i+1/2} + \sum_{i=m-m_6}^{m+m_5} c(i)_{k+1/2}\, H^{\psi y}_{l+1/2,i+1/2} \Big) \quad , \end{aligned}$$

The finite-difference equations for $D^{(\phi,\psi)z}$ and $H^{(\phi,\psi)y}$ are similar. For all simulations, a parabolic distribution of the conductivity σ is used in the PML region (N cells):

$$\sigma^{E,H}_{(m\Delta z)} = \sigma^{E,H}_{max}\left(\frac{m}{N}\right)^2 \qquad \text{for m=0,1,..,N,} \tag{4}$$

with $\sigma^{E,H}_{max}$ the maximum conductivity at the end of the absorbing layer. As in [5], the "magnetic" conductivity σ^H is given by:

$$\frac{\sigma^E_{(m\Delta z)}}{\epsilon} = \frac{\sigma^H_{(m\Delta z)}}{\mu} \qquad \text{for m=0,1,..,N,} \tag{5}$$

and the MRTD mesh is terminated by a perfect electric conductor (PEC) at the end of the PML region. This PEC is modelled by applying the image theory.

III Space/Time Adaptive Meshing

The wavelet components' amplitudes have negligible values away from the discontinuities or at regions where the excitation pulse has not propagated yet. There are numerous ways of taking advantage of the above feature. The simplest one is to threshold the wavelet components to a fraction (usually $\leq 0.1\%$) of the scaling component at the same cell (space adaptivity) for each time-step. All components below this threshold are eliminated from the subsequent calculations for the same time-step (time adaptivity). This procedure offers only a moderate economy in memory (factor close to 2). Also, this algorithm allows for the dynamic memory allocation in its programming implementation, while maintaining a low complexity.

The above space-/time- adaptive meshing scheme is applied to the analysis of the partially-loaded parallel-plate waveguide of (Fig.1) for the frequency range 0-22.5GHz. The waveguide is half-filled with air and half-filled with dielectric with $\epsilon_r = 2.56$. An FDTD 16×640 (10240 cells) mesh and an MRTD 2×80 (160 cells) mesh (160 grid points with $dx = 0.18\lambda_o$, $dz = 0.3\lambda_o$ - close to the Nyquist Limit for $f = 22.5GHz$) are used for the Time-Domain simulations (3,000 time-steps). The 160 grid points of the MRTD mesh express the number of the used scaling functions. The number of the wavelets is varying with time and depends on the predefined threshold. For consistency, the time step for both schemes is chosen to be equal to the 1/8 of the FDTD maximum Δt.

The waveguide is excited with a Gabor function 0-22.5GHz along a vertical line for the FDTD simulation and for a rectangular region of 12 cells to the longitudinal direction (due to the non-localized character of the Battle-Lemarie scaling and wavelet functions) for the MRTD simulations. Other excitations (e.g.Gaussian) can be applied i a straightforward way. For both cases, a PML region of 16 cells and σ^E_{max}=0.4S/m absorbs the waves in the front and back open planes. The capability of the MRTD technique to provide space- and time- adaptive gridding is verified by thresholding the wavelet components to the 0.1% of the value of the scaling function at the same cell for each time-step. The accuracy achieved by using only the wavelets with values above the threshold is equal to what would be if wavelets were used everywhere. Though this number is varying in time , its maximum value is 36 out of a total of 160 to the z-direction (economy in memory by a factor of 52 instead of 32). In addition, execution time is reduced by a factor 4-5. For larger thresholds, the ringing effect due to the elimination of the wavelets deteriorates the performance of the algorithm. For example, using a threshold of 1% (13 out of a 160 wavelets to the z-direction) increases the error by a factor of 2.1.

The results for the Reflection Coefficient for 10 GHz are validated by comparison to the theoretical value $|R| = 0.231$ $(=(\sqrt{2.56}\text{-}1.0)/(\sqrt{2.56}\text{+}1.0))$. MRTD gives the value 0.2296 and FDTD gives 0.2304 (similar accuracy). The normal electric field is probed at a distance 10 cells away from the source and is plotted in (Fig.2) in time-domain. Similar accuracy can be observed for

the FDTD and the MRTD meshes.

Fig.3 demonstrates the space- and time-adaptive character of the meshing algorithm. It is clearly shownw that the wavelets follow the propagating exciation pulse before and after the incidence to the dielectric interface and can be omitted elsewhere. The location and the number of the wavelet coefficients with values above the threshold ("effective wavelets") are different for each time-step, something that creates a mesh with high resolution ("dense") in regions of strong field variations, while maintaining a much lower resolution ("coarse") for the rest cells.

IV Conclusion

A simple space- and time- adaptive meshing algorithm based on an MRTD scheme has been proposed and has been validated for a parallel-plate waveguide problem. The electric field value and the reflection coefficient have been calculated and verified by comparison to reference data. The proposed scheme exhibits memory savings by a factor of 52 in 2D, as well as execution time savings by a factor of 4-5, while maintaining a similar accuracy with Yee's conventional FDTD scheme. In addition, this algorithm doesn't increase the programming complexity and can be effectively extended to 3D problems.

References

[1] M.Krumpholz, L.P.B.Katehi, "MRTD: New Time Domain Schemes Based on Multiresolution Analysis", IEEE Trans. Microwave Theory and Techniques, vol. 44, no. 4, pp. 555-561, April 1996.

[2] E.Tentzeris, M.Krumpholz and L.P.B. Katehi, "Application of MRTD to Printed Transmission Lines", Proc. MTT-S 1996, pp. 573-576.

[3] R. Robertson, E. Tentzeris, M. Krumpholz, L.P.B. Katehi, "Application of MRTD Analysis to Dielectric Cavity Structures", Proc. MTT-S 1996, pp. .

[4] E.Tentzeris, R.Robertson, M.Krumpholz and L.P.B. Katehi, "Application of the PML Absorber to the MRTD Technique", Proc. AP-S 1996, pp. 634-637.

[5] J.-P. Berenger, "A Perfectly Matched Layer for the Absorption of Electromagnetic Waves", J. Computational Physics, vol. 114, pp. 185-200, 1994.

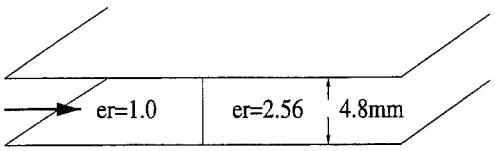

Figure 1: Dielectric-loaded Waveguide.

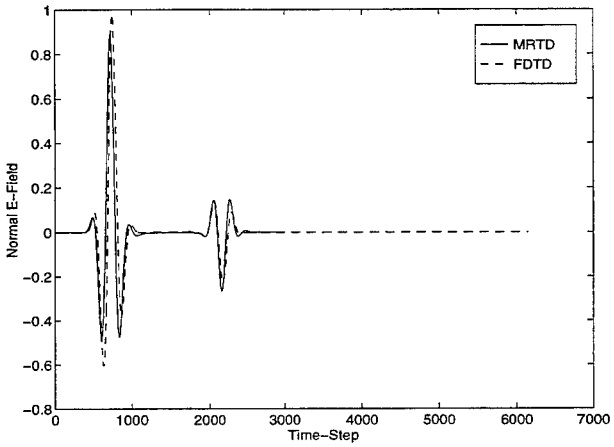

Figure 2: Normal E-field Time Evolution.

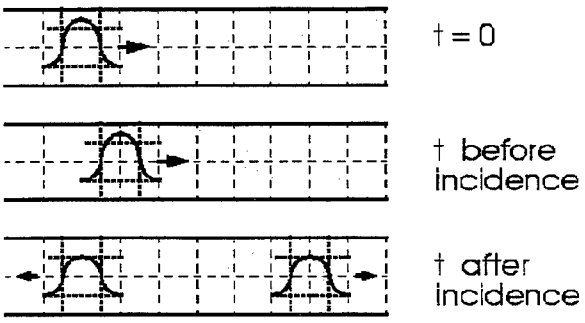

Figure 3: Space-/Time- Adaptive Meshing Demonstration.

Static extraction, "static" basis functions and regularization in the analysis of printed antennas

Giuseppe Vecchi, Ladislau Matekovits, Paola Pirinoli and Mario Orefice
Dipartimento di Elettronica, Politecnico, I-10129 Torino, Italy

Abstract

A novel approach is applied to the EFIE-MoM analysis of printed antennas of arbitrary shape, based on the suitably extracted singular, frequency-independent parts of the integral operator. We first address the basis function decomposition that allows the separation of these terms, and discuss the regularizing effects of their inverse. The eigenfunctions of these singular terms, called "static modes", are entire-domain basis functions that extend and generalize the TM and TE modes of a magnetic-wall cavity to arbitrary geometries. Their use as basis functions is described, giving criteria to select the modes that efficiently represent the solution, including also "attachment" modes that represent the feed structure discontinuities. Other applications of the presented general framework are related to quasi-wavelet representation and sparse conditioning.

1 Introduction

In this paper we will be concerned with the analysis of planar printed antennas of general shape, formulated in terms of an Electric-Field Integral Equation (EFIE), discretized and numerically solved via the Method of Moments (MoM) procedure. For conductors with negligible losses the EFIE numerically behaves as the first-kind equation obtained in the limit of zero losses; this will be the case dealt with in this paper. As well known, the kernel of this equation is strongly singular. For two-dimensional problems for printed structures in layered media, the integral operator associated to the singular part of the kernel can be inverted in closed form, and this allows one to transform the EFIE into a second-kind Fredholm equation with strongly improved numerical properties.

This technique, called here "regularization", has been recently extended by the authors to handle three-dimensional printed structures of general shapes, via a proper separation of the singular and regular parts of the dyadic kernels, and a numerical approach to the inversion of the static-related, frequency-independent singular parts [1]. The resulting formulation shows that the convergence of the solution is guaranteed by the singular behavior of the kernels, provided it is correctly accounted for. This formulation shows that in order to correctly represent the singular part, and invert it, one needs to split the solution space into a solenoidal part, and a remainder that can be called irrotational for ease of reference, although it is not eaxctly so in a strong (pointwise) sense. This separation, introduced first in [2], applied recently by several others, and recently reviewd for an analogous (FEM) problem [3], is dealt with here in Sec. 2 in an alternative manner, that allows an easy generation of the necessary basis functions for these two subspaces, allows for uselful generalizations, and sheds some light on the general setup of the EFIE.

For the sake of clarity and ease of reference, the essentials of the regularization technique are summarized in Sec. 3. It also emerges that the eigenfunctions of the two frequency-independent singular operators are a set of entire-domain basis functions that approximate the (dynamical) solution with a reduced number of terms [1, 4]; the performance can be further enhanced by the introduction of an alternative representation of one of the two classes of functions [7]. In Sec. 4, this will be used to reduce the computational efforts associated with complex structures, like an array, by blending the use of these shape-conforming entire functions functions on the resonant elements (patches) with conventional subsectional functions on the feed structure, including attachment modes for the description of feed-related discontinuities. This way the numerical effort needed to solve the problem is reduced, essentially preserving the same accuracy obtained with a large number of subdomain basis functions, as reported in Sec. 4.1.

2 Loop-Star Decomposition

The necessity for a correct representation of the solenoidal part of the solution (surface current) has emerged from different works and viewpoints [2, 3]. It turns out that the solution of an EFIE problem has to be div-conforming, i.e. able to represent a zero divergence; equivalently, one has to find a set of basis functions able to represent the

solenoidal part of the solution. This is usually done by recognizing that solenoidal currents form closed paths, leading to *loop*-type basis functions [2, 5], or tree and co-tree groupings [3]. As to the remainder subspace, we note that even using infinitely continuous functions (like on separable simple domains) the solution cannot be irrotational in a strong sense, since it must be defined over the entire plane, but vanishing outside the conductors [6]. The irrotational property has therefore to be understood in a weak sense (almost everywhere), especially using subsectional functions.

In the following we will consider only this case, and denote rooftops by $\underline{R}_n$.

The basis functions for the solenoidal and "irrotational" subspaces will be linear combinations of the initial, shape-conforming rooftops, subject to the condition that the mesh be able to close all loops. We adopt a procedure that is naturally suited to our further treatment, but that has the advantage of easily generating these functions on any mesh, and of further allowing for promising extensions.

Beginning with the solenoidal part $\underline{J}''$, we note that the condition $\nabla_t \cdot \underline{J}'' = 0$ everywhere implies

$$\underline{J}''(\underline{\rho}) = \frac{1}{j\omega\mu_0}\nabla_t \times \hat{z}M(\underline{\rho}), \quad \nabla_t \cdot \underline{J}'' = 0, \quad \forall \underline{\rho} \in I\!R^2, \tag{1}$$

(the factor in front of the curl is arbitrary), and therefore this part of the current is represented by the scalar function M, and the solenoidal basis functions are naturally derived from those chosen for M. It is easy to show that the regularity condition for the rooftops translates into the requirement for M to be piecewise linear. As a result, the simplest choice is to employ the scalar linear Lagrange (or nodal interpolating) basis, i.e. piecewise linear functions $\Lambda_\alpha(\underline{\rho})$ going to zero on all neighboring nodes. In the rectangular mesh that will be used in the following for the sake of illustration, each rooftop extends over two rectangular cells of the mesh, and the Lagrange basis functions are pyramids over a rectangle formed by four adjacent cells. The curl operation in (1),

$$\underline{L}_\alpha(\underline{\rho}) = \nabla_t \times \hat{z}\Lambda_\alpha(\underline{\rho}) \tag{2}$$

will generate the rectangular loop basis functions, shown in Fig. 1. These basis functions will be denoted by $\underline{L}(\underline{\rho})$ in the following, i.e.

$$\underline{J}''(\underline{\rho}) = \sum_\alpha I''_\alpha \underline{L}_\alpha(\underline{\rho}) \tag{3}$$

As to the "irrotational part" $\underline{J}'$, it is actually defined to be non-solenoidal, i.e. $\nabla_t \cdot \underline{J}' \neq 0$, which makes $\underline{J}'$ be defined (uniquely) by its divergence, called in the following "charge", and denoted by $q(\underline{\rho})$. We denote by $\underline{X}_\alpha(\underline{\rho})$ the basis functions spanning the space of $\underline{J}'$, each being a combination of rooftops $\underline{R}_n(\underline{\rho})$, i.e.

$$\underline{J}'(\underline{\rho}) = \sum_\alpha I'_\alpha \underline{X}_\alpha(\underline{\rho}), \quad \underline{X}_\alpha(\underline{\rho}) = \sum_n x_{\alpha n}\underline{R}_n(\underline{\rho}) \tag{4}$$

so that the "irrotational" basis is defined by the coefficient matrix $[X] = [x_{\alpha n}]$ that specifies the (contractive) passage from the rooftops to the $\underline{X}$ basis. On the other hand, we represent the charge q as

$$\nabla_t \cdot \underline{J}' = q(\underline{\rho}) = \sum_a C_a q_a(\underline{\rho}) \tag{5}$$

For zero-degree rooftops, the charge has to be piecewise constant, and this is the regularity required for the q_a: they will be a combination of the pulse functions $p_a(\underline{\rho})$, that are vanishing on all but one cell,

$$q_a(\underline{\rho}) = \sum_b q_{ab} p_a(\underline{\rho}) \tag{6}$$

In the following, we will call N the number of rooftops and N_c the number of cells in the mesh. Note that the total charge has to be zero in a dynamic problem, so that there are only $N_c - 1$ terms in the sum (5).

Substituting now (4) into (5) and testing it onto the charge space, we find

$$[\Pi]\,[C] = ([Q]\,[X]^{\mathrm{T}})\,[I'], \quad Q_{an} = \langle q_a, \nabla_t \cdot \underline{R}_n \rangle, \quad \Pi_{ab} = \langle q_a, q_b \rangle \tag{7}$$

where $[C]$ and $[I']$ are the column vectors of the homonimous coefficients in (4) and (5).

Equation (7) expresses the relationship between the charge and the irrotational current in the adopted discretization, and therefore imposes the condition on the basis functions $\underline{X}_\alpha$ that the product matrix $([Q]\,[X]^{\mathrm{T}})$ be non-singular: all convenient choices for the coeffcients $[X]$ that lead to a non-singular $([Q]\,[X]^{\mathrm{T}}$ are valid choices for the definition of the irrotational basis functions.

It is important to note how the above approach leads to the definition of the solenoidal and irrotational basis functions in terms of operations on *scalar* functions with specified regularity, that opens up interesting prespectives for choosing a more efficient structure. In particular, this approach seems an ideal candidate for the generation of wavelet basis functions.

Lastly, we note that inversion of (7) allows to use the charge directly in stead of the irrotational current; in this case $([Q]\,[X]^{\mathrm{T}})^{-1}$ represents the discretized form of the irrotational part of Helmholtz representation of $\underline{J}$, completing, in a weak sense, the representation of $\underline{J}$ in terms of two scalar functions (the solenoidal generating function M and the charge q). However, this option so far has not been found to be numerically efficient.

2.1 The star choice

The most natural choice for q_a are the pulse functions $p_a(\underline{\rho})$ themselves, for which $[\Pi]$ is identity. Excluding any cell from the count (because of zero total charge), there are clearly $N_c - 1$ degrees of freeedom for the charge, and the matrix $[Q]$ thus obtained has rank $N_c - 1$; therefore if one takes $[X]^{\mathrm{T}} = [Q]^{\mathrm{T}}$ the product matrix $([Q]\,[X]^{\mathrm{T}}) = [X]\,[X]^{\mathrm{T}}$ is non-singular. This choice turns out to be the choice that leads to irrotational basis functions called "stars" [2, 5] because of their form, shown in Fig. 1.

2.2 Semi-Wavelet irrotational functions

As an example of a more flexible basis generation, we now turn our attention to a particular choice of $\underline{X}$ that leads to wavelet-like properties. Namely, we begin by numbering all cells in a consecutive fashion ("snake-like" numbering), so that each cell with index i is contiguous with those having index $i-1$ and $i+1$, and the first being continguous with the last; note that this is possible because a div-conforming mesh implies loop-representability, and that in turn cells must be grouped by four (on a rectangular mesh). This generates a full-cyclic one-dimensional domain s, over which conventional wavelets can be employed. Since the functions are piecewise-constant, the use of the Haar basis is obvious; in this case, the only scaling function is everywhere constant, and is excluded to represent zero total charge. The coefficient matrix $[q]$ is made up by the coefficients of the wavelets $\psi_{jk}(s)$ that are the standard "doublet" detail functions. The irrotational functions can be derived from the same consideration as before, i.e. taking $[X] = [Q]$; they appear wavelet-like, in that they have decreasing domains, and are essentially translatable. Their use will be shown in Sec. 2.2. The definition of wavelets for the solenoidal scalar functions is a bit more complicated by their higher regularity, being nonetheless standard with the one-dimensional reduction explained above. We will not address this aspect here.

3 Summary of numerical regularization

For a metalization occupying a region Σ the EFIE for the unknown surface currents $\underline{J}$ on the conductors can be written in terms of an integral operator $\mathcal{Z}$,

$$\begin{aligned} \mathcal{Z}\underline{J}(\underline{\rho}) &= -\underline{E}_0, \quad \forall \underline{\rho} \in I\!R^2; \\ \mathcal{Z}\underline{J}(\underline{\rho}) &\equiv \chi_\Sigma(\underline{\rho}) \int_\Sigma d^2\underline{\rho}'\, \underline{\underline{G}}(\underline{\rho} - \underline{\rho}') \cdot \underline{J}(\underline{\rho}') \end{aligned} \tag{8}$$

where $\chi_\Sigma(\underline{\rho}) = 1$ on Σ and zero elsewhere, $\underline{E}_0$ is the driving term (tangential "incident" field times χ_Σ), and the kernel $\underline{\underline{G}}$ is the usual dyadic Green's function of the grounded layered medium (without conductors), stratified along the $\hat{z}$ axis.

The leading TM term of $\underline{\underline{G}}$ corresponds to an operator $(1/j\omega\epsilon_0)\mathcal{S}^{\mathrm{TM}}$ with a strongly singular kernel in the space domain, that behaves like $1/|\underline{\rho} - \underline{\rho}'|^3$ as $|\underline{\rho} - \underline{\rho}'| \to 0$; the leading TE term $\mathcal{W}^{\mathrm{TE}}$ has a a weak spatial singularity, i.e. with kernels of the kind $1/|\underline{\rho} - \underline{\rho}'|$. The term $\mathcal{S}$ accounts for the near electrostatic field, and $\mathcal{W}^{\mathrm{TE}}$ for the near magnetostatic field.

It can be easily recognized that the purely solenoidal functions $\underline{J}''$, are the nullspace of the TM operator. Therefore, the strongly singular part (usually employed in the two-dimensional case) is not enough for regularization purposes in the vector, three-dimensional case, and we must first separate the solenoidal subspace, following the procedures of Sec. 2.

Having separated the space spanned by the rooftops into the two parts spanned by loops and stars, it turns out [1] that testing the EFIE (8) separately onto these two sets is equivalent to stating that the EFIE splits into two problems for the scalar function M in (1), and for the non-solenoidal part $\underline{J}'$. These two problems have the form

$$\begin{aligned} \left(\frac{1}{j\omega\epsilon_0}\mathcal{S} + \mathcal{Z}_r^{\mathrm{TM}} + \mathcal{Z}^{\mathrm{TB}}\right)\underline{J}' + T^{\mathrm{MB}}M &= -\underline{E}_0' \\ \left(\frac{1}{j\omega\mu_0}\mathcal{B} + \mathcal{Y}\right)M + T^{\mathrm{BM}}\underline{J}' &= -\frac{1}{j\omega\mu_0}\nabla_t\cdot(\hat{z}\times\underline{E}_0) \end{aligned} \tag{9}$$

with $\mathcal{Z}_r^{\mathrm{TB}} \equiv \mathcal{Z}^{\mathrm{TB}} - j\omega\mu_0 W^{\mathrm{TB}}$, The explicit expressions of the kernels of the above operators can be found in [1].

The kernel B of the singular operator $\mathcal{B}$ accounts for the asymptotic, magnetostatic behaviour, and can be shown to express the same singular behaviour as the TM singular (electrostatic) part $\mathcal{S}$, and as $\mathcal{S}$ is frequency-independent. The remaining kernels are all regular or weakly singular (integrable).

If one knew the inverse of singular operators $\mathcal{S}^{-1}$ and $\mathcal{B}^{-1}$, the regularization of the two coupled equations (9) would obtain by left multiplying the first one by $\mathcal{S}^{-1}$ and the second one times $\mathcal{B}^{-1}$, generating second-kind equations. Although $\mathcal{S}^{-1}$ and $\mathcal{B}^{-1}$ are not expressible in closed form, the procedure becomes numerically explicit on choosing two sets $\{\underline{J}_n'\}$ and $\{M_n\}$ of basis functions for $\underline{J}'$ and M, and then applying the MoM to the formal equations obtained by pre-multiplication of (9) as said above; $\underline{J}_n'$ and M_n can be any functions that can be approximated by stars and pyramids.

In fact, note that by doing so the identity operators are represented by the projection matrices $[P']$ and $[P'']$ with entries $P'_{mn} = \langle \underline{J}'_m, \underline{J}'_n\rangle$ and $P''_{mn} = \langle M_m, M_n\rangle$: these matrices appear as key elements in defining in what space the operations are actually performed. The discretized version of the regularized equations is equivalent to the algebraic linear system obtained from the non-regularized (9) by using the basis functions $\underline{J}'_n$ and M_n, *but* testing (9) onto the functions $\underline{\vartheta}_n$ and Θ_n defined by the linear systems

$$\begin{aligned} \langle \underline{\vartheta}_m, \mathcal{S}\underline{J}'_n\rangle &= P'_{mn} = \langle \underline{J}'_m, \underline{J}'_n\rangle, \\ \langle \Theta_m, \mathcal{B}M_n\rangle &= P''_{mn} = \langle M_m, M_n\rangle \end{aligned} \tag{10}$$

As an example, if one chooses $\underline{J}'_n = \underline{X}_n$ and $M_n = \Lambda_n$, and letting $\underline{\vartheta}_n = \sum_\alpha \theta_{n\alpha}\underline{X}_\alpha$, $\Theta_n = \sum_\alpha \Theta_{n\alpha}\Lambda_\alpha$, one gets, from (10), the linear systems:

$$\sum_\alpha \theta_{m\alpha}\langle \underline{X}_\alpha, \mathcal{S}\underline{X}_n\rangle = \langle \underline{X}_m, \underline{X}_n\rangle, \qquad \sum_\alpha \Theta_{m\alpha}\langle \Lambda_\alpha, \mathcal{B}\Lambda_n\rangle = \langle \Lambda_m, \Lambda_n\rangle \tag{11}$$

3.1 Example of semi-wavelet application

We remark that from the example above, the regularization technique appears as a preconditioning procedure. In particular, the choice of the θ functions in (11) as basis functions corresponds to a direct pre-multiplicative conditioning, efficient if one finds sparse (conditioning) matrices $[\theta]$, $[\Theta]$. Note that both matrices representing singular operators can be defined and calculated directly in terms of the scalar functions, so that a possible wavelet representation directly impacts on these matrices. As an example, we employ the semiwavelet basis in Sec. 2.2 for the charge; for a square patch with seven rooftop nodes along each direction ($N_c = 64$), we get a matrix $[S]$ (not shown) with the "pine-tree" like structure typical of wavelet appplication. The matrix $[\theta]$ of the coefficients of the regularizing functions $\underline{\vartheta}$ in the standard star basis of Sec.2.1 (and shown in Fig. 1) is the sparse matrix shown in Fig. 2: clipping it columnwise to a relative threshold value of 1% the relative error (in two-norm) is 5%, yielding a matrix with a filling index of 15%. This makes it a good candidate for sparse conditioning.

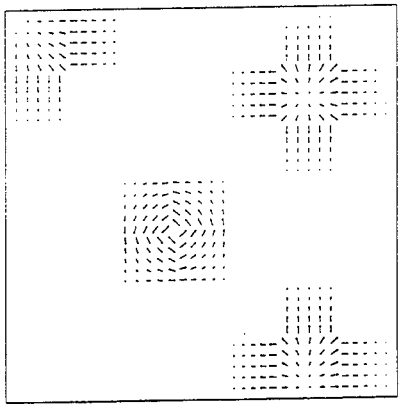

Figure 1. *Loop and star basis functions.*

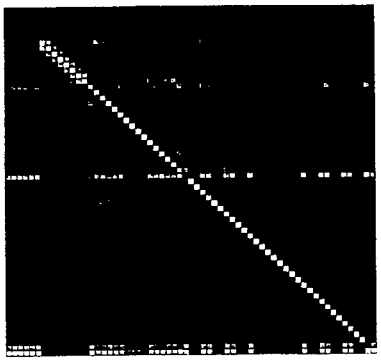

Figure 2. *Magnitude plot of the matrix of the coefficients [θ]; here black is zero, white is max.*

4 Use of Static Modes

A convenient approach for the analysis of printed antennas, as discussed in [1, 4, 7], is to employ as basis functions the eigenfunctions of the singular (static) operators $\mathcal{S}$ and $\mathcal{B}$, to be called $\underline{\varphi}$ and Ψ, respectively. The functions Ψ generate solenoidal vector functions $\underline{\psi}$ via application of (1), and the $\underline{\varphi}$ are weakly irrotational. They are entire-domain basis functions and appear to be a generalization of the TM and TE modes of a magnetic-wall cavity to arbitrary geometries, and to the presence of singular edge terms; therefore, they will be termed TE and TM in the following. The eigensystems can be computed by standard MoM discretization of the corresponding operator eigenproblems, giving rise to generalized algebraic eigenproblems; note that the dimensions of the two (separated) problems are N_S and N_L, and that $N_L \sim N_S \sim N/2$, and that the matrices are positive-definite and real symmetric, thus allowing the use of efficient iterative solvers. Note also, that in many practical cases, like patch arrays, the structure lends itself to decomposition into smaller parts, and one has to solve several smaller eigenproblems, or only a few (like in the array case) if many elements of the structure are identical.

It can be shown [1] that problem is intrinsiacally numerically robust and stable, and it is apparent that this choice is a regularizing one. Also, it can be shown that the TE eigenfunctions have both the edge singular behavior for the current components parallel and normal to the edge, while the TM have only a singular normal derivative of the current normal to the edge. This implies that the TE terms will be coupled in to satisfy the edge condition.

Note that since the singular edge behavior is essentially due to the static part, the use of the static eigenfunctions allows direct incorporation of the edge singularity into the solution. In the proposed technique, we employ the static modes as basis functions for the representation of the current on the radiating element(s), using instead conventional rooftop functions on the feed structure (typically, a microstrip line or network).

In using these static modes as basis functions for the full-wave analysis of printed antennas, two issues are of primary importance for the (numerical) efficiency of the solution: the selection of the "right" terms, and the inclusion, into the static modes, of the relevant features of the discontinuity between the feed structure and the radiating element. This latter aspect will lead us to the introduction of functions that will be termed "attachment" modes, since they are analogous to the terms usually called with this name in the literature; in fact, they appear as an extension of these latter.

Mode selection. It appears that TE modes present singular currents parallel to the edges, while TM only show singular normal current derivative (singular charge). As a result, the selection is made difficult by the fact

that the TE and TM functions are strongly coupled at the boundary, and that TE-TM interaction involves curl terms, that "scramble" the spectral ordering. Since TM are the dominant modes in realistic patch antennas, the selection is guided by them. The choice of static modes is based on the matrix obtained with the asymptotic part of the coupling terms. First, the number of TM modes necessary for obtaining a specific accuracy, at a given frequency, is established. Then the modes coupled to the above selected TM are found, looking at the asymptotic coupling matrices. The validity of the criterion has been checked verifying what static modes contribute to the solution obtained with subdomain functions: it appears that the most contributing terms are actually those selected according to the described scheme.

A second option [7] is based on the analysis of the range of the static TM-TE coupling operator: since the TM eigenfunctions are used to represent its domain, we want to "optimize" the number of solenoidal functions necessary to represent the image of each TM mode, that means to optimize the projections of these basis functions onto the TM images. A possible choice consists in taking an orthonormal basis, so that the projection matrix results almost triangular and the matrix associated to $\mathcal{B}$ almost-diagonal. These TE functions are called "Orthogonal-Range Solenoidal" functions, or ORS for short. These ORS functions are significantly non zero only in correspondance to the edges, providing the singular behavior missing in TM modes but not altering sensibly the current in the inner part of the patch, that is well represented by TM terms.

Attachment modes. While the above discussion essentially refers to "free-standing" patches, it is possible to include, in the structure for which the modes are calculated, a portion of the feed structure. Most of the modes of this "extended" patch are essentially undistinguishable from the modes of the patch free-standing patch, and will be called "intrinsic" modes of the radiating element in the following. On the other hand, a number (generally small) of modes present some differences with respect to those of the patch alone: these different modes constitute the *attachment* modes, that efficiently represent the storage of static-dominated reactive energy near the feed discontinuity.

4.1 Application

The concepts outlined above are now clarified by the application to a specific structure, composed by a rectangular patch with recessed monolithic microstrip-line feed, as shown in Fig. 3, printed on a dielectric substrate of heigth $h = 1.57\,\text{mm}$ and $\epsilon_r = 2.2$; the patch outer dimensions are $46{,}7\,\text{mm} \times 32.9\,\text{mm}$, the recess depth and width are $16.67\,\text{mm}$ and $4.7\,\text{mm}$, and the line width is $4.7\,\text{mm}$. Note that structure is clearly non-separable.

The current on the patch is discretized by rectangular rooftops along $\hat{x}$ and $\hat{y}$ directions, for a total of 435 rooftops, further grouped in 198 loops and 237 stars. The rooftop solution has been checked against independent results [8], and will be taken as reference.

The "free-standing" patch is taken to be the part up to the junction with the recessed line, and a portion of the feed line is included in the structure for which the static modes are computed, and subsequently removed. Some of the modes present a peak in the vicinity of the feed-patch discontinuity; these modes constitute the feed-dependent attachment modes, the first being reported in Fig 4, "cut" to conform to the choice for the "free-standing" patch. Other modes, like the dominant TM, TE and ORS shown in Figs. 5, 6, 7, respectively, are indistinguishable from those of the free-standing patch: they are the "intrinsic" modes, independent from the feed configuration, and the related impedance matrix entries are not modified when the feed line changes.

The performances of the static modes emerge from the plot of Fig. 8, in which the input reflection coefficient obtained with static modes is reported, together the reference rooftop solution. It emerges that twelve modes are sufficient to correctly represent the solution, and that the convergence is uniform.

For a reference case with 24 modes, the total CPU time (including base change) for one frequency point is less than five seconds, against 28.5 s taken for the (LU) solution with rooftops; the mode generation frequency-independent overhead CPU time is below 10 s, thus proving the potentials of the method.

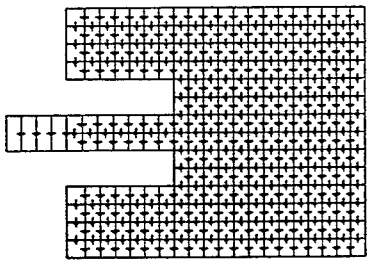

Figure 3. *Geometry of the recess-fed patch.*

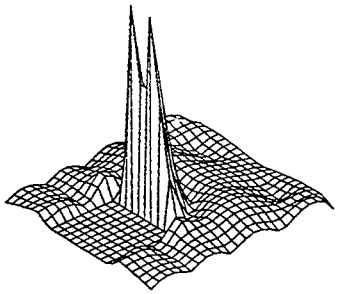

Figure 4. *Magnitude plot of the first TM attachment mode.*

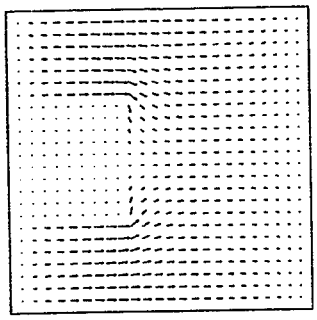

Figure 5. *Arrow plot of the dominant TM intrinsic mode.*

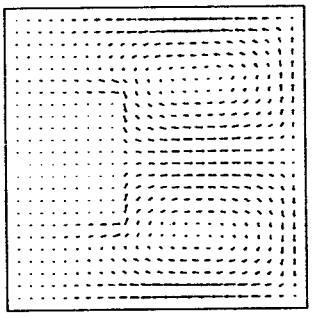

Figure 6. *Arrow plot of the dominant TE intrinsic mode.*

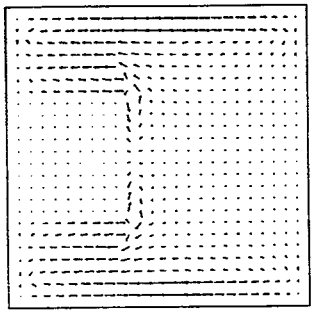

Figure 7. *Arrow plot of the dominant ORS intrinsic mode.*

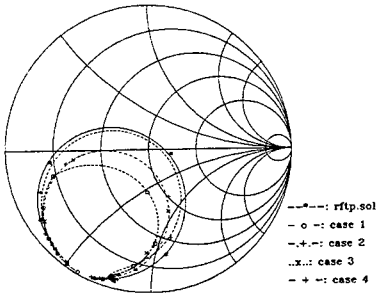

Figure 8. *Input reflection coefficient for 5, 7, 9, 12 modes, and as obtained with rooftop solution.*

References

[1] G. Vecchi, L. Matekovits, P. Pirinoli, M. Orefice, "A numerical regularization of the EFIE for three-dimensional planar structures in layered media", to appear on *Int. J. of Microwave and Millimeter-Wave Computer-Aided Engineering*, Spec. Issue on "Frequency domain modeling of planar circuits and antennas".

[2] Wilton, D.R., "Topological considerations in surface patch and volume cell modelling of electromagnetic scatters", *1983 URSI International Symposium on Electromagnetic Theory*, Santiago de Compostela (E), pp. 65–68, Aug. 1983.

[3] D.Sun, J.Manges, X.Yuan, Z.Cendes, Spurious modes in Finite-Element Methods, *IEEE Antennas and Propagation Magazine*, vol. 37. no. 5, October 1995; pp. 12-24.

[4] G. Vecchi, P. Pirinoli, L. Matekovits, M. Orefice, "Hybrid spectral-spatial method for the analysis of printed antennas", *Radio Science*, Vol. 31, no. 5, pp. 1263-1270, Sep.-Oct. 1996; Special Issue on Computational Electromagnetics.

[5] Lim, J.S. and S.M. Rao, "A novel technique to calculate the electromagnetic scattering in the entire frequency range", *Asia-Pacific Microwave Conference Proc.*, Taejon (Korea), pp. 345-348, Oct. 1995.

[6] G. Vecchi, M. Orefice, C. Vai, P. Pirinoli, "Spectral analysis of printed circular rings for use with a general coupling", *Proc. of International Conference on Electromagnetics in Advanced Applications*, Torino (I), Sept. 1995, pp. 23-26.

[7] G. Vecchi, L. Matekovits, P. Pirinoli, M. Orefice, "Application of numerical regularization options to the Integral-Equation analysis of printed antennas", to appear on *IEEE Trans. Antennas and Propag.*, Special issue on "Advanced numerical techniques", March 1997.

[8] G. Splitt, "Improved numerical strategies for rigorous analysis of microstrip antennas", *Proc. 23rd Europ. Microwave Conf.*, pp. 354-356; Madrid (E), Sept. 1993.

WAVELET-BASED MODELING OF WIRE ANTENNAS AND SCATTERERS

Kazem F. Sabet†, Linda P.B. Katehi‡, and Kamal Sarabandi‡

† EMAG Technologies, Inc., 2901 Hubbard Rd., Suite E-116, Ann Arbor, MI 48105
‡ Department of Electrical Engineering and Computer Science, The University of Michigan, Ann Arbor, MI 48109-2122

I. INTRODUCTION

During the past two decades, the method of moments (MoM) has widely been used to analyze wire antennas and scatterers in open boundary environments. This has led to the emergence of popular computer codes such as NEC and its derivatives, that are able to treat complex wire structures with a high degree of accuracy. These codes are of great practical interest not only due to the importance of wire antennas as popular radiating elements, but because many sophisticated structures can be modeled using wiregrid equivalents amenable to the thin-wire approximation.

Although theoretically, the conventional MoM-based codes offer infinite capability in view of complexity of the wire structure, they have a limited scope in practice due to the fullness of the moment matrices. As the number of unknowns increases, so does the size of the linear system to be solved. The treatment of very large linear systems often poses three major computational problems: 1) memory usage for the storage of the system, 2) computation time for inversion of the system, and 3) stability of the numerical solution. The storage dilemma has traditionally become the bottleneck of conventional integral-based numerical techniques. Computational speed is another major issue which quickly turns into a limiting factor when solving full linear systems. This is especially critical if the full-wave simulation is part of the antenna design process. In the meantime, large densely populated moment matrices suffer from poor condition numbers. This fact leads to some adverse consequences which directly affect the computational cost. For instance, to achieve numerical stability, it is often necessary to maintain a very high degree of precision in the numerical evaluation of the moment integrals. Poor condition numbers also deteriorate the convergence of iterative linear system solvers.

In the past couple of years, the newly developed theory of multiresolution analysis has opened new horizons for the application of the method of moments by making it possible to generate highly sparse linear systems [1]-[5]. It has been demonstrated the due to the cancellation property of wavelet basis functions, a wavelet-dominated moment matrix can be thresholded to render it highly sparse. The error introduced to the system solution due to the thresholding process can be kept minimum depending on the thresholding scheme and the threshold level. Retaining a high level of accuracy in spite of discarding a sizable number of negligible matrix elements is a clear indication of the improvement in the system condition number. This phenomenon originates from the mathematical properties of the multiresolution analysis leading to matrix regularization. An interesting and unique feature of multiresolution expansions is the fast wavelet transform (FWT), which establishes a recursive relationship among the basis functions at different resolution levels. When implemented, this algorithm can improve the computational efficiency by speeding up the matrix fill process in many cases. The wavelet concepts have been applied successfully to the modeling of printed microwave circuits and antennas, dielectric structures and scattering from two-dimensional geometries, to name a few [2]-[5].

In this paper, we investigate the modeling of wire antennas and scatteres using intervallic multiresoultion expansions. It will be shown how the fast wavelet transform (FWT) can easily transform a high resolution grid into a multiresolution wavelet-dominated grid. The radiation and scattering properties of various wire antenna arrays will be examined, and the major improvements in the computational speed, memory usage and numerical convergence of the solution will be discussed.

II. FORMULATION

The formulation of the wire structure in this paper is based on the generalized Pocklington integral equation. In order to avoid the source singularity of the free space Green's function, the thin wire approximation is utilized. In other words, filament currents are assumed at the center of the conducting wires for MoM expansion, and the testing procedure is carried out on the surface of the wire. Denoting by G(**r**|**r**′) the free space Green's function:

$$G(\mathbf{r}|\mathbf{r}') = \frac{e^{-jk_0|\mathbf{r}-\mathbf{r}'|}}{4\pi|\mathbf{r}-\mathbf{r}'|}, \tag{1}$$

one can then write:

$$\hat{\mathbf{s}}.\mathbf{E}^{\mathrm{i}}(\mathbf{r}) = jk_0 Z_0 \int_C \left[\hat{\mathbf{s}}.\hat{\mathbf{s}}' I(s') + \frac{1}{{k_0}^2} \frac{\partial I(s')}{\partial s'} \frac{\partial}{\partial s} \right] G(\mathbf{r}|\mathbf{r}') ds', \tag{2}$$

where k_0 and Z_0 are the free space propagation constant and characteristic impedance, respectively, the space curve C traces the wire geometry, and $\hat{\mathbf{s}}$ is the unit tangent vector along this curve. In the method of moments, the unknown wire current I(s) is discretized using a suitable set of basis functions. Pulse, triangular, cubic spline and piecewise sinusoidal functions are some of the popular choices for the expansion basis. The discretized integral equation is then tested using a suitable testing scheme to produce a system of linear algebraic equations. Point matching and Galerkin's technique are the most widely used testing schemes in MoM implementations. Once the linear system is solved and the unknown expansion coefficients are determined, the current distribution on the wires and near-field and far-field characteristics of the antenna such as input impedance, radiation pattern, beamwidth, etc., can easily be calculated.

In a wavelet-based MoM implementation of the wire structure, the unknown wire current is expanded in a multiresolution basis, containing scaling functions at the lowest resolution level plus wavelets at this and higher resolution levels up the desired degree of accuracy. We utilize an intervallic multiresolution analysis (MRA) which is naturally defined over a bounded interval. Specifically, the B-spline intervallic MRA is used in this paper. Intervallic expansions contain inner basis functions identical to the regular multiresolution expansions plus special edge basis functions which satisfy the desired boundary conditions of the problem. Thus, a typical intervallic multiresolution expansion looks like the following form:

$$\begin{aligned} f(x) \approx & \sum_{n=1}^{N_\varphi^{(i)}(m_0)} c_n^{(i)} \phi(2^{m_0}x - n) + \sum_{l=1}^{N_\varphi^{(e)}} c_l^{(e)} \phi_l^{(e)}(2^{m_0}x) \\ & + \sum_{m=m_0}^{M-1} \left[\sum_{n=1}^{N_w^{(i)}(m)} d_{m,n}^{(i)} \psi(2^m x - n) + \sum_{l=1}^{N_w^{(e)}} d_l^{(e)} \psi_l^{(e)}(2^m x) \right], \end{aligned} \tag{3}$$

where M is the highest resolution level required in the problem, $\phi(x)$ and $\psi(x)$ are the inner scaling function and wavelet, respectively, and $\phi_l^{(e)}(x)$ and $\psi_l^{(e)}(x)$ are the edge scaling functions and wavelets, respectively. Note that the number of shifted inner scaling functions and shifted inner wavelets depend on the resolution levels, while the number of edge scaling functions and edge wavelets are independent of the resolution levels and depend only on the order of the intervallic MRA. According to the definition of the MRA, the expansion of equation (3) is equivalent to the following high-resolution expansion made up of only scaling functions:

$$f(x) \approx \sum_{n=1}^{N_\phi^{(i)}(M)} c_n^{(i)} \phi(2^M x - n) + \sum_{l=1}^{N_\phi^{(e)}} c_l^{(e)} \phi_l^{(e)}(2^M x). \tag{4}$$

The equivalence between the two expansions (3) and (4) is a very important feature of the MRA, which indeed forms the basis of the fast wavelet transform (FWT). Using this algorithm, it suffices to compute the expansion coefficients of only scaling functions at the highest resolution level. The expansion coefficients of all other basis functions at lower resolutions can be computed recursively from these high resolution scaling coefficients. The aforementioned equivalence can be exploited in a very useful way. Suppose that the wire structure has already been discretized using a high resolution grid, and the impedance matrix has been computed at this resolution level. A MoM expansion composed of only high resolution scaling functions leads to a full moment matrix as discussed before. However, using the FWT, one can transform the high resolution scaling-only grid into a wavelet-dominated multiresolution grid at lower resolution levels. It is now the cancellation effect of the wavelet basis functions which will render the impedance matrix highly sparse. It should be noted that such transformation does not involve the tedious numerical integration task, which is carried out once during the computation of the original high resolution scaling-only matrix.

III. RESULTS AND CONCLUSION

The formulation developed in the previous section has been applied to a variety of wire antennas and scatterers including dipole arrays, loops, helical and other curvilinear antennas, etc. In all cases, the geometry of the antenna or scatterer is parameterized appropriately, and integral equation (2) is implemented. The structure is first discretized using a high resolution scaling grid. At this stage, one can employ the symmetries of the geometry, if any, to speed up the matrix fill process. Then using the fast wavelet transform, a wavelet-dominated multiresolution grid is generated, and its associated impedance matrix is computed from the original matrix through simple digital filters. The resulting sparse matrices are thresholded by discarding all the elements whose magnitudes fall below a certain threshold level with respect to the largest matrix element. Two or three resolution levels are typically used for the multiresolution grid, and normally threshold levels as high as 0.1% yield very satisfactory results. This is mostly due to the fact that the singularity of the kernel of the integral equations is avoided through the use of the thin wire approximation. Another important feature of this formulation is that in large structures which involve a large number of basis functions spread all over the geometry, it is possible to identify all negligible interactions which will be subject to thresholding. This pre-sorting is based on the premise that the Green's function is a function of only the distance between the source and observation points and not their absolute positions. A major acceleration of the matrix fill process can thus be achieved by skipping the numerical evaluation of the trivial interactions. After the impedance matrix has been rendered sparse due to thresholding, a sparse-based preconditioned biconjugate gradient (BiCG) solver is employed to solve the linear system. Due to the improvement of the system condition number, the BiCG solver usually converges very fast.

As an example, here we consider a two-element and a three-element array of full-wavelength dipoles of identical feeds with half wavelength separations. Figs. 1 and 2 show the current distribution on the center dipole of these arrays. The effect of the thresholding process and the threshold level on the current distribution have been explored in these figure. It is seen that at a threshold level of 0.1%, the current distribution is almost indistinguishable from the original distribution with no thresholding applied at all. While, the resulting wavelet-dominated matrices exhibit sparsity levels of 83% and 94.3% for the two- and three-element arrays, respectively. In particular, when the far-field characteristics are of primary interest, the threshold level can be raised to a much higher value without affecting the radiation pattern drastically. More numerical results including different types of wire antennas will be presented at the conference.

REFERENCES

[1] B.Z. Steinberg and Y. Leviatan, "On the use of wavelet expansions in the method of moments," *IEEE Trans. Antennas Propagat.*, vol. AP-41, pp. 610-619, May 1993.

[2] K.F. Sabet, "Wavelet-based modeling of microwave circuits and antennas," in *MTT-S Workshop Digest: Applications of Wavelets to Electromagnetics*, Organizers: L.P.B. Katehi and H. Ling, June 1996.

[3] K.F. Sabet and L.P.B. Katehi, "Analysis of integrated millimeter-wave and submillimeter-wave waveguides using orthonormal wavelet expansions," *IEEE Trans. Microwave Theory Tech.*, vol. MTT-42, pp. 2412-2422, Dec. 1994.

[4] K.F. Sabet, J-C. Cheng and L.P.B. Katehi, "Efficient wavelet-based modeling of printed circuit antennas and arrays," submitted for publication.

[5] K.F. Sabet, K. Sarabandi and D. Zahn, "A Study of scattering from curvilinear surfaces based on wavelet concepts," in *URSI Radio Science Meeting*, July 1996.

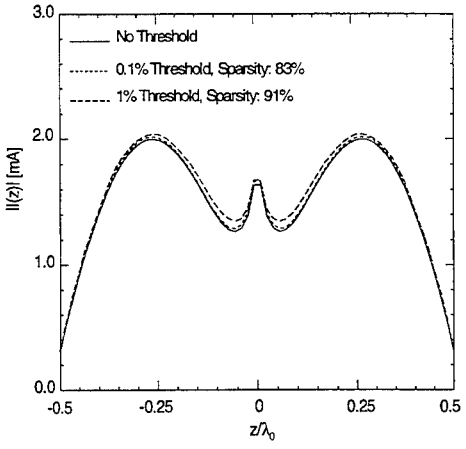

Fig. 1. Current distribution on a two-element dipole array (l=λ, s= λ/2).

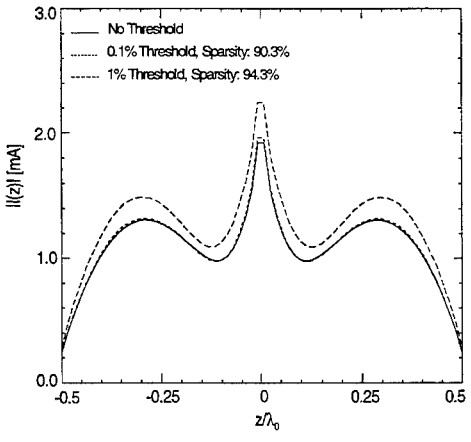

Fig. 2. Current distribution on the center dipole of a three-element dipole array (l=λ, s= λ/2).

AUTHOR INDEX